Nucleic acid-mediated fluorescence activation and chromophore assembly

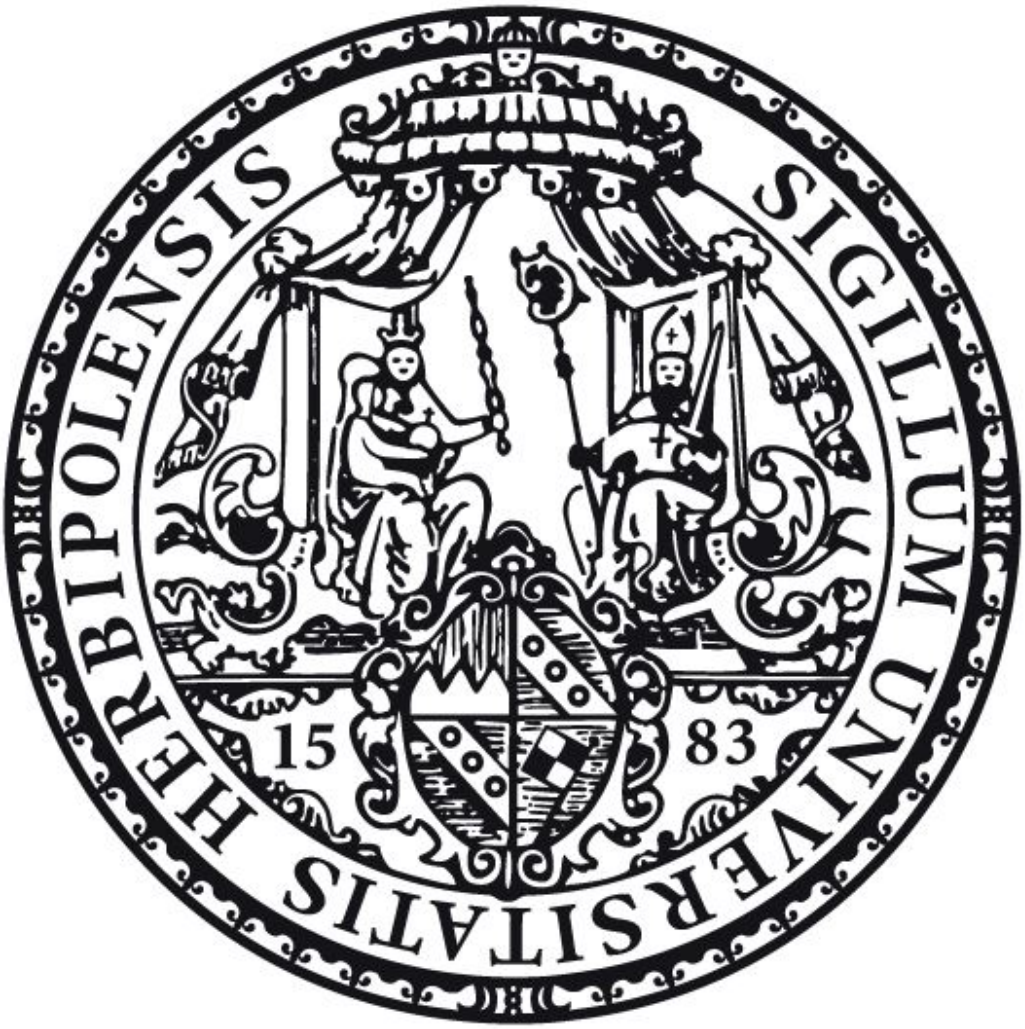

Dissertation zur Erlangung des naturwissenschaftlichen Doktorgrades der Julius-Maximilians-Universität Würzburg

vorgelegt von

Julia Dietzsch

aus Kassel

Würzburg 2022

Eingereicht bei der Fakultät für Chemie und Pharmazie am

11.01.2022

Gutachter der schriftlichen Arbeit

1. Gutachter: Prof. Dr. Claudia Höbartner

2. Gutachter: Prof. Dr. Frank Würthner

Prüfer des öffentlichen Promotionskolloquiums

1. Prüfer: Prof. Dr. Claudia Höbartner

2. Prüfer: Prof. Dr. Frank Würthner

3. Prüfer: Prof. Dr. Agnieszka Nowak-Król

Datum des öffentlichen Promotionskolloquiums

25.02.2022

Doktorurkunde ausgehändigt am

Für meinen Großvater

Mein besonderer Dank gebührt meiner Doktormutter Prof. Dr. Claudia Höbartner für die Möglichkeit, ein so interessantes Thema in ihrer Arbeitsgruppe bearbeiten zu dürfen, die Unterstützung und das mir entgegengebrachte Vertrauen. Ich weiß es sehr zu schätzen, dass du jederzeit für Diskussionen offen warst und mir bei allen Problemen und Fragestellungen mit Rat und Tat zu Seite gestanden hast.

Außerdem möchte ich Herrn Prof. Dr. Frank Würthner für die zahlreichen Anregungen im Rahmen unserer Subgroup-Meetings sowie die Übernahme des Zweitgutachtens danken.

Dr. Vladimir Stepanenko danke ich für die Messung und Auswertung der AFM-Bilder, Dr. David Bialas und Florian Seitz für das Durchführen theoretischer Rechnungen, Bernhard Mahlmeister für die Hilfe am CPL-Gerät und Dr. Irene Bessi für die Messung von Oligo-NMR-Proben.

Mein Dank gilt auch den Mitarbeitern der NMR- und Massenabteilung, vor allem Michaela Schraut und Sebastian Mayer für das Messen meiner zahlreichen Oligoproben. Außerdem möchte ich mich bei Manuela Michel, Ann-Kathrin Lenz und Celine Pfeuffer sowie Doris Feineis für die Unterstützung im Laboralltag bedanken.

Danke an alle Mitglieder der Arbeitsgruppe Höbartner für die angenehme Arbeitsatmosphäre, die gemeinsamen Unternehmungen und die interessanten Gespräche. Ein besonderer Dank gilt meinen Bürokollegen Hermann und Carina für die unterhaltsame Zeit, sowie Taku, Ai und Florian für die gemeinsamen Boulderabende und Carina, Manu, Celine und Ann-Kathrin für die lustigen Mittagspausen. Ohne euch wäre meine Zeit in der Arbeitsgruppe nur halb so schön gewesen! Und danke, Carina, für die seelische und moralische Unterstützung und alles andere!

Vielen Dank auch an meine Praktikanten und Bachelorstudenten Katja, Dominik, Nadine, Felix, Theresa, Jonas, Julian, Johannes und Maria. Es hat Spaß gemacht, mit euch zu arbeiten!

Außerdem danke ich Carina, Hermann, Irene und vor allem Florian für das Korrekturlesen dieser Arbeit.

Von ganzem Herzen möchte ich mich bei meiner Familie, meinen Freunden und vor allem bei Florian bedanken, die mich immer unterstützt und mein Leben bereichert haben.

List of publications

Research articles

J. Dietzsch, D. Bialas, J. Bandorf, F. Würthner, C. Höbartner "Tuning Exciton Coupling of Merocyanine Nucleoside Dimers by RNA, DNA and GNA Double Helix Conformations", *Angew. Chem. Int. Ed.* **2022**, doi: 10.1002/anie.202116783, *Angew. Chem.* **2022**, doi: 10.1002/angew.202116783, first published: December 22nd, 2021.

Reviews

J. Dietzsch, D. Feineis, C. Höbartner "Chemoselective labeling and site-specific mapping of 5-formylcytosine as a cellular nucleic acid modification", *FEBS Lett.* **2018**, *592*, 2032–2047.

Contents

Abstract

Nucleic acids are not only one of the most important classes of macromolecules in biochemistry but also constitute a promising platform for the defined spatial arrangement of small functional molecules such as chromophores. Thanks to their precise structural organization by directional polar and hydrophobic interactions, oligonucleotides can be exploited as suitable templates for covalent and non-covalent multichromophore assemblies with predictable spectroscopic properties. Although a plethora of such chromophoric systems has been reported, most of the chromophore designs exclusively rely on hydrophobic interchromophore stacking interactions but do not take advantage of the intrinsic complementary base pairing capability of canonical nucleobases. However, not only further stabilization of the oligonucleotide secondary structure, but also a more straightforward interpretation of observed spectroscopic effects might be achieved under consideration of these polar interactions.

To expand the toolbox of artificial emissive nucleobase analogs and to adress the additional effect introduced by the mentioned polar interactions, several barbituric acid merocyanine (BAM) chromophores were designed in the course of this thesis. The barbituric acid acceptor moiety of these artificial nucleobase surrogates resembles the Watson-Crick site of natural thymine (T) and uracil (U), facilitating base pair formation with adenine (A). By attachment of differently constituted aromatic donors such as indolenines and benzothiazoles to this acceptor unit, merocyanines with tunable spectroscopic properties were readily accessed.

Since the constitution of the nucleic acid backbone has a significant impact on the structural parameters and thermodynamic stability of the resulting duplex, the synthesized BAM chromophores were converted into phosphoramidite building blocks for covalent assembly within different oligonucleotide scaffolds. Therefore, besides the synthesis of the respective DNA and RNA nucleosides, BAM chromophores were prepared as glycol nucleic acid (GNA) building blocks with an acyclic backbone. Incorporation of the generated artificial nucleosides was successfully achieved by solid phase synthesis, leading to over 100 modified oligonucleotide single strands.

Upon hybridization of the modified oligonucleotides with their respective complementary counterstrands a multitude of short duplex structures containing up to ten BAM chromophores in

different mutual arrangements was obtained. Detailed analysis of these multichromophoric systems by a variety of spectroscopic methods revealed the presence of dipolarly coupled merocyanine dimers and multimers evoked by the unusual *syn*-conformation of the BAM chromophores which was further supported by oligonucleotide NMR spectra. The distinct spectroscopic and thermodynamic properties of BAM modified nucleic acids showed to be strongly dependent on the chromophore orientation toward each other and the backbone conformation. These characteristics were exploited for various applications such as FRET pair formation and the use as internal fluorescent stop nucleotides in polymerase chain reaction (PCR) experiments. The formation of higher-order aggregates observed by atomic force microscopy (AFM) implies future applications of these new oligonucleotide-chromophore systems as light-harvesting materials or in DNA nanotechnology.

Besides extensive studies on the covalent assembly of chromophores templated by oligonucleotides also non-covalent nucleic acid-chromophore complexes are currently a broad field of research. Among these, fluorogenic RNA aptamers are of special interest with the most versatile ones based on derivatives of hydroxybenzylidene imidazolone (HBI), a chromophore found in the naturally occurring green fluorescent protein (GFP). However, many reported aptamer-ligand systems suffer from severe drawbacks such as unspecific binding, a strong tendency toward photoisomerization and poor cell permeability, just to mention a few. Therefore, new HBI-derived chromophores with an expanded conjugated system and an additional exocyclic amino group for an enhanced binding affinity were synthesized and characterized in complex with the reported Chili aptamer. Among these, structurally new fluorogenes with strong fluorescence activation upon binding to the aptamer were identified and further analyzed. These hold great promise for further derivatization and application as color-switching sensor devices for example.

Zusammenfassung

Nukleinsäuren sind nicht nur eine der wichtigsten Klassen biochemisch relevanter Makromoleküle, sondern stellen auch eine vielversprechende Plattform für die definierte räumliche Organisation kleiner funktioneller Moleküle, wie beispielsweise Chromophore, dar. Oligonukleotide können aufgrund ihrer präzise gegliederten Struktur, die durch gerichtete polare und hydrophobe Wechselwirkungen hervorgerufen wird, als nützliche Template für die mehrfache kovalente und nicht-kovalente Anordnung von Chromophoren zu Aggregaten mit vorhersagbaren spektroskopischen Eigenschaften genutzt werden. Obwohl eine Vielzahl solcher Chromophorsysteme bereits in der Literatur beschrieben ist, basieren die meisten Chromophordesigns nur auf hydrophoben Wechselwirkungen zwischen den einzelnen Chromophoren und lassen die intrinsische Fähigkeit kanonischer Nukleobasen, komplementäre Basenpaare zu bilden, außen vor. Allerdings liegt es auf der Hand, dass die Berücksichtigung dieser polaren Wechselwirkungen nicht nur zu einer Stabilisierung der Oligonukleotid-Sekundärstruktur führen kann, sondern auch die Interpretation spektroskopischer Effekte vereinfacht.

Um das bekannte Spektrum emittierender Nukleobasen-Analoga zu erweitern und den zusätzlichen Einfluss dieser polaren Wechselwirkungen auszunutzen, wurden im Zuge dieser Arbeit verschiedene, strukturell unterschiedliche Barbitursäure-Merocyanin-Chromophore (BAM) entworfen. Die Barbitursäure-Akzeptoreinheit dieser künstlichen Nukleobasensurrogate ähnelt der Watson-Crick-Basenpaarungsseite der natürlichen T- und U-Nukleobasen und soll somit die Basenpaarung mit Adenosin ermöglichen. Durch die Kombination dieses Akzeptors mit unterschiedlich aufgebauten aromatischen Donoreinheiten, wie zum Beispiel Indol und Benzothiazol, konnten Merocyanine mit interessanten spektroskopischen Eigenschaften erhalten werden.

Da die Konstitution des Nukleinsäurerückgrates einen starken Einfluss auf die Strukturparameter und die thermodynamische Stabilität der resultierenden Duplexstruktur hat, wurden die synthetisierten BAM-Chromophore in Phosphoramiditbausteine für die kovalente Assemblierung innerhalb verschiedener Oligonukleotidsysteme umgewandelt. Neben der Synthese entsprechender DNA- und RNA-Nukleotide wurden die BAM-Chromophore auch als Glykolnukleinsäure-Bausteine (GNA) mit einem azyklischen Rückgrat hergestellt. Der erfolgreiche Einbau der erhaltenen künstlichen Nukleoside konnte durch Festphasensynthese erreicht werden, wobei über 100 modifizierte Einzelstränge erhalten werden konnten.

Die Hybridisierung der künstlichen Oligonukleotid-Einzelstränge mit ihren jeweiligen Gegensträngen führte zu einer Vielzahl kurzer Duplexstrukturen mit bis zu zehn BAM-Chromophoren in unterschiedlicher Anordnung. Mithilfe verschiedenster spektroskopischer Methoden konnte ein Einblick in die strukturelle Organisation der Merocyanine innerhalb dieser Systeme erhalten werden, wobei sich die Bildung dipolar-gekoppelter Merocyanin-Dimere und -Multimere zeigte. Die hierfür erforderliche ungewöhnliche *syn*-Konformation der BAM-Chromophore wurde weiterhin durch Oligonukleotid-NMR bestätigt. Erstaunlicherweise wiesen die spektroskopischen und thermodynamischen Eigenschaften BAM-modifizierter Nukleinsäuren eine starke Abhängigkeit von der Chromophororientierung und der Konformation des Rückgrates auf. Dieser Effekt konnte für verschiedene Anwendungen wie die Bildung von FRET-Paaren und die Verwendung als internes fluoreszentes Stop-Nukleotid in Polymerasekettenreaktionen ausgenutzt werden. Mithilfe von Rasterkraftmikroskopie wurde außerdem die Bildung von Aggregaten höherer Ordnung beobachtet, was eine zukünftige Verwendung dieser neuen Oligonukleotid-Chromophor-Systeme als Materialien für Lichtsammelkomplexe oder für die DNA-Nanotechnologie denkbar macht.

Ein weiteres großes Forschungsfeld neben kovalenten Chromophoranordnungen mit Oligonukleotiden als Templat sind nicht-kovalente Nukleinsäure-Chromophorkomplexe. Insbesondere fluorogene RNA-Aptamere sind hier von großer Bedeutung wobei die wichtigsten auf der Fluoreszenzaktivierung von Derivaten 4-Hydroxybenzylidenimidazolon-Fluorophors (HBI), dem Chromophor des natürlich vorkommenden grün fluoreszierenden Proteins (GFP), beruhen. Allerdings zeigen viele der berichteten Aptamer-Ligand-Systeme signifikante Nachteile wie unter anderem unspezifische Bindung, eine starke Tendenz zu Photoisomerisierung oder ineffiziente Zellpermeabilität. Deshalb wurden im Zuge dieser Arbeit neue, von HBI abgeleitete Chromophore mit einem vergrößerten konjugierten π-System und einer zusätzlichen exozyklischen Aminogruppe für eine erhöhte Bindungsaffinität synthetisiert und im Komplex mit dem bekannten Chili-Aptamer untersucht. Einige dieser strukturell neuen Chromophore zeigten einen starken Anstieg der Emission bei Bindung an dieses Aptamer und wurden daher weiter charakterisiert. Sie stellen eine vielversprechende Möglichkeit für weitere Derivatisierung und die zukünftige Anwendung beispielsweise als schaltbare Aptamer-basierte Fluoreszenzsensoren dar.

Chapter 1

Objectives and outline

The capability of natural organisms to control the flow of electronic energy by photosynthetic light-harvesting systems is essential for nearly all domains of life. Within these light-harvesting systems the required chromophores are organized with nanoscale presicion in electronically coupled networks to ensure effective excitation and following exciton transport. The underlaying systems are in most cases proteins which provide a defined chromophore environment with specified distances and orientations for electrodynamic coupling interactions. However, due to their structural complexity and the interplay of multiple electronic couplings, proteins are poor synthetic model systems to further investigate these complex dynamical properties. Instead, oligonucleotide scaffolds for templated assembly of chromophores have recently been developed as functional designer materials since their reliable base pairing pattern ensures the formation of precise nanoarchitectures. The organization of chromophores within oligonucleotide scaffolds leads to inter-chromophore coupling with programmable excitonic states and a defined spatial organization, providing access to highly predictable nanostructures. This sequence-specific positioning of fluorophores can be used to design dimers and multimers with distinct electronic characteristics and gives rise to the development of light-harvesting antennae and materials for molecular electronics with properties dependent on intermolecular electronic interactions. However, multichromophore assemblies based on DNA were for a long time limited to single dimers. Recently, the self-assembly of chromophores on a DNA platform leading to non-covalent as well as covalent higher-order aggregates with long-distance exciton transport has been described. With these defined structures, new materials with pronounced electronic properties and geometries for a wide range of applications can be accessed.

The aim of this thesis was to generate fluorescent multichromophore systems based on differently substituted merocyanine chromophores with spectroscopic properties influenced by the helix environment. To achieve this goal, several merocyanine chromophores constituted of a barbituric acid moiety as electronic acceptor and a heteroaromatic core as electronic donor were generated as phosphoramidite building blocks for DNA, RNA and GNA synthesis (Figure 1.1). The chromophores were designed to be able to base pair with an opposite adenine in the duplex *via* the barbituric acid amide function, giving rise to defined helical chromophore arrangements for double and multiple modified duplex structures. By the attachment of

different functional groups to the aromatic ring system, the spectroscopic properties of the incorporated chromophores could be further tuned. In addition, the three diverse backbones were supposed to provide access to distinct helical scaffolds, which were supposed to lead to various modes of chromophore aggregation due to directional electrostatic, dipolar, π-stacking and hydrogen bonding interactions between the merocyanine chromophores. The hereby obtained oligonucleotide systems were meant to be characterized by spectroscopic and thermodynamic measurements, providing insight into chromophore aggregate constitution and stability. By engaging additional methods such as molecular dynamics (MD) simulations and NMR studies on nucleic acids the influence of the chromophores' orientation towards each other as well as of the sequence context on the spectroscopic characteristics of formed fluorophore assemblies should be revealed. With these results in hand, different applications based on these new molecular synthons such as fluorescent labeling oligonucleotides and the use as environment-sensitive probe were to be developed.

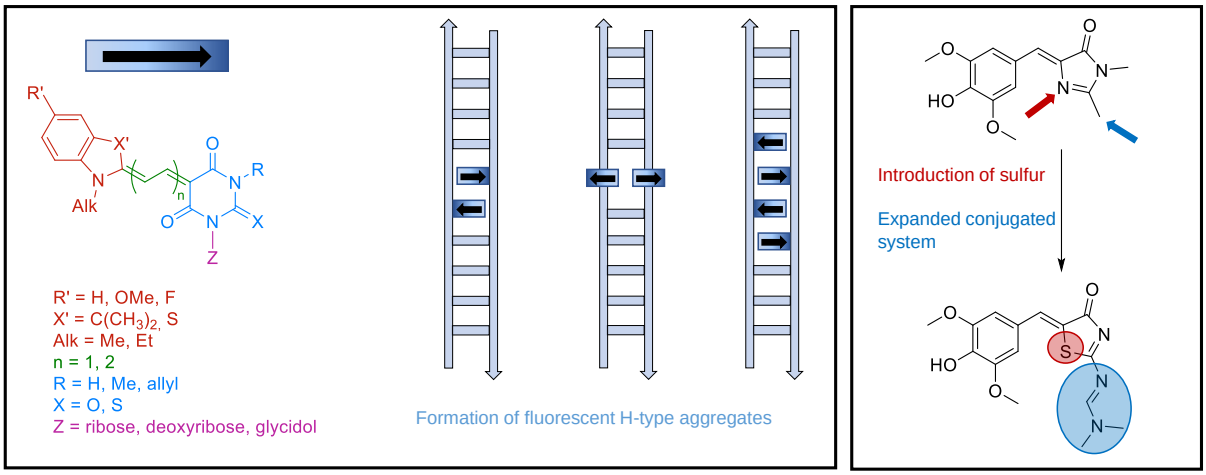

Figure 1.1: General structure of the merocyanine building blocks synthesized in the course of this thesis and schematic representation of double and multiple modified oligonucleotide duplex structures with the direction of the merocyanine's dipole moment shown as black arrow (left). In the second part of this thesis, novel HBI-derived chromophores with an additional amino group, an expanded conjugated system and a sulfur-containing five-membered ring were synthesized and characterized (right).

Besides a number of natural organisms with the ability to harvest light by photosynthesis, other creatures exhibit remarkable photophysical properties upon excitation with light of a specific wavelength. The most important organisms among these comprise fluorescent proteins, for example the widely-known jellyfish *Aequorea victoria* comprising the green fluorescent protein (GFP). This luminescent protein is of outstanding importance for biological and medicinal research since it can be used as potent biomarker for all kinds of cell labeling applications. Using the GFP chromophore as a model, a large number of similar but structurally simpler fluorogenic systems based on artificial RNA aptamers have been designed during the last decade. One example of these fluorogenic RNA systems is the Chili aptamer which shows the best fluorescence enhancement with positively charged chromophores having an expanded ring system compared

to the natural GFP chromophore. Within this thesis, new GFP-derived chromophores with an additional amino group and an enlarged aromatic system were synthesized and characterized with regard to their fluorescence properties in complex with the Chili aptamer. Furthermore, the potential of these newly developed fluorogenic systems for further applications and for the design of environment-sensitive switchable aptamer-fluorogene systems was supposed to be tested.

Chapter 2 gives an introduction into the theoretical background of artificial backbone modifications and differently constituted fluorescent nucleosides. In addition, reported covalent and non-covalent multichromophore assemblies as well as fluorogenic RNA aptamers are discussed.

In **Chapter 3** the results obtained in the course of this thesis are summarized and discussed with regard to similar systems published in literature. This chapter is divided into two main parts; the first section deals with the synthesis of RNA, DNA and GNA merocyanine building blocks, their incorporation into oligonucleotides and the spectroscopic and thermodynamic characterization of the hereby obtained single, double and multiple modified oligonucleotide duplex structures. Data interpretation is further supported by MD simulations and NMR analyses and possible applications of the designed fluorescent systems, such as FRET pair formation, are described. In addition, DNA-GNA hybrid structures containing up to ten consecutively incorporated merocyanine building blocks are discussed. The spectroscopic features of these systems are compared with regard to the number and orientation of the chromophores toward each other.
In the second part of Chapter 3, the synthesis and spectroscopic characterization of novel HBI-derived chromophores with additional amino groups and expanded aromatic systems is described.

Chapter 4 summarizes the advances achieved in the course of this thesis and provides an outlook on the design of future DNA-based multichromophoric systems and fluorogenic aptamers as well as potential applications for these emissive systems.

Finally, **Chapter 5** and **Chapter 6** contain all experimental procedures and the appendix with supporting data, respectively.

Chapter 2

Theoretical background

2.1 Nucleic acids: general features

Nucleic acids are besides proteins the most important macromolecules for the continuity of life since they do not only carry the whole genetic information of an organism but do also contain instructions for cell functions and serve as blueprints for proteins. The two types of nucleic acids which are most abundant in nature are deoxyribonucleic acid (DNA) and ribonucleic acid (RNA). DNA consists of the four canonical nucleosides deoxyadenosine (dA), deoxycytidine (dC), deoxyguanosine (dG) and thymidine (T) while RNA is based on the corresponding ribonucleosides A, C, G and uridine (U). The nucleobases are each linked *via* a glycosidic bond between the N1 nitrogen of pyrimidines or the N9 nitrogen of purines to the C1 carbon of the respective ribose sugar moiety in *anti*-conformation to form nucleosides. Individual nucleosides are connected by phosphodiester bonds between the 5'-hydroxyl of one sugar moiety and the 3'-hydroxyl of the next one, forming linear single strands. Since the four nucleobases are capable of forming Watson-Crick base pairs by hydrogen bonding between A and T or C and G, two complementary single strands can hybridize to form an antiparallel duplex which is stabilized by these and other non-covalent interactions such as stacking and hydrophobic interactions (Figure 2.1).

The double-helical structure for DNA was first proposed by James Watson, Francis Crick and Rosalind Franklin based on X-ray diffraction data and published in 1953; it is until today one of the most important discoveries to understand the function and properties of nucleic acids.[1,2] In its naturally occurring form, DNA is constituted as a right-handed B-form helix with a major and a minor groove caused by the different distances of the 1'-carbons of two opposing nucleotides from the helical axis. Within this structure, the base paired nucleobases are located in the more hydrophobic helix center while the phosphate backbone points outwards and is in contact with the aqueous surrounding.[3] The length, sequence composition and stability of DNA are almost not restricted which makes this nucleic acid suitable for short- and also long-time storage of genetic information.

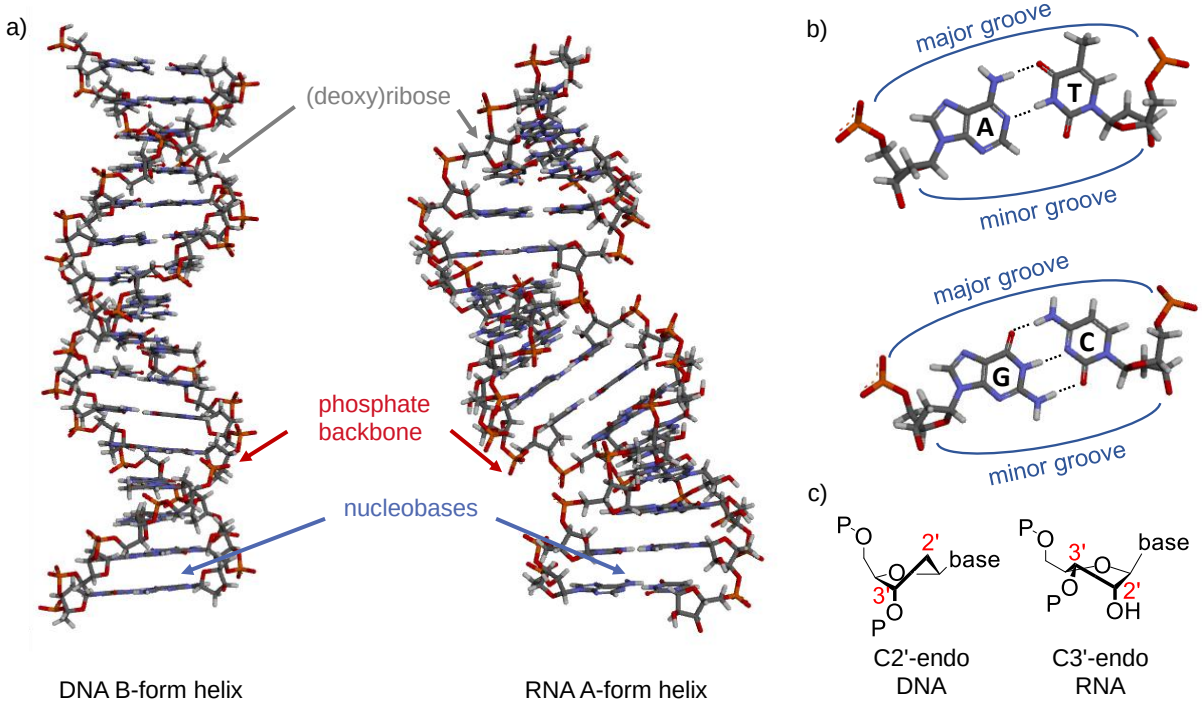

Figure 2.1: a) Structural model for a DNA B-form helix (left) and an RNA A-form helix (right). b) Hydrogen bonding pattern for the A-T (top) and the G-C base pair (bottom) in DNA. c) Conformations of the ribose sugar pucker: the C2'-endo conformation is found in the B-form helix while the C3'-endo conformation exists in the A-form helix.

Although the monomeric building blocks of DNA and RNA are fairly similar with respect to their molecular structure, the two corresponding oligonucleotides show significantly different features in their polymeric constitutions (Figure 2.1a). This is due to the different conformations of the ribose sugar puckers which are in C3'-endo conformation for RNA while in C2'-endo conformation for DNA (Figure 2.1c).[4] The different sugar pucker of the A-from RNA helix induces the formation of a deep and narrow major groove and a shallow and wide minor groove which increases the accessibility for degrading enzymes and leads, along with the additional 2'-hydroxy group, to a higher reactivity and lower duplex stability compared to DNA. The distinct helical parameters of A- and B-form duplex structures will be discussed in greater detail in section 2.2.1.

Similar to DNA, most biologically active RNAs comprise self-complementary sequences that allow parts of the RNA to fold and pair with itself.[5] However, these highly organized helical structures are in general not as long as for DNA, but are rather collections of shorter helices, giving rise to a great variety of three-dimensional shapes. Apart from the widely known protein-coding messenger RNA (mRNA), which plays a vital role in protein biosynthesis and other regulatory processes,[6,7] around 97% of the eukaryotic RNA is non-coding (ncRNA).[8,9] The most abundant and functionally important regulatory ncRNAs include transfer RNA (tRNA) and ribosomal RNA (rRNA) as well as shorter structures such as microRNA (miRNA), small interfering RNA (siRNA), small nucleolar RNA (snoRNA) and small nuclear

RNA (snRNA) and long ncRNAs such as the X-inactive specific transcript (Xist) and HOX transcript antisense RNA (HOTAIR). However, the exact number of ncRNAs within the human genome is still not known and the biological functions of many of the already discovered ones remain to be elucidated although there is some evidence that ncRNAs might contribute to the development of for example cancer[10] and Alzheimer's.[11,12]

Apart from the four canonical nucleobases, RNA, especially tRNA, often contains modified nucleobases mostly formed by methylation reactions, such as 5-methyl cytidine (m^5C). Since RNA influences a multitude of posttranscriptional processes in the cell, the position and chemical structure of these modifications build up a second layer of information which is important to understand the origin of different diseases for example.[6,13,14] The structure and impact of such simple nucleobase modifications on biochemical processes will be discussed in the next section, along with the role of hypermodified nucleobases and artificial backbone modifications.

2.2 Modified nucleosides

Besides the role of nucleic acids as carrier of the hereditary information of an organism they also have a variety of regulatory functions. While DNA and RNA are based on almost the same four-letter alphabet and share a similar Watson-Crick base pairing pattern, RNA is responsible for additional cellular tasks within the regulation of gene expression, protein synthesis and intracellular communication which requires further structural and functional properties.[15] To achieve these, nature has introduced a plethora of modifications, mainly at the nucleobase level, leading to an increased stability of local topologies and assisting the formation of complex secondary and tertiary structures.

Thanks to their easily programmable nature, nucleic acids are not only the material of choice to store genetic information in living organisms but have been exploited for various sophisticated applications such as the construction of nanomaterials or the use in therapeutics and diagnostics, just to mention a few. However, some intrinsic properties of native nucleic acids limit their functional scope and in particular their potential for therapeutic *in vivo* applications. The major deficiencies in this regard are the susceptibility of nucleic acids towards degradation by endo- and exo-nucleases, their contribution to immune activation and their poor pharmacokinetic properties.[16,17] Therefore, the effectiveness of treatments with nucleic acid based therapeutics largely depends on chemical modifications designed to increase the resilience of nucleic acids to nuclease cleavage and to ensure their stability in the circulation, the localization to the target tissue and efficient intracellular delivery. To achieve this and to overcome the stability drawbacks of natural nucleosides, modifications at several different positions such as the sugar moiety, the heterocyclic nucleobase and the phosphate group have been reported (Figure 2.2).[16,18] Based on these modification sites, numerous synthetic nucleic acid analogs

were developed, giving rise to various structures divergent from native oligonucleotides with unnatural physicochemical properties.

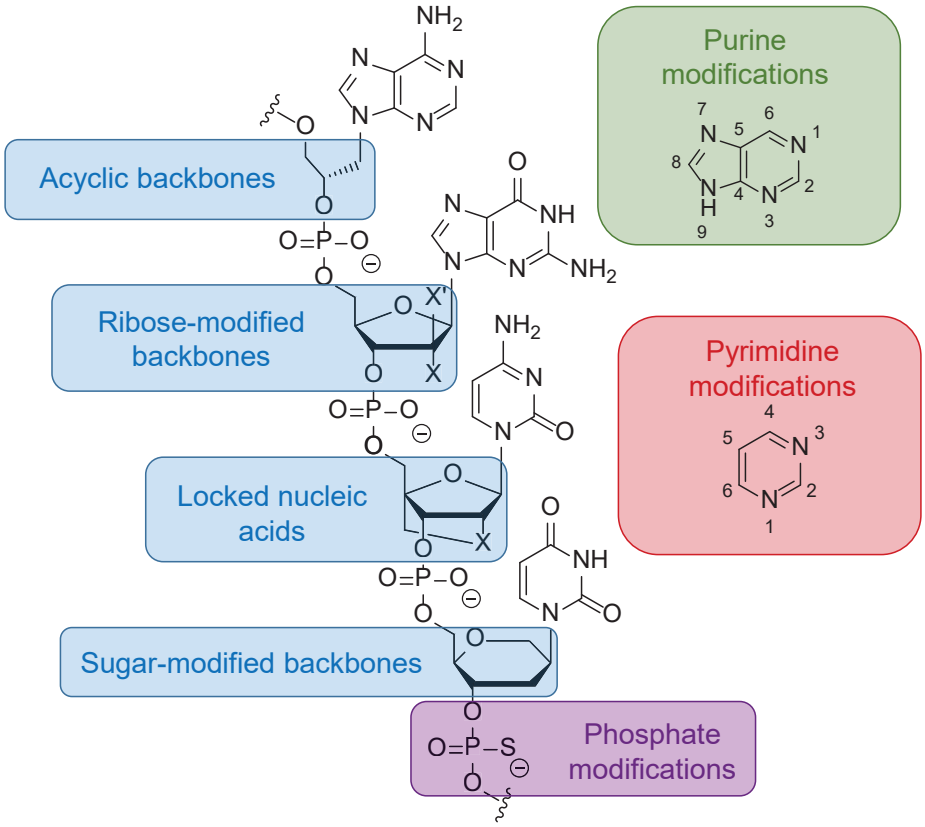

Figure 2.2: Oligonucleotides can be modified at multiple positions, for example the sugar moieties (blue), the phosphate backbone (purple) and the purine and pyrimidine nucleobases (green and red).[16]

In this section, a short overview of reported backbone modifications including sugar- and ribose-modified ones is given, with the main focus on acyclic backbones. In addition, the most important naturally occurring purine and pyrimidine nucleobase modifications along with artificially accessible ones for different applications are discussed whereas phosphodiester modifications such as phosphorthioates will not be taken into account.

2.2.1 Backbone modifications: Xeno Nucleic Acids (XNA)

Nucleic acids with sugar moieties different from the naturally occurring (deoxy)ribose were mainly developed to overcome their high *in vivo* instability and are called xeno nucleic acids (XNAs).[19–22] While for these systems the Watson-Crick base pairing ability is retained, the profound structural changes of the sugar backbone can at the same time lead to different local geometries and have an impact on the oligonucleotide flexibility. These new features give rise to many *in vivo* and *in vitro* applications, including the use of XNA as fluorogenic probes[23] for the analysis of nucleic acid-protein interactions, the generation of higher-order

nanostructures[24] and the potential to generate artificial life.[22] Besides minor modifications of the furanose ring, this five-membered ribose can be replaced by a six-membered ring and by bi-, tri- or even acylic sugar backbone analogs which are still able to crosspair with naturally composed nucleic acids. Some prominent examples for these ribose- and sugar-modified XNAs are to be discussed briefly in the next part of this thesis. In the structures shown in the following figures, the backbones are colored in blue while the nucleobase linkage to these backbones are marked red.

2.2.1.1 Ribose- and sugar-modified backbones

Among all XNAs, the ones with ribose-modified backbones can be considered most similar to native nucleic acids since the natural five-membered ring structure of the ribose backbone is maintained while only the ring substituents or the substitution pattern is altered. Most of the described nucleosides for this family can be incorporated into oligonucleotides by solid phase synthesis or triphosphate chemistry, which gives rise to a broad range of possible oligonucleotide sequences.

One of the most widely known XNAs is certatinly the ribose-modified 2'-methyl-RNA (2'-*O*-Me-RNA, Figure 2.3a), which is a posttranscriptional modification of mRNA in functionally essential regions of the ribosome and spliceosome. 2'-*O*-Me-RNA has for example been incorporated into chimeric antisense oligonucleotides (ASOs), which are applied for the treatment of various diseases to increase the stability and binding affinity to the target.[25]

Another famous ribose-modified XNA is the 2'-epimer of RNA, arabino nucleic acid (ANA),[26] along with its structurally derived 2'-fluoro-ANA (FANA, Figure 2.3a).[27] These two nucleic acid analogs are capable of forming duplex structures with a complementary RNA strand, presumably due to the DNA-like C2'-endo conformation of their sugar pucker, which makes them favorable systems to study and control gene expression in cells and organisms.[28]

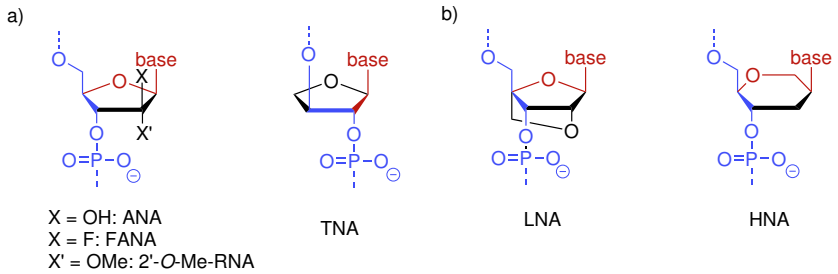

Figure 2.3: Nucleic acid analogs with ribose and sugar-modified backbones. Shown are the general structures of arabino and 2'-fluoro arabino nucleic acid (ANA and FANA), 2'-methyl-RNA (2'-*O*-Me-RNA), threose nucleic acid (TNA) in a), and of locked nucleic acid (LNA) and hexitol nucleic acid (HNA) in b).

The alteration of the number of sugar carbons gives rise to other groups of ribose modifications, for example threose nucleic acid (TNA), which comprises a tetrose rather than a hexose moiety. TNA is constituted of 3'-2'-linked α-L-threofuranosyl building blocks and undergoes efficient base pairing with DNA as well as RNA.[29] These properties make TNA useful for therapeutic and diagnostic applications, for example through *in vitro* selection of TNA aptamers.[30]

2.2.1.2 Locked nucleic acids and sugar-modified backbones

The sugar moiety of nucleic acids cannot only be altered by attaching additional substituents to the ribose ring or changing the connectivity but also by introducing bridges, expanding the ring size or incorporating additional heteroatoms. The synthesis of the phosphoramidite building blocks required for solid phase synthesis is more challenging for these XNA variants.

An example for this type of modifications is locked nucleic acid (LNA, Figure 2.3b), also called bridged nucleic acid (BNA), with a bridge between the 2'- and 4'-carbon of the ribose, fixing the C3'-endo sugar pucker which leads to structurally rigid oligonucleotides with pre-organized backbones and increased hybridization properties.[31,32] Due to excellent single-mismatch discrimination and good nuclease resistance, LNAs can be used for applications in antigene and antisense technology. The properties of LNA can be tuned further by changing the length of the bridge and attaching functional groups, leading to a variety of different structures.[33]
The best studied XNA among the ones with an expanded sugar ring size is hexitol nucleic acid (HNA, Figure 2.3b); it can strongly and selectively bind to RNA single strands, forming an antiparallel A-type heteroduplex with reduced conformational flexibility.[34,35] HNA is resistant toward degradation by RNaseH and has therefore been used for the development of highly stable aptamers.[35,36]

2.2.1.3 Acyclic backbones

Although the scaffold structure of XNAs with acyclic backbones does not mimic the natural oligonucleotide structure, many of these artificial systems have been described and extensively reviewed.[19,20,22,33,37] The advantage of building blocks with acyclic backbones is their facile synthesis and the high nuclease resistance of the resulting oligonucleotides, making them valuable tools for a variety of biological applications including fluorescent probes[38] and nucleic-acid based drugs.[39]

Peptide Nucleic Acid (PNA)
The probably most famous nucleic acid analogs with an acyclic backbone is the peptide nucleic acid (PNA, Figure 2.4 left) which can be synthesized using standard peptide chemistry. PNA is built from repeating *N*-(2-aminoethyl)-glycine units linked by peptide bonds with the

nucleobases attached by methylcarbonyl linkers.[40] Since the peptide backbone is uncharged, the overall electrostatic repulsion within the system is considerably lowered compared to native nucleic acid structures.[41] The advantage of this neutral backbone is its ability to strongly bind to RNA and ssDNA, while a drawback is its enhanced hydrophobic character which requires coupling to a cell penetrating peptide for cell delivery. Therefore, numerous strategies to improve the physicochemical properties, cellular permeability and duplex stability of PNA have been described as well as the incorporation of different ligands or other functional molecules for diverse applications.[42] Since PNA is, as many other XNAs, not recognized by enzymes it has evolved into an excellent biomolecular instrument, also due to the mentioned structural improvements.[43]

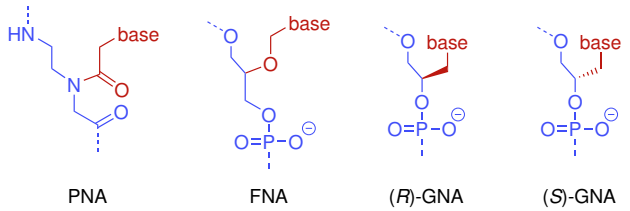

Figure 2.4: Nucleic acid analogs with acyclic backbones: peptide nucleic acid (PNA, left), flexible nucleic acid (FNA, middle) and (*R*)- and (*S*)-glycol nucleic acid (GNA, right).

Flexible Nucleic Acid (FNA)

Flexible Nucleic Acids (FNAs) were first proposed by Orgel *et al.* as primitive nucleic acid analogs (Figure 2.4).[44] FNA lacks the 2'-carbon, which on the one hand increases the flexibility but on the other hand leads to severe destabilization of FNA-comprising duplex structures. Thus, an FNA-T_{12} oligonucleotide does not form any stable structure with dA_{12}, rA_{12} or FNA-A_{12} and the melting temperature of an FNA-A_{12}/T_{12} duplex is reduced by 15 °C compared to a native dA_{12}/dT_{12} duplex. Despite these drawbacks some applications for FNA have been reported, for example its use as a primer for Klenow extension or as a template for nonenzymatic oligomerization of RNA.[45,46] However, FNA is much less commonly used compared to other nucleic acid analogs with acyclic backbones such as PNA or GNA.

Glycol nucleic acid (GNA)

Glycol or glycerol nucleic acid (GNA) is a non-natural, simplified nucleic acid structure which was developed by Meggers and coworkers (Figure 2.4 right).[47] It is composed of canonical nucleobases linked to glycol units, which are themselves connected by phosphodiester bonds. The phosphoramidites for this XNA are easily accessible by an epoxide ring-opening reaction of (*R*)- or (*S*)-glycidol with the respective nucleobase and the introduction of required protection groups.

GNA was the first described example of acyclic XNA to form highly stable homoduplexes with a by 24 °C increased melting temperature compared to a DNA-15mer homoduplex. This remar-

kable thermodynamic stability is explained by the strong preorganization of the single stranded GNA and the favorable stacking between two neighboring base pairs.[48] However, GNA is not compatible with DNA or RNA, since partial modification of these native nucleic acids with GNA building blocks leads to strong destabilization and cross-hybridization is impossible.[49] These characteristics are due to the difference in the helical parameters for a GNA double helix compared to A- and B-form duplexes.[50]

Table 2.1: Graphic representation of helical parameters (top left) and model structures with top and side view of (*S*)-GNA, B-DNA and A-DNA duplexes (top right) and comparison of the corresponding helical parameters (bottom). The structure for the (*S*)-GNA duplex was derived from PDB 2JJA.

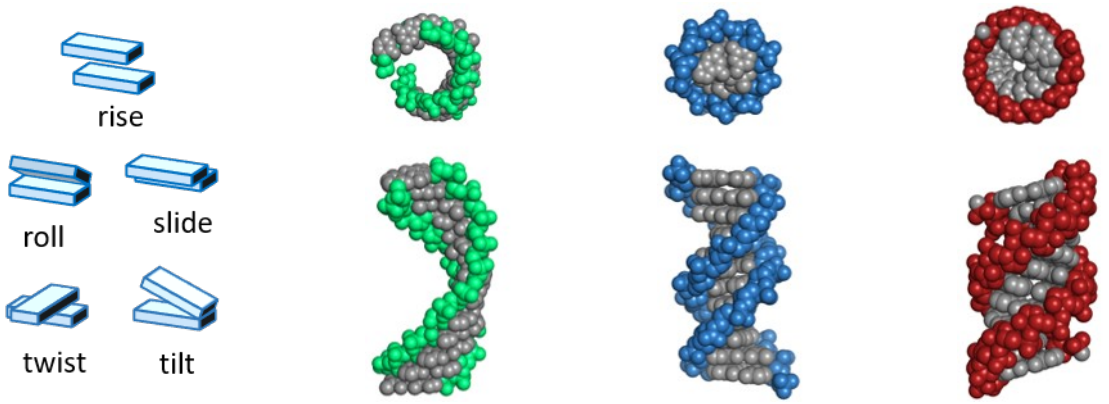

	(*S*)-GNA	**B-DNA**	**A-DNA**
helical sense	right	right	right
residues per turn	16	10	12
helical pitch (Å)	60	34	34
helical rise (Å)	3.8	3.4	2.9
tilt (°)	0	-0.1	0.1
roll (°)	-2.8	0.6	8.0
twist (°)	22.9	36	31
slide (Å)	-3.4	0.2	-1.5
P-P distance (Å)	5.4	7.0	5.9

Table 2.1 shows model structures for right-handed double helices of (*S*)-GNA, B-DNA and A-DNA as well as the corresponding parameters. The most obvious difference between these three structures is the large helical pitch of 60 Å with 16 base pairs per turn and a comparably large helical rise for the GNA duplex. Additionally, the position and orientation of the nucleobases in the three dimensional structure described by the tilt, roll and twist values varies among the three structures. Due to the large backbone-base inclination of 42–50° compared

to 0° for B-DNA the slide between neighboring base pairs is significantly elevated in GNA and similar to the HNA duplex, leading to a lack of intrastrand stacking but instead to extensive interstrand stacking interactions which contribute to the high duplex stability. As expected for the simplified GNA backbone, rather short intrastrand phosphorous-phosphorous distances are observed.[51–53]

The combination of all of these parameters leads to the formation of a helical ribbon-like structure for GNA with a large groove corresponding to the DNA minor groove and a convex surface which resembles the DNA major groove.

GNA has been utilized for different applications such as the formation of stable nanostructures or as a scaffold for chromophore clusters.[54,55] Furthermore, several GNA-derived XNAs were developed to alter duplex stability and hybridization properties. The most important ones among these are ZNA with an additional methylene linker between the phosphine and oxygen compared to the GNA scaffold,[56] isoGNA as a structural isomer of GNA with the nucleobase attached directly to the backbone[57] and BuNA where the C2-linker of the main chain of GNA is extended to a C3-linker[58] (Figure 2.5).

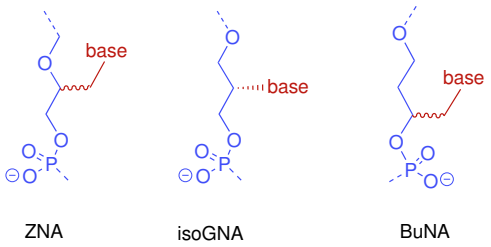

Figure 2.5: Examples for GNA-derived XNAs: ZNA (left), isoGNA (middle) and butyl nucleic acid (BuNA, right).

As will be discussed in Chapter 3, the three different helical structures can be used to organize chromophore aggregates. The differently constituted backbones are shown to have a significant influence on the orientation of the chromophores as artificial nucleobase surrogates in the duplex and toward each other as well as on the resulting chromophore-chromophore interactions.

2.2.2 Nucleobase modifications

While the backbone of nucleic acids can be artificially modified to generate oligonucleotides with improved properties, this type of modification is rarely found in nature. In contrast to this, DNA and especially RNA contain a large number of modified nucleobases besides the four canonical ones to extend their information content and enhance their chemical diversity. The first part of this section introduces the structure and function of the most important and well-studied natural nucleobase modifications. In the second part, the development of several artificial nucleobase analogs to further expand the functional scope of native nucleic acids will

be discussed.

2.2.2.1 Natural nucleobase modifications

Around 170 RNA nucleobase modifications in all types of RNA have been discovered within the last decades with the largest variety found in tRNA with about 10–15% of known non-canonical nucleobases.[59] Besides simple modifications arising from methylation or acetylation processes, also hypermodified nucleobases with different heterocyclic structures or large substituents were identified in RNA.[6,13]

Simple natural nucleobase modifications

The most abundant modifications of native nucleobases, which have only a small structural impact on the oligonucleotide scaffold, are obtained from posttranscriptional methylation which has a significant influence on many biological processes.[60]

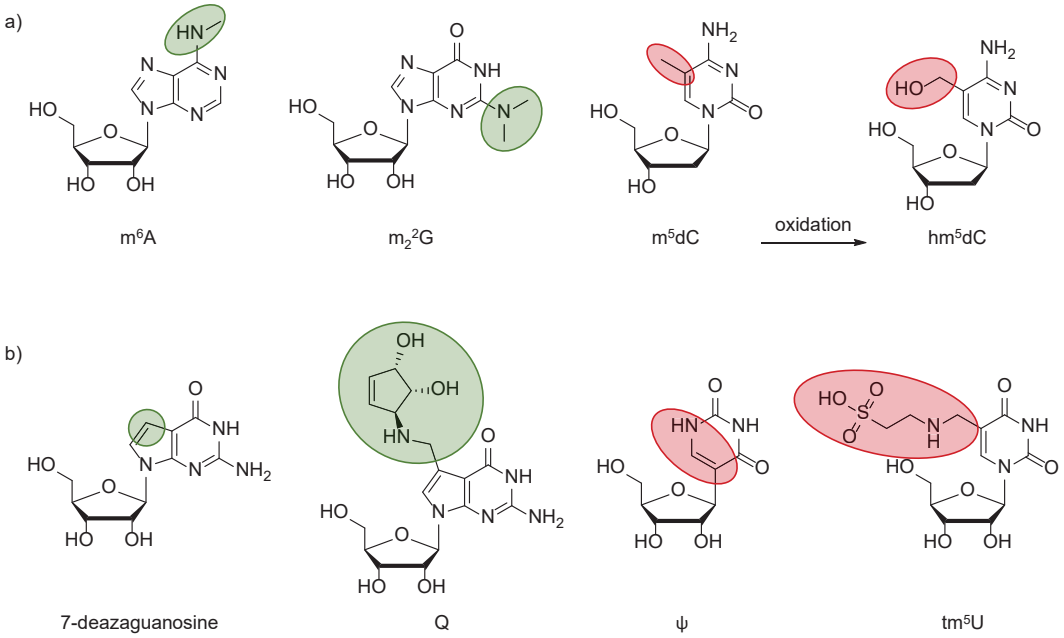

Figure 2.6: a) Simple nucleobase modifications arising from methylation and oxidation processes. b) Examples for hypermodified nucleobases. Purine modifications are shown in green while pyrimidine modifications are colored in red.

Among these methylated nucleobases, N^6-methyl-A (m^6A) is an abundant modification predominantly found in mRNA and its structure and function have been studied in great detail.[61,62] m^6A is conserved across most organisms and appears in the favored *syn*-conformation in which the steric clash between the methyl group and the purine scaffold is minimized (Figure 2.6a).[63] Recent studies revealed the important role of m^6A in human physiology and pathology, especially in the development of several types of cancer. This is further emphasized by the existence of specific m^6A-recognizing enzymes, the so-called m^6A-readers, m^6A-writers and

m^6A-erasers, which are responsible for the regulation of m^6A levels in the cell.[64]
Along with single-methylated nucleosides also double-methylated ones such as N^2,N^2-dimethyl guanosine (m_2^2G) are common RNA modifications. However, these are less prevalent and are not capable to undergo Watson-Crick base pairing with their complementary nucleobases, thereby leading to duplex distortions.[59]

In contrast to RNA, the nucleobase modifications present in DNA are much less complex and are mainly restricted to methylation followed by oxidation. However, some of these bases play a crucial role in epigenetics as well as the development of several diseases.[65,66]
Among them is m^5dC which is the best-understood regulatory epigenetic modification with its methyl group introduced by DNA methyltransferases (Figure 2.6a).[67,68] m^5dC accounts for up to 5% of all cytidines in vertebrates' DNA and plays an important biological role, in for example cancer evolution and as a biomarker of aging.[69] It is gradually oxidized to 5-hydroxymethyl-C (hm^5dC) and further to 5-formyl-C (f^5dC) and 5-carboxyl-C (ca^5dC) by ten-eleven-translocation (TET) enzymes during the nucleobase demethylation pathway.[70] All of these epigenetic nucleotides control the transcriptional activity of the genes in which they are embedded, although the underlying mechanism is still poorly understood.[71]

Hypermodified natural nucleobases

Unlike the described simple modifications, hypermodified nucleobases show a larger variety of structural patterns but are almost exlusively present in RNA. Some of these modifications are lacking ring nitrogen atoms, for example 7-deazapurines, which are secondary metabolites with an own chemical diversity (Figure 2.6b). Queuosine (Q) for example has a 7-deaza-guanine core structure covalently linked to an amino-methyl side chain and a cyclo-pentanediol moiety. It can be found at the wobble position of the anticodon loop of tRNA, where it restricts the flexibility of this structural element and might therefore be involved in regulation of gene expression.[72,73] Furthermore, it has also been associated with other biological processes such as cell differentiation and cancer progression.[74] Several glycosylated derivatives of Q have been detected although the biochemical functions of all of the members of the Q base family remain unidentified.[75,76]
One of the most famous hypermodified pyrimidine RNA nucleosides found in all domains of life is pseudouridine (Ψ), also called the fifth nucleobase, where the nucleobase is connected with the C5-atom *via* a C-C bond to the ribose by a posttranscriptional enzymatic isomerization reaction. The C-C bond leads to a higher rotational freedom and conformational flexibility compared to normal U and can therefore induce the formation of stabilized RNA secondary structures. This stabilizing effect has been proven to be important for translational efficiency and accuracy.[77]
The last example of hypermodified RNA nucleosides to be mentioned here is 5-taurinomethyluridine (tm^5U), a non-canonical nucleoside present at the wobble position of the anticodon loop

in mitochondrial tRNA. Here, a sulfonic acid is attached to the 5-position of uridine *via* an aminomethyl linker. As it is the case for most of the natural nucleobase modifications, the function of tm^5U is not completely understood, but there is good evidence that it is associated with mitochondrial translation defects.[78]

Altogether, DNA and in particular RNA contain a great diversity of possible nucleobase modifications. The resulting non-canonical nucleobases serve different biological roles and establish a second layer of information within the genome although many of their functions have not yet been conclusively elucidated.

2.2.2.2 Artificial nucleobase analogs

Nucleic acids are naturally responsible for storing, reading and writing genetic information, but their preorganized structure, programmability and easy synthetic accessibility also makes DNA and RNA attractive tools for applications in medicine and technology. Many artificial modifications have been introduced; among them some which only slightly modify the canonical nucleobase structure and others where the nucleobase is completely substituted by an unnatural nucleobase analog.

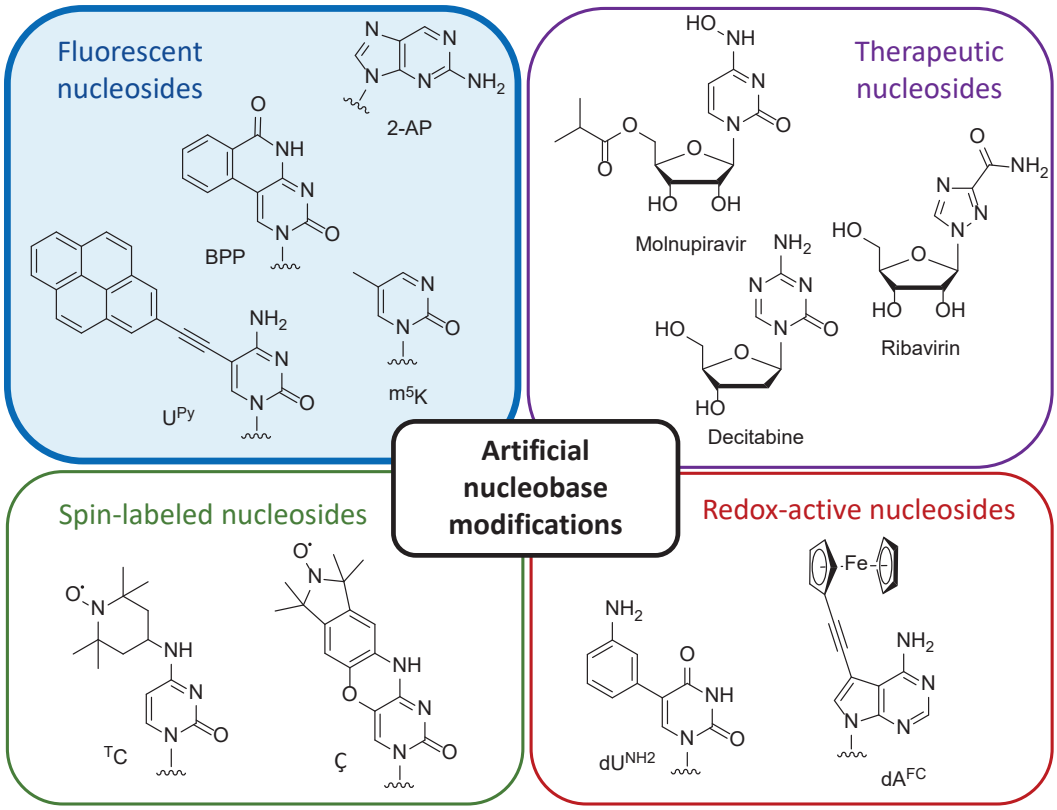

Figure 2.7: Overview of artificial nucleobase modifications for different applications, including fluorescent, therapeutic, spin-labeled and redox-active nucleosides.

To get an impression of the synthetic and functional potential of artificially modified nucle-

obases some examples of these with different implemented properties are illustrated in Figure 2.7.

A huge field of research is the potential of nucleoside analogs as therapeutics and antimetabolites for medicinal applications. Since the 1950s, nucleoside analogs have been studied as potential antiviral or antitumor agents and many effective drugs based on these compounds with high potency and a high barrier to resistance could be developed.[79] Besides the well-known gemcitabine, a dC analog with a difluorinated sugar, and its derivatives such as sapacitabine, also decitabine shown in Figure 2.7 is widely used in chemotherapy. This compound is another dC analog with a triazine nucleobase; it is applied for the treatment of acute myeloid leukemia as it irreversibly inhibits methyltransferases after its incorporation into DNA strands.[80] Examples for nucleoside analogs with antiviral properties are molnupiravir and ribavirin which are administered as prodrugs and metabolized in the human body to their active forms. Nucleosides with antiviral activity show different mechanisms of action; ribavirin for example is a G-analog and interferes with the RNA metabolism required for viral replication. It can therefore be used to treat infections with different DNA- and also RNA-viruses such as hepatitis C and influenza.[81] Molnupiravir, in contrast, inhibits viral RNA replication by the introduction of copying errors; it leads to G-to-A and C-to-U mutations in MHV, MERS-CoV and SARS-CoV-2 viruses.[82,83]

Nucleobase analogs are not only used for therapeutic applications but also for structural elucidation of nucleic acid biopolymers. A valuable method for this is electron paramagnetic resonance (EPR) spectroscopy which has been used to investigate the structure and dynamics of proteins as well as oligonucleotides. EPR spectroscopy requires unpaired electrons; since radicals cannot be found in natural nucleic acids due to their high reactivity, they need to be introduced artificially, resulting in the so-called nucleoside spin-labels. Several flexible spin-labels derived from TEMPO as well as rigid ones such as ^{T}C[84] and Ç[85] have been described and mainly used for distance measurements in duplex structures.

In addition, also electrochemical methods have proven to be well suited for the analysis of nucleic acid functions and structures. Even though A, C and G themselves are reducible on mercury electrodes, their intrinsic electrochemical properties can be further tuned by labeling with external redox-active groups, for example ferrocene in dA^{FC} or an aminobenzyl moiety attached to dU in dU^{NH2} (Figure 2.7).[86,87] Recently, redox-labeled nucleic acids have not only been reported to be useful biosensors for the investigation of DNA hybridization and the detection of mutations and SNPs but also to monitor DNA–protein interactions which is advantageous for many different fields of research such as molecular diagnostics, biomedicine and environmental analysis.[88] However, the use of fluorescent nucleosides as biochemical markers for a plethora of different applications is much more common and numerous publications in

this research area are available.[89–92]

Fluorescent nucleobase analogs (FNAs) are chemically modified nucleic acid building blocks that, if designed carefully, do not only retain most biological DNA and RNA functions such as base pairing and base stacking but also show improved fluorescent properties. Whereas native nucleobases are basically non-fluorescent due to ultrafast non-radiative decay of their excited states and no naturally occuring FNA is known, appropriate labels or chromophores need to be introduced leading to a fluorescence turn-on.[93,94] Here, minor changes to the canonical nucleobase structure like shifting exocyclic residues as in the case of 2-aminopurine (2-AP) and m^5K as well as larger structural changes leading to extended and expanded nucleobase analogs such as benzopyridopyrimidine (BPP) or U^{Py} have been introduced. Since different FNAs have been synthesized and characterized in the course of this thesis, this type of nucleoside modifications will in the following be described in more detail.

2.3 Fluorescent nucleobase analogs (FNAs)

To get an better understanding of the spectroscopic properties of FNAs, the first part of this section deals with the underlying photochemical processes of fluorescence. Based on this, different types of fluorescent nucleobases and applications of the resulting emissive biopolymers will be discussed, all of which have extensively been reviewed.[89,91,95–97]

2.3.1 Fluorescence theory: the origin of fluorescent properties

Fluorescence is the spontaneous emission of light and results from a three-stage process which can be depicted by a simple electronic state diagram, the Jablonski term scheme shown in Figure 2.8.

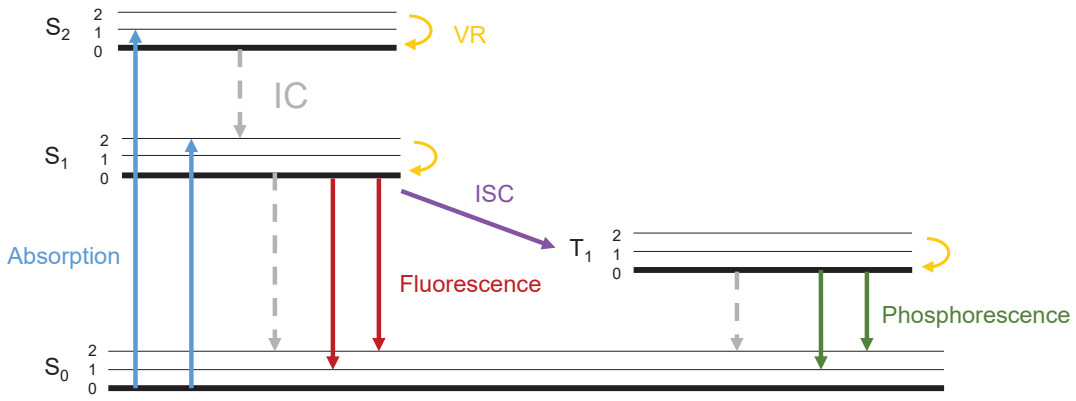

Figure 2.8: The Jablonski term scheme shows possible transitions between electronic ground and excited states for an organic fluorophore. Depicted are absorption processes (blue), fluorescence processes (red), phosphorescence processes (green), vibrational relaxation (VR, yellow), intersystem crossing (ISC, purple) and internal conversion (IC, grey). S indicates singlet states while T stands for triplet states.[98,99]

The ground, the first and the second excited singlet states are abbreviated S_0, S_1 and S_2, respectively, while T_1 denotes the first excited triplet state. These electronic energy levels are each split into several vibrational energy levels with different distances in between. Absorption of a photon with a suitable energy leads to excitation of a fluorophore from the electronic ground state S_0 to an excited state S_1 or S_2. This transition is on a timescale of about 10^{-15} s, which is much faster than all of the following processes and can be described by the Franck-Condon principle.
After excitation, several deactivation events by radiative and non-radiative mechanisms can take place. First of all, the excited electron can lose its excess vibrational energy by collision with other molecules in a non-radiative vibrational relaxation (VR) process and fall to the lowest vibrational energy state within its excited electronic state ($S_{1,0}$ or $S_{2,0}$). From there, a radiationless decay process called internal conversion (IC) can occur if the vibrational state of this electronically excited state overlaps with a vibrational state of an energetically lower electronic state. IC can be observed on a timescale of 10^{-12} s or less. By a similar mechanism called intersystem crossing (ISC), the electron's energy is redistributed to a vibrationally excited state of an electronic state with a different multiplicity, for example the T_1 triplet state, which causes reversion of the spin of the excited electron. In most organic molecules, the ISC process is comparably inefficient because it is a spin forbidden process.

From the T_1 state, either a non-radiative dissipation pathway through IC can occur or the fluorophore can lose its excess energy by the emission of light by phosphorescence. Since the transition from the T_1 state to the S_0 ground state is also forbidden, phosphorescence is mostly observed for molecules containing heavy atoms which facilitate ISC processes and therefore enhance phosphorescence quantum yields. If the excited electron is located in an electronically excited singlet state, stabilization of the fluorophore can also be achieved by the loss of a fluorescence photon. This photon is of lower energy than the one absorbed in the excitation product, leading to a red-shift in the fluorescence spectra, the so called Stokes shift. Since the lifetime of the excited S_1 state with 10^{-10} to 10^{-7} s is much longer compared to the possible non-radiative decay pathway from the S_2 to the S_1 state, fluorescence usually results from an electron populated in the energetically lower S_1 state.
Besides the pathways for excitation and deactivation of a fluorophore marked in the simplified Jablonski term scheme in Figure 2.8, additional interactions such as collisional quenching, energy transfer, for example Förster resonance energy transfer (FRET), and solvent interactions have to be taken into account to fully describe the spectroscopic properties of a fluorescent system.[98,99]
To exhibit fluorescence properties, a molecule needs to be able to absorb and emit light in defined wavelengths ranges. For the processes summarized in the Jablonski diagram, excitable electrons are required that need to be stabilized by delocalization, which is why many fluorophores contain an extended aromatic systems. This structural feature is also be found in

most of the FNAs described in the following part.

2.3.2 The structural constitution of FNAs

For the design of FNAs in general, some aspects need to be taken into account, in particular if these emissive nucleobase analogs are meant to be recruited for *in vivo* applications. To avoid background emission by native cell compounds and to diminish cytotoxicity caused by ultraviolet radiation, it is often required to shift the excitation and emission wavelengths of FNAs toward the red. This can be achieved by extending the conjugated π-system or the incorporation of heteroatoms. Based on their molecular constitution and structural relation to the canonical nucleobases, FNAs can be divided into four groups (Figure 2.9).[100] Isomorphic FNAs can either bear additional substituents at the natural nucleobase core or have an altered ring structure with different numbers or positions of the heteroatoms present. Expanded FNAs contain additional rings fused to the purine or pyrimidine nucleobase, therefore expanding the aromatic system. In extended FNAs, on the other hand, the complete native nucleobase structure is conserved with a chromophore tethered to the heterocycle by a C-C bond or a conjugated linker. Finally, in chromophoric nucleoside analogs the whole nucleobase is replaced by a fluorophore.

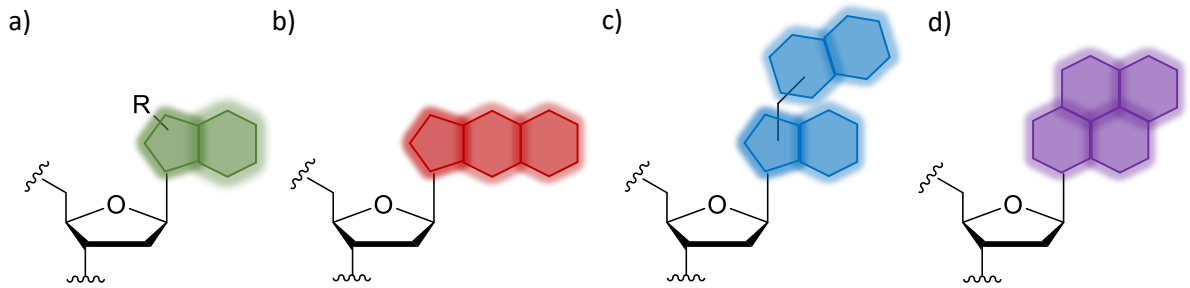

Figure 2.9: General structure of FNAs: a) isomorphic, b) expanded, c) extended and d) chromophoric nucleosides analogs. For isomorphic FNAs, either purine- (shown) or pyrimidine-derived scaffolds are possible.[100]

2.3.2.1 Isomorphic FNAs

Isomorphic FNAs preserve the molecular size as well as intrinsic properties like base pairing and the participation in inter- and intramolecular interactions of the native nucleobase from which they are derived. This makes them especially useful for labeling applications where only small structural perturbations are acceptable. Additionally, due to their structural similarity to canonical nucleosides, isomorphic FNAs can often enzymatically be incorporated into oligonucleotides. They are further divided into different subgroups, depending on their parent ring structure.

The most prominent examples for isomorphic FNAs are shown in Figure 2.10.

2-Aminopurine (2-AP)

2-AP was first reported by Stryer in 1969 and is the most widely used FNA.[101] It is a constitutional isomer of A and can base pair with T but also with C in a wobble structure.[102] The 2-AP monomer is highly fluorescent in aqueous solution with a quantum yield of 0.66 to 0.72 and a fluorescence lifetime of around 11 ns; it possesses a single emission band at 370 nm and an absorption maximum at 303 nm.[101,103] Upon incorporation into oligonucleotides, the quantum yield of 2-AP is decreased by up to two orders of magnitude with the largest reduction if located next to a G. This fluorescence quenching is based on a complex mechanism with a charge transfer assumed to be the predominant radiationless deactivation pathway.[104] Recent studies also reveal that the fluorescence intensity is not as reliable as initially thought because it strongly depends on the presence of water. 2-AP has to be completely hydrated for full fluorescence activation which needs to be taken into account for the interpretation of changes of its fluorescence intensity in the oligonucleotide environment.[105] Unfortunately, the practical scope of 2-AP for *in vivo* applications, for example cell microscopy, is limited because of the drastically decreased fluorescence upon hybridization and the excitation and emission spectra located in the UV region of the electromagnetic spectrum.[106] Despite this drawback, 2-AP has been used for a broad range of applications, mostly to probe the activity of enzymes, the folding mechanisms of nucleic acids and interactions with nucleic acid binding proteins. However, also more sophisticated applications have been described, including the construction of a DNA walker[107] and several biosensors to detect miRNA,[108] metal ions[109] and organic compounds such as theophylline.[110]

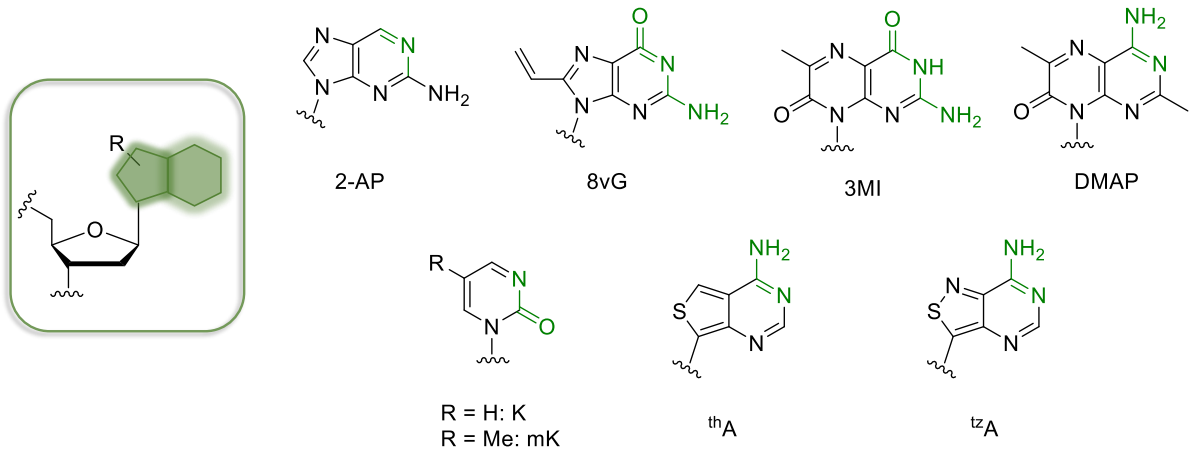

Figure 2.10: The most prominent examples in the group of isomorphic FNAs are shown here. The schematic representation of their general structure is depicted on the left side and the parts marked in green in each molecule indicate the Watson-Crick base pairing site.

8-Vinylated purine analogs

The spectroscopic properties of emissive nucleoside analogs cannot only be tuned by varying the substitution pattern of canonical nucleosides but also by the introduction of small addi-

tional groups to the nucleobase core. Prominent examples for this are 8-vinyl-adenosine (8vA) and -guanosine (8vG) which exhibit a redshift in absorption to 382 or 400 nm, respectively, compared to their native parent nucleobases.[111,112] The fluorescent characteristics of these two free nucleosides are strongly dependent on the solvent polarity, which is according to quantum mechanical calculations due to unfavored ISC processes in polar solvents and results in a higher fluorescence emission intensity. However, upon incorporation into oligonucleotides, both 8vA and 8vG experience an almost 10-fold reduction in fluorescence caused by intrastrand quenching and H-bond formation.[111] Meanwhile, the introduction of either 8vA or 8vG has a minimal impact on the thermal duplex stability and induces only minor perturbations of the duplex structure when incorporated into DNA or PNA.[113] In particular 8vG has been used for robust and sensitive fluorescence detection and has for example been applied to monitor the formation of G-quadruplexes as a hybridization sensitive probe.[112]

Pteridine-derived FNAs

3-Methyl isoxanthopterin (3MI) and 4-amino-2,6-dimethyl pteridone (DMAP) shown in Figure 2.10 as well as the structurally similar 6-methyl isoxanthopterin (6MI) and 4-amino-6-methyl pteridone (6MAP) belong to the family of pteridine-derived FNAs. Compared to native nucleosides, these chemical variants are composed of a different heterocyclic core with additional methyl groups. 3MI and 6MI are G-like nucleoside analogs, DMAP and 6MAP are A-like analogs and all of them except for 3MI are able to base pair. Pteridine-derived FNAs show fluorescence in buffered aqueous solution in the range of 380 to 500 nm, caused by the increased conjugation compared to natural A or G. While the free nucleosides feature fluorescence quantum yields between 0.39 and 0.88, fluorescence emission is significantly quenched in oligonucleotides, especially when incorporated next to purines. This is a limiting factor if bright fluorophores are required but useful to report on local structures. By taking advantage of the environment-dependent changes in fluorescence intensity, pteridine-derived FNAs have been employed to monitor the cleavage activity of HIV-1 integrase and the binding of the non-specific histone-like DNA binding protein, just to mention two examples.[114,115]

2-Pyrimidinone-derived FNAs

By eliminating the C4 and replacing the C5 substituent in natural pyrimidine nucleobases, K, mK and rK (zebularine) were synthesized, based on a 2-pyrimidinone heterocycle. All of these nucleobase analogs exhibit only weak base pairing with G, leading to a strong destabilization of the duplex due to their high local mobility.[116,117] The absorption maxima of the free K and mK nucleosides are at 303 to 315 and 314 to 321 nm, respectively, while the peak fluorescence emission is detected at 365 or 385 nm.[118,119] However, the quantum yield for the free as well as the incorporated nucleosides are comparably low with less than 1%. Although there is only a small decrease of fluorescence intensity upon implementation into oligonucleotides, this drawback makes 2-pyrimidinone-derived FNAs less favorable

tools for environment-sensitive fluorescence detection.[120] Additionally, 2-pyrimidone-derived nucleosides have shown to be potentially harmful to DNA upon UV-irradiation, resulting in photolesions and backbone breaks.[121,122] Thus, K, mK and rK are rarely used as fluorogenic probes but instead as potential anti-cancer drugs in the case of rK, since it acts as DNA-methyltransferase and cytidine deaminase inhibitor.[123]

Heteroatom-containing nucleobase analogs

The last class of isomorphic FNAs to be mentioned here are heteroatom-containing nucleobase analogs. In representation of this family of fluorescent nucleosides, thA and ^{tz}A are illustrated in Figure 2.10. Similar alterations of the nucleobase heterocycle have been made to all of the four canonical RNA nucleobases, resulting in a new emissive RNA alphabet. thA and ^{tz}A are based on thieno[3,4-*d*]-pyrimidines or isothiazolo[4,3-*d*]-pyrimidines, respectively. Because of the incorporation of sulfur as an electron-rich atom, the absorption and emission maxima are similarily red-shifted for both compounds to 341 and 420 nm for thA or 338 and 410 nm for ^{tz}A. Albeit the spectroscopic properties do not differ significantly, only ^{tz}A contains an intrinsic hydrogen bond acceptor in form of the N7 nitrogen. It can therefore enzymatically be converted to other emissive purines by deamination with adenosine deaminase.[124,125] The families of thN as well as ^{tz}N with N representing each of the canonical nucleobases were successfully applied for real-time monitoring of various biological processes.[126–128]

By expanding the heterocyclic nucleobase ring system the fluorescence properties of FNAs can be tuned to a greater extent, as described in the next part.

2.3.2.2 Expanded FNAs

Expanded FNAs are characterized by additional aromatic rings fused to the canonical nucleobase core, therefore enabling better electronic conjugation and shifting the spectroscopic properties toward the visible range of the electromagnetic spectrum. With the attachment of additional electron-donating or electron-withdrawing substituents on the aromatic system environment-sensitive chromophores which are often still able to undergo Watson-Crick base pairing can be developed. In Figure 2.11, some examples for purine- as well as pyrimidine-derived expanded FNAs are shown which will be discussed in the following.

Pyrimidine-derived expanded FNAs

The conjugated system of pyrimidine nucleobases can be extended at the 4- and 5-position or the 5- and 6-position, respectively, if the ability to form Watson-Crick base pairs is supposed to be maintained. One example for the first case mentioned is pyrrolo-C (pC) with a five-membered ring fused to cytidine.[129] The free pC nucleobase has a maximum absorption at 340 nm and a fluorescence emission maximum at 449 nm with a quantum yield of 0.38.[130] If a ribose moiety is attached to the pC nucleobase, the fluorescence is red-shifted and the

quantum yield reduced to 0.2 which can be explained by an increased IC rate. The fluorescence intensity of pC is further lowered by 60 or 75%, respectively, upon incorporation into single- or double-stranded DNA (ssDNA and dsDNA); especially if pC is flanked by G. Thus, pC can be recruited to directly probe single-nucleotide polymorphisms (SNPs).[131] In addition, since the fluorescence intensity of pC correlates well with thermal duplex stability, pC was applied to probe the hybridization of modified metal-ion-chelating oligonucleotides with their unmodified counterstrands.[132]

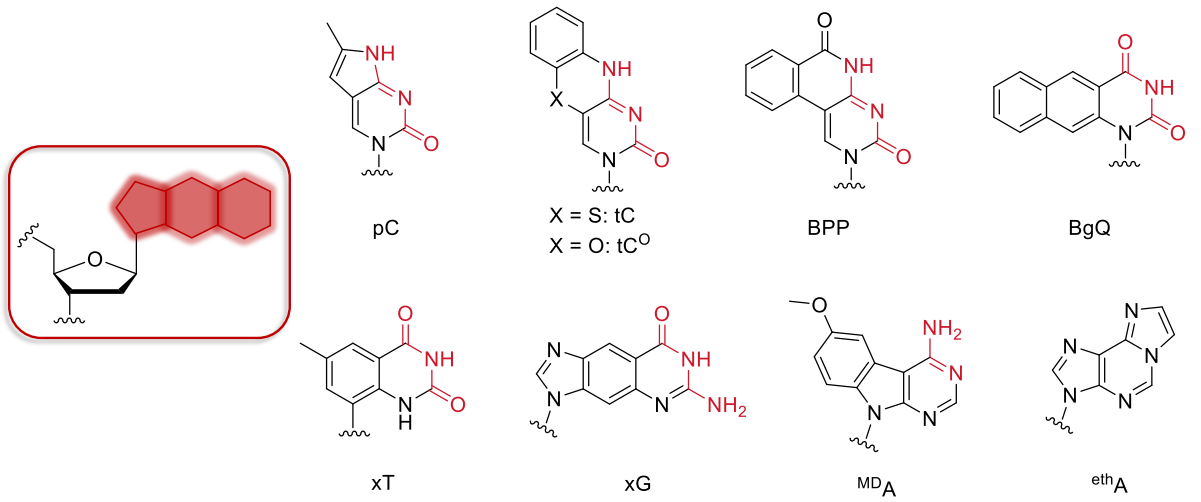

Figure 2.11: Shown are important examples of expanded FNAs. The schematic representation of the general structure is depicted on the left side and the parts marked in red in each molecule show the Watson-Crick base pairing site.

However, not only bicyclic expanded FNAs such as pC but also tricyclic ones are useful biochemical sensing tools. The thiol-appended tC is one of these emissive tricyclic FNA versions; it was initially developed to design duplex structures with improved stabilities. The free tC nucleobase has an absorption maximum at 375 nm and emits at 505 nm with a quantum yield of 0.17. Upon incorporation into oligonucleotides, fluorescence exhibits a 25 nm red-shift which is attributed to stacking interactions.[133] Additionally, tC is still brightly fluorescent when base paired to G, with negligible sensitivity to the surrounding sequence context. tC shows interesting properties for anisotropy-based sensing applications and thanks to its long fluorescence lifetime can be used as a donor for lifetime-based FRET experiments.[134] For this purpose, tC^O, with the sulfur atom replaced by an oxygen, was developed. Compared to tC, the absorption maximum of tC^O is blue-shifted by 15 nm and its emission maximum at 461 nm as well as the quantum yield of 0.3 are only moderately altered upon incorporation into the oligonucleotide. Together with its variant tC_{nitro}, which bears an additional nitro group at the aromatic core, tC^O forms a FRET pair used to obtain structural information on DNA duplexes.[135,136]

Structurally similar to tC is the phenyl-appended pyrimidine derivative benzopyridopyrimidine

(BPP). The absorption maximum of BPP is located at 347 nm and fluorescence emission is highest at 390 nm; meanwhile, BPP is emitting less brightly compared to tC with a quantum yield of only 0.04. The fluorescence of BPP is quenched if base paired with purines; opposite A the fluorescence quantum yield is diminished to 0.035 while it is decreased by a factor of twenty when incorporated opposite G. The explanation for this phenomenon is presumably the lower ionization potential of G, making the CT process more selective.[137] Although this dynamic quenching process limits its general utility, BPP can still be used for SNP typing of genes, since it is able to distinguish between A and G in the duplex structure.[138]

Much more remarkable are the fluorescence properties of BgQ, a tricyclic expanded FNA with a naphthalene fused to the 5- and 6-position of T. Due to its planar and rigid ring structure, BgQ has a fluorescence quantum yield of 0.82 with maximum emission at 434 nm. Similar to BPP, its fluorescence properties are strongly dependent on the sequence context: if BgQ is flanked by C and T, the fluorescence quantum yield is decreased by only 15%, whereas a 100-fold reduction is observed when it is flanked by two Gs. This environmental sensitivity is advantageous, not only for SNP detection but also to monitor DNA triplex formation.[139]
Related to BgQ, a complete DNA series, the so-called xDNA family developed by Kool and coworkers, with only one aromatic ring fused to the nucleobase core has been reported.[140–142] In representation of the xDNA nucleobases, xT and xG are shown in Figure 2.11. Although all of these nucleobases are by 2.4 Å larger than their natural counterparts, the corresponding nucleosides can be copied by DNA polymerase in live bacterial cells, showing their high biocompatibility.[143] Despite the high local backbone strain introduced by the xDNA nucleobases, all of them are still able to form Watson-Crick base pairs. The depicted xT nucleobase shows an emission maximum at 385 nm in aqueous solution. Its fluorescence quantum yield is highly dependent on the sequence context, similar to BPP and BgQ. If xT is flanked by A and T in ssDNA, the quantum yield is reduced from 0.3 to 0.01, while it remains unchanged if xT is surrounded by T and C.

Purine-derived expanded FNAs

The xG modification, belonging to purine-derived expanded FNAs with a six-membered ring implemented between the five- and the six-membered purine rings, resembles the spectroscopic properties of xT but has a somewhat higher quantum yield of 0.4.[142] Therefore, it can also be used to detect mismatches as well as abasic sites similar to all other nucleosides of the xDNA series. The structure of methoxy benzodeaza-adenosine (^{MD}A) shown in Figure 2.11 differs from xG and xA in the location of the attached conjugated ring system, which is in this case only bound to the imidazole ring. With a quantum yield of 0.12, ^{MD}A is less fluorescent than all of the other nucleobases belonging to the xDNA family, which is presumably due to dissipation of rotational energy by the methoxy group. The absorption and emission maxima of ^{MD}A are at 327 and 427 nm, respectively. Upon incorporation of ^{MD}A into ssDNA and

matched dsDNA, the fluorescence intensity is 24- to 100-fold decreased, depending on the sequence context, while the quantum yield is reduced to a smaller extent in mismatched dsDNA. On the basis of its environment-sensitive properties, ^{MD}A can be used to detect SNPs and has successfully been applied to investigate on the T/C SNP sequence of the human breast cancer 1 gene.[144] Later, ^{MD}A was refined to naphthodeaza-adenosine (NDA) with a naphthyl instead of a phenyl ring attached to the native nucleobase. NDA exhibits similar features as ^{MD}A and has been used for FRET-based distance measurements with fluorescein as FRET acceptor.[145]

The expanded FNAs described so far are all able to form Watson-Crick base pairs; an exception is etheno adenosine (^{eth}A), which was the first described heterocyclic non-canonical fluorescent nucleobase analog.[146] Here, the exocyclic amino group and the N1 ring nitrogen are connected by an ethylene bridge, forming an additional five-membered ring. ^{eth}A has an absorption maximum at 294 nm and emits fluorescence at 410 nm, with a remarkably high quantum yield of 0.6 and a long-lived excited state of 23 ns. This long fluorescence lifetime makes ^{eth}A suitable for applications with time-resolved fluorescence measurements. Although ^{eth}A leads to perturbation of the duplex upon incorporation due to the lack of base pairing ability, it can replace ATP in enzymatic reactions such as primer elongations with DNA polymerase I, making it a reliable tool for biological experiments.[146–148]

If the aromatic nucleobase ring system is not expanded by direct attachment of additional aromatic scaffolds but chromophores are installed *via* a linker, the family of extended FNAs described in the next part is obtained.

2.3.2.3 Extended FNAs

In Figure 2.12, selected examples of extended FNAs are shown. Chromophores of all kinds can be attached to canonical nucleosides at different positions and with variable conjugated linkers, giving rise to a plethora of emissive nucleobase analogs.

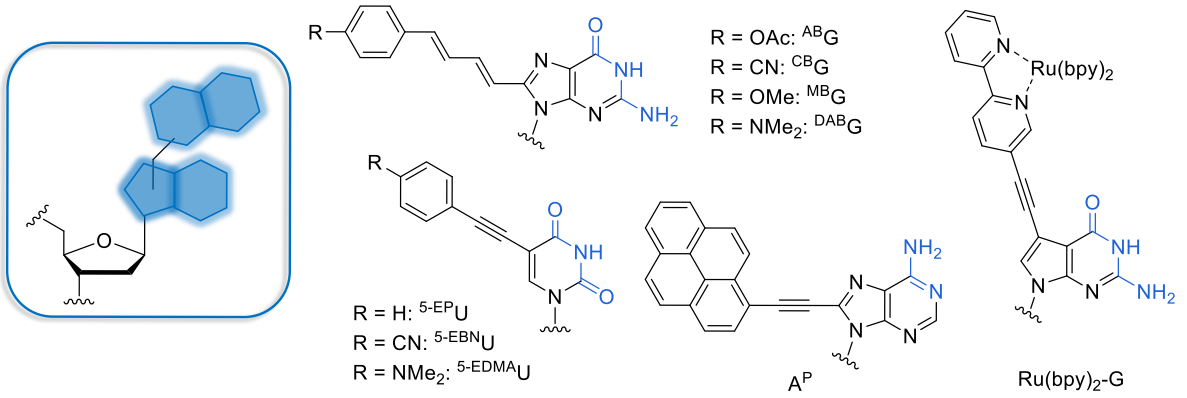

Figure 2.12: Shown are important examples of extended FNAs. The general structure is depicted on the left side and the parts marked in blue in each molecule show the Watson-Crick base pairing site.

Extended FNAs exhibit conjugation between the extended chromophore and the aromatic ring system of native nucleobases, thus allowing the optical properties of the whole scaffold to be influenced by base pairing and the local environment. This environmental sensitivity arises from internal charge transfer between the extended moiety and the natural nucleobase and results in redshifts and quantum yield changes.[138,149]

One possibility to extend the conjugated system of canonical nucleobases is to equip them with differently substituted phenyl rings with altered electronic properties attached *via* an acetylene or a butadiene linker. Butadiene linkers are not as commonly used as acetylene linkers; however, para-substituted phenyl rings have been tethered to the 8-position of G using this handle, leading to ^{AB}G, ^{CB}G, ^{MB}G and ^{DAB}G shown in Figure 2.12. These four extended FNAs consist of a push-pull system and exhibit remarkable solvatochromic and solvatofluorochromic properties dependent on the electronic nature of the functional group at the aromatic core. ^{DAB}G for example has an fluorescence emission maximum at 554 nm in methanol with a quantum yield of only 0.02, while its fluorescence brightness is significantly enhanced in acetonitrile, showing a quantum yield increase to 0.57. Because of such an environmentally sensitive strong fluorescence and no observed photoisomerization processes, all of the four mentioned FNAs were exploited for structural studies of nucleic acids and molecular diagnostics.[150]

Similar electronic effects are obtained if para-substituted phenyl rings are attached by an acetylene linker to for example the 5-position of pyrimidine nucleobases, such as in $^{5\text{-EP}}$U, $^{5\text{-EBN}}$U and $^{5\text{-EDMA}}$U. Although these FNAs have not been used for further applications, they exhibit interesting spectroscopic properties tuned by their different electron-donating and -withdrawing groups. While the absorption and emission maxima for $^{5\text{-EP}}$U are located at 320 and 400 nm, respectively, a red-shift of these maxima to 330 and 450 nm was observed upon introduction of a dimethyl amino group in $^{5\text{-EDMA}}$U, in contrast to $^{5\text{-EBN}}$U where the electron-withdrawing cyano substituent leads to a blue-shift.[151]

Besides single phenyl rings also highly conjugated carbohydrate chromophores, for example pyrenes and perylenes, can be attached to different positions of natural nucleobases. A^P shown in Figure 2.12 as well as U^P with the pyrene chromophore tethered to the 5-position of U are examples of this type of extended FNAs. The pyrene moiety allows excitation in the long UV to short blue range between 380 to 420 nm, while emission of blue light with wavelengths between 450 and 480 nm is observed. A^P has been incorporated as a terminal modification into oligonucleotides, stabilizing hairpin structures through π-stacking with neighboring nucleobases. The free nucleoside has a quantum yield of 0.73 at the emission maximum at 413 nm in water, and upon incorporation the fluorescence is strongly quenched by proton-coupled electron transfer. However, the quenching effiency proved to be controlled by the nucleobases adjacent to A^P, enabling its use for the detection of single nucleotide alterations.[152]

If not only fluorophores but in addition also transition metal ions are included in the nucleobase scaffold, characterization of these systems can be achieved using spectroscopic as well as electrochemical detection methods.[153,154] The most commonly used transition metal ions are Ru^{2+} and Os^{2+}, for example in the 7-deazapurine conjugate $Ru(bpy)_2$-G (Figure 2.12). Upon excitation at 450 nm, the $Ru(bpy)_2$-G triphosphate exhibits strong red luminescence at around 640 nm, which is quenched to a certain degree after incorporation by primer extension. However, the fluorescence detection limit for $Ru(bpy)_2$-G still is around 10^{-8} M, which is in the same range as required for detection by cyclovoltammetric methods.[154]

Some of the chromophores mentioned in this section can also directly be attached to the ribose moiety *via* a C-C bond, leading to the formation of chromophoric FNAs as described next.

2.3.2.4 Chromophoric FNAs

Chromophoric FNAs are fully non-canonical nucleobase analogs based on either aromatic hydrocarbons or planar heterocyclic fluorophores. These fluorophores are lacking a Watson-Crick site for base pairing, stabilization of nucleic acid structures can instead be achieved by extensive π-stacking interactions. π-stacking interactions are especially strong for aromatic hydrocarbons but less pronounced for heterocyclic fluorophores. In this case, the weak π-stacking interactions and the absence of hydrogen bonds are compensated by the distinct energy states of the heteroatoms. In addition, the incorporation of heteroatoms leads to a broader accessible range of possible emission wavelengths. The major advantage of chromophoric FNAs is the even further red-shifted emission compared to all of the other FNA families, helping to avoid toxicity and background emission after excitation. Furthermore, chromophoric FNAs are capable of forming extended multichromophore assemblies and excited state dimers, so-called excimers, which are characterized by a far-red shifted emission band.[155] However, the practical scope of chromophoric FNAs is hampered by the size of these nucleobases, since they are too large to fit into a natural dsDNA context and are therefore poor substrates for polymerases.[156] To overcome these limitations, several strategies for the enzymatic incorporation of chromophoric FNAs have been developed.[157,158]

Five examples of chromophoric FNAs based on different organic chromophore scaffolds are shown in Figure 2.13. Among them, the most widely used chromophoric FNAs are constructed from pyrene, 1-naphthalene, perylene or phenanthrene topologies. All of these are able to form excimers with higher quantum yields compared to the monomeric building blocks.[159] A single pyrene nucleoside, for example, can be excited in the long UV range at 341 nm and emits at 395 nm; upon excimer or exciplex formation, the pyrene emission is red-shifted to 500 nm.[160] This 100 nm red-shift can be observed for all of the mentioned aromatic hydrocarbon chromophores and makes these FNAs applicable to monitor DNA base excision repair.[161,162]
Exciton coupling can also be observed by circular dichroism (CD) spectroscopy when two

stilbene chromophores are attached to the DNA backbone. The length of *trans*-stilbene perfectly matches the size of a canonical purine-pyrimidine base pair, making it an effective base pair surrogate with intrinsic fluorescence properties. Similar to most other FNAs, stilbene exhibits a strongly reduced fluorescence intensity upon incorporation. Additionally, it can only be excited in the UV range of the electromagnetic spectrum which limits its application as environment- and hybridization-sensitive fluorescence probe.[163]

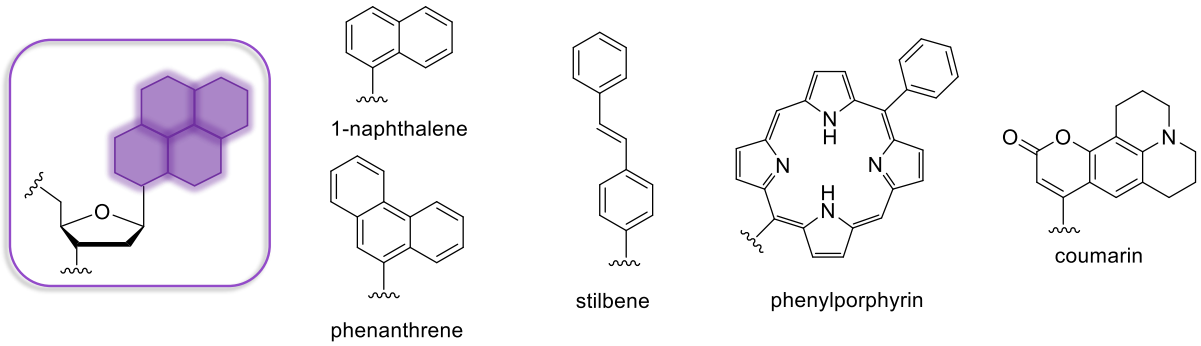

Figure 2.13: Shown are important examples of chromophoric FNAs. The general structure is depicted on the left side. The name of the fluorophore moiety is given below every structure.

Chromophores which are suitable to further tune the spectroscopic properties of nucleic acids are for example the heterocycle-containing building blocks phenylporphyrine and coumarin. Both chromophores can be incorporated as 2'-deoxy-C-ribosides and lead to an only minimal distortion of DNA duplexes with similar thermodynamic stabilities compared to unmodified ones.[164,165] Since the fluroescence quantum yield of porphyrines showed to be independent from the sequence context and was not decreased upon incorporation, it can potentially be used for many different applications, among them the design of supramolecular devices and the establishment of light-harvesting arrays.[166] Coumarin, on the other hand, shows a large Stokes shift, suitable to study ultrafast DNA dynamics in solution.[167]

In summary, FNAs display a great diversity in means of chemical structure, spectroscopic properties and possible biochemical and biophysical applications. The choice of an appropriate chromophore for a desired application depends on the context of the experiment and requires careful design of the used fluorescent probe. In the following section, some of the most prominent examples for the application of FNAs are demonstrated.

2.3.3 Selected applications for FNAs

As pointed out in the previous part of this chapter, the reliable detection of SNPs in the human genome is highly desirable since these variations have an impact on the development of various diseases and are of particular interest in pharmacokinetics as they influence the response to different agents such as drugs, pathogens and vaccines. Many methods for SNP

detection have been developed, based on FRET experiments using molecular beacons,[168] on PNA-mediated PCR-clamping[169] or on electrochemical mismatch detection.[170,171]

However, all of these techniques strongly rely on hybridization efficiencies and the sequence context of the SNP of interest, limiting their practical scope. Base-discriminating fluorophores (BDFs), as shown in Figure 2.14a, overcome the aforementioned drawbacks and offer convenient detection of SNPs by fluorescence response. Labeling of an oligonucleotide single strand with a BDF probe can be achieved easily by different methods and upon hybridization of the labeled single strand with a mismatched or matched complementary counterstrand, the fluorescence properties remain either unchanged or the fluorophore's brightness is significantly enhanced. However, with some BDFs it is not only possible to differenciate between the matched and the mismatched situtation, but also to distinguish between opposite nucleobases.[172] Ethynyl uridines for example, which were also illustrated in Figure 2.12, show considerable fluorescence quenching when opposite a mismatched guanine, while their fluorescence intensity is only reduced to an intermediary degree when opposite thymine and duplexes with a cytosine mismatch are not quenched significantly.[173] By taking advantage of the strong response of BDFs to their local environment, DNA damages at different positions in the genome can be elucidated and localized structural phenomena as well as nucleic acid-ligand interactions can be monitored by this hybridization-based mismatch detection method.

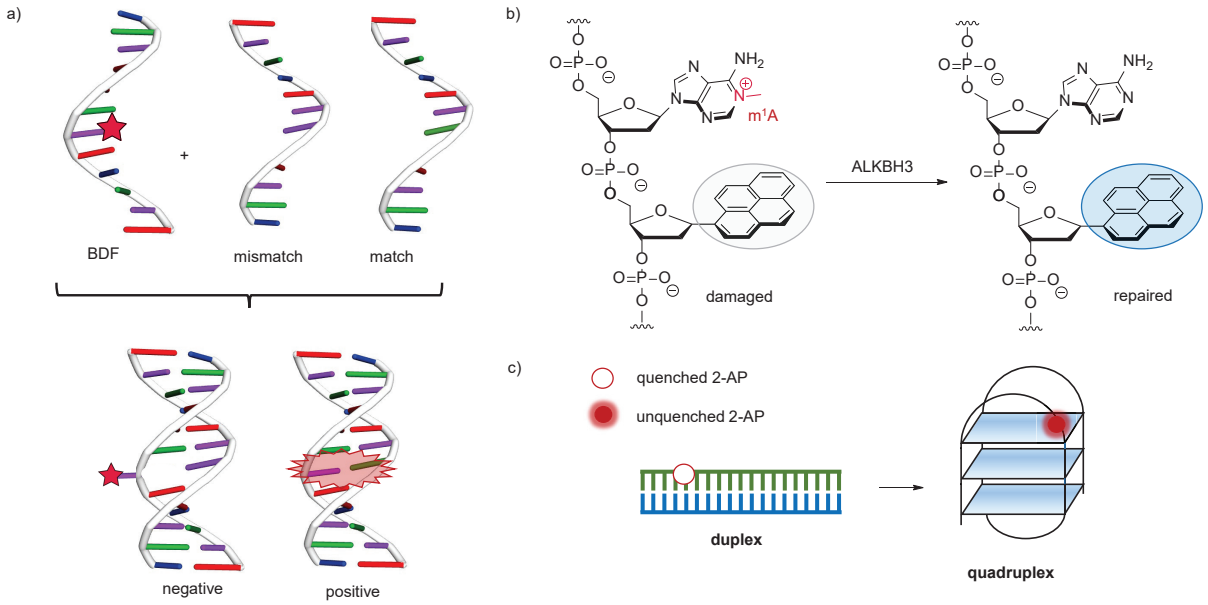

Figure 2.14: Common examples for applications of FNAs. a) By using base-discriminating fluorophores (BDFs), hybridization-based mismatch detection can be achieved.[172] b) Pyrene-based chromophoric FNAs can be recruited as fluorescent probes to monitor DNA repair, for example the activity of the ALKBH3 enzyme in m^1A demethylation.[174] c) 2-AP can be applied to probe structural changes. In the duplex structure, the 2-AP fluorescence is quenched while it lights up upon quadruplex formation.

In a similar approach, fluorescent probes were used to track DNA repair activities by direct readout of fluorescence intensities. Probes used for this application need to be designed in a way that their fluorescence is directly quenched by the DNA damage and not by the DNA duplex structure itself; thus, the repaired product must provide only minimal quenching. Many examples of fluorescent reporters for DNA repair have been reported, for example an uracil DNA glycosylase (UDG) probe which benefits from the fluorescence turn-on of pyrene upon excision of the flanking uridines.[160] In addition, the already mentioned tC^O nucleoside has been applied to record the activity of OGG1 glycosylase in the removal of 8-oxoguanine. This lesion considerably quenches tC^O fluorescence; upon removal of 8-oxoguanine by OGG1, tC^O lights up and thus directly reports on this enzyme's efficiency.[175] More recently, fluorescent probes have been developed to observe the repair of methylated nucleobases like m^1A and m^3C. The probe design and the repair detection of this lesions by demethylases is challenging since methylated nucleobases induce only small perturbations in the oligonucleotide structure. However, it has been found that pyrene is a suitable reporter on the activity of the Fe(II)- and oxoglutarate-dependent demethylase ALKBH3 toward m^1A demethylation (Figure 2.14b). m^1A is positively charged and thus electron-deficient; it strongly quenches the fluorescence of pyrene, an electron-rich fluorophore with high LUMO energy levels, by photoinduced charge transfer. With this method, demethylase activity can directly be reported *in vitro*, in cell lysates and in live cells, showing the benefit of probes quenched by specific nucleobases with the potential to screen and identify enzyme inhibitors.[174]

FNAs cannot only be used to detect mismatches and to provide insight into enzyme activity, but also to report on changes of oligonucleotide secondary structures. One widely used probe for this purpose is 2-AP, which, as mentioned in the previous section, shows strong fluorescence quenching after incorporation into oligonucleotides.[176] Majima *et al.* took advantage of this property and incorporated 2-AP in the G-quartet-comprising human telomeric DNA sequence $d[AGGG(TTAGGG)_3]$ (Figure 2.14c).[177,178] While 2-AP did not have a significant influence on the stability of this structure, it experienced a fluorescence turn-on upon conformational change from the duplex to the quadruplex structure, which is attributed to different base stacking and solvent accessibility in the TTA-loop. Furthermore, it was not only possible to distinguish between duplex and quadruplex structures but also between the basket- and the propeller-type G-quadruplex with the latter one showing weaker fluorescence since here 2-AP is intercalated between to thymidines. Thus, 2-AP is able to provide information on local changes of G-qadruplex structures and their interactions with small ligands.

The aforementioned selection of applications, including SNP detection,[179] the monitoring of enzyme activity and structural changes *in vivo* and *in vitro*[180] as well as the analysis of A-to-I editing mechanisms[181] and the probing of nucleoside transporter activity,[182] demonstrates the versatility of FNAs as analytical probes. However, not only oligonucleotides containing a

single FNA but multiple fluorescent nucleobases are useful tools in many areas of research. In the next section, the structural and spectroscopic properties of covalent and non-covalent DNA-based multichromophore arrays along with possible applications are discussed.

2.4 Multichromophore assemblies

Multichromophore assemblies have gained more and more interest in the last decades, with systems based on conjugated polymers, oligoamides, viral nanoparticles and photonic wires having been developed. Their applications are wide-spread, they range from light-harvesting antennae,[183] synthetic photosystems[184] and photovoltaics[185] to organic semiconductors[186] and other supramolecular materials. Multichromophore assemblies serve different purposes: first, they support highly efficient excitation and energy transfer suitable for the use in organic electronic materials and sensors. Second, their higher collective absorption compared to the monomer building blocks can be exploited for solar cells and light-harvesting applications. In addition, multichromophore assemblies are highly tunable as their spectral properties depend on the number, the arrangement and the relative orientation of the chromophores toward each other. Finally, the array of multiple chromophores leads to new spectroscopic features due to interactions of fluorophores in the ground states with others in excited states, for example the formation of excimers and exciplexes, which leads to broadened and red-shifted emission spectra.[187] In this section, the theory behind the distinct fluorescence properties of ordered chromophore aggregates will be discussed first, followed by examples for covalent as well as non-covalent multichromophore assemblies on DNA.

2.4.1 The theory behind multichromophore fluorescence

The incorporation of fluorophores into oligonucleotide structures gives rise to ordered, self-organized supramolecular assemblies templated by the oligonucleotide backbone. Since chromophores often adopt a planar molecular structure, the interactions between them are mostly driven by π-π-stacking. Depending on their geometry, fluorophore dimers can exhibit either a blue-shift (hypsochromic) or a red-shift (bathochromic) in absorption. Bathochromic shifts are characteristic for J-type aggregates, which are named after Jelley, one of their explorers.[188] In J-type aggregates, chromophores are assembled in a head-to-tail arrangement, exhibiting a narrow and intense absorption band as well as nearly resonant fluorescence. H-type aggregates, on the other hand, consist of chromophores arranged in a face-to-face or sandwich-type fashion. Here, the dimer absorption band shows a width similar to the monomer band and often exhibits a rich vibrational structure.[188,189] The strong difference in the optical properties of H- and J-type aggregates can be explained by the distinct coupling between the transition dipole moments according to Kasha's exciton model.[190] If the transition dipole moments of two monomers are coupled, the degenerate pairs of the monomers' excited states combine

and form an exciton state. This state is split into two excitonic energy levels S_1' and S_1" belonging either to a dimer with parallel or antiparallel transition dipole moments. H- and J-type aggregates can also be classified by the angle θ between the transition dipole moment of the monomer and the chromophore chain axis: if θ is smaller than the magic angle of 54.7°, H-type aggregates are formed whereas with θ higher than 54.7°, the formation of J-type aggregates can be observed.[191]

Upon direct absorption of light, the excited states with the transition dipole moments arranged in parallel fashion are occupied. In the case of J-type aggregates, this is the lower excitonic state (Figure 2.15). From there, the electron can directly fall into the ground state under emission of fluorescence. For H-type aggregates, the excitonic state with parallel transition dipole moments is the higher-energy excitonic state. However, due to a rapid IC process, the excited electron has a higher probability to be located in the lower excitonic state, characterized by antiparallel dipole moments. From there, transition back into the ground state is not allowed and can only occur by non-radiative IC. This explains why H-type aggregates in contrast to J-type aggregates are generally considered non-fluorescent.[192] Despite the forbidden electronic transition, some fluorescent H-type aggregates have been described in literature, for example for merocyanines.[193] In general, H-type aggregates are much more common for organic molecules; they can be found for perylenebisimides (PBIs), cyanine dyes, oligophenylenevinylenes, carotenoids and oligothiphenes for example. Meanwhile, J-aggregates have only been reported for selected organic fluorophores, such as cyanines, PBIs and porphyrines.[194]

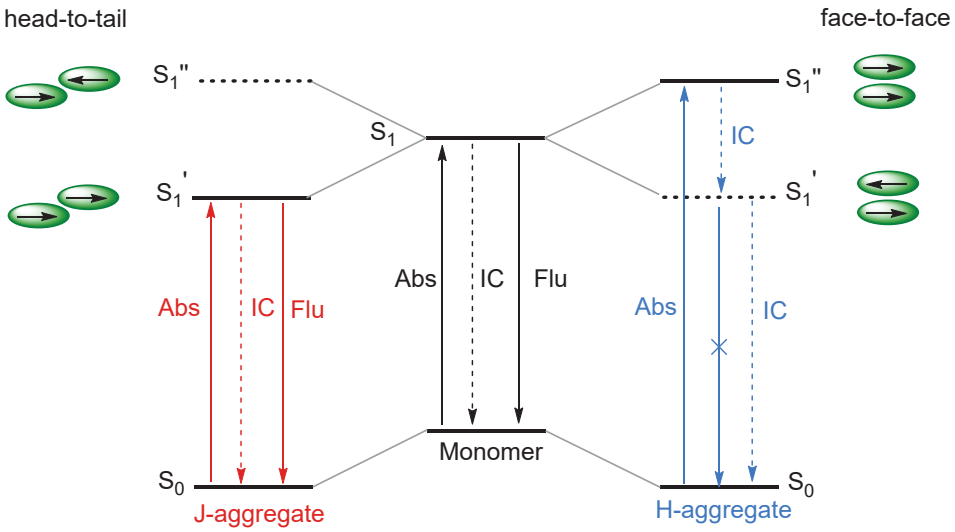

Figure 2.15: Energy diagram for J- and H-type dimers. The allowed absorption, fluorescence and IC pathways between the ground state S_0 and the split excited states S_1' and S_1" are marked with arrows. The exciton coupling energy *J* corresponds to half of the distance between S_1' and S_1". The green oval shapes depict the fluorophores with the small black arrow indicating the direction of their transition dipole moments.[191]

H- and also J-type aggregates have also been observed for a number of multichromophore systems attached to the DNA scaffold, which will be further discussed in the following part of this thesis.

2.4.1.1 Covalent DNA-based multichromophore assemblies

Nucleic acids are, thanks to their organized, well-defined structure, a favored scaffold to assemble fluorophores in a predictable manner. Chromophores can be covalently attached to nucleic acid structures at different positions, leading to distinct stacking interactions by intercalation, groove binding or backbone stacking in defined regions of a duplex.

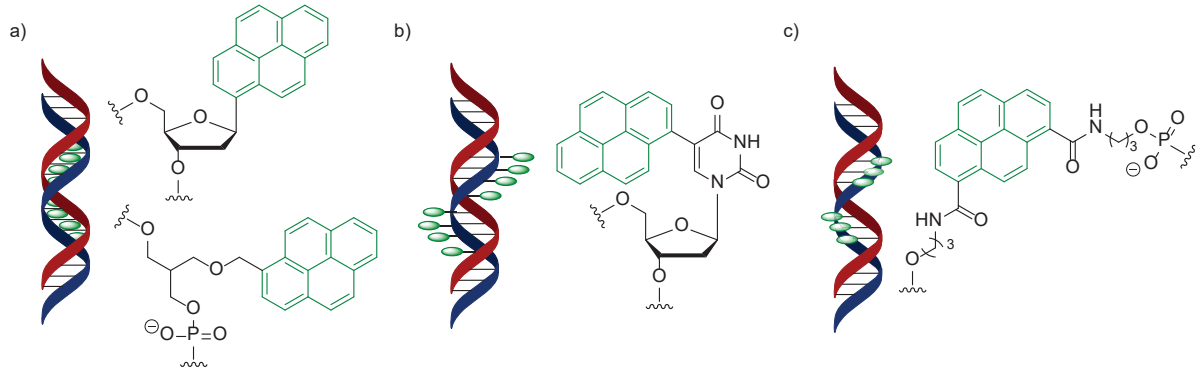

Figure 2.16: Aggregation modes within covalent multichromophore assemblies. a) Intercalation, b) stacking in the groove and c) aggregation of chromophores directly implemented into the backbone.

As shown in Figure 2.16a with pyrene as an example, intercalation of nucleobases can on the one hand be obtained with chromophoric nucleosides as discussed in section 2.3.2. Within these, the sugar puckering and the helical structure of the duplex are retained if the introduced chromophores are similar in size to canonical nucleobases. On the other hand, intercalating chromophores can also be incorporated using a non-nucleosidic approach where the ribose is replaced by a linker and the chromophore is directly attached to the backbone. Another type of assembly is achieved by chromophore aggregation in the minor or major groove of the DNA helix, for example with chromophores directly attached to the non-Watson-Crick site of canonical nucleobases (Figure 2.16b). Additionally, chromophores can directly be implemented into the backbone, giving rise to backbone assemblies shown in Figure 2.16c.

Since a huge amount of covalent multichromophore assemblies have been reported, only some selected systems can be shown in the course of this thesis. However, there are multiple review articles which cover most of the multichromophore systems described so far.[187,195,196]

Covalent assembly by chromophore intercalation

The smallest possible multichromophore assembly based on DNA can be imagined to contain

two interacting chromophores. Two examples of these intercalating fluorophore dimers were described by Asanuma *et al.* and Park *et al.* to form a FRET pair.[197,198]

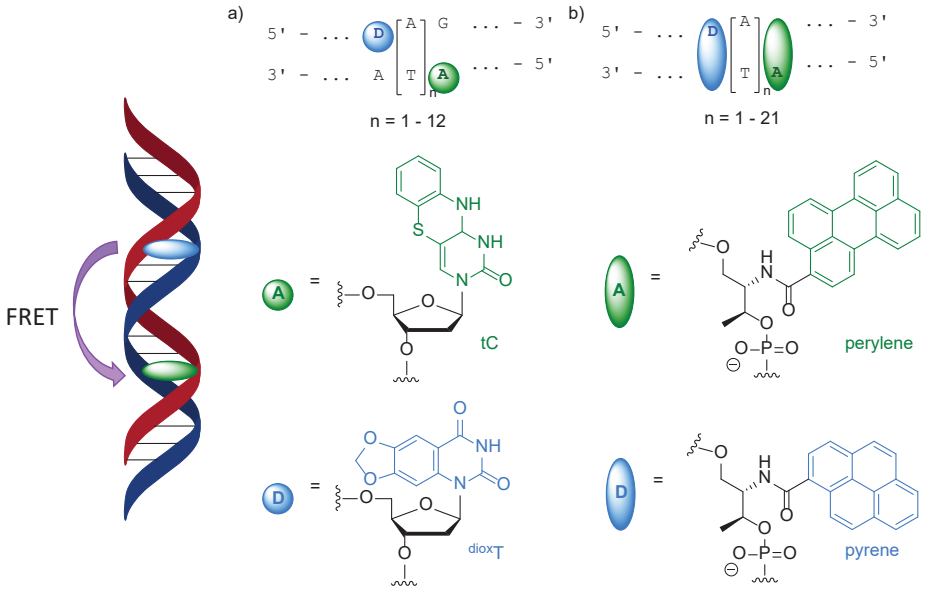

Figure 2.17: FRET pair formation by DNA-intercalating fluorophores. On the left side, the setup of the two FRET experiments is depicted schematically. In a), two isomorphic pyrimidine analogs are used as FRET donor (blue) and acceptor (green); this system was described by Park *et al.*[198] Similarly, Asanuma *et al.* reported a FRET system based on perylene and pyrene attached to a D-threoninol linker (b).[197] In both systems, the donor and acceptor moiety are separated by up to 21 A-T base pairs.

FRET is, due to its high spatial sensitivity, often used as molecular ruler to measure distances but there are only limited examples of orientation-dependent FRET effects. As shown in Figure 2.17a, Park *et al.* used the isomorphic pyrimidine analogs tC and ^{diox}T for such distance- and orientation-dependent FRET experiments.[198] Due to the strong stacking between the intercalated dyes and the natural nucleobases, the free movement of these chromophores is restricted and they are therefore fixed within the duplex. To control the distance and orientation of the donor and the acceptor fluorophores within the helical structure, a varied number of 1 to 12 A-T pairs was introduced in between them.

The experimental FRET efficiency, which was obtained from the static fluorescence intensities of both donor and acceptor and the lifetime of the donor, showed to change periodically, indicating its strong dependence on the chromophore orientation. Similarly, Asanuma *et al.* used perylene as a FRET acceptor and pyrene as the donor (Figure 2.17b). These two chromophores were attached by D-threoninol linkers to the DNA backbone and incorporated opposite abasic sites. Also here, 1 to 21 A-T pairs were implemented in between the two chromophores. Interestingly, the FRET effiency did not decrease linearly with higher number of A-T base pairs but dropped significantly every five base pairs, which corresponds to a half turn of a B-helix.[197] These two described FRET systems emphasize the orientation- and distance-dependence of the energy transfer efficiency between two chromophores covalently linked to the DNA scaffold

and can be used for further nucleotide-based FRET experiments.

The non-polar, weakly H-bonding aromatic hydrocarbons pyrene and perylene mentioned above were not only used for double- but also as nucleobase analogs for multiple modified DNA duplexes. Along with other polycyclic aromatic systems such as terphenyl, benzo[*a*]pyrene, phenanthrenes and naphthalenes, some of them shown in Figure 2.18a, they were incorporated into different DNA systems, mainly by Kool and coworkers, to test the effects of chromophore surface area, electrostatics, polarizability and hydrophobicity on π-stacking in aqueous solution.[159]

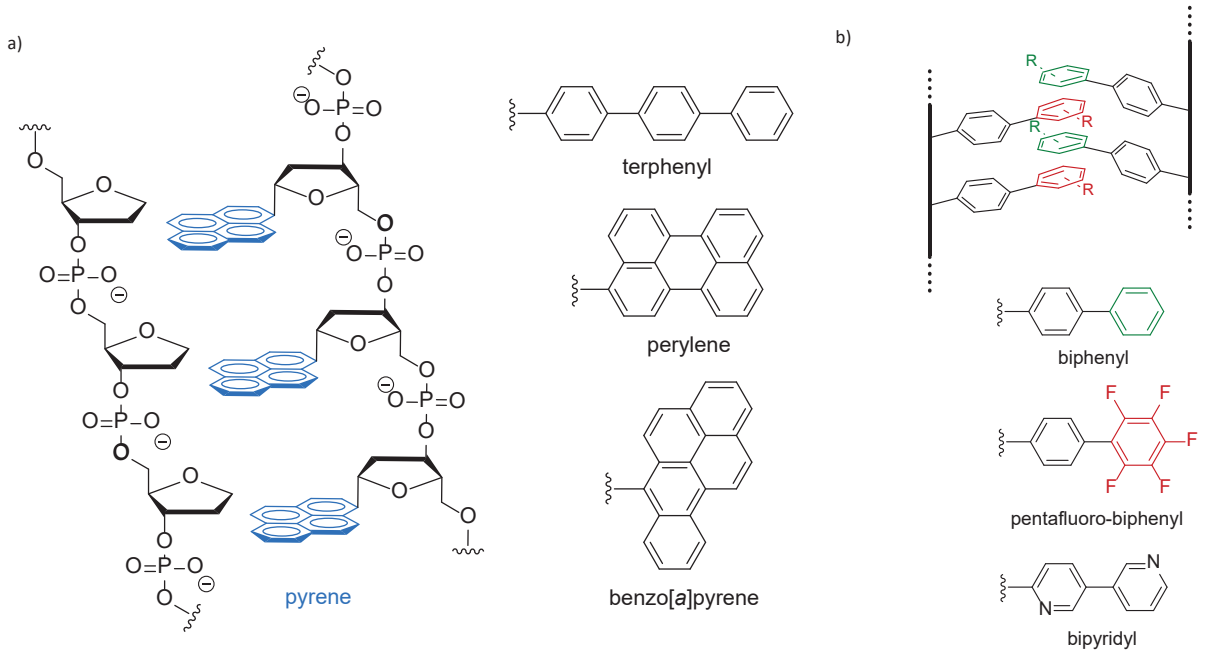

Figure 2.18: a) Structure of a duplex with chromophoric pyrene FNAs incorporated opposite abasic sites (left) and examples for different oligodeoxyfluoroside (ODF) chromophores established by Kool and coworkers (right).[199–201] b) Simplified representation of a biphenyl/pentafluoro-biphenyl modified duplex structure (top) and biaromatics used as chromophoric FNAs by Leumann *et al.* (bottom).[202]

In the first attempts using these chromophoric FNAs, more than 20% of the base pairs of a DNA duplex were replaced by pyrenes positioned opposite abasic sites; depending on the number of substitutions, this led to either a weak destabilization or in some cases even a slight stabilization of the DNA duplex.[203] Based on these findings, Kool *et al.* established a system of base-replacing chromophores, the so-called oligodeoxyfluorosides (ODFs), as molecular sensors. The aromatic fluorophores here are also attached to the anomeric position of deoxyribose, forming the monomeric fluorosides which can be converted into phosphoramidite building blocks and incorporated into oligonucleotides by solid phase synthesis. Libraries of up to 14,000 ODFs composed of four different aromatic nucleoside analog building blocks have been produced; although these remain single-stranded, the chromophores are stacked, leading to electronic interactions between the ground and the excited states which vary with

the oligonucleotide sequence. ODFs exhibit salient Stokes shifts of up to 200 nm, and are able to form numerous types of excimers, exciplexes and H-type dimers. Upon excitation with a single wavelength, multiple emission colors can be observed for these libraries, making ODFs useful tools with unusual sensing and highly efficient quenching properties for *in vivo* and *in vitro* applications.[199–201]

Similar to FNAs shown in the previous section (Figure 2.12) with spectral properties tuned by the attachment of either electron-donating or -withdrawing phenyl substituents, Leumann *et al.* incorporated biphenyl with variable functional groups, pentafluoro-biphenyl as well as bipyridyl scaffolds as chromophoric FNAs into DNA duplex structures (Figure 2.17b). Up to seven biphenyl and bipyridyl pairs were consecutively implemented into the DNA helix, showing a gradual increase of the duplex melting temperature in the case of the biphenyl and a thermal destabilization for the bipyridyl nucleobase. Both aromatic systems are characterized by efficient and selective self-recognition arising from the stacking of the distal rings in a zipper-like conformation without major distortion of the DNA backbone. In addition to the homooligomer formation also heterooligomers containing both pentafluoro-biphenyl and bipyridyl nucleobase analogs proved to be sufficiently stable which can be attributed to the dehydration of the aromatic rings in the stacked conformation.[202] This assumption was further supported by the formation of interstrand stacking motifs with biphenyl and pentafluoro-biphenyl FNAs incorporated opposite each other. Also here, the terminal rings are overlapped upon distortion of the bond connecting the two aromatic rings. This interaction was again attributed to aromatic dehydration while van der Waals dispersion forces and electrostatic interactions only play a minor role according to molecular dynamics (MD) simulations.[204] Leumann and coworkers were able to further fine-tune the electronic, spectroscopic and recognition properties of these self-recognizing building blocks by introducing modified biphenyl FNAs bearing π-donor and π-acceptor aromatic substituents. If for example an unsubstituted biphenyl moiety is placed opposite an amino-substituted one, clear electronic coupling between those two chromophores is observable, presumably due to charge transfer processes.[205,206] These different electronic and recognition properties might be favorable for the construction of a primitive genetic code as well as for applications as novel DNA nanomaterials.

The examples for multichromophore assemblies based on intercalating interactions shown so far are all composed of chromophoric FNAs. As already depicted in Figure 2.16a, also non-nucleosidic building blocks with the fluorophore directly attached to the DNA backbone are able to form assemblies by mutual intrastrand intercalation. The attachment of these nucleoside surrogates to the backbone can be achieved using different anchors, among them are carboxamide, threoninol, (*S*)-aminopropan-2,3-diol and glycerol linkers.[187]
The chiral (*S*)-aminopropan-2,3-diol linker was used by Asanuma and coworkers to introduce a variety of chromophores such as methyl and naphthyl red, azobenzenes and pyrenes.[207–209]

Upon sequential incorporation of methyl red into DNA strands, the formation of an H-aggregate with a narrow, blue-shifted absorption band and an intense exciton coupled CD signal was observed. As shown in Figure 2.19, methyl red was also incorporated with naphthyl red in an alternating manner to form heteroaggregates.

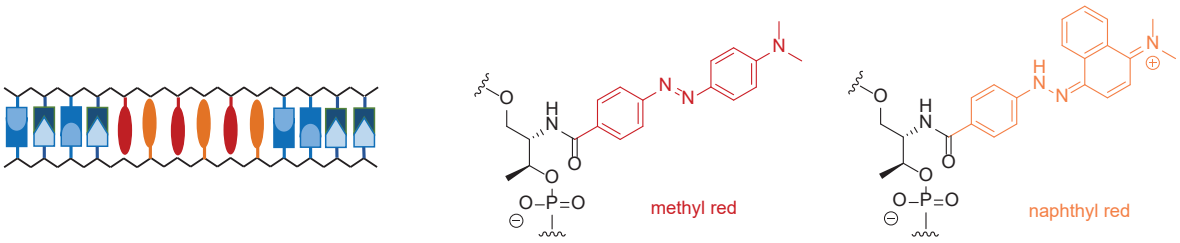

Figure 2.19: Graphical representation of a DNA duplex with methyl and naphthyl red incorporated in a consecutive, alternating manner (left) and molecular structure of the two chromophores tethered to an (*S*)-aminopropan-2,3-diol linker (right).[207–209]

Within the resulting stacked assemblies, up to six chromophores were installed consecutively. With spacer groups between the chromophores resembling abasic sites, positive and negative CD signals were induced by hybridization, which indicates the formation of a right-handed B-form-like helix. If these spacers were removed, no CD signals were observable. This finding can be attributed to unwinding of the duplex because of the high steric demand of the two fluorophores. However, although the helical structure is partially destroyed, its thermal stability is nearly unchanged, which shows that the chromophores remain stacked, enabled by the flexible (*S*)-aminopropan-2,3-diol linker. These DNA-dye conjugates are useful to develop novel materials and could be applicable as highly sensitive DNA probes, thanks to their nonlinear optical activity.[207–209]

In addition to the relatively small chromophores employed by Asanuma, a number of sterically more demanding fluorophores such as PBIs and pyrenes have been incorporated by direct linkage to the DNA backbone. The hereby obtained dye clusters can for instance be used to induce hybridization and dimerization of two duplex structures when attached to the 5'-end of a DNA helix or as probes for the detection of one-base deletions, just to name a few possible applications.[210,211]

Covalent assembly by stacking in the groove

Besides chromophores interacting by intercalation, stacking in the helical groove is a common type of assembly, especially for extended FNAs. The advantage of these extended FNAs, as mentioned before, is their retained ability to form Watson-Crick base pairs since the chromophore moiety is in most cases attached to the 5-position of pyrimidines, the 7-position of 7-deazapurines or the 8-position of purines by a simple C-C bond or by conjugated linkers.

One example for the first case mentioned are di- and tetraphenylporphyrins linked to dU and incorporated into DNA oligonucleotides, forming zipper-like DNA-chromophore hybrids with up to eleven chromophores (Figure 2.20). To minimize their conformational energy, the porphyrins are already helically stacked in the single-stranded state. Upon hybridization with another modified DNA strand, the chromophore stack is desolvated, located in the helix major groove and substantially stabilized by hydrophobic chromophore-chromophore interactions. The resulting duplex is characterized by a two-step melting behavior, with one melting temperature belonging to the melting of the duplex and the other to the unwinding of the porphyrin stack.[166,212,213]

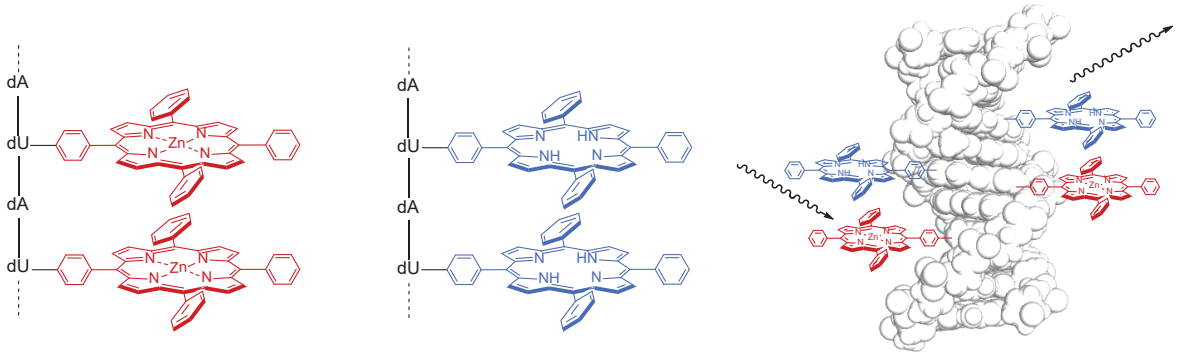

Figure 2.20: DNA single strands equipped with multiple metalated (red) and free (blue) tetraphenylporphyrins can form duplex structures stabilized by hydrophobic chromophore-chromophore interactions. Due to charge transfer between the two porphyrin variants, the fluorescence of the metalated ring system is quenched while the free ring systems remain emissive.[213]

If porphyrins are incorporated adjacent to each other, highly ordered structures are obtained in which the ground and excited states of each chromophore are influenced by the neighboring porphyrin ring. Further tuning of the spectroscopic properties was achieved by metalation of one single-strand with Zn(II), leading to mixed metalated and free-base porphyrin arrays. Due to energy transfer between these two moieties, the fluorescence of the Zn(II)-containing porphyrin was strongly quenched. These well-defined, long arrays are theoretically not restricted in the length of the porphyrin stack, providing access to potent photonic wires and light-harvesting antennae.[213]

The direct attachment of chromophores to the DNA backbone by C-C bonds leads to electronic coupling between the chromophore and the nucleobase, which has not only been used for the formation of porphyrin clusters but also served as the basis for the covalent arrangement of oligochromophoric structures. Wagenknecht *et al.* incorporated multiple dU nucleosides with a pyrene chromophore attached to the 5-position into DNA strands; by the introduction of up to five adjacent pyrenes, these assembled into a right-handed helical π-array in the major groove of the duplex and showed exciplex formation with an intense red-shifted emission band at 475 nm and a positive exciton-coupled CD signal.[214] The same chromophore was later tethered to dU

by the longer acetylene linker to give Py-dU (Figure 2.21), leading to improved chromophore-chromophore interactions. This blue emitting Py-dU building block was incorporated together with the perylene-based green-emitting Pe-dU and the red-emitting Nile red building block Nr-dU into DNA oligonucleotides. By combination of these three chromophores, DNA-based nanoarchitectures with distinct electronic and spectroscopic properties were obtained.[215]

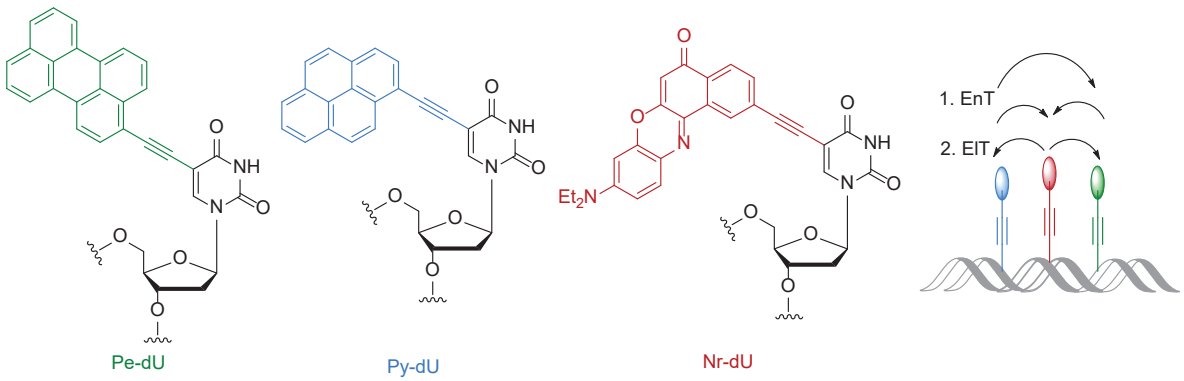

Figure 2.21: Perylene-, pyrene- and Nile red-based DNA building blocks Pe-dU, Py-dU and Nr-dU were incorporated into one DNA duplex. By excitation with light of a single wavelength, an energy (EnT) and electron (EIT) transfer cascade was observed, leading to the formation of charge-separated states. The direction of the energy transfer is indicated by black arrows.[215]

Excitation of the triple-modified DNA helix with any wavelength in the range of 350 to 700 nm triggered an energy transfer (EnT) cascade from Py-dU over Pe-dU to Nr-dU and subsequent electron transfer (EIT) in the opposite direction from Nr-dU to Py-dU and Pe-dU. Hereby, charge-separated states emerged, tunable by the distance between the chromophores. Charge separation is a desirable feature for the design of light-harvesting systems and photocatalysts, making these ordered DNA-dye scaffolds beneficial for further physicochemical applications.[215] Thanks to their convenient fluorescent properties, pyrenes and also phenanthrenes are among the most widely-used chromophores for multichromophore assemblies. Thus, their derivatives have also been applied for the DNA backbone assembly of fluorophores as shown in Figure 2.16c.

Covalent assembly by backbone-implemented chromophores

If fluorophores are meant to be directly implemented into the backbone structure, two linkers need to be installed on the chromophoric ring system. Prominent examples for this type of building blocks were described by Häner *et al.* who used carboxamide linkers to covalently tether a series of base surrogates based on pyrene,[216] phenanthrene[217,218] and phenanthrolines[219] to a DNA oligonucleotide (Figure 2.22). All of these aromatic systems noticeably increased the duplex melting temperature when placed opposite an abasic site by stacking between the polyaromatic rings and the adjacent base pairs. In addition, the incorporation of up to seven phenanthrene units into a DNA 21mer led to an only small

reduction of the thermal stability and from the lengthening of the duplex structure interactions between the phenanthrenes by intrastrand stacking were predicted.

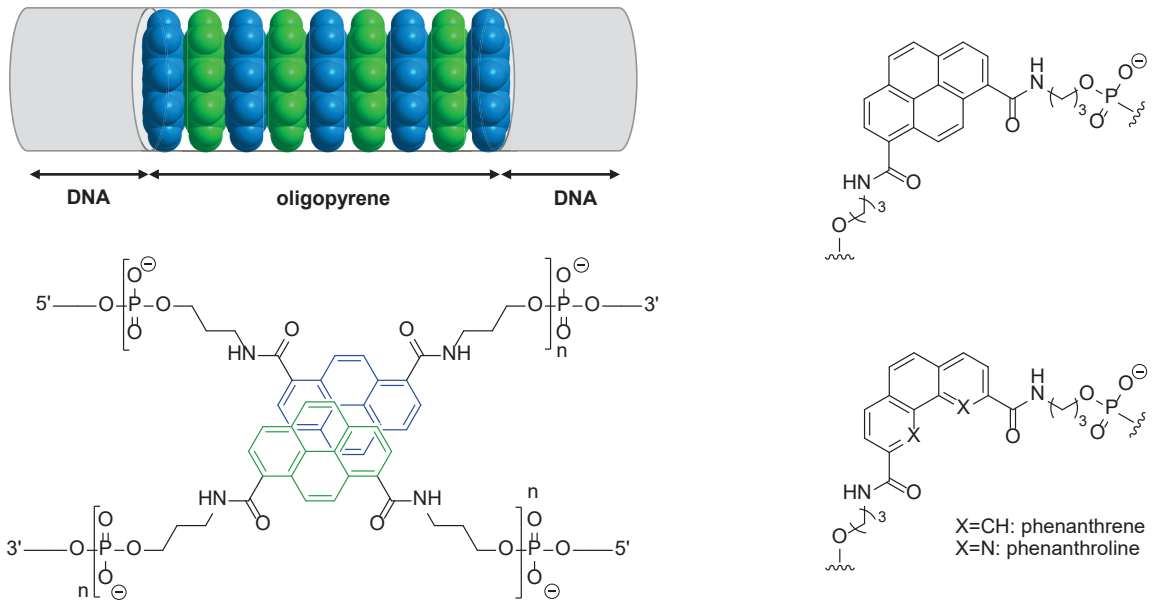

Figure 2.22: Oligopyrene stacks were implemented in the core of a DNA duplex; the pyrene chromophores of the two single-strands are colored blue and green, respectively.[220] On the right side, chromophores for similar foldamer structures are shown.[216–219]

Later, self-organizing dsDNA systems with up to 14 pyrenes stacked in the duplex were synthesized (Figure 2.22, left). The presumed existence of intra- and interstrand chromophore-chromophore stacking interactions within the helical structure was further supported by the observation of two melting transitions and the formation of excimers, leading to broadened absorption spectra. The long oligopyrene foldamer stacks are orientated in a right-handed helical fashion which is caused by chirality transfer from the DNA helix and was proven by exciton-coupled CD experiments. Since the formed foldamers are considered to be dynamic, their structure is susceptible to external influences such as temperature and salt concentration, leading to oligomeric systems with easily adjustable properties for various applications.[220]

Although covalently attached chromophores provide access to highly ordered, well-defined and stable structures, they are sometimes not suitable for a desired application. Instead, non-covalent DNA-templated self assembly offers an alternative to reversibly organize small fluorescent molecules in structured arrays. The underlaying interactions as well as some examples for fluorophores non-covalently bound to nucleic acids are reviewed in the next section.

2.4.1.2 Non-covalent DNA-based multichromophore assemblies

Non-covalent binding interactions include hydrogen bonding, electrostatic forces, van der Waals forces and hydrophobic effects; all of these are critical for many biological functions although they are generally weaker compared to covalent bonds and are often transient.[187]

However, less complicated synthetic steps are necessary to obtain the required building blocks. DNA serves as an attractive template for the non-covalent binding of small molecules, among them fluorophores, since it provides water-solubility and a programmable structure as well as a high information density to encode data for potential storage. To obtain a selective and directed assembly of fluorophores on the DNA scaffold, interactions by either intercalation, groove binding or recognition by hydrogen bonding play an important role. In the following some examples of non-covalent multichromophore assemblies templated by DNA structures are discussed.

Non-covalent DNA-multichromophore assemblies by intercalation and groove binding

Intercalation in the core of DNA duplex structures is typical for chromophores with planar, cationic rings and results in expansion of the helix along its main axis. Electrostatic interactions between the intercalating molecules and the DNA nucleobases are crucial for the stabilization of these systems, primarily to overcome the stability loss by the formation of a binding pocket by two adjacent base pairs. Here, typical binding constants are in a range between 10^3 and 10^7 M. dsDNA exhibits multiple binding sites for poly-intercalation, which in general occurs as a multi-step process in a non-cooperative manner.[196] Poly-intercalation was for example used by Armitage and coworkers in developing a multichromophore system similar to phycobiliproteins found in photosynthetic cyanobacteria. Here, multiple bilin chromophores are encapsulated in the protein matrix, leading to efficient light-harvesting and energy transfer to the reaction center of the protein.[221]

Using this protein complex as a model, the fluorescent intercalating oxazole yellow dyes YOYO-1 and YO-PRO-1 (Figure 2.23a), which are a mono- and a bisintercalator, respectively, were assembled on linear and branched DNA templates, for example two-way junctions (2WJ) and three-way junctions (3WJ) as well as 3D DNA-tetrahedrons. Both chromophores are basically non-fluorescent in solution, but upon intercalation into DNA, YOYO-1 shows a quantum yield of 0.52 and YO-PRO-1 of 0.44. By frequent intercalation of either of these two fluorophores, a high chromophore density can be achieved, leading to brightly fluorescent systems with molar extinction coefficients ϵ in the order of 10^6 M^{-1} cm^{-1}.[222,223]
Due to separation of the two oxazole yellow dyes within the formed non-covalent assemblies by around 7 Å from each other, self-quenching events are prevented. The two described systems based on oxazole yellow chromophores exhibit favorable light-harvesting properties and, upon combination with a FRET acceptor covalently attached to the DNA scaffold, tunable wavelengths with red-shifted emission. Since both of these non-covalent multichromophore assemblies show a light absorbance efficiency which is more than 10-fold enhanced compared to the single chromophore in solution, they provide effective labels for confocal microscopy.[222,223]

DNA scaffolds with YOYO-1 or YO-PRO-1 as intercalators are furthermore suitable tools for flow cytometry since labeling of mouse T-cells can be achieved upon biotinylation of the intercalated systems.[222]

However, not only intercalation but also binding to the groove of nucleic acid structures is a common assembly mode for small molecules. Cationic dyes are normally bound to the minor groove, following the helical twist and stabilized by electrostatic interactions with the phosphate backbone. Binding to the DNA major groove is rare for small molecules but more common for proteins, peptides or other oligoucleotides through hydrogen bonding to the Hoogsteen faces of the nucleobases. Groove binding of fluorophores is most widely found for cyanine dyes which leads to the formation of photonic wires with long-range energy transfer properties.[187]

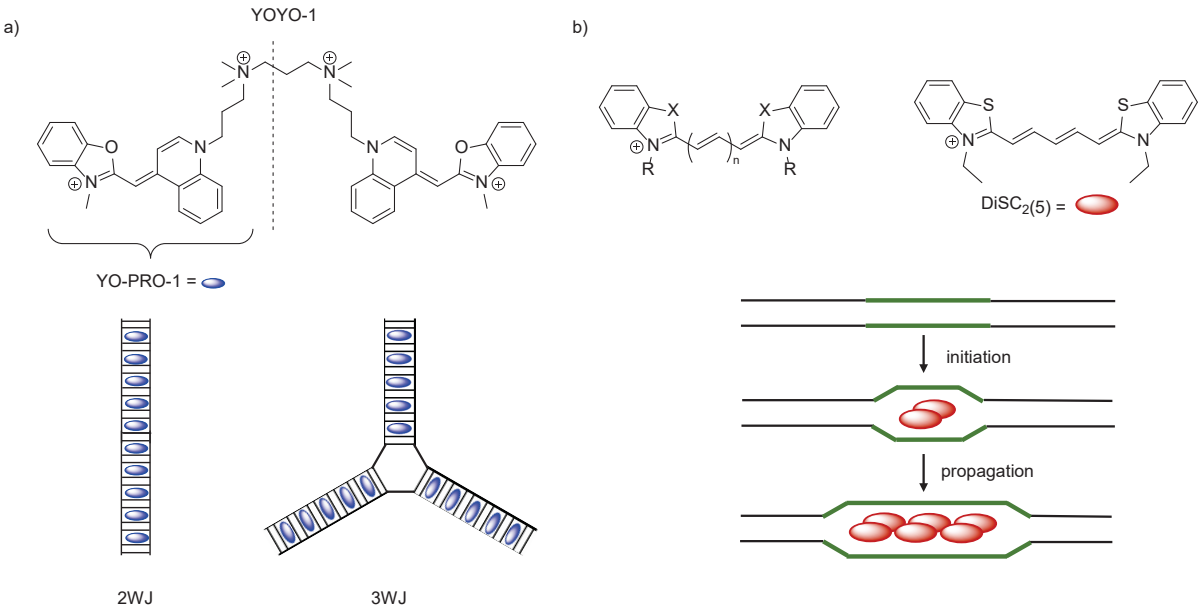

Figure 2.23: Fluorophores can be assembled on DNA templates by intercalation or minor groove binding. a) Intercalation of the oxazole yellow dyes YOYO-1 and YO-PRO-1 into two-way and three-way junctions (2WJ and 3WJ).[222,223] b) General structure of symmetric benzothiazole cyanine dyes, structure of $DiSC_2(5)$ used by Armitage and its cooperative dimerization in the minor groove. Green lines represent regions of alternating A/T pairs.[224–226]

One example of the non-covalent assmebly of cyanine chromophores in the groove was reported by Armitage *et al.*, who studied the spontaneous assemblies of some symmetrical cationic cyanine dyes, most importantly 3,3'-diethylthiadicarbocyanine ($DiSC_2(5)$, Figure 2.23b), in the minor groove of DNA templates, forming J-type aggregates. The $DiSC_2(5)$ chromophores assembled to face-to-face dimers in the presence of alternating A/T and I/C pairs, indicated by a shift of the absorption maximum from 647 nm for the monomeric dye to 590 nm, an exciton splitting observable by CD and a strongly quenched fluorescence. This dimerization induced a cooperative aggregation process of multiple dimers, with the spatial dimensions of the formed assemblies controlled by the DNA template.[224–226] In further studies, a tricationic variant of

$DiSC_2(5)$ was assembled in the DNA minor groove to either H- or J-type aggregates.[227] In this case, it was possible to control the aggregation mode by external parameters such as the length of the DNA template, the dye concentration, the temperature and the ionic strength, providing access to assemblies with easily tunable spectroscopic properties.

An extensively used method to assemble chromophores on DNA templates is to make advantage of their intrinsic recognition mechanism based on the Watson Crick and Hoogsteen H-bonding properties of canonical nucleobases. Figure 2.24 shows some examples employing this technique for different fluorophores.

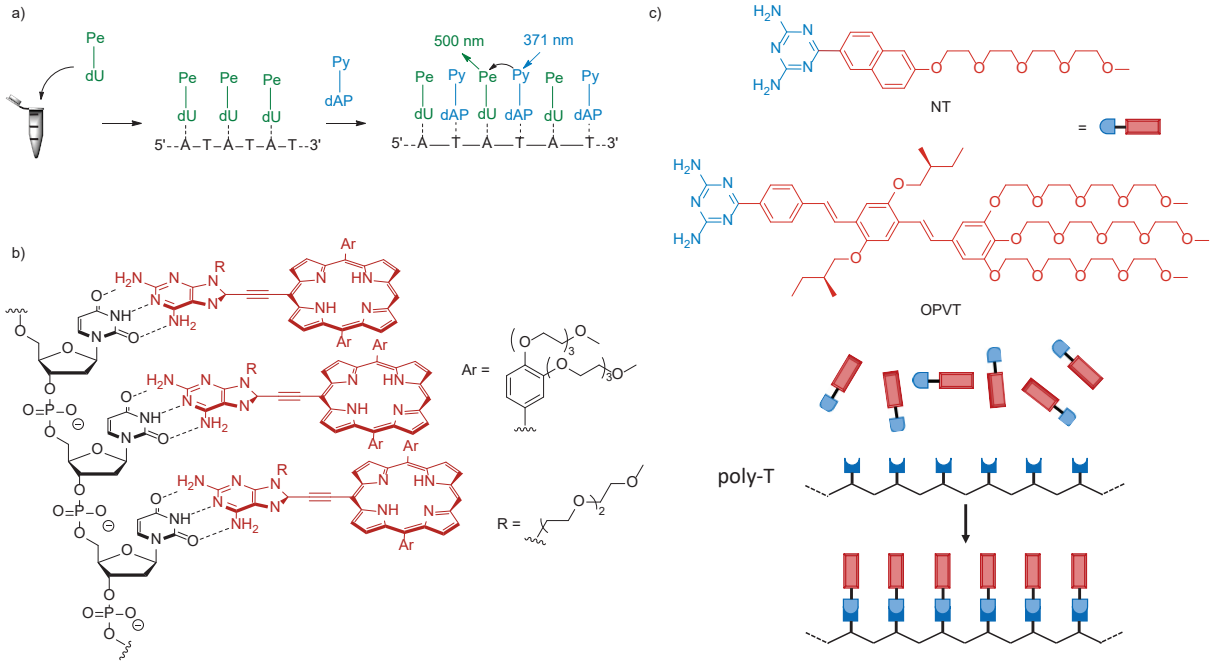

Figure 2.24: Non-covalent multichromophore assembly on ssDNA is often achieved by hydrogen bonds between the respective chromophores and the canonical nucleobases. In a), perylene- and pyrene-derived expanded FNAs are assembled on A-T templates for efficient energy transfer.[228] b) shows the formation of non-covalently bound porphyrin nanoladders[229] and in c) the precise arrangement of naphthalene (NT)- and oligo(*p*-phenylene)vinylene (OPVT)-based fluorophores on poly-T templates is illustrated.[230]

Self-assembly of fluorophores by hydrogen bonding on a DNA template allows the construction of precise chromophore arrays. These are in most cases arranged in single- or double-zipper structures, with the guest molecule providing either one or two sites for base pairing with ssDNA. Most frequently, artificial nucleobases with an increased number of hydrogen bonding sites are used for this method to expand the assembly capacity and to permit orthogonal binding if different guest molecules are present.

The mentioned single-zipper approach was for example used by Wagenknecht *et al.* to assemble the previously mentioned expanded FNAs Pe-dU and Py-dAP with a perylene or pyrene chromophore, respectively, as donor and acceptor pairs on ssDNA with mixed A-T sequences

(Figure 2.24a).[228,231] By careful design of the single-stranded templates, it was possible to control the energy transfer between these two chromophores by the oligonucleotide sequence. In the mixed assemblies, absorption maxima at 383 nm and 497 nm belonging to both Py-dAP and Pe-dU were observed while fluorescence emission maxima were only detected at 502 and 536 nm, which was attributed to perylene fluorescence emission. The fluorescence intensity of the assembled mixtures increased from $A_{10}T_{10}$ over $(AATT)_5$ to $(AT)_{10}$, emphasizing the programmability of chromophore aggregation and its potential for fluorescence readout. These observations are in contrast to previous ones on the self-assembly of Py-dAP and the Nile red derivative Nr-dU, leading to fluorescence quenching instead of enhancement by energy transfer.[232,233] The possibility to affect the energy transfer and therefore light-harvesting properties by the template sequence context makes the described multichromophore systems promising candidates in materials science and nanoelectronics, for example for the design of solar cells.[234]

However, not only planar polyaromatic chromophores have been used for non-covalent assembly on ssDNA but also heteroaromatic systems such as porphyrins (Figure 2.24b).[229,235] Balaz and coworkers designed porphyrin nanoladders based on the helical organization of substituted diphenyl porphyrins on dT_{40} templates by directional hydrogen bonding. Successful assembly was verified by spectroscopic measurements, most importantly CD spectroscopy. What makes this system stand out from all other known ones is that the handedness of the assembly can be influenced by the conditions during sample preparation: dependent on the annealing rate, the presence of sodium chloride and the template:guest ratio, either left-or right-handed helices are formed, making these systems well suited for several applications in electronics.[229]

Single-stranded oligonucleotide templates have also been applied for dynamic and reversible polymerization reactions of chromophores, mainly by Schenning and coworkers who used naphthalene (NT)- and π-conjugated oligo(*p*-phenylene)vinylene (OPVT)-based fluorophores with appended polyethylene glycol linkers for better solubility. Here, many differently designed systems with various base pairing patterns and template lengths have been developed and studied extensively.[230,236–241] One early example is shown in Figure 2.24c where NT and OPVT are both equipped with a diaminotriazine moiety which is able to assemble on poly-T strands by hydrogen bonding in a nucleation growth mechanism. The arising right-handed helical structures are further stabilized by π-π-stacking and hydrophobic interactions between adjacent chromophores.[230] Similar NT and OPVT chromophores have later been used for the development of more elaborated systems for example by encapsulation into virus protein nanotubes,[242] the assembly on PNA instead of DNA templates[243] and the formation of chromophore stacks for energy transfer to covalently bound cyanine dyes.[244]

In conclusion, numerous techniques employing either covalent or non-covalent multichro-

mophore assemblies on DNA have been described leading to a broad range of artificial systems with unusual spectroscopic characteristics. Especially their capacity for light-harvesting and the substantial fluorescence intensity enhancement make DNA-based multichromophore assemblies promising candidates for electronics and novel functional materials. However, it often remains challenging to predict the photophysical properties of newly designed DNA-chromophore hybrids. Thus, a deeper understanding of the underlaying electronic processes by mechanistic studies and theoretical calculations might be helpful for the design of future multichromophore arrays, also for further improvement of already known systems. As discussed in this section, the precise arrangement of chromophores often leads to a fluorescence turn-on compared to the monomer. A similar luminescence enhancement can be achieved by other methods, in particular non-covalent binding of specifically designed fluorogenes to RNA aptamers. In the following section, some selected fluorogenic aptamers with their respective chromophores will be discussed. The main focus of this section will be on the Chili aptamer for which novel chromophores with altered electronic and steric properties were synthesized in the course of this thesis.

2.5 Fluorogenic RNA aptamers

For a long time, the evolution of fluorescent probes for cellular imaging applications has been a major goal in biochemistry. The starting point for the development of a diverse fluorescent protein toolbox was the discovery of the green fluorescent protein (GFP) from the jellyfish *Aequorea victoria*. This naturally occurring protein exhibits luminescence by an autocatalytic cyclization of the three amino acids serine, tyrosine and glycine; the resulting emissive structure is rigidified and located in the center of an 11-sheet β-barrel.[245] Since less than 3% of the human genome is translated into proteins while a much larger fraction is transcribed into RNA, it was desirable to not only have access to fluorescent proteins but also to RNA.[246] However, no naturally fluorescent RNA has been discovered so far. Nonetheless, systematic evolution of ligands by exponential enrichment (SELEX) allowed the identification of a variety of fluorogenic RNA aptamers and their cognate ligands.[247] The advantage of fluorogenic in contrast to fluorescent chromophores is the reduced background emission since fluorogenic dyes are non-emissive when free in solution but light up when bound by an aptamer. This fluorescence enhancement can be achieved by different activation mechanisms: either by twisted intramolecular charge transfer (TICT) where the rotational freedom of the two heterocyclic rings is decreased, by excited state proton transfer (ESPT) or by intramolecular quenching (IQ) if both fluorophore and quencher are present in one molecule.[248] The first fluorogenic RNA aptamer developed was the Malachite-green aptamer;[249] since then, a huge number of fluorogenic RNA-aptamer/chromophore systems with emission wavelengths covering the whole visible spectrum have been described.[250] A selection of these systems is illustrated in Figure 2.25 and briefly discussed in the following.

2.5.1 Important light-up RNA aptamers

After the discovery of the Malachite-green aptamer, in 2011 Jaffrey *et al.* were able to isolate and characterize a number of new fluorogenic aptamers.[251] All of the cognate chromophores were based on the 4-(4-hydroxybenzylidene)-1*H*-imidazol-5-(4*H*)-one (HBI) chromophore found in native GFP, which is non-fluorescent in solution due to a non-radiative energy dissipation pathway by intermolecular rotation. Among these biomimetic fluorogens, 3,5-difluoro-4-hydroxybenzylidene imidazolinone (DFHBI) was the brightest one, emitting green fluorescence at 501 nm with a quantum yield of 0.74; its 98 nt long activating aptamer was called Spinach in analogy to the fruit nomenclature for fluorescent proteins.

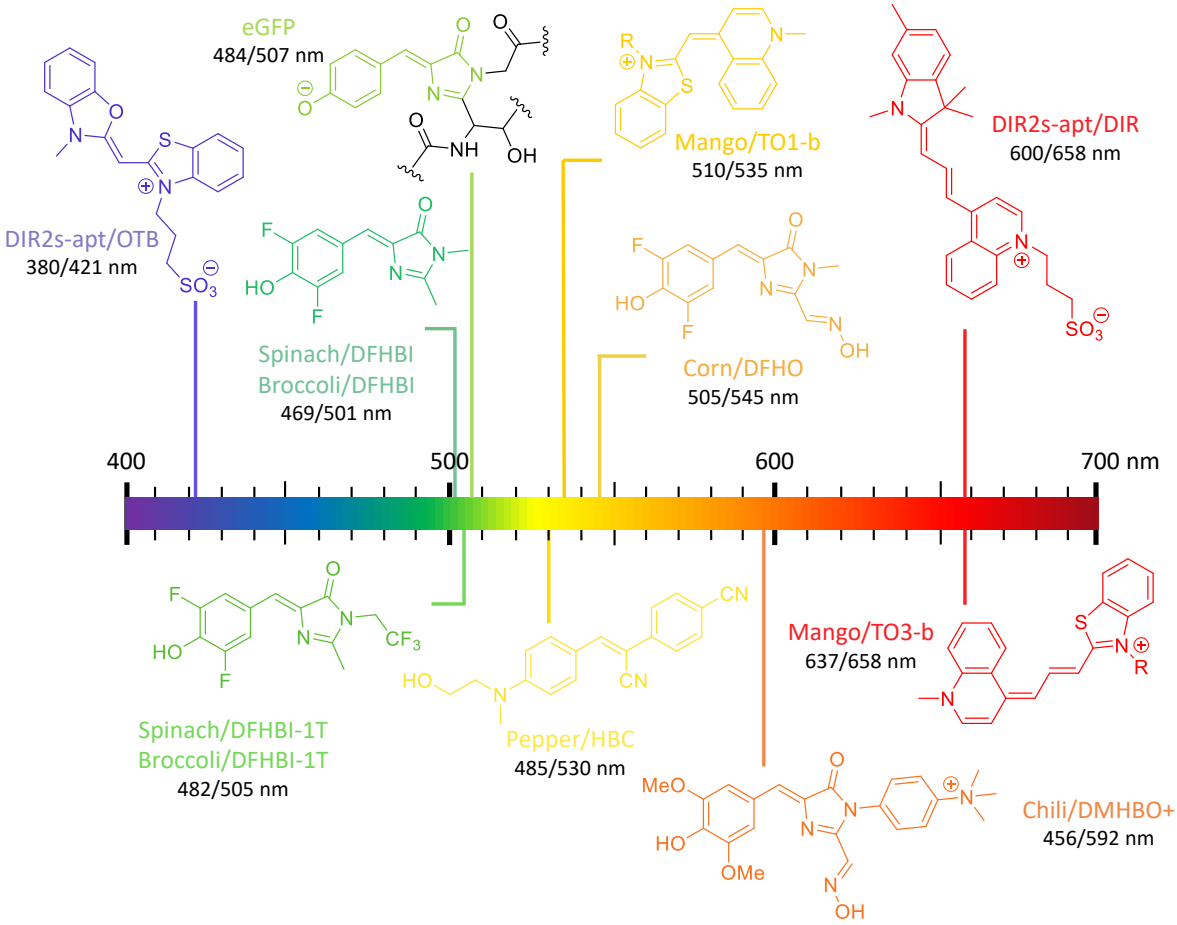

Figure 2.25: Overview of the wildtype GFP chromophore and several fluorophores for selected fluorogenic RNA aptamers. The name of the aptamers and their cognate chromophores as well as the respective excitation and emission wavelengths are given. Figure adapted from reference [250] and corrected.

According to the crystal structure, the fluorescence turn-on of DFHBI is supported by a G-quadruplex within the aptamer structure, which restrains the two chromophore ring systems in one plane and inhibits fluorescence deactivation by energy loss through tortional motion around the ring-connecting bond.[252,253] The Spinach/DFHBI system was improved by further *in vitro* and *in vivo* selections with the evolution of the 49 nt Broccoli aptamer and the new

trifluoromethyl-substituted ligand DFHBI-1T, which exhibits a bathochromic shift of 13 nm in the excitation and 4 nm in the emission compared to its parent system.[254]
With the goal to enhance the photostability by higher H-bonding capacity, the DFHBI ligand was further developed into the DsRed mimicking chromophore 3,5-difluoro-4-hydroxybenzylidene imidazolinone-2-oxime (DFHO) with an additional oxime moiety. DFHO can be activated by the Corn aptamer and shows an almost 1000-fold enhanced photostability compared to Spinach as well as a red-shifted emission wavelength of 545 nm.[255] Surprisingly, the crystal structure revealed that Corn is a homodimer where DFHO binds to the interpromoter face in a coplanar conformation.[256]
Independently, the Chili aptamer was developed by truncation and optimization of the 3,5-dimethoxy-4-hydroxybenzylidene imidazolinone (DMHBI)-binding 13-2 aptamer,[251] giving access to a broad spectral emission range and showing with around 130 nm the largest Stokes shifts reported so far for fluorogenic RNA aptamers.[257,258] Its cognate ligands $DMHBI^+$ and 3,5-dimethoxy-4-hydroxybenzyli-dene imidazolinone-2-oxime ($DMHBO^+$) are characterized by extended aromatic systems and additional cationic substituents compared to the inital HBI chromophore.[257] Fluorescence activation with the Chili aptamer again relies on the presence of a G-quartet; the structure and spectroscopic properties of this system will be discussed in more detail in sections 2.5.2 and 3.7.1.[259]

An alternative approach with a G-quadruplex as structurally important component for fluorescence activation was the development of the Mango aptamer. Mango selectively encloses the thiazole orange (TO) derived chromophores TO1-b and TO3-b, with the latter one emitting strongly red-shifted fluorescence at 658 nm.[260] However, Mango only displays a modest quantum yield of 0.14 which is attributed to the chromophore structure in the bound state since the two aromatic ring systems are not coplanar but instead are arranged in an angle of 45° with respect to each other.[261] Reselection of Mango led to additional variants of this aptamer with improved brightness.[262,263]
Only recently, the new Pepper aptamer was selected, which enhances the fluorescence of its highly photoresistant ligand (4-((2-hydroxyethyl)(methyl)amino)-benzylidene)-cyanophenylacetonitrile (HBC) up to 3000-fold upon binding. By the introduction of different heteroatomic substituents to the chromophore structure or expansion of the aromatic π-system, the spectral properties of the Pepper/HBC system were tuned over a large part of the visible spectrum.[264]
This year, also the crystal structure of Pepper has been solved and revealed a fluorescence activation mechanism independent from the presence of a G-quadruplex. The near-planar HBC fluorophore here is intercalated between one non-G-quadruplex base quadruple and one G-U wobble base pair while the ligand-recognition pocket tolerates specific modifications of HBC, giving rise to higher affinity or broader spectral properties.[265]
Besides the many described fluorogenic RNA aptamers containing G-quadruplexes, also other aptamers with difference mechanisms leading to fluorescence enhancement are known. One of

these is the DIR2s aptamer which either activates the oxazole thiazole blue (OTB) or dimethyl indole red (DIR) chromophore, inducing fluorescence emission at the blue and the red edge of the visible spectrum, respectively.[266] Here, the ligands are bound to a two-tiered stack of base triplets and an upaired A, restricting rotational freedom.[267]

In summary, the development of fluorogenic RNA aptamers provides access to brightly emitting systems with excitation and emission wavelengths spanning the whole visible spectrum. This diversity results from the combination of many structurally different chromophores selectively bound by RNAs and can be further optimized by additional *in vitro* and *in vivo* selection steps. Fluorogenic RNA aptamers are useful as fluorescent sensors, especially for super-resolution imaging of RNA complexes in cells to reveal spatial and dynamic aspects of the genome. In future it is desirable to further expand the fluorogenic aptamer toolbox by developing RNA aptamer/chromophore complexes with additional photoactivatable, photoconvertible and photoswitchable properties.

2.5.2 Chili - a multicolor fluorogenic RNA aptamer with a exceptional Stokes shift

As mentioned in the last section, the 52 nt Chili aptamer mimics large Stokes shift fluorescent proteins, for example LSSmOrange[268] and LSSmKate.[269] In contrast to Spinach, Chili exclusively recognizes the protonated phenol-form of various HBI-derived chromophores but enhances green and red fluorescence of the deprotonated phenolate form. The two ligands with the most remarkable fluorescence properties, $DMHBI^+$ and $DMHBO^+$, are characterized by a cationic side chain which increases RNA affinity, minimizes Mg^{2+}-dependency and enhances fluorescence brightness. With the latter chromophore, a low nanomolar binding constant along with red-shifted emission at 592 nm was observed, promoting FRET-pair formation with the rhodamine acceptor dye Atto 590 or the fluorescent FNA 4-cyanoindole.[257,270]
In Figure 2.26, the sequence as well as the secondary and the crystal structure of the Chili aptamer in complex with $DMHBO^+$ are shown. Chili exhibits a G-rich fluorophore binding domain (FBD) marked in green, which is connected to the two base paired regions P1 (purple) and P2 (red) by a small loop region L2 (blue). Its structure when bound to either $DMHBO^+$ or $DMHBI^+$ was solved at a resolution of 2.25 and 2.95 Å, respectively. Within the aptamer core, the chromophores are stabilized and immobilized in a rigid conformation by stacking to a G-quadruplex. Unlike other HBI-activating chromophores, the ligand here obtains a twisted instead of a coplanar conformation in the bound state. In addition, the fluorophore binding site is distinct from previously described fluorogenic RNA aptamer systems: by a hydrogen bond between the phenolic hydroxy group of the chromphore and the Hoogsteen edge at the N7-nitrogen of G15, the protonation state of the chromophore is controlled in response to excitation, leading to ESPT on a 100 fs-scale which is much faster than in wildtype-GFP.[259]

The role of the N7 of G15 as a proton acceptor was further confirmed by atomic mutagenesis experiments. In addition, the central K^+ bound to the G-quadruplex contributes to the orientation and stabilization of the fluorogenic ligands; it can be replaced by Tl^+ with retained spectroscopic properties but not that easily by divalent cations.[259]

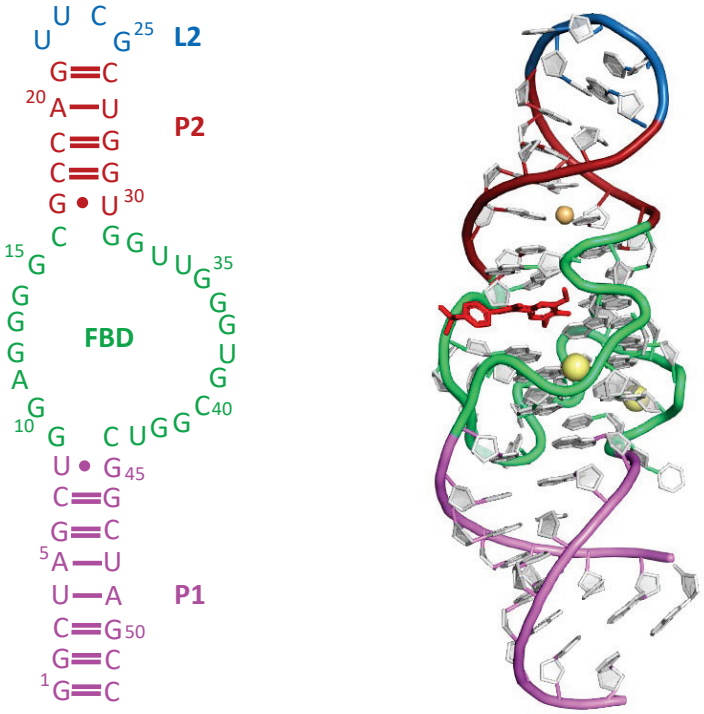

Figure 2.26: On the left side, the sequence and the secondary structure of the Chili aptamer are illustrated. P stands for the paired regions, L for the loop region and FBD for the fluorophore binding domain. On the right side, the crystal structure of the Chili-DMHBO$^+$ complex is depicted (PDB: 7OAX, 2.25 Å resolution). The sequence color code is the same in both figures, the bound ligand is shown in red and the yellow and orange spheres represent potassium and iridium cations, respectively.[259]

Thanks to its unique spectroscopic properties such as the large Stokes shift, Chili is a promising candidate for future *in vitro* and live cell imaging applications. In addition, its performance was further tuned by simple variations of the chromophore structure, such as the introduction of additional heteroatoms or the expansion of the aromatic ring system. In the course of this thesis, attempts to design and synthesize such novel ligands will be described in section 3.7, which might give rise to new photoswitchable fluorogenic RNA aptamer systems with desirable environment-dependent fluorescence characteristics.

Overall, the development of emissive nucleic acid structures by either incorporation of fluorescent nucleoside analogs or fluorescence activation of chromophores by fluorogenic RNA aptamers is a huge research field, providing access to many sophisticated *in vitro* and *in vivo* labeling methods as well as a plethora of other applications to shed light on the structure and function of nucleic acids in the genome. Within this thesis, new fluorescent merocyanine

building blocks with either RNA, DNA or GNA backbones were synthesized, incorporated into oligonucleotides and characterized with respect to their spectroscopic properties in single-, double- and also multichromophoric arrays. Furthermore, new HBI-derived chromophores with an additional amino group for further functionalization were developed, their emission properties in complex with the Chili aptamer were evaluated and compared to reported fluorogenic RNA aptamer systems.

Chapter 3

Results and Discussion

This chapter provides an overview over all the results obtained in the course of this thesis. The chemical synthesis of several free merocyanine chromophores, their conversion into phosphoramidites with different backbones as well as their incorporation into oligonucleotides by solid phase synthesis will be discussed. In addition, the spectroscopic and thermodynamic characterization of the obtained single, double and multiple modified oligonucleotides will be described. Included is also the progress in elucidating the constitution of formed merocyanine dimeric structures by enzymatic and spectroscopic approaches as well as MD simulations and nucleic acid NMR experiments. The final part of this chapter deals with the synthesis of novel HBI-derived chromophores as well as the examination of their fluorescent properties in complex with the fluorogenic Chili RNA aptamer.

3.1 Synthesis and spectroscopy of merocyanines

Cyanine dyes, also called polymethine dyes, are one of the most important classes of chromophores; during the last century they gained more and more importance in different scientific fields with a broad palette of applications such as in laser[271] and solar technology.[272] Especially in the last two decades cyanines became popular as fluorescent labels for proteins and nucleic acids.[273]

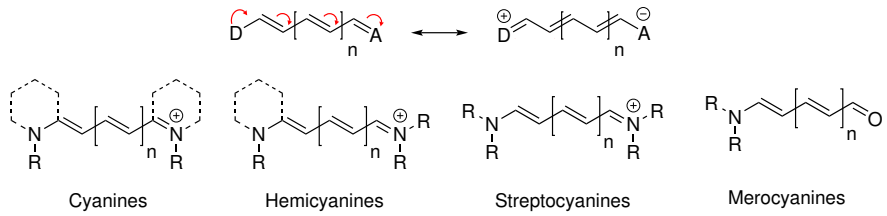

Figure 3.1: Cyanines are push-pull chromophores, consisting of an electron-donor D and an electron-acceptor A connected by a polymethine linker with the variable length of n (top). Cyanine chromophores can be divided into different subclasses, depending on their structural constitution and charge (bottom). R is a variable substituent and the dashed ring indicates a nitrogen-containing heterocycle such as indole, oxazole or benzothiazole.

Cyanines are composed of an electron-donating and an electron-withdrawing group connected

by a conjugated polymethine linker, leading to the formation of a push-pull chromophoric system.[274] Depending on their structure and overall charge, cyanine dyes can be divided into different categories with cationic cyanines including hemicyanines and streptocyanines and neutral cyanine dyes such as merocyanines being the most important ones (Figure 3.1). The classification of these chromophores is based on the nature of the donor and acceptor groups: cyanines, hemicyanines and streptocyanines comprise a nitrogen-containing donor as well as acceptor group of which either two, one or none is embedded in a heteroaromatic systems. Meanwhile, in uncharged merocyanines the acceptor part does not necessarily include a nitrogen which is part of the conjugated system, thereby providing access to a number of differently constituted acceptor moieties including carbonyl or thiocarbonyl groups. This structural variability gives rise to a multitude of possible merocyanine scaffolds with tunable properties, making this class of chromophores suitable for the covalent modification of oligonucleotides as done in the course of this thesis.

3.1.1 General synthetic approaches toward merocyanines

Synthetic approaches toward merocyanine chromophores, characterized by an even number of π-electrons and an odd number of π-center groups, are in general dependent on the length of the polymethine linker.[275] Here, only synthetic routes toward merocyanines with a two-carbon bridge will be described since these compounds were mainly used within this thesis.
The classical route for the synthesis of these asymmetric cyanine dyes bridged by two carbons is a condensation of a heterocyclic enamine or its corresponding salt with hydroxybenzaldehyde or derivatives (Scheme 3.1a); it has for example been applied in the reported synthesis of coumarin- and hydroxyquinoline-derived merocyanines.[276,277]
However, in some cases it is suitable to transfer the formyl group to the nitrogen containing moiety, especially if the required heterocyclic aldehydes are difficult to obtain. The condensation reaction with an active methylene compound was also used in the course of this thesis and is in general conducted in either absolute ethanol or acetic anhydride, leading to moderate yields of the desired chromophores (Scheme 3.1b).[278]

A versatile approach with similar starting materials was described by Würthner *et al.*, using quarternary salts and active methylene compounds with DMF in acetic anhydride as solvent in a one-pot reaction (Scheme 3.1c). The advantage of this route is that the starting material does not necessarily has be purified beforehand to obtain the desired merocyanine in good yield, making it a useful step for combinatorial syntheses.[279]
Methyl-substituted quarternary salts of nitrogen-containing heterocycles have also been applied in many other procedures described for the synthesis of merocyanine chromophores, using either anilinomethylene derivatives (Scheme 3.1d), acetanilidomethylene-substituted heterocycles (Scheme 3.1e) or dimethylaminomethylene derivatives of heterocyclic ketones (Scheme 3.1f).[280–282]

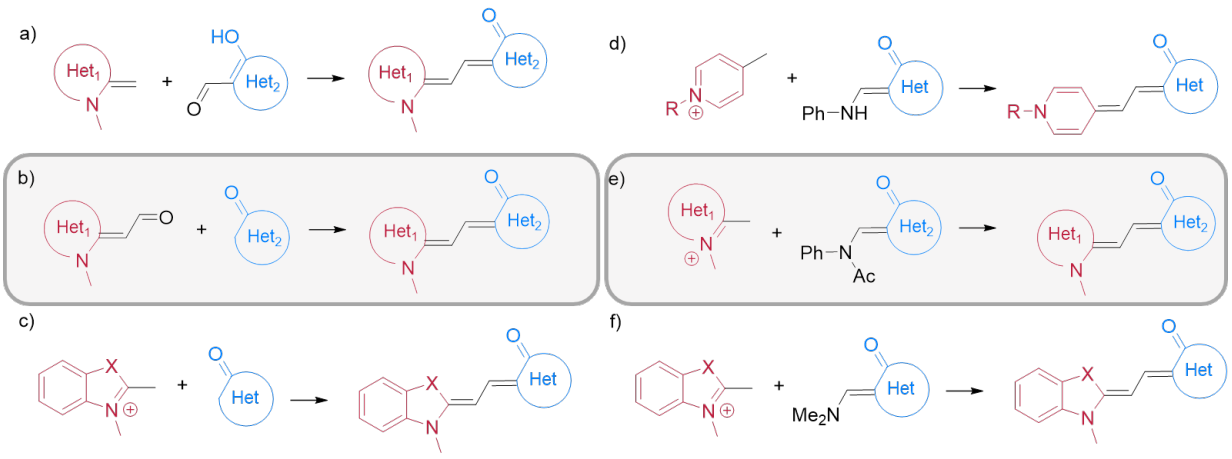

Scheme 3.1: General synthetic approaches toward merocyanine chromophores. The electron-donating and -accepting groups are colored in red and blue, respectively, and the two methods used within this thesis are framed. a) Reaction of heterocyclic enamines with hydroxybenzaldehydes. b) Condensation of active methylene compounds with heterocyclic aldehydes. c) One-pot reaction of quarternary salts with active methylene compounds in the presence of *N,N*-DMF and Ac_2O. d) Coupling of quarternary salts with anilinomethylene derivatives, acetanilidomethylene-substituted heterocycles (e) or dimethylaminomethylene derivatives of heterocyclic ketones (f). Het_n is abbreviated for heterocycles, X is either S, O or $C(CH_3)_2$ and the counter ion is typically iodide or tosylate.

All of the described synthetic routes have extensively been used for the preparation of a plethora of different merocyanine chromophores. However, the most suitable method for a specific merocyanine depends on the molecular composition as well as constitution of the desired chromophore.

3.1.2 Synthesis of free barbituric acid-derived merocyanines

Merocyanine dyes comprising a barbituric or thiobarbituric acid as a terminal electron-accepting group have been investigated by several research groups for different purposes such as the design of supramolecular systems, for example functional polymers and liquid crystals.[283–286] Since these chromophores exhibit hydrogen bond donating as well as accepting properties due to the amide groups of the barbituric acid moiety they are suitable biomedical probes with environment- and polarity-sensitive spectroscopic behavior.[287] Thus, barbituric acid merocyanine dyes provide a promising platform for stabilized complexes with proteins or nucleic acids by mimicking the Watson-Crick site of a natural T or U nucleobase for base pairing with A.[288,289] With this in mind, differently substituted barbituric acid merocyanine chromophores with a two-carbon polymethine bridge were synthesized and subsequently converted into the respective phosphoramidites for incorporation into oligonucleotides. Due to their short polymethine bridge, the synthesized merocyanine dyes are, similar as thiazole orange, expected to exhibit a better photostability than the widely used Cy3 chromophore. As a starting point, the free chromophores shown in Figure 3.2 were generated and evaluated concerning their spectral

characteristics.

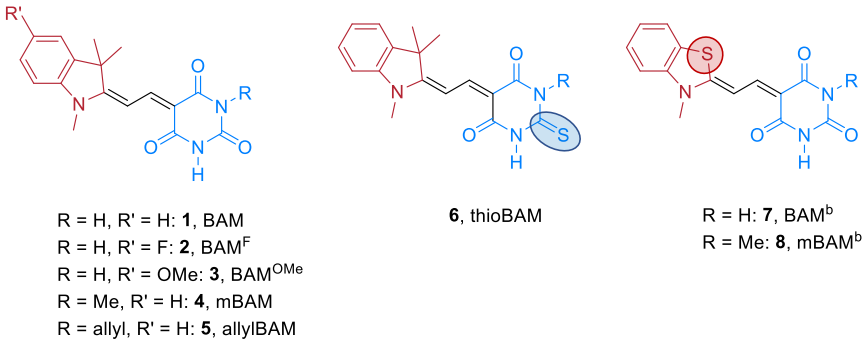

Figure 3.2: Overview of the free barbituric acid merocyanine chromophores synthesized and characterized in the course of this thesis. In the molecular structures of the synthesized dyes, the electron-donating part is colored in red while the electron-accepting moiety is shown in blue. Changes of the chromophore structure are circled in addition.

The synthesis and a comparative spectroscopic characterization of the **B**arbituric **A**cid **M**erocyanine **1** (BAM) and its *N*-methylated variant **4** (mBAM) as well as the dimethylated variant of this indolenine-derived barbituric acid dye have already been reported.[290–292] Within this thesis, only one amide nitrogen of the barbituric acid structure was methylated to investigate the Watson-Crick base pairing behavior of the merocyanine building blocks when incorporated into oligonucleotides, while the allyl residue in allylBAM **5** was meant to be used for further derivatization.

To achieve a farther red-shifted emission and absorption behavior desirable for biological applications, additional substituents such as fluorine and a methoxy group in compounds **2** (BAM^F) and **3** (BAM^{OMe}) were introduced at the aromatic core of the indolenine moiety, as similarly described by Armitage and coworkers for non-covalent aggregation of cyanine dyes in the minor groove of a DNA duplex.[293] A bathochromic shift in absorption can also be obtained by the implementation of sulfur atoms, which was done here either at the electron-accepting terminal group by replacing the barbituric acid with thiobarbituric acid (thioBAM, **6**) or at the electron-donating group. Since indolin-2-yl and benzothiazolyl groups are the most common heterocyclic electron-donating groups used in cyanine chemistry, the latter one was the system of choice to achieve farther red-shifted maxima, leading to compounds **7** (BAM^b) and its *N*-methylated variant **8** ($mBAM^b$).

In the following, the syntheses of the different chromophores **1** to **8** will be discussed, together with their spectroscopic characterization by UVvis absorption and fluorescence measurements. Especially BAM (**1**) will be examined in detail with regard to its solvatochromic as well as polarity- and pH-dependent behavior, since the majority of the modified oligonucleotide systems described in this thesis is based on this chromophore.

The free indolenine-derived merocyanine chromophores **1** to **6** were synthesized *via* an aldol or aldol-type reaction. In the first step, an aldehyde-modified electron donor moiety was prepared. For this purpose, the substituted 2,3,3-trimethyl indolenines **9** and **10** were generated by Fischer indole synthesis from the respective phenylhydrazine hydrochlorides and methyl isopropyl ketone in presence of a Brønsted acid (Scheme 3.2). The obtained indolenine precursors were then methylated at the N1-position with methyl iodide to give the 1,2,3,3-tetramethyl-3*H*-indolium-salts **11** to **13**, followed by generation of an exocyclic double bond under basic conditions, leading to the Fischer's base **14** and its two substituted variants **15** and **16**. These heterocycles were subjected to a Vilsmeier-Haack formylation reaction; here, the commercially available Vilsmeier reagent was directly used instead of generating it *in situ* from $POCl_3$ and DMF. Alkaline hydrolysis of the formed intermediates finally afforded the desired aldehydes **17** to **19**.[278,294]

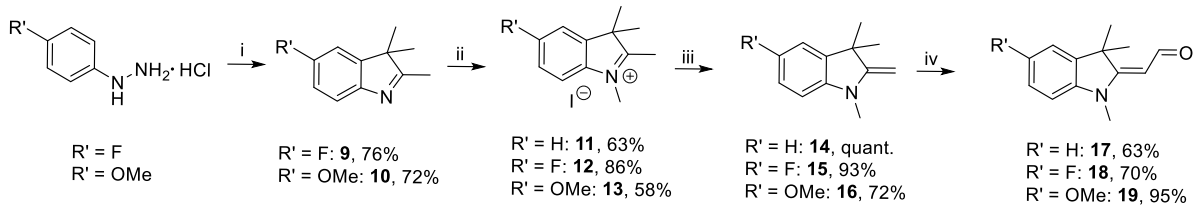

Scheme 3.2: Synthesis of the precursor for indolenine-derived merocyanine chromophores **17** to **19**. Conditions: i) 3-methyl-2-butanone and acetic acid (for **9**) or *p*-toluene sulfonic acid in ethanol (for **10**), reflux, 22 h; ii) MeI, 40 °C, 20 h; iii) 3 M NaOH, 50 °C, 30 min; iv) 1. (chloromethylene)dimethylammonium chloride, *N,N*-DMF, r. t. 1 h, 2. THF, sat. aq. K_2CO_3, r. t., 12 h.

However, the aldehyde precursor required for the following aldol condensation reaction is not easily accessible with benzothiazole heterocycles. Therefore, an alternative approach, which is commonly used for the synthesis of symmetric as well as asymmetric cyanine chromophores, had to be used to generate the chromophores BAM^b (**7**) and mBAM^b (**8**).[295] Here, *N,N*-diphenylformamidine (**20**) is used as the condensing reagent, which reacts with the alkylated heteroarene **21** to furnish the half-dye **22** (Scheme 3.3).[296]

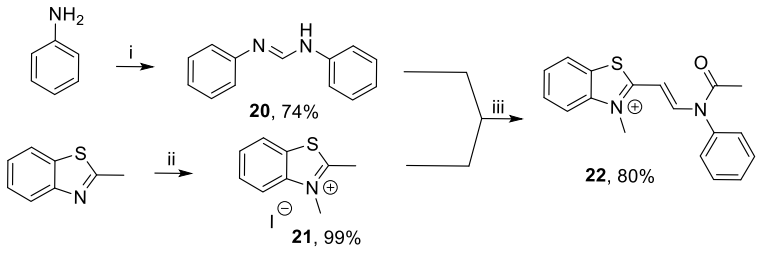

Scheme 3.3: Synthesis of the precursor half-dye **22** for benzothiazole-containing merocyanines BAM^b (**7**) and mBAM^b (**8**). Conditions: i) triethyl orthoformate, acetic acid, 150 °C, 16 h; ii) MeI, *N,N*-DMF, 60 °C, 16 h; iii) acetic anhydride, 140 °C, 2 h.

In the final step, the aldehydes **17** to **19** and the acetanilidomethylene-substituted precursor **22** were coupled in aldol-type condensation reactions to the barbituric acid terminal groups

(Scheme 3.4), according to the general routes shown in Scheme 3.1b and e. Here, either free commercially available barbituric and thiobarbituric acid or its *N*-substituted variant, synthesized according to described procedures, were employed. *N*-methyl barbituric acid (**23**) was generated from malonic acid and *N*-methyl urea in acetic anhydride, while for the *N*-allyl compound **24** *N*-allyl urea and diethyl malonate were used as starting materials.[297,298] The indolenine- as well as benzothiazole-derived chromophores **1** to **8** were accessed by heating the two precursor molecules in absolute ethanol to reflux and afterwards collecting the formed products as bright orange to red powders by filtration.

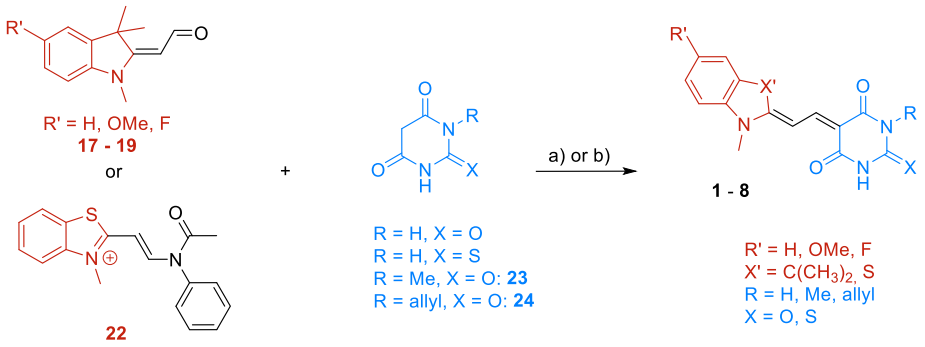

Scheme 3.4: Synthesis of the free merocyanine chromophores **1** to **8**. Conditions: a) abs. EtOH, 70 °C, 2–16 h for indolenine-derived chromophores; b) 1) Ac_2O, Et_2O, 150 °C, 2 h; 2) NEt_3, EtOH, 95 °C, 2 h for benzothiazole-derived chromophores.

The yields obtained for all of the merocyanine chromophores synthesized according to Scheme 3.4 are summarized in Table 3.1.

Table 3.1: Yields obtained by filtration of the precipitated products for all free merocyanine chromophores with different aromatic substituents, electron donors and acceptors.

Compound	**No.**	donor	acceptor	R	R'	yield
					%	
BAM	**1**	indole	BA	H	H	61
BAM^{F}	**2**	indole	BA	H	F	92
BAM^{OMe}	**3**	indole	BA	H	OMe	89
mBAM	**4**	indole	BA	Me	H	52
allyl-BAM	**5**	indole	BA	allyl	H	62
thio-BAM	**6**	indole	thio-BA	H	H	69
BAM^{b}	**7**	benzothiazole	BA	H	H	quant.
mBAM^{b}	**8**	benzothiazole	BA	Me	H	quant.

All of the procedures shown in Schemes 3.2 to 3.4 only required simple workup steps, such as precipitation, filtration or extraction. This led to sufficient product purity and, with one

exception, to yields above 60%, demonstrating the simplicity and versatility of the majority of reactions in merocyanine chemistry.

The free chromophores **1** to **8** were characterized regarding their spectroscopic properties, prior to using them for the preparation of phosphoramidite building blocks. The recorded absorption and fluorescence spectra as well as estimated molar extinction coefficients for some merocyanines selected from the ones described above will be discussed in the next section.

3.1.3 Spectroscopic characterization of free merocyanine derivatives

3.1.3.1 Absorption and fluorescence behavior of selected free merocyanines

For a detailed spectroscopic characterization, stock solutions of the free merocyanine chromophores in dimethyl sulfoxide (DMSO) were prepared and diluted with water to the required concentrations. Aqueous conditions were used here for UVvis and fluorescence measurements for a better comparability with data obtained for merocyanine-modified oligonucleotides.

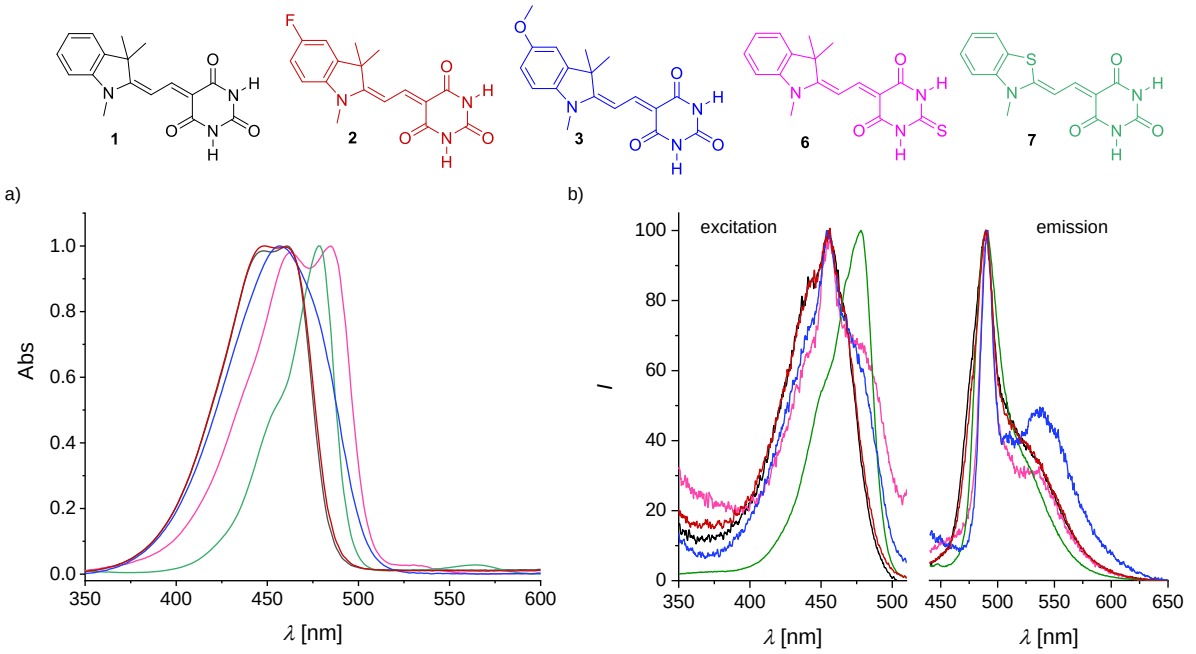

Figure 3.3: Normalized UVvis absorption (a) and fluorescence emission and excitation spectra (b) for selected free merocyanine chromophores; the color of the molecular structures matches the curve color. Conditions: 5 µM chromophore in water (UVvis); 1 µM chromophore in water, excitation at 420 nm, emission at 540 nm (fluorescence).

All of the investigated merocyanine chromophores show an absorption maximum at around 460 nm; however, in each spectrum except in the one for the methoxy-substituted variant an additional blue-shifted absorption band is visible, which has similarly been reported for structurally akin two-carbon bridge merocyanines (Figure 3.3).[299] It has to be noted that

the spectra for the methylated chromophores are not shown here since they exhibit the same features as their unmethylated counterparts. Theoretically, the arising of a second band in absorption can be traced back to different reasons. First, it could be caused by the presence of a (*Z*)-configurated isomer along with the (*E*)-isomer. However, this is unlikely since the double bond configuration here is dictated by the conformation of the aldehyde precursor, exclusively leading to (*E*)-configured chromophores with the symmetric barbituric acid acceptor unit. Also, so far no direct route for double bond isomerization of the (*E*)-isomer has been observed.[300] To clarify the double bond configuration of the BAM chromophore **1**, a NOESY spectrum was recorded (Figure 3.4).

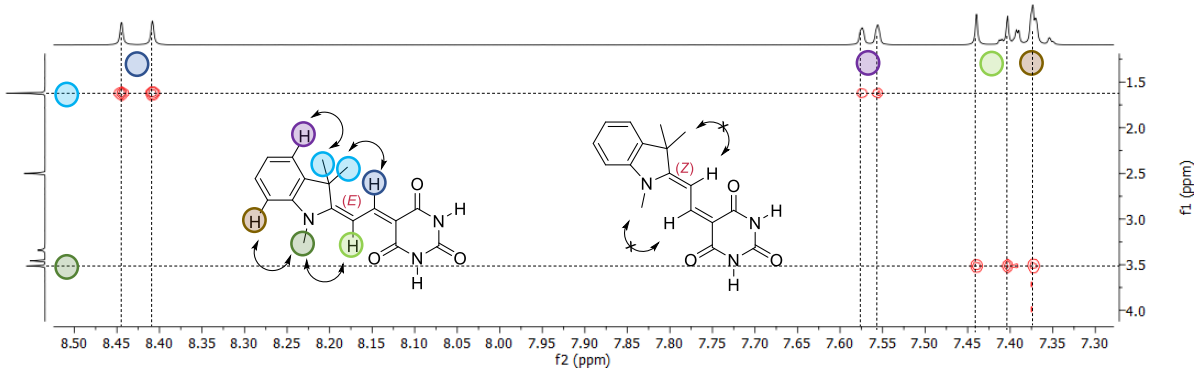

Figure 3.4: The excerpt from the NOESY spectrum of the free BAM chromophore **1** proves the presence of only the (*E*)-isomer. The visible NOE contacts are indicated as black double-headed arrows in the molecular structure.

Indeed, NOESY contacts between the dimethyl and *N*-methyl groups of the indolenine and the respective polymethine bridge hydrogen atom were observed, proving the presence of exclusively the expected (*E*)-isomer . Due to the symmetry of barbituric acid, the constitution of the second double bond cannot be estimated but becomes important for *N*-substituted barbituric acid derivatives as discussed at a later point in this thesis (section 3.2.2).

Since the additional absorption maximum is neither supposed to arise from the prescence of two or more excited states in the visible range, according to theoretical calculations, nor from dimer formation or aggregation as proven by concentration dependent absorption measurements, the most plausible explanation for the second band in the UVvis spectrum is the existence of different tautomers in solution (Scheme 3.5).[299,301] Merocyanines are so-called push-pull D-π-A chromophores; upon electronic excitation, they undergo both charge resonance between the positions adjacent to the polymethine chain and light-induced intramolecular charge transfer from the donor (here the indolenine part) to the acceptor group (here the barbituric acid moiety), accompanied by interconversion between single and double bonds in the π-bridge. Therefore, three fictious states corresponding to a dipolar and a neutral polyene with localized π-electrons as well as a polymethine structure with maximal π-electron delocalization can be achieved. Importantly, the neutral polyene form in the case of BAM (**1**) is able to undergo keto-

enol tautomerism, although this is not expected to have an impact on its spectral properties.

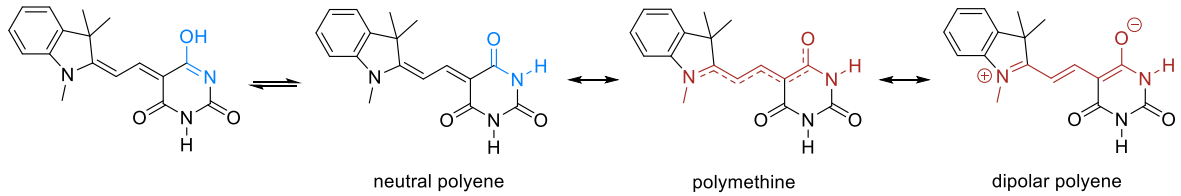

Scheme 3.5: Keto-enol tautomerism and resonance forms for barbituric acid-derived merocyanines, exemplarily shown for BAM (**1**). For simplification, only one possible tautomer is shown for each structure.

The neutral and the dipolar polyene structure are treated as basis states; their linear combinations comprise the electronic ground and first excited state with the relative contribution of the two basis states depending on the nature of the donor and acceptor groups as well as on the solvent. If the ground state is mainly neutral and the first excited state largely zwitterionic, a significant change in charge distribution and therefore equilibrium bond length takes place upon excitation. With increased proportion of the zwitterionic tautomer the ground state becomes more polar while the polarity of the excited state decreases. If both structures contribute equally to these two electronic states, the highest possible degree of conjugation is reached within the polymethine state. In this case, the dipole moment of the chromophores does not change anymore when excited and all conjugated bonds are of equal order of 1.5. This condition is called cyanine limit referring to symmetric cyanine dyes where the proportions of the neutral and the dipolar polyene are equally distributed.[302] Merocyanines at the cyanine limit typically exhibit a strong, narrow absorption band with a short-wavelength shoulder and a relatively weak vibronic structure in absorption. The absorption band of chromophores at the cyanine limit is bathochromically shifted compared to the neutral form and hypsochromically shifted compared to the zwitterionic form of the same dye.[303] The spectroscopic pattern of a chromophore at the cyanine limit is observed for almost all of the synthesized dyes shown in Scheme 3.4; it has in addition been reported to occur for structurally similar merocyanines, for example a chromophore composed of a 1,3-diphenylbenzimidazole donor linked to a thiobarbituric acid acceptor by a two-carbon bridge.[304]

The absorption spectrum for the thiobarbituric acid containing chromophore **6** differs from all the other spectra as it is red-shifted with a pronounced maximum at 485 nm and a weaker shoulder at 462 nm. This is expected since sulfur atoms included in the acceptor group of merocyanines usually lead to spectral broadening and a bathochromic shift of the maximum.[305] In contrast, the sulfur atom in the donor group of chromophore **7** only leads to a less pronounced blue-shifted shoulder compared to the indolenine-derived chromophores but not to a change in the maximum position. The same holds true for the substituted variants **2** and **3**. Here, neither the electron-withdrawing fluorine substituent nor the electron-donating methoxy

group have a pronounced influence on the spectral properties.

In accordance with the results obtained from UVvis measurements, the fluorescence excitation maxima for all of the chromophores discussed are positioned below 460 nm, except for compound **7**, where it is red-shifted by 22 nm. However, the maximum emission wavelength for this chromophore is the same as for all of the other dyes, located at 491 nm. Similar to the absorption also in the fluorescence spectra complex band structures can be found, which is again due to the presence of two tautomers, leading to a more complex vibrational band structure.

The absorption as well as excitation and emission maxima along with the calculated Stokes shift are summarized in Table 3.2. Also the molar extinction coefficients calculated from dilution series by the Beer-Lambert law are listed; the detailed procedure to estimate these parameters and the raw data can be found in sections 5.4.1.4 and 6.2, respectively. It has to be noted that the parameters given for mBAM[b] (**8**) were measured in DMSO instead of aqueous solution due to solubility issues. The obtained results are compared to reported values for the structurally similar unsymmetrical cyanine dye thiazole orange (TO), which shows a significantly red-shifted absorption and fluorescence emission maximum compared to the chromophores synthesized in the course of this thesis while its molar extinction coefficient ϵ is in the same order as for BAM (**1**). The bathochromic shift of TO can be explained by its reduced electron density in the conjugated system due to the positive charge.

Table 3.2: Spectroscopic parameters for selected free merocyanine chromophores and thiazole orange (TO) in water. Given is the absorbance maximum along with the position of the shorter-wavelength shoulders, the excitation and emission maxima, respectively, as well as the molar extinction coefficient ϵ with standard deviation of the mean from triplicate measurements and the Stokes shift $\Delta\lambda$. n d. is for not determined values.

Compound	λ_{Abs} nm	$\epsilon\pm$s.d.m. 10^3 $M^{-1}cm^{-1}$	λ_{Ex} nm	λ_{Em} nm	$\Delta\lambda$ nm
BAM	447, 461	41±1	455	491	36
BAM^{OMe}	458	n. d.	455	491	36
BAM^{F}	448, 461	n. d.	455	491	36
thio-BAM	462, 484	104±1	455	491	36
mBAM$^{b[a]}$	446, 461	91±2	478	491	13
TO[306]	502	63	512	533	21

[a] measured in DMSO due to its poor solubility in water

Since the synthesis of the unsubstituted chromophore BAM (**1**) is comparably straighforward

and the spectroscopic properties do not change significantly by the attachment of substituents to the aromatic system, this chromophore was chosen as the main building block for the following synthetic steps. Accordingly, it was characterized in more detail, which will briefly be described in the next section.

3.1.3.2 Additional characterization of the free BAM chromophore

To gain further insight into the chemical and spectroscopic properties of the BAM chromophore **1**, its behavior in solvents and solvent mixtures of different polarity as well as at different pH-values was studied.

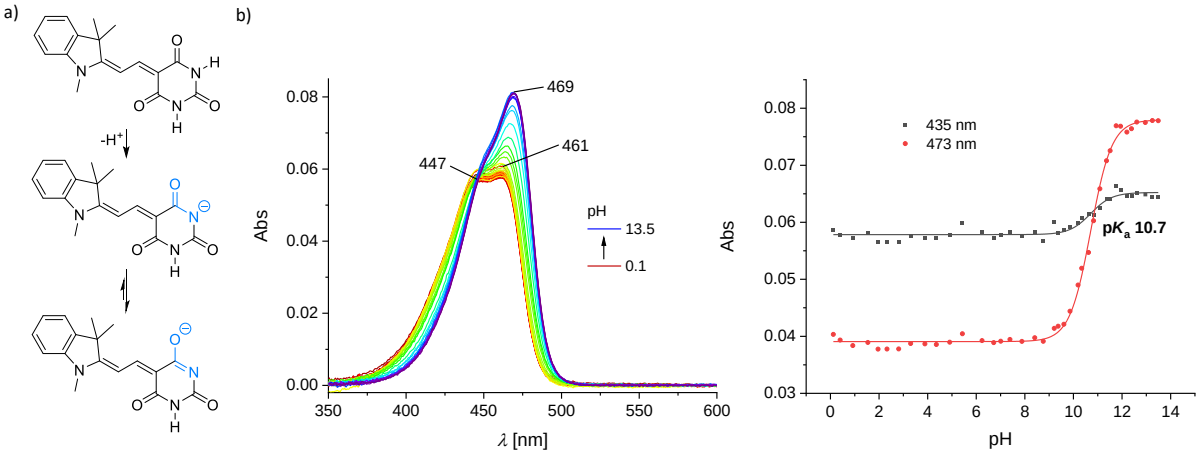

Figure 3.5: a) Upon deprotonation of BAM under basic conditions, two resonance structures are conceivable, of which the one with the negative charge located at the oxygen is more probable. b) Absorption spectra for the pK_a titration of BAM (left) and intensities plotted *versus* the corresponding pH (right), giving a pK_a of 10.7 by global fitting according to the Henderson-Hasselbalch equation. Conditions: 1 µM chromophore in 30 mM Britton-Robinson buffer of the respective pH.

Since especially the pH-dependency of a chromophore's spectral characteristics is of importance for biochemical and biological applications, the spectroscopic response of BAM to acidic and basic conditions was examined by a pK_a titration. The obtained spectra for a range of pH-values between 0.1 and 13.5 are shown in Figure 3.5. Below pH 9, the absorption spectrum of BAM (**1**) shows the two previously described maxima at 447 and 461 nm in an almost 1:1 ratio. By further increasing the pH, a new sharp absorption maximum at 469 nm arises, which is attributed to a deprotonated form of BAM (Figure 3.5a). The absorption intensities at 453 and 473 nm were globally fitted according to the Henderson-Hasselbalch equation and yielded a pK_a of 10.7±0.1 (Figure 3.5b).

The obtained pK_a value is reasonable when compared to reported ones; free barbituric acid has a pK_a of 4.01 while barbital, a barbituric acid derivative with two ethyl residues, is a much weaker acid with a pK_a of 8.0.[307] Within the BAM structure, the indolenine has an even stronger electron-donating character than the two alkyl chains of barbital, therefore further

increasing the electron density of the N-H bond and making the barbituric acid moiety less prone to deprotonation, which leads to a higher pK_a. In addition, the pK_a of BAM can be further elevated by attaching substituents to one of the barbituric acid nitrogens; thus, the pK_a of the BAM ribonucleoside was found to be 11.0±0.2 (see section 6.2.4).

The spectral characteristics of chromophores in environments of distinct polarity and proticity are another important factor when choosing dyes for biochemical purposes. Therefore, absorption spectra of BAM in a range of different solvents as well as in water/dioxane mixtures of different compositions were recorded and analyzed regarding its solvatochromic behavior (Figure 3.6).

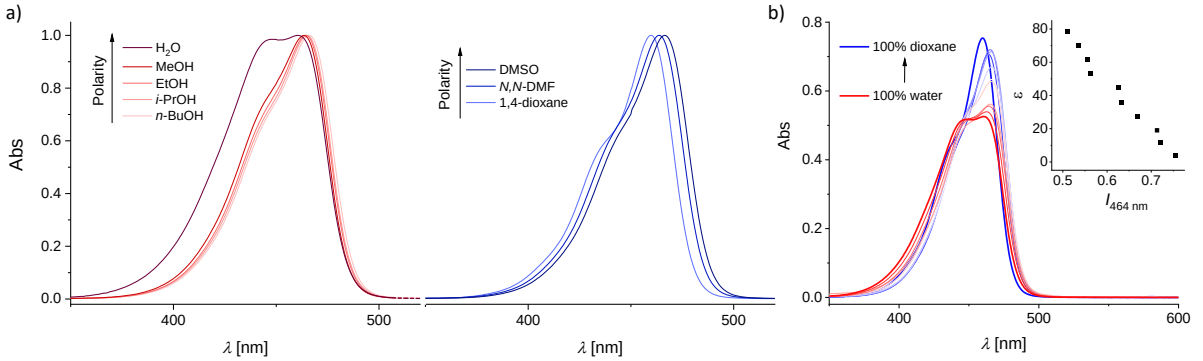

Figure 3.6: a) Normalized absorption spectra for 5 µM BAM (**1**) in different solvents. Protic and aprotic solvents are shown in red and blue, respectively. b) Polarity dependence of BAM absorption in water/1,4-dioxane mixtures of different ratios. Insert: linear relationship between the dielectric constant of the solvent mixture and the absorption intensity at 464 nm.

As mentioned before, BAM is supposed to be relatively close to the cyanine limit. Therefore, the dipole moments of the ground and the excited state should be similarly affected by solvent polarity and only a weak solvatochromic behavior is expected. This is indeed observed for the BAM chromophore since the absorption maximum is shifted by only about 7 nm from the solvent of lowest to the one of highest polarity. Interestingly, the nature of the solvatochromicity depends on the proticity of the solvent: in protic solvents, a negative solvatochromism characterized by a hypsochromic shift with increasing solvent polarity and dielectric constant ϵ from *n*-BuOH to water is observed, while in aprotic solvents the absorption maximum is shifted bathochromically from 1,4-dioxane to DMSO (Figure 3.6a). This can be traced back to the distinct H-bonding ability of protic solvents to the dye's acceptor moiety, stabilizing the dipolar resonance form of the chromophore and therefore blue-shifting the absorption maximum compared to the delocalized polymethine at higher polarity. In aprotic, non-H-bonding solvents the tautomeric equilibrium is shifted toward the neutral polyene structure; upon increased solvent polarity, the chromophores are brought closer to the cyanine limit, leading to a red-shift in absorption.[308,309] A very similar behavior has already been reported for other thiobarbituric acid merocyanine chromophores with a benzothiazole donor terminal group and was rational-

ized by the same reasons.[308] However, it has to be taken into account that the position of the absorption maximum is not only influenced by the polarity but also the polarizability of the respective solvent, which can have a significant impact on data interpretation, especially if only small changes are observed. Therefore, the absorption maxima of BAM obtained from the solvatochromicity measurements are summarized in Table 3.3, along with the dielectric constant ϵ which characterizes the solvent polarity and the refractive index n_D as parameter for the polarizability of the respective solvent.[307]

Table 3.3: Absorption maxima of BAM in different solvents along with the dielectric constant ϵ and the n_D as solvent parameters. Aprotic and protic solvents with increasing polarity from top to bottom are listed in the upper and lower part, respectively.

Solvent	λ_{max} nm	ϵ[307]	n_D[307]
Dioxane	459.7	2.21	1.422
***N,N*-DMF**	463.7	36.7	1.431
DMSO	466.6	47.2	1.479
***n*-BuOH**	466.0	17.1	1.399
***i*-PrOH**	465.1	18.3	1.376
EtOH	464.3	22.4	1.361
MeOH	463.5	32.6	1.329
H_2O	461.0	79.7	1.333

The spectral behavior of BAM was not only studied in different solvents but also in water/dioxane mixtures of various composition (Figure 3.6b). Here, the absorption intensity was found to be highest in apolar dioxane, which is to be expected since in general the molar extinction coefficient is drastically decreased with increased solvent polarity.[304] In addition, also here a blue-shift of the higher-wavelength absorption maximum with a larger proportion of water is observed, again explicable by the formation of hydrogen bonds between the solvent and the barbituric acid terminal group. Concomitantly, a linear increase of the red-shifted absorption band at 464 nm with decreasing water content in the sample, leading to a lower total dielectric constant of the system, was obtained (insert Figure 3.6b).

In summary, the free BAM chromophore is characterized by absorption and fluorescence of blue light at around 460 nm. It exhibits two equally intense absorption bands, a comparably small Stokes shift of 36 nm and a poor solvatochromic behavior, which is attributed to its cyanine-like spectroscopic behavior. Since the spectral characteristics of BAM and BAM^b are

only weakly dependent on the solvent polarity and not influenced by changes of the pH in the biologically relevant region, they were considered suitable chromophores for biochemical labeling and were therefore transformed into phosphoramidite building blocks with different sugar moieties. In addition, BAM^{F} and BAM^{OMe} were incorporated into oligonucleotides to study the influence of substitutents on the indolenine donor with different electronic properties on the spectroscopic and thermodynamic behavior of modified nucleic acid analogs.

In addition, the structure of these four chromophores was geometry optimized and the electrostatic potential as well as different molecular parameters were calculated by ab initio calculations. As expected, the results reveal an overall positive electrostatic potential for all of the aromatic donors and the barbituric acid nitrogens, while the negative electrostatic potential is mainly concentrated on the barbituric acid oxygen atoms (Figure 3.7).

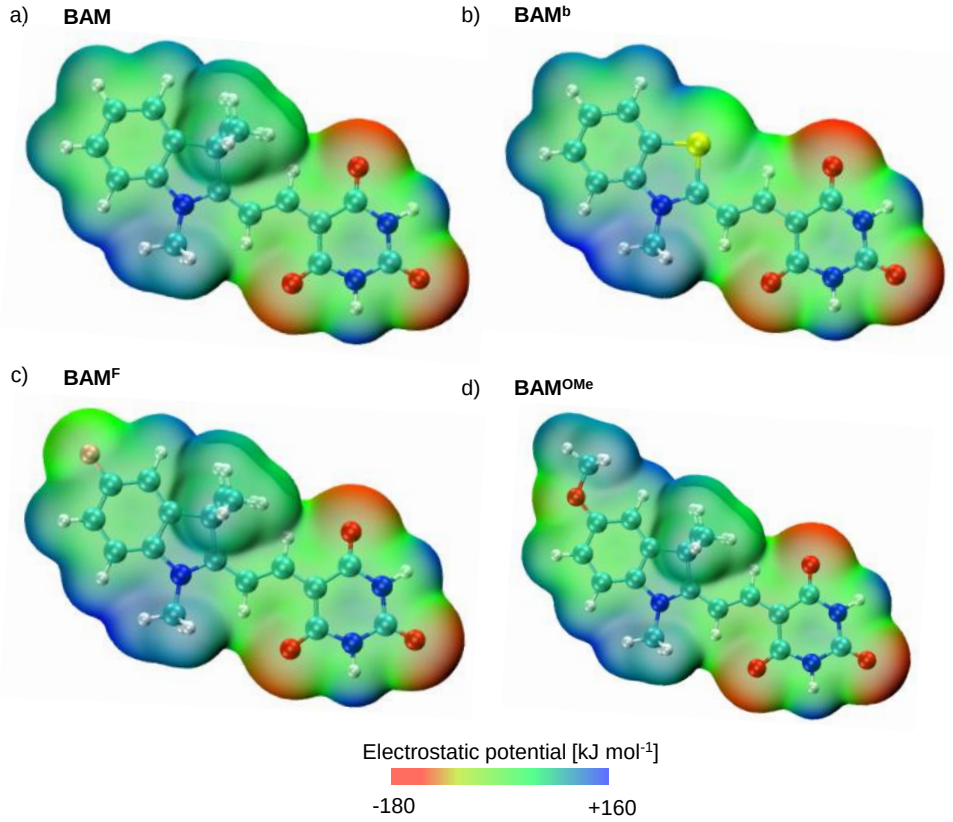

Figure 3.7: The electrostatic potential for geometry optimized BAM (**1**, a), BAM^{b} (**7**, b), BAM^{F} (**2**, c) and BAM^{OMe} (**3**, d) chromophores shows has a positive value for both aromatic donors and the barbituric acid nitrogens, while it is negative at the barbituric acid oxygens. Geometry optimization was done in ORCA Version 5.0[310] at the level of density functional theory employing the B3LYP functional[311,312] together with the def2-SVP basis set.[313] Maps of the electrostatic potential on the electron density isosurface with a resolution of 80x80x80 grid points were generated using the Multiwfn software[314–316]

Between BAM (**1**) and BAM^{b} (**7**), no pronounced difference of the electrostatic potential distribution is observed apart from a stronger negative electrostatic potential at the sulfur in BAM^{b} compared to the quartary carbon of the indolenine five-membered ring of BAM (**1**). In

BAM^{F} (**2**) and BAM^{OMe} (**3**), the electrostatic potential on the individual atoms of the barbituric acid is not influenced by the electronic character of the substituents on the indolenine moiety. Within the donor part of these two chromophores, the lowest electrostatic potential is found on the fluorine of BAM^{F} (**2**) and the oxygen atom of the BAM^{OMe} (**3**) methoxy group due to their electronegative character.

Along with the electrostatic potential, the ground state dipole moments μ of the four chromophores were calculated. For BAM (**1**) and BAM^{b} (**7**), 7.70 and 9.14 D were obtained for this parameter, respectively, which is comparable to the reported value of 6.12 D for *N,N*-dimethyl BAM[291] and higher than for TO with 4.14 D.[317] With regard to these results, enhanced dipolar stacking interactions are expected for centrosymmetric BAM^{b} dimers compared to BAM dimers, which was indeed observed and will be explained in more detail in section 3.5.5.
The lowest dipole moment with 6.54 D was obtained for BAM^{F}, while the methoxy-substituted chromophore BAM^{OMe} exhibited an intermediary dipole moment of 8.30 D. Along with the permanent ground state dipole moments, the HOMO-LUMO band gaps and the LUMO energies were calculated for all of the four chromophores. These values and their impact on the spectroscopic properties of multiply-modified oligonucleotide duplex structures is discussed in section 3.6.3.

As a starting point for such multichromophore assemblies, different BAM-derived ribonucleosides for incorporation into oligonucleotides were synthesized and spectroscopically characterized, which is described in the next part of this thesis.

3.2 Synthesis and spectroscopy of merocyanine ribonucleosides

For covalent incorporation of chromophores into an oligonucleotide scaffold, the synthesis of protected nucleoside phosphoramidite building blocks is required. Since the chromophores are here directly attached to the ribose moiety without a linker, they are supposed to occupy the position of a canonical nucleobase, enforcing stacking interactions and a fluorescence turn-on compared to the free dyes. In this section, the preparation of different free barbituric acid merocyanine ribonucleosides to explore their spectroscopic behavior upon attachment of a ribose moiety to one of the barbituric acid nitrogens will be discussed. Furthermore, the absorption and fluorescence characteristics of these novel compounds are to be described.

3.2.1 General synthetic approaches toward artificial nucleosides

Most artificially modified nucleosides are accessible by nucleosidation reactions which comprise the coupling of the protected sugar moieties to nucleobase analogs of interest. In principle, three general methods for the preparation of nucleosides have been reported: two of them include a nucleophilic substitution reaction with the leaving group either at the anomeric center of the sugar or at the nucleobase, while in the third method the heterocyclic nucleobase is not used as a synthon but constructed from scratch on the sugar ring. The nucleosidation by nucleophilic substitution is the most widely used method (Scheme 3.6); only if this reaction yields primarily wrong regioisomers or the nucleobase does not react at all the third technique mentioned is applied.

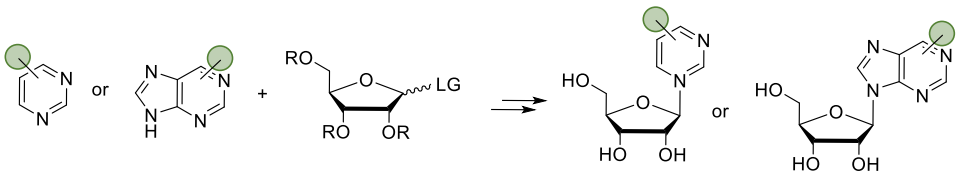

Scheme 3.6: Schematic representation of the *N*-glycosylation reaction based on nucleophilic substitution of the leaving group (LG) at the protected sugar (R = acetyl, benzoyl) by a nucleobase analog with variable substitution pattern (indicated by green circles), leading to the formation of the desired β-anomer.

In early years, nucleosides were mostly synthesized by the Fischer-Helferich or Koenigs-Knorr method, based on an S_N2 reaction between soft heavy metal salts (Ag^+ or Hg^{2+}) of the nucleobase heterocycle as nucleophile and a 1'-chloro- or 1'-bromosugar.[318,319] Although these methods lead to the correct regiochemical connectivity between sugar and nucleobase, they are rarely used nowadays due to several drawbacks such as the poor solubility of heavy metal salts in organic solvents and the easily hydrolyzable halogenated sugar building blocks. Heavy metal salts are avoided in the Hilbert-Johnson method which was developed later and em-

ploys alkylated nucleobases that by themselves are nucleophilic enough for the substitution reaction.[320]

The Hilbert-Johnson method was further refined to the commonly applied Silyl-Hilbert-Johnson or Vorbrüggen nucleosidation.[321,322] This technique uses a more stable sugar precursor with for example an acetate as the leaving group at the anomeric center. Prior to coupling with the nucleobase, the sugar is activated by a Lewis acid such as the weak trimethylsilyl trifluoromethanesulfonate (TMSOTf) or the stronger $SnCl_4$, leading to the formation of a cyclic oxocarbenium ion as intermediate (Scheme 3.7).

For the following coupling step, persilylated nucleobases with increased nucleophilicity compared to the unprotected ones are employed. These attack at the 1'-position of the activated sugar in an S_N1-type reaction, leading to a mixture of the β- and the undesired α-anomer. However, if the C2'-atom of the sugar moiety is acetyl (Ac) or benzoyl (Bz) protected, the intermediary oxocarbenium ion is stabilized by participation of this neighboring group and, according to Bakers-1,2-trans rule, the nucleophilic attack can only take place *trans* to the C2'-group. Therefore, the main product for nucleosidation reactions with acyl-protected D-ribose is the desired β-anomer.[323] The silyl protecting groups of the nucleobase which still remain after the coupling step can be hydrolyzed afterwards by aqueous workup. Since the regio- and stereoselectivity of the nucleosidation reaction are critical for almost every nucleoside of interest, the Lewis acid catalyst and the reaction solvent need to be chosen carefully.

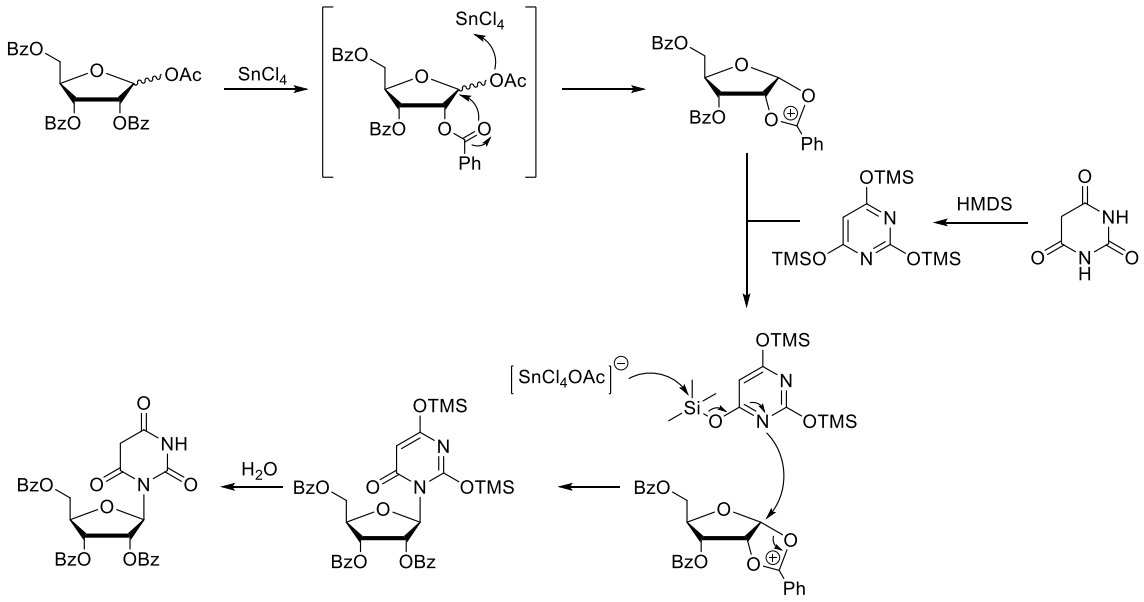

Scheme 3.7: Mechanism of the Silyl-Hilbert-Johnson nucleosidation of persilylated barbituric acid with benzoyl-protected ribose. First, the 1'-position of the sugar is activated by a Lewis acid catalyst, leading to the formation of a cyclic oxocarbenium ion. In an S_N1-type reaction, the silylated nucleobase attacks at the activated 1'-carbon under formation of the glycosidic bond. The remaining silyl protecting groups can be removed by hydrolysis, yielding the desired β-anomer. Ac: acetyl, Bz: benzoyl, HMDS: hexamethyldisilazane.

Under optimized conditions the Silyl-Hilbert-Johnson reaction has an exceptional substrate scope and is characterized by its high reliability. Given these facts, this synthetic approach was also used within this thesis for the preparation of barbituric acid merocyanine ribonucleosides (rBAM).

3.2.2 Synthesis of free rBAM and derivatives

Two synthons are required for the preparation of the different rBAM building blocks shown in Scheme 3.8: the first one is the unprotected barbituric acid ribonucleoside, the second one is the aldehyde precursor for the formation of the chromophore's donor terminal group.

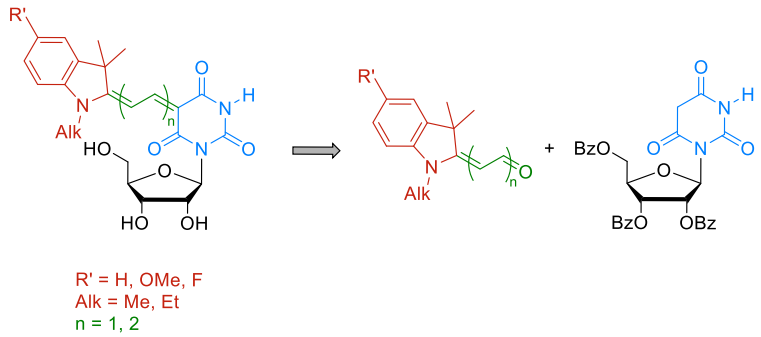

Scheme 3.8: Retrosynthetic scheme for the preparation of differently substituted rBAM nucleosides. Required are the aldehyde precursor of the chromophore and the barbituric acid ribonucleoside.

As explained in the previous section, the necessary ribonucleoside was synthesized by a Lewis acid catalyzed condensation of persilylated barbituric acid **25** and 1-*O*-acetyl-2,3,5-tri-*O*-benzoyl-β-D-ribofuranose inspired by a reported procedure.[324–326] The silylated nucleobase analog **25** was obtained by refluxing barbituric acid in HMDS and had to be used immediately for the following nucleosidation reaction with the commercially available protected ribose since it appeared to decompose upon storage, even if kept under nitrogen at -18 °C for only one day.

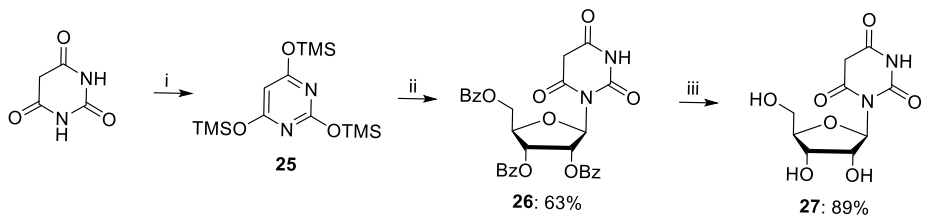

Scheme 3.9: Synthesis of the free barbituric acid ribonucleoside **27** by Silyl-Hilbert-Johnson nucleosidation. Conditions: i) HMDS, reflux; ii) 1) $SnCl_4$, 1-*O*-acetyl-2,3,5-tri-*O*-benzoyl-β-D-ribofuranose, 1,2-DCE, r. t., 6.5 h, 2) sat. aq. $NaHCO_3$, r. t., 12 h; iii) 0.5 M NaOMe in MeOH, r. t., 3 h.

In addition, the ratio of the sugar and the nucleobase precursor as well as the choice of the solvent proved to be important: if less than 1.10 equivalents (eq.) of the persilylated barbituric

acid were used, a significant amount of double glycosylated product was obtained, which was identified by both electrospray mass spectrometry (ESI-MS, Figure 3.8) and ^{1}H-NMR.

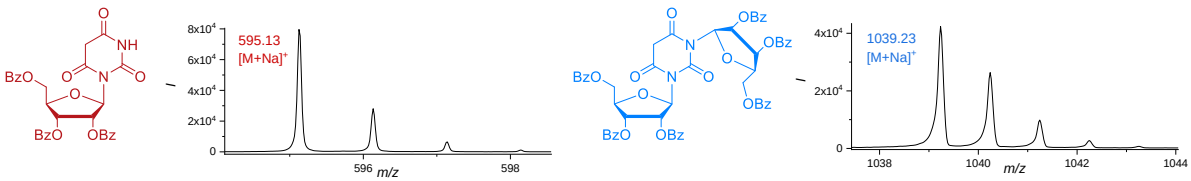

Figure 3.8: ESI(+) mass spectra for the desired single- and undesired double-glycosylated barbituric acid.

This is due to the presence of two equally reactive nitrogen atoms in the nucleobase analog: the strong Lewis acid stannic chloride leads to an enhanced σ-complexation during the reaction, therefore facilitating a nucleophilic attack of the second barbituric acid nitrogen to an additional sugar moiety. With careful optimization of the reaction conditions, the highest yield of the single-glycosylated product **26** in β-conformation was achieved with 1.20 eq. of silylated barbituric acid **25** and 1.90 eq. of $SnCl_4$ in 1,2-dichloroethane. If acetonitrile was used as a solvent instead, again a larger amount of the undesired double-glycosylated product was isolated.

In the following step, the benzoyl protecting groups were hydrolyzed with sodium methoxide in methanol. Hereby, the free nucleoside **27** was obtained as trisodium salt along with benzoic methyl ester as a byroduct. The trisodium salt was converted into the free uncharged nucleoside by dissolving in water and adjusting the pH of this solution to 4 with an acidic ion exchange resin. The resulting barbituric acid β-ribonucleoside **27** proved to be of exceptionally high polarity and purification was only possible by reversed phase column chromatography.

The purified unprotected barbituric acid ribonucleoside **27** was in the following used to generated a palette of rBAM nucleosides with different spectroscopic properties. The synthesis of the respective chromophore precursors required for this has already been described in section 3.1.2, except for the *N*-ethyl and the nitro-substituted ones **33** and **34** which were generated following a similar procedure (Scheme 3.10). For the nitro-substituted aldehyde **34**, the starting compound **28** was synthesized by Fischer indole synthesis, followed by *N*-alkylation and conversion by Vilsmeier-Haack formylation into the active aldehyde. The *N*-ethyl substituted indolenine precursor **33** was synthesized accordingly, using ethyl instead of methyl iodide for *N*-alkylation and commercially available 1,3,3-trimethyl indolenine as starting material.

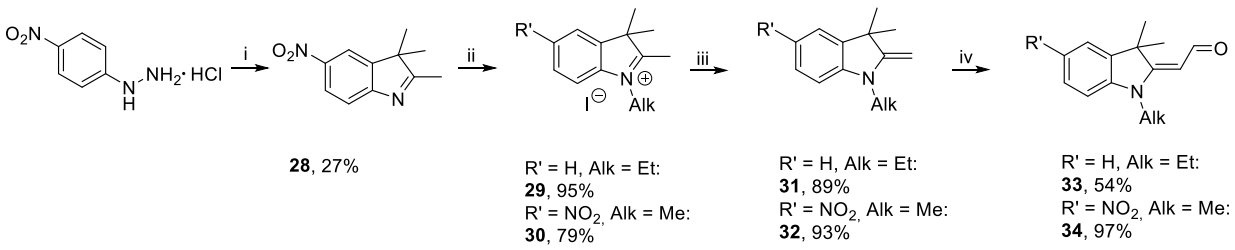

Scheme 3.10: Synthesis of the precursors **33** and **34** for indolenine-derived merocyanine chromophores. Conditions: i) 3-methyl-2-butanone, acetic acid, H_2SO_4, reflux, 21 h; ii) EtI, MeCN, 70 °C, 3 d for **33** or MeI, 40 °C, 20 h for **34**; iii) 3 M NaOH, 50 °C, 30 min; iv) 1. (chloromethylene)dimethylammonium chloride, *N,N*-DMF, r. t. 1 h, 2. THF, sat. aq. K_2CO_3, r. t., 12 h.

In addition to merocyanine chromophores with a two-carbon polymethine bridge also one variant with a four-carbon bridge was synthesized. However, the aldehyde derivative with the by two carbons elongated polymethine linker **35** required for this dye cannot be accessed by the described formylation reaction. Instead, a reported procedure based on a Wittig condensation reaction was followed (Scheme 3.11).[327]

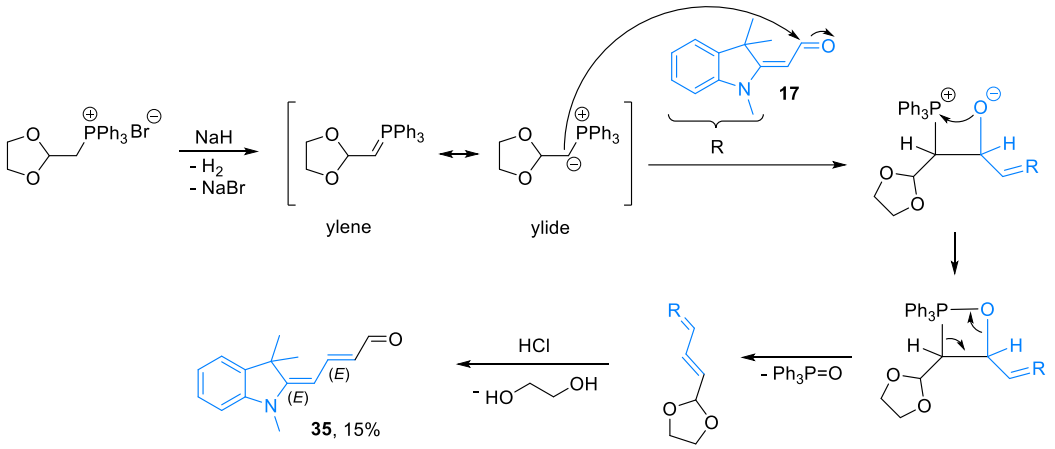

Scheme 3.11: The elongated aldehyde **35** is prepared by a Wittig condensation with (1,3-dioxolan-2-ylmethyl)triphenyl-phosphonium bromide as Wittig reagent. In the presence of sodium hydride as a base and the catalyst 18[crown]-6, the active ylide is formed which attacks at the carbonylic hydrogen of aldehyde **17**, leading to the formation of a cyclic oxaphosphetane intermediate. Upon release of triphenylphosphine oxide and following hydrolysis, the target compound **35** in all-*trans* configuration can be accessed.

Here, (1,3-dioxolan-2-ylmethyl)triphenyl-phosphonium bromide is used as Wittig reagent which deprotonated by NaH is in the first step. To increase the reactivity of the hydride, [18]crown-6 is employed as a catalyst chelating the sodium cation. Upon the deprotonation step an uncharged ylene is formed which is in equilibrium with the ionic ylide. By nucleophilic attack of the negatively charged ylide carbon to the aldehydic C-atom of the chromophore precursor **17**, a cyclic oxaphosphetane is formed which decomposes due to the strong oxygen-phosphorous bond into triphenylphosphine oxide and the acetal protected target compound. The acetal can

in the following be cleaved by acidic hydrolysis to the desired aldehyde **35**, releasing ethylene glycol as the side product.

The target compound **35** comprises two (*E*)-configurated C-C double bonds. While the constitution of the double bond at the indolenine moiety is already specified in the starting molecule **17**, the constitution of the second C=C bond is given by the reactivity of the ylide. If the ylide is stabilized by electron withdrawing substituents at the phosphorous such as phenyl rings in the present case, predominantly an (*E*)-configuration is obtained. The correct stereochemistry of **35** was confirmed by NMR spectroscopy; an excerpt from the proton NMR spectrum is shown in Figure 3.9. H5 and H6 as well as H6 and H7 are coupling with 12.6 and 14.2 Hz, respectively.

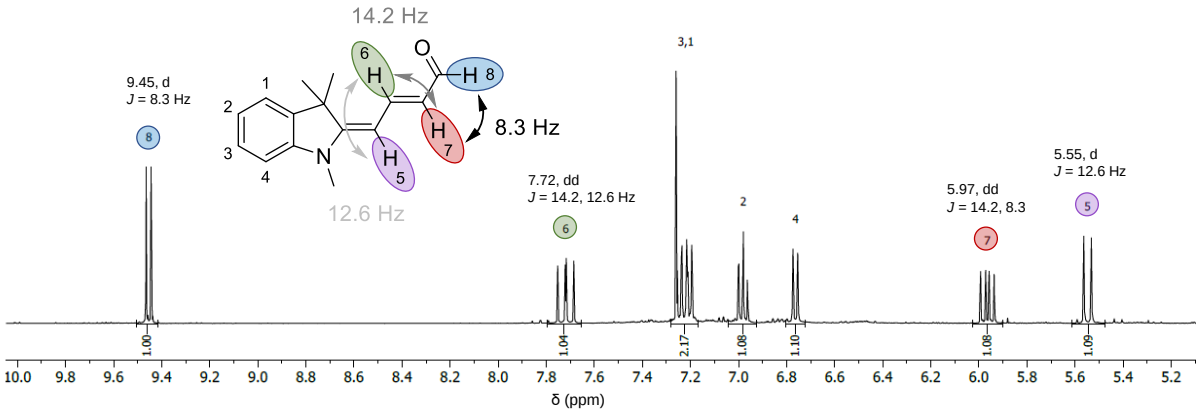

Figure 3.9: Excerpt from the ^{1}H-NMR spectrum of compound **35**. The double bond protons and the coupling constants are marked and prove an all-*trans* configuration.

Since typical coupling constants for protons of double bonds in *trans*-configuration are between 10 and 16 Hz, while the ones for *cis*-standing double bond protons are lower with 5 to 12 Hz, the two C=C bonds of the elongated aldehyde **35** are most likely in (*E*)-configuration.

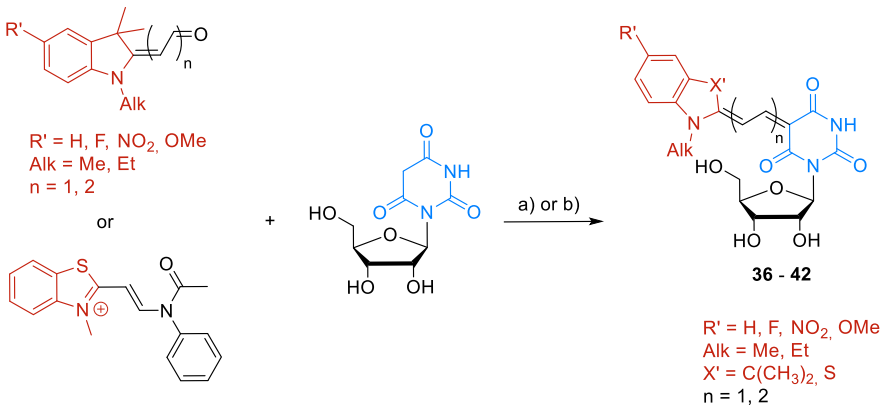

Scheme 3.12: The free rBAM chromophores **36** to **42** were generated by an uncatalyzed aldol condensation reaction of the deprotected barbituric acid ribonucleoside and the aldehyde precursors. The respective yields can be found in Table 3.4. Conditions: a) abs. EtOH, 70 °C, 2-3 h for indolenine-derived chromophores; b) i) Ac_2O, Et_2O, 150 °C, 2 h; ii) NEt_3, EtOH, 95 °C, 2 h for benzothiazole-derived chromophores.

The elongated aldehyde **35** as well as its shorter, substituted variants (Scheme 3.2 and 3.10) and also the already described precursor for BAM^{b} **22** were in the next reaction steps coupled to the deprotected barbituric acid ribonucleoside **27** in an uncatalyzed aldol condensation (Scheme 3.12). Here, the same reaction conditions as described in section 3.1.2 for the free BAM chromophores were employed, leading to the desired target compounds with yields between 44 and 68%.

All of the synthesized rBAM nucleosides were purified by column chromatography on silica gel and obtained as brightly colored powders. The yields for these chromophores along with the aromatic substituents R', the alkyl residue Alk and the chain length n are summarized in Table 3.4.

Table 3.4: Summarized yields for the different isolated rBAM chromophores **36** to **42**. Given are also the substituents at the aromatic core R', the alkyl residue Alk and the length of the polymethine chain n.

Compound	**No.**	R'	Alk	n	yield %
rBAM	**36**	H	Me	1	61
rBAM^{F}	**37**	F	Me	1	44
rBAM^{OMe}	**38**	OMe	Me	1	46
rBAM^{NO2}	**39**	NO_2	Me	1	55
rBAM^{Et}	**40**	H	Et	1	52
rBAM^{2}	**41**	H	Me	2	68
rBAM^{b}	**42**	H	Me	1	45

However, it has to be noted here that the aldol condensation reaction leads to the formation of two double bond isomers in almost 1:1 ratio for all cases. While the configuration of the double bond next to the electron donor is given as (*E*) for indolenine- and (*Z*) for benzothiazole-derived chromophores, the configuration of the second vinyl unit depends on the orientation of the aldehyde precursor in this reaction step (Scheme 3.13). Therefore, in the case of the indolenine BAM chromophores an (*E,E*)- along with an (*E,Z*)-stereoisomer and a (*Z,Z*)- along with an (*Z,E*)-stereoisomer for the BAM^{b} chromophore is obtained. Since the superposition of these two isomers in both cases shows their almost equal steric demand and their dipole moments are essentially overlapping, both are considered equal in the following interpretation of the spectroscopic characteristics of chromophore dimers.

The energetic difference between these two stereoisomers was estimated by geometry optimization on the level of density functional theory. For simplification, the *N*-methyl-substituted

mBAM and mBAM^b chromophores were used as model systems for these calculations and the energy of the energetically lower isomer was set to 0 kJ/mol. The optimized structures showed only an insignificant energy difference of 0.70 kJ/mol for the BAM chromophores, with the (*E,Z*)-stereoisomer being higher in energy.

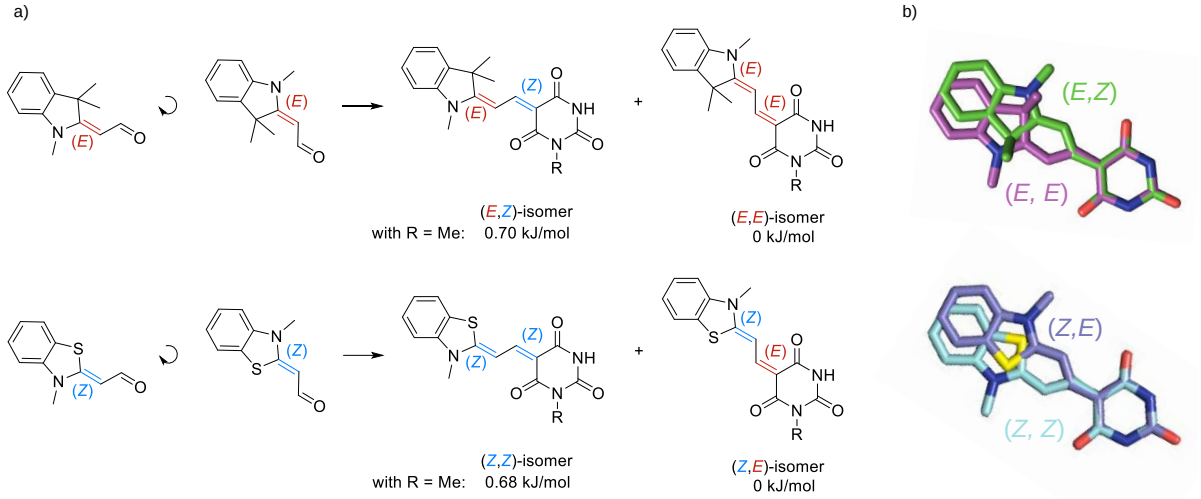

Scheme 3.13: During the aldol condensation, two double bond isomers are formed, dependent on the orientation of the precursor aldehyde or the respective nucleosidated barbituric acid nitrogen (a). By geometry optimization, the energy difference between the two isomers was estimated, revealing a by 0.70 and 0.68 kJ/mol higher energy for the (*E,Z*)- and the (*Z,Z*)-isomer of the BAM:BAM and BAM^b:BAM^b dimers, respectively. The overlay of the two isomers shows their equal steric demand and almost the same direction of the dipole moments (b). Geometry optimization was done by Dr. David Bialas on the level of DFT theory employing the long-range correct CAM-B3LYP functional[328] together with the def2-SVP basis set[313] as implemented in the Gaussian 09 package.[329]

Accordingly, a similar result was obtained for the BAM^b systems with an energy gap of 0.68 kJ/mol between the two stereoisomers. Since the two isomeric structures do not differ significantly in energetic means, the 1:1 ratio observed in NMR can be rationalized. The influence of both stereoisomers on the chromophore orientation and interactions in an oligonucleotide duplex will be discussed in section 3.3.5.

The synthesized rBAM chromophores were further characterized by absorption as well as fluorescence measurements and their molar extinction coefficients ϵ were estimated. The hereby obtained results will be described in the next section.

3.2.3 Spectroscopic characterization of the free rBAM chromophores

For spectroscopic characterization of rBAM and related derivatives, stock solutions of each compound were prepared in DMSO and diluted with water to the required concentration. The results for the absorption and fluorescence measurements are shown in Figure 3.10.

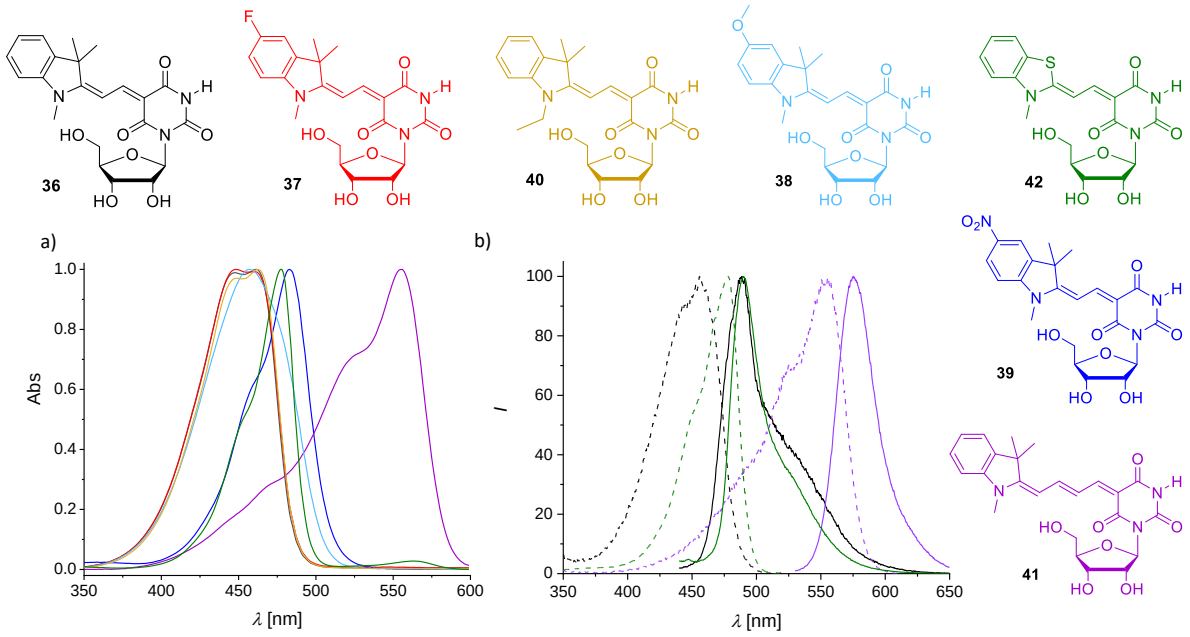

Figure 3.10: In a), the normalized absorption spectra for the different rBAM chromophores are depicted. b) shows normalized fluorescence excitation and emission spectra for the three selected rBAM derivatives **36**, **41** and **42**. Conditions: 5 µM chromophore in water (UVvis); 1 µM chromophore in water, excitation at 420 nm, emission at 540 nm or excitation at 510 nm, emission at 630 nm for **41** (fluorescence).

In the absorption, the parent compound rBAM **36** as well as its fluorine and *N*-ethyl substituted derivatives **37** and **40** all exhibit two maxima at 447 and 461 nm, similar to the respective free chromophores (Figure 3.10). This shows that both the electron-withdrawing character of the fluorine and the sterically more demanding ethyl group on the indolenine nitrogen only marginally influence the absorption behavior of the rBAM chromophores. In addition, also the spectrum for the methoxy derivative rBAM^{OMe} (**38**) is comparable to its unglycosylated counterpart.

The benzothiazole-derived chromophore rBAM^{b} (**42**) and the nitro variant rBAM^{NO2} (**39**) differ from these modified nucleoside as they only exhibit one pronounced, slightly red-shifted maximum at 477 and 483 nm, respectively. This observed bathochromic shift is expected, since the nitro group is an antiauxochrome due to its electron-accepting properties and negative mesomeric effect (-M effect). An electron-accepting group reduces the electron density within the system and therefore stabilizes the lowest unoccupied molecular orbital (LUMO) while the energy of the highest occupied molecular orbital (HOMO) remains unchanged, leading to a smaller HOMO-LUMO gap. This entails the observed red-shift of the absorption band and was confirmed for the free BAM^{b} chromophore by MD simulation as discussed in section 3.6.3.2.

rBAM^{2} (**41**) with a four instead of a two carbon polymethine bridge shows an absorption maxi-

mum at 555 nm, which is bathochromically shifted by around 100 nm compared to the shorter variant rBAM (**36**). This 100 nm red-shift has been reported for many symmetric cyanine chromophores and merocyanines near the cyanine limit upon increasing the chain length by one vinylene unit; it is also called vinylene shift and corresponds to a 0-0 electronic transition. If this shift is larger than 100 nm, the first excited state S_1 is assumed to have an especially high electronic symmetry.[330,331] In addition, the absorption band of rBAM^2 (**41**) is broadened and shows a more pronounced vibronic fine structure with shoulders at 473 and 527 nm. The broadening of the spectrum can be explained by enhanced intermolecular interactions with increased polymethine chain lengths while the distinct vibronic fine structure is mainly due to enhanced vibronic interactions.

However, it has to be mentioned that the purity of rBAM^2 (**41**) was only determined by RP-HPLC, since no conclusive NMR spectrum of this compound was obtained. Instead, in DMSO as well as in chloroform and acetonitrile extensive signal splitting and line broadening was observed which can be traced back to aggregation at the high concentration in the mM range required for NMR measurements. These aggregation effects were not observed at µM concentrations used for spectroscopic analyses.

Since the fluorescent properties of the already described free chromophores and their glycosylated variants do not differ in means of fluorescence intensity and maxima positions, only three selected normalized fluorescence spectra for structurally different rBAM chromophores are shown in Figure 3.10b. Here, the fluorescence spectra of rBAM (**36**) and rBAM^b (**42**) are akin to the respective free chromophores, with the benzothiazole-based rBAM^b (**42**) displaying an exceptionally small Stokes shift of only 13 nm. The novel elongated rBAM^2 (**41**) nucleoside exhibits excitation and emission maxima at 554 and 576 nm, respectively, which again constitutes a bathochromic shift of about 100 nm compared to its shorter counterpart rBAM (**36**). Interestingly, the fluorescence emission band for rBAM^2 (**41**) is significantly narrowed compared to the absorption band, although according to the Franck-Condon principle both are expected to have the same width and a mirror-image symmetry. However, this is often not observed for large conjugated chromophores. In these cases, the different energetic levels are overlapped to a larger extent; therefore, not only the first excited state S_1 but also energetically higher levels (S_2, S_3, ...) are occupied upon excitation. The energetically lowest transition from the ground state to the first excited state is marked in the schematic representation in Figure 3.11a. It corresponds to the longest-wavelength absorption maximum at 560 nm.

The two observed shoulders in the absorption spectrum at shorter wavelengths are attributed to transitions from the ground to the second and third excited states S_2 and S_3. In contrast to the three transitions visible in the absorption spectrum, only the lowest one from the S_1 to the S_0 state is observed in the fluorescence emission spectrum (Figure 3.11b). This can

be explained by the significantly shorter fluorescence lifetimes for transitions from the second or higher energetic levels to the ground state and therefore only the S_1-S_0 transition can be detected as a mirror image of the absorption spectrum.[331]

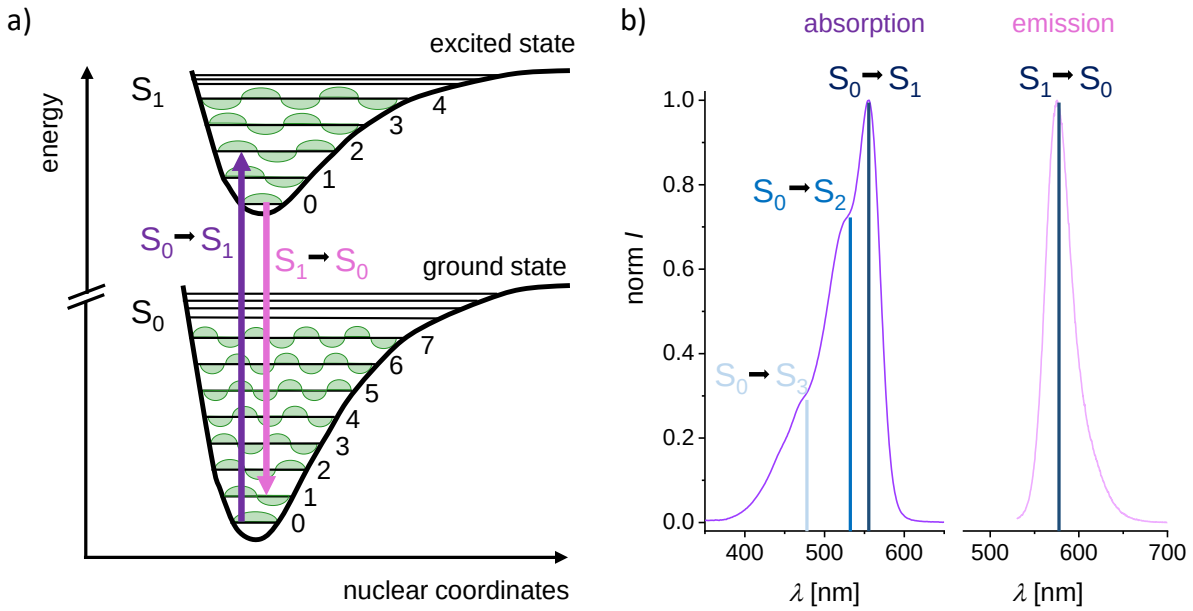

Figure 3.11: The Franck-Condon principle, schematically drawn in a), explains the arising of absorption and fluorescence bands by electronic transitions. Here, the excitation and relaxation between the vibronic ground state and the second excited vibronic state is marked. In b), the absorption and emission spectra for rBAM^2 (**41**) are shown; indicated are the most probable electronic transitions.

The fluorescence intensities for all rBAM chromophores with a two carbon bridge were in the same magnitude, except for the nitro-substituted variant rBAM^{NO2} (**39**). For this chromophore, the emission and excitation intensities are reduced by a factor of roughly four compared to the parent compound rBAM (**36**, Figure 6.1 in the appendix). The photoquenching characteristics of the nitro group attached to the aromatic system are not unexpected since this functionality is commonly recognized as a fluorescence quencher due to two reasons. First, the two lone-pair electrons on the oxygen of the nitro group are located at a comparably high energetic level caused by resonance within the O-N-O configuration. Therefore, the transition from a non-bonding electron (n) to the π^* orbital, leading to a $n\pi^*$ configuration, can serve as the lowest singlet excited state.[332] The transition to this state is optically forbidden and enhances radiationless deactivation such as heat dissipation or IC in nitro-functionalized chromophores. Second, the strong electron-withdrawing nature of the nitro group can act as an electron trapping site which forms a charge transfer state and suppresses the radiative decay channel.[332–334] Due to its low fluorescence intensity, rBAM^{NO2} (**39**) can be considered a poor label for further applications and was therefore not further characterized.

All estimated photophysical parameters for every rBAM chromophore are summarized in Table 3.5. Here, also the pK_a values and the calculated molar extinction coefficients ϵ are listed. Compared to the free BAM chromophore (**1**), the values for ϵ are higher for the ribose-attached merocyanines by around 50% while there is not much deviation between the differently substituted rBAM compounds. The same holds true for the pK_a values of all of the merocyanine ribonucleosides.

Table 3.5: pK_a values (standard deviation of the mean $\pm$0.1 for all values) and spectroscopic parameters for rBAM chromophores in water. Given are the absorbance maximum along with the position of the shorter-wavelength shoulders, the excitation and emission maxima, respectively, as well as the molar extinction coefficient ϵ with standard deviation of the mean from triplicate measurements and the Stokes shift $\Delta\lambda$ in nm and $\Delta\tilde{\nu}$ in cm^{-1}. n. d. stands for not determined values.

Name	pK_a	λ_{Abs} nm	$\epsilon\pm$s.d.m. 10^3 M^{-1} cm^{-1}	λ_{Ex} nm	λ_{Em} nm	$\Delta\lambda$ nm	$\Delta\tilde{\nu}$ 10^5 cm^{-1}
rBAM	11.0	447, 462	61$\pm$1	457	489	32	3.13
rBAM^{F}	11.5	447, 462	59$\pm$1	456	490	34	2.94
rBAM^{OMe}	12.2	456	63$\pm$1	456	492	36	2.78
rBAM^{NO2}	10.4	483	67$\pm$2	456	491	35	2.86
rBAM^{Et}	11.9	447, 462	58$\pm$1	456	489	33	3.03
rBAM^{2}	12.1	472, 527, 555	64$\pm$1	554	575	21	4.76
rBAM^{b}	n.d.	477	n. d.	477	490	13	7.69

In addition, all rBAM chromophores were subjected to fluorescence quantum yield measurements which revealed quantum yields of below 1% for all of these compounds. This low quantum yield can be explained by the chromophore structure: for high fluorescence quantum yields, the donor and acceptor moiety need to be in a coplanar arrangement, facilitating efficient delocalization of the electrons upon excitation. Since the two ring systems here are connected by the flexible polymethine bridge, the fluorescence is quenched by tortional motion around this linker. Upon rigidification of the chromophore structure by for example implementation into an oligonucleotide scaffold this rotation should be inhibited, presumably leading to increased fluorescence quantum yields. To support this assumption, the relative quantum yields of BAM-modified oligonucleotides have been determined and will be discussed in sections 3.3 and 3.4.

For follow-up experiments, rBAM (**36**) and rBAM^{b} (**42**) were chosen since the first one is synthetically the easiest one to access and the latter one shows red-shifted excitation properties which is desired for biochemical applications. Both nucleosides were converted into the corre-

sponding phosphoramidite building blocks and incorporated into oligonucleotides. The hereby obtained supramolecular systems were characterized regarding their thermodynamic and spectroscopic features. In the next part, the synthesis of the rBAM and rBAM^{b} phosphoramidites, followed by the preparation of modified oligonucleotides will be described.

3.3 rBAM chromophores in the RNA scaffold

3.3.1 Protection strategies for phosphoramidite building blocks

Solid phase synthesis of natural and artifical DNA and RNA oligonucleotides is based on phosphoramidite chemistry, which was first described by Caruthers in the early 1980s.[335] Phosphoramidites are suitable building blocks for the sequence specific preparation of oligonucleotides with lengths of up to 200 bases; however, appropriate protecting groups need to be introduced for reactive functions to avoid side reactions during the synthetic process.[336] An overview over the most commonly used protecting groups is given in Figure 3.12.

Protection of the nucleobase

Exocyclic nucleobase amino groups need to be protected by permanent protecting groups which stay on during the complete solid phase synthesis procedure and can be cleaved afterwards by treatment with a base. While for unmodified oligonucleotides often protecting groups that can only be removed under harsh conditions are used, such as benzoyl (Bz) for A and C and isobutyryl (Ib) for G, for many modified oligonucleotides cleavage under much milder conditions is required.[335] Therefore, the exocyclic amino group of A is often protected by phenoxy acetyl (PAc) while C and G can be acetyl (Ac)- or dimethylformamidine (dmf)-protected, respectively.[337,338] Besides base-labile nucleobase protecting groups also photo- and fluoride-labile ones have been reported, but these are rarely used.[339,340]

Protection of the 5'-hydroxy group

In contrast to the protecting groups at the nucleobase, the one at the 5'-hydroxy function of the ribose is only meant for temporary protection as it is cleaved at the beginning of each cycle during solid phase synthesis. Therefore, it has to be orthogonal to the nucleobase protecting groups. Almost exclusively, a 4,4'-dimethoxytrityl (DMT) functionality is introduced at this position of the sugar moiety since it can be removed under mildly acidic conditions and allows monitoring of the nucleoside coupling efficiency during oligonucleotide synthesis by measurement of the absorbance of the brightly colored cleaved trityl cation.[341] Another advantage of the DMT protecting group is its efficient site-specific introduction during the preparation of the phosphoramidite, even in the presence of free 2'- and 3'-OH groups: due to its bulkiness, DMT chloride reacts much faster with the primary 5'-OH compared to the two secondary hydroxy groups, which in most cases leads to exclusive formation of the 5'-DMT protected nucleoside.

Protection of the 2'-hydroxy group

Compared to DNA, an additional protecting group for 2'-OH is needed for RNA phosphoramidite synthesis. The chosen protecting group needs to be orthogonal to the nucleobase protecting groups, being stable under acidic as well as basic conditions; if this is not the

case, the free 2'-OH can be deprotonated at higher pH values, which leads to oligonucleotide degradation due to the formation of cyclic 2',3'-phosphates.[342] In addition, a suitable 2'-protecting group should not be too sterically demanding to not interfere with the coupling step in the solid phase synthesis process. Fluoride-labile silyl groups have been found to be the best choice for 2'-OH protection; among them especially the silyl ethers [(tri-*iso*-propylsilyl)oxy]methyl (TOM), *tert*-butyldimethylsilyl (TBDMS) and tri-*iso*-propylsilyl (TIPS) are widely used.[343,344]

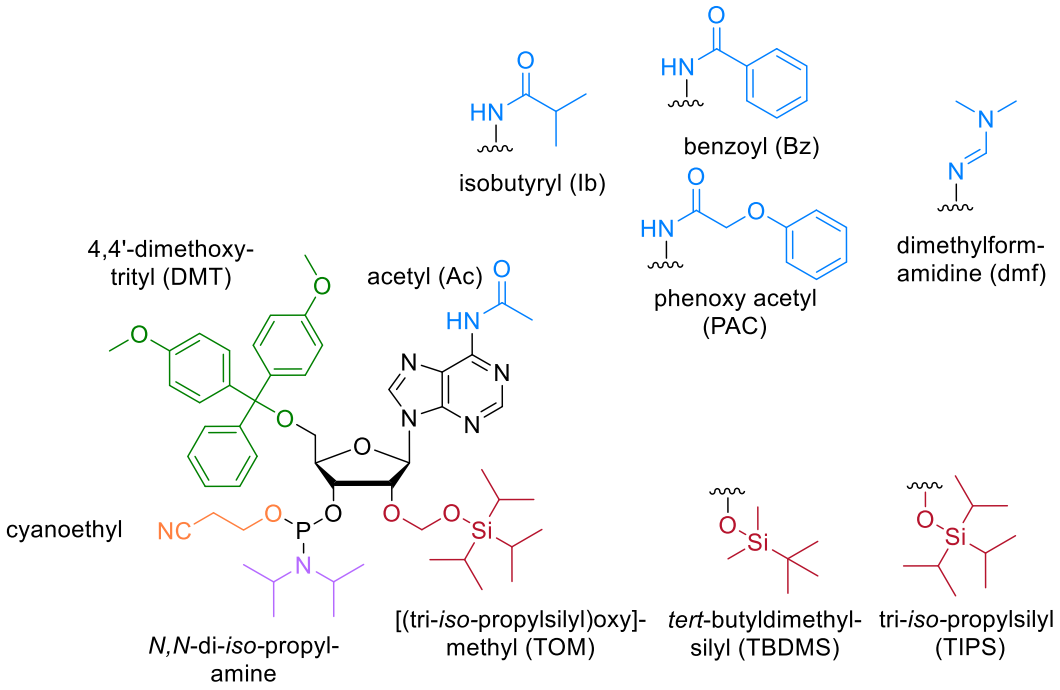

Figure 3.12: Common protection groups for phosphoramidite building blocks, exemplarily shown for an rA building block. The nucleobase protection groups are colored blue, 2'-OH protecting groups are colored red and the 5'-OH protecting group is shown in green. The leaving and protecting groups at the phosphoramidite moiety are marked in purple and orange, respectively.

Since the 2'-functionalization needs to be accomplished prior to the introduction of the phosphoramidite, isomeric mixtures of 2'- and 3'-protected nucleosides are often obtained. If for example TBDMS is used for protection, the yield of the desired 2'-silylated building block can be increased by the addition of $AgNO_3$ while for the preparation of TOM-protected nucleosides the vicinal 2'/3'-OH groups are often activated by a dialkyl tin reagent.[345] However, the TOM protection group has several advantages compared to the TBDMS group: it is, on the one hand, sterically less hindered and on the other hand not as prone to migration from 2'- to 3'-position during phosphoramidite synthesis.[344]

In addition to the protection of free hydroxy and amino groups also the phosphoramidite functionality contains an *N,N*-di-*iso*-propyl amino protecting group which is removed after each synthetic cycle by activation with a tetrazole catalyst. Meanwhile, the phosphite hydroxy group

bears a cyanoethyl residue which is cleaved under basic conditions during the deprotection of the full-length oligonucleotide.

The protection strategy described above employing a 5'-DMT and a 2'-TOM protecting group was used for the preparation of the two modified building blocks rBAM (**36**) and rBAM^b (**42**). Since the artificial nucleobase analogs within these two structures do not exhibit any reactive functionality, additional protecting groups were omitted. A detailed description and discussion of the synthetic pathway toward these two phosphoramidites will be given in the next section.

3.3.2 Synthesis of the rBAM and rBAM^b phosphoramidite building blocks

In the first step of the synthesis toward the desired rBAM and rBAM^b phosphoramidite building blocks **49** and **50**, both free nucleosides were 5'-DMT-protected with DMT chloride in an S_N1-type reaction (Scheme 3.14). If the vicinal 2'- and 3'-hydroxy groups were transformed into an acetal using dimethylformamide dimethyacetal (DMFDMA) prior to the introduction of DMT, they were blocked for possible side reactions and the yields of the tritylated compounds **43** and **44** improved significantly. Since such dimethyl acetal intermediates are known to be fairly unstable, they were only generated *in situ* and directly used for the DMT protection step. After removal of the temporary acetal protective group with methanol, **43** and **44** were obtained in moderate to good yields.

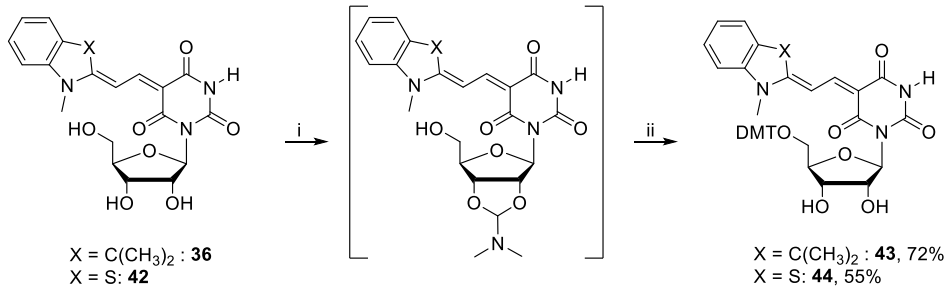

Scheme 3.14: Introduction of the DMT group to the free rBAM (**36**) and rBAM^b (**42**) nucleosides *via* an acetal intermediate. Conditions: i) DMFDMA, dry pyridine, r. t., 18 h ii) DMT-Cl, dry pyridine, r. t., 2.5 h.

As mentioned before, the TOM group was chosen for protection of the free 2'-OH. The reagent TOM chloride which is required for this reaction was prepared beforehand according to a reported procedure.[344] In the first step, an ethylthiomethanol intermediate was synthesized from paraformaldehyde and ethanethiol (Scheme 3.15). Upon silylation of this intermediary compound with triisopropylsilyl chloride in the presence of imidazole, intermediate **45** was generated and finally transformed into the target compound **46**, which was purified by distillation.

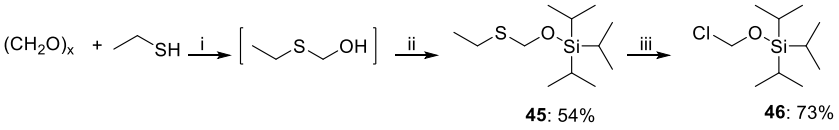

Scheme 3.15: Preparation of TOM chloride required for the protection of the 2'-OH of rBAM (**36**) and rBAM^b (**42**). Conditions: i) 2 M NaOH, 0 to 40 °C, 1 h; ii) imidazole, TIPS-Cl, r. t., 14 h; iii) SO_2Cl_2, CH_2Cl_2, 0 °C to r. t., 1 h. TIPS-Cl: tri-*iso*-propylsilyl chloride.

For the protection of the 2'-OH group with TOM chloride, the reaction conditions need to be chosen carefully to improve the yield of the desired 2'-isomer and prevent major protection of the 3'-position. As described by Pitsch and coworkers, best reaction outcomes can be obtained by activation of the free hydroxy groups with a tin dialkyl dichloride reagent under basic conditions (Scheme 3.16).[344]

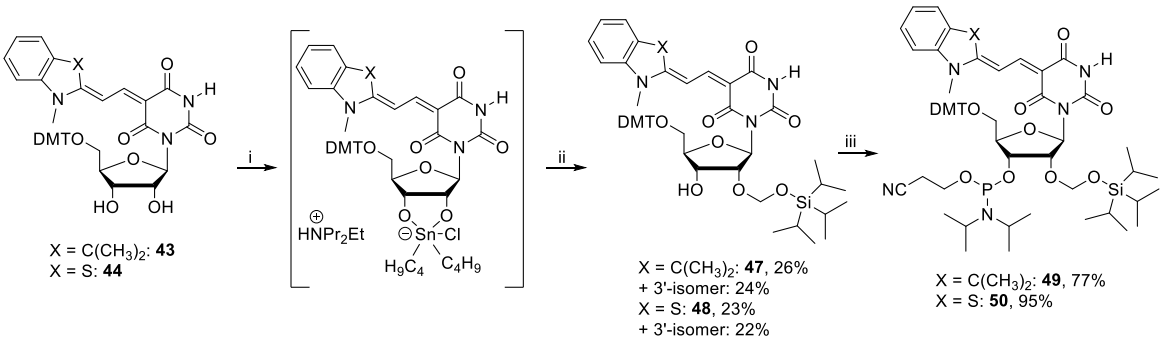

Scheme 3.16: 2'-TOM protection and phosphitylation of the DMT-protected RNA nucleosides **43** and **44**. Shown is also the activation of the two nucleosides with a tin dialkyl dichloride reagent prior to TOM-protection. Conditions: i) DIPEA, tBu$_2$SnCl$_2$, 1,2-DCE, 70 °C, 40 min; ii) TOM-Cl, r. t. 1.5 h; iii) Me_2NEt, CEP-Cl, CH_2Cl_2, r. t., 2 h.

Here, the use of tBu$_2$SnCl$_2$ is preferred over nBu$_2$SnCl$_2$ for the generation of the activated cyclic intermediate since it finally leads to higher yields of the 2'-protected nucleoside. The intermediary 2'-3'-*O*-dibutylstannilydene derivative was treated with TOM chloride under optimized conditions and after aqueous workup the 2'- or 3'-TOM-protected phosphoramidite precursors were separated by column chromatography on silica gel. The position of the introduced TOM protecting group was in the following elucidated by 2D-NMR spectroscopy. In the ^{1}H-^{1}H-COSY NMR spectra of the faster eluting compounds, a correlation between the 3'-H and the proton of the free 3'-OH is visible while the 2'-H does not show any correlation to an OH proton. This is examplarily shown in Figure 3.13 for the desired 2'-TOM protected rBAM nucleoside **47**. The spectra of the slower eluting derivatives show converse correlations; therefore, the desired protected 2'-isomers **47** as well as **48** and the undesired 3'-isomers are in the first and second isolated fraction, respectively.

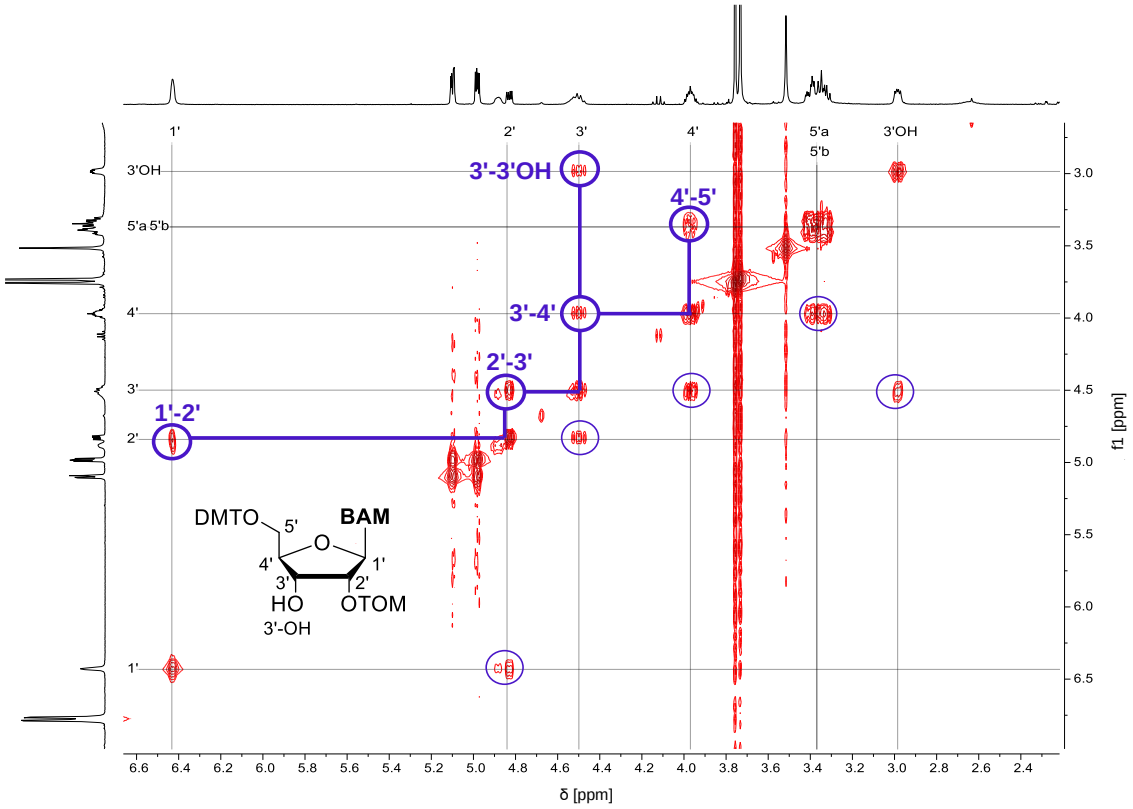

Figure 3.13: ^{1}H-^{1}H COSY NMR spectrum for the desired 2'-TOM protected rBAM nucleoside **47**. The important H-H couplings are marked; the coupling between the 3'-H and the 3'-OH proton confirms the identity of the desired 2'-TOM isomer.

Finally, the rBAM and rBAM^{b} phosphoramidite building blocks **49** and **50** were prepared by phosphitylation. In general, two main procedures to access nucleoside phosphoramidites are known: the 3'-unprotected nucleoside precursor can either be treated with a diamidite such as 2-cyanoethyl *N,N,N',N'*-tetra-*iso*-propylphosphorodiamidite under the catalysis of a weak acid, or with 2-cyanoethyl *N,N*-di-*iso*-propylchlorophosphoramidite (CEP-Cl) in the presence of an organic base. Here, the latter method was employed and the two phosphoramidites **49** and **50** were isolated with reasonable yields after purification. The formation of the correct products was confirmed by NMR spectroscopy. However, especially the rBAM^{b} phosphoramidite **50** showed to decompose to phosphonate and phosphate triester in several NMR solvents already after only one hour, making it impossible to record a clean carbon spectrum. The interpretation of the recorded NMR spectra for the phosphoramidites **49** and **50** was further hampered by the existence of four different isomers due to the two double bond configurations described earlier and the stereocenter at the phosphorous atom.

These isomers are also visible in the ^{31}P NMR spectra: normally, two signals at around 150 ppm are expected for the P(III) atom, while in the case of **49** and **50**, several overlapped signals with a chemical shift in this region are observed. In addition, the benzothiazole-derived compound **50** still contained a H-phosphonate species after purification, leading to a ^{31}P NMR signal with a chemical shift of 13.4 ppm for the P(V) atom. The formation of phosphite triesters,

which would lead to signals with a chemical shift of around 138 to 140 ppm, is not observed in the ^{31}P NMR spectrum of this freshly prepared sample.

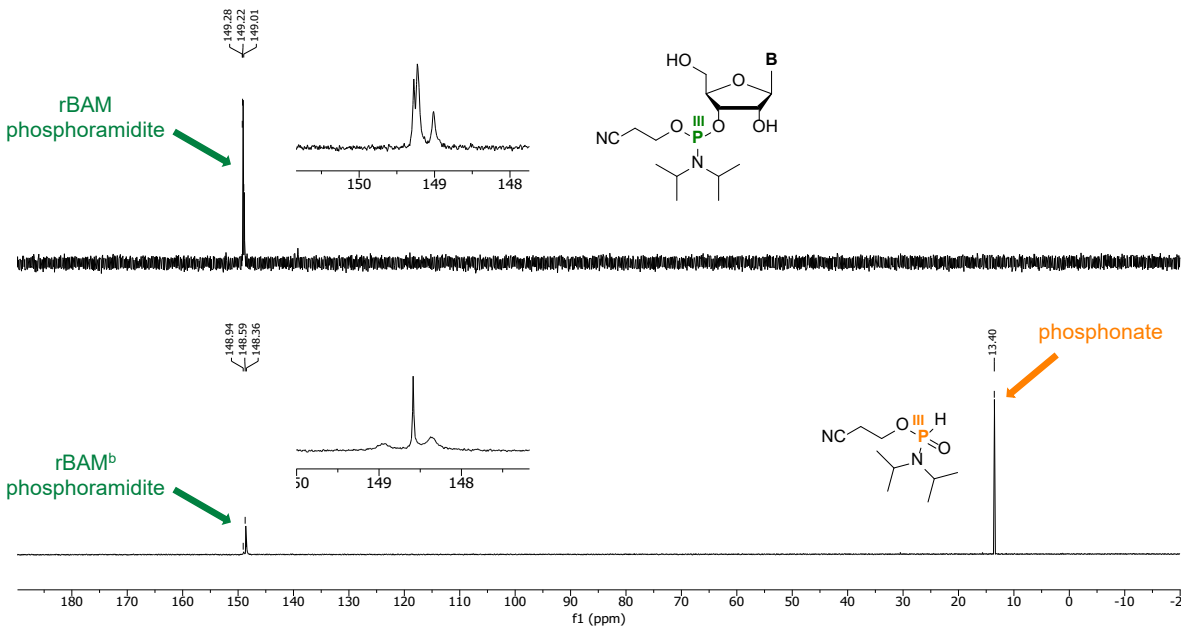

Figure 3.14: ^{31}P NMR spectra for rBAM and rBAM^{b} phosphoramidites **49** and **50**. The chemical shift regions of these phosphoramidites are shown enlarged as inserts. In the spectrum of the rBAM^{b} phosphoramidite **50**, at 13.4 ppm the signal for a phosphonate due to hydrolysis of CEP chloride is visible. **B** is abbreviated for nucleobase.

However, this low molecular weight byproduct arises from hydrolysis of the phosphitylating reagent CEP-Cl and is to some extent tolerated in solid phase synthesis. Therefore, the sensitive phosphoramidite **50** was used without a second purification step for oligonucleotide synthesis described in the next section.

3.3.3 Design and synthesis of rBAM- and rBAM^{b}-modified RNA oligonucleotides

In the first part of this section, the basic principles of oligonucleotide solid phase synthesis will be explained. Based on this, the preparation, purification and characterization of merocyanine containing RNA oligonucleotides is to be discussed.

3.3.3.1 A general overview of oligonucleotide solid phase synthesis

Solid phase synthesis is the most widely used method for the chemical preparation not only of oligonucleotides but also of peptides and oligosaccharides. It gives access to the rapid preparation of artificial oligonucleotide strands with variable sequences and a length of up to 200 nucleotides.[346]

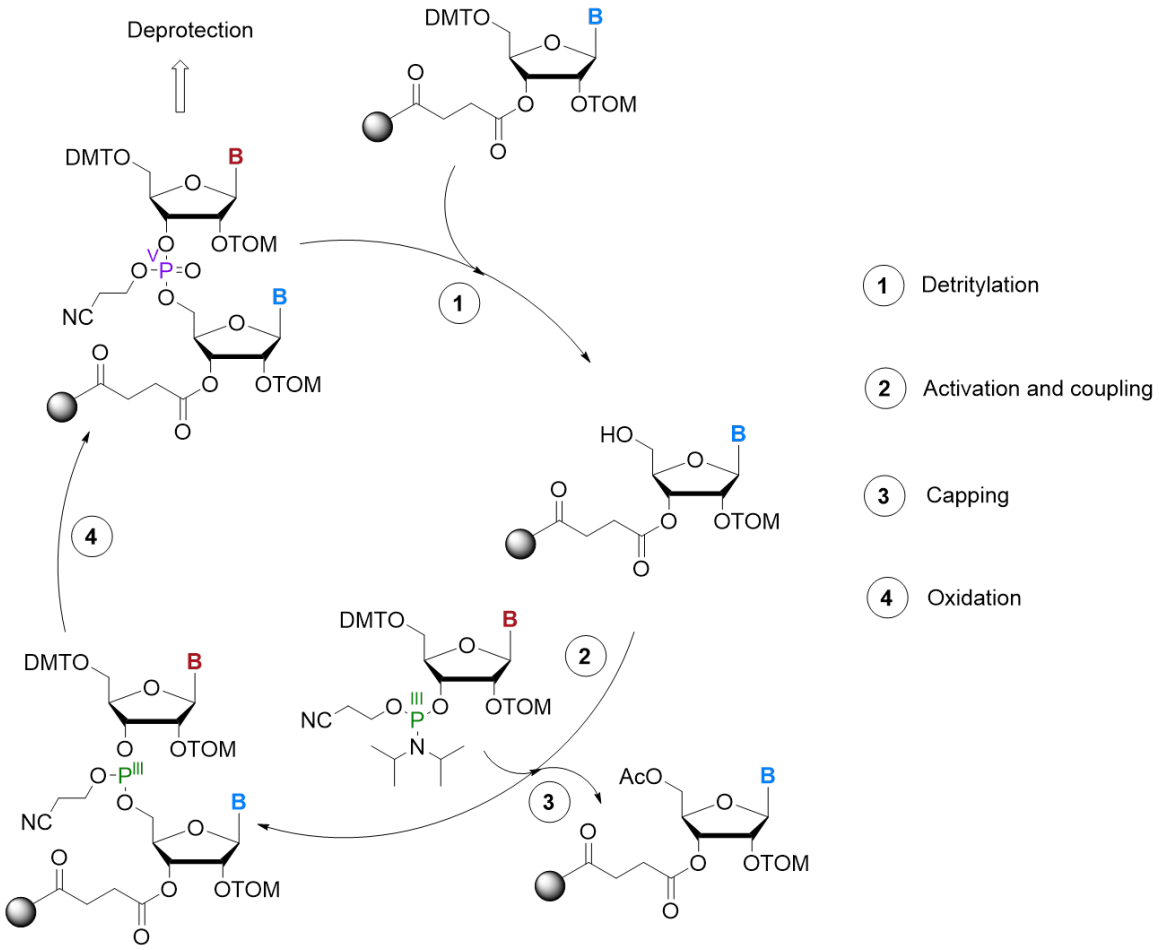

Scheme 3.17: General scheme for oligonucleotide solid phase synthesis. In the first step, the DMT group at the 5'-position of the nucleoside bound to the solid phase is cleaved, followed by tetrazole activation, coupling of the first phosphoramidite and oxidation of P(III) to P(V) by iodine. Unreacted free 5'-OH groups are capped with acetyl groups. The cycle is repeated until the desired oligonucleotide length is reached. **B** is abbreviated for nucleobase.[346,347]

The main advantage of oligonucleotide solid phase synthesis is the easy removal of impurities by washing the solid support with organic solvents. In addition, high yields are achievable as single reaction steps can be driven close to completion by using a large excess of reactant solutions. Although the entire automated solid phase synthesis process mimicks RNA replication in nature, it does not proceed in 5'- to 3'-direction but from the 3'- to the 5'-end (Scheme 3.17).

The cyclic process starts with the detritylation of the first nucleoside, which is bound to a controlled pore glass (CPG) solid support, a rigid and non-swelling material, and later constitutes the first nucleotide at the 3'-end of the strand (step 1). After the removal of the DMT group with di- or trichloroacetic acid, the phosphoramidite for the next nucleotide in the sequence is activated by a tetrazole catalyst which protonates the di-*iso*-propyl amino group, converting it into a good leaving group (step 2). The phosphorous of the activated nucleoside is activated by a tetrazole catalyst and then rapidly attacked by the free 5'-OH of the resin-bound nucleoside

under formation of an acid-labile phosphite triester. At this point of the synthetic cycle the capping of all unreacted 5'-OH functions with acetyl groups is crucial to prevent them from further reaction, leading for example to deletion mutations (step 3). The phosphite triester is oxidized by iodine in pyridine and converted into a stable P(V) species (step 4). This cycle is repeated until the desired oligonucleotide length is reached; the synthesized oligonucleotide is afterwards cleaved from the solid support and deprotected.

However, oligonucleotide solid phase synthesis is restricted to comparably short sequences of up to 200 nt. To access longer DNA or RNA strands, other biochemical methods such as *in vitro* transcription or ligation of shorter oligonucleotides need to be employed.
Despite its many advantages and the high yields of oligonucleotides that can be obtained by solid phase synthesis, this process is highly sensitive to contaminations and humidity, especially if RNA strands are synthesized. Therefore, it was especially important to freshly prepare rBAM and rBAM^b phosphoramidite solutions in dry acetonitrile and store them overnight over molecular sieves prior to solid phase synthesis.

3.3.3.2 Synthesis of rBAM- and rBAM^b-containing RNA oligonucleotides

To study the influence of merocyanine modifications on the stability of RNA duplex structures and to investigate chromophore-chromophore interactions, suitable oligonucleotide sequences had to be designed. It was decided to use RNA 12mers since this length corresponds to one helix turn in A-form RNA. In addition, 12mer oligonucleotides can easily be precipitated in 70% ethanol and their duplex structures show melting temperatures appropriate for thermodynamic analyses.

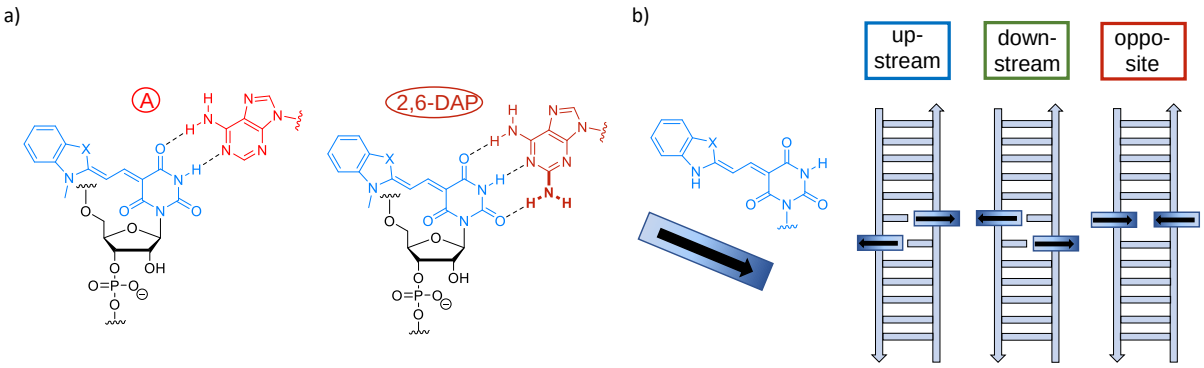

Figure 3.15: a) Base pairing of merocyanine RNA nucleosides with either A or 2,6-DAP, leading to the formation of two or three hydrogen bonds, respectively. b) Schematic representation of merocyanine chromophore orientation in double-modified duplex structures. The arrow indicates the direction of the dipole moment.

Since the barbituric acid moiety of rBAM and rBAM^b mimicks a natural U nucleobase, the sequence was chosen to facilitate the incorporation of the merocyanine ribonucleosides into

both strands in the duplex core opposite A. In addition, two strands for an unmodified reference duplex were synthesized as well as complementary strands for helix structures with each of the canonical nucleosides opposite rBAM or rBAM^b for investigation of base pairing properties. To enhance the probability of base pairing between the modified and its opposing nucleoside by increasing the number of possible H-bonding sites, an additional sequence with 2,6-diaminopurine (2,6-DAP) was generated (Figure 3.15). For further examination of the merocyanines base pairing behavior, also a 12 nt m^{6}A-containing oligomer was synthesized since the sterically demanding *syn*-oriented *N*6-methyl group of this nucleobase affects the strength of the formed Watson-Crick base pair.

Commercially available phosphoramidites and CPG solid supports for canonical nucleosides as well as a standard RNA synthesis protocol with a final detritylation step were used for solid phase synthesis. A detailed synthetic procedure including the required reagent solutions can be found in section 5.2. The crude oligonucleotides obtained by solid phase synthesis were purified by denaturing polyacrylamide gel electrophoresis (PAGE); their quality and identity was verified by anion exchange high performance liquid chromatography (HPLC) and high-resolution electrospray mass spectrometry (HR-ESI MS), respectively (Figure 3.16).

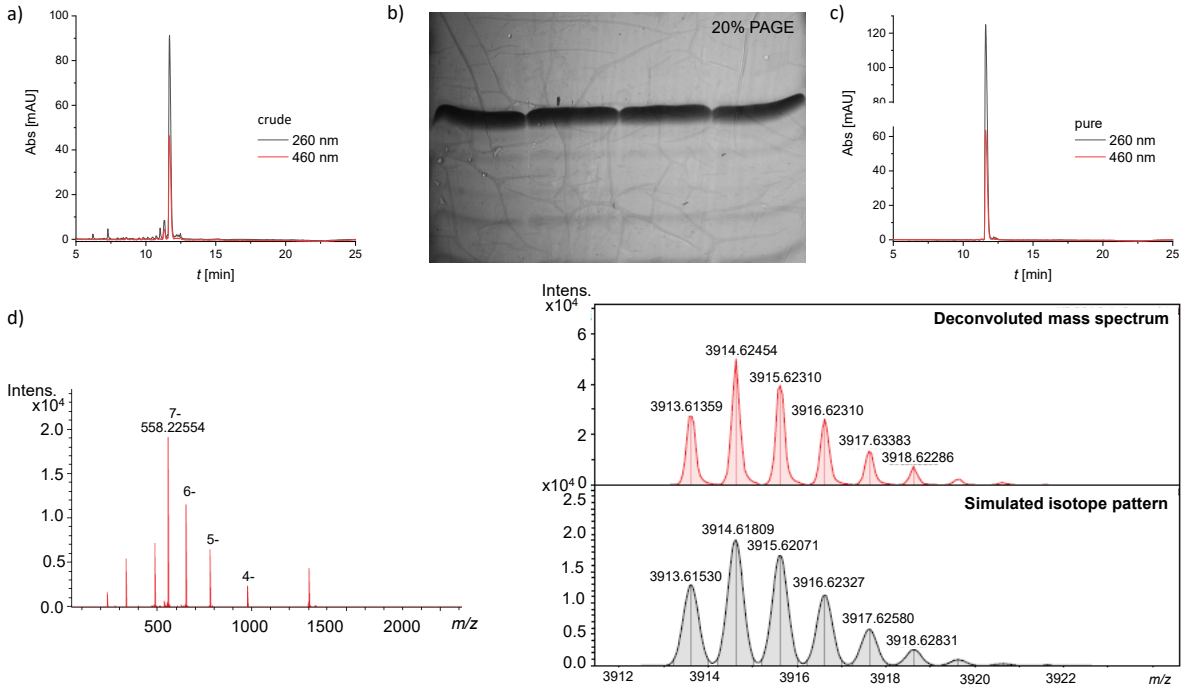

Figure 3.16: HPLC trace for the deprotected crude oligonucleotide **R14** (a), PAGE image of this oligonucleotide (b) and the corresponding HPLC trace for the pure sample for quality verification (c). The identity of the synthesized oligonucleotide is proven by deconvolution of the HR-ESI-MS spectrum (left) and comparison of the simulated isotope pattern (gray) with the deconvoluated mass spectrum (red, d).

Native and rBAM-modified oligonucleotides were obtained with reasonable yields and high quality after purification, while the amount obtained of the 2,6-DAP- and rBAM^b-modified

oligomers showed to be fairly low. For **R7**, the commercially available 2,6-DAP phosphoramidite with formamidine-protected exocyclic amino groups was used; these protecting groups can readily be cleaved under basic conditions.

However, the formamidine protecting group at the 2-amino function is susceptible to exchange by an acetyl group during the capping step of the solid phase synthesis procedure. This *N*2-acetyl group is known to be comparably stable under ultramild conditions such as incubation overnight at 37 °C in aqueous ammonia used here.[348]

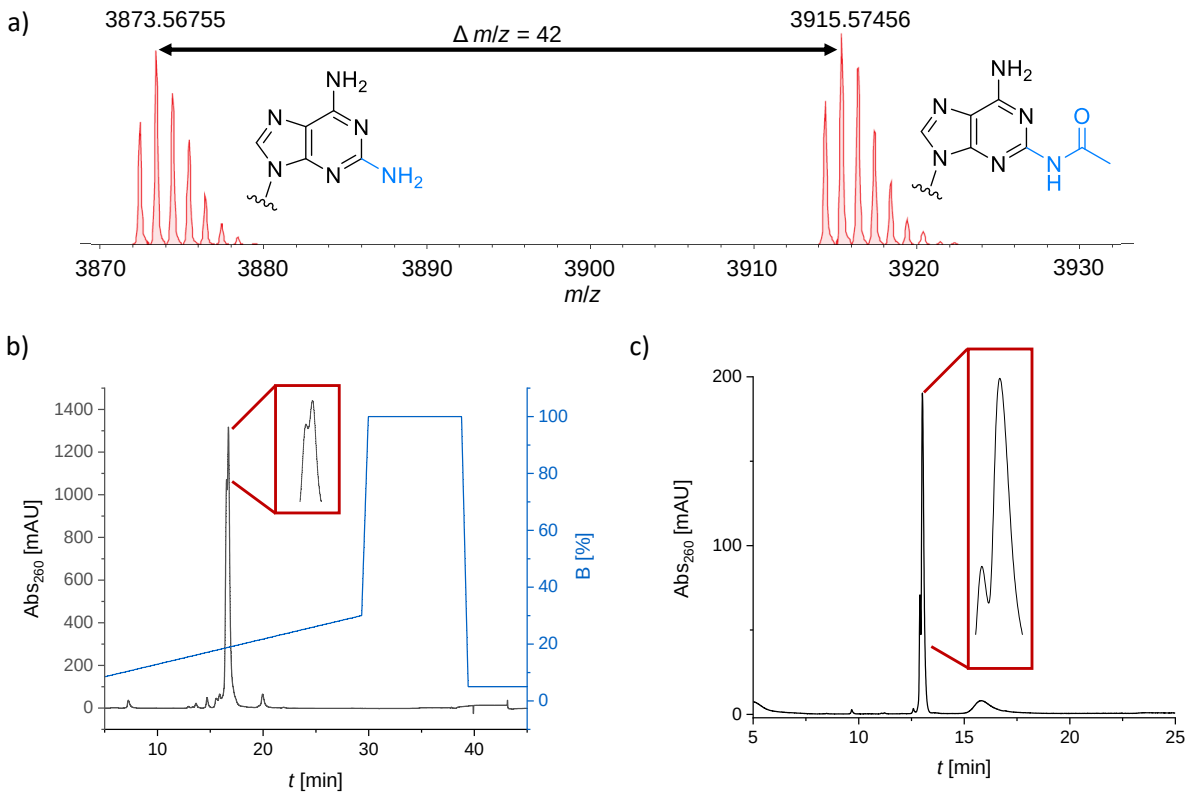

Figure 3.17: a) The deconvoluted ESI mass spectrum of **R7** after PAGE purification shows the presence of the fully deprotected oligonucleotide along with an *N*2-acetylated byproduct which is also visible in the RP-HPLC chromatogram of PAGE-purified **R7** (b). The ion exchange HPLC chromatogram of **R7** after purification by RP HPLC still shows the presence of the *N*2-acetylated byproduct (c). Conditions can be found in section 5.2.3.

In Figure 3.17a, the deconvoluted ESI spectrum of **R7** after PAGE purification is shown; it clearly contains the completely deprotected oligonucleotide along with the by 42 mass units heavier single-acetyl protected one in almost 1:1 ratio. Therefore, the mixture was subjected to RP-HPLC (Figure 3.17b). Although both species unfortunately had almost the same retention time, the desired deprotected oligonucleotide was partially purified from the byproduct by fractional peak collection. The ion exchange HPLC trace recorded after RP HPLC purification is shown in Figure 3.17c; the acetylated side product can be seen as impurity at shorter retention time compared to the fully deprotected oligomer. To prevent the acetylation of the

exocyclic nitrogen of 2,6-DAP, phenoxyacetyl anhydride instead of acetic acid anhydride could be used for capping in the solid phase synthesis process since the PAC protecting group is easier to remove. Despite the presence of the side product, **R7** was later anyway used for duplex stability measurements.

The low yields for the rBAM^b-containing oligonucleotides **R9**, **R11**, **R13** and **R15** can be explained by the instability of the rBAM^b chromophore toward ammonia used for basic oligonucleotide deprotection, leading to aminolysis of the benzothiazole-derived merocyanine and formation of colorless byproducts. Therefore, these oligonucleotides had to be further purified by RP-HPLC after gel electrophoresis and were finally obtained in pure form. The formation and constitution of the aminolysis byproducts will be discussed in section 3.4.2.

Table 3.6: Sequences, yields and masses for native and modified RNA 12 nt oligomers obtained by solid phase synthesis. Particularly important nucleobases are shown in bold, modified ones are colored in addition.

Name	5'-sequence-3'	yield[a] nmol	*M* calc. g mol^{-1}	*M* meas.[b] g mol^{-1}
R1	GAUGAU**A**GCUAG	32	3857.56124	3857.57503
R2	CUAGCUAUCAUC	23	3714.51558	3714.52176
R3	GAUGAU**C**GCUAG	39	3833.55001	3833.54554
R4	GAUGAU**G**GCUAG	43	3873.55616	3873.56620
R5	GAUGAU**U**GCUAG	43	3834.53403	3834.52933
R6	GAUGAU**A**GCUAG	94	3871.57744	3871.61737
R7	GAUGAU**A**GCUAG	10	3872.57214	3872.59076
R8	GAUGA**X**AGCUAG	34	4056.66096	4056.64911
R9	GAUGA**X**AGCUAG	12	4046.58608	4046.58471
R10	CUAGC**X**AUCAUC	44	3913.61530	3913.61359
R11	CUAGC**X**AUCAUC	11	3903.54042	3903.53311
R12	CUAGCU**X**UCAUC	42	3890.58808	3890.59383
R13	CUAGCU**X**UCAUC	10	3880.51320	3880.51386
R14	CUAGCUA**X**CAUC	47	3913.61530	3913.62010
R15	CUAGCUA**X**CAUC	13	3903.54042	3903.54073

[a] 600 nmol synthesis scale

[b] monoisotopic masses obtained by charge deconvolution of the raw spectra

A = m^{6}A, **A** = 2,6-DAP, **X** = rBAM, **X** = rBAM^b.

An overview of the RNA sequences prepared in the course of this thesis is provided in Table 3.6; given are the sequence, the yields of the purified oligonucleotides and the observed as well

as calculated molecular masses.

The purified RNA oligonucleotides were in the following hybridized to their respective complementary counterstrands to obtain differently duplex structures (Figure 3.18). In the single-nucleotide mutants, either one of the four canonical nucleobases, m^6A or 2,6-DAP is located opposite rBAM or $rBAM^b$. Additionally, double-modified duplex structures with different chromophore positions and orientations toward each other were generated to analyse the dependence of duplex stability and chromophore-chromophore interactions on the spatial arrangements of the merocyanine modifications. The resulting double-modified systems will in the following be named downstream, upstream and opposite and indicated with the color code blue for downstream, green for upstream and red for opposite.

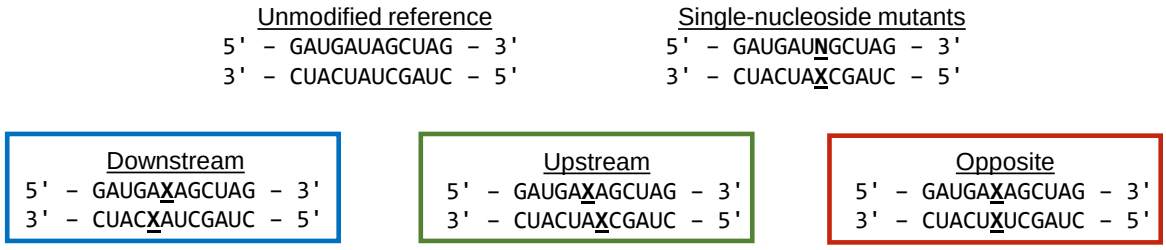

Figure 3.18: Duplex sequences for unmodified and modified RNA structures. **N** is the abbreviation for any of the nucleobases A, C, G, U, m^6A and 2,6-DAP while **X** is either rBAM or $rBAM^b$.

In the next section, the thermodynamic properties of the duplex structures shown in Figure 3.18 will be compared to each other and discussed.

3.3.4 Thermodynamic properties and structural parameters of rBAM- and $rBAM^b$-modified RNA oligomers

An important parameter for the complete characterization of modified duplex structures is their thermodynamic stability. To further investigate this property, thermal melting profiles of duplex structures can be recorded to estimate the duplex melting temperature T_m as well as the changes in free enthalpy ΔH^0 and free entropy ΔS^0.
The melting temperature T_m of an oligonucleotide duplex structure is defined as the temperature at which half of the duplex structure is denatured and present in single-stranded form or as random coil; it can be assessed by changes in the UV absorbance. Unwinding of the duplex upon heating can be explained by breaking of hydrophobic stacking interactions since these interactions are the main factors for duplex stability. In general, the melting temperature of a given duplex is influenced by three main factors which are the buffer composition, the length and the sequence of the oligonucleotide. For the analysis of the thermodynamic behavior of nucleic acid duplex structures, the typical sigmoidal-shaped melting curves are analyzed by

assuming a two-state melting transition, which neglects possible intermediary binding states and yields the duplex melting temperature from the curve's inflection point (Figure 3.19).

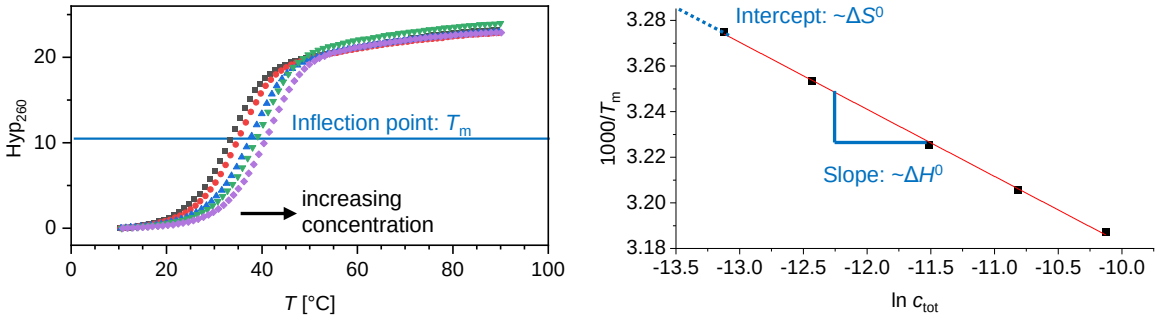

Figure 3.19: The thermal melting profiles for an oligonucleotide at five different concentrations show increasing melting temperatures with increasing oligonucleotide concentration (left). The hyperchromicity at 260 nm, which is the difference in absorbance between low and high temperatures corresponding here to the presence of duplex and single-stranded oligonucleotides, is plotted against the sample temperature. The estimated melting points can be used to generate a van't Hoff plot from which the free enthalpy ΔH^0 and the free entropy ΔS^0 can be derived (right).

Since heteroduplexes, in contrast to hairpin forming systems, have a molecularity greater than one, the association constant K for duplex formation as well as the related T_m are dependent on the oligonucleotide concentration, with increasing T_m values for higher concentrations. However, this only holds true for short oligomers but not for longer ones. The reason for this is that duplex formation includes an initiation step, which describes the encounter of two strands followed by base pair formation, and a propagation step in which the initiation complex is further elongated. While the initiation step is dominant for shorter oligonucleotides, for larger oligonucleotides the propagation step plays a more important role but since the number of strands present does not change in this step, it is independent from the sample concentration, leading to a pseudomonomolecular behavior. For DNA duplexes, this behavior is observed for lengths roughly between 12 and 50 base pairs.[349]

By assuming the two-state model for oligonucleotide melting behavior, a van't Hoff plot can be used to derive the thermodynamic parameters ΔH^0 and ΔS^0 (Figure 3.19). ΔH^0 is mainly influenced by short-range van der Waals and base stacking interactions, with a small net contribution from hydrogen bonding within the Watson-Crick base pairs, while ΔS^0 represents changes in the order of the two states, including conformation changes and rearrangements of associated solvent molecules and counter ions. From these, the free Gibbs enthalpy ΔG^0 at 298 K can be calculated by application of the Gibbs-Helmholtz equation. An explanation of the formulas necessary for parameter calculation is given in section 5.4.1.6.

Within this thesis, thermal denaturation curves were measured for duplex samples at different concentrations (1, 2, 5, 10 and 20 µM) in phosphate-buffered saline (PBS, 100 mM NaCl, 10 mM

sodium phosphate, pH 7.0). Measurements started with an initial annealing ramp followed by two cooling/heating cycles. For all of the modified duplex structures, sigmoidal shaped melting curves were obtained, suggesting a cooperative melting behavior. From these curves, the concentration-dependent duplex melting temperatures T_m were extracted; a deviation of 0.5 °C is assumed for the obtained values which is considered the limiting accuracy of this type of experiment.[350] In Table 3.7, the observed melting temperatures together with derived thermodynamic para-meters for single-modified rBAM and rBAM^b duplex structures are summarized and compared to the unmodified reference duplex **R1/R2**.

Table 3.7: Abbreviated sequences, melting temperatures and thermodynamic parameters for RNA duplex structures with a single merocyanine modification. Particularly important nucleobases are shown in bold, non-native ones are colored in addition. Given are also the differences in melting temperature relative to the unmodified reference sequence **R1/R2**.

Name	sequence	$T_m^{[a]}$ °C	$\Delta T_m^{[b]}$ °C	ΔH^0 kcal mol^{-1}	ΔS^0 cal mol^{-1} K^{-1}	ΔG^0_{298K} kcal mol^{-1}
R1/R2	5'-...AUA...-3' 3'-...UAU...-5'	54.4	-	-119	-337	-18.4
R8/R2	5'-...A**X**A...-3' 3'-...U**A**U...-5'	38.1	-16.3	-98.7	-291	-11.9
R1/R10	5'-...AU**A**...-3' 3'-...UA**X**...-5'	38.2	-16.2	-105	-312	-12.3
R6/R10	5'-...AU**A**...-3' 3'-...UA**X**...-5'	36.7	-17.7	-91.3	-269	-11.0
R7/R10	5'-...AU**A**...-3' 3'-...UA**X**...-5'	42.6	-11.8	-107	-312	-13.7
R3/R10	5'-...AU**C**...-3' 3'-...UA**X**...-5'	34.7	-19.7	-89.9	-266	-10.6
R4/R10	5'-...AU**G**...-3' 3'-...UA**X**...-5'	36.8	-17.6	-93.4	-276	-11.3
R5/R10	5'-...AU**U**...-3' 3'-...UA**X**...-5'	35.0	-19.4	-89.1	-264	-10.5
R9/R2	5'-...A**X**A...-3' 3'-...U**A**U...-5'	39.1	-15.3	-113	-336	-12.8

[a] values for 5 µM samples in PBS (100 mM NaCl, 10 mM phosphate, pH 7.0); 0.5 °C/min heating rate; a standard error of ±0.5 °C is assumed

[b] difference relative to unmodified duplex

A = m^{6}A, **A** = 2,6-DAP, **X** = rBAM, **X** = rBAM^b.

Here, the color of the X refers to the modification incorporated with **X** standing for rBAM and **X** for rBAM^b. The unmodified RNA 12mer duplex shows a melting temperature of 54.4 °C which is a reasonable value for an RNA duplex of this length and in agreement with values calculated by the nearest-neighbor model.[351,352] In comparison to this reference structure, all of the modified duplexes show a reduced melting point by 15 to 20 °C which is attributed to the loss of hydrogen bonding within the duplex structure and a perturbation of the helix caused by the steric demand of the introduced chromophores.

Among the duplex structures with an A or its variants m^{6}A and 2,6-DAP opposite rBAM, the one with 2,6-DAP (**R7/R10**) possessing three instead of two sites for hydrogen bonding shows the highest melting temperature with 42.6 °C while the m^{6}A-containing system **R6/R10** is only slightly destabilized since m^{6}A has to adopt the energetically unfavored *anti*-conformation to engage in base pairing (Figure 3.20b). However, the duplex structures with either C, G or U opposite rBAM are destabilized to a similar extent as **R1/R10** (Figure 3.20a).

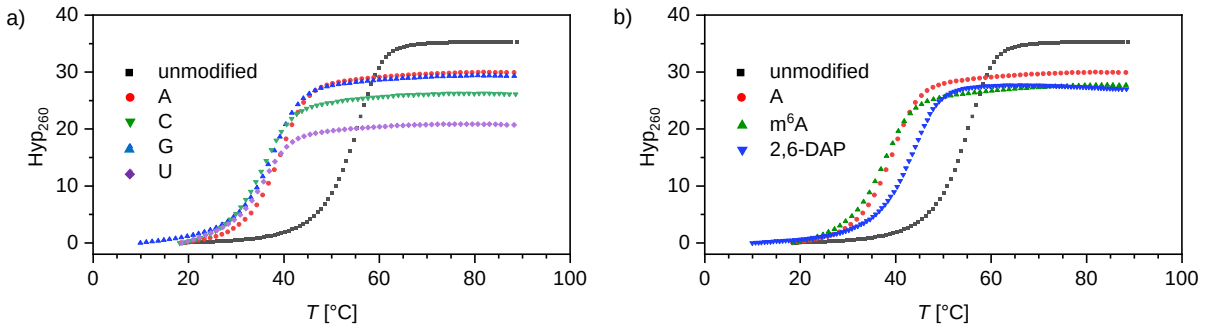

Figure 3.20: All of the RNA duplex structures with different canonical nucleobases opposite rBAM displayed very similar melting temperatures which showed to be noticably reduced compared to the unmodified reference (a). For duplex structures with different A-variants, the highest T_m value was obtained with 2,6-DAP while the *N*6-methyl group in m^{6}A did only have a small influence on the thermal duplex stability (b). Data are shown for 5 µM samples and the second heating ramp.

Therefore, it can be concluded that the indolenine-derived chromophore is not able to base pair with A or any other nucleobase within the duplex. Since the melting temperatures for **R8/R2** and **R1/R10** containing the rBAM chromophore opposite A are equal, it can furthermore be assumed that the impact of the merocyanine modification on the duplex stability is independent from the surrounding sequence context. The T_m value for **R9/R2** with rBAM^b is by 1 °C higher compared to the same duplex structure with rBAM, **R8/R2**. Since this is only a minor difference, rBAM^b can be considered not base pairing in the RNA duplex as well.

If the thermodynamic parameters of the single-modified duplex structures are compared to the unmodified reference duplex **R1/R2**, a significant increase of the calculated ΔG^0_{298K}-values by +4.5 to 7 kcal mol^{-1} becomes obvious which exceeds the loss of the hydrogen bond strength of approximately 2 kcal mol^{-1} assumed for the replaced A-U Watson-Crick base pair.[353] There-

fore, additional effects such as structural perturbation of the oligonucleotide scaffold by the bulky merocyanine modification need to play a role for the lowering of the free Gibbs energy. One of these effects has already been described for DNA oligonucleotides modified with hydrophobic, not base pairing nucleobase analogs.[354] Here, it was reported that the difference in ΔG^0_{298K} after incorporation of such modifications can be attributed to changes in the solvation shell of unpaired nucleobases. In general, unhybridized nucleobases are surrounded by hydrogen bonding water molecules; upon formation of a base pair this solvation shell gets lost. During this process, hydrogen bonds are rearranged, leading to an overcompensation of the solvation energy. When the non-base pairing rBAM or rBAM^b modifications are incorporated, the nucleobases located opposite these merocyanines presumably shed their solvation shell due to steric constraints. In the following, the system cannot be stabilized again by newly formed interbase hydrogen bonds, leading to the observed differences in ΔG^0_{298K}. Since one A-U base pair is replaced in all of the duplex structures, the increase in the free Gibbs energy is always similar.

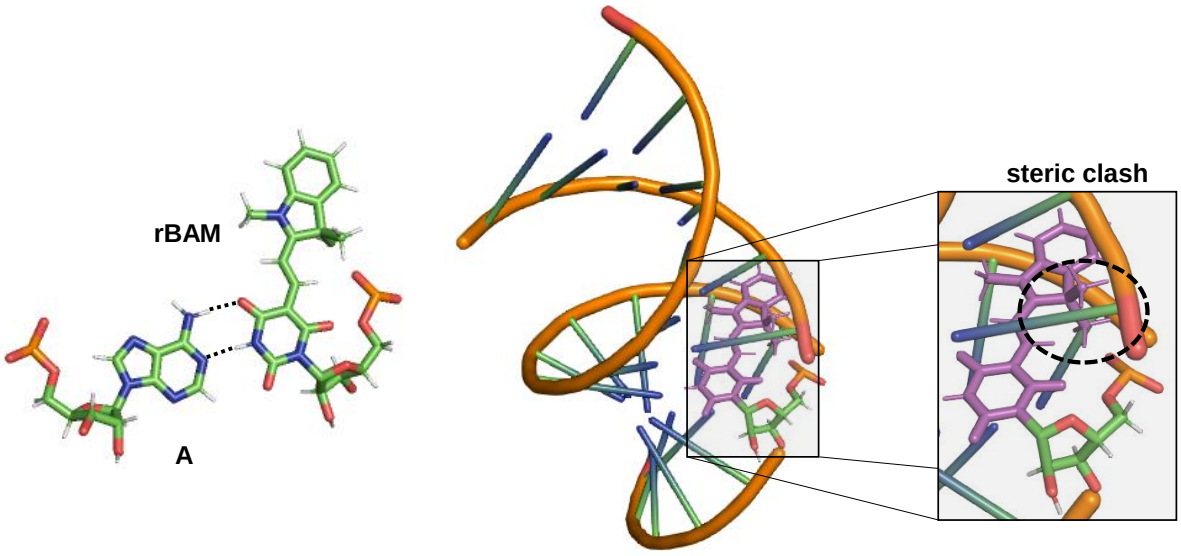

Figure 3.21: Modeled rBAM-A base pair in the 12mer duplex structure (left) and orientation of the rBAM chromophore upon base pairing in the helix (right). The double bonds of the chromophore are drawn in the (*E*),(*E*)-form; the presence of the indolenine methyl groups leads to a steric clash with the phosphate backbone upon base pairing, as shown in the magnified detail. Structures were built with ChemDraw, Discovery Studio and Pymol.

In parallel with the increase in ΔG^0_{298K}, a less favored enthalpic contribution which is to some extent compensated by a more favored entropic component is observed for single-modified duplex structures. This indicates an overall increase of conformational freedom next to the modification site due to partial unwinding of the duplex structure upon incorporation of the sterically demanding merocyanine chromophore.

One reason for this non-base pairing behavior might be the already mentioned steric demand

of the merocyanines. If a natural U in the unmodified RNA duplex is replaced by the rBAM chromophore in the 3D-modeled structure, a steric clash between the two methyl groups of the indolenine and the phosphate backbone is observed which presumably prevents base pairing between rBAM and A (Figure 3.21). Although not shown here, a similar effect is visible for the methyl group at the aromatic nitrogen of the benzothiazole-derived rBAM^b chromophore. In addition, the rather hydrophobic chromophore might favor to be located in the core of the helix, shielded from the polar aqueous environment. In this case, the merocyanine nucleobase analog would be rotated around the glycosidic bond and the barbituric acid moiety instead of the aromatic electron donor points into the duplex major groove.

Table 3.8: Sequences, melting temperatures and thermodynamic parameters for RNA duplex structures with two merocyanine modifications incorporated; the blue, green and red colored duplex name indicates upstream, downstream and opposite chromophore positioning, respectively. rBAM and rBAM^b are abbreviated as differently colored X. Given are also the differences in melting temperature relative to the unmodified reference sequence **R1/R2**.

Name	sequence	$T_m^{[a]}$ °C	$\Delta T_m^{[b]}$ °C	ΔH^0 kcal mol^{-1}	ΔS^0 cal mol^{-1} K^{-1}	ΔG^0_{298K} kcal mol^{-1}
R1/R2	5'-...AUA...-3' 3'-...UAU...-5'	54.4	-	-119	-337	-18.4
R8/R14	5'-...AXA...-3' 3'-...XAU...-5'	36.0	-18.4	-77.3	-224	-10.4
R8/R10	5'-...AXA...-3' 3'-...UAX...-5'	35.9	-18.5	-118	-357	-12.0
R8/R12	5'-...AXA...-3' 3'-...UXU...-5'	39.2	-15.2	-86.5	-252	-11.5
R9/R15	5'-...AXA...-3' 3'-...XAU...-5'	42.4	-12.0	-102	-296	-13.4
R9/R11	5'-...AXA...-3' 3'-...UAX...-5'	~53.5	~0.9	n.d.	n.d.	n.d.
R9/R13	5'-...AXA...-3' 3'-...UXU...-5'	50.1	-4.3	-165	-484	-20.8

[a] values for 5 µM samples in 1× PBS (100 mM NaCl, 10 mM phosphate, pH 7.0); 0.5 °C/min heating rate; a standard error of ±0.5 °C is assumed
[b] difference relative to unmodified duplex
X = rBAM, X = rBAM^b.

However, the destabilizing effect observed for single-modified RNA structures is not enhanced any further if two merocyanine chromophores are incorporated into the duplex structure. In Table 3.8, the melting temperatures as well as the thermodynamic parameters for the down-

stream (green), upstream (blue) and opposite (red) duplex structures are listed.

In the case of double-rBAM modified duplex structures **R8/R14**, **R8/R10** and **R8/R12** the observed melting temperatures are within the same range as for only single-rBAM modified systems. Therefore, there need to be stabilizing interactions between the two chromophores which compensate further structural perturbations and thus the reduction of the duplex melting temperature upon incorporation of a second space-consuming merocyanine. Regarding the derived thermodynamic parameters, also here no significant deviations from the single-modified systems are observed, which makes the conclusions drawn previously applicable for these double-modified structures as well.

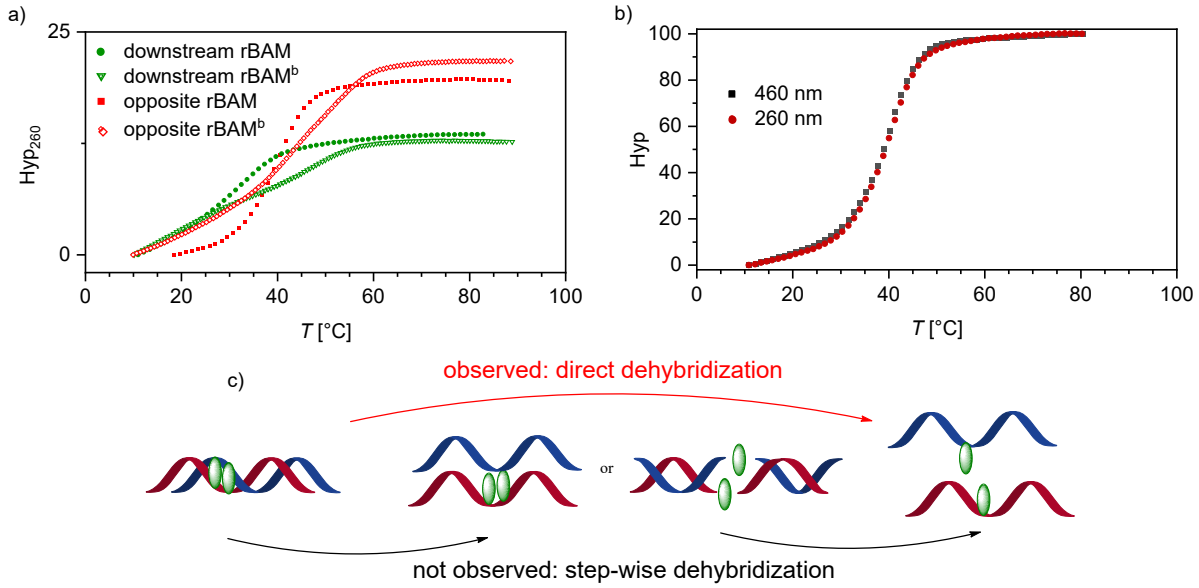

Figure 3.22: The observed duplex melting temperatures are in general higher for structures containing rBAM^b dimers compared to those with rBAM dimers, which is exemplarily shown for the opposite and upstream dimers in a). The normalized change in absorption with increasing temperature for the 5 µM rBAM/rBAM opposite RNA duplex structure **R8/R12** shows the same melting temperature at the nucleobase and chromophore absorption wavelengths of 260 nm and 460 nm (b). Thus, only direct dehybridization is observed for BAM-modified structures, indicating that the dye-dye interactions strongly depend on the structural framework of the helix (c). Data are shown for 5 µM samples and the second heating ramp.

The stabilizing effect becomes even more pronounced for double-rBAM^b modified duplexes compared to the respective duplexes containing rBAM dimers (Figure 3.22a). In the case of downstream and opposite chromophore-chromophore orientation **R9/R11** and **R9/R13**, the melting temperature is decreased by only up to 4.3 °C compared to the unmodified reference **R1/R2** while in the upstream case **R9/R15** the structure is destabilized by 12 °C which is also less than for the single-modified duplex **R9/R2**. Additionally, the ΔG^0_{298K} value for the duplex with opposite chromophore orientation **R9/R13** exceeds the one of the reference duplex **R1/R2** which supports the assumption that further stabilizing interactions between the

well-ordered chromophores themselves seem to be of importance. Since for these two systems the entropic component is more favorable, the conformational freedom seems to be even more enhanced compared to double-rBAM- and single-modified structures.

Interestingly, the thermal dehybridization of all of the merocyanine dimers can be detected at 460 nm at temperatures very similar to the T_m values obtained for the whole duplex. As an example, a melting curve for the double-modified duplex **R8/R12** recorded at the nucleobase absorption of 260 nm and the merocyanine absorption at 460 nm is shown in Figure 3.22b, revealing the same curve inflection point for both wavelengths. This indicates that there is no stepwise melting process but instead a direct thermal dehybridization suggesting strong cooperativity within the overall duplex structure (Figure 3.22c). However, stepwise melting was later observed for BAM^b-modified DNA structures (section 3.4.3), where either the canonical outer parts of the duplex or the chromophore-containing inner part melts first.

To gain further insight into the stacking interactions within double-rBAM modified duplex structures, the hyperchromicities, which reflect the change in absorbance upon duplex melting, can be compared among these systems (Figure 3.23). At 260 nm, the highest value for the hyperchromicity is observed for the unmodified reference **R1/R2** while lower but similar values are obtained for the modified systems. This is in agreement with the highest melting temperature obtained for the reference duplex **R1/R2** since large changes in absorbance by denaturation indicate stronger stacking interactions between the nucleobases. However, the hyperchromicity values at 460 nm do not reflect the ones at 260 nm. The overall hyperchromicities are much larger with the most significant change in absorbance for the duplex **R8/R12** with the two rBAM directly facing each other. This behavior already gives a hint at strong chromophore-chromophore interactions within the double-rBAM modified structures and was observed in a similar fashion for duplex structures containing rBAM^b dimers.

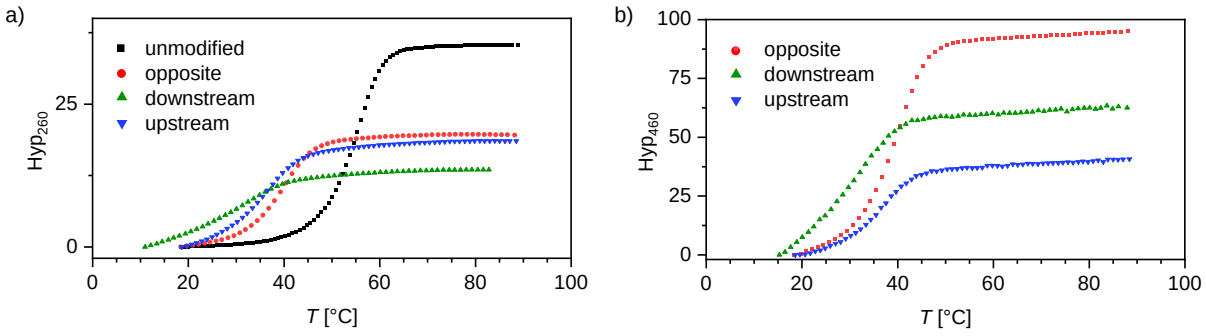

Figure 3.23: Comparison of the hyperchromicities at 260 (a) and 460 nm (b) for 5 µM double-rBAM modified duplex structures, revealing a different extent of stacking interactions among these systems. Data are shown for 5 µM samples and the second heating ramp.

Although the sequence context is the same for all of the three different systems, the positioning of the chromophores and their orientation toward each other in the helical structure seems to

have a huge influence on duplex stability, which is a striking observation. A duplex stabilizing effect of two chromophores located opposite each other has already been described for multiple incorporations of not base pairing thiazole orange chromophores into oligonucleotides.[355] In this case, the chromophores were attached to the backbone by a flexible linker and the duplex stabilizing effect was explained by stacking between the thiazole orange dye with adjacent nucleobases or neighboring chromophores. Also with the merocyanine chromophores described here, stacking might play a role for rBAM/rBAM and $rBAM^b$/$rBAM^b$ interactions. However, these interactions cannot be realized if the merocyanines are in the base pairing *anti*-conformation as shown in Figure 3.24a since then the two chromophore ring systems are located separated from each other in the duplex major groove.

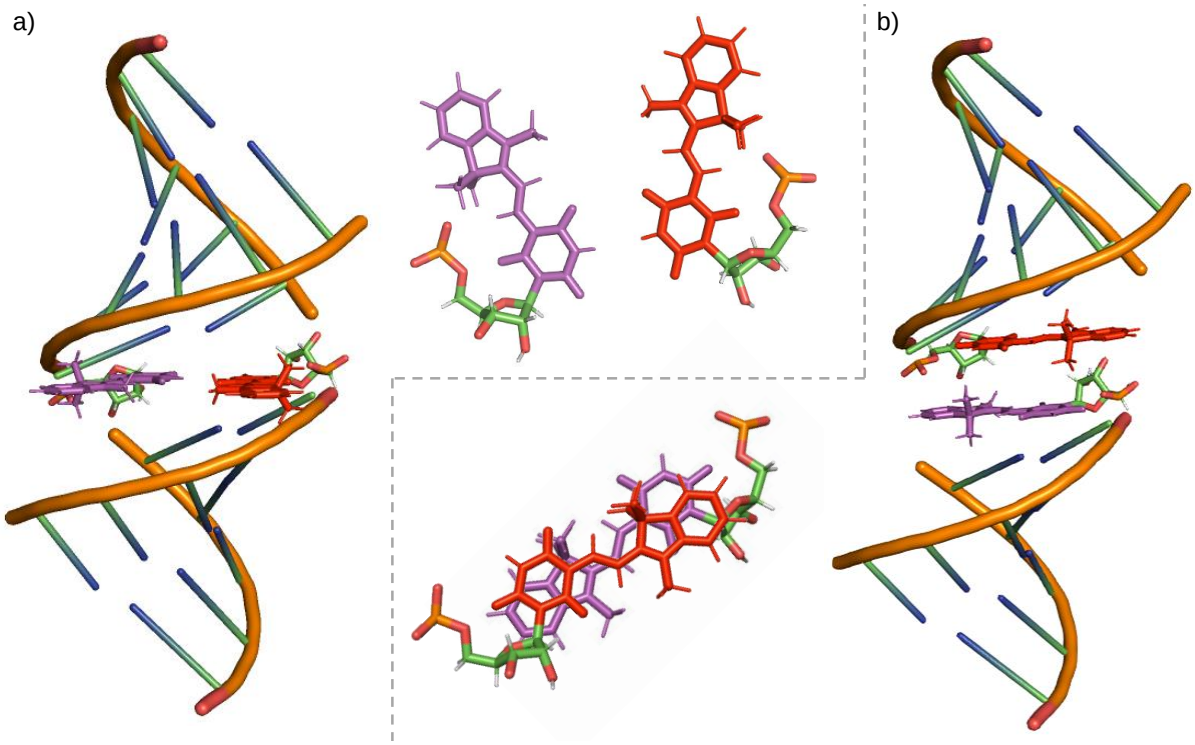

Figure 3.24: Modeled RNA duplex structures with two rBAM chromophores located opposite each other; shown are a side view of the helix and the top view of the two chromophores in this structure. In a), both chromophores are drawn in the base pairing *anti*-conformation with the indolenine moieties pointing into the duplex major groove. In b), the merocyanines are present in *syn*-conformation, leading to stacking of the chromophores in the inner core of the helix. Models were built with ChemDraw, Discovery Studio and Pymol. The duplex structure in b) was stretched for better illustration of the chromophore positions.

In contrast, if both chromophores are present in *syn*- instead of the normally occuring *anti*-conformation, the barbituric acid base pairing site faces the duplex major groove and the indolenine or benzothiazole ring system penetrates the base stack in the core of the helix (Figure 3.24b). In this case the two merocyanines are stacked in a coplanar fashion which might lead to duplex stabilization. This assumption is in accordance with the literature where the dime-rization of dipolar merocyanines in antiparallel orientation by strong, directional

dipole-dipole interactions due to their significant zwitterionic character and the resulting large molecular ground state dipole moment has been reported to be favored.[356] However, it has to be considered that the double helical structure does not provide sufficient space for both chromophores rotating inward. Therefore, the helix needs to be stretched as done in the modeled structure in Figure 3.24, which implies that stacking of the chromophores likely goes hand in hand with an increase in the phosphate-phosphate distance.

The stabilizing effect by BAM:BAM stacking instead of base pair formation can be rationalized by steric as well as electronic aspects. As already shown for the single-modified system, a significant steric clash between the chromophore's methyl groups and the phosphate backbone occurs if BAM is in the base pairing *anti*-conformation. This effect might be even more enhanced with two instead of one BAM chromophores in the structure, leading to a strong destabilization which contradicts the experimentally found melting temperatures. Regarding electronic interactions, it is a common perception that dipolar coupling interactions are weak, but this does not hold true for dipolar D-π-A scaffolds such as merocyanines in antiparallel cofacially stacked dimers. The averaged attractive interactions between an ensemble of two of these constantly rotating dipoles is described by the Keesom interaction, which depends on the inverse sixth power of the chromophore-chromophore distance:

$$E = -\frac{2\ \mu_g^4}{3 \cdot (4 \cdot \pi \cdot \epsilon_0)^2 \cdot k \cdot T \cdot r^6} \tag{1}$$

with the chromophore dipole moment μ_g, the permittivity of free space ϵ_0, the Boltzmann constant k, the temperature T and the distance r between the two dipoles.[357] With the antiparallel orientation of two dipolar chromophores, π-stacks with dipole-dipole distances between 3.2 and 3.5 Å become possible, leading to strong intermolecular interactions due to the much larger dipole moments of these dyes compared to their hydrogen-bonded counterparts. Here, the chromophore's large dipole moments compensate for the larger π-π-stacking distance compared to the interchromophore distances required for hydrogen bonding (around ~1.8 Å). For the modeled upstream and downstream BAM:BAM dimer structures, the interchromophore distance has been indeed found between 3.2 and 3.7 Å, providing effective dipolar coupling (compare Figure 3.34). To compare the stability of dipole-dipole and hydrogen-bonding interactions by energetic means, the factor σ, which is the ratio of the Gibbs binding energy and the required area for molecular contact, is employed. This has exemplarily been done for Watson-Crick base pairs and a dipolar merocyanine in organic solvents (Figure 3.25).[357]

Although all measurements conducted in the course of this thesis were carried out in aqueous solution, an organic solvent as a model system is considered an appropriate approximation for the environment of the BAM:BAM dimer and the Watson-Crick base pairs located in the hydrophobic inner core of the RNA duplex structure. The surface size-related binding strength

σ for a classical A-T base pair has been found by almost a factor of three lower compared to the dipolar model merocyanine. Since this dipolar chromophore is similar in size to BAM, the favored formation of coupled BAM:BAM dimers by dipolar interactions over Watson-Crick H-bonding interactions is reasonable.

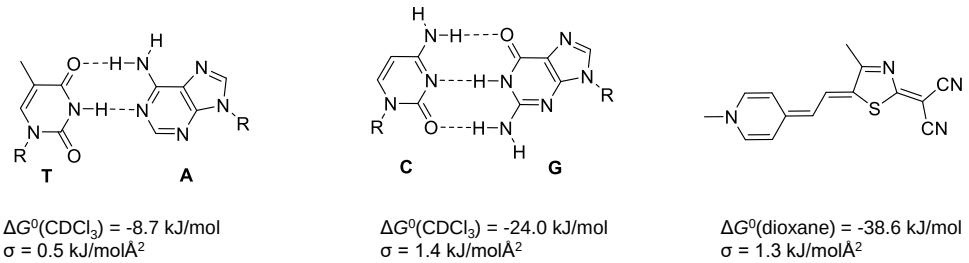

Figure 3.25: The size-related parameter σ, calculated from the ratio of the Gibbs binding energy and the molecular surface, reveals distinct binding strengths for hydrogen bonded Watson-Crick base pairs and dipolar merocyanines in organic solvents.[357]

The divergence in the duplex destabilization for systems with either two rBAM or two rBAM^b chromophores might be deduced to differently pronounced chromophore stacking due to the distinct steric demand of the two merocyanines. For the indolenine-derived rBAM, the additional methyl groups are pointing out of the chromophore's plane, therefore hindering efficient parallel chromophore-chromophore stacking while the sulfur atom in the benzothiazole system is much less sterically demanding. Additionally, the already mentioned calculated larger ground state dipole moment of the BAM^b chromophore leads to enhanced dipolar stacking.

An overview of the three different chromophore orientations downstream, upstream and opposite is given in Figure 3.26. Here, the rBAM (top, purple and red) and the rBAM^b (bottom, orange and blue) chromophores are depicted in the non-base pairing *syn*-conformation. Within these structural models, the mentioned steric clash for the indolenine-derived rBAM chromophores becomes more obvious and can therefore indeed be an explanation for stronger duplex destabilization compared to the rBAM^b modified systems. For the latter ones, almost the same T_m values for the downstream and opposite **R9/R11** and **R9/R13** were observed while a stronger duplex destabilization for the upstream chromophore-chromophore orientation in **R9/R15** was measured. In accordance with these melting temperatures, the chromophore positions in downstream and opposite orientation are fairly similar with nearly antiparallel stacking. However, in the upstream case the two merocyanines are not as perfectly antiparallel aligned but slightly shifted, therefore leading to less pronounced stacking interactions and a lower melting point.

It has to be noted that the model structures shown are not energetically optimized by MD simulations since for this a parameterization of the chromophores would be required. Thus, the depicted structures are only preliminary models to support a rationalization the observed

thermodynamic and spectroscopic properties. In addition, not only steric factors but also other parameters need to be taken into account which might play a role in chromophore-chromophore interactions and influence the spectral characteristics of these assemblies.

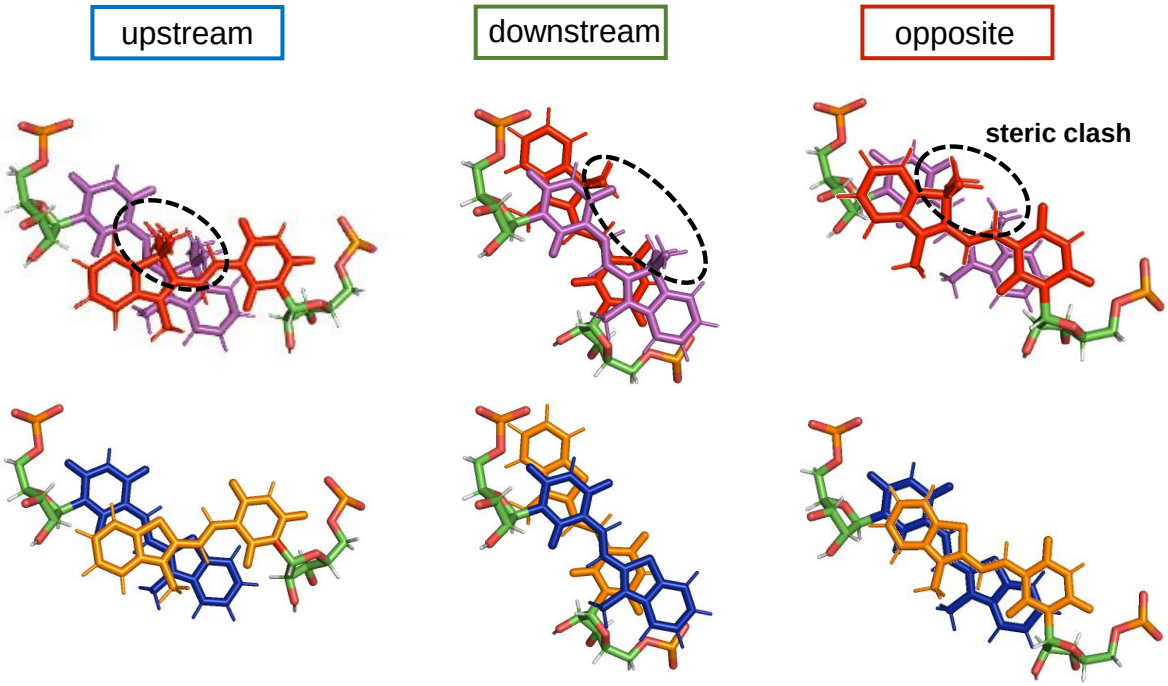

Figure 3.26: Top views of the chromophore positions in upstream, downstream and opposite double-modified RNA duplex structures. On top, systems with two rBAM chromophores shown in red and purple are illustrated, below, systems with two rBAM^{b} chromophores shown in orange and blue are depicted. In all structures the two chromophores are stacked on top of each other; however, for rBAM modified structures there seems to be a significant steric clash due to the methyl groups of the indolenine donor.

The structural models shown in Figure 3.26 will in the following section be used to discuss the spectroscopic features observed for single- and double-modified rBAM and rBAM^{b} duplex structures.

3.3.5 Spectroscopic characterization of rBAM- and rBAM^{b}-modified RNA duplex structures

One of the most famous merocyanine chromophores which is widely used in the oligonucleotide context as a DNA stain is thiazole orange (TO). This dye has attracted much attention because of its environment-sensitive emission properties: it exhibits an up to 3200-fold fluorescence enhancement upon binding to DNA by intercalation and can therefore be used as fluorogenic hybridization probe.[358] However, not only the non-covalent assembly of TO on DNA has been reported but also its covalent attachment by several different linker units, giving access to a range of single- and multiple TO-modified DNA structures with inter- as well as intrastrand

TO-dimers (Figure 3.27).[355,359–363]

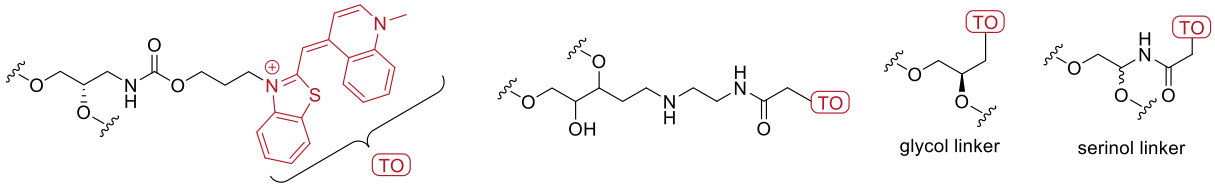

Figure 3.27: Thiazole orange (TO) has been covalently attached to oligonucleotide scaffolds by different linkers, among them a glycol and a serinol linker. Hereby, multiple modified duplex structures containing TO dimers and trimers were obtained[355,359–363]

Although no TO ribonucleoside has been described so far, the reported TO-modified oligonucleotide systems can be used for comparison of their spectral features with BAM-modified nucleic acids, which will turn out to be especially useful for the analysis of the BAM orientation within the oligonucleotide scaffold. Starting with the simplest modified nucleic acid systems, single-rBAM and -rBAM^b containing duplex structures will be discussed in the first part of this subchapter.

3.3.5.1 Investigations on single-rBAM and -rBAM^b modified systems

To gain insight into the photophysical behavior of the merocyanine chromophores incorporated into RNA, temperature-dependent absorption as well as fluorescence excitation and emission spectra of single- and double-modified RNA duplex structures were measured.

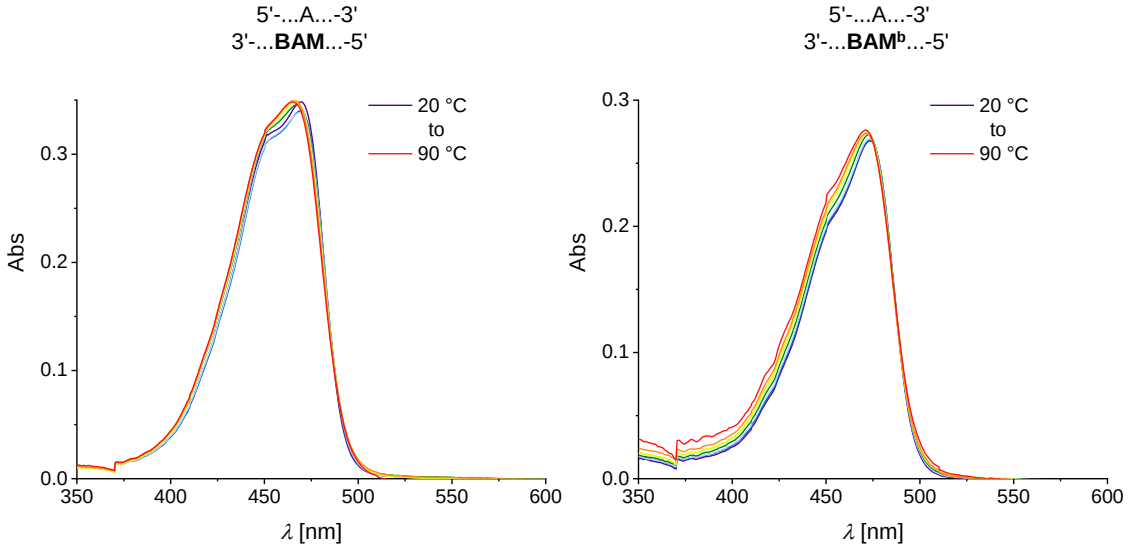

Figure 3.28: Temperature-dependent absorption spectra for single rBAM- (left) and rBAM^b-modified (right) RNA 12mer duplexes **R8/R2** and **R9/R2**. Upon thermal dehybridization, the absorption spectra for both systems only change marginally which indicates neglectable influence of the surrounding nucleobases on the merocyanine's absorption behavior. Conditions: 5 µM samples in 1× PBS (100 mM NaCl, 10 mM phosphate, pH 7.0).

As a starting point for these analyses, the temperature-dependent UVvis spectra of the two single-modified dsRNAs **R8/R2** (left) and **R9/R2** (right) are shown Figure 3.28. According to the estimated melting points, both RNA systems are supposed to exist in duplex conformation at the lowest temperature of 20 °C and are completely dehybridized at 90 °C. Obviously, the shape and intensity of the charge transfer (CT) absorption band at 460 nm of the two modified duplex structures undergoes only minimal changes upon increased temperature. This indicates that the absorption properties of rBAM and rBAM^b are not significantly influenced by the surrounding nucleobases in the double helix and can therefore easily be compared to the respective free chromophores. In addition, this finding was supported by spectroscopic characterization of the duplex structures with rBAM opposite each of the canonical nucleobases, since here same spectra shapes and intensities for absorbance as well as fluorescence measurements were observed (see sections 6.1.1 and 6.3.1.1).

Next, the fluorescence emission and excitation spectra for single-modified ssRNA and dsRNA were recorded and compared with the ones for the free merocyanines measured under the same conditions (Figure 3.29).

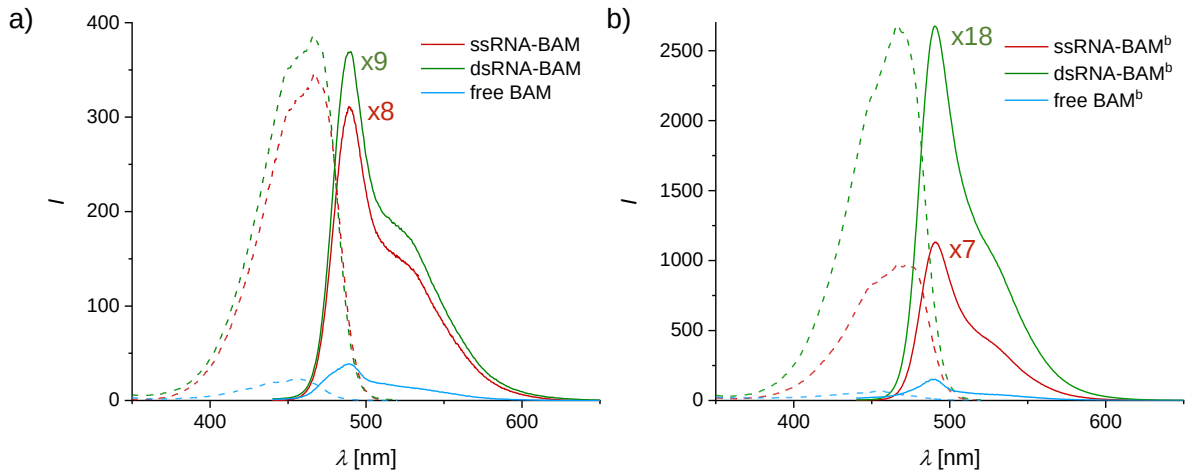

Figure 3.29: Fluorescence excitation and emission spectra for single-rBAM (a) and single-rBAM^b (b) labelled ssRNA compared to dsRNA and the respective free chromophore. Given is also the intensity enhancement of the merocyanines in the oligonucleotide systems relative to the unbound ones, obtained by comparison of the intensities at the maximum. Conditions: 1 µM samples in 1× PBS (100 mM NaCl, 10 mM phosphate, pH 7.0), excitation at 420 nm, emission at 540 nm.

By evaluation of the obtained data, some interesting features can be discovered: first, the position of the excitation and emission maxima does not change upon incorporation of the two chromophores into oligonucleotides, similar to the position of the absorption maxima. Therefore, the influence of the surrounding nucleobases on the excited states of rBAM and rBAM^b can also be neglected. Second, the fluorescence intensity for rBAM as well as the rBAM^b is highest in dsRNA, lowered to some extent in ssRNA and significantly reduced for the free chromophores. This effect is more pronounced for the benzothiazole-derived rBAM^b with a 7-

and 18-fold fluorescence increase in ssRNA and dsRNA, respectively, compared to rBAM with an 8- and 9-fold enhancement. This can be explained by the higher conformational flexibility of the free merocyanine chromophores which causes rapid fluorescence quenching through non-emissive rotational relaxation around the central polymethine bridge and has been described for many cyanine and merocyanine chromophores.[364]

In ssRNA, the dye scaffold is rigidified to some extent and the tortional motion is partially restricted, preventing nonradiative deactivation and leading to an increase in fluorescence intensity.[365] If the modified ssRNA is hybridized with its complementary counterstrand, the non-radiative relaxation pathway is even more suppressed, similar as of TO by intercalation into the duplex.[366,367] Since the rBAM chromophore is sterically more demanding due to the methyl groups at the indolenine core compared to the rBAM^b chromophore, the described fluorescence decay channel might already almost be closed in ssRNA; therefore, the fluorescence intensity difference between ssRNA-BAM and dsRNA-BAM is comparably low.

Although rBAM and rBAM^b only differ in the substitution pattern of their aromatic systems, the fluorescence intensity for dsRNA-BAM^b is almost 7-fold higher than for dsRNA-BAM. The fluorescence brightness FB of a chromophore can be calculated according to equation (2) by multiplying the exctinction coefficient ϵ and the fluorescence quantum yield ϕ.

$$\mathrm{FB} = \epsilon \cdot \phi \tag{2}$$

Since ϵ at the absorption maximum was only double as high for BAM^b compared to the one for BAM (see Table 3.2), the ϕ-value for the rBAM^b-modified duplex **R9/R2** is expected to exceed the one for the rBAM-modified system **R1/R10**.

ϕ is an important selection criterion for the application of a chromophore as a fluorescent probe since it testifies the fluorescence quality. By constant illumination of a fluorophore described by k_{abs}, a population of excited states F* is generated which reaches a steady state according to the following equation:

$$\mathrm{d[F^*]}/\mathrm{d}t = k_{abs} - (k_r + k_{IC} + k_{ISC}) \cdot [\mathrm{F^*}] = k_{abs} - (k_r + k_{nr}) \cdot [\mathrm{F^*}] = 0 \tag{3}$$

Here, the rate constants for radiative and non-radiative decay are given as k_r and k_{nr}, respectively, with the latter one summarizing the rate constants of all non-emissive events such as IC and ISC. In general, non-radiative decay proceeds on a much faster timescale than radiative decay and can only be observed if the difference in energy between the two respective energy levels is small. From the steady state conditions

$$k_{abs} = (k_r + k_{nr}) \cdot [\mathrm{F^*}] \tag{4}$$

follows. Since the quantum yield ϕ is determined by the ratio of absorbed and emitted photons by a chromophore, it is described by equation (5):

$$\phi = \frac{k_{nr}}{k_r + k_{nr}} \tag{5}$$

For the relative estimation of ϕ for the two BAM derivatives, first the absolute quantum yield for fluorescein was determined as ϕ=0.67 at pH 7.0. The relative quantum yield for **R1/R10** was obtained as approximately 0.016 as shown in Figure 3.30a.

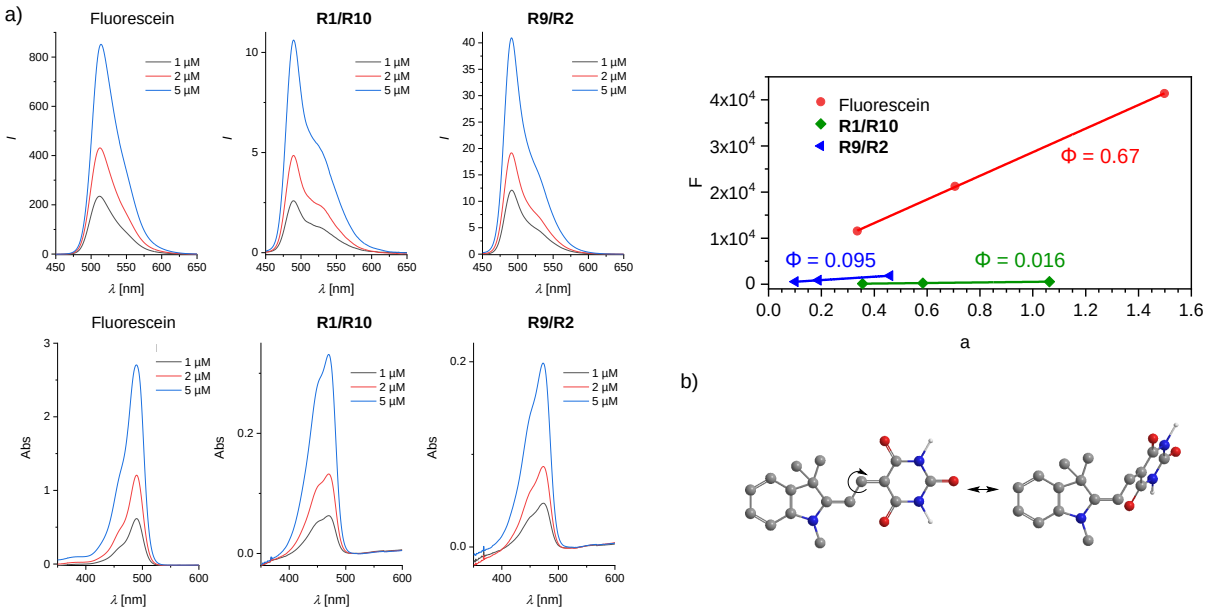

Figure 3.30: The quantum yield ϕ of the single-modified RNA duplexes **R1/R10** and **R9/R2** was determined relative to fluorescein as a standard. In a), the recorded concentration-dependent emission and absorption spectra are shown together with the plot of the integrated fluorescence emission F *versus* the absorption factor *a* as derived from integration of the absorption maximum for quantum yield calculation. In b), the assumed fluorescence quenching process by rotational relaxation is illustrated. Conditions: 1 to 5 µM duplex in 1× PBS (100 mM NaCl, 10 mM phosphate, pH 7.0), excitation at 435 nm. Details for the calculation of ϕ are given in section 5.4.3.6.

Although this value is low compared to fluorescein, it is in the same range as the reported quantum yield of 0.017 for the structurally similar TO chromophore incorporated into ssDNA.[355] The estimated low fluorescence quantum yield leads to the assumption that a partial unwinding of the modified RNA helix takes place upon incorporation of the sterically demanding BAM chromophore, leading to a high conformational flexibility which induces fluorescence quenching by enhanced rotational motion around the polymethine bridge, similar as for the free chromophore in solution. This is also in accordance with the strongly decreased melting points observed for rBAM-modified RNA duplex structures. In comparison, ϕ is 0.095 for the rBAM^b-modified system **R9/R2** which constitutes a 6-fold enhancement and is presumably explained by the difference in the aromatic chromophore system. ϕ increases with a lower probability for vibrational deactivation of the first excited state S_1 due to a larger S_0-S_1 gap

which is supposed to be the case for rBAM^b compared to rBAM due to the electronegative sulfur atom in the benzothiazole moiety.

With the estimated fluorescence quantum yield ϕ and the molar extinction coefficient ϵ (see Table 3.2) for the BAM- and the BAM^b-chromophores, the fluorescence brightness FB is calculated as 8600 M^{-1} cm^{-1} for the single-rBAM^b modified duplex **R9/R2**. This constitutes, as expected, an almost 9-fold enhancement compared to the single-rBAM modified system **R1/R10** with an FB of 980 M^{-1} cm^{-1} and is comparable to the reported value of 5800 M^{-1} cm^{-1} for a single-thiazole orange modified DNA duplex.[361] However, it has to be noted that the ϵ used for this calculation was estimated for the free chromophores and in DMSO in the case of BAM^b, which might lead to small differences in the here calculated brightness for oligonucleotides in the aqueous environment.

To conclude, the increased fluorescence brightness for rBAM^b-modified systems is attributed to an enhanced fluorescence quantum yield relative to rBAM rather than a difference in the extinction coefficient. Details on the calculation of the plotted integrated fluorescein intensity F and the absorption factor a as well as the estimation of the relative quantum yield ϕ can be found in section 5.4.3.6.

Besides ϕ, the fluorescence lifetime τ, an intrinsic chromophore property, is important for a fluorophore's characterization. It describes the average time elapsed between the excitation of a fluorophore and the emission of a photon and is found to be in the range of 0.1 to 20 ns nanoseconds for organic chromophores.[368] τ is considered to be a kinetic parameter and is determined to be inversely proportional to the sum of k_r and k_{nr}.

$$\tau = \frac{1}{k_r + k_{nr}} \tag{6}$$

In this thesis, the fluorescence lifetimes of the RNA duplexes **R1/R10** and **R9/R2** were estimated by a time-correlated single photon counting (TCSPC) setup; the obtained results with the prompt as instrument response function are shown in Figure 3.31. The fluorescence decay curves in a) and b) were fitted with tri-exponential fitting functions to estimate the fluorescence lifetimes. These higher order decays indicate the presence of different fluorophore conformations with distinct lifetimes. For the rBAM-modified system **R1/R10**, a weighted average lifetime $<\tau>$ of ca. 150 ps was estimated while this parameter was with 760 ps by more than five times higher for the rBAM^b-modified duplex **R9/R2**. These comparably low values obtained for τ are traced back to different fluorescence deactivation pathways, similar as the low quantum yield. Since the fluorescence lifetime is a relatively long process on the time scale of molecular events, a fluorophore can undergo a variety of transformations during this process, including electronic redistribution and geometric alterations which both induce non-radiative decay mechanisms. In the present case, the already mentioned tortional motion

of the polymethine bridge facilitating a non-radiative internal conversion deactivation pathway is assumed to be the major factor for fluorescence quenching and a reduced lifetime.

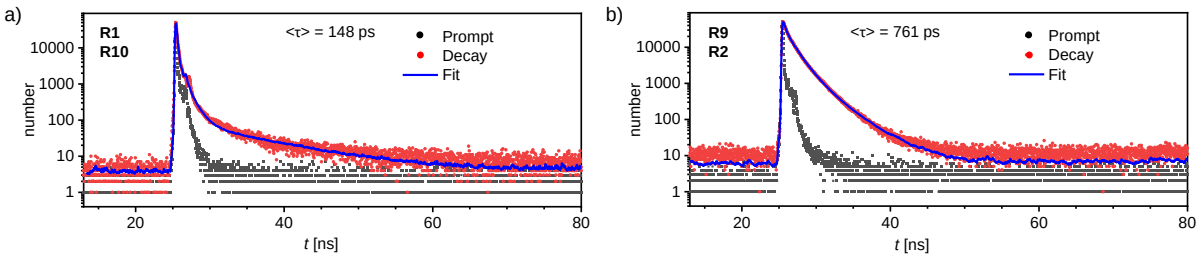

Figure 3.31: Fluorescence decay curves for the single-rBAM (a) and single-rBAM^{b}-modified (b) RNA duplexes **R1/R10** and **R9/R2**. From this data, fluorescence lifetimes of 148 and 761 ps were derived by exponential fitting. Conditions: 1 µM duplex in 1× PBS (100 mM NaCl, 10 mM phosphate, pH 7.0), excitation at 477 nm, emission detected at 492 nm.

From equations (5) and (6), k_r and k_{nr} can be calculated:

$$k_r = \frac{\phi}{\tau} \tag{7}$$

and

$$k_{nr} = \frac{1}{\tau} - k_r. \tag{8}$$

The hereby obtained values for **R1/R10** and **R9/R2** are summarized in Table 3.9. For **R1/R10**, k_{nr} is higher than k_r by a factor of 60, while it was only a factor of ten for **R9/R2**. Since very similar values for k_r were obtained for both **R1/R10** and **R9/R2**, the difference in ratio is caused by k_{nr} which is almost six-fold higher for **R1/R10** than for **R9/R2**. A similar ratio of radiative and non-radiative decay rates as found for **R1/R10** has recently been described for structurally akin merocyanines.[356]

Table 3.9: Fluorescence lifetimes τ, quantum yields ϕ and the corresponding radiative and non-radiative decay rates k_r and k_{nr} for single-modified RNA duplexes **R1/R10** and **R9/R2**.

sample	τ ps	ϕ[a]	k_r s^{-1}	k_{nr} s^{-1}
R1/R10	150	0.016	$1.07 \cdot 10^8$	$6.66 \cdot 10^9$
R9/R2	760	0.095	$1.25 \cdot 10^8$	$1.19 \cdot 10^9$

[a] determined relative to fluorescein

This indicates that rBAM^{b} is rigidified to a larger extent within the oligonucleotide scaffold compared to rBAM, having a reduced probability for non-radiative events by tortional motions

around the central polymethine bridge. Therefore, the calculated rate constants are in accordance with the conclusions drawn from thermal denaturation and spectroscopic measurements and it can be assumed that the introduction of the sterically demanding merocyanine chromophores leads to a partial widening of the duplex structures. It has to be noted that the calculated values for radiative and non-radiative decay rates must be treated with caution due to the extremely short lifetimes of the merocyanine chromophores which are on the lower edge of the measurement range of the used TCSPC lifetime fluorometer setup.

Since the spectroscopic properties of the single-modified RNA duplexes have been determined in detail, further characterization of the merocyanine dimers formed upon hybridization of two modified single-strands was required. This will be described in the following part of this thesis.

3.3.5.2 Investigations on double-rBAM and -rBAM^b modified systems

To investigate on ground and excited state interactions between the rBAM and rBAM^b chromophores, all of the double-modified RNA duplex structures were analyzed by temperature-dependent UVvis, fluroescence and CD spectroscopy and compared to the respective single-modified systems. In addition, circularly polarized luminescence (CPL) spectra were recorded and compared.

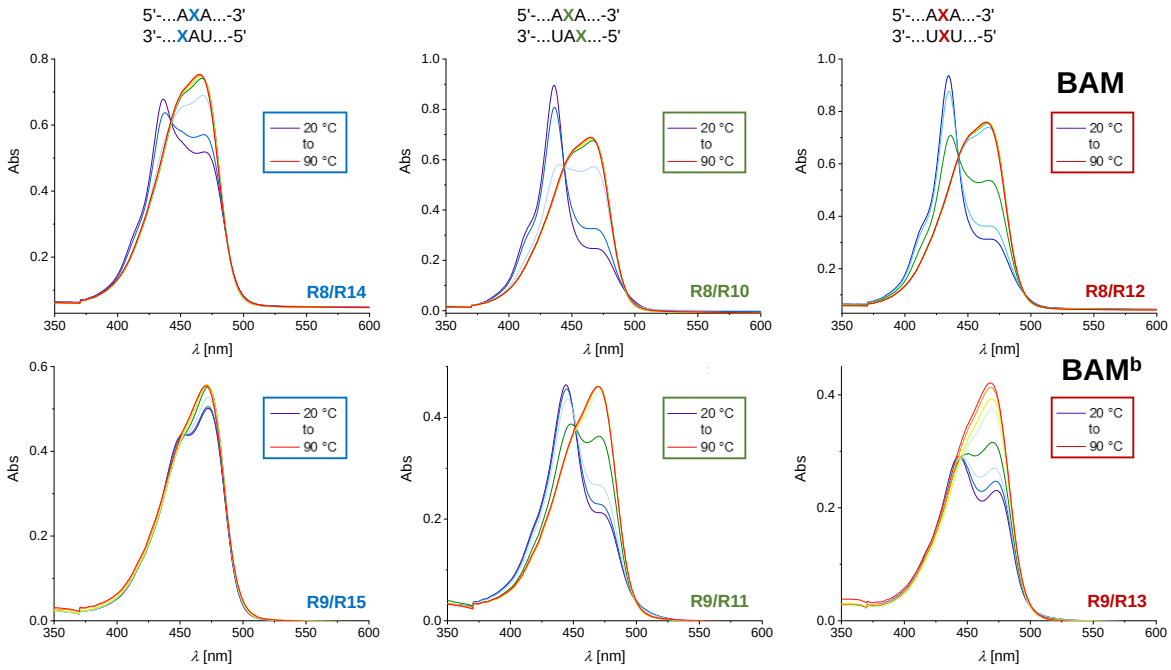

Figure 3.32: Temperature-dependent absorption spectra for double rBAM- (top) and rBAM^b-modified (bottom) RNA 12mer duplexes in upstream (blue), downstream (green) and opposite (red) orientation. Upon dehybridization, the absorption spectra for all of the systems change drastically: the main band shifts from the H-type dimer absorption at approximately 436 nm to the monomer absorption at approximately 466 nm. Conditions: 5 µM samples in 1× PBS (100 mM NaCl, 10 mM phosphate, pH 7.0).

In Figure 3.32, the temperature-dependent absorbance spectra for RNA duplex structures with either two rBAM or rBAM^b chromophores in upstream, downstream and opposite orientation are shown. Interestingly, the UVvis spectra for all of the examined systems change drastically upon heating; not only in terms of absorption intensity but also of the spectral shapes. At temperatures below the duplex melting point, all of the absorption spectra except for the rBAM^b/rBAM^b upstream orientation **R9/R15** exhibit a sharp peak at approximately 436 nm which is hypsochromically shifted by 30 nm compared to the monomer absorption at 466 nm.

The pronounced blue-shifted peak can be attributed to the formation of H-type dimers by excitonic interaction; as described before, H-aggregates are in general characterized by a strong hypsochromic shift in absorption. The observation of this kind of aggregates is reasonable if the rBAM and rBAM^b chromophores are indeed present in *syn*- instead of *anti*-conformation. As shown in Figure 3.24, the *syn*-conformation would give rise to the formation of electronically coupled face-to-face stacked dimers with the hydrophobic merocyanine chromophores located in an antiparallel fashion in the duplex center. However, the strong absorption at 436 nm still exhibits two less intense shoulders with about one third of the maximum intensity, one at the monomer absorption wavelength, the other is even more blue-shifted at 413 nm. The long-wavelength band is explained by a slight deviation of the transition dipole moments from the parallel alignment; it is observed for many merocyanine chromophore and usually overlaps with the monomer absorption.[369]

Upon thermal dehybridization at elevated temperatures, the hypsochromically shifted absorption band decreases in intensity while the monomer absorption with the typical vibronic fine structure intensifies. This observation is in accordance with the similar melting temperatures observed for the RNA duplex and the merocyanine dimer, indicating the dependence of chromophore-chromophore interactions on the duplex architecture. The presence of only two spectroscopic species in equilibrium, namely the merocyanine dimer and monomer, is in addition supported by an isosbestic point which is located at 442 nm for the majority of the examined systems.

However, among the examined RNA duplex structures are some with remarkably intense absorption bands attributed to H-type aggregate formation and some with an only weak or almost no blue-shifted peak in absorption. In the case of double-rBAM modified downstream and opposite duplex structures **R8/R10** and **R8/R12**, strong H-type assemblies are observed in the absorption spectra, while the upstream duplex **R8/R14** shows less separated bands at 20 °C. Although the melting temperatures for both the down- and the upstream case **R8/R10** and **R8/R14** are similar, this suggests differenct excitonic coupling strengths for these systems. This result is in accordance with the later discussed CD spectra and the modeled structures

shown in Figure 3.26 where the chromophore stacking interactions are much more pronounced for the downstream and opposite duplexes. Similarly, also for the upstream rBAM^b-modified duplex **R9/R15** no excitonic dye-dye interaction can be observed which complies with the dimer model as well as the low melting temperature for this system. In contrast, the strongest H-type assembly here is observed for the downstream case **R9/R11** which also shows the highest melting temperature of all double-modified duplex structures. Therefore, it can be concluded that the chromophore-chromophore stacking interactions observed by UVvis spectroscopy are indeed leading to duplex stabilization.

Although the modeled structure for the opposite rBAM^b/rBAM^b-modified duplex **R9/R13** suggests similar intense dye stacking interactions, a less pronounced absorption band attributed to H-type dimer formation is observed for this intact helix. This indicates that the incorporation of the sterically demanding merocyanine base surrogates does not only lead to rotation of the chromophore around the glycosidic bond giving rise to nucleoside analogs in *syn*-conformation, but implies further disruption of the helical structure due to the restricted space in the helix architecture. These findings will later be supported by the detailed analysis of double-BAM modified DNA structures in section 3.4.4.2.

Comparable spectroscopic observations have already been reported by Wagenknecht *et al.* on inter- and intrastrand TO-dimers in DNA.[363] Concomitantly, the arising blue-shifted absorption for intrastrand dimers was attributed to excimer formation due to stacking of the TO chromophores in the duplex framework and was explained, similar as here, by the exciton coupling theory. In addition, multiple incorporations of TO into DNA double helical structures led to duplex stabilization by strong chromophore-chromophore stacking interactions, comparable to the discussed double-rBAM^b-modified systems.

For further characterization of the double-rBAM and -rBAM^b modified RNA duplex structures, temperature-dependent fluorescence spectra were recorded (Figure 3.33). Here, the fluorescence intensity decreases upon heating by 70 to 80%, which is in agreement with the known thermochromic behavior of cyanine dyes and can be rationalized by the previously explained tortional motion around the polymethine bridge in ssRNA.[370] At elevated temperatures, this non-radiative decay pathway is even more preferred due to the energetically lowered rotation barrier. Surprisingly, the spectral pattern for the excitation of rBAM-modified duplexes below the helix melting temperature exhibit similar features as the respective absorption spectra.

For the downstream and the opposite rBAM-chromophore orientation **R8/R10** and **R8/R12** the already discussed H-type aggregate formation can clearly be observed in the fluorescence excitation as well as emission spetra although these types of assemblies are generally considered non-emissive. Here, this excimer-type fluorescence is characterized by a peak at approximately

435 nm in the excitation and a red-shifted emission peak at 531 nm which both disappear upon thermal duplex dehybridization since an intact helix scaffold is required for efficient chromophore interaction. The emissive character of the observed H-type aggregates is still in accordance with the exciton coupling theory and attributed to the restricted conformational freedom of the chromophores which are directly attached to the RNA backbone without employing a linker. This might restrain the rBAM from maximizing chromophore interactions, leading to a non-perfect antiparallel chromophore-chromophore arrangement. Within the dimers, the transition probability between the ground and the lowest exciton state does not vanish as it is normally the case but instead gives rise to a red-shifted emission band. In addition, since the rBAM chromophores are covalently fixed to the oligonucleotide scaffold, a helical twist is likely to be induced in the coplanar chromophore arrangement which disturbs their antiparallel arrangement and was later confirmed by CD spectroscopy (see Figure 3.35).

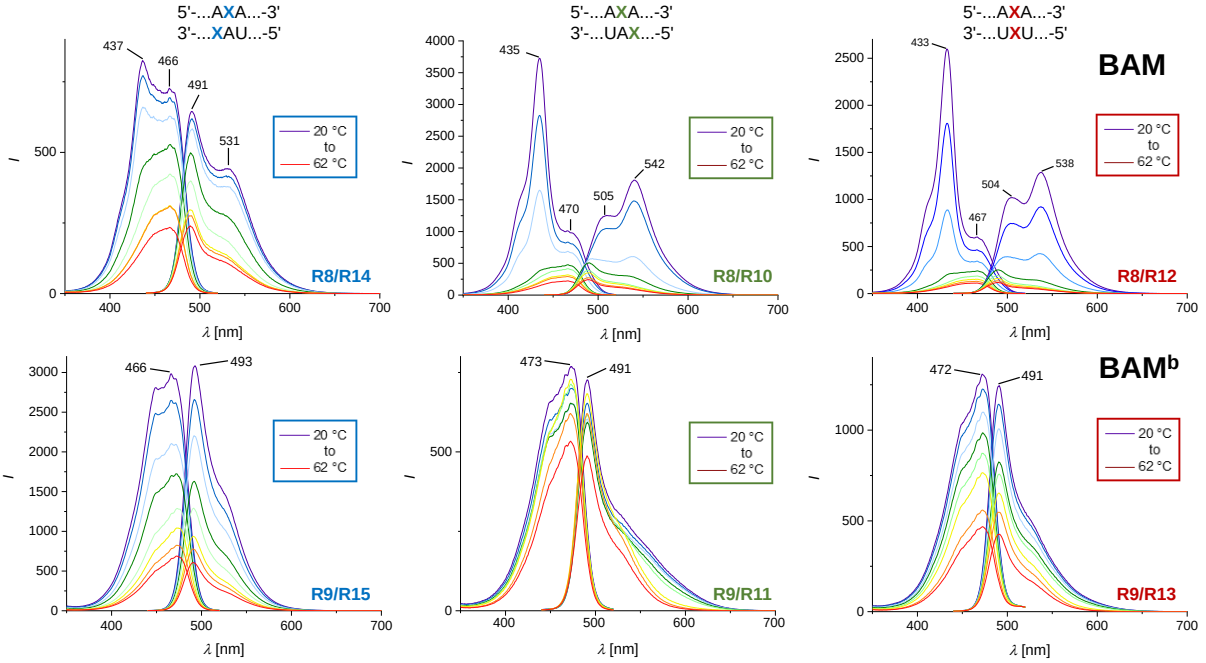

Figure 3.33: Temperature-dependent fluorescence spectra for double rBAM- (top) and rBAM^b-modified (bottom) RNA 12mer duplexes in upstream (blue), downstream (green) and opposite (red) orientation. The rBAM-modified duplex structures show the formation of fluorescent H-type aggregates while these cannot be observed for rBAM^b-modified systems. Conditions: 1 µM samples in 1× PBS (100 mM NaCl, 10 mM phosphate, pH 7.0), excitation at 420 nm, emission at 540 nm.

Similar as in the absorption spectra, also here no complete dimer formation can be observed but a fraction of the present chromophores always remains in unstacked conformation. This is especially pronounced for the upstream system **R8/R14**, where the monomer and dimer excitation at 466 nm and 437 nm and emission intensities at 491 nm and 531 nm, respectively, contribute almost equally to the spectral pattern.

Interestingly, the rBAM^b-modified duplex structures exhibit completely different fluorescent

properties compared to rBAM-modified systems. Here, no H-type aggregate attributed excitation and emission spectra can be observed; at temperatures below as well as above the duplex melting temperature only monomer fluorescence with excitation and emission at approximately 470 nm and 490 nm, respectively, is detected. These findings can be explained by the differences in steric demand between rBAM and rBAM^b: while the coplanar chromophore arrangement for rBAM might be hindered by the additional methyl groups at the indolenine moiety, the latter chromophore is missing these groups and can therefore adopt a more planar conformation. Thus, rBAM^b chromophores might more efficiently be stacked in an antiparallel fashion which leads to a forbidden optical transition from the ground to the first excited state and therefore non-fluorescent H-type aggregates. By density functional theory (DFT), the optimized structures for one possible dimer of the free BAM and BAM^b were calculated and indeed show a difference in planarity between these two chromophores (Figure 3.34a).

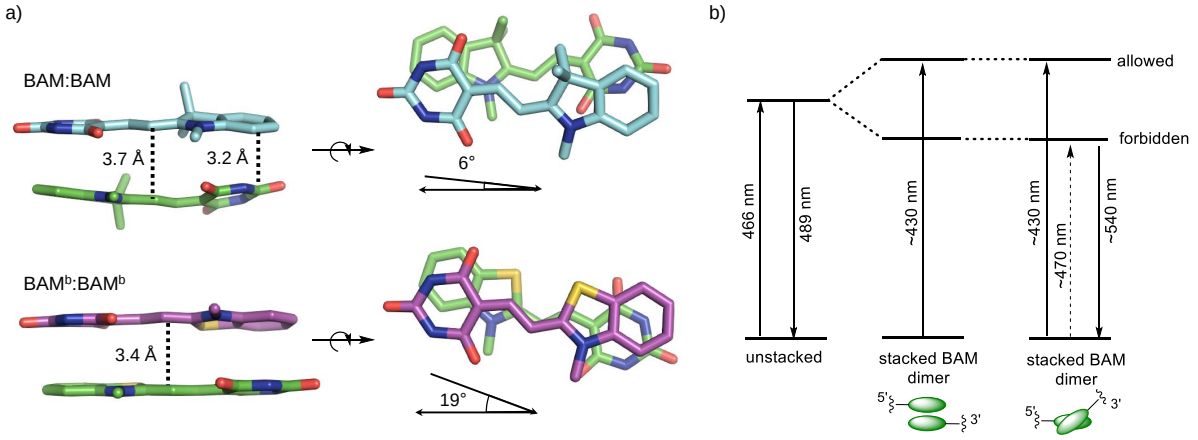

Figure 3.34: a) The geometry optimized BAM:BAM and BAM^b:BAM^b dimers obtained by DFT calculations show obvious differences in planarity: while the BAM chromophores in the dimer are slightly bent, the BAM^b dyes are aligned in almost perfect coplanar fashion. Geometry optimizations were carried out by Dr. David Bialas. For better visualization, the single chromophores within the dimer are differently colored. b) Schematic representation of the transition between the ground and the first excited state for unstacked merocyanines compared to the proposed BAM^b dimer with the two chromophores in almost perfectly antiparallel alignment and the slightly oblique chromophore stack in the BAM dimer.

While the BAM^b chromophores are almost coplanar with a calculated chromophore-chromophore distance of 3.4 Å, the edges of the BAM chromophores are slightly bent toward each other to maximize dipolar interactions. Within the BAM:BAM dimer, a interchromophore distance of 3.2 to 3.7 Å can be determined, therefore preventing as efficient antiparallel stacking as observed for the BAM^b:BAM^b dimer. In addition, in both cases the chromophores are rotated slightly against each other by 6 and 19°, respectively, which can be attributed to the bulky methyl groups at the donor moiety and has in a similar way already been observed for Cy3-dimers.[371] It has to be noted, that here only one out of four possible dimer structures, arising

from the two earlier discussed double-bond stereoisomers, is shown. However, all of these four possibilities are assumed to be similar in means of their spatial arrangement.

In Figure 3.34b, the observed transitions between the ground and the first excited states are summarized for unstacked BAM monomers and differently stacked dimers. For an ideal antiparallel chromophore arrangement, only the allowed transition to the upper excitonic state is observed, while for an inclined chromophore orientation also the otherwise forbidden state can be occupied and leads to the occurrence of fluorescent H-type aggregates.

The different chromophore arrangements for rBAM and rBAM^b dimers within a duplex structure were further supported by CD spectroscopy. CD spectroscopy is a powerful method for determining the absolute configurations and conformations of chiral molecules. It originates from the differential absorption of right- and left-handed circularly polarized light and therefore the observed Cotton effect is normally located at the absorption wavelength.[372] For most cases, either the ellipticity in mdeg or the the observable molar dichroism $\Delta\epsilon$ obtained from the respective extinction coefficients for left- and right-handed polarized light ϵ_L and ϵ_R according to

$$\Delta\epsilon = \epsilon_L - \epsilon_R \tag{9}$$

are plotted against the wavelength λ. The magnitude of a CD spectrum is quantified by the absorptive dissymmetry factor g_{Abs} described by equation (10).

$$g_{Abs} = \frac{2 \cdot (\epsilon_L - \epsilon_R)}{\epsilon_L + \epsilon_R} \tag{10}$$

Since CD spectroscopy can provide additional structural information about the chromophore arrangement in merocyanine-conjugated oligonucleotides, CD spectra for all of the double-modified RNA duplexes were measured and compared to the reference sample (Figure 3.35). In the region between 200 and 300 nm, the typical CD pattern of a right-handed A-form duplex can be observed for all of the examined systems, proving that the overall duplex structure is maintained upon merocyanine incorporation.

With rBAM or rBAM^b implemented into the duplex, bisignate positive Cotton effects in the respective absorption region were observed. Since these are not visible for modified RNA single strands, the chirality of the chromophore dimer is induced by the oligonucleotide scaffold and the bisignate CD signal can be explained by the formation of a chromophore exciton pair. If two chromophores with identical or very similar excited states are in spatial proximity within a chiral environment and undergo intense π-π^* transitions, the individual monomer excited states are lost and delocalized over both chromophores in this dimer. Thus, the two excitons interact with each other and are coupled, giving rise to CD exciton couplets which are characterized by two bands with opposite signs but comparable band areas. The sign of the observed bisignate

CD signals depends on the helical sense and reflects the absolute arrangement of the two chromophores within the supramolecular structure. The constitution of the electric transition dipole moments of the two chromophores in a clockwise screw sense leads to a positive Cotton effect with a positive CD band at longer and a negative CD band at shorter wavelengths, while an anti-clockwise screw sense gives rise to a negative Cotton effect.[373,374] Furthermore, if the two chromophores are perfectly coplanar, the systems chirality is broken at this position and no or only a very weak CD signal can be detected.

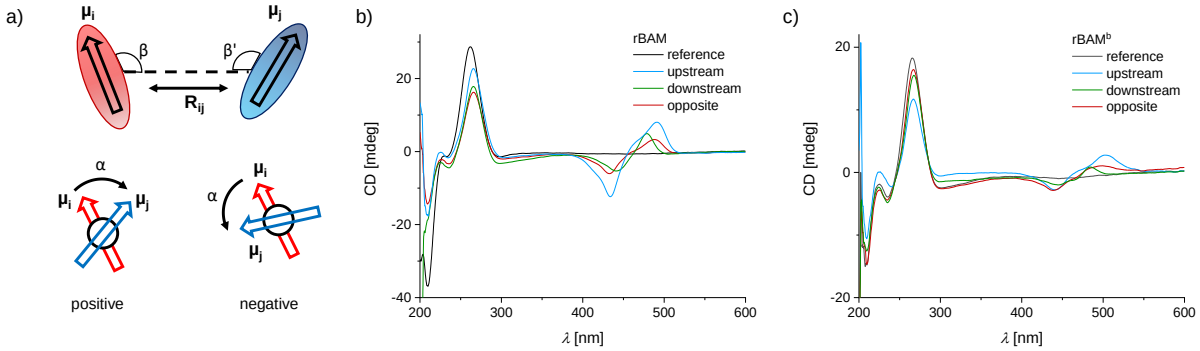

Figure 3.35: a) The constitution of two electric transition dipole moments indicated by arrows in a clockwise screw sense leads to a positive Cotton effect for the CD band while a counterclockwise screw sense provokes a negative Cotton effect. The bisignate CD signal can be described quantitatively by the distance between the positive and the negative CD band. In b) and c), the CD spectra for double-rBAM and double-rBAM^b modified RNA duplex strucures are shown. Conditions: 5 μM samples in 1× PBS (100 mM NaCl, 10 mM phosphate, pH 7.0).

Here, a good match between the absorption maximum wavelength and the CD crossover is observed, a typical signature of degenerate exciton coupling. These CD bands in the chromophore absorption region are more intense for rBAM- than for rBAM^b-modified structures which is in accordance with the UVvis and fluorescence data. For the rBAM:rBAM dimer, a helical arrangement with a slight offset between the excitonically coupled chromophores is expected, leading to the observed Cotton effect, while in the rBAM^b:rBAM^b dimer with nearly coplanar chromophores only a weak CD band is visible. The different exciton coupling strengths observed for the downstream and upstream rBAM:rBAM dimer in the absorption are also reflected in the distance between the positive and negative CD band. For the upstream dimer, this shift was 56 nm, while it was reduced to 36 nm for the downstream dimer, indicating much weaker coupling for the latter one and a larger BAM-BAM distance.

As the rBAM-modified RNA duplex structures combine a chiral scaffold and covalently bound fluorophores, not only CD but also circularly polarized luminescence (CPL) spectra were recorded. This method takes advantage of the different emission intensities of left- and right-handed CPL by a chiral fluorescent sample upon excitation and can be considered the emission counterpart of electronic CD (ECD) which takes place in the absorption. CPL spectroscopy has recently not only found many applications in different fields such as the chirality sensing

of biomolecules[375] and amino acids,[376] but was also used for more general studies of biological systems including oligonucleotides[377] and proteins.[378] It is established as a powerful tool to obtain stereochemical, conformational and three-dimensional structural information on complex supramolecular systems.

CPL effects are described by the differential emission intensity ΔI of the left- and right-handed circularly polarized light instead of the molar dichroism $\Delta\epsilon$ as for CD according to the following equation, with I_L and I_R referring to the intensity of left- and right-handed circularly polarized light:

$$\Delta I = I_L - I_R \tag{11}$$

Since the quantification of absolute I_L and I_R values is not easily achieved, the CPL effect can quantitatively be described by the luminescence dissymmetry factor g_{lum}. g_{lum} is derived from a similar mathematical equation as g_{Abs} for CD with the difference in intensities divided by the average total luminescence intensity:

$$g_{lum} = \frac{2 \cdot (I_L - I_R)}{I_L + I_R} \tag{12}$$

Theoretically, g_{lum} is approximated by

$$g_{lum} = \frac{4 \cdot |\mathbf{m}| \cdot \cos\theta}{|\boldsymbol{\mu}|} \tag{13}$$

where $|\mathbf{m}|$ and $|\boldsymbol{\mu}|$ are the magnitudes of the magnetic and electronic transition dipole moment vectors and θ is the angle between these vectors. For magnetic dipole-allowed and electric dipole-forbidden transitions, high values for the dissymmetry factors are obtained.

The CPL and the corresponding emission spectra for double-rBAM modified RNA 12mer duplexes are shown in Figure 3.36.

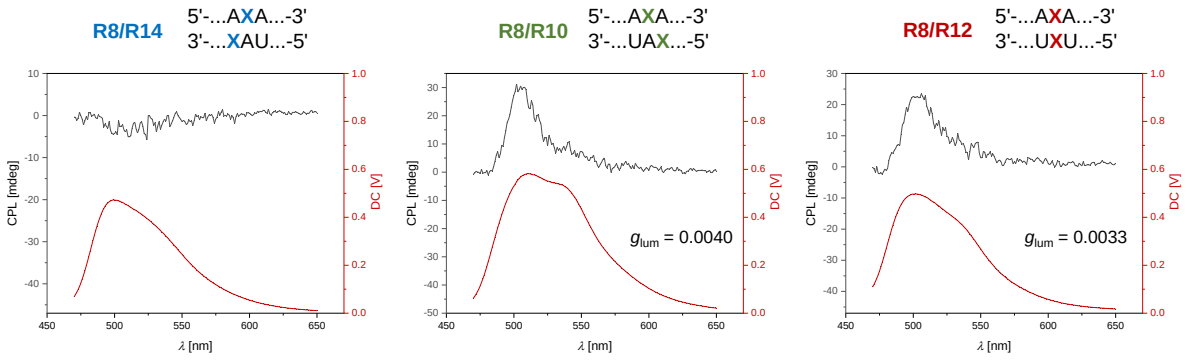

Figure 3.36: CPL spectra for double-rBAM modified RNA 12mer duplex structures. Conditions: 5 µM samples in 1× PBS (100 mM NaCl, 10 mM phosphate, pH 7.0).

Interestingly, for the red-shifted excimer emission band no CPL was observed for all of the

systems which could on the one hand be due to the fast relaxation of this excited state with a lifetime beyond the detection limit of the CPL device. On the other hand, chromophores within an excimer show a much larger polarizability compared to chromophores in the ground state. Thus, a more efficient antiparallel stacking is facilitated, inducing the formation of a point symmetric dimer within the chiral oligonucleotide scaffold which does not show CPL.

While no CPL effect is observed for the rBAM dimer in upstream orientation **R8/R14**, for both the downstream and the opposite case **R8/R10** and **R8/R12** positive CPL signals with a g_{lum} value between 0.003 and 0.004 at around 500 nm are observed, reflecting the right-handed arrangement of the chromophores. The observed CPL is on a similar scale as the typically observed $|g_{lum}|$ values between 10^{-5} and 10^{-3} for organic molecules in solution.[379] In addition, similar CPL direction and magnitude have been reported for pyrene excimers in right-handed helical peptides and serinol nucleic acids.[380,381]

However, not all of the obtained data can easily be interpreted by the simple model for the double-modified duplex structures depicted in Figure 3.26. Especially the spectral features observed for some of the double-modified systems contradict the assumed chromophore orientation and the estimated duplex melting temperatures. Therefore, a more detailed examination of the actual constitution of BAM:BAM and BAM^b:BAM^b is required. To achieve this, the same sequences were synthesized as simplified DNA oligonucleotides with the respective dBAM and dBAM^b building blocks incorporated. In addition, the alteration of the oligonucleotide scaffold might provide additional insight into the influence of the backbone nature on chromophore-chromophore interactions. The synthesis of the required phosphoramidites, their incorporation into DNA oligonucleotides and the characterization of the modified duplex structure obtained hereby will be described in section 3.4. Subsequently, further experiments such as salt-dependent titration and oligonucleotide NMR studies to reveal the actual chromophore arrangement are to be discussed.

3.3.6 Enzymatic incorporation of rBAM

Prior to the synthesis of modified DNA strands by solid phase synthesis, the enzymatic incorporation of an rBAM triphosphate was tested in primer extension and transcription experiments. The enzymatic polymerization of triphosphates constitutes a mild and facile alternative for the generation of functionalized oligonucleotides by solid phase synthesis and since the invention of the polymerase chain reaction (PCR) a multitude of thermostable polymerases with a broad substrate tolerance has been developed for this type of applications. The required triphosphate building blocks are in most cases synthesized by the Ludwig-Eckstein method or the Yoshikawa protocol; the latter one comprises less synthetic steps and was therefore also used for the preparation of the rBAM triphosphate.[382,383]

3.3.7 Synthesis and purification of the rBAM triphosphate

For the synthesis of the triphosphate, the free unprotected rBAM nucleoside **36** was in the first step 5'-monophosphorylated with $POCl_3$, leading to the formation of a labile phosphorodichlorate intermediate (Scheme 3.18). The *in situ* reaction of this intermediate with bis(tetrabutylammonium) pyrophosphate generated from tetrasodium pyrophosphate by protonation with an ion exchange resin and titration with tetrabutylammonium hydroxide solution gave the cyclic triphosphate which was hydrolyzed to the desired rBAM triphosphate **51**.

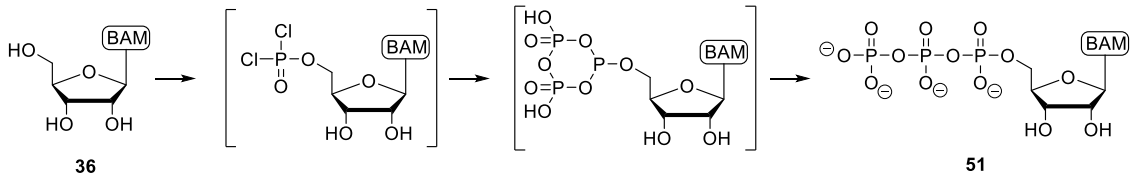

Scheme 3.18: Synthetic scheme for the synthesis of the rBAM triphosphate **51** showing the *in situ* generated intermediary structures. Conditions: 1) proton sponge, $(MeO)_3PO$, $POCl_3$, -20 °C, 3 h, 2) $(NBu_4)_2PP_i$, NBu_3, *N,N*-DMF, 0 °C, 1 h, 3) 0.1 M triethylammonium bicarbonate (TEAB) buffer pH 7.5, r. t., 30 min; yield estimated by UVvis absorbance: 6%.

The crude reaction mixture was purified by ion exchange and RP-HPLC. The HPLC traces and the proton NMR spectrum of the pure compound are depicted in Figure 3.37; the latter one shows the typical signal multiplicities expected for a triphosphate.

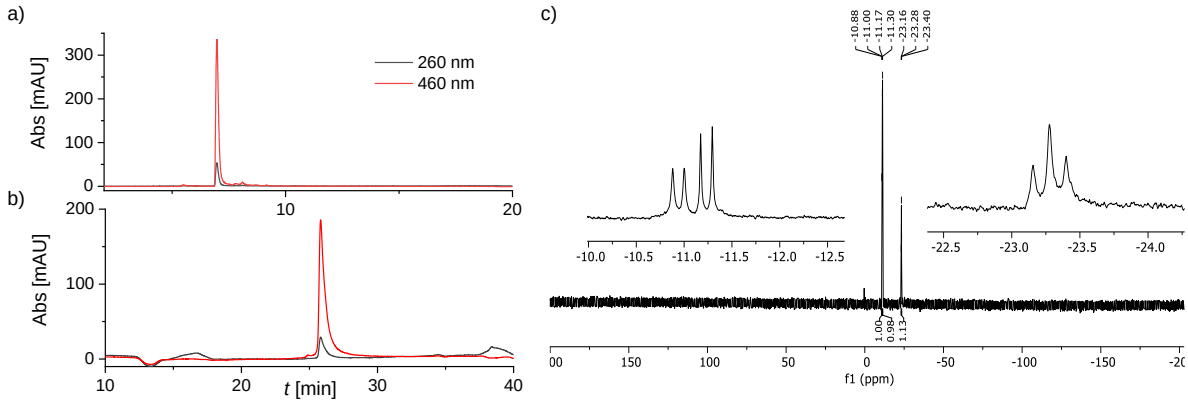

Figure 3.37: Analytical IEX- (a) and RP-HPLC (b) traces recorded at 260 and 460 nm and proton NMR spectrum (c) of the pure rBAM triphosphate **51**. Conditions: 0-32% Dionex buffer B over 8 CV (IEX); 0-60% buffer B over 40 min (RP).

The pure rBAM triphosphate **51** was in the following used for transcription and primer extension assays with different polymerases to explore its versatility as a substrate for enzymes.

3.3.8 Transcription and primer extension assays with the rBAM triphosphate

Besides the preparation by phosphoramidite solid phase synthesis, *in vitro* transcription is the second method of choice to prepare long unmodified oligonucleotides and also to test enzymatic incoporation of modified triphosphates. It requires a linear DNA template which codes for the target RNA transcript sequence downstream of a promoter region (red in Figure 3.38). After annealing of the promotor to the template, transcription proceeds in 5'-3'-direction. Here, a 38nt template together with the T7-promotor was used to investigate the potential of enzymatic incorporation of the rBAM triphosphate **51** by T7 RNA polymerase, for which the structural requirements of the initiation site require two consecutive guanines at the 5'-end of the transcript.[384] In addition to a transcription containing ATP, CTP, GTP and **51** instead of UTP giving the transcript Tr402, a positive and a negative control experiment were carried out with either all of the four NTPs, leading to the full-length transcript Tx001, or all of the NTPs except for UTP, leading to the by 9 nucleotides shorter transcript Tx001a.

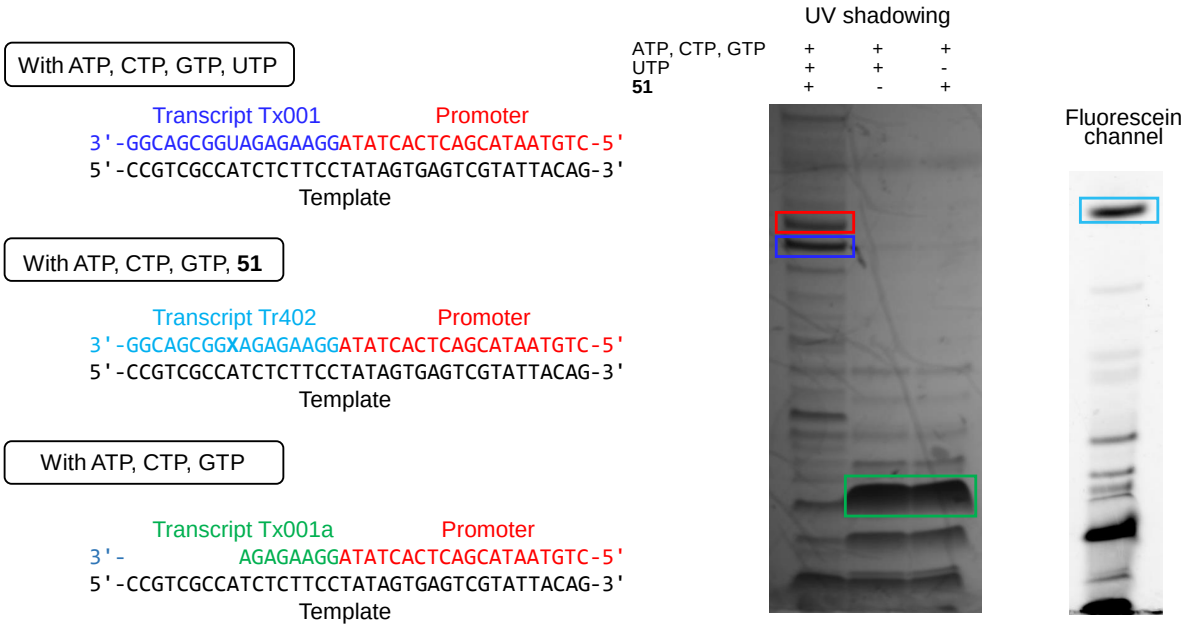

Figure 3.38: The transcription of a template with T7 RNA polymerase in the presence of all four NTPs is expected to give the full length transcript Tx001 (darkblue), while upon substitution of UTP by **51** the modified transcript Tr402 should be obtained (lightblue). If neither UTP nor **51** are present in the reaction mixture, only the short transcript Tx001a (green) is formed. The modified transcript Tr402 was only visible under the fluorescein channel but not by UV shadowing on a TLC plate. It has to be noted that the two gel pictures cannot be compared regarding their dimensions since they were imaged with two different devices. Conditions: 100 µL final volume, 1 µM template and promoter, 4 mM dNTPs, 30 mM $MgCl_2$, 40 mM Tris, 10 mM DTT, 2 mM spermidine.

The three transcriptions were carried out in parallel and incubated overnight at 37 °C before they were quenched by addition of EDTA solution and subjected to PAGE (Figure 3.38).

Unfortunately, visualization of the bands by UV shadowing on a TLC plate only showed the elongation to the full 17nt transcript for the positive control, while for both the negative control and the sample containing **51** only the short Tx001a transcript was visible. Since it had been observed before that the incorporation of BAM nucleosides leads to only weak fluorescence quenching under UV, the gel was imaged again using the fluorescein detection method of a BioRad Chemidoc imager system. Indeed, under these settings a pronounced band for an oligonucleotide of the correct length was detected. A direct comparison between this gel image and the one taken under UV light with respect to their dimensions to proof the correct length of the formed modified transcript is not possible here, however, since different devices were used for imaging.

Nevertheless, it was shown that the rBAM triphosphate **51** can be incorporated by T7 RNA polymerase under *in vitro* transcription conditions, despite its large steric demand and the observation that is not capable of forming Watson-Crick base pairs. It would be required to further analyze the generated transcripts, for example by ESI-MS or HPLC, to prove their correct lengths.

To further investigate the possibility for enzymatic incorporation of the rBAM triphosphate **51**, a primer extension assay with Taq DNA polymerase was carried out (Figure 3.39).

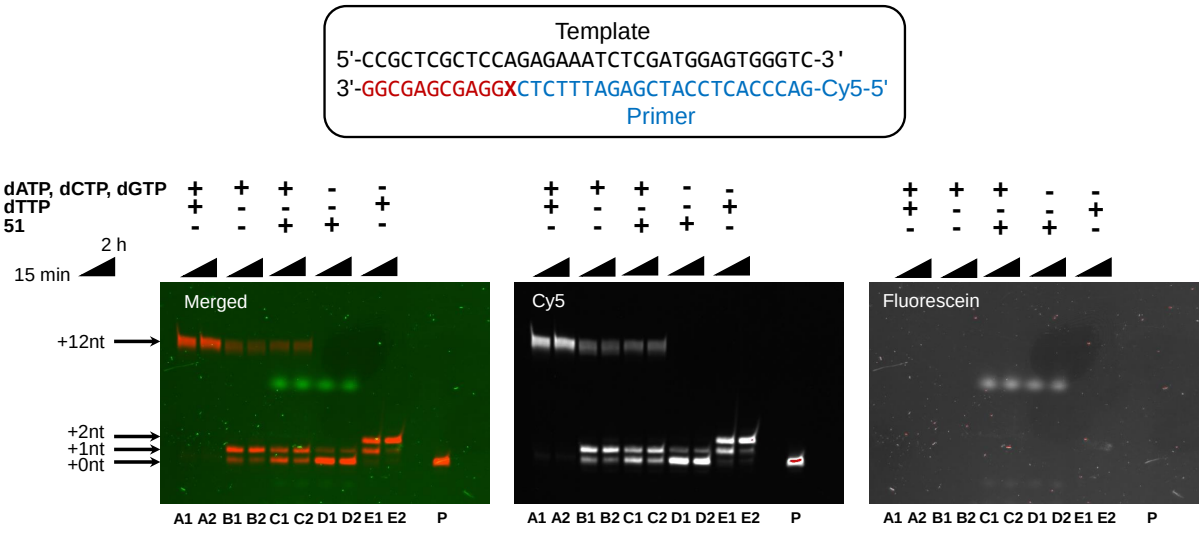

Figure 3.39: In a primer extension assay, the incorporation of the modified triphosphate **51** by Taq polymerase was tested. While the positive control with all canonical dNTPs led to full elongation of the primer (lane A), the absence of one or more dNTPs and the presence of **51** did not yield fully elongated product. The weak upwards shifted band in lane D, however, indicates that **51** is incorporated at least to a small extent. P = primer; conditions: 1 µM template, 2 µM primer, 200 µM dNTP, 0.05 u/µL polymerase, 20 µL final volume.

Although **51** is a ribose triphosphate it was assumed that it might be recognized by this

polymerase which has an enhanced ability to incorporate modified triphosphates. For primer extension experiments, a template and a complementary primer, which is elongated in 5'-3' direction, are required. Here, the alkyne-modified primer was 5'-labelled with sulfo-Cy5 azide in a copper(I)-catalyzed azide-alkyne cycloaddition (CuAAC) to enable imaging under two different settings for either Cy5 or **51** detection. The template was chosen that the first nucleotide to be incorporated is a T or instead the modified triphosphate **51**. Primer extension assays were set up with either all dNTPs (lane A), all dNTPs except for dTTP (lane B), with dATP, dCTP, dGTP and **51** (Lane C), and only **51** (lane D) or dTTP (lane E). Time points were taken after 15 min and 2 h as indicated by the bars. If all canonical dNTPs were present in the reaction mixture, exclusively a band for the fully elongated primer was observed, even after only 15 min of incubation (lane A). Without dTTP (lane B), however, the primer is still fully elongated to some extent due to misincorporations although the most intense band is detected for the elongation by only one nucleotide. A similar obervation is made with dATP, dCTP, dGTP and **51** instead of dTTP (lane C). If **51** is the only triphosphate in the reaction mixture, however, only a small fraction of the labeled primer is elongated, as indicated by the weakly fluorscent bands in both the Cy5 and fluorescein channel (lane D). In contrast, dTTP is incorporated twice by the polymerase but no further elongation is observed (lane E).

Therefore, the artificial triphosphate **51** can be installed by Taq polymerase under the tested conditions, although only to a low extent. Due to the large size of the BAM nucleobase analog and its hydrophobic character, further optimization of the reaction conditions is required to ensure efficient incorporation by the polymerase. Besides the concentration of **51**, the incubation time as well as the used polymerase are adjustable parameters for a higher incorporation efficiency. In addition, the primer extension assay could again be tested using the respective dBAM DNA triphosphate which might be more readily accepted by the Taq polymerase. It has to be noted, that the blurred band observed in the fluorescein channel for all of the reactions containing **51** does not belong to an oligonucleotide but rather appears due to unspecific binding or dimer formation of **51**.

To summarize, rBAM and rBAM^b were synthesized as artificial RNA phosphoramidite building blocks and successfully incorporated into several oligonucleotides. These were analyzed by different spectroscopic techniques regarding their thermodynamic and spectral characteristics. Furthermore, it was shown that the rBAM triphosphate is recognized by RNA as well as DNA polymerases which shows the potential of this fluorescent nucleoside analog for further biochemical applications.

In general, however, RNA is chemically not as stable as DNA, showing a much higher sensitivity toward degradation, and is structurally more complex. Furthermore, modified DNA phosphoramidites are often easier to access since their preparation requires less synthetic

steps. Therefore, it was decided to prepare BAM and BAM^{b} as DNA nucleosides and analyze their behavior in the DNA context.

3.4 dBAM chromophores in the DNA scaffold

For a detailed examination of dBAM- and dBAM^b-modified DNA scaffolds, both chromophores were synthesized as phosphoramidite building blocks and incorporated by solid phase synthesis. The high stability and predictable structure of DNA duplex structures were expected to provide access to additional experiments and lead to easier data interpretation for analysis of the chromophore dimer structures. The preparation of the required building blocks as well as the synthesis and purification of modified DNA oligonucleotides will be described in the first part of the following section.

3.4.1 Synthesis of the dBAM and dBAM^b phosphoramidite building blocks

The direct glycosylation of the free BAM chromophore **1** was considered the easiest approach toward the indolenine-derived dBAM building block. Therefore, the synthetic route toward the dBAM phosphoramidite was started by glycosylation of **1** with 1-chloro-2-deoxy-3,5-di-*O*-toluoyl-α-D-ribofuranose (Hoffer's chlorosugar), a commonly used sugar precursor for deoxyribonucleosides (Scheme 3.19). First, glycosylation was attempted using either only NaH or a combination of NaH and K_2CO_3 as a base for nucleobase activation (entry 1 and 2 in Table 3.10). The nucleobase analog **1** was used in excess to prevent the formation of the double-glycosylated side product. However, even after stirring the reaction mixture for 24 h at 60 °C no product formation was observed. Therefore, it was decided to first silylate the free chromophore **1** *in situ* with *N,O*-bis(trimethylsilyl)acetamide (BSA) and afterwards react it with the sugar compound (entries 3 to 5). Indeed, the formation of the desired product was observed in different solvents at r. t. and also at 0 °C.

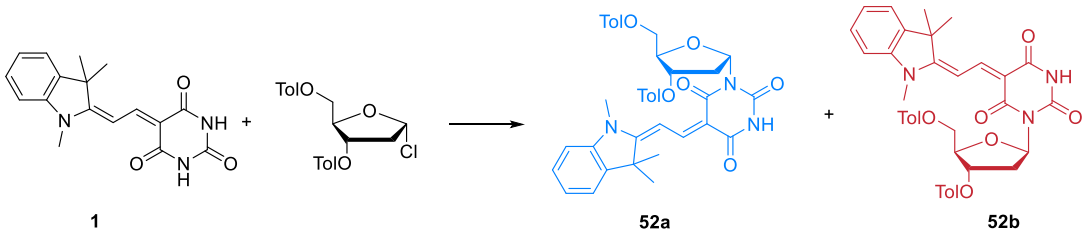

Scheme 3.19: Glycosylation of the free BAM chromophore **1** led to an inseparable 1:1 mixture of α- and β-anomer **52a** and **52b**. See Table 3.10 for reaction conditions.

As discussed previously, due to the lacking 2'-protection group, the activated DNA sugar compound cannot form a cyclic oxocarbenium ion as it is observed for the ribose sugar. Therefore, the exclusive formation of the desired β-anomer is not favored in this case but instead both the α- and the β-anomer **52a** and **52b** are obtained in a 1:1 ratio. This was also the case here and since these two anomers proved to be inseparable by column chromatography,

it was decided to follow a procedure described for the glycosylation of persilylated barbituric acid with Hoffer's chlorosugar instead (Scheme 3.20).[325]

Table 3.10: The direct glycosylation of the free BAM chromophore **1** with Hoffer's chlorosugar under different reaction conditions only led to the formation of a 1:1 mixture of α- and β-anomer **52a** and **52b** of the dBAM nucleoside.

Entry	Conditions	Outcome
1	1.0 eq. **1**, 0.7 eq. Hoffer's chlorosugar, 5.0 eq. NaH, MeCN, 24 h, 60 °C	no reaction
2	1.0 eq. **1**, 0.7 eq. Hoffer's chlorosugar, 5.0 eq. NaH, 1.0 eq. K_2CO_3, MeCN, 24 h, 60 °C	no reaction
3	1) 1.0 eq. **1**, 6.0 eq . BSA, 50 °C, 1 h; 2) 1.0 eq. Hoffer's chlorosugar, 2.0 eq. NaH, MeCN, 24 h, r.t.	1:1 α/β
4	1) 1.0 eq. **1**, 6.0 eq . BSA, 50 °C, 1 h;, 2) 1.0 eq. Hoffer's chlorosugar, 2.0 eq. NaH, THF, 24 h, r.t.	1:1 α/β
5	1) 1.0 eq. **1**, 6.0 eq . BSA, 50 °C, 1 h;, 2) 1.0 eq. Hoffer's chlorosugar, 2.0 eq. NaH, THF, 20 h, 0 °C	1:1 α/β

This protocol is very similar to the one used for the synthesis of the rBAM building block: it is also carried out at ambient temperature in 1,2-DCE and employs $SnCl_4$ for activation of the sugar compound. Since also here separation of the two anomers was not achieved by column chromatography, the purified anomeric mixture was recrystallized from methanol as reported.[325] Hereby, around 70% of the β-anomer **53b** precipitated while the other part together with the α-anomer **53a** remained in the filtrate.

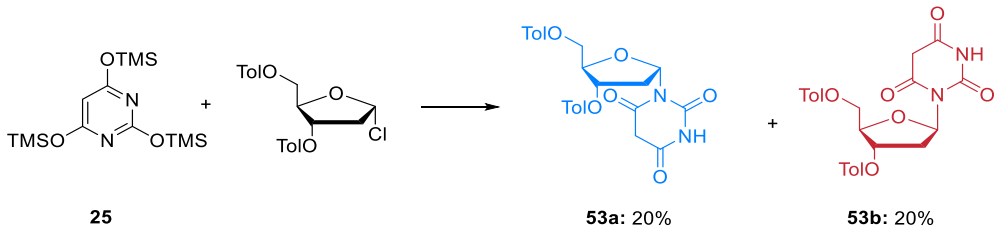

Scheme 3.20: The glycosylation of persilylated barbituric acid with Hoffer's chlorosugar gives an 1:1 mixture of α- and β-anomer **53a** and **53b**. Conditions: $SnCl_4$, 1,2-DCE, r. t., 3 h.[325]

The proton NMR signals were assigned unambiguously for both anomers by 2D NMR. To elucidate the conformation of the anomeric center, a NOESY spectrum of the filtrate containing the two anomers was recorded and by analysis of the visible NOESY contacts both isomers were clearly identified (Figure 3.41).

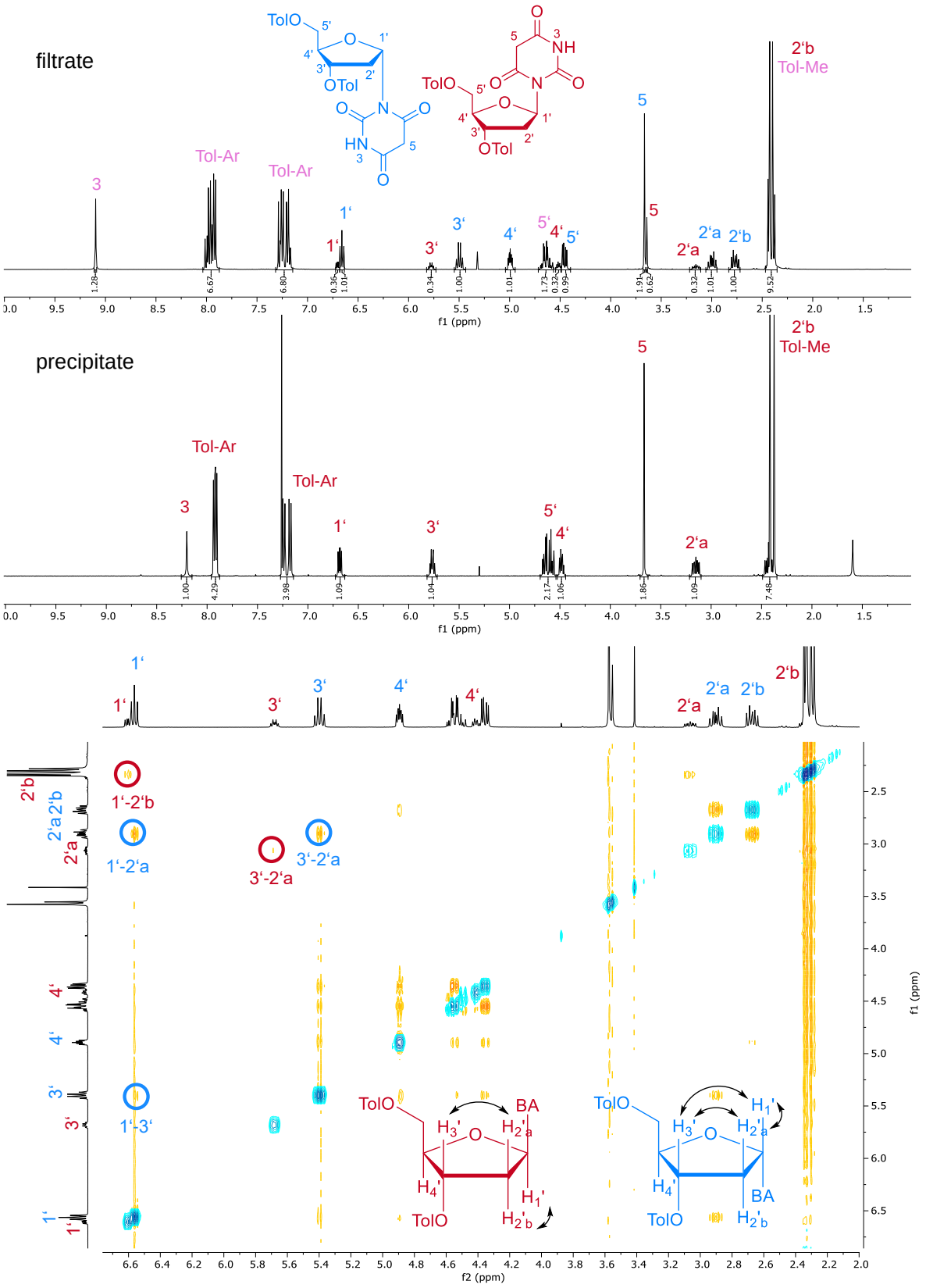

Figure 3.40: The proton NMR spectra after recrystallization of the anomeric mixture of barbituric acid DNA nucleosides shows the α-anomer **53a** (blue) and the β-anomer **53b** (red) in 3:1 ratio in the mother liquor whereas only the desired β-anomer **53b** precipitated (top). The α- and β-anomer were unambiguously assigned by analysis of the NOESY contacts for the filtrate; signals belonging to both compounds are colored purple.

The β-nucleoside **53b** was used for aldol condensation with the precursor aldehyde **17** and subsequently deprotected with methanolic NaOH, which *in situ* generates sodium methoxide (Scheme 3.21). The hereby obtained free dBAM nucleoside **54** was afterwards 5'-DMT-protected to give **55** and then converted into the target phosphoramidite **56**. All synthetic steps proceeded smoothly and gave high yields of the desired compounds after purification by column chromatography.

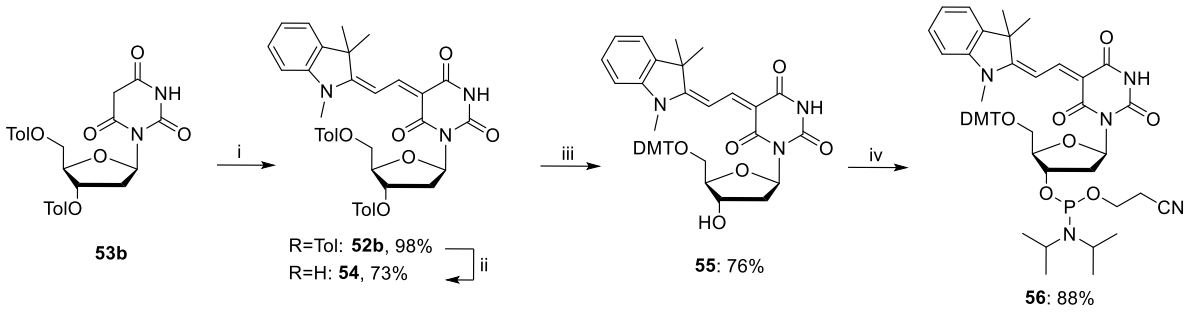

Scheme 3.21: Synthesis scheme for the preparation of the dBAM phosphoramidite building block **56**. Conditions: i) aldehyde **17**, abs. EtOH, 70 °C, 18 h; ii) 1% methanolic NaOH, r. t., 45 min; iii) DMT-Cl, DMAP, pyridine, r. t., 20 h; iv) CEP-Cl, *N,N*-ethyldimethylamine, anhydrous CH_2Cl_2, r. t., 90 min.

Since the BAM^b chromophore showed to be more prone to degradation and oxidation compared to the BAM chromophore, the barbituric acid nucleoside **53b** was deprotected to give compound **57** prior to building up the chromophoric system in an aldol-type reaction with the precursor **22** (Scheme 3.22). Also in this case, the merocyanine nucleoside **58** was 5'-DMT protected, yielding compound **59**, which was further converted into the target phosphoramidite **60** by phosphitylation.

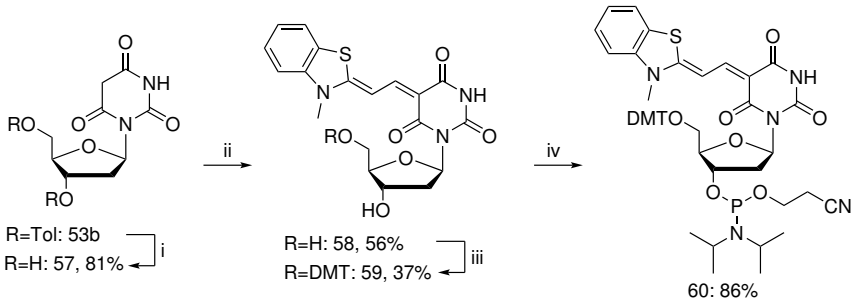

Scheme 3.22: Schematic scheme for the synthesis of the dBAM^b phosphoramidite building block **60**. i) 1% methanolic NaOH, r. t., 20 min; ii) precursor **22**, NEt_3, abs. EtOH, 70 °C, 2 h; iii) DMT-Cl, DMAP, pyridine, r. t., 30 h; iv) CEP-Cl, *N,N*-di-*iso*-propylethylamine, anhydrous CH_2Cl_2, r. t., 3 h.

As already mentioned for the rBAM and rBAM^b nucleosides, it has to be noted that upon introduction of the aromatic chromophore donor two double bond isomers are formed, namely the (*E,E*)- along with the (*E,Z*)-stereoisomer. Both are assumed to be energetically very similar according to geometry optimizations (compare Scheme 3.13) with nearly identical directions of

their transition dipole moments; they are not expected to influence the spectroscopic properties of the chromophore but lead to NMR spectra with complex coupling patterns. Thus, not only one but two sets of signals with the same integral are observed for the two protons of the polymethine bridge as well as for the NH of the barbituric acid which is exemplarily shown for the free dBAM nucleoside **54** in Figure 3.41.

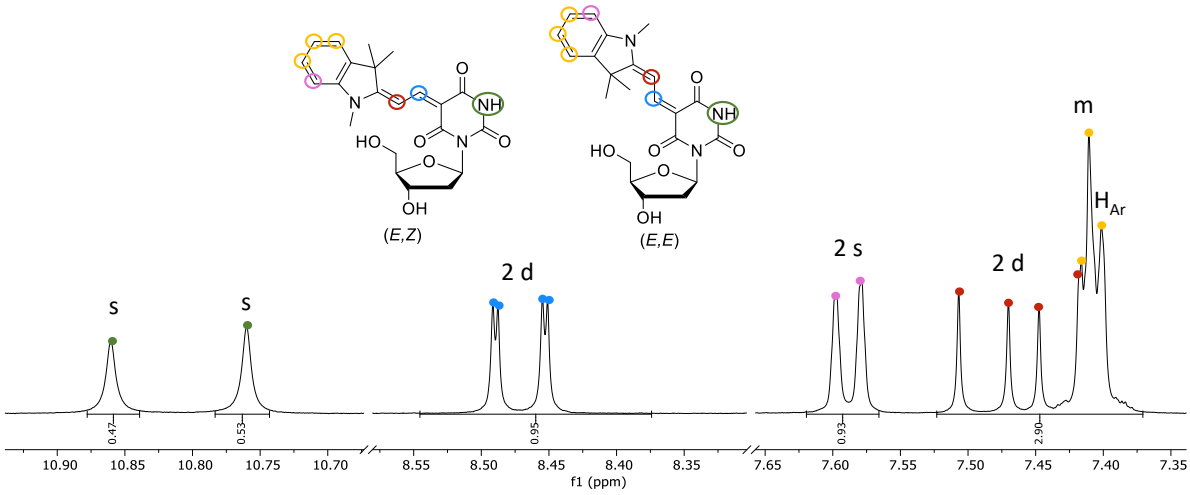

Figure 3.41: The aromatic region of the proton NMR spectrum for the free dBAM nucleoside **54** reveals two sets of signals for the protons of the polymethine bridge and the barbituric acid NH due to the presence of double bond isomers.

The two obtained pure phosphoramidites were afterwards incorporated into DNA oligonucleotides by solid phase synthesis which will be described in the following section.

3.4.2 Incoporation of the dBAM and dBAM^b phosphoramidites into DNA oligonucleotides

In accordance with the RNA sequences shown in Table 3.6, analoguous DNA strands were synthesized following a standard coupling protocol (Table 3.11). In addition to the canonical reference strands, one oligonucleotide with 2AP for FRET experiments and one with an abasic site for additional stability measurements were prepared. Pure unmodified and dBAM-modified oligonucleotides were isolated in excellent yields after PAGE purification while dBAM^b-modified sequences had to be purified by RP-HPLC in addition which led to reduced yields of the isolated oligonucleotides. The additional HPLC purification was neccessary due to the formation of byproducts by aminolysis reactions during basic deprotection, as already mentioned for the rBAM^b-containing RNA strands. Exemplarily, an ESI mass spectrum for **D9** after gel electrophoresis is shown in Figure 3.42. Here, four species are obtained; the one with the highest molecular weight is the desired target strand, the other species are lighter by 42, 93 and 146 mass units, respectively, and are colorless which indicates the decomposition of the chromphore structure.

Table 3.11: Sequences, yields and masses for native and modified DNA 12 nt oligomers obtained by solid phase synthesis. Important nucleobases are shown in bold, modified ones are colored in addition.

Name	5'-sequence-3'	yield[a] nmol	*M* calc. g mol^{-1}	*M* meas.[b] g mol^{-1}
D1	GATGAT**A**GCTAG	249	3707.66977	3707.69796
D2	CTAGCTATCATC	162	3578.63975	3578.65536
D3	GATGAT**C**GCTAG	173	3683.65853	3683.68621
D4	GATGAT**G**GCTAG	193	3723.66468	3723.66893
D5	GATGAT**T**GCTAG	214	3698.65820	3698.70495
D6	GATGAT**A**GCTAG	157	3707.66922	3707.66874
D7	GATGAT**Y**GCTAG	279	3532.61981	3532.62184
D8	GATGA**X**AGCTAG	235	3892.75328	3892.72682
D9	GATGA**X**AGCTAG	46	3882.65924	3882.67840
D10	CTAGC**X**ATCATC	211	3763.72327	3763.69965
D11	CTAGC**X**ATCATC	11	3753.65499	3753.64839
D12	CTAGCT**X**TCATC	194	3754.71170	3754.71066
D13	CTAGCT**X**TCATC	84	3744.64374	3744.63682
D14	CTAGCTA**X**CATC	206	3763.72327	3763.72978
D15	CTAGCTA**X**CATC	95	3753.66226	3753.64839

[a] 600-800 nmol synthesis scale

[b] monoisotopic masses obtained by charge deconvolution of the raw spectra

Y = C3-linker (abasic site), **A** = 2AP, **X** = dBAM, **X** = dBAM^{b}.

To reveal the degradation mechanism of the BAM^{b} chromophore under basic conditions, the exact masses of conceivable decomposition intermediates (colored) were calculated and compared to the observed ones (black, Figure 3.42). The decomposition of dBAM^{b} containing oligonucleotides seems to be initiated by a nucleophilic attack on the polymethine bridge, leading to the introduction of additional amino or hydroxy groups. The products formed upon this nucleophilic substitution degrade afterwards, until only a methylene unit with an NH_2 remains at the barbituric acid core which leads to a by 146 mass units reduced molecular weight (blue). However, the actual chemical composition of the observed degradation products with Δ=42 (red), 44 (yellow) and 93 *m/z* (purple) cannot be proven reliably by only mass analysis, and therefore only the deconvoluted and calculated spectra for possible intermediates are shown in Figure 3.42. Interestingly, similar decomposition events were not observed for dBAM-modified oligonucleotides. This might be due to the electron-withdrawing character of the sulfur atom in dBAM^{b}, which reduces the electron density of the polymethine bridge and

hereby makes it more prone to nucleophilic attacks.

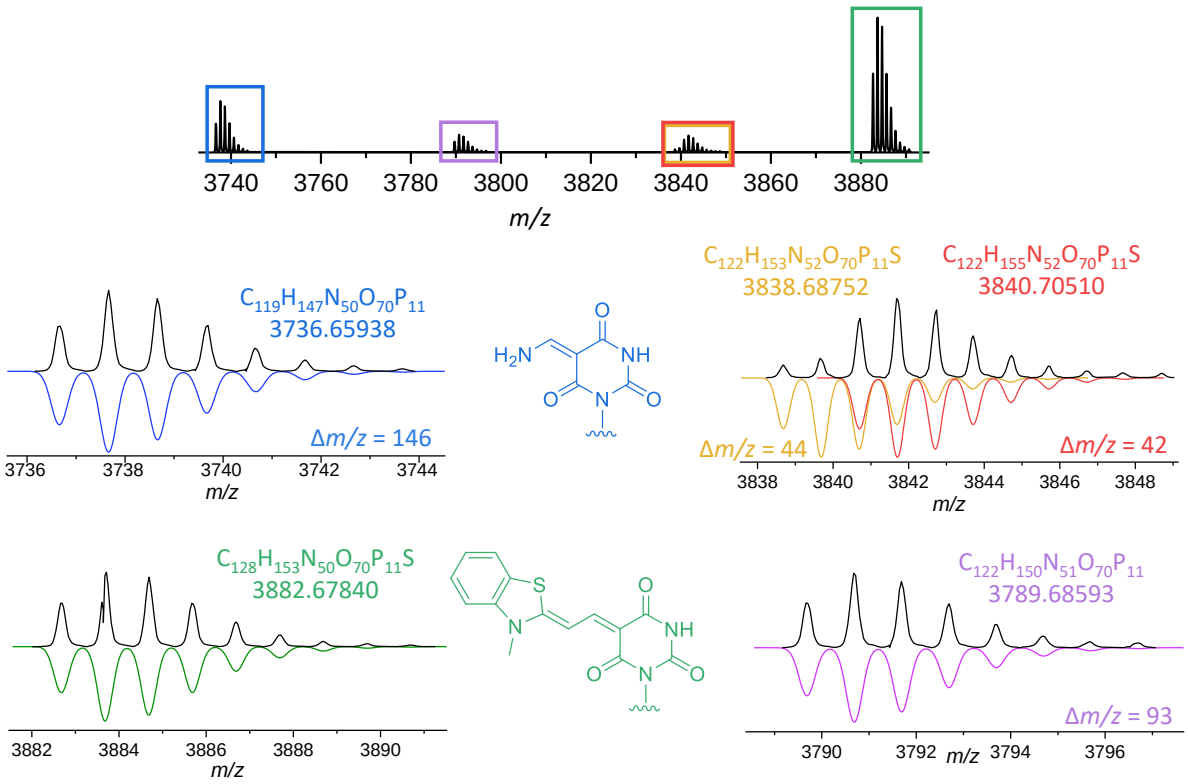

Figure 3.42: The deconvoluted ESI mass spectrum for **D9** after PAGE purification reveals the presence of four different species. Deconvoluted measured spectra are shown black, simulated spectra are colored and the respective masses as well as conceivable molecular formulas are given above every spectrum.

For further elucidation of the decomposition intermediates, the free BAM^{b} chromophore **7** was treated with aqueous ammonia at elevated temperature. HPLC-MS data were recorded for this sample after overnight incubation (Figure 3.43). With this experiment, the presumed nucleophilic substitution reaction was confirmed since three chromophores with either a hydroxy group, an amine or both functions attached were detected in the 230 nm UV trace. In the 460 nm trace, only the intact chromophore was visible. This is interesting since also in the substitution products shown on the upper left side the conjugated chromophoric system remains undisturbed. This might indicate that these compounds are rather present in the keto than in the drawn enol ether form. The degradation products with only a methylene unit bearing an amino group bound to either barbituric acid or benzothiazole found in the oligonucleotide were also present here (last structure on left side of Figure 3.43). However, as already stated for the dBAM^{b}-containing oligonucleotide **D9**, the shown molecular structures are not confirmed since the final elucidation of the molecular constitution and the mechanism for the formation of the observed degradation products requires more detailed analysis of the treated samples. In addition, for simplification only one isomer out of two possible ones is shown for each structure.

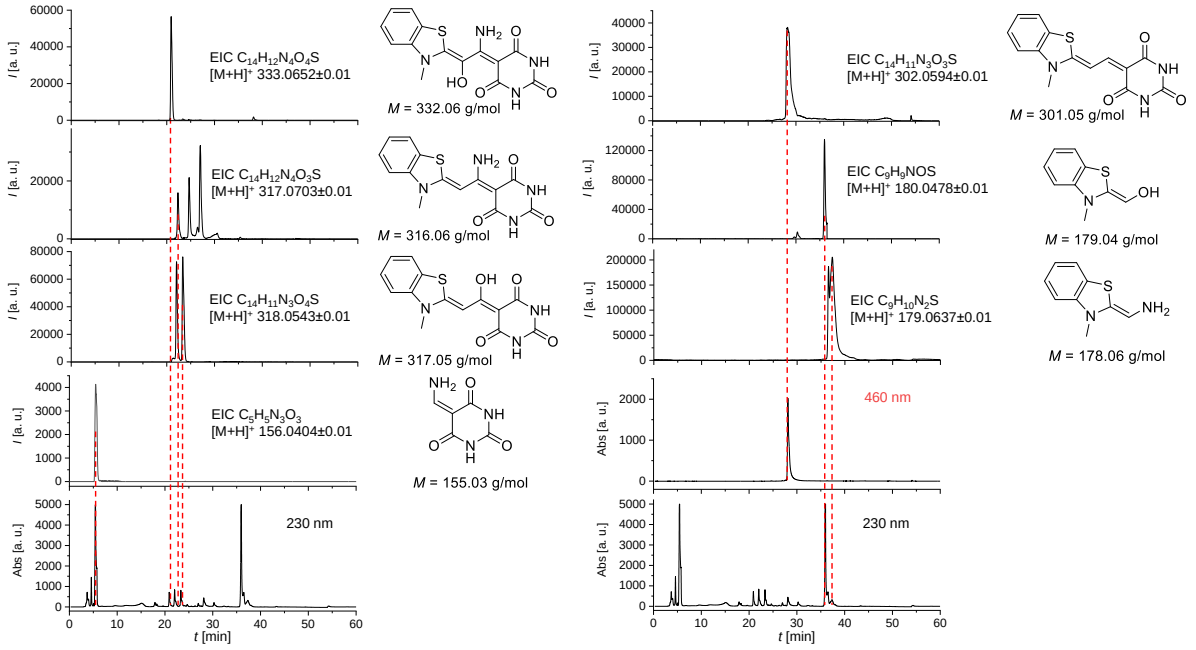

Figure 3.43: LCMS traces for the free BAM^{b} chromophore **7** after overnight incubation with ammonia at 60 °C reveal the degradation of the chromophore under basic conditions by nucleophilic attack on the double bonds of the polymethine bridge. For simplification, only one isomer is shown for each spectrum.

The PAGE- and HPLC-purified DNA oligonucleotides were in the following used for duplex formation with their respective counterstrands. The hereby obtained helical systems are structurally comparable to their RNA variants with single-modified duplex structures having either each of the canonical nucleobases or 2AP opposite the merocyanine modification as well as double-modified ones in downstream, upstream and opposite direction (Figure 3.44).

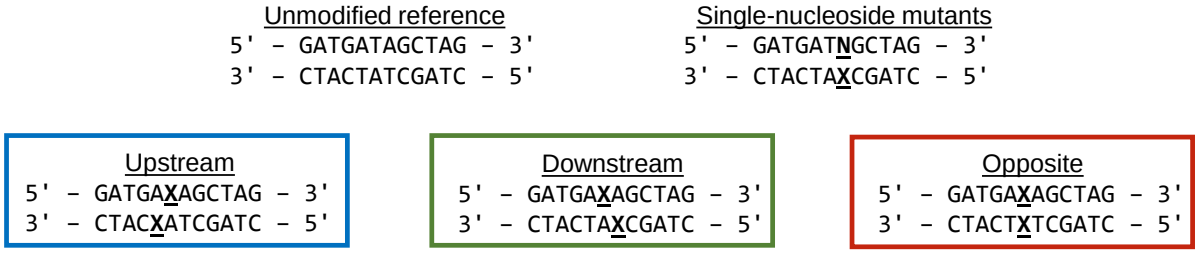

Figure 3.44: Duplex sequences for unmodified and modified DNA structures. **N** is the abbreviation for any of the nucleobases A, C, G, T and 2AP while **X** is either dBAM or dBAM^{b}.

Besides these DNA 12mers, 34 nt DNA oligonucleotides were synthesized for thermodynamic analyses and further experiments. Despite their lengths, the two unmodified as well as the modified strands were obtained with excellent yields (Table 3.12).

Table 3.12: Sequences, yields and masses for native and modified DNA 34 nt oligomers obtained by solid phase synthesis.

Name	5'-sequence-3'
D16	CAACAACAACAACTGGAGTCGCCAACTGAATGAA
D17	TTCATTCAGTTGGCGACTCCAGTTGTTGTTGTTG
D18	CAACAACAACAAC**X**GGAGTCGCCAACTGAATGAA

Name	yield[a] nmol	*M* calc. g mol^{-1}	*M* meas.[b] g mol^{-1}
D16	119	10425.82493	10425.92603
D17	169	10446.71612	10446.84153
D18	94	10615.98306	10616.04446

[a] 600-800 nmol synthesis scale
[b] monoisotopic masses obtained by charge deconvolution of the raw spectra
X = dBAM.

The purified oligonucleotides were afterwards used for thermodynamic and spectroscopic analyses which are going to be discussed in the following sections.

3.4.3 Thermodynamic properties and structural parameters of dBAM- and dBAM^{b}-modified DNA oligomers

As already mentioned before, the melting point and derived thermodynamic parameters are important characteristics of modified oligonucleotide duplex structures. Similar as for the rBAM- and rBAM^{b}-modified RNA structures, the base pairing properties for the structurally akin respective DNA systems with either dBAM or dBAM^{b} opposite different nucleobases were determined and compared to an unmodified reference duplex (Table 3.13).

Since RNA is capable of forming twice as many hydrogen bonds than DNA, the DNA reference duplex **D1/D2** with a melting temperature of 43.6 °C is by 10.8 °C destabilized compared to the respective RNA duplex and therefore lowered melting points are obtained for all modified systems.[385] In general, the duplex melting points for single-dBAM- and single-dBAM^{b}-modified systems are decreased by 8 to 11 °C and 4 to 9 °C, respectively. The effect that the overall thermal stability of dBAM^{b}-modified duplexes is higher than for dBAM-modified ones can also here be attributed to the smaller steric demand of the benzothiazole-derived chromophore. The decrease of the melting temperature shows to be independent from the nucleobase opposite the merocyanine for both modified systems. Thus, also in the DNA context

dBAM and dBAM^{b} do not maintain the optimal conformation for Watson-Crick base pairing with A. In addition, the values for ΔH^0, ΔS^0 and ΔG^0 are in the same range for all structures, revealing a similar thermodynamic behavior for both dBAM- and dBAM^{b}-modified duplexes.

Table 3.13: Sequences, melting temperatures and thermodynamic parameters for DNA duplex structures with a single merocyanine modification. Important nucleobases are shown in bold. Given are also the differences in melting temperature relative to the unmodified reference sequence.

Name	sequence	$T_m^{[a]}$ °C	$\Delta T_m^{[b]}$ °C	ΔH^0 kcal mol^{-1}	ΔS^0 cal mol^{-1} K^{-1}	ΔG^0_{298K} kcal mol^{-1}
D1/D2	5'-...ATA...-3' 3'-...TAT...-5'	43.6	-	-86.9	-248	-12.9
D8/D2	5'-...A**X**A...-3'	35.4	-8.2	-77.9	-227	-10.2
D9/D2	3'-...T**A**T...-5'	34.7	-8.9	-79.7	-233	-10.2
D1/D10	5'-...AT**A**...-3'	33.5	-10.1	-79.0	-232	-9.90
D1/D11	3'-...TA**X**...-5'	36.7	-6.9	-66.6	-189	-10.3
D3/D10	5'-...AT**C**...-3'	33.5	-10.1	-78.6	-231	-9.85
D3/D11	3'-...TA**X**...-5'	39.2	-4.4	-70.6	-200	-10.8
D4/D10	5'-...AT**G**...-3'	32.3	-11.3	-76.1	-224	-9.34
D4/D11	3'-...TA**X**...-5'	38.7	-4.9	-70.3	-200	-10.8
D5/D10	5'-...AT**T**...-3'	32.5	-11.1	-70.4	-205	-9.33
D5/D11	3'-...TA**X**...-5'	37.6	-6.0	-80.3	-233	-11.0
D7/D10	5'-...AT**Y**...-3'	36.9	-6.7	-77.9	-226	-10.7
D7/D11	3'-...TA**X**...-5'	42.9	-0.7	-84.1	-240	-12.5
D6/D10	5'-...TA**A**...-3' 3'-...TA**X**...-5'	34.9	-8.7	-66.8	-192	-9.69

[a] values for 5 µM samples in 1× PBS (100 mM NaCl, 10 mM phosphate, pH 7.0); 0.5 °C/min heating rate; a standard error of ±0.5 °C is assumed

[b] difference relative to unmodified duplex

Y = C3-linker (abasic site), **A** = 2AP, names in blue for dBAM, names in red for dBAM^{b}.

If the merocyanine modification is located opposite an abasic site, which provides enhanced conformational freedom of the chromophore, the thermodynamic parameters obtained for the dBAM-modified duplex **D7/D10** are very similar to the ones for all of the duplexes with the canonical nucleobases opposite dBAM. In contrast, the respective dBAM^{b}-modified helix **D7/D11** shows almost the same values for T_m, ΔH^0, ΔS^0 and ΔG^0_{298K} as the unmodified reference **D1/D2**. This indicates that the additional space provided by the abasic site can be occupied by the dBAM^{b} chromophore without destabilization of the structure. Meanwhile,

the indolenine-derived dBAM chromophore still leads to structural perturbation, presumably due to its increased steric demand. For better comparison, the melting curves for all of the duplex structures given in Table 3.13 containing either BAM or BAM^b opposite the different canonical nucleobases and the abasic site are summarized in Figure 3.45.

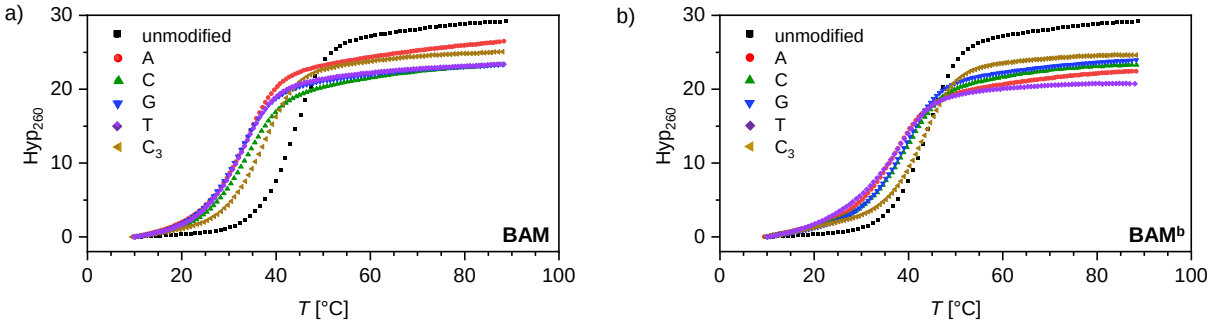

Figure 3.45: For duplexes with different canonical nucleosides or an abasic site opposite to dBAM (a) or dBAM^b (b) very similar melting temperatures were obtained with the highest ones for systems with an abasic site opposite the modification. In general, dBAM^b-modified duplex structures displayed a better thermal stability than dBAM-modified systems. Data are shown for 5 µM samples and the second heating ramp.

The values for the free Gibbs energy ΔG^0_{298K} are elevated by around 3 kcal mol^{-1} for dBAM-modified duplex structures which is a significant smaller increase than for all of the RNA systems and is in the range of the loss of hydrogen bond strength for the replaced A-T base pair (approximately 2.5 kcal mol^{-1}). For the dBAM^b-modified systems, the enhancement of ΔG^0_{298K} is even smaller. Therefore, the introduction of the sterically demanding merocyanine modifications into DNA has a smaller impact on the thermodynamic parameters compared to the incorporation of the rBAM or rBAM^b chromophore into RNA.

Quantitative analysis of the melting temperatures obtained for modified DNA and RNA duplex structures shows an overall larger helix destabilization by 30 to 40% for RNA compared to 10 to 25% for DNA upon incorporation of BAM and similarly BAM^b. To explain this difference in stability, the simplified 3D-model of the single-BAM-modified DNA duplex can be consulted (Figure 3.46). In comparison with the RNA model in Figure 3.21, a much less pronounced steric clash between the methyl groups of the chromophore and the phosphate backbone is observed, which also holds true for the single-dBAM^b-modified DNA duplex.

However, it has to be noted that the chromophore in Figure 3.46 is drawn in base pairing conformation with the indolenine being located in the duplex major groove although the melting points already indicate that BAM and BAM^b rather are in a similar orientation as in the RNA helix. This assumption was further supported by the thermodynamic and spectroscopic analysis of double-modified duplex structures discussed in the next section.

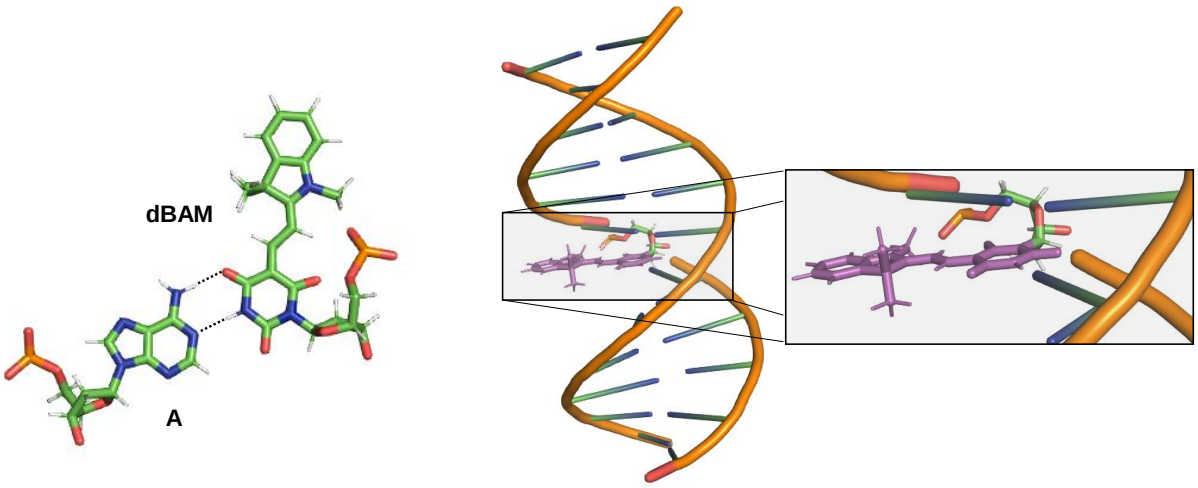

Figure 3.46: Modeled dBAM-A base pair in the 12mer duplex structure (left) and orientation of the dBAM chromophore upon base pairing in the helix (right). The chromophore is drawn in the (*E*),(*E*)-conformation; as shown in the magnified detail, a much less significant steric clash between the chromophore and the phosphate backbone is observed in comparison to the respective RNA system. Structures were built with ChemDraw, Discovery Studio and Pymol.

In addition to the single-dBAM-modified DNA 12mer duplex structures the melting temperatures of DNA 34mer duplexes containing only one dBAM were estimated (Table 3.14). Here, the duplex **D18/D17** was destabilized by only 2.2 °C upon introduction of one dBAM chromophore compared to the reference system **D16/D17**, indicating that dBAM leads to only a minor disturbance of the duplex structure in longer strands.

Table 3.14: Sequences and melting temperatures for the DNA 34mer duplex structure with a single dBAM modification. Given is also the difference in melting temperature relative to the unmodified reference sequence.

Name	sequence	$T_m^{[a]}$ °C	$\Delta T_m^{[b]}$ °C
D16/D17	5'-...T...-3' 3'-...A...-5'	75.6	-
D18/D17	5'-...**X**...-3' 3'-...A...-5'	73.4	-2.2

[a] values for 5 µM samples in 1× PBS (100 mM NaCl, 10 mM phosphate, pH 7.0); 0.5 °C/min heating rate; a standard error of ±0.5 °C is assumed.
[b] difference relative to unmodified duplex.
X = dBAM.

The estimation of the thermodynamic parameters for these two system by van't Hoff analysis was not done here since they showed only a slight dependence of the denaturation tempera-

ture on the sample concentration (Figure 3.47). This is reasonable for longer oligonucleotides due to the larger influence of the propagation compared to the initiation step on the melting behavior as explained in section 3.3.4. However, since not only the melting temperatures but also the curve shapes for both the modified and unmodified duplex structures are almost equal, a similar thermodynamic behavior for these two systems is expected.

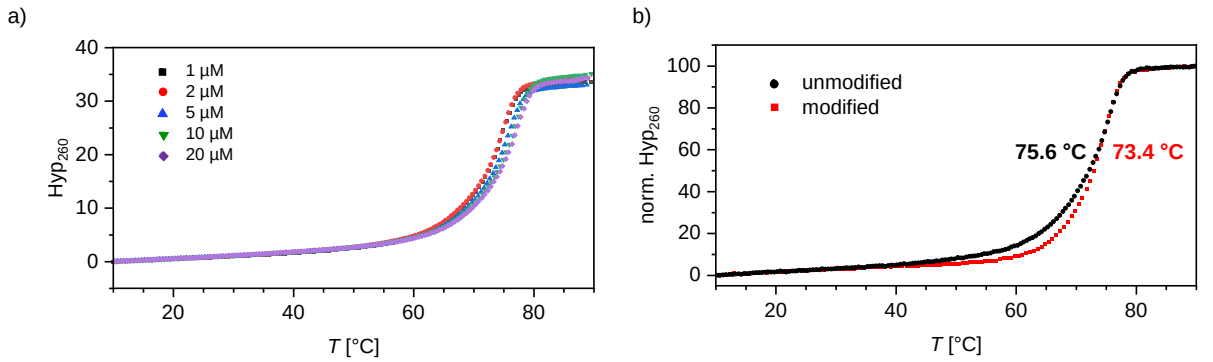

Figure 3.47: The melting curves for the single-dBAM-modified DNA 34mer duplex **D18/D17** show only a weak dependence of the denaturation temperature on the sample concentration (a), and the melting point as well as the curve shape of this system almost resemble the ones of the unmodified reference **D16/D17** (b).

Furthermore, the melting temperatures for the double-modified structures shown in Figure 3.44 with the related thermodynamic parameters were estimated and are presented in Table 3.15. Here, all of the double-dBAM-modified duplex structures showed to be destabilized by 3 to 9 °C compared to the reference system. This destabilizing effect is in the same range as for single-dBAM-modified duplex structures and shows that a second chromophores is well tolerated. In addition, both the enthalpic and entropic factors are decreased while the values for ΔG^0_{298K} correlate with the trend in the melting temperatures.

In stark contrast to these findings, the second chromophore in double-dBAM^b-modified duplex structures even partially rescued the drop in duplex stability caused by the first dBAM^b. This stabilizing effect is most pronounced with the two chromophores located directly opposite each other in **D9/D13** with a significant increase of the melting temperature by 15.4 °C for the 5 µM sample. In parallel, for the down- and upstream case **D9/D11** and **D9/D15** only a slight stabilization of 4.0 and 2.2 °C, respectively, was observed. The stabilizing effect is presumably caused by dipolar interactions between stacking merocyanine chromophores and outweighs the duplex destabilization due to the introduction of the sterically demanding chromophores. Similar positive impacts on the duplex stability by chromophore stacking in a face-to-face H-type fashion have already been reported for pyrenes, PDIs and fluorenes.[386–388] However, the degree of duplex stabilization in the dimer systems described here is strongly dependent on the position of the chromophores in the helix and their orientation toward each other.

Table 3.15: Sequences, melting temperatures and thermodynamic parameters for DNA duplex structures with two merocyanine modifications incorporated; the blue, green and red colored duplex names indicates upstream, downstream and opposite chromophore positioning, respectively. dBAM and dBAM^{b} are abbreviated as differently colored X. Given are also the differences in melting temperature relative to the unmodified reference sequence.

Name	sequence	$T_m^{[a]}$ °C	$\Delta T_m^{[b]}$ °C	ΔH^0 kcal mol^{-1}	ΔS^0 cal mol^{-1} K^{-1}	ΔG^0_{298K} kcal mol^{-1}
D1/D2	5'-...ATA...-3' 3'-...TAT...-5'	43.6	-	-86.9	-248	-12.9
D8/D14	5'-...AXA...-3' 3'-...XAT...-5'	37.2	-6.4	-76.6	-221	-10.8
D8/D10	5'-...AXA...-3' 3'-...TAX...-5'	34.9	-8.7	-74.0	-215	-9.99
D8/D12	5'-...AXA...-3' 3'-...TXT...-5'	40.4	-3.2	-73.7	-209	-11.3
D9/D15	5'-...AXA...-3' 3'-...XAT...-5'	45.8	+2.2	-61.7	-174	-9.75
D9/D11	5'-...AXA...-3' 3'-...TAX...-5'	47.6	+4.0	-57.1	-155	-10.8
D9/D13	5'-...AXA...-3' 3'-...TXT...-5'	59.0	+15.4	-56.5	-145	-13.4

[a] values for 5 µM samples in 1× PBS (100 mM NaCl, 10 mM phosphate, pH 7.0); 0.5 °C/min heating rate; a standard error of ±0.5 °C is assumed
[b] difference relative to unmodified duplex
X = dBAM, X = dBAM^{b}.

If the duplex melting curves for all dBAM-modified systems are compared to their dBAM^{b}-modified counterparts, an apparent difference in the curve shapes becomes obvious (Figure 3.48). While for the first ones mentioned sigmoidal shaped curves for all concentrations were observed, for the latter ones the melting behavior showed to be strongly dependent on the sample concentration. At low concentrations, the melting curves are lacking a pronounced inflection point which hampers exact determination of the denaturation temperature. With higher duplex concentrations, the curve shape becomes almost sigmoidal and therefore the duplex melting point can more easily be calculated. These findings indicate a strong dependence of the duplex stability and melting behavior on the chromophore position in the oligonucleotide scaffold.

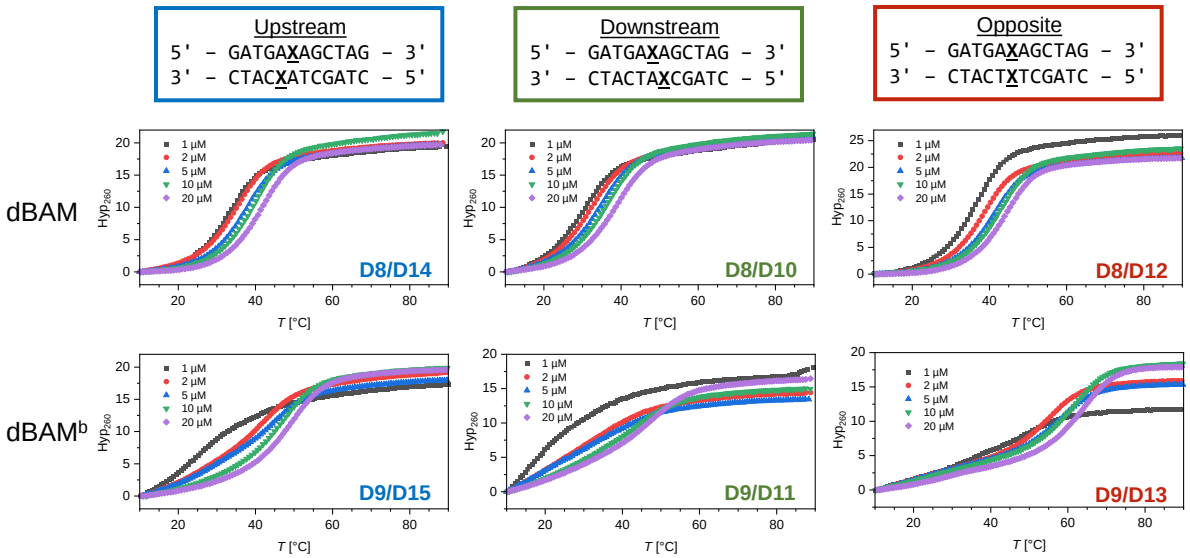

Figure 3.48: The melting curves for double-dBAM-modified duplexes (top row) show a sigmoidal shape for all concentrations while the melting behavior of double-dBAM^b-modified duplexes (bottom row) exhibits a strong dependence on the sample concentration. Data shown are for the second heating ramp for samples in 1× PBS (100 mM NaCl, 10 mM phosphate, pH 7.0); 0.5 °C/min heating rate.

If the thermodynamic parameters for double-dBAM- and double-dBAM^b-modified duplexes are compared, it becomes obvious that both the enthalpic as well as the entropic contribution are increased. The difference in entropy might be attributed to the distinct conformational freedom of the two chromophores in the helix scaffold: similar as for the RNA case, the benzothiazole-derived chromophore dBAM^b is sterically less demanding and therefore fits better into the tight duplex environment while the methyl groups of the indolenine-derived dBAM chromophore prevent efficient coplanar alignment of the merocyanines, presumably leading to a partial unwinding of the duplex structure and hereby destabilizing the system.

In analogy to the modified RNA systems, 3D models for the respective DNA duplex structures with upstream, downstream and opposite chromophore-chromophore orientation were built (Figure 3.49). Although these structures are energetically not optimized, it is evident that the steric hindrance between the two chromophores is reduced compared to RNA which might be due to the larger base-base distance in the DNA B-form duplex (3.4 compared to 2.9 Å in the A-form duplex). However, the melting temperatures for the three different duplex variants are only partially in accordance with these preliminary models. The most stable structures are observed for the opposite chromophore orientation which is expected since here both merocyanines do not have an opposite canonical nucleobase which needs to be displaced and the artificial nucleobase surrogates are stacked in almost parallel alignment. For the up- and downstream case, the modeled structures suggest a higher stability for the second system. This is indeed observed for the downstream dBAM^b-modified helix **D9/D11** whereas for the dBAM-modified structure the melting temperature of the upstream dimer **D8/D14** slightly exceeds

the one of the downstream orientation **D8/D10**. However, it has to be noted that in the up- and downstream dimers still the two A opposite the BAM modifications are present. The positions and orientations of these canonical nucleobases is not elucidated so far; presumably, they are rotated outward of the duplex center or might be located in the major groove.

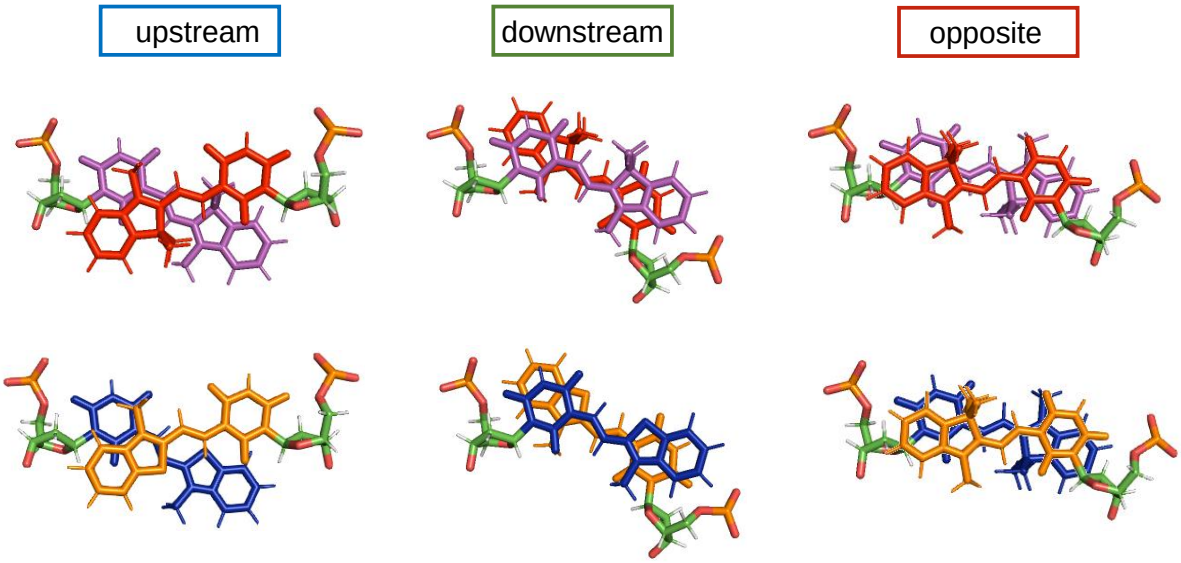

Figure 3.49: Top views of the chromophore positions in upstream, downstream and opposite double-modified DNA duplex structures. On top, systems with two dBAM chromophores shown in red and purple are illustrated, below, systems with two dBAM^{b} chromophores shown in orange and blue are depicted. In all of the structures the two chromophores are stacked on top of each other; compared to the respective RNA models, a larger overlap of the chromophore aromatic systems becomes obvious.

Thus, the actual structures of double-modified duplexes cannot easily be rationalized by simple modeling and additional experiments are required to elucidate the conformation of these merocyanine-containing systems. Toward this goal, similar spectroscopic analyses as for the RNA helical structures were conducted and are discussed in the next section of this thesis.

3.4.4 Spectroscopic characterization of dBAM- and dBAM^{b}-modified DNA duplex structures

To explore the spectroscopic characteristics of the dBAM and dBAM^{b} monomers, absorption and fluorescence spectra of single-modified DNA duplex structures were recorded. In addition, also the respective downstream, upstream and opposite dimers were analyzed regarding their temperature-dependent spectroscopic properties.

3.4.4.1 Investigations on single-dBAM- and single-dBAM^{b}-modified systems

First, the temperature-dependent absorption spectra of single-BAM- and -BAM^{b}-modified DNA duplex structures were analyzed (Figure 3.50). Obviously, the absorption behavior only

changes slightly for both systems upon heating from 20 to 80 °C. For the dBAM-containing helix, the absorption maximum is hypsochromically shifted by 3 nm from 469 to 466 nm and shows an intensity decrease of less than 5% at high temperatures compared to lower ones. These minor changes can be attributed to the loss of stacking interactions between the chromophore and adjacent nucleobases at temperatures above the duplex melting temperature, although these interactions do not have a significant impact in the fully hybridized duplex. A similar trend is obtained for the single-dBAM^{b}-modified helix albeit here the blue-shift of the maximum is with 7 nm from 477 to 470 nm a bit more pronounced. In general, no remarkable differences in the absorption behavior of single-modified DNA and RNA is observed, both reflecting similar characteristics as the respective monomeric chromophores.

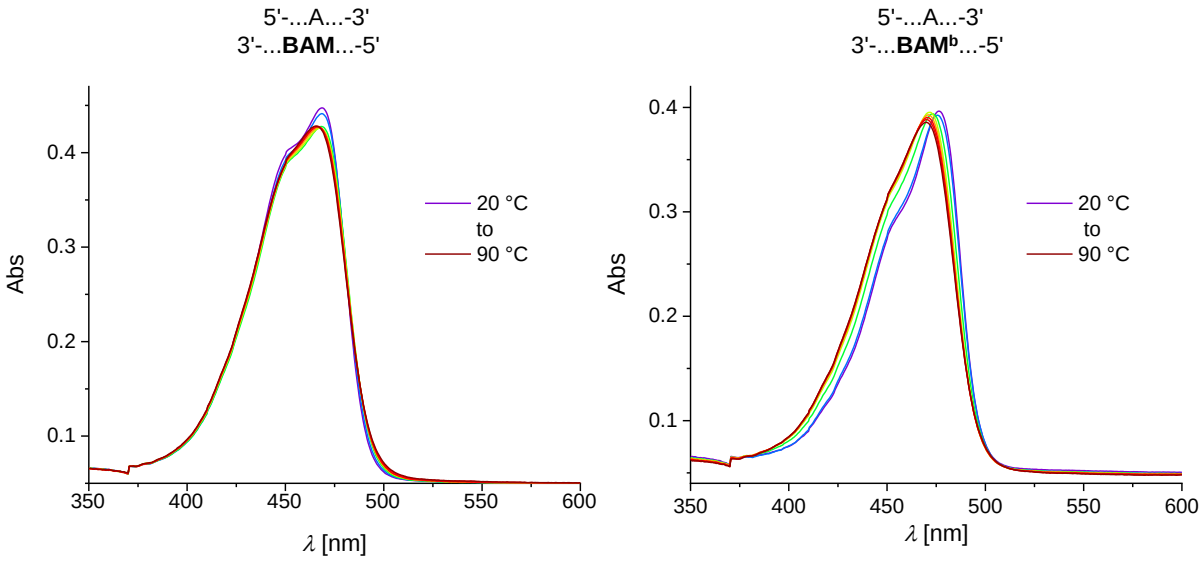

Figure 3.50: Temperature-dependent absorption spectra for single-dBAM- (left) and -dBAM^{b}-modified (right) DNA 12mer duplexes. Upon thermal dehybridization, the absorption spectra for both systems undergo only minor changes due to loss of stacking interactions with adjacent nucleobases. Conditions: 5 µM samples in 1× PBS (100 mM NaCl, 10 mM phosphate, pH 7.0).

By integration of the steady state absorption spectra at 20 °C, the transition dipole moments μ_{ag} of BAM and BAM^{b} were calculated according to

$$|\mu_{ag}^2| = \frac{3 \cdot h \cdot c_0 \cdot \epsilon_0 \cdot \ln 10}{2 \cdot \pi^2 \cdot N_A} \cdot \int_{\tilde{\nu}_1}^{\tilde{\nu}_2} \frac{\epsilon(\tilde{\nu})}{\tilde{\nu}} d\tilde{\nu} \tag{14}$$

with the Planck's constant h, the speed of light c_0, the permittivity of the vacuum ϵ_0, the Avogadro's number N_A, the molar extinction coefficient $\epsilon(\tilde{\nu})$ and the wavenumber $\tilde{\nu}$.[356] To estimate μ_{ag}, the absorbance was converted into $\epsilon/\tilde{\nu}$ and plotted *versus* the wavenumber $\tilde{\nu}$. By integration of the longest wavelength absorption band, transition dipole moments for the S_0-S_1 transition of 6.5 and 5.8 D for BAM and BAM^{b}, respectively, were obtained. These values are in accordance with reported ones between 6.3 and 7.1 for the structurally related

thiazole orange and oxazole yellow.[389,390]

Although the absorption characteristics of the two merocyanines are only marginally influenced by the surrounding canonical nucleobases, the situation is different for the fluorescence properties as revealed by the excitation and emission spectra for single-modified DNA duplex structures with the chromophores positioned opposite each of the canonical nucleosides or an abasic site (Figure 3.51).

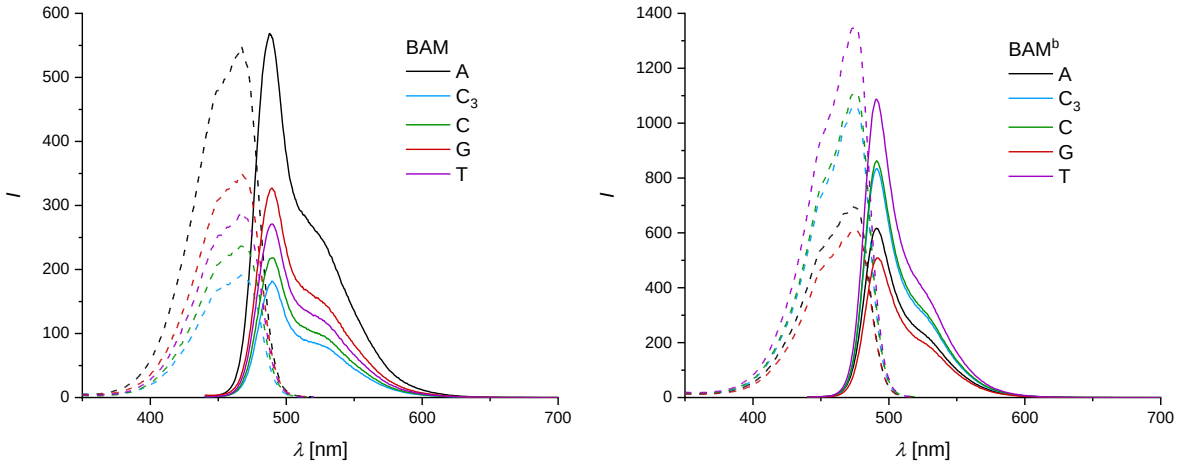

Figure 3.51: The fluorescence excitation and emission spectra for single-dBAM- (left) and -dBAM^b-modified (right) DNA 12mer duplexes illustrate the influence of the counterbase on the emissive behavior of the two chromophores. Conditions: 1 µM samples in 1× PBS (100 mM NaCl, 10 mM phosphate, pH 7.0), excitation at 420 nm, emission at 540 nm.

In the case of dBAM-modified duplex structures, highest absolute fluorescence intensities are observed with the purine bases A and G in the counterstrand, while the emission and excitation intensities are strongly decreased by around 50% with a pyrimidine base opposite dBAM and even lower with an abasic site in the counterstrand. These observations are in accordance with the steric demand of the different nucleobases: the larger the size of the nucleobase is, the lower is the degree of rotational freedom for the merocyanine chromophore in the helical structure. As already discussed, an increased steric hindrance leads to higher fluorescence intensities since the rotational deactivation of the excited chromophore is prevented, which explains the higher fluroescence intensity of dBAM opposite purine nucleobases.

However, the fluorescence features for single-dBAM^b modified duplexes differ strongly from the dBAM-modified ones. Here, the most pronounced luminescence is obtained for dBAM^b opposite a pyrimidine nucleobase or an abasic site while the fluorescence intensity is reduced for systems with a purine nucleobase opposite dBAM^b. Thanks to its reduced steric demand, the BAM^b chromophore is able to undergo stronger π-π stacking interactions with the aromatic systems of adjacent nucleobases. Assuming that the chromophore is located in the duplex core and not in the major groove, these stacking interactions are expected to be more pro-

nounced with the larger purine ring systems than the pyrimidine aromatic systems, therefore leading to fluorescence quenching as extensively described in the literature for many fluorescent nucleobase analogs.[391,392]
Thus, for the distinct luminescence of dBAM and dBAM^{b} opposite different nucleobases the steric hindrance of the chromophores as well as their ability to stack are of importance. In agreement with the conclusions drawn for modified RNA systems, also for the DNA structures the overall fluorescence intensity is enhanced for dBAM^{b}- over dBAM-modified duplexes, although here this effect is less pronounced.

The interpretation of the spectroscopic behavior of single-modified duplex structures was followed by a detailed analysis of the spectral characteristics of double-modified DNA systems which will be discussed in the next section. Also, additional spectroscopic parameters such as the fluorescence quantum yields and lifetimes for both single- and double- modified DNA structures will be described and interpreted with regard to the already obtained data for modified RNA systems.

3.4.4.2 Investigations on double-dBAM- and double-dBAM^{b}-modified systems

Similar as for the double-modified RNA duplex structures, temperature-dependent absorption as well as fluorescence and CD spectra were recorded for DNA 12mer helices to investigate the ground and excited states chromophore-chromophore interactions.

To elucidate the influence of the helical oligonucleotide scaffold on the absorption behavior of dBAM:dBAM and dBAM^{b}:dBAM^{b} dimers in different orientations, absorption spectra between 20 and 90 °C were measured (Figure 3.52). Interestingly, the observed patterns vary strongly compared to the ones for the merocyanine dimers in RNA. While for the opposite BAM:BAM dimer in both DNA (**D8/D12**) and RNA (**R8/R12**) the formation of H-type aggregates, indicated by a sharp blue-shifted absorption band at 437 nm due to pronounced exciton coupling is observed, a similarly strong coupling was obtained for the downstream rBAM:rBAM **R8/R10** dimer but can be seen here for the upstream dBAM:dBAM dimer **D8/D14**.

Meanwhile, a much less pronounced chromophore-chromophore interaction is obtained for the dBAM:dBAM downstream dimer **D8/D10**. This strengthens the assumption that the dimerization of the indolenine-derived BAM dyes strongly depends on the backbone constitution and the duplex conformation. One reason for these findings might be the distinct structural differences between the A-form RNA and the B-form DNA helix: while the first one is characterized by a strong base pair inclination and deep major groove, the Watson-Crick base pairs are essentially perpendicular to the helix axis with a higher base-base distance in the latter one which allows an increased conformational freedom for sterically demanding nucleobase surrogates.

However, one would not conclude this when only comparing the model dimers illustrated in Figures 3.26 and 3.49 since here no remarkable difference between the systems with either a ribose or a deoxyribose backbone is evident. Therefore, additional effects must play a role such as the already mentioned partial unwinding of the duplex structure due to the incorporation of the sterically demanding merocyanine. This will also later be discussed by analyzing the NOESY NMR spectrum of the duplex with the upstream dBAM:dBAM dimer **D8/D14** in section 3.4.7.

The spectroscopic characteristics for the downstream and opposite dBAM^{b}:dBAM^{b} dimers **D9/D11** and **D9/D13** are inverted compared to their RNA counterparts but resemble those observed for the respective dBAM:dBAM dimers **D8/D10** and **D8/D12** with strong coupling only present for the opposite case. However, similar to the situation in RNA, also here the upstream dBAM^{b}:dBAM^{b} dimer **D9/D15** shows only weak chromophore-chromophore interactions.

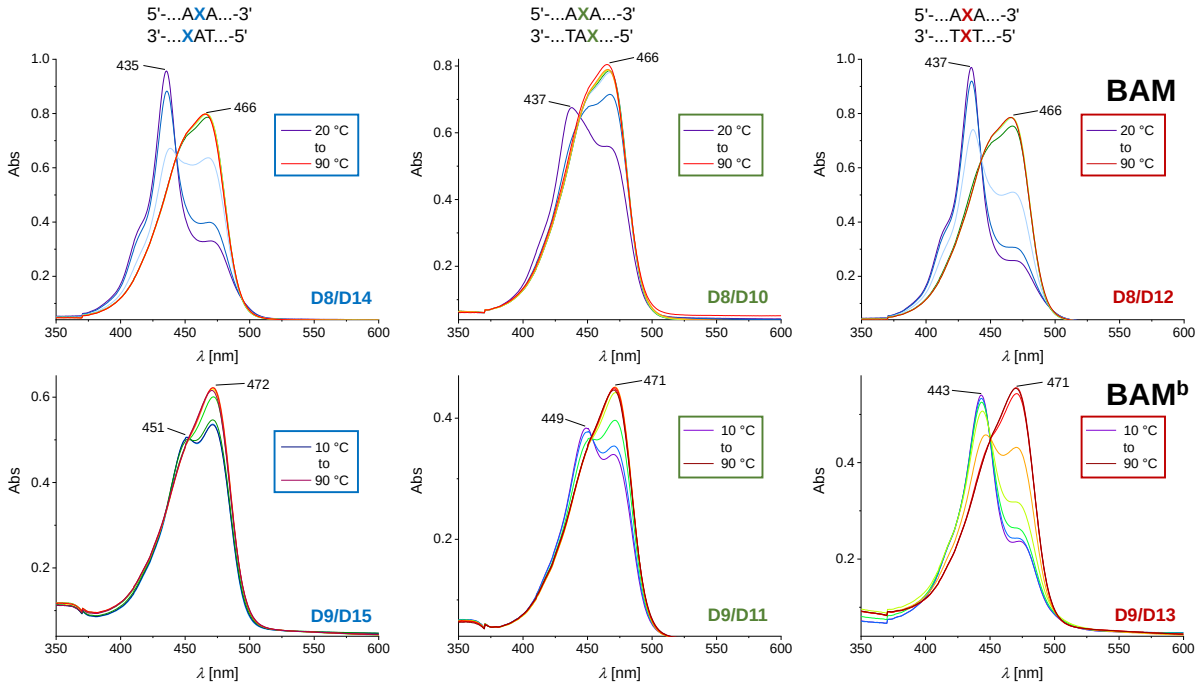

Figure 3.52: Temperature-dependent absorption spectra for double-dBAM- (top) and -dBAM^{b}-modified (bottom) DNA 12mer duplexes in upstream (blue), downstream (green) and opposite (red) orientation. Upon dehybridization, the absorption spectra for all of the systems change remarkably: the main band shifts from the H-type dimer absorption at approximately 440 nm to the monomer absorption at approximately 470 nm. Conditions: 5 µM samples in 1× PBS (100 mM NaCl, 10 mM phosphate, pH 7.0).

All of the six samples depicted in Figure 3.52 exhibit a noticeable change upon duplex dehybridization, indicating dipolar and π-π stacking interactions of different strength for all cases. The detectable transition from coupled chromophores to non-interacting ones is in accordance with the respective estimated melting points for all duplex structures. The maximum for the

monomer absorption is located at 466 nm for dBAM- and 471 nm for dBAM^b-modified systems, which is comparable to the values found in the RNA context. Also the H-type aggregate absorption at 437 and 440 to 451 nm for dBAM:dBAM and dBAM^b:dBAM^b, respectively, emerges at the same wavelengths as observed previously. These findings demonstrate that the overall structure of the stacked dimer is similar regardless from the chemical backbone composition of the underlying oligonucleotide scaffold.

Very similar spectral features have recently been reported not only for covalent merocyanine dimers,[393,394] but also for dimeric Cy5 constructs on DNA scaffolds.[370,395,396] Here, the presence of excitonic coupling effects along with vibronic progression was attributed to partially twisted transition dipole moments and confirmed by time-resolved spectroscopy as well as quantum chemical calculations. Therefore, to gain deeper insight into the dimerization behavior of the BAM and BAM^b chromophores, time-dependent DFT calculations for the respective monomers and the geometry optimized dimers were performed. The monomer spectra were calculated first to adjust the required parameters. With a transition energy E_g of 21,400 cm^{-1} and a vibrational frequency ω_0 of 1,200 cm^{-1} the best agreement with the experimental monomer absorption spectra of the denatured single strands was obtained. In addition, the Huang-Rhys factor λ^2, which determines the ratio between the 0-1 and the 0-0 absorption bands of the vibronic progression, was set to 0.74 and 0.71 for BAM and BAM^b, respectively. The resulting simulated monomer spectra are reminiscent of the experimental ones (Figure 3.53a and b).

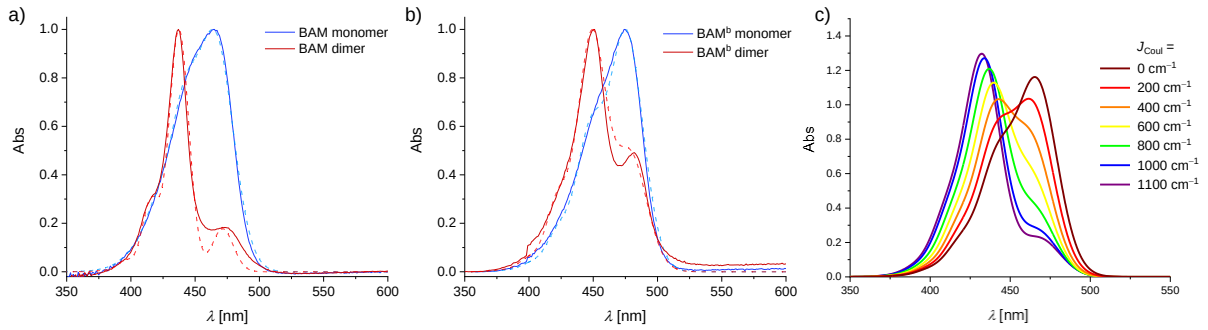

Figure 3.53: The normalized experimental spectra (a and b, solid lines) at 10 and 90 °C are in good agreement with DFT-calculated spectra (dashed lines) for the respective monomers (blue) and the geometry-optimized dimers (red, **D8/D12** and **D9/D13**). The simulated dimer spectra with a wider range of coupling energies reflect the partially unfolded duplex states at increasing temperatures (c). Spectra simulations were done by Dr. David Bialas.

The absorption spectra of the two dimers were calculated using a Holstein-type Hamiltonian[397] with the two-particle approximation[398] and a Coulomb coupling of the chromophores' transition dipole moments along the dimer axis of 1,100 cm^{-1} for BAM (1,050 cm^{-1} for BAM^b), which is in a similar range as calculated for Cy3 dimers.[399–401] Furthermore, the Huang-Rhys

factor λ^2 had to be reduced to 0.61 (0.56 for BAM^b) to obtain the best agreement with the experimental spectrum. The lower Huang-Rhys factor can be rationalized by the polarizability effect of the neighboring chromophore in the stacked dimer, moving the chromophore closer to the cyanine limit compared to the monomeric merocyanine.[402,403] To adjust the position of the absorption maximum to the one of the experimental spectrum, a gas-to-crystal shift of -150 cm^{-1}, which denotes the shift of electronic excitation energy for a molecule transferred from the gas to the bulk phase, had to be applied in addition.
If BAM:BAM dimer spectra with a wider range of coupling energies were simulated, the curve shapes resembled the ones of the partially dehybridized duplex. Thus, the results from these MD simulations are further evidence for the formation of chromophore dimers due to dipolar interactions guided by the oligonucleotide scaffold (Figure 3.53c).

To investigate not only the ground but also the excited state chromophore-chromophore interactions, excitation and emission spectra in a temperature range between 20 and 62 °C were recorded for all of the dBAM:dBAM and dBAM^b:dBAM^b dimers (Figure 3.54).

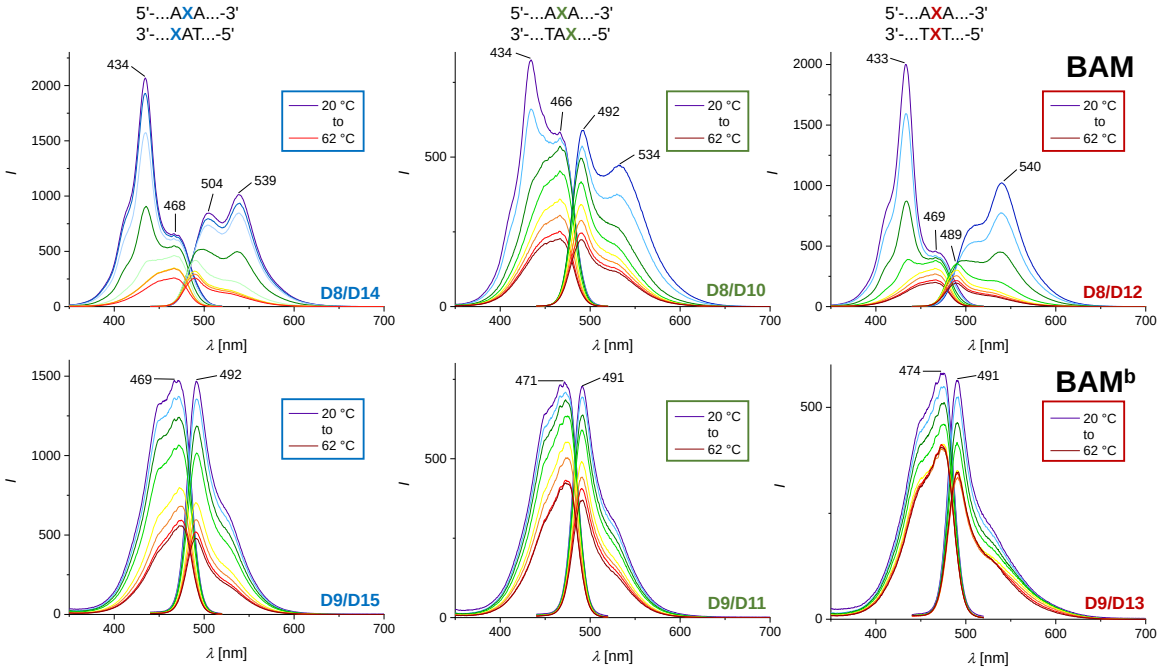

Figure 3.54: Temperature-dependent fluorescence spectra for double-dBAM- (top) and -dBAM^b-modified (bottom) RNA 12mer duplexes in upstream (blue), downstream (green) and opposite (red) orientation. The dBAM-modified duplex structures show the formation of fluorescent H-type aggregates while dBAM^b:dBAM^b dimers showed no emissive excitonic coupling. Conditions: 1 µM samples in 1× PBS (100 mM NaCl, 10 mM phosphate, pH 7.0), excitation at 420 nm, emission at 540 nm.

As already discovered for the double-rBAM-modified structures, also the excitation spectra of the dBAM:dBAM dimers resemble the shape of the corresponding absorption spectra. The excitation spectra for all of the three fully hybridized systems are characterized by a sharp, intense band at 434 nm with hypso- and bathochromically shifted shoulders at 415 and ap-

proximately 467 nm, respectively. Again, this spectral pattern can unambiguously be assigned to the formation of excitonically coupled merocyanine dimers which is further evidenced by the emission spectra. Here, the bathochromically shifted band at 540 nm for low temperatures arises due to excimer emission while furthermore a second transition at 490–505 nm is observed, which is also slightly red-shifted compared to the monomer emission of the denatured duplex at temperatures above the melting point.

These spectroscopic results are consistent with the already described preferred orientation of the BAM chromophores in which the hydrophobic indole part is rotated toward the duplex core, implying a *syn*-conformation of the glycosidic bond in dBAM. However, the presence of the adenosine in the opposite strand together with the sterically demanding methyl groups in the indole likely prevent an ideal antiparallel alignment and enforce a twisted chromophore arrangement.
The existence of excimer emission in the dBAM:dBAM opposite dimer was further proven by a matrix scan of emission spectra at variable excitation wavelengths (Figure 3.55, b). Since strong excimer emission at 540 nm is induced upon excitation at 430 nm, these two maxima detected in the fluorescence spectra indeed belong to the same spectroscopic species. Meanwhile, the monomer emission at 490 nm by excitation at 470 nm detectable in the matrix scan of the single strand (Figure 3.55, a) is drastically reduced for the dimeric system.

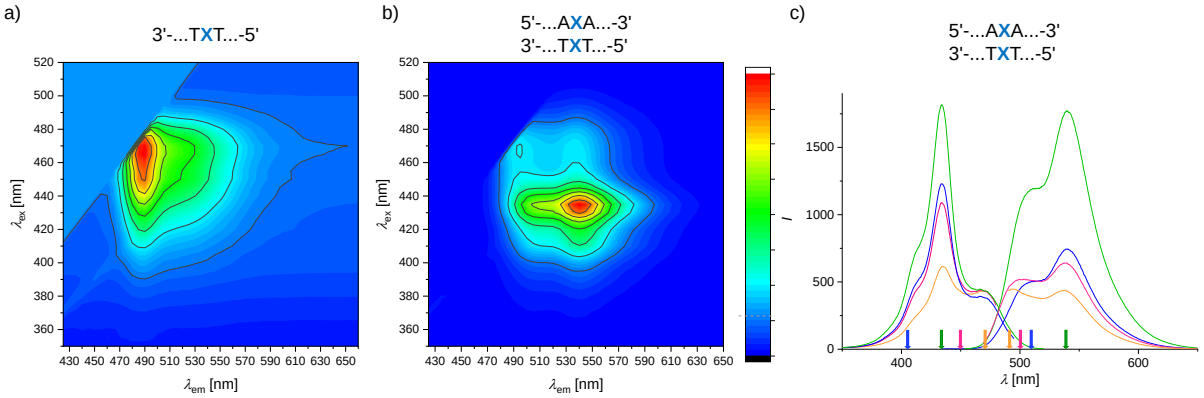

Figure 3.55: The 3D emission matrix scans with variable excitation wavelengths reveal a pronounced difference between the monomer emission (a) and the emission of the excitonically coupled dimer (b). In addition, the shape of the fluorescence spectra of the opposite dBAM:dBAM dimer **D8/D12** recorded at different excitation and emission wavelengths shows to change slightly with regard to the intensity ratio of the different maxima (c, blue: ex 420, em 540; green: ex 435, em 505; pink: ex 450, em 500; orange: ex 470, em 490 nm). Conditions: 1 µM samples in 1× PBS (100 mM NaCl, 10 mM phosphate, pH 7.0), 20 °C.

Furthermore, fluorescence spectra for the dBAM:dBAM dimer at different excitation and emission wavelengths were recorded (Figure 3.55c). Here, not the position of the maxima but rather their intensity ratio changes: the longer the excitation wavelengths is, the more intense is the blue-shifted emission maximum at just below 500 nm while with longer emission wavelengths

the blue-shifted excitation maximum becomes more pronounced. This behavior supports the assumption of the presence of two different spectroscopic species, presumably different conformers.

In contrast to the dBAM:dBAM dimers, no H-type aggregate attributed excitation and emission behavior was detected for the dBAM^{b}:dBAM^{b} dimers. The excitation maxima at approximately 470 nm as well as the emission maxima at 491 nm remained unchanged at elevated temperatures and can be assigned to the monomer fluorescence. Since these observations have also previously been made for the respective RNA dimers, similar conclusions can be drawn: the benzothiazole-derived chromophore lacking two of the sterically demanding methyl groups present in the indolenine-derived dBAM might be able to adopt a much better planar conformation, enabling more efficient antiparallel stacking. Within these perfectly aligned chromophores, transitions between the ground and the first excited state are forbidden and therefore no excimer fluorescence is observed.

Along with the recorded steady state spectra, the time-dependent fluorescence decay for dBAM-modified DNA single- and double-strands was recorded at different excitation and detection wavelengths, providing access to the average fluorescence lifetime $<\tau>$ as an important parameter for the characterization of fluorophore assemblies (Figure 3.56).

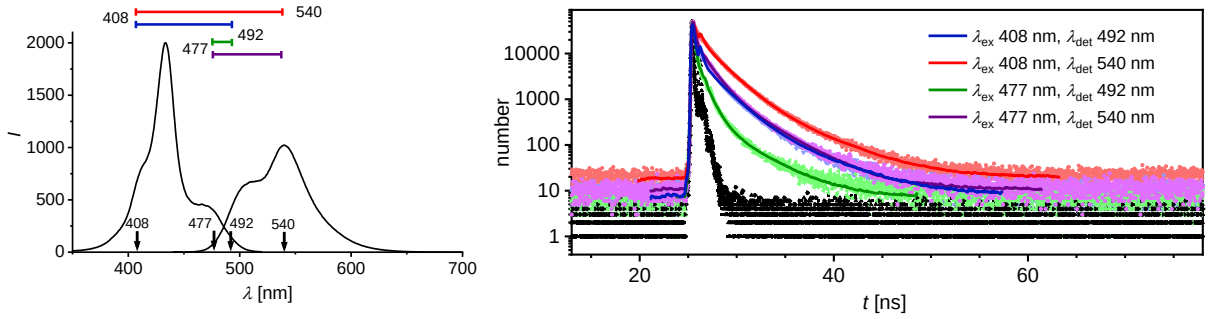

Figure 3.56: The fluorescence decay for the opposite dBAM-modified DNA system **D8/D12** measured by TCSPC reveals different excited state lifetimes dependent on the excitation and detection wavelengths.

The results obtained for the three investigated systems are summarized in Table 3.16. To obtain a goood fitting result, a two- or three-exponential fitting function had to be applied which reveals the coexistence of multiple spectroscopic species. From the obtained individual lifetimes and their corresponding weighting factors the average fluorescence lifetime $<\tau>$ for each system was calculated.

For the dBAM-modified single and single-modified double strands **D12** and **D1/D12**, very short lifetimes of 0.17 and 0.06 ns, respectively, were detected at 492 nm upon excitation at 477 nm which is in the same range as the τ-value for an rBAM-containing RNA duplex and reported values for the structurally akin YOYO.[404] Note, that these low values are not fully

reliable due to the detection limit of the lifetime measuring device. The fluorescence lifetime for the dBAM:dBAM opposite dimer **D8/D12** was measured at both the emission wavelength of the monomer (492 nm) and the dimer (540 nm). In addition, this duplex was excited with the two different laser wavelengths 408 and 477 nm. Compared to the single strand **D12** and the single-modified duplex **D1/D12**, increased τ values for **D8/D12** under all conditions were observed which can reasonably be explained by the suppressed deactivation of the excited state by non-radiative decay events in the stacked, conformationally more rigid dimer structure as described for other fluorescent merocyanine H-type aggregates.[193]

Table 3.16: Fluorescence lifetimes τ_n with the corresponding weighting factors A_n and the average lifetime $<\tau>$ for BAM-modified DNA structures.

sample	λ_{ex} nm	λ_{det} nm	A_1	τ_1 ns	A_2	τ_2 ns	A_3	τ_3 ns	$<\tau>$ ns
D12	477	492	0.05	0.67	0.002	2.79	0.95	0.13	0.17
D1/D12	477	492	0.06	0.27	–	–	0.92	0.04	0.06
D8/D12	477	492	0.06	0.83	0.004	3.28	0.93	0.15	0.20
D8/D12	477	540	0.16	1.21	0.020	3.45	0.81	0.18	0.43
D8/D12	408	492	0.08	1.83	0.007	4.74	0.92	0.20	0.35
D8/D12	408	540	0.24	1.87	0.023	4.73	0.74	0.32	0.80

$<\tau>$ was comoposed in all cases of τ_1 between one and two ns, τ_2 between three and five ns and τ_3 of below 0.35 ns with the largest contribution to $<\tau>$. Interestingly, the average liftime $<\tau>$ showed to be strongly dependent on the measurement parameters: excitation at 408 nm rather than 477 nm and detection at the dimer emission maximum of 540 nm rather than the monomer emission maximum at 492 nm led to an overall increase of $<\tau>$. This finding supports the assumption that at least to independent species are present in the double-modified duplex structure, which presumably differ in their structural conformation. However, the obtained lifetimes are still comparably short which is in accordance with reported data for the DNA-templated formation of H- and J-aggregates of Cy5 chromophores, for which fluorescence quenching by non-radiative pathways was described and rationalized by analysis of TCSPC measurements in the context of molecular exciton theory.[405]

In analogy to the calculations for k_r and k_{nr} for merocyanine-modified RNA systems, the radiative and non-radiative decay rates were estimated for the single- and the double-dBAM-modified DNA duplex structures **D1/D10** and **D8/D12**. Both values were found to be essentially the same for the single-modified RNA **R1/R10** as well as DNA structure **D1/D10**. In contrast, k_r was reduced for the opposite dBAM:dBAM dimer **D8/D12** compared to the

single-modified system **D1/D10** at the two different detection wavelengths. The most pronounced decrease of the radiative decay rate was observed at the excimer emission wavelength of 540 nm, indicating a slower decay and therefore leading to the enhanced observed fluorescence lifetime of this excited state. Due to the strong dipolar stacking of the two dBAM chromophores, the distance between them is reduced which facilitates the occurrence of non-radiative decay pathways, similar as reported for TO dimers covalently linked to DNA.[363]

Table 3.17: Fluorescence lifetimes τ, quantum yields ϕ and the corresponding radiative and non-radiative decay rates k_r and k_{nr} for BAM-modified DNA structures.

sample	λ_{em} nm	τ[a] ns	ϕ[b]	k_r s^{-1}	k_{nr} s^{-1}
D1/D10	492	0.14	0.031	$2.21 \cdot 10^8$	$6.92 \cdot 10^9$
D8/D12	492	0.20	0.030	$1.50 \cdot 10^8$	$4.85 \cdot 10^9$
D8/D12	540	0.43	0.030	$6.98 \cdot 10^7$	$2.26 \cdot 10^9$

[a] determined for $\lambda_{ex} = 477$ nm
[b] determined relative to fluorescein

To gain additional information on the relative arrangement of the two merocyanine chromophores in the dimer, CD spectra were recorded (Figure 3.57). While no or only a negligible CD effect was seen for the flexible single strands, for all of the double-modified systems no strong deviation from the unmodified reference duplex was observed in the nucleobase absorption range between 200 and 300 nm.

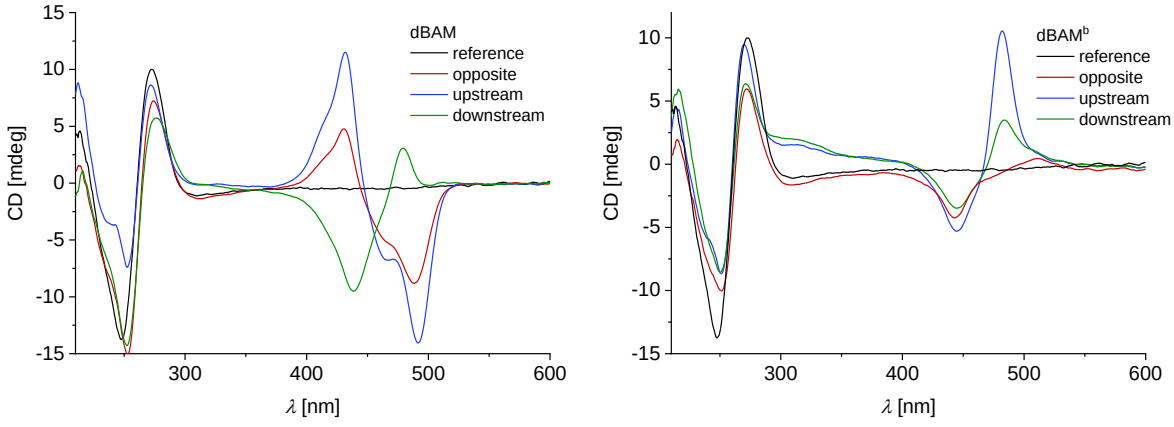

Figure 3.57: The CD spectra for double-dBAM- and double-dBAM^b-modified DNA duplex structures are shown, revealing a marked distance and geometry dependence of the exciton coupling within the chromophore dimers. Conditions: 5 µM samples in 1× PBS (100 mM NaCl, 10 mM phosphate, pH 7.0).[406]

This proves that the two fluorescent nucleobase surrogates are well tolerated within the duplex structure which is only slightly perturbed upon their incorporation. Nevertheless, distinct CD

bisignate patterns are observed for the different dimer orientations in the visible range. These varying CD bands can be attributed to the distance and geometry dependent exciton coupling between the merocyanine chromophores. Usually, the exciton coupled CD of H-type assembled chromophores is of symmetrical shape with both couplets having comparable intensities, which can be attributed to the main electronic transition. However, most of the CD bands shown in Figure 3.57 are not fully symmetric which supports the assumption of the formation of non-perfect exciton coupled H-type aggregates.

While for rBAM:rBAM containing RNA helices only positive CD couplets were observed, within the DNA B-form helix this is only the case for the downstream dimer **D8/D10**, while the opposite and upstream dimers **D8/D12** and **D8/D14** provoke a negative CD signal, indicating opposite chirality.

The sign and amplitude of split Cotton effects are dictated by the exciton chirality, which is given by $\mathbf{R}_{ij}\cdot(\mu_i x \mu_j)V_{ij}$ with $\mathbf{R}_{ij}$ as the distance vector between the centers of the two chromophores i and j, μ_i and μ_j the transition dipole moments for the 0-1 excitation and V_{ij} the electronic interaction energy between the chromophores (compare Figure 3.35). If the two chromophores are dipole-coupled, the angle between their two local transition dipole moments is given as α and the rotary strength is approximately proportional to $\sin 2\alpha$. Therefore, the Cotton effect is inversed by a difference of 90° in the chromophore orientation.[363]

The inversed Cotton effect can be explained by the more crowded environment and the larger base pair inclination in RNA which forces the chromophores into a determined position while the parallel stacked base pairs in DNA provide more space for larger nucleobase analogs. Furthermore, the inner core of the DNA duplex needs to be structurally widened to allow for a chromophore arrangement in an anti-clockwise screw sense instead of the expected clockwise orientation.

The obtained CD patterns for the dBAM^b:dBAM^b dimers, however, are showing only positive Cotton effects, consistent with the situation observed in the RNA duplex. In general, the intensity of the CD signals for the dBAM^b:dBAM^b dimers are lower than for the dBAM:dBAM dimers which can be attributed to a preferable antiparallel alignment of the two chromophores with a benzothiazole instead of an indole donor moiety. Upon coplanar orientation, a nearly pointsymmetric antiparallel dimer is obtained where the transition dipole moments of the individual chromophores are cancelled out by each other, leading to a vanishing CD band.

For a better overview, the absorption together with the fluorescence and CD spectra for the single-dBAM-modified duplex **D8/D2** and the dBAM:dBAM opposite dimer **D8/D12** are summarized in Figure 3.58. The weak negative CD band of the single-modified system

D8/D2 corresponds here to the excitation/absorption maximum at 466 nm, while the weak positive band can be attributed to the emission maximum at 488 nm. In comparison, also the stronger positive CD signal for **D8/D12** at 431 nm is located at the excitation/absorption maximum while the negative signal arises at the emission wavelength of the monomer and not at the 540 nm excimer emission, similar to TO dimers in DNA. As expected, the zero-line crossing is in the absorption range of the dBAM chromophores at 451 nm.[363]

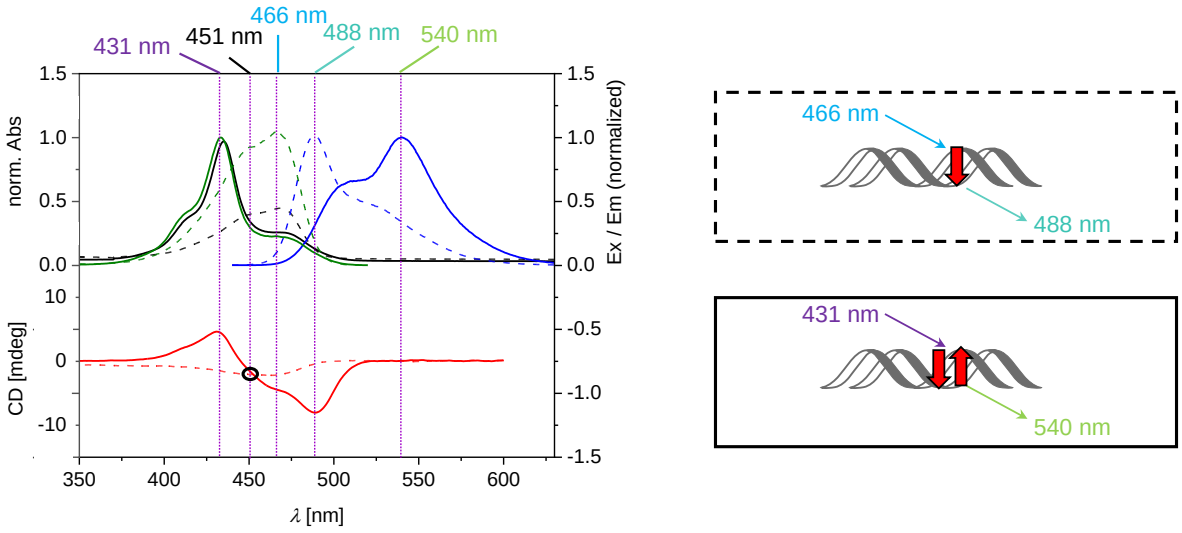

Figure 3.58: Absorption (black), excitation (green), emission (blue) and CD (red) spectra of **D8/D12** (solid lines) and **D8/D2** (dashed lines). The respective absorption/excitation and emission wavelengths for the two systems are in addition shown on the right side.

The formation of excitonically coupled dimers suggested to probe the extent of chiral fluorescence dissymmetry in the excited state by CPL (Figure 3.59).

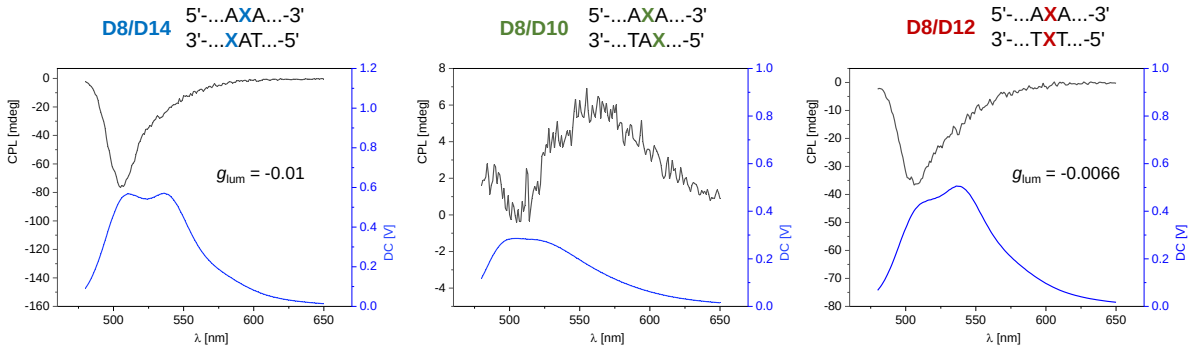

Figure 3.59: CPL spectra for double-dBAM-modified DNA 12mer duplex structures with different dimer orientations. Conditions: 5 µM samples in 1× PBS (100 mM NaCl, 10 mM phosphate, pH 7.0).

Indeed, for the upstream and opposite dBAM:dBAM dimer **D8/D14** and **D8/D12** exceptionally strong negative CPL bands were observed, indicating left-handed chromophore arrangement. These findings are in accordance with the recorded CD and fluorescence spectra as for both cases a pronounced negative CD signal and strong H-type coupling is found. The

calculated g_{lum} of -0.01 and -0.0066 are surprisingly high for organic chromophores as such increased absolute values have only been reported for dye aggregates such as rhodamine B in a chiral medium[407] or pyrene zipper arrays on RNA with a g_{lum} of 0.0035.[377] Meanwhile, the downstream case **D8/D10** with a positive CD band and only a weak excitonic interaction shows, if any, a markedly reduced CPL.

Altogether, the collected spectroscopic data prove the assumptions made for merocyanine dimers in the oligonucleotide scaffold: first, the chromophore prefers being located in the central core of the nucleic acid duplex structure, due to its hydrophobic nature and its tendency to form excitonically coupled aggregates by dipolar interactions. Second, the spectral characte-ristics of the formed dimers strongly depend on the backbone conformation and the orientation of the chromophores toward each other. In addition, the formed H-type aggregates are fluorescent in the case of BAM chromophores, caused by the sterically demanding methyl groups at the chromophore donor moiety, while BAM^b chromophores lacking these alkyl groups do only form non-emissive hypsochromically shifted dimers. Further investigations on the BAM:BAM dimers revealed distinct fluorescence parameters as well as CD and CPL effects but the exact structure, especially for the dimer with the two chromophores directly facing each other, is only partially elucidated due to the absence of a 3D structure for this modified system. To investigate the characteristics of the dBAM:dBAM opposite dimer **D8/D12** in DNA, additional experiments were conducted which will be discussed in the next section.

3.4.5 How to shed light on the structure of the dBAM:dBAM dimer in DNA?

To gain a deeper understanding of the dBAM:dBAM opposite dimer structure **D8/D12**, the spectroscopic response of this double-modified system to variations of the solvent polarity and the sample salt content were studied. In addition, the changes in absorption and fluorescence behavior upon addition of melamine and Hg^{2+} to alter the coordination environment as well as the potential to enzymatically control the dimer formation by a helicase were explored. Due to its suitable fluorescent properties, BAM was furthermore used as a FRET acceptor for the widely known 2AP nucleobase. Finally, imino as well as NOESY spectra of the upstream BAM:BAM dimer **D8/D14**, which showed strong excitonic coupling, were recorded to elucidate the spatial orientation of the merocyanine dimer.

3.4.5.1 Influence of the salt effect on the dBAM:dBAM dimer formation

To reveal the influence of the NaCl concentration in the sample on the duplex and hereby BAM:BAM dimer formation, both single strands **D8** and **D12** were mixed in equimolar ratio in deionized water. Without the presence of any cations, only monomer fluorescence at 460 and 490 nm was detected (Figure 3.60). Upon stepwise addition of NaCl over 45 titration steps up

to a concentration of 300 mM, the excitation and emission maxima of the excitonically coupled dBAM:dBAM dimer consecutively increased. To calculate the required NaCl concentration for 50% of the duplex structure formed, the normalized excimer excitation and emission at 433 and 540 nm, respectively, were plotted against the NaCl concentration on a logarithmic scale. For fitting, a multi-binding site model was applied according to the Hill-Langmuir equation $I=x^n/(k^n+x^n)$ with the NaCl concentration x, the dissociation constant k and the Hill coefficient n. n quantifies the degree of cooperativity of ligand binding and since it amounts here to 1.95±0.11, a positive cooperativity effect is proven. From this mathematical analysis, a c_{50} concentration of 28 mM NaCl for duplex formation was derived.

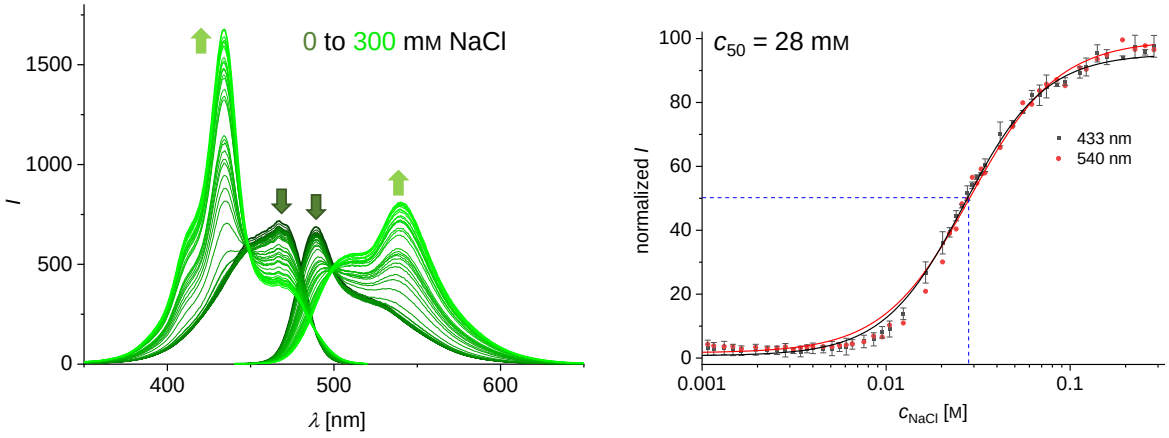

Figure 3.60: The titration of an equimolar mixture of **D8** and **D12** with sodium chloride showed the induced formation of excitonically coupled dimers (left). By plotting the normalized intensities at the excitation and emission maxima against the NaCl concentration and applying a multi-binding site Hill fit, a c_{50} value of 28 mM was calculated for half of the duplex structures formed (right, shown are the mean values of triplicates with s. d. m. as error bars). Conditions: 1 µM concentration of each single strand, excitation at 420 nm, emission at 540 nm.

These findings correlate with the line-charge counterion condensation theory and the Poisson-Boltzmann distribution which assume the uniform distribution of small, mobile ions on polyelectrolytes upon duplex formation.[408,409] Therefore, the salt effect on the hybridization of dBAM-modified single strands by the stepwise increase of the NaCl concentration can spectroscopically be followed and analyzed. To investigate if the formation of the dBAM:dBAM dimer can in addition be triggered by unpolar additives, duplex melting curves in the presence of different amounts of glycerol were recorded.

3.4.5.2 dBAM:dBAM dimer formation in the presence of glycerol

As mentioned before, the denaturation behavior of **D8/D12** with the opposite dBAM:dBAM dimer shows a strong cooperative effect since the melting curves at 260 and 460 nm are superimposable, leading to the same melting temperature at both the nucleobase and the dBAM absorption (section 3.4.3). This suggested a direct thermal duplex denaturation with strong

dependence of the dBAM:dBAM dimer formation on the folding state of the oligonucleotide scaffold. In addition to duplex denaturation at elevated temperatures, a similar effect can also be achieved by the addition of apolar solvents. DNA as a polyelectrolyte is highly polar and mainly stable in dielectric environments, such as in aqueous buffered solution, where the water and the countercations neutralize the anionic charge of the phosphate backbone and favor hydrophobic base stacking interactions. It has been reported that DNA undergoes significant structural changes or even complete unfolding and single strand separation in some organic solvents such as methanol, formamide, pyridine or dimethyl sulfoxide while in others, for example glycerol, the duplex structure is maintained but with strongly reduced stability.[410–412] Since the excitonically coupled antiparallel dBAM:dBAM dimer is comparably hydrophobic with the two individual dipole moments almost cancelling each other out, it was assumed that this dimer might be more stable compared to the surrounding native oligonucleotide sequence with an increased percentage of glycerol in the sample solution.

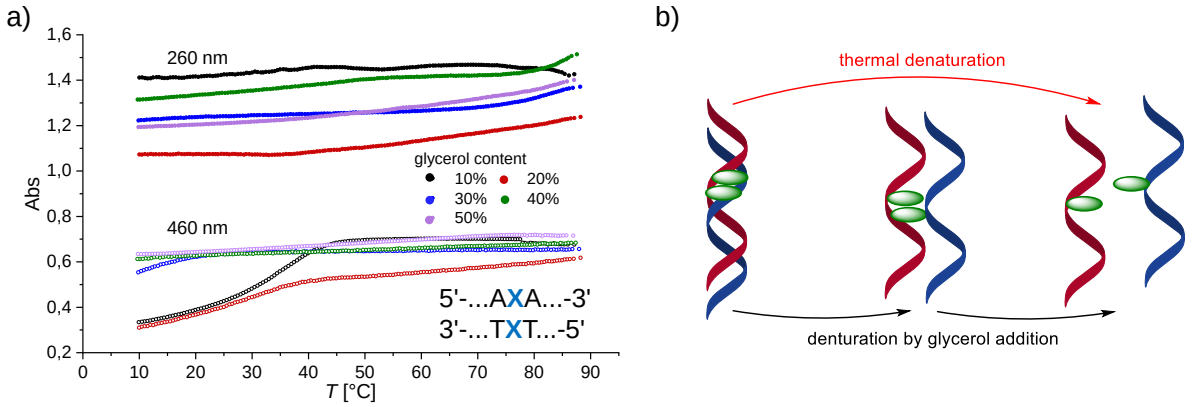

Figure 3.61: With a glycerol content of up to 30%, hyperchromicity is still observed for **D8/D12** at the BAM absorption wavelength of 460 nm, indicating dimer formation at low temperatures, while in the 260 nm absorption trace no transition from the single- to the double-stranded state is visible (a). This indicates a stepwise dehybridization process with dimer stabilization in apolar solvents, which is in contrast to the one-step dehybridization at increased temperature (b).

To prove this assumption, a buffered stock solution of the **D8/D12** duplex was prepared and 10 to 50% percent by volume of glycerol were added. Upon heating and slow cooling of these samples, the change of the absorption at 260 as well as 460 nm was recorded and revealed remarkable differences (Figure 3.61a). The absorption at 260 nm changed only marginally by cooling from 90 to 10 °C for all samples, lacking a sigmoidal melting transition. Since it is known that the thermostability of a DNA duplex is significantly reduced in non-aqueous solvents, the short 12mer duplex is already completely unfolded at 10 °C even at only low glycerol concentrations.[410]

Meanwhile, the 460 nm absorption intensity changes notably by decreasing the sample temper-

ature. Here, with 10% of glycerol a duplex melting point at approximately 32 °C is observed. Also with a higher glycerol concentration of 20 and 30% the cooling curve still exhibits a sigmoidal shape although the denaturation temperature is significantly reduced. This is in strong contrast to the thermal denaturation behavior of double-dBAM-modified DNA systems where a high degree of cooperativity in the melting behavior was observed. It clearly shows the high stability of the hydrophobic BAM:BAM dimer in apolar solvents: although the oligonucleotide scaffold no longer maintains its helical structure, the two chromophores are still strongly interacting. The thermodynamic driving force of these interactions can be described by an excitonic coupling model based on the point dipole approximation, which neglects all geometrical considerations and assumes a spherical molecular shape. If the surrounding solvent molecules are also treated as point dipoles, a solvation as shown in Figure 3.62 is obtained.

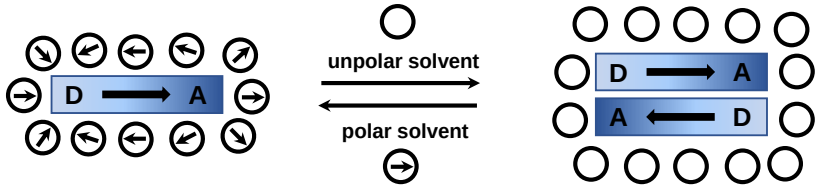

Figure 3.62: Polar solvent molecules, which are treated as point dipoles, are oriented along the dipolar monomer while in apolar solvents the formation of an electronically coupled dimer with vanishing total dipole moment is facilitated.[357]

For polar solvents, the dipole moments of the solvent molecules are oriented according to the dipole moment of the dissolved dipolar chromophore. In apolar solvents, however, the solvent molecules do not possess a dipole moment per definition and the chromophores are best stabilized when their dipole moments are cancelled out by stacking into antiparallel dimers. Therefore, also for the BAM chromophore the dipolar chromophore-chromophore interactions facilitate an increased stability of the dimer in non-polar solvents while the electrostatic repulsion of the charged phosphate backbone leads to dehybridization of the surrounding oligonucleotide structure at much lower temperatures.

The BAM chromophore is not only able to undergo dipolar interactions but its barbituric acid moiety also has the potential to act as hydrogen bond acceptor. This feature could be exploited by the addition of the hydrogen bond donor melamine, which was expected to lead to the disruption of the dBAM:dBAM dimer in the DNA duplex. In addition, the barbituric acid moiety is structurally similar to T and U; for the first one mentioned, the formation of Hg^{II}-mediated T-T base pairs has been reported.[413,414] Thus, besides the addition of melamine, also Hg^{II} could have the capability to break the hydrophobic BAM:BAM dimer within the oligonucleotide scaffold.

3.4.5.3 Probing of the dBAM:dBAM dimer stability

Barbituric as well as cyanuric acid and their complementary counterparts 2,4,6-triaminopyrimidine and melamine as hydrogen bond donors have widely been used to access a plethora of supramolecular structures by non-covalent interactions. These small molecules represent the so-called Janus type nucleobases[415] with identical duplicate or triplicate sets of the H-bonding faces of T or A, respectively, and are considered as candidates for the arising of prebiotic RNA variants. In aqueous solutions, mixtures of these free hydrogen bond donors and acceptors and their substituted variants are known to self-assemble into hexameric rosettes[288,416–421] with large hydrophobic surfaces (Figure 3.63a), and helicene-like structures.[422–424] In addition, melamine has been found to associate with poly-T strands in a defined manner to form triplex structures.[425] However, not only the simple cyanuric acid monomer but also derived merocyanines have been used for controlled self-assembly with melamine hydrogen-bond donors, as for example described by Würthner *et al.* (Figure 3.63b). For instance, barbituric acid containing merocyanine chromophores were arranged in a chiral screw sense by excitonic coupling, in colloidal assemblies as well as in well-ordered columnar mesophases.[279,426,427]

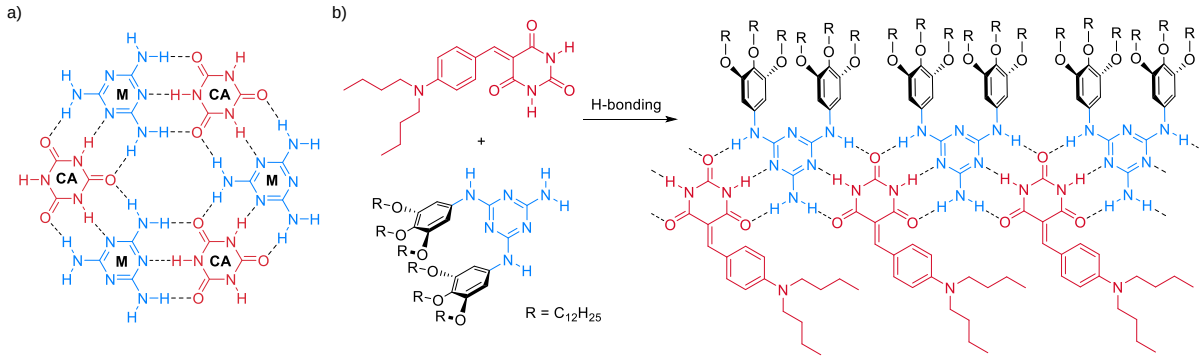

Figure 3.63: a) Structure of a hexad rosette formed by hydrogen-bonded melamine (M) and cyanuric acid (CA) in aqueous solution.[420] b) Sheet-type assembly of a barbituric acid-based merocyanine by intermolecular interactions, including hydrogen bonds. These sheets can give ribbons by π-π stacking which finally assmemble into columnar structures.[426]

With BAM containing the barbituric acid moiety, the formation of similar structures seemed to be conceivable. Since the free BAM chromophore itself is not soluble in water and can therefore not directly be used for self-assembly with melamine, 10 eq. of melamine were instead added to a solution of the duplex **D8/D12** with the opposite dBAM:dBAM dimer in 1× PBS where strong excitonic coupling had been observed before.

Due to its multiple H-bonding faces, melamine was expected to be able to incorporate in between the two opposing chromophores (Figure 3.64a). This requires disruption of the dipolar chromophore-chromophore interactions by energetically more favored hydrogen bonds, leading to a red-shift in the UVvis spectrum toward the monomer absorption. However, even after annealing, no change in the absorption behavior of **D8/D12** compared to the untreated control

(black) and the not-annealed sample (dashed line) was observed. Since the H-type aggregate absorption of the dimer did not show decreased intensity, it can be concluded that the dipolar dBAM:dBAM interactions are considerably strong, exceeding the presumed structural stabilization by multiple hydrogen bonds between the barbituric acid donor and the melamine monomer.

As already discussed for the formation of rBAM:rBAM dimers in RNA, the binding strength of coplanar antiparallel D-π-A chromophores by dipolar interactions markedly overcomes the one of triple- and even quadruple hydrogen-bonded base pairs. In addition, also the restricted space within the context of the DNA scaffold might be a reason for the non-perturbed chromophore dimers in the presence of an excess of melamine. Presumably, the BAM:melamine:BAM construct simply is sterically too demanding to still provide stabilization of the short duplex structure.

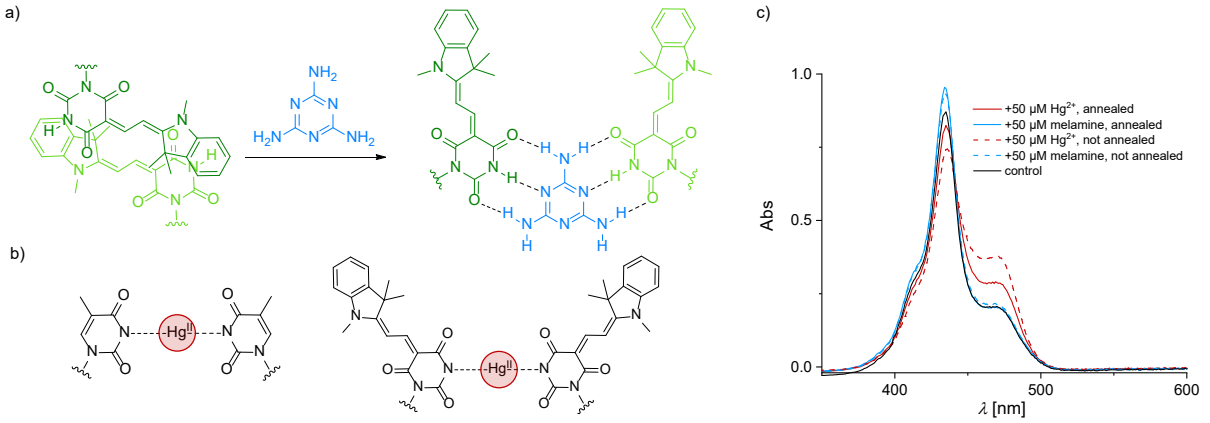

Figure 3.64: The excitonically coupled dBAM:dBAM dimers in the DNA scaffold are potentially broken by the formation of multi-hydrogen bond triplex structures with melamine (a) or Hg^{II}, forming metal-mediated base pairs similar to the T-Hg^{II}-T pair (b).[413,414] However, the interchromophore interaction showed to be surprisingly strong; even after annealing in the presence of 10 eq. of melamine or Hg^{II} no change in the H-type aggregate absorption pattern indicating dimer disruption was observed.

D8/D12 was not only treated and annealed with melamine, but also with 10 eq. of $HgCl_2$ to induce the formation of a Hg^{II}-mediated dBAM:dBAM base pair similar to reported T-Hg^{II}-T mispairs with N3 coordination of Hg^{2+} by two deprotonated thymidine residues and increased thermodynamic stability.[413,414] However, also upon addition of Hg^{2+} no disruption of the excitonically coupled dBAM:dBAM dimer was observed which is explained not only by steric but also by electronic effects. Due to the electron-donating character of the indolenine, the electron density of the barbituric acid moiety is increased, leading to a pK_a of around 11 for BAM in the DNA scaffold which is higher compared to T with a pK_a of 9.9.[428] Consequently, dBAM is not as easily deprotonated as T in the presence of Hg^{II} and dBAM:Hg^{II}:dBAM complex formation is hampered.

Although not achieved here, a better design of the oligonucleotide sequence and careful optimization of the experimental conditions might allow the formation of dBAM:melamine:dBAM or dBAM:Hg^{II}:dBAM triplets. It might for example be helpful to incorporate abasic sites in the vicinity of dBAM to reduce the crowdedness, providing a larger conformational freedom of the merocyanine chromophore. Furthermore, it might be beneficial to subject the duplex samples with the respective additive to multiple heating-cooling cycles to ensure efficient structural organization.

As already shown, the distinct spectroscopic pattern of the dBAM:dBAM dimer and the respective monomer can be used to track duplex formation by absorption and fluorescence measurements. This can for example be useful to probe the activity of enzymes such as helicases by spectroscopic read-out. Therefore, duplex unwinding experiments with Tte UvrD helicase on the double-BAM-modified opposite DNA system **D8/D12** have been carried out and are discussed in the following.

3.4.5.4 Spectroscopic tracking of helicase-mediated duplex unwinding

DNA helicases are able to unwind DNA duplexes by breaking the hydrogen bonds linking the two single strands using energy generated by the hydrolysis of nucleoside triphosphates. The widely known ATP-dependent Tte UvrD helicase is isolated from a strain of *E. coli* which carries the cloned UvrD gene from the thermophilic organism *Thermoanaerobacter tengcongensis*. It is a repair helicase which unwinds DNA duplexes in 3'-5' direction and is active for a wide range of different DNA substrates.[429] Therefore, it was used for the dehybridization of the dBAM:dBAM H-type dimer containing duplex **D8/D12** which is expected to lead to diminished exciton fluorescence and give rise to enhanced monomeric BAM emission. Since there is a fast recombination of DNA single strands in solution, an unmodified strand complementary to **D8** was added in 10-fold molar excess to capture the released single strands (Figure 3.65a).

The duplex of interest was prepared as 5 µM solution in a fluorescence cuvette in thermal amplification buffer and treated with Tte UvrD and excess of ATP in the absence and presence of the capture strand **D2**. After incubation for 20 min at 20 °C, the sample without the capture strand showed the same fluorescence characteristics as the untreated control duplex. For the system including **D2**, the excimer fluorescence was strongly decreased while an enhanced monomer excitation and emission was detected, indicating the breakup of the dipolar coupling between the two BAM chromophores. Unfortunately, an additional control experiment where the modified duplex was incubated only with the capture strand **D2** in the absence of any enzyme led to the same fluorescence behavior. Therefore, the used 12mers are presumably too short and form thermodynamically too labile duplex structures with strand displacement taking place even at room temperature. To prevent this side reaction, longer oligonucleotides with

dehybridization occuring only at higher temperatures could be used instead, such as modified 34mers as described in for DNA/GNA hybrid structures in section 3.6. Then, the samples could be incubated at 65 °C, the optimal temperature for Tte UvrD, and a more reliable fluorescence readout can be expected.

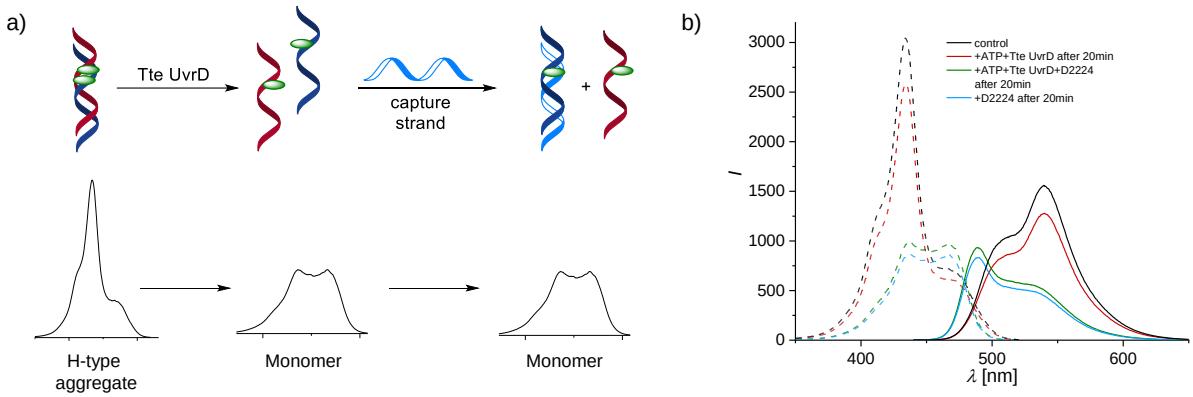

Figure 3.65: By unwinding the DNA duplex containing the opposite dBAM:dBAM dimer with Tte UvrD helicase and capturing the released modified single strand, the dimer fluorescence is expected to be reduced while the monomer fluorescence should increase (a). Fluorescence spectra for **D8/D12** treated with Tte UvrD and ATP in the presence and absence of a capture strand as well as two control samples reveal fast recombination of the indiviual single strands even in the absence of the helicase (b). Conditions: 5 µM **D8/D12**, 20 ng of Tte UvrD, 1 mM ATP, 1x thermal amplification buffer, incubation at 20 °C, excitation at 420 nm, emission at 540 nm.

Although no further conclusions can be drawn from the described helicase-mediated DNA unwinding experiments, it has become obvious that dipolar coupling interactions of cofacially stacked antiparallel BAM chromophores are favored over classical Watson-Crick base pairing with A in DNA as well as RNA. Due to the localization of the hydrophobic BAM chromophore in the inner core of the oligonucleotide duplex structure and its fluorescent character, it was considered to be suitable for FRET experiments as described in the next section.

3.4.6 BAM - a new FRET acceptor for 2AP

The FRET effect describes an incoherent dipole-dipole interaction with non-radiative energy transfer from an excited donor to a non-excited acceptor and competes with emission as well as other non-radiative deactivation pathways. Since it depends on the resonant Coulomb coupling of the donor and acceptor transition dipole moments, the FRET efficiency is strongly distance-dependent and can be used as a molecular ruler in the range of 2–10 nm. For the occurrence of FRET effects, several prerequisites need to be fulfilled: the donor needs a sufficiently long fluorescence lifetime for energy transfer, the donor-acceptor separation is required to be within the Foerster radius R_0, the acceptor absorption and the donor emission need to overlap to an adequate extent and the dipole moments of the interacting chromophores must be approximately parallel.[430] For an isolated donor-acceptor pair in the absence of short

range interactions the rate of the energy transfer k_{ET} can be described as

$$k_{ET} = \frac{1}{\tau_D} \cdot \left(\frac{R_0^6}{r_{DA}^6} \right) \tag{15}$$

with the donor lifetime τ_D, the Foerster radius R_0 and the donor-acceptor distance r_{DA}. The efficiency E of a FRET effect is calculated from the steady state emission intensity of the donor alone and in the presence of the acceptor and can also be described including the rates for the energy transfer as well as for radiative and non-radiative processes according to equation (16):

$$E = 1 - \frac{I_{DA}}{I_D} = 1 - \frac{\tau_{DA}}{\tau_D} = 1 - \frac{k_{ET}}{k_{ET} + k_r + k_{nr}} = \frac{k_{ET}}{k_{ET} + \tau_D^{-1}} \tag{16}$$

With equation (15), the distance-dependency of the FRET effect becomes obvious:

$$E = \frac{R_0^6}{R_0^6 + r_{DA}} \tag{17}$$

Per definition, the Foerster radius R_0 describes the required donor-acceptor distance for a FRET efficiency of 50% and is given by

$$R_0^6 = \frac{9 \cdot \ln 10 \cdot \kappa^2 \cdot \phi_D}{128 \cdot \pi^5 \cdot N_A \cdot \eta^4} \cdot J_{DA} \tag{18}$$

Here, ϕ_D is the donor quantum yield, η is the refractive index of the solvent, κ^2 is the orientation factor and J_{DA} is the spectral overlap integral of the donor-acceptor pair, described by

$$J_{DA} = \int_0^\infty I_D(\lambda) \cdot \epsilon_A(\lambda) \cdot \lambda^4 d\lambda \tag{19}$$

with the donor emission $I_D(\lambda)$ and the acceptor absorption $\epsilon_A(\lambda)$ in ϵ units. The orientation factor κ^2 provides information on the spatial arrangement of the donor and the acceptor according to the following vector equation

$$\kappa^2 = [\mu_A \cdot \mu_D - 3 \cdot (\mu_A \cdot r_A) \cdot (\mu_D \cdot r_{DA})]^2 = (\sin\theta_D \cdot \sin\theta_A \cdot \cos\varphi - 2 \cdot \cos\theta_D \cdot \cos\theta_A)^2 \tag{20}$$

The last part of equation (20) is much more comprehensive with the visualized orientation of the donor and acceptor transition dipole moments and the corresponding angles (Figure 3.66).

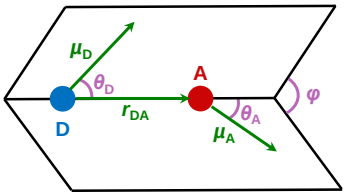

Figure 3.66: Illustration of the orientations of the donor and acceptor transition dipole moments and the respective angles needed to calculate the orientation factor κ^2.

Therefore, the maximum value for κ^2 is 4, which corresponds to a collinear orientation of the two transition dipole moments while it amounts to 0 with perpendicular orientation. If the two FRET partners can isotropically reorient during the lifetime of the excited donor, a dynamically averaged value of $2/3$ is obtained for κ^2. However, this assumption is only valid if the fluorophores are not rigidified within a supramolecular complex. For the systems described in this thesis, this is a weak approximation since the BAM chromophores are in all cases covalently attached to the spatially restricted oligonucleotide scaffold. If no information on the mutual orientation of the FRET partners is available, the donor-acceptor separation r_{DA} can be described as a function of the orientation factor:

$$r_{DA} = \left(\frac{1 - E}{E} \cdot \frac{9 \cdot \ln 10 \cdot \kappa^2 \cdot \phi_D \cdot J_{DA}}{128 \cdot \pi^5 \cdot N_A \cdot \eta^4} \right)^{1/6} \tag{21}$$

Since the fluorescence excitation of the BAM chromophore ranges from 370 to 510 nm, a sufficient overlap of the 2AP donor emission with a maximum at 380 nm and the BAM acceptor excitation for FRET effects is provided. This allows excitation of 2AP at 320 nm and, upon energy transfer to the BAM chromophore, detection of the emission at 490 nm if both are in close proximity (Figure 3.67). To ensure spacial vicinity of donor and acceptor, 2AP was incorporated directly opposite or by one or two base pairs apart from BAM in the counterstrand.

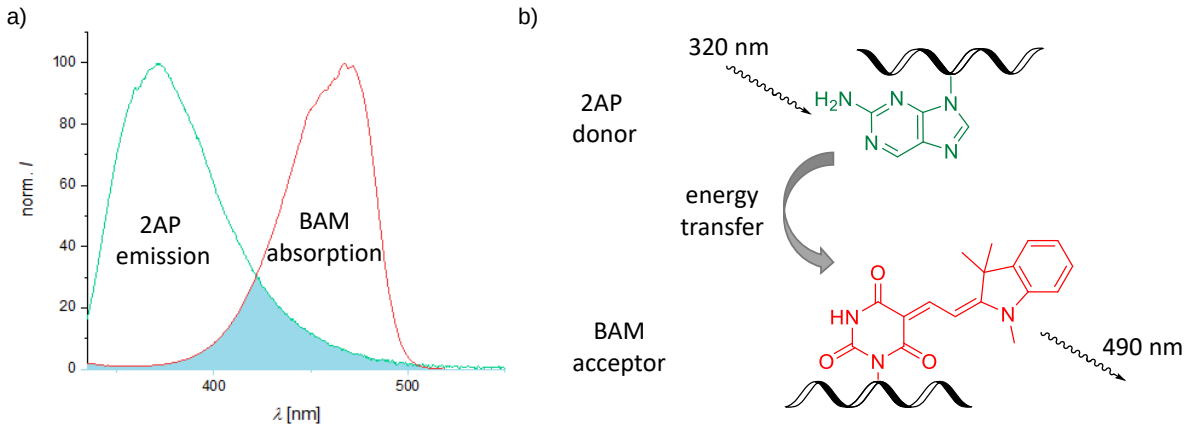

Figure 3.67: The overlap of the 2AP donor emission and the BAM acceptor absorption allows the evaluation of FRET effects (a). Upon excitation of 2AP at 320 nm and subsequent energy transfer to the BAM chromophore, emission at 490 nm is detected (b).

For the DNA duplexes shown in Figure 3.68, fluorescence emission spectra with excitation at 320 nm were recorded. In the depicted graphs, the 2AP emission is located between 340 and 480 nm, while the BAM chromophore emits in the range of 450 to 620 nm. As expected, the highest 2AP emission intensity is recorded for the 2AP-modified single strand (grey) while the 2AP fluorescence is strongly quenched for the hybridized duplex structure containing a 2AP-T base pair (red). Intermediary 2AP emission is observed for duplex systems modified with both 2AP and BAM, which is also reflected by the integral of the 2AP emission represented in the bar graph.

Regarding the BAM emission, the lowest intensity is detected for the control duplex without 2AP, in which BAM is excited directly (orange). If BAM together with 2AP is incorporated in the duplex structure, the BAM emission intensity is significantly increased. This enhanced fluorescence is dependent on the distance between 2AP and BAM: with both of them opposite each other, the most efficient energy transfer occurs and highest BAM emission is obtained (blue). With a distance of one base pair between 2AP and BAM, the merocyanine emission is reduced by around 30% (green) while with BAM and 2AP by two base pairs apart, BAM emission is even further reduced to only 40% of the initial value (purple). These values are in addition shown in the bar graph on the right for better comparison and can be rationalized by the strong distance dependence of the FRET efficiency according to equation 17.

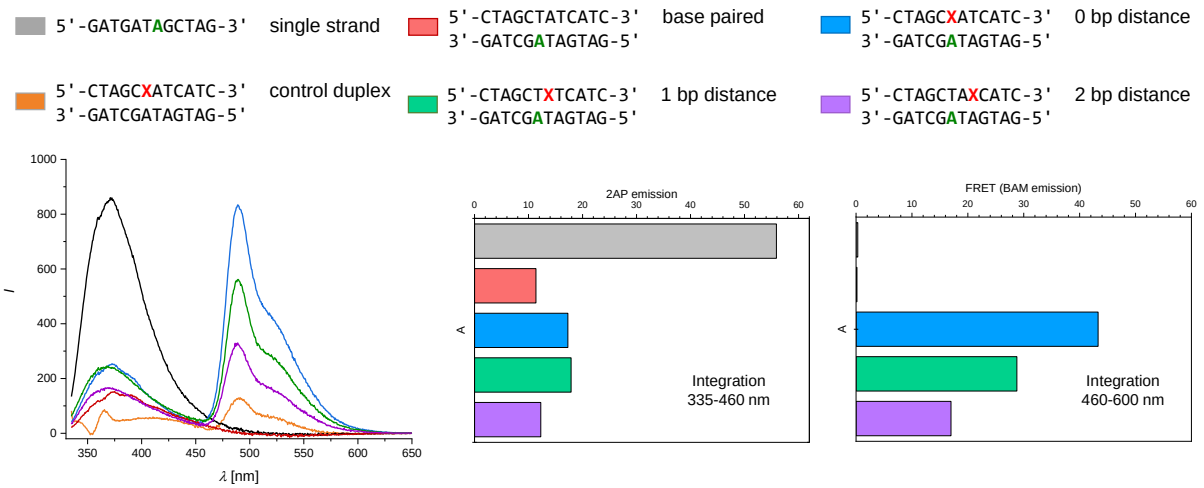

Figure 3.68: Fluorescence emission upon excitation at 320 nm for three BAM-2AP-modified DNA duplex structures along with three control samples was measured, shown on the left side. The integrated 2AP and BAM emission depicted in the two bar graphs showed distance-dependent energy transfer from the 2AP donor to the BAM acceptor.

For the duplex with dBAM directly opposite each other, the FRET efficiency was calculated according to equation (16). For this, the donor emission was corrected by substraction of the residual fluorescence of 2AP in the single strand, which led to a FRET efficiency E of 0.88. In addition, the Foerster radius R_0 of BAM was estimated using equation (18). For this purpose, the overlap integral was calculated from the area-normalized donor emission spectrum

and the acceptor absorption spectrum in ϵ units. Due to the λ^4 term in equation (19), J_{DA} is skewed to longer wavelength and its integral different from the actual overlapping area of these two spectra (Figure 3.69a). Since during the calculation the donor emission is area-normalized to one, the unit of the y-axis is formally nm^{-1} leading to an integrand unit of $L \cdot mol^{-1} \cdot cm^{-1} \cdot nm^3$.

J_{DA} was obtained as $3.1069 \cdot 10^{14}$ $mol^{-1}cm^{-1}nm^4$ and further used to calculate the Foerster radius R_0 after equation (18), with $\phi_D(2AP) = 0.68$, $N_A = 6.022 \cdot 10^{23}$ mol^{-1} and $\eta = 1.333$ (refractive index of water). For the orientation factor κ^2 a value of 2/3 was assumed for simplification, yielding an Foerster radius R_0 of 40 Å. Despite the weak approximation of an isotropic orientation factor, this value is in good accordance with reported ones for a thiazole orange dimer and a thiazole orange-Cy3 pair with 23±7 and 32±9, respectively.[431]

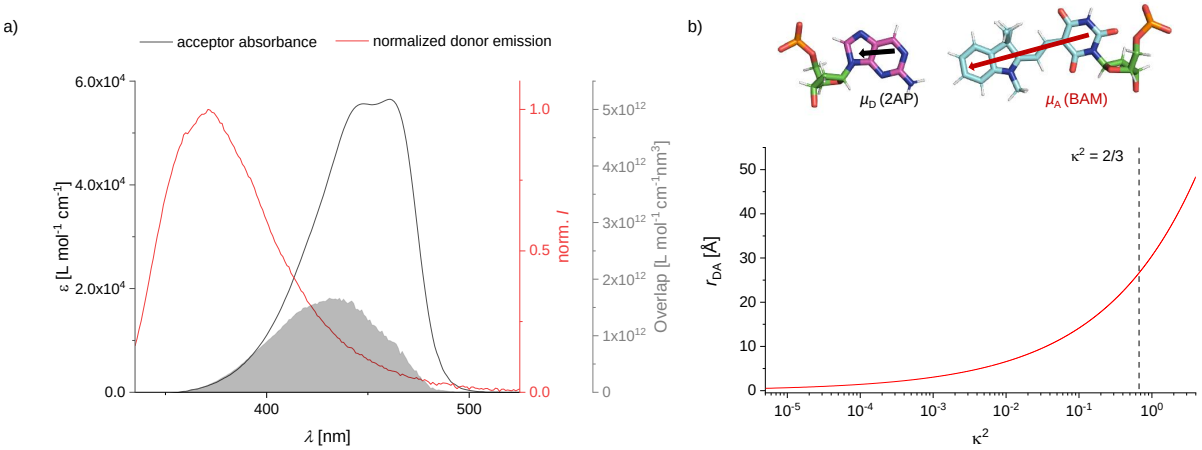

Figure 3.69: a) From the normalized donor emission and the acceptor absorbance plotted in extinction coefficient units of the duplex with dBAM directly opposite 2AP, the overlap integral J_{DA} can be calculated. The integral is shown as shaded area and does not correspond to the actual overlapping area of the two curves but is larger due to the λ^4 term in equation (19). b) If 2AP and dBAM are incorporated directly opposite each other, their dipole moments are essentially collinear, which is the prerequisite for a high FRET efficiency. The distance between donor and acceptor r_{DA} can be plotted dependent on the orientation factor κ^2 if no information about the mutual orientation of the donor and acceptor is available.

As already mentioned, the maximum value of four for the orientation factor κ^2 is obtained with collinear orientation of the donor and acceptor dipole moments. For the case with 2AP opposite BAM, a 3D model was constructed to clarify the direction of the dipole moments for these two nucleobase analogs in the DNA duplex. In analogy to the model structures shown before, 2AP and BAM were introduced into the helical system by base pair fitting to A and T, respectively. For simplication, only the 2AP and BAM nucleosides with their relative orientation in the DNA duplex are shown in Figure 3.69b, all of the others are masked. The BAM chromophore is drawn in *syn*-conformation here with the hydrophobic ring system being localized in the core of the duplex. The approximate directions of the dipole moments are furthermore indicated by the inserted arrows. Indeed, for the shown case the dipole moments

of 2AP and BAM are almost collinear, fulfilling the required criterion for high FRET efficiency. Since no information about the mutual orientation of the 2AP donor and the dBAM acceptor is available, the donor-acceptor distance r_{DA} was plotted as a function of κ^2 according to equation (21) in Figure 3.69b. If both fluorophores are located in the core of the duplex, they are in close proximity as the intrastrand distance in B-form DNA is only approximately 10 Å. This suggests a donor-acceptor orientation resulting in a κ^2 value lower than $2/3$, emphasizing the deficiency of an isotropic orientation factor for the covalently fixed dBAM chromophore.

However, also here it has to be considered that the structure shown in Figure 3.69b is not energy- or geometry-optimized and can therefore only serve as a preliminary model to explain the observed FRET effects. In addition, the FRET efficiency and the calculated Foerster radius R_0 need to be treated with caution since the 2AP fluorescence is dependent not only on the presence of dBAM as FRET acceptor but on many different factors. This is the reason why no further calculations were done for the duplexes with 2AP and dBAM apart by one or two base pairs as here the 2AP emission does not concurrently increase with larger donor-acceptor separation.

3.4.7 NMR analysis of the dBAM-dBAM upstream dimer

For detailed investigations on the structure of modified nucleic acids at atomic resolution, X-ray crystallography and NMR spectroscopy are the methods of choice. Both methods require comparably large amounts of pure material but are widely used for structural analysis of oligonucleotides containing natural and artificial modifications. The main advantage of oligonucleotide NMR is that it yields the oligonucleotide structure in the solution state rather than in the crystal lattice. In the course of this thesis, several attempts were made to crystallize dBAM-dBAM dimer containing duplex structures under different conditions. Despite the growth of some uniformely shaped single crystals, no high resolution scattering patterns were obtained, which might be due to the presence of double-bond isomers in the chromophore structure. Therefore, it was decided to further analyze the upstream dBAM-dBAM dimer structure **D8/D14** by NMR spectroscopy.

Nucleic acids are highly polymorphic molecules; their structure and dynamics strongly depend on the solvent, the salt concentration and the temperature. They are composed of building blocks with only a limited amount of non-exchangable protons, particularly at the nucleobases, which results in crowded spectra with limited chemical shift dispersion of the signals. Nevertheless, different assignment strategies have been developed and can be used to assign most of the proton signals in the standard helical regions by 1D imino and 2D NOESY spectra.[432,433] Hereby, not only the spatial proximity required for NOE contacts but also structural parameters such as the helical handedness of up to 50nt double strands can be estimated at high resolution.[434]

First, 1D proton spectra at various temperatures between 283 and 318 K were recorded for **D8/D14** containing the upstream dBAM:dBAM dimer (Figure 3.70).

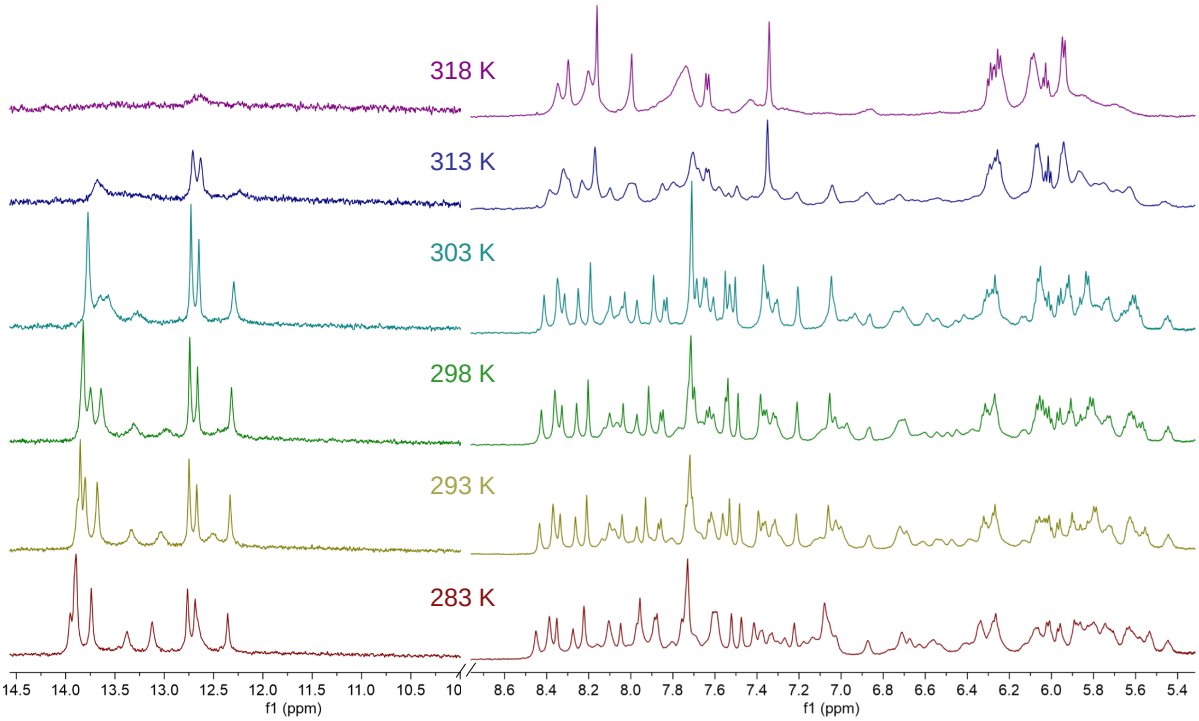

Figure 3.70: Imino (left) and anomeric aromatic (right) region of the 1D proton spectrum of **D8/D14** at various temperatures. Conditions: 200 µM duplex, 1× PBS (100 mM NaCl, 10 mM phosphate, pH 7.0), 90% H_2O/10% D_2O, 600 MHz. Spectra were recorded by Dr. Irene Bessi.

The imino region of these spectra already contains valuable information. Thus, the number of signals is related to the number of imino protons involved in base pairing which are protected from solvent exchange while the chemical shift gives a hint on the nature of the base pairs. In particular, imino protons involved in base pairing are resonating between 12 and 15 ppm. For the examined modified duplex, twelve imino signals are expected in this region of the spectrum. However, only ten imino signals are indeed observed. This indicates on the one hand the formation of a stable duplex and on the other hand the lacking of two of the expected base pairs, presumably the two A-dBAM base pairs. At elevated temperatures, the imino signals vanish concomitant to the hydrogen bond breaking between the Watson-Crick base pairs upon melting. Above 318 K, no signal is detectable in the imino region anymore which is in accordance with the observed duplex melting temperature of 309 K.

The aromatic region of the 1D proton NMR of **D8/D14** is shown in Figure 3.70 as well. Between 7 and 8.5 ppm, typically H8 and H2 of purines and H6 of pyrimidines in addition to the nucleobase amino protons are visible, while between 5.5 and 7 ppm H5 of C and the sugar H1' protons are observed. For the double-dBAM-modified duplex **D8/D14** also the signals for the aromatic protons of the two chromophores are expected in this region. With

increasing temperature, most signals between 5.5 and 8.5 ppm are broadened significantly or even disappear while some are also getting sharper. However, the 1D proton NMR spectrum is not sufficient to assign the observed signals to the corresponding protons.

To achieve this, a 2D proton homonuclear nuclear Overhauser effect (2D NOE) spectrum was recorded which allows a preliminary assingment of many of the observed signals. The starting point of the assignment was the G8-G16 contact shown in the spectrum excerpt in Figure 3.71a. By a sequential walk on the H1'-to-base pathway the contacts between sequentially connected nucleotides were then assigned in a step-wise manner. While the downfield shifted signals belong to the H3 of four of the Ts in the duplex, only a weak signal is observed for the imino proton of T18 which indicates that this particular nucleoside might not be base paired. For the imino protons of all Gs in the duplex, however, signals are detected and can also be unambiguously assigned, except for the terminal Gs (Figure 3.71b). Besides these imino protons for Ts and Gs, another signal at 13.35 ppm is visible which cannot be assigned due to missing NOE contacts but might belong to the proton at the barbituric acid of one of the merocyanine chromophores.

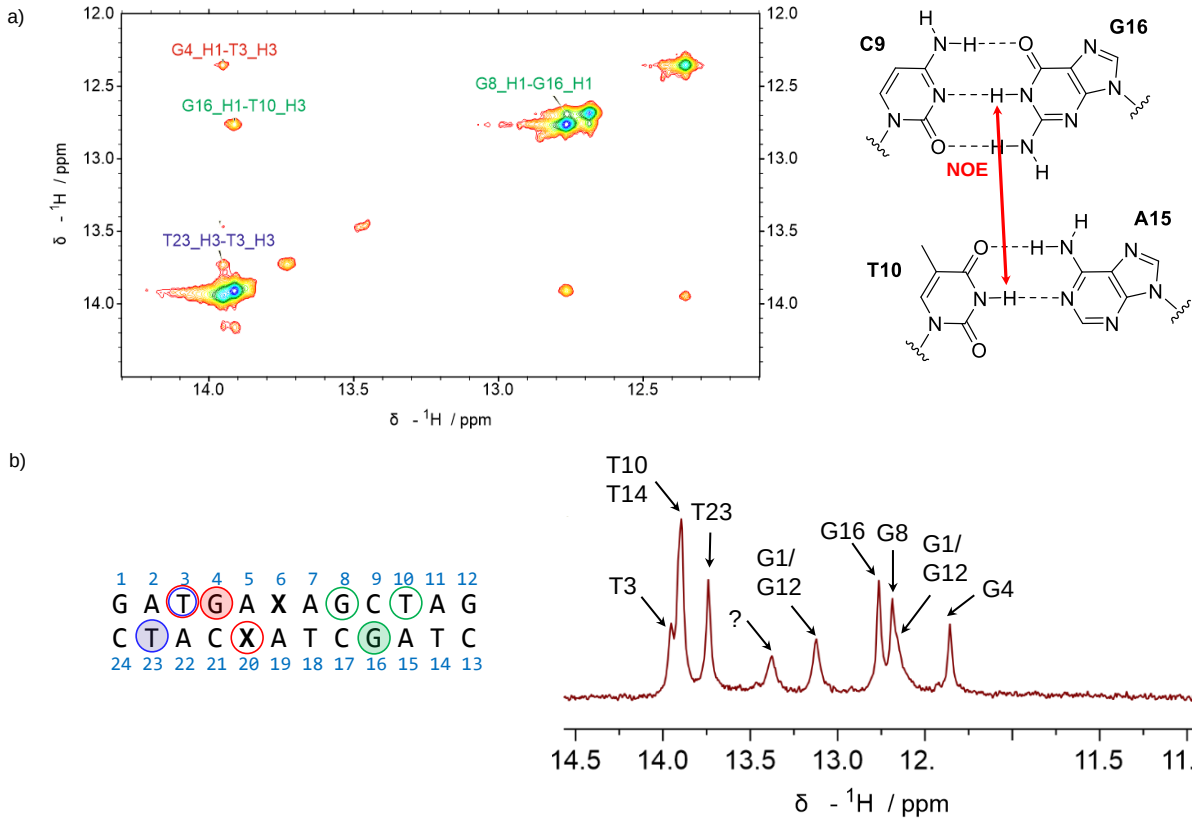

Figure 3.71: The signals in the imino region of the proton NMR can be assigned by a 2D NOESY spectrum by analysis of the contacts of the imino protons of two adjacent nucleobases. Hereby, all of the imino signals except for ones of the end-standing Gs can be assigned. Conditions: 220 µM (imino) or 440 µM (NOESY) duplex, 1× PBS (100 mM NaCl, 10 mM phosphate, pH 7.0), 90% H_2O/10% D_2O, 600 MHz, 200 ms mixing time. Spectra were recorded by Dr. Irene Bessi.

An enlarged detail of the aromatic and H1' region of the 2D NOESY spectrum for **D8/D14** which was used for preliminary assignment is shown in Figure 3.72. In general, the assignment of individual NOE signals in this part of the spectrum is facilitated by intraresidue contacts between the nucleobase proton and the H1' of the same sugar (top left, red arrows) as well as interresidue contacts between the H1' of one nucleoside and the nucleobase proton of the next (blue arrows).

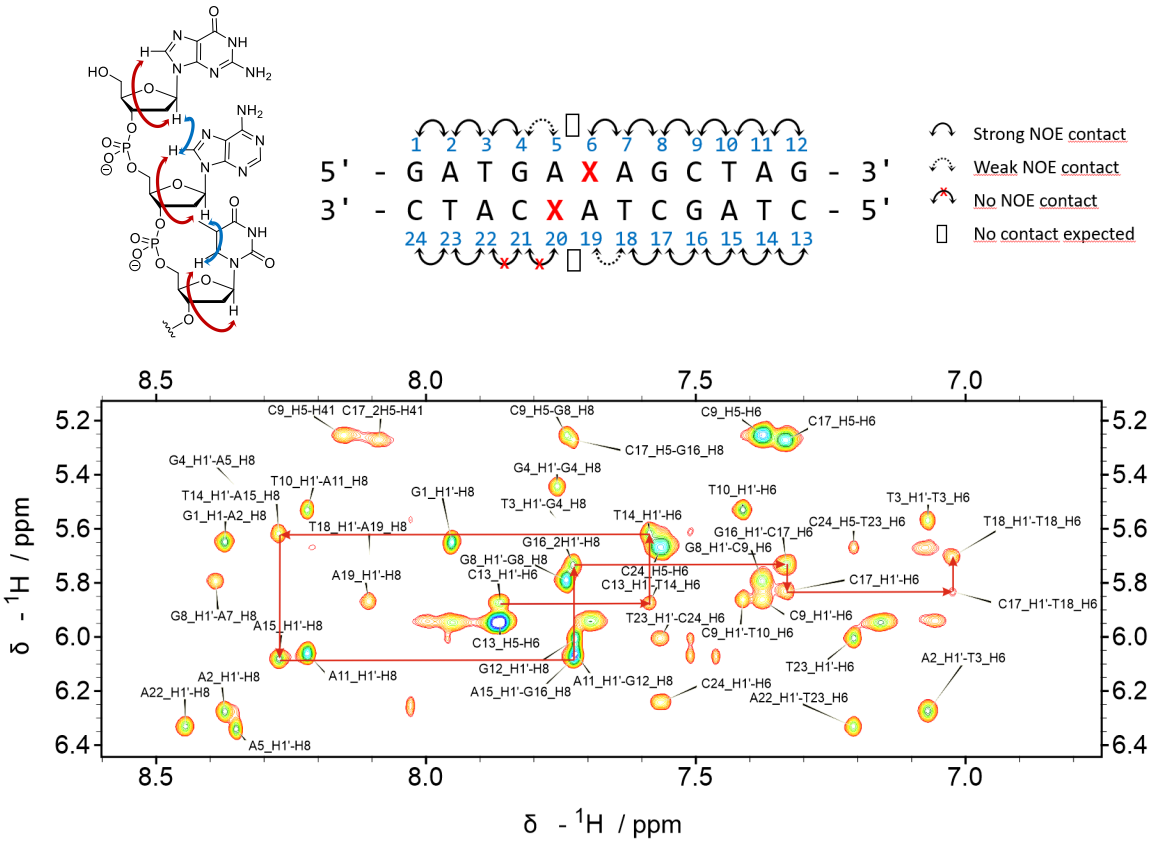

Figure 3.72: In the aromatic region of a 2D NOESY interresidue contacts (red) between the nucleobase aromatic proton and its own H1' as well as intraresidue contacts (blue) from the H1' of one nucleoside to the aromatic nucleobase protons of the next are observed (top left). An excerpt from the aromatic region of the NOESY spectrum of **D8/D14** measured at 283 K shows the preliminary signal assignment with the sequential-walk on the H1'-to-base pathway exemplarily shown from C13 to T18 with red arrows. The extracted NOE contacts are summarized in the schematic sequence above. Conditions: 440 µM duplex, 1× PBS (100 mM NaCl, 10 mM phosphate, pH 7.0), 90% H_2O/10% D_2O, 600 MHz, 200 ms mixing time. Spectra were recorded by Dr. Irene Bessi.

A part of the sequential pathway from the H1'-H6 contact of C13 to the H1'-H6 contact of T18 is exemplarily indicated by red arrows in Figure 3.72. However, regions of conformational instability or unusual residues will lead to interruptions of the base-to-sugar pathways, which is observed here for the nucleosides adjacent to the two merocyanine modifications. While between G4 and A5 as well as T18 and A19 only weak NOE contacts are visible, none are observed between C21 and the neighboring nucleosides BAM20 and A22. This hints to a major perturbation of the duplex structure induced by the sterically demanding artificial nucleobases.

Since the main purpose of recording a 2D NOESY spectrum was to obtain information on the chromophore orientation in **D8/D14**, special attention was paid to the contacts of BAM6 and BAM20 to neighboring nucleosides. One important NOE contact toward this goal is observed between two of the aromatic protons on the indolenine ring of BAM6 and H8 of the adjacent A7 (Figure 3.73a). These protons are only in close spatial proximity if the chromophore is in *syn*-orientation with its aromatic donor being located in the duplex core, supporting the conclusions drawn from spectrocopic analysis.

Further evidence for this particular chromophore orientation is obtained by analysis of the aliphatic and imino regions of the 2D NOESY spectrum. Here, NOE contacts between the H3 and the methyl protons within the same T nucleobase as well as between the imino protons or T methyl protons of nucleosides located diagonally opposite or next to each other are observed (Figure 3.73b). The most important contact visible in this region is shown in the upper spectrum excerpt between the methyl protons of BAM20 and the imino proton of G4, which only emerges if BAM is in the non-base pairing *syn*-conformation.

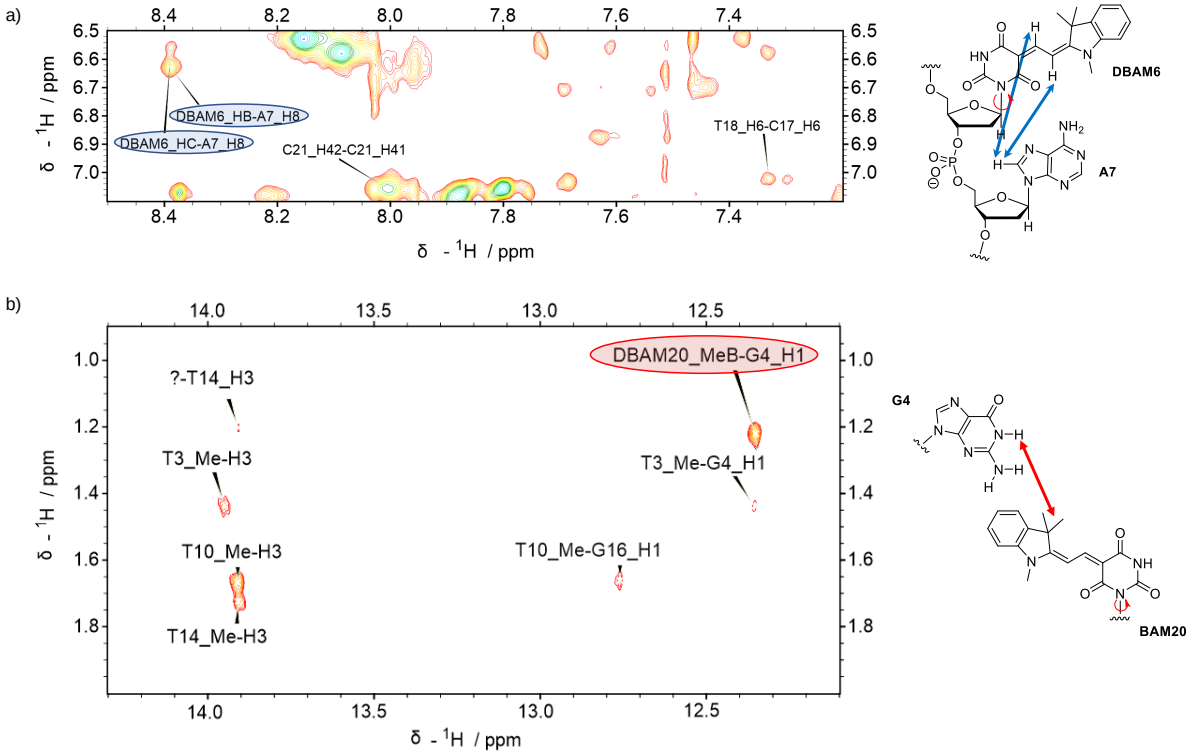

Figure 3.73: In both the aromatic (a) and aliphatic (b) imino region of the 1D proton spectrum contacts between the BAM chromophores and neighboring nucleobases are visible. Conditions: 440 µM duplex, 1× PBS (100 mM NaCl, 10 mM phosphate, pH 7.0), 90% H_2O/10% D_2O, 600 MHz, 200 ms mixing time. Spectra were recorded by Dr. Irene Bessi.

However, direct contacts between the aromatic protons of BAM6 and BAM20 are not observed here although these nucleobase analogs are assumed to be in close proximity due to dipolar

stacking interactions. The calculated distance for the geometry optimized dimer structure (see Figure 3.34) was between 3 and 4 Å while NOE contacts are typically obtained for intermolecular distances of up to 6 Å.[435] Therefore, NOE contacts between the two chromophores should theoretically be visible. One reason for the absence of these contacts might be the hydrophobic nature of BAM: despite repeated precipitation from acetone and extensive lyophilization, a significant amount of ethanol remained in the freeze-dried duplex sample which is usually not observed for other oligonucleotide samples. Thus, the observation of NOE contacts between the two BAM chromophores might be hampered by the non-covalent integration of ethanol in proximity of these two nucleobase surrogates. In addition, the molecular dynamics of the chromophores might play a role for the lacking of detectable proton signals for these artificial nucleobase analogs, leading to undetectable signals for exchanging protons. It has to be noted that the discussed assignments are only preliminary and additional experiments to confirm these are required.

Despite this, the preliminary assignments of the observed NOE contacts already provide good evidence for the assumed positioning of the two BAM chromophores in the duplex core and indicate a structural perturbation of this part of the DNA duplex, leading to the weakening of the A7-T18 Watson-Crick base pair. To get further insight into the structure of the double-modified duplex **D8/D14** it is required to record additional 2D NMR spectra such was HMBC and HSQC in pure D_2O to confirm these preliminary assignments. In this deuterated solvent, only non-exchangable protons such as H3' and H4' and all of the signals close to the H_2O signal will be detectable which might simplify the interpretation of the recorded spectra and enable the detection of aromatic chromophore protons, leading to a reliable proposal for the 3D duplex structure.

Since the simplification of the backbone structure from the RNA to DNA scaffold provided access to additional experiments such as oligonucleotide NMR for the interpretation of the interesting spectroscopic properties of these modified systems, it might be advantageous to even more reduce the backbone complexity. Although DNA is the most simple naturally occuring nucleic acid, many artificial oligonucleotide analogs with even more simplified backbone structures have been reported. One of them is GNA, which has already been discussed in the theoretical part of this thesis (section 2.2.1.3). Since GNA employs a synthetically easy to access acyclic backbone structure and leads to the formation of duplex structures with exceptional thermodynamic stabilities, it was decided to use this particular nucleic acid analog as the basis for further investigations of multichromophore assemblies on oligonucleotide scaffolds. The preparation of the therefore required phosphoramidite building blocks and oligonucleotide systems as well as the observed spectroscopic properties are discussed in the following section.

3.5 gBAM chromophores in the GNA scaffold

3.5.1 Preparation of canonical GNA and different variants of gBAM phosphoramidites and oligonucleotides

GNA features remarkably different structural characteristics compared to DNA and RNA as already introduced in Chapter 2. It combines structural simplicity and atom economy with a high duplex stability that significantly exceeds the stabilities of analogous duplexes of DNA and RNA.[48] In contrast to the naturally occurring oligonucleotides, the GNA structure of the antiparallel Watson-Crick duplex is rather comparable to a helically wound ribbon with a large helical pitch and a higher number of residues per turn showing a remarkable thermodynamic stability. Since the GNA duplex provides much more space for sterically demanding nucleobase surrogates, it was assumed that the GNA-BAM building block gBAM might be able to form a base pair with A instead of stacking in the shielded center of the duplex structure. Therefore, an additional scaffold for the incorporation of BAM dimers is accessible, which could give rise to thermodynamic and spectroscopic properties distinct from natural oligonucleotides.
The protected GNA phosphoramidites for the canonical nucleobases are commercially available but were nevertheless synthesized according to described procedures in the course of this thesis. In addition, the gBAM building block along with different variants for spectroscopic analyses was prepared. GNA oligonucleotides were in the following synthesized on a 3'-phosphate CPG solid support and deprotected under suitable conditions to yield GNA strands in high yields and quality after purification.

3.5.1.1 Synthesis of canonical GNA phosphoramidites

The first synthetic routes described for GNA phosphoramidite building blocks employed the traditional amide protection scheme.[436] However, these suffered from low yields, the formation of byproducts and extensive work-up procedures. Especially the G phosphoramidite showed to be unstable and decomposed upon storage. Later, the synthetic pathway was improved by using dmf protecting groups for A and G as well as an acetyl group for the exocyclic amino function of C (Scheme 3.23).[437] These can be cleaved under much milder deprotection conditions and resulted in higher yields of isolated, purified GNA oligonucleotides. In the course of this thesis, the desired GNA phosphoramidites were synthesized using these reported conditions, but slightly modified procedures as described in the following section.

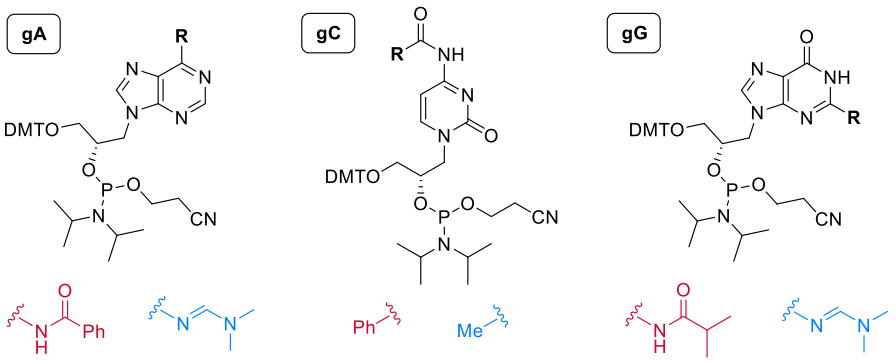

Scheme 3.23: Protecting groups for the canonical gA, gC and gG phosphoramidites used in earlier reports (red) and the previously described ones which can be cleaved under ultramild conditions (blue).

Synthesis of gT

The gT phosphoramidite building is synthetically the easiest one to acess due to the lack of exocyclic amino groups. In the first step, DMT-protected (*R*)-glycidol (**61**), prepared according to a standard procedure, was used for a ring-opening reaction with the T nucleobase in the presence of catalytic amounts of NaH, yielding **62** with (*S*)-configuration of the stereocenter (Scheme 3.24). This intermediate was then directly converted into the desired phosphoramidite **63** by phosphitylation with CEP-Cl.

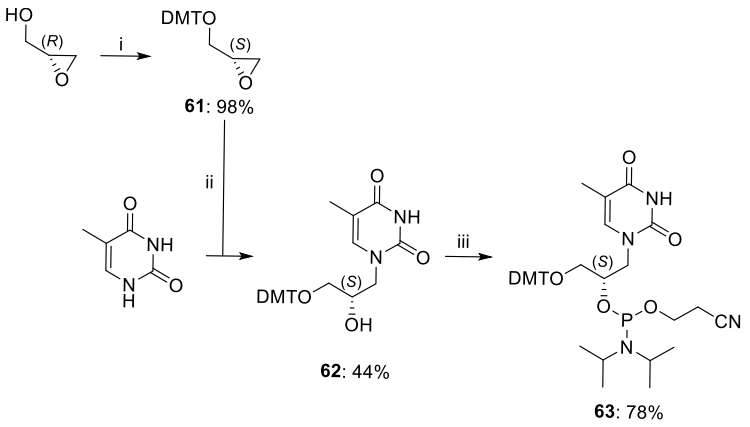

Scheme 3.24: Synthesis of DMT-protected (*R*)-glycidol **61** and the gT phosporamidite building block **63**. i) DMT-Cl, dry CH_2Cl_2, r. t., 2 h; ii) 1) NaH, dry *N,N*-DMF, r. t., 1 h, 2) **61**, 110 °C, 21 h; iii) DIPEA, CEP-Cl, dry CH_2Cl_2, r. t., 3 h.

The formation of the product with the required regioselectivity is strongly influenced by the conditions during the ring-opening reaction.[438] Under basic conditions, the nucleophile attacks at the least hindered β-position of the three-membered ring system, presumably controlled by steric interactions between the nucleophile and the epoxide, and the desired product is obtained (Scheme 3.25). Meanwhile, acidic reaction conditions lead to a nucleophilic attack at the α-position of the epoxide, stabilized by a carbocation-like intermediate.

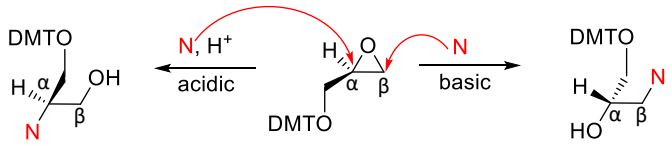

Scheme 3.25: The conditions of the epoxide ring-opening reaction have a significant impact on the stereoselectivity: under basic conditions, the nucleophile attacks at the less hindered position of the epoxide, while the nucleophilic attack under acid conditions takes place at the sterically more crowded carbon.[438]

The described epoxide ring-opening conditions under basic conditions were applied for the synthesis of all the of the GNA phosphoramidites prepared in this thesis.

Synthesis of N^4-acetyl gC

The synthesis of the other GNA pyrimidine phosphoramidite, gC, required the acetyl-protection of the exocyclic amino group in the first step in analogy to N^4-acetyl cytidine DNA phosphoramidites which are widely used for ultramild oligonucleotide deprotection (Scheme 3.26). The acetyl-protected nucleobase **64** was used without further purification for the epoxide ring-opening reaction with the DMT-protected (*R*)-glycidol **61**, giving compound **65** with a similar yield as obtained for the ring-opening with T. Following the general protocol for the phosphitylation, the final building block **66** was in the last step obtained with a sufficient yield.

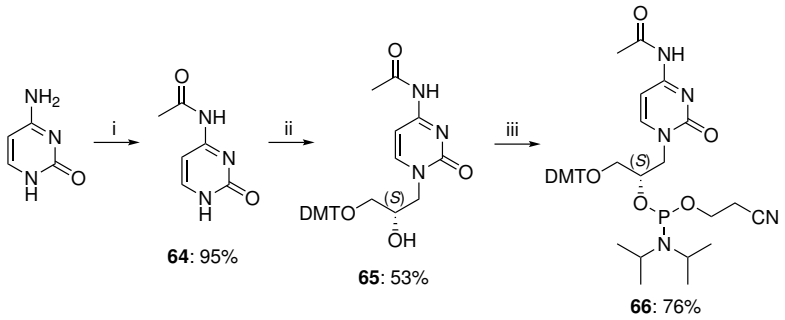

Scheme 3.26: Synthesis of the gC phosporamidite building block **66**. i) Ac_2O, DMAP, toluene, pyridine, 50 °C, 17 h; ii) 1) NaH, dry *N,N*-DMF, r. t., 1 h, 2) **61**, 110 °C, 18 h; iii) DIPEA, CEP-Cl, dry CH_2Cl_2, r. t., 3 h.

Therefore, both pyrimidine nucleobases were easily converted into the protected GNA phosphoramidite building blocks according to reported procedures.[436,437]

Synthesis of N^6-dmf gA

Amidine groups have been investigated for the protection of adenosine nucleosides to prevent acid catalyzed depurination during oligonucleotide synthesis. Therefore, DMFDMA was chosen as a suitable reagent for the introduction of a dmf-protecting group on the exocyclic amino group. Thus, after attaching the DMT-protected glycidol backbone using catalytic amounts of NaH, compound **67** was converted into the nucleobase-protected precursor **68** which was

used for subsequent phosphitylation to give the target compound **69** (Scheme 3.27).

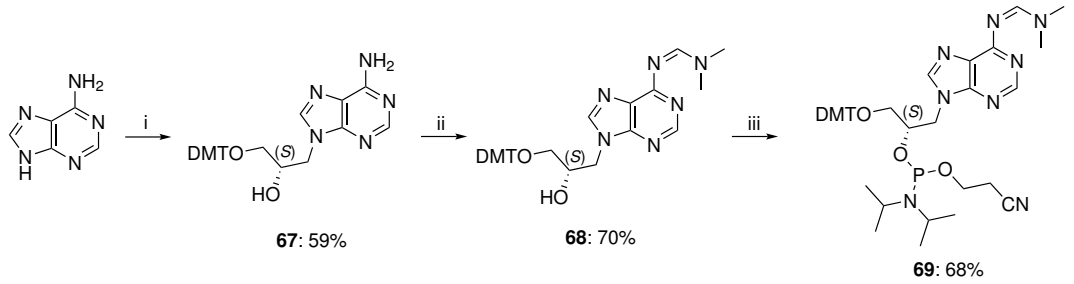

Scheme 3.27: Synthesis of the gA phosporamidite building block **69**. i) 1) NaH, dry *N,N*-DMF, r. t., 1 h, 2) **61**, 110 °C, 18 h; ii) DMFDMA, dry *N,N*-DMF, 60 °C, 1 h; iii) DIPEA, CEP-Cl, dry CH_2Cl_2, r. t., 2.5 h.

So far, all of the synthetic pathways were straighforward and yielded the protected phosphoramidites in good yields. However, the synthesis and purification of the gG building block proved to be more difficult.

Synthesis of N^2-dmf gG

Toward the gG phosphoramidite, two different procedures are reported which were combined here.[437,439] First, commercially available 2-amino-6-chloropurine was treated with unprotected (*R*)-glycidol. For this reaction, K_2CO_3 instead of NaH was used as a base for the nucleophilic ring-opening reaction to yield the free GNA nucleoside **70** (Scheme 3.28). This intermediary compound was then hydrolyzed under acidic conditions to the guanosine nucleoside analog **71**.

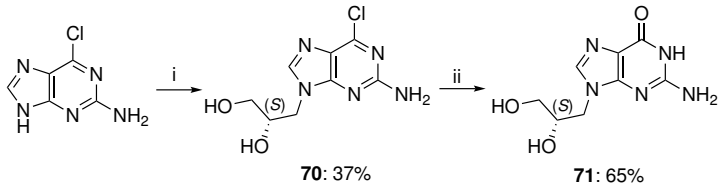

Scheme 3.28: Synthesis of the gG phosporamidite precursor **71**. i) (*R*)-glycidol, K_2CO_3, dry *N,N*-DMF, 90 °C, 20 h; ii) 1 M HCl, 85 °C, 3 h.

The exocyclic amino group of this free GNA nucleoside was protected with a dimethyl formamidine protecting group (Scheme 3.29). However, the intermediate **72** was not purified but directly subjected to the following tritylation reaction toward **73** and subsequently phosphitylated to give the phosphoramidite **74**. The isolation of the DMT-protected precursor and the phosphoramidite building block showed to be challenging, since both compounds partially decomposed during column chromatography on silica gel. By careful optimization of the purification conditions and precipitation of the crude phosphoramidite **74** prior to column chromatography, the final compound was obtained in sufficient amount for multiple incorporations into oligonucleotides by solid phase synthesis. However, it has to be noted that along with the

gG phosphoramidite always a significant amount of CEP-Cl hydrolyzed to phosphonate was obtained, which could not be removed in the purification steps. Nevertheless, the gG building block **74** was used for solid phase synthesis and the prescence of the phosphonate byproduct did not show to have any negative impact on the stepwise coupling yield.

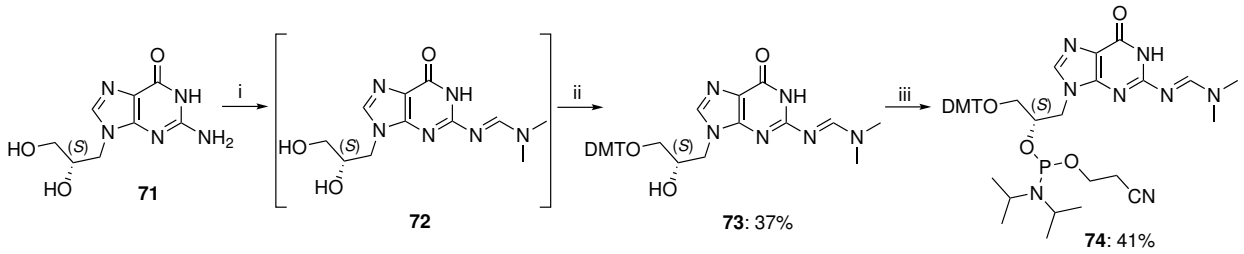

Scheme 3.29: Synthesis of the gG phosporamidite building block **74**. i) DMFDMA, MeOH, r. t., 18 h; ii) DMT-Cl, dry pyridine, r. t., 5 h; iii) DIPEA, CEP-Cl, dry CH_2Cl_2, 0 °C to r. t., 5 h.

All of the synthesized GNA phosphoramidite building blocks were afterwards used for oligonucleotide solid phase synthesis on a phosphate solid support. The phosphate blocks the 3'-hydroxy group but does not hamper the thermodynamic and spectroscopic properties of the generated oligonucleotides, while preventing degradation of the oligonucleotides under basic deprotection conditions.[440] The preparation of this solid support is described in the following part.

Preparation of the 3'-phosphate solid support

For the preparation of the 3'-phosphate CPG support, 4-bromomethylbenzoic acid was reacted with 2-mercaptoethanol to give thioether **75** in excellent yield (Scheme 3.30). After DMT-protection, compound **76** was loaded onto an amino-functionalized CPG support by standard amide coupling chemistry using BOP (benzotriazol-1-yloxytris(dimethylamino) phosphonium hexafluorophosphate) as a coupling reagent. Then, unreacted amino groups were capped with acetyl groups and the thioether was oxidized with *m*CPBA.

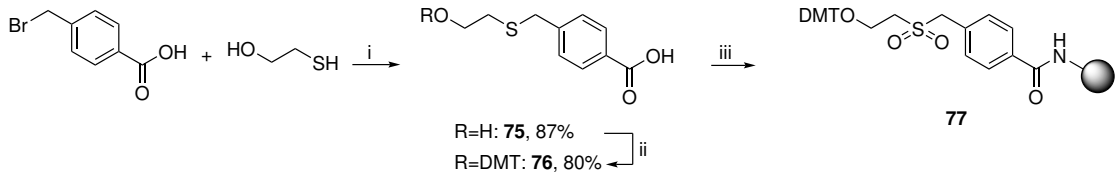

Scheme 3.30: Synthesis of the CPG solid support for the preparation of 3'-phosphate modified oligonucleotides. i) NEt_3, MeOH, r. t., 18 h; ii) DMT-Cl, pyridine, r. t., 15 h; iii) 1) BOP, *i*PrNEt$_2$, 40 °C, 2 h, 2) Ac_2O, 2,6-lutidine, *N*-methylimidazole, THF, r. t., 10 min, 3) *m*CPBA, CH_2Cl_2, r. t., 30 min.

The loading density of the prepared solid support **77** was finally determined by measurement of the trityl cation absorption after treatment with dichloroacetic acid. Typical values for the loading density were around 50 µmol/g which is higher than for the commercial DNA CPG

supports used in this work with a loading density of 25–35 µmol/g.

In addition to the canonical GNA phosphoramidites, building blocks composed of BAM and its variants attached by the N1 of the barbituric acid moiety to the chiral glycol backbone were generated. The synthesis of these modifications is discussed in the next section.

3.5.2 Synthesis of different gBAM phosphoramidites

The synthesis of gBAM phosphoramidite building blocks can be approached from different directions (Scheme 3.31). One possibility is to conduct the same epoxide ring-opening conditions as for the canonical nucleobases using DMT-protected glycidol. However, since the two nitrogen atoms of BAM are not equivalent, these conditions would not only lead to the formation of double-bond isomers for the desired single-glycosylated nucleoside, but also to the formation of a double-glycosylated compound as a byproduct. An alternative synthetic pathway starts with the stereospecific dihydroxylation of *N*-allyl BAM, followed by tritylation and phosphitylation. Although this pathway includes more reaction steps, no double-glycosylation is expected, leading to a higher total yield of the phosphoramidite.

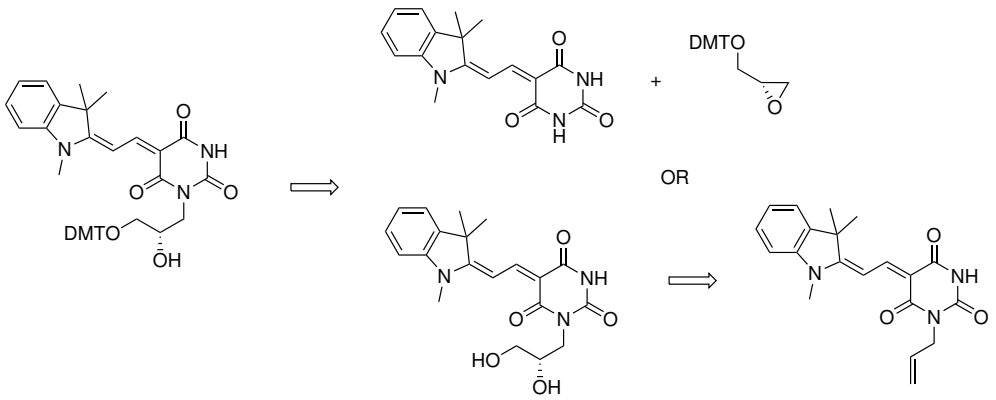

Scheme 3.31: The retrosynthesis of the DMT-protected glycidol BAM building block can be approached from two different directions. Either, the same epoxide ring-opening reaction as for the canonical nucleobases can be applied, leading to the formation of isomers and an undesired double-glycosylated byproduct, or the free *N*-allyl BAM chromophore can be dihydroxylated stereospecifically, which requires more synthetic steps.

Therefore, the *N*-allyl BAM chromophore **5** was synthesized as described at the beginning of this chapter and it was attempted to oxidize the allylic double bond to the vicinal diol (Scheme 3.32). The dihydroxylation worked smoothly under Upjohn dihydroxylation conditions in the presence of OsO_4 and stoichiometric amounts of *N*-methylmorpholine *N*-oxide (NMO) to generate the active osmium catalyst.[441] However, this reaction does in general not proceed stereospecifically but leads to a mixture of two stereoisomers which is not suitable for solid phase synthesis. To prevent this, the asymmetric dihydroxylation of *N*-allyl BAM was conducted under Sharpless conditions. Here, commercially available AD-mix-β, which

contains $K_2OsO_2(OH)_4$ as source of OsO_4, potassium ferricyanide $K_3Fe(CN)_6$ as a re-oxidant in the catalytic cycle, K_2CO_3 and the chiral ligand $(DHQD)_2PHAL$, a phthalazine adduct with dihydroquinidine, was used.

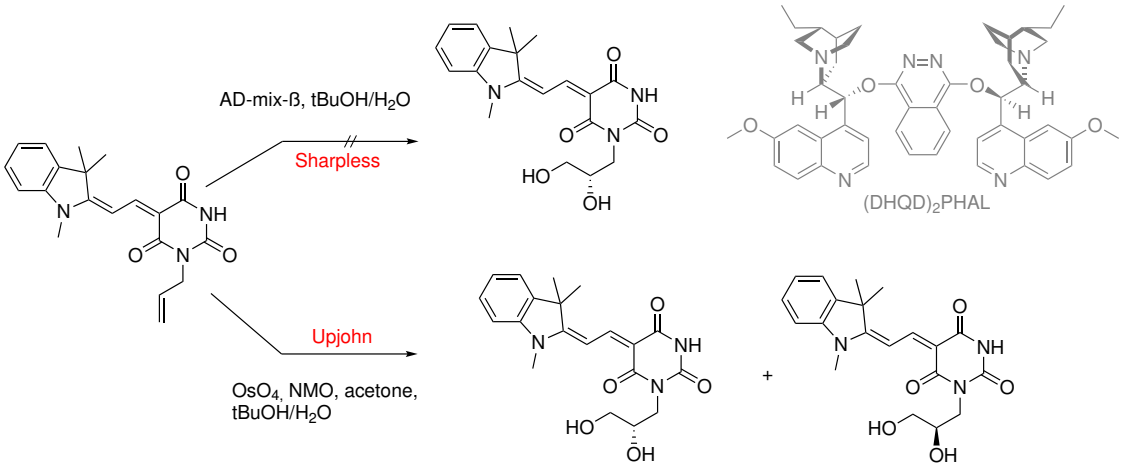

Scheme 3.32: Dihydroxylation under Sharpless and Upjohn conditions. While under the latter one a mixture of stereoisomers was obtained, the asymmetric dihydroxylation in the presence of AD-mix-β containing the chiral catalyst $(DHQD)_2PHAL$ did no lead to product formation.

The reaction was carried out in the biphasic solvent mixture $tBuOH/H_2O$, which is supposed to prevent the premature re-oxidation of the cyclic osmate intermediate, and was afterwards reduced with Na_2SO_3. However, the *N*-allyl BAM chromophore showed to be too unreactive, which might be due to its poor solubility in the solvent system, and no product was obtained for this asymmetric dihydroxylation, even after stirring for several days. Thus, the second possible reaction pathway was followed, employing the base-mediated epoxide ring-opening of DMT-protected (*R*)- and also (*S*)-glycidol **61** and **78** by the free BAM chromophore **1** to give compounds **79** and **80** (Scheme 3.33).

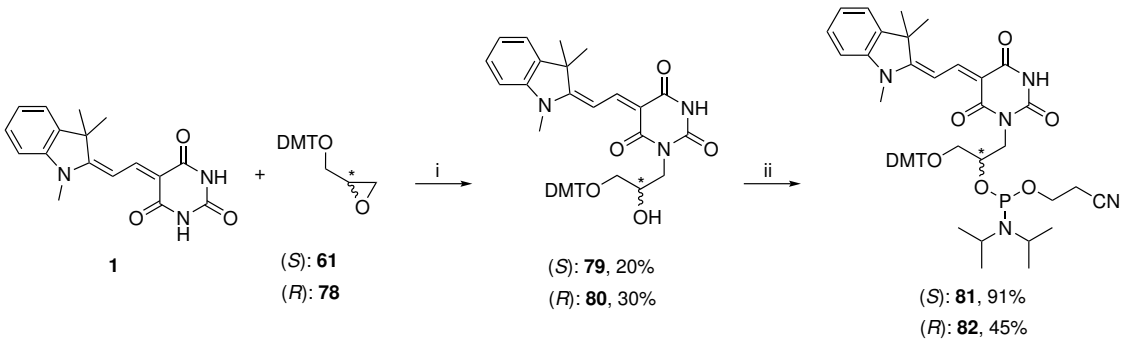

Scheme 3.33: Synthesis of the gBAM phosphoramidite with (*S*)- or (*R*)-configured stereocenter, **81** and **82**. Conditions: i) 1) NaH, K_2CO_3, dry *N,N*-DMF, r. t., 2 h; 2) **61** or **78**, 110 °C, 15 h; ii) Me_2NEt, CEP-Cl, dry CH_2Cl_2, r. t., 2 h.

These two precursors were in the next step phosphitylated to yield the phosphoramidites **81** and **82** which were used to analyze the influence of the stereocenter on the spectroscopic

characteristics of gBAM in the DNA duplex structure.

The reaction conditions for the attachment of the glycidol backbone had to be carefully optimized by adjusting the required amounts and ratio of NaH and K_2CO_3. With 1.5 eq. of NaH and 2.2 eq. of potassium carbonate, the best, although still low, yields of the desired compounds **79** and **80** were obtained.

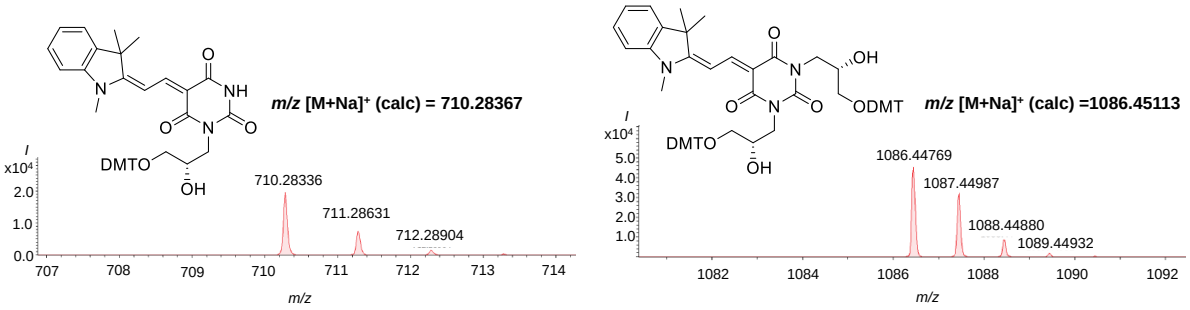

Figure 3.74: High resolution ESI mass spectra for the single- and double-glycosylated DMT-protected gBAM building block.

This is on the one hand caused by the formation of a significant amount of double-glycosylated byproduct, which could not prevented under any of the tested reaction conditions, and on the other hand presumably by the poor solubility of the free BAM chromophore **1** in *N,N*-DMF. The single- and double-substituted compounds were separated by column chromatography and analyzed by ESI-mass spectrometry (Figure 3.74) and NMR. Despite the low yield of the desired protected precursors **79** and **80**, several hundred milligrams of these compounds were synthesized and incorporated more than 70 times by solid phase synthesis into GNA as well as DNA oligonucleotides. It has to be noted, that the two double bond isomers are inseparable, but are assumed to be equal, similar as for the dBAM and rBAM building blocks, and therefore no difference in their chemical and spectroscopic behavior is expected. It was in addition tried to synthetically access *N*3-acetyl and -benzyl protected variants of BAM to prevent the formation of these isomers. While is was impossible to obtain the acetyl-protected BAM chromophore, the benzyl-protected compound was accessible but not used for further reactions since it can only be removed under harsh conditions and blocking of one barbituric acid nitrogen did not lead to improved yields in the epoxide ring-opening reaction as later observed for *N*-methylated barbituric acid.

The described epoxide ring-opening reaction and the phosphitylation were in the following also conducted with several variants of BAM: besides the *N*3-methylated building block mBAM (**4**), also the phosphoramidites of BAM^F (**2**) and BAM^{OMe} (**3**) with additional substituents at the aromatic indole systems as well as the methylated benzothiazole-derived compound $mBAM^b$ (**8**) were synthesized (Scheme 3.34).

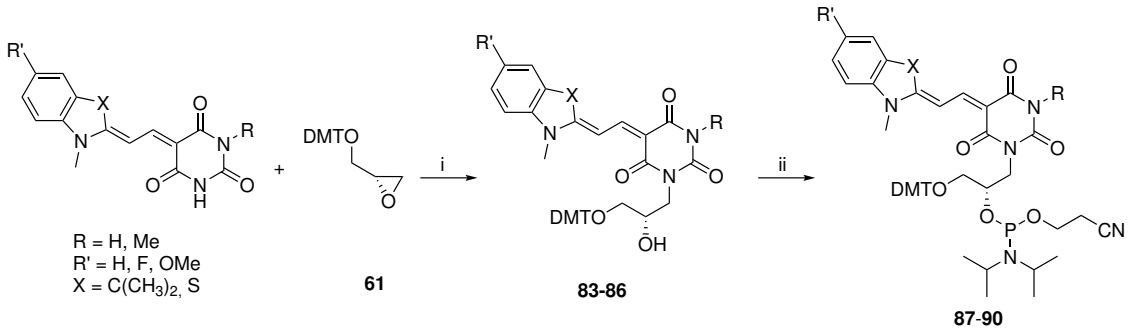

Scheme 3.34: Synthesis of phosphoramidites for further modified gBAM variants. Conditions: i) 1) NaH, K_2CO_3, dry *N,N*-DMF, r. t., 2 h; 2) **61**, 90–110 °C, 15–22 h; ii) Me_2NEt, CEP-Cl, dry CH_2Cl_2, r. t., 2 h. Yields are given in Table 3.18, for exact conditions see experimental section.

While the preparation of the free chromophores has already been discussed earlier in this thesis (Table 3.1), the yields for the obtained ring-opening products and phosphoramidites are summarized in Table 3.18. For all of the chromophores except gmBAM^b, between 15 and 30% conversion were observed in the alkylation reaction under very similar reaction conditions (for details see the experimental part). This is rationalized by electronic effects: the electron-rich sulfur atom in the aromatic donor moiety increases the electron density in the chromophoric system, therefore this nucleophile is more reactive and the obtained yield increases. However, sufficient yields for the introduction of the phosphoramidite functionality were obtained for all of the substrates.

Table 3.18: Yields obtained for the epoxide ring-opening reaction and the phosphitylation of different BAM variants.

Compound	R	R'	X	yield step i %	yield step ii %
gmBAM	Me	H	$C(CH_3)_2$	26 (**83**)	69 (**87**)
gmBAM^b	Me	H	S	65 (**84**)	77 (**88**)
gBAM^F	H	F	$C(CH_3)_2$	15 (**85**)	75 (**89**)
gBAM^{OMe}	H	OMe	$C(CH_3)_2$	20 (**86**)	46 (**90**)

Detailed reaction conditions can be found in the experimental part.

It has to be noted that the full assignment of the proton and carbon NMR spectra of the phosphoramidites proved to be difficult and remained incomplete. Due to the presence of two or four isomers, a large number of signals with overlapping coupling patterns were observed for which the assignment to designated protons was only partially achieved. However, the identity of the synthesized compounds was confirmed by HR-ESI-MS and gBAM as well as the gmBAM phosphoramidites were subsequently incorporated into 12mer GNA oligonucleotides

by solid phase synthesis. In analogy to the already discussed modified DNA and RNA systems, also gBAM-single as well as -double-modified duplex structures were used for thermodynamic and spectroscopic analyses. In addition, GNA 12mers with up to two or three gBAM modifications and short single strands exclusively built from gBAM were synthesized to investigate the behavior of this chromophore in larger complexes.

gmBAM^{b}, gBAM^{F} and gBAM^{OMe} were used for the preparation of DNA-GNA hybrid systems which will be discussed at a later point of this thesis (section 3.6). The conditions for oligonucleotide solid phase synthesis and deprotection as well as purification of the obtained GNA strands are described in the next section.

3.5.3 Incoporation of gBAM and gmBAM phosphoramidites into GNA oligonucleotides

In analogy to the strands synthesized for DNA and RNA, similar gBAM- and gmBAM-containing GNA oligonucleotides were prepared using a standard coupling protocol. All strands were synthesized on the in-house-made phosphate CPG support. To prevent alkaline hydrolysis during basic deprotection, the GNA oligonucleotides can either be synthesized in DMT-on mode or the 5'-end can be capped with a canonical DNA nucleoside. Since it was desired to obtain homogenous GNA strands in analogy to the pure DNA and RNA strands and the removal of the 5'-DMT-group only required a short additional step, it was decided to follow the first method.

Deprotection and cleavage from the solid support was achieved by overnight incubation at 37 °C in aq. ammonia. Indeed, degradation was observed if the DMT-group had been removed prior to the deprotection step, revealing a much larger fraction of shorter oligonculeotides in the HPLC analysis, while only one main peak remained with the capped 5'-hydroxy group (Figure 3.75).

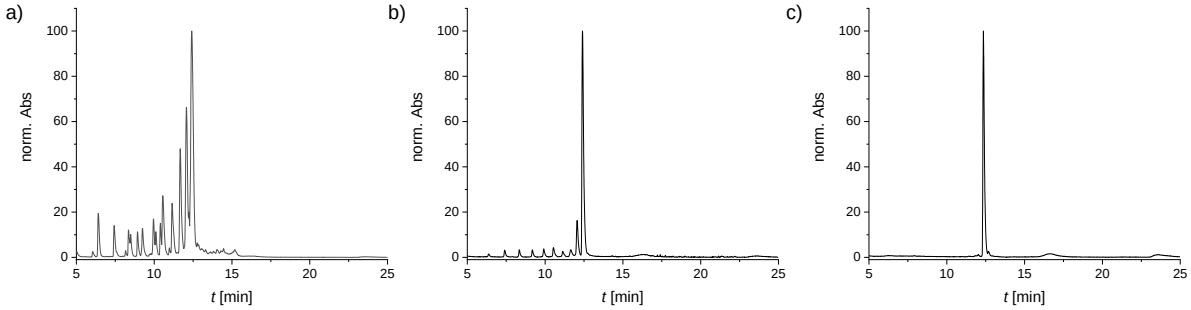

Figure 3.75: Anion exchange HPLC traces for an unmodified GNA strand: crude sample after deprotection of strand synthesized in DMT-off mode (a), in DMT-on mode (b) and purified oligonucleotide (c).

Afterwards, the DMT-groups were cleaved by incubation in 50% acetic acid for 30 min, the

crude oligonucleotides were precipitated and purified by PAGE. Precipitation from 70% ethanol as well as isopropanol was tested and both proceeded without further problems.

Table 3.19: Sequences, yields and masses for GNA 12mers obtained by solid phase synthesis. Important nucleobases are shown in bold, modified ones are colored in addition.

Name	3'-sequence-2'[a]	yield[b] nmol	*M* calc. g mol^{-1}	*M* meas.[c] g mol^{-1}
G1	GATGA**T**AGCTAG	199	3283.50932	3283.51387
G2	CTAGCTATCATC	124	3154.47931	3154.48223
G3	GATGA**A**AGCTAG	100	3292.52034	3292.54139
G4	GATGA**C**AGCTAG	103	3268.50911	3268.52156
G5	GATGA**G**AGCTAG	162	3308.51525	3308.53476
G6	CTAGC**TTT**CATC	187	3145.46719	3145.48367
G7	GATGA**Y**AGCTAG	114	3159.48149	3159.52953
G8	GATGA**X**AGCTAG	101	3468.59338	3468.58403
G9	GATGA**X**AGCTAG	106	3482.60849	3482.62047
G10	CTAGCT**X**TCATC	163	3330.55181	3330.55426
G11	CTAGCT**X**TCATC	121	3344.56691	3344.60009
G12	CTAGC**X**ATCATC	108	3339.56282	3339.54139
G13	CTAGCTA**X**CATC	128	3339.56282	3339.55835
G14	CTAGC**X**A**X**CATC	95	3524.64689	3524.61320
G15	CTAGC**XXX**CATC	71	3700.71938	3700.67227

[a] all oligonucleotides with 3'-phosphate
[b] 600-800 nmol synthesis scale
[c] monoisotopic masses obtained by charge deconvolution of the raw spectra
Y = C3-linker (abasic site), **X** = gBAM, **X** = gmBAM.

All GNA oligonucleotides were obtained with high quality and in good yields although the overall isolated amounts of the double- and triple-modified oligonucleotides **G14** and **G15** showed to be lower compared to all of the other strands (Table 3.19). This is presumably caused by the sterically demanding BAM chromophores, blocking the surface of the solid support to some extent for solvents and reagents and hereby leading to reduced coupling efficiencies.

With the sequences synthesized according to Table 3.19, duplex structures resembling the ones designed for DNA as well as RNA were prepared. Besides an unmodified reference, also here all of the canonical nucleobases as well as an abasic site were incorporated opposite gBAM. In addition, the same single-modified duplex structures with the methylated gBAM building

block, gmBAM, were prepared to investigate the base pairing properties of this chromophore in the GNA scaffold. To gain further insight into the behavior of gBAM in larger chromophore stacks, not only double-modified duplexes with upstream, downstream and opposite dimer orientation were generated but also structures with two or three gBAM in the same strand (Figure 3.76).

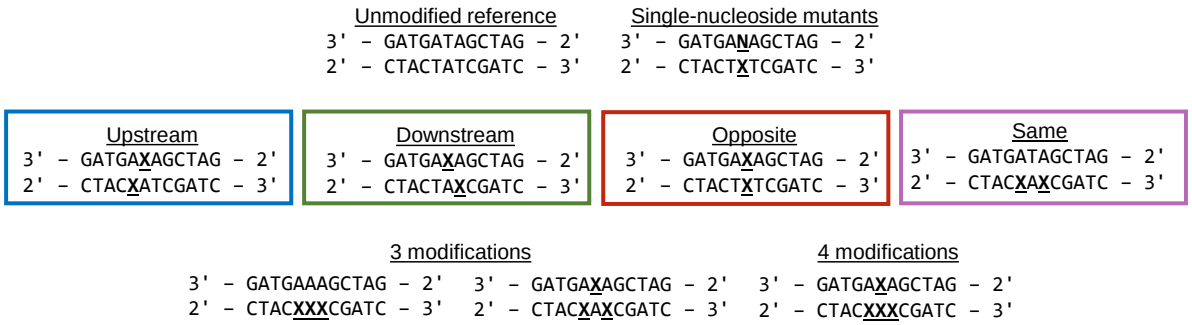

Figure 3.76: Duplex sequences for unmodified and modified GNA structures. **N** is the abbreviation for any of the nucleobases A, C, G and T or an abasic site while **X** is either gBAM or gmBAM.

Furthermore, 6- and 10mers composed of exclusively gA, gT or gBAM were synthesized for investigations of larger chromophore aggregates. Precipitation of the 6- and 10mers composed of only gA or gT shown in Table 3.20 was not possible after PAGE purification due to their short lengths. Instead, the purified oligonucleotides were desalted by size exclusion chromatography after extraction from the gel, yielding pure GNA single strands.

Table 3.20: Sequences, yields and masses for GNA 6mers and 10mers.

Name	3'-sequence-2'[a]	yield[b] nmol	*M* calc. g mol^{-1}	*M* meas.[c] g mol^{-1}
G16	AAAAAA	130	547.09033[d]	547.08575[d]
G17	TTTTTT	88	529.06719[d]	529.06968[d]
G18	XXXXXX	85	2700.72778	2700.71435
G19	AAAAAAAAAA	137	2728.48097	2728.48936
G20	TTTTTTTTTT	150	2638.36529	2638.36932
G21	XXXXXXXXXX	19	4489.20593	4489.20026

[a] all oligonucleotides with 3'-phosphate
[b] 600-800 nmol synthesis scale
[c] monoisotopic masses obtained by charge deconvolution of the raw spectra
[d] too few data points for deconvolution; shown is the mass for $[M\text{-}3H]^{3-}$
X = gBAM

However, this method was not suitable for the gBAM 6- and 10mer **G18** and **G21** because these coeluted with the salts remaining in the samples after PAGE. Therefore, these two strands were purified over a SepPak cartridge by gradient elution with a water/acetonitrile mixture. Compared to the canonical GNA oligonucleotides, the yield dropped significantly for **G21** which can partly be due to poor coupling yields as already explained or due to the lengthy purification procedure and the higher hydrophobicity of this heavily modified oligonucleotide. Despite the apolar character of gBAM, both **G18** and **G21** were still soluble in water, which facilitated the use of the standard buffer system for spectroscopic analyses, although **G21** showed the tendency to adhere to glass as well as plastic surfaces.

The GNA 6- and 10mers summarized in Table 3.20 were not only used for thermodynamic and spectroscopic analyses, but **G21** was in addition investigated by atomic force microscopy (AFM) to examine the formation of higher-order assemblies by dipolar and hydrophobic chromophore-chromophore interactions.

In the next section, thermodynamic stability measurements for single- and multiple-modified GNA structures are discussed first, followed by spectroscopic analyses of the formed BAM dimers, trimers and tetramers. Finally, the spectroscopic properties of duplex systems containing either six or ten gBAM chromophores are reported and evaluated.

3.5.4 Thermodynamic properties of gBAM- and gmBAM-modified GNA

The duplex melting temperatures and the derived thermodynamic parameters for single-gBAM and gmBAM-modified structures are summarized in Table 3.21. Here, the denaturation temperature for the unmodified reference duplex **G1/G2** shows a markedly increased thermal stability with 67.0 °C which is by 12.6 and 23.4 °C higher than for the equal RNA and DNA systems **R1/R2** and **D1/D2**, respectively.

The high thermal stability of GNA is at first glance surprising since for a long time it was assumed that the conformational preorganization of nucleic acid analog single strands required for stable duplex formation can only be achieved with cyclic phosphodiester backbones.[48] Compared to DNA, GNA duplex formation is less exothermic and at the same time entropically more favored than for DNA, which is unexpected since due to the flexible backbone an entropically less favorable duplex formation for GNA would be expected. These effects have been explained by a strong structural preorganization of the GNA single strands, as confirmed by CD spectroscopy, and different stacking interactions. These contribute to the increase in entropy through partial dehydration of the nucleobases upon hybridization of the single strands. In GNA, base-base interstrand stacking interactions are predominant whereas in

DNA intrastrand stacking plays a more important role.[52] Together with the strong backbone-base inclination already present in single-stranded GNA and the zipperlike interstrand stacking by attractive van-der-Waals forces additionally contributing to the duplex stability, duplex formation is thermodynamically more favored for GNA in comparison to DNA.

Table 3.21: Sequences, melting temperatures and thermodynamic parameters for GNA duplex structures with a single merocyanine modification. Important nucleobases are shown in bold. Given are also the differences in melting temperature relative to the unmodified reference sequence.

Name	sequence	T_m[a] °C	ΔT_m[b] °C	ΔH^0 kcal mol^{-1}	ΔS^0 cal mol^{-1} K^{-1}	ΔG^0_{298K} kcal mol^{-1}
G1/G2	3'-...ATA...-2' 2'-...TAT...-3'	67.0	-	-89.5	-238	-18.6
G8/G2	3'-...A**X**A...-2'	60.6	-6.4	-90.1	-244	-17.3
G9/G2	2'-...T**A**T...-3'	52.3	-14.7	-92.2	-258	-15.3
G3/G10	3'-...A**A**A...-2'	64.4	-2.6	-93.7	-252	-18.6
G3/G11	2'-...T**X**T...-3'	54.8	-12.2	-89.2	-247	-15.6
G4/G10	3'-...A**C**A...-2'	56.5	-10.5	-91.0	-250	-16.4
G4/G11	2'-...T**X**T...-3'	55.8	-11.2	-67.7	-179	-14.3
G5/G10	3'-...A**G**A...-2'	57.7	-9.3	-82.7	-224	-16.0
G5/G11	2'-...T**X**T...-3'	54.7	-12.3	-93.3	-260	-16.0
G1/G10	3'-...A**T**A...-2'	56.5	-10.4	-91.0	-250	-16.4
G1/G11	2'-...T**X**T...-3'	58.1	-8.9	-91.4	-251	-16.8
G7/G10	3'-...A**Y**A...-2'	56.0	-11.0	-85.8	-236	-15.5
G7/G11	2'-...T**X**T...-3'	56.5	-11.5	-87.6	-241	-15.8

[a] values for 5 µM samples in 1× PBS (100 mM NaCl, 10 mM phosphate, pH 7.0); 0.5 °C/min heating rate; a standard error of ±0.5 °C is assumed
[b] difference relative to unmodified duplex
Y = C3-linker (abasic site), names in blue for gBAM, names in red for gmBAM.

Upon incorporation of one gBAM opposite A in **G3/G10** and **G8/G2**, the GNA duplex is slightly destabilized by 2.6 to 6.4 °C, depending on the sequence context, which can be attributed to the large steric demand of the chromophore. This reduced thermal stability is also reflected in the thermodynamics with a small decrease of ΔH^0 and a slight increase of ΔS^0. If **G3/G10** is compared to the duplex structures with gBAM opposite C, G, T or the abasic site instead of A, a significant drop in melting temperatures by almost 10 °C is apparent. This indicates that gBAM is able to discriminate counterbases in the GNA context by classical Watson-Crick base pair formation with A, which is in stark contrast to the already discussed

RNA and DNA systems. The analysis of the melting temperatures of gmBAM-modified GNA structures with a blocked BAM-Watson-Crick base pairing site strengthens this assumption (Figure 3.77).

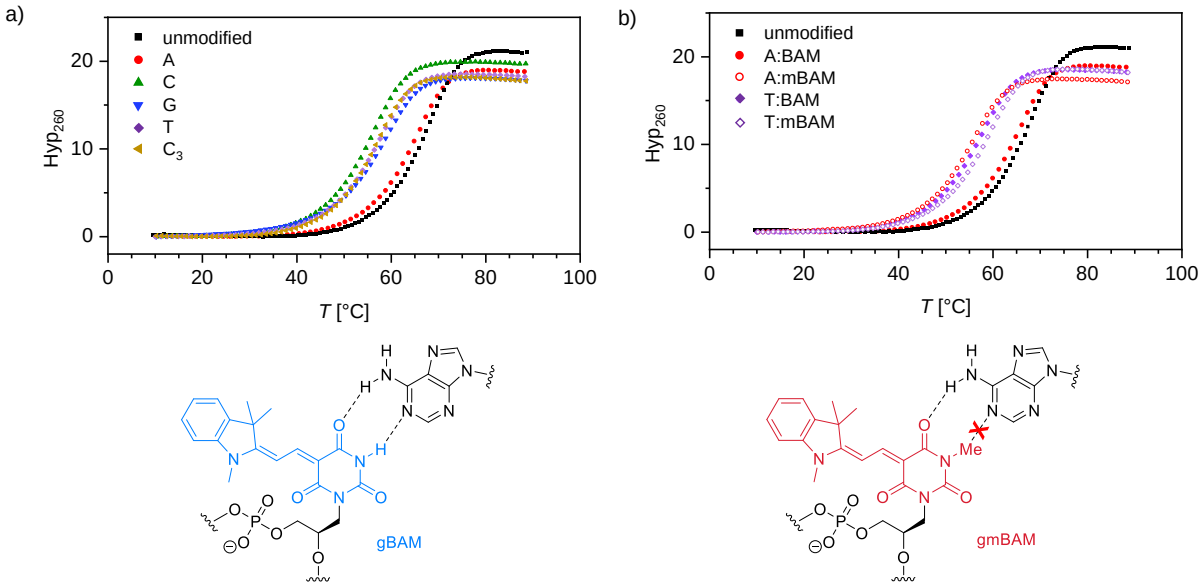

Figure 3.77: If gBAM is incorporated opposite A in the GNA scaffold, almost the same melting temperature as for the unmodified reference is obtained while incoporation opposite other canonical nucleosides drastically reduces the thermal duplex stability (a). With gmBAM having a blocked base-pairing site opposite to A, the T_m value of the duplex is strongly decreased and comparable to structures with mismatched BAM (b). Data are shown for 5 µM samples and the second heating ramp.

Here, the lowest melting temperatures of approximately 55 °C are observed for gmBAM opposite the purine nucleobases A and G in **G3/G11** and **G5/G11**, while dehybridization of systems with gmBAM opposite the pyrimidines C or T in **G4/G11** and **G1/G11** occurs at slightly higher temperatures. The slight stability difference between purine and pyrimidine nucleobases is explained by the increased molecular size of gmBAM, which is not well accommodated when opposite the large purine nucleobases, as also observed for porphyrines incorporated into a GNA scaffold.[54]

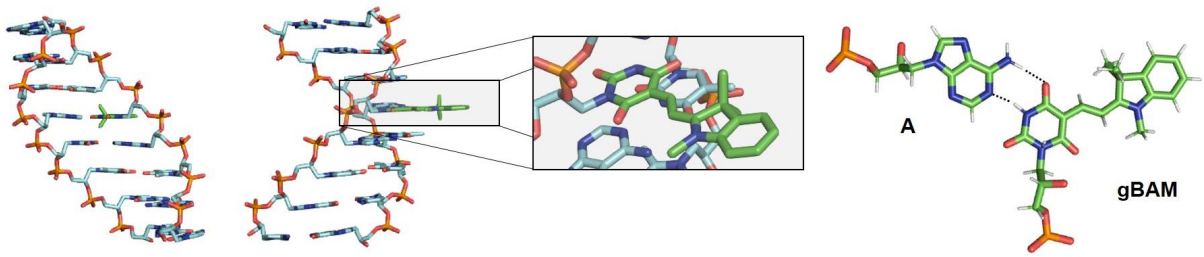

Figure 3.78: The model of a GNA duplex with gBAM forming a Watson-Crick base pair with A reveals no noteworthy steric clash between the chromophore and the phosphate backbone. Modeled with PDB 2JJA in Pymol.

The base pairing ability of gBAM in GNA is rationalized by the widened GNA duplex structure

where no considerable steric clash between the chromophore methyl groups and the phosphate backbone is observed (Figure 3.78). Therefore, the GNA duplex structure provides enough space to accommodate the sterically demanding merocyanine chromophore in base-pairing conformation.
To summarize, the BAM chromophore is so far only able to base pair in the GNA context, where the localization of the indolenine moiety in the duplex major groove is sterically not hindered. In DNA as well as in RNA, in contrast, the hydrophobic chromophore is not base paired but rather positioned in the helix center, stabilized by stacking interactions with the neighboring nucleobases.

In addition to the investigations on the base pairing properties of gBAM in single-modified duplexes, the thermodynamic parameters for GNA duplexes with two, three or even four gBAM modifications were estimated (Table 3.22). As already observed for the single-modified GNA systems, GNA duplexes containing gBAM dimers show decreased duplex stability compared to the unmodified reference **G1/G2**. However, the degree of destabilization is strongly dependent on the orientation of the chromophores toward each other (Figure 3.79). While for the upstream dimer **G8/G13** the melting temperature is decreased by only 4.3 °C, the downstream dimer **G8/G12** is by 7.8 °C less stable; for both, the drop in stability observed upon incorporation of the first gBAM modification is partially rescued. This might be caused by stabilizing chromophore-chromophore stacking interactions which are more obvious in the absorption and fluorescence spectra and will be discussed at that point. The GNA duplexes with the two gBAM either directly opposite each other (**G8/G10**) or in one strand (**G1/G14**) show the lowest thermal stability of all double-modified systems.

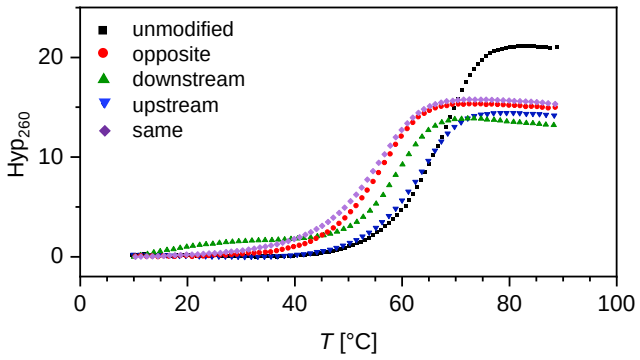

Figure 3.79: The duplex melting temperature of GNA hybrid structures depends on the mutual orientation of the two gBAM chromophores. The highest melting temperature was observed with the two modifications in upstream orientation (blue) while the lowest thermal stability was obtained for the opposite dimer (red) and the duplex with the two gBAM in the same strand (purple). Data are shown for 5 µM samples and the second heating ramp.

The strong destabilization of these two systems is explained by the two directly adjacent located chromophores, leading to a disturbed duplex structure due to the increased steric demand of

gBAM compared to native nucleobases. Compared to DNA, this result is surprising since in that case the opposite dimer showed to be the most stable one which might be caused by more pronounced dipolar stacking interactions between the two chromophores.

Table 3.22: Sequences, melting temperatures and thermodynamic parameters for GNA duplex structures with two merocyanine modifications incorporated; the blue, green, red and purple colored duplex name indicates upstream, downstream and opposite as well as chromophore positioning in the same strand, respectively. gBAM is abbreviated as **X**. Given are also the differences in melting temperature relative to the unmodified reference sequence.

Name	sequence	$T_m^{[a]}$ °C	ΔT_m °C	ΔH^0 kcal mol^{-1}	ΔS^0 cal mol^{-1} K^{-1}	ΔG^0_{298K} kcal mol^{-1}
G1/G2	3'-...ATA...-2' 2'-...TAT...-3'	67.0	-	-89.5	-238	-18.6
G3/G11	3'-...AAA...-2' 2'-...TTT...-3'	54.8	-12.2[b]	-89.2	-247	-15.6
G8/G13	3'-...A**X**A...-2' 2'-...**X**AT...-3'	62.7	-4.3[b]	-88.5	-238	-17.6
G8/G12	3'-...A**X**A...-2' 2'-...TA**X**...-3'	59.2	-7.8[b]	-116	-325	-19.4
G8/G10	3'-...A**X**A...-2' 2'-...T**X**T...-3'	55.4	-11.6[b]	-86.8	-239	-15.7
G1/G14	3'-...ATA...-2' 2'-...**X**A**X**...-3'	55.0	-12.0[b]	-87.8	-242	-15.6
G3/G15	3'-...AAA...-2' 2'-...**XXX**...-3'	49.2	-6.6[c]	-81.4	-228	-13.6
G8/G14	3'-...A**X**A...-2' 2'-...**X**A**X**...-3'	56.3	+1.5[c]	-87.2	-240	-15.8
G8/G15	3'-...A**X**A...-2' 2'-...**XXX**...-3'	49.5	-5.3[c]	-82.3	-230	-13.7

[a] values for 5 µM samples in 1× PBS (100 mM NaCl, 10 mM phosphate, pH 7.0); 0.5 °C/min heating rate; a standard error of ±0.5 °C is assumed
[b] difference relative to unmodified reference G001G002 or [c] G008G013
blue = upstream, green = downstream, red = opposite, purple = same.

Regarding their thermodynamic characteristics, all of the different gBAM:gBAM dimer structures are essentially similar and comparable to the single-modified systems, except for the downstream dimer orientation in **G8/G12**. Here, the enthalpic as well as the entropic com-

ponent are increased, which means duplex formation is more exothermic and entropically less favored. The reason for this thermodynamic phenomenon is not easily explained but can to some extent be elucidated by 3D models for the dimeric systems (Figures 3.80 and 3.81).

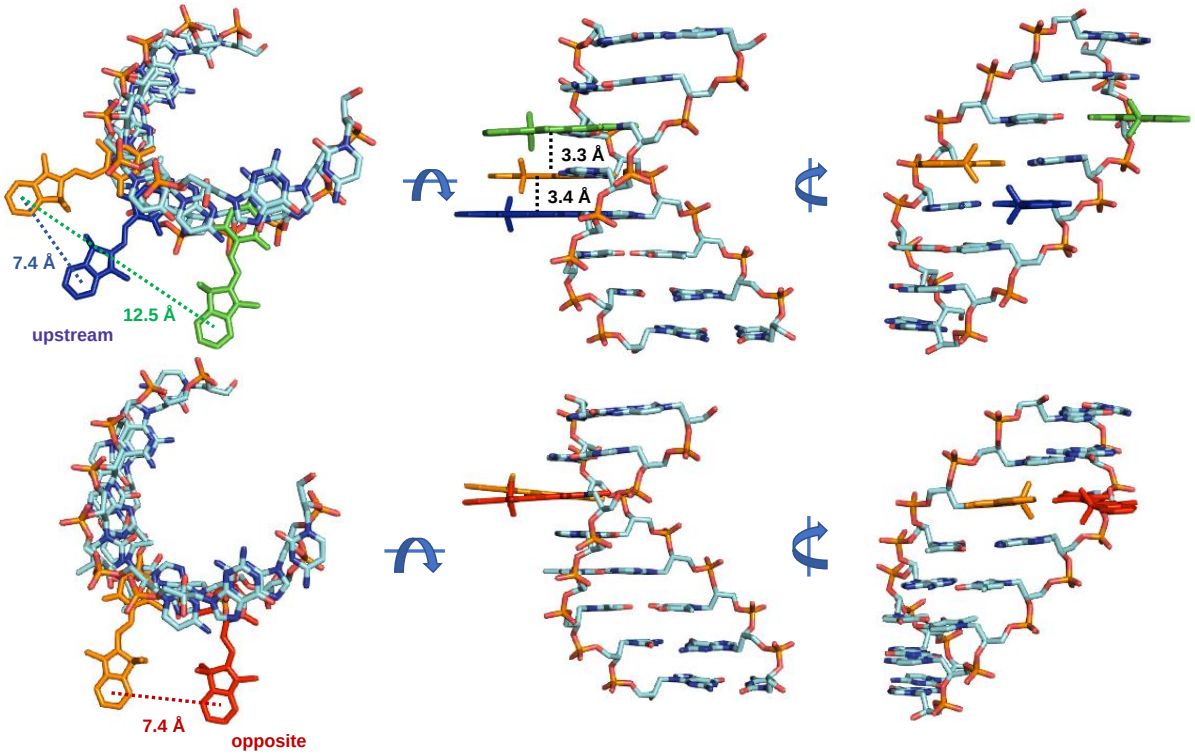

Figure 3.80: The side and top view of gBAM downstream (green), upstream (blue) and opposite (red) dimers within a 3D model of a GNA duplex reveals different interchromophore distances depending on the dimer orientation. Model taken from PDB 2JJA, processed with Pymol.

For these 3D models, a published GNA crystal structure (PDB: 2JJA) was used as the basic scaffold. Within this system, T nucleobases were systematically substituted by gBAM chromophores in the base pairing conformation with the chromophore pointing into the major groove. Although the underlying sequence for these model does not resemble the one in which gBAM was actually incorporated, it can still be used to illustrate the orientation of two chromophores toward each other in the GNA context. Obviously, the relative orientation and distance between the chromophore dramatically depends on their localization in the duplex structure. In Figure 3.80, the blue, green and red gBAM are located upstream, downstream and opposite from the orange gBAM, respectively. From both the side and the top view, the vertical distance to this particular gBAM in upstream or opposite direction is essentially the same with 3.3 Å (downstream) and 3.4 Å (upstream), which are suitable distances for efficient dipolar stacking interactions. However, the larger horizontal shift of the chromophores in the upstream chromophores might enable more efficient stacking interactions due to a higher conformational freedom of gBAM, while in the opposite dimer both chromophores are rather located in one plane which might prevent pronounced interchromophore interactions. The ab-

sence of stacking and excitonic coupling of the two gBAM is also expected for the downstream dimer, where the chromophores are with approximately 12 Å much farther apart compared to the upstream and opposite dimer with distances of approximately 7.5 Å. These findings are summarized in Figure 3.81 and were later indeed supported by spectroscopic analyses of the different double-substituted GNA systems (section 3.5.5.1).

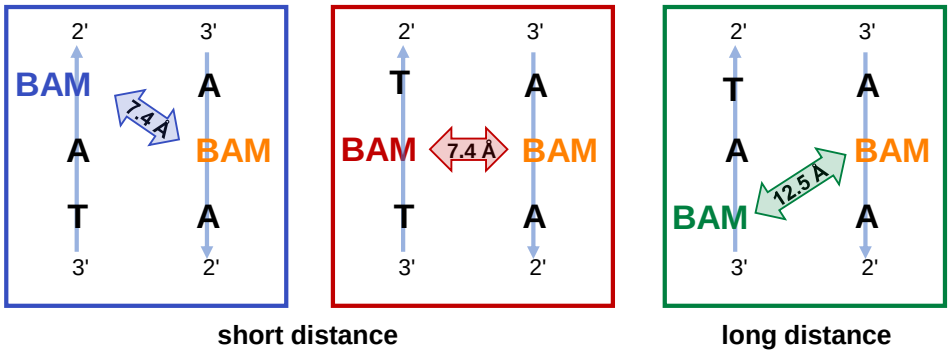

Figure 3.81: The side and top view of the gBAM opposite dimer within a 3D model of a GNA duplex reveals a similar interchromophore distance as for the upstream dimer while this distance is much larger for the downstream dimer. Model taken from PDB 2JJA, processed with Pymol.

The melting temperatures for the multiple-modified GNA duplexes **G3/G15**, **G8/G14** and **G8/G15** were compared to the second reference strand **G3/G11** with a AAA/TTT context in the center of the sequence. Since the two GNA systems with three consecutive gBAM in one strand were both thermally slightly destabilized and exhibited almost the same thermodynamic characteristics, the additional chromophore in the counterstrand in **G8/G15** does not have any negative impact on the duplex stability. Meanwhile, the duplex **G8/G14** with the three offset chromophores was surprisingly even more stable than the respective unmodified system **G3/G11**. These observed stabilizing effects can be ascribed to stabilizing stacking interactions between the hydrophobic, almost coplanar merocyanine chromophores and will be further discussed in the following section.

Besides the mixed duplex structures composed of canonical GNA nucleotides and gBAM, also gA_{10}/gT_{10} as well as $gA_{10}/gBAM_{10}$ systems and the respective 6mers were analyzed regarding their thermal stability. In Table 3.23, only the results for the 10mer duplex structures **G19/G20** and **G19/G21** are shown since the shorter variants showed to be thermally too unstable for melting point determinations. Compared to the unmodified reference duplex **G1/G2**, the GNA system composed of only the canonical GNA nucleosides gA and gT **G19/G20** showed a by 20 °C decreased melting temperature. This is explained by the shorter sequence and the lower thermal stability of A-T Watson-Crick base pairs compared to C-G base pairs.

Table 3.23: Thermal stability for gA_{10}/gT_{10} and gA_{10}/gX_{10} duplex structures.

Name	3'-sequence-2'	T_m[a] heat °C	T_m[a] cool °C
G19/G20	3'-AAAAAAAAAA-2' 2'-TTTTTTTTTT-3'	46.8	46.4
G19/G21	3'-AAAAAAAAAA-2' 2'-**XXXXXXXXXX**-3'	40.4	19.9

[a] values for 5 µM samples in 1× PBS (100 mM NaCl, 10 mM phosphate, pH 7.0); 0.5 °C/min heating rate; a standard error of ±0.5 °C is assumed
X = gBAM

If the melting temperatures obtained for the heating and cooling ramps are compared, the obtained values for **G19/G20** do not differ significantly (Figure 3.82). In contrast, for the $gA_{10}/gBAM_{10}$ duplex **G19/G21** the denaturation temperature was 40.4 °C when heating from 10 to 90 °C, while T_m was reduced to approximately 20 °C upon cooling. This strong hysteresis has been reported for many other multichromophoric systems such as the nucleated self-assembly of triple-stranded nucleic acid structures[442] and the assembly of DNA-conjugated squaraine oligomers.[443]

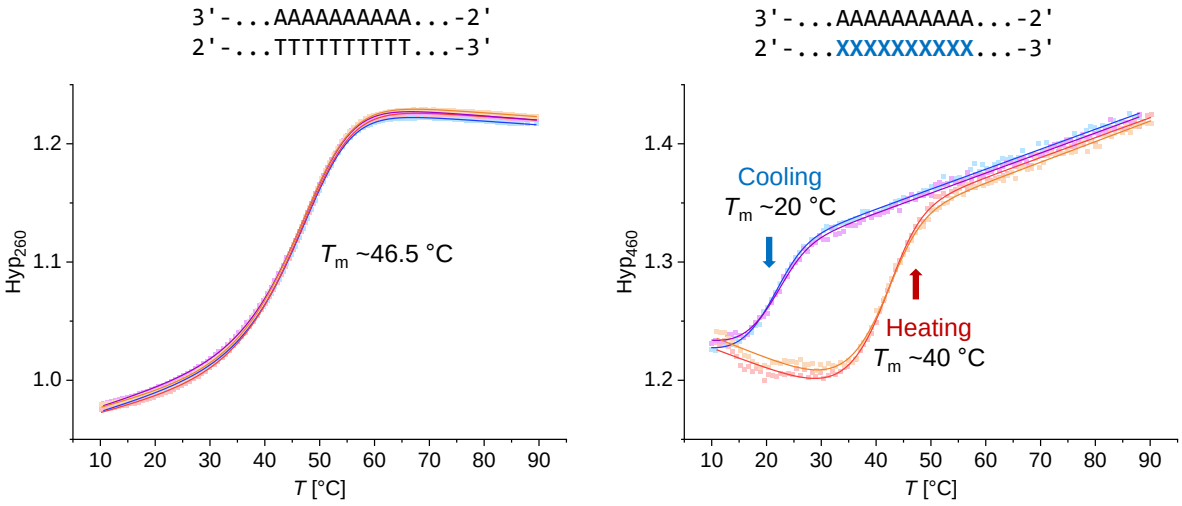

Figure 3.82: For the unmodified gA_{10}/gT_{10} duplex **G19/G20**, the same T_m value for heating and cooling ramps was obtained while the melting curves for the $gA_{10}/gBAM_{10}$ system **G19/G21** exhibited a strong hysteresis. Conditions: 5 µM samples, 1× PBS (100 mM NaCl, 10 mM phosphate, pH 7.0); 0.5 °C/min heating rate.

These self-assemble in a cooperative supramolecular polymerization process with a large kinetic barrier in the assembly or disassembly pathway, for example when self-assembly is dominated by homogeneous nucleation which can in the case of the $gA_{10}/gBAM_{10}$ system **G19/G21** be

explained by extensive inter- and intrastrand chromophore stacking interactions.[444] Therefore, it appears surprising that a double-helical structure is still formed for this short-sequence system and leads to the question how the chromophores are organized within this scaffold which will be further elucidated by CD and UVvis spectroscopy as well as AFM measurements.

In summary, also for gBAM dimers within the GNA scaffold the destabilizing effect on the oligonucleotide duplex strongly depends on the constitution of the dimers. The only slightly reduced melting temperatures for the upstream dimer **G8/G13** as well as the triple- and quadruple-modified samples **G3/G15**, **G8/G14** and **G8/G15** are likely induced by dipolar chromophore-chromophore stacking interactions while the 3D-model of the downstream and opposite dimers **G8/G12** and **G8/G10** revealed either too large interchromophore distances or a too pronounced steric hindrance for stacking. Besides the mixed canonical and modified sequences, also the gA_{10}/gT_{10} and $gA_{10}/gBAM_{10}$ systems **G19/G20** and **G19/G21** still form stable duplexes, while the latter one shows a strong hysteresis of about 20 °C in the UVvis melting curves.

3.5.5 Spectroscopic characterization of gBAM-modified GNA duplexes

For investigations on the behavior of gBAM in the GNA scaffold, the single- and multiple-modified oligonucleotide duplex structures were studied by different spectroscopic methods. In addition, AFM images for the $gA_{10}/gBAM_{10}$ system were recorded and are discussed in the following section with regard to the formation of supramolecular complexes.

3.5.5.1 Spectroscopic characterization of single- and double-gBAM-modified GNA systems

In the following, the single-modified GNA system reflecting the spectroscopic behavior of the monomeric gBAM is compared to the different gBAM dimers within the GNA scaffold as well as to the triple- and quadruple-modified structures with respect to the absorption and fluorescence behavior.

The temperature-dependent absorption and fluorescence spectra for single-gBAM-modified GNA show only minimal changes with increasing temperature (Figure 3.83). Therefore, similar as for DNA and RNA scaffolds, also in the GNA context the spectroscopic behavior of BAM is almost not influenced by stacking interactions with neighboring nucleobases. The decrease in fluorescence intensity at elevated temperatures can also here be attributed to the larger proportion of non-radiative deactivation pathways through rotation around the polymethine bridge.

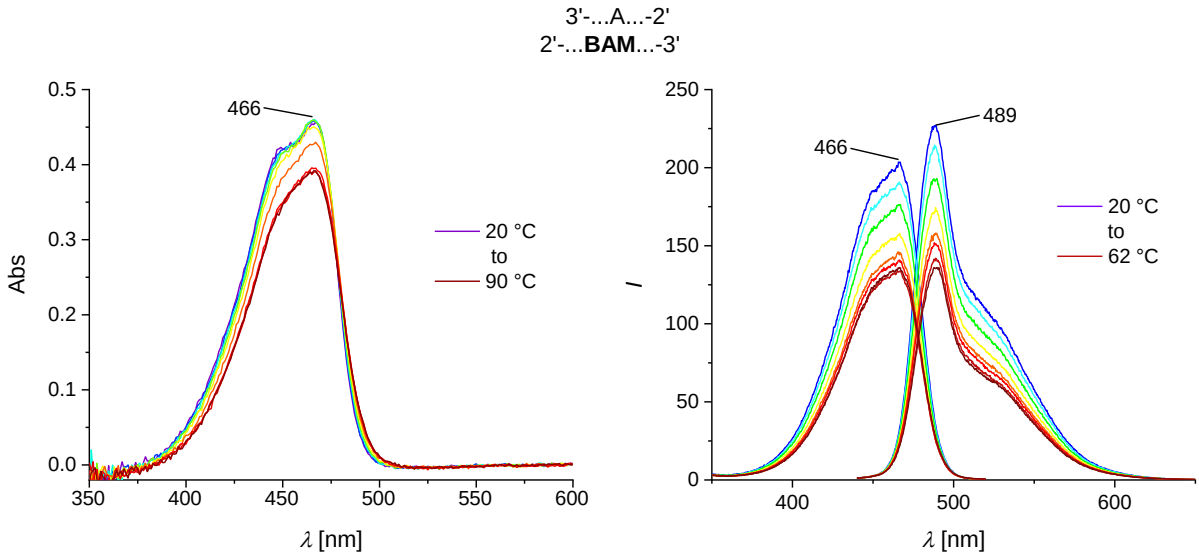

Figure 3.83: Temperature-dependent absorption (left) and fluorescence (right) spectra for a single-gBAM-modified GNA 12mer duplex. Conditions: 1 or 5 μM samples in 1× PBS (100 mM NaCl, 10 mM phosphate, pH 7.0), for fluorescence excitation at 420 nm, emission at 540 nm.

If not only one but two gBAM chromophores are incorporated into the GNA duplex, different spectroscopic patterns are observed (Figure 3.84). For the system with downstream as well as opposite chromophore orientation **G8/G12** and **G8/G10** as well as the dimer in the same strand **G1/G14** two maxima at approximately 450 and 466 nm of almost equal intensity are detected, resembling the absorption behavior of the monomeric gBAM. The absorption signature of the upstream dimer **G8/G13** differs from the three other orientations: here, again a sharp, blue-shifted band is visible which vanishes at temperatures above the melting point, indicating H-type aggregation due to dipolar chromophore-chromophore interactions. This can be explained by the previously discussed 3D model structure where both chromophores are arranged in a parallel fashion, giving rise to the observed spectroscopic pattern. The formation of gBAM:gBAM dimers dependent on the oligonucleotide scaffold is further supported by the superimposable melting curves at the nucleobase and the chromophore absorption of 260 and 460 nm. Therefore, in contrast to the already discussed DNA and RNA scaffolds, in the GNA context attractive dipolar stacking interactions between two merocyanine chromophores are present in addition to Watson-Crick base pairing of the barbituric acid moiety with A. This requires the two chromophores to be in close proximity and the duplex structure to provide sufficient flexibility for stacking interactions of the two gBAM in the major groove. The presence of H-type aggregates in the absorption is in accordance with the high melting temperature observed for the upstream duplex **G8/G13** where the presumed disturbance of the duplex structure is partially compensated by the stabilizing chromophore stacking interactions. However, since the acyclic GNA backbone is much more flexible compared to the ones based on ribose, the overall duplex structure is expected to be less disrupted and is therefore destabilized to a lower extent.

The CD spectra recorded for the four different gBAM dimers all show the typical pattern for GNA duplex structures in the nucleobase absorption region between 200 and 300 nm, proving the presence of an intact helix (Figure 3.84). In the chromophore absorption range, weak negative CD couplets are observed for the opposite and upstream dimers **G8/G10** and **G8/G13**, while asymmetric positive Cotton effects are detected for the chromophores in downstream direction in **G8/G12** or in the same strand in **G1/G14**. These trends cannot easily be rationalized in the absence of a 3D structure but indicate excitonic gBAM:gBAM interactions of different strength for all of the modified GNA duplex structures.

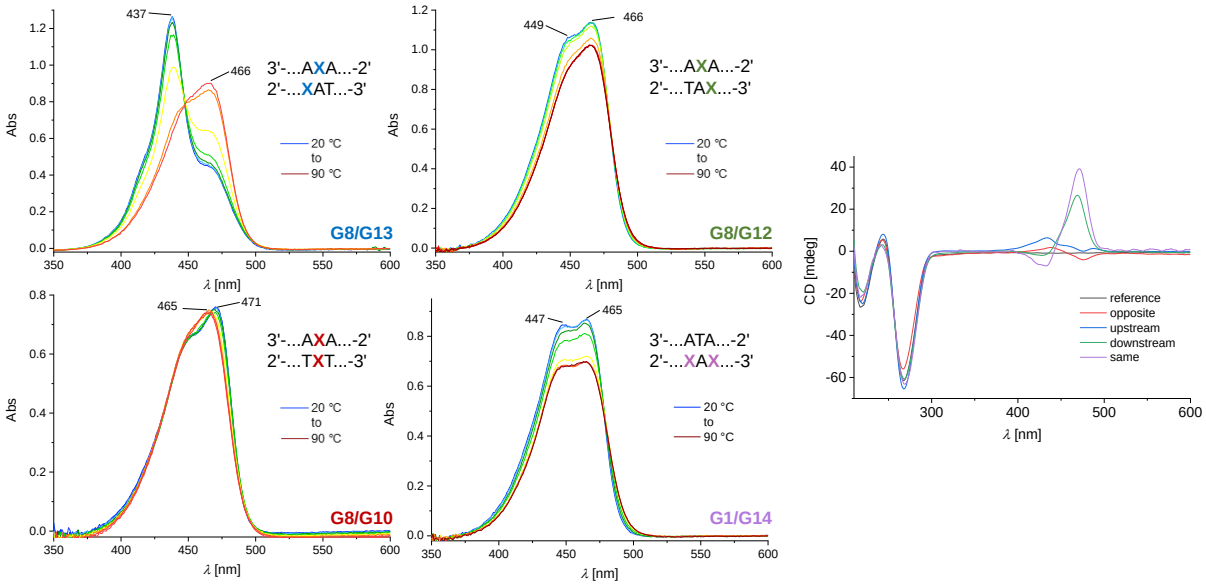

Figure 3.84: Temperature-dependent absorption and CD spectra for double-gBAM-modified GNA 12mer duplexes in upstream (blue), downstream (green) or opposite (red) orientation or in the same strand (purple). Conditions: 5 µM samples in 1× PBS (100 mM NaCl, 10 mM phosphate, pH 7.0).

The emission and excitation spectra for all of the dimers except the upstream one **G8/G13** reflect the monomer fluorescence of non-interacting chromophores with decreased fluorescence intensity at higher temperatures. In contrast, the upstream dimer **G8/G13** behaves totally different: luminescence arising from excitonically coupled chromophores in H-type assemblies is only detected as a weak band at 437 nm in the excitation, but not in the emission spectrum. Interestingly, the fluorescence intensity for this dimer increases at elevated temperatures, being more than twofold higher at 62 °C compared to room temperature. The gBAM fluorescence is therefore quenched in the hybridized duplex, which has not yet been observed for any other merocyanine-modified oligonucleotide scaffold in this thesis. However, the same effect has been described *vice versa* for structurally similar thiazole-orange based exciton-controlled hybridization-sensitive fluorescence emission (ECHO) probes (Figure 3.86). Here, two thiazole orange derivatives are covalently linked, showing hybridization-dependent absorption shifts and emission switching regulated by H-type aggregation.[445]

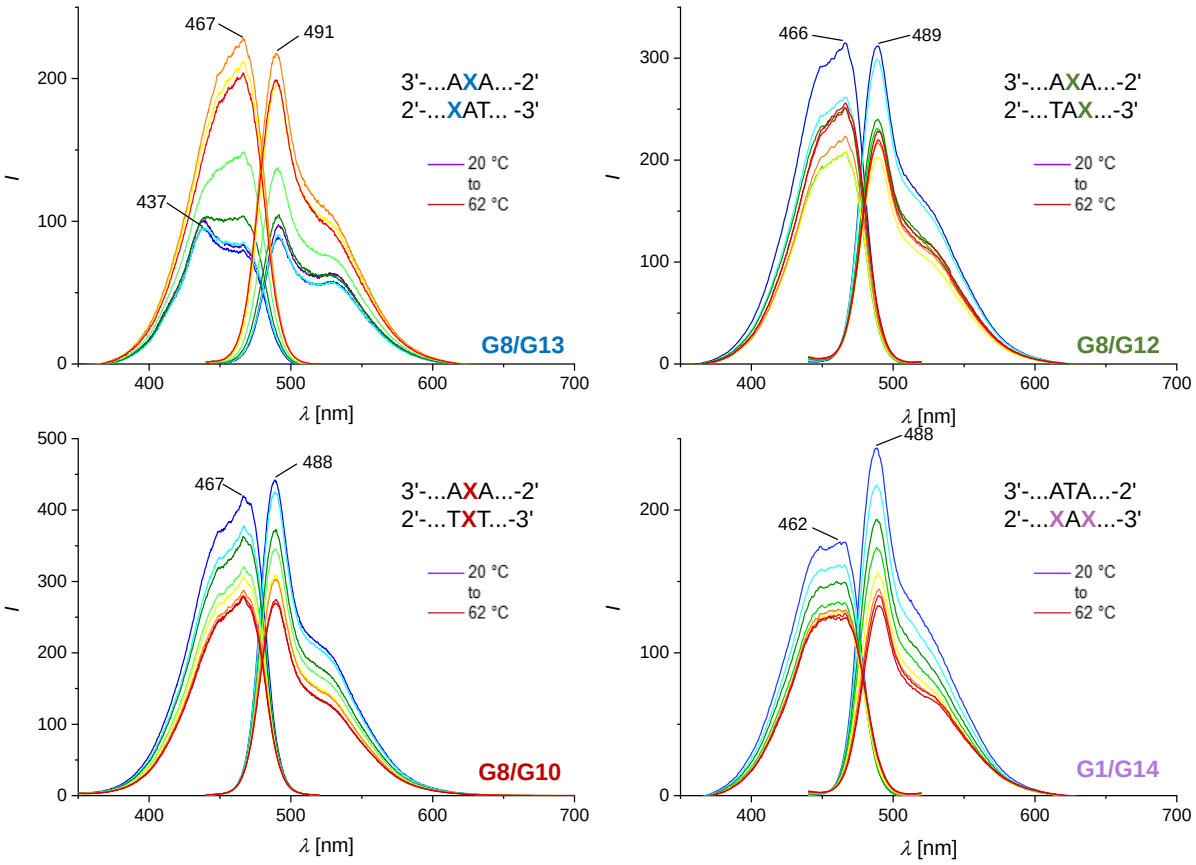

Figure 3.85: Temperature-dependent fluorescence spectra for double-gBAM-modified GNA 12mer duplexes in upstream (blue), downstream (green) and opposite (red) orientation as well as with the two gBAM in one strand (purple). All gBAM-modified duplex structures show monomer fluorescence, except for the upstream case **G8/G13** where a weak exciton fluorescence is observed. Conditions: 1 µM samples in 1× PBS (100 mM NaCl, 10 mM phosphate, pH 7.0), excitation at 420 nm, emission at 540 nm.

ECHO probes can serve as a fluorescence detection readout for target oligonucleotides for a variety of different biological applications.[359,445,446] In the single strand, the two chromophores form a parallel stack and show fluorescence quenching by the excitonic coupling effect.

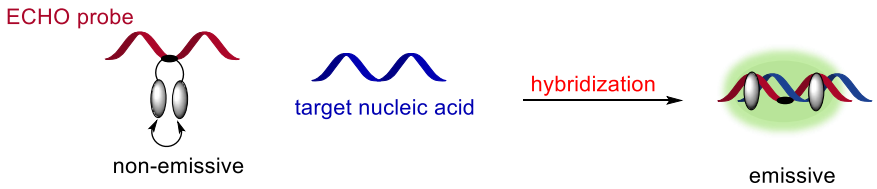

Figure 3.86: Thiazole-orange based exciton-controlled hybridization-sensitive fluorescence emission (ECHO) probes show hybridization-sensitive fluorescence behavior, suitable for different biological applications.[445]

The chromophore dimer exhibits a split excited state, where only transition to the upper excitonic states is allowed for H-aggregates, but this rapidly relaxes into the lower excitonic state. Since from there the transition into the ground state is theoretically forbidden, the aggregate

stays trapped in a state with strongly suppressed emission. Upon hybridization of the ECHO probe with the target oligonucleotide, the H-type aggregate is broken up and emission of thiazole orange due to intercalation into the duplex is detected.

The situation for the upstream gBAM:gBAM dimer **G8/G13** reported here is similar, although reversed: in the hybridized duplex, the two chromophores are excitonically coupled, leading to the formation of a non-emissive H-type aggregate by contact quenching. At elevated temperatures, this dimer is disrupted, giving rise to monomer emission which is still low due to non-radiative deactivation but enhanced compared to the quenched dimer emission.

The spectroscopic results obtained for double-gBAM-modified GNA structures provide an interesting additional insight into the spectroscopic behavior of merocyanine chromophores in different oligonucleotide scaffolds. In contrast to nucleic acids with a natural ribose or deoxyribose backbone, gBAM is arranged in parallel, base pairing dimers when covalently attached to the acyclic GNA backbone, forming non-emissive H-type assemblies. Since gBAM interferes only slightly with the stability of the GNA helix, also structures with three and four modifications were analyzed and are discussed in the following part.

3.5.5.2 Spectroscopic characterization of triple- and quadruple-gBAM-modified GNA systems

The triple- and quadruple-gBAM-modified GNA duplex structures were designed to include intra- as well as interstrand multichromophore assemblies to provide additional insight into hybridization-independent chromophore interactions. Indeed, the temperature-dependent absorption and fluorescence spectra exhibit interesting features.

For all of the GNA structures with three or four gBAM chromophores, the formation of H-type assemblies is observed in the absorption spectra of the hybridized duplexes, proven by the sharp, blue-shifted band at around 440 nm (Figure 3.87). For the **G8/G14** duplex, which combines the up- and downstream dimer, this hypsochromically shifted absorption maximum decreases in intensity with increasing temperature, with only the monomer absorption present at temperatures above the duplex melting point. For the other two systems **G3/G15** and **G8/G15** with three gBAM chromophores consecutively incorporated into one strand, the aggregate absorption does not vanish, even not at 90 °C, which is well above the denaturation temperature of these duplexes. Therefore, the blue-shifted absorption maximum is attributed to intrastrand chromophore stacking which is still present in the single strand. The two triple-gBAM-modified duplexes **G3/G15** and **G8/G14** exhibited similar spectroscopic characteristics, showing the minor influence of the additional fourth chromophore opposite the intrastrand gBAM trimer in **G8/G15**.

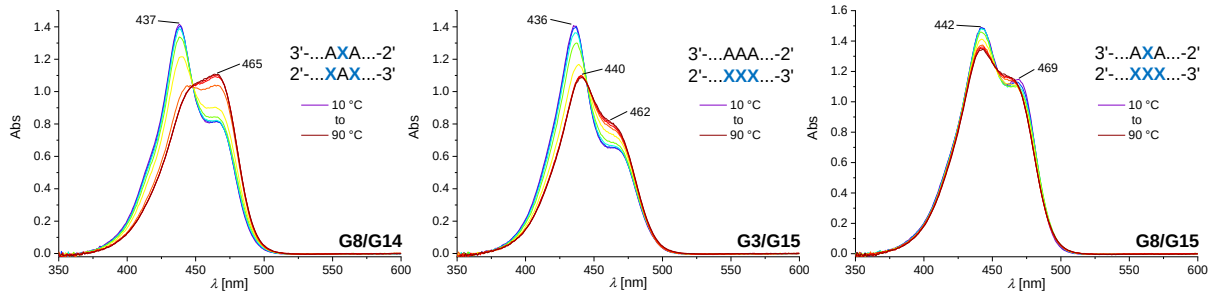

Figure 3.87: Temperature-dependent absorption spectra for a triple- and quadruple-gBAM-modified GNA 12mer duplexes **G8/G14** (left), **G3/G15** (middle) and **G8/G15** (right). Conditions: 5 µM samples in 1× PBS (100 mM NaCl, 10 mM phosphate, pH 7.0).

The fluorescence spectra recorded for these three multiple-modified GNA systems fit to the respective absorption spectra (Figure 3.88). The fluorescence pattern of the GNA duplex **G8/G14** with the gBAM each displaced by one position is akin to the excitation and emission pattern of the upstream gBAM dimer **G8/G13** with weak excitonic fluorescence in the hybridized state attributed to contact quenching, and enhanced intensity for the single strands.

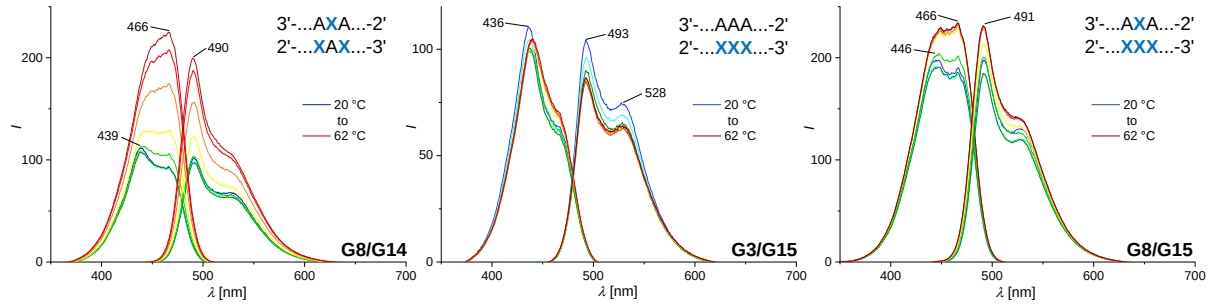

Figure 3.88: Temperature-dependent fluorescence spectra for triple- and quadruple-gBAM-modified GNA 12mer duplexes. Conditions: 1 µM samples in 1× PBS (100 mM NaCl, 10 mM phosphate, pH 7.0), excitation at 420 nm, emission at 540 nm.

No significant change of the fluorescence behavior is observed for the intrastrand gBAM trimer **G3/G15**, as expected. Since in this case the chromophore-chromophore interactions are not disturbed upon dehybridization, the spectral shape and intensity do not show remarkable differences below and above the duplex melting temperature, indicating extensive intrastrand stacking interactions. Therefore, also for the quadruple-modified GNA system **G8/G15** only minor changes are detected, such as a slight increase of the luminescence intensity and monomer fluorescence also at elevated temperatures.

Due to the presence of the strong intrastrand stacking it was assumed that pure gBAM oligonucleotides might give access to spectroscopically unique properties. Therefore, the spectral features of the GNA 10mers presented in Table 3.20 were surveyed by absorption, fluorescence and CD spectroscopy as well as by AFM.

3.5.5.3 Investigations on multiple-gBAM-modified GNA systems

To evaluate the influence of Watson-Crick base pair formation on the spectroscopic properties of the gBAM 10mer **G21**, the temperature-dependent fluorescence of this single strands was compared to the hybridized duplex **G19/G21** (Figure 3.89a). The concentration of the **G21** stock solution was calculated with Lambert-Beer from the UVvis absorbance and was diluted with 5× PBS and water to the required concentration.

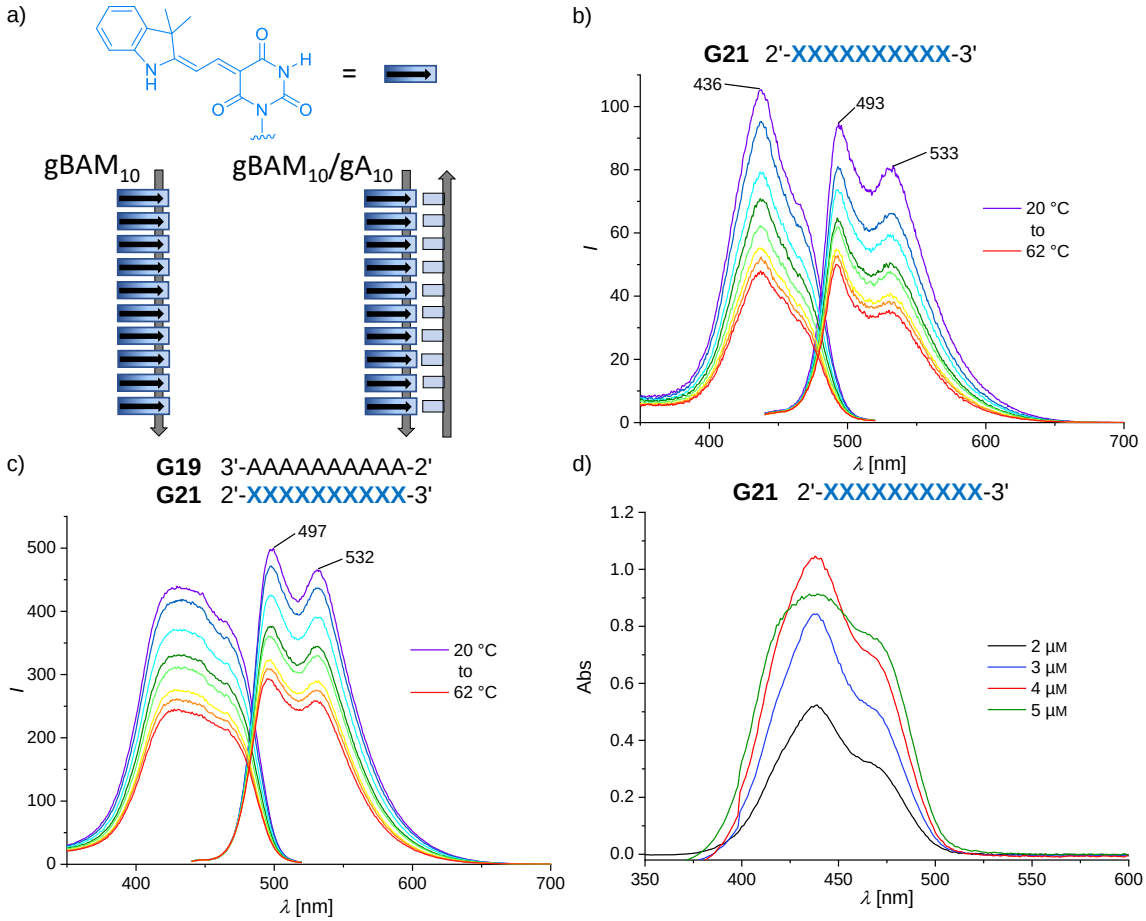

Figure 3.89: Schematic structure of the $gBAM_{10}$ single strand **G21** and duplex $gA_{10}/gBAM_{10}$ (**G19/G21**, a), temperature-dependent fluorescence spectra for the the $gBAM_{10}$ single strand **G21** (b) as a well as the $gA_{10}/gBAM_{10}$ duplex **G19/G21** (c) and concentration-dependent absorption spectra for the $gBAM_{10}$ single strand **G21** (d). Samples in 1× PBS (100 mM NaCl, 10 mM phosphate, pH 7.0), excitation at 420 nm, emission at 540 nm.

The $gBAM_{10}$ single strand **G21** shows an only weak fluorescence, especially when compared to the modified DNA and RNA dimer systems, although the total chromophore concentration is five times higher (Figure 3.89b). This is attributed to contact quenching by intrastrand excitonic coupling in H-type aggregates, proven by the compared to the monomer blue-shifted excitation maximum at 436 nm and the red-shifted emission band at 533 nm. These assemblies are not disrupted at elevated temperatures, indicating the high thermal stability of the underlying dipolar interactions. For the hybridized gBAM 10mer **G19/G21**, very similar

spectral features are observed (Figure 3.89c). However, only a broad, structureless excitation band lacking a pronounced maximum is obtained, which hints to a combination of different stacking conformations and stacking modes within this heavily modified short GNA duplex.

H-type aggregates are also visible in the concentration-dependent absorption spectrum, showing a maximum at 435 nm and a shoulder of lower intensity at the monomer absorption of 460 nm (Figure 3.89d). Here, a linear rise of the absorbance is observed when the duplex concentration is increased from 2 to 4 µM. At higher concentrations, however, the absorption band is decreased in intensity and significantly broadened, indicating further conglomeration of the hydrophobic single strands.

The formation of such higher-order aggregates is supported by concentration-dependent CD spectra with a complex CD pattern observed for the gBAM$_{10}$ single strand **G21** (Figure 3.90a).

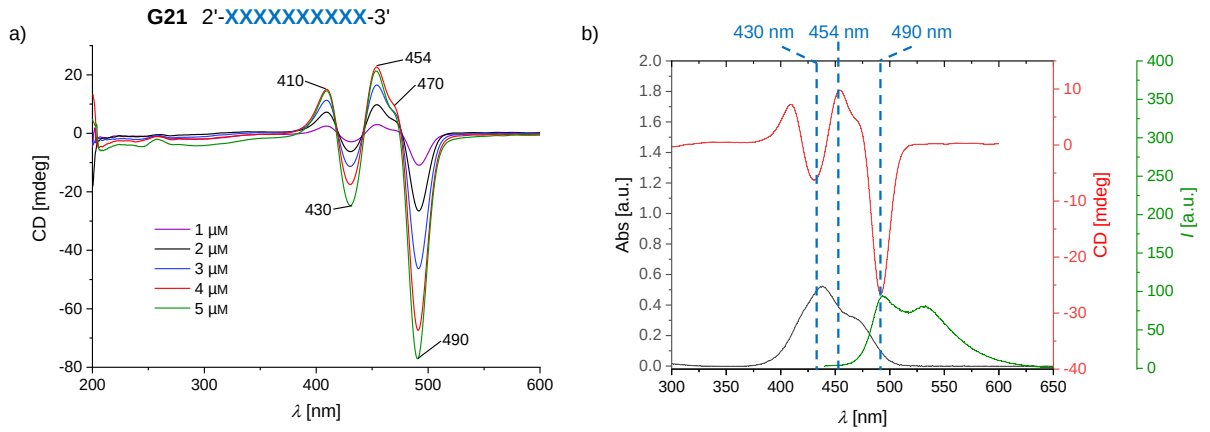

Figure 3.90: Concentration-dependent CD spectra for the gBAM$_{10}$mer **G21** (a) and overlay with the absorption and emission spectra (b). Samples measured in 1× PBS (100 mM NaCl, 10 mM phosphate, pH 7.0).

Surprisingly, several Cotton effects are evident at 410, 430, 454, 470 and 490 nm, respectively. The two minima as well as the local maximum at 454 nm are assigned to the absorption and blue-shifted emission maxima (Figure 3.90b). In the absorption range of 380 to 540 nm, the overall integral of the negative signal is notably enhanced by a factor of three compared to the overall integral of the positive signal and this ratio remains constant for all of the concentrations investigated. The detection of such well-defined Cotton effects is astonishing since it shows that even the gBAM$_{10}$ single strand **G21** adopts an organized conformation. Exciton coupled CD spectra of H-type aggregates are usually of symmetrical shape with comparable intensities of positive and negative CD couplets, which can be described under consideration of only the main transitions. The complexity of the CD pattern for gBAM$_{10}$ (**G21**) is therefore presumably attributed to additional J-type coupling interactions which leads to a narrowing and substantial increase of the oscillator strength of the negative low energy band at 490 nm, similarly described for Cy5-Cy5 dimers in a DNA scaffold.[370]

Although the existence of J-type coupled chromophores cannot be confirmed by spectroscopic measurements in the present case, it is rationalized by the qualitative 3D model of a GNA duplex with multiple gBAM in one strand, exemplarily shown with four gBAM in Figure 3.91a. In this structure, the chromophores are oriented perpendicular to the aggregate axis and are not aligned perfectly parallel but inclined, which is the prerequisite for J-type coupling interactions.

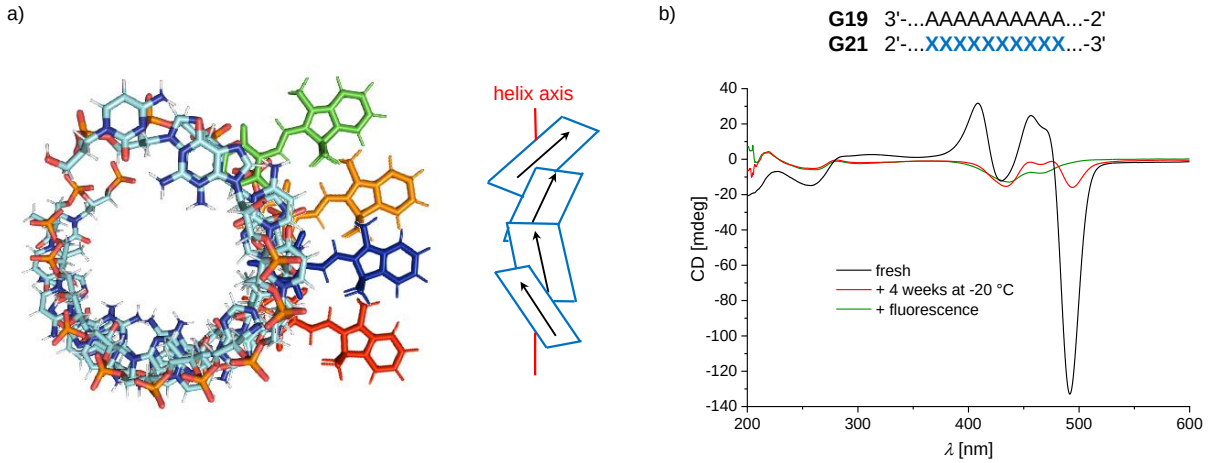

Figure 3.91: The structural model for a duplex with multiple gBAM in one strand and the schematic representation with the dipole moments illustrated as arrows show the slight shift of the chromophores with respect to each other (a) along the helix axis (red).[447] In the CD spectrum of the $gBAM_{10}/gA_{10}$ duplex **G19/G21** the same pattern as for the single strand **G21** is observed, in addition to an aging effect over time (b). Samples measured in 1× PBS (100 mM NaCl, 10 mM phosphate, pH 7.0).

Here, it has to be taken into account that the gBAM 10mer **G21** certainly does not form a duplex structure but rather a nanoparticle-type aggregate with the monomers helically arranged with respect to the aggregate axis, leading to spectroscopically active assemblies. However, in this type of assembly a combination of H- and J-type coupling is expected due to the multitude of possible chromophore orientations.

Besides for the $gBAM_{10}$ single strand **G21** also for the 10mer duplex $gBAM_{10}/gA_{10}$ **G19/G21** CD spectra were recorded (Figure 3.91b). Here, the CD couplet pattern matched those of the single strand **G21** and only a weak typical pattern in the nucleobase absorption region indicating duplex formation was detected. This observation is in accordance with the large hysteresis of the melting curves and supports the assumption that the self-assembly of $gBAM_{10}$ is dominated by homogeneous nucleation while formation of a duplex by Watson-Crick-type base pairing only plays a minor rule. Surprisingly, this short GNA duplex experienced a reproducable aging effect by storage at -20 °C for four weeks: all of the signals showed a significant loss of intensity, with the positive Cotton effect at 410 nm completely disappearing. This observation, which was even enhanced after additional fluorescence measurement, is not easily explained but might be caused by further aggregation to supramolecular structures and hereby

precipitation of the optically active polymers.

The formation of nanoparticles was further investigated by AFM measurements. AFM is a suitable method to obtain high resolution images of surface textures and provides the possibility to measure the height and size of macromolecular assemblies, unraveling intermolecular forces at nanoscale level.[448] Here, AFM images of freshly prepared $gBAM_{10}$ (**G21**) in water as well as 1× PBS spin-coated on a mica surface pretreated with $NiCl_2$ to promote sample adhesion were taken.

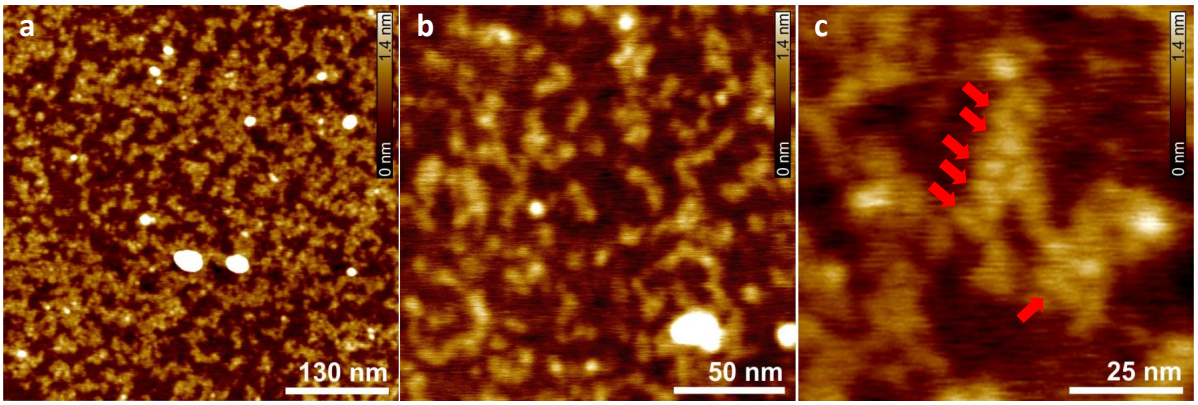

Figure 3.92: Height AFM images of $gBAM_{10}$ (**G21**) spin-coated on a mica surface pretreated with $NiCl_2$ revealed the formation of short spherical particles and rod-like aggregates, marked by red arrows. Conditions: 18 µM sample in water, silicon cantilever with a resonance frequency of approximately 70 kHz and a spring constant of approximately 1.7 Nm^{-1}. AFM measurements were conducted by Dr. Vladimir Stepanenko.

Height AFM images for $gBAM_{10}$ (**G21**) in water revealed the presence of a thin film consisting of short spherical nanoparticles with a diameter of 5.0±0.5 nm and rod-like aggregates with a height of 0.55 to 0.65 nm and a length of up to 7.5 nm, indicated by red arrows (Figure 3.92). It has to be noted that the AFM resolution is limited by the tip size of the cantilever, which was in this case around 6 nm and therefore aggregates shorter than this appear as spherical particles. Furthermore, the white spots correspond to a second aggregate layer. In addition, it cannot be excluded that the apolar GNA 10mer **G21** exists in a collapsed state due to strong adhesion to the substrate surface. However, these AFM images are in accordance with the already conducted spectroscopic measurements, suggesting strong intrastrand chromophore stacking leading to nucleation of the single strands.

Besides AFM images of $gBAM_{10}$ (**G21**) spin-coated on mica, additional ones for the same single strand on mica in a fluid cell were recorded. Also here, the mica surface was pretreated with $NiCl_2$ and after incubation with the modified single strand for five minutes the adsorption of small, particle-like aggregates marked by red arrows was observed in the phase image (Figure 3.93). The height of these particles varied between 0.55 and 0.75 nm and the lateral diameter was estimated with 5.0 to 6.0 nm.

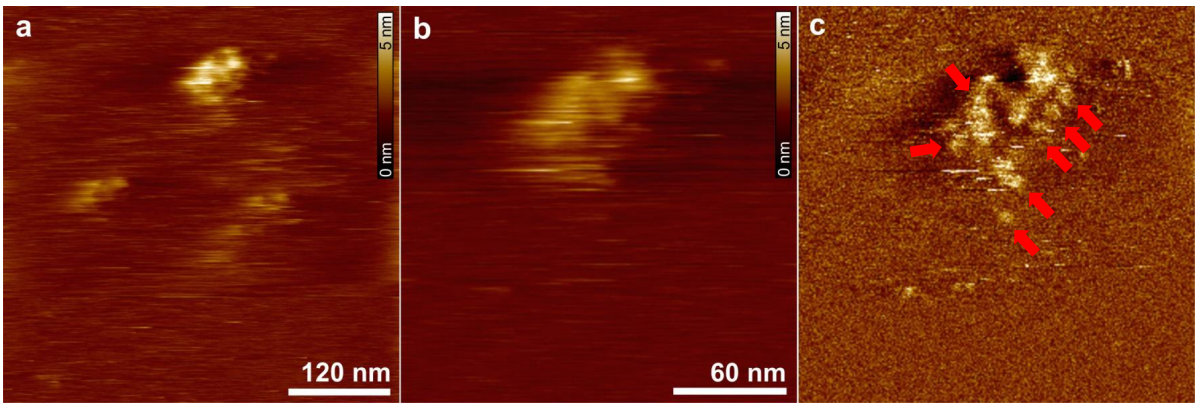

Figure 3.93: Height (a, b) and phase (c) AFM images of $gBAM_{10}$ in 1× PBS on mica in a fluid cell shows the adsorption of particle-like aggregates, indicated by red arrows. Conditions: 9 µM sample in 1× PBS, silicon cantilever with a resonance frequency of approximately 25 to 65 kHz and a spring constant of approximately 0.12 to 0.35 Nm^{-1}. AFM measurements were conducted by Dr. Vladimir Stepanenko.

The sizes measured for the formed nanoparticles on mica clearly indicate aggregation of $gBAM_{10}$ (**G21**). If this single strand were present in the completely unfolded state, which is according to spectroscopic results not the case, it would have a length of approximately 75 Å. This matches the measured diameter of the uniformly shaped nanoparticles, indicating the formation of small supramolecular structures containing more than one molecule.

In conclusion, gBAM-modified GNA oligonucleotides exhibit unique spectroscopic patterns differing from the ones observed for the canonical DNA and RNA scaffolds. This is attributed to the distinct structural parameters of the GNA duplex which facilitate the formation of gBAM:A Watson-Crick base pairs. The presence of gBAM dimers can, dependent on the dimer orientation, lead to a stabilized duplex structure by dipolar interactions between parallelly aligned chromophores. This is in stark contrast to the dimeric structures expected in DNA and RNA and gives rise to non-emissive H-type dimers, which are also found in triple- and quadruple-modified GNA duplexes. In addition, short 10mers composed of only gBAM showed surprisingly complex CD patterns, presumably caused by a combination of H- and J-type coupled chromophores upon formation of spherical and rod-like nanoparticles as suggested by AFM images.

The unique spectroscopic features observed for multiple-modified GNA structures led to the design of DNA-gBAM hybrid structures. With DNA providing a stable oligonucleotide scaffold recognized by enzymes, gBAM chromophores were incorporated into DNA sequences of different lengths to further investigate the behavior of this merocyanine with the flexible acyclic backbone within preorganized structures. The synthesis of these systems as well as their spectroscopic characterization and additional experiments are discussed in the following section.

3.6 Multiple-modified gBAM-DNA hybrid structures

To gain further insight into the behavior of GNA-based merocyanine chromophores within the DNA scaffold, the phosphoramidites of the six different gBAM variants described in section 3.5.2, namely gmBAM (**87**), gmBAM^{b} (**88**), gBAM^{F} (**89**), gBAM^{OMe} (**90**) as well as (*S*)- and (*R*)-gBAM (**81** and **82**), were incorporated into DNA 12mers and also 17mers. With these strands, duplex structures containing up to ten gBAM chromophores were successfully constructed and analyzed by thermodynamic and spectroscopic means. In addition, (*S*)-gBAM, which is in the following only named gBAM, was incorporated in the core or as overhangs at the 3'- and 5'-ends of the Dickerson-Drew dodecamer (DDD) for structural probing and the formation of higher-order molecular aggregates by dipolar intrastrand interactions mediated by non-base paired gBAM. Since the chemical synthesis toward the different gBAM phosphoramidites has already been discussed, the next part of this thesis deals with the design and synthesis of gBAM-modified DNA oligonucleotides.

3.6.1 Design and synthesis of gBAM-containing DNA oligonucleotides

All gBAM-modified DNA strands were synthesized by solid-phase synthesis; cleavage from the solid support and deprotection were achieved under ultramild conditions by overnight incubation in aq. ammonia at 37 °C. Hereby, oligonucleotides modified with each of the six gBAM variants were obtained in high yields and excellent quality without the formation of major side products. All strands except for those with gBAM at the 3'- or 5'-end were synthesized in DMT-off mode while end-gBAM modified oligonucleotides had to be treated with 50% acetic acid after basic deprotection to remove the trityl protecting group. Furthermore, no chromophore degradation under basic conditions was observed in the case of the gmBAM^{b} dye, which is in contrast to the respective rBAM^{b} and dBAM^{b}-modified RNA and DNA systems and attributed to the *N*-methyl group providing a better chromophore stability.

3.6.1.1 Single-modified DNA 12mers with different gBAM variants

All of the single-modified GNA-DNA hybrid strands are summarized in Table 3.24, with the respective modifications shown in color. Besides the different gBAM variants, also gT was incoporated into two DNA strands for a better comparison of thermodynamic stabilities. (*S*)-gBAM was incorporated into four different positions in these single-modified oligonucleotides, providing access to all of the three chromophore dimers already described for pure DNA, RNA and GNA systems. All of the other gBAM variants were implemented into at least two different strands for spectroscopic analyses.

Table 3.24: Sequences, yields and masses for single-modified DNA 12 nt oligomers obtained by solid phase synthesis. Modified nucleobases are colored.

Name	5'-sequence-3'	yield[a] nmol	*M* calc. g mol^{-1}	*M* meas.[b] g mol^{-1}
DG1	GATGA**T**AGCTAG	210	3665.65920	3665.70344
DG2	GATGA**X**AGCTAG	158	3850.74327	3850.77673
DG3	GATGA**X**AGCTAG	170	3864.75837	3864.76701
DG4	GATGA**X**AGCTAG	154	3854.68349	3854.67628
DG5	GATGA**X**AGCTAG	152	3868.73384	3868.73784
DG6	GATGA**X**AGCTAG	156	3880.75383	3880.78272
DG7	GATGA**X**AGCTAG	206	3850.74272	3850.75056
DG8	CTAGC**T**ATCATC	232	3536.62919	3536.66762
DG9	CTAGC**X**ATCATC	216	3721.71325	3721.73845
DG10	CTAGC**X**ATCATC	121	3735.72890	3735.72627
DG11	CTAGC**X**ATCATC	149	3725.65348	3725.66988
DG12	CTAGC**X**ATCATC	316	3739.70383	3739.71323
DG13	CTAGC**X**ATCATC	197	3751.72382	3751.75157
DG14	CTAGC**X**ATCATC	126	3721.71271	3721.70606
DG15	CTAGCT**X**TCATC	196	3712.70114	3712.72352
DG16	CTAGCT**X**TCATC	121	3726.71679	3726.73631
DG17	CTAGCT**X**TCATC	77	3716.64191	3716.61563
DG18	CTAGCT**X**TCATC	193	3712.70114	3712.69100
DG19	CTAGCTA**X**CATC	166	3721.71271	3721.71058

[a] 600-800 nmol synthesis scale
[b] monoisotopic masses obtained by charge deconvolution of the raw spectra
T = gT, **X** = gBAM, **X** = gmBAM, **X** = gmBAM^{b}, **X** = gBAM^{F}, **X** = gBAM^{OMe}, **X** = (*S*)-gBAM.

3.6.1.2 Multiple-modified gBAM-DNA hybrid 12mers

In addition to single-gBAM-modified DNA oligonucleotides, also those with successive substitution of every T in the sequence by the merocyanine nucleobase surrogate have been synthesized, leading to single strands with up to four gBAM (Table 3.25). Furthermore, to compare the spectral features of these strands with the individual gBAM nucleotides each separated by at least one nucleotide, one DNA strand with three consecutive gBAM in the sequence center was designed. For this purpose, also the unmodified sequences **D19** and **D20** for the canonical, base paired duplex were generated.

Table 3.25: Sequences, yields and masses for DNA 12 nt oligomers with multiple gBAM, obtained by solid phase synthesis. Modified nucleobases are colored.

Name	5'-sequence-3'	yield[a] nmol	*M* calc. g mol^{-1}	*M* meas.[b] g mol^{-1}
D19	GATGAAAGCTAG	149	3716.68079	3716.68086
D20	CTAGCTTTCATC	190	3569.62764	3569.63160
DG20	CTAGC**X**A**X**CATC	129	3864.78620	3864.80093
DG21	GA**X**GA**X**AGC**X**AG	157	4136.89026	4136.88583
DG22	C**X**AGC**X**A**X**CA**X**C	158	4150.93375	4150.98998
DG23	CTAGC**XXX**CATC	138	3998.84814	3998.84185

[a] 600-800 nmol synthesis scale
[b] monoisotopic masses obtained by charge deconvolution of the raw spectra
X = gBAM.

gBAM was not only incorporated into the designed 12mer sequences used for all oligonucleotide scaffolds within this thesis, but also into the DDD (Table 3.26). This palindromic sequence is often used as a model system as it is easy to crystallize and present in either bimolecular duplex or monomolecular hairpin conformation, depending on the strand and salt concentration.[449,450]

Table 3.26: Sequences, yields and masses for unmodified and gBAM-modified DDD DNA strands obtained by solid phase synthesis. Modified nucleosides are colored.

Name	5'-sequence-3'	yield[a] nmol	*M* calc. g mol^{-1}	*M* meas.[b] g mol^{-1}
D21	CGCGAATTCGCG	203	3644.64709	3644.63939
D22	CGCG**Y**ATTCGCG	72	3510.62644	3510.61436
DG24	CGCGAAT**X**CGCG	230	3787.72058	3787.72750
DG25	CGCGAA**X**TCGCG	188	3787.72058	3787.74733
DG26	**X**CGCGAATTCGCG**X**	90	4618.85249	4618.86749
DG27	**XX**CGCGAATTCGCG**X**	98	5065.97203	5065.99478

[a] 600-800 nmol synthesis scale
[b] monoisotopic masses obtained by charge deconvolution of the raw spectra
X = gBAM, **Y** = C3-linker (abasic site).

It was suspected that incorporation of gBAM as internal or terminal modification might lead

to distinct spectrocopic properties and provide a platform for the formation of higher-order aggregates.

Therefore, gBAM was used to substitute either of the two T in the center of the DDD sequence to test the influence of this sterically demanding modification on the formation of a hairpin or duplex secondary structure. In addition, gBAM was incorporated as overhangs at the 3'- and 5'-end of the DDD since it was suspected that this might give rise to higher-molecular complexes by dipolar interstrand stacking interactions.

3.6.1.3 Multiple-modified gBAM-DNA hybrid 17mers

GNA nucleotides are known to have a strong destabilizing effect if incorporated into DNA strands. To enhance the thermodynamic stability of gBAM-modified DNA duplexes and enable the incorporation of more than four merocyanines while maintaining a sufficiently high thermodynamic duplex stability, also gBAM-DNA 17mer hybrids were synthesized.

Table 3.27: Sequences, yields and masses for unmodified and gBAM-modified DNA 17mers obtained by solid phase synthesis. Modified nucleosides are colored.

Name	5'-sequence-3'	yield[a] nmol	*M* calc. g mol^{-1}	*M* meas.[b] g mol^{-1}
D23	GGACTCTTTTTCTCAGG	244	5164.87782	5164.90647
D24	CCTGAGAAAAAGAGTCC	273	5209.93566	5209.92683
D25	CCTGAGAAGAAGAGTCC	180	5225.93057	5225.93961
D26	CCTGAGAGGGAGAGTCC	96	5257.92040	5257.94694
DG28	GGACTCTT**X**TTCTCAGG	281	5307.95132	5307.95756
DG29	CCTGAGAA**X**AAGAGTCC	193	5343.99759	5344.01111
DG30	GGACTCTT**XX**TCTCAGG	169	5451.02427	5451.04142
DG31	GGACTCT**XXX**TCTCAGG	116	5594.09777	5594.11004
DG32	CCTGAGA**XXX**AGAGTCC	170	5612.12091	5612.14974
DG33	GGACTC**XXXXX**CTCAGG	64	5880.24477	5880.26860
DG34	CCTGAG**XXXXX**GAGTCC	113	5880.24477	5880.26489

[a] 600-800 nmol synthesis scale
[b] monoisotopic masses obtained by charge deconvolution of the raw spectra
X = gBAM.

Comparable to the modified DNA 12mers, also the gBAM-modified DNA 17mer single strands were obtained in satisfactory yields and quality after PAGE purification, even with up to five

incorporated merocyanines.

In the following, the influence of different gBAM-variants as well as the impact of a larger number of gBAM chromophores on the duplex stability will be discussed on the basis of thermal denaturation experiments and derived thermodynamic parameters.

3.6.2 Thermodynamic properties of gBAM-DNA hybrid structures

For gBAM-DNA hybrid structures, extensive thermodynamic analyses have been carried out, covering all single- and double-modified systems containing the different gBAM variants as well as heavily gBAM-modified structures with up to ten chromophores.

3.6.2.1 gBAM-Modified DNA 12mer duplexes

The incorporation of acyclic building blocks with for example aminopropyl backbones into DNA strands has been described to induce a significant decrease in duplex stability.[451,452] This is also true for GNA-DNA hybrids, where the incorporation of a single (*S*)-gT into a DNA 15mer caused a reduction of the melting temperature from 47 to 34 °C while a higher number of implemented glycol nucleotides decreased the duplex stability even stronger.[453] The cross-pairing incompatibility of GNA and DNA manifested in a pronounced destabilizing effect was also observed for the 12mer DNA/GNA strands synthesized in the course of this thesis.

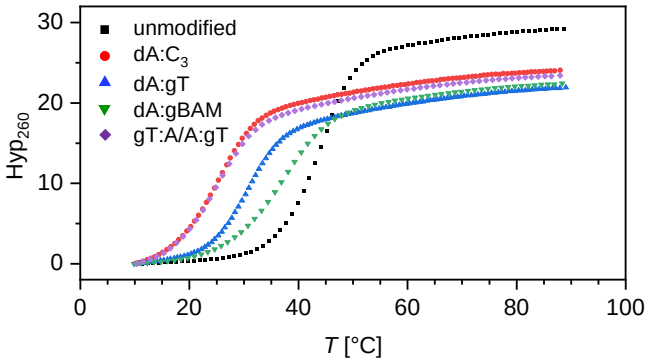

Figure 3.94: The incorporation of an abasic site (red) or two gT (purple) induces a significant destabilization of the DNA duplex while modification with one sterically demanding gBAM (green) does have a less negative impact on the duplex stability than incorporation of one gT (blue). Data are shown for 5 µM samples and the second heating ramp.

To get an insight into the relationship of the thermal stabilities between pure DNA and DNA-GNA hybrid duplexes, the melting temperatures for systems containing one gT, one C3-linker as abasic site or one gBAM were compared (Table 3.28). The incorporation of either of these three modifications led to a noticable drop of the melting temperatures, which is also visible

in the combined graph in Figure 3.94. Here, the strongest duplex destabilization by 18.0 °C compared to the reference **D1/D2** was observed for the C3-linker-modified system **D7/D2** while the melting temperature of the gBAM-modified duplex **DG2/D2** was reduced by only 7.8 °C despite the presence of the bulky merocyanine chromophore.

Also the single- as well as the double-gT-modified DNA duplexes **DG1/D2** and **DG1/DG8** showed a strong decrease of their duplex denaturation temperatures, with the latter one being even less stable. These reduced duplex stabilities are in accordance with the reported destabilizing effect of acyclic nucleosides on DNA scaffolds, which is attributed to structural distortions due to the more flexible sugar surrogate.[453] Since the drop in thermal stability for the gBAM-modified system **DG2/D2** was not as strong and still a sufficiently high melting temperature was measured, it was decided to further investigate similar modified DNA/GNA hybrids.

Table 3.28: Sequences, melting temperatures and thermodynamic parameters for DNA/GNA duplex structures with a single merocyanine modification. Important nucleobases are colored. Given are also the differences in melting temperature relative to the unmodified reference sequence.

Name	sequence	T_m[a] °C	ΔT_m[b] °C	ΔH^0 kcal mol^{-1}	ΔS^0 cal mol^{-1} K^{-1}	ΔG^0_{298K} kcal mol^{-1}
D1/D2	5'-...ATA...-3' 3'-...TAT...-5'	43.6	-	-86.9	-248	-12.9
D7/D2	5'-...A**Y**A...-3' 3'-...TAT...-5'	25.6	-18.0	-91.1	-280	-7.76
DG1/D2	5'-...A**T**A...-3' 3'-...TAT...-5'	29.6	-14.0	-82.7	-249	-8.60
DG2/D2	5'-...A**X**A...-3' 3'-...TAT...-5'	35.8	-7.8	-76.9	-223	-10.3
DG1/DG8	5'-...A**T**A...-3' 3'-...TA**T**...-5'	21.6	-22.0	-38.2	-104	-7.14

[a] values for 5 µM samples in 1× PBS (100 mM NaCl, 10 mM phosphate, pH 7.0); 0.5 °C/min heating rate; a standard error of ±0.5 °C is assumed
[b] difference relative to unmodified duplex
T = gT, **Y** = C3-linker (abasic site), **X** = gBAM.

For elucidation of the Watson-Crick base pairing capability of gBAM in DNA scaffolds, duplex structures containing either gBAM or its methylated variant gmBAM opposite each of the

canonical nucleobases were investigated with regard to their thermal stability and compared to the unmodified DNA reference duplex **D1/D2** (Table 3.29).

Table 3.29: Sequences, melting temperatures and thermodynamic parameters for DNA/GNA duplex structures with gBAM and gmBAM opposite different nucleobases. Important nucleobases are shown in bold. Given are also the differences in melting temperature relative to the unmodified reference sequence.

Name	sequence	$T_m^{[a]}$ °C	$\Delta T_m^{[b]}$ °C	ΔH^0 kcal mol^{-1}	ΔS^0 cal mol^{-1} K^{-1}	ΔG^0_{298K} kcal mol^{-1}
D1/D2	5'-...ATA...-3' 3'-...TAT...-5'	43.6	-	-86.9	-248	-12.9
D1/DG9	5'-...AT**A**...-3'	36.9	-6.7	-67.6	-192	-10.2
D1/DG10	3'-...TA**X**...-5'	36.5	-7.1	-69.8	-200	-10.3
D3/DG9	5'-...AT**C**...-3'	38.7	-4.9	-76.6	-219	-11.2
D3/DG10	3'-...TA**X**...-5'	37.6	-6.0	-71.7	-204	-10.5
D4/DG9	5'-...AT**G**...-3'	42.2	-1.4	-84.6	-243	-12.3
D4/DG10	3'-...TA**X**...-5'	41.3	-2.3	-78.3	-224	-11.7
D5/DG9	5'-...AT**T**...-3'	38.2	-5.4	-75.4	-217	-10.8
D5/DG10	3'-...TA**X**...-5'	38.0	-5.6	-78.5	-227	-11.0
D7/DG9	5'-...AT**Y**...-3'	39.6	-4.0	-56.8	-156	-10.4
D7/DG10	3'-...TA**X**...-5'	39.2	-4.4	-72.9	-208	-10.9

[a] values for 5 µM samples in 1× PBS (100 mM NaCl, 10 mM phosphate, pH 7.0); 0.5 °C/min heating rate; a standard error of ±0.5 °C is assumed
[b] difference relative to unmodified duplex
name in blue for gBAM-modified systems, name in purple for gmBAM-modified systems, **X** = gBAM or gmBAM, **Y** = C3-linker (abasic site).

All of the modified systems showed a reduced thermal stability in comparison to **D1/D2**, no matter which nucleobase was located opposite the merocyanine chromophore. Most important, gBAM- and gmBAM-modified duplexes did show only slight deviations in their melting temperatures, proving that the gBAM chromophore is not able to undergo Watson-Crick base pairing when implemented into a DNA construct. Since not only the melting temperatures but also the thermodynamic parameters are almost the same for gBAM- and gmBAM-modified duplexes, it can be assumed that all of these systems adopt a similar structure and the Watson-Crick base pairing face of the BAM head group is not involved in essential hydrogen bonding interactions for formation of these structures.

The overall highest thermal stability was found for both merocyanines opposite G in **D4/DG9**

and **D4/DG10**, which indicates structural stabilization by stacking interactions between the chromophore and this nucleobase (Figure 3.95). Apparently, these interactions are not as pronounced between gBAM or gmBAM and A or the pyrimidine nucleobases since here lower melting temperatures were observed. Interestingly, the thermal stability for the duplex with gBAM opposite the abasic site **D7/DG9** was reduced by only 4.0 °C compared to the reference **D1/D2**, although the melting temperature for the duplex **D7/D2** with the abasic site opposite A showed a much stronger destabilization by 18.0 °C. Therefore, the incorporation of the hydrophobic merocyanine chromophore induces a pronounced stabilizing effect which is consistent with π-π stacking with its neighboring nucleobases.

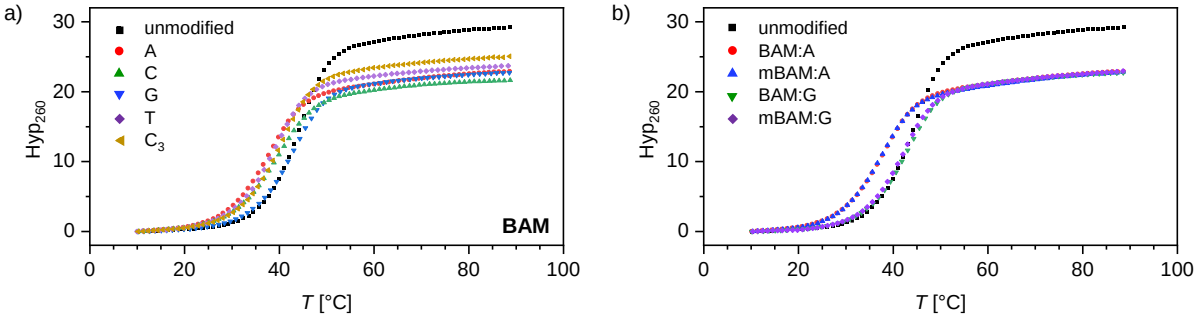

Figure 3.95: The thermal stability of DNA-GNA hybrids slightly depends on the nucleobase opposite to the merocyanine modification as exemplarily shown for BAM in a). However, the observed melting temperature does not change upon methylation of the barbituric acid nitrogen (b). Data are shown for 5 μM samples and the second heating ramp.

A very striking observation is made if the thermal stabilities of the DNA/GNA hybrid structures are compared to the already discussed dBAM-modified DNA systems: for the first ones mentioned, the duplex melting temperatures are by 3 to 10 °C higher than for the latter ones. This is unexpected, since in the dBAM-modified DNA systems only the sterically demanding chromophore needs to be accommodated while in the hybrid structures additional structural perturbations by the acyclic glycol nucleoside are introduced. However, the more flexible acyclic sugar surrogate might provide better accommodation of the merocyanine in *syn*-conformation within the core of the duplex structure, with stabilizing nucleobase-chromophore stacking interactions partially overcoming the duplex destabilization after the incorporation of gBAM. With the rigid deoxyribose, the duplex structure is presumably more distorted with BAM rotated around the glycosidic bond, leading to a decreased thermal stability and most likely to a partial unwinding of the duplex core.

The character of gBAM as a universal nucleobase was further proven by the thermal stability analysis of RNA/DNA/GNA hybrid duplexes (Table 3.30). Here, the gBAM-containing DNA strand **DG9** was hybridized to a complementary RNA strand with either A (**R1**) or m^6A (**R6**) opposite the merocyanine chromophore. As expected, the melting temperature for the m^6A containing reference **R6/D2** is slightly decreased compared to the canonical system **R1/D2**, presumably due to the steric demand of the methyl group. For both duplex structures **R1/DG9**

and **R6/DG9** comprising gBAM, however, almost the same T_m value is obtained which indicates that the duplex stability is dictated by the bulky chromophore while the presence of the additional methyl group of m^6A only plays a minor role.

Table 3.30: Sequences, melting temperatures and thermodynamic parameters for RNA/DNA/GNA duplex structures. Important nucleobases are colored. Given are also the differences in melting temperature relative to the unmodified reference sequence.

Name	sequence	$T_m^{[a]}$ °C	$\Delta T_m^{[b]}$ °C	ΔH^0 kcal mol^{-1}	ΔS^0 cal mol^{-1} K^{-1}	ΔG^0_{298K} kcal mol^{-1}
R1/D2	5'-...AUA...-3' 3'-...TA**T**...-5'	42.9	-	-105	-303	-13.7
R6/D2	5'-...AU**A**...-3' 3'-...TA**T**...-5'	40.9	-2.0	-85.9	-248	-12.0
R1/DG9	5'-...AUA...-3' 3'-...TA**X**...-5'	34.6	-8.3	-79.6	-233	-10.2
R6/DG9	5'-...AU**A**...-3' 3'-...TA**X**...-5'	34.3	-8.6	-75.2	-219	-9.91

[a] values for 5 µM samples in 1× PBS (100 mM NaCl, 10 mM phosphate, pH 7.0); 0.5 °C/min heating rate; a standard error of ±0.5 °C is assumed
[b] difference relative to unmodified duplex
A = m^6A, **X** = gBAM.

Besides single-modified 12nt DNA/GNA hybrid structures also those with gBAM-dimers and multimers were investigated (Table 3.31). The orientation of the different dimers corresponds to the already discussed ones for pure DNA, RNA and GNA systems with the chromophores in downstream or upstream direction and directly opposite each other. Surprisingly, the upstream dimer **DG2/DG19** showed a slightly increased melting temperature compared to the unmodified reference **D1/D2** while the downstream and the opposite dimer **DG2/DG9** and **DG2/DG15** were slightly decreased in their thermal stabilities. Compared to the respective dBAM-containing DNA systems, all of the gBAM-modified DNA/GNA hybrid structures here are less destabilized which is also reflected in higher total values for ΔG^0_{298K}. Although two Watson-Crick base pairs are lost upon incorporation of the gBAM dimers into the 12mer duplex structure, the increase of the free Gibbs energy is much smaller than expected. The loss of the hydrogen bond strength of two A-T base pairs amounts to approximately 4 kcal mol^{-1}; here, the largest increase of ΔG^0_{298K} with +2.2 kcal mol^{-1} is observed for the downstream dimer **DG2/DG9**. Therefore, additional stabilizing interactions are expected to influence the overall duplex stability, such as the already mentioned chromophore-chromophore interstrand stacking

and stacking with adjacent nucleobases. These interactions are remarkably strong: if the T_m value for the downstream dimer **DG2/DG9** is compared to the double-gT-modified duplex **DG1/DG8** (see Table 3.28), the latter one is by 17 °C more destabilized only by changing the backbone of two nucleotides from cyclic to acyclic without altering the nucleobase structure.

Table 3.31: Sequences, melting temperatures and thermodynamic parameters for DNA/GNA duplex structures with two or more gBAM modifications incorporated; the blue, green and red colored duplex name indicates upstream, downstream and opposite chromophore positioning, respectively. dBAM is abbreviated as differently colored **X**. Given are also the differences in melting temperature relative to the unmodified reference sequence.

Name	sequence	T_m[a] °C	ΔT_m[b] °C	ΔH^0 kcal mol^{-1}	ΔS^0 cal mol^{-1} K^{-1}	ΔG^0_{298K} kcal mol^{-1}
D1	5'-...ATA...-3'	43.6	-	-86.9	-248	-12.9
D2	3'-...TAT...-5'					
DG2	5'-...A**X**A...-3'	45.2	+1.6	-77.2	-217	-12.5
DG19	3'-...**X**AT...-5'					
DG2	5'-...A**X**A...-3'	38.6	-5.0	-69.5	-197	-10.7
DG9	3'-...TA**X**...-5'					
DG2	5'-...A**X**A...-3'	41.5	-2.1	-78.7	-225	-11.7
DG15	3'-...T**X**T...-5'					
D1	5'-...ATA...-3'	34.4	-9.2	-54.7	-153	-9.23
DG20	3'-...**X**A**X**...-5'					
DG2	5'-...A**X**A...-3'	40.1	-3.5	-55.8	-153	-10.2
DG20	3'-...**X**A**X**...-5'					
DG2	5'-...A**X**A...-3'	40.0	-3.6	-37.2	-95	-8.93
DG22[c]	3'-**X**.**X**A**X**.**X**-5'					

[a] values for 5 µM samples in 1× PBS (100 mM NaCl, 10 mM phosphate, pH 7.0); 0.5 °C/min heating rate; a standard error of ±0.5 °C is assumed
[b] difference relative to unmodified duplex
[c] sequence for **DG22** 3'-C**X**AC**X**A**X**CGA**X**C-5'
X = dBAM.

Besides interstrand gBAM dimers, also one system containing an intrastrand dimer (**D1/DG20**) was synthesized, exhibiting a markedly reduced T_m value compared to the interstrand dimers which indicates the lack of dipolar interactions between the chromophores due to their unfavorable mutual orientation within the oligonucleotide scaffold (Figure 3.96). If the counterstrand contains an additional gBAM chromophore, the T_m value for this gBAM trimer in **DG2/DG20** is increased again. Thus, despite the presence of this third sterically demading chromophore with the backbone-disturbing acyclic glycol, the dipolar stacking interactions between the two

chromophores exceed the hereby induced destabilizing effect. Surprisingly, the duplex structure is not further destabilized if all dT in one strand are replaced by gBAM, leading to a gBAM pentamer in **DG2/DG22**. Meanwhile, the changes in enthalpy and entropy are less negative for this system which is reasonable: the large gBAM content leads to a less ordered duplex structure and therefore an increased ΔS^0 value.

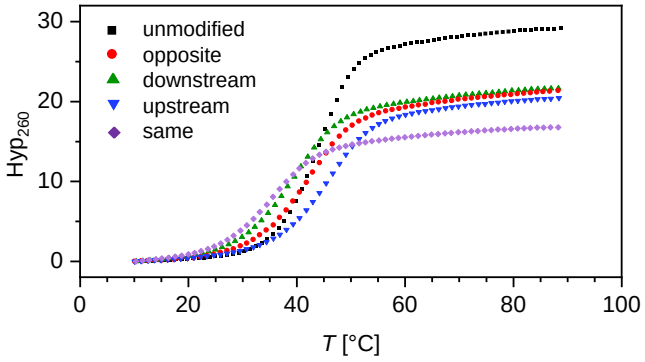

Figure 3.96: The duplex melting temperature of DNA-GNA hybrid structures strongly depends on the mutual orientation of the two gBAM chromophores. With the two modifications in upstream orientation (blue) the duplex structure displayed an even higher thermal stability than the unmodified reference (black). Data are shown for 5 µM samples and the second heating ramp.

Concomitantly, also ΔH^0, dominated by short-range interactions such as van der Waals contacts and base stacking, is increased which is attributed to the partial loss of these interactions due to the structural duplex disturbance by gBAM. For the other possible multiple-modified DNA/GNA hybrids no thermodynamic analysis was carried out due to inconclusive results from the thermal dehybridization experiments attributed to a reduced duplex stability of systems with two heavily modified strands.

The gBAM chromophores incorporated so far all comprised an (S)-configured backbone. To investigate if the configuration of the glycol stereocenter has an influence on the thermal stability of DNA/GNA hybrids, also the (R)-configured gBAM phosphoramidite **82** was incorporated, providing access to $(R)/(S)$-mixed dimers besides the $(R)/(R)$- and $(S)/(S)$-only dimers (Table 3.32).

However, the configuration of the glycol stereocenter does not play a significant role for the duplex destabilization of DNA/GNA hybrid structures: not only for the single-modified systems almost the same melting temperatures and thermodynamic parameters are obtained, but also for the double-modified duplexes with either pure (R),(R)- and (S),(S)- or mixed (R),(S)-gBAM dimers which is visualized in Figure 3.97. This hints to a high flexibility of the gBAM chromophores within the DNA scaffold, which allows the chromophores to adopt similar conformations regardless from their backbone configuration and is very likely only possible if the core of the helix containing the two merocyanine modifications is partially unwound.

Table 3.32: Sequences, melting temperatures and thermodynamic parameters for DNA duplex structures with (*R*)- and (*S*)-gBAM. Important nucleobases are colored. Given are also the differences in melting temperature relative to the unmodified reference sequence.

Name	sequence	$T_m^{[a]}$ °C	$\Delta T_m^{[b]}$ °C	ΔH^0 kcal mol^{-1}	ΔS^0 cal mol^{-1} K^{-1}	ΔG^0_{298K} kcal mol^{-1}
D1/D2	5'-...ATA...-3' 3'-...TAT...-5'	43.6	-	-86.9	-248	-12.9
D1/**DG9**	3'-...ATA...-5'	36.9	-6.7	-67.6	-192	-10.2
D1/**DG14**	5'-...TA**X**...-3'	35.9	-7.7	-77.2	-223	-10.6
DG2/DG9	5'-...A**X**A...-3' 3'-...TA**X**...-5'	38.6	-5.0	-69.5	-197	-10.7
DG7/DG14		38.6	-5.0	-67.0	-189	-10.7
DG2/**DG14**		38.9	-4.7	-72.4	-207	-10.9
DG2/DG15	5'-...A**X**A...-3' 3'-...T**X**T...-5'	41.5	-2.1	-78.7	-225	-11.7
DG7/DG18		42.9	-0.7	-80.9	-230	-12.3
DG2/**DG18**		43.3	-0.3	-88.8	-256	-12.6

[a] values for 5 µM samples in 1× PBS (100 mM NaCl, 10 mM phosphate, pH 7.0); 0.5 °C/min heating rate; a standard error of ±0.5 °C is assumed

[b] difference relative to unmodified duplex

names in lightblue for (*S*)-gBAM containing strands, names in blue for (*R*)-gBAM containing strands.

Among the investigated systems, the thermodynamically most stable duplex structures are the ones with the two chromophores opposite each other with T_m values between 41.5 and 43.3 °C, suggesting the presence of pronounced dipolar stacking of the two *syn*-configured merocyanines in the helix core as similarly discussed for other double helixes containing an opposite BAM:BAM dimer.

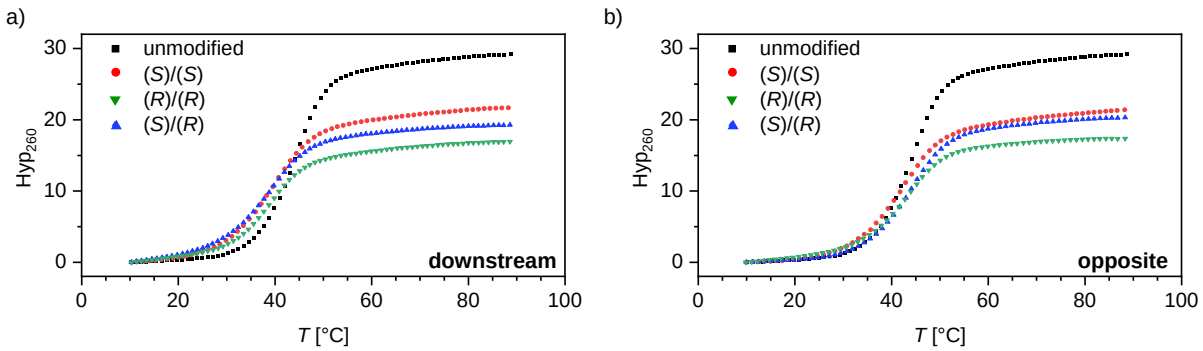

Figure 3.97: In both the downstream and the opposite dimer orientation almost the same melting temperatures are obtained for duplex structures containing (*R*),(*R*)-, (*S*),(*S*)- or mixed (*R*),(*S*)-gBAM dimers. Data are shown for 5 µM samples and the second heating ramp.

Meanwhile, also the melting temperatures for the downstream dimers are slightly increased by approximately 2 °C compared to the respective single-modified duplex structures, indicating the presence of stabilizing dipolar stacking interactions although these are not as pronounced as for the opposite dimers. The independence of the dimer formation from the backbone constitution also manifests in the spectroscopic characteristics of these double-modified duplex structures which will be discussed in the next section of this thesis.

The spectral properties of merocyanines can be further tuned by introduction of heteroatoms or additional aromatic substituents. To evaluate the influence of these modifications on the duplex melting behavior, single- and double-modified structures containing either gBAM^{F} or gBAM^{OMe} with a fluorine and a methoxy groups attached to the indolenine ring system, resepectively, or the benzothiazole-derived gmBAM^{b}, were analyzed (Table 3.33).

Table 3.33: Sequences, melting temperatures and thermodynamic parameters for DNA duplex structures including gBAM variants. Given are also the differences in melting temperature relative to the unmodified reference sequence.

Name	sequence	$T_m^{[a]}$ °C	$\Delta T_m^{[b]}$ °C	ΔH^0 kcal mol^{-1}	ΔS^0 cal mol^{-1} K^{-1}	ΔG^0_{298K} kcal mol^{-1}
D1/D2	5'-...ATA...-3' 3'-...TAT...-5'	43.6	-	-86.9	-248	-12.9
D1/DG9	5'-...ATA...-3' 3'-...TA**X**...-5'	36.9	-6.7	-67.6	-192	-10.2
D1/DG10		36.5	-7.1	-69.8	-200	-10.3
D1/DG11		39.2	-4.4	-63.5	-178	-10.6
D1/DG12		36.3	-7.3	-66.8	-190	-10.1
D1/DG13		~35	n.d.	n.d.	n.d.	n.d.

[a] values for 5 µM samples in 1× PBS (100 mM NaCl, 10 mM phosphate, pH 7.0); 0.5 °C/min heating rate; a standard error of ±0.5 °C is assumed

[b] difference relative to unmodified duplex

names in lightblue for gBAM-containing strands, names in violet for gmBAM-containing strands, names in red for gmBAM^{b}-containing strands, names in green for gBAM^{F}-containing strands, names in orange for gBAM^{OMe}-containing strands.

If the gBAM variants were incorporated opposite A, the melting temperature dropped slightly, but for all modifications to a similar extent with a decrease of T_m by 4 to 7 °C. Again, the lowest destabilization was observed for the gmBAM^{b}-modified duplex **D1/DG11** with a melting temperature of 39.2 °C despite the additional methyl group on the barbituric acid nitrogen. The estimated melting temperature for this system is only by 4.4 °C lower than for the unmodified reference **D1/D2** which is attributed to the decreased steric hindrance due to the lacking methyl groups at the donor moiety.

Unfortunately, no defined melting transition was observed for the gBAM^{OMe}-containing duplex **D1/DG13**, although from the hyperchromicity at 460 nm a T_m value of approximately 35 °C was estimated. This strong destabilization might be due to the methoxy substituent which increases the molecular size of the merocyanine nucleoside analog even further, preventing effective accommodiation of this chromophore within the DNA scaffold.

In addition, the additional fluorine substituent in gBAM^{F} and the *N*-methyl group in gmBAM did not have a significant impact on the duplex stability compared to the parent chromophore gBAM. For the single-gBAM^{F} and -gmBAM modified duplex structures **D1/DG12** and **D1/DG10**, T_m values of 36.3 and 36.5 °C were obtained, respectively, which is by 0.6 or 0.4 °C lower than for the single-gBAM modified system **D1/DG9**. Therefore, these structural changes lead to a small increase of the chromophore's steric demand and do not interfere with the accommodation of these modifications in the double-helical structure.

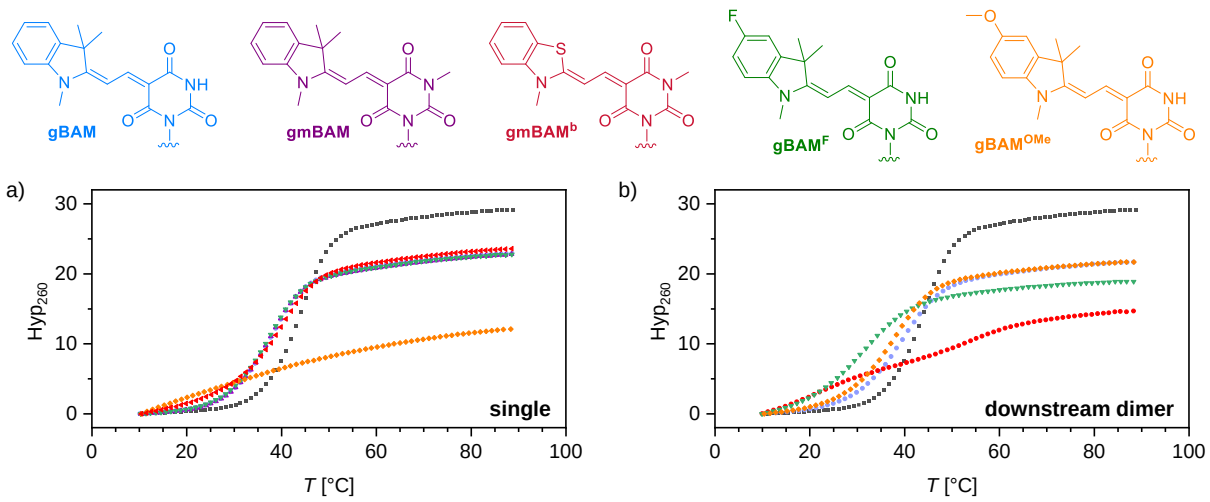

Figure 3.98: The hyperchromicity at 260 nm plotted against the sample temperature reveals a very similar melting behavior for duplex structures containing a single gBAM, gmBAM, gmBAM^{b} or gBAM^{F} while no melting transition is observed for the gBAM^{OMe}-modified duplex (a). For duplex structures with downstream merocyanine dimers, the highest melting temperatures are obtained for the systems containing gBAM- and gBAM^{OMe}-dimers while for the double-gmBAM^{b}-modified helix a biphasic melting behavior is observed (b). Data are shown for 5 µM samples and the second heating ramp.

To get a better impression of the different denaturation characteristics of DNA duplex structures modified with the different gBAM variants, the hyperchromicities at 260 nm for these systems are summarized in Figure 3.98a. Here, the apparent difference between the individual samples is illustrated: while the curve shape for the gBAM-, gmBAM^{b}- and gBAM^{F}-containing systems **D1/DG9**, **D1/DG11** and **D1/DG12** are almost identical, the unmodified reference strand **D1/D2** shows an overall higher hyperchromicity whereas the gBAM^{OMe}-modified duplex **D1/DG13** does not show a pronounced inflection point. Overall, substitutions on the aromatic donor moiety have a stronger influence on the duplex stability of single-modified

systems compared to the introduction of an additional methyl group on the acceptor part of the molecule. This observation coincides with the assumed *syn*-conformation of the different merocyanine chromophores as discussed earlier in this thesis, as the bulkiness of the aromatic donor rather than the acceptor is the determining factor for the coplanarity of two chromophores within a dimer and thus also for efficient dipolar stacking interactions. Since GNA duplex structures containing gBAM dimers exhibited interesting thermodynamic and also spectroscopic properties, also DNA/GNA hybrid structures with downstream and opposite dimers of the gBAM variants were generated of which the melting profiles of the first ones mentioned are shown in Figure 3.98b.

While the gBAM and gBAM^{OMe} downstream dimers **DG2/DG9** and **DG6/DG13** showed very similar thermodynamic parameters and melting temperatures which were interestingly slightly higher than for the respective single-modified structures **DG1/DG9** and **DG1/DG13**, the gBAM^{F} downstream dimer **DG5/DG12** was strongly destabilized (Table 3.34). This is attributed to electronic effects due to the electronegative fluorine substituent which leads to a decreased electron density within the delocalized chromophore system, an energetically lowered LUMO and different dipole moments as well as an increased hydrophobic character of the merocyanine chromophores. These effects seem to prevent the efficient dipolar stacking of gBAM^{F} in the oligonucleotide context.

However, the thermodynamic analysis for the downstream gmBAM^{b}-dimer **DG4/DG11** was hampered since this duplex showed two independent melting transitions. The first melting point of 22 °C was only visible in the 260 nm UV trace while the second melting temperature at 54 °C was detected at both 260 and 460 nm. This indicates that the melting process deviates from the cooperative model, suggesting that the loss of the hydrogen-bonded base pairs at the 3'- and 5'-ends occur at lower temperatures while the strongly stacked dipolar gmBAM^{b}-gmBAM^{b} dimer is only broken up at higher temperatures.

By comparison of the gBAM/gBAM and gmBAM^{b}/gmBAM^{b} opposite dimers **DG2/DG15** and **DG4/DG17** the strong influence of the chromophores steric demand on the strength of the dipolar stacking interactions becomes obvious. While the first one mentioned showed a similar dehybridization behavior as the reference strand **D1/D2**, the latter one had a markedly increased thermal stability and concomitantly more negative free energy change. The absolute ΔG^{0}_{298K} value for this system was even higher than for the unmodified reference, with the dipolar chromophore-chromophore stacking interactions making up for the loss of the A-T base pair. Therefore, the absence of the two methyl groups at the benzothiazole ring system allows for a more favorable antiparallel alignment of the two chromophores in the duplex center, as also observed for BAM^{b}-containing DNA and RNA systems.

Table 3.34: Sequences, melting temperatures and thermodynamic parameters for DNA duplex structures including dimers of gBAM variants. Given are also the differences in melting temperature relative to the unmodified reference sequence.

Name	sequence	$T_m^{[a]}$ °C	$\Delta T_m^{[b]}$ °C	ΔH^0 kcal mol^{-1}	ΔS^0 cal mol^{-1} K^{-1}	ΔG^0_{298K} kcal mol^{-1}
D1/D2	5'-..ATA..-3' 3'-..TAT..-5'	43.6	-	-86.9	-248	-12.9
DG2/DG9	5'-..A**X**A..-3' 3'-..TA**X**..-5'	38.6	-5.0	-69.5	-197	-10.7
DG3/DG10		38.7	-4.9	-67.9	-192	-10.7
DG4/DG11[c]		22, 54	n.d.	n.d.	n.d.	n.d.
DG5/DG12		28.7	-14.9	-52.4	-148	-8.4
DG6/DG13		36.7	-6.9	-89.5	-263	-11.1
DG2/DG15	5'-..A**X**A..-3'	41.5	-2.1	-78.7	-225	-11.7
DG4/DG17	3'-..T**X**T..-5'	52.0	+8.4	-71.9	-196	-13.6

[a] values for 5 µM samples in 1× PBS (100 mM NaCl, 10 mM phosphate, pH 7.0); 0.5 °C/min heating rate; a standard error of ±0.5 °C is assumed

[b] difference relative to unmodified duplex

[c] two melting transitions observed for this sample

names in lightblue for gBAM-containing strands, names in purple for gmBAM-containing strands, names in red for gmBAM^b-containing strands, names in green for gBAM^F-containing strands, names in orange for gBAM^{OMe}-containing strands.

3.6.2.2 Multiple gBAM-modified DNA 17mer duplexes

Since the thermal stability of a DNA 12mer duplex is comparably low and the short length does not support the consecutive incorporation of multiple gBAM building blocks, longer strands consisting of 17 nt were designed. This provided access to duplex structures containing up to ten gBAM chromophores (Tables 3.35 and 3.36). The single-modified 17mer duplex structure **D23/DG29** with T opposite gBAM shows a by 8% reduced melting temperature compared to the unmodified reference **D23/D24**. For the respective 12mer duplex, a higher reduction by 15% upon gBAM incorporation was observed which is expected since the longer DNA duplex is better capable of compensating the structural disturbance introduced by this artificial nucleobase. As observed before, the melting temperature for the opposite gBAM dimer **DG28/DG29** is also here increased compared to the single-modified duplex **D23/DG29** which is explained by stabilizing dipolar stacking interactions between the two chromophores in *syn*-conformation. The assumption of the merocyanines located in the core of the helical structure is further supported by the comparably low thermal stability of **DG30/D24** with the

two gBAM next to each other in one strand. Here, the antiparallel chromophore-chromophore stacking is inhibited due to their spatially fixed mutual arrangement which prevents thermal stabilization.

Table 3.35: Sequences, melting temperatures and thermodynamic parameters for DNA/GNA 17mer duplex structures. Given are also the differences in melting temperature relative to the unmodified reference sequence.

Name	sequence	$T_m^{[a]}$ °C	$\Delta T_m^{[b]}$ °C	ΔH^0 kcal mol^{-1}	ΔS^0 cal mol^{-1} K^{-1}	ΔG^0_{298K} kcal mol^{-1}
D23	5'-...TTTTT...-3'	56.8	-	-126	-357	-19.9
D24	3'-...AAAAA...-5'					
D23	5'-...TTTTT...-3'	52.1	-4.7	-130	-373	-18.4
DG29	3'-...AA**X**AA...-5'					
DG28	5'-...TT**X**TT...-3'	55.9	-0.9	-128	-362	-19.7
DG29	3'-...AA**X**AA...-5'					
DG30	5'-...TT**XX**T...-3'	48.6	-8.2	-110	-315	-15.7
D24	3'-...AAAAA...-5'					

[a] values for 5 µM samples in 1× PBS (100 mM NaCl, 10 mM phosphate, pH 7.0); 0.5 °C/min heating rate; a standard error of ±0.5 °C is assumed
[b] difference relative to unmodified duplex
X = gBAM

In the following, the number of gBAM modifications within the 17mer duplex structure was increased stepwise to evaluate the effect of gBAM multimers on the thermal stability (Table 3.36). The most striking result of this analysis is that the overall duplex melting temperatures are all within the same range, being unrelated to the systems gBAM content although a stronger destabilization would be expected with a higher degree of modification (Figure 3.99a). Instead, the T_m values are linked to the number of gBAM within the individual single strands (Figure 3.99b). If only one strand of the duplex is gBAM-modified or the difference in the total number of gBAM is greater than two among the two strands, melting temperatures between 44 and 48 °C are observed (red values in Table 3.36), independent of the total amount of gBAM. Concomitantly, the change in entropy is less negative, indicating the formation of a less ordered structure.

Table 3.36: Sequences, melting temperatures and thermodynamic parameters for multiple-modified DNA/GNA 17mer duplex structures. Given are also the differences in melting temperature relative to the unmodified reference sequence.

Name	sequence	T_m[a] °C	ΔT_m[b] °C	ΔH^0 kcal mol^{-1}	ΔS^0 cal mol^{-1} K^{-1}	ΔG^0_{298K} kcal mol^{-1}
D23	5'-...TTTTT...-3'	56.8	-	-126	-357	-19.9
D24	3'-...AAAAA...-5'					
D23	5'-...TTTTT...-3'	40.3	-	-95.9	-280	-12.4
D26	3'-...AGGGA...-5'					
DG31	5'-...T**XXX**T...-3'	47.0	-9.8	-95.1	-271	-14.3
D24	3'-...AAAAA...-5'					
DG30	5'-...TT**XX**T...-3'	52.8	-4.0	-111	-316	-16.9
DG29	3'-...AA**X**AA...-5'					
DG31	5'-...T**XXX**T...-3'	46.2	+5.9[c]	-91.6	-261	-13.8
DG26	3'-...AGGGA...-5'					
DG31	5'-...T**XXX**T...-3'	50.1	-6.7	-96.9	-274	-15.1
DG29	3'-...AA**X**AA...-5'					
DG33	5'-...**XXXXX**...-3'	44.5	-12.3	-80.7	-229	-12.5
D24	3'-...AAAAA...-5'					
DG30	5'-...TT**XX**T...-3'	52.9	-3.9	-100	-282	-16.2
DG32	3'-...A**XXX**A...-5'					
DG31	5'-...T**XXX**T...-3'	52.4	-4.6	-113	-321	-17.1
DG32	3'-...A**XXX**A...-5'					
DG33	5'-...**XXXXX**...-3'	47.9	-8.9	-84.3	-237	-13.5
DG29	3'-...AA**X**AA...-5'					
DG30	5'-...TT**XX**T...-3'	47.7	-9.1	-84.2	-237	-13.5
DG34	3'-...**XXXXX**...-5'					
DG33	5'-...**XXXXX**...-3'	49.5	-7.3	-86.1	-242	-14.1
DG32	3'-...A**XXX**A...-5'					
DG33	5'-...**XXXXX**...-3'	52.8	-4.0	-83.9	-232	-14.7
DG34	3'-...**XXXXX**...-5'					

[a] values for 5 µM samples in 1× PBS (100 mM NaCl, 10 mM phosphate, pH 7.0)
0.5 °C/min heating rate; a standard error of ±0.5 °C is assumed
[b] difference relative to unmodified duplex **D23/D24** or [c] **D23/D26**
values in green for weak, values in red for strong destabilization **X** = gBAM

On the other hand, if both strands are modified to a similar extent, T_m values between 50

and 53 °C are measured which corresponds to only a slight difference of up to $\Delta T_m = 7$ °C to the unmodified reference **D23/D24** (green values). This observed behavior is explained by pronounced interstrand chromophore-chromophore stacking interactions, significantly exceeding the strength of intrastrand dipolar stacking. Simultaneously, the total entropic as well as enthalpic contributions to the thermodynamic stability of the stronger destabilized duplex structures decrease which indicates a less structured double helix due to the loss of stabilizing low-range interactions.

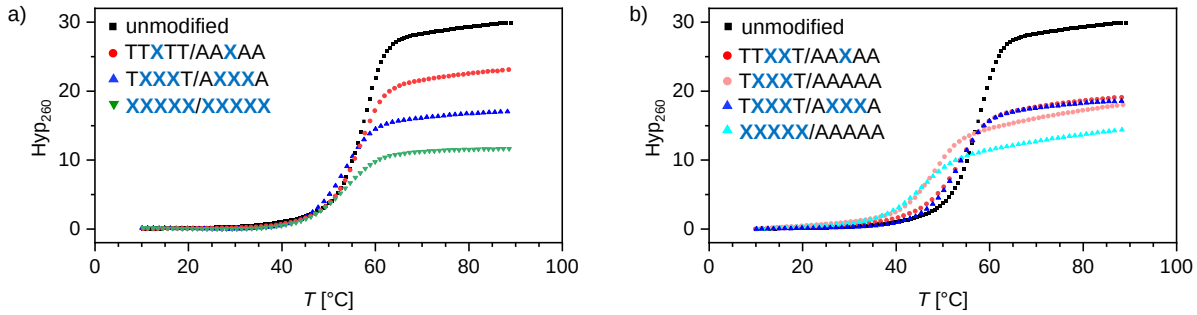

Figure 3.99: The consecutive incorporation of one, three or five opposite gBAM:gBAM dimers into the duplex core leads to almost similar melting temperatues (a). Meanwhile, the melting temperatures for duplexes with only one modified strand showed to be noticeably decreased compared to duplex structures with the same number of modifications but distributed in both strands (a). The drop of the hyperchromicity at 260 nm with an increased number of modifications is due to the low extinction coefficient of the barbituric acid moiety at this wavelength compared to the canonical nucleobases. Data are shown for 5 µM samples and the second heating ramp.

However, the consecutive incorporation of multiple gBAM chromophores into one strand of the duplex still leads to a higher thermal stability compared to the comparable system with the same number of mismatches, similar as described for DNA-based pyrene- and phenanthrene light harvesting systems.[454] As an example, the melting temperature for the triple-gBAM-modified **DG31/D26** duplex is by 5.9 °C higher than for **D23/D26** with three G-T wobble pairs, indicating the presence of either weak chromophore-chromophore or chromophore-base stacking interactions.

In summary, the overall thermal stabilities of these heavily-modified DNA/GNA hybrid structures are astonishingly high with the strength of the dipolar chromophore-chromophore stacking interactions significantly exceeding the loss of Watson-Crick base pairs and the structural perturbation introduced by the sterically demanding merocyanine nucleobase analog and the acyclic backbone.

3.6.2.3 Self-complementary DNA duplexes with internal and terminal gBAM modifications

So far, gBAM modifications were only implemented in the center of the duplex but never at 3'- or 5'-end. Since such pronounced dipolar stacking within duplex structures consisting of two

modified strands have been observed, it was assumed that these interactions might also occur in between two duplex structures with gBAM as overhangs. Therefore, gBAM was attached to both ends of the self-complementary DNA Dickerson-Drew sequence which is able to either form a duplex or a hairpin structure.

The concentration-dependent increase of the melting temperature for the unmodified reference **D21** clearly indicated formation of a duplex instead of a hairpin with the T_m value and the thermodynamic parameters matching reported ones under similar conditions (Table 3.37).[455] Interestingly, upon incorporation of gBAM, all modified DDD structures showed a by 4 to 10 °C higher thermal stability compared to this strand. For single-modified DDD, the type of the formed secondary structure proved to be dependent on the position of gBAM in the sequence: if the T in proximity to the 3'-end was substituted in **DG24**, hairpin formation was observed while substitution of the T closer to the 5'-end in **DG25** led to duplex formation, which is also obvious in the melting curves illustrated in Figure 3.100.

Table 3.37: Sequences, melting temperatures and thermodynamic parameters for DNA/GNA duplex structures with gBAM and gmBAM opposite different nucleobases. Important nucleobases are shown in bold. Given are also the differences in melting temperature relative to the unmodified reference sequence.

Name	sequence	T_m[a] °C	ΔT_m[b] °C	ΔH^0 kcal mol^{-1}	ΔS^0 cal mol^{-1} K^{-1}	ΔG^0_{298K} kcal mol^{-1}
D21	5'-...AATT...-3'	53.6	-	-57.4	-150	-12.7
DG24	5'-...AAT**X**...-3'	64.4	+10.8	n.d.[c]	n.d.[c]	n.d.[c]
DG25	5'-...AA**X**T...-3'	58.7	+5.1	-60.2	-156	-13.7
DG26	5'-**X**...**X**-3'	59.2	+5.6	n.d.[d]	n.d.[d]	n.d.[d]
DG27	5'-**XX**...**X**-3'	57.7	+4.1	n.d.[d]	n.d.[d]	n.d.[d]

[a] values for 5 µM samples in 1× PBS (100 mM NaCl, 10 mM phosphate, pH 7.0); 0.5 °C/min heating rate; a standard error of ±0.5 °C is assumed
[b] difference relative to unmodified system
[c] not determined due to hairpin formation
[d] not determined due to complex melting behavior
X = gBAM

The influence of the gBAM position on the secondary structure can be explained by the differently pronounced dipolar stacking interactions and van der Waals contacts. For **DG24**, the two merocyanine modifications would be by three base pairs apart from each other in the duplex, therefore basically not able to interact. However, if gBAM is in *syn*-conformation, the indolenine part can rotate inside the hydrophobic cavity of the hairpin's tetraloop and presumably stack with the adjacent G which, according to the melting temperatures of the gBAM-G

mismatch duplex discussed earlier, leads to thermal stabilization. In contrast, the two gBAM nucleoside analogs are only shifted by one position in the **DG25** duplex, thus being able to undergo dipolar stacking interactions, which will be further discussed in section 3.6.3.4 by the interpretation of the spectroscopic data. In the respective hairpin, gBAM would be positioned in the middle of the tetraloop which is expected to lead to major structural disturbances due to the flexible acyclic glycol backbone of gBAM. Therefore, formation of the duplex with an increased number of base pairs is thermodynamically preferred over the monomolecular hairpin.

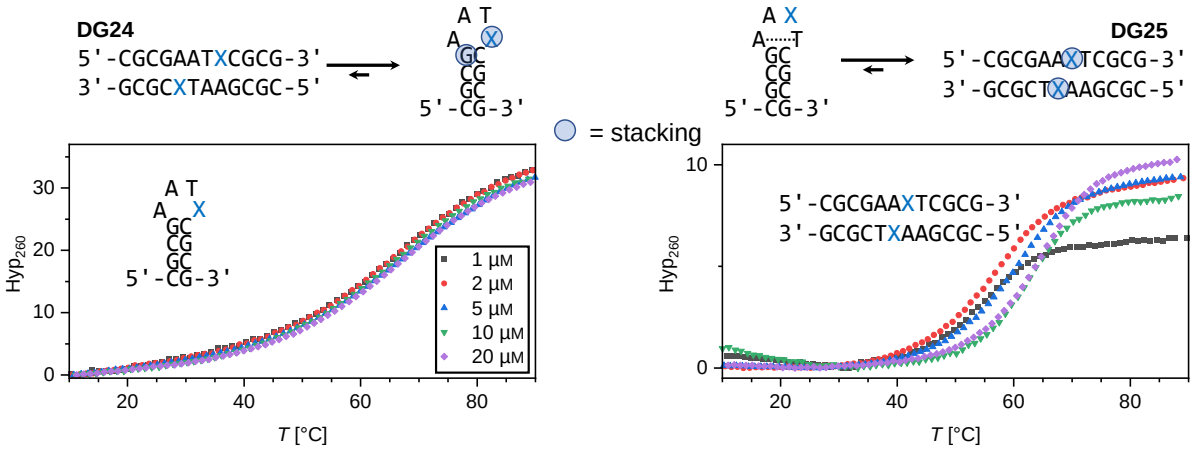

Figure 3.100: The secondary structure adopted by the single-gBAM-modified DDD **DG24** and **DG25** is dependent on the position of the modification in the sequence, which is attributed to differently pronounced stacking interactions. Data shown are for the second heating ramp for samples in 1× PBS (100 mM NaCl, 10 mM phosphate, pH 7.0); 0.5 °C/min heating rate.

For the end-modified DDD **DG26** and **DG27**, a very complex melting behavior is observed, which is not as easy to interpret. Here, the shape of the melting curve is strongly dependent on the oligonucleotide concentration in the sample and the wavelength (Figure 3.101). While nearly sigmoidal-shaped curves with at least two melting transitions are observed in the 260 nm UV trace for higher oligonucleotide concentrations, at 460 nm no defined curve inflection point is obtained for any of the samples. This unusual dehybridization behavior likely arises due to the formation of higher-order molecular structures beyond the monomolecular and bimolecular hairpin and duplex structures, presumably due to end-to-end stacking of the single strands mediated by dipolar interactions between the gBAM overhangs. At elevated temperatures, the hybridized canonical parts of these assemblies denature, leading to the observed melting transition in the nucleobase absorption region. Meanwhile, the broad, undefined melting transition at the merocyanine absorption can be attributed to a stepwise disruption of dipolar interstrand chromophore interactions at elevated temperatures. Similar systems, where the self-assembly of amphiphilic DNA equipped with tetraphenylethylene sticky ends led to vesicle formation, have been reported recently.[456]

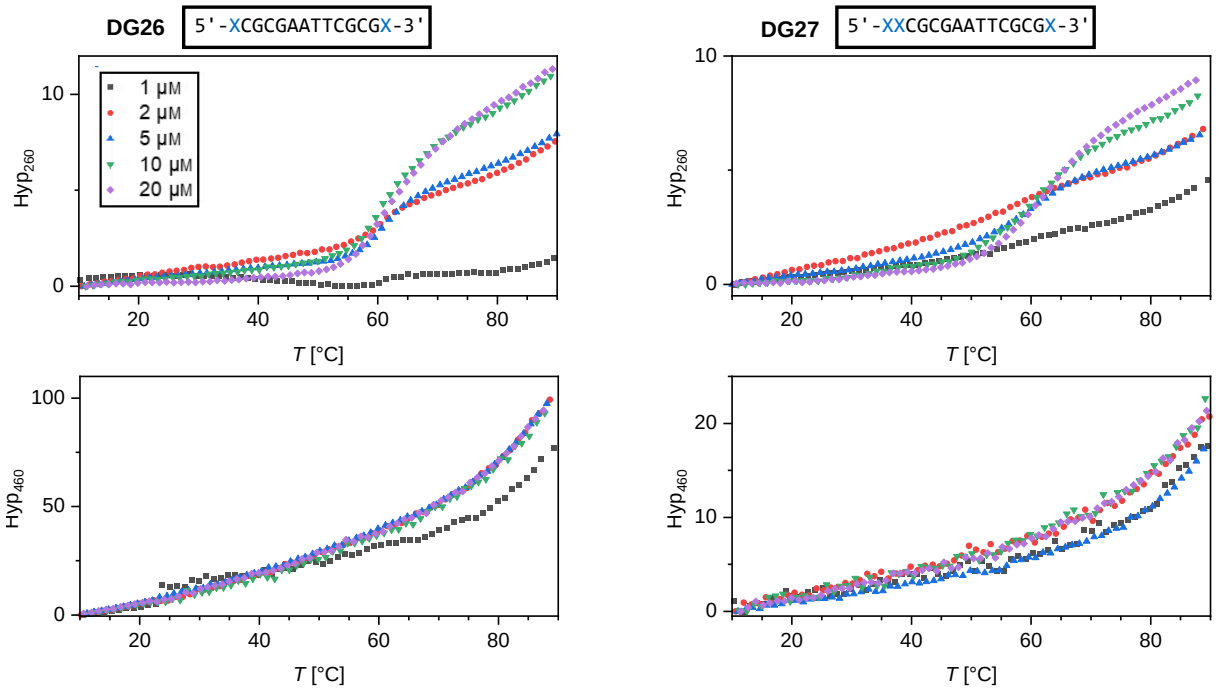

Figure 3.101: End-modified DDD **DG26** and **DG27** showed complex melting behaviors dependent on the sample concentration and the wavelength. Data shown are for the second heating ramp for samples in 1× PBS (100 mM NaCl, 10 mM phosphate, pH 7.0) at 260 nm (top) and 460 nm (bottom); 0.5 °C/min heating rate.

The assumed self-assembly to larger supramolecular aggregates here will be discussed in the next section by means of spectroscopic analyses and AFM images. Prior to this, the spectral properties for most of the prepared DNA/GNA hybrid systems with a single or multiple gBAM chromophores and gBAM variants are described and evaluated.

3.6.3 Spectroscopic characterization of gBAM-DNA hybrid structures

In the following, the spectroscopic characterization of single-modified DNA/GNA 12mer hybrids with different gBAM variants will be discussed first, followed by the spectral analysis of the chromophore dimers in different orientations. Finally, the characteristics of interactions between multiple merocyanines within the core of 17mer DNA duplexes or attached to the 3'- and 5'-end of the shorter DDD system are evaluated.

3.6.3.1 Spectroscopic properties of single-modified gBAM-DNA hybrids

To evaluate the influence of the DNA scaffold on the spectroscopic properties of the distinct gBAM variants, temperature-dependent absorption as well as fluorescence spectra were recorded (Figure 3.102).

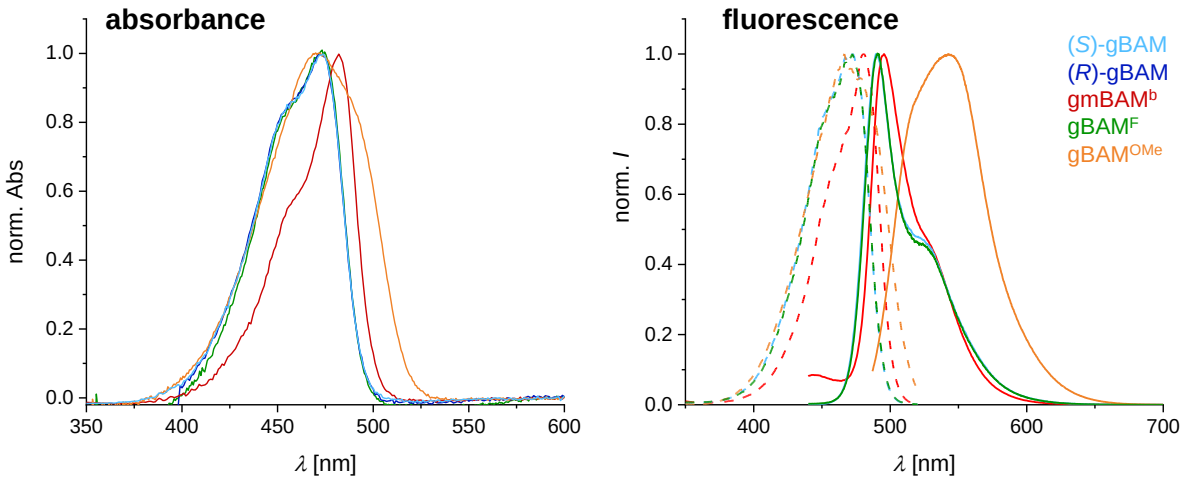

Figure 3.102: The normalized absorption (left) and fluorescence (right) spectra for DNA-12mers modified with different gBAM variants do not differ from the ones recorded for the free nucleosides, emphasizing the negligible influence of the oligonucleotide scaffold on the spectral features of these artificial nucleobase analogs. Conditions: 1 (fluorescence) or 5 (absorption) µM samples in 1× PBS (100 mM NaCl, 10 mM phosphate, pH 7.0). Excitation at 420 nm, emission at 540 nm.

Since the curve shapes do not change for any of the samples, in Figure 3.102 only the normalized absorption, emission and excitation spectra at ambient temperature are shown for better comparison. Apparently, neither the stereocenter configuration of the GNA backbone nor the introduction of a fluorine to the indolenine donor moiety have any influence on the spectroscopic properties since the absorption, excitation and emission maxima for single-modified duplexes with (*S*)-gBAM, (*R*)-gBAM or gBAM^{F} are all located at 473, 472 and 491, respectively. As also observed for the free ribonucleosides, the absorption and excitation maxima for the benzothiazole-derived gmBAM^{b}-modified system are red-shifted by approximately 10 nm due to the electronic effect of the electronegative sulfur. In contrast, the gBAM^{OMe}-modified duplex comprising an electron-donating methoxy function shows broader bands with less defined maxima. Only the emission maximum is red-shifted to 544 nm for this system, therefore leading to the highest Stokes shift of 77 nm of all variants. Since all of the gBAM-chromophores incorporated into DNA 12mer duplexes resemble the spectral features of the respective free chromophores, the influence of the oligonucleotide scaffold on their spectroscopic properties can be neglected. With the knowledge of these characteristics for monomeric, non-interacting chromophores the absorption and fluorescence spectra of gBAM-dimers are evaluated in the next section.

3.6.3.2 Spectroscopic properties of double- and multiple-modified gBAM-DNA 12mer hybrids

In analogy to the dimeric chromophore systems discussed for pure RNA, DNA and GNA backbones, also for the gBAM-DNA hybrids upstream (**DG2/DG19**), downstream (**DG2/DG9**)

and opposite (**DG2/DG15**) oriented dimers were designed. The spectral behavior of these systems was compared to the intrastrand dimer **D1/DG20** with the two gBAM chromophores separated by one nucleoside and the triple-modified duplex **DG2/DG20** combining downstream and upstream orientation as well as **DG2/DG22** comprising five separated gBAM units (Figure 3.103). It has to be mentioned, that for the DNA/GNA hybrids no crystal structures are available and therefore no 3D models of the different systems can be built as done for all of the other backbones so far. In addition, the actual chromophore orientation is not easily predictable due to the higher conformational freedom of the acyclic glycidol building block within the organized DNA scaffold.

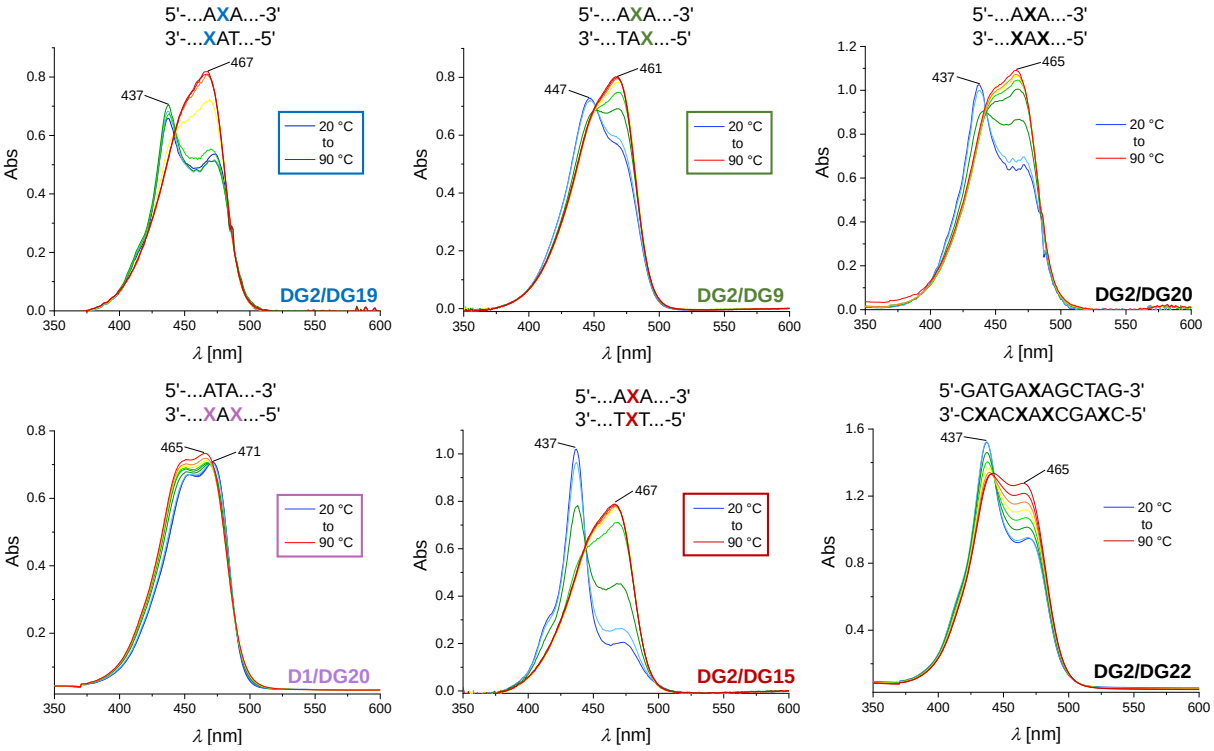

Figure 3.103: Temperature-dependent absorption spectra for double gBAM-modified DNA/GNA hybrid duplexes in upstream (blue), downstream (green) and opposite (red) orientation or with both chromophores in the same strand (purple) as well as structures containing multiple gBAM chromophores. Upon dehybridization, the absorption spectra for systems having two modified strands change markedly with a shift of the main band from H-type dimer absorption at 430–440 nm to the monomer absorption at approximately 470 nm. Conditions: 5 µM samples in 1× PBS (100 mM NaCl, 10 mM phosphate, pH 7.0).

Interestingly, the absorption behaviors for the upstream and downstream dimer (**DG2/DG19** and **DG2/DG9**, Figure 3.103) are very similar in both the fully hybridized and dehybridized states with maxima at approximately 440 and 465 nm, respectively, which is in contrast to all of the other systems discussed so far. Upon combination of these two chromophore orientations giving the triple-modified structure **DG2/DG20**, the overall absorption intensity is increased, as expected, while the position of the absorption maxima still does not change, only the red-shifted shoulder at low temperatures becomes less pronounced. However, the incorporation of

two gBAM chromophores in the same strand or directly opposite each other as in **D1/DG20** and **DG2/DG15** reveals a completely different picture. While for the system **D1/DG20** with only one modified strand solely monomer absorption is observed at all temperatures, two opposing gBAM lead to the formation of the previously observed strong H-type aggregates characterized by a sharp peak at 437 nm with two less intense red- and blue-shifted shoulders for **DG2/DG15**. The formation of these strongly coupled H-type dimers is also here explained by rotation of the BAM nucleobase surrogate around the glycosidic bond, leading to localization of the hydrophobic chromophore in the duplex core shielded from the surrounding water molecules and the charged phosphate backbone.

Therefore, two gBAM chromophores are only able to interact by dipolar coupling if they are located close to each other in the different single strands. This can be explained by the mutual antiparallel orientation of the merocyanines required for H-type assembly which is only realizable for interstrand dimers.

However, the formation of these dipolarly coupled aggregates is also observed for the quintuple-modified duplex **DG2/DG22** although with a larger proportion of residual monomer absorption. For this system, the absorption maximum attributed to chromophore aggregation does not vanish upon duplex melting, indicating the presence of comparably strong intrastrand chromophore-chromophore stacking interactions. Only if the individual chromophores in the single strand are at least three base pairs apart from each other, dipolar intrastrand coupling is enabled even in the random coil state at elevated temperatures which is in contrast to interstrand coupling interactions observed for chromophores directly opposite each other.

The temperature-dependent fluorescence behavior of all of the six systems discussed above resembles the patterns observed in the absorption with a modest H-type dimer excitation maximum at 436 to 444 nm and an emission between 530 and 540 nm along with monomer luminescence at 468 nm in the excitation and approximately 490 nm in the emission for the up- and downstream case **DG2/DG19** and **DG2/DG9** as well as their combination **DG2/DG20** (Figure 3.104). Concomitantly, for the interstrand dimer **D1/DG20** only monomer fluorescence is observed at ambient as well as elevated temperatures. For the duplex **DG2/DG15** with two gBAM directly opposite each other, the overall strongest H-type aggregate fluorescence is recorded with a nicely visible transition to monomer fluorescence in the temperature range of duplex dehybridization, as would be predicted from the observations made for the previously discussed modified structures. Also here, the two chromophores are expected to not be in perfectly antiparallel alignment due to their bulky indolenine methyl groups, leading to a partially allowed transition from the excited aggregate state to the ground state. In the case of the five-fold modified structure **DG2DG22**, only the intensity decrease at elevated temperatures attributed to enhanced non-radiative decay is observed, as for all of the other discussed samples, while the spectra shape remains unchanged. This indicates, as already mentioned,

the presence of pronounced interstrand chromophore-chromophore stacking interactions, not only in the hybridized duplex but also in the single strand.

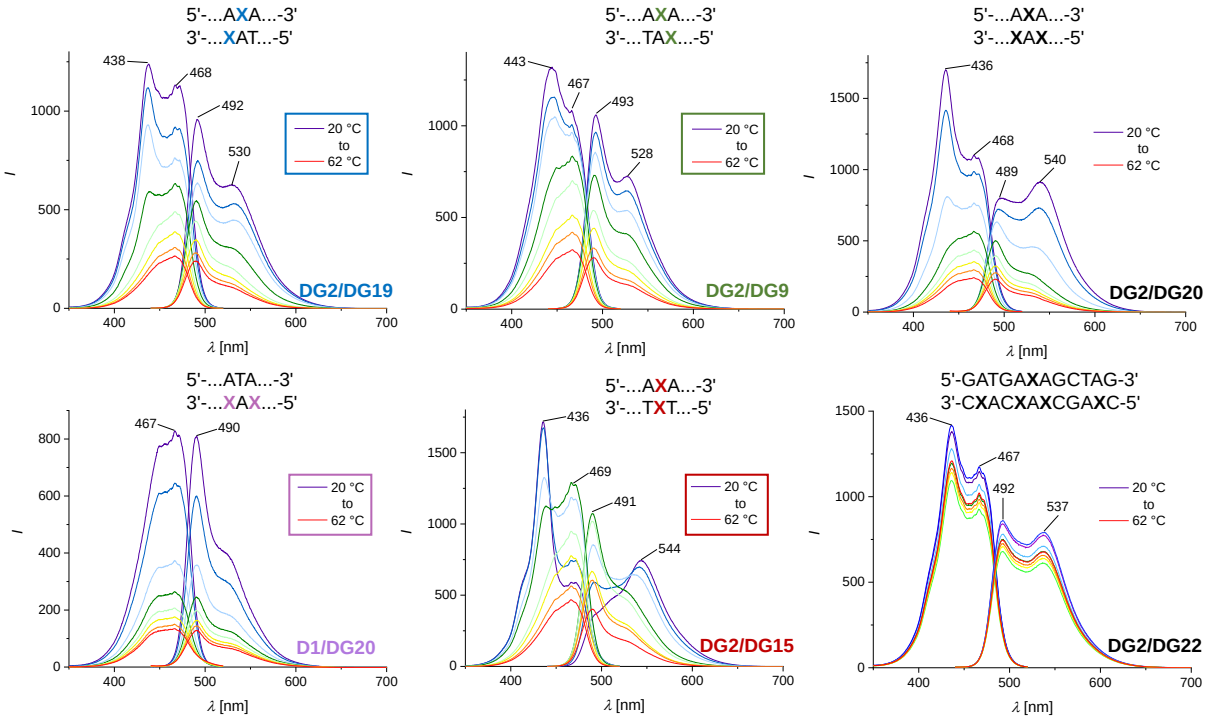

Figure 3.104: The temperature-dependent fluorescence spectra for double-gBAM-modified DNA/GNA hybrid duplexes in upstream (blue), downstream (green) and opposite (red) orientation or with both chromophores in the same strand (purple) as well as structures containing multiple gBAM chromophores reveal the formation of fluorescent interstrand gBAM:gBAM dimers. Conditions: 1 µM samples in 1× PBS (100 mM NaCl, 10 mM phosphate, pH 7.0), excitation at 420 nm, emission at 540 nm.

To further study the influence of an altered donor ring system on the spectroscopic behavior of gBAM interstrand dimers, DNA/GNA hybrids comprising either a gmBAM^{b}:gmBAM^{b} (**DG4/DG11**), a gBAM^{F}:gBAM^{F} (**DG5/DG12**) or a gBAM^{OMe}:gBAM^{OMe} (**DG6/DG13**) dimer in downstream orientation were investigated by temperature-dependent absorption and fluorescence spectroscopy (Figure 3.105). In contrast to the parent gBAM:gBAM downstream dimer **DG2/DG9**, H-type coupling is observed neither in the absorption nor in the fluorescence for **DG4/DG11** containing the two gmBAM^{b} chromophores. At all temperatures, only the spectroscopic features of the monomer are detected, exhibiting a remarkably small Stokes shift of only 15 nm. On the other hand, the hybridized duplex with the gBAM^{F}:gBAM^{F} downstream dimer **DG5/DG12** shows a weakly coupled, fluorescent H-type aggregate which is broken upon melting. Also the maximum of the gBAM^{OMe}:gBAM^{OMe} downstream dimer **DG6/DG13** is hypsochromically shifted by approximately 15 nm at ambient compared to elevated temperatures in both the absorption and fluorescence excitation. However, the dipolar coupling in this case is assumed to be very weak since the bands attributed to H-type aggregates are not sharp but only slightly less broadened in contrast to the bands belonging to the chromophore monomers.

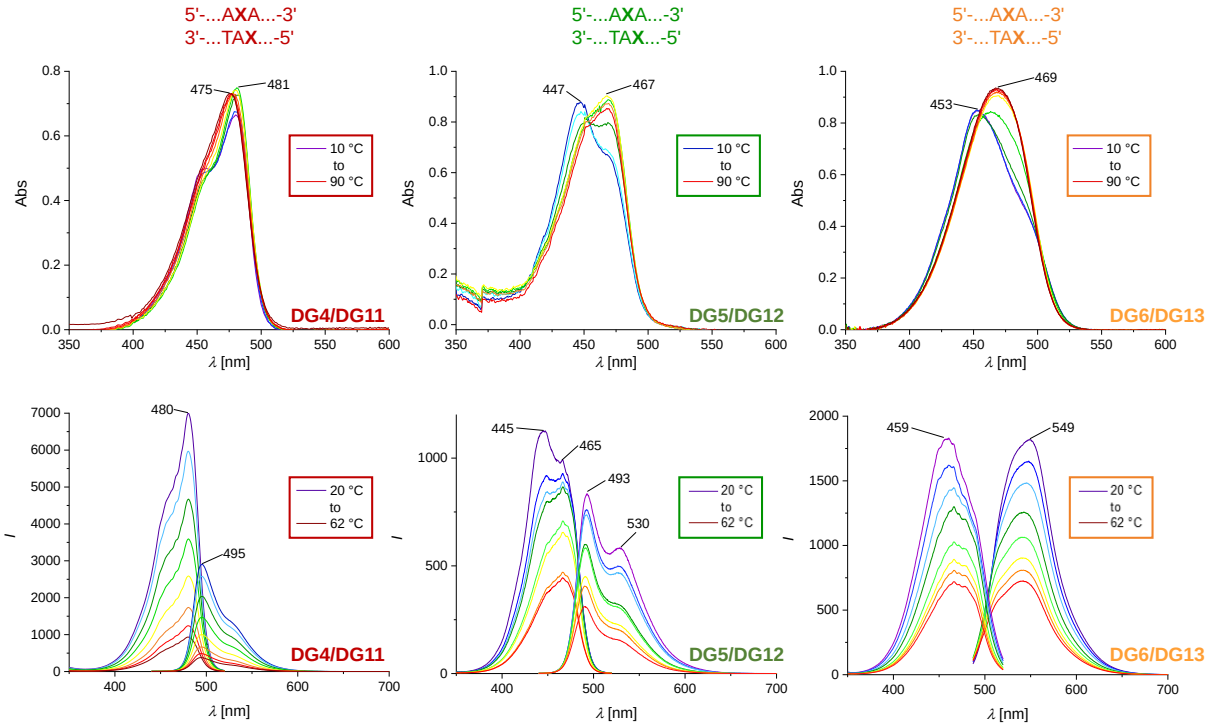

Figure 3.105: Temperature-dependent absorption (top) and fluorescence (bottom) spectra for double-gBAM-modified DNA/GNA hybrid duplexes with either gmBAM^{b}:gmBAM^{b} (red), gBAM^{F}:gBAM^{F} (green) or gBAM^{OMe}:gBAM^{OMe} (orange) dimers in downstream orientation. The change from the indolenine to the benzothiazole donor and the attachment of an additional electron-donating or -withdrawing aromatic substituent leads to pronounced changes of the dimer's spectral properties. Conditions: 1 or 5 µM samples in 1× PBS (100 mM NaCl, 10 mM phosphate, pH 7.0). Excitation at 420 nm, emission at 540 nm, for gBAM^{OMe}-modified oligonucleotides excitation and emission at the maximum.

The explanation of the distinct spectroscopic behavior and coupling strength of these different downstream dimers must be based on mostly steric rather than electronic reasons. The gBAM^{F}-modified duplex **DG5/DG12** contains chromophores which are structurally very similar to the initial gBAM, therefore showing consistent spectral patterns. gmBAM^{b} and gBAM^{OMe} comprise a methyl or an additional methoxy groups at either the barbituric acid moiety or the aromatic system, respcetively, which might prevent these dyes from adopting the conformation required efficient stacking due to their steric demand. Interestingly, the methyl group attached to the barbituric acid acceptor seems to have a larger influence here since for the gmBAM^{b}:gmBAM^{b} system **DG4/DG11** not even weak H-type dipolar coupling is observed although for both the dBAM^{b}:dBAM^{b} and rBAM^{b}:rBAM^{b} downstream dimers in DNA and RNA, respectively, the formation of these dimers was clearly detected.

The spectroscopic properties of the differently substituted chromophores can also to some extent be explained by molecular parameters obtained from ab initio calculations. These were carried out for the geometry-optimized free merocyanine chromophores and are summarized in

Table 3.38 for comparison with reported values for TO. Given are the absorption, excitation and emission maxima for BAM, BAM^{b}, BAM^{F} and BAM^{OMe} in the fully dehybridized downstream dimer containing duplex as well as the calculated values for the permanent ground state dipole moment μ (discussion see section 3.1.3.), the LUMO energy E_{LUMO} and the HOMO-LUMO energy gap $\Delta E_{HOMO\text{-}LUMO}$ for the respective free chromophores.

The HOMO-LUMO energy gap explains the charge transfer interaction within the molecule and is useful to determine molecular electrical transport properties. Molecules with a high HOMO-LUMO gap have a comparably low chemical reactivity and a higher kinetic stability because it is energetically unfavorable to add an electron to the high-lying LUMO in order to remove electrons from the low-lying HOMO.[457] Furthermore, the HOMO-LUMO gap is correlated with the spectroscopic properties of a molecule, as nicely visible for the emission maxima of the investigated merocyanine chromophores. For instance, the highest band gap of 3.398 eV was obtained for BAM which displayed the most blue-shifted emission maximum at 491 nm for the HOMO-LUMO transition while for gBAM^{OMe} with a red-shifted emission at 549 nm a smaller band gap of 3.265 eV was observed, comparable to the values reported for TO.[306,458,459]

Table 3.38: Parameters for geometry-optimized free merocyanine chromophores obtained by ab initio calculations. Given are the positions of the most intense absorption, excitation and emission maxima of fully dehybridized duplex structures containing the downstream dimer of the respective chromophore along with the calculated values for the permanent ground state dipole moment μ, the LUMO energy E_{LUMO} and the HOMO-LUMO band gap $\Delta E_{HOMO\text{-}LUMO}$.

Compound	λ_{Abs} nm	λ_{Ex} nm	λ_{Em} nm	μ D	E_{LUMO} eV	$\Delta E_{HOMO\text{-}LUMO}$ eV
BAM	467	467	491	7.70	-2.219	3.398
BAM^{F}	467	465	493	6.54	-2.279	3.379
BAM^{b}	481	480	495	9.14	-2.228	3.346
BAM^{OMe}	469	459	549	8.30	-2.116	3.265
TO[306,458,459]	502	512	533	4.14	-2.72	3.27

Furthermore, the LUMO energy is related to the electronic properties of the substituents on the aromatic merocyanine donors. The methoxy group in BAM^{OMe} is electron-donating by conjugation, therefore increasing the electron density in the conjugated system and leading to the least negative LUMO energy of -2.116 eV. Compared to the parent compound BAM, the two chromophores BAM^{F} and BAM^{b} contain either the strongly electron-withdrawing fluorine or the only weakly electron-withdrawing sulfur atom, respectively, which leads to a

lower electron density within the system and therefore more negative LUMO energies.

In conclusion, the theoretical molecular parameters of the individual chromophores obtained by ab initio calculations correlate well with the observed spectroscopic properties within the oligonucleotide scaffold. Since these characteristics also have an influence on chromophore-chromophore interactions, the potential of the gmBAM^{b} chromophore to form dipolarly coupled H-type aggregates was explored by generating the DNA/GNA hybrid system with the respective opposite dimer **DG4/DG17**. For this structure, the arising of the relative to the monomer hypsochromically shifted absorption band at 450 nm at low temperatures is unambiguously assigned to strong dipolar chromophore-chromophore coupling interactions, also reflected by the high duplex melting temperature of this sample (Figure 3.106). However, in the fluorescence no such blue-shift but only monomer luminescence is observed and the emission spectrum is a mirror image only for the monomeric state, rendering the H-type dimers as non-fluorescent. A reason for this behavior of the opposite dimer, especially in comparison to the fully uncoupled chromophores in the downstream orientation in **DG4/DG11**, might be the closer proximity of the two merocyanine nucleoside analogs here. To administer both gBAM nucleobase surrogates in the duplex core, a structural distortion and partial unwinding of the oligonucleotide scaffold is required. In the opposite dimer, none of the two chromophores has a counterbase for Watson-Crick base pairing which might cause steric restrictions with the barbituric acid methyl group and interfere with chromophore stacking due to its hydrophobic aromatic ring system. Therefore, dipolar stacking is facilitated for the opposite structure **DG4/DG17** compared to the downstream gmBAM^{b}:gmBAM^{b} dimer **DG4/DG11**.

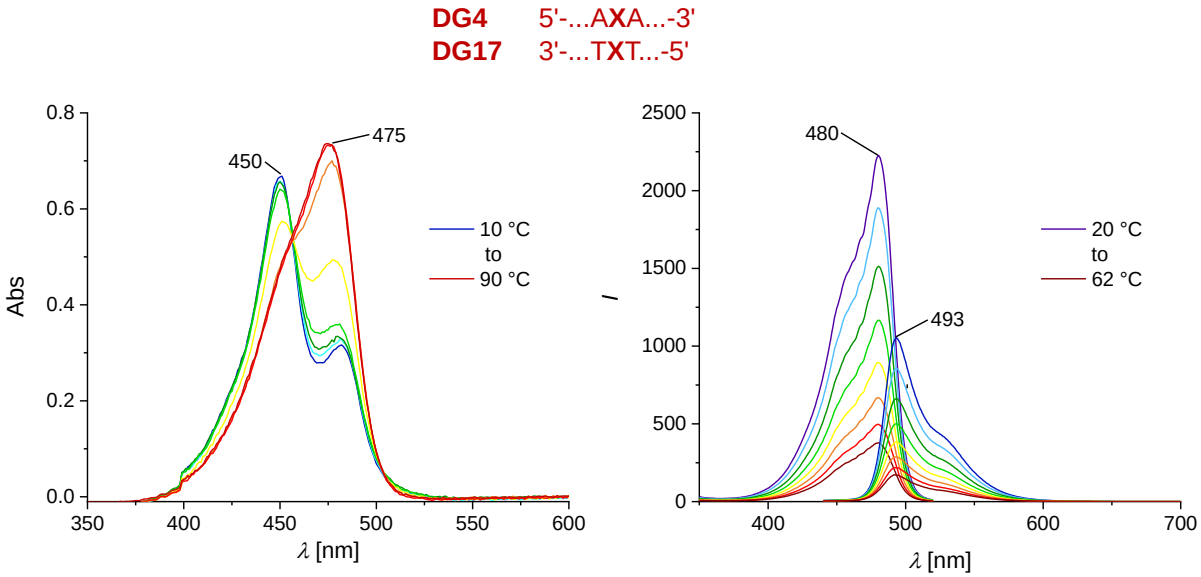

Figure 3.106: The temperature-dependent absorption and fluorescence spectra for the opposite gmBAM^{b}:gmBAM^{b} dimer **DG4/DG17** show the presence of non-fluorescent H-type aggregates which vanish upon duplex melting. Conditions: 1 or 5 µM samples in 1× PBS (100 mM NaCl, 10 mM phosphate, pH 7.0). Excitation at 420 nm, emission at 540 nm.

To further investigate the relative arrangement of the two merocyanines in the different chromophore dimers, CD spectra were recorded for all of the samples (Figure 3.107). The Cotton effects observed in the nucleobase absorption region resemble those found for pure DNA strands with only minor deviations, indicating that all of the different gBAM variants are well tolerated within the oligonucleotide scaffold. Only for the quintuple-modified system **DG2/DG22** the observed CD bands between 200 and 300 nm are slightly less intense, which might be attributed to the lower nucleobase content in this system. As expected, pronounced CD couplets for gBAM:gBAM-dimer modified duplexes are only observed for systems with weakly coupled H-type aggregates (Figure 3.107a), which were recorded for the upstream as well as the downstream gBAM:gBAM dimer in **DG2/DG19** and **DG2/DG9** and the systems containing more than two merocyanines. The downstream dimer **DG2/DG9** exhibits the most intense positive Cotton effect with zero-crossing at 460 nm and two similar intense couplets attributed to the main electronic transition of the H-type dimer. Also for the upstream dimer **DG2/DG19** a positive Cotton effect is observed, although here the two bands are not symmetric but the higher wavelength band shows a higher ellipticity. This lower energy band in excitonic CD spectra is attributed to attractive, stabilizing processes which implies the presence of further modes of chromophore-chromophore coupling interactions within this duplex structure.

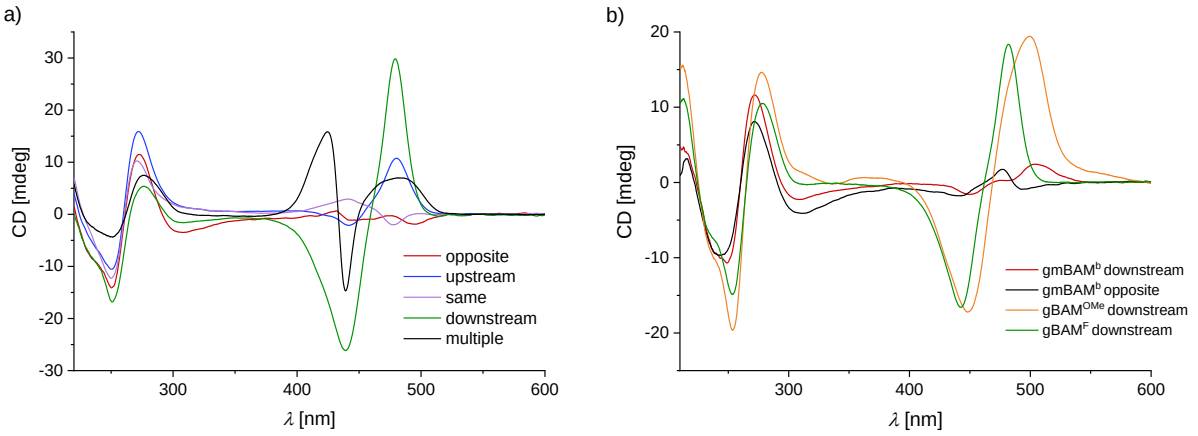

Figure 3.107: The CD spectra for gBAM-dimers and the gBAM-pentamer within 12mer DNA/GNA hybrid structures reveal a pronounced distance and geometry dependence of the exciton coupling (a). For structures containing dimers of different gBAM variants, only the methoxy- and fluorine-substituted chromophore exhibit Cotton effects in the merocyanine absorption region (b). Conditions: 5 µM samples in 1× PBS (100 mM NaCl, 10 mM phosphate, pH 7.0).

This also holds true for the five gBAM-containing duplex **DG2/DG22** with an additional positive CD band detected at 410 nm. Meanwhile, the uncoupled interstrand dimer in **DG1/DG20** is expectedly CD silent between 350 and 550 nm, such as the opposite dimer. The intensity of the exciton CD is described by the *A*-factor which is inversely proportional to the square of the interchromophoric distance and a function of the dihedral angle between the two transition moments. If the dipole moments of the two chromophores are coplanar and antiparallel

aligned, the dihedral angle between them approaches zero, leading to the disappearance of the CD signal.

Very similar observations are made for the DNA/GNA hybrids modified with gBAM-variants: while the downstream gBAM^{F} and gBAM^{OMe} dimers **DG5/DG12** and **DG6/DG13** show a strongly defined positive Cotton effect, neither of the gmBAM^{b}:gmBAM^{b} dimers **DG4/DG11** and **DG4/DG17** show a CD band, which matches the conclusions drawn before (Figure 3.107b).

Since gBAM dimers in the DNA scaffold showed interesting spectroscopic features, DNA/GNA hybrid structures with an stepwise increasing number of chromophores were analyzed and are discussed in the following section.

3.6.3.3 Spectroscopic properties of multiple-modified gBAM-DNA 17mer hybrids

As a basis for the discussion of multiple-gBAM-modified DNA/GNA hybrids, the structurally akin intrastrand and interstrand gBAM dimers **DG30/D24** and **DG28/DG29** within the core of the 17mer DNA duplex are compared with regard to their absorption and fluorescence behavior at different temperatures (Figure 3.108).

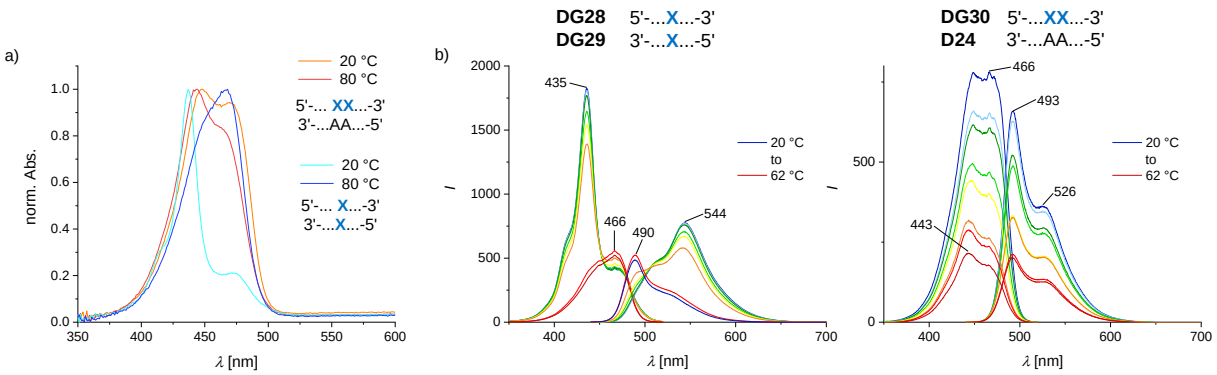

Figure 3.108: Inter- and intrastrand gBAM dimers **DG30/D24** and **DG28/DG29** show a remarkably diverse absorption (a) and fluorescence (b) behavior in both the fully hybridized and denatured duplex, attributed to differently pronounced dipolar coupling interactions. Conditions: 1 or 5 µM samples in 1× PBS (100 mM NaCl, 10 mM phosphate, pH 7.0).

The interstrand dimer with the two chromophores directly opposite each other remsembles the absorption pattern observed for the shorter 12mer opposite dimer **DG2/DG15** with a sharp, hypsochromically shifted band at ambient temperature attributed to the formation of an H-type assembly. Meanwhile, at elevated temperatures above the duplex melting point only monomer absorption is detected.
In contrast, the blue-shifted absorption band for the intrastrand dimer **DG30/D24** is much less pronounced and possesses a longer-wavelength shoulder with an intensity of over 80% of

the maximum. Even in the dehybridized state the absorption band associated with dipolar coupling is still present although the monomeric absorption is intensified with around 95% of the maximum's absorbance.

The remarkable difference between the inter- and the intrastrand gBAM dimer becomes obvious also in the excitation and emission spectra: while the H-type fluoresence of the opposite gBAM dimer **DG28/DG29** is assigned to the intense sharp excitation band at 435 nm and the red-shifted emission maximum at 544 nm (Figure 3.108b), a much less pronounced aggregate luminescence is observed for the intrastrand dimer **DG30/D24**. For this case, the peaks' shapes remain similar upon increasing temperatures, with a comparably high monomer fluorescence intensity in the hybridized duplex and fluorescence maxima belonging to dipolar coupled chromophores also visible for the single-stranded state.
Interestingly, the spectroscopic properties of this system with the two chromophores positioned directly next to each other strongly differ from the shorter 12mer duplex **D1/DG20** were the two merocyanines were separated by one nucleoside and no dipolar coupling was observed. Thus, the two chromophores need to be located in close proximity for efficient dipolar coupling. The resulting interactions show to be remarkably strong and independent from the organized oligonucleotide scaffold as they are still present at 80 °C, which is well above the duplex melting point and the single strands are expected to exist as random coils.

To expand the chromophore stack, up to five gBAM modifications were consecutively incorporated into the single strands and hybridized with different counterstrands. For all of these samples, the temperature-dependent absorption and fluorescence characteristics were analyzed. For simplification, only the absorption spectra for the hybridized and denatured duplex at 20 and 80 °C, respectively are shown while the complete data sets can be found in the appendix. At ambient temperature, H-type aggregate absorption is observed for all of the four duplexes summarized in Figure 3.109, with the most pronounced hypsochromically shifted band and the least intense monomer band for the dimer **DG28/DG29** (**2**). With increasing gBAM content, the absorption band assigned to H-type assembly formation is broadened and the proportion of monomer absorbance depends on the number of gBAM opposite a canonical nucleobase. For both the triple- and the quintuple-modified duplex **DG30/DG29** (**3**) and **DG30/DG32** (**5**) with one gBAM each opposite either A or T, the monomer band intensity constitutes to 50% of the aggregate absorbance, while for the quadruple-modified system **DG31/DG29** (**4**) with two gBAM having A in the counterstrand the monomer intensity is approximately 70% of the maximum. These observations support the hypothesis of stable interstrand dimer formation with the two chromophores positioned directly opposite each other while two adjacent gBAM in the same strand only form weakly interacting dimers with a larger proportion of monomer absorption.

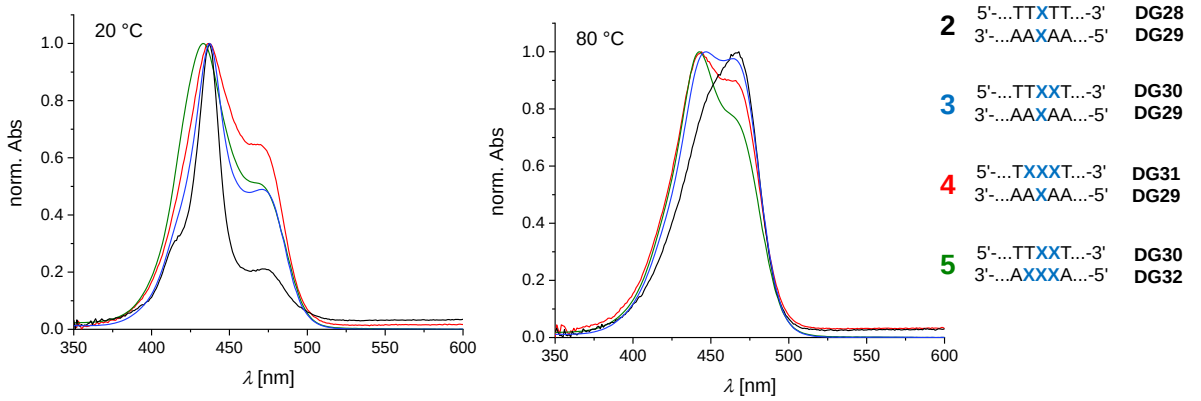

Figure 3.109: For multiple-gBAM-modified DNA/GNA 17mers with up to five chromophores, H-type aggregation is observed in the normalized absorption of the hybridized duplexes. Upon heating, these dipolarly coupled chromophores are only detected for systems containing at least three modifications, attributed to intrastrand stacking interactions. Conditions: samples in 1× PBS (100 mM NaCl, 10 mM phosphate, pH 7.0), concentration adjusted for a maximum absorbance of approximately one.

In the fully denatured state at 80 °C, dipolar chromophore coupling is still observed for systems containing more than two gBAM with the intensity of the monomer absorbance inversely proportional to the total dye content within the sample (78%, 90% and 98% of the maximum's absorbance for the monomer absorption within the quintuple-, quadruple- and triple-modified systems, respectively).

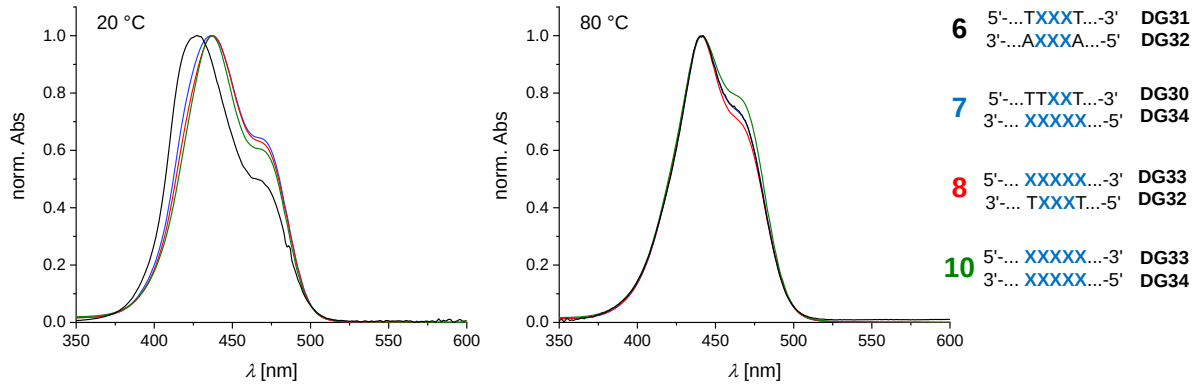

Figure 3.110: All of the multiple-gBAM-modified DNA/GNA 17mers containing five to ten chromophores show absorption characteristics attributed to H-type aggregation in both the hybridized and fully denatured duplex at 20 and 80 °C, respectively. Conditions: samples in 1× PBS (100 mM NaCl, 10 mM phosphate, pH 7.0), concentration adjusted to a maximum absorbance of approximately one.

If the chromophore content of the examined systems is even further increased up to ten, the overall shape of the absorption spectra is independent from the number of modifications (Figure 3.110). For both ambient and elevated temperature, aggregate absorption is observed, experiencing a small red-shift from 436 to 441 nm between 20 and 80 °C. Additionally, the intensity of the monomer absorption band does not rely on the chromophore distribution in

the individual single strands of the duplex anymore.

Therefore, for systems with up to five chromophores a statement about the chromophore content within the system and their mutual orientation can be made by evaluating the absorption behavior. If the number of gBAM nucleosides is even more increased, the absorption spectra shape remains unaltered for systems with six to ten chromophores due to extensive concurrent intra- and intrastrand stacking interactions.

The spectroscopic patterns observed in the absorption can be transferred to the fluorescence spectra of the multiple-modified DNA/GNA hybrid systems. Exemplarily, the temperature-dependent excitation and emission spectra for duplexes with either three, five or ten chromophores are shown in Figure 3.111; the temperature-dependent fluorescence spectra for all of the other modifed DNA/GNA hybrids can be found in the appendix.

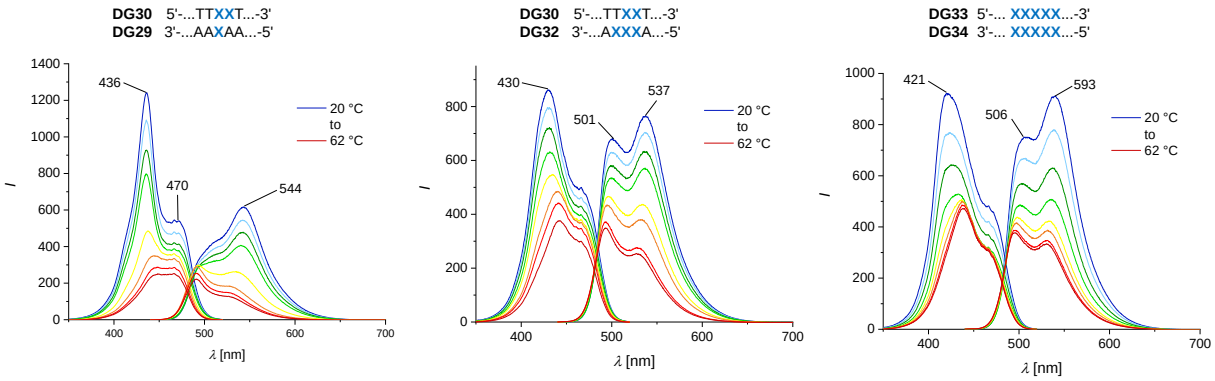

Figure 3.111: Temperature-dependent fluorescence analyses show the presence of emissive H-type aggregates in both the hybridized and denatured duplex for DNA/GNA hybrids containing at least three gBAM chromophores. Conditions: 1 µM samples in 1× PBS (100 mM NaCl, 10 mM phosphate, pH 7.0), excitation at 420 nm, emission at 540 nm.

Also here, the formation of emissive H-type aggregates is observed for every system. The excitation maximum between 420 and 440 nm assigned to these dipolarly coupled assemblies is gradually broadened and shifts to shorter wavelengths with increasing gBAM content. Besides these effects, the fluorescence behavior is comparable for quintuple- or higher modified systems, making them basically indistinguishable by spectroscopic means. For all of the studied multichromophore systems, chromophore assembly is also observed at temperatures above the melting temperatures due to extensive intrastrand stacking interactions, as discussed previously for other samples with at least two gBAM incorporated consecutively into one strand. Notably, the fluorescence intensity does not show a correlation to the number of merocyanines in the sequence but is comparable for all of the samples which implies the partial quenching of gBAM within multichromophore stacks. Furthermore, this observation is also due to the preferred antiparallel dimerization of the BAM chromphores by strong electrostatic dipole-dipole

interactions while further aggregation into larger chromophore stacks is only guided by weaker dispersion forces as the ground state dipole moment of the dimer is close to zero.[356]

For the complete spectroscopic analysis of the observed hydrophobic π-π excitonic interactions, CD spectra were recorded also for the heavily modified DNA/GNA hybrid systems; some selected ones are shown in Figure 3.112. Independent from the degree of modification, most of the examined duplex structures show a positive Cotton effect in the chromophore absorption region centered around the absorption maximum of the isolated monomer at approximately 460 nm, indicating a clockwise arrangement of the chromophores induced by the oligonucleotide secondary structure.

The recorded excitonic CD bands are not fully symmetric: while the positive CD bands for systems comprising up to five gBAM chromophores all show a split positive band with two maxima of almost equal intensity, the negative CD band only shows one sharp maximum (Figure 3.112a). However, the CD band for duplex structures with even more modifications only exhibits one positive pronounced maximum with a shoulder at the blue-shifted edge, reflecting the shape of the absorption spectrum (Figure 3.112b). It also has to be noted that the CD spectrum for the ten-fold modified duplex is slightly shifted to longer wavelengths, presumably due to the combination of various different chromophore stacking modes. An additional interesting experiment would be to record temperature-dependent CD spectra for the samples shown here, which was not done here due to the lacking of a temperature-adjustable CD device. CD spectra at temperatures above the duplex melting temperature will reveal the degree of single strand preorganization and the resulting handedness introduced by directional dipolar chromophore stacking interactions.

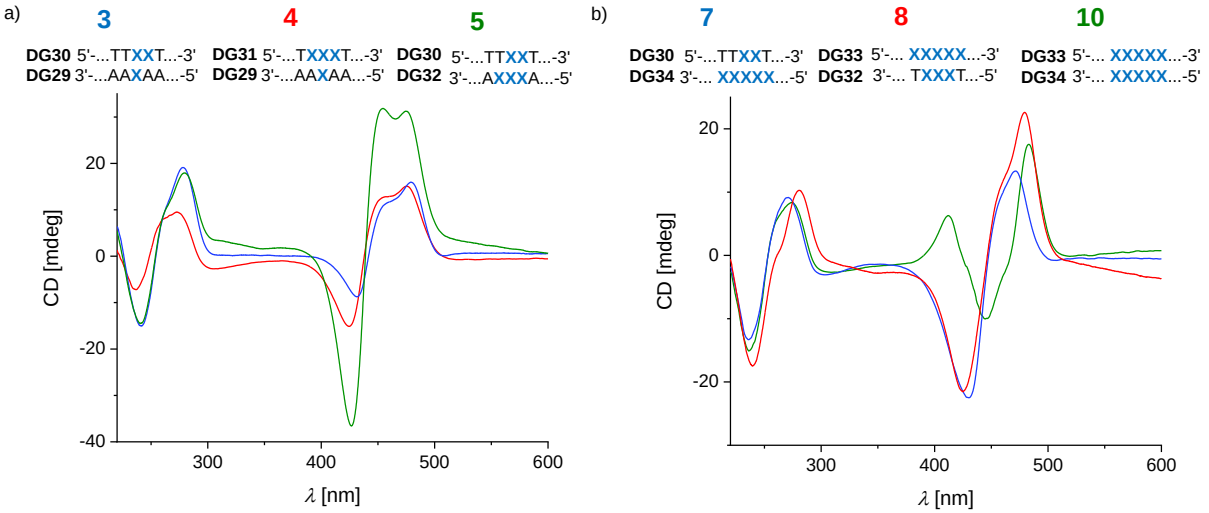

Figure 3.112: The CD spectra for all of the multichromophoric DNA/GNA hybrid structures show strong positive Cotton effects with split positive bands for systems with less than six modifications, indicating extensive inter- and intrastrand stacking interactions. Conditions: 5 μM samples in 1× PBS (100 mM NaCl, 10 mM phosphate, pH 7.0).

In summary, short 17mer DNA duplexes were extensively gBAM-modified, substituting up to 30% of the original canonical nucleobases. These structures are still capable of stable duplex formation, as proven by the good quality of the duplex melting curves and the typical B-DNA helix pattern observed in the individual CD spectra. The multichromophoric stacks accessible by hybridization of two heavily core-modified single strands exhibit interesting spectroscopic characteristics attributed to strong inter- and intramolecular H-type aggregate formation. The spectral features of DNA/GNA hybrids containing more than five merocyanine nucleoside analogs are repetitive since they are apparently dominated by intra- rather than interstrand stacking interactions.

As the dipolar coupling of two gBAM chromophores showed to be strongly dependent on the spatial arrangement of these nucleobase surrogates, it was assumed that this feature could be exploited for oligonucleotide structure analysis. As a suitable oligonucleotide sequence, the palindromic DDD was chosen since it comprises two T at different positions for gBAM substitution and can also be modified at both the 3'- and the 5'-end to investigate dipolar stacking interactions in duplex as well as hairpin structures. The spectroscopic properties of these systems are discussed in the following section.

3.6.3.4 Spectroscopic properties of gBAM-modified Dickerson Drew dodecamers

The thermodynamic analysis of DDD modified with a single gBAM at two different positions, namely **DG24** and **DG25**, already proved the formation of a hairpin or duplex structure if the chromophore was incorporated either closer to the 3'- or 5'-end, respectively.

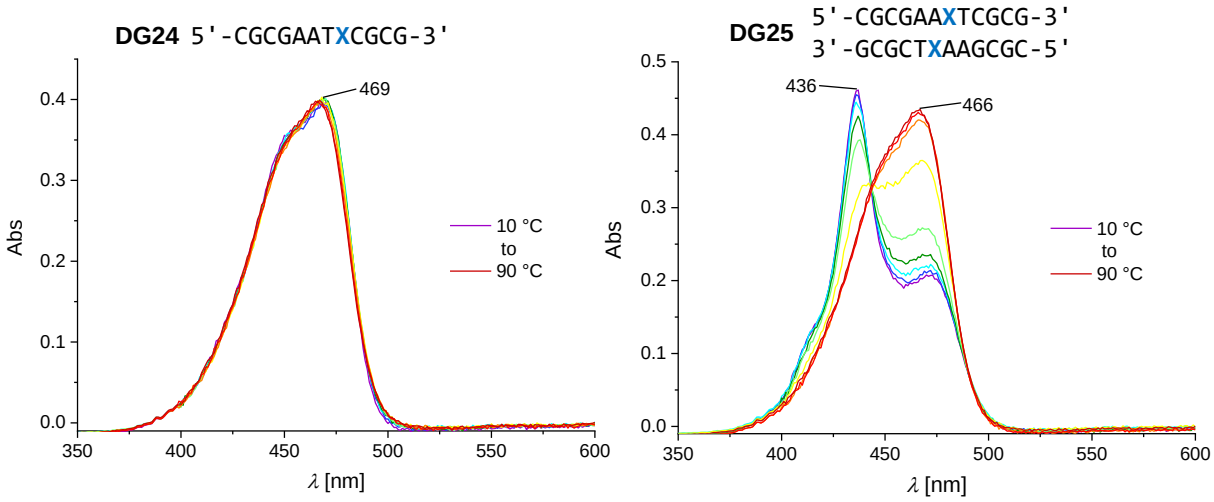

Figure 3.113: The substitution of either of the two T in the DDD sequences gives rise to remarkably different absorption spectra caused by the presence and absence of proximity-dependent dipolar coupling interactions. Conditions: 5 µM samples in 1× PBS (100 mM NaCl, 10 mM phosphate, pH 7.0).

Due to the useful spectral characteristics of dipolarly coupled gBAM-dimers, these findings are

unequivocally confirmed by temperature-dependent absorption as well as fluorescence spectra. In contrast, substitution of the other T in **DG25** provokes strong H-type aggregate absorption for the hybridized duplex, indicated by the characteristic hypsochromically shifted maximum at 436 nm. The conclusions drawn from the different temperature-dependent absorption experiments are clearly supported by fluorescence spectroscopy. Here, for the assumed DDD hairpin structure **DG24** only monomer excitation and emission is detected while for the expected duplex of **DG25** emissive dipolarly coupled chromophore dimers with excitation and emission maxima at 435 and 535 nm, respectively, are found (Figure 3.114). For the DDD variant with gBAM closer to the 3'-end, **DG24**, even at ambient temperature only monomer absorption is recorded which excludes the presence of electronically interacting merocyanines .

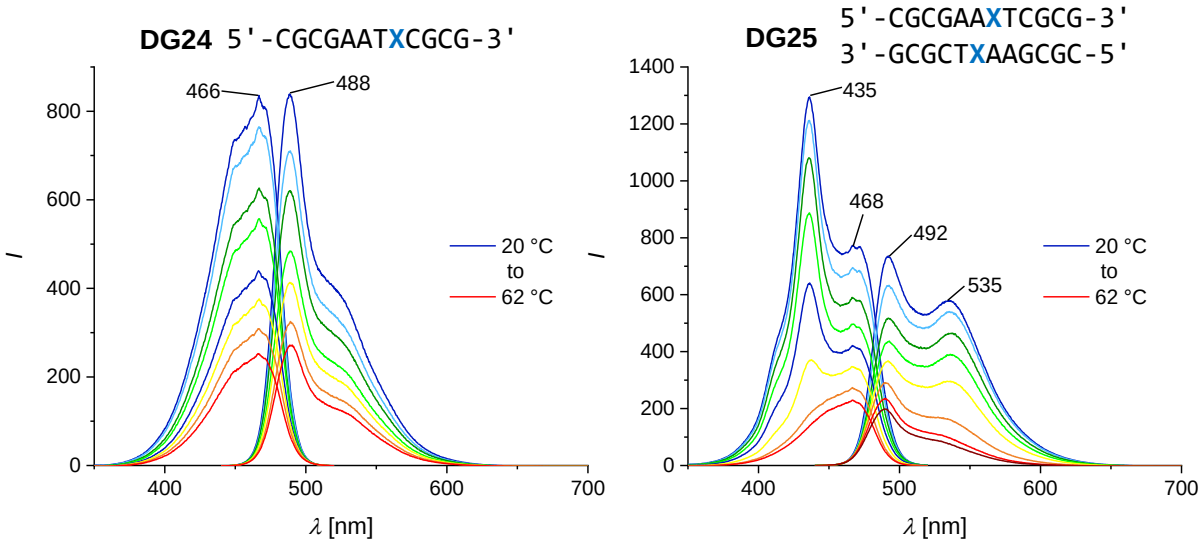

Figure 3.114: The temperature-dependent fluorescence spectra confirm the formation of H-type aggregates for **DG25** while for the DDD variant with gBAM by one position closer to the 3'-end (**DG24**) only monomer excitation and emission is recorded. Conditions: 1 µM samples in 1× PBS (100 mM NaCl, 10 mM phosphate, pH 7.0), excitation at 420 nm, emission at 540 nm.

If the gBAM nucleoside analogs are not incorporated in the core but as overhangs on the 3'- and 5'-ends of the DDD in **DG26** and **DG27**, a similar spectral behavior as observed for the **DG25** duplex is obtained (Figure 3.115). Here, the hypsochromically shifted absorption band is much sharper if the self-complementary sequence contains not only two but three merocyanines, which is rationalized by the more intense monomer absorption for the latter case. Also for these systems, the results from absorption and fluorescence spectroscopy are consistent since for both examined modified 12mers emissive H-type aggregates are recorded (Figure 3.116).

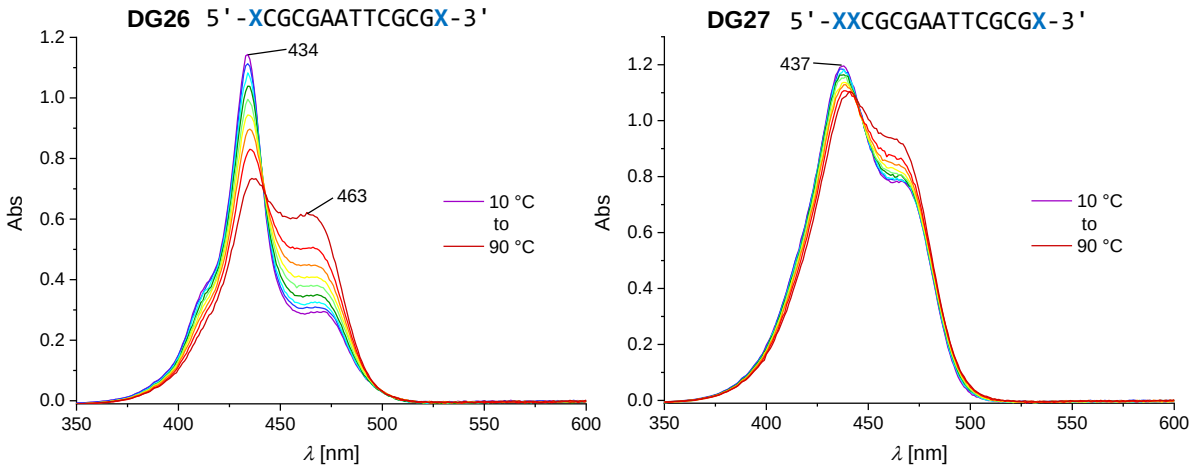

Figure 3.115: DDD sequences end-modified with gBAM show intense H-type aggregate absorption with the proportion of monomer absorption depending on the number of chromophores at the 5'-end. Conditions: 5 µM samples in 1× PBS (100 mM NaCl, 10 mM phosphate, pH 7.0).

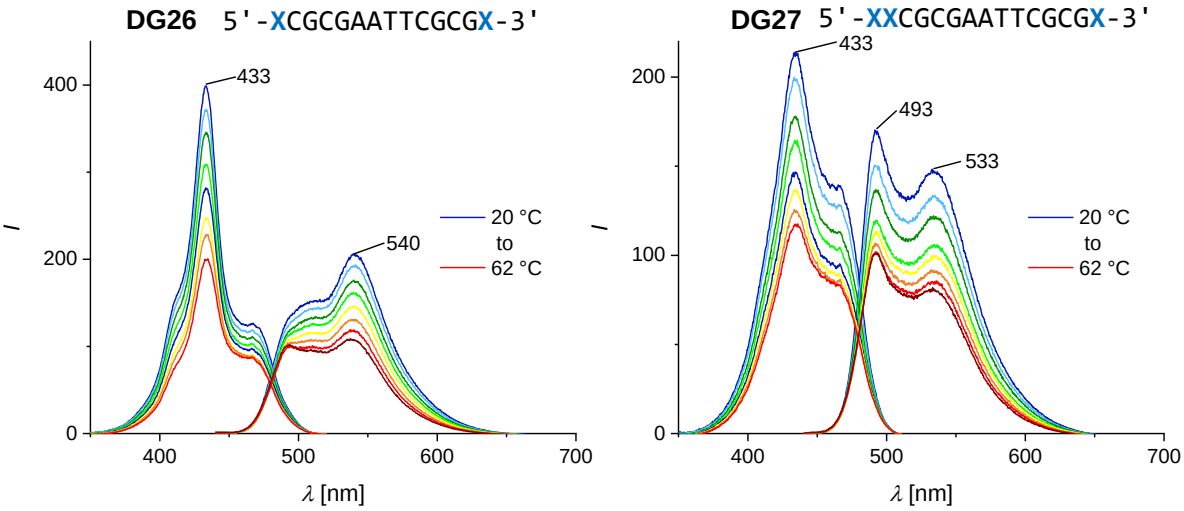

Figure 3.116: The formation of emissive dipolarly coupled chromophore stacks is certified by temperature-dependent fluorescence spectra of end-modified DDD sequences. Conditions: 1 µM samples in 1× PBS (100 mM NaCl, 10 mM phosphate, pH 7.0), excitation at 420 nm, emission at 540 nm.

Obviously, the two or three overhanging gBAM chromophores are still partially stacked at 90 °C which becomes evident by the small change in the position of absorption and fluorescence maxima at increasing temperatures. Therefore, it can be concluded that the hydrophobic chromophore-chromophore interactions are either due to intrastrand stacking, if both strands are present in hairpin conformation, or to the formation of larger, thermally stable multi-strand assemblies.

To further investigate these interactions, CD spectra were recorded (Figure 3.117).

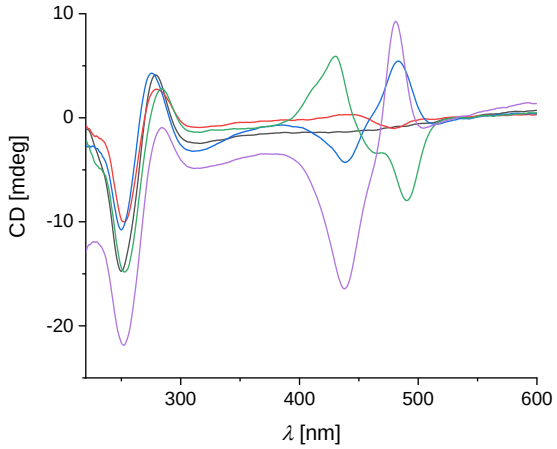

D21 5'-CGCGAATTCGCG-3'
3'-GCGCTTAAGCGC-5'

DG25 5'-CGCGAAXTCGCG-3'
3'-GCGCTXAAGCGC-5'

DG26 5'-XCGCGAATTCGCGX-3'

DG27 5'-XXCGCGAATTCGCGX-3'

DG24
A T
A X
G C
C G
G C
5'-C G-3'

Figure 3.117: The CD signals for single-gBAM-modified DDD sequences show the expected patterns while end-modified dodecamers lead to negative Cotton effects, implying a counter-clockwise chromophore arrangement. Conditions: 5 µM samples in 1× PBS (100 mM NaCl, 10 mM phosphate, pH 7.0).

These confirm B-form duplex formation by the typical pattern in the nucleobase absorption region for all DDD variants. As expected, for the unmodified reference **D21** and the single-modified **DG24** present in hairpin conformation no CD band is observed while the **DG25** duplex with the dipolarly coupled upstream dimer shows a positive Cotton effect. Contrary to this, strong bisignate CD signals with negative Cotton effects are recorded for both end-modified DDD sequences **DG26** and **DG27**. Thus, the chromophores here are arranged with counterclockwise screw sense although their orientation is still dictated by the DNA scaffold.

Since it was suspected that the two end-modified dodecamers **DG26** and **DG27** might form higher-order aggregates, these two sequences were prepared for AFM imaging by spin-coating on a hydrophilic mica surface pre-treated with $NiCl_2$ to immobilize the negatively charged oligonucleotides. For the double-modified sequence **DG26**, only short rod-like aggregates with a diameter of 0.63±0.05 nm and a length of up to 16 nm were measured (Figure 3.118). In contrast, the aggregates observed for the triple-modified DDD **DG27** were of the same diameter with 0.62±0.03 nm but almost double as long with lengths up to 30 nm (Figure 3.119). Since the length of the 12meric DDD duplex is expected to be approximately 3.8 nm (calculated for a 12 bp B-form DNA helix with 10.4 base pairs and a length of 3.32 nm per turn) which is also in accordance with a reported persistence length of roughly 4 nm, the observed small rods must be attributed to the formation of higher molecular aggregates by end-to-end aggregation.[460]

The measured heights of approximately 0.6 nm are much smaller than the expected diameter of a B-form DNA duplex of 2 nm. However, reported heights of DNA in AFM are often below 2 nm, except for contact AFM in aqueous solutions, and depend on the AFM conditions, with values ranging from 0.5 to 1.9 nm in air and propanol. The discrepancy between the measured and expected height is probably due to compression of the DNA by the cantilever tip.[461]

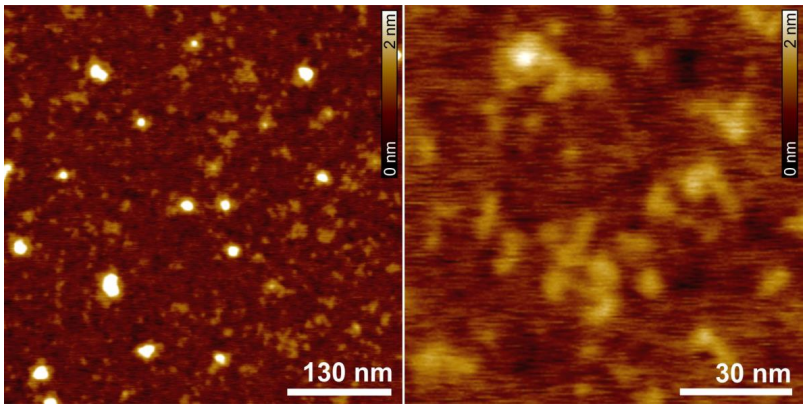

Figure 3.118: The height AFM image of **DG26** on mica shows the formation of short rod-like aggregates with lengths of up to 16 nm. Conditions: 10 µM sample in water, silicon cantilever with a resonance frequency of ~70 kHz and a spring constant of ~1.7 Nm^{-1}. AFM measurements were conducted by Dr. Vladimir Stepanenko.

The formed aggregates of **DG27** were easily destroyed by the cantilever tip due to the weak adhesion of the single aggregates to the mica surface, making it difficult to take multiple close-up images of this sample.

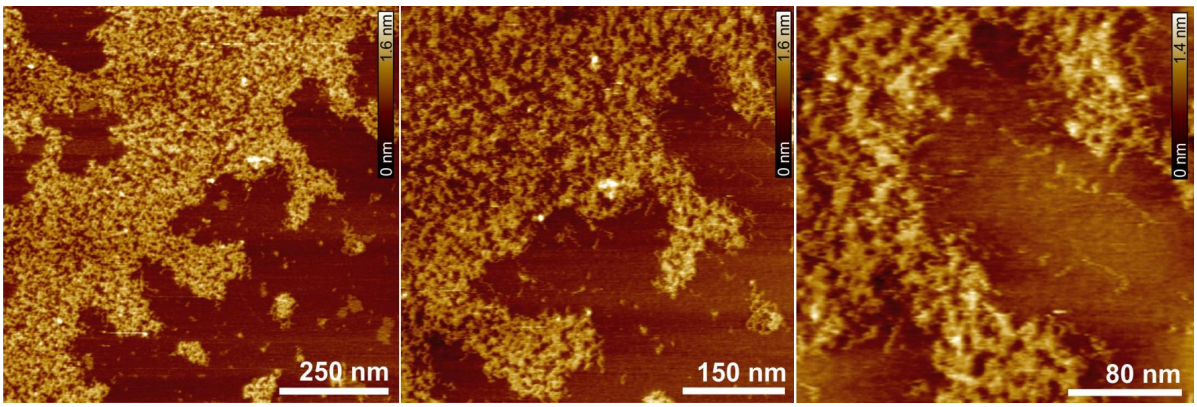

Figure 3.119: The height AFM image of **DG27** on mica shows the formation of a thin film consisting of rod-like assemblies with an approximate length of 60 nm. Conditions: 10 µM sample in water, silicon cantilever with a resonance frequency of ~70 kHz and a spring constant of ~1.7 Nm^{-1}. AFM measurements were conducted by Dr. Vladimir Stepanenko.

The preferred formation of longer and more stable aggregates for the triple-modified DDD sequence **DG27** compared to the double-modified variant **DG26** can be explained by a different extent of end-to-end stacking of the single duplexes. For **DG26** with only one overhanging gBAM on each end the single duplexes can only interact by weak dipolar inter-helical chromophore interactions by face-to-face arrangement of the individual single strands (Figure 3.120). On the other hand, the additional modification in **DG27** leads to a head-to-tail arrangement, promoting the formation of larger aggregates due to a higher chromophore content.

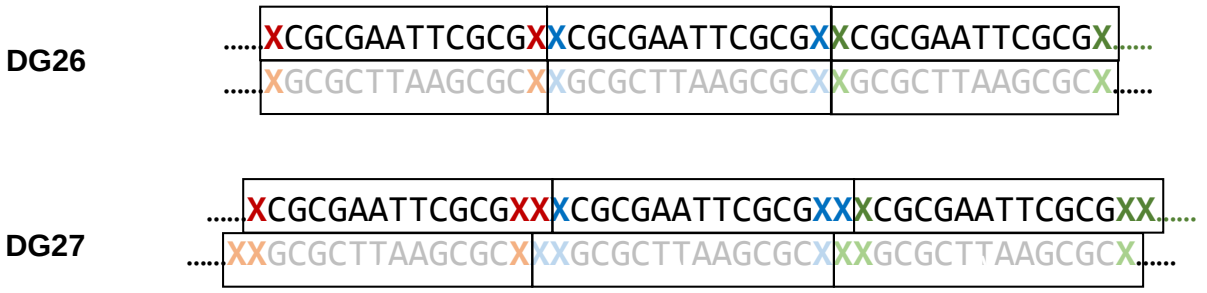

Figure 3.120: Due to the asymmetric structure of **DG27**, the individual duplexes are slightly oblique in larger aggregates and dipolar end-to-end stacking interactions can be assumed to be stronger than for **DG26** in parallel face-to-face arrangement.

To summarize, height AFM images of the two different end-gBAM modified DDD sequences **DG26** and **DG27** reveal the formation of higher-order aggregates illustrated as short rods. A higher number of chromophores in the sequence leads to larger assemblies which show to be rather unstable under AFM measuring conditions. The stability of these aggregates might be improved by using a higher concentration of $NiCl_2$ for mica pre-treatment to enhance adhesion of the negatively-charged oligonucleotides to the surface. With the observed non-covalently connected fluorescent aggregates, access toward functional, spectroscopically active nanomaterials is provided, for example to be used as light-harvesting antennae.

3.6.4 Enzymatic recognition of gBAM in the DNA scaffold

The spectroscopic analysis of DNA-GNA hybrid structures revealed the interesting spectral properties of these structures. Due to the fluorescence emission of gBAM, the prepared chromophore-oligonucleotide structures might not only be useful for applications in light-harvesting applications or DNA nanotechnology but also in the field of oligonucleotide labeling. For the application as a labeling agent, the presence of the gBAM building block needs to tolerated by polymerase enzymes. To test this tolerance, primer extension assays using Klenow exo- polymerase were carried out. A 17nt single-modified strand (red) was used as a template in this setup, together with a Cy5-labeled primer which was supposed to be elongated in 3'-direction, starting with the incorporation of dATP opposite gBAM in the first elongation step (Figure 3.121). Different reaction conditions were tested, using either all four dNTPs (conditions A) or only one of them (conditions B to E) and incubation times of 1 or 3 h. Upon incubation of the reaction mixture with all dNTPs (lanes A1 and A2), the primer was elongated by only one nucleotide, as indicated by the band shift in the Cy5-channel. Elongation of the primer was otherwise only observed in the presence of dATP (lanes B1 and B2) but not with the other dNTPs. Therefore, it can be concluded that exclusively A is incorporated opposite gBAM although it has been shown that this artificial nucleobase does not undergo Watson-Crick base pairing. However, this unexpected observation is presumably due to the preference of Klenow exo- polymerase to incorporate one or more nucleotides in a non-templated fashion,

for example to the 3'-terminus of blunt-end DNA substrates.[462] The reason for the stop of the elongation after incorporation of the first triphosphate might be the steric demand and unfavorable orientation of the merocyanine modification, preventing efficient orientation in the active site of the enzyme.

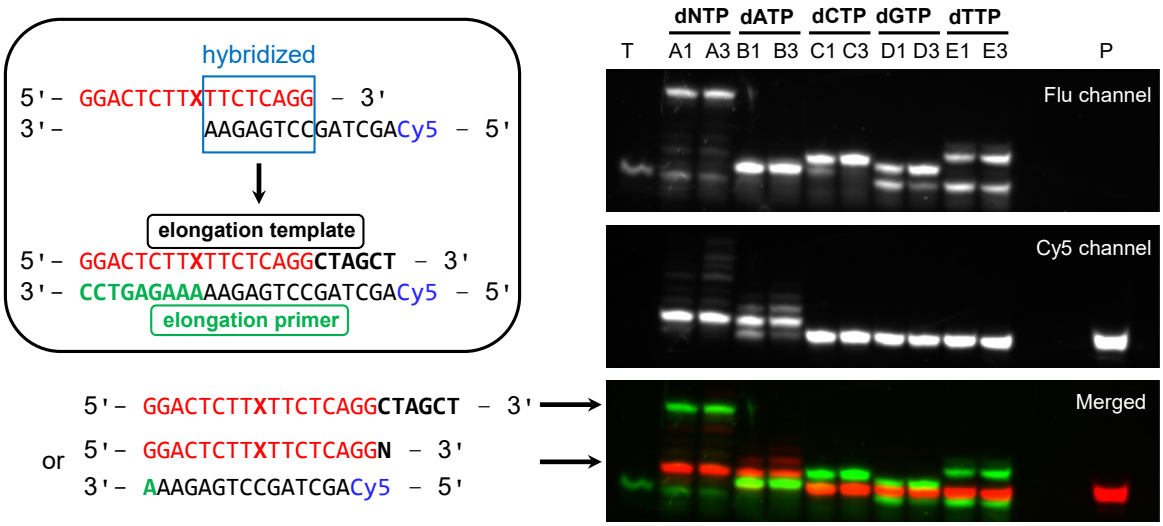

Figure 3.121: The primer extension assay with Klenow exo- polymerase shows selective incorporation of A opposite gBAM but no further elongation while the template itself was fully elongated in the presence of all dNTPs. Nucleotides added to the primer are shown bold. T: template (red), P: primer (black). Conditions A: all dNTPs; B: only dATP; C: only dCTP; D: only dGTP; E: only dTTP; 1: 1 h reaction time; 3: 3 h reaction time. Final concentrations: 200 µM dNTPs, 1 µM template, 2 µM primer, 0.05 u/µL polymerase. The exact procedure can be found in section 5.3.4.2.

If all of the four dNTPs are present in the reaction mixture, full extension of the template was observed along with elongation of the primer, indicated by the highest shifted band in the fluorescein channel. With only dCTP, dGTP or dTTP (lanes C to E) the template was elongated by one nucleotide, although this is only expected in the presence of dCTP and must therefore be due to misincorporation. The elongation of the template is an undesired side effect, it can be prevented by designing the primer-template system more carefully with the 5'-end of the primer completely hybridized to the template. Notably, incubation for 1 h showed to be sufficient since no further change occurred after 3 h of reaction time.

The stop of the primer elongation observed with a gBAM modification in the template was further exploited for polymerase chain reaction (PCR) experiments. PCR is a simple enzymatic assay which allows amplification of a specific sequence in a complex DNA pool. It requires a DNA template, primers, nucleotide triphosphates and a suitable DNA polymerase which links individual nucleotides together to form the PCR product. The primers, short DNA fragments complementary to the target sequence, specify the sequence to be amplified and serve as extension sites for the DNA polymerase. With the use of a thermocycler, the reaction mixture

is first heated to 95 °C to ensure complete denturation. Then, the temperature is lowered in the so-called annealing step to allow binding of the primers to the target DNA segments. By increasing the temperature again, the DNA polymerase extends the bound primers which are amplified by consecutive repetition of these three steps.[463] Due to its simplicity, PCR is widely used within the course of *in vitro* selections for DNA amplification. Thus, an already known PCR sytem was used here, consisting of a 50nt template, a 34nt reverse primer and a 17nt forward primer (Figure 3.122). To simplify the purification by gel electrophoresis of the amplified PCR product, the reverse primer was equipped with an overhang separated by a primer stop from the desired binding sequence.

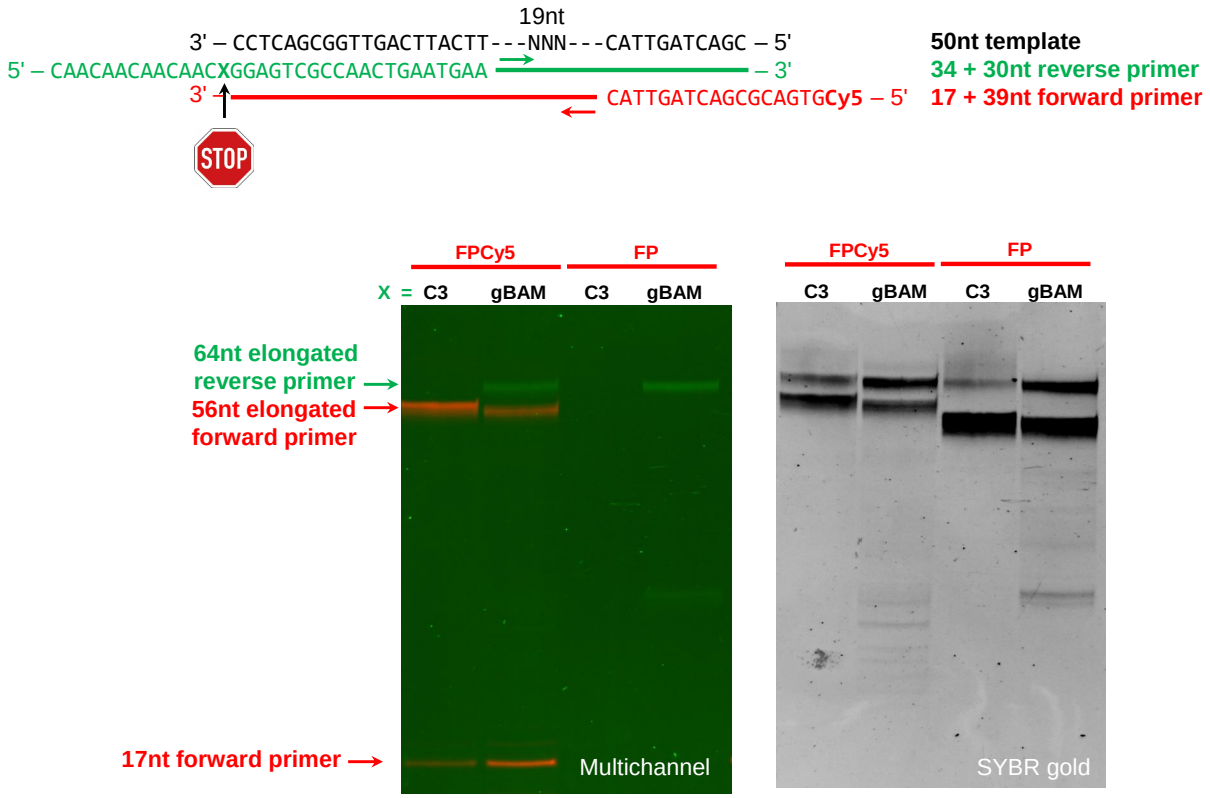

Figure 3.122: The system used for PCR consisted of a 50nt template, a 34nt reverse primer with either an abasic site or gBAM as stop nucleotide and a 17nt forward primer, labeled with Cy5 for some experiments. In the multichannel image only the labeled elongated primers are visible while staining with SYBR gold reveals the presence of both the elongated forward and reverse primer in all of the four reactions. Therefore, gBAM can be applied as a fluorescent primer stop for such PCR experiments. FP: forward primer, C3: abasic site. Conditions: 1 pmol template, 20 pmol primer, 20 mM dNTPs, 0.01 u/µL DreamTaq polymerase; initial annealing step with 4 min at 95 °C, then 25 cycles of 30 s at 95 °C, 30 s at 60 °C and 30 s at 72 °C. The exact procedure can be found in section 5.3.3.

Initially, an abasic site was installed as a polymerase stop but was here in two of the reactions replaced by gBAM. Furthermore, the forward primer was either Cy5-labeled or unlabeled to prove the utility of the intrinsically fluorescent reverse primer. After multiple amplification steps using DreamTaq polymerase, the PCR reaction mixture was separated by PAGE and imaged

under different settings for gBAM and Cy5. As expected, with suitable imaging parameters for gBAM a band for the elongated 64nt reverse primer only emerged for the PCR setups containing the gBAM-modified reverse primer. In addition, imaging under Cy5 settings revealed a band for the elongated 56nt forward primer. Staining of the gel with SYBR gold, however, showed the presence of both the elongated reverse and forward primers for all reactions. The shift of the band for the unlabeled elongated forward primer is explained by the absence of the Cy5 label which influences the migration of oligonucleotides in gel electrophoresis.

Therefore, these experiments demonstrate that gBAM cannot only be used as a reliable polymerase stop but is also intrinsically fluorescent which allows direct visualization without additional gel staining. It has to be noted that here only the initial 17nt forward primer but not the reverse primer is visible on the gel image which is due to the low fluorescence quantum yield of gBAM, requiring a larger concentration for more intense bands.

To summarize, it has been shown that gBAM can efficiently be incorporated into DNA structures, providing access to heavily modified oligonucleotides with interesting thermodynamic and spectroscopic properties. Thanks to dipolar inter- and intrachromophoric interactions, DNA duplex structures are sufficiently stable at ambient temperature even with a modification degree of up to 30%. Furthermore, it was proven that the gBAM chromophore is recognized by the Klenow exo- polymerase, which incorporates dATP opposite this modified nucleotide in primer extension assays. Since no further elongation was observed, gBAM was furthermore applied as a synthetically easily accessible fluorescent primer stop for PCR.

With the incorporation of BAM with different backbones into oligonucleotides, covalently labelled nucleic acid structures were obtained. As discussed in Chapter 2 of this thesis, not only covalent but also non-covalent labeling of oligonucleotides is a large field of scientific research. Very prominent examples for fluorescence activation by non-covalent interactions are fluorogenic RNA-aptamer-ligand complexes derived from the naturally occurring GFP. Although a plethora of examples for these systems has been described, many of them suffer from severe drawbacks. Therefore, new ligands for the Chili aptamer with improved properties such as a red-shifted emission and a large Stokes shift have been synthesized and characterized, which will be discussed in the following section.

3.7 Design of new ligands for the Chili aptamer

3.7.1 Structural considerations for fluorescence activation by Chili

In 2011, Jaffrey *et al.* reported the now famous Spinach RNA aptamer, which binds the and activates fluorescence of DFHBI, a fluorogen related to the chromophore of GFP. In the same paper, the authors also reported the selection and screening of various aptamers for the GFP-related fluorogen DMHBI.[251] Within these, the minimized 60 nt aptamer 13-2min showed the highest fluorescence turn-on when bound to DMHBI, with a single emission peak at 529 nm and a quantum yield of 12% relative to natural GFP. However, back then these new DMHBI-aptamer systems were not analyzed since the major focus was on the DFHBI-binding Spinach aptamer and its applications. Using the 13-2min aptamer as a structural model, a variant called 13-2min2 was engineered in our lab, aiming at a lower conformational heterogeneity and a higher fluorophore binding affinity by replacing the original loop region by a stable UUCG tetraloop. 13-2min2, later nicknamed Chili, indeed showed an astonishing fluorescence enhancement of DMHBI *in vitro*.[257,258] To improve the aptamer folding, to obtain a bright emission along with a high quantum yield and to increase the binding strength between aptamer and fluorophore, Chili was in the following further optimized by screening of potential chemically modified ligands. This resulted in the two new fluorophores DMHBI$^+$ and DMHBO$^+$ with a quarternary ammonium in the side chain (Figure 3.123).

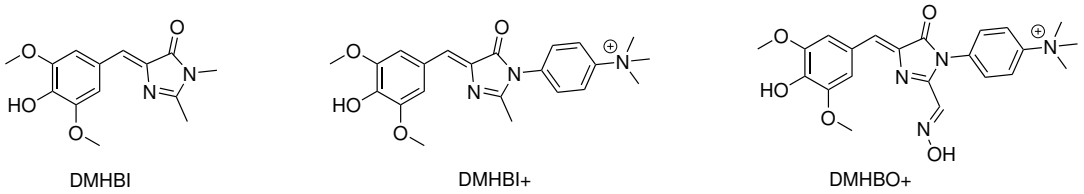

Figure 3.123: The orginial DMHBI structure was further optimized by the introduction of quarternary ammonium in the side chain and an oxime moiety in DMHBO$^+$ for stabilizing interactions with the phosphate backbone.

The trimethylammonium-substituted phenyl rings at N3 in both DMHBI$^+$ and DMHBO$^+$ were chosen to provide additional stacking interactions with adjacent nucleobases and assist electrostatic interactions with the negatively charged RNA backbone. Hereby, the chromophore is rigidified and stabilized at the binding site, provoking a strong fluorescence turn-on upon binding. The extension of the C2-position with an oxime in DMHBO$^+$ was chosen as a hydrolytically stable acylimine mimic which might act as ambidentate hydrogen bond donor and acceptor. Indeed, both DMHBI$^+$ and DMHBO$^+$ tightly bound to Chili, exhibiting a large Stokes shift and fluorescence intensities increased by factors of 7.35 and 1.47 relative to DMHBI, respectively.[257,258] Later, similar stabilizing effects were also observed for the DFHO/Corn system.[464]

Since back then no crystal structure for Chili was available, it was attempted to understand its mechanism of action by biochemical and ligand mutation experiments. These revealed fluoresecence activation based on an ESPT process, with a hydrogen acceptor located at the chromophore binding site to facilitate ligand binding in the ground state and proton abstraction in the excited state (Figure 3.124).[258] Therefore, ligands are bound in the protonated state to the Chili aptamer but emit in the deprotonated form which is manifested in the observed large pseudo Stokes shifts of up to 130 nm and distinguishes Chili from other fluorogenic aptamer-ligand systems with Stokes shifts well below 80 nm.[465,466]

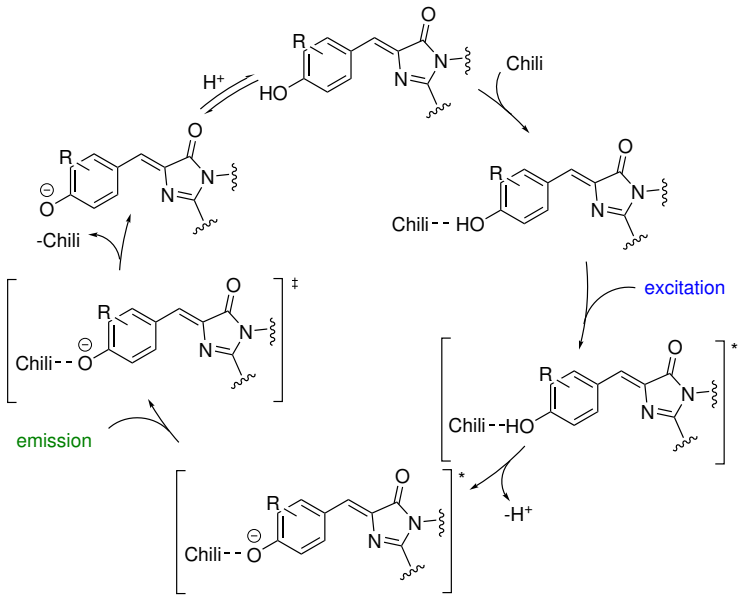

Figure 3.124: Proton transfer cycle for the binding and fluorescence activation of HBI chromophores by Chili. The ligand can only be excited in the protonated form; upon deprotonation, the chromophore emits in its phenolic form, followed by dissociation of the aptamer-dye complex.[258]

To understand the mechanism for fluorescence activation, a 3D RNA structure is required. Therefore, DMHBI$^+$ and DMHBO$^+$ were cocrystallized with Chili; both crystal structures were solved by molecular replacement and refined at resolutions of 2.95 and 2.25 Å, respectively.[259] As already discussed in section 2.5.2, Chili RNA folds into a single, 70 Å long coaxial helical stack which contains two A-form duplexes, namely the basal stem P1 and the apical stem P2, separated by the central fluorophore binding domain (FBD) that accommodates the fluorophore binding site. The architecture of the two-tiered G-quadruplex core of Chili bound to DMHBO$^+$ is characterized by three consecutive guanine steps (G12/G13, G36/G37 and G41/G42) with mixed parallel and antiparallel strand orientation in between and one non-consecutive edge (G9/G32) (Figure 3.125a). Within the G-quartets, all G are in *anti*-conformation with torsion angles between -120 and -160°; only G32 is in high-anti conformation with a torsion angle of -79°.

The DMHBO$^+$ fluorophore adopts a non-planar conformation in the binding site, dictated by

stacking interactions with neighboring nucleobases. In detail, the benzylidene moiety stacks on top of the G13:G32 plane of T2 and G31 in the direction of the apical stem. Meanwhile, the imidazolone ring projects outwards from the quadruplex center, stacking with G14 and also the cationic side chain is not accommodated in the binding site. Besides stacking interactions, the core of Chili is stabilized by polar interactions: the oxime moiety undergoes hydrogen bonding with the phosphate of G10 and the 2'-OH of G9, leading to a higher binding affinity compared to $DMHBI^+$ (12 *versus* 65 nM) as well as a higher thermal stability of the aptamer-dye complex.

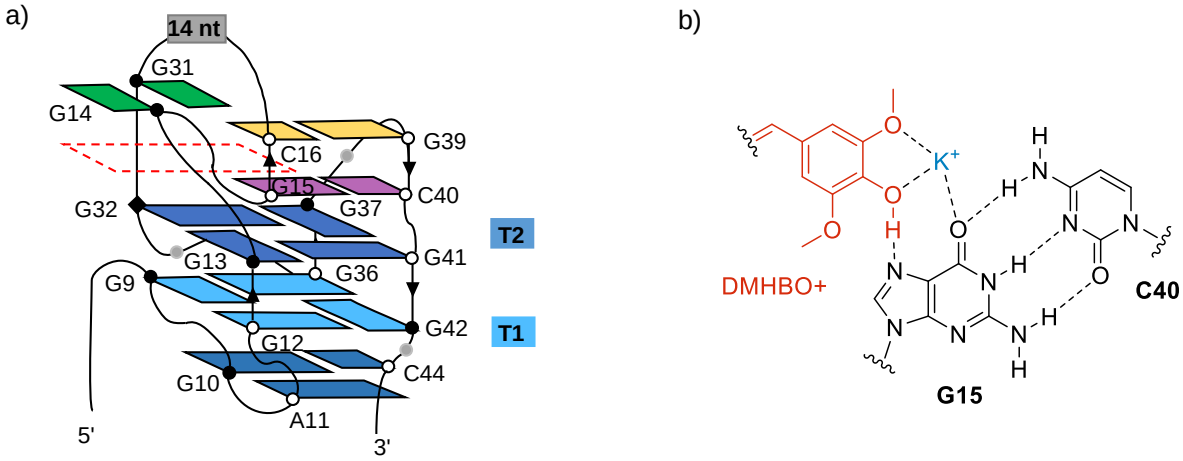

Figure 3.125: Schematic representation of the Chili aptamer core architecture with white and black circles denoting different sugar pucker conformations, respectively (a). The black outline indicates *anti*-conformation for all G and T in the G-quartets 1 and 2 (T1 and T2), except G32 in high anti conformation (black diamond). The position of the ligand is shown by the red dashed square. Nucleotides of the same color interact by hydrogen bonding in base pairs (green, purple and yellow), base triple (dark blue) or G-quartets (light and middle blue). In b), the hydrogen bonding between the $DMHBO^+$ ligand and the N7 of G15 in Chili as a proton acceptor with the whole structure stabilized by K^+ is shown. Figures adapted from ref. [259].

The G-quadruplex structure is stabilized by a central octacoordinate K^+ ion and a second K^+ coordinated to T2, the phenolic hydroxy group and one of the chromophore's methoxy groups as well as O6 of G15. To unravel the nucleobase participating in the proton transfer cycle required for fluorescence activation, NMR studies and mutation of G15 to 7-deazaguanine were carried out. Since replacement by this modified nucleobase led to complete loss of the fluorescence, the N7 of G15 was unambiguously assigned as proton acceptor for the ultrafast excited state proton transfer (Figure 3.125b).

Since many of the reported GFP-like chromophore-aptamer complexes suffer from severe drawbacks such as poor cell permeability, toxicity, unspecific binding, high magnesium dependency, low thermal stability, a high tendency toward photobleaching or cis-trans isomerization, valuable chromophores with improved biochemical and spectroscopic properties while maintaining a robust fluorescence are still required. With the design of $DMHBI^+$ and $DMHBO^+$, modification of the N3 or C2 position of the imidazolone ring showed to provide access to tightly

binding and brightly fluorescent new DMHBI analogs. Therefore, replacement of the C2-methyl group by a hydrogen-donating functional group such as amino might not only give rise to even higher binding affinities due to polar interactions of the ligand with the RNA backbone and better cell permeability, similar as for $DMHBO^+$, but also introduces an additional site for further derivatizations to obtain various emission colors. Furthermore, mutation of the N1 to other heteroatoms such as sulfur has the potential to further tune the spectral properties of the Chili-chromophore complexes by shifting the emission maximum to longer wavelengths (Scheme 3.35).

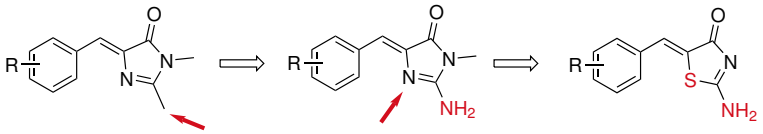

Scheme 3.35: To enhance the affinity and spectroscopic properties of DMHBI analogs, the C2 methyl group was substituted by a polar amino function for improved binding affinities and further derivatization, leading to a guanidine-like chromophore structure. In addition, the N1 of the imidazolone was replaced by sulfur for spectral tuning. R represents different substituents.

Taking these considerations into account, a pseudothiohydantoin containing chromophore is considered an especially promising new fluorogen. In this context, it is also interesting to note that rhodanine-derived chromopohres were used as ligand for fluorogenic proteins.[467] Within these systems, 4-hydroxybenzylidene-rhodanine (HBR) and its methylated variant HMBR with a push-pull structure analogous to the HBI chromophore are applied for *in vivo* labeling by fluorescence activation upon specific and reversible binding to a **Y**ellow **F**luorescence-**A**ctivating and absorption-**S**hifting **T**ag (Y-FAST), a small monomeric protein tag engineered from the photoactive yellow protein (Figure 3.126).

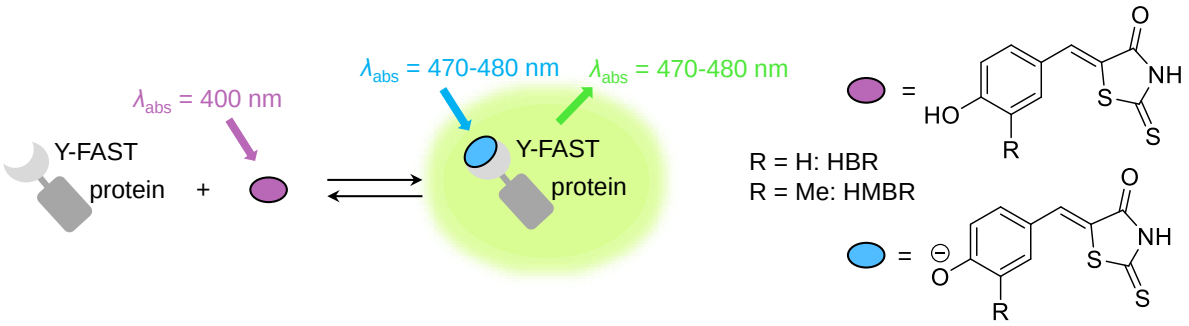

Figure 3.126: Y-FAST can be used to label proteins of interest by binding the fluorogenic chromophores HBR and HMBR and activating their fluorescence, provoking an increase in quantum yield and a red-shift in absorption.[467]

Both HBR and HMBR are almost completely protonated at physiological pH, having a pK_a of 8.4 and 8.7, respectively, and undergo a red-shift of 50 nm in the absorption upon deprotonation. These two chromophores are not only advantageous due to their highly environment-

sensitive fluorescence but also their enhanced cell permeability and low toxicity, their low fluorescence background and their specific, fully reversible binding. This allows the Y-FAST system to spectroscopically monitor rapid processes in various organelles and hosts.
With these suitable spectral characteristics in mind, different fluorophores according to Scheme 3.35 were synthesized and screened as potential candidates for strong fluorescence activation by Chili. The required reactions steps toward these new chromophores are discussed in the following section.

3.7.2 Synthesis of four new ligands for the Chili aptamer

Since the characterization of new chromophores with regard to their brightness and binding affinity requires comparison to appropriate known aptamer-dye complexes, DMBHI derivatives with different substituents at the phenyl ring were synthesized in addition. In general, the preparation of HBI-derived chromophores can be approached from different directions. Commonly, these dyes are accessed by aminolysis of an oxazolone prepared *via* an Erlenmeyer azlactone synthesis. Due to the fact that this reaction is hampered by electron-poor substituents at the N3 of the imidazolone, HBI derivatives are alternatively obtained by Knoevenagel condensation between an aromatic aldehyde and the imidazolone[468] or by 1,3-dipolar cycloaddition of an aromatic imine and an imidate.[469] While the first method was used to access the new 3,5-dimethoxy-4-hydroxybenzylaminoimidazolinone (DMHBI-NH_2) chromophores, the latter one was used for already reported DMHBI chromophores.[257,258]

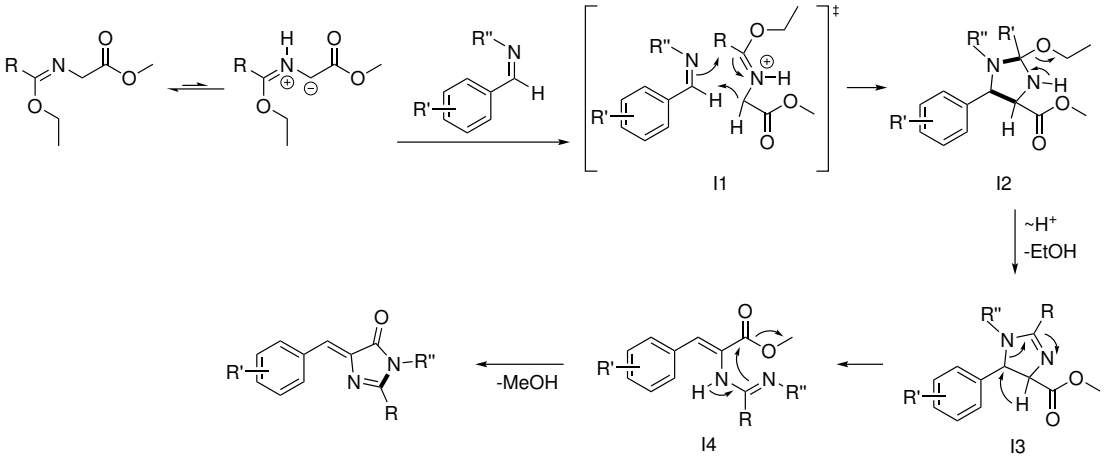

Scheme 3.36: In the first step of the cycloaddition, the 1,3-dipolar azomethine ylide tautomer of the imidate reacts with the imine to form the intermediary imidazolone **I2**, which is finally reorganized *via* **I3** and the ring-opened intermediate **I4** to the final HBI chromophore. Newly formed bonds are shown bold.[469]

The mechanism of the 1,3-dipolar cycloaddition is not intuitive, it is therefore illustrated in Scheme 3.36. Here, the imidate is in equilibrium with the 1,3-dipole azomethine ylide which reacts with an imine to form the intermediary imidazoline **I2**. Upon loss of ethanol, the un-

saturated intermediate **I3** is obtained, which rearranges *via* the ring-opened **I4** to the final imidazolone.[469]

The required aromatic imines and the imidate were synthesized according to reported procedures (Scheme 3.37).[257,258] Here, all of the required aromatic aldehydes were commercially available, except for the di-fluoro substituted compound for DFHBI derivatives, which was generated by formylation of 2,6-difluorophenol under Duff conditions.[470] These aldehydes were converted into their respective *N*-methyl imines **91** to **96** and then reacted with imidate **97**. The obtained target compounds **98** to **103** only vary in the aromatic substitution pattern, providing access to a palette of chromophores with different electronic properties. All of these chromophores were purified by column chromatography on silica and obtained as brightly colored powders in modest to good yields with exclusively (*Z*)-configured bridging double bonds.

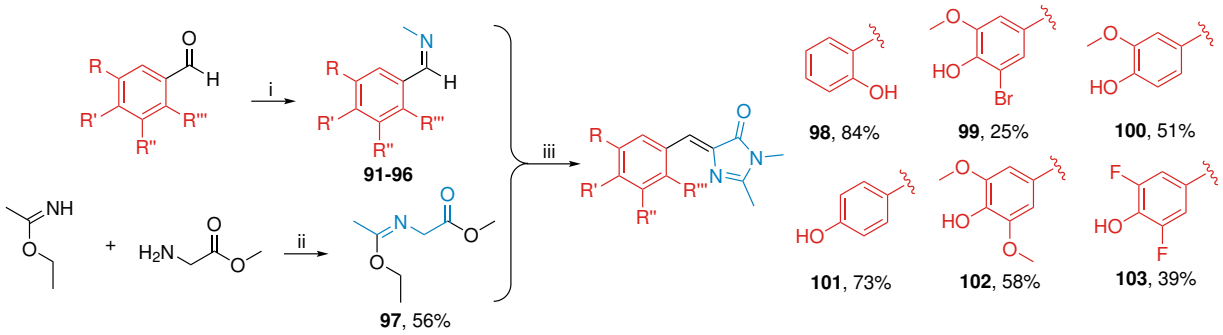

Scheme 3.37: Synthesis of HBI chromophores with differently substituted aromatic ring systems. Conditions: i) $MeNH_2$ in EtOH, $MgSO_4$, r. t., 16 h; ii) glycine methyl ester hydrochloride, NEt_3, CH_2Cl_2, r. t., 3 h; iii) EtOH, r. t., 16 h.[257,258]

As already mentioned, the HBI-NH_2 derivatives were synthesized under Knoevenagel conditions. The therefore required 2-aminoimidazolin-4-one (**106**) had to be synthesized beforehand (Scheme 3.38). In the first step, commercially available *N*-methyl thiourea underwent facile *S*-alkylation with iodoethane, resulting in quantitative conversion of the starting material to *N*-methyl-*S*-ethylisothiouronium iodide (**104**). By reaction of this intermediate with glycine in aqueous sodium hydroxide, *N*'-methyl guanidino acetic acid **105** was obtained and finally converted into the target compound **106** by treatment with hydrochloric acid.[471]

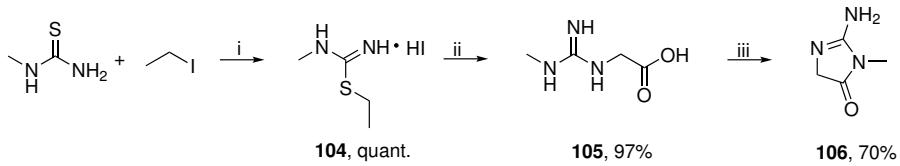

Scheme 3.38: Synthesis of 2-aminoimidazolin-4-one (**106**) as a presursor for DMHBI-NH_2 chromophores. Conditions: i) 60 °C, 3.5 h; ii) glycine, 4 M NaOH, r. t., 16 h; iii) 6 M HCl, 120 °C, 22 h.[471]

Subsequent reaction of the five-membered ring precursor **106** with the differently substituted aromatic aldehydes under Knoevenagel conditions led to the formation of the desired DMHBI-NH_2 chromophores **107** to **112** (Scheme 3.39). All of the members of this new class of HBI derivatives were isolated in sufficient yield and with high purity after column chromatography.

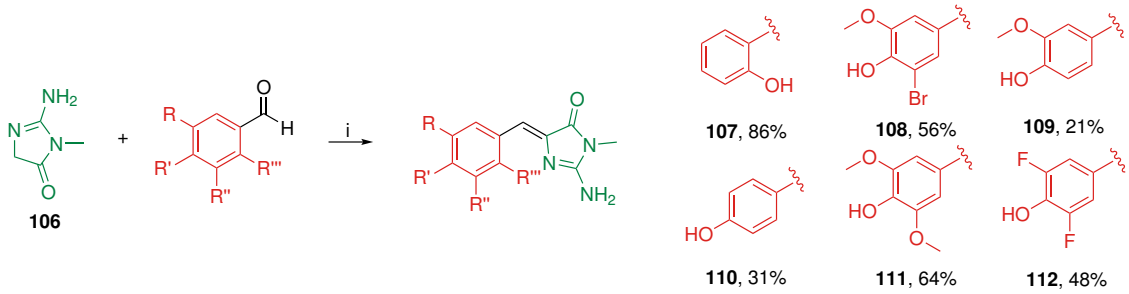

Scheme 3.39: The different HBI-NH_2 chromophores **107** to **112** were obtained by Knoevenagel condensation of the respective aromatic aldehydes and 2-aminoimidazolin-4-one (**106**). Conditions: i) NEt_3, EtOH, 90 °C, 5.5 h.

To explore the potential of other heterocyclic five-membered ring systems besides the natural imidazolone for efficient fluorescence turn-on, it was decided to replace this moiety by the similarly sized pseudothiohydantoin. Pseudothiohydantoin does not only employ the exocyclic amino group auspicious for a higher cell permeability but has in addition one of the ring nitrogens replaced by sulfur which is expected to lead to a red-shifted emission, desirable for *in vivo* experiments.

The DMHB-PTH chromophore **113** was synthesized under similar conditions as the DMHBI-NH_2 dyes (Scheme 3.40). However, here not the classical Knoevenagel condensation but the Verley modification was used, employing β-alanine instead of piperidine as a „green“catalyst.[472]

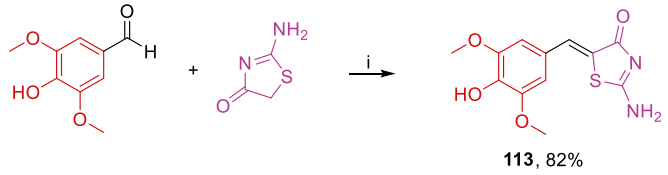

Scheme 3.40: Formation of DMHB-PTH (**113**) catalyzed by β-alanine under Knoevenagel conditions. Conditions: i) β-alanine, AcOH, 115 °C, 4 h.[473]

Not only the introduction of electron-donating heteroatoms such as sulfur but also an expansion of the conjugated system leads to a bathochromic shift of the fluorescence emission. With the exocyclic amino group as a functionalizable moiety, DMHB-PTH (**113**) and DMHBI-NH_2 (**111**) with the 3,5-dimethoxy-4-hydroxy-substituted phenyl ring were further derivatized. The introduction of a *N,N*-dimethyl aminomethylene (DMAM) group was considered to be resonable since it contains an additional double bond in conjugation with the chromophore aromatic system and is small enough to not interfere with binding of the chromophore to the aptamer. Introduction of the DMAM moiety was achieved using a standard protocol and

yielded DMAM-DMHB-PTH (**114**) and DMAM-DMHBI-NH_2 (**115**) in good yields (Scheme 3.41).

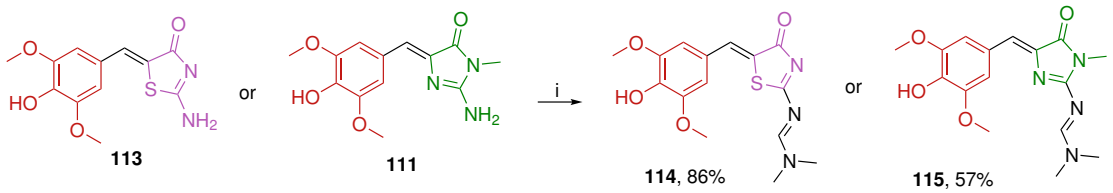

Scheme 3.41: DMHBI-NH_2 (**111**) and DMHB-PTH (**113**) were further derivatized by attachment of a DMAM function to the exocyclic amino group. Conditions: DMFDMA, MeOH, r. t., 3 h.

All of the prepared chromophores were initially screened to explore their fluorescence activation by Chili. The results are discussed in the next section by comparison of the fluorescence properties of the new chromophores with the respective DMHBI-related parent compounds.

3.7.3 Screening of HBI-NH_2 and DMHB-PTH chromophores as potential candidates for fluorescence activation by the Chili aptamer

For investigation of the potential for fluorescence activation of the new DMHB-PTH and HBI-NH_2 chromophore family by Chili, excitation and emission spetra were recorded and the emission bands were integrated for better comparison. The results are summarized and compared to the DMHBI-Chili parent in Figure 3.127. Interestingly, the emission intensity of DMHBI-NH_2 (**111**) is significantly reduced compared to the DMHBI chromophore **102** although it is structurally akin, only possessing one additional exocyclic amino group. This decreased fluorescence is also observed for the substituted variants MHBI-NH_2 (**109**) and BMHBI-NH_2 (**108**), although to a lower extent, while for the fluorine-containing DFHBI-NH_2 (**112**) negligible fluorescence is observed in complex with Chili. In the case of the simple HBI chromophores **101** and **110**, the latter one having the amino groups shows a stronger fluorescence activation, resembling the one obtained for the DMHBI parent compound.

The most interesting observation here is made for DMHB-PTH (**113**) with the imidazolone replaced by pseudothiohydantoin. Surprisingly, the emission intensity is restored only by introduction of a ring sulfur atom in comparison to DMHBI-NH_2 (**111**), even showing an almost four-fold fluorescence enhancement relative to DMHBI (**102**). This bright fluorescence is not maintained if the conjugated system is expanded by an additional double bond in DMAM-DMHB-PTH (**114**); this chromophores is intensity-wise again comparable to the parent DMHBI. However, the structurally similar DMAM-DMBHI-NH_2 (**115**) still shows a by approximately 50% lower emission intensity.

For better comparison of their fluorescence properties, the excitation and emission maxima as well as the Stokes shift and the fluorescence intensity relative to DMHBI-Chili of the nine new chromophores are compared in Table 3.39. In general, the excitation and emission maxima are for most HBI-NH_2 variants slightly blue-shifted in comparison to the HBI-derived chromophores with the same phenyl substitution pattern. This trend is expected since the exocyclic amino group has a +M- and -I-effect with the latter one being more dominant here, leading to a reduced electron density in the conjugated system which therefore requires higher energy for excitation. Interestingly, for DMHBI-NH_2 (**111**) and BMHBI-NH_2 (**108**) a dual-emission is observed which hints to the presence of two different excited species.

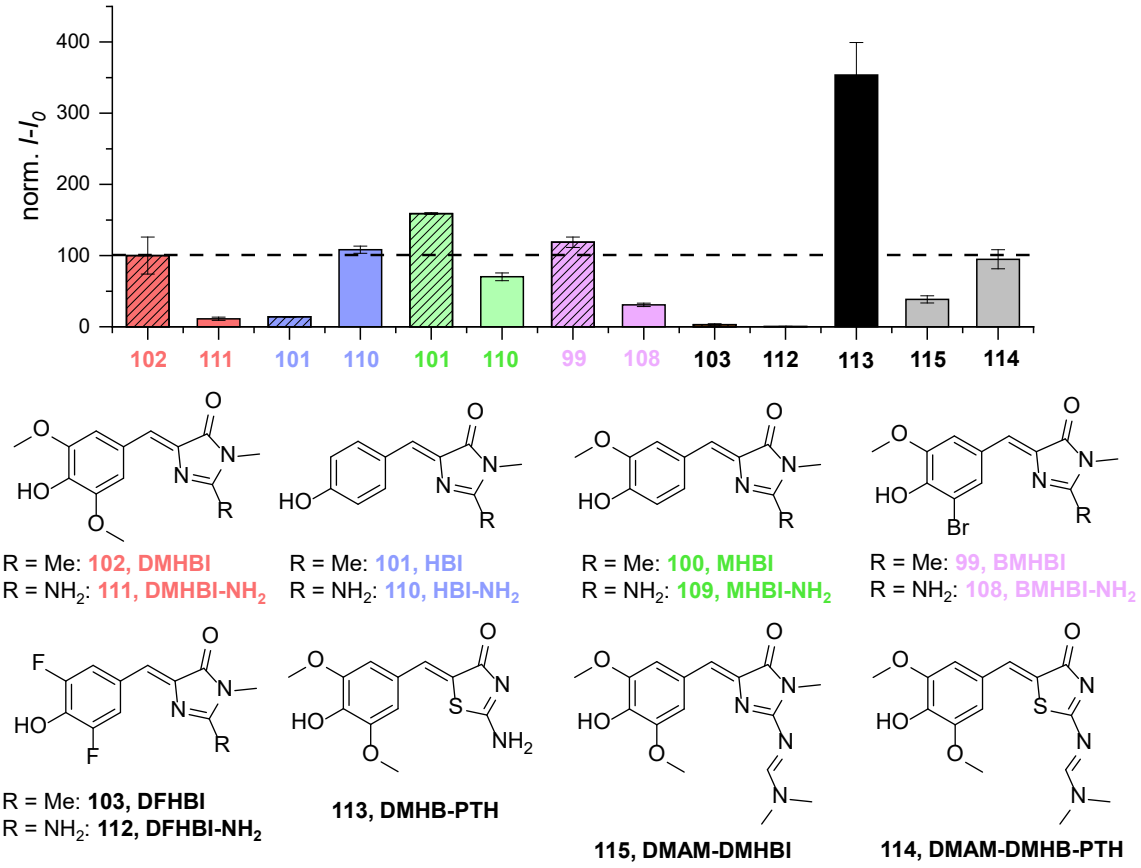

Figure 3.127: Screening results for the fluorescence activation of new HBI chromophores by the Chili aptamer. Shown is the average integrated emission intensity with standard deviation of the mean after blank correction, normalized against DMHBI-Chili. Conditions: 0.5 µM chromophore, 0.5 µM Chili, 125 mM KCl, 5 mM $MgCl_2$, 80 mM HEPES pH 7.5; emission and excitation at the maximum.

While the complete removal of the aromatic methoxy groups leads to a significant loss of fluorescence for HBI-Chili (**101**) with only 14% of the DMHBI-Chili intensity, the HBI-NH_2-Chili complex (**110**) shows an even stronger emission than this system. Therefore, unlike as for DMHBI-derived dyes where the methoxy groups contribute to the optimal occupation of the binding site due to steric effects, it is preferable to remove these substituents if the

chromophore contains 4-aminoimidazolinone instead of imidazolinone.[259] The fluorescence behavior of MHBI-NH_2 (**109**) fits to this observation as it shows enhanced fluorescence in comparison to DMHBI-NH_2 (**111**) with two methoxy group but reduced emission intensity compared to HBI-NH_2 (**110**).

Table 3.39: Summary of the emission and excitation maxima as well as the resulting Stokes shifts for the screened DMHBI-NH_2 and DMHB-PTH chromophore family in comparison to the HBI parent compounds. The intensity is given relative to DMHBI-Chili. For fluorophores showing dual-emission, the more intense maximum is shown in bold.

Name	No.	R	R'	R''	R'''	λ_{ex} nm	λ_{em} nm	Stokes nm	rel. *I*
DMHBI	**102**	OMe	OH	OMe	H	405	537	132	1.00
DMHBI-NH_2	**111**					396	**544**/484	148/88	0.11
HBI	**101**	H	OH	H	H	379	464	85	0.14
HBI-NH_2	**110**					376	446	70	1.08
o-HBI	**98**	H	H	H	OH	_[a]	_[a]	_[a]	_[a]
o-HBI-NH_2	**107**					_[a]	_[a]	_[a]	_[a]
MHBI	**100**	OMe	OH	H	H	392	503	111	1.59
MHBI-NH_2	**109**					388	461	73	0.70
BMHBI	**99**	OMe	OH	Br	H	385	521	136	1.19
BMHBI-NH_2	**108**					381	**533**/493	152/112	0.30
DFHBI	**103**	F	OH	F	H	377	496	119	0.03
DFHBI-NH_2	**112**					_[a]	_[a]	_[a]	_[a]
DMHB-PTH	**113**	OMe	OH	OMe	H	387	553	166	3.54
DMHB-PTH*	**114**	OMe	OH	OMe	H	389	550	161	0.95
DMHBI-NH_2*	**115**					420	**546**/478	126/67	0.39

Conditions: 0.5 µM chromophore, 0.5 µM Chili, 125 mM KCl, 5 mM $MgCl_2$, 80 mM HEPES pH 7.5; emission and excitation at the maximum.
[a] not emissive
* for DMAM variants

For fluorescence activation, the presence of a para-OH group on the phenyl ring seems to be mandatory also for the amino-modified HBI dyes as no emission was detected for *o*-HBI-NH_2 (**107**). Furthermore, also the fluorine-containing DFHBI-NH_2 (**112**) is non-emissive in the presence of Chili, resembling the behavior of DFHBI. These chromophores are already completely deprotonated at neutral pH (pK_a 5.5 for DFHBI)[251] due to the electron-withdrawing fluorine atoms which hampers fluorescence activation by ESPT in complex with the Chili ap-

tamer.

The most remarkable fluorescence behavior is observed for DMHB-PTH (**113**): compared to DMHBI-Chili, it shows a hypsochromic shift in excitation as well as a bathochromic shift in emission due to the electon-donating sulfur, resulting in a Stokes shift of 166 nm which is even larger than for DMHBI and $DMHBO^+$. Stokes shifts of similar magnitude have not yet been reported for fluorgene-aptamer complexes but only for engineered fluorescent proteins such as LSS-mKate1, LSS-mKate2 and LSS-mCherry1.[269,474] Intensity-wise, DMHB-PTH (**113**) is located in between $DMHBO^+$ and $DMHBI^+$ with a fluorescence enhancement by a factor of approximately 3.5 compared to DMHBI (**102**).[257] By enlargement of the conjugated chromophore system upon addition of DMAM to the amino group, unexpectedly no pronounced shift of either the exciation or emission maxima is detected. Meanwhile, the emission intensity of DMAM-DMHB-PTH (**114**) is reduced by a factor of approximately 3.5 to the level of the parent complex DMHBI-Chili; therefore, the exocyclic amino group in DMHB-PTH (**113**) is detrimental for efficient fluorescence activation. DMAM-$DMHBI-NH_2$ (**115**), however, still shows a lower fluorescence response, although around four-fold enhanced in comparison to $DMHBI-NH_2$ (**111**). A more detailed analysis of the spectroscopic characteristics of the new $DMHBI-NH_2$ and DMHB-PTH chromophore family is provided in the next section.

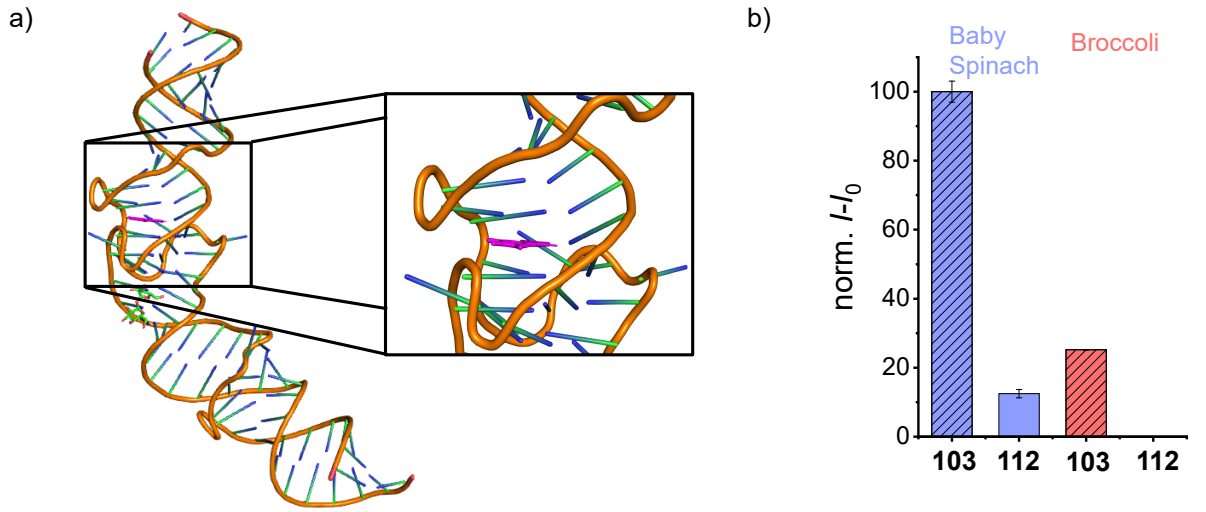

Figure 3.128: Crystal structure for the 98nt Spinach aptamer with the DHFBI chromophore shown in pink (a, taken from PDB 4TS2).[252] The DFHBI (**103**) fluorescence is activated by both Baby Spinach and Broccoli, to a much larger extent than $DFHBI-NH_2$ (**112**) (b). Shown is the average integrated emission intensity with standard deviation of the mean after blank correction, normalized against Baby Spinach-DFHBI. Conditions: 0.5 µM chromophore, 0.5 µM Chili, 125 mM KCl, 5 mM $MgCl_2$, 80 mM HEPES pH 7.5; emission and excitation at the maximum.

Since it was shown that the two DFHBI fluorophores **103** and **112** were non-emissive in complex with Chili, fluorescence spectra were recorded with 51nt Baby Spinach and the 49nt Broccoli aptamer instead. Baby Spinach is a truncated variant of the DFHBI-binding 98

nt Spinach aptamer which retains 95% of the brightness of wild-type Spinach, and was later further optimized by reselection, resulting in the Broccoli aptamer with higher thermal stability and reduced Mg^{2+}-dependency.[252,254] The crystal structures of Spinach is shown in Figure 3.128a; apparently, it varies from the Chili secondary structure illustrated in Figure 2.26 in the introduction part of this thesis, although both comprise a fluorophore-binding G-quadruplex. Screening of DFHBI-NH_2 (**112**) revealed fluorescence activation only by Baby Spinach while the chromophore remained non-emissive in complex with Broccoli (Figure 3.128b). However, in comparison to the normalized fluorescence of DFHBI-Baby Spinach (**103**), only 12% of the emission intensity is retained for DFHBI-NH_2 (**112**). This reduction is similar to the difference in emission intensity between DMHBI-Chili and DMHBI-NH_2-Chili. The fluorescence parameters for DFHBI (**103**) and DFHBI-NH_2 (**112**) in complex with Baby Spinach as well as Broccoli are summarized in Table 3.40.

Table 3.40: Summary of the emission and excitation maxima as well as the resulting Stokes shifts for DFHBI (**103**) and DFHBI-NH_2 (**112**). The intensity is given relative to DFHBI-Baby Spinach.

Name	No.	RNA	λ_{ex} nm	λ_{em} nm	Stokes nm	rel. *I*
DHFBI	**103**	Baby Spinach	453	493	40	1.00
DFHBI-NH_2	**112**		435	512	77	0.12
DHFBI	**103**	Broccoli	455	494	39	0.25
DFHBI-NH_2	**112**		_[a]	_[a]	_[a]	_[a]

Conditions: 0.5 µM chromophore, 0.5 µM Chili, 125 mM KCl, 5 mM $MgCl_2$, 80 mM HEPES pH 7.5; emission and excitation at the maximum.
[a] not emissive

DFHBI (**103**) exhibits maximum exciation and emission at almost the same wavelengths independent from the binding aptamer. Compared to these, DFHBI-NH_2 (**112**) in complex with Baby Spinach shows a blue-shift in excitation and a red-shift in emission, resulting in a by 37 nm larger Stokes shift, while the DFHBI-NH_2-Broccoli complex remains non-emissive.

However, the explanation of the remarkable differences in fluorescence activation of HBI-NH_2 and DMHB-PTH fluorophores by different aptamers is not straightforward. In general, several aspects need to be considered for weak fluorescence activation, among them steric and electronic influences. Here, it is very unlikely that steric hindrance prevents efficient fluorescence activation since on the one hand an amino group is of similar size than a methyl group and on the other hand it has already been reported that chromophores with larger substituents at C2 of the imidazolinone ring are readily accepted, such as the Kaede-like

DMHBI-Imi.[257] Thus, electronic effects remain as the main reason for poor fluorescence emission and need to be investigated by a more detailed analysis and comparison of the spectral properties of the structurally very similar but spectroscopically very different DMHBI-NH_2 (**111**) and DMHB-PTH (**113**) chromophores.
For in-depth spectroscopic characterization, these two dyes as well as their DMAM-substituted variants DMAM-DMHB-PTH (**114**) and DMAM-DMHBI-NH_2 (**115**) were selected and the obtained results will be discussed in the next section.

3.7.4 Characterization of selected new fluorophores for the Chili aptamer

Since the molar extinction coefficient ϵ is an important photophysical parameter of a chromophore, ϵ values for the four mentioned chromophores were determined by concentration-dependent absorption measurements. The obtained values for ϵ at the higher-wavelength maximum were found to be in a range between 24,000 and 30,000 L^{-1}mol cm^{-1} and are therefore slightly elevated compared to the reported value of 19,500 L^{-1}mol cm^{-1} for the protonated form of DMHBI (Table 3.41). Interestingly, the two chromophores bearing the DMAM group, DMAM-DMHBI-NH_2 (**115**) and DMAM-DMHB-PTH (**114**), exhibited two absorption maxima at approximately 300 and 400 nm, respectively, indicating the presence of two independent parts within the chromophore structure. However, for both cases ϵ of the higher-energy absorption maximum was lower by about one third of the value for the more red-shifted maximum.

Table 3.41: Molar extinction coefficients ϵ for new chromophores in comparison to DMHBI.

Name	No.	λ nm	$\epsilon\pm$s.d.m. 10^3 M^{-1} cm^{-1}
DMHBI-NH_2	**111**	374	28.0±4.0
DMAM-DMHBI-NH_2	**115**	280	20.9±0.3
		407	29.6±0.1
DMHB-PTH	**113**	367	24.1±0.4
DMAM-DMHB-PTH	**114**	310	16.6±0.2
		401	25.3±0.3
DMHBI[a]	**102**	385	19.5
		470	28.6

[a] values for protonated and deprotonated species, taken from ref. [257]
Conditions: dilution from 44.4 to 1.39 µM dye in water, measured in triplicates

HBI derivatives in aqueous environment can exist in either cationic, neutral or anionic pro-

tonation state, with protonation of the imidazolinone-N in the positively and deprotonation of the phenol hydroxy group in the negatively charged form, respectively.[475,476] The pK_a value for the transition between these states is influenced by the electronic nature of the substituents attached to either the phenyl or the imidazolinone ring which can consequently be exploited to tune the protonation state of this type of push-pull chromophores. For a better understanding of the absorption behavior of the four new HBI-derived compounds, their pK_a values were determined by spectrophotometric titration with Britton-Robinson buffer. Compared to the parent structure DMHBI (**102**), the pK_a value for the protonation/deprotonation step of the phenolic hydroxy group was found to be increased for all of the chromophores from the DMHBI-NH_2 and DMHB-PTH family (Table 3.42). Since the aromatic substitution pattern is the same for all of these molecules, the electron-donating nature of the exocyclic amino group must be responsible for these elevated pK_a values. This electronic effect is also the reason for the slight decrease of the pK_a upon introduction of the DMAM group and is furthermore observed for the DFHBI-NH_2 (**112**) chromophore in comparison to DFHBI (**103**).

Table 3.42: Estimated pK_a values and absorption maxima for protonated phenol and deprotonated phenolate forms of new chromophores.

Name	No.	$\lambda_{Abs,1}$ nm	$\lambda_{Abs,2}$ nm	$I(\lambda_{Abs,1})/I(\lambda_{Abs,2})$	pK_a±s.d.m.
DMHBI-NH_2	**111**	368	432	12	8.78±0.01
DMAM-DMHBI-NH_2	**115**	397	474	6.1	8.49±0.03
DMHB-PTH	**113**	367	443	2.6	8.02±0.04
DMAM-DMHB-PTH	**114**	401	493	2.0	7.88±0.11
DMHBI[257]	**102**	385	470	3	7.96±0.01
DFHBI-NH_2	**112**	344	399	n.d.	5.67±0.26
DFHBI[476]	**103**	363	418	n.d.	5.4

Conditions: 11 µM dye, 30 mM Britton-Robinson buffer, measured in triplicates
$\lambda_{Abs,1}$ for protonated form, $\lambda_{Abs,2}$ for deprotonated form

Surprisingly, the ratio of the phenolate and phenol absorbance $\lambda_{Abs,1}/\lambda_{Abs,2}$ at pH 7.5, used for spectroscopic analyses in the prescence of Chili, strongly differs between the different chromophores. For DMHB-PTH (**113**) and DMAM-DMHB-PTH (**114**), a ratio of 2.6 is observed which resembles the behavior of DMHBI (**102**). In contrast, the fraction of the protonated phenol form is significantly increased for DMHBI-NH_2 (**111**) and DMAM-DMHBI-NH_2 (**115**) at this pH, although these two chromophores show nearly the same pK_a value as the DMHB-

PTH chromophores, indicating a much sharper phenol-phenolate transition at a well-defined pH.

However, DMHBI-NH_2 (**111**) and DMHB-PTH (**113**) as well as their DMAM-containing variants **114** and **115** are all present in the protonated form at physiological pH while DFHBI-NH_2 (**112**) is completely deprotonated due the low pK_a induced by the strongly electronegative fluorines.

Another interesting observation can be made by direct analysis of the absorption spectra at different pH values, exemplarily shown for DMHB-PTH (**113**) in Figure 3.129. For all of the four new chromophores, maxima at not only two, but three or four wavelengths are detected: besides the phenol and phenolate absorption at 367 and 443 nm, respectively, an additional red-shifted absorption at 383 nm for pH values below 1 and a blue-shift in absorption to 420 nm at pH values above 10 are observed, although the latter shift is only visible for DMHB-PTH (**113**) and DMAM-DMHB-PTH (**115**). This indicates the presence of additional protonation states besides the two described ones as shown for DMHB-PTH (**113**) on the right side of Figure 3.129. Thus, the red-shifted absorption under strongly acidic conditions arises from protonation of one nitrogen either in the five-membered ring or more likely at the exocyclic amino group while the blue-shift in absorption under strongly basic conditions is attributed to deprotonation of the pseudothiohydantoin, requiring its presence in the imino form. However, here the second negative charge can either be located at the ring nitrogen or oxygen, as indicated by the double-headed arrow, with the latter case being favored due to the higher electronegativity of oxygen.

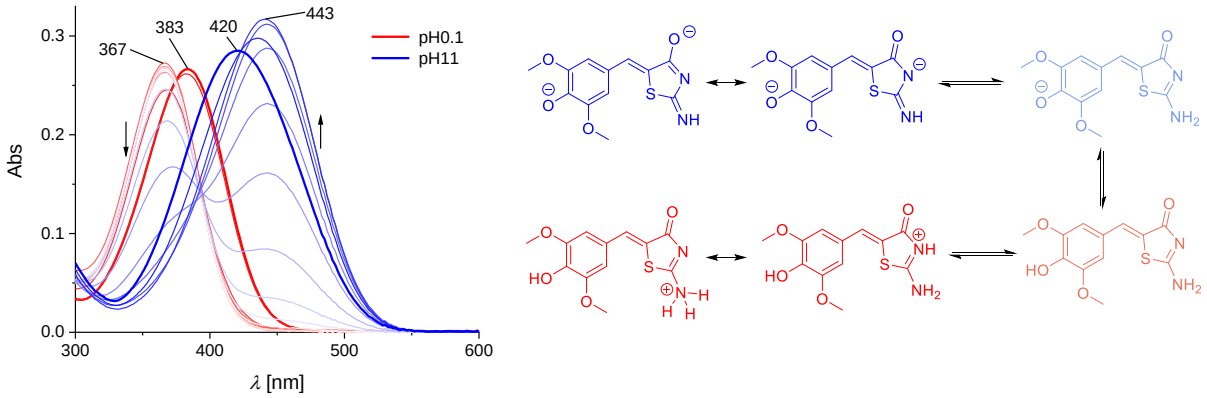

Figure 3.129: Absorption spectra for DMHB-PTH (**113**) in aqueous buffer for pH values between 0.1 and 11 show the presence of four different maxima in total which are attributed to the different protonation states shown on the right side. Conditions: 11 µM dye, 30 mM Britton-Robinson buffer.

The missing blue-shift at high pH values for DMHBI-NH_2 (**111**) and DMAM-DMHBI-NH_2 (**115**) is perfectly reasonable since the formation of the double-deprotonated species is prevented by the methylated imidazolinone nitrogen.

To evaluate the influence of the solvent on the protonation state of the four new chromophores, absorption spectra in protic (water, methanol, ethanol, isopropanol, *n*-butanol) as well as in aprotic (toluene, DMSO, *N,N*-DMF, dioxane) were recorded. In Figure 3.130, the normalized absorption spectra for water and toluene are shown as representatives for protic and aprotic solvents. Here, differences in the absorption behavior between these two solvents are only observed for DMHBI-NH_2 (**111**) and DMHB-PTH (**113**), while the two DMAM-substituted chromophores **114** and **115** exhibit identical spectra for both systems, therefore showing an absorbance rather independent from H-bonding ability and solvent polarity. However, DMHB-PTH (**113**) is more sensitive toward the solvent environment, showing a slight blue-shift of the absorption maximum when going from water to toluene, presumably due to destabilization attributed to the loss of hydrogen bonds to the phenolic hydroxy group.[477,478] This hypsochromic shift is not observed for DMHBI-NH_2 (**111**); instead it exhibits two pronounced absorption maxima at 393 and 373 nm in toluene and all of the other aprotic solvents while only the more red-shifted maximum is retained in protic solvents such as water.

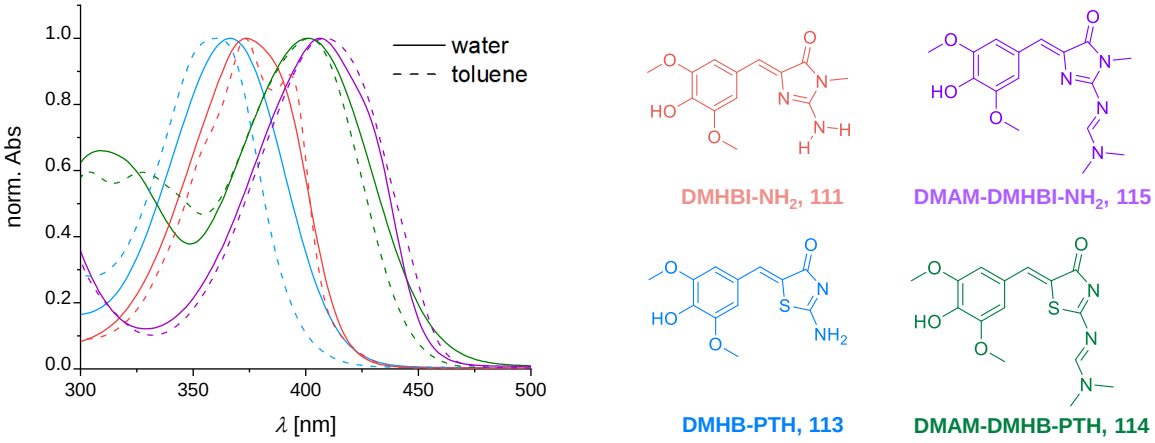

Figure 3.130: Absorption spectra for DMHBI-NH_2 (**111**), DMHB-PTH (**113**), DMAM-DMHB-PTH (**114**) and DMAM-DMHBI-NH_2 (**115**) in water (solid lines) and toluene (dashed lines).

The observation of two maxima indicates the presence of two energetically different conformations of which the farther red-shifted one displaying a larger HOMO-LUMO gap is not present in protic solvents. Therefore, the maximum at the lower wavelength might be attributed to a hydrogen-bonded conformation but since aprotic solvents are by definition not able to contribute to these intermolecular interactions, it might arise due to an intermolecular hydrogen bridge between the exocyclic amino protons or the unmethylated imidazolinone nitrogen of two DMHBI-NH_2 chromophores. However, this effect is neither observed for DMHB-PTH (**113**) nor the two DMAM-modified chromophores **114** and **115** which might be due to electronic effects.

The assumed capacity of DMHBI-NH_2 (**111**) to form stabilizing intermolecular hydrogen bonds might also play a role in the weak fluorescence activation of this chromophore by the Chili aptamer which remains to be elucidated. To have a closer look into their fluorescence behavior, the excitation and emission spectra of the four new chromophores in comparison to $DMHBI^+$ (**116**) and DMHBI (**102**) are shown in Figure 3.131, where the already discussed remarkably low emission intensity of DMHBI-NH_2 (**111**) becomes obvious. In addition, if the absorption and emission maxima observed here are compared to the ones of the free chromophores at different pH values, it can clearly be stated that DMHB-PTH (**113**) and DMAM-DMHB-PTH (**114**) are bound to the Chili aptamer in their protonated form but emit in their unprotonated form, similar as for other DMHBI derivatives.[258]

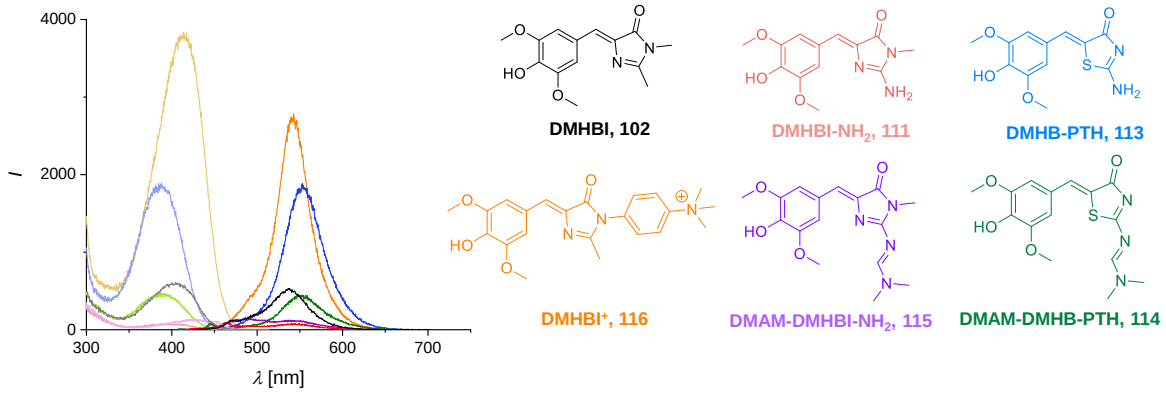

Figure 3.131: Overview of fluorescence excitation and emission spectra for DMHBI-NH_2 (**111**), DMAM-DMHBI-NH_2 (**115**), DMHB-PTH (**113**) and DMAM-DMHB-PTH (**114**) in comparison to DMHBI (**102**) and $DMHBI^+$ (**116**). Conditions: 0.5 µM chromophore, 0.5 µM Chili, 125 mM KCl, 5 mM $MgCl_2$, 80 mM HEPES pH 7.5; emission and excitation at the maximum.

The difference in fluroescence intensities is also reflected by the quantum yield ϕ summarized in Table 3.43. ϕ was determined for the free and the bound chromophores relative to Coumarin153.

While all of the free chromophores do not emit, displaying quantum yields of well below 1%, DMHB-PTH (**113**) bound to Chili is as expected the chromophore-RNA complex with the highest ϕ of nearly 19%, which is roughly half of the quantum yield of $DMHBI^+$ (**116**). Furthermore, all of the other values for ϕ match the expectations, being almost identical for both DMAM-containing structures **114** and **115** while the lowest for ϕ is obtained for DMHBI-NH_2 (**111**).

For additional characterization and to investigate the binding strength between Chili and its ligands, dissociation constants K_D were determined by the titration of the RNA aptamer into solutions with fixed ligand concentrations. By plotting the relative intensity of the emission

maximum against the aptamer concentration and fitting according to a single-site binding model, the K_D values shown in Table 3.43 were obtained. It has to be noted that for DMHBI-NH_2 (**111**) and DMAM-DMHBI-NH_2 (**115**) no K_D was calculated due to the low fluorescence emission intensity of these two chromophores.

Table 3.43: Quantum yields ϕ for free and bound chromophores as well as K_D values for the chromophore-Chili complexes.

Name	No.	ϕ_{free}±s.d.m.[a] %	ϕ_{bound}±s.d.m.[a] %	K_D±s.d.m. nM
DMHBI-NH_2	**111**	0.21±0.05	1.34±0.02	n.d.
DMAM-DMHBI-NH_2	**115**	0.46±0.03	4.89±0.04	n.d.
DMHB-PTH	**113**	0.15±0.05	18.6±2.8	137±5
DMAM-DMHB-PTH	**114**	0.18±0.05	5.07±0.08	45±6
DMHBI[257]	**102**	0.07±0.01	7.6±0.1	570±120
DMHBI$^+$[257]	**116**	0.11±0.01	40±1	63±16
DMHBO$^+$[257]	**117**	0.10±0.01	9.4±0.4	12±1

[a] measured relative to Coumarin 153 in ethanol with an estimated absolute quantum yield of 53%
Conditions for ϕ estimation: 17.0/11.2/7.41 µM RNA, 10.0/6.66/3.33 µM ligand, 125 mM KCl, 5 mM $MgCl_2$, 80.0 mM HEPES pH 7.5.
n. d. for not determined values
Conditions for K_D estimation: 8.00 µM to 0.49 µM RNA (15-step dilution series with water), 0.1 µM ligand, 125 mM KCl, 5 mM $MgCl_2$, 80 mM HEPES pH 7.5.

The estimated dissociation constants for DMHB-PTH (**113**) and DMAM-DMHB-PTH (**114**) are with 137 and 45 nM in a similar range as for DMHBI$^+$ (**116**) with 63 nM, indicating a comparably strong binding of these ligands. However, DMHBO$^+$ (**117**) still exhibits the strongest binding to Chili with a K_D of 12 nM due to the additional stabilizing interactions between the oxime moiety and the phosphate backbone as discussed previously.

The reason for the low fluorescence activation of DMHBI-NH_2 (**111**) might be due to inefficient or slow binding by the Chili aptamer or due to an intrinsically low fluorescence of this chromophore. To investigate the dependence of the emission intensity on the incubation time of the aptamer with the different chromophores, time-dependent fluorescence spectra were recorded and compared by integration of the emission bands (Figure 3.132).

Here, only for DMHB-PTH (**113**) and DMAM-DMHB-PTH (**114**) an increase in emission intensity by approximately 25% between incubation for 0 min and 104 h was observed, while the fluorescence intensity for DMHBI-NH_2 (**111**) and DMAM-DMHBI-NH_2 (**115**) remained

virtually unchanged. Therefore, a slow binding of the ligand cannot be the reason for the low luminescence of Chili-DMHBI-NH_2.

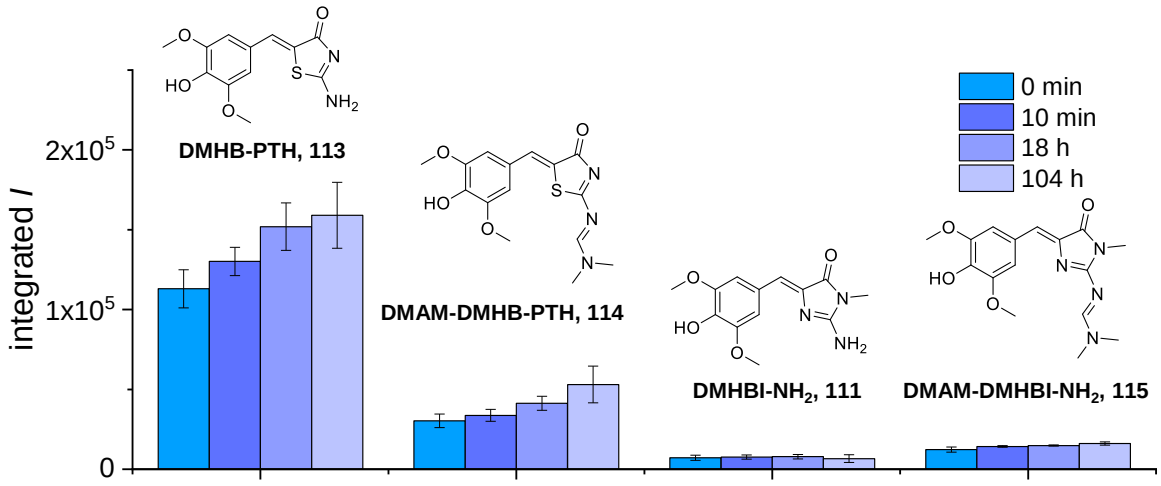

Figure 3.132: The fluorescence intensity only increases for DMHB-PTH (**113**) and DMAM-DMHB-PTH (**114**) upon prolonged incubation time, while it remains basically unchanged for DMHBI-NH_2 (**111**) and DMAM-DMHBI-NH_2 (**115**). Plotted is the area of the integrated emission after blank correction. Conditions: 0.5 µM chromophore, 0.5 µM Chili, 125 mM KCl, 5 mM $MgCl_2$, 80 mM HEPES pH 7.5; emission and excitation at the maximum.

Thus, the weak fluorescence activation of DMHBI-NH_2 (**111**) might arise because of the intrinsically low fluorescence of this chromophore. To address this issue, fluorescence spectra of DMHBI (**102**), DMHBI-NH_2 (**111**) and DMHB-PTH (**113**) in 50% water/glycerol were recorded since with glycerol the solvent viscosity is significantly enhanced, slowing down the rotation around the benzylidene bridge to increase the probability of radiative decay pathways (Figure 3.133).

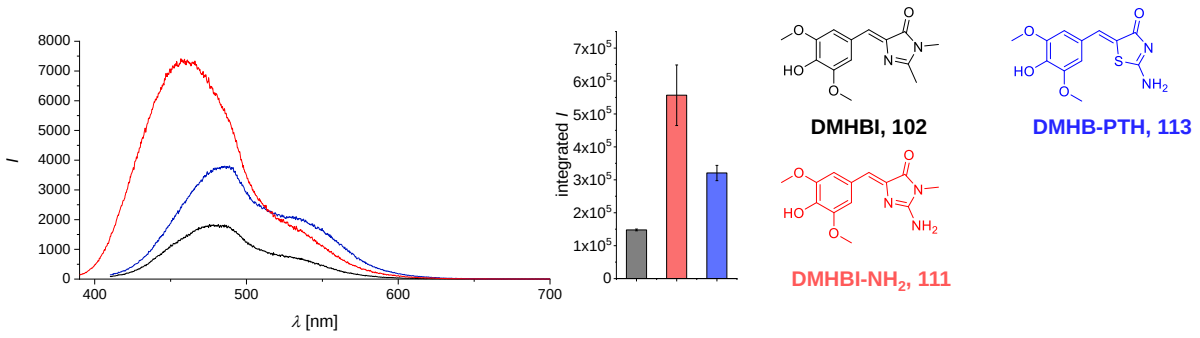

Figure 3.133: The fluorescence intensity recorded for the free chromophores in 50% glycerol/water is highest for DMHBI-NH_2 (**111**) which becomes obvious from the blank-corrected spectra and integrated intensity of the emission band. This is in strong contrast to the only weak fluorescence activation of this compound by the Chili aptamer which must therefore be due to inefficient binding of this ligand or binding in a non-emissive conformation. Conditions: 50 µM chromophore, glycerol/water 50/50 (v/v), excitation at the maximum.

Interestingly, the fluorescence behavior observed in this environment does not at all reflect the one described for the Chili-ligand complexes: although DMHBI-NH_2 (**111**) was nearly non-emissive when bound to the aptamer, it showed a twice as high fluorescence intensity in 50% glycerol compared to DMHB-PTH (**113**) which is much more efficiently activated by Chili. However, the emission intensity of DMHBI (**102**) in the glycerol/water mixture is even lower than for DMHB-PTH (**113**). Therefore, the chromophore structure itself is not responsible for the weak emission of the Chili-DMHBI-NH_2 but it must be due to either inefficient binding to the aptamer or due to binding in a non-emissive conformation. It has furthermore to be noted that the observed emission maxima for the HBI derivatives in the water/glycerol mixture strongly differ from the ones found for these chromophores in complex with Chili. Since the maximum emission is noticeably red-shifted for the chromophore-RNA complexes, no pronounced ESPT process seems to take place in the water/glycerol mixture, leading to the observation of only the emission of the protonated chromophores.

For further investigations of this phenomenon it might be useful to combine the the DMHBI (**102**) and DMHB-PTH (**113**) structure by synthesizing a DMHB-PTH variant with a methyl instead of the exocyclic amino group to estimate the influence of the exocyclic amino group on the binding efficiency to the Chili aptamer.

However, some of the effects detected in the course of the spectroscopic analysis of the DMHBI-NH_2 and DMHB-PTH chromophore family can be rationalized by comparison with computational results. Therefore, the chromophore structures were geometry-optimized and their electrostatic potential as well as different molecular parameters were calculated.

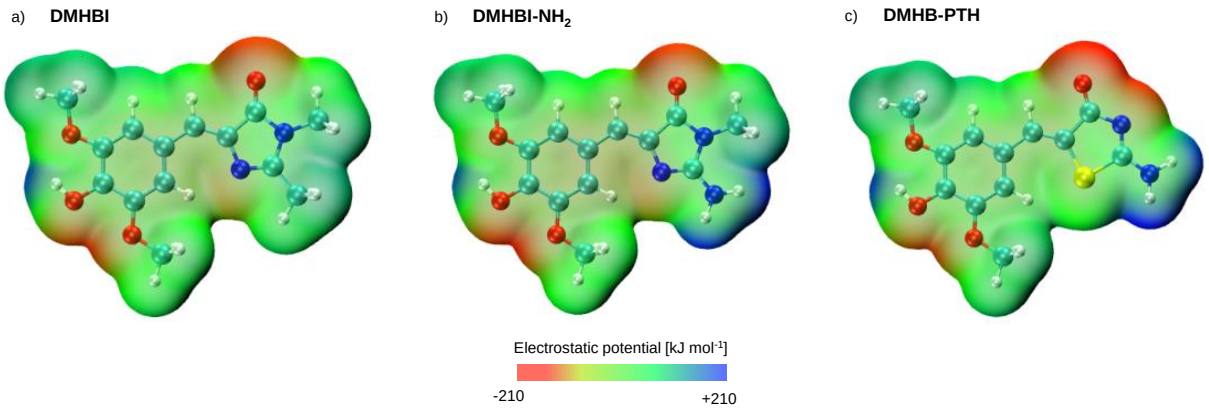

Figure 3.134: The electrostatic potential of geometry-optimized DMHBI (**102**,a), DMHBI-NH_2 (**111**, b) and DMHB-PTH (**113**, c) strongly depends on the nature of the five-membered ring system, leading to a differently pronounced positive electrostatic potential at the phenol hydroxy group. Geometry optimization was done in ORCA Version 5.0[310] at the level of density functional theory employing the B3LYP functional[311,312] together with the def2-SVP basis set.[313] Maps of the electrostatic potential on the electron density isosurface with a resolution of 80x80x80 grid points were generated using the Multiwfn software[314–316]

As shown in Figure 3.134, the nature of the five-membered ring strongly influences the positive electrostatic potential at the hydrogen of the phenol hydroxy group: while it is most positive for DMHBI (**102**), it is decreased in DMHB-PTH (**113**) and even lower for DMBHI-NH_2 (**111**). These results are in perfect accordance with the estimated pK_a values for these chromophores (see Table 3.42), which increase with a less positive electrostatic potential at this OH-group. Furthermore, the observation of a double-deprotonated form for DMHB-PTH (**113**) can be supported by these calculations since the negative electrostatic potential within the pseudothiohydantoin ring is not only concentrated on the oxygen atom but also equally pronounced at the ring nitrogen.

For the two chromophores with the electron-donating exocyclic amino function, the main part of the positive electrostatic potential is consequently located there and the dipole moments μ are elevated compared to DMHBI (**102**, 1.34 D), with 3.76 D for DMHB-PTH (**113**) and 4.03 D for DMHBI-NH_2 (**111**). Therefore, the assumption that a higher dipole moment of the chromophore is beneficial for efficient fluorescence activation is true for DMHB-PTH (**113**), while as already mentioned different factors need to play a role for the low emission intensity of Chili-DMHBI-NH_2.

Even larger dipole moments μ were obtained for the two DMAM-containing chromophores, with 5.65 D for DMAM-DMHBI-NH_2 (**115**) and 7.06 D for DMAM-DMH-PTH (**114**, Figure 3.135). For these, the main part of the positive electrostatic potential is located at the DMAM functionality and the electrostatic potential of the phenyl ring differs only marginally between DMAM-DMHBI-NH_2 (**115**) and DMAM-DMHB-PTH (**114**).

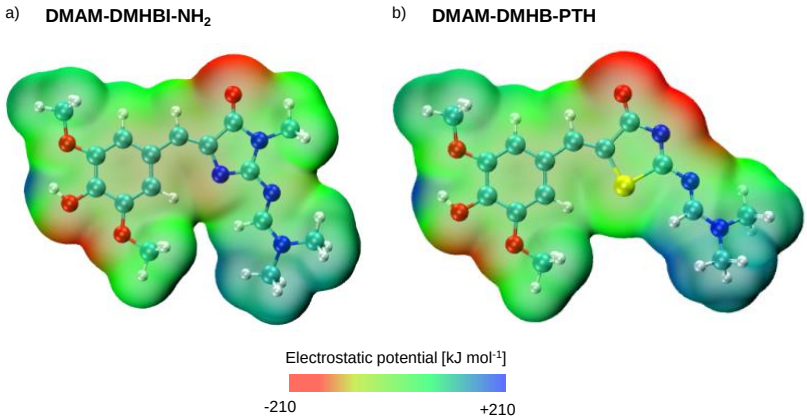

Figure 3.135: For DMAM-DMHBI-NH_2 (**115**, a) and DMAM-DMHB-PTH (**114**, b), the positive electrostatic potential is concentrated on the DMAM group, which is almost in plane with the conjugated system in the first case but rotated out of this plane for the second chromophore.

Interestingly, the geometry optimization of the two structures showed different orientations of the DMAM group: while it is almost in plane with the conjugated system in the case of

DMAM-DMHBI-NH_2 (**115**), it is rotated by around 30° out of this plane in DMAM-DMHB-PTH (**114**). Therefore, the presence of the *N*-methyl group and the substitution of one ring-nitrogen by sulfur leads to non-negligible structural changes which need to be taken into account for further investigations of this type of chromophores.

In summary, four structurally new DMHBI-derived chromphores have been synthesized and characterized with respect to their spectroscopic properties in both their free form or when bound to the Chili aptamer. All of the chromophores bind to Chili in their protonated form and emit in their deprotonated state with the most efficient fluorescence activation and the largest Stokes shift of 166 nm observed for DMHB-PTH (**113**), where the imidazolinone ring is replaced by pseudothiohydantoin, while DMHBI-NH_2 (**111**) with an aminoimidazolinone remained basically non-emissive. Attachment of a *N,N*-dimethyl aminomethylene group resulted in either strong decrease or slight enhancement of the emission intensity for DMAM-DMHB-PTH (**114**) and DMAM-DMHBI-NH_2 (**115**), respectively. Furthermore, it was shown that DMHBI-NH_2 (**111**) can be deprotonated twice under strongly basic conditions, indicated by a blue-shift of the absorption and rationalized by the calculated electrostatic potential at the phenolic hydroxy group. Since it was excluded that the chromophore by itself is non-emissive, the low emission intensity of the Chili-DMHBI-NH_2 must either be due to inefficient and weak binding or due to binding of the ligand in a non-emitting conformation. This might be attributed to the influence of the electron-donating exocyclic group on the pK_a of the phenol hydroxy group in complex with Chili, presumably preventing the ESPT mechanism required for fluorescence activation. To further investigate the underlying effects of the inefficient fluorescence activation of DMHBI-NH_2 (**111**), additional structural and spectroscopic characterization is needed.

Chapter 4

Conclusion and outlook

In the course of this thesis, the spectroscopic and biochemical properties of a variety of non-covalent and especially covalent fluorophore-oligonucleotide systems were studied. For the preparation of covalent chromophore assemblies on nucleic acids, some of the most promising candidates out of a library of differently constituted barbituric acid merocyanines were chosen and prepared as phosphoramidite building blocks. With these in hand, more than 100 single-, double- and multiple-modified DNA, RNA and also GNA strands were successfully synthesized by oligonucleotide solid phase synthesis and hybridized, providing access to a plethora of duplex structures containing up to ten merocyanine chromophores in a well-defined arrangement. These generated modified systems constitute the first described xample of the covalent incorporation of base pairing merocyanine chromophores as nucleobase surrogates into oligonucleotide scaffolds with different backbones. The thermodynamic and spectroscopic properties of these (multi)chromophoric duplex structures were analyzed by a range of different methods and surprisingly revealed a significant dependence of these characteristics not only on the backbone and chromophore constitution but also on the position of the chromophores in the sequence and their mutual orientation. Thus, despite being located in the same sequence context, formation of excitonically-coupled fluorescent H-type dimers was only observed for selected chromophore orientations within the different oligonucleotide scaffolds as summarized in Figures 4.1 to 4.4. Here, temperature-dependent absorption (Figures 4.1 and 4.3.) as well as fluorescence spectra (Figures 4.2 and 4.4) for BAM:BAM and BAM^{b}:BAM^{b} dimers within homogenous RNA, DNA and GNA scaffolds or DNA/GNA hybrid structures are shown. Among these modified oligonucleotides, H-type coupling within these dimers is only observed for some systems, for example the BAM:BAM opposite dimer in RNA (Figure 4.1, top right panel), while for others no chromophore-chromophore interactions are visible despite the close spatial proximity of the two nucleobase surrogates. Surprisingly, excitonically coupled BAM:BAM dimers showed to be strongly emissive (Figure 4.3), while BAM^{b}:BAM^{b} dimers remained non-emissive, indicating a strong influence of the chromophore's electronic and steric properties on the spectroscopic characteristics.

The dipolar character of the prepared merocyanines became even more obvious within duplex structures containing multiple chromophores consecutively incorporated into one of the

strands. Here, strong dipolar coupling interactions were not only present in the hybridized but also in the dehybridized state which gives rise to future applications of these easily accessible multichromophoric systems. Since furthermore the formation of higher-order aggregates caused by dipolar interstrand stacking interactions was observed by AFM, conceivable areas of application could be the design of light-harvesting systems, as similarly reported for DNA-phenanthrene systems, or the use as fluorescent synthons in DNA nanotechnology. In addition, further elaboration of the chromophore's structure by elongation of the poylmethine linker or stronger rigidification due to the introduction of a dioxaborine barbituryl moiety will not just improve its spectroscopic performance but also allow the use of additional analytical techniques such as pump-probe and time-resolved spectroscopy.

However, the generated merocyanine-oligonucleotide systems might not only be useful as building blocks for supramolecular structures but due to their sequence-specific emissive properties also for labeling and probing experiments in biochemistry. Promising preliminary results for these applications have already been obtained in the course of this thesis. Thus, it was for example shown that the barbituric acid merocyanine is able to serve as a fluorescent primer stop in PCR. To increase the scope of this chromophore as a substrate for enzymatic reactions, additional tests with available enzymes are required, for example to explore its suitability for end-labeling of oligonucleotides by terminal transferases. Furthermore, both the capability of these chromophores for orientation-dependent H-type aggregate formation and their combination with the widely known 2AP nucleobase, leading to the formation of a FRET pair, are useful to probe nucleic acid structures and conformations.

With regard to non-covalent oligonucleotide-chromophore complexes, the toolbox of fluorogenic ligands for the Chili RNA-aptamer was expanded by four new compounds. Structural changes of the five-membered ring system allowed the identification of one very promising chromophore containing a pseudothiohydantoin moiety which showed strong fluorescence activation upon binding to the aptamer. The presence of an exocyclic amino group within this new chromophore provides a platform for additional derivatizations and might lead to enhanced cell permeability required for *in vivo* experiments. Furthermore, this new chromophore is a potential candidate for future applications as a switchable biosensor or similar analytical device.

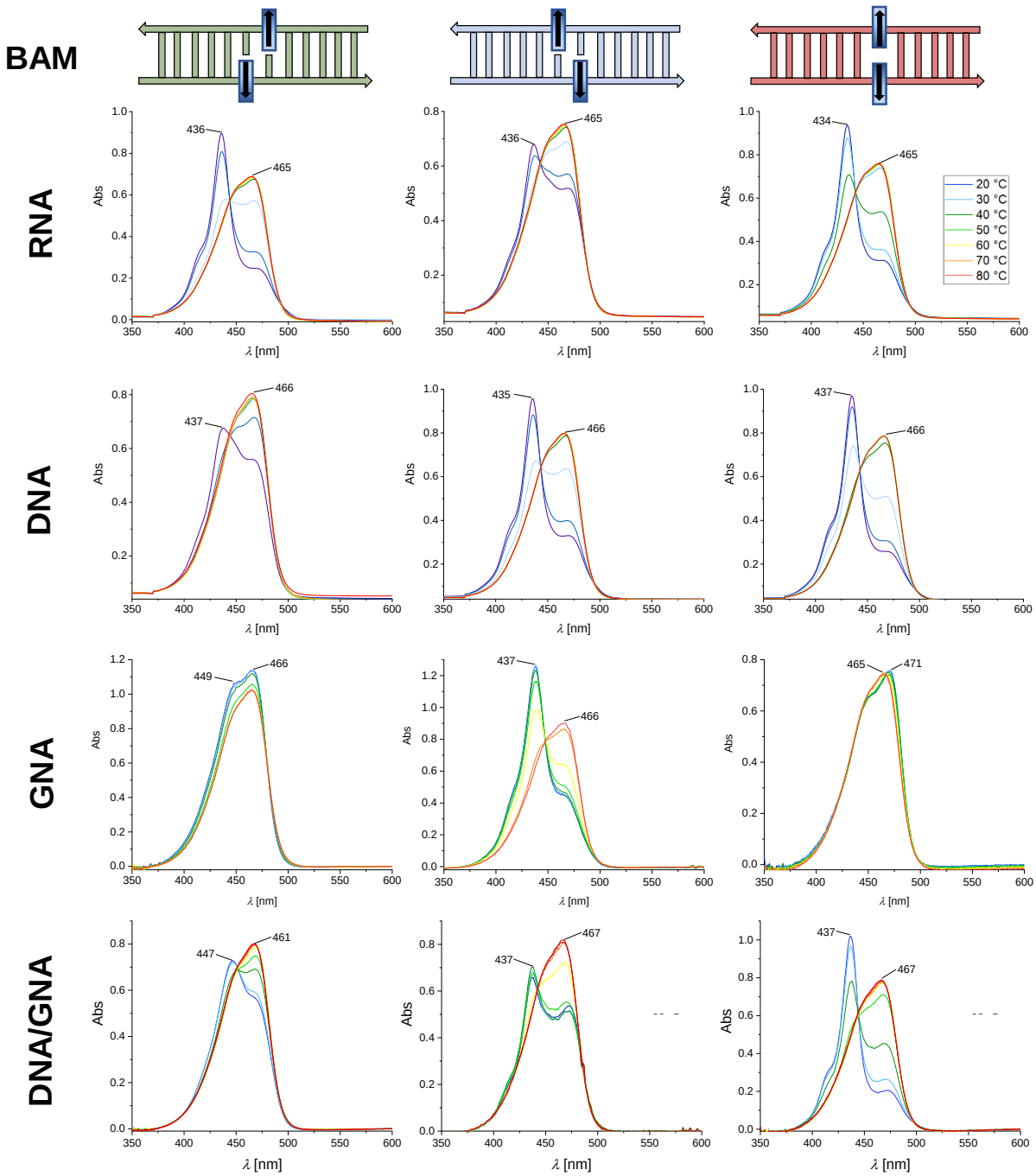

Figure 4.1: The overview of temperature-dependent absorption spectra for downstream (green), upstream (blue) and opposite (red) BAM:BAM dimers in the RNA, DNA, GNA and DNA/GNA context shows the strong dependence of the strength of the dipolar chromophore coupling on the backbone conformation and chromophore orientation.

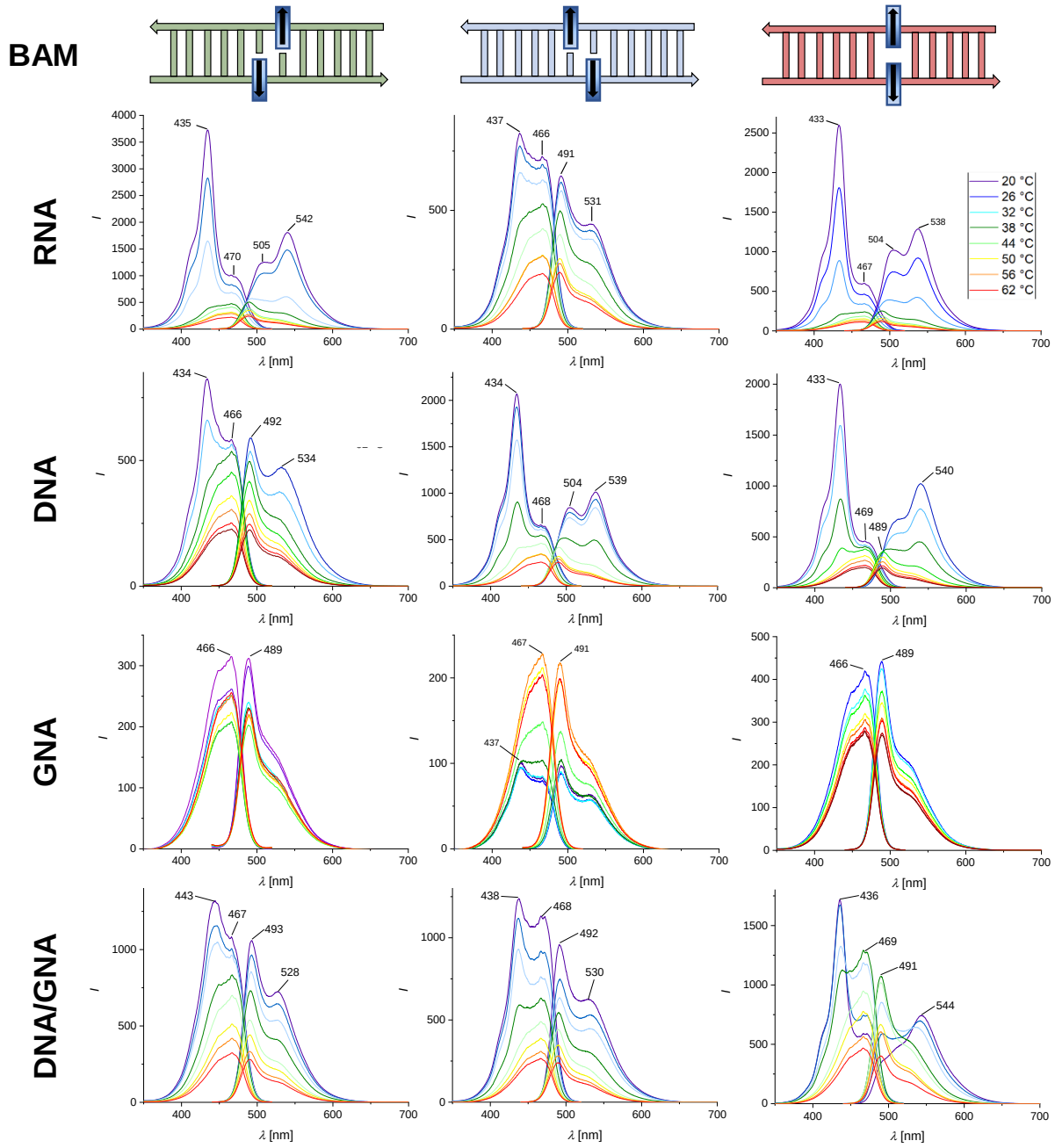

Figure 4.2: The overview of temperature-dependent fluorescence spectra for downstream (green), upstream (blue) and opposite (red) BAM:BAM dimers in the RNA, DNA, GNA and DNA/GNA context shows the strong dependence of the strength of the dipolar chromophore coupling on the backbone conformation and chromophore orientation.

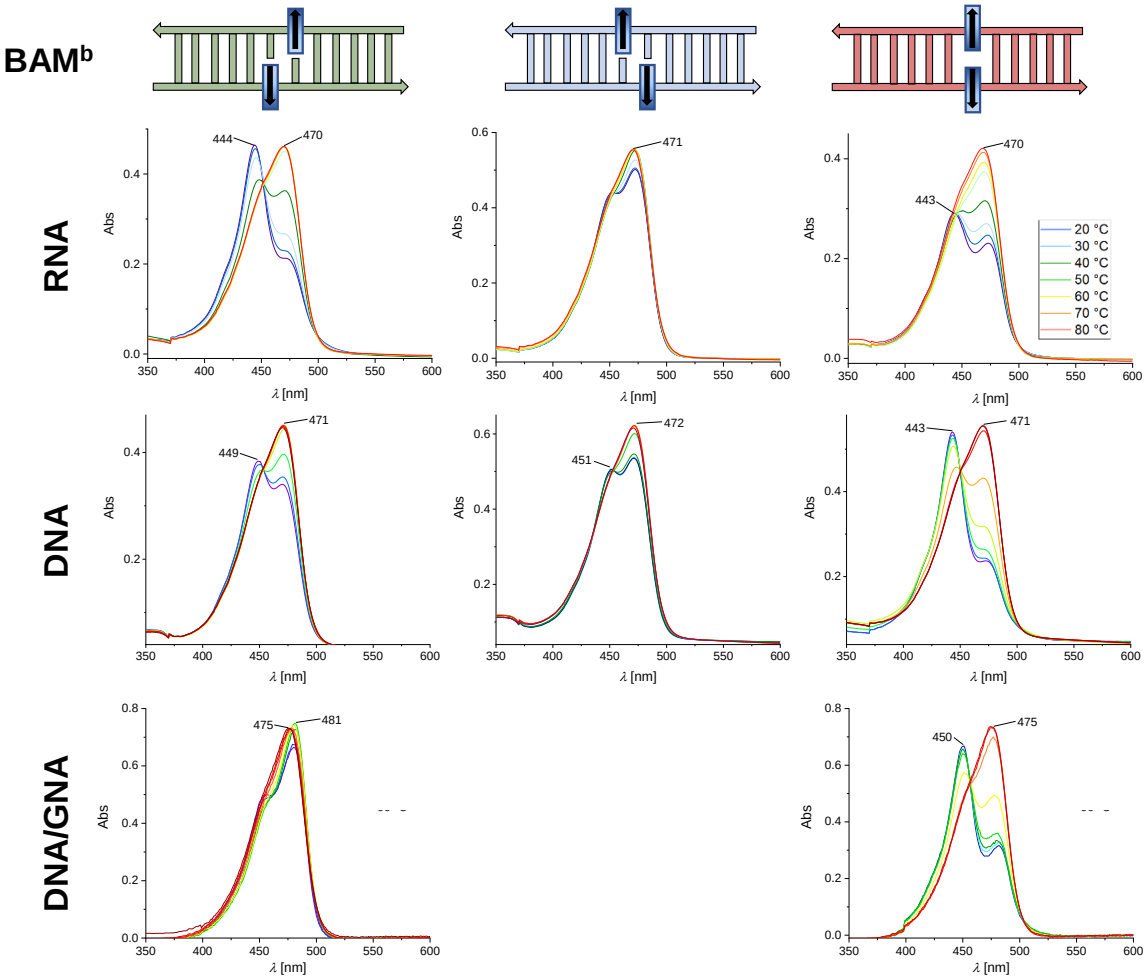

Figure 4.3: The overview of temperature-dependent absorption spectra for downstream (green), upstream (blue) and opposite (red) BAM^b:BAM^b dimers in the RNA, DNA and DNA/GNA context shows the strong dependence of the strength of the dipolar chromophore coupling on the backbone conformation and chromophore orientation.

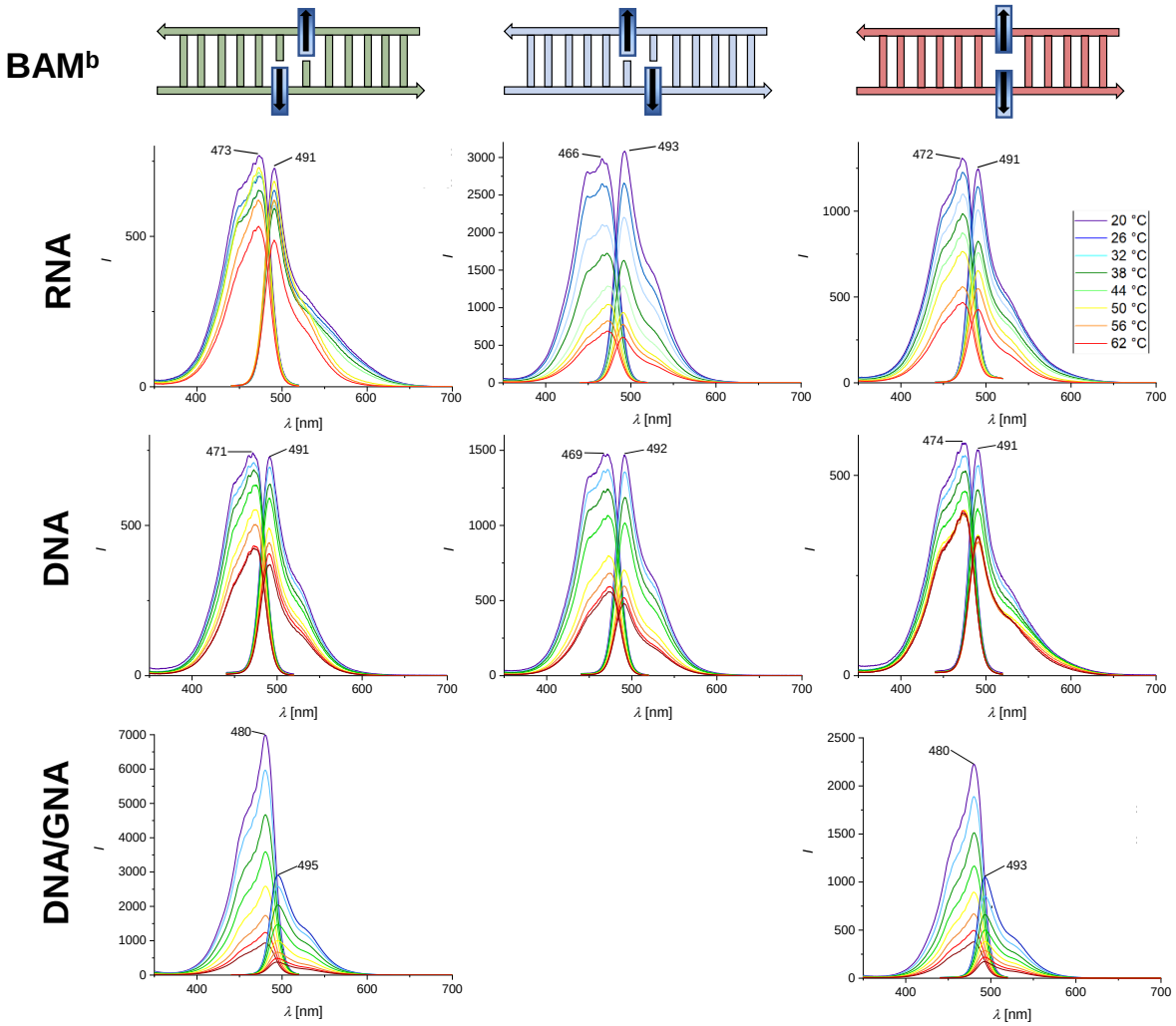

Figure 4.4: The overview of temperature-dependent fluorescence spectra for downstream (green), upstream (blue) and opposite (red) BAM^b:BAM^b dimers in the RNA, DNA and DNA/GNA context shows the strong dependence of the strength of the dipolar chromophore coupling on the backbone conformation and chromophore orientation.

Chapter 5

Experimental part

5.1 Chemical syntheses

5.1.1 General remarks

5.1.1.1 Materials

All standard chemicals and solvents were purchased from commercial suppliers. Organic solvents were used in pro analysis or for synthesis quality without further purification. Solvents for extraction and column chromatography were purchased in technical quality and distilled prior to use. Anhydrous solvents (dichloromethane, THF, *N,N*-DMF, acetonitrile) were obtained from a solvent purification system (SPS). Organic solvents for optical spectroscopy were purchased from Acros Organics. Thin layer chromatography (TLC) was performed on silica gel pre-coated aluminum plates (Alugram SIL G/UV254, Macherey-Nagel). Visualization was accomplished by irradiation with UV light at 254 nm. 4,4'-Dimethoxytrityl(DMT)-protected compounds were stained with 5% sulfuric acid in ethanol, which rendered them orange. Column chromatography was carried out on silica gel (Kieselgel 60, Merck, 0.063–0.200 mm).

5.1.1.2 NMR spectroscopy and mass spectrometry

NMR spectra of small molecules were measured on a Bruker Avance III HD 400 spectrometer at 400 MHz. For NMR samples of phosphoramidites the solvent was filtered through basic aluminum oxide prior to use. Chemical shifts (δ) were referenced to the residual solvent signals as internal standards (in ppm; $CDCl_3$: $^1H = 7.26$, $^{13}C = 77.16$; DMSO-d_6: $^1H = 2.50$, $^{13}C = 39.52$; CD_3CN: $^1H = 1.94$, $^{13}C = 118.26$; acetone-d_6: $^1H = 2.05$, $^{13}C = 29.84$; D_2O: $^1H = 4.79$) or on the unified scale for ^{31}P. Coupling constants (J) were reported in Hz. Multiplets were abbreviated as following: s (singlet), s_{br} (broad singlet), d (doublet), t (triplet), q (quartet) and m (multiplet). Spectral assignments were verified by 2D NMR experiments. Typical sample concentrations were in the range of 2–5 µmol of sample in 0.5 mL of solvent. High resolution ESI mass spectra were measured on a Bruker micrOTOF-Q III spectrometer. Monoisotopic masses for oligonucleotides were obtained by charge deconvolution of the raw spectra.

5.1.2 Synthetic procedures

5.1.2.1 Preparation of free merocyanine chromophores

General procedure I: Fischer indole synthesis

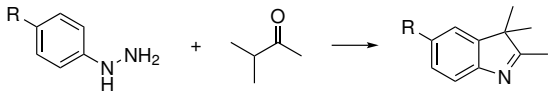

Substituted phenylhydrazine or the respective hydrochloride (1.00 eq.) was mixed with methyl-isopropylketone (1.00 to 1.50 eq.) in acetic acid (2 mL per mmol) and heated to reflux for up to 24 h. The solvent was removed in vacuum and the residue was redissolved in CH_2Cl_2 (4 mL per mmol starting material). This solution was washed with the same volume of each sat. aq. $NaHCO_3$, H_2O and brine. The organic phase was dried over Na_2SO_4 and the solvent was removed under reduced pressure to obtain the target compound.

5-Fluoro-2,3,3-trimethyl-3*H*-indole (9)

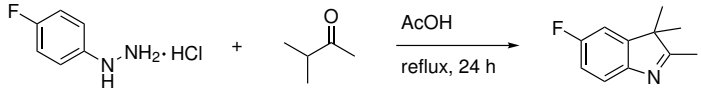

$C_6H_8ClFN_2$ 162.59 g mol^{-1} | $C_5H_{10}O$ 86.07 g mol^{-1} | $C_{11}H_{12}FN$ 177.22 g mol^{-1} **9**

Compound **9** was synthesized according to general procedure I on a 24.6 mmol scale with 1.50 eq. of methyl-isopropylketone by heating the reaction mixture for 24 h. The target compound **9** was obtained as brown needles (3.30 g, 18.6 mmol, 76%). Spectral data matched those reported previously.[479]

^{1}H NMR (400 MHz, $CDCl_3$): δ = 7.49 - 7.37 (m, 1 H, *H*-6), 7.05 - 6.88 (m, 2 H, *H*-4, *H*-7), 2.25 (d, J = 0.6 Hz, 3 H, CH_3), 1.29 (s, 6 H, 2×CH_3) ppm;
^{13}C{^{1}H} NMR (100 MHz, $CDCl_3$): δ = 187.87 (*C*-2), 187.83 (*C*-2), 162.51 (*C*-5), 160.09 (*C*-3a), 149.72 (*C*-7a), 149.70 (*C*-7a), 120.62 (*C*-7), 120.53 (*C*-7), 114.32 (*C*-4), 114.09 (*C*-4), 109.31 (*C*-6), 109.07 (*C*-6), 54.29 (*C*-3), 54.27 (*C*-3), 23.14 (2×*C*H$_3$), 15.53 (*C*H$_3$) ppm;
^{19}F NMR (376 MHz, $CDCl_3$): δ = -117.71 ppm;
HR-MS (ESI+): *m/z* calc. ($C_{11}H_{13}FN$, $[M+H]^+$): 178.1027, found: 178.0996.

5-Methoxy-2,3,3-trimethyl-3*H*-indole (10)

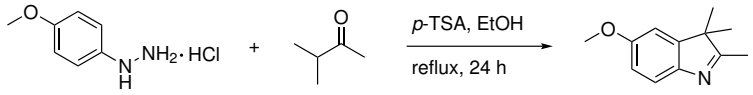

$C_7H_{11}ClN_2O$ 174.63 g mol^{-1} | $C_5H_{10}O$ 86.13 g mol^{-1} | $C_{12}H_{15}NO$ 189.26 g mol^{-1} **10**

p-Methoxyphenylhydrazine hydrochloride (2.50 g, 14.5 mmol, 1.00 eq.), methylisopropylketone (1.55 mL, 14.5 mmol, 1.00 eq.) and *p*-toluenesulfonic acid (273 mg, 1.45 mmol, 0.10 eq.) were dissolved in abs. EtOH (125 mL) and heated for 24 h to reflux. The solvent was removed in vacuum and the residue was taken up in 1 M HCl (25 mL). The resulting solution was washed with EtOAc (2×30 mL) and *n*-hexane (1×30 mL). Afterwards, the aqueous phase was neutralized with sat. aq. $NaHCO_3$ and extracted with CH_2Cl_2 (2×100 mL). The combined organic phases were dried over Na_2SO_4 and removal of the solvent in vacuum afforded the target compound **10** as a brown liquid (1.98 g, 10.5 mol, 72%). Spectral data matched those reported previously.[480]

^{1}H NMR (400 MHz, $CDCl_3$): $\delta = 7.42$ (dd, $J = 8.1$, 0.7 Hz, 1 H, *H*-7), 6.87 - 6.74 (m, 2 H, *H*-4, *H*-6), 3.83 (s, 3 H, OCH_3), 2.24 (s, 3 H, CH_3), 1.28 (s, 6 H, 2×CH_3) ppm;
^{13}C{^{1}H} NMR (100 MHz, $CDCl_3$): $\delta = 185.99$ (*C*-5), 158.04 (*C*-3a), 147.39 (*C*-7a), 120.18 (*C*-7), 112.14 (*C*-6), 108.27 (*C*-4), 55.83 (OCH_3), 53.90 (*C*-3), 23.38 (2×CH_3), 15.45 (CH_3) ppm;
HR-MS (ESI+): *m/z* calc. ($C_{12}H_{16}NO$, $[M+H]^+$): 190.1226, found: 190.1222.

5-Nitro-2,3,3-trimethyl-3*H*-indole (28)

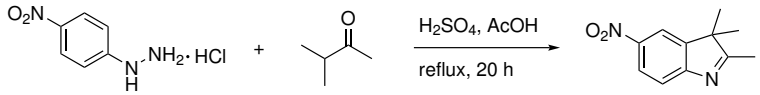

$C_6H_8ClN_3O_2$ 189.60 g mol^{-1} | $C_5H_{10}O$ 86.13 g mol^{-1} | $C_{11}H_{12}N_2O_2$ 204.23 g mol^{-1} **28**

Compound **28** was synthesized according to general procedure I on a 32.6 mmol scale with 1.00 eq. of methyl-isopropylketone and in the presence of 3.50 eq. of conc. H_2SO_4 by heating the reaction mixture for 20 h to reflux. The target compound **28** was obtained as brown needles (1.80 g, 8.80 mmol, 27%) after column chromatography on silica gel (100% CH_2Cl_2). Spectral data matched those reported previously.[480]

^{1}H NMR (400 MHz, $CDCl_3$): $\delta = 8.24$ (dd, $J = 8.5$, 2.3 Hz, 1 H, *H*-4), 8.15 (dd, $J = 2.3$, 0.5 Hz, 1 H, *H*-6), 7.65 - 7.54 (m, 1 H, *H*-7), 2.34 (s, 3 H, CH_3), 1.36 (s, 6 H, 2×CH_3) ppm;
^{13}C{^{1}H} NMR (100 MHz, $CDCl_3$): $\delta = 194.28$ (*C*-2), 159.04 (*C*-7a), 146.79 (*C*-3a), 145.73 (*C*-5), 124.64 (*C*-4), 120.14 (*C*-7), 117.27 (*C*-6), 54.61 (*C*-3), 22.83 (2×CH_3), 16.09 (CH_3)

ppm;
HR-MS (ESI+): *m/z* calc. ($C_{11}H_{13}N_2O_2$, $[M+H]^+$): 205.0972, found: 205.0972.

General procedure II: *N*-methylation

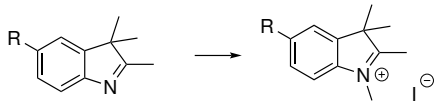

Indolenine or benzothiazole derivatives (1.00 eq.) were mixed with MeI (1.00 to 5.00 eq.) and heated to 50 °C for up to 24 h. The precipitate was filtered off and washed with cold EtOH and Et_2O for afford the target compound.

1,2,3,3-Tetramethyl-3*H*-indoline iodide (11)

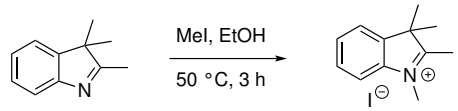

$C_{11}H_{13}N$
159.23 g mol^{-1}

$C_{12}H_{16}IN$
301.17 g mol^{-1}
11

Compound **11** was synthesized according to general procedure II on a 31.1 mmol scale with 1.35 eq. of MeI by heating for 3 h in abs. EtOH (7.80 mL). Hereby, the target compound **11** was obtained as slightly pink crystals (5.92 g, 19.7 mmol, 63%). Spectral data matched those reported previously.[296]

^{1}H NMR (400 MHz, DMSO-d_6): δ = 7.95 - 7.88 (m, 1 H, 7-H), 7.86 - 7.80 (m, 1 H, 4-H), 7.67 - 7.58 (m, 2 H, 5-H, 6-H), 3.97 (s, 3 H, NCH_3), 2.77 (s, 3 H, CH_3), 1.53 (s, 6 H, 2×CH_3) ppm;
^{13}C{^{1}H} NMR (100 MHz, DMSO-d_6): δ = 196.46 (*C*-2), 142.57 (*C*-3a), 142.06 (*C*-7a), 129.79 (*C*-5), 129.28 (*C*-6), 123.75 (*C*-4), 115.57 (*C*-7), 54.38 (*C*-3), 35.07 (N*C*H$_3$), 22.15 (2×*C*H$_3$), 14.47 (*C*H$_3$) ppm;
HR-MS (ESI+): *m/z* calc. ($C_{12}H_{16}N$, $[M]^+$): 174.1277, found: 174.1281.

5-Fluoro-1,2,3,3-tetramethyl-3*H*-indoline iodide (12)

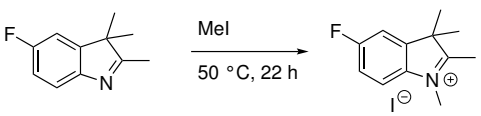

$C_{11}H_{12}FN$
177.22 g mol^{-1}
9

$C_{12}H_{15}FIN$
319.16 g mol^{-1}
12

Compound **12** was synthesized according to general procedure II on a 11.3 mmol scale with 5.00 eq. of MeI by heating for 22 h. Hereby, the target product **12** was obtained as brown solid (3.11 g, 9.75 mmol, 86%). Spectral data matched those reported previously.[481]

^{1}H NMR (400 MHz, DMSO-d_6): δ = 8.43 (ddd, J = 8.8, 4.2 Hz, 1 H, *H*-7), 7.84 (dd, J = 8.2, 2.5 Hz, 1 H, *H*-4), 7.51 (td, J = 9.1, 2.6 Hz, 1 H, *H*-6), 3.97 (s, 3 H, NCH_3), 2.76 (s, 3 H, CH_3), 1.54 (s, 6 H, 2×CH_3) ppm;
^{13}C{^{1}H} NMR (100 MHz, DMSO-d_6): δ = 196.06 (*C*-2), 196.03 (*C*-2), 163.80 (*C*-5), 161.35 (*C*-3a), 144.25 (*C*-7a), 144.15 (*C*-7a), 138.39 (*C*-7), 138.37 (*C*-7), 115.95 (*C*-6), 115.71 (*C*-6), 111.50 (*C*-4), 111.24 (*C*-4), 54.15 (*C*-3), 54.13 (*C*-3), 35.01 (N*C*H$_3$), 21.53 (2×*C*H$_3$), 14.30 (*C*H$_3$) ppm;
^{19}F NMR (376 MHz, DMSO-d_6): δ = -111.46 ppm;
HR-MS (ESI+): *m/z* calc. ($C_{12}H_{15}FN$, $[M]^+$): 192.1183, found: 192.1177.

5-Methoxy-1,2,3,3-tetramethyl-3*H*-indoline iodide (13)

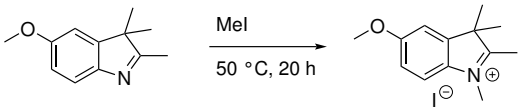

$C_{12}H_{15}NO$
189.26 g mol^{-1}
10

$C_{13}H_{18}INO$
331.20 g mol^{-1}
13

Compound **13** was synthesized according to general procedure II on a 7.00 mmol scale with 5.00 eq. of MeI by heating for 20 h. Hereby, the target product **13** was obtained as brown crystals (1.35 g,4.08 mmol, 58%). Spectral data matched those reported previously.[480]

^{1}H NMR (400 MHz, DMSO-d_6): δ = 7.81 (d, J = 8.8 Hz, 1 H, *H*-7), 7.47 (d, J = 2.5 Hz, 1 H, *H*-4), 7.15 (dd, J = 8.8, 2.5 Hz, 1 H, *H*-6), 3.93 (d, J = 1.0 Hz, 3 H, NCH_3), 3.86 (s, 3 H, OCH_3), 2.70 (d, J = 1.0 Hz, 3 H, CH_3), 1.51 (s, 6 H, 2×CH_3) ppm;
^{13}C{^{1}H} NMR (100 MHz, DMSO-d_6): δ = 193.57 (*C*-2), 161.02 (*C*-5), 144.10 (*C*-3a), 135.82 (*C*-7a), 116.52 (*C*-7), 114.60 (*C*-6), 109.68 (*C*-4), 56.55 (O*C*H$_3$), 54.19 (*C*-3), 35.08 (N*C*H$_3$), 22.24 (2×*C*H$_3$), 14.21 (*C*H$_3$) ppm;
HR-MS (ESI+): *m/z* calc. ($C_{13}H_{18}NO$, $[M]^+$): 204.1383, found: 204.1383.

2,3-Dimethylbenzothiazolium iodide (21)

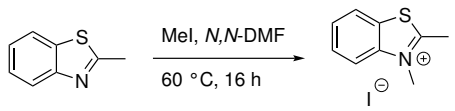

C_8H_7NS
149.21 g mol^{-1}

$C_9H_{10}INS$
291.15 g mol^{-1}
21

2-Methylbenzothiazole (2.56 mL, 20.1 mmol, 1.00 eq.) and methyl iodide (5.00 mL, 80.4 mmol, 4.00 eq.) were mixed with *N,N*-DMF (10 mL) and stirred for 16 h at 60 °C. The reaction mixture was cooled to r. t. and EtOAc (100 mL) was slowly added. The precipitate was filtered off and washed with EtOAc (3×20 mL). The target compound **21** was obtained as pink crystals (5.83 g, 20.0 mmol, quant.). Spectral data matched those reported previously.[296]

^{1}H NMR (400 MHz, DMSO-d_6): δ = 8.43 (ddd, J = 8.1, 1.3, 0.6 Hz, 1 H, *H*-7), 8.29 (dt, J = 8.5, 0.9 Hz, 1 H, *H*-4), 7.90 (ddd, J = 8.5, 7.3, 1.3 Hz, 1 H, *H*-5), 7.81 (ddd, J = 8.3, 7.3, 1.1 Hz, 1 H, *H*-6), 4.20 (s, 3 H, NCH_3), 3.16 (s, 3 H, CH_3) ppm;
^{13}C{^{1}H} NMR (100 MHz, DMSO-d_6): δ = 177.32 (*C*-2), 141.61 (*C*-3a), 129.29 (*C*-4), 128.73 (*C*-5), 128.12 (*C*-6), 124.52 (*C*-7), 116.79 (*C*-7a), 36.17 (N*C*H$_3$), 17.08 (*C*H$_3$) ppm;
HR-MS (ESI+): *m/z* calc. ($C_9H_{10}NS$, [M]$^+$): 164.0528, found: 164.0529.

1-Ethyl-2,3,3-trimethyl-3*H*-indoline iodide (29)

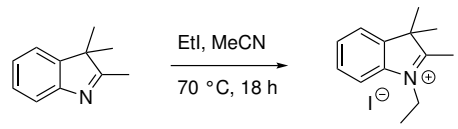

$C_{11}H_{13}N$
159.23 g mol^{-1}

$C_{13}H_{18}IN$
315.20 g mol^{-1}
29

2,3,3-Trimethylindolenine (1.00 g, 6.25 mmol, 1.00 eq.) was dissolved in ethyl iodide (5.00 mL, 63.2 mmol, 10.1 eq.) and MeCN (10 mL). The reaction mixture was heated for 18 h to 70 °C. Afterwards, the solvent was removed under reduced pressure and the residue was washed with cold Et_2O (50 mL in total) to obtain the target compound **29** as violet crystals (1.88 g, 5.96 mmol, 95%). Spectral data matched those reported previously.[481]

^{1}H NMR (400 MHz, DMSO-d_6): δ = 8.05 - 7.92 (m, 1 H, *H*-7), 7.92 - 7.78 (m, 1 H, *H*-6), 7.72 - 7.50 (m, 2 H, *H*-4, *H*-5), 4.50 (q, J = 7.3 Hz, 2 H, NCH_2), 2.84 (s, 3 H, CH_3), 1.54 (s, 6 H, 2×CH_3), 1.45 (t, J = 7.3 Hz, 3 H, NCH$_2$CH_3) ppm;
^{13}C{^{1}H} NMR (100 MHz, DMSO-d_6): δ = 128.82 (*C*-3a), 127.81 (*C*-7a), 96.11 (*C*-6), 95.65 (*C*-5), 92.33 (*C*-4), 90.82 (*C*-7), 49.35 (N*C*H$_2$), 41.61 (*C*-3), 36.36 (2×*C*H$_3$), 33.42 (NCH$_2$*C*H$_3$), 26.08 (*C*H$_3$) ppm;

HR-MS (ESI+): *m/z* calc. ($C_{13}H_{18}N$, $[M]^+$): 188.1434, found: 188.1434.

5-Nitro-1,2,3,3-tetramethyl-3*H*-indoline iodide (30)

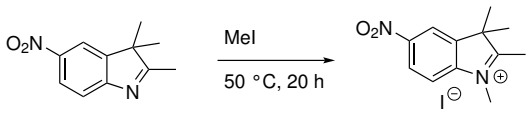

$C_{11}H_{12}N_2O_2$
204.23 g mol^{-1}
28

$C_{12}H_{15}IN_2O_2$
346.17 g mol^{-1}
30

Compound **30** was synthesized according to general procedure II on a 4.90 mmol scale with 3.20 eq. of MeI by heating for 20 h. Hereby, the target product **30** was obtained as a brown solid (1.36 g, 3.93 mmol, 79%). Spectral data matched those reported previously.[480]

^{1}H NMR (400 MHz, DMSO-d_6): δ = 8.20 - 7.97 (m, 2 H, *H*-4, *H*-6), 6.85 (d, J = 8.8 Hz, 1 H, *H*-7), 4.20 (d, J = 13.0 Hz, 3 H, NCH_3), 3.14 (s, 3 H, CH_3), 1.33 (s, 6 H, 2×CH_3) ppm;
^{13}C{^{1}H} NMR (100 MHz, DMSO-d_6): δ = 161.32 (*C*-2), 152.11 (*C*-7a), 139.62 (*C*-3a), 138.50 (*C*-5), 126.72 (*C*-4), 118.54 (*C*-7), 105.55 (*C*-6), 43.56 (N*C*H$_3$), 29.69 (2×*C*H$_3$), 29.49 (*C*H$_3$) ppm;
HR-MS (ESI+): *m/z* calc. ($C_{12}H_{15}N_2O_2$, $[M]^+$): 219.1128, found: 219.1129.

General procedure III: generation of the exocyclic double bond

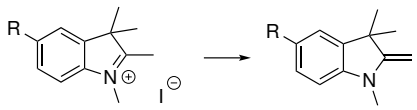

Methylated indolenines or benzothiazoles (2 to 4 mmol) were dissolved in 3 M NaOH (150 mL) and heated to 50 °C for 30 min. After cooling to r. t., the aqueous phase was extracted with Et_2O (3×100 mL). The combined organic phases were dried over Na_2SO_4 and the solvent was removed in vacuum to afford the pure product.

1,3,3-Trimethyl-2-methyleneindoline (14)

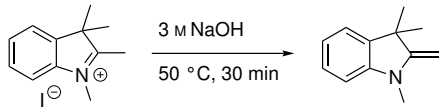

$C_{12}H_{16}IN$
301.17 g mol^{-1}
11

$C_{12}H_{15}N$
173.26 g mol^{-1}
14

Compound **14** was synthesized according to general procedure III on a 4.98 mmol scale and was obtained as a pink oil (873 mg, 4.94 mmol, 99%). Spectral data matched those reported previously.[296]

^{1}H NMR (400 MHz, $CDCl_3$): δ = 7.18 - 7.03 (m, 2 H, *H*-4, *H*-6), 6.76 (td, J = 7.4, 1.0 Hz, 1 H, *H*-5), 6.55 (dd, J = 7.9, 0.9 Hz, 1 H, *H*-7), 3.85 (s, 2 H, CH_2), 3.04 (s, 3 H, NCH_3), 1.35 (s, 6 H, 2×CH_3) ppm;
^{13}C{^{1}H} NMR (100 MHz, $CDCl_3$): δ = 163.24 (*C*-2), 146.79 (*C*-7a), 137.97 (*C*-3a), 127.91 (*C*-6), 122.15 (*C*-4), 118.70 (*C*-5), 105.27 (*C*-7), 73.35 (CH_2), 53.83 (*C*-3), 30.34 (2×CH_3), 29.14 (CH_3) ppm;
HR-MS (ESI+): *m/z* calc. ($C_{12}H_{16}N$, $[M+H]^+$): 174.1277, found: 174.1276.

5-Fluoro-1,3,3-trimethyl-2-methyleneindoline (15)

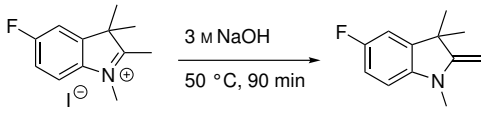

$C_{12}H_{15}FIN$
319.16 g mol^{-1}
12

$C_{12}H_{14}FN$
191.25 g mol^{-1}
15

Compound **15** was synthesized according to general procedure III on a 6.27 mmol scale by heating for 90 min and was obtained as an orange oil (1.12 g, 5.86 mmol, 93%).

^{1}H NMR (400 MHz, $CDCl_3$): δ = 6.89 - 6.72 (m, 2 H, *H*-4, *H*-6), 6.39 (dd, J = 9.1, 4.0 Hz, 1 H, *H*-7), 3.82 (q, J = 2.0 Hz, 2 H, CH_2), 3.01 (s, 3 H, NCH_3), 1.33 (s, 6 H, 2×CH_3) ppm;
^{13}C{^{1}H} NMR (100 MHz, $CDCl_3$): δ = 162.91 (*C*-2), 158.45 (*C*-5), 142.63 (*C*-3a), 139.17 (*C*-7a), 113.40 (*C*-7), 113.17 (*C*-4), 110.13 (*C*-6), 73.34 (CH_2), 53.58 (*C*-3), 29.95 (NCH_3), 29.13 (2×CH_3) ppm;
HR-MS (ESI+): *m/z* calc. ($C_{12}H_{15}FN$, $[M+H]^+$): 192.1183, found: 192.1185.

5-Methoxy-1,3,3-trimethyl-2-methyleneindoline (16)

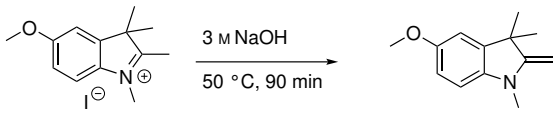

$C_{13}H_{18}INO$
331.20 g mol^{-1}
13

$C_{13}H_{17}NO$
203.29 g mol^{-1}
16

Compound **16** was synthesized according to general procedure III on a 3.02 mmol scale by heating for 90 min and was obtained as a violet oil (440 mg, 2.16 mmol, 72%). Spectral data matched those reported previously.[482]

^{1}H NMR (400 MHz, $CDCl_3$): δ = 6.74 (d, J = 2.6 Hz, 1 H, *H*-7), 6.67 (dd, J = 8.4, 2.6 Hz, 1 H, *H*-6), 6.42 (d, J = 8.3 Hz, 1 H, *H*-4), 3.77 (s, 3 H, NCH_3), 3.00 (s, 3 H, OCH_3), 1.54 (s, 2 H, CH_2), 1.33 (s, 6 H, 2×CH_3) ppm;
^{13}C{^{1}H} NMR (100 MHz, $CDCl_3$): δ = 163.41 (*C*-2), 153.33 (*C*-5), 140.94 (*C*-3a), 139.22 (*C*-7a), 112.25 (*C*-6), 110.21 (*C*-7), 104.77 (*C*-4), 72.39 (*C*H_2), 56.28 (*C*-3), 44.68 (O*C*H_3), 30.15 (N*C*H_3), 29.16 (2×*C*H_3) ppm;
HR-MS (ESI+): *m/z* calc. ($C_{13}H_{18}NO$, $[M+H]^+$): 204.1383, found: 204.1376.

1-Ethyl-3,3-dimethyl-2-methyleneindoline (31)

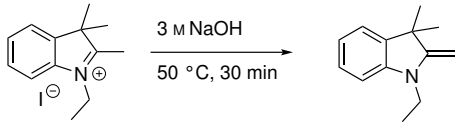

$C_{13}H_{18}IN$
315.20 g mol^{-1}
29

$C_{13}H_{17}N$
187.29 g mol^{-1}
31

Compound **31** was synthesized according to general procedure III on a 3.17 mmol scale and was obtained as a pink oil (527 mg, 2.81 mmol, 89%). Spectral data matched those reported previously.[483]

^{1}H NMR (400 MHz, $CDCl_3$): δ = 7.09 - 6.97 (m, 2 H, *H*-4, *H*-6), 6.68 (td, J = 7.4, 1.0 Hz, 1 H, *H*-5), 6.46 (dt, J = 7.9, 0.8 Hz, 1 H, *H*-7), 3.78 (dd, J = 18.1, 1.9 Hz, 2 H, CH_2), 3.49 (q, J = 7.1 Hz, 2 H, N*C*H_2), 1.26 (s, 6 H, 2×CH_3), 1.10 (t, J = 7.1 Hz, 3 H, NCH_2CH_3) ppm;
^{13}C{^{1}H} NMR (100 MHz, $CDCl_3$): δ = 161.10 (*C*-2), 145.48 (*C*-7a), 137.71 (*C*-3a), 127.59 (*C*-6), 121.86 (*C*-4), 118.16 (*C*-5), 108.19 (*C*-7), 72.59 (*C*H_2), 53.45 (*C*-3), 44.11 (N*C*H_2), 29.98 (2×*C*H_3), 12.74 (NCH_2CH_3) ppm;
HR-MS (ESI+): *m/z* calc. ($C_{13}H_{18}N$, $[M+H]^+$): 188.1434, found: 188.1432.

5-Nitro-1,3,3-trimethyl-2-methyleneindoline (32)

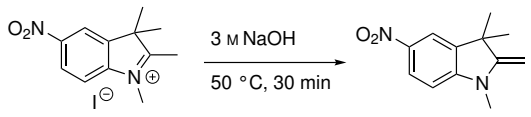

$C_{12}H_{15}IN_2O_2$
346.17 g mol^{-1}
30

$C_{12}H_{14}N_2O_2$
218.26 g mol^{-1}
32

Compound **32** was synthesized according to general procedure III on a 2.89 mmol scale and was obtained as red crystals (587 mg, 2.69 mmol, 93%).

^{1}H NMR (400 MHz, $CDCl_3$): δ = 8.14 (dd, J = 8.8, 2.3 Hz, 1 H, *H*-4), 7.94 (d, J = 2.3 Hz, 1 H, *H*-6), 6.52 (d, J = 8.8 Hz, 1 H, *H*-7), 4.16 - 4.03 (m, 2 H, CH_2), 3.13 (s, 3 H, NCH_3),

1.37 (s, 6 H, 2×CH_3) ppm;
^{13}C{^{1}H} NMR (100 MHz, $CDCl_3$): δ = 161.36 (*C*-2), 151.67 (*C*-7a), 140.12 (*C*-3a), 138.28 (*C*-5), 126.40 (*C*-4), 118.26 (*C*-6), 104.02 (*C*-7), 79.02 (CH_2), 43.60 (*C*-3), 29.84 (2×CH_3), 29.21 (NCH_3) ppm;
HR-MS (ESI+): *m/z* calc. ($C_{12}H_{14}N_2NaO_2$, $[M+Na]^+$): 241.0948, found: 241.0947.

General procedure IV: Vilsmeier-Haack formylation

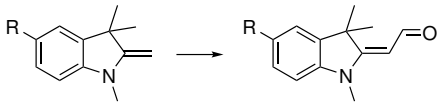

The Vilsmeier reagent (chloromethylene)dimethylammonium chloride (3.00 eq.) was dissolved under nitrogen atmosphere in anhydrous CH_2Cl_2 (1 mL per mmol). The indolenine or benzothiazole derivative (1.00 eq.) in CH_2Cl_2 (1 mL per mmol) was added dropwise and the reaction was stirred for 1 to 5 h at ambient temperature. After removal of the solvent in vacuum, the residue was taken up in THF (1 mL per mmol) and sat. aq. K_2CO_3 was added until the formation of CO_2 ceased. The biphasic mixture was stirred for 12 h before the organic solvent was evaporated. After extraction of the aqueous phase with CH_2Cl_2 (3×50 mL), the combined organic phases were dried over Na_2SO_4 and removal of the solvent under reduced pressure afforded the target compound.[294]

(*E*)-2-(1,3,3-Trimethylindolin-2-ylidene)acetaldehyde (17)

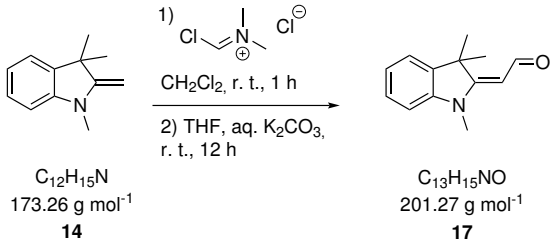

Compound **17** was synthesized on a 4.94 mmol scale according to general procedure IV by stirring for 1 h in the first reaction step and obtained as an orange oil (625 mg, 3.11 mmol, 63%). Spectral data matched those reported previously.[278]

^{1}H NMR (400 MHz, $CDCl_3$): δ = 10.00 (d, *J* = 9.0 Hz, 1 H, C*H*O), 7.34 - 7.17 (m, 2 H, *H*-4, *H*-5), 7.05 (td, *J* = 7.5, 0.9 Hz, 1 H, *H*-6), 6.84 (dt, *J* = 7.9, 0.8 Hz, 1 H, *H*-7), 5.38 (d, *J* = 8.9 Hz, 1 H, NCC*H*), 3.23 (s, 3 H, NCH_3), 1.65 (s, 6 H, 2×CH_3) ppm;
^{13}C{^{1}H} NMR (100 MHz, $CDCl_3$): δ = 186.93 (*C*HO), 174.07 (*C*-2), 143.92 (*C*-7a), 139.77 (*C*-3a), 128.48 (*C*-6), 122.91 (*C*-4), 122.27 (*C*-5), 108.44 (*C*-7), 99.38 (NC*C*H), 47.89 (*C*-3), 29.95 (N*C*H_3), 24.80 (2×*C*H_3) ppm;
HR-MS (ESI+): *m/z* calc. ($C_{13}H_{15}NNaO$, $[M+Na]^+$): 224.1046, found: 224.1041.

(*E*)-2-(5-Fluoro-1,3,3-trimethylindolin-2-ylidene)acetaldehyde (18)

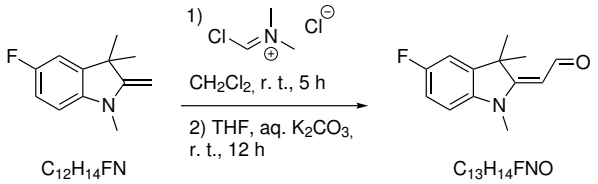

$C_{12}H_{14}FN$
191.25 g mol^{-1}
15

$C_{13}H_{14}FNO$
219.26 g mol^{-1}
18

Compound **18** was synthesized on a 5.23 mmol scale according to general procedure IV by stirring for 5 h in the first reaction step and obtained as a red oil (822 mg, 3.68 mmol, 70%).

^{1}H NMR (400 MHz, $CDCl_3$): $\delta = 9.97$ (d, $J = 8.9$ Hz, 1 H, C*H*O), 7.03 - 6.87 (m, 2 H, *H*-4, *H*-6), 6.83 - 6.65 (m, 1 H, *H*-7), 5.36 (d, $J = 8.9$ Hz, 1 H, NCC*H*), 3.21 (d, $J = 5.5$ Hz, 3 H, NCH_3), 1.65 (s, 6 H, 2×CH_3) ppm;
^{13}C{^{1}H} NMR (100 MHz, $CDCl_3$): $\delta = 186.46$ (*C*HO), 174.23 (*C*-2), 158.27 (*C*-5), 141.27 (*C*-3a), 139.60 (*C*-7a), 114.55 (*C*-7), 110.24 (*C*-4), 108.40 (*C*-6), 99.25 (NC*C*H), 47.76 (*C*-3) , 29.97 (N*C*H$_3$), 29.57 (2×*C*H$_3$) ppm;
HR-MS (ESI+): *m/z* calc. ($C_{13}H_{15}FNO$, $[M+H]^+$): 220.1059, found: 220.1061.

(*E*)-2-(5-Methoxy-1,3,3-trimethylindolin-2-ylidene)acetaldehyde (19)

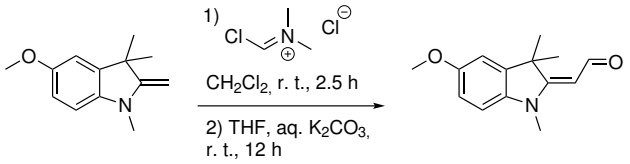

$C_{13}H_{17}NO$
203.29 g mol^{-1}
16

$C_{14}H_{17}NO_2$
231.30 g mol^{-1}
19

Compound **19** was synthesized on a 2.16 mmol scale according to general procedure IV by stirring for 2.5 h in the first reaction step and obtained as a red oil (471 mg, 2.04 mmol, 95%).

^{1}H NMR (400 MHz, $CDCl_3$): $\delta = 9.96$ (d, $J = 9.0$ Hz, 1 H, C*H*O), 6.92 - 6.72 (m, 3 H, *H*-4, *H*-6, *H*-7), 5.33 (d, $J = 9.0$ Hz, 1 H, NCC*H*), 3.81 (s, 3 H, OCH_3), 3.21 (s, 3 H, NCH_3), 1.65 (s, 6 H, 2×CH_3) ppm;
HR-MS (ESI+): *m/z* calc. ($C_{14}H_{17}NaNO_2$, $[M+Na]^+$): 254.11515, found: 254.11533.

(*E*)-2-(1-Ethyl-3,3-dimethylindolin-2-ylidene)acetaldehyde (33)

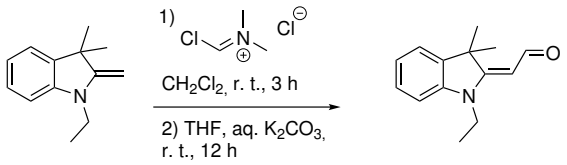

$C_{13}H_{17}N$
187.29 g mol^{-1}
31

$C_{14}H_{17}NO$
215.30 g mol^{-1}
33

Compound **33** was synthesized on a 2.81 mmol scale according to general procedure IV by stirring for 3 h in the first reaction step and was obtained as a red oil (330 mg, 1.53 mmol, 54%).

^{1}H NMR (400 MHz, $CDCl_3$): δ = 10.02 (d, J = 9.0 Hz, 1 H, C*H*O), 7.31 - 7.17 (m, 2 H, *H*-4, *H*-6), 7.09 - 7.02 (m, 1 H, *H*-5), 6.88 - 6.82 (m, 1 H, *H*-7), 5.42 (d, J = 9.0 Hz, 1 H, NCC*H*), 3.81 - 3.68 (m, 2 H, NCH_2), 1.66 (s, 6 H, 2×CH_3), 1.30 - 1.23 (m, 3 H, NCH_2CH_3) ppm;
HR-MS (ESI+): *m/z* calc. ($C_{14}H_{18}NO$, $[M+H]^+$): 216.1310, found: 216.1312.

(*E*)-2-(5-Nitro-1,3,3-trimethylindolin-2 ylidene)acetaldehyde (34)

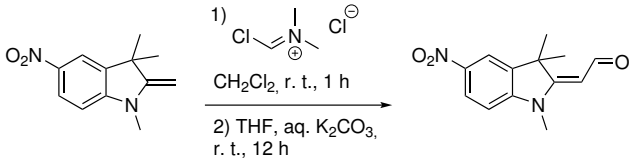

$C_{12}H_{14}N_2O_2$
218.26 g mol^{-1}
32

$C_{13}H_{14}N_2O_3$
246.27 g mol^{-1}
34

Compound **34** was synthesized on a 2.69 mmol scale according to general procedure IV by stirring for 1 h in the first reaction step and obtained as a brown solid (748 mg, 2.56 mmol, 97%).

^{1}H NMR (400 MHz, $CDCl_3$): δ = 10.07 (d, J = 8.5 Hz, 1 H, C*H*O), 8.25 (dd, J = 8.8, 2.2 Hz, 1 H, *H*-4), 8.09 (d, J = 2.2 Hz, 1 H, *H*-6), 6.87 (d, J = 8.8 Hz, 1 H, *H*-7), 5.49 (d, J = 8.5 Hz, 1 H, NCC*H*), 3.29 (s, 3 H, NCH_3), 1.72 (s, 6 H, 2×CH_3) ppm;
HR-MS (ESI+): *m/z* calc. ($C_{13}H_{15}N_2O_3$, $[M+H]^+$): 247.1077, found: 247.1068.

(*E*)-4-((*E*)-1,3,3-Trimethylindolin-2-ylidene)but-2-enal (35)

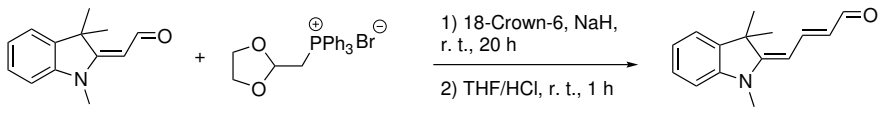

$C_{13}H_{15}NO$
201.27 g mol^{-1}
17

$C_{22}H_{22}BrO_2P$
429.29 g mol^{-1}

$C_{15}H_{17}NO$
227.31 g mol^{-1}
35

Aldehyde **17** (1.20 g, 6.00 mmol, 1.00 eq.) and triphenyl-(1,3-dioxolan-2-ylmethyl)phosphonium bromide (5.67 g, 13.2 mmol, 2.20 eq.) were dissolved under nitrogen atmosphere in anhydrous THF (15 mL). 18-Crown-6 (320 mg, 1.20 mmol, 0.20 eq.) and NaH (60% oil dispersion, 2.40 g, 60.0 mmol, 10.0 eq.) were added slowly. The reaction mixture was stirred for 20 h at r. t. Afterwards, the reaction was stopped by addition of THF/HCl 1:1 (5 mL) and stirred for one additional hour at ambient temperature. It was extracted with EtOAc (3×50 mL), the combined organic phases were dried over $MgSO_4$ and the solvent was removed in vacuum. The target compound **35** was obtained after column chromatography on silica gel (CH_2Cl_2/MeOH 99:1 to 9:1) as a dark violet solid (201 mg, 0.89 mmol, 15%).

^{1}H NMR (400 MHz, $CDCl_3$): δ = 9.45 (d, J = 8.2 Hz, 1 H, C*H*O), 7.72 (dd, J = 14.2, 12.6 Hz, 1 H, CHOC*H*), 7.26 - 7.18 (m, 2 H, *H*-4, *H*-6), 6.98 (td, J = 7.5, 0.9 Hz, 1 H, *H*-5), 6.76 (dt, J = 7.8, 0.7 Hz, 1 H, CHOCHC*H*), 6.01 - 5.92 (m, 1 H, *H*-7), 5.55 (d, J = 12.6 Hz, 1 H, CHOCHCHC*H*), 3.23 (s, 3 H, NCH_3), 1.63 (s, 6 H, 2×CH_3) ppm;
^{13}C{^{1}H} NMR (100 MHz, $CDCl_3$): δ = 192.45 (*C*HO), 165.62 (*C*-2), 150.29 (CHOCH*C*H), 144.05 (*C*-7a), 139.07 (*C*-3a), 128.04 (*C*-6), 127.65 (CHO*C*H), 123.19 (*C*-4), 121.73 (*C*-5), 107.29 (*C*-7), 94.99 (CHOCHCH*C*H), 46.77 (*C*-3), 29.46 (N*C*H_3), 28.47 (2×*C*H_3) ppm;
HR-MS (ESI+): *m/z* calc. ($C_{15}H_{17}NNaO$, $[M+Na]^+$): 250.1202, found: 250.1197.

N,N-Diphenylformamidine (20)

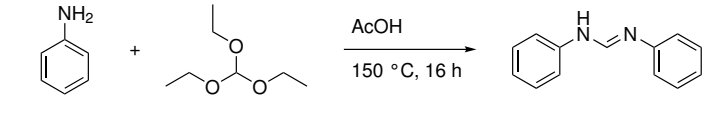

C_6H_7N 93.13 g mol^{-1} | $C_7H_{16}O_3$ 148.20 g mol^{-1} | $C_{13}H_{12}N_2$ 196.25 g mol^{-1} **20**

Aniline (5.50 mL, 60.2 mmol, 1.82 eq.), triethyl orthoformate (5.00 mL, 33.1 mmol, 1.00 eq.) and acetic acid (0.10 mL, 1.80 mmol, 0.05 eq.) were mixed and stirred for 16 h at 150 °C. The reaction mixture was cooled to r. t., the precipitate was filtered off and washed with *n*-hexane (2×10 mL). The product **20** was obtained as yellowish crystals (4.82 g, 24.6 mmol, 74%). Spectral data matched those reported previously.[484]

^{1}H NMR (400 MHz, $CDCl_3$): δ = 8.23 (s, 1 H, C*H*), 7.36 - 7.01 (m, 10 H, Ph-*H*) ppm;
^{13}C{^{1}H} NMR (100 MHz, $CDCl_3$): δ = 149.45 (*C*H), 145.22 (Ph-1-*C*), 129.52 (Ph-3,5-*C*), 123.51 (Ph-2,4,6-*C*), 119.17 (Ph-2,4,6-*C*) ppm;
HR-MS (ESI+): *m/z* calc. ($C_{13}H_{13}N_2$, $[M+H]^+$): 197.1073, found: 197.1078.

3-Methyl-2-(2-*N*-phenylacetamidovinyl)benzothiazolium iodide (22)

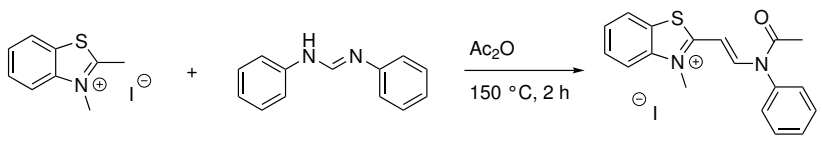

$C_9H_{10}INS$
291.15 g mol^{-1}
21

$C_{13}H_{12}N_2$
196.25 g mol^{-1}
20

$C_{18}H_{17}IN_2OS$
336.31 g mol^{-1}
22

Compound **21** (3.16 g, 11.4 mmol, 1.00 eq.) and *N,N*-diphenylformamidine (**20**, 2.72 g, 13.8 mmol, 1.21 eq.) were dissolved in acetic anhydride (20 mL) and stirred for 2 h at 150 °C. The reaction mixture was cooled to r. t. and Et_2O (60 mL) was added within 30 min. The precipitate was filtered off and washed with Et_2O (3×20 mL) and H_2O (2×10 mL). The target compound **22** was obtained as deep purple crystals (3.96 g, 9.08 mmol, 80%). Spectral data matched those reported previously.[296]

^{1}H NMR (400 MHz, DMSO-d_6): δ = 8.80 (d, J = 13.9 Hz, 1 H, NC*H*), 8.31 (dd, J = 8.1, 1.3 Hz, 1 H, *H*-7), 8.10 (d, J = 8. Hz, 1 H, *H*-4), 7.83 - 7.49 (m, 7 H, *H*-5, *H*-6, Ph-*H*), 5.69 (d, J = 13.9 Hz, 1 H, NCC*H*), 3.88 (s, 3 H, NCH_3), 2.06 (s, 3 H, acetyl-CH_3) ppm;
^{13}C{^{1}H} NMR (100 MHz, DMSO-d_6): δ = 171.93 (*C*-2), 170.08 (carbonyl-*C*), 144.98 (*C*-3a), 141.73 (Ph-1-*C*), 136.94 (N*C*H), 130.66 (*C*-5), 130.14 (*C*-4), 129.06 (*C*-6), 128.66 (Ph-4-*C*), 128.30 (Ph-2,6-*C*), 127.89 (Ph-3,5-*C*), 126.56 (*C*-7a), 124.03 (*C*-7), 96.42 (*C*HCHN), 35.62 (N*C*H$_3$), 23.19 (acetyl-*C*H$_3$) ppm;
HR-MS (ESI+): *m/z* calc. ($C_{18}H_{17}N_2OS$, $[M]^+$): 309.1056, found: 309.1052.

General procedure V: synthesis of *N*-substituted barbituric acid derivatives

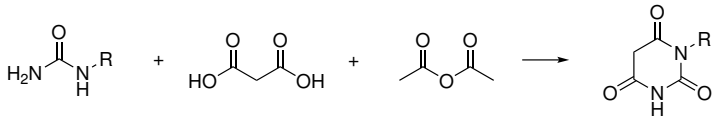

The required urea derivative (1.00 eq.), acetic anhydride (2.05 eq.) and malonic acid (1.00 eq.) were mixed and heated for 3 to 18 h to 70 to 90 °C. After cooling to r. t., the reaction volume was reduced to approximately 3 mL and a small amount abs. EtOH was added for complete precipitation. The formed solid was filtered off, washed with cold abs. EtOH and dried in vacuum to afford the desired target compound.

N-Methylbarbituric acid (23)

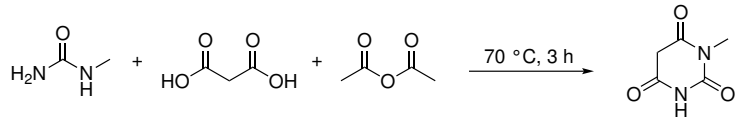

$C_2H_6N_2O$ 74.08 g mol^{-1} | $C_3H_4O_4$ 104.06 g mol^{-1} | $C_4H_6O_3$ 102.09 g mol^{-1} | $C_5H_6N_2O_3$ 142.11 g mol^{-1} **23**

N-Methylbarbituric acid (**23**) was synthesized on a 3.85 mmol scale according to general procedure V by heating the reaction mixture for 3 h to 70 °C. The target compound **23** was obtained as a pale yellow solid (3.45 g, 2.43 mmol, 63%).

^{1}H NMR (400 MHz, DMSO-d_6): δ = 11.33 (s, 1 H, N*H*), 3.59 (s, 2 H, CH_2), 3.06 (s, 3 H, CH_3) ppm;
^{13}C{^{1}H} NMR (100 MHz, DMSO-d_6): δ = 167.47 (carbonyl-*C*), 167.00 (carbonyl-*C*), 152.39 (NR-carbonyl-*C*-NR), 27.28 (*C*H$_3$) ppm;
HR-MS (ESI+): *m/z* calc. ($C_5H_6N_2NaO_3$, [M+Na]$^+$): 165.0271, found: 165.0269.

N-Benzylbarbituric acid (118)

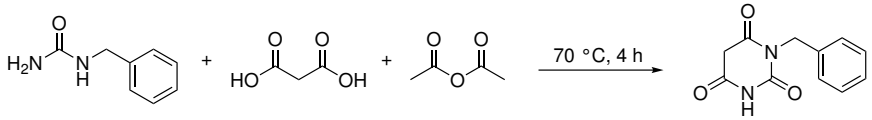

$C_8H_{10}N_2O$ 150.18 g mol^{-1} | $C_3H_4O_4$ 104.06 g mol^{-1} | $C_4H_6O_3$ 102.09 g mol^{-1} | $C_{11}H_{10}N_2O_3$ 218.21 g mol^{-1} **118**

N-Benzylbarbituric acid (**118**) was synthesized on a 13.2 mmol scale according to general procedure V by heating the reaction mixture for 3 h to 70 °C. The target compound **118** was obtained as a colorless solid (1.22 g, 5.57 mmol, 43%).

^{1}H NMR (400 MHz, DMSO-d_6): δ = 11.41 (s, 1 H, N*H*), 7.34–7.11 (m, 5 H, Bn-*H*), 4.87 (s, 2 H, Bn-CH_2), 3.69 (s, 2 H, BA-CH_2) ppm;
^{13}C{^{1}H} NMR (100 MHz, DMSO-d_6): δ = 167.45 (carbonyl-*C*), 166.98 (carbonyl-*C*), 152.21 (NR-carbonyl-*C*-NR), 137.40 (Bn-*C*1), 128.85 (Bn-*C*), 128.69 (Bn-*C*), 127.79 (Bn-*C*), 127.67 (Bn-*C*), 127.52 (Bn-*C*), 127.41 (Bn-*C*), 43.49 (Bn-*C*H$_2$) ppm.

N-Allylbarbituric acid (24)

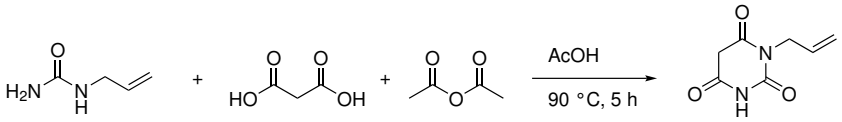

$C_4H_8N_2O$ 100.12 g mol^{-1} + $C_3H_4O_4$ 104.06 g mol^{-1} + $C_4H_6O_3$ 102.09 g mol^{-1} → $C_7H_8N_2O_3$ 168.15 g mol^{-1}

24

N-Allylurea (2.00 g, 20.0 mmol, 1.00 eq.) was dissolved under nitrogen atmosphere in acetic acid (60 mL). Malonic acid (2.10 g, 20.0 mmol, 1.00 eq.) was added and the reaction mixture was heated to 60 °C. After addition of acetic anhydride (40 mL) the reaction was stirred for 5 h at 90 °C. The reaction volume was reduced to approximately 3 mL by evaporation of the solvent and abs. EtOH (5 mL) was added. The hereby resulting precipitate was filtered off, washed with abs. EtOH (3×5 mL) and dried in vacuum to afford the target compound **24** as a brownish powder (1.09 g, 6.48 mmol, 32%). Spectroscopic data matched those reported.[298]

^{1}H NMR (400 MHz, DMSO-d_6): δ = 11.36 (s, 1 H, N*H*), 5.82-5.72 (m, 1 H, allyl-C*H*), 5.17 (dq, J = 17.2, 1.6 Hz, 1 H, allyl-CH_2), 5.08 (dq, J = 10.3, 1.5 Hz, 1 H, allyl-CH_2), 4.27 (d, J = 5.1 Hz, 2 H, CH_2-allyl), 3.64 (s, 2 H, terminal-allyl-CH_2) ppm;
^{13}C{^{1}H} NMR (100 MHz, DMSO-d_6): δ = 166.98 (carbonyl-*C*), 151.84 (NR-carbonyl-*C*-NR), 132.98 (allyl-*C*H), 116.67 (terminal-allyl-*C*H$_2$), 42.38 (allyl-*C*H$_2$) ppm.

General procedure VI: aldol condensation with barbituric acid derivatives

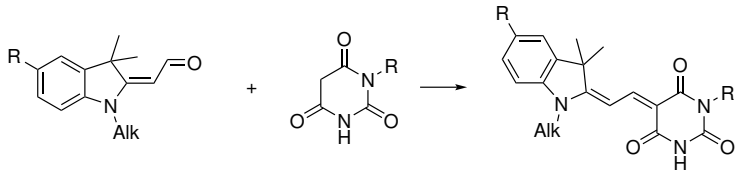

The aldehyde chromophore precursor (1.00 eq.) and the required barbituric acid derivative (1.00 to 2.00 eq.) were dissolved in abs. EtOH (1 mL per mmol) and heated to 70 °C for up to 22 h. Filtration of the precipitate and washing with cold abs. EtOH afforded the target compound which was either pure enough for further reactions or again purified by column chromatography on silica gel.

(*E*)-5-(2-(1,3,3-Trimethylindolin-2-ylidene)ethylidene)pyrimidine-2,4,6-(1*H*,3*H*,5*H*)-trione (BAM, 1)

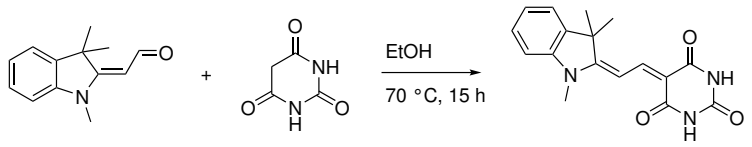

$C_{13}H_{15}NO$ 201.27 g mol^{-1} **17** + $C_4H_4N_2O_3$ 128.09 g mol^{-1} → $C_{17}H_{17}N_3O_3$ 311.34 g mol^{-1} **1**

Compound **1** (BAM) was synthesized according to general procedure VI on a 0.71 mmol scale with 1.22 eq. of barbituric acid and was obtained as an orange solid (135 mg, 430 µmol, 61%). Analytical data were consistent with those reported previously.[290]

^{1}H NMR (400 MHz, DMSO-d_6): $\delta = 10.64$ (d, $J = 1.9$ Hz, 1 H, N*H*), 10.53 (d, $J = 2.0$ Hz, 1 H, N*H*), 8.43 (d, $J = 14.5$ Hz, 1 H, COCC*H*), 7.60 - 7.54 (m, 1 H, *H*-4), 7.46 - 7.34 (m, 3 H, *H*-6, *H*-7, NCC*H*), 7.25 - 7.18 (m, 1 H, *H*-5), 3.51 (s, 3 H, NCH_3), 1.62 (s, 6 H, 2×CH_3) ppm;
^{13}C{^{1}H} NMR (100 MHz, DMSO-d_6): $\delta = 176.56$ (carbonyl-*C*), 165.00 (carbonyl-*C*), 164.56 (carbonyl-*C*), 151.26 (carbonyl-*C*), 149.72 (COC*C*H), 143.21 (*C*-7a), 141.00 (*C*-3a), 128.78 (CO*C*), 124.80 (*C*-6), 122.66 (*C*-4), 111.18 (*C*-5), 100.96 (*C*-7), 97.76 (NC*C*H), 48.88 (N*C*H_3), 46.12 (*C*-3), 28.64 (2×*C*H_3) ppm;
HR-MS (ESI+): *m/z* calc. ($C_{17}H_{17}N_3NaO_3$, $[M+Na]^+$): 334.1162, found: 334.1159.

(*E*)-5-(2-(5-Fluoro-1,3,3-trimethylindolin-2-ylidene)ethylidene)pyrimidine-2,4,6-(1*H*,3*H*,5*H*)-trione (BAM^F, 2)

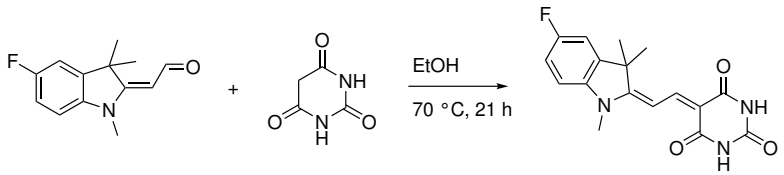

$C_{13}H_{14}FNO$ 219.26 g mol^{-1} **18** + $C_4H_4N_2O_3$ 128.09 g mol^{-1} → $C_{17}H_{16}FN_3O_3$ 329.33 g mol^{-1} **2**

Compound **2** (BAM^F) was synthesized according to general procedure VI on a 1.74 mmol scale with 1.20 eq. of aldehyde precursor and was obtained as an orange solid (436 mg, 1.33 mmol, 92%).

^{1}H NMR (400 MHz, DMSO-d_6): δ =10.59 (2 s, 2 H, N*H*), 8.40 (d, $J = 14.5$ Hz, 1 H, COCC*H*), 7.57 (dd, $J = 8.4$, 2.6 Hz, 1 H, *H*-7), 7.42 - 7.35 (m, 2 H, *H*-6, *H*-4), 7.20 - 7.28 (m, 1 H, NCC*H*), 3.40 - 3.52 (m, 3 H, NCH_3), 1.63 (s, 6 H, 2×CH_3) ppm;
^{13}C{^{1}H} NMR (100 MHz, DMSO-d_6): $\delta = 176.12$ (*C*-2), 167.81 (carbonyl-*C*), 164.53 (carbonyl-*C*), 158.63 (*C*-5), 151.70 (*C*-7a), 150.80 (*C*-3a), 149.10 (COC*C*H), 139.07 (CO*C*),

111.82 (*C*-7), 110.27 (*C*-6), 100.55 (*C*-4), 97.38 (NC*C*H), 56.04 (*C*-3), 48.69 (O*C*H$_3$), 27.98 (N*C*H$_3$), 18.59 (2×*C*H$_3$) ppm;
^{19}F NMR (376 MHz, DMSO-d_6): δ = -128.53 ppm;
HR-MS (ESI+): *m/z* calc. ($C_{17}H_{16}FN_3NaO_3$, $[M+Na]^+$): 352.1068, found: 352.1063.

(*E*)-5-(2-(5-Methoxy-1,3,3-trimethylindolin-2-ylidene)ethylidene)pyrimidine-2,4,6-(1*H*,3*H*,5*H*)-trione (BAM^{OMe}, 3)

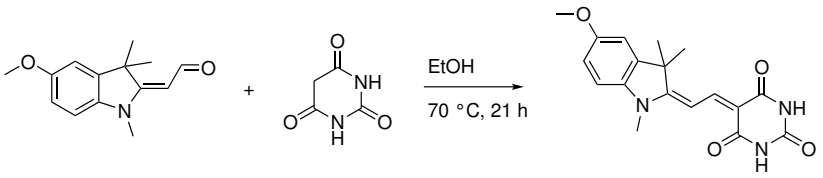

$C_{14}H_{17}NO_2$
231.30 g mol^{-1}
19

$C_4H_4N_2O_3$
128.09 g mol^{-1}

$C_{18}H_{19}N_3O_4$
341.37 g mol^{-1}
3

Compound **3** (BAM^{OMe}) was synthesized according to general procedure VI on a 6.55 mmol scale with 1.30 eq. of barbituric acid and was obtained as an orange solid (2.00 g, 5.68 mmol, 89%).

^{1}H NMR (400 MHz, DMSO-d_6): δ = 10.51 (2 s, 2 H, N*H*), 8.38 (d, *J* = 14.7 Hz, 1 H, COCC*H*), 7.39 (d, *J* = 14.8 Hz, 1 H, *H*-4), 7.32 (d, *J* = 8.7 Hz, 1 H, *H*-4), 7.27 (d, *J* = 2.5 Hz, 1 H, *H*-6), 6.96 (dd, *J* = 8.7, 2.5 Hz, 1 H, NCC*H*), 3.80 (s, 3 H, OC*H*$_3$), 3.51 (s, 3 H, NC*H*$_3$), 1.63 (s, 6 H, 2×C*H*$_3$) ppm;
^{13}C{^{1}H} NMR (100 MHz, DMSO-d_6): δ = 176.12 (*C*-2), 168.02 (carbonyl-*C*), 164.83 (carbonyl-*C*), 164.34 (COC*C*H), 157.63 (*C*-5), 151.91 (*C*-3a), 151.06 (*C*-7a), 148.75 (CO*C*), 113.50 (*C*-7), 111.78 (*C*-6), 109.13 (*C*-4), 99.50 (NC*C*H), 55.99 (O*C*H$_3$, 49.04 (N*C*H$_3$), 28.31 (2×*C*H$_3$) ppm;
HR-MS (ESI+): *m/z* calc. ($C_{18}H_{19}N_3NaO_4$, $[M+Na]^+$): 364.1268, found: 364.1283.

(*E*)-5-(2-(1,3,3-Trimethylindolin-2-ylidene)ethylidene)-3-methylpyrimidine-2,4,6-(1*H*,3*H*,5*H*)-trione (mBAM, 4)

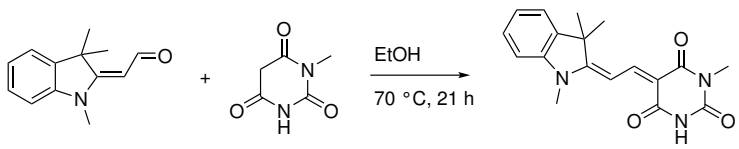

$C_{13}H_{15}NO$
201.27 g mol^{-1}
17

$C_5H_6N_2O_3$
142.11 g mol^{-1}
23

$C_{18}H_{19}N_3O_3$
325.37 g mol^{-1}
4

Compound **4** (mBAM) was synthesized according to general procedure VI on a 5.06 mmol scale with 1.00 eq. of *N*-methyl barbituric acid (**23**) and was obtained as an orange solid (859 mg, 2.63 mmol, 52%). Spectral data matched those reported previously.[282]

^{1}H NMR (400 MHz, DMSO-d_6): δ = 8.68 (2 d, J = 14.5 Hz, 1 H, COCC*H*), 8.13 - 7.90 (m, 1 H, N*H*), 7.60 (dd, J = 14.5 Hz, 1 H, NCC*H*), 7.31 - 7.45 (m, 2 H, *H*-7, *H*-5), 7.20 - 7.26 (m, 1 H, *H*-6), 7.06 (dd, J = 7.8, 1.1 Hz, 1 H, *H*-4), 3.57 (2 s, 3 H, BA-NCH_3), 3.34 (2 s, 3 H, NCH_3), 1.73 (s, 6 H, 2×CH_3) ppm;
^{13}C{^{1}H} NMR (100 MHz, DMSO-d_6): δ = 163.29 (COC*C*H), 152.40 (carbonyl-*C*), 151.51 (carbonyl-*C*), 151.21 (carbonyl-*C*), 142.74 (*C*-7a), 141.09 (*C*-3a), 128.59 (CO*C*), 125.04 (*C*-6), 122.30 (*C*-5), 110.06 (NC*C*H), 101.08 (*C*-4), 98.95 (*C*-7), 49.24 (*C*-3), 31.16 (N*C*H$_3$), 28.95 (2×*C*H$_3$), 27.61 (BAM-*C*H$_3$) ppm;
HR-MS (ESI+): *m/z* calc. ($C_{18}H_{20}N_3O_3$, $[M+H]^+$): 326.1499, found: 326.1506.

(*E*)-5-(2-(1,3,3-trimethylindolin-2-ylidene)ethylidene)-3-allylpyrimidine-2,4,6-(1*H*,3*H*,5*H*)-trione (allylBAM, 5)

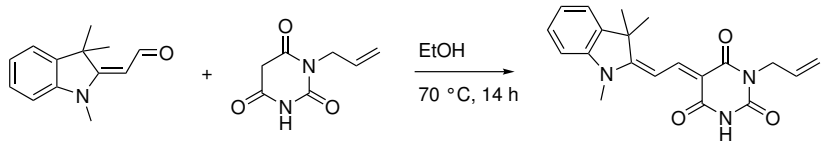

$C_{13}H_{15}NO$ 201.27 g mol^{-1} **17**
$C_7H_8N_2O_3$ 168.15 g mol^{-1} **24**
$C_{20}H_{21}N_3O_3$ 351.41 g mol^{-1} **5**

Compound **5** (allyl-BAM) was synthesized according to general procedure VI on a 0.59 mmol scale with 1.20 eq. of allyl barbituric acid **24** and was obtained as an orange solid (364 mg, 0.36 mmol, 62%).

^{1}H NMR (400 MHz, DMSO-d_6): δ = 10.84 (2 s, 1 H, N*H*), 8.45 (d, JJ = 14.6 Hz, 1 H, COCC*H*), 7.58 (ddd, J = 8.3, 2.6, 0.7 Hz, 1 H, *H*-4), 7.46 - 7.38 (m, 2 H, *H*-7, NCC*H*), 7.27 - 7.21 (m, 1 H, *H*-6), 5.88 - 5.75 (m, 1 H, allyl-C*H*), 5.10 - 5.02 (m, 2 H, terminal-allyl-CH_2), 4.36 (dq, J = 3.1, 1.5 Hz, 2 H, allyl-CH_2), 3.53 (2 s, 3 H, NCH_3), 1.64 (s, 6 H, 2×CH_3) ppm;
^{13}C{^{1}H} NMR (100 MHz, DMSO-d_6): δ = 176.93 (*C*-2), 163.90 (carbonyl-*C*), 163.60 (carbonyl-*C*), 163.23 (carbonyl-*C*), 151.11 (carbonyl-*C*), 150.43 (*C*-5), 149.81 (CO*C*), 143.23 (*C*-3a), 139.42 (*C*-7a), 133.97 (allyl-*C*H), 133.91 (allyl-*C*H), 116.32 (terminal-allyl-*C*), 115.11 (terminal-allyl-*C*), 112.38 (*C*-6), 110.96 (*C*-4), 100.45 (NC*C*H), 98.08 (CO*C*), 49.23 (*C*-3), 42.32 (allyl-*C*H$_2$, 31.58 (N*C*H$_3$), 28.35 ppm (2×*C*H$_3$) ppm;
HR-MS (ESI+): *m/z* calc. ($C_{20}H_{21}N_3NaO_3$, $[M+Na]^+$): 374.1475, found: 374.1478.

(*E*)-2-Thioxo-5-(2-(1,3,3-trimethylindolin-2-ylidene)ethylidene)dihydropyrimidine-4,6-(1*H*,5*H*)-dione (thioBAM, 6)

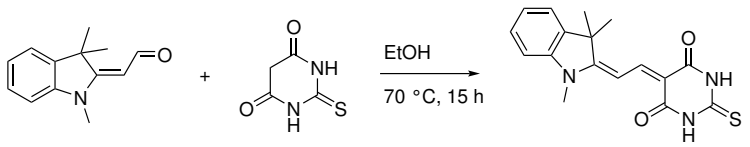

$C_{13}H_{15}NO$
201.27 g mol^{-1}
17

$C_4H_4N_2O_2S$
144.15 g mol^{-1}

$C_{17}H_{17}N_3O_2S$
327.40 g mol^{-1}
6

Compound **6** (thio-BAM) was synthesized according to general procedure VI on a 3.98 mmol scale with 1.00 eq. of thiobarbituric acid and was obtained as an orange solid (902 mg, 2.74 mmol, 69%).

^{1}H NMR (400 MHz, DMSO-d_6): δ = 11.75 (2 s, 2 H, N*H*), 8.40 (d, J = 14.8 Hz, 1 H, COCC*H*), 7.60 (dd, J = 7.4, 1.1 Hz, 1 H, *H*-7), 7.54 (d, J = 14.8 Hz, 1 H, NCC*H*), 7.48 - 7.35 (m, 2 H, *H*-4, *H*-6), 7.34 - 7.23 (m, 1 H, *H*-5), 3.58 (s, 3 H, NCH_3), 1.63 (s, 6 H, 2×CH_3) ppm;
^{13}C{^{1}H} NMR (100 MHz, DMSO-d_6): δ = 177.37 (*C*S), 176.86 (*C*-2), 162.70 (carbonyl-*C*), 161.90 (carbonyl-*C*), 149.29 (COC*C*H), 142.56 (*C*-7a), 140.95 (*C*-3a), 128.43 (CO*C*), 125.09 (*C*-6), 122.30 (*C*-4), 111.42 (*C*-5), 100.91 (*C*-7), 99.08 (NC*C*H), 48.94 (*C*-3), 31.24 (N*C*H$_3$), 27.96 (2×*C*H$_3$) ppm;
HR-MS (ESI+): *m/z* calc. ($C_{17}H_{18}N_3O_2S$, $[M+H]^+$): 328.1120, found: 328.1118.

(*Z*)-5-(2-(3-Methylbenzo[*d*]thiazol-2(3*H*)-ylidene)ethylidene)pyrimidine-2,4,6-(1*H*,3*H*,5*H*)-trione (BAM^b, 7)

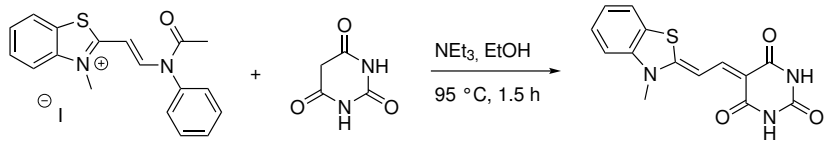

$C_{18}H_{17}IN_2OS$
336.31 g mol^{-1}
22

$C_4H_4N_2O_3$
128.09 g mol^{-1}

$C_{14}H_{11}N_3O_3S$
301.32 g mol^{-1}
7

Compound **22** (1.75 g, 4.01 mmol, 1.00 eq.) and barbituric acid (0.51 g, 4.01 mmol, 1.00 eq.) were dissolved in abs. EtOH (100 mL) and triethylamine (1.80 mL, 13.0 mmol, 3.20 eq.) was added slowly. The solution was stirred for 90 min at 95 °C. Afterwards, the reaction mixture was cooled to r. t. and Et_2O (180 mL) was added over 30 min. The precipitate was filtered off and washed with Et_2O (3×20 mL) and H_2O (2×10 mL) which yielded the product **7** (BAM^b) as a red solid (1.19 g, 3.96 mmol, 99%).

^{1}H NMR (400 MHz, DMSO-d_6): δ = 10.45 (2 s, 2 H, N*H*), 8.05 (d, J = 14.0 Hz, 1 H, COCC*H*), 7.97 (dd, J = 8.0, 1.2 Hz, 1 H, *H*-7), 7.78 - 7.71 (m, 1 H, *H*-4), 7.60 - 7.48 (m,

2 H, *H*-5, NCC*H*), 7.40 (ddd, J = 8.2, 7.4, 1.0 Hz, 1 H, *H*-6), 3.79 (s, 3 H, NCH_3) ppm;
^{13}C{^{1}H} NMR (100 MHz, DMSO-d_6): δ = 169.57 (*C*-2), 164.37 (carbonyl-*C*), 164.30 (carbonyl-*C*), 150.88 (carbonyl-*C*), 146.86 (COC*C*H), 141.94 (*C*-3a), 127.87 (CO*C*), 125.15 (*C*-5), 124.74 (*C*-7), 122.99 (*C*-7a), 113.68 (*C*-4, *C*-6), 96.54 (NC*C*H), 33.56 (N*C*H$_3$) ppm;
HR-MS (ESI-): *m/z* calc. ($C_{14}H_{10}N_3O_3S$, [M-H]$^-$): 300.0448, found: 300.0458.

(*E*)-1-Methyl-5-(2-(3-methylbenzo[*d*]thiazol-2(3*H*)-ylidene)ethylidene)pyrimidine-2,4,6-(1*H*,3*H*,5*H*)-trione (mBAM^b, 8)

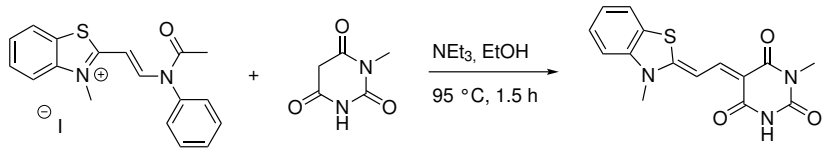

$C_{18}H_{17}IN_2OS$
336.31 g mol^{-1}
22

$C_5H_6N_2O_3$
142.11 g mol^{-1}
23

$C_{15}H_{13}N_3O_3S$
315.35 g mol^{-1}
8

Compound **22** (1.75 g, 4.01 mmol, 1.00 eq.) and barbituric acid **23** (0.57 g, 4.01 mmol, 1.00 eq.) were dissolved in abs. EtOH (100 mL) and triethylamine (1.80 mL, 13.0 mmol, 3.20 eq.) was added slowly. The solution was stirred for 90 min at 95 °C. Afterwards, the reaction mixture was cooled to r. t. and Et_2O (180 mL) was added over 30 min. The precipitate was filtered off and washed with Et_2O (3×20 mL) and H_2O (2×10 mL) which yielded the product **8** (mBAM^b) as a brown solid (1.26 g, 4.01 mmol, quant.). Due to its poor solubility, no ^{13}C spectrum of compound **8** was recorded.

^{1}H NMR (400 MHz, DMSO-d_6): δ = 10.69 (2 s, 1 H, N*H*), 8.11 (dd, J = 13.9, 8.7 Hz, 1 H, COCC*H*), 8.00 (d, J = 7.7 Hz, 1 H, *H*-7), 7.77 (t, J = 6.9 Hz, 1 H, *H*-4), 7.64 - 7.52 (m, 2 H, *H*-5, NCC*H*), 7.42 (t, J = 7.5 Hz, 1 H, *H*-6), 3.81 (d, J = 6.6 Hz, 3 H, BA-NCH_3), 3.11 (s, 3 H, NCH_3) ppm;
HR-MS (ESI-): *m/z* calc. ($C_{15}H_{12}N_3O_3S$, [M-H]$^-$): 314.0605, found: 314.0605.

5.1.2.2 Preparation of rBAM phosphoramidites

NMR signals for protected ribonucleosides were assigned as far as possible; especially the assignment of ^{13}C signals was in most cases hampered by the presence of double bond isomers.

((Ethylthio)methoxy)tri-*iso*-propylsilane (45)

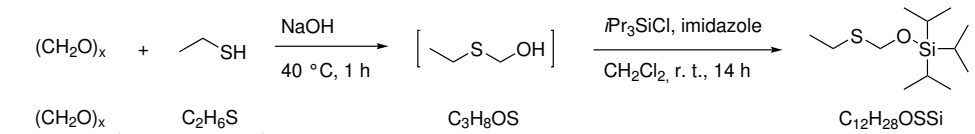

$(CH_2O)_x$
(30.01 g mol^{-1})$_x$

C_2H_6S
62.13 g mol^{-1}

C_3H_8OS
92.16 g mol^{-1}

$C_{12}H_{28}OSSi$
248.50 g mol^{-1}
45

A suspension of paraformaldehyde (3.00 g, 99.9 mmol, 1.00 eq.) in ethylsulfide (6.95 mL, 99.9 mmol, 1.00 eq.) was cooled to 0 °C under nitrogen atmosphere. Two drops of NaOH (2 M) were added and the mixture was allowed to slowly warm up to r. t. Afterwards, the reaction mixture was stirred for 1 h at 40 °C. After cooling to r. t., anhydrous CH_2Cl_2 (98 mL), imidazole (13.6 g, 200 mmol, 2.00 eq.) and *i*Pr_3SiCl (21.4 mL, 99.9 mmol, 1.00 eq.) were added. The solution was stirred for 14 h at r. t. After dilution with *n*-hexane (200 mL) the mixture was washed with 10% aq. NaH_2PO_4 (200 mL). The organic phase was dried over $MgSO_4$ and the solvent was removed in vacuum. Vacuum distillation yielded the product **45** (13.3 g, 53.7 mmol, 57%) as a colorless liquid. Spectroscopic data matched those reported previously.[344]

^{1}H NMR (400 MHz, $CDCl_3$): δ = 4.87 (s, 2 H, SCH_2O), 2.70 (q, J = 7.61 Hz, 2 H, SCH_2CH$_3$), 1.30 (t, J = 7.33 Hz, 3 H, CH$_2$CH_3), 1.16 - 1.04 (m, 21 H, *i*Pr-*H*) ppm;
^{13}C{^{1}H} NMR (100 MHz, $CDCl_3$): δ = 66.06 (S*C*H$_2$O), 24.66 (CH$_2$*C*H$_3$), 17.91 (*i*Pr-*C*H$_3$), 14.94 (*i*Pr-*C*H), 11.96 (CH$_2$*C*H$_3$) ppm;
HR-MS (ESI+): *m/z* calc. ($C_{12}H_{28}NaOSSi$, $[M+Na]^+$): 271.1522, found: 271.1514.

(Tri-*iso*-propylsiloxy)methyl chloride (TOM-Cl, 46)

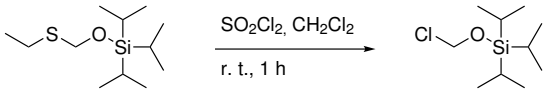

$C_{12}H_{28}OSSi$
248.50 g mol^{-1}
45

$C_{10}H_{23}ClOSi$
222.83 g mol^{-1}
46

Compound **45** (13.3 g, 53.7 mmol, 1.00 eq.) was dissolved under nitrogen atmosphere in anhydrous CH_2Cl_2 (38 mL) and cooled to 0 °C. SO_2Cl_2 (4.33 mL, 53.7 mmol, 1.00 eq.) was added and the solution was allowed to warm up to r. t. After stirring for 1 h and vacuum distillation, the target product **46** (8.73 g, 39.2 mmol, 73%) was obtained as a colorless liquid. Spectroscopic data matched those reported previously.[344]

^{1}H NMR (400 MHz, $CDCl_3$): δ = 5.66 (s, 2 H, CH_2), 1.23 - 1.07 (m, 21 H, *i*Pr-*H*) ppm;
^{13}C{^{1}H} NMR (100 MHz, $CDCl_3$): δ = 76.39 (*C*H$_2$), 17.66 (*i*Pr-*C*H$_3$), 11.82 (*i*Pr-*C*H) ppm.

Tris(trimethylsilyl) barbituric acid (25)

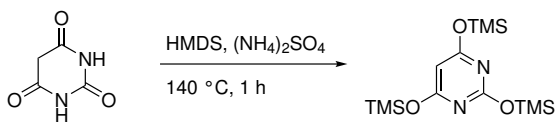

$C_4H_4N_2O_3$
128.09 g mol^{-1}

$C_{13}H_{28}N_2O_3Si_3$
344.63 g mol^{-1}
25

Barbituric acid (2.00 g, 15.6 mmol, 1.00 eq.) was mixed with hexamethyldisilazane (12.0 mL, 55.4 mmol, 3.55 eq.) and $(NH_4)_2SO_4$ (40.0 mg, 0.31 mmol, 0.02 eq.) under nitrogen atmosphere. This mixture was heated to 140 °C until the barbituric acid was completely dissolved (approximately 1 h). After cooling to r. t., the solvent was removed in vacuum and the target compound **25** was obtained as a colorless solid which was used for the next reaction step without further purification.

2',3',5'-Tri-*O*-benzoyl barbituric acid ribonucleoside (26)

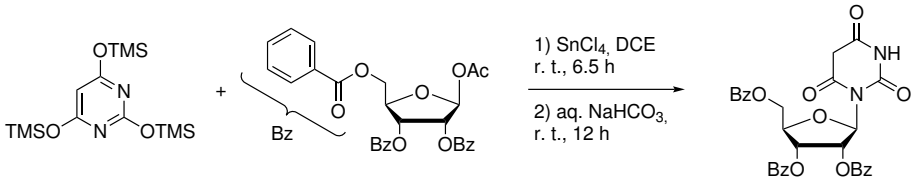

$C_{13}H_{28}N_2O_3Si_3$
344.63 g mol^{-1}
25

$C_{28}H_{24}O_9$
504.49 g mol^{-1}

$C_{30}H_{24}N_2O_{10}$
572.53 g mol^{-1}
26

Tris(trimethylsilyl) barbituric acid (**25**, 4.62 g, 13.4 mmol, 1.15 eq.) was dissolved under nitrogen atmosphere in anhydrous DCE (60 mL) and carefully treated with $SnCl_4$ (2.50 mL, 5.58 g, 22.2 mmol, 1.90 eq.). Afterwards, a solution of 1-acetyl-2,3,5-tri-*O*-benzoyl-β-D-ribofuranose (5.89 g, 11.7 mmol, 1.00 eq.) in DCE (60 mL) was added to the resulting suspension. The reaction mixture was stirred at r. t. for 6.5 h, then poured into sat. aq. $NaHCO_3$ (50 mL) and left to stand overnight. The layers were separated and the aqueous phase was extracted with CH_2Cl_2 (5×30 mL). The combined organic phases were dried over Na_2SO_4, filtered and concentrated under reduced pressure. The crude product was purified by column chromatography on silica gel (CH_2Cl_2/MeOH 98:2) to afford the target compound **26** as a slightly yellow foam (4.38 g, 7.66 mmol, 63%).

^{1}H NMR (400 MHz, $CDCl_3$): δ = 9.34 (s, 1 H, N*H*), 8.09 - 8.00 (m, 2 H, Bz-*H*), 7.96 (dq, J = 8.2, 1.4 Hz, 2 H, Bz-*H*), 7.88 - 7.81 (m, 2 H, Bz-*H*), 7.56 - 7.40 (m, 3 H, Bz-*H*), 7.39 - 7.29 (m, 4 H, Bz-*H*), 7.31 - 7.22 (m, 2 H, Bz-*H*), 6.43 (d, J = 2.0 Hz, 1 H, *H*-1'), 6.10 - 6.01 (m, 2 H, *H*-2', *H*-3'), 4.79 (dd, J = 11.9, 3.6 Hz, 1 H, *H*-5'), 4.68 (ddd, J = 7.2, 5.7, 3.6 Hz, 1 H, *H*-4'), 4.58 (dd, J = 11.9, 5.7 Hz, 1 H, *H*-5'), 3.67 (s, 2 H, BA-CH_2) ppm;
^{13}C{^{1}H} NMR (100 MHz, $CDCl_3$): δ = 166.35 (Bz-carbonyl-*C*), 165.65 (Bz-carbonyl-*C*), 165.35 (Bz-carbonyl-*C*), 165.27 (BA-carbonyl-*C*), 164.63 (BA-carbonyl-*C*), 149.81 (BA-carbonyl-*C*), 133.58 (Bz-*C*), 133.49 (Bz-*C*), 133.14 (Bz-*C*), 129.85 (Bz-*C*), 129.81 (Bz-*C*), 129.79 (Bz-*C*), 129.56 (Bz-*C*), 128.80 (Bz-*C*), 128.71 (Bz-*C*), 128.41 (Bz-*C*), 128.33 (Bz-*C*), 86.78 (*C*-1'), 79.10 (*C*-4'), 73.94 (*C*-2'), 70.99 (*C*-3'), 63.70 (*C*-5'), 39.67 (BA-*C*H_2) ppm;
HR-MS (ESI+): *m/z* calc. ($C_{30}H_{24}N_2NaO_{10}$, $[M+Na]^+$): 595.1323, found: 595.1342.

Barbituric acid ribonucleoside (27)

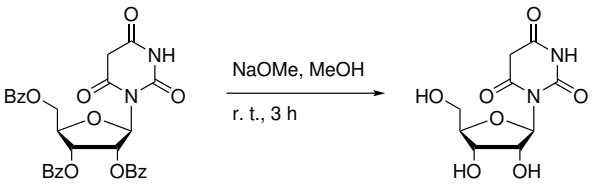

$C_{30}H_{24}N_2O_{10}$
572.53 g mol^{-1}
26

$C_9H_{12}N_2O_7$
260.20 g mol^{-1}
27

To a solution of benzoyl-protected barbituric acid ribonucleoside **26** (4.07 g, 7.11 mmol, 1.00 eq.) in anhydrous MeOH (25 mL), 0.5 M NaOMe in MeOH (45.0 mL, 22.5 mmol, 3.16 eq.) was added under nitrogen atmosphere and the mixture was stirred at r. t. for 3 h. After removal of the solvent, the residue was redissolved in H_2O (150 mL) and cleared from benzoic acid methyl ester formed in the deprotection reaction by repeated extraction with Et_2O (3×150 mL). The pH of the aqueous layer was adjusted to 4 by addition of Dowex 50WX8 (hydrogen form). The ion exchange resin was filtered off and the solvent was removed under reduced pressure yielding the free barbituric acid nucleoside **27** as a colorless powder (1.66 g, 6.38 mmol, 89%).

^{1}H NMR (400 MHz, DMSO-d_6): δ = 11.39 (s, 1 H, N*H*), 5.90 (s, 1 H, *H*-1'), 5.01 (s_{br}, 1 H, O*H*), 4.92 (s_{br}, 1 H, O*H*), 4.56 (s_{br}, 1 H, O*H*), 4.35 (s, 1 H, *H*-2'), 4.05 (t, J = 6.5 Hz, 1 H, *H*-3'), 3.66 (td, J = 6.7, 3.5 Hz, 1 H, *H*-4'), 3.59 (dd, J = 11.6, 3.5 Hz, 1 H, *H*-5'), 3.39 (dd, J = 11.6, 6.6 Hz, 1 H, *H*-5') ppm;
^{13}C{^{1}H} NMR (100 MHz, DMSO-d_6): δ = 166.70 (BA-carbonyl-*C*), 150.83 (N*C*ON), 87.64 (*C*-1'), 83.97 (*C*-4'), 71.21 (*C*-2'), 69.76 (*C*-3'), 62.10 (*C*-5') ppm;
HR-MS (ESI+): *m/z* calc. ($C_9H_{12}N_2NaO_7$, [M+Na]$^+$): 283.0537, found: 283.0539.

Barbituric acid merocyanine ribonucleoside (rBAM, 36)

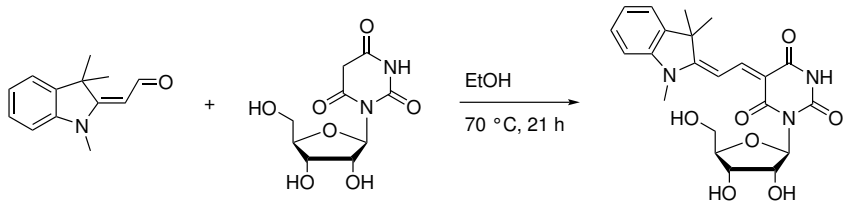

$C_{13}H_{15}NO$
201.27 g mol^{-1}
17

$C_9H_{12}N_2O_7$
260.20 g mol^{-1}
27

$C_{22}H_{25}N_3O_7$
443.46 g mol^{-1}
36

Aldehyde **17** (600 mg, 2.31 mmol, 1.00 eq.) and the free barbituric acid ribonucleoside **27** (603 mg, 3.00 mmol, 1.30 eq.) were suspended in abs. EtOH (11 mL). The reaction mixture was stirred for 21 h at 70 °C. After removal of the solvent under reduced pressure, the resulting residue was purified by column chromatography on silica gel (CH_2Cl_2/MeOH 95:5) to afford a 1:1 mixture of (*E*),(*Z*)- and (*E*),(*E*)-double bond isomers of the pure nucleoside **36** (rBAM)

as a dark red solid (625 mg, 1.41 mmol, 61%).

^{1}H NMR (400 MHz, DMSO-d_6): δ = 10.92 and 10.82 (2 s, 1 H, N*H*), 8.48 (2 d, J = 14.8 Hz, 1 H, COCC*H*), 7.59 (d, J = 7.4 Hz, 1 H, Ind-*H*-7), 7.54 - 7.38 (m, 3 H, NCC*H*, Ind-*H*-4, Ind-*H*-5), 7.29 - 7.21 (m, 1 H, Ind-*H*-6), 6.08 (s, 1 H, *H*-1'), 5.02 (2 d, J = 5.1 Hz, 1 H, 2'-O*H*), 4.82 (2 d, J = 6.6 Hz, 1 H, 3'-O*H*), 4.60 (t, J = 6.4 Hz, 1 H, 5'-O*H*), 4.47 (q, J = 5.0 Hz, 1 H, *H*-2'), 4.15 - 4.07 (m, 1 H, *H*-3'), 3.70 - 3.65 (m, 1 H, *H*-4'), 3.64 - 3.57 (m, 1 H, *H*-5'), 3.56 (2 s, 3 H, NCH_3), 3.48 - 3.39 (m, 1 H, *H*-5'), 1.67 - 1.59 (m, 6 H, 2×CH_3). ppm;
^{13}C{^{1}H} NMR (100 MHz, DMSO-d_6): δ = 177.20 (Ind-*C*-2), 176.97 (Ind-*C*-2), 163.74 (BA-carbonyl-*C*), 163.03 (BA-carbonyl-*C*), 162.85 (BA-carbonyl-*C*), 162.59 (BA-carbonyl-*C*), 150.52 (COC*C*H), 149.84 (COC*C*H), 142.64 (Ind-*C*-7a), 140.76 (Ind-*C*-3a), 128.39 (Ind-*C*-5), 124.77 (Ind-*C*-6), 122.27 (Ind-*C*-7), 111.13 (Ind-*C*-4), 98.32 (NC*C*H), 97.93 (NC*C*), 87.83 (*C*-1'), 84.09 (*C*-4'), 71.31 (*C*-2'), 70.15 (*C*-3'), 62.46 (*C*-5'), 48.75 (Ind-*C*-3), 48.72 (Ind-*C*-3), 31.05 (N*C*H$_3$), 28.14 (*C*H$_3$), 28.02 (*C*H$_3$) ppm;
HR-MS (ESI+): *m/z* calc. ($C_{22}H_{25}N_3NaO_7$, $[M+Na]^+$): 466.1585, found: 466.1578.

5-Fluoro-barbituric acid merocyanine ribonucleoside (rBAM^F, 37)

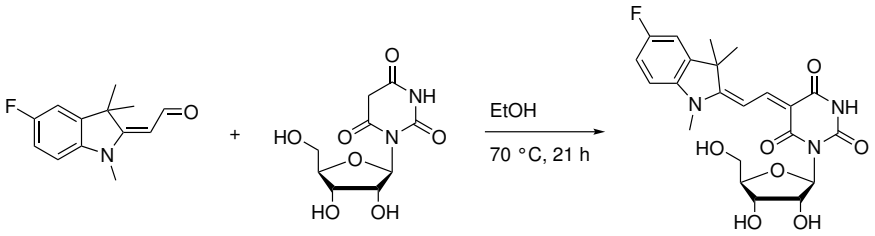

$C_{13}H_{14}FNO$
219.26 g mol^{-1}
18

$C_9H_{12}N_2O_7$
260.06 g mol^{-1}
27

$C_{22}H_{24}FN_3O_7$
461.45 g mol^{-1}
37

Aldehyde **18** (338 mg, 1.53 mmol, 2.00 eq.) and the free barbituric acid ribonucleoside **27** (200 mg, 765 µmol, 1.00 eq.) were suspended in abs. EtOH (8 mL). The reaction mixture was stirred for 21 h at 70 °C. After removal of the solvent under reduced pressure, the resulting residue was purified by column chromatography on silica gel (CH_2Cl_2/MeOH 95:5 to 9:1) to afford a 1:1 mixture of (*E*),(*Z*)- and (*E*),(*E*)-double bond isomers of the pure nucleoside **37** (rBAM^F) as a red solid (165 mg, 339 µmol, 44%).

^{1}H NMR (400 MHz, DMSO-d_6): δ = 10.87 (2 s, N*H*), 8.45 (2 d, J = 14.7 Hz, 1 H, COCC*H*), 7.59 (dd, J = 8.3, 2.6 Hz, 1 H, Ind-*H*-6), 7.53 - 7.36 (m, 2 H, Ind-*H*-4, NCC*H*), 7.32 - 7.20 (m, 1 H, Ind-*H*-7), 6.08 (s, 1 H, *H*-1'), 5.02 (dd, J = 5.1, 2.1 Hz, 1 H, 2'-O*H*), 4.82 (dd, J = 6.7, 0.8 Hz, 1 H, 3'-O*H*), 4.60 (dd, J = 6.4, 5.2 Hz, 1 H, 5'-O*H*), 4.45 - 4.41 (m, 1 H, *H*-2'), 4.17 - 4.02 (m, 1 H, *H*-3'), 3.72 - 3.58 (m, 3 H, *H*-4', *H*-5'), 3.55 (2 s, 3 H, NCH_3), 1.64 (s, 6 H, 2×CH_3) ppm;
^{13}C{^{1}H} NMR (100 MHz, DMSO-d_6): δ = 177.67 (Ind-*C*-2), 177.44 (Ind-*C*-2), 164.18

(BA-carbonyl-*C*), 163.47 (BA-carbonyl-*C*), 163.29 (BA-carbonyl-*C*), 163.03 (BA-carbonyl-*C*), 159.32 (BA-carbonyl-*C*), 150.85 (COC*C*H), 150.13 (COC*C*H), 139.39, 118.58 (Ind-*C*-6), 115.45 (Ind-*C*-7), 115.22 (Ind-*C*-7), 112.64 (Ind-*C*-4), 111.00 (Ind-*C*-4), 98.84 (NC*C*H), 98.45 (NC*C*H), 87.77 (*C*-1'), 84.54 (*C*-4'), 71.75 (*C*-2'), 70.59 (*C*-3'), 63.25 (*C*-5'), 62.89 (*C*-5'), 49.43 (Ind-*C*-3), 31.73 (N*C*H_3), 28.38 (*C*H_3), 28.26 (*C*H_3) ppm;
^{19}F NMR (376 MHz, DMSO-d_6): δ = -117.80 ppm;
HR-MS (ESI+): *m/z* calc. ($C_{22}H_{24}FN_3NaO_7$, $[M+Na]^+$): 484.1491, found: 484.1488.

5-Methoxy-barbituric acid merocyanine ribonucleoside (rBAM^{OMe}, 38)

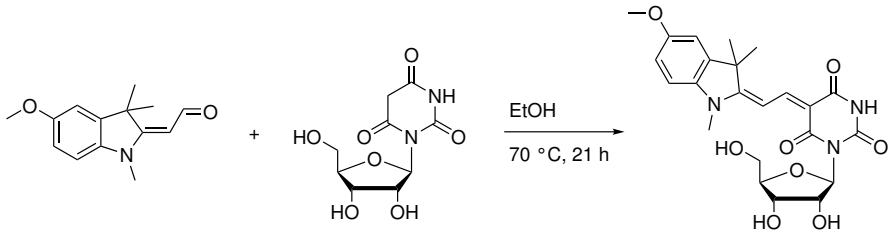

$C_{14}H_{17}NO_2$ 231.30 g mol^{-1} **19**
$C_9H_{12}N_2O_7$ 260.06 g mol^{-1} **27**
$C_{23}H_{27}N_3O_8$ 473.48 g mol^{-1} **38**

Aldehyde **19** (93.2 mg, 383 µmol, 2.00 eq.) and the free barbituric acid ribonucleoside **27** (100 mg, 383 µmol, 1.00 eq.) were suspended in abs. EtOH (3 mL). The reaction mixture was stirred for 21 h at 70 °C. After removal of the solvent under reduced pressure, the resulting residue was purified by column chromatography on silica gel (CH_2Cl_2/MeOH 95:5 to 8:2) to afford a 1:1 mixture of (*E*),(*Z*)- and (*E*),(*E*)-double bond isomers of the pure nucleoside **38** (rBAM^{OMe}) as a bright orange solid (85.9 mg, 176 µmol, 46%).

^{1}H NMR (400 MHz, $CDCl_3$): δ = 8.55 (d, *J* = 14.8 Hz, 1 H, COCC*H*), 7.62 - 7.46 (m, 1 H, Ind-*H*-4), 7.04 - 6.98 (m, 1 H, *H*-6), 6.93 - 6.84 (m, 2 H, *H*-7, NCC*H*), 6.50 - 6.33 (m, 1 H, *H*-1'), 5.01 - 4.82 (m, 1 H, *H*-2'), 4.71 - 4.52 (m, 1 H, *H*-3'), 4.09 (s, 1 H, *H*-5'), 4.06 - 3.88 (m, 2 H, *H*-4', *H*-5'), 3.86 - 3.81 (m, 3 H, NCH_3), 3.75 (s, 3 H, OCH_3), 1.75 - 1.55 (m, 6 H, 2×CH_3) ppm.
Due to its poor solubility, no ^{13}C spectrum of compound **38** was recorded.
HR-MS (ESI+): *m/z* calc. ($C_{23}H_{27}N_3NaO_8$, $[M+Na]^+$): 496.1690, found: 496.1693.

5-Nitro-barbituric acid merocyanine ribonucleoside (rBAM^{NO2}, 39)

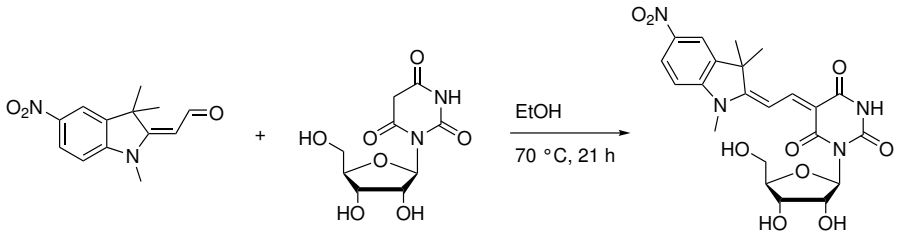

$C_{13}H_{14}N_2O_3$
246.27 g mol^{-1}
34

$C_9H_{12}N_2O_7$
260.20 g mol^{-1}
27

$C_{22}H_{24}N_4O_9$
488.45 g mol^{-1}
39

Aldehyde **34** (169 mg, 383 µmol, 2.00 eq.) and the free barbituric acid ribonucleoside **27** (100 mg, 383 µmol, 1.00 eq.) were suspended in abs. EtOH (5 mL). The reaction mixture was stirred for 21 h at 70 °C. After removal of the solvent under reduced pressure, the resulting residue was purified by column chromatography on silica gel (CH_2Cl_2/MeOH 95:5 to 7:3) to afford a 1:1 mixture of (*E*),(*Z*)- and (*E*),(*E*)-double bond isomers of the pure nucleoside **39** (rBAM^{NO2}) as a bright orange solid (103 mg, 211 µmol, 55%).

^{1}H NMR (400 MHz, DMSO-d_6): δ = 11.09 (2 s, N*H*), 8.59 - 8.45 (m, 2 H, COCC*H*, Ind-*H*-4), 8.32 (ddd, J = 8.8, 2.3, 0.9 Hz, 1 H, Ind-*H*-6), 7.61 - 7.48 (m, 2 H, Ind-*H*-7, NCC*H*), 6.07 (s, 1 H, *H*-1'), 5.04 (dd, J = 5.1, 0.9 Hz, 1 H, 2'-O*H*), 4.85 (d, J = 6.6 Hz, 1 H, 3'-O*H*), 4.60 (t, J = 5.8 Hz, 1 H, 5'-O*H*), 4.45 - 4.42 (m, 1 H, *H*-2'), 4.17 - 4.02 (m, 1 H, *H*-3'), 3.71 - 3.58 (m, 3 H, *H*-4', *H*-5'), 3.55 (2 s, 3 H, NCH_3), 1.70 (s, 6 H, 2×CH_3) ppm;
^{13}C{^{1}H} NMR (100 MHz, DMSO-d_6): δ = 171.95 (Ind-*C*-2), 163.22 (BA-carbonyl-*C*), 144.12, 141.90, 118.63 (Ind-*C*-6), 112.53 (Ind-*C*-4), 111.18 (Ind-*C*-4), 99.35 (NC*C*H), 88.44 (*C*-1'), 84.56 (*C*-4'), 71.73 (*C*-2'), 70.55 (*C*-3'), 63.25 (*C*-5'), 62.85 (*C*-5'), 49.07 (Ind-*C*-3), 31.60 (N*C*H_3), 28.44 (2×*C*H_3) ppm;
HR-MS (ESI+): *m/z* calc. ($C_{22}H_{24}N_4NaO_9$, [M+Na]$^+$): 511.1436, found: 511.1420.

Ethyl barbituric acid merocyanine ribonucleoside (rBAM^{Et}, 40)

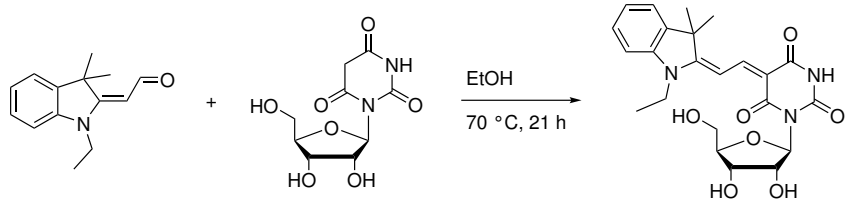

$C_{14}H_{17}NO$
215.30 g mol^{-1}
33

$C_9H_{12}N_2O_7$
260.20 g mol^{-1}
27

$C_{23}H_{27}N_3O_7$
457.48 g mol^{-1}
40

Aldehyde **33** (282 mg, 1.31 mmol, 1.00 eq.) and the free barbituric acid ribonucleoside **27** (682 mg, 2.62 mmol, 2.00 eq.) were suspended in abs. EtOH (3 mL). The reaction mixture was stirred for 21 h at 70 °C. After removal of the solvent under reduced pressure, the resulting residue was purified by column chromatography on silica gel (CH_2Cl_2/MeOH 95:5 to 9:1) to

afford a 1:1 mixture of (*E*),(*Z*)- and (*E*),(*E*)-double bond isomers of the pure nucleoside **40** (rBAM^{Et}) as an orange solid (311 mg, 682 µmol, 52%).

^{1}H NMR (400 MHz, $CDCl_3$): δ = 8.60 (2 d, J = 14.7 Hz, 1 H, COCC*H*), 7.63 (d, *J* = 14.7 Hz, 1 H, Ind-*H*-4), 7.44 - 7.32 (m, 2 H, Ind-*H*-6, Ind-*H*-5), 7.30 - 7.19 (m, 1 H, Ind-*H*-7), 7.10 - 6.98 (m, 1 H, NCC*H*), 6.45 (s, 1 H, *H*-1'), 4.70 - 4.56 (m, 1 H, *H*-2'), 4.15 - 3.99 (m, 2 H, NC*H*, *H*-3'), 3.91 - 3.85 (m, 1 H, *H*-5'), 3.82 - 3.76 (m, 2 H, *H*-4', *H*-5'), 3.49 (s, 3 H, NCH_3), 1.76 - 1.61 (m, 6 H, 2×CH_3), 1.48 - 1.32 (m, 3 H, NCH_2CH_3) ppm.
Due to its poor solubility, no ^{13}C spectrum of compound **40** was recorded.
HR-MS (ESI+): *m/z* calc. ($C_{23}H_{27}N_3NaO_7$, $[M+Na]^+$): 480.1741, found: 480.1745.

Elongated barbituric acid merocyanine ribonucleoside (rBAM^2, 41)

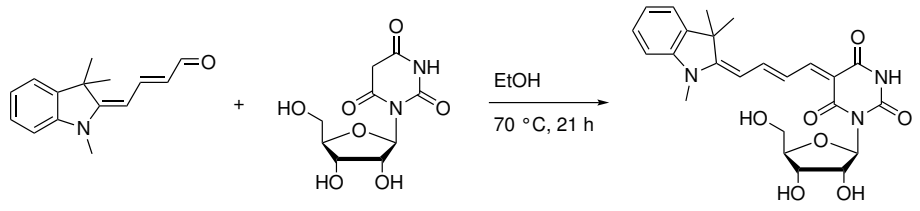

$C_{15}H_{17}NO_2$
227.31 g mol^{-1}
35

$C_9H_{12}N_2O_7$
260.20 g mol^{-1}
27

$C_{24}H_{27}N_3O_7$
469.49 g mol^{-1}
41

Aldehyde **35** (38 mg, 167 µmol, 1.00 eq.) and the free barbituric acid ribonucleoside **27** (87 mg, 334 µmol, 2.00 eq.) were suspended in abs. EtOH (1 mL). The reaction mixture was stirred for 21 h at 70 °C. After removal of the solvent under reduced pressure, the resulting residue was purified by column chromatography on silica gel (CH_2Cl_2/MeOH 95:5 to 8:2) to afford the nucleoside **41** (rBAM^2) as a violet solid (63 mg, 134 µmol, 68%).

Since compound **41** led to very complex NMR spectra in several solvents presumably due to decomposition, assignment of the signals was not possible.
HR-MS (ESI+): *m/z* calc. ($C_{24}H_{27}N_3NaO_7$, $[M+Na]^+$): 492.1741, found: 492.1729.

Benzothiazole barbituric acid merocyanine ribonucleoside (rBAM^b, 42)

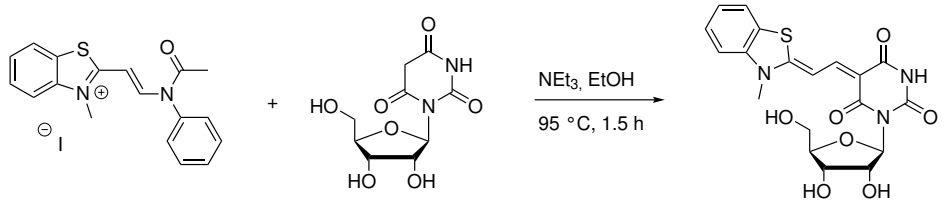

$C_{18}H_{17}IN_2OS$
336.31 g mol^{-1}
22

$C_9H_{12}N_2O_7$
260.20 g mol^{-1}
27

$C_{19}H_{19}N_3O_7S$
433.44 g mol^{-1}
42

Compound **22** (904 mg, 2.07 mmol, 1.20 eq.) and barbituric acid nucleoside **27** (450 g, 1.73 mmol, 1.00 eq.) were dissolved in abs. EtOH (60 mL) and triethylamine (770 µL,

559 mg, 5.53 mmol, 3.20 eq.) was added slowly. The solution was stirred for 90 min at 95 °C. Afterwards, the reaction mixture was cooled to r. t. and Et_2O (180 mL) was added over 30 min. The precipitate was filtered off and washed with Et_2O (3×20 mL) and H_2O (2×10 mL). Column chromatography on silica gel (CH_2Cl_2/MeOH 95:5 to 8:2) afforded a 1:1 mixture of (*E*),(*Z*)- and (*E*),(*E*)-double bond isomers of the pure nucleoside **42** (rBAM^b) as a red solid (340 mg, 784 µmol, 45%).

^{1}H NMR (400 MHz, DMSO-d_6): δ = 10.70 (2 s, 1 H, N*H*), 8.09 (2 d, *J* = 14.1 Hz, 1 H, CONC*H*), 8.00 (d, *J* = 7.9 Hz, 1 H, arom-*H*-7), 7.79 (d, *J* = 8.3 Hz, 1 H, arom-*H*-4), 7.65 - 7.50 (m, 2 H, NCC*H*, arom-*H*-5), 7.47 - 7.41 (m, 1 H, arom-*H*-6), 6.16 - 5.99 (m, 1 H, *H*-1'), 5.02 (dd, *J* = 5.2, 3.5 Hz, 1 H, 2'-O*H*), 4.82 (d, *J* = 6.6 Hz, 1 H, 3'-O*H*), 4.61 (dt, *J* = 9.3, 4.5 Hz, 1 H, 5'-O*H*), 4.52 - 4.43 (m, 1 H, *H*-2'), 4.14 - 4.08 (m, 1 H, *H*-3'), 3.83 (2 s, 3 H, NCH_3), 3.72 - 3.56 (m, 2 H, *H*-4', *H*-5'), 3.49 - 3.37 (m, 1 H, *H*-5') ppm;
^{13}C{^{1}H} NMR (100 MHz, DMSO-d_6): δ = 170.40 (arom-*C*-2), 163.39 (BA-carbonyl-*C*), 162.84 (BA-carbonyl-*C*), 162.68 (BA-carbonyl-*C*), 162.62 (BA-carbonyl-*C*), 146.82 (COC*C*H), 141.79 (arom-*C*-3a), 127.88 (arom-*C*-5), 125.38 (arom-*C*-6), 124.85 (arom-*C*-7a), 122.98 (arom-*C*-7), 113.89 (arom-*C*-4), 97.71 (NC*C*H), 97.30 (NC*C*H), 96.81 (NC*C*H), 87.63 (*C*-1'), 84.02 (*C*-4'), 83.89 (*C*-4'), 71.20 (*C*-3'), 70.09 (*C*-2'), 62.40 (*C*-5'), 33.68 (N*C*H$_3$) ppm;
HR-MS (ESI+): *m/z* calc. ($C_{19}H_{19}N_3NaO_7S$, $[M+Na]^+$): 456.0843, found: 456.0839.

5'-*O*-(4,4'-Dimethoxytrityl) barbituric acid merocyanine ribonucleoside (43)

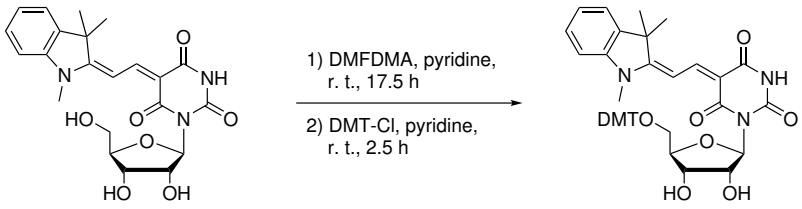

$C_{22}H_{25}N_3O_7$
443.46 g mol^{-1}
36

$C_{43}H_{43}N_3O_9$
745.83 g mol^{-1}
43

Barbituric acid merocyanine ribonucleoside **36** (331 mg, 746 µmol, 1.00 eq.) was dissolved in anhydrous pyridine (10 mL) under nitrogen atmosphere and DMFDMA (222 mg, 1.87 mmol, 2.51 eq.) was added. The mixture was stirred at r. t. for 17.5 h. Afterwards, the solvent was removed in vacuum and the residue re-dissolved in dry pyridine (10 mL) under nitrogen atmosphere. DMT-Cl (278 mg, 821 µmol, 1.10 eq.) was added and the mixture was stirred at r. t. for 2.5 h. After addition of MeOH (5 mL) the reaction mixture was stirred for additional 20 min. The solvent was removed under reduced pressure and the crude product was purified via column chromatography on silica gel (CH_2Cl_2/MeOH 95:5 + 4% NEt_3) to obtain the target compound **43** as a red foam (401 mg, 538 µmol, 72%).

^{1}H NMR (400 MHz, $CDCl_3$): δ = 8.71 (s, 1 H, N*H*), 8.64 - 8.55 (m, 1 H, COCC*H*), 7.55

(2 d, J = 14.6 Hz, 1 H, NCC*H*), 7.40 - 7.08 (m, 16 H, DMT-*H*, *H*-4, *H*-5, *H*-6), 7.06 - 6.97 (m, 1 H, *H*-7), 6.80 - 6.74 (m, 4 H, DMT-*H*), 6.39 (2 d, J = 2.4 Hz, 1 H, *H*-1'), 4.79 - 4.66 (m, 1 H, *H*-2'), 4.63 - 4.55 (m, 1 H, *H*-3'), 4.02 - 3.92 (m, 1 H, *H*-4'), 3.79 (s, 3 H, NCH_3), 3.75 - 3.69 (m, 6 H, DMT-OCH_3), 3.50 - 3.34 (m, 2 H, *H*-5'), 1.73 - 1.58 (m, 6 H, 2×CH_3) ppm;

^{13}C{^{1}H} NMR (100 MHz, $CDCl_3$): δ = 178.00 (Ind-*C*-2), 177.79 (Ind-*C*-2), 164.02 (BA-carbonyl-*C*), 163.51 (BA-carbonyl-*C*), 163.27 (BA-carbonyl-*C*), 163.24 (BA-carbonyl-*C*), 158.69 (BA-carbonyl-*C*), 158.39 (BA-carbonyl-*C*), 152.56 (COC*C*H), 151.64 (COC*C*H), 150.34, 149.74 (COC*C*H), 147.46 (DMT-*C*), 145.18 (DMT-*C*), 145.14 (DMT-*C*), 142.65 (Ind-*C*-7a), (Ind-*C*-3a), 136.43 (DMT-*C*), 136.39 (DMT-*C*), 136.34 (DMT-*C*), 136.26 (DMT-*C*), 130.31 (DMT-*C*), 130.26 (DMT-*C*), 129.25 (DMT-*C*), 128.53 (DMT-*C*), 128.44 (DMT-*C*), 127.95 (DMT-*C*), 127.88 (DMT-*C*), 127.82 (DMT-*C*), 127.17 (DMT-*C*), 126.68 (DMT-*C*), 125.10 (DMT-*C*), 123.92 (DMT-*C*), 122.25 (Ind-*C*-4), 122.21 (Ind-*C*-4), 113.25 (DMT-*C*), 113.12 (DMT-*C*), 110.23 (DMT-*C*), 100.59 (DMT-*C*), 100.55 (DMT-*C*), 99.41 (NC*C*H), 99.10 (CNC*C*H), 88.85 (*C*-1'), 88.23 (*C*-1'), 86.24, 86.20, 82.18 (*C*-4'), 82.14 (*C*-4'), 81.52, 72.77 (*C*-2'), 71.38 (*C*-3'), 71.35 (*C*-3'), 64.78 (*C*-5'), 55.36 (DMT-O*C*H_3), 55.27 (DMT-O*C*H_3), 55.25 (N*C*H_3), 49.33 (Ind-*C*-3), 49.26 (Ind-*C*-3), 31.06, 28.85 (*C*H_3), 28.72 (*C*H_3) ppm;

HR-MS (ESI+): *m/z* calc. ($C_{43}H_{43}N_3NaO_9$, $[M+Na]^+$): 768.2892, found: 768.2895.

5'-*O*-(4,4'-Dimethoxytrityl)-2'-*O*-tri-*iso*-propylsilyloxymethyl barbituric acid indolenine merocyanine ribonucleoside (47)

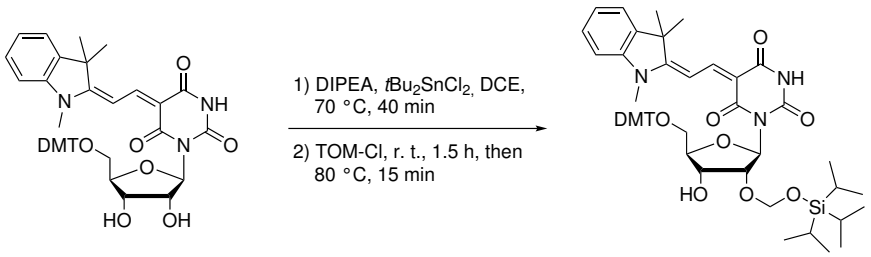

$C_{43}H_{43}N_3O_9$
745.83 g mol^{-1}
43

$C_{53}H_{65}N_3O_{10}Si$
932.20 g mol^{-1}
47

Merocyanine ribonucleoside **43** (602 mg, 807 µmol, 1.00 eq.) and DIPEA (415 mg, 3.21 mmol, 3.98 eq.) were dissolved in anhydrous DCE (15 mL) under nitrogen atmosphere. tBu$_2$SnCl$_2$ (294 mg, 968 µmol, 1.20 eq.) was added and the mixture was heated to 70 °C and stirred for 40 min at this temperature. The reaction mixture was cooled to r. t., TOM-Cl (216 mg, 968 µmol, 1.20 eq.) was added and the reaction mixure was stirred at this temperature for 1.5 h and then for 15 min at 80 °C. The solvent was removed under reduced pressure and the crude product was purified by column chromatography on silica gel (EtOAc/*n*-hexane 3:1 to 2:1 + 4% NEt$_3$). The pure product **47** was obtained as a red foam (200 mg, 215 µmol, 26%), along with an equal amount of the undesired 3'-silylated compound which both were identified by ^{1}H-^{1}H COSY NMR.

^{1}H NMR (400 MHz, $CDCl_3$): δ = 8.65 (2 d, J = 14.6 Hz, 1 H, COCC*H*), 7.57 (2 d, J = 14.6 Hz, 1 H, NCC*H*), 7.52 - 7.45 (m, 2 H, DMT-*H*), 7.41 - 7.32 (m, 7 H, *H*-5, *H*-7, DMT-*H*), 7.28 - 7.18 (m, 3 H , DMT-*H*), 7.18 - 7.10 (m, 1 H, *H*-4), 7.08 - 7.00 (m, 1 H, *H*-6), 6.81 - 6.73 (m, 4 H, DMT-*H*), 6.43 (s, 1 H, *H*-1'), 5.10 (dd, J = 4.8, 1.8 Hz, 1 H, TOM-CH_2), 4.98 (dd, J = 4.8, 2.6 Hz, 1 H, TOM-CH_2), 4.91 - 4.80 (m, 1 H, *H*-2'), 4.57 - 4.46 (m, 1 H, *H*-3'), 4.02 - 3.91 (m, 1 H, *H*-4'), 3.75 (2 s, 6 H, DMT-OCH_3), 3.52 (s, 3 H, NCH_3), 3.45 - 3.28 (m, 2 H, *H*-5'), 3.02 - 2.93 (m, 1 H, 3'-O*H*), 1.77 - 1.59 (m, 6 H, 2×CH_3), 1.15 - 1.00 (m, 21 H, TOM-*i*Pr-*H*) ppm;
^{13}C{^{1}H} NMR (100 MHz, $CDCl_3$): δ = 177.82 (Ind-*C*-2), 177.68 (Ind-*C*-2), 163.04 (CO*C*), 162.79 (BA-carbonyl-*C*), 158.38 (DMT-*C*), 152.76 (COC*C*H), 145.37 (DMT-*C*), 145.31 (DMT-*C*), 142.69 (Ind-*C*-7a), 141.15 (DMT-*C*), 136.62 (DMT-*C*), 136.56 (DMT-*C*), 130.38 (DMT-*C*), 130.32 (DMT-*C*), 128.58 (DMT-*C*), 128.53 (DMT-*C*), 127.78 (Ind-*C*-5), 126.60 (Ind-*C*-4), 125.08 (DMT-*C*), 122.29 (Ind-*C*-7), 113.10 (DMT-*C*), 113.08 (DMT-*C*), 110.13 (Ind-*C*-6), 99.14 (NC*C*H), 98.91 (NC*C*H), 90.56 (TOM-*C*H_2), 90.42 (TOM-*C*H_2), 86.10 (*C*-1'), 86.07 (*C*-1'), 83.14 (*C*-4'), 79.80 (*C*-2'), 79.61 (*C*-2'), 70.55 (*C*-3'), 64.63 (*C*-5'), 64.55 (*C*-5'), 55.30 (DMT-O*C*H_3), 55.28 (DMT-O*C*H_3), 49.28 (Ind-*C*-2), 31.09 (N*C*H_3), 28.95 (2×*C*H_3), 17.94 (TOM-*i*Pr-*C*H_3), 17.92 (TOM-*i*Pr-*C*H_3), 12.02 (TOM-*i*Pr-*C*H) ppm;
HR-MS (ESI+): *m/z* calc. ($C_{53}H_{65}N_3NaO_{10}Si$, $[M+Na]^+$): 954.4331, found: 954.4324.

5'-*O*-(4,4'-Dimethoxytrityl)-2'-*O*-tri-*iso*-propylsilyloxymethyl barbituric acid indolenine merocyanine ribonucleoside-3'-(2-cyanoethyl-*N,N*-di-*iso*-propyl) phosphoramidite (49)

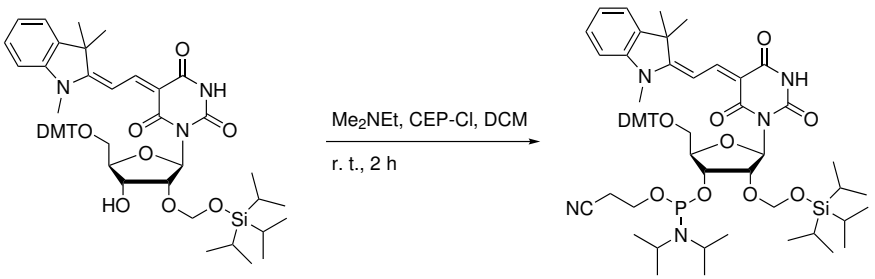

$C_{53}H_{65}N_3O_{10}Si$
932.20 g mol^{-1}
47

$C_{62}H_{82}N_5O_{11}PSi$
1132.42 g mol^{-1}
49

The protected ribonucleoside **47** (150 mg, 161 µmol, 1.00 eq.) was dissolved in dry CH_2Cl_2 (5 mL) under nitrogen atmosphere. Me_2NEt (0.21 mL, 1.61 mmol, 10.0 eq.) and CEP-Cl (57.0 mg, 242 µmol, 1.50 eq.) were added to the mixture which was then stirred at r. t. for 2 h. The solvent was removed in vacuum. Purification of the crude product by column chromatography on silica gel (EtOAc/*n*-hexane 3:1 to 2:1 + 1% NEt_3) yielded the target compound **49** as a red foam (141 mg, 125 µmol, 77%).

^{1}H NMR (400 MHz, $CDCl_3$): δ = 8.72 - 8.60 (m, 1 H, COCC*H*), 7.64 - 7.42 (m, 3 H,

NCC*H*), 7.41 - 7.30 (m, 7 H, DMT-*H*), 7.29 - 7.18 (m, 3 H), 7.19 - 7.11 (m, 1 H), 7.09 - 7.01 (m, 1 H), 6.83 - 6.70 (m, 4 H, DMT-*H*), 6.53 - 6.39 (m, 1 H, *H*-1'), 5.08 - 5.03 (m, 1 H, TOM-CH_2), 5.02 - 4.89 (m, 2 H), 4.78 - 4.46 (m, 1 H), 4.22 - 4.07 (m, 1 H), 4.02 - 3.79 (m, 1 H, POCH_2), 3.80 - 3.70 (m, 8 H, DMT-OCH_3), 3.59 - 3.45 (m, 4 H, NCH_3, POCH_2), 3.45 - 3.34 (m, 1 H), 3.32 - 3.18 (m, 1 H), 2.66 (td, J = 7.0, 6.5, 2.2 Hz, 1 H, $POCH_2CH_2$), 2.34 (td, J = 6.8, 4.6 Hz, 1 H, $POCH_2CH_2$), 1.75 - 1.68 (m, 6 H, 2×C_3), 1.17 - 0.95 (m, 32 H, *i*Pr-CH_3) ppm;

^{13}C{^{1}H} NMR (100 MHz, $CDCl_3$): δ = 158.24, 151.50 (CON*C*H), 145.14, 142.61, 140.99, 136.40, 130.25, 128.41, 127.62, 126.46, 124.83, 122.15, 112.92, 109.87, 98.66 (NC*C*H), 89.40 (TOM-*C*H_2), 85.91, 81.71, 60.40, 55.17 (DMT-O*C*H_3), 55.15 (DMT-O*C*H_3), 49.06, 42.95, 30.95 (N*C*H_3), 28.79 (2×*C*H_3), 24.67 (PN*C*H), 24.59 (PN*C*H), 21.07, 20.23 ($POCH_2CH_2$), 19.99 ($POCH_2CH_2$), 17.86 (TOM-*i*Pr-*C*H_3), 17.82 (TOM-*i*Pr-*C*H_3), 17.78 (TOM-*i*Pr-*C*H_3), 14.20, 12.01 (TOM-*i*Pr-*C*H), 11.99 (TOM-*i*Pr-*C*H), 11.97 (TOM-*i*Pr-*C*H), 11.89 (TOM-*i*Pr-*C*H) ppm;

^{31}P NMR (162 MHz, $CDCl_3$): δ = 149.25, 149.20, 148.99 ppm;

HR-MS (ESI+): *m/z* calc. ($C_{62}H_{82}N_5NaO_{11}PSi$, $[M+Na]^+$): 1154.5419, found: 1154.5419.

5'-*O*-(4,4'-Dimethoxytrityl) barbituric acid benzothiazole merocyanine ribonucleoside (44)

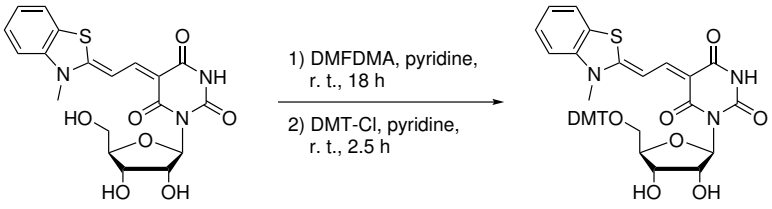

$C_{19}H_{19}N_3O_7S$
433.44 g mol^{-1}
42

$C_{40}H_{37}N_3O_9S$
735.81 g mol^{-1}
44

Barbituric acid merocyanine ribonucleoside **42** (340 mg, 784 µmol, 1.00 eq.) was dissolved in anhydrous pyridine (6 mL) under nitrogen atmosphere and DMFDMA (234 mg, 1.96 mmol, 2.51 eq.) was added. The mixture was stirred at r. t. for 18 h. Afterwards, the solvent was removed in vacuum and the residue re-dissolved in anhydrous pyridine (10 mL) under nitrogen atmosphere. DMT-Cl (319 mg, 0.941 mmol, 1.20 eq.) was added and the mixture was stirred at r. t. for 2.5 h. Since after this reaction time a significant amount of starting material was still present in the reaction mixture, again 0.50 eq. of DMT-Cl were added and it was stirred for 1 h. After addition of MeOH (6 mL) the reaction mixture was stirred for additional 20 min. The solvent was removed under reduced pressure and the crude product was purified by column chromatography on silica gel (CH_2Cl_2/MeOH 95:5 + 4% NEt_3) to obtain the target compound **44** as an orange foam (320 mg, 435 µmol, 55%).

^{1}H NMR (400 MHz, $CDCl_3$): δ = 10.71 (2 s, 1 H, N*H*), 8.19 - 7.96 (d, J = 14.2 Hz, 1 H,

COCC*H*), 8.04 - 7.75 (m, 2 H, arom-*H*), 7.79 (dd, J = 8.3, 2.7 Hz, 1 H, arom-*H*-7), 7.69 - 7.51 (m, 1 H, arom-*H*-6), 7.48 - 7.35 (m, 3 H, arom-*H*, DMT-*H*, NCC*H*), 7.33 - 7.15 (m, 7 H, arom-*H*, DMT-*H*), 6.84 (ddd, J = 11.2, 8.0, 2.4 Hz, 4 H, DMT-*H*), 6.14 (s, 1 H, *H*-1'), 5.08 (s, 1 H, 2'-O*H*), 4.83 (s, 1 H, 3'-O*H*), 4.34 (s, 1 H, *H*-2'), 4.19 (s, 1 H, *H*-3'), 3.89 - 3.62 (m, 9 H, DMT-OCH_3), 3.20 - 3.05 (m, 2 H, *H*-5') ppm;

^{13}C{^{1}H} NMR (100 MHz, $CDCl_3$): δ = 170.30 (BA-carbonyl-*C*O, 162.69 (BA-carbonyl-*C*O), 157.90, 157.85, 146.86 (COC*C*H), 144.99, 141.78, 135.71, 129.72, 129.65, 127.88, 127.65, 126.46, 125.36, 124.85, 122.99, 113.86, 113.01, 112.97, 97.63 (NC*C*H), 89.07 (*C*-1'), 85.16, 81.73 (*C*-4'), 71.94 (*C*-2'), 70.06 (*C*-3'), 64.83 (*C*-5'), 54.87 (DMT-O*C*H$_3$), 48.35, 40.05, 33.66 (CN*C*H$_3$), 16.74 ppm;

HR-MS (ESI+): *m/z* calc. ($C_{40}H_{837}N_3NaO_9S$, $[M+Na]^+$): 758.2144, found: 758.2171.

5'-*O*-(4,4'-Dimethoxytrityl)-2'-*O*-tri-*iso*-propylsilyloxymethyl barbituric acid benzothiazole merocyanine ribonucleoside (48)

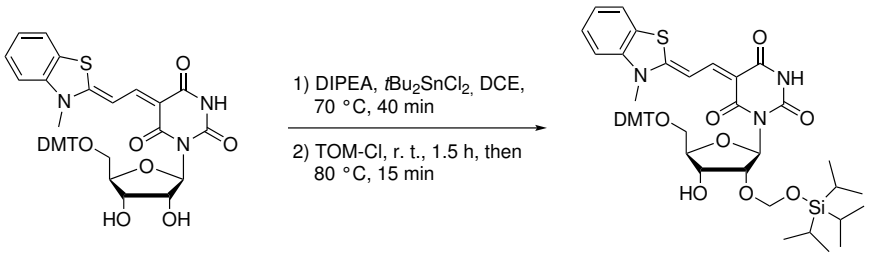

$C_{41}H_{37}N_3O_9$
735.81 g mol^{-1}
44

$C_{50}H_{59}N_3O_{10}SSi$
922.18 g mol^{-1}
48

Merocyanine ribonucleoside **44** (650 mg, 883 µmol, 1.00 eq.) and DIPEA (457 mg, 3.53 mmol, 4.00 eq.) were dissolved in anhydrous DCE (15 mL) under nitrogen atmosphere. tBu$_2$SnCl$_2$ (322 mg, 1.06 mmol, 1.20 eq.) was added and it was heated to 70 °C and stirred for 40 min at this temperature. The reaction mixture was cooled to r. t., TOM-Cl (236 mg, 1.06 mmol, 1.20 eq.) was added and the reaction mixure was stirred at this temperature for 1.5 h and then for 15 min at 80 °C. The solvent was removed under reduced pressure and the crude product was purified by column chromatography on silica gel (CH_2Cl_2/MeOH 98:2 to 9:1 + 4% NEt_3). The pure product **48** was obtained as a red foam (193 mg, 209 µmol, 23%), along with an equal amount of the undesired 3'-silylated compound which both were identified by ^{1}H-^{1}H COSY NMR.

^{1}H NMR (400 MHz, acetone-d_6): δ = 9.35 (d, J = 8.3 Hz, 1 H, N*H*), 8.18 (dd, J = 14.0, 11.7 Hz, 1 H, COCC*H*), 7.87 (dd, J = 7.9, 1.2 Hz, 1 H, arom-*H*), 7.70 - 7.62 (m, 1 H, NCC*H*), 7.57 - 7.12 (m, 11 H, arom-*H*, DMT-*H*), 6.83 (dddd, J = 8.8, 6.7, 3.7, 1.7 Hz, 4 H, DMT-*H*), 6.43 (2 s, 1 H, *H*-1'), 5.06 (dd, J = 4.9, 1.5 Hz, 1 H, OCH_2O), 4.99 (dd, J = 4.9, 2.9 Hz, 1 H, OCH_2O), 4.75 - 4.62 (m, 2 H, *H*-2', *H*-3'), 4.24 - 4.10 (m, 1 H, *H*-4'), 3.87 (s, 3 H, NCH_3), 3.77 - 3.70 (m, 6 H, DMT-OCH_3), 3.49 - 3.31 (m, 2 H, *H*-5'), 1.14 - 1.01 (m,

21 H, TOM-*i*Pr-*H*) ppm;
^{13}C{^{1}H} NMR (100 MHz, acetone-d_6): $\delta =$ 169.28 (BA-carbonyl-*C*O), 162.05 (BA-carbonyl-*C*O), 161.61 (BA-carbonyl-*C*O), 157.60, 157.54, 147.57, 146.70 (COC*C*H), 144.64, 144.60, 141.13, 141.07, 135.29, 135.26, 135.17, 129.21, 129.20, 129.11, 129.09, 127.25, 127.22, 126.92, 126.60, 125.48, 124.35, 124.20, 124.17, 121.68, 112.35, 111.91, 111.88, 96.37, 96.19 (NC*C*H), 89.11 (O*C*H$_2$O), 88.88, 84.79 (*C*-1'), 84.74 (*C*-1'), 79.92 (*C*-4'), 77.53, 71.94 (*C*-2', *C*-3'), 63.87, 63.61, 53.59, 53.57, 53.54, 32.23, 32.18 (N*H*$_3$), 16.43 (TOM-*i*Pr-*C*), 16.41 (TOM-*i*Pr-*C*), 10.75 (TOM-*i*Pr-*C*) ppm;
HR-MS (ESI+): *m/z* calc. ($C_{50}H_{59}N_3NaO_{10}SSi$, $[M+Na]^+$): 944.3585, found: 944.3551.

5'-*O*-(4,4'-Dimethoxytrityl)-2'-*O*-tri-*iso*-propylsilyloxymethyl barbituric acid benzothiazole merocyanine ribonucleoside-3'-(2-cyanoethyl-*N,N*-di-*iso*-propyl phosphoramidite (50)

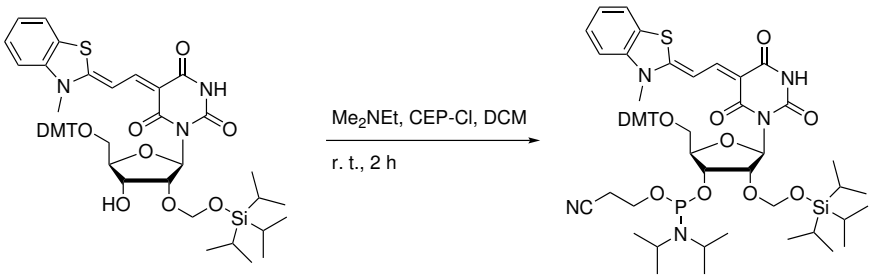

$C_{50}H_{59}N_3O_{10}SSi$
922.18 g mol^{-1}
48

$C_{59}H_{76}N_5O_{11}PSSi$
1122.40 g mol^{-1}
50

The protected ribonucleoside **48** (150 mg, 163 µmol, 1.00 eq.) was dissolved in anhydrous CH_2Cl_2 (5 mL) under nitrogen atmosphere. Me_2NEt (0.21 mL, 1.63 mmol, 10.0 eq.) and CEP-Cl (58 mg, 244 µmol, 1.50 eq.) were added to the mixture which was then stirred at r. t. for 2 h. The solvent was removed in vacuum. Purification of the crude product by column chromatography on silica gel (EtOAc/*n*-hexane 100:0 to 9:1 + 1% NEt_3) yielded the target compound **50** as a red foam (173 mg, 155 µmol, 95%).

Due to its low stability in all of the tested NMR solvents and the extensively overlapping individual signals assignment of the proton signals was not possible and no ^{13}C spectrum was recorded.
^{1}H NMR (400 MHz, acetone-d_6): $\delta =$ 9.43 (s, 1 H, N*H*), 8.38 - 8.19 (m, 1 H, COCC*H*), 7.96 - 7.90 (m, 1 H), 7.75 - 7.66 (m, 2 H), 7.62 - 7.49 (m, 3 H), 7.47 - 7.35 (m, 5 H), 7.33 - 7.24 (m, 2 H), 7.23 - 7.15 (m, 1 H), 6.93 - 6.79 (m, 4 H), 6.48 (s, 1 H, *H*-1'), 5.21 - 4.86 (m, 3 H), 3.90 (s, 3 H), 3.81 - 3.62 (m, 6 H, DMT-OC*H*$_3$), 3.66 - 3.38 (m, 3 H), 3.38 - 3.20 (m, 1 H), 2.62 - 2.52 (m, 1 H), 1.30 - 0.99 (m, 35 H, TOM-*i*Pr-*H*, PN-*i*Pr-*H*) ppm;
^{31}P NMR (162 MHz, acetone-d_6): $\delta =$ 148.96, 148.59, 148.38 ppm;
HR-MS (ESI+): *m/z* calc. ($C_{59}H_{76}N_5NaO_{11}PSSi$, $[M+Na]^+$): 1144.4678, found: 1144.4557.

5.1.2.3 Preparation of the rBAM triphosphate

Bis(tetra-*n*-butylammonium) dihydrogen pyrophosphate (119)

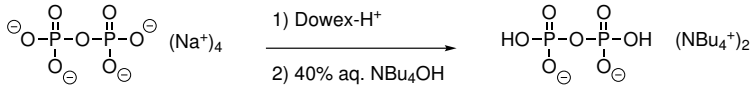

$Na_4O_7P_2$
265.90 g mol^{-1}

$C_{32}H_{74}N_2O_7P_2$
660.90 g mol^{-1}
119

A solution of tetrasodiumpyrophosphate decahydrate (1.12 g, 2.51 mmol) was dissolved in H_2O (9 mL) and applied to a column of Dowex-50WX80 (H^+ form), which was pre-washed with MeOH. The product was eluted with H_2O and washed until a neutral pH was reached. The eluate was afterwards titrated with 40% aq. NBu_4OH until pH 3.5 was reached. The solvent was removed in vacuum (water bath at 30 °C maximum) which yielded the product **119** as a colorless oil.

^{1}H NMR (400 MHz, D_2O): δ = 3.13 - 3.03 (m, 24 H, $CH_3CH_2CH_2CH_2$), 1.59 - 1.48 (m, 24 H, $CH_3CH_2CH_2$), 1.31 - 1.18 (m, 24 H, CH_3CH_2), 0.83 (t, J = 7.4 Hz, 32 H, CH_3) ppm;
^{31}P NMR (162 MHz, D_2O): δ = -10.2 ppm.

Barbituric acid merocyanine ribonucleoside triphosphate (51)

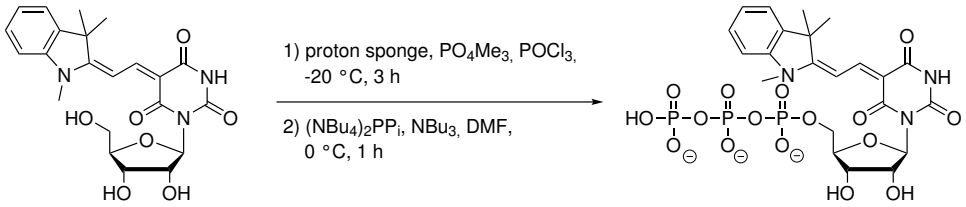

$C_{22}H_{25}N_3O_7$
443.46 g mol^{-1}
36

$C_{22}H_{25}N_3O_{16}P_3^{3-}$
680.37 g mol^{-1}
51

Barbituric acid merocyanine ribonucleoside **36** (20 mg, 45 µmol, 1.00 eq.) and proton sponge (14 mg, 63 µmol, 1.40 eq.) were dried overnight under high vacuum, dissolved in PO_4Me_3 (0.9 mL, dried over molecular sieves) under nitrogen atmosphere and cooled to -20 °C. Freshly distilled $POCl_3$ (8 µL, 68 µmol, 1.50 eq.) was added and the mixture was stirred for 3 h at -20 °C. NBu_3 (76 µL, 315 µmol, 7.00 eq.) and a solution of $(NBu_4)_2PP_i$ (**119**, 202 mg, 306 µmol, 6.80 eq.) in *N,N*-DMF (360 µL) were added and the mixture stirred for 1 h at 0 °C. TEAB buffer (1 M, pH 7.5, 5 mL) was added and the mixture was warmed to r. t. The reaction mixture was concentrated under reduced pressure and the crude product was purified by ion exchange HPLC (A: 0.1 M TEAB buffer pH 7.5, B: 1 M TEAB buffer pH 7.5, gradient: 0 to 100% B in 40 min) and then by RP HPLC (A: 100 mM TEAA in H_2O , B: 100 mM TEAA in 90% MeCN, gradient: 0 to 60% B in 30 min). Hereby, the pure product was obtained as triethylammonium salt which was dissolved in H_2O (200 µL). The concentration

of this solution was measured by UVvis spectroscopy (120 µM, 24 nmol, 5.3%). To half of the sample, MeOH (1 mL) was added and the resulting mixture was added dropwise to 5% w/w $LiClO_4$ in acetone (40 mL). The solution was centrifuged at 4 °C and 4,200 rpm for 2 h upon which the triphosphate precipitated as lithium salt. The precipiate was washed with acetone (5 mL), the supernatant was removed, the target compound **51** was dried in vacuum and afterwards redissolved in H_2O (50 µL).

^{1}H NMR (400 MHz, D_2O): δ = 8.53 (d, J = 15.3 Hz, 1 H, COCC*H*), 7.61 - 7.55 (m, 1 H, arom-*H*), 7.54 - 7.46 (m, 2 H, arom-*H*, NCC*H*), 7.45 - 7.37 (m, 2 H, arom-*H*), 6.37 - 6.24 (m, 1 H, *H*-1'), 4.75 - 4.69 (m, 1 H, *H*-2'), 4.61 - 4.54 (m, 1 H, *H*-3'), 4.53 - 4.46 (m, 1 H, *H*-3'), 4.35 - 4.25 (m, 1 H, *H*-5'), 4.20 - 4.06 (m, 2 H, *H*-4', *H*-5'), 3.99 - 3.85 (m, 2 H, *H*-4', *H*-5'), 3.77 (dd, J = 12.4, 6.1 Hz, 1 H, *H*-5'), 3.72 (s, 3 H, NCH_3), 1.70 (s, 6 H, 2×CH_3) ppm;
^{31}P NMR (162 MHz, D_2O): δ = -5.49 (d, J = 19.0 Hz), -10.63 (d, J = 18.2 Hz), -20.48 – -21.22 (t, J = 18.7 Hz) ppm.

5.1.2.4 Preparation of dBAM phosphoramidites

3',5'-Di-*O*-toluoyl barbituric acid 2'-deoxyribonucleoside (53)

$C_{13}H_{28}N_2O_3Si_3$
344.63 g mol^{-1}
25

$C_{21}H_{21}ClO_5$
388.84 g mol^{-1}

$C_{25}H_{24}N_2O_8$
480.47 g mol^{-1}
53a

$C_{25}H_{24}N_2O_8$
480.47 g mol^{-1}
53b

Under nitrogen atmosphere, silylated barbituric acid **25** (5.82 g, 16.9 mmol, 1.22 eq.) in anhydrous DCE (80 mL) was added to a solution of Hoffer's chlorosugar (5.40 g, 13.9 mmol, 1.00 eq.) in 80 mL of the same solvent. $SnCl_4$ (0.36 mL, 3.48 mmol, 0.25 eq.) in anhydrous 1,2-dichloroethane (25 mL) was added and the reaction mixture was stirred at r. t. for 3 h. Afterwards, the solvent was removed in vacuum and the crude product was purified by column chromatography on silica gel (CH_2Cl_2/MeOH 98:2 to 95:5) to yield the product as a 1:1 mixture of α- and β-anomer. The obtained white foam was recrystallized from methanol, where the desired β-anomer precipitated upon cooling while the α-anomer stayed in solution. The protected β-nucleoside **53b** was obtained as white solid (1.65 g, 3.44 mmol, 20%).

^{1}H NMR (400 MHz, $CDCl_3$): δ = 8.20 (s, 1 H, N*H*), 7.96 - 7.88 (m, 4 H, Tol-*H*), 7.27 - 7.14 (m, 4 H, Tol-*H*), 6.68 (dd, J = 8.5, 5.0 Hz, 1 H, *H*-1'), 5.77 (dt, J = 8.0, 5.3 Hz, 1 H, *H*-3'), 4.70 - 4.54 (m, 2 H, *H*-5'), 4.48 (dt, J = 6.7, 4.8 Hz, 1 H, *H*-4'), 3.67 (s, 2 H,

BA-CH_2), 3.15 (ddd, J = 14.1, 8.1, 5.0 Hz, 1 H, H-2'), 2.49 - 2.35 (m, 7 H, H-2', Tol-CH_3) ppm;

^{13}C{^{1}H} NMR (100 MHz, $CDCl_3$): δ = 166.42 (Tol-C), 165.99 (Tol-C), 164.98 (BA-carbonyl-C), 163.56 (BA-carbonyl-C), 149.25 (NCON), 144.21 (Tol-C), 143.74 (Tol-C), 129.82 (Tol-C), 129.76 (Tol-C), 129.18 (Tol-C), 129.02 (Tol-C), 127.03 (Tol-C), 126.60 (Tol-C), 82.42 (C-4'), 82.34 (C-1'), 74.69 (C-3'), 64.29 (C-5'), 39.95 (BA-CH$_2$), 35.62 (C-2'), 21.72 (Tol-CH$_3$), 21.66 (Tol-CH$_3$) ppm;

HR-MS (ESI+): m/z calc. ($C_{25}H_{24}N_2NaO_6$, $[M+Na]^+$): 503.1439, found: 503.1430.

3',5'-Di-*O*-toluoyl barbituric acid indolenine merocyanine 2'-deoxyribonucleoside (52b)

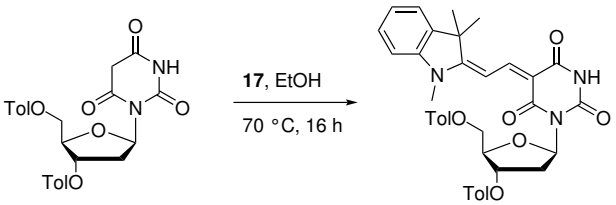

$C_{25}H_{24}N_2O_8$
480.47 g mol^{-1}
53b

$C_{38}H_{37}N_3O_8$
663.73 g mol^{-1}
52b

The protected barbituric acid deoxyribonucleoside **53b** (1.00 g, 2.08 mmol, 1.00 eq.) and aldehyde **17** (503 mg, 2.50 mmol, 1.20 eq.) were dissolved in abs. EtOH (12 mL) and heated to 70 °C for 16 h. Then, the reaction mixture was cooled to r. t. and the solvent was removed in vacuum. Column chromatography on silica gel (CH_2Cl_2/MeOH 98:2) yielded the merocyanine nucleoside **52b** as an orange foam (1.35 g, 2.03 mmol, 98%).

^{1}H NMR (400 MHz, $CDCl_3$): δ = 8.66 (2 d, J = 14.6 Hz, 1 H, COCH), 8.25 (2 s, 1 H, NH), 8.00 - 7.89 (m, 4 H, Tol-H), 7.61 (t, J = 14.2 Hz, 1 H, NCCH), 7.38 - 7.34 (m, 2 H, Ind-H-5, Ind-H-6), 7.26 - 7.11 (m, 6 H, Ind-H-4, Tol-H), 7.11 - 7.05 (m, 1 H, Ind-H-7), 6.99 - 6.84 (m, 1 H, H-1'), 5.89 (dd, J = 8.3, 4.2 Hz, 1 H, H-3'), 4.78 - 4.59 (m, 2 H, H-5'), 4.54 - 4.45 (m, 1 H, H-4'), 3.57 (2 s, 3 H, NCH_3), 3.36 - 3.24 (m, 1 H, H-2'), 2.49 - 2.26 (m, 7 H, H-2', Tol-CH_3), 1.74 - 1.69 (m, 6 H, 2×CH_3) ppm;

^{13}C{^{1}H} NMR (100 MHz, $CDCl_3$): δ = 177.97 (C-2), 177.68 (C-2), 166.60 (Tol-C), 166.12 (Tol-C), 164.03 (BA-carbonyl-C), 163.40 (BA-carbonyl-C, NCON), 163.20 (BA-carbonyl-C, NCON) , 163.02 (BA-carbonyl-C, NCON), 152.60 (CONCH), 151.79 (CONCH), 150.19 (BA-carbonyl-C), 144.03 (Tol-C), 144.00 (Tol-C), 143.54 (Tol-C), 141.14 (Ind-C-3a), 129.97 (Tol-C), 129.88 (Tol-C), 129.21 (Tol-C), 129.05 (Tol-C), 128.57 (Tol-C), 127.41 (Ind-C-5), 127.12 (Ind-C-5), 125.11 (Ind-C-4), 125.05 (Ind-C-4), 122.35 (Ind-C-6), 122.29 (Ind-C-6), 122.25 (Ind-C-6), 110.20 (Ind-C-7), 110.15 (Ind-C-7), 99.31 (NCCH), 98.80 (CNCCH), 82.34 (C-1', C-4'), 82.05 (C-1', C-4'), 81.90 (C-1', C-4'), 75.74 (C-3'), 65.21 (C-5'), 49.33 (Ind-C-3), 49.27 (Ind-C-3), 35.79 (C-2'), 35.69 (C-2'), 31.23 (NCH$_3$), 28.96 (CH$_3$), 28.87 (CH$_3$), 21.82 (Tol-CH$_3$), 21.77 (Tol-CH$_3$) ppm;

HR-MS (ESI+): *m/z* calc. ($C_{38}H_{37}N_3NaO_6$, $[M+Na]^+$): 686.2478, found: 686.2515.

Barbituric acid indolenine merocyanine 2'-deoxyribonucleoside (dBAM, 54)

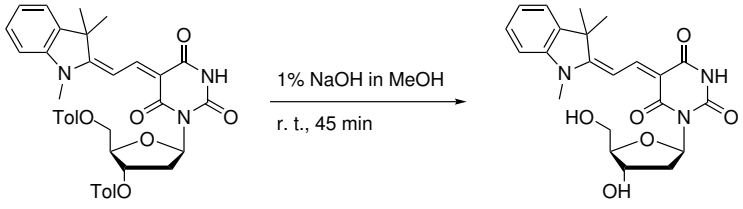

$C_{38}H_{37}N_3O_8$
663.73 g mol^{-1}
52b

$C_{22}H_{25}N_3O_6$
427.46 g mol^{-1}
54

The protected nucleoside **52b** (1.00 g, 1.51 mmol, 1.00 eq.) was dissolved in 45 mL of 1% methanolic NaOH and stirred at r. t. for 45 min. Afterwards, the solvent was removed in vacuum and the crude material was purified by column chromatography on silica gel (CH_2Cl_2/MeOH 95:5 to 8:2) to give the desired product **54** as an orange solid (466 mg, 1.09 mmol, 73%).

^{1}H NMR (400 MHz, DMSO-d_6): δ = 10.86, 10.76 (2 s, 1 H, N*H*), 8.47 (2 d, J = 14.8 Hz, 1 H, COCC*H*), 7.59 (d, J = 7.5 Hz, 1 H, Ind-*H*-7), 7.52 - 7.37 (m, 3 H, NCC*H*, Ind-*H*-4, Ind-*H*-5), 7.32 - 7.18 (m, 1 H, Ind-*H*-6), 6.56 (ddd, J = 8.2, 6.3, 4.7 Hz, 1 H, *H*-1'), 5.07 (d, J = 5.1 Hz, 1 H, 3'-O*H*), 4.64 - 4.52 (m, 1 H, 5'-O*H*), 4.37 - 4.25 (m, 1 H, *H*-3'), 3.70 - 3.57 (m, 2 H, *H*-4', *H*-5'), 3.55 (2 s, 3 H, NCH_3), 3.51 - 3.41 (m, 1 H, *H*-5'), 2.71 (dddd, J = 13.3, 7.6, 6.2, 1.6 Hz, 1 H, *H*-2'), 1.91 (td, J = 8.2, 4.1 Hz, 1 H, *H*-2'), 1.67 - 1.56 (m, 6 H, 2×CH_3) ppm;
^{13}C{^{1}H} NMR (100 MHz, DMSO-d_6): δ = 177.10 (Ind-*C*-2), 176.84 (Ind-*C*-2), 163.81 (BA-carbonyl-*C*), 163.03 (BA-carbonyl-*C*), 162.97 (BA-carbonyl-*C*), 162.60 (BA-carbonyl-*C*), 150.51 (COC*C*H), 150.40 (COC*C*H), 150.32 (COC*C*H), 149.79 (COC*C*H), 142.66 (Ind-*C*-7a), 140.74 (Ind-*C*-3a), 128.39 (Ind-*C*-4), 124.72 (Ind-*C*-6), 122.27 (Ind-*C*-7), 111.07 (Ind-*C*-5), 99.84 (CO*C*), 99.77 (CO*C*), 98.23 (CO*C*), 97.87 (NC*C*H), 87.18 (*C*-4'), 81.15 (*C*-1'), 80.51 (*C*-1'), 71.18 (*C*-3'), 62.40 (*C*-5'), 48.72 (Ind-*C*-3), 48.68 (Ind-*C*-3), 37.08 (*C*-2'), 31.03 (N*C*H_3), 28.17 (2×*C*H_3), 28.13 (2×*C*H_3), 28.03 (2×*C*H_3) ppm;
HR-MS (ESI+): *m/z* calc. ($C_{22}H_{25}N_3NaO_6$, $[M+Na]^+$): 450.1641, found: 450.1658.

5'-*O*-(4,4'-Dimethoxytrityl) barbituric acid indolenine merocyanine 2'-deoxyribonucleoside (55)

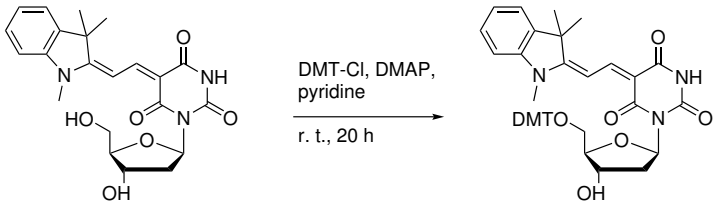

$C_{22}H_{25}N_3O_6$
427.46 g mol^{-1}
54

$C_{43}H_{43}N_3O_8$
729.83 g mol^{-1}
55

The unprotected nucleoside **54** (400 mg, 936 µmol, 1.00 eq.) and DMAP (5.7 mg, 47 µmol, 0.05 eq.) were dissolved in anhydrous pyridine (15 mL) under nitrogen atmosphere. The reaction mixture was cooled to 0 °C and DMT-Cl (476 mg, 1.40 mmol, 1.50 eq.) was added. After warming up to r. t., the reaction mixture was stirred at this temperature for 20 h. The solvent was removed in vacuum and the crude product was purified by column chromatography on silica gel (CH_2Cl_2/MeOH 100:0 to 97:3) to give the target compound **55** as an orange foam (533 mg, 732 µmol, 78%).

^{1}H NMR (400 MHz, $CDCl_3$): $\delta = 10.82$, 10.72 (2 s, 1 H, N*H*), 8.60 - 8.38 (m, 1 H, COCC*H*), 7.60 - 7.53 (m, 1 H, Ind-*H*-4), 7.50 - 7.32 (m, 5 H, NCC*H*, DMT-*H*), 7.31 - 7.19 (m, 7 H, DMT-*H*, Ind-*H*-5), 7.20 - 7.12 (m, 1 H), 6.87 - 6.76 (m, 4 H, DMT-*H*), 6.61 (dd, $J = 9.1$, 4.2 Hz, 1 H, *H*-1'), 5.05 (dd, $J = 5.5$, 3.7 Hz, 1 H, 3'-O*H*), 4.32 - 4.24 (m, 1 H, *H*-3'), 3.85 - 3.78 (m, 1 H, *H*-4'), 3.72 - 3.63 (m, 6 H, DMT-OCH_3), 3.49 (2 s, 3 H, NCH_3), 3.30 - 3.21 (m, 1 H, *H*-5'), 3.04 (td, $J = 9.5$, 3.2 Hz, 1 H, *H*-5'), 2.68 - 2.54 (m, 1 H, *H*-2'), 2.09 - 1.95 (m, 1 H, *H*-2'), 1.66 - 1.51 (m, 6 H, 2×CH_3) ppm;
^{13}C{^{1}H} NMR (100 MHz, $CDCl_3$): $\delta = 176.84$ (Ind-*C*-2), 176.69 (Ind-*C*-2), 163.07, 162.80, 162.66, 157.99 (DMT-*C*), 157.90 (DMT-*C*), 149.65 (COC*C*H), 145.27, 145.24, 142.66, 140.70, 135.90 (DMT-*C*), 135.84 (DMT-C), 135.79, 129.86, 129.80, 129.66, 128.38, 127.80, 127.69, 126.54, 124.67, 123.95, 122.26 (Ind-*C*-4), 113.06 (DMT-*C*), 113.01 (DMT-*C*), 111.00, 100.03 (CO*C*), 98.08 (NC*C*H), 85.44 (*C*-4'), 85.21 (*C*-4'), 71.40 (*C*-3'), 54.99 (DMT-O*C*H_3), 54.96 (DMT-O*C*H_3), 54.93 (DMT-O*C*H_3), 54.90 (DMT-O*C*H_3), 48.63 (Ind-*C*-3), 48.60 (Ind-*C*-3), 37.96 (*C*-2'), 37.96 (*C*-2'), 28.16 (*C*H_3), 28.09 (*C*H_3) ppm;
HR-MS (ESI+): *m/z* calc. ($C_{43}H_{43}N_3NaO_8$, [M+Na]$^+$): 752.3050, found: 752.3039.

5'-*O*-(4,4'-Dimethoxytrityl) barbituric acid indolenine merocyanine 2'-deoxyribonucleoside 3'-(2-cyanoethyl-*N,N*-di-*iso*-propyl) phosphoramidite (56)

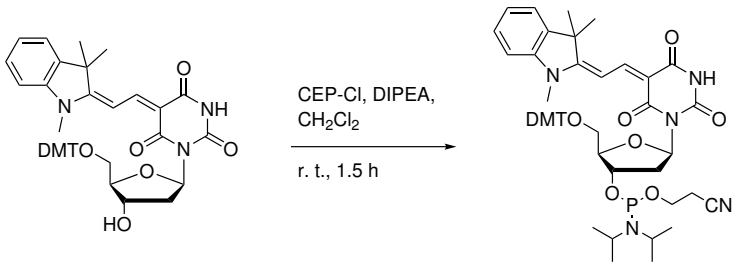

$C_{43}H_{43}N_3O_8$
729.83 g mol^{-1}
55

$C_{52}H_{60}N_5O_9P$
929.41 g mol^{-1}
56

The DMT-protected nucleoside **55** (400 mg, 537 µmol, 1.00 eq.) was dissolved in anhydrous CH_2Cl_2 (9 mL) under nitrogen atmosphere. DIPEA (0.80 mL, 4.30 mmol, 8.00 eq.) and CEP-Cl (191 mg, 806 µmol, 1.50 eq.) were added dropwise and the reaction mixture was stirred at r. t. for 1.5 h. After removal of the solvent under reduced pressure, the crude product was purified by column chromatography on silica gel (EtOAc/*n*-hexane 90:10 to 80:20+2% NEt_3) to obtain the phosphoramidite building block **56** as an orange foam (436 mg, 473 µmol, 88%).

^{1}H NMR (400 MHz, $CDCl_3$): δ = 8.73 - 8.53 (m, 1 H, COCC*H*), 7.90 (s_{br}, 1 H, N*H*), 7.62 - 7.45 (m, 3 H, NCC*H*), 7.43 - 7.31 (m, 6 H, Ind-*H*-5, DMT-*H*), 7.27 - 7.18 (m, 3 H), 7.18 - 7.09 (m, 1 H), 7.04 (d, J = 8.0 Hz, 1 H, Ind-*H*-4), 6.86 - 6.72 (m, 5 H, *H*-1', DMT-*H*), 4.85 - 4.71 (m, 0.5 H, *H*-3'), 4.72 - 4.60 (m, 0.5 H, *H*-3'), 4.17 - 4.04 (m, 1 H, *H*-4'), 3.82 - 3.69 (m, 7 H, POCH_2, DMT-OCH_3), 3.61 - 3.45 (m, 4 H, NCH_3, POCH_2, *i*Pr-C*H*), 3.45 - 3.23 (m, 3 H, *H*-5'), 2.99 - 2.80 (m, 1 H, *H*-2'), 2.63 - 2.54 (m, 1 H, $POCH_2CH_2$), 2.42 - 2.35 (m, 1 H, $POCH_2CH_2$), 2.28 (ddd, J = 13.3, 5.8, 4.5 Hz, 1 H, $POCH_2CH_2$), 1.75 - 1.58 (m, 6 H, 2×CH_3), 1.19 - 1.10 (m, 9 H, *i*Pr-CH_3), 1.00 (dd, J = 6.8, 3.2 Hz, 3 H, *i*Pr-CH_3) ppm;
^{13}C{^{1}H} NMR (100 MHz, $CDCl_3$): δ = 177.57 (Ind-*C*-2), 177.40 (Ind-*C*-2), 163.98 (BA-carbonyl-*C*), 163.39 (BA-carbonyl-*C*), 163.05 (BA-carbonyl-*C*), 162.77, 158.24 (DMT-*C*), 158.21 (DMT-*C*), 152.58 (COC*C*H), 151.44 (COC*C*H), 149.91, 149.81, 145.18, 145.15, 145.12, 145.09, 142.58, 141.00 (Ind-*C*-3a), 136.54 (DMT-*C*), 136.48 (DMT-*C*), 136.45 (DMT-*C*), 136.40 (DMT-*C*), 136.36 (DMT-*C*), 130.25, 130.22, 130.16, 128.45, 128.39, 127.62, 127.59, 126.52, 126.46, 124.88, 122.15, 117.61 (C-21), 112.90 (DMT-*C*), 109.94 (Ind-*C*-4), 100.97, 98.94 (NC*C*H), 98.66 (NC*C*H), 85.95 (DMT-*C*), 85.92 (DMT-*C*), 85.90 (DMT-*C*), 85.00 (*C*-4'), 84.87 (*C*-4'). 84.82 (*C*-4'), 81.72 (*C*-1'), 81.55 (*C*-1'), 81.24 (*C*-1'), 81.10 (*C*-1'), 74.38 (*C*-3'), 74.32 (*C*-3'), 74.21 (*C*-3'), 74.15 (*C*-3'), 73.78 (*C*-3'), 73.73 (*C*-3'), 73.59 (*C*-3'), 73.53 (*C*-3'), 64.52 (*C*-5'), 64.27 (*C*-5'), 58.53 (PO*C*H_2), 58.35 (PO*C*H_2), 58.16 (PO*C*H_2), 55.18 (DMT-O*C*H_3), 55.15 (DMT-O*C*H_3), 55.12 (DMT-O*C*H_3), 49.11 (Ind-*C*-2), 49.07 (Ind-*C*-2), 43.20 (N*C*H_3), 43.18 (N*C*H_3), 43.14 (N*C*H_3), 43.12 (N*C*H_3), 43.08 (N*C*H_3), 43.06 (N*C*H_3), 43.01 (N*C*H_3), 42.99 (N*C*H_3), 37.34 (*C*-2'), 37.17 (*C*-12'), 30.92

(*i*Pr-*C*H), 30.75 (*i*Pr-*C*H), 28.82 (*C*H_3), 28.77 (*C*H_3), 28.69 (*C*H_3), 24.66 (*i*Pr-*C*H_3), 24.59 (*i*Pr-*C*H_3), 24.46 (*i*Pr-*C*H_3), 24.42 (*i*Pr-*C*H_3), 24.39 (*i*Pr-*C*H_3), 24.34 (*i*Pr-*C*H_3), 20.34 (POCH$_2$*C*H$_2$), 20.27 (POCH$_2$*C*H$_2$), 20.11 (POCH$_2$*C*H$_2$), 20.04 (POCH$_2$*C*H$_2$) ppm;
^{31}P NMR (162 MHz, $CDCl_3$): δ = 148.42, 148.33, 148.27, 148.12 ppm;
HR-MS (ESI+): *m/z* calc. ($C_{52}H_{60}N_5NaO_9P$, $[M+Na]^+$): 952.4026, found: 952.4022.

Barbituric acid 2'-deoxyribonucleoside (57)

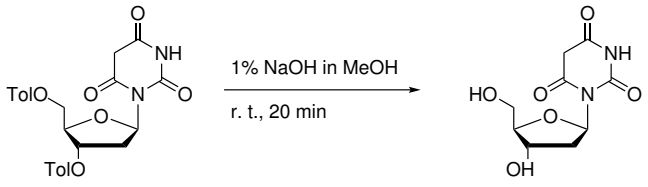

$C_{25}H_{24}N_2O_8$
480.47 g mol^{-1}
53b

$C_9H_{12}N_2O_6$
244.20 g mol^{-1}
57

The protected barbituric acid nucleoside **53b** (560 mg, 1.17 mmol, 1.00 eq.) was dissolved in 1% methanolic NaOH (35 mL) and stirred for 20 min at ambient temperature. After removal of the solvent under reduced pressure, the residue was redissolved in H_2O (50 mL). The aqueous phase was washed with CH_2Cl_2 (3×30 mL) and brought to pH 4.0 with Dowex-50WX80 (hydrogen form). Removal of the solvent in vacuum afforded the free nucleoside **57** as a colorless solid (232 mg, 950 µmol, 81%).

^{1}H NMR (400 MHz, DMSO-d_6): δ = 6.42 (s, 1 H, *H*-1'), 5.06 (s, 1 H, 3'-O*H*), 4.26 (dt, *J* = 8.3, 4.4 Hz, 1 H, *H*-3'), 3.64 (dt, *J* = 5.4, 4.2 Hz, 1 H, *H*-4'), 3.56 (dd, *J* = 11.5, 4.1 Hz, 1 H, *H*-5'), 3.41 (dd, *J* = 11.4, 5.5 Hz, 1 H, *H*-5'), 3.16 (s, 2 H, BA-CH_2), 2.74 - 2.56 (m, 1 H, *H*-2'), 1.86 (s, 1 H, *H*-2') ppm;
^{13}C{^{1}H} NMR (100 MHz, DMSO-d_6): δ = 167.39 (BA-carbonyl-*C*), 143.09 (N*C*ON), 87.19 (*C*-4'), 81.05 (*C*-1'), 62.34 (*C*-3'), 48.65 (*C*-5'), 40.15 (BA-*C*H_2), 36.86 (*C*-2') ppm;
HR-MS (ESI+): *m/z* calc. ($C_9H_{12}N_2NaO_6$, $[M+Na]^+$): 267.0595, found: 267.0593.

Barbituric acid benzothiazole merocyanine 2'-deoxyribonucleoside (dBAM^b, 58)

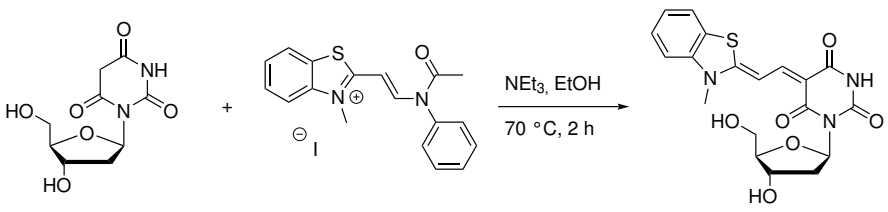

$C_9H_{12}N_2O_6$
244.20 g mol^{-1}
57

$C_{18}H_{17}IN_2OS$
336.31 g mol^{-1}
22

$C_{19}H_{19}N_3O_6S$
417.45 g mol^{-1}
58

Compound **22** (493 mg, 1.13 mmol, 1.20 eq.) and barbituric acid 2'-deoxyribonucleoside **57** (230 mg, 0.94 mmol, 1.00 eq.) were dissolved in abs. EtOH (15 mL) and triethylamine

(400 µL, 3.01 mmol, 3.20 eq.) was added slowly. The solution was stirred for 2 h at 70 °C. Afterwards, the reaction mixture was cooled to r. t. and Et_2O (30 mL) was added over 30 min. The precipitate was filtered off and washed with Et_2O (3×20 mL) and H_2O (2×10 mL). Column chromatography on silica gel (EtOAc/MeOH 95:5 to 8:2) afforded a 1:1 mixture of (*E*),(*Z*)- and (*E*),(*E*)-double bond isomers of the pure nucleoside **58** as a red solid (220 mg, 530 µmol, 56%).

^{1}H NMR (400 MHz, DMSO-d_6): δ = 10.68 (s, 1 H, N*H*), 8.10 (dd, *J* = 14.1, 6.2 Hz, 1 H, COCC*H*), 8.01 (ddd, *J* = 8.0, 3.4, 1.2 Hz, 1 H, arom-*H*-7), 7.80 (dd, *J* = 8.3, 3.7 Hz, 1 H, arom-*H*-4), 7.65 - 7.51 (m, 2 H, arom-*H*-5, NCC*H*), 7.44 (t, *J* = 7.7 Hz, 1 H, arom-*H*-6), 6.56 (ddd, *J* = 10.7, 7.9, 6.4 Hz, 1 H, *H*-1'), 5.10 (s, 1 H, 3'-O*H*), 4.62 (s, 1 H, 5'-O*H*), 4.30 (dt, *J* = 8.8, 4.5 Hz, 1 H, *H*-3'), 3.83 (d, *J* = 3.8 Hz, 3 H, NCH_3), 3.66 (q, *J* = 4.7 Hz, 1 H, *H*-4'), 3.62 - 3.55 (m, 1 H, *H*-5'), 3.53 - 3.42 (m, 1 H, *H*-5'), 2.71 (dt, *J* = 13.8, 7.0 Hz, 1 H, *H*-2'), 1.90 (td, *J* = 8.5, 4.1 Hz, 1 H, *H*-2') ppm;
^{13}C{^{1}H} NMR (100 MHz, DMSO-d_6): δ = 170.24 (BA-carbonyl-*C*), 163.59 (BA-carbonyl-*C*), 150.48 (BA-carbonyl-*C*), 147.62 (COC*C*H), 146.98 (arom-*C*-3a), 141.93 (arom-*C*-2), 127.99 (arom-*C*-5), 125.44 (arom-*C*-6), 124.95 (arom-*C*-7a), 123.10 (arom-*C*-7), 113.99 (arom-*C*-4), 97.75 (NC*C*H), 97.26 (NC*C*H), 87.08 (*C*-4'), 81.13 (*C*-1'), 71.24 (*C*-3'), 62.41 (*C*-5'), 37.05 (*C*-2'), 33.77 (N*C*H_3) ppm;
HR-MS (ESI+): *m/z* calc. ($C_{19}H_{19}N_3NaO_6S$, $[M+Na]^+$): 440.0892, found: 440.0892.

5'-*O*-(4,4'-Dimethoxytrityl) barbituric acid benzothiazole merocyanine 2'-deoxyribonucleoside (59)

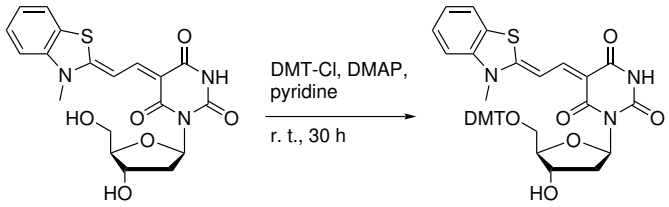

$C_{19}H_{19}N_3O_6S$
417.45 g mol^{-1}
58

$C_{40}H_{37}N_3O_8S$
719.81 g mol^{-1}
59

The unprotected nucleoside **58** (200 mg, 481 µmol, 1.00 eq.) and DMAP (2.1 mg, 22 µmol, 0.05 eq.) were dissolved in anhydrous pyridine (8 mL) under nitrogen atmosphere. The reaction mixture was cooled to 0 °C and DMT-Cl (210 mg, 622 µmol, 1.50 eq.) was added. After warming up to r. t., the reaction mixture was stirred at this temperature for 20 h. Since after this reaction time still a significant amount of starting material was present in the reaction mixture, additional 0.5 eq. of DMT-Cl were added and it was stirred again for 10 h at r. t. The solvent was removed in vacuum afterwards and the crude product was purified by column chromatography on silica gel (CH_2Cl_2/MeOH 95:5 to 9:1) to give the target compound **59** as an orange foam (128 mg, 178 µmol, 37%).

^{1}H NMR (400 MHz, $CDCl_3$): δ = 10.64 (2 s, 1 H, N*H*), 8.11 (d, J = 14.1 Hz, 1 H, COCC*H*), 8.01 (ddd, J = 8.0, 2.8, 1.2 Hz, 1 H, arom-*H*-7), 7.79 (dd, J = 8.4, 4.6 Hz, 1 H, arom-*H*-4), 7.66 - 7.35 (m, 5 H, DMT-*H*, NCC*H*), 7.31 - 7.22 (m, 6 H, DMT-*H*), 7.21 - 7.15 (m, 1 H, arom-*H*-5), 6.83 (ddd, J = 15.4, 7.6, 2.1 Hz, 4 H, DMT-*H*), 6.62 (ddd, J = 12.9, 8.9, 4.3 Hz, 1 H, *H*-1'), 5.05 (dd, J = 5.5, 2.5 Hz, 1 H, 3'-O*H*), 4.33 - 4.24 (m, 1 H, *H*-3'), 3.86 - 3.74 (m, 3 H, NCH_3, *H*-4'), 3.74 - 3.63 (m, 6 H, OCH_3), 3.25 (dd, J = 18.5, 9.6 Hz, 1 H, *H*-5'), 3.07 (dd, J = 9.7, 3.4 Hz, 1 H, *H*-5'), 2.68 - 2.57 (m, 1 H, *H*-2'), 2.04 - 1.96 (m, 1 H, *H*-2') ppm;
^{13}C{^{1}H} NMR (100 MHz, $CDCl_3$): δ = 170.68 (BA-carbonyl-*C*), 163.32 (BA-carbonyl-*C*), 158.43 (DMT-*C*), 145.70 (COC*C*H), 142.38, 136.36, 130.29, 130.10, 128.25, 128.15, 126.99 (arom-*C*-5), 125.84, 125.37, 124.40, 123.55 (arom-*C*-7), 114.37 (arom-*C*-4), 113.51 (DMT-*C*), 85.66 (*C*-4'), 81.06 (*C*-1'), 71.98 (*C*-3'), 65.27 (*C*-5'), 60.24, 55.41 (DMT-*C*H_3), 55.35 (DMT-*C*H_3), 46.18, 38.22 (*C*-2'), 34.17 (N*C*H_3), 21.25, 14.56 ppm;
HR-MS (ESI+): *m/z* calc. ($C_{40}H_{37}N_3NaO_8S$, $[M+Na]^+$): 742.2224, found: 742.2199.

5'-*O*-(4,4'-Dimethoxytrityl) barbituric acid benzothiazole merocyanine 2'-deoxyribonucleoside 3'-(2-cyanoethyl-*N,N*-di-*iso*-propyl) phosphoramidite (60)

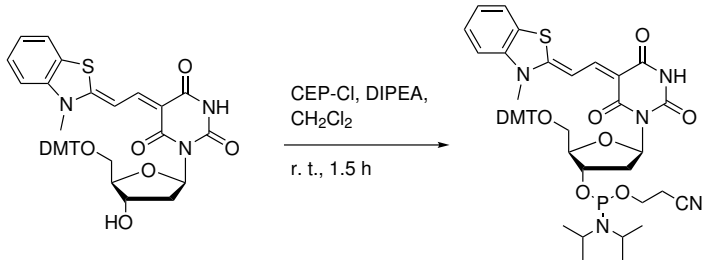

$C_{40}H_{37}N_3O_8S$
719.81 g mol^{-1}
59

$C_{49}H_{54}N_5O_9PS$
920.03 g mol^{-1}
60

The DMT-protected nucleoside **59** (100 mg, 136 µmol, 1.00 eq.) was dissolved in anhydrous CH_2Cl_2 (2 mL) under nitrogen atmosphere. DIPEA (0.20 mL, 1.09 mmol, 8.00 eq.) and CEP-Cl (48 mg, 204 µmol, 1.50 eq.) were added dropwise and the reaction mixture was stirred at r. t. for 3 h. After removal of the solvent under reduced pressure, the crude product was purified by column chromatography on silica gel (EtOAc/*n*-hexane 100:0 to 90:10+2% NEt_3) to obtain the phosphoramidite building block **60** as an orange foam (121 mg, 117 µmol, 86%).

NMR signals for compound **60** were not assigned unambiguously due to significant overlapping and the presence of multiple sets of signals for all of the protons.

^{1}H NMR (400 MHz, $CDCl_3$): δ = 8.32 - 8.18 (m, 1 H, COCC*H*), 7.77 - 7.61 (m, 3 H), 7.49 (dtd, J = 8.3, 4.3, 1.4 Hz, 3 H), 7.42 - 7.30 (m, 7 H), 7.27 - 7.10 (m, 6 H), 6.82 - 6.73 (m, 6 H), 6.15 (s, 1 H), 4.66 (d, J = 8.4 Hz, 1 H), 4.28 - 4.06 (m, 3 H), 3.84 - 3.69 (m, 9 H),

3.64 (d, J = 4.6 Hz, 2 H), 3.26 - 3.21 (m, 6 H), 2.93 - 2.78 (m, 1 H), 2.78 - 2.70 (m, 2 H), 2.60 (t, J = 6.5 Hz, 1 H), 2.39 (dq, J = 7.1, 2.5 Hz, 1 H), 2.35 - 2.18 (m, 1 H), 1.27 (dd, J = 6.8, 5.5 Hz, 13 H), 1.19 - 1.11 (m, 10 H), 1.01 (dd, J = 6.8, 1.1 Hz, 3 H) ppm;
^{13}C{^{1}H} NMR (100 MHz, $CDCl_3$): δ = 170.46, 158.33, 142.05, 141.54, 136.37, 130.31, 128.43, 127.67, 126.59, 125.45, 124.39, 122.55, 112.96, 91.52, 58.16, 55.18, 45.35, 45.29, 43.04, 33.32, 31.77, 24.49, 23.39, 23.01, 22.99, 22.93, 22.90, 20.10 ppm;
^{31}P NMR (162 MHz, $CDCl_3$): δ = 148.56, 148.42, 148.33, 148.28 ppm;
HR-MS (ESI-): m/z calc. ($C_{49}H_{53}N_5O_9PS$, $[M-H]^-$): 919.3380, found: 919.3372.

5.1.2.5 Preparation of canonical GNA phosphoramidites

Canonical phosphoramidites were synthesized according to reported procedures. Spectral data matches those reported for all compounds.[436,437]

(4,4'-Dimethoxytrityloxy)-glycidol (61 and 78)

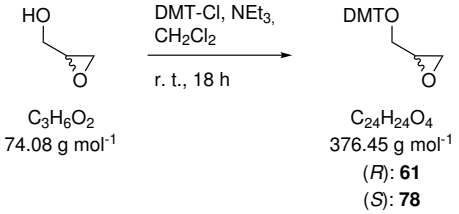

Glycidol (1.00 g, 13.6 mmol, 1.00 eq.) and NEt_3 (4.86 mL, 34.8 mmol, 2.56 eq.) were dissolved in anhydrous CH_2Cl_2 (31 mL) under nitrogen atmosphere. The reaction mixture was stirred at r. t. for 16 h and then filtered through a celite pad. After removal of the solvent in vacuum, the crude product was purified by column chromatography on silica gel (*n*-hexane/EtOAc 98:2 + 2% NEt_3). The pure product was obtained as a colorless oil (**61**: 5.01 g, 13.3 mmol, 98%; **78**: 3.91 g, 10.4 mmol, 77%).

The obtained spectral data were the same for both isomers.

^{1}H NMR (400 MHz, $CDCl_3$): δ = 7.50 - 7.43 (m, 2 H, DMT-*H*), 7.39 - 7.03 (m, 7 H, DMT-*H*), 6.87 - 6.80 (m, 4 H, DMT-*H*), 3.79 (s, 6 H, DMT-OCH_3), 3.32 (dd, J = 10.3, 2.6 Hz, 1 H, 1-CH_2), 3.18 - 3.08 (m 2 H, 1-CH_2, 2-C*H*), 2.78 (dd, J = 5.1, 4.0 Hz, 1 H, 3-CH_2), 2.63 (dd, J = 5.1, 2.6 Hz, 1 H, 1-CH_2) ppm;
^{13}C{^{1}H} NMR (100 MHz, $CDCl_3$): δ = 158.60 (DMT-*C*), 144.92 (DMT-*C*), 136.15 (DMT-*C*), 130.16 (DMT-*C*), 128.26 (DMT-*C*), 127.98 (DMT-*C*), 126.91 (DMT-*C*), 113.25 (DMT-*C*), 86.23 (DMT-C_{quart}), 64.72 (3-CH_2), 55.35 (DMT-OCH_3), 51.26 (2-*C*H), 44.81 (1-CH_2) ppm;
HR-MS (ESI+): m/z calc. ($C_{24}H_{24}NaO_4$, $[M+Na]^+$): 399.4421, found: 399.4425.

3'-*O*-(4,4'-Dimethoxytrityloxy)methyl-(*S*)-9-(2,3-dihydroxypropyl)adenine (67)

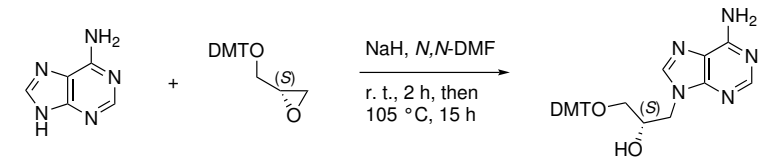

$C_5H_5N_5$
135.13 g mol^{-1}

$C_{24}H_{24}O_4$
376.45 g mol^{-1}
61

$C_{29}H_{29}N_5O_4$
511.58 g mol^{-1}
67

Adenine (710 mg, 5.25 mmol, 1.00 eq.) and NaH (60% oil dispersion, 43 mg, 1.07 mmol, 0.20 eq.) were suspended in anhydrous *N,N*-DMF (8 mL) under nitrogen atmosphere. The suspension was stirred for 2 h at r. t. Then, the DMT-protected glycidol **61** (1.86 g, 4.95 mmol, 0.94 eq.) in anhydrous *N,N*-DMF (13 mL) was added and the mixture was heated for 15 h to 105 °C. After cooling to r. t., the precipitate was filtered off and washed with EtOAc (50 mL). The solvent of the filtrate was removed in vacuum and column chromatography on silica gel (CH_2Cl_2/MeOH 98:2 to 95:5 + 2% NEt_3) afforded the product **67** as a white foam (1.57 g, 3.09 mmol, 59%).

^{1}H NMR (400 MHz, $CDCl_3$): δ = 8.22 (s, 1 H), 7.70 (s, 1 H), 7.47 - 7.39 (m, 2 H), 7.35 - 7.25 (m, 6 H), 7.24 - 7.19 (m, 1 H), 6.87 - 6.74 (m, 4 H), 6.07 (s_{br}, 2 H), 4.45 - 4.16 (m, 3 H), 3.77 (d, J = 3.7 Hz, 6 H), 3.27 (dd, J = 9.6, 5.3 Hz, 1 H), 3.08 (dd, J = 9.6, 6.0 Hz, 1 H) ppm;
HR-MS (ESI+): *m/z* calc. ($C_{24}H_{24}NaO_4$, $[M+Na]^+$): 399.1567, found: 399.1566.

(*S*)-9-(3-(4,4'-Dimethoxytrityloxy)-2-hydroxypropyl)-N^6-[(dimethylamino)methylene]adenine (68)

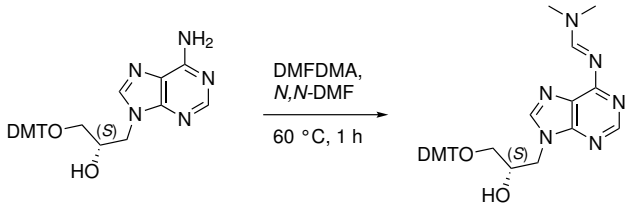

$C_{29}H_{29}N_5O_4$
511.58 g mol^{-1}
67

$C_{32}H_{34}N_6O_4$
566.66 g mol^{-1}
68

Compound **67** (1.32 g, 2.58 mmol, 1.00 eq.) was dissolved under nitrogen atmosphere in anhydrous *N,N*-DMF (8 mL) and DMFDMA (1.21 mL, 9.04 mmol, 3.50 eq.) was added dropwise. The reaction mixture was heated to 60 °C for 1 h. After cooling to r. t., the solvent was removed in vacuum and the residue was redissolved in CH_2Cl_2 (100 mL). The organic phase was washed with sat. aq. $NaHCO_3$ solution (100 mL) and afterwards dried over Na_2SO_4. The solvent was removed in vacuum and column chromatography on silica gel (EtOAc/MeOH 100:0 to 9:1 + 2% NEt_3) afforded the target compound **68** as a white foam

(1.02 g, 1.79 mmol, 79%).

^{1}H NMR (400 MHz, $CDCl_3$): δ =8.91 - 8.87 (m, 1 H), 8.43 (s, 1 H), 7.83 (s, 1 H), 7.45 - 7.38 (m, 2 H), 7.33 - 7.16 (m, 8 H), 6.84 - 6.77 (m, 4 H), 5.03 (s, 1 H), 4.49 - 4.40 (m, 1 H), 4.31 - 4.19 (m, 2 H), 3.77 (s, 6 H), 3.27 (dd, J = 9.5, 5.1 Hz, 1 H), 3.22 (d, J = 0.6 Hz, 3 H), 3.19 (s, 3 H), 3.07 (dd, J = 9.6, 6.2 Hz, 1 H) ppm;
HR-MS (ESI+): *m/z* calc. ($C_{32}H_{35}N_6O_4$, $[M+H]^+$): 567.2714, found: 567.2709.

(*S*)-9-(3-(4,4'-Dimethoxytrityloxy)-2-hydroxypropyl)-N^6-[(dimethylamino)methylene]-adenine phosphoramidite (gA-PA, 69)

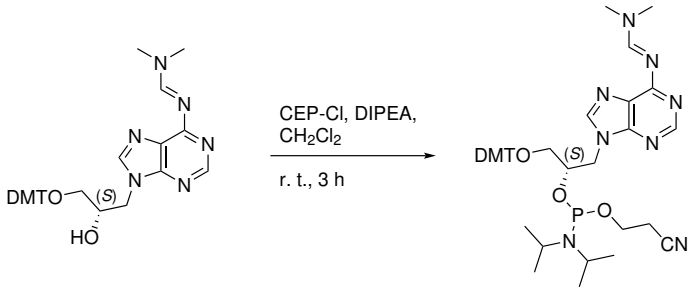

$C_{32}H_{34}N_6O_4$
566.66 g mol^{-1}
68

$C_{41}H_{51}N_8O_5P$
766.88 g mol^{-1}
69

Compound **68** (800 mg, 1.51 mmol, 1.00 eq.) was dissolved under nitrogen atmosphere in anhydrous CH_2Cl_2 (26 mL). DIPEA (2.25 mL, 12.1 mmol, 8.00 eq.) and CEP-Cl (0.52 mL, 2.27 mmol, 1.50 eq.) were added dropwise and the reaction mixture was stirred for 3 h at ambient temperature. Afterwards, the solvent was removed in vacuum and column chromatography on silica gel (EtOAc/acetone 1:1 + 2% NEt_3) afforded the target compound **69** as a white foam (792 mg, 1.08 mmol, 68%).

^{1}H NMR (400 MHz, $CDCl_3$): δ = 8.95 (d, J = 5.0 Hz, 1 H), 8.51 (d, J = 3.8 Hz, 1 H), 7.90 (d, J = 4.1 Hz, 1 H), 7.45 (ddd, J = 8.2, 2.9, 1.3 Hz, 2 H), 7.35 - 7.15 (m, 6 H), 6.85 - 6.75 (m, 4 H), 4.58 - 4.30 (m, 3 H), 4.25 - 4.08 (m, 1 H), 3.78 (d, J = 2.4 Hz, 6 H), 3.69 - 3.39 (m, 3 H), 3.25 (d, J = 2.1 Hz, 4 H), 3.20 (d, J = 2.6 Hz, 3 H), 2.79 - 2.72 (m, 1 H), 2.47 - 2.31 (m, 2 H), 1.27 (dd, J = 6.8, 5.6 Hz, 6 H), 1.13 - 0.95 (m, 12 H) ppm;
^{31}P NMR (162 MHz, $CDCl_3$): δ = 149.89, 149.67 ppm;
HR-MS (ESI+): *m/z* calc. ($C_{41}H_{51}N_8O_5P$, $[M+H]^+$): 767.3798 found: 767.3793.

N^4-Acetylcytosine (64)

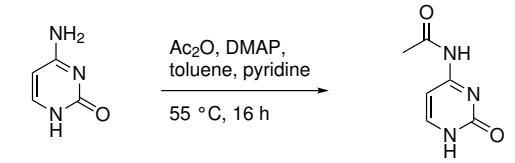

$C_4H_5N_3O$
111.10 g mol^{-1}

$C_6H_7N_3O_2$
153.14 g mol^{-1}
64

Cytosine (4.00 g, 36.0 mmol, 1.00 eq.) was suspended in toluene (12 mL) and pyridine (4.40 mL, 54.6 mmol, 1.52 eq.) and DMAP (20 mg, 161 µmol, 0.002 eq.) were added. After addition of acetic anhydride (4.02 mL, 42.3 mmol, 1.18 eq.) in toluene (7 mL) the reaction mixture was heated for 16 h to 55 °C. The mixture was cooled to r. t., the precipitate was filtered off and washed with toluene (2×10 mL) and H_2O (3×10 mL). After drying in high vacuum the target compound **64** was obtained as a slightly yellow solid (5.24 g, 34.3 mmol, 95%).[485]

^{1}H NMR (400 MHz, DMSO-d_6): δ = 11.51 (s, 1 H, N*H*-1), 10.75 (s, 1 H, N*H*-4), 7.80 (d, J = 7.1 Hz, 1 H, *H*-6), 7.09 (d, J = 7.1 Hz, 1 H, *H*-5), 2.08 (s, 3 H, COC*H*H_3) ppm;
^{13}C{^{1}H} NMR (100 MHz, DMSO-d_6): δ = 171.36 (*C*O), 163.72 (*C*-4), 156.65 (*C*-2), 147.62 (*C*-6), 94.96 (*C*-5), 24.79 (CO*C*H_3) ppm;
HR-MS (ESI+): *m/z* calc. ($C_6H_7N_3NaO_2$, [M+Na]$^+$): 176.0731, found: 176.0432.

(*S*)-1-(3-(4,4'-Dimethoxytrityloxy)-2-hydroxypropyl)-N^4-acetylcytosine (65)

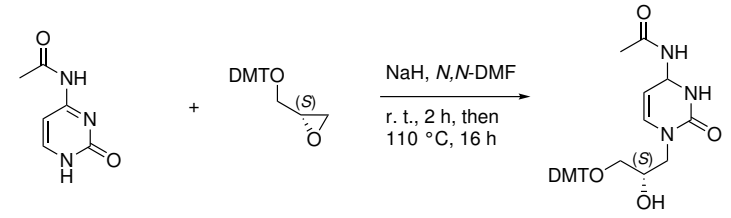

$C_6H_7N_3O_2$
153.14 g mol^{-1}
64

$C_{24}H_{24}O_4$
376.45 g mol^{-1}
61

$C_{30}H_{32}N_3O_6$
530.60 g mol^{-1}
65

Acetyl-protected cytosine **64** (1.16 g, 7.57 mmol, 1.05 eq.) and NaH (60% oil dispersion, 60 mg, 1.50 mmol, 0.20 eq.) were suspended in anhydrous *N,N*-DMF (15 mL) under nitrogen atmosphere and stirred for 1 h at r. t. After addition of DMT-protected glycidol **61** (2.71 g, 7.20 mmol, 1.00 eq.) in anhydrous *N,N*-DMF (15 mL) the reaction mixture was heated for 16 h to 110 °C. The mixture was cooled to r. t., the solvent was removed in vacuum and column chromatography on silica gel (acetone/*n*-hexane 3:2 + 2% NEt_3) afforded the target compound **65** as a slightly yellow foam (2.02 g, 3.82 mmol, 53%).

^{1}H NMR (400 MHz, $CDCl_3$): δ = 9.92 (s, 1 H), 7.57 (d, J = 7.3 Hz, 1 H), 7.45 - 7.39 (m, 2 H), 7.32 - 7.23 (m, 7 H), 7.22 - 7.16 (m, 1 H), 6.85 - 6.75 (m, 4 H), 4.32 (dd, J = 13.4,

2.4 Hz, 1 H), 4.21 (d, J = 8.2 Hz, 2 H), 3.76 (s, 7 H), 3.21 (dt, J = 10.2, 4.9 Hz, 1 H), 3.14 - 3.05 (m, 1 H), 2.20 (s, 3 H) ppm;
HR-MS (ESI+): m/z calc. ($C_{30}H_{31}N_3NaO_6$, $[M+Na]^+$): 552.2105, found: 552.2108.

(*S*)-1-(3-(4,4'-Dimethoxytrityloxy)-2-hydroxypropyl)-*N*^{4}-acetylcytosine phosphoramidite (gC-PA, 66)

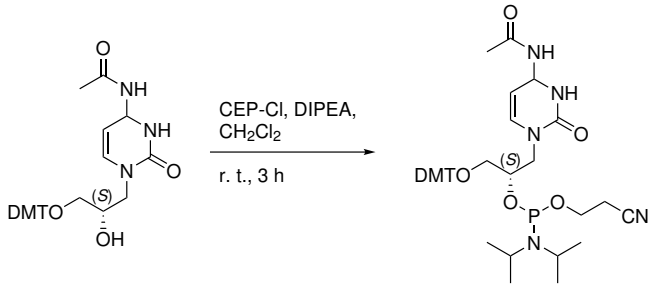

$C_{30}H_{32}N_3O_6$
530.60 g mol^{-1}
65

$C_{39}H_{50}N_5O_7P$
731.83 g mol^{-1}
66

Compound **65** (1.00 g, 1.89 mmol, 1.00 eq.) was dissolved under nitrogen atmosphere in anhydrous CH_2Cl_2 (32 mL). DIPEA (2.81 mL, 15.1 mmol, 8.00 eq.) and CEP-Cl (0.65 mL, 2.84 mmol, 1.50 eq.) were added dropwise and the reaction mixture was stirred for 3 h at ambient temperature. Afterwards, the solvent was removed in vacuum and column chromatography on silica gel (EtOAc + 2% NEt_3) afforded the target compound **66** as a white foam (1.01 g, 1.44 mmol, 76%).

^{1}H NMR (400 MHz, $CDCl_3$): δ = 9.23 (2 s, 1 H), 7.55 (dd, J = 13.8, 7.3 Hz, 1 H), 7.49 - 7.43 (m, 2 H), 7.38 - 7.13 (m, 8 H), 6.86 - 6.77 (m, 4 H), 4.45 - 4.05 (m, 2 H), 3.89 - 3.34 (m, 11 H), 3.29 - 3.06 (m, 1 H), 2.80 - 2.49 (m, 1 H), 2.44 - 2.36 (m, 1 H), 2.23 (d, J = 4.3 Hz, 3 H), 1.31 - 1.23 (m, 7 H), 1.18 - 1.06 (m, 12 H) ppm;
^{31}P NMR (162 MHz, $CDCl_3$): δ = 149.60, 149.43 ppm;
HR-MS (ESI+): m/z calc. ($C_{39}H_{50}N_5O_7P$, $[M+H]^+$): 731.3442, found: 731.3400.

(*S*)-9-(2,3-dihydroxypropyl)-2-amino-6-chloropurine (70)

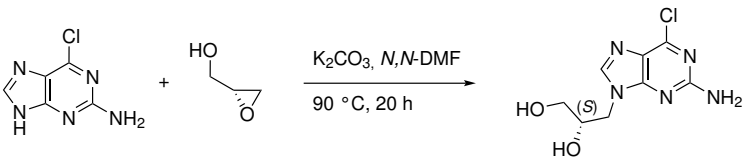

$C_5H_4ClN_5$
169. 57 g mol^{-1}

$C_3H_6O_2$
74.08 g mol^{-1}

$C_8H_{10}ClN_5O_2$
243.65 g mol^{-1}
70

2-Amino-6-chloropurine (4.80 g, 28.4 mmol, 1.00 eq.), (*R*)-glycidol (1.92 mL, 29.0 mmol, 1.02 eq.) and K_2CO_3 (660 mg, 4.80 mmol, 0.17 eq.) were dissolved in *N,N*-DMF (90 mL). The reaction mixture was heated to 90 °C for 20 h after which the solvent was removed in

vacuum. The residue was suspended in MeOH (100 mL), silica gel (2 g) was added and the solvent was again removed under reduced pressure. Column chromatography on silica gel (EtOAc/MeOH 25:3 to 20:3) afforded the target compound **70** as a white powder (2.55 g, 10.5 mmol, 37%).

^{1}H NMR (400 MHz, DMSO-d_6): δ = 8.02 (s, 1 H), 6.90 (s, 2 H), 5.11 (d, J = 5.4 Hz, 1 H), 4.83 (t, J = 5.6 Hz, 1 H), 4.19 (dd, J = 13.8, 3.3 Hz, 1 H), 3.90 (dd, J = 13.8, 8.7 Hz, 1 H), 3.85 - 3.75 (m, 1 H), 3.47 - 3.24 (m, 2 H) ppm;
HR-MS (ESI+): m/z calc. ($C_8H_{10}ClN_5NaO_2$, $[M+Na]^+$): 266.0415, found: 266.0419.

(*S*)-9-(2,3-Dihydroxypropyl)-guanine (71)

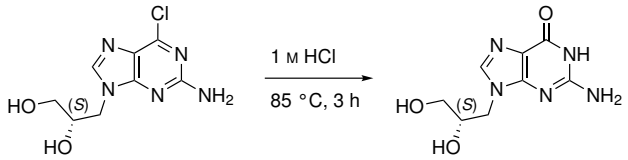

$C_8H_{10}ClN_5O_2$
243.65 g mol^{-1}
70

$C_8H_{11}N_5O_3$
225.21 g mol^{-1}
71

Compound **70** (2.00 g, 8.17 mmol, 1.00 eq.) was dissolved in 1 M HCl and heated for 3 h to 85 °C. After cooling to r. t., aq. NH_3 was added until a pH of 9 was reached. The formed precipitate was filtered off and dried in high vacuum which gave the target compound **71** as a white powder (1.20 g, 5.34 mmol, 65%).

^{1}H NMR (400 MHz, DMSO-d_6): δ = 10.72 (s, 1 H), 7.60 (s, 1 H), 6.63 (s, 2 H), 5.10 (d, J = 4.7 Hz, 1 H), 4.84 (s, 1 H), 4.08 (dd, J = 13.4, 3.2 Hz, 1 H), 3.84 - 3.69 (m, 2 H), 3.40 - 3.23 (m, 2 H) ppm;
HR-MS (ESI+): m/z calc. ($C_8H_{11}N_5NaO_3$, $[M+Na]^+$): 248.0754, found: 248.0758.

(*S*)-9-(3-(4,4'-Dimethoxytrityloxy)-2-hydroxypropyl)-N^2-[(dimethylamino)methylene]-guanine (73)

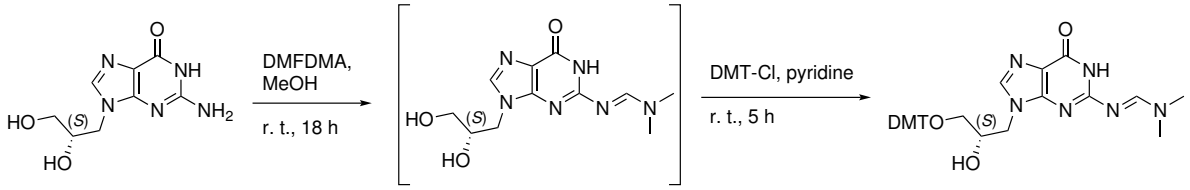

$C_8H_{11}N_5O_3$
225.21 g mol^{-1}
71

$C_{11}H_{16}N_6O_3$
280.29 g mol^{-1}
72

$C_{32}H_{34}N_6O_5$
582.66 g mol^{-1}
73

Compound **71** (630 mg, 2.77 mmol, 1.00 eq.) was suspended under nitrogen atmosphere in anhydrous MeOH (12 mL). DMFDMA (1.48 mL, 11.1 mmol, 4.00 eq.) was added and the reaction mixture was stirred at r. t. for 18 h. Afterwards, the solvent was removed

in vacuum and the residue was dried in high vacuum. The residue was then redissolved in anhydrous pyridine (15 mL) and DMT-Cl (1.12 g, 3.32 mmol, 1.20 eq.) was added in three portions within 3 h under nitrogen atmosphere. After stirring for additional 2 h at r. t., the solvent was removed under reduced pressure and column chromatography on silica gel (CH_2Cl_2/MeOH 100:1 to 9:1 + 2% NEt_3) afforded the target compound **73** as a white foam (591 mg, 1.01 mmol, 37% over two steps).

^{1}H NMR (400 MHz, $CDCl_3$): δ = 8.85 (s, 1 H), 8.46 (d, J = 0.9 Hz, 1 H), 7.48 - 7.43 (m, 3 H), 7.41 - 7.14 (m, 7 H), 6.85 - 6.77 (m, 4 H), 4.38 (td, J = 13.6, 4.9 Hz, 2 H), 4.05 (dd, J = 13.8, 7.2 Hz, 1 H), 3.78 (s, 6 H), 3.33 (dd, J = 9.4, 5.0 Hz, 1 H), 3.09 - 3.01 (m, 4 H), 2.94 (s, 3 H) ppm;
HR-MS (ESI+): *m/z* calc. ($C_{32}H_{34}N_6NaO_5$, $[M+Na]^+$): 605.2483, found: 605.2484.

(*S*)-9-(3-(4,4'-Dimethoxytrityloxy)-2-hydroxypropyl)-*N*^{2}-[(dimethylamino)methylene]-guanine phosphoramidite (gG-PA, 74)

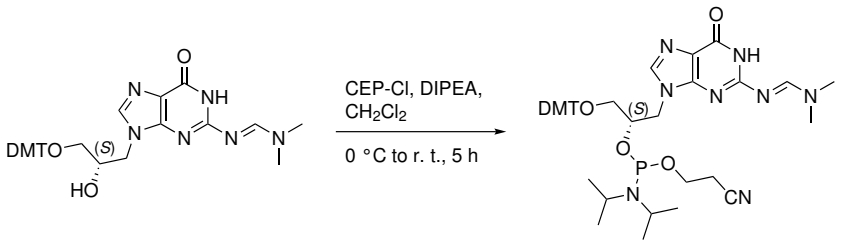

$C_{32}H_{34}N_6O_5$
582.66 g mol^{-1}
73

$C_{41}H_{51}N_8O_6P$
782.88 g mol^{-1}
74

Compound **73** (800 mg, 1.37 mmol, 1.00 eq.) was dissolved under nitrogen atmosphere in anhydrous CH_2Cl_2 (24 mL). The resulting solution was cooled to 0 °C, DIPEA (2.55 mL, 13.7 mmol, 10.0 eq.) and CEP-Cl (0.47 mL, 2.06 mmol, 1.50 eq.) were added dropwise and the reaction mixture was stirred for 35 h at ambient temperature. Afterwards, the solvent was removed in vacuum and column chromatography on silica gel (acetone/*n*-hexane 2:1 + 2% NEt_3) afforded the target compound **74** as a white foam (440 mg, 562 µmol, 41%).

^{1}H NMR (400 MHz, $CDCl_3$): δ = 9.25 (s, 1 H), 8.51 (s, 1 H), 7.49 - 7.43 (m, 2 H), 7.36 - 7.15 (m, 7 H), 6.85 - 6.76 (m, 4 H), 4.49 (ddd, J = 20.3, 14.0, 3.2 Hz, 1 H), 4.42 - 4.30 (m, 1 H), 4.17 (ddd, J = 14.1, 7.4, 3.1 Hz, 1 H), 3.78 (d, J = 3.1 Hz, 6 H), 3.68 - 3.42 (m, 3 H), 3.27 (ddd, J = 32.0, 9.6, 4.9 Hz, 1 H), 3.17 - 2.99 (m, 3 H), 2.81 (d, J = 2.3 Hz, 3 H), 2.56 - 2.29 (m, 2 H), 1.19 - 0.98 (m, 12 H) ppm;
^{31}P NMR (162 MHz, $CDCl_3$): δ = 149.62, 149.28 ppm;
HR-MS (ESI+): *m/z* calc. ($C_{41}H_{51}N_8NaO_6P$, $[M+Na]^+$): 805.3561, found: 805.3550.

3-*O*-(4,4'-dimethoxytrityloxy)methyl (*S*)-1-(2,3-dihydroxypropyl) thymine (62)

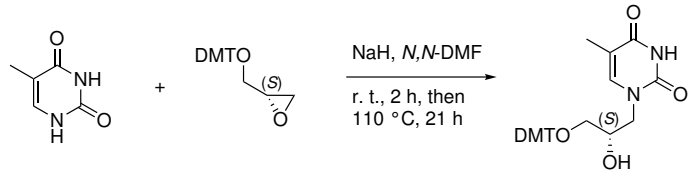

$C_5H_6N_2O_2$ 126.12 g mol^{-1}

$C_{24}H_{24}O_4$ 376.45 g mol^{-1} **61**

$C_{29}H_{30}N_2O_6$ 502.57 g mol^{-1} **62**

Thymine (1.25 g, 9.81 mmol, 1.06 eq.) and NaH (60% oil dispersion, 85.0 mg, 1.85 mmol, 0.22 eq.) in anhydrous *N,N*-DMF (20 mL) were stirred for 1 h at r. t. under nitrogen atmosphere. Afterwards, DMT-protected glycidol **61** (3.53 g, 9.26 mmol, 1.00 eq.) in anhydrous *N,N*-DMF (15 mL) was added and the mixture was heated for 21 h to 110 °C. The reaction was cooled to r. t., the precipitate was filtered off and the solvent of the filtrate was removed in vacuum. Column chromatography on silica gel (CH_2Cl_2/MeOH 98:2 to 95:5 + 1% NEt_3) afforded the target compound **62** as a white foam (2.05 g, 4.08 mmol, 44%).

^{1}H NMR (400 MHz, $CDCl_3$): δ = 7.43 - 7.38 (m, 2 H), 7.33 - 7.18 (m, 7 H), 7.04 (q, J = 1.2 Hz, 1 H), 6.85 - 6.80 (m, 4 H), 4.11 - 3.98 (m, 2 H), 3.79 (s, 6 H), 3.69 - 3.59 (m, 1 H), 3.17 (d, J = 5.5 Hz, 2 H), 1.83 (d, J = 1.2 Hz, 3 H) ppm;
HR-MS (ESI+): *m/z* calc. ($C_{29}H_{30}N_2NaO_6$, $[M+Na]^+$): 525.1996, found: 525.1997.

3-*O*-(4,4'-Dimethoxytrityloxy)methyl (*S*)-1-(2,3-dihydroxypropyl) thymine phosphoramidite (gT-PA, 63)

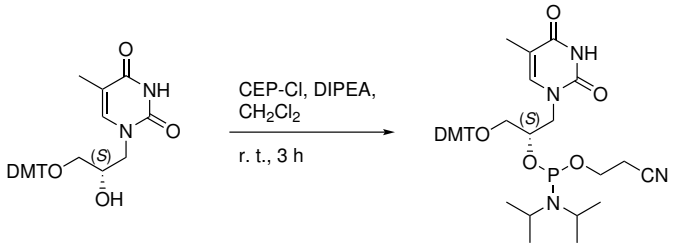

$C_{29}H_{30}N_2O_6$ 502.57 g mol^{-1} **62**

$C_{38}H_{47}N_4O_7P$ 702.79 g mol^{-1} **63**

Compound **62** (1.10 g, 2.20 mmol, 1.00 eq.) was dissolved under nitrogen atmosphere in anhydrous CH_2Cl_2 (36 mL). DIPEA (2.20 mL, 11.7 mmol, 5.32 eq.) and CEP-Cl (0.68 mL, 3.10 mmol, 1.41 eq.) were added dropwise and the reaction mixture was stirred for 3 h at ambient temperature. Afterwards, the solvent was removed in vacuum and column chromatography on silica gel (EtOAc/*n*-hexane 2:1 + 2% NEt_3) afforded the target compound **63** as a white foam (1.21 g, 1.72 mmol, 78%).

^{1}H NMR (400 MHz, $CDCl_3$): δ = 8.61 (s, 1 H), 7.48 - 7.42 (m, 2 H), 7.37 - 7.16 (m, 8 H), 7.09 - 7.00 (m, 1 H), 6.91 - 6.75 (m, 4 H), 4.28 - 4.17 (m, 1 H), 4.10 - 4.03 (m, 1 H), 3.86 -

3.48 (m, 10 H), 3.33 - 3.09 (m, 2 H), 2.63 - 2.55 (m, 1 H), 1.83 (dd, J = 2.4, 1.2 Hz, 3 H), 1.21 - 1.09 (m, 12 H) ppm;
^{31}P NMR (162 MHz, $CDCl_3$): δ = 149.56, 149.39 ppm;
HR-MS (ESI+): *m/z* calc. ($C_{38}H_{47}N_4NaO_7P$, $[M+Na]^+$): 725.3075, found: 725.3071.

5.1.2.6 Preparation of gBAM phosphoramidites

For gBAM phosphoramidites, NMR assignments are only given for signals which were assigned unambiguously.

General procedure VII: epoxide ring-opening reaction with DMT-protected glycidol

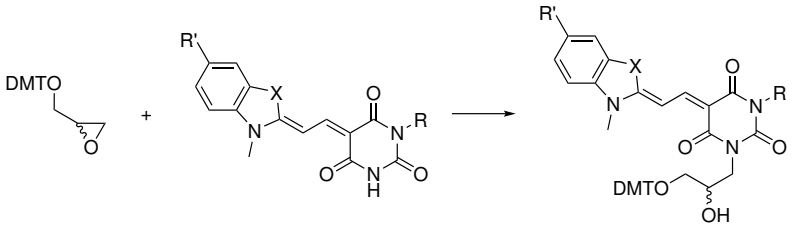

The free chromophore (1.43 eq.), K_2CO_3 (2.21 eq.) and NaH (1.43 eq.) were suspended under nitrogen atmosphere in anhydrous DMF (3 mL per mmol chromophore) and stirred for 2 h at r. t. DMT-protected glycidol (1.00 eq.) in anhydrous DMF (9 mL per mmol glycidol) was added and the reaction mixture was heated to 110 °C for up to 12 h. The reaction mixture was cooled to r. t. and filtered over celite. After removal of the solvent in vacuum the residue was purified by column chromatography. For chromophores with two equal unmethylated barbituric acid nitrogens comparably low yields were obtained since the reaction had to be stopped before the starting material was completely consumed due to the formation of a double-substituted side product.

3-*O*-(4,4'-Dimethoxytrityloxy)methyl (*S*)-1-(2,3-dihydroxypropyl) barbituric acid indolenine merocyanine (DMT-gBAM, 79)

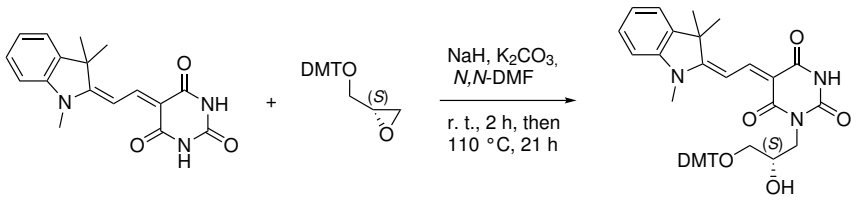

$C_{17}H_{17}N_3O_3$ 311.34 g mol^{-1} **1**
$C_{24}H_{24}O_4$ 376.45 g mol^{-1} **61**
$C_{41}H_{41}N_3O_7$ 687.79 g mol^{-1} **79**

Compound **79** was synthesized according to general procedure VII on a 1.80 mmol scale and was obtained as a bright orange foam (251 mg, 360 µmol, 20%) after column chromatography on silica gel (packed with acetone/*n*-hexane 1:1 + 2% NEt_3, eluted with acetone/*n*-hexane

3:2 to 1:1 + 2% NEt_3).

^{1}H NMR (400 MHz, $CDCl_3$): δ = 8.66 (d, J = 14.6 Hz, 1 H, COCC*H*), 7.59 (2 d, J = 14.5 Hz, 1 H, NCC*H*), 7.52 - 7.15 (m, 17 H, DMT-*H*), 7.09 - 7.04 (s, 1 H), 6.89 - 6.75 (m, 4 H, DMT-*H*), 4.26 (dd, J = 13.9, 9.1 Hz, 1 H, glycido-3-CH_2), 4.20 - 4.03 (m, 2 H, glycido-2-C*H*, glycido-3-CH_2), 3.78 (2 s, 6 H, DMT-OCH_3), 3.56 (2 s, 3 H, NCH_3), 3.31 - 3.14 (m, 2 H, glycido-1-CH_2), 2.31 (s, 2 H), 1.72 (s, 6 H, 2×CH_3) ppm;
^{13}C{^{1}H} NMR (100 MHz, $CDCl_3$): δ = 177.74 (Ind-*C*-2), 177.59 Ind-*C*-2), 165.60 (BA-carbonyl-*C*), 164.85 (BA-carbonyl-*C*), 162.54, 158.41 (DMT-*C*), 158.38 (DMT-*C*), 152.36 (COC*C*H), 151.61 (COC*C*H), 151.51 (COC*C*H), 144.94, 144.89, 144.86, 142.55 (Ind-*C*-7a), 140.99 (Ind-*C*-3a), 136.11 (DMT-*C*), 136.08 (DMT-*C*), 130.12, 130.06, 130.00, 128.47, 128.23, 128.16, 128.05, 127.90, 127.79, 126.71, 126.68, 124.99, 122.16, 113.17 (DMT-*C*), 113.08 (DMT-*C*), 110.02 (Ind-*C*-5), 100.88, 100.81, 99.06 (NC*C*H), 98.65 (NC*C*H), 85.92 (DMT-*C*), 70.51 (glycido-2-*C*H), 70.46 (glycido-2-*C*H), 66.89 (glycido-1-*C*H_2), 66.15 (glycido-1-*C*H_2), 65.73 (glycido-1-*C*H_2), 65.64 (glycido-1-*C*H_2), 62.54, 55.20 (DMT-O*C*H_3), 49.16 (Ind-*C*-3), 45.41, 44.81 (glycido-3-*C*H_2), 44.04 (glycido-3-*C*H_2), 36.49, 31.43 (N*C*H_3), 28.84 (2×*C*H_3) ppm;
HR-MS (ESI+): *m/z* calc. ($C_{41}H_{41}N_3NaO_7$, $[M+Na]^+$): 710.2837, found: 710.2837.

3-*O*-(4,4'-Dimethoxytrityloxy)methyl (*R*)-1-(2,3-dihydroxypropyl) barbituric acid indolenine merocyanine (DMT-gBAM^R, 80)

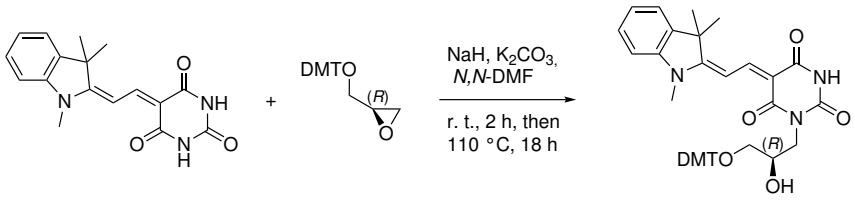

$C_{17}H_{17}N_3O_3$ 311.34 g mol^{-1} **1**
$C_{24}H_{24}O_4$ 376.45 g mol^{-1} **78**
$C_{41}H_{41}N_3O_7$ 687.79 g mol^{-1} **80**

Compound **80** was synthesized according to general procedure VII on a 1.52 mmol scale and was obtained as a bright orange foam (241 mg, 350 µmol, 23%) after column chromatography on silica gel (packed with acetone/*n*-hexane 1:1 + 2% NEt_3, eluted with acetone/*n*-hexane 3:2 to 1:1 + 2% NEt_3).

^{1}H NMR (400 MHz, $CDCl_3$): δ = 8.70 - 8.62 (m, 1 H, COCC*H*), 7.80 - 7.15 (m, Ind-*H*, DMT-*H*), 7.11 - 7.05 (m, 1 H), 6.88 - 6.78 (m, 4 H, DMT-*H*), 4.28 (dd, J = 13.9, 9.2 Hz, 1 H, glycido-3-CH_2), 4.20 - 4.03 (m, 2 H, glycido-2-C*H*, glycido-3-CH_2), 3.78 (2 s, 6 H, DMT-OCH_3), 3.61 - 3.52 (m, 3 H, NC_3), 3.29 - 3.16 (m, 2 H, glycido-1-CH_2), 1.72 (s, 6 H, 2×CH_3) ppm;
^{13}C{^{1}H} NMR (100 MHz, $CDCl_3$): δ = 177.75 (Ind-*C*-2), 177.58 Ind-*C*-2), 165.60 (BA-

carbonyl-*C*), 164.85 (BA-carbonyl-*C*), 162.54, 158.41 (DMT-*C*), 158.38 (DMT-*C*), 152.36 (COC*C*H), 151.61 (COC*C*H), 151.51 (COC*C*H), 144.94, 144.89, 144.86, 142.55 (Ind-*C*-7a), 140.98 (Ind-*C*-3a), 136.11 (DMT-*C*), 136.08 (DMT-*C*), 130.12, 130.06, 130.00, 128.47, 128.23, 128.16, 128.05, 127.90, 127.79, 126.71, 126.68, 124.99, 122.16, 113.17 (DMT-*C*), 113.08 (DMT-*C*), 110.02 (Ind-*C*-5), 100.88, 100.81, 99.06 (NC*C*H), 98.65 (NC*C*H), 85.92 (DMT-*C*), 70.51 (glycido-2-*C*H), 70.46 (glycido-2-*C*H), 66.91 (glycido-1-*C*H_2), 66.15 (glycido-1-*C*H_2), 65.73 (glycido-1-*C*H_2), 65.64 (glycido-1-*C*H_2), 62.54, 55.20 (DMT-O*C*H_3), 49.16 (Ind-*C*-3), 45.41, 44.81 (glycido-3-*C*H_2), 44.04 (glycido-3-*C*H_2), 36.49, 31.43 (N*C*H_3), 28.83 (2×*C*H_3) ppm;
HR-MS (ESI+): *m/z* calc. ($C_{41}H_{41}N_3NaO_7$, $[M+Na]^+$): 710.2837, found: 710.2836.

3-*O*-(4,4'-Dimethoxytrityloxy)methyl (*S*)-1-(2,3-dihydroxypropyl) barbituric acid 5-methoxy-indolenine merocyanine (DMT-gBAM^F, 85)

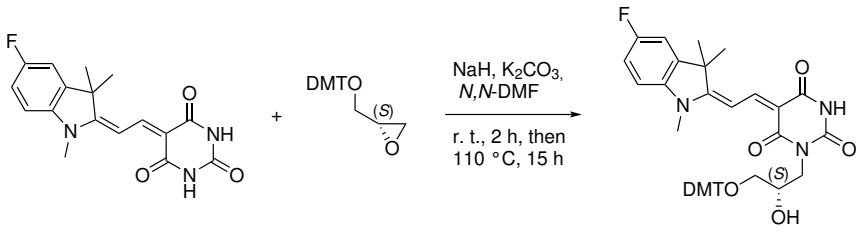

$C_{17}H_{16}FN_3O_3$
329.33 g mol^{-1}
2

$C_{24}H_{24}O_4$
376.45 g mol^{-1}
61

$C_{41}H_{40}FN_3O_7$
705.78 g mol^{-1}
85

Compound **85** was synthesized according to general procedure VII on a 6.07 mmol scale and was obtained as a bright orange foam (442 mg, 620 µmol, 15%) after column chromatography on silica gel (EtOAc + 2% NEt_3).

^{1}H NMR (400 MHz, $CDCl_3$): δ = 8.63 (dd, J = 14.6, 2.7 Hz, 1 H, COCC*H*), 7.68 (2 s, 1 H, N*H*), 7.55 (dd, J = 14.5, 1.3 Hz, 1 H, NCC*H*), 7.50 - 7.46 (m, 2 H), 7.38 - 7.34 (m, 4 H, DMT-*H*), 7.31 - 7.27 (m, 2 H), 7.23 - 7.18 (m, 1 H), 7.10 - 7.05 (m, 2 H), 7.01 - 6.97 (m, 1 H), 6.85 - 6.81 (m, 4 H, DMT-*H*), 4.27 (dd, J = 13.9, 9.2 Hz, 1 H, glycido-2-C*H*), 4.15 - 4.10 (m, 2 H, glycido-3-CH_2), 3.79 (2 s, 6 H, DMT-OCH_3), 3.55 (2 s, 3 H, NCH_3), 3.27 - 3.16 (m, 3 H, glycido-1-CH_2), 1.72 (2 s, 6 H, 2×CH_3) ppm;
^{13}C{^{1}H} NMR (100 MHz, $CDCl_3$): δ = 162.93 (BA-carbonyl-*C*), 158.87 (DMT-*C*), 136.55 (DMT-*C*), 130.57 (DMT-*C*), 128.68 (DMT-*C*), 128.27 (DMT-*C*), 127.17 (DMT-*C*), 113.55 (DMT-*C*), 111.09 (Ind-*C*), 96.07 (DMT-C_{quart}), 86.41, 77.80, 70.90 (glycido-3-*C*H_2), 66.06 (glycido-2-*C*H), 55.67 (DMT-O*C*H_3), 29.23 (2×*C*H_3), 28.13 (N*C*H_3) ppm;
HR-MS (ESI+): *m/z* calc. ($C_{41}H_{40}FN_3NaO_7$, $[M+Na]^+$): 728.2743, found: 728.2747.

3-*O*-(4,4'-Dimethoxytrityloxy)methyl (*S*)-1-(2,3-dihydroxypropyl) barbituric acid 5-fluoro-indolenine merocyanine (DMT-gBAM^{OMe}, 86)

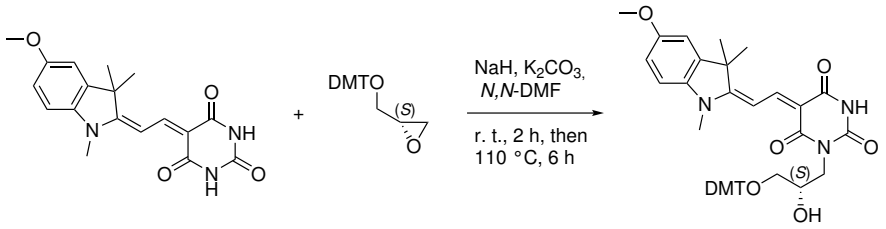

$C_{18}H_{19}N_3O_4$ 341.37 g mol^{-1} **3**

$C_{24}H_{24}O_4$ 376.45 g mol^{-1} **61**

$C_{42}H_{43}N_3O_8$ 717.82 g mol^{-1} **86**

Compound **86** was synthesized according to general procedure VII on a 2.05 mmol scale and was obtained as a bright orange foam (301 mg, 412 µmol, 20%) after column chromtography on silica gel (EtOAc + 2% NEt_3).

^{1}H NMR (400 MHz, $CDCl_3$): δ = 8.61 (d, J = 14.7 Hz, 1 H, COCC*H*), 7.50 - 7.43 (m, 3 H, NCC*H*), 7.38 - 7.27 (m, 8 H), 6.85 - 6.80 (m, 4 H, DMT-*H*), 3.85 (2 s, 3 H, OCH_3), 3.79 (2 s, 8 H, DMT-OCH_3), 3.56 (s, 3 H, NCH_3), 3.24 - 3.15 (m, 2 H), 3.06 (dd, J = 9.4, 4.9 Hz, 1 H), 1.72 (2 s, 6 H, 2×CH_3). ppm;
^{13}C{^{1}H} NMR (100 MHz, $CDCl_3$): δ = 165.86 (BA-carbonyl-*C*), 165.09 (BA-carbonyl-*C*), 162.68 (BA-carbonyl-*C*), 158.53 (DMT-*C*), 151.71, 145.08, 142.93, 142.01, 136.27, 130.26, 130.21, 128.31, 127.93, 126.83, 113.22, 110.88, 109.14, 99.91, 99.23, 98.85, 86.06, 67.06, 66.30, 62.64, 56.08 (DMT-O*C*H_3), 55.35, 45.64, 31.58 (2×*C*H_3), 28.93 (N*C*H_3) ppm;
HR-MS (ESI+): *m/z* calc. ($C_{42}H_{43}N_3NaO_8$, $[M+Na]^+$): 740.2942, found: 740.2944.

3-*O*-(4,4'-Dimethoxytrityloxy)methyl (*S*)-1-(2,3-dihydroxypropyl) 3-methyl-barbituric acid indolenine merocyanine (DMT-gmBAM, 83)

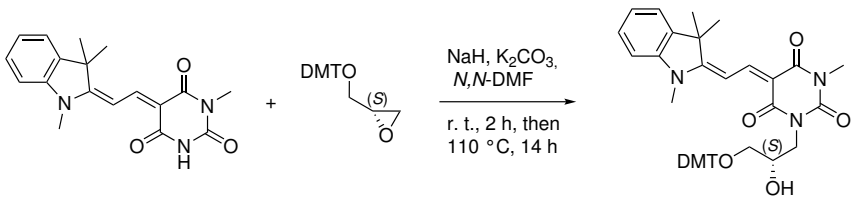

$C_{18}H_{19}N_3O_3$ 325.37 g mol^{-1} **4**

$C_{24}H_{24}O_4$ 376.45 g mol^{-1} **61**

$C_{42}H_{43}N_3O_7$ 701.82 g mol^{-1} **83**

Compound **83** was synthesized according to general procedure VII with 1.00 eq. of free chromophore **4**, DMT-protected glycidol and K_2CO_3 and 0.50 eq. of NaH and **61** on a 1.53 mmol scale and was obtained as a bright orange foam (272 mg, 391 µmol, 26%) after column chromatography on silica gel (packed with acetone/*n*-hexane 1:1 + 2% NEt_3, eluted with acetone/*n*-hexane 3:2 to 1:1 + 2% NEt_3).

^{1}H NMR (400 MHz, $CDCl_3$): δ = 8.72 (2 d, J = 14.5 Hz, 1 H, COCC*H*), 7.60 (2 d, J = 14.5 Hz, 1 H, NCC*H*), 7.52 - 7.17 (m, 12 H, DMT-*H*, Ind-*H*), 7.09 - 7.02 (m, 1 H, Ind-*H*), 6.86 - 6.75 (m, 4 H, DMT-*H*), 4.32 (dd, J = 13.9, 9.2 Hz, 1 H, glycido-1-CH_2), 4.17 (ddd, J = 13.9, 2.9, 2.1 Hz, 1 H, glycido-1-CH_2), 4.08 (dd, J = 12.2, 6.3 Hz, 1 H, glycido-2-C*H*), 3.78 (s, 6 H, DMT-OCH_3), 3.56 (d, J = 5.1 Hz, 3 H, NCH_3), 3.39 - 3.31 (m, 4 H, BAM-NCH_3, glycido-2-O*H*), 3.21 (qdd, J = 9.4, 4.7, 2.1 Hz, 2 H, glycido-3-CH_2), 1.72 (2 s, 6 H, 2×CH_3) ppm;
^{13}C{^{1}H} NMR (100 MHz, $CDCl_3$): δ = 177.41 (BA-carbonyl-*C*), 164.87 (Ind-*C*-2), 164.19 (BA-carbonyl-*C*), 163.93 (BA-carbonyl-*C*), 158.51 (DMT-*C*), 152.96 (COC*C*H), 145.06 (BA-N*C*ON), 145.03, 142.78, 141.11, 136.27, 136.24, 130.26, 128.56, 128.36, 127.92, 126.80, 124.91, 122.29, 113.21 (DMT-*C*), 109.96 (Ind-*C*), 98.77 (NC*C*H) 86.04 (DMT-C_{quart}), 70.73 (glycido-2-*C*H), 70.70 (glycido-2-*C*H), 55.33 (DMT-O*C*H_3), 53.90 (glycido-2-*C*H_2), 49.18 (Ind-*C*), 44.83 (glycido-1-*C*H_2), 31.73 (N*C*H_3), 29.40 (2×*C*H_3), 14.27 (N*C*H_3) ppm;
HR-MS (ESI+): m/z calc. ($C_{42}H_{43}N_3NaO_7$, $[M+Na]^+$): 724.2993, found: 724.2990.

3-*O*-(4,4'-Dimethoxytrityloxy)methyl (*S*)-1-(2,3-dihydroxypropyl) 3-methyl-barbituric acid benzothiazole merocyanine (DMT-gmBAM^b, 84)

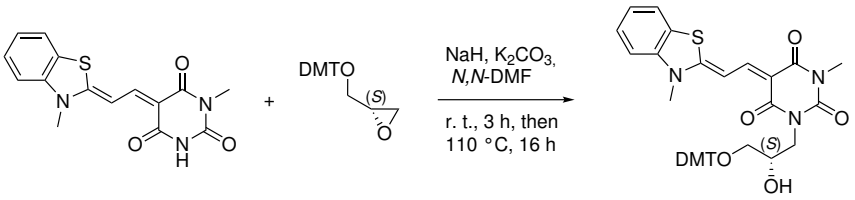

$C_{15}H_{13}N_3O_3S$ | 315.35 g mol^{-1} | **8**
$C_{24}H_{24}O_4$ | 376.45 g mol^{-1} | **61**
$C_{39}H_{37}N_3O_7S$ | 691.80 g mol^{-1} | **84**

Compound **84** was synthesized according to general procedure VII with 1.00 eq. of free chromophore **8**, K_2CO_3 and NaH and 1.60 eq. of DMT-protected glycidol **61** on a 2.53 mmol scale and was obtained as a bright orange foam (1.13 g, 1.64 mmol, 65%) after column chromatography on silica gel (packed with acetone/*n*-hexane 1:1 + 2% NEt_3, eluted with acetone/*n*-hexane 3:2 to 1:1 + 2% NEt_3).

^{1}H NMR (400 MHz, $CDCl_3$): δ = 8.26 (ddd, J = 18.5, 14.0, 1.9 Hz, 1 H, COCC*H*), 7.73 - 7.60 (m, 2 H, arom-*H*-7, NCC*H*), 7.51 - 7.25 (m, 13 H, arom-*H*-4, arom-*H*-5, DMT-*H*), 7.23 - 7.16 (m, 1 H, arom-*H*-6), 6.86 - 6.80 (m, 4 H, DMT-*H*), 4.24 (ddd, J = 13.9, 9.2, 1.8 Hz, 1 H, glycido-1-CH_2), 4.13 (ddd, J = 13.4, 10.0, 2.7 Hz, 1 H, glycido-1-CH_2), 4.06 (s, 1 H, glycido-2-C*H*), 3.80 - 3.71 (m, 9 H, NCH_3, DMT-OCH_3), 3.49 (dd, J = 14.4, 6.0 Hz, 1 H, glycido-2-O*H*), 3.26 (dd, J = 5.2, 1.1 Hz, 3 H, BAM-NCH_3), 3.24 - 3.19 (m, 2 H, glycido-3-CH_2) ppm;
^{13}C{^{1}H} NMR (100 MHz, $CDCl_3$): δ = 170.29 (CO*C*), 170.25 (CO*C*), 164.63 (BA-carbonyl-*C*), 164.32 (BA-carbonyl-*C*), 163.35 (arom-*C*-2), 158.50 (DMT-*C*), 152.76 (BA-N*C*ON),

152.69 (BA-N*C*ON), 149.62 (COC*C*H), 149.48 (COC*C*H), 145.06, 145.04, 141.71, 136.28, 136.25, 136.23, 130.27, 130.25, 130.23, 128.35, 127.92, 127.84, 126.80, 125.65, 125.63, 125.39, 125.34, 122.59, 113.20, 112.41, 112.36, 99.24, 99.17, 97.81, 97.78, 86.03, 86.02, 70.81 (glycido-2-*C*H), 70.78 (glycido-2-*C*H), 69.62, 65.97 (glycido-3-CH_2), 65.93 (glycido-3-CH_2), 55.32 (DMT-OCH_3), 53.89, 45.95, 45.58 (glycido-1-CH_2), 44.95, 33.58 (NCH_3), 33.53 (NCH_3), 31.87, 31.07, 29.39, 28.26, 27.58 (BA-NCH_3) ppm;
HR-MS (ESI+): *m/z* calc. ($C_{39}H_{37}N_3NaO_7S$, $[M+Na]^+$): 714.2424, found: 714.2426.

General procedure VIII: phosphitylation

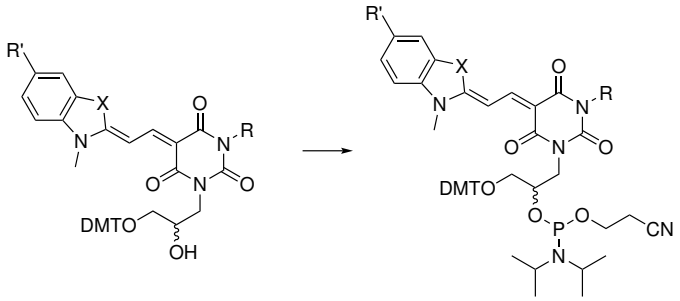

DMT-protected glycidol merocyanines (1.00 eq.) were dissolved in anhydrous CH_2Cl_2 (20 mL per mmol) under nitrogen atmosphere. Me_2NEt (10.0 eq.) and CEP-Cl (1.50 eq.) were added dropwise and the reaction mixture was stirred at r. t. for 2 h. After the reaction was completed, the solvent was removed in vacuum and the crude product was purified by column chromatography on silica gel.

3-*O*-(4,4'-Dimethoxytrityloxy)methyl (*S*)-1-(2,3-dihydroxypropyl) barbituric acid indolenine merocyanine phosphoramidite (gBAM-PA, 81)

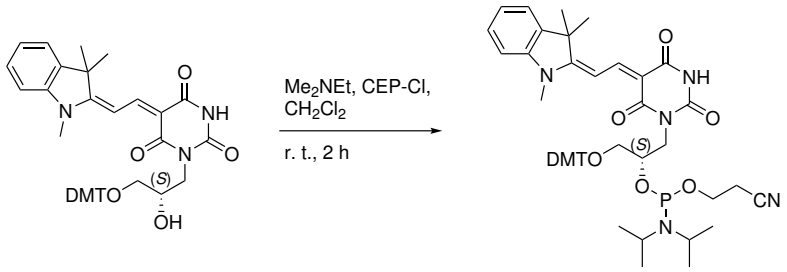

$C_{41}H_{41}N_3O_7$
687.79 g mol^{-1}
79

$C_{50}H_{58}N_5O_8P$
888.01 g mol^{-1}
81

Compound **81** was synthesized according to general procedure VIII on a 230 µmol scale and was isolated after column chromatography on silica gel (EtOAc/*n*-hexane 8:2 + 2% NEt_3) as an orange foam (187 mg, 210 µmol, 91%).

^{1}H NMR (400 MHz, $CDCl_3$): δ = 8.71 - 8.49 (m, 1 H, COCC*H*), 7.59 - 7.46 (m, 1 H, NCC*H*), 7.46 - 7.07 (m, 13 H, Ind-*H*-4, Ind-*H*-5, Ind-*H*-6, DMT-*H*), 7.02 - 6.95 (m, 1 H,

Ind-*H*-7), 6.80 - 6.69 (m, 4 H, DMT-*H*), 4.47 - 4.20 (m, 2 H), 4.19 - 3.79 (m, 1 H), 3.71 (2 s, 6 H, DMT-OCH_3), 3.53 - 3.44 (m, 3 H, *i*Pr-C*H*), 3.43 - 3.09 (m, 1 H), 3.07 - 2.97 (m, 1 H), 2.72 - 2.59 (m, 1 H), 2.57 - 2.46 (m, 1 H), 2.37 - 2.27 (m, 1 H), 1.91 (s, 1 H), 1.71 - 1.58 (m, 6 H, 2×CH_3), 1.24 - 0.94 (m, 12 H, *i*Pr-CH_3) ppm;

^{13}C{^{1}H} NMR (100 MHz, $CDCl_3$): δ = 177.48 (Ind-*C*-2), 177.30 (Ind-*C*-2), 177.19 (Ind-*C*-2), 177.14 (Ind-*C*-2), 164.70 (BA-carbonyl-*C*), 164.42 (BA-carbonyl-*C*), 164.06 (BA-carbonyl-*C*), 163.70 (BA-carbonyl-*C*), 163.53 (BA-carbonyl-*C*), 163.36 (BA-carbonyl-*C*), 163.25 (BA-carbonyl-*C*), 158.66 (DMT-*C*), 158.43 (DMT-*C*), 152.30 (COC*C*H), 151.99 (COC*C*H), 151.33, 151.15, 150.95, 150.91, 145.02, 144.98, 142.74, 141.03, 136.35, 136.32, 136.25, 136.22, 136.20, 130.27 (DMT-*C*), 130.24 (DMT-*C*), 130.19 (DMT-*C*), 128.52, 128.40, 128.34, 127.82, 127.80, 126.74, 126.70, 124.88, 124.83, 122.22, 117.97, 117.88, 117.79, 113.30 (DMT-*C*), 113.12 (DMT-*C*), 113.08 (DMT-*C*), 110.01 (Ind-*C*-7), 109.93 (Ind-*C*-7), 101.43, 101.37, 101.33, 98.82 (NC*C*H), 98.21 (CNC*C*H), 86.13, 86.02, 77.48, 77.16, 76.84, 69.80, 69.69, 65.51, 58.67, 58.47, 58.26, 58.20, 58.08, 55.29 (DMT-O*C*H_3), 49.18 (Ind-*C*-3), 49.10 (Ind-*C*-3), 45.41, 45.35, 43.47, 43.31, 43.18, 43.04, 42.94, 42.47, 28.89 (2×*C*H_3), 24.86 (*i*Pr-*C*H_3), 24.78 (*i*Pr-*C*H_3), 24.71 (*i*Pr-*C*H_3), 24.64 (*i*Pr-*C*H_3), 24.56 (*i*Pr-*C*H_3), 24.47 (*i*Pr-*C*H_3), 23.08, 23.06, 23.00, 22.97, 20.16, 20.01 ppm;

^{31}P NMR (162 MHz, $CDCl_3$): δ = 149.27, 149.23, 149.16, 149.12 ppm;

HR-MS (ESI+): *m/z* calc. ($C_{50}H_{58}N_5NaO_8P$, $[M+Na]^+$): 910.3915, found: 910.3914.

3-*O*-(4,4'-Dimethoxytrityloxy)methyl (*R*)-1-(2,3-dihydroxypropyl) barbituric acid indolenine merocyanine phosphoramidite (gBAM^R-PA, 82)

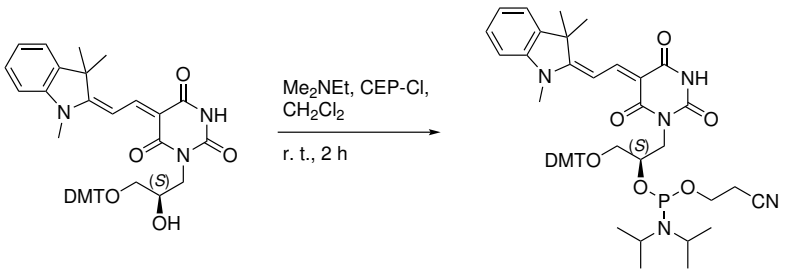

$C_{41}H_{41}N_3O_7$
687.79 g mol^{-1}
80

$C_{50}H_{58}N_5O_8P$
888.01 g mol^{-1}
82

Compound **82** was synthesized according to general procedure VIII on a 350 µmol scale and was isolated after column chromatography on silica gel (EtOAc/*n*-hexane 7:3 + 2% NEt_3) as an orange foam (277 mg, 312 µmol, 89%).

^{1}H NMR (400 MHz, $CDCl_3$): δ = 8.71 - 8.48 (m, 1 H, COCC*H*), 7.57 - 7.46 (m, 1 H, NCC*H*), 7.46 - 7.07 (m, 13 H, Ind-*H*-4, Ind-*H*-5, Ind-*H*-6, DMT-*H*), 7.02 - 6.95 (m, 1 H, Ind-*H*-7), 6.80 - 6.69 (m, 4 H, DMT-*H*), 4.46 - 4.20 (m, 2 H), 4.19 - 3.79 (m, 1 H), 3.71 (2 s, 6 H, DMT-OCH_3), 3.53 - 3.44 (m, 3 H, *i*Pr-C*H*), 3.43 - 3.09 (m, 1 H), 3.08 - 2.97 (m, 1 H), 2.72 - 2.61 (m, 1 H), 2.57 - 2.46 (m, 1 H), 2.37 - 2.27 (m, 1 H), 1.91 (s, 1 H), 1.71 -

1.59 (m, 6 H, 2×CH_3), 1.24 - 0.94 (m, 12 H, *i*Pr-CH_3) ppm;
^{13}C{^{1}H} NMR (100 MHz, $CDCl_3$): δ = 177.48 (Ind-*C*-2), 177.31 (Ind-*C*-2), 177.19 (Ind-*C*-2), 177.14 (Ind-*C*-2), 164.70 (BA-carbonyl-*C*), 164.42 (BA-carbonyl-*C*), 164.06 (BA-carbonyl-*C*), 163.70 (BA-carbonyl-*C*), 163.53 (BA-carbonyl-*C*), 163.36 (BA-carbonyl-*C*), 163.25 (BA-carbonyl-*C*), 158.66 (DMT-*C*), 158.43 (DMT-*C*), 152.30 (COC*C*H), 151.99 (COC*C*H), 151.32, 151.15, 150.97, 150.91, 145.02, 144.98, 142.74, 141.03, 136.35, 136.32, 136.25, 136.22, 136.20, 130.27 (DMT-*C*), 130.24 (DMT-*C*), 130.19 (DMT-*C*), 128.52, 128.40, 128.34, 127.82, 127.80, 126.74, 126.70, 124.88, 124.83, 122.24, 117.97, 117.88, 117.81, 113.30 (DMT-*C*), 113.12 (DMT-*C*), 113.08 (DMT-*C*), 110.01 (Ind-*C*-7), 109.93 (Ind-*C*-7), 101.43, 101.37, 101.33, 98.82 (NC*C*H), 98.21 (CNC*C*H), 86.13, 86.02, 77.48, 77.16, 76.84, 69.80, 69.69, 65.51, 58.67, 58.47, 58.26, 58.20, 58.08, 55.28 (DMT-OCH_3), 49.18 (Ind-*C*-3), 49.10 (Ind-*C*-3), 45.41, 45.35, 43.45, 43.31, 43.17, 43.04, 42.94, 42.47, 28.89 (2×CH_3), 24.86 (*i*Pr-CH_3), 24.78 (*i*Pr-CH_3), 24.71 (*i*Pr-CH_3), 24.65 (*i*Pr-CH_3), 24.56 (*i*Pr-CH_3), 24.47 (*i*Pr-CH_3), 23.08, 23.06, 23.00, 22.97, 20.16, 20.00 ppm;
^{31}P NMR (162 MHz, $CDCl_3$): δ = 149.28, 149.23, 149.15, 149.11 ppm;
HR-MS (ESI+): *m/z* calc. ($C_{50}H_{58}N_5NaO_8P$, $[M+Na]^+$): 910.3915, found: 910.3914.

3-*O*-(4,4'-Dimethoxytrityloxy)methyl (*S*)-1-(2,3-dihydroxypropyl) barbituric acid 5-methoxy-indolenine merocyanine phosphoramidite (gBAM^F-PA, 89)

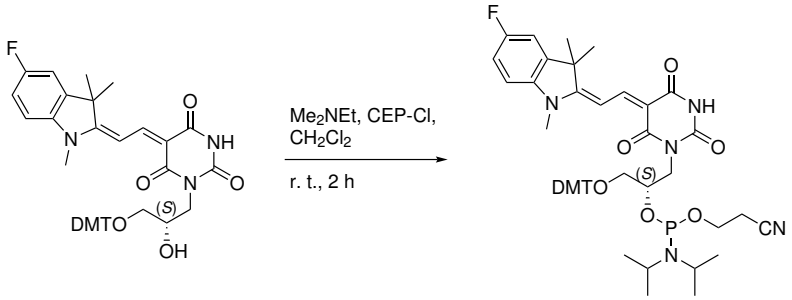

$C_{41}H_{40}FN_3O_7$
705.78 g mol^{-1}
85

$C_{50}H_{57}FN_5O_8P$
918.04 g mol^{-1}
89

Compound **89** was synthesized according to general procedure VIII on a 280 µmol scale and was isolated after column chromatography on silica gel (EtOAc/*n*-hexane 8:2 + 2% NEt_3) as an orange foam (192 mg, 212 µmol, 75%).

^{1}H NMR (400 MHz, $CDCl_3$): δ = 8.69 - 8.55 (m, 1 H, COCC*H*), 7.61 - 7.52 (m, 1 H, NCC*H*), 7.51 - 7.44 (m, 2 H, Ind-*H*), 7.39 - 7.31 (m, 4 H, DMT-*H*), 7.31 - 7.22 (m, 2 H), 7.22 - 7.15 (m, 1 H), 7.11 - 7.04 (m, 2 H), 7.01 - 6.94 (m, 1 H), 6.85 - 6.77 (m, 4 H, DMT-*H*), 4.50 - 4.23 (m, 1 H), 4.04 - 3.85 (m, 1 H), 3.78 (2 s, 6 H, DMT-OCH_3), 3.74 - 3.40 (m, 4 H, NCH_3), 3.37 - 3.02 (m, 1 H), 2.65 - 2.54 (m, 1 H), 2.44 - 2.35 (m, 1 H), 1.77 - 1.61 (m, 6 H, 2×CH_3), 1.19 - 0.97 (m, 13 H, *i*Pr-CH_3) ppm;
^{13}C{^{1}H} NMR (100 MHz, $CDCl_3$): δ = 177.13, 171.19 (Ind-*C*-2), 164.53, 164.25, 163.93,

163.57, 162.99, 162.86, 158.35, 152.01 (COC*C*H), 151.71 (COC*C*H), 150.86 (COC*C*H), 150.68 (COC*C*H), 150.65 (COC*C*H), 144.90, 144.86, 138.64, 136.20 (DMT-*C*), 136.15 (DMT-*C*), 136.11 (DMT-*C*), 136.09 (DMT-*C*), 130.17, 130.14, 130.09, 128.29, 128.24, 127.73, 127.70, 126.65, 126.62, 117.82, 115.14, 114.90, 113.03 (DMT-*C*), 112.99 (DMT-*C*), 110.48, 110.40, 110.15, 101.50, 101.35, 98.71, 86.05, 85.94, 77.02, 60.41, 58.55, 58.16, 57.97, 55.20 (DMT-O*C*H$_3$), 49.13, 45.33, 45.26, 43.21, 43.09, 42.96, 42.84, 42.47, 28.84 (2×*C*H$_3$), 28.74 (2×*C*H$_3$, 24.76 (*i*Pr-*C*H$_3$), 24.68 (*i*Pr-*C*H$_3$), 24.60 (*i*Pr-*C*H$_3$), 24.53 (*i*Pr-*C*H$_3$), 24.45 (*i*Pr-*C*H$_3$), 24.37 (*i*Pr-*C*H$_3$), 21.07, 20.15, 20.07 ppm;
^{31}P NMR (162 MHz, CDCl$_3$): δ = 149.29, 149.25, 149.13, 149.07 ppm;
HR-MS (ESI+): *m/z* calc. (C$_{50}$H$_{57}$FN$_5$NaO$_8$P, [M+Na]$^+$): 941.3821, found: 941.3817.

3-*O*-(4,4'-Dimethoxytrityloxy)methyl (*S*)-1-(2,3-dihydroxypropyl) barbituric acid 5-fluoro-indolenine merocyanine phosphoramidite (gBAM^{OMe}-PA, 90)

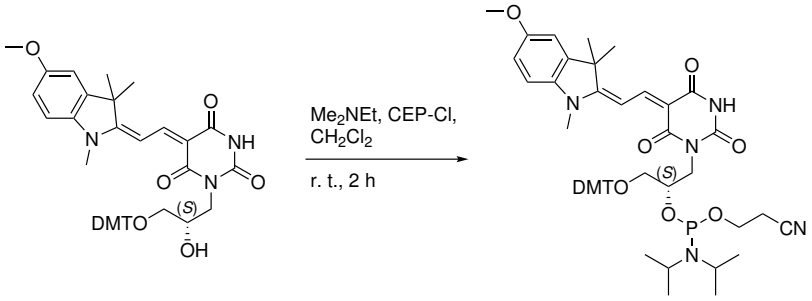

C$_{42}$H$_{43}$N$_3$O$_8$
717.82 g mol^{-1}
86

C$_{51}$H$_{60}$N$_5$O$_9$P
917.41 g mol^{-1}
90

Compound **90** was synthesized according to general procedure VIII on a 280 µmol scale and was isolated after column chromatography on silica gel (EtOAc/*n*-hexane 7:3 + 2% NEt$_3$) as an orange foam (119 mg, 129 µmol, 46%).

^{1}H NMR (400 MHz, CDCl$_3$): δ = 8.67 - 8.52 (m, 1 H, COCC*H*), 7.59 - 7.51 (m, 1 H, NCC*H*), 7.51 - 7.42 (m, 2 H), 7.39 - 7.31 (m, 4 H), 7.30 - 7.22 (m, 1 H), 7.22 - 7.15 (m, 1 H), 7.00 - 6.95 (m, 1 H), 6.94 - 6.86 (m, 2 H), 6.84 - 6.78 (m, 4 H, DMT-*H*), 4.50 - 4.05 (m, 4 H), 3.84 (2 s, 3 H, OC*H*$_3$), 3.78 (2 s, 6 H, DMT-OC*H*$_3$), 3.76 - 3.62 (m, 1 H), 3.59 - 3.45 (m, 6 H, NC*H*$_3$), 3.36 - 3.03 (m, 2 H), 2.79 - 2.73 (m, 2 H), 2.63 - 2.54 (m, 1 H), 2.44 - 2.35 (m, 1 H), 1.75 - 1.68 (m, 6 H, 2×C*H*$_3$), 1.18 - 1.06 (m, 8 H, *i*Pr-C*H*$_3$), 1.06 - 0.98 (m, 4 H, *i*Pr-C*H*$_3$) ppm;
^{13}C{^{1}H} NMR (100 MHz, CDCl$_3$): δ = 158.36, 144.90, 136.14, 131.65, 130.17, 130.12, 128.27, 127.75, 127.72, 117.73, 113.05, 110.52, 109.02, 106.26, 100.24, 98.45, 85.94, 83.98, 82.17, 71.11, 69.44, 65.40, 58.17, 58.11, 55.95, 55.23, 49.36, 45.35, 45.29, 43.24, 43.11, 42.84, 30.98, 28.86, 28.78, 24.79, 24.71, 24.71, 24.47, 24.46, 24.39, 23.01, 22.99, 22.93, 22.90, 20.17, 20.10, 20.00 ppm;
HR-MS (ESI+): *m/z* calc. (C$_{51}$H$_{60}$N$_5$NaO$_9$P, [M+Na]$^+$): 940.4021, found: 940.4006.

3-*O*-(4,4'-Dimethoxytrityloxy)methyl (*S*)-1-(2,3-dihydroxypropyl) 3-methyl-barbituric acid indolenine merocyanine phosphoramidite (gmBAM-PA, 87)

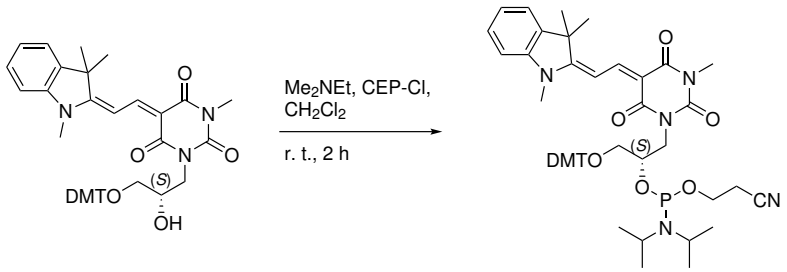

$C_{42}H_{43}N_3O_7$
701.82 g mol^{-1}
83

$C_{51}H_{60}N_5O_8P$
902.04 g mol^{-1}
87

Compound **87** was synthesized according to general procedure VIII on a 290 µmol scale and was isolated after column chromatography on silica gel (EtOAc/*n*-hexane 7:3 + 2% NEt_3) as an orange foam (183 mg, 204 µmol, 69%).

^{1}H NMR (400 MHz, $CDCl_3$): δ = 8.71 - 8.53 (m, 1 H, COCC*H*), 7.57 - 7.43 (m, 1 H, NCC*H*), 7.43 - 6.88 (m, Ind-*H*, DMT-*H*), 6.76 - 6.67 (m, 4 H, DMT-*H*), 4.49 - 4.22 (m, 1 H, glycido-3-C H_2), 3.99 - 3.73 (m, 1 H, glycido-2-C*H*), 3.69 (2 s, 6 H, DMT-OCH_3), 3.65 - 3.31 (m, 5 H, NCH_3), 3.31 - 3.19 (m, 4 H, BA-NCH_3), 3.19 - 2.93 (m, 1 H, glycido-1-C*H*), 2.78 - 2.37 (m, 1 H, POCH$_2$CH_2), 2.35 - 2.16 (m, 1 H, POCH_2), 1.68 - 1.54 (m, 6 H, 2×CH_3), 1.10 - 0.97 (m, 12 H, *i*Pr-CH_3), 0.97 - 0.92 (m, 2 H, *i*Pr-C*H*) ppm;
^{13}C{^{1}H} NMR (100 MHz, $CDCl_3$): δ = 158.24 (BA-carbonyl-*C*), 152.03 (COC*C*H), 151.50 (COC*C*H), 144.84, 142.59, 140.71, 136.04, 130.05, 128.21, 128.09, 127.59, 126.53, 126.09, 124.50 (*C*N), 122.00, 117.56, 112.88, 109.54, 101.86, 98.11 (NC*C*H), 85.82 (DMT-C_{quart}), 65.35 (glycido-1-*C*H$_2$), 55.10 (DMT-O*C*H$_3$), 42.98 (glycido-3-*C*H$_2$), 42.85 (glycido-1-*C*H), 28.84 (N*C*H$_3$), 28.01 (BA-N*C*H$_3$), 27.32 (2×*C*H$_3$), 24.67 (*i*Pr-*C*H$_3$), 24.60 (*i*Pr-*C*H$_3$), 24.36 (*i*Pr-*C*H$_3$), 24.20 (*i*Pr-*C*H$_3$), 20.97 (PO*C*H$_2$), 19.94 (*i*Pr-*C*H$_3$), 24.20 (*i*Pr-*C*H), 19.82 (*i*Pr-*C*H$_3$), 24.20 (*i*Pr-*C*H) ppm;
^{31}P NMR (162 MHz, $CDCl_3$): δ = 149.28, 149.21, 149.17, 149.15 ppm;
HR-MS (ESI+): *m/z* calc. ($C_{51}H_{60}N_5NaO_8P$, $[M+Na]^+$): 924.4072, found: 924.4241.

3-*O*-(4,4'-Dimethoxytrityloxy)methyl (*S*)-1-(2,3-dihydroxypropyl) 3-methyl-barbituric acid benzothiazole merocyanine phosphoramidite (gmBAM^{b}-PA, 88)

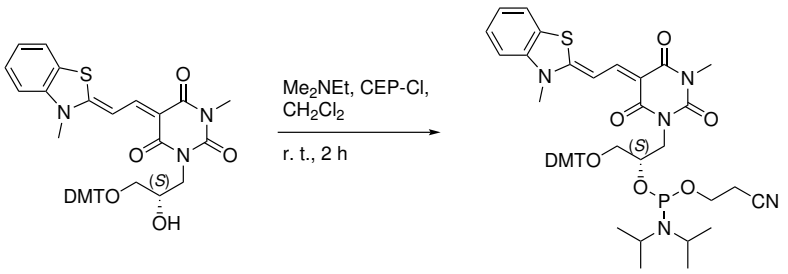

$C_{39}H_{37}N_3O_7S$
691.80 g mol^{-1}
84

$C_{48}H_{54}N_5O_8PS$
892.02 g mol^{-1}
88

Compound **88** was synthesized according to general procedure VIII on a 430 µmol scale and was isolated after column chromatography on silica gel (EtOAc/*n*-hexane 8:2 + 2% NEt_3) as an orange foam (301 mg, 338 µmol, 77%).

^{1}H NMR (400 MHz, $CDCl_3$): δ = 8.41 - 8.29 (m, 1 H, COCC*H*), 7.77 - 7.68 (m, 1 H, NCC*H*), 7.67 - 7.61 (m, 1 H), 7.47 (dtt, J = 9.6, 6.8, 1.5 Hz, 3 H), 7.39 - 7.31 (m, 5 H), 7.31 - 7.23 (m, 4 H), 7.18 (tt, J = 6.9, 1.6 Hz, 1 H), 6.81 (dq, J = 6.9, 2.8, 2.4 Hz, 4 H, DMT-*H*), 4.55 - 4.27 (m, 2 H), 4.06 - 3.88 (m, 1 H), 3.78 (s, 10 H, NCH_3, DMT-OCH_3), 3.72 - 3.61 (m, 1 H), 3.60 - 3.42 (m, 1 H), 3.36 - 3.26 (m, 3 H, BA-NCH_3), 3.25 - 3.03 (m, 1 H), 2.63 - 2.50 (m, 1 H), 2.40 (td, J = 6.6, 2.6 Hz, 1 H), 1.80 (s, 2 H), 1.31 - 1.20 (m, 2 H, *i*Pr-C*H*), 1.17 – 0.98 (m, 12 H, *i*Pr-CH_3) ppm;
^{13}C{^{1}H} NMR (100 MHz, $CDCl_3$): δ = 169.85 (arom-*C*-2), 169.70 (arom-*C*-2), 169.60 (arom-*C*-2), 163.79 (CO*C*), 163.69 (CO*C*), 163.59 (CO*C*), 163.41 (CO*C*), 163.34 (CO*C*), 163.01 (CO*C*), 158.33, 152.08 (BA-carbonyl-*C*), 151.95 (BA-carbonyl-*C*), 149.86 (COC*C*H), 149.53 (COC*C*H), 144.95, 141.67, 136.28, 136.17, 136.11, 130.14, 130.09, 128.31, 128.28, 128.25, 128.22, 127.72, 127.69, 126.62, 125.48, 125.13, 122.43, 117.85, 113.01, 112.98, 112.96, 112.18, 112.05, 99.98, 99.94, 99.90, 99.72, 97.31 (NC*C*H), 97.21 (NC*C*H), 86.03, 85.89, 65.49, 58.20, 58.01, 55.20 (DMT-O*C*H$_3$), 43.18, 43.07, 42.90, 42.78, 33.45 (N*C*H$_3$), 33.33 (N*C*H$_3$), 33.30 (N*C*H$_3$), 33.26 (N*C*H$_3$), 28.04, 27.37 (BA-N*C*H$_3$), 24.77 (*i*Pr-*C*H$_3$), 24.68 (*i*Pr-*C*H$_3$), 24.60 (*i*Pr-*C*H$_3$), 24.47 (*i*Pr-*C*H$_3$), 24.40 (*i*Pr-*C*H$_3$), 24.32 (*i*Pr-*C*H$_3$), 20.06, 20.00, 19.93 ppm;
^{31}P NMR (162 MHz, $CDCl_3$): δ = 149.31, 149.24, 149.22, 149.08 ppm;
HR-MS (ESI+): *m/z* calc. ($C_{48}H_{54}N_5NaO_8PS$, $[M+Na]^+$): 914.3323, found: 914.3304.

5.1.2.7 Preparation of the 3'-phosphate CPG support

4-(((2-Hydroxyethyl)thio)methyl)benzoic acid (75)

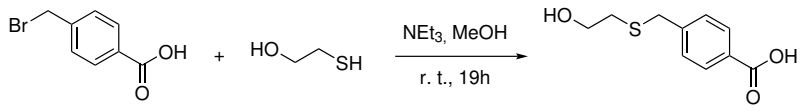

$C_8H_7BrO_2$ 215.05 g mol^{-1} | C_2H_6OS 78.13 g mol^{-1} | $C_{10}H_{12}O_3S$ 212.26 g mol^{-1} **75**

4-Bromomethylbenzoic acid (300 mg, 1.48 mmol, 1.00 eq.) and 2-mercaptoethanol (126 mg, 1.62 mmol, 1.16 eq.) were dissolved under nitrogen atmosphere in a mixture of NEt_3 (280 mg, 2.76 mmol, 1.98 eq.) and MeOH (6 mL). The reaction mixture was stirred at ambient temperature for 18 h. Afterwards, the solvent was evaporated and the residue was redissolved in H_2O (12 mL). The resulting solution was acidified with 1 M HCl until precipitation of a white solid was completed. The suspension was extracted with EtOAc (3×20 mL) and the combined organic phases were dried over Na_2SO_4. Removal of the solvent under reduced pressure and drying in vacuum provided the crude product **75** as a colorless solid (274 mg, 1.29 mmol, 87%) which was sufficiently pure for the next reaction step. Spectral data matched those reported previously.[270]

^{1}H NMR (400 MHz, CD_3CN): δ = 7.98 - 7.88 (m, 2 H, Ph-2,6-H), 7.47 - 7.40 (m, 2 H, Ph-3,5-H), 3.80 (s, 2 H, S-CH_2-Ph), 3.58 (t, J = 6.6 Hz, 2 H, CH_2-OH), 2.53 (t, J = 6.6 Hz, 2 H, S-CH_2) ppm.

4-(((2-(4,4'-Dimethoxytrityl)oxyethyl)thio)methyl)benzoic acid (76)

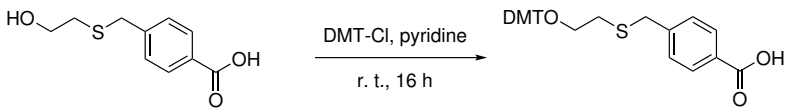

$C_{10}H_{12}O_3S$ 212.26 g mol^{-1} **75** | $C_{31}H_{30}O_5S$ 514.64 g mol^{-1} **76**

Compound **75** (274 mg, 1.29 mmol, 1.00 eq.) was coevaporated with pyridine (3×5 mL) and redissolved in anhydrous pyridine (7 mL) under nitrogen atmosphere. 4,4'-Dimethoxytrityl chloride (657 mg, 1.94 mmol, 1.50 eq.) was added in three portions over the course of 1 h and the reaction mixture was stirred at ambient temperature for 16 h. The solvent was removed under reduced pressure, the residue was coevaporated with toluene (3×5 mL), taken up in CH_2Cl_2 (20 mL) and washed with citric acid (5% aq. solution, 3×20 mL). The organic phase was dried over Na_2SO_4, the solvent was removed in vacuum and the crude product was purified by column chromatography (CH_2Cl_2/MeOH 10:1 to 9:1 + 1% NEt_3) to afford the target compound **76** as an off-white foam (534 mg, 1.04 mol, 80%). Spectral data matched those reported previously.[270]

^{1}H NMR (400 MHz, CD_3CN): δ = 7.92 - 7.83 (m, 2 H, Ph-2,6-*H*), 7.43 - 7.39 (m, 2 H, Ph-3,5-*H*), 7.33 - 7.19 (m, 9 H, DMT-*H*), 6.88 - 6.81 (m, 4 H, DMT-*H*), 3.76 (s, 6 H, DMT-OCH_3), 3.68 (s, 2 H, S-CH_2-Ph), 3.09 (t, J = 6.7 Hz, 2 H, CH_2-OH), 2.60 (t, J = 6.7 Hz, 2 H, S-CH_2) ppm.

3'-Phosphate CPG support (77)

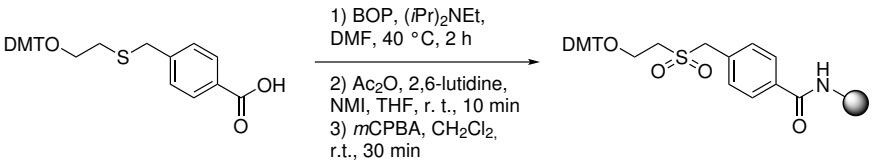

$C_{31}H_{30}O_5S$
514.64 g mol^{-1}
76

77

In the following procedure, washing of the solid supports includes brief agitation with the respective solvent followed by centrifugation at 4,200 rpm for 10 min and removal of the supernatant.

Native amino CPG support (250 mg, 18.5 µmol, 1.00 eq.) was washed with DMF (1.5 mL) and treated with a solution of compound **76** (25.0 mg, 48.7 µmol, 2.63 eq.), BOP reagent (22.0 mg, 49.8 µmol, 2.69 eq.) and (iPr)$_2$NEt (12 µL, 67.7 µmol, 3.66 eq.) in anhydrous DMF (1.5 mL). The reaction mixture was shaken for 2 h at 40 °C in the dark. Afterwards, the mixture was centrifuged at 4,200 rpm for 5 min, the supernatant was removed by decanting and the remaining solid was washed with anhydrous DMF (5 mL) followed by anhydrous MeCN (5 mL). Capping solution A (pyridine/Ac_2O/THF 10/10/80, configured for ABI synthesizer, 2 mL) and B (16% NMI in THF, configured for ABI synthesizer, 2 mL) were added and the mixture was shaken at ambient temperature for 10 min. The supernatant was removed and the solid support was successively washed with MeCN, MeOH and CH_2Cl_2 (5 mL each). Afterwards, a solution of *m*CPBA (75% by weight, 173 mg, 750 µmol, 40.5 eq.) in CH_2Cl_2 (12 mL) was added and the mixture was shaken at r. t. for 30 min. The supernatant was removed, the residual solid was successively washed with MeCN and CH_2Cl_2 (5 mL each) and the CPG support was carefully dried in a desiccator.

To determine the success of the capping reaction, approximately 0.5 mg of **77** were suspended in ninhydrin solution (0.5 mL, 0.025% in EtOH) and heated to 65 °C for 2 min. No blue coloration due to uncapped amino groups was observed.

The loading density of the CPG support was determined by suspending approximately 3 mg of **77** in dichloroacetic acid (10 mL, 3% in dichloroethane). An absorbance spectrum of an aliquot of this solution between 200 and 800 nm was recorded in a 1 cm cuvette. From the absorbance a of the DMT cation at 498 nm (ϵ = 70,000 L mol^{-1} cm^{-1}) and the exact mass

m, the loading density was calculated according to

$$\frac{n}{m} = \frac{A}{\epsilon \cdot 1\ \text{cm}} \cdot \frac{10\ \text{mL}}{m} \tag{22}$$

Two batches of **77** with loading densities of 46 and 48 µmol g^{-1} were obtained.

5.1.2.8 Preparation of HBI-derivatives

(Methyl-2-((1-ethoxyethylidene)amino)acetate (97)

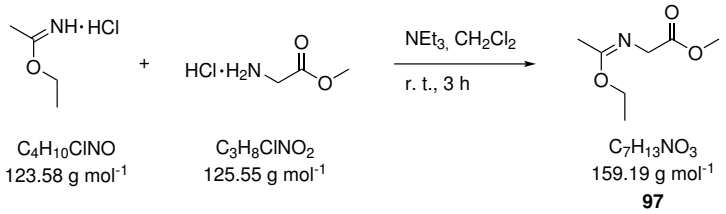

Ethylacetimidate hydrochloride (2.47 g, 20.0 mmol, 1.00 eq.) and glycinmethylester hydrochloride (2.52 g, 20.0 mmol, 1.00 eq.) were dissolved in anhydrous, degassed CH_2Cl_2 (80 mL) and stirred for 3 h at r. t. The reaction mixture was washed with H_2O (2×40 mL) and brine (1×40 mL) and dried over Na_2SO_4. After removal of the solvent in vacuum, the target compound **97** was obtained as a yellow oil (1.77 g, 11.1 mmol, 56%). Spectroscopic data matched those reported previously.[257]

^{1}H NMR (400 MHz, $CDCl_3$): δ = 4.07 (q, J = 7.1 Hz, 2 H, OCH_2CH$_3$), 4.05 (s, 2 H, NCH_2), 3.72 (s, 3 H, OCH_3), 1.86 (s, 3 H, CCH_3), 1.25 (t, J = 7.1 Hz, 3 H, OCH_2CH_3) ppm;
^{13}C{^{1}H} NMR (100 MHz, $CDCl_3$): δ = 171.39 (O*C*N), 164.55 (carbonyl-*C*), 60.74 (O*C*H$_2$), 51.68 (O*C*H$_3$), 50.88 (N*C*H$_2$), 15.03 (OCH$_2$*C*H$_3$), 13.93 (NC*C*H$_3$) ppm;
HR-MS (ESI+): *m/z* calc. ($C_7H_{13}NNaO_3$, $[M+Na]^+$): 182.0788, found: 182.0791.

3,5-Difluoro-4-hydroxybenzaldehyde (120)

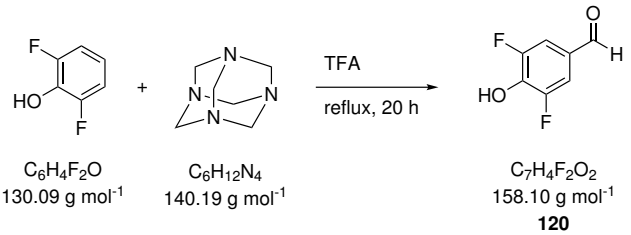

2,6-Difluorophenol (4.50 g, 34.6 mmol, 1.00 eq.) and urotropin (4.85 g, 34.6 mmol, 1.00 eq.) were dissolved in TFA (35 mL) and heated to reflux for 20 h. Afterwards, the solvent was removed in vacuum and CH_2Cl_2 (200 mL) was added. The resulting solution was extracted with sat. aq. $NaHCO_3$ (3×150 mL). Then, the aqueous phase was neutralized with 1 M NaOH, the pH was adjusted to 1 by addition of conc. HCl and it was extracted with CH_2Cl_2

(1×250 mL, 2×150 mL). The combined organic phases were dried over Na_2SO_4 and the solvent was removed under reduced pressure to afford the target compound **120** as an orange solid (4.39 g, 27.8 mmol, 80%). Spectroscopic data matched those reported previously.[470]

^{1}H NMR (400 MHz, acetone-d_6): δ = 9.85 (t, J = 1.9 Hz, 1 H, C*H*O), 7.63 - 7.51 (m, 2 H, Ph-2,6-*H*) ppm;
^{13}C{^{1}H} NMR (100 MHz, acetone-d_6): δ = 190.06 (*C*HO), 153.41 (Ph-3,5-*C*), 150.91 (Ph-3,5-*C*), 140.12 (Ph-4-*C*), 126.71 (Ph-1-*C*), 113.14 (Ph-2,6-*C*) ppm;
HR-MS (ESI-): *m/z* calc. ($C_7H_3F_2O_2S$, [M-H]$^-$): 157.0107, found: 157.0109.

General procedure IX: imine synthesis

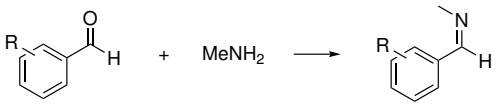

The respective aromatic aldehyde (1.00 eq.) was dissolved in $MeNH_2$ (33% in EtOH, 10.0 eq.) and DMF (1.3 mL per mmol aldehyde) under nitrogen atmosphere. After stirring for 16 h at ambient temperature, the solution was filtered over celite and the solvent was removed in vacuum. The resulting product was usually sufficiently pure for the next reaction step.

2-Hydroxy-*N*-methylbenzaldimine (91)

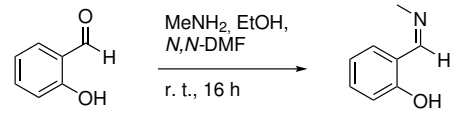

$C_7H_6O_2$
122.12 g mol^{-1}

C_8H_9NO
135.17 g mol^{-1}
91

Compound **91** was synthesized according to general procedure IX on a 8 mmol scale. The product was obtained as a slightly yellow liquid which was used without further purification for the next reaction step.

3-Bromo-4-hydroxy-5-methoxy-*N*-methylbenzaldimine (92)

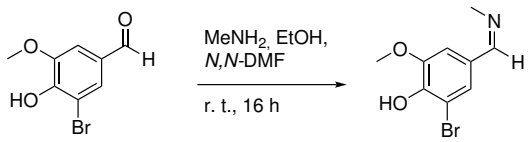

$C_8H_7BrO_3$
231.05 g mol^{-1}

$C_9H_{10}BrNO_2$
244.09 g mol^{-1}
92

Compound **92** was synthesized according to general procedure IX on a 4 mmol scale. The product was obtained as a dark red solid which was used without further purification for the

next reaction step.

4-Hydroxy-3-methoxy-*N*-methylbenzaldimine (93)

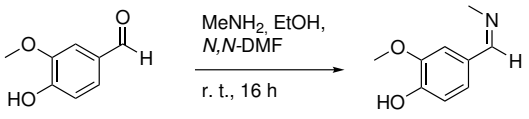

$C_8H_8O_3$
152.15 g mol^{-1}

$C_9H_{11}NO_2$
165.19 g mol^{-1}
93

Compound **93** was synthesized according to general procedure IX on a 6 mmol scale. The product was obtained as a yellow solid which was used without further purification for the next reaction step.

4-Hydroxy-*N*-methylbenzaldimine (94)

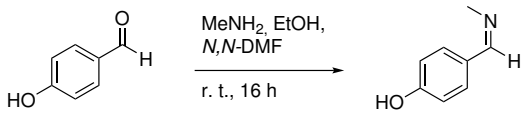

$C_7H_6O_2$
122.12 g mol^{-1}

C_8H_9NO
135.17 g mol^{-1}
94

Compound **94** was synthesized according to general procedure IX on a 9 mmol scale. The product was obtained as slightly yellow solid (724 mg, 5.36 mmol, 65%) and was sufficiently pure for further reactions.

^{1}H NMR (400 MHz, $CDCl_3$): δ = 9.87 (s, 1 H, O*H*), 8.18 (q, J = 1.6 Hz, 1 H, imino-*H*), 7.50 - 7.56 (m, 2 H, Ph-3,5-*H*), 6.75 - 6.85 (m, 2 H, Ph-2,6-*H*), 3.35 (d, J = 1.5 Hz, 3 H, NC*H*$_3$) ppm;
HR-MS (ESI+): *m/z* calc. ($C_8H_{10}NO$, $[M+H]^+$): 136.0757, found: 136.0760.

4-Hydroxy-3,5-dimethoxy-*N*-methylbenzaldimine (95)

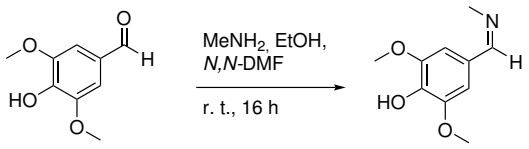

$C_9H_{10}O_4$
182.18 g mol^{-1}

$C_{10}H_{13}NO_3$
195.22 g mol^{-1}
95

Compound **95** was synthesized according to general procedure IX on a 25 mmol scale. The product was obtained as slightly yellow solid (4.05 g, 20.8 mmol, 83%) and was sufficiently pure for further reactions. Spectroscopic data matched those reported previously.[257]

^{1}H NMR (400 MHz, $CDCl_3$): $\delta = 8.15$ (s, 1 H, imino-*H*), 6.97 (s, 2 H, Ph-2,6-*H*), 3.92 (s, 6 H, OCH_3), 3.49 (s, 3 H, NCH_3) ppm;
^{13}C{^{1}H} NMR (100 MHz, $CDCl_3$): $\delta = 162.07$ (imino-*C*), 147.28 (Ph-3,5-*C*), 137.58 (Ph-4-*C*), 127.29 (Ph-1-*C*), 104.74 (Ph-2,6-*C*), 56.20 (OCH_3), 47.76 (NCH_3) ppm;
HR-MS (ESI-): *m/z* calc. ($C_{10}H_{14}NO_3$, [M-H]$^-$): 194.0823, found: 194.0822.

3,5-Difluoro-4-hydroxy-*N*-methylbenzaldimine (96)

$C_7H_4F_2O_2$
158.10 g mol^{-1}
120

$C_8H_7F_2NO$
171.15 g mol^{-1}
96

Compound **96** was synthesized according to general procedure IX on a 6 mmol scale. The product was obtained as a red oil which was used without further purification for the next reaction step.

General procedure X: cycloaddition

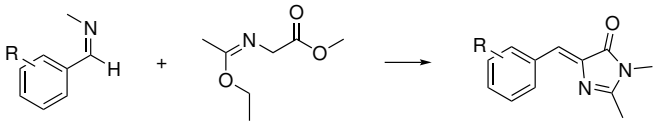

The aromatic imine (1.00 eq.) and the imidate (1.00 eq.) were dissolved under nitrogen atmosphere in abs. EtOH (1 mL per mmol) and stirred for 16 h at ambient temperature. Et_2O (4 mL per mmol) was added, the precipitate was filtered off and again washed with cold Et_2O (2 mL per mmol). The resulting product was dried under reduced pressure and was in most cases sufficiently pure for spectroscopic analyses.

(*Z*)-5-(2-Hydroxybenzylidene)-2,3-dimethyl-3,5-dihydro-4*H*-imidazol-4-one (o-HBI, 98)

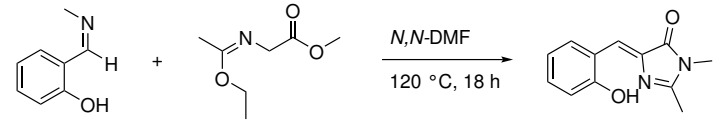

C_8H_9NO
135.17 g mol^{-1}
91

$C_7H_{13}NO_3$
159.19 g mol^{-1}
97

$C_{12}H_{12}N_2O_2$
216.24 g mol^{-1}
98

A solution of imine **91** (1.08 g, 8.19 mmol, 1.00 eq.) and imidate **97** (1.43 g, 9.01 mmol, 1.10 eq.) was heated for 18 h to 120 °C under nitrogen atmosphere. Afterwards, the reaction mixture was cooled to r. t. and the solvent was removed under reduced pressure. Et_2O (20 mL) was added, the precipitate was filtered off and dried in vacuum. The product **98** was

obtained as an orange solid (1.48 g, 6.86 mmol, 84%). Spectral data matched those reported previously.[251]

^{1}H NMR (400 MHz, DMSO-d_6): δ = 11.81 (s, 1 H, O*H*), 8.17 (dd, J = 7.8, 1.7 Hz, 1 H, Ph-6-*H*), 7.27 (ddd, J = 8.3, 7.2, 1.8 Hz, 1 H, Ph-3-*H*), 7.23 (s, 1 H, benzylidene-*H*), 6.82 - 6.70 (m, 2 H, Ph-4,5-*H*), 3.11 (s, 3 H, NCH_3), 2.36 (s, 3 H, CH_3) ppm;
^{13}C{^{1}H} NMR (100 MHz, DMSO-d_6): δ = 168.73 (carbonyl-*C*), 162.18 (NR-*C*-NR), 157.61 (Ph-2-*C*), 135.69 (N-*C*-CO), 133.93 (Ph-3-*C*), 132.54 (Ph-6-*C*), 122.48 (Ph-5-*C*), 120.34 (Ph-3-*C*), 119.31 (Ph-1-*C*), 116.91 (benzylidene-*C*), 26.38 (N*C*H$_3$), 15.25 (*C*H$_3$) ppm;
HR-MS (ESI+): *m/z* calc. ($C_{12}H_{13}N_2O_2$, $[M+H]^+$): 217.0972, found: 217.0971.

(*Z*)-5-(3-Bromo-4-hydroxy-5-methoxybenzylidene)-2,3-dimethyl-3,5-dihydro-4*H*-imidazol-4-one (BMHBI, 99)

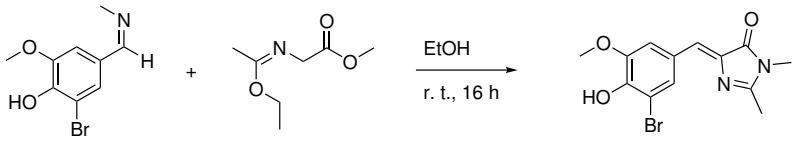

$C_9H_{10}BrNO_2$
244.09 g mol^{-1}
92

$C_7H_{13}NO_3$
159.19 g mol^{-1}
97

$C_{13}H_{13}BrN_2O_3$
325.16 g mol^{-1}
99

Compound **99** was synthesized according to general procedure X on a 4.33 mmol scale. Column chromatography on silica gel (CH_2Cl_2/MeOH 100:1) afforded the product **99** as an orange solid (349 mg, 1.07 mmol, 25%).

^{1}H NMR (400 MHz, DMSO-d_6): δ = 10.19 (s, 1 H, O*H*), 8.12 (d, J = 1.6 Hz, 1 H, Ph-2-*H*), 7.87 (d, J = 1.9 Hz, 1 H, Ph-6-*H*), 6.89 (s, 1 H, benzylidene-*H*), 3.86 (s, 3 H, OCH_3), 3.09 (s, 3 H, NCH_3), 2.35 (s, 3 H, CH_3) ppm;
^{13}C{^{1}H} NMR (100 MHz, DMSO-d_6): δ = 169.73 (carbonyl-*C*), 163.54 (NR-*C*-NR), 148.06 (Ph-5-*C*), 145.77 (Ph-4-*C*), 137.49 (Ph-1-*C*), 128.62 (N-*C*-CO), 126.56 (Ph-2-*C*), 124.02 (Ph-3-*C*), 114.56 (benzylidene-*C*), 109.50 (Ph-6-*C*), 56.24 (O*C*H$_3$), 26.29 (N*C*H$_3$), 15.51 (*C*H$_3$) ppm;
HR-MS (ESI+): *m/z* calc. ($C_{13}H_{14}BrN_2O_3$, $[M]^+$): 325.0182, found: 325.0180.

(*Z*)-5-(4-Hydroxy-3-methoxybenzylidene)-2,3-dimethyl-3,5-dihydro-4*H*-imidazol-4-one (MHBI, 100)

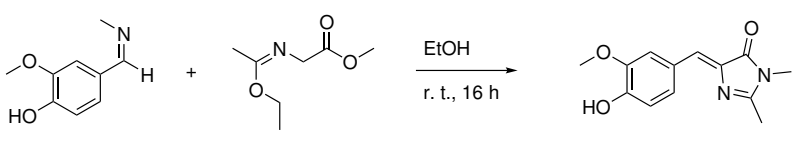

$C_9H_{11}NO_2$
165.19 g mol^{-1}
93

$C_7H_{13}NO_3$
159.19 g mol^{-1}
97

$C_{13}H_{14}N_2O_3$
246.27 g mol^{-1}
100

Compound **100** was synthesized according to general procedure X on a 6.57 mmol scale and afforded as an orange solid (818 mg, 3.32 mmol, 51%). Spectral data matched those reported previously.[486]

^{1}H NMR (400 MHz, DMSO-d_6): δ = 7.94 (d, J = 1.93 Hz, 1 H, Ph-2-*H*), 7.64 (dd, J = 8.49, 1.93 Hz, 1 H, Ph-6-*H*), 6.88 (s, 1 H, benzylidene-*H*), 6.82 (d, J = 8.58 Hz, 1 H, Ph-5-*H*), 3.79 (s, 3 H, OCH_3), 3.08 (s, 3 H, NCH_3), 2.33 (s, 3 H, CH_3) ppm;
^{13}C{^{1}H} NMR (100 MHz, DMSO-d_6): δ = 169.84 (carbonyl-*C*), 162.20 (NR-*C*-NR), 149.44 (Ph-3-*C*), 147.60 (Ph-4-*C*), 126.75 (N-*C*-CO), 125.81 (Ph-6-*C*), 125.69 (Ph-5-*C*), 115.71 (benzylidene-*C*), 115.56 (Ph-1-*C*), 55.58 (O*C*H$_3$), 26.22 (N*C*H$_3$), 15.43 (*C*H$_3$) ppm;
HR-MS (ESI+): *m/z* calc. ($C_{13}H_{14}N_2NaO_3$, $[M+Na]^+$): 269.0897, found: 269.0890.

(*Z*)-5-(4-Hydroxybenzylidene)-2,3-dimethyl-3,5-dihydro-4*H*-imidazol-4-one (HBI, 101)

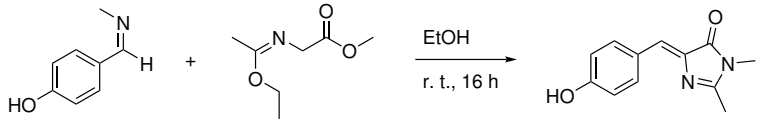

C_8H_9NO
135.17 g mol^{-1}
94

$C_7H_{13}NO_3$
159.19 g mol^{-1}
97

$C_{12}H_{12}N_2O_2$
216.24 g mol^{-1}
101

Compound **101** was synthesized according to general procedure X on a 6.57 mmol scale and afforded as an orange solid (845 mg, 3.91 mmol, 73%). Spectral data matched those reported previously.[251]

^{1}H NMR (400 MHz, DMSO-d_6): δ = 10.11 (s, 1 H, O*H*), 8.01 - 8.18 (m, 2 H, Ph-2,6-*H*), 6.89 (s, 1 H, benzylidene-*H*), 6.83 (m, 2 H, Ph-3,5-*H*), 3.07 (s, 3 H, NCH_3), 2.32 (s, 3 H, CH_3) ppm;
^{13}C{^{1}H} NMR (100 MHz, DMSO-d_6): δ = 169.85 (carbonyl-*C*), 162.31 (NR-*C*-NR), 159.58 (Ph-4-*C*), 136.29 (N-*C*-CO), 134.12 (Ph-2,6-*C*), 134.01 (Ph-2,6-*C*), 125.49 (Ph-3,5-*C*), 125.37 (Ph-3,5-*C*), 115.76 (benzylidene-*C*), 26.22 (N*C*H$_3$), 15.30 (*C*H$_3$) ppm;
HR-MS (ESI+): *m/z* calc. ($C_{12}H_{13}N_2O_2$, $[M+H]^+$): 217.0972, found: 217.0966.

(*Z*)-5-(4-Hydroxy-3,5-dimethoxybenzylidene)-2,3-dimethyl-3,5-dihydro-4*H*-imidazol-4-one (DMHBI, 102)

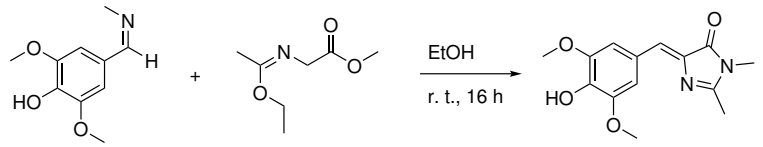

$C_{10}H_{13}NO_3$
195.22 g mol^{-1}
95

$C_7H_{13}NO_3$
159.19 g mol^{-1}
97

$C_{14}H_{16}N_2O_4$
276.29 g mol^{-1}
102

Compound **102** was synthesized according to general procedure X on a 7.59 mmol scale and afforded as an orange solid (1.22 g, 4.42 mmol, 58%). Spectral data matched those reported previously.[251]

^{1}H NMR (400 MHz, DMSO-d_6): $\delta = 7.63$ (s, 2 H, Ph-2,6-*H*), 6.89 (s, 1 H, benzylidene-*H*), 3.79 (s, 6 H, OCH_3), 3.08 (s, 3 H, NCH_3), 2.33 (s, 3 H, CH_3) ppm;
^{13}C{^{1}H} NMR (100 MHz, DMSO-d_6): $\delta = 169.85$ (carbonyl-*C*), 162.39 (NR-*C*-NR), 147.85 (Ph-3,5-*C*), 136.57 (Ph-4-*C*), 136.05 (N-*C*-CO), 125.73 (benzylidene-*C*), 124.48 (Ph-1-*C*), 110.15 (Ph-2,6-*C*), 56.05 (O*C*H$_3$), 26.25 (N*C*H$_3$), 15.54 (*C*H$_3$) ppm;
HR-MS (ESI+): *m/z* calc. ($C_{14}H_{17}N_2O_4$, $[M+H]^+$): 277.1183, found: 277.1178.

(*Z*)-5-(3,5-Difluoro-4-hydroxybenzylidene)-2,3-dimethyl-3,5-dihydro-4*H*-imidazol-4-one (DFHBI, 103)

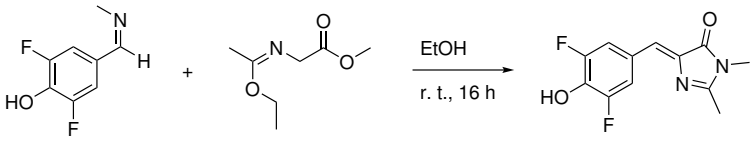

$C_8H_7F_2NO$ 171.15 g mol^{-1} **96** + $C_7H_{13}NO_3$ 159.19 g mol^{-1} **97** → $C_{12}H_{10}F_2N_2O_2$ 252.22 g mol^{-1} **103**

Compound **103** was synthesized according to general procedure X on a 2.05 mmol scale and afforded as an orange solid (202 mg, 0.80 mmol, 39%). Spectral data matched those reported previously.[251]

^{1}H NMR (400 MHz, DMSO-d_6): $\delta = 10.99$ (s, 1 H, O*H*), 7.96 (d, $J = 8.6$ Hz, 2 H, Ph-2,6-*H*), 6.90 (s, 1 H, benzylidene-*H*), 3.09 (s, 3 H, NCH_3), 2.36 (s, 3 H, CH_3) ppm;
^{13}C{^{1}H} NMR (100 MHz, DMSO-d_6): $\delta = 170.03$ (carbonyl-*C*), 164.80 (NR-*C*-NR), 153.57 (Ph-3,5-*C*), 153.50 (Ph-3,5-*C*), 136.57 (Ph-4-*C*, N-*C*-CO), 123.31 (benzylidene-*C*), 115.72 (Ph-2,6-*C*), 115.65 (Ph-2,6-*C*), 115.56 (Ph-2,6-*C*), 115.49 (Ph-2,6-*C*), 26.84 (N*C*H$_3$), 15.88 (*C*H$_3$) ppm;
HR-MS (ESI+): *m/z* calc. ($C_{12}H_{10}F_2N_2NaO_2$, $[M+Na]^+$): 275.0603, found: 275.0608.

5.1.2.9 Preparation of HBI-NH$_2$-derivatives

Ethyl methylcarbamimidothioate hydroiodide (104)

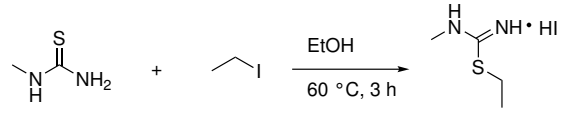

$C_2H_6N_2S$ 90.14 g mol^{-1} + C_2H_5I 155.97 g mol^{-1} → $C_4H_{11}IN_2S$ 246.11 g mol^{-1} **104**

N-Methylthiourea (3.54 g, 39.3 mmol, 1.00 eq.) was dissolved in abs. EtOH (13 mL) under nitrogen atmosphere. Iodoethane (3.78 mL, 47.4 mmol, 1.21 eq.) was added. The solution was stirred for 3.5 h at 60 °C. Afterwards, the solvent was removed in vacuum and the target compound **104** was obtained as a dark-yellow oil (10.0 g, 40.7 mmol, quant.). Spectral data matched those reported previously.[471]

^{1}H NMR (400 MHz, DMSO-d_6): $\delta = 9.19$ (s, 2 H, N*H*), 3.17 (q, $J = 7.3$ Hz, 2 H, S-CH_2), 2.90 (s, 3 H, N-CH_3), 1.26 (t, $J = 7.3$ Hz, 3 H, CH_2-CH_3) ppm;
^{13}C{^{1}H} NMR (100 MHz, DMSO-d_6): $\delta = 166.76$ (NH-*C*-S), 31.05 (N*C*H_3), 25.65 (*C*H_2), 14.68 (CH_2*C*H_3) ppm;
HR-MS (ESI+): *m/z* calc. ($C_4H_{11}N_2S$, $[M+H]^+$): 119.0637, found: 119.0641.

(*N*-Methylcarbamimidoyl)glycine (105)

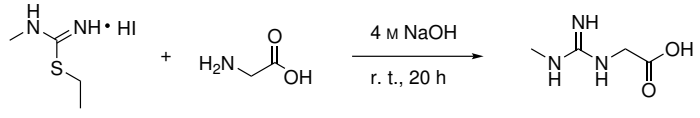

$C_4H_{11}IN_2S$
246.11 g mol^{-1}
104

$C_2H_5NO_2$
75.07 g mol^{-1}

$C_4H_9N_3O_2$
131.14 g mol^{-1}
105

Glycine (2.77 g, 36.9 mmol, 1.00 eq.) was added to aqueous 4 M NaOH (10 mL). The mixture was cooled to 0 °C, compound **104** (10.0 g, 40.6 mmol, 1.10 eq.) in water (20 mL) was added over 1 h and the reaction mixture was stirred for 20 h at r. t. Afterwards, cold Et_2O (2×5 mL) was added and the resulting white suspension was stirred again for 22 h at 0 °C. The organic solvent was removed in vacuum and the residue was filtered off, washed with water and dried in vacuum to give the target compound **105** as a colorless solid (4.69 g, 35.8 mmol, 97%). Spectral data matched those reported previously.[471]

^{1}H NMR (400 MHz, D_2O): $\delta = 3.74$ (s, 2 H, CH_2), 2.81 (s, 3 H, CH_3) ppm;
^{13}C{^{1}H} NMR (100 MHz, D_2O): $\delta = 175.28$ (*C*O_2H), 156.56 (guanidinium-*C*), 44.48 (*C*H_2), 27.34 (*C*H_3) ppm;
HR-MS (ESI+): *m/z* calc. ($C_4H_{10}N_3O_2$, $[M+H]^+$): 132.0768, found: 132.0772.

2-Amino-3-methyl-3,5-dihydro-4*H*-imidazol-4-one (106)

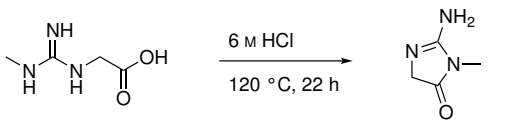

$C_4H_9N_3O_2$
131.14 g mol^{-1}
105

$C_4H_7N_3O$
113.12 g mol^{-1}
106

Compound **105** (3.00 g, 22.9 mmol, 1.00 eq.) was dissolved in 6 M HCl (65 mL) and heated to 120 °C for 22 h. After cooling down to r. t., Et_2O (25 mL) and H_2O (35 mL) were added and the reaction was stirred for additional 3 h at ambient temperature before it was stored at -20 °C overnight. The formed precipitate was filtered off and dried in high vacuum to afford compound **106** as a colorless solid (1.62 g, 14.3 mmol, 62%). Spectral data matched those reported previously.[471]

^{1}H NMR (400 MHz, DMSO-d_6): δ = 9.54 (s, 2 H, NH_2), 4.15 (s, 2 H, CH_2), 3.06 (s, 3 H, CH_3) ppm;
^{13}C{^{1}H} NMR (100 MHz, DMSO-d_6): δ = 175.89 (*C*O), 158.57 (*C*NH_2), 51.53 (*C*H_2), 26.11 (*C*H_3) ppm;
HR-MS (ESI+): *m/z* calc. ($C_4H_8N_3O$, $[M+H]^+$): 114.0662, found: 114.0665.

General procedure XI: Knoevenagel condensation

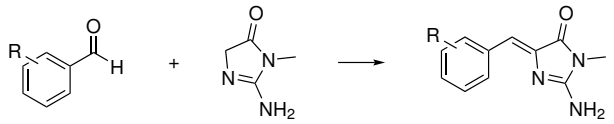

A solution of the aromatic aldehyde (1.00 eq.), 2-amino-3-methyl-3,5-dihydro-4*H*-imidazol-4-one (2.00 eq.) and NEt_3 (0.10 eq.) in abs. EtOH (3.2 mL per mmol) was heated to 90 °C for 5 - 22 h. After cooling to r. t., the volatiles were removed under reduced pressure and the crude product was purified by column chromatography on silica gel.

(*Z*)-2-Amino-5-(2-hydroxybenzylidene)-3-methyl-3,5-dihydro-4*H*-imidazol-4-one (o-HBI-NH_2, 107)

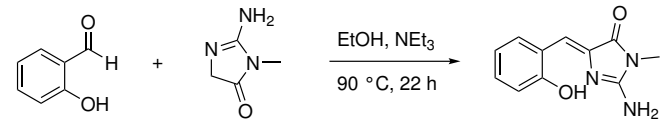

$C_7H_6O_2$
122.12 g mol^{-1}

$C_4H_7N_3O$
113.12 g mol^{-1}
106

$C_{11}H_{11}N_3O_2$
217.23 g mol^{-1}
107

Compound **107** was synthesized according to general procedure XI by heating the reaction mixture for 22 h to 90 °C. The product o-HBI-NH_2 was obtained as an orange solid (410 mg, 1.89 mmol, 86%) after column chromatography on silica gel (CH_2Cl_2/MeOH 50:1).

^{1}H NMR (400 MHz, DMSO-d_6): δ = 12.66 (s, 1 H, O*H*), 7.82 (s, 2 H, NH_2), 7.63 - 7.56 (m, 1 H, Ph-6-*H*), 7.13 (ddd, J = 8.1, 7.2, 1.76 Hz, 1 H, Ph-4-*H*), 6.81 - 6.70 (m, 2 H, Ph-3,5-*H*), 6.51 (s, 1 H, benzylidene-*H*), 3.06 (s, 3 H, NCH_3) ppm;
^{13}C{^{1}H} NMR (100 MHz, DMSO-d_6): δ = 167.73 (carbonyl-*C*), 156.63 (NR-*C*-NR), 156.42

(Ph-2-*C*), 133.26 (N-*C*-CO), 133.93 (Ph-3-*C*), 132.54 (Ph-6-*C*), 122.48 (Ph-5-*C*), 130.31 (Ph-4,6-*C*), 121.64 (Ph-5-*C*), 118.87 (Ph-3-*C*), 117.56 (Ph-1-*C*), 112.69 (benzylidene-*C*), 25.82 (N*C*H$_3$) ppm;
HR-MS (ESI-): *m/z* calc. ($C_{11}H_{10}N_3O_2$, $[M-H]^-$): 216.0779, found: 216.0775.

(*Z*)-2-Amino-5-(3-bromo-4-hydroxy-5-methoxybenzylidene)-3-methyl-3,5-dihydro-4*H*-imidazol-4-one (BMHBI-NH$_2$, 108)

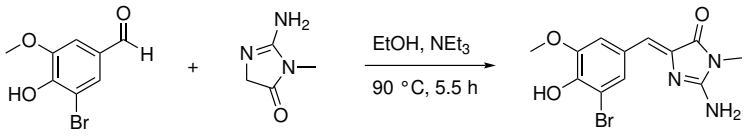

$C_8H_7BrO_3$
231.05 g mol^{-1}

$C_4H_7N_3O$
113.12 g mol^{-1}
106

$C_{12}H_{12}BrN_3O_3$
326.15 g mol^{-1}
108

Compound **108** was synthesized according to general procedure XI on a 2.21 mmol scale by heating the reaction mixture for 5.5 h to 90 °C. Column chromatography on silica gel (CH_2Cl_2/MeOH 50:1) afforded the product **108** as an orange solid (403 mg, 1.24 mmol, 56%).

^{1}H NMR (400 MHz, DMSO-d_6): $\delta = 9.67$ (s, 1 H, O*H*), 8.08 (d, $J = 1.8$ Hz, 1 H, Ph-2,6-*H*), 7.54 (s, 2 H, NH_2), 7.51 (d, $J = 1.8$ Hz, 1 H, Ph-2,6-*H*), 6.30 (s, 1 H, benzylidene-*H*), 3.83 (s, 3 H, OCH_3), 3.03 (s, 3 H, NCH_3) ppm;
^{13}C{^{1}H} NMR (100 MHz, DMSO-d_6): $\delta = 169.60$ (carbonyl-*C*), 159.44 (NR-*C*-NR), 147.95 (Ph-5-*C*), 143.32 (Ph-4-*C*), 139.59 (N-*C*-CO), 128.45 (Ph-1-*C*), 126.05 (Ph-2,6-*C*), 113.40 (Ph-3-*C*), 111.49 (benzylidene-*C*), 56.21 (O*C*H$_3$), 25.65 (N*C*H$_3$) ppm;
HR-MS (ESI+): *m/z* calc. ($C_{12}H_{13}BrN_3O_3$, $[M]^+$): 326.0135, found: 326.0135.

(*Z*)-2-Amino-5-(4-hydroxy-3-methoxybenzylidene)-3-methyl-3,5-dihydro-4*H*-imida-zol-4-one (MHBI-NH$_2$, 109)

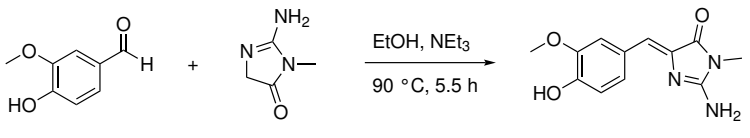

$C_8H_8O_3$
152.15 g mol^{-1}

$C_4H_7N_3O$
113.12 g mol^{-1}
106

$C_{12}H_{13}N_3O_3$
247.25 g mol^{-1}
109

Compound **109** was synthesized according to general procedure XI on a 2.21 mmol scale by heating the reaction mixture for 5.5 h to 90 °C. Column chromatography on silica gel (CH_2Cl_2/MeOH 20:1) afforded the product **109** as an orange solid (113 mg, 0.46 mmol, 21%).

^{1}H NMR (400 MHz, DMSO-d_6): $\delta = 9.24$ (s, 1 H, O*H*), 7.73 (d, $J = 1.9$ Hz, 1 H, Ph-2-*H*), 7.51 (dd, $J = 8.5$, 1.9 Hz, 1 H, Ph-6-*H*), 7.35 (s, 2 H, NH_2), 6.75 (d, $J = 8.2$ Hz, 1 H, Ph-5-*H*), 6.33 (s, 1 H, benzylidene-*H*), 3.79 (s, 3 H, OCH_3), 3.03 (s, 3 H, NCH_3) ppm;

$^{13}C\{^1H\}$ NMR (100 MHz, DMSO-d_6): δ = 169.80 (carbonyl-*C*), 158.81 (NR-*C*-NR), 149.44 (Ph-3-*C*), 147.60 (Ph-4-*C*), 147.34 (Ph-3-*C*), 146.81 (Ph-4-*C*), 138.38 (N-*C*-CO), 127.62 (Ph-1-*C*), 124.26 (Ph-6-*C*), 115.46 (Ph-5-*C*), 114.55 (benzylidene-*C*), 113.63 (Ph-2-*C*), 55.74 (O*C*H_3), 25.63 (N*C*H_3) ppm;
HR-MS (ESI+): *m/z* calc. ($C_{12}H_{14}N_3O_3$, $[M+H]^+$): 248.1030, found: 248.1032.

(*Z*)-2-Amino-5-(4-hydroxybenzylidene)-3-methyl-3,5-dihydro-4*H*-imidazol-4-one (HBI-NH_2, 110)

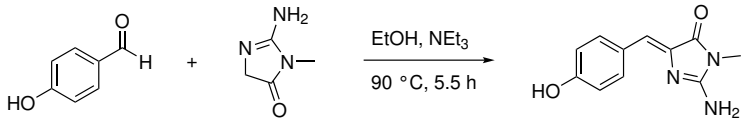

$C_7H_6O_2$ 122.12 g mol^{-1} | $C_4H_7N_3O$ 113.12 g mol^{-1} **106** | $C_{11}H_{11}N_3O_2$ 217.23 g mol^{-1} **110**

Compound **110** was synthesized according to general procedure XI on a 1.34 mmol scale by heating the reaction mixture for 5.5 h to 90 °C. Column chromatography on silica gel (CH_2Cl_2/MeOH 20:1 to 9:1) afforded the product **110** as an orange solid (90.0 mg, 0.41 mmol, 31%).

^1H NMR (400 MHz, DMSO-d_6): δ = 9.66 (s, 1 H, O*H*), 8.08 - 7.96 (m, 2 H, Ph-2,6-*H*), 6.78 - 6.70 (m, 2 H, Ph-3,5-*H*), 6.32 (s, 1 H, benzylidene-*H*), 3.02 (s, 3 H, NCH_3) ppm;
$^{13}C\{^1H\}$ NMR (100 MHz, DMSO-d_6): δ = 169.73 (carbonyl-*C*), 158.79 (NR-*C*-NR), 157.26 (Ph-4-*C*), 138.15 (N-*C*-CO), 131.92 (Ph-2,6-*C*), 127.01 (Ph-1-*C*), 115.28 (Ph-3,5-*C*), 113.27 (benzylidene-*C*), 25.61 (N*C*H_3) ppm;
HR-MS (ESI+): *m/z* calc. ($C_{11}H_{12}N_3O_2$, $[M+H]^+$): 218.0924, found: 218.0921.

(*Z*)-2-Amino-5-(4-hydroxy-3,5-dimethoxybenzylidene)-3-methyl-3,5-dihydro-4*H*-imidazol-4-one (DMHBI-NH_2, 111)

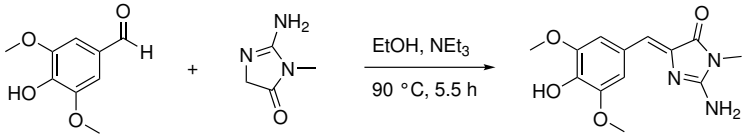

$C_9H_{10}O_4$ 182.18 g mol^{-1} | $C_4H_7N_3O$ 113.12 g mol^{-1} **106** | $C_{13}H_{15}N_3O_4$ 277.28 g mol^{-1} **111**

Compound **111** was synthesized according to general procedure XI on a 1.34 mmol scale by heating the reaction mixture for 5.5 h to 90 °C. Column chromatography on silica gel (CH_2Cl_2/MeOH 20:1 to 9:1) afforded the product **111** as an orange solid (495 mg, 1.42 mmol, 64%).

^{1}H NMR (400 MHz, DMSO-d_6): δ = 8.66 (s, 1 H, O*H*), 7.44 (s, 2 H, Ph-2,6-*H*), 7.35 (s, 2 H, NH_2), 6.33 (s, 1 H, benzylidene-*H*), 3.77 (s, 6 H, OCH_3), 3.03 (s, 3 H, NCH_3) ppm;
^{13}C{^{1}H} NMR (100 MHz, DMSO-d_6): δ = 169.75 (carbonyl-*C*), 158.80 (NR-*C*-NR), 147.70 (Ph-3,5-*C*), 138.61 (N-*C*-CO), 136.19 (Ph-4-*C*), 126.41 (Ph-1-*C*), 113.75 (benzylidene-*C*), 108.63 (Ph-2,6-*C*), 56.11 (O*C*H$_3$), 25.60 (N*C*H$_3$) ppm;
HR-MS (ESI+): *m/z* calc. ($C_{13}H_{16}N_3O_4$, $[M+H]^+$): 278.1135, found: 278.1140.

(*Z*)-2-Amino-5-(3,5-difluoro-4-hydroxybenzylidene)-3-methyl-3,5-dihydro-4*H*-imidazol-4-one (DFHBI-NH$_2$, 112)

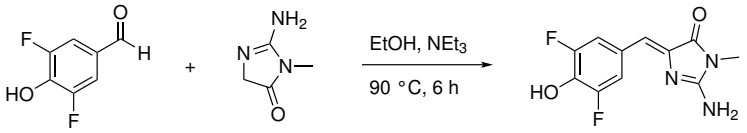

$C_7H_4F_2O_2$ | 158.10 g mol^{-1} | **120**
$C_4H_7N_3O$ | 113.12 g mol^{-1} | **106**
$C_{11}H_9F_2N_3O_2$ | 253.21 g mol^{-1} | **112**

Compound **112** was synthesized according to general procedure XI on a 2.21 mmol scale by heating the reaction mixture for 6 h to 90 °C. Column chromatography on silica gel (CH_2Cl_2/MeOH 20:1 to 10:1) afforded the product **112** as an orange solid (271 mg, 1.06 mmol, 48%).

^{1}H NMR (400 MHz, DMSO-d_6): δ = 10.37 (s, 1 H, O*H*), 7.82 - 7.75 (m, 2 H, Ph-2,6-*H*), 7.64 (s, 2 H, NH_2), 6.29 (s, 1 H, benzylidene-*H*), 3.03 (s, 3 H, NCH_3) ppm;
^{13}C{^{1}H} NMR (100 MHz, DMSO-d_6): δ = 169.47 (carbonyl-*C*), 159.90 (NR-*C*-NR), 153.08 (Ph-3,5-*C*), 140.64 (N-*C*-CO), 133.00 (Ph-1-*C*), 127.00 (Ph-4-*C*), 113.00 (benzylidene-*C*), 110.10 (Ph-2,6-*C*), 25.65 (N*C*H$_3$) ppm;
HR-MS (ESI+): *m/z* calc. ($C_{11}H_{10}F_2N_3O_2$, $[M+H]^+$): 254.0736, found: 254.0742.

(*Z*)-2-Amino-(*N,N*-dimethylformamidine)-5-(4-hydroxy-3,5-dimethoxybenzylidene)-3-methyl-3,5-dihydro-4*H*-imidazol-4-one (DMAM-DMBHI-NH$_2$, 115)

$C_{13}H_{15}N_3O_4$ | 277.28 g mol^{-1} | **111**
$C_{16}H_{20}N_4O_4$ | 332.36 g mol^{-1} | **115**

DMHBI-NH$_2$ (**111**, 250 mg, 0.81 mmol, 1.00 eq.) was dissolved under nitrogen atmosphere in anhydrous MeOH (11 mL). Subsequently, DMFDMA (428 mg, 3.60 mmol, 4.00 eq.) was added and the resulting red solution was stirred for 3 h at r. t. The solvent was afterwards removed in vacuum and the residue was purified by column chromatography on silica

gel (CH_2Cl_2/MeOH 95:5) to afford the target compound **115** as a yellow solid (171 mg, 0.51 mmol, 57%).

^{1}H NMR (400 MHz, DMSO-d_6): δ = 8.80 - 8.74 (m, 2 H, O*H* and DMAM-C*H*), 7.56 (s, 2 H, Ph-2,5-*H*), 6.54 (s, 1 H, benzylidene-*H*), 3.81 (s, 6 H, OCH_3), 3.24 - 3.10 (m, 6 H, DMAM-CH_3), 3.03 (s, 3 H, NCH_3) ppm;
^{13}C{^{1}H} NMR (100 MHz, DMSO-d_6): δ = 169.97 (carbonyl-*C*), 163.08 (N-*C*-NMe), 158.19 (Ph-4-*C*), 147.69 (Ph-3,5-*C*), 138.31 (DMAM-*C*H), 136.59 (Ph-1-*C* or N-*C*-CO), 125.99 (Ph-1-*C* or N-*C*-CO), 117.65 (benzylidene-*C*), 108.75 (Ph-2,5-*C*), 55.86 (O*C*H_3), 41.10 (DMAM-*C*H_3), 34.75 (DMAM-*C*H_3), 25.45 (N*C*H_3) ppm;
HR-MS (ESI+): *m/z* calc. ($C_{16}H_{20}N_4NaO_4$, $[M+Na]^+$): 355.1377, found: 355.1370.

5.1.2.10 Preparation of DMHB-PTH derivatives

(*Z*)-2-Amino-5-(4-hydroxy-3,5-dimethoxybenzylidene)thiazol-4(5*H*)-one (DMHB-PTH, 113)

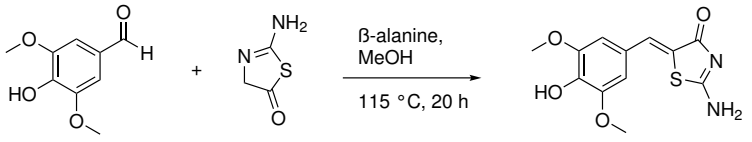

$C_9H_{10}O_4$
182.18 g mol^{-1}

$C_3H_4N_2OS$
116.14 g mol^{-1}
106

$C_{12}H_{12}N_2O_4S$
280.30 g mol^{-1}
113

4-Hydroxy-3,5-dimethoxybenzaldehyde (600 mg, 3.29 mmol, 1.00 eq.), pseudothiohydantoin (380 mg, 3.27 mmol, 1.00 eq.) and β-alanine (59 mg, 0.66 mmol, 0.20 eq.) were dissolved in MeOH (6 mL). The reaction mixture was stirred for 20 h at 115 °C. The resulting orange suspension was afterwards cooled to 0 °C, the precipitate was filtered off and washed with H_2O (4×5 mL), EtOH (2×5 mL), Et_2O (2×5 mL) and CH_2Cl_2 to obtain the target compound **113** as an orange solid (752 mg, 2.68 mmol, 82%).

^{1}H NMR (400 MHz, DMSO-d_6): δ = 9.10 (s, 2 H, NH_2), 7.53 (s, 1 H, benzylidene-*H*), 6.88 (s, 2 H, Ph-2,6-*H*), 3.81 (s, 6 H, OCH_3) ppm;
^{13}C{^{1}H} NMR (100 MHz, DMSO-d_6): δ = 181.72 (carbonyl-*C*), 175.39 (S-*C*-N), 148.07 (Ph-3,5-*C*), 137.50 (Ph-1-*C*), 130.07 (benzylidene-*C*), 125.71 (S-*C*-CO), 124.71 (Ph-4-*C*), 107.21 (Ph-2,6-*C*), 55.87 (O*C*H_3) ppm;
HR-MS (ESI+): *m/z* calc. ($C_{12}H_{12}N_2NaO_4S$, $[M+Na]^+$): 303.0410, found: 303.0412.

(*Z*)-2-Amino-(*N,N*-dimethylformamidine)-5-(4-hydroxy-3,5-dimethoxybenzylidene)-thiazol-4(5*H*)-one (DMAM-DMHB-PTH, 114)

$C_{12}H_{12}N_2O_4S$
280.30 g mol^{-1}
113

$C_{15}H_{17}N_3O_4S$
335.38 g mol^{-1}
114

DMHB-PTH (**113**, 400 mg, 1.43 mmol, 1.00 eq.) was dissolved under nitrogen atmosphere in anhydrous MeOH (16 mL). Subsequently, DMFDMA (721 mg, 6.05 mmol, 4.20 eq.) was added and the resulting red solution was stirred for 3 h at r. t. The solvent was afterwards removed in vacuum and the residue was purified by column chromatography on silica gel (CH_2Cl_2/MeOH 10:1) to afford the target compound **114** as an orange solid (414 mg, 1.23 mmol, 86%).

^{1}H NMR (400 MHz, DMSO-d_6): δ = 9.18 (s, 1 H, O*H*), 8.84 (s, 1 H, DMAM-C*H*), 7.59 (s, 1 H, benzylidene-*H*), 6.92 (s, 2 H, Ph-2,5-*H*), 3.82 (s, 6 H, OCH_3), 3.30 (d, J = 0.7 Hz, 3 H, NCH_3), 3.17 (d, J = 0.9 Hz, 3 H, NCH_3) ppm;
^{13}C{^{1}H} NMR (100 MHz, DMSO-d_6): δ = 185.53 (carbonyl-*C*), 181.20 (S-*C*-N), 159.72 (DMAM-*C*H), 148.19 (Ph-3,5-*C*), 137.92 (Ph-1-*C*), 131.67 (benzylidene-*C*), 126.72 (S-*C*-CO), 124.38 (Ph-4-*C*), 107.58 (Ph-2,6-*C*), 56.03 (O*C*H_3), 41.71 (N*C*H_3), 35.77 (N*C*H_3) ppm;
HR-MS (ESI+): *m/z* calc. ($C_{15}H_{17}N_3NaO_4S$, [M+Na]$^+$): 358.0832, found: 358.0825.

5.2 Oligonucleotide solid phase synthesis

5.2.1 Synthetic procedure and oligonucleotide deprotection

Automated solid phase synthesis was carried using an Applied Biosystems ABI 392 DNA/RNA synthesizer on a 0.6 µmol scale. Standard 5'-*O*-DMT-2'-*O*-TOM-protected RNA and 5'-*O*-DMT-protected DNA phosphoramidites for solid phase synthesis as well as standard 5'-*O*-DMT-protected CPG supports (1000 Å, 25 - 35 µmol/g for DNA, 20 - 30 µmol/g for RNA) were purchased from ChemGenes or Sigma Aldrich. The following solutions were used: 0.25 M ethylthiotetrazole (ETT) in anhydrous acetonitrile as activator, 3% dichloro acetic acid in 1,2-dichloroethane for detritylation of RNA oligonucleotides and 3% trichloro acetic acid in 1,2-dichloroethane for DNA and GNA oligonucleotides, 20 mM iodine in THF/water/pyridine 66/12/22 for oxidation, pyridine/acetic anhydride/THF 10/10/80 as Cap A solution and 16% NMI in THF as Cap B solution. RNA and DNA oligonucleotides were prepared on commercially

available CPG solid supports using 70 mM solutions for standard phosphoramidites and 80 - 100 mM solutions for self-made phosphoramidites in acetonitrile dried over molecular sieves. GNA oligonucleotides were prepared on an in-house made 3'-phosphate solid support. DNA oligonucleotides were synthesized using a standard protocol with a coupling time of 2 min, while RNA and GNA were synthesized with a coupling time of 4 min. Stepwise coupling yields were assessed from the absorbance of the trityl cation released during the detritylation step. DNA and RNA syntheses were carried out in DMT-off mode while GNA oligonucleotides were synthesized in DMT-on mode to prevent degradation during alkaline deprotection.[47,436,440]

RNA oligonucleotides were cleaved from the solid support and deprotected by incubation with aqueous ammonia/abs. ethanol 3/1 overnight at 37 °C. Afterwards, the solid support was filtered off and the solvent was removed in vacuum. The crude samples were redissolved in 1 M TBAF solution in THF (500 µL) and shaken overnight at r. t. After addition of 1 M Tris-HCl pH 8.0 (500 µL), the THF was removed in vacuum and the oligonucleotide samples were desalted by size exclusion chromatography using an Äkta start purification system with three HiTRAP Desalting columns (each 5 mL volume, 2 mL/min flow rate) from GE Healthcare. The water was removed under reduced pressure and the samples were redissolved in 600 µL of nanopure water.

DNA oligonucleotides were cleaved from the solid support and deprotected by incubation in 1 mL of aqueous ammonia overnight at 37 °C. After filtration and removal of the solvent in vacuum, the crude oligonucleotides were redissolved in 600 µL of nanopure water.

GNA oligonucleotides were cleaved from the solid support and deprotected by incubation with 1 mL of aqueous ammonia overnight at 37 °C. After filtration and removal of the solvent under reduced pressure, the crude oligonucleotides were dissolved in 600 µL of nanopure water. The samples were divided into four portions of 150 µL each and to each portion 150 µL of acetic acid was added for cleavage of the 5'-DMT group. After incubation for 30 min at r. t., 3 M NaCl solution was added to a final NaCl concentration of 300 mM. The crude oligonucleotides were then precipitated with abs. ethanol (70% final concentration) and the dried pellets were redissolved in 600 µL of nanopure water.

5.2.2 Oligonucleotide purification and characterization

Crude oligonucleotide mixtures were purified according to their charge state by denaturing polyacrylamide gel electrophoresis (PAGE). Gels were prepared from acrylamide stock solutions containing 5% bis-acrylamide as a crosslinker and 7 M urea as a denaturing agent. The concentration of acrylamide was chosen based on the length of the respective oligonucleotide, with 20% for oligonucleotides shorter than 20nt and 15% for oligonucleotides longer than 20nt. Polymerization was initiated by addition of 130 µL of 25% ammonium peroxodisulfate (APS)

and 35 µL of tetramethylethylenediamine (TEMED) to 50 mL of the polyacrylamide gel stock solution. Gels were polymerized for 30 min at ambient temperature and pre-run for 30 min at 35 W using 1× TBE buffer (89 mM Tris, 89 mM boric acid, 2 mM EDTA, pH 8.3) as running buffer.

Preparative gel purification of the crude oligonucleotides was performed with 300×200×0.7 mm polyacrylamide gels with four pockets which were loaded with a 1:1 mixture of crude oligonucleotide solution and high dye (80% formamide (99%), 100 mM Tris pH 8.0. 0.1 mM boric acid, 70 mM EDTA pH 8.0, 0.25 mg/mL bromophenol blue, 0.25 mg/mL xylene cyanol). The oligonucleotide bands were visualized by UV shadowing on a TLC plate using a Serva DIAS-II imaging and analysis system. The oligonucleotide bands were excised from the gel, the gel pieces were soaked overnight at 4 °C for oligonucleotide extraction in 450 µL of TEN buffer (10 mM Tris-HCl, 0.1 mM EDTA, 300 mM NaCl, pH 8.0). After removal of the supernatant, the gel pieces were again incubated in 450 µL of TEN buffer for 2 h at 37 °C. For oligonucleotide precipitation, the TEN buffer was mixed with abs. ethanol (70% final concentration), frozen in liquid nitrogen and centrifuged for 30 min at 4 °C and 15,000 rpm. The supernatant was removed carefully, the remaining pellets were covered with 75 µL of 70% ethanol and again centrifuged for 10 min. After removal of the supernatant, the oligonucleotide pellets were dried in vacuum and resuspended in 400 µL of deionized water.

For analytical assays, gels (300×200×0.4 mm) with up to 28 sample pockets were used. These gels were run in 1× TBE for 90 min at a constant voltage of 25 V. Bands were visualized by a BioRad Universal Hood III under either the fluorescein (530/28 filter, blue epi illumination) or the Cy5 (695/55 filter, red epi illumination) channel. Some gels were stained by incubation with 1× SYBR gold in TBE for 5 min prior to imaging.

To estimate the concentration of crude and pure oligonucleotide solutions, an Implen NanoPhotometer P 360 was used. Concentrations of DNA, RNA and GNA samples were determined from their UV absorbance at 260 nm based on reported extinction coefficients of the individual nucleosides (15,400 L mol^{-1} cm^{-1} for A, 7,300 L mol^{-1} cm^{-1} for C, 11,700 L mol^{-1} cm^{-1} for G, 8,800 L mol^{-1} cm^{-1} for T and 9,900 L mol^{-1} cm^{-1} for U) with neglection of the nearest-neighbor effect. The concentrations of modified oligonucleotides were calculated by using the extinction coefficient estimated for the free chromophores.

High-resolution ESI mass spectra in negative ion mode were recorded on a Bruker micrOTOF-Q III instrument, using 200 pmol of oligonucleotide in 8 µL of nanopure water. The monoisotopic masses of pure oligonucleotides were obtained by charge deconvolution of the raw spectra. Samples were diluted with hexafluoroisopropanol (HFIP) in acetonitrile and directly injected into the ESI source.

5.2.3 HPLC

5.2.3.1 Anion exchange HPLC

The quality of PAGE-purified oligonucleotides was checked using an ÄKTApurifier from GE Healthcare with a DNAPac PA200 column (2×250 mm) from Thermo Scientific with a sample concentration of 100 pmol in 15 µL of nanopure water. Runs were performed using Dionex buffer A (6 M urea, 250 mM Tris-HCl pH 8.0) and B (6 M urea, 0.5 M $NaClO_4$, 250 mM Tris-HCl pH 8.0) with a gradient of 0–48% B over 12 CV, a flow rate of 0.5 mL min^{-1} and a temperature of 60 °C.

5.2.3.2 Reverse-phase HPLC

Some oligonucleotides had to be further purified by RP-HPLC as mentioned in the discussion part of this thesis. Runs were performed on an ÄKTA micro system from GE Healthcare at 30 °C with a 8×250 mm Nucleosil 100-7 C18 column from Macherey-Nagel and a buffer gradient from 5% to 30% of triethylammonium acetate (TEAA) buffer B over 4.8 column volumes (buffer A: water, 100 mM TEAA, pH 7.0; buffer B: 90% MeCN, 10% water, 100 mM TEAA pH 7.0). The solvent of the collected samples was removed under reduced pressure and the pure oligonucleotides were redissolved in water.

5.2.4 5'-Labeling

5'-Alkinyl-modified oligonucleotides were labeled with 6-FAM- or sulfo-Cy5-azide in a CuAAC reaction. 10 nmol of the respective oligonucleotide were dissolved in 10 µL of nanopure water and mixed with 6 µL of DMSO/*t*BuOH 3:1. To this solution, 1.25 µL of the chromophore azide (50 mM in DMSO), 1.25 µL of freshly prepared 10 mM CuBr in DMSO/*t*BuOH 3:1 and 2.5 µL of 100 mM tris[(1-benzyl-1*H*-1,2,3-triazol-4-yl)methyl]amin (TBTA) in DMSO/*t*BuOH 3:1 were added. The reaction mixture was incubated for 4 h at 37 °C in the dark and then stopped by addition of 30 µL of stop solution (80% formamide (99%), 100 mM Tris pH 8.0. 0.1 mM boric acid, 70 mM EDTA pH 8.0). Purification of the labeled oligonucleotides was achieved by preparative PAGE.

5.2.5 Oligonucleotide NMR spectroscopy

For NMR spectroscopy, the required amount of aqueous oligonucleotide solution was diluted 1:5 with acetone/$LiClO_4$ (2% w/v) and kept at -20 °C for 6 h. The sample was then centrifuged for 30 min at 4 °C and 15,000 rpm. After removal of the supernatants, the pellets were dried in vacuum, redissolved in 350 µL of nanopure water and lyophilized overnight on a Christ Alpha 2-4 LSCbasic lyophilizer. The pellets were again dissolved in 300 µL of nanopure water and an equal amount of both single strands was taken out, mixed with 9 µL of 200 mM sodium phosphate pH 7.0 and 18 µL of 1 M NaCl to final concentrations of 10 and 100 mM, respectively. These samples were annealed for 3 min at 95 °C, cooled to r. t. and again lyophilized overnight. Successful annealing was controlled by native PAGE: after lyophilization, 100 pmol of each strand was dissolved in 5 µL of 1 M NaCl (100 mM final concentration), 2.5 µL of 200 mM sodium phosphate (10 mM final concentration) and 40.25 µL of water. After annealing for 3 min at 95 °C, the sample was loaded onto an native (no urea containing) 15% gel (1.0×80×100 mm) with ten pockets and run in 1× TBE buffer for 1 h at a constant voltage of 100 V. If only a single band was visible after staining with SYBR gold, sucessfull annealing of the two single strands was assumed. For sample preparation, the lyophilized duplex was dissolved in 162 µL of H_2O, 18 µL of D_2O and 0.4 µL of 7 mM sodium trimethylsilylpropanesulfonate (DSS) standard and filled into a 3 mm NMR tube. Duplex concentrations were 200 µM for 1D imino and 440 µM for 2D NOESY measurements. NMR spectra were recorded on a Bruker Avance III HD 600 spectrometer equipped with a DCH13C/1H cryoprobe at variable temperatures.

5.3 Enzymatic assays

5.3.1 General remarks

Enzymes and the respective reaction buffers for enzymatic assay were either purchased from commercial suppliers (New England BioLabs Inc., ThermoFisher Scientific) or, in the case of T7 RNA polymerase, in-house made following a reported procedure.[487]

5.3.2 *In vitro* transcription

In vitro transcription was performed using 100 pmol of template and 100 pmol of T7 promoter. Both were mixed with 5 µL of 10× TxAB annealing buffer and filled up with deionized water to a total volume 50 µL. For annealing, the sample was incubated for 5 min at 95 °C and then cooled to r. t. for 20 min. Afterwards, 4 µL of 1 M Tris-HCl pH 8.0 (40 mM final concentration), 4 µL of 250 mM dithiothreitol (DTT, 10 mM final concentration), 4 µL of each NTP (100 mM stock, 4 mM final concentration), 3 µL of 1 M $MgCl_2$ (30 mM final concentration) and 2 µL of 100 mM spermidine (2 mM final concentration) were added to the annealed mixture and the total volume was brought up to 98 µL using deionized water. After mixing properly,

2 µL of T7 RNA polymerase were added and the sample was incubated overnight at 37 °C. The reaction was stopped by the addition of 80 µL of high dye. The final transcript was then purified by PAGE.

5.3.3 PCR

PCR experiments were conducted with 1 pmol of template, 20 pmol of both forward and reverse primer and a dNTP concentration of 20 mM in a reaction volume of 50 µL. DreamTaq DNA polymerase (0.01 u/µL) was used as an enzyme. To obtain optimal conditions for this enzyme, the PCR mixture was incubated in 1× DreamTaq buffer (contains KCl, $(NH_4)_2SO_4$ and 2 mM $MgCl_2$). After initial sample denaturation for 4 min at 95 °C, a PCR cycle including a denaturing step (30 s, 95 °C), an annealing step (30 s, 60 °C) and an amplification step (30 s, 72 °C) was repeated 25 times, followed by cooling of the reaction mixture to 4 °C (Figire 5.1).

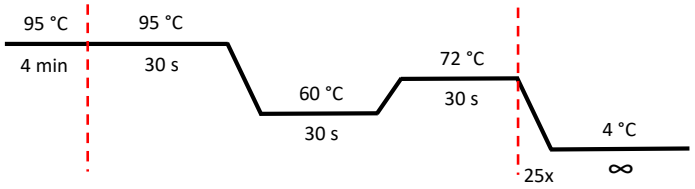

Figure 5.1: PCR conditions 25× repetition of the denaturing, annealing and amplification step.

The PCR mixture was purified by 15% analytical PAGE (300×200×0.4 mm) which was run for 90 min at 25 W. Oligonucleotide bands were visualized with a ChemiDoc imager under imaging settings for fluorescein and Cy5 as well as by staining with SYBR gold.

5.3.4 Primer extension

5.3.4.1 Primer extension with the modified triphosphate 51

For primer extension assays in the presence of the modified triphosphate **51** final concentrations of 1 µM of primer and 2 µM of template were used. In addition, the reaction mixture contained 200 µM dNTPs and 0.05 u/µL Taq DNA polymerase. The volume was filled up to 20 µL with 1× Standard Taq Reaction buffer (10 mM Tris-HCl, 50 mM KCl, and 1.5 mM $MgCl_2$, pH 8.3) and the mixture was incubated at 72 °C for the required reaction time. The reaction was stopped by addition of 10 µL of stop solution and aliquots were loaded onto 15% analytical PAGE (300×200×0.4 mm) which was run for 90 min at 20 W. Oligonucleotide bands were visualized with a ChemiDoc imager under imgaging settings for fluorescein and Cy5.

5.3.4.2 Primer extension with a modified template

For primer extension assays with modified triphosphate templates final concentrations of 1 µM of primer and 2 µM of template were used. In addition, the reaction mixture contained 200 µM dNTPs and 0.05 u/µL Klenow exo- polymerase. The volume was filled up to 20 µL with 1× Klenow buffer (50 mM Tris-HCl pH 7.2, 10 mM $MgSO_4$ and 100 µM DTT) and the mixture was incubated at 37 °C for the required reaction time. The reaction was stopped by addition of 10 µL of stop solution and aliquots were loaded onto 20% analytical PAGE (300×200×0.4 mm) which was run for 90 min at 20 W. Oligonucleotide bands were visualized with a ChemiDoc imager under imgaging settings for fluorescein and Cy5.

5.3.5 Helicase assay

To test the capability of Tte UvrD helicase to unwind a 12nt DNA duplex, 1 µM samples of the duplex of interest in 20 µL of 1× Isothermal Amplification buffer (20 mM Tris-HCl, 10 mM $(NH_4)_2SO_4$, 50 mM KCl, 2 mM $MgSO_4$, 0.1% Tween® 20, pH 8.8) in the presence of 10 mM ATP and 10 µM capture strand were prepared. The reaction volume was filled up to 20 µL and 20 ng of Tte UvrD helicase were added before the sample was incubated at 25 °C in a Hellma ultra-micro quartz cuvette (1.5×1.5 mm). Fluorescence spectra were recorded at different time points as described in section 3.4.5.4.

5.4 Spectroscopy

5.4.1 UVvis spectroscopy

5.4.1.1 General remarks

Absorption spectra were collected on a JASCO V-770 spectrophotometer equipped with a PAC-743 cell changer, a VARIAN CARY 100 Bio spectrophotometer equipped with a 6×6 Multicell Block Peltier Series II cell changer and a VARIAN CARY Temperature Controller or an Agilent Cary 3500 spectrophotometer with an Agilent Cary UV-Vis Multicell Peltier. Standard absorption spectra were measured in VARIAN semi-micro quartz cuvettes or in Roth semi-micro polystyrene cuvettes (10 mm path length, for pK_a-titrations) at ambient temperature unless noted otherwise. Scan speed, spectral bandwidths and integration time were adjusted to record a stable signal within a reasonable timeframe. Spectra were blank corrected by subtraction of a spectrum of pure buffer or solvent in the same cuvette. If constant residual baseline offsets occurred for measurements in cuvettes with small window sizes, the entire spectra were shifted up- or downwards to achieve the same baseline level.

Measurement parameters at the Agilent Cary 3500 spectrophotometer:

- measurement range 200 - 800 nm

- 2 nm spectral bandwidth
- 3000 nm/min scan speed
- 1 nm data interval
- 20 ms averaging time

Measurement parameters at the VARIAN CARY 100 Bio spectrophotometer:

- measurement range 200 - 800 nm
- 2 nm spectral bandwidth
- 600 nm/min scan speed
- 1 nm data interval
- 100 ms averaging time

Measurement parameters at the JASCO V-770 spectrophotometer:

- measurement range 200 - 800 nm
- 2 nm spectral bandwidth
- 1000 nm/min scan speed
- 0.5 nm data interval
- 60 ms averaging time

5.4.1.2 Temperature-dependent absorption spectra

Temperature-dependent absorption spectra were recorded for 5 µM samples between 10 and 90 °C by stepwise increasing the temperature by 10 °C. For oligonucleotides with high chromophore content, an appropriate sample concentration was chosen to obtain an absorbance of approximately one for qualitative comparison. To guarantee a stable sample temperature, spectra were recorded 2 min after the respective temperature had been reached.

5.4.1.3 pK_a-titrations

pK_a-titrations between pH 1 and 12 were conducted for 11 µM samples in 30 mM Britton-Robinson buffer (2.30 mL of AcOH, 2.72 mL of phosphoric acid and 2.48 g of boronic acid in 1 L of H_2O) in Roth semi-micro polystyrene cuvettes (10 mm path length). For sample preparation, 10 µL of a 1 mM stock of the chromophore in DMSO were diluted with 680 µL of 40 mM Britton-Robinson buffer and 210 µL of H_2O. Samples with pH 0.1 were prepared with the same amount of chromophore stock in 680 µL of 1 M HCl and 210 µL of H_2O. Blank spectra were recorded prior to addition of the ligand.

The investigated chromophores are only weak acids; the equilibrium of these acids HA with the respective deprotonated base A^- can therefore be described by the Henderson-Hasselbalch

equation

$$\mathrm{pH} = \mathrm{p}K_\mathrm{a} - \log\frac{[\mathrm{HA}]}{[\mathrm{A}^-]} \tag{23}$$

with the concentrations [HA] and [A^-]. Since the absorbances of the base and the acid vary proportionally with the pH, the absorbance values of these two are weighted by their mole fractions χ:

$$A = A_\mathrm{HA} \cdot \chi_\mathrm{HA} + A_{\mathrm{A}^-} \cdot \chi_{\mathrm{A}^-} = A_\mathrm{HA} \cdot \chi_\mathrm{HA} + A_{\mathrm{A}^-} \cdot (1 - \chi_\mathrm{HA}) \tag{24}$$

This equation can be rearreanged, leading to a mathematical expression for the mole fraction of the acid

$$\chi_\mathrm{HA} = \frac{A - A_{\mathrm{A}^-}}{A_\mathrm{HA} - A_{\mathrm{A}^-}} \tag{25}$$

and in analogy also for the mole fraction of the base

$$\chi_{\mathrm{A}^-} = \frac{A_\mathrm{HA} - A}{A_\mathrm{HA} - A_{\mathrm{A}^-}} \tag{26}$$

These two parts are combined in the Henderson-Hasselbalch equation (27):

$$\mathrm{pH} = \mathrm{p}K_\mathrm{a} - \log\frac{\chi_\mathrm{HA}}{\chi_{\mathrm{A}^-}} = \mathrm{p}K_\mathrm{a} - \log\frac{(A - A_{\mathrm{A}^-}) \cdot (A_\mathrm{HA} - A_{\mathrm{A}^-})}{(A_\mathrm{HA} - A_{\mathrm{A}^-}) \cdot (A_\mathrm{HA} - A)} \tag{27}$$

which gives after simplification and reorganization

$$10^{\mathrm{p}K_\mathrm{a} - \mathrm{pH}} = \frac{A - A_{\mathrm{A}^-}}{A_\mathrm{HA} - A} \tag{28}$$

From equation (28), the experimentally measured absorbance A is described by

$$A = A_\mathrm{HA} + \frac{A_\mathrm{HA} - A_{\mathrm{A}^-}}{1 + 10^{\mathrm{p}K_\mathrm{a} - \mathrm{pH}}} \tag{29}$$

The absorbance A at the absorption maximum of each observed deprotonation state was fitted to a suitable form of equation (29) to estimate the pK_a value of a chromophore of interest.

5.4.1.4 Molar extinction coefficient ϵ

For the estimation of the molar extinction coefficient ϵ dilution series of the free chromophores of interest in either water or 1× PBS (100 mM NaCl, 10 mM phosphate, pH 7.0) were prepared. The highest concentration was chosen to obtain an absorbance of approximately one to ensure the validity of the Beer-Lambert law. Samples were gradually diluted 1:1 with the respective solvent until no absorbance was detectable anymore, which was typically after six dilution steps. For data evaluation, the absorbance A at the maximum was plotted against the chromophore concentration c and a linear fit was applied. ϵ was calculated according to the Beer-Lambert

law

$$A = \epsilon \cdot c \cdot d \tag{30}$$

with the path length $d = 1$ cm.

5.4.1.5 Solvatochromism

Solvatochromism studies were carried out with 5 µM solutions of merocyanines or 11 µM solutions of DMHBI-derived chromophores. Samples were prepared from 1 mM chromophore stock solutions in DMSO, which were diluted with the respective solvents to the final concentration. Spectra were blank-corrected by subtraction of a spectrum of the pure respective solvent.

5.4.1.6 Oligonucleotide melting curves

To probe the stability of modified oligonucleotide duplex structures, UVvis melting curves were recorded. All of the samples were prepared in 1× PBS (100 mM NaCl, 10 mM phosphate, pH 7.0). 500 µL of samples with a duplex concentration of 1, 2 and 5 µM were measured in VARIAN semi-micro cuvettes (1 cm path length) while 300 µL of samples with a duplex concentration of 10 and 20 µM were measured in Hellma macro cuvettes (0.1 cm path length). The samples were covered with a 0.5 cm thick layer of silicon oil to prevent evaporation upon heating which would distort the sample concentration. In addition, a constant flow of nitrogen through the measurement chamber to limit condensation of air humidity was applied. Five temperature ramps between 10 and 90 °C were collected.

Measurement parameters:

- detection wavelengths 250, 260, 280 and 460 nm
- 1 nm spectral bandwidth
- 2 s averaging time
- 0.5 °C/min heating rate

The thermal denaturation of a duplex manifests in a sigmoidal increase of the absorbance in the nucleobase absorption region, which is typically described by the percentage hyperchromicity H with the absorbance Abs of the two single strands in the fully denatured state and the minimal absorbance $\mathrm{Abs_{min}}$ of the hybridized duplex:

$$H = 100 \cdot \frac{\mathrm{Abs} - \mathrm{Abs_{min}}}{\mathrm{Abs_{min}}} \tag{31}$$

In general, the melting temperature T_m of a duplex corresponds to the inflection point of the sigmoidal melting curve. A reliable value for T_m is obtained by applying a linear fit to the data points of a plot of $1/T_\mathrm{m}$ *vs.* $\ln c_\mathrm{tot}$ with the total oligonucleotide concentration c_tot.

According to the van't Hoff equation

$$\frac{1}{T_m} = \frac{(n-1)\cdot R}{\Delta H^0} \cdot \ln(c_{tot}) + \frac{[\Delta S^0 - (n-1)\cdot R \cdot \ln 2n]}{\Delta H^0} \quad (32)$$

with the molecularity n and the ideal gas constant the change in free enthalpy ΔH^0 upon melting can be calculated.[349] For the equilibrium of two non-self complementary strand, n is 2 and equation (32) simiplifies to

$$\frac{1}{T_m} = \frac{R}{\Delta H^0} \cdot \ln(c_{tot}) + \frac{[\Delta S^0 - R \cdot \ln 4]}{\Delta H^0} \quad (33)$$

Therefore, the slope m of the linear fit provides the change in enthalpy ΔH^0

$$\Delta H^0 = \frac{R}{m} \quad (34)$$

and from the intercept b the change in entropy ΔS^0 is obtained:

$$\Delta S^0 = (\Delta H^0 \cdot b) + R \cdot \ln 4 \quad (35)$$

If both values are inserted into the Gibbs-Helmholtz equation, ΔG^0 can be determined in addition:

$$\Delta G^0 = \Delta H^0 - T \cdot \Delta S^0 \quad (36)$$

ΔG^0 is typically estimated for 298 K which was also done in the course of this thesis. An accurancy of the melting temperature of ± 0.5 °C was assumed for all of the measurements.

5.4.2 CD and CPL spectroscopy

5.4.2.1 CD spectroscopy

CD spectra were recorded on a Jasco J-715 Spectropolarimeter equipped with a PS-150J Power Supply in VARIAN semi-micro quartz cuvettes (10 mm pathlength). Sample concentrations were 5 µM in 1× PBS (100 mM NaCl, 10 mM phosphate, pH 7.0) and spectra were blank-corrected by subtraction of a spectrum recorded for pure buffer. The measurement parameters were chosen to obtain a high tension (HT) voltage of below 400 V.

Measurement parameters:

- measurement range 190 - 600 nm
- 500 nm/min scan speed
- 0.1 nm data pitch
- 10 nm bandwith

- 1 s response
- accumulation: 2

5.4.2.2 CPL spectroscopy

CPL spectra were recorded on a customized JASCO CPL-300/J-1500 hybrid spectrometer equipped with a PM-539 detector and a RSC-502 Standard Cell Holder. Sample concentrations were 5 µM in 1× PBS (100 mM NaCl, 10 mM phosphate, pH 7.0) and samples were measured in VARIAN semi-micro quartz cuvettes (10 mm pathlength). The measurement range, the excitation wavelength and the bandwidths were adjusted to obtain a HT voltage of below 1000 V.

Measurement parameters:

- 50 nm/min scan speed
- 1 nm data pitch
- 2 s digital integration time per data (D. I. T.)
- continuous scanning mode
- accumulation: 15

5.4.3 Fluorescence spectroscopy

5.4.3.1 General remarks

Steady-state fluorescence spectra were recorded on a JASCO FP-8300 spectrofluorometer equipped with an FCT-817S water thermostatted automatic 8-position cell changer with stirrer and a Julabo F12 temperature control unit. Samples were measured in Hellma ultra-micro quartz cuvettes (10×2 mm or 1.5×1.5 mm) at appropriate excitation and emission wavelengths. These were either at the respective maximum or chosen to obtain a full spectrum for better qualitative comparability. The spectral bandwidths and photomultiplier tube (PMT) voltage were adjusted to achieve the highest possible signal intensity with the best signal-to-noise ratio and the scan speed and integration time were chosen to obtain a stable signal while minimizing the exposure time of the sample to the excitation light. Where indicated, excitation and emission spectra were manually background-corrected by subtraction of a blank spectrum. Spectral intensities were either reported at the spectra maximum or as integrated peak areas for a more reliable comparison with other data.

5.4.3.2 Temperature-dependent fluorescence

Temperature-dependent emission and excitation spectra of merocyanine-modified oligonucleotides were recorded for 1 µM samples in 1× PBS (100 mM NaCl, 10 mM phosphate, pH 7.0). The thermostat temperature was uniformely increased from 20 to 90 °C in steps of

10 °C, resulting in temperatures of up to 62 °C of the sample holder.

Measurement parameters:

- measurement range adjusted to obtain the complete excitation and emission peak
- 5 nm excitation bandwidth
- 5 nm emission bandwidth
- 500 nm/min scan speed
- 0.2 nm data interval
- 50 ms response
- 400 V PMT voltage

5.4.3.3 Fluorescence screening of DMHBI variants

The fluorescence of DMBHI variants was screened in the presence and absence of an aptamer. For these measurements, 100 µL of both a 2× aptamer and 2× ligand solution were prepared. For the preparation of the first sample mentioned, the amount of aptamer required for a final concentration of 1 µM was mixed with 12.5 µL of 1 M KCl (125 mM final concentration) and 16 µL of 500 mM HEPES pH 7.5 (80 mM final concentration) and annealed for 3 min at 95 °C. After incubation for 20 min at ambient temperature, 5 µL of 100 mM $MgCl_2$ (5 mM final concentration) were added and the sample was filled up to 100 µL with H_2O. The aptamer solution was stored at 4 °C overnight prior to measurement.

For the 2× ligand solution, 1 µL of 100 µM ligand in DMSO (1 µM final concentration) was mixed with with 12.5 µL of 1 M KCl (125 mM final concentration), 16 µL of 500 mM HEPES pH 7.5 (80 mM final concentration) and 5 µL of 100 mM $MgCl_2$ (5 mM final concentration) and filled up with H_2O to a total volume of 100 µL.

Samples for fluorescence measurements were prepared by combining each 7.5 µL of the 2× ligand and aptamer solutions and mixing thoroughly. For negative control, 7.5 µL of the ligand solution was combined with 7.5 µL of buffer (125 mM KCl, 80 mM HEPES pH 7.5, 5 mM $MgCl_2$). Samples were measured in Hellma ultra-micro quartz cuvettes (1.5×1.5 mm) and spectra were blank-corrected by subtraction of spectra of 7.5 µL buffer and 7.5 µL 2× aptamer solution recorded at the respective emission and excitation wavelength.

Measurement parameters:

- excitation and emission wavelengths were adjusted to the specific RNA-ligand complex
- 2.5 nm excitation bandwidth
- 5 nm emission bandwidth
- 500 nm/min scan speed
- 0.5 nm data interval

- 50 ms response
- 680 V PMT voltage

5.4.3.4 K_D estimation

For the K_D estimation of Chili-ligand complexes, varying concentrations of aptamer were titrated into a fixed concentration of ligand. First, 45 µL of a 16 µM stock solution of Chili in H_2O were prepared. This solution was diluted 1:1 with H_2O in a stepwise manner to obtain 2× aptamer solutions with concentrations between 8 µM and 0.49 nM. Then, 7.5 µL of each diluted sample was mixed with 4× buffer (500 mM KCl, 160 mM HEPES pH 7.5), annealed for 3 min at 95 °C and kept at ambient temperature for 20 min. Afterwards, 3.75 µL of 4× ligand solution (0.4 µM ligand, 20 mM $MgCl_2$) were added to a final volume of 15 µL. This protocol results in a dilution series containing 0.5 nM to 8 µM aptamer and 100 nM ligand. Before measurement, the samples were incubated for 16 h at 4 °C. For blank correction a sample with 7.50 µL of H_2O, 3.75 µL of ligand solution and 3.75 µL of buffer solution was prepared. Measurements were conducted in Hellma ultra-micro quartz cuvettes (1.5×1.5 mm).

Measurement parameters:

- 2.5 nm excitation bandwidth
- 5 nm emission bandwidth
- 500 nm/min scan speed
- 0.2 nm data interval
- 1 s response
- 680 V PMT voltage

The evaluation of the obtained data was based on several assumptions. In general, the dissociation constant K_D is the inverse of the association constant K_A and describes the tendency of a complex C to dissociate into the receptor R and the ligand L as an equilibrium constant:

$$R + L \overset{K}{\rightleftharpoons} C$$

Therefore, K_D can be expressed as

$$K_D = \frac{[R] + [L]}{[C]} \tag{37}$$

with the equilibrium concentrations [R], [L] and [C] and the fractional occupation θ of each receptor

$$\theta = \frac{[C]}{[C] + [R]} \qquad \text{or} \qquad 1 - \theta = \frac{[R]}{[R] + [C]} \tag{38}$$

According to the law of mass action, K_D corresponds to

$$K_D = \frac{(1-\theta)\cdot[L]}{\theta} = \frac{[L]-\theta\cdot[L]}{\theta} \tag{39}$$

By rearraging equation (39) and taking a number of binding sites n into account, the well known Hill-Langmuir equation is obtained:

$$\theta = \frac{[L]^n}{K_D + [L]^n} \tag{40}$$

Since the equilibrium concentrations of unbound R and L are usually not known, they need to be calculated from their concentration $[R]_0$ and $[L]_0$ prior to reaching the equilibrium:

$$[R] = [R_0] - [C] \qquad \text{and} \qquad [L] = [L_0] - [C] \tag{41}$$

θ can then be expressed depending on the initial concentrations

$$\theta = \frac{[C]}{[R_0]} \tag{42}$$

which leads to the complex concentration [C] as

$$[C] = [R_0] \cdot \frac{[L]^n}{K_D + [L]^n} \tag{43}$$

Since the emission intensity is proportional to the concentration of the formed aptamer-ligand complex, the normalized integrated area of the emission peak was plotted against the ligand concentration and fitted according to equation (43), which provided the Hill coefficient n and K_D.

5.4.3.5 NaCl titration

For titrations of oligonucleotides with NaCl, 2× stock solutions of NaCl in H_2O were mixed 1:1 with a 2 µM solution of both single strands in H_2O (1 µM final concentration) and measured immediately. 45 titration steps with an increasing NaCl concentration from 9.8 µM to 310 mM were conducted in Hellma ultra-micro quartz cuvettes (10×2 mm).

Measurement parameters:

- 5 nm excitation bandwidth
- 5 nm emission bandwidth
- 1000 nm/min scan speed
- 0.2 nm data interval
- 50 ms response

- 400 V PMT voltage

For data analysis, the intensities of the excitation at 433 nm and emission at 540 nm were normalized to 100 and plotted against the respective NaCl concentration on a logarithmic scale. Since the concentration of the dimer is proportional to its fluorescence intensity *I*, the data points were fitted according to a modified Hill-Langmuir equation

$$I = \frac{x^n}{k^n + x^n} \tag{44}$$

with the NaCl concentration *x*, the dissociation constant *k* and the Hill coefficient n as empirical cooperativity parameter. Since the Hill-Langmuir equation fundamentally describes a binding hyperbola, it is useful to determine the degree of cooperativity of ligand binding with n quantifying the degree of interaction between the ligand and the binding site (Figure 5.2).[488]

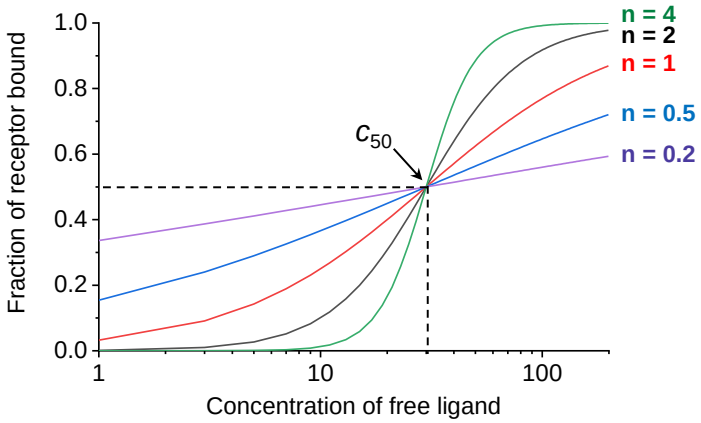

Figure 5.2: The Hill–Langmuir equation leads to characteristically sigmoidal curves to model cooperative binding. The saturation curve becomes steeper with increasing Hill coefficient and the inflection point of the curve reflects the required ligand concentration for occupation of half of the binding sites.

Positively cooperative binding is obtained for n>1 which means that binding of the first ligand increases the binding affinity for additional ligands. Meanwhile, n<1 indicates negatively cooperative binding with decreased affinity after binding of the first ligand. From the Hill-Langmuir plot, n and the c_{50} value of NaCl were determined (see section 3.4.5.1).

5.4.3.6 Quantum yield determination

The quantum yield ϕ describes the ratio of emitted and absorbed photons and can either be estimated by the absolute or the relative method. Absolute quantum yields are measured in special setups, so-called integrating spheres, which are sample compartments with a highly reflectant surface coating, allowing the instrument to count all of the emitted photons from the sample.[489] The total number of these emitted photons is then simply compared to the

total number of absorbed photons which directly provides the value of ϕ. For relative quantum yields measurements where the fluorescence intensity of a chromophore is compared to a sample of known ϕ, a conventional fluorescence spectrometer is sufficient. For the latter method, however, the absorbance of both the sample of interest and the reference needs to be known. In the course of this thesis, absolute quantum yields were determined for the two standards Coumarin 153 (C153) and fluorescein under given conditions. Since this method requires a comparably large amount of analyte, ϕ of all of the synthesized compounds was estimated relative to these two reference samples.

Absolute quantum yield

Absolute fluorescence quantum yield measurements were conducted with an ILF-835 integrating sphere in a Jasco 6808-H150A liquid cell (1×10×250 mm side length). 50 µM samples in either 1× PBS (100 mM NaCl, 10 mM phosphate, pH 7.0, Fluorescein) or abs. EtOH (C153) were prepared and serially diluted 1:1 with the respective solvent to a concentration of 0.1 µM.

Measurement parameters for C153/Fluorescein:

- excitation at 418 (C153)/435 (Fluorescein) nm
- 403 - 750 (C153)/420 - 750 (Fluorescein) nm emission range
- 2.5 nm excitation bandwidth
- 2.5 nm emission bandwidth
- 100 nm/min scan speed
- 0.2 nm data interval
- 1 s response
- 450 V PMT voltage

For the estimation of the absolute quantum yield of a chromophore, two measurements were necessary. First, an emission spectrum including the scattering peak of the chromophore's solvent was recorded. The area of this scattering peak S_0 is proportional to the reduction of the incident light flux by absorption of the sphere while the area of the emission peak F_0 is expected to be close to zero for this blank measurement. Second, an emission spectrum of the chromophore of interest in the respective solvent was recorded under identical conditions. The area of the scattering peak S_x is in this case reduced due to additional absorption of the fluorophore while the area of the emission peak F_x is increased (Figure 5.3). From these areas, the absolute fluorescence quantum yield ϕ_{abs} is obtained according to

$$\phi_{abs} = \frac{F_x - F_0}{S_0 - S_x} \tag{45}$$

with the nominator and denominator being proportional to the number of emitted and absorbed photons, respectively. Measurements were carried out with at least five different sample concentrations to rule out inner filter effects and aggregation.

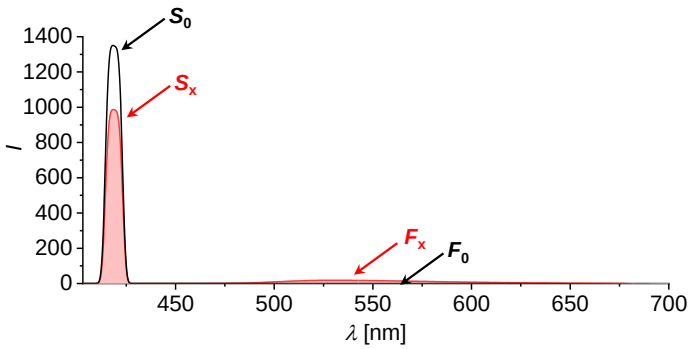

Figure 5.3: The absolute quantum yield ϕ_{abs} is calculated from the area of the scattering peaks of standard S_0 and analyte S_x as well as the area of the emission peaks F_0 and F_x.

The spectra were integrated over Ex ±15 nm to obtain the area of the scattering peak as well as between Ex+15 nm and 750 nm to obtain the area of the emission peak.

Relative quantum yield

The relative estimation of fluorescence quantum yields is more widely used than the absolute method. In contrast to the integration sphere, the conventional fluorescence spectrometer allows the detection of only a fraction of the emitted light due to for example the scattering of light by the sample and the 90° arrangement of the optics.

For relative quantum yield determination, a dilution series of the analyte in a suitable buffer was prepared. Fluorescence measurements were conducted in Hellma ultra-micro quartz cuvettes (1.5×1.5 mm or 10×2 mm) and spectra were blank-corrected by subtraction of a spectrum of pure buffer. After fluorescence measurement, the samples were transferred into VARIAN semi-micro quartz cuvettes with a path length of 10 mm for absorption measurements.

Sample preparation for merocyanine-modified oligonucleotides:

For the estimation of ϕ_{rel} of merocyanine-modified oligonucleotides, 1, 2, and 5 µM samples in 1× PBS (100 mM NaCl, 10 mM phosphate, pH 7.0) of the analytes of interest as well as of fluorescein were prepared and used for emission and absorbance measurements.

Measurement parameters:

- excitation at 435 nm
- 440 - 750 nm emission range
- 2.5 nm excitation bandwidth

- 2.5 nm emission bandwidth
- 200 nm/min scan speed
- 0.2 nm data interval
- 1 s response
- 300 V PMT voltage (adjusted for an optimal signal intensity of the standard)

Sample preparation for DMHBI-derived chromophores:
250 µL of the RNA-ligand sample were prepared by annealing a solution of Chili (required amount for a final concentration of 17 µM) with 31.25 µL of 1 M KCl (125 mM final concentration) and 20 µL of 500 mM HEPES pH 7.5 (40 mM final concentration) for 3 min at 95 °C. After incubation for 20 min at ambient temperature, 12.5 µL of 100 mM $MgCl_2$ (5 mM final concentration) and 25 µL of 100 µM ligand in DMSO (10 µM final concentration) were added and the sample was filled up with H_2O to the final volume.

Only-ligand samples were prepared by mixing 25 µL of 100 µM ligand stock solutions in DMSO (10 µM final concentration) with 31.25 µL of 1 M KCl (125 mM final concentration), 20 µL of 500 mM HEPES pH 7.5 (40 mM final concentration) and 12.5 µL of 100 mM $MgCl_2$ (5 mM final concentration) and filling up to a total volume of 250 µL with H_2O.

For the reference C153, 250 µL of a 10 µM sample in abs. EtOH were prepared.

For all of the samples, emission and absorption spectra were recorded. Afterwards, the samples were diluted twice 1:2 with buffer (125 µL of 1 M KCl, 80 µL of 500 mM HEPES pH 7.5 and 50 µL of 100 mM $MgCl_2$ in a total volume of 1 mL) or abs. EtOH (for C153). Hereby, samples with 17.0/11.2/7.41 µM RNA and 10/6.67/3.33 µM of ligand were obtained. All of the spectra were blank-corrected by subtraction of a spectrum of pure buffer or ethanol.

Measurement parameters:
- excitation at the maximum of the RNA-ligand complex
- Ex+20 - 750 nm emission range
- 2.5 nm excitation bandwidth
- 2.5 nm emission bandwidth
- 200 nm/min scan speed
- 0.2 nm data interval
- 1 s response
- 500 V PMT voltage (adjusted for an optimal signal intensity of the standard)

For calculation of ϕ_{rel} of an unknown chromophore, the integrated fluorescence and absorption intensities I_x and A_x of this sample were compared to the intensities I_S and A_S of a standard with a known quantum yield. Herefore, the standard and the analyte must absorb and emit in a similar wavelength range and the concentration of the reference need to be chosen as such that the absorbance approximately matches the one of the analyte at the excitation wavelength. By integration, the absorption factor *a* was calculated:

$$a = \int_{\lambda_{ex}+\Delta\lambda_{ex}/2}^{\lambda_{ex}-\Delta\lambda_{ex}/2} 1\text{-}10^{-A} d\lambda \tag{46}$$

Equation (46) takes the finite bandwith $\Delta\lambda$ of the exitation monochromator of the fluorescence spectrometer into account, which was here set to 2.5 nm. The emission spectra were blank-corrected by subtraction of a spectrum of pure buffer and integrated over the whole range to obtain the two factors F_x and F_S. These factors provide access to the relative quantum yield ϕ_{rel} according to

$$\phi_{rel} = \phi_S \cdot \frac{F_x}{a_x} \cdot \frac{a_S}{F_S} \cdot \frac{\eta_x^2}{\eta_S^2} \tag{47}$$

which includes the refractive indices η_x and η_S of the sample and the reference if two different solvents are used. The measurements were conducted at three different sample concentrations to allow plotting of *F versus a* and fitting of these data points by a linear model with an intercept at the origin and the slope m to calculate ϕ_{rel}

$$\phi_{rel} = \phi_S \cdot \frac{m_x}{m_S} \cdot \frac{\eta_x^2}{\eta_S^2} \tag{48}$$

By comparison with the absolute quantum yield of the standard ϕ_S, values for ϕ_{rel} were obtained.

5.4.3.7 Fluorescence lifetime

Fluorescence lifetime data were collected at a Horiba DeltaFlex system with a DeltaDiode excitation source (DD-405L or DD-485L) and polarization filters. The excitation and emission polarizer were oriented in the vertical position or at an angle of 54.7° from the vertical orientation to minimize anisotropic effects. Samples were measured in Hellma ultra-micro quartz cuvettes (10×2 mm) at a concentration of 1 µM. The excitation source and emission monochromator wavelengths were chosen to be close to the steady-state excitation and emission maxima of the chromophore. The emission bandwidth was adjusted for a stop rate of close to 2%. An excitation pulse repetition rate of 10 MHz was used which corresponds to a measurement interval of 105 ns. The photon arrival time was set to 4096 channels, resulting in a width of 0.026 ns per channel. Data points was collected until 50,000 counts had accumulated in the peak channel. The instrument response function was recorded from buffer sample

by setting the emission monochromator to the peak wavelength of the excitation source.

Fluorescence decay curves were analyzed by iterative reconvolution fitting with a suitable instrument response function using a proprietary algorithm implemented in Horiba DAS6 (version 6.8). Only data with photon counts above the noise level were used for fitting, starting from a monoexponential model. If the fit did not convert properly, up to three additional exponential terms were included until the fit statistics (χ^2) did not changed significantly anymore and the autocorrelation of the weighted fit residuals did not show systematic variations. The average lifetime was calculated from the weighted individual lifetimes.

5.4.4 AFM

AFM measurements were performed under ambient conditions using a Bruker Multimode 8 SPM system operating in tapping mode in air. Silicon cantilevers (OMCL-AC240TS, Olympus) with a resonance frequency of ~70 kHz and a spring constant of ~1.7 N m^{-1} were used. For preparation of the AFM samples, the oligonucleotide solution in sodium phosphate buffer (100 mMNaCl, 10 mM Na-phosphate) was spin-coated with 3,000 rpm onto mica substrate pre-treated with $NiCl_2$ solution to promote sample adhesion.

AFM measurements in fluid cell were performed under ambient conditions using a Bruker Multimode 8 SPM system operating in tapping mode. Soft silicon nitride probes (SNL, Bruker) with a resonance frequency of ~25 - 65 kHz, a spring constant of ~0.12 - 0.35 Nm^{-1} and a typical tip radius below 5 nm were used. The silicon ring supplied with the fluid cell by Bruker seals the fluid cell environment and was used to prevent spillage of the liquid onto the scanner. Cleavage of mica followed by treatment with $NiCl_2$ was performed always just before the solution for AFM measurement was deposited and samples were incubated for 5 minutes prior to measurement.

5.4.5 LC-MS

For analysis of the degradation products of a free chromophore upon alkaline hydrolysis, 1 mg of the chromophore of interest was incubated for 12 h at 37 °C in 1 mL of aq. ammonia. 100 µL aliquots were taken out, the solvent was removed in vacuum and the residual was redissolved in 50 µL of H_2O. Samples were measured using an RP-18 column (Synergi, 4 µm Fusion-RP C18 80 Å, 250×2 mm, Phenomenex) at 25 °C with aqueous mobile phase A (5 mM NH_4OAc, pH 5.3) and organic mobile phase B (100% acetonitrile) on a Dionex UltiMate3000 system by ThermoScientific. The flow rate was set to 0.2 mL/min with a 0% B in the first 5 min, followed by a gradient of 5–70% B in 40 min. The micrOTOF-Q III with an ESI ion source was operated in positive-ion mode, with a capillary voltage of 4.5 kV, an end plate offset of 500 V, a nitrogen nebulizer pressure of 1.4 bar, a dry gas flow 9 L/min and a dry

temperature of 200 °C. Data were analyzed with the Data Analysis software DA 4.2 by Bruker Daltonics.

5.5 Theoretical calculations

5.5.1 Geometry optimization

Geometry optimization for the two stereoisomers of BAM have been performed in order to estimate the energy difference between the two species. The structure was optimized at the level of density functional theory employing the long-range correct CAM-B3LYP functional[328] together with the def2-SVP basis set[313] as implemented in the Gaussian 09 package.[329]

5.5.2 Spectra simulation

The absorption spectra for the BAM:BAM dimer were calculated employing a Holstein-type Hamiltonian[397] with the two-particle approximation[398] following the procedure as previously described.[399,400] A collinear assignment of the chromophores was assumed with a long-range Coulomb coupling J_{Coul} between the transition dipole moments of the chromophores. First, the monomer spectrum was calculated to adjust the parameters. Best agreement with the experimental absorption spectrum of the monomer was obtained with a transition energy of E_g = 21,400 cm^{-1} and a vibrational frequency of ω_0= 1,200 cm^{-1} assuming a one-effective mode. For the dimer spectrum, a Coulomb coupling of J_{Coul} = 1,050 cm^{-1} (1,100 cm^{-1} for BAM^b) was applied. Furthermore, the Huang-Rhys factor had to be decreased to $\lambda^2 = 0.56$ (0.61 for BAM^b) in order to obtain best agreement with the experimental dimer spectrum. Additionally, a gas-to-crystal shift of –150 cm^{-1} was applied to adjust the position of the absorption maximum with the experimental spectrum. For all simulated spectra, a maximum number of 7 vibrational quanta has been used for each chromophore.

The absorption spectra were simulated by

$$A(E) = \sum_{n=1} E_{eg}| < \Psi_g|\widehat{\mu}|\Psi_e > |^2 \exp(-(E - E_{eg})^2/\sigma^2 \quad (49)$$

Here, $A(E)$ is the absorption at photon energy E and E_{eg} is the transition energy between the ground state with wave function Ψ_g and the respective excited state Ψ_e. σ is the band-width with $2\sqrt{\ln(2)}\sigma$ being the full width at half height. A value of σ = 830 cm^{-1} and σ = 520 cm^{-1} has been used for the simulation of the monomer and dimer spectrum, respectively. According to equation 49, Gaussian line shape functions were used to simulate the spectra. In addition,

$\widehat{\mu}_{eg}$ is the transition dipole moment operator and defined as

$$\widehat{\mu}_{eg} = \mu_{eg} \sum_{n=1,2} \{|n><g| + |g><n|\} \quad (50)$$

with the transition dipole moment μ_{eg} of the monomeric chromophore. |n> means that chromophore n is electronically excited, whereas |g> indicates that all chromophores are in the electronic ground state.

5.5.3 Electrostatic potential

The geometry optimization for electrostatic potential calculations was done in ORCA Version 5.0[310] at the level of density functional theory employing the B3LYP functional[311,312,490] together with the def2-SVP basis set.[313] Maps of the electrostatic potential on the electron density isosurface with a resolution of 80×80×80 grid points were generated using the Multiwfn software[314–316] and visualized with VMD version 1.9.3.[491]

Chapter 6

Appendix

6.1 Supplementary temperature-dependent absorption spectra

6.1.1 RNA

Temperature-dependent absorption spectra were recorded for 5 µM oligonucleotides in 1× PBS (100 mM NaCl, 10 mM phosphate, pH 7.0).
A = m^6A, **A** = 2,6-DAP, **X** = rBAM, **X** = $rBAM^b$

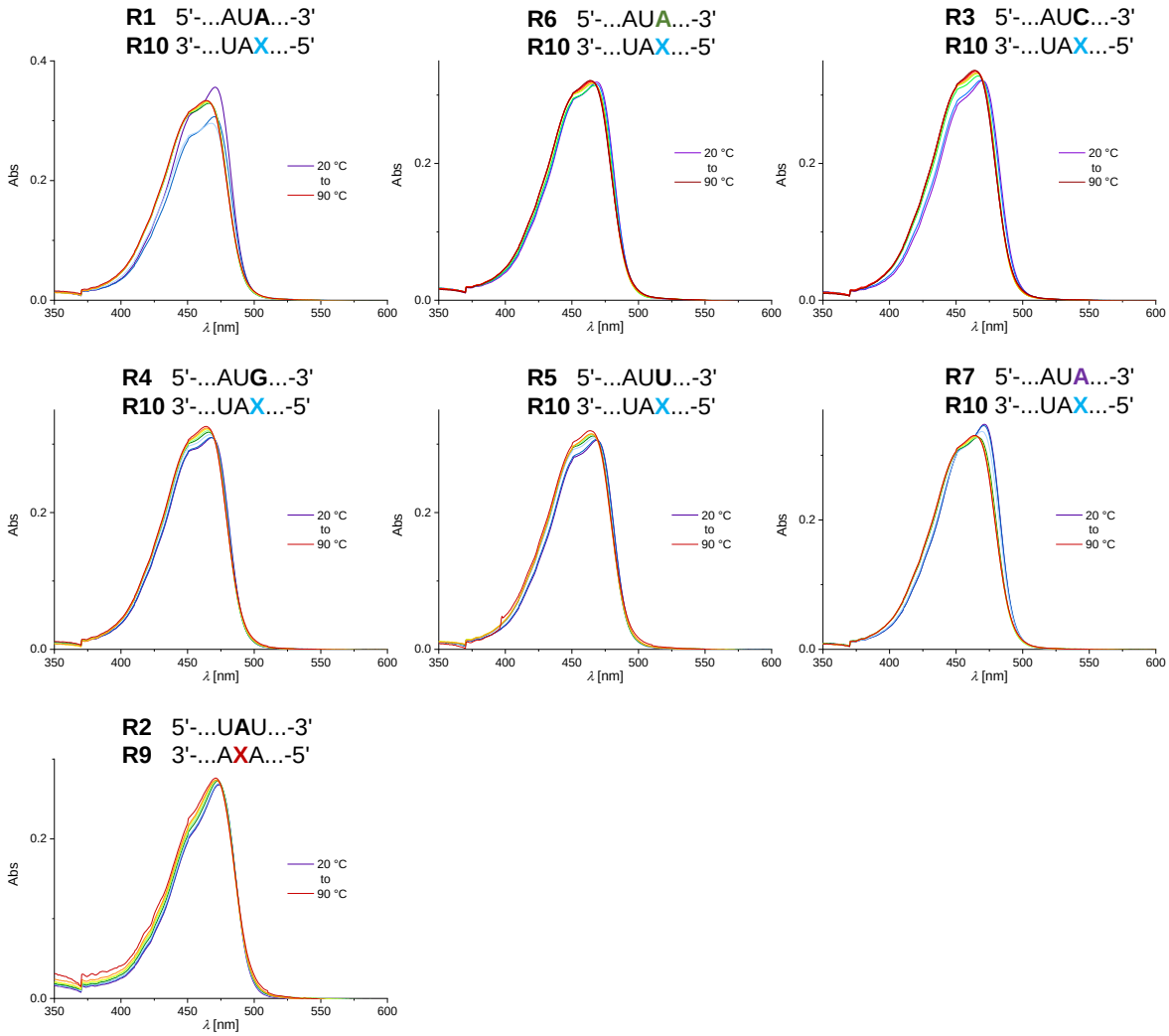

6.1.2 DNA

Temperature-dependent absorption spectra were recorded for 5 µM oligonucleotides in 1× PBS (100 mM NaCl, 10 mM phosphate, pH 7.0).
X = dBAM, **Y** = C3-linker (abasic site)

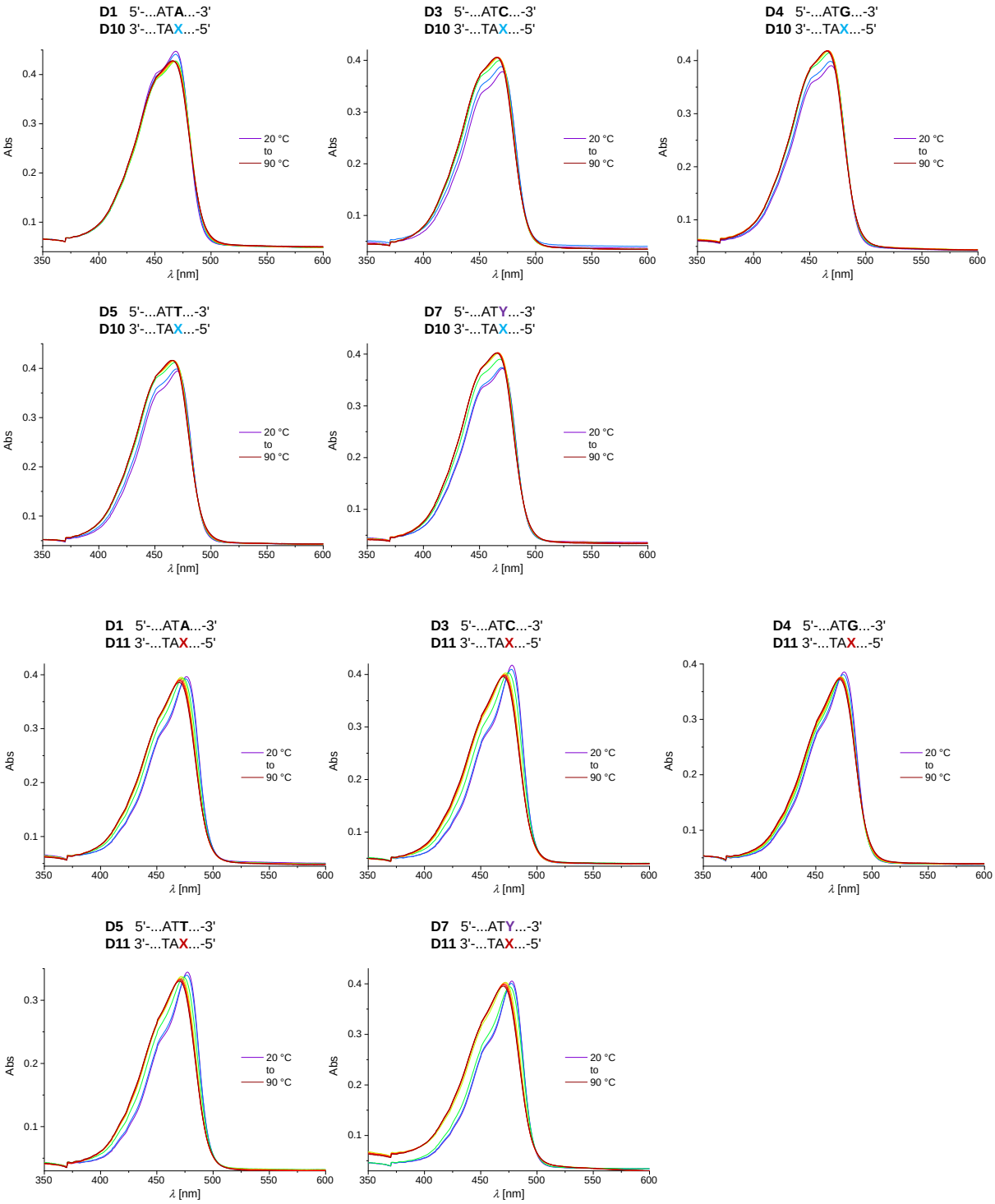

6.1.3 GNA

Temperature-dependent absorption spectra were recorded for 5 µM oligonucleotides in 1× PBS (100 mM NaCl, 10 mM phosphate, pH 7.0).

Y = C3-linker (abasic site), **X** = gBAM, **X** = gmBAM

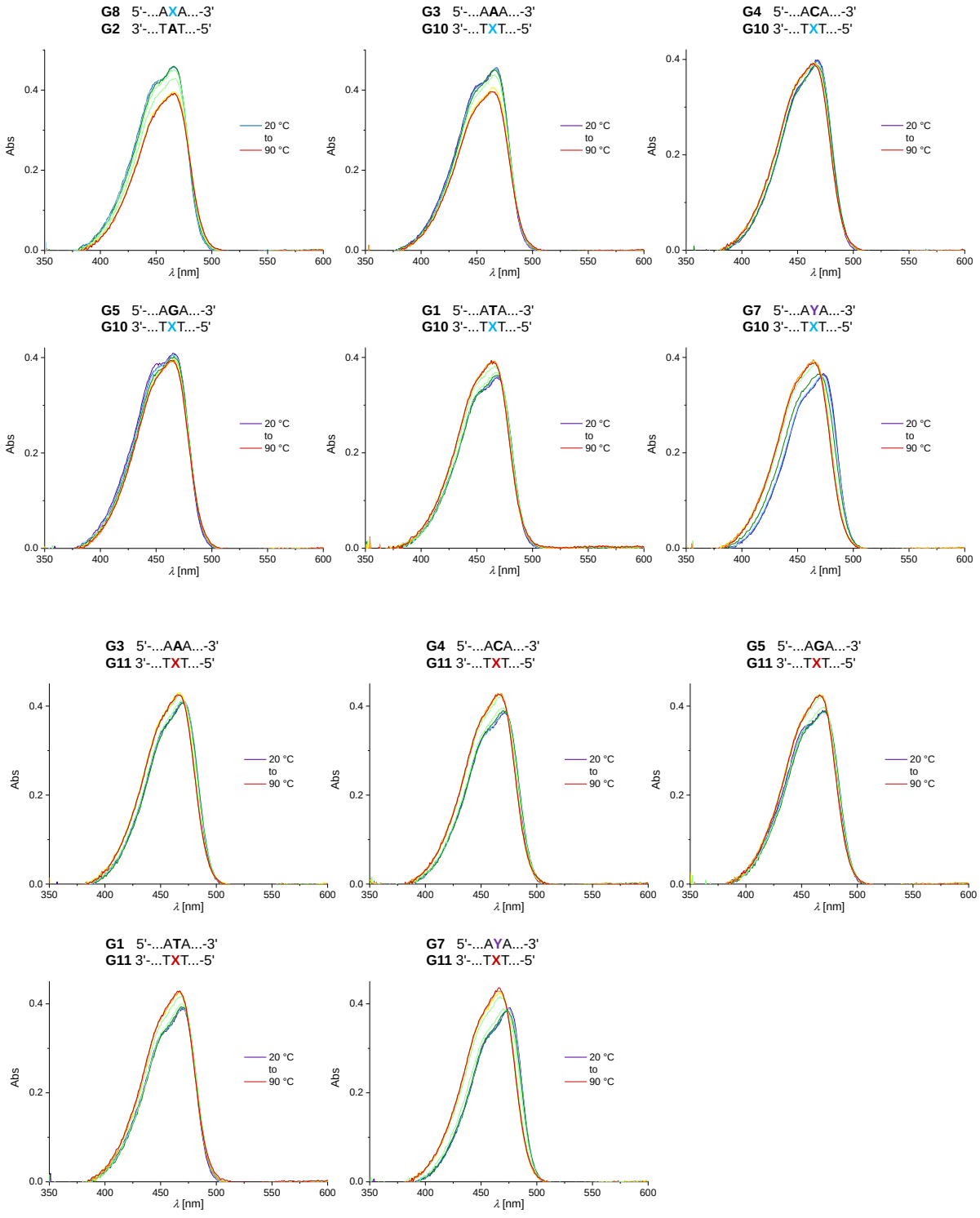

6.1.4 DNA/GNA hybrids

Temperature-dependent absorption spectra were recorded for 5 µM oligonucleotides in 1× PBS (100 mM NaCl, 10 mM phosphate, pH 7.0).
X = gBAM, X = gmBAM, x = gmBAM^{b}, X = gBAM^{F}, X = gBAM^{OMe}, X for (*R*)-gBAM.

D1 5'-...AT**A**...-3'
DG9 3'-...TA**X**...-5'

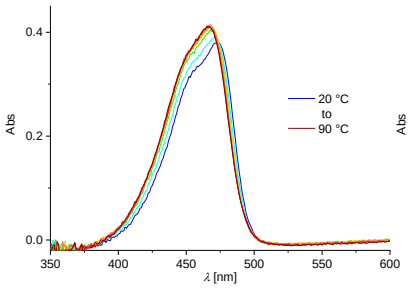

D3 5'-...AT**C**...-3'
DG9 3'-...TA**X**...-5'

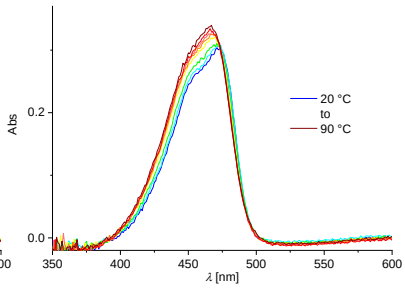

D4 5'-...AT**G**...-3'
DG9 3'-...TA**X**...-5'

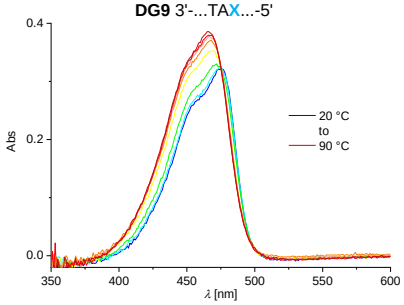

D5 5'-...AT**T**...-3'
DG9 3'-...TA**X**...-5'

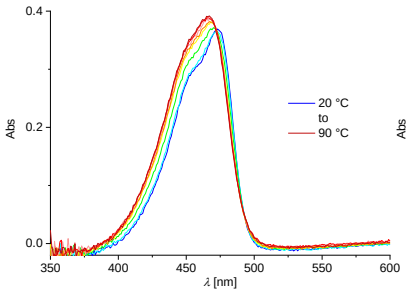

D7 5'-...AT**Y**...-3'
DG9 3'-...TA**X**...-5'

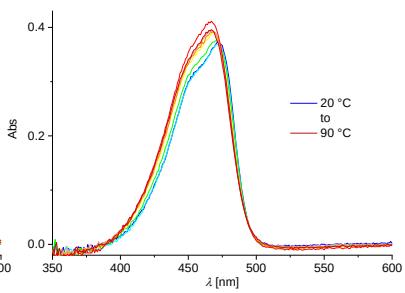

D1 5'-...AT**A**...-3'
DG14 3'-...TA**X**...-5'

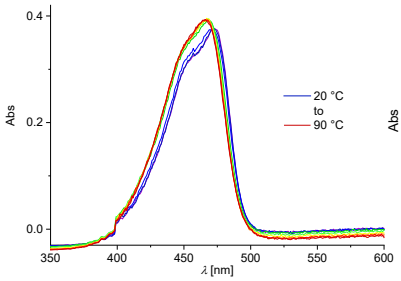

D1 5'-...AT**A**...-3'
DG12 3'-...TA**X**...-5'

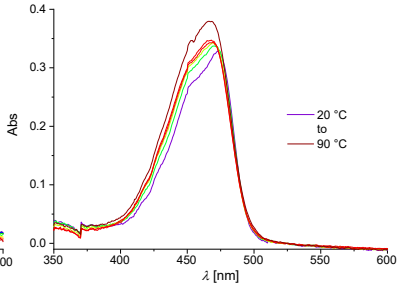

D1 5'-...AT**A**...-3'
DG13 3'-...TA**X**...-5'

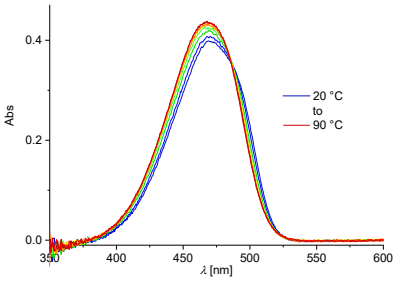

D1 5'-...AT**A**...-3'
DG11 3'-...TA**X**...-5'

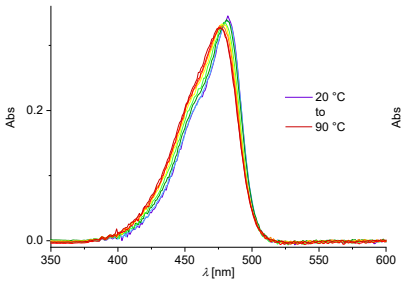

DG7 5'-...A**X**A...-3'
DG14 3'-...TA**X**...-5'

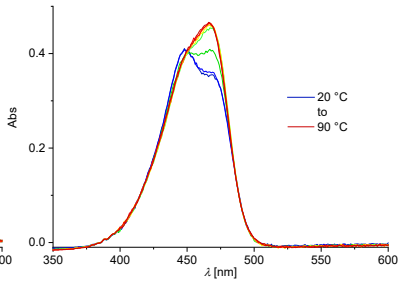

DG2 5'-...A**X**A...-3'
DG14 3'-...TA**X**...-5'

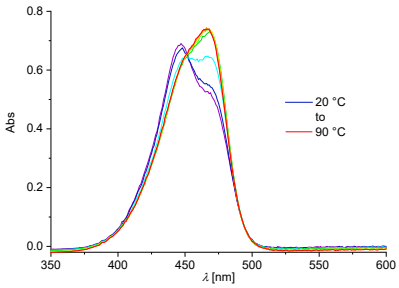

DG7 5'-...A**X**A...-3'
DG18 3'-...T**X**T...-5'

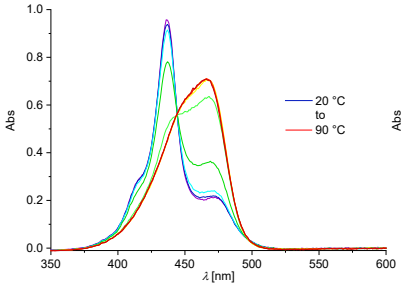

DG2 5'-...A**X**A...-3'
DG18 3'-...T**X**T...-5'

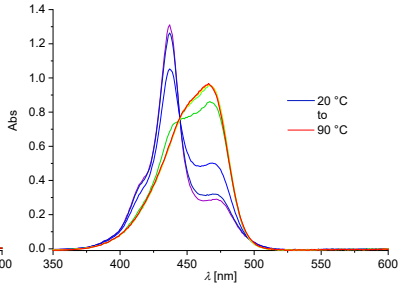

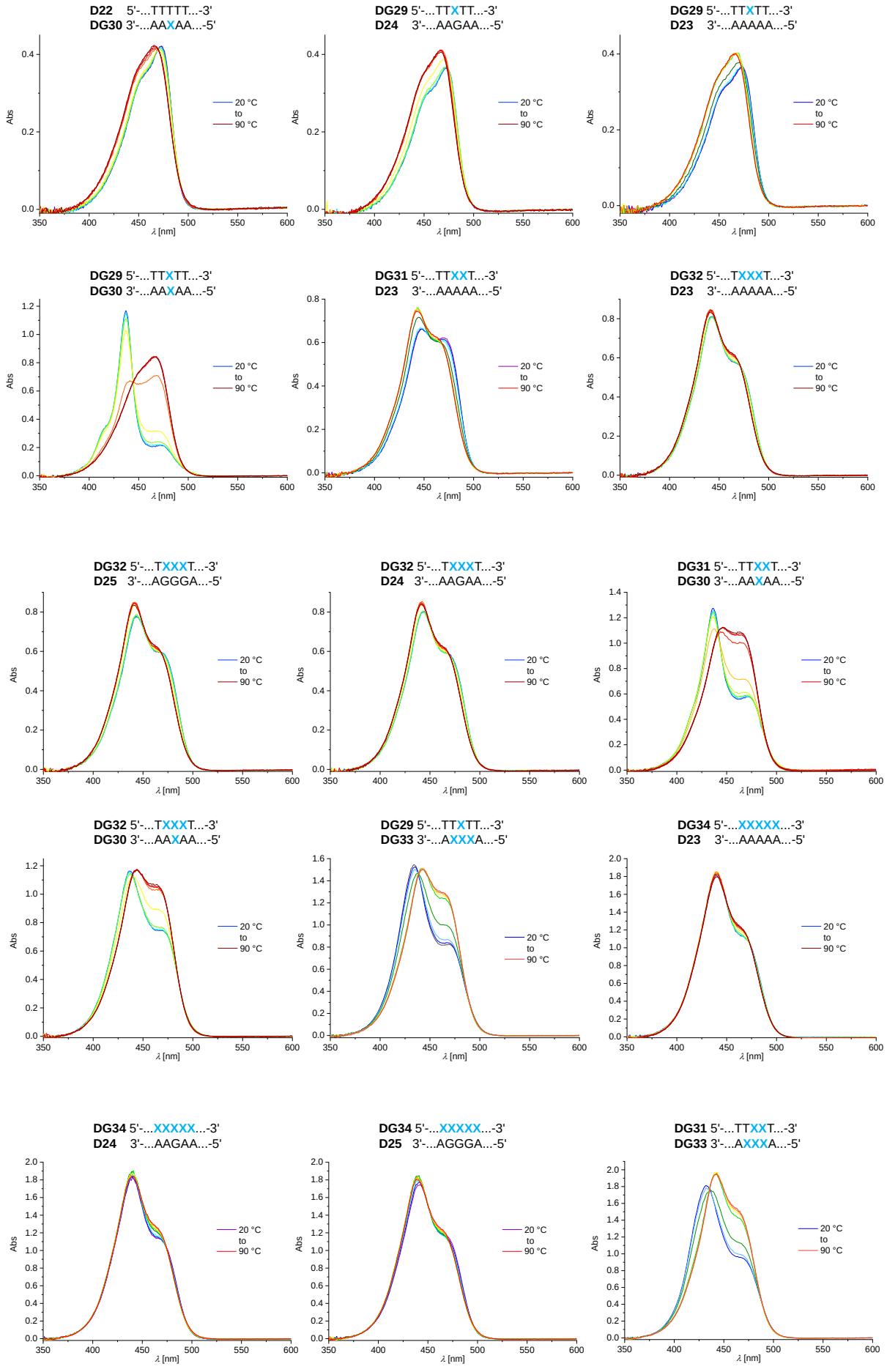
D22 5'-...TTTTT...-3'
DG30 3'-...AAXAA...-5'
DG29 5'-...TTXTT...-3'
D24 3'-...AAGAA...-5'
DG29 5'-...TTXTT...-3'
D23 3'-...AAAAA...-5'
DG29 5'-...TTXTT...-3'
DG30 3'-...AAXAA...-5'
DG31 5'-...TTXXT...-3'
D23 3'-...AAAAA...-5'
DG32 5'-...TXXXT...-3'
D23 3'-...AAAAA...-5'
DG32 5'-...TXXXT...-3'
D25 3'-...AGGGA...-5'
DG32 5'-...TXXXT...-3'
D24 3'-...AAGAA...-5'
DG31 5'-...TTXXT...-3'
DG30 3'-...AAXAA...-5'
DG32 5'-...TXXXT...-3'
DG30 3'-...AAXAA...-5'
DG29 5'-...TTXTT...-3'
DG33 3'-...AXXXA...-5'
DG34 5'-...XXXXX...-3'
D23 3'-...AAAAA...-5'
DG34 5'-...XXXXX...-3'
D24 3'-...AAGAA...-5'
DG34 5'-...XXXXX...-3'
D25 3'-...AGGGA...-5'
DG31 5'-...TTXXT...-3'
DG33 3'-...AXXXA...-5'
Abs
λ [nm]
20 °C
to
90 °C

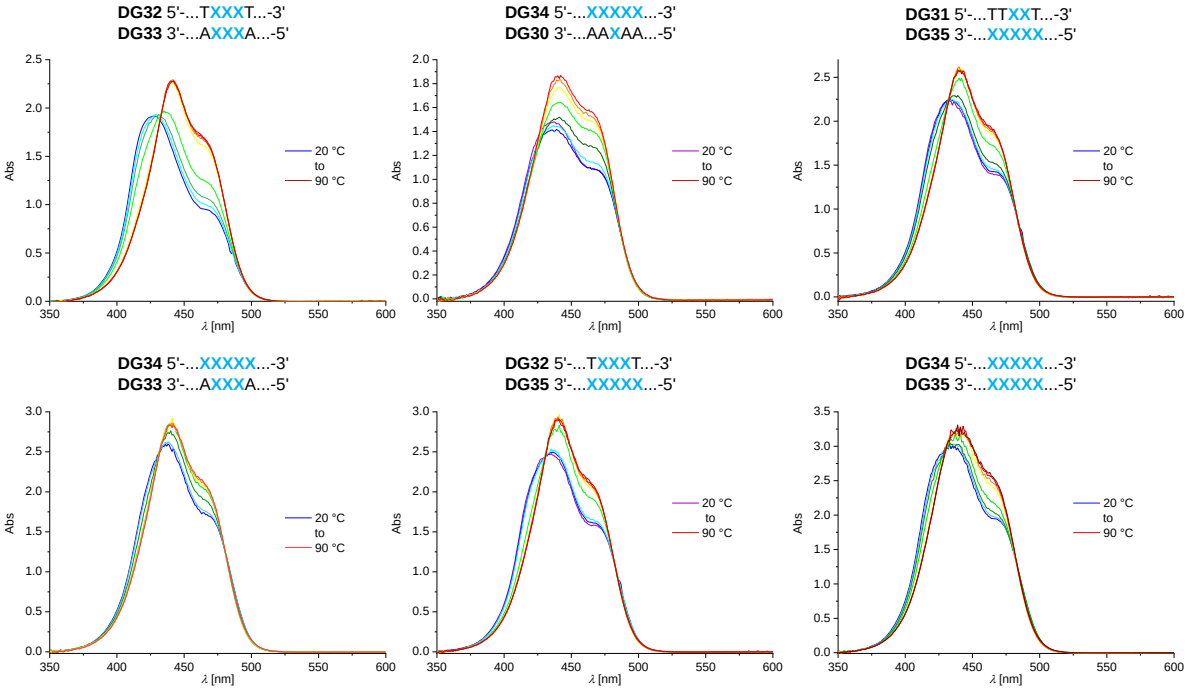

6.2 Determination of molar extinction coefficients

6.2.1 Merocyanine chromophores

Concentration-dependent absorption spectra for a dilution series of different merocyanine chromophores with concentrations between 10 to 0.3 µM in water (top) and linear fit of the intensity at the absorption maximum for the calculation of the molar extinction coefficient (bottom). Measurements for mBAM^b were conducted in DMSO instead of water.

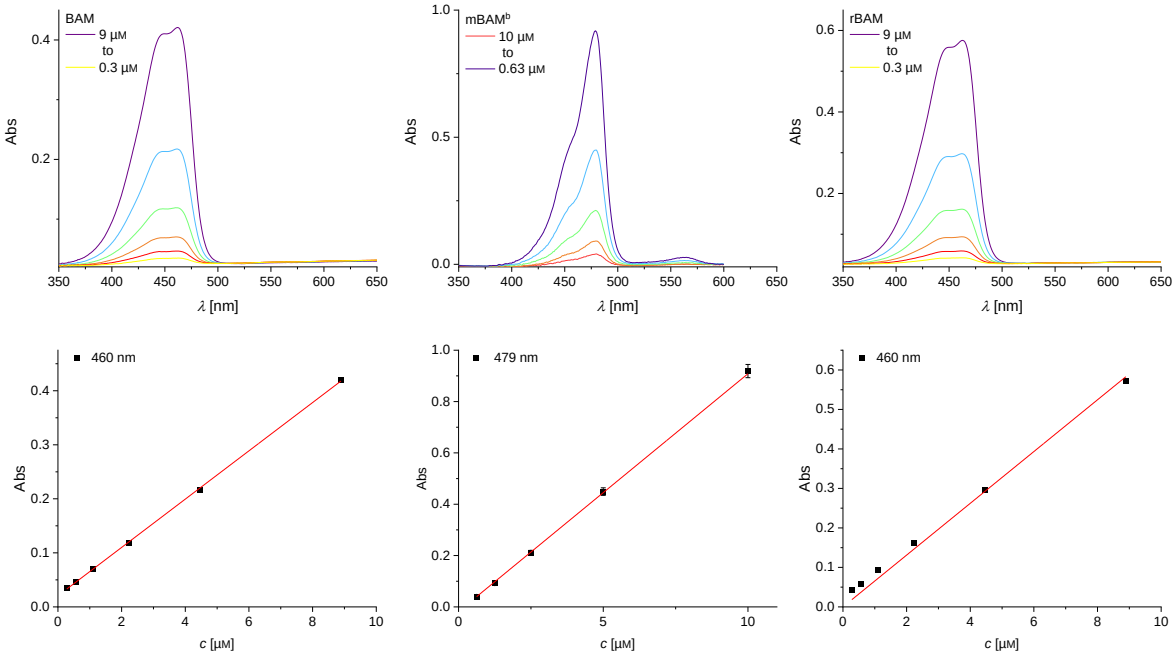

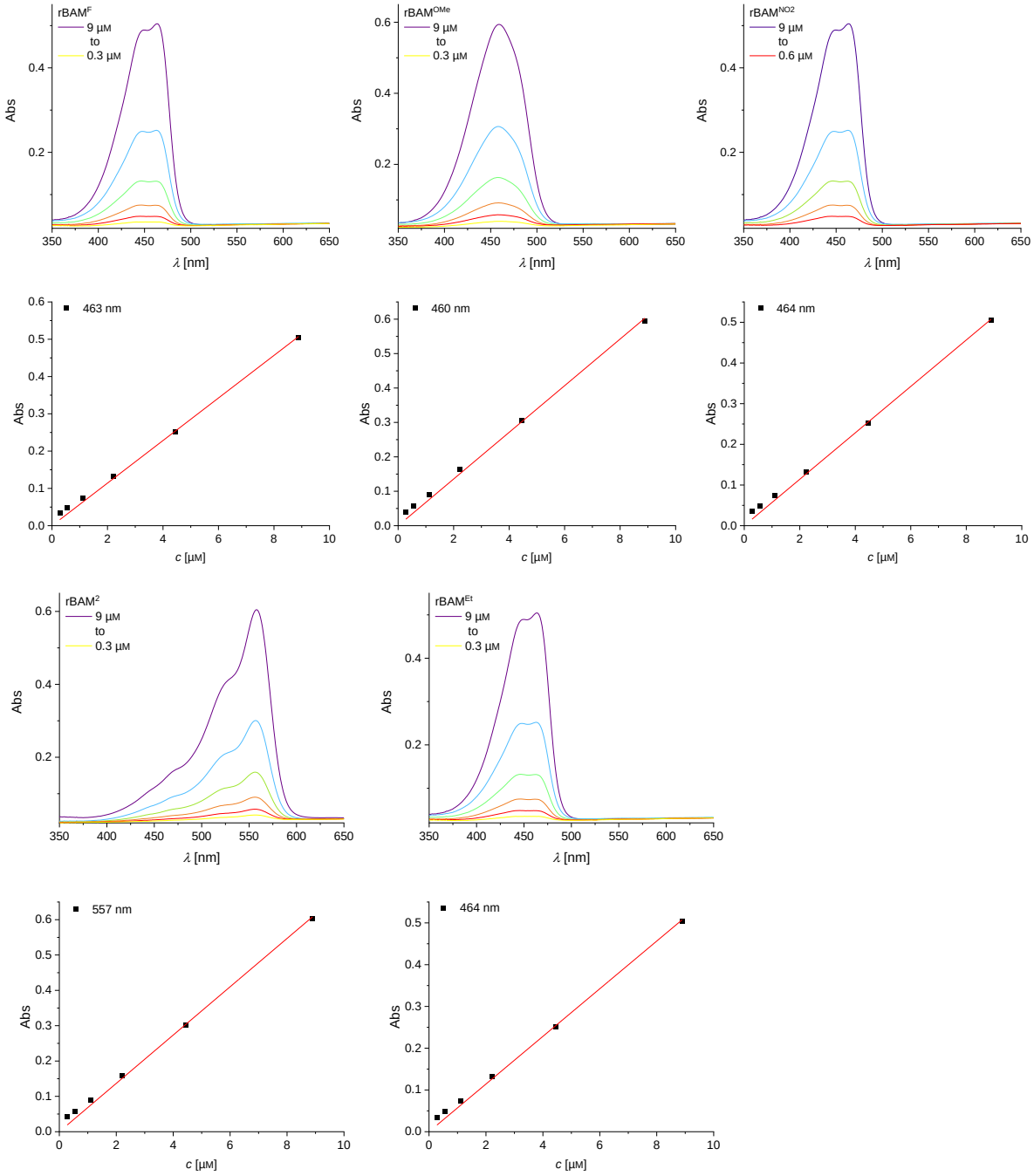
rBAM^F
9 µM
to
0.3 µM
Abs
λ [nm]
rBAM^OMe
9 µM
to
0.3 µM
Abs
λ [nm]
rBAM^NO2
9 µM
to
0.6 µM
Abs
λ [nm]
463 nm
Abs
c [µM]
460 nm
Abs
c [µM]
464 nm
Abs
c [µM]
rBAM^2
9 µM
to
0.3 µM
Abs
λ [nm]
rBAM^Et
9 µM
to
0.3 µM
Abs
λ [nm]
557 nm
Abs
c [µM]
464 nm
Abs
c [µM]

6.2.2 DMHBI variants

Concentration-dependent absorption spectra for a dilution series of different DMHBI variants with concentrations between 40 to 1.25 µM in water (top) and linear fit of the intensity at the absorption maximum for calculation of the molar extinction coefficient (bottom). The error bars represent the standard deviation of the mean of triplicates.

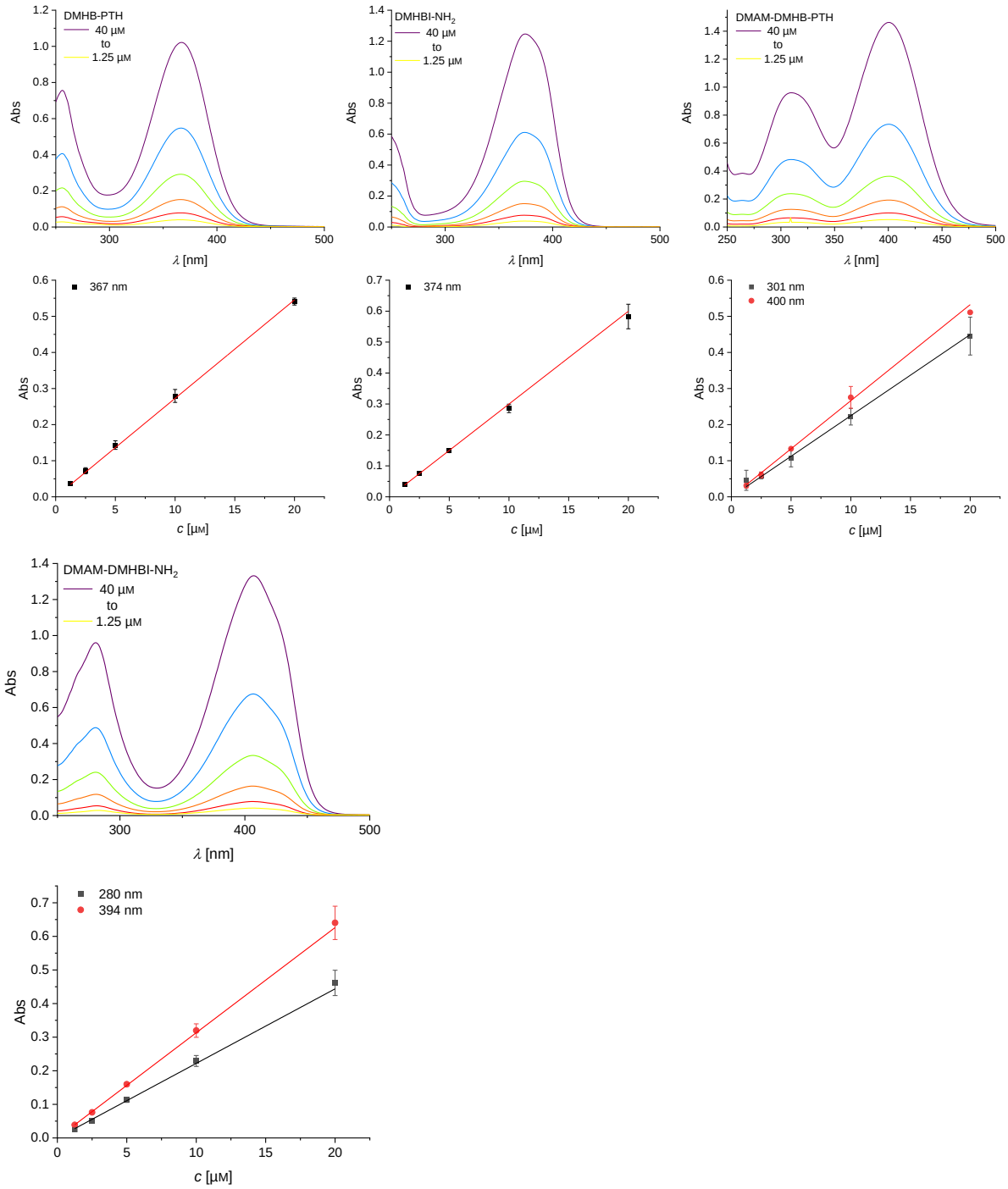

6.2.3 pK_a titrations

6.2.4 Merocyanine chromophores

UVvis spectra (top) and titration curves (bottom) at the absorption maxima of the cationic (black) and anionic (blue) form of different merocyanine ribonucleosides in aqueous buffer. Spectra were measured between pH 0 and 13 in steps of 0.5. pK_a values were obtained by global fitting of the absorbance according to the Henderson-Hasselbalch equation and are given in the experimental part. Conditions: 11 µM ligand in 30 mM Britton-Robinson buffer.

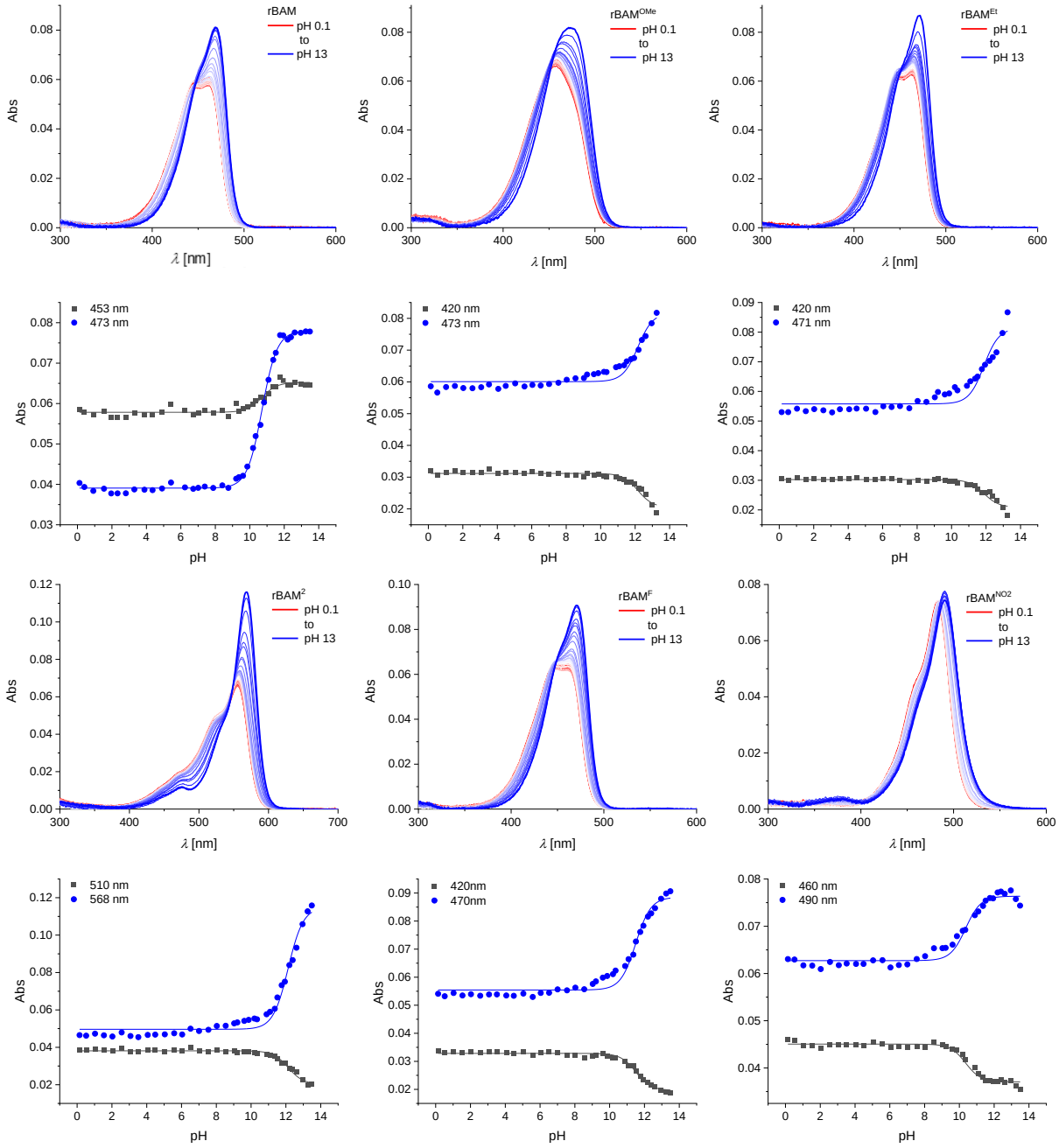

6.2.5 DMHBI variants

UVvis spectra (top) and titration curves (bottom) at the absorption maxima of the cationic (black) and anionic (blue) form of different DMHBI derivatives in aqueous buffer. Spectra

were measured between pH 0 and 12 in steps of 0.5. pK_a values were obtained by global fitting of the absorbance according to the Henderson-Hasselbalch equation and are given in the experimental part. Data points marked in red were excluded from fitting. Conditions: 11 µM ligand in 30 mM Britton-Robinson buffer.

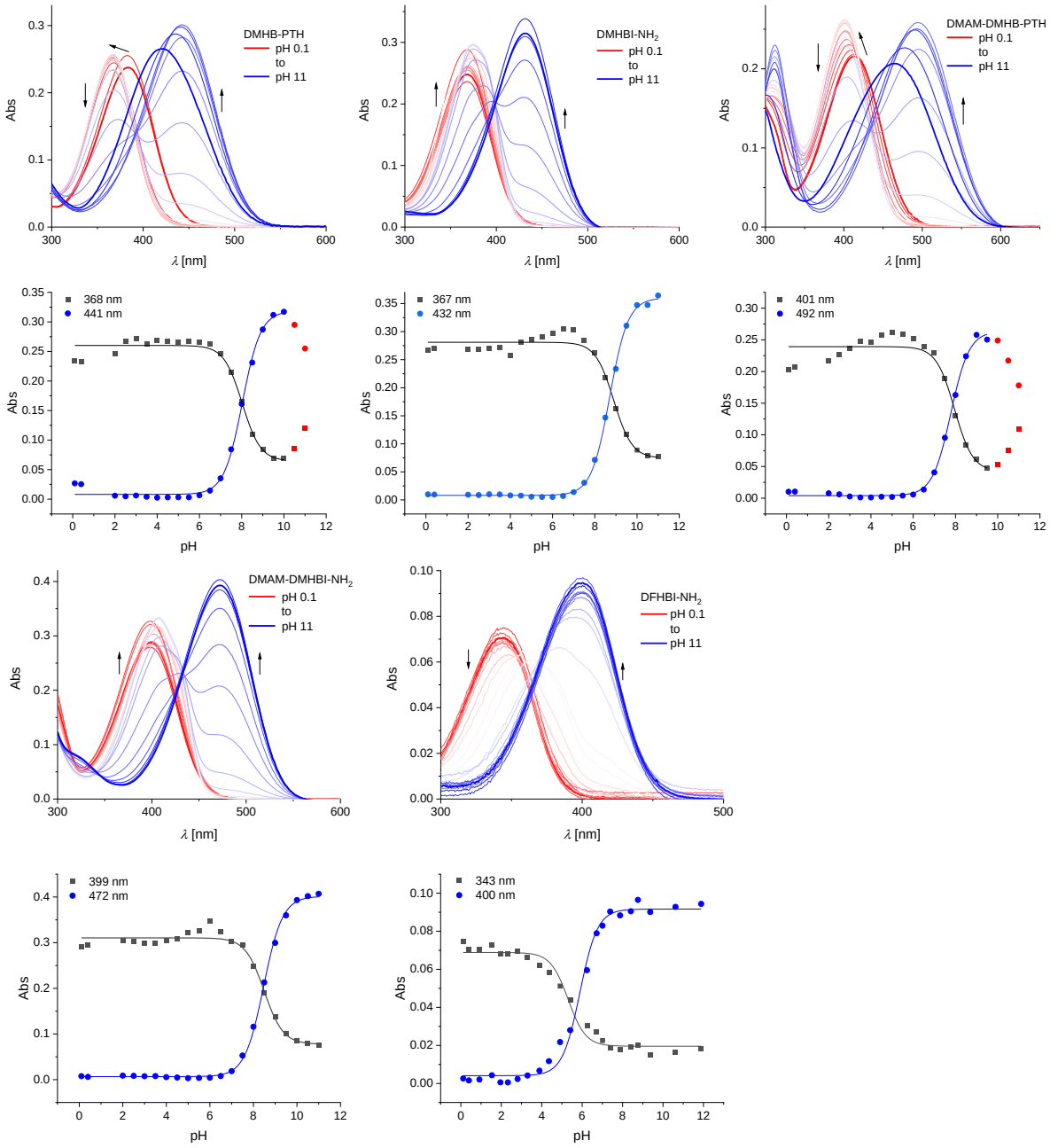

6.3 Supplementary fluorescence data

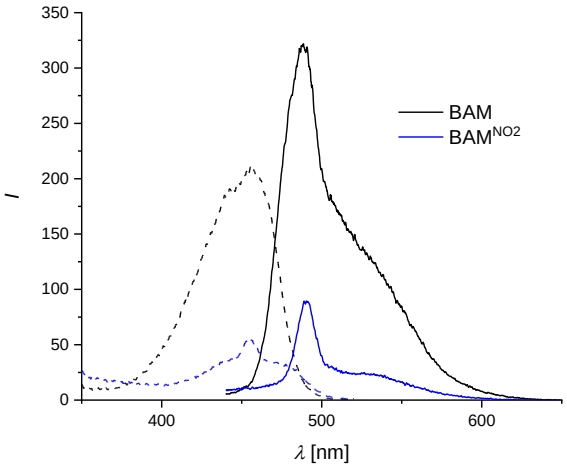

Figure 6.1: Comparison of the excitation and emission spectra of the free rBAM and rBAM^{NO2} nucleosides. Conditions: 1 µM chromophore in water, excitation at 420 nm, emission at 540 nm.

6.3.1 Temperature-dependent fluorescence

6.3.1.1 RNA

Temperature-dependent fluorescence spectra were recorded for 1 µM oligonucleotides in 1× PBS (100 mM NaCl, 10 mM phosphate, pH 7.0). Excitation and emission wavelengths were 420 and 540 nm, respectively.
A = m^{6}A, **A** = 2,6-DAP, **X** = rBAM, **X** = rBAM^b

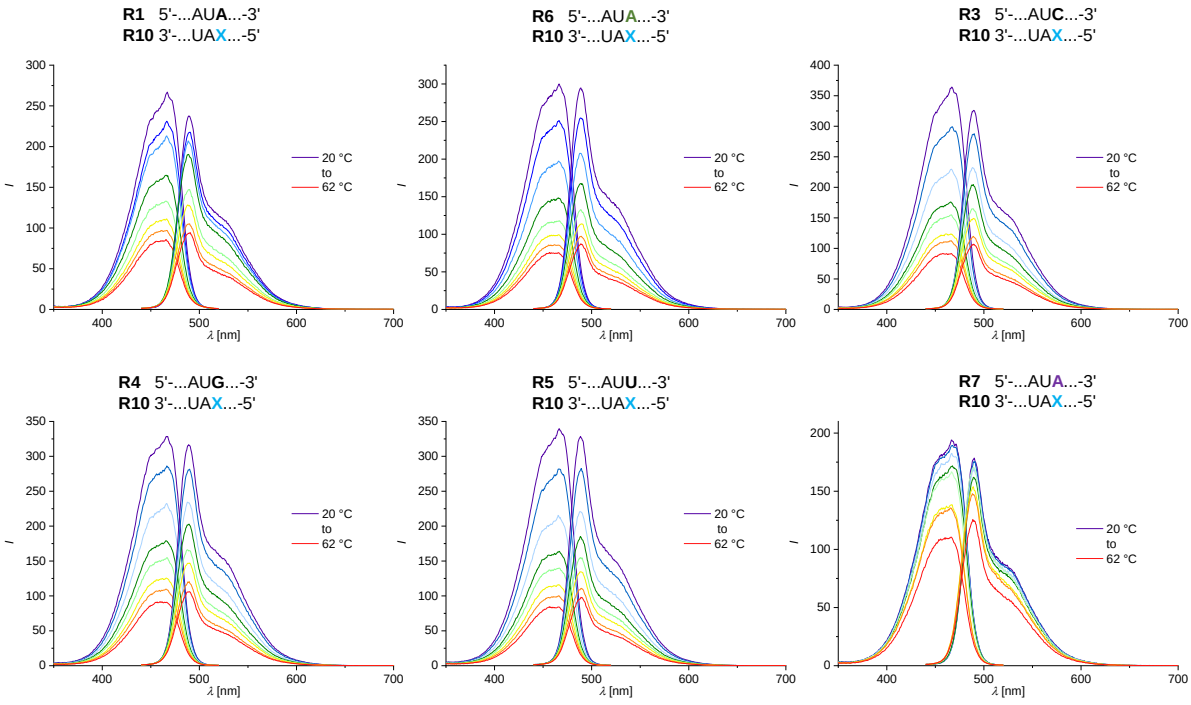

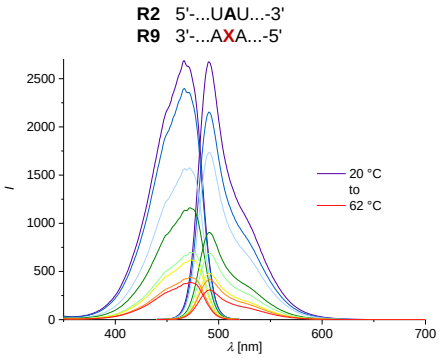

6.3.1.2 DNA

Temperature-dependent fluorescence spectra were recorded for 1 µM oligonucleotides in 1× PBS (100 mM NaCl, 10 mM phosphate, pH 7.0). Excitation and emission wavelengths were 420 and 540 nm, respectively.
X = dBAM, **Y** = C3-linker (abasic site)

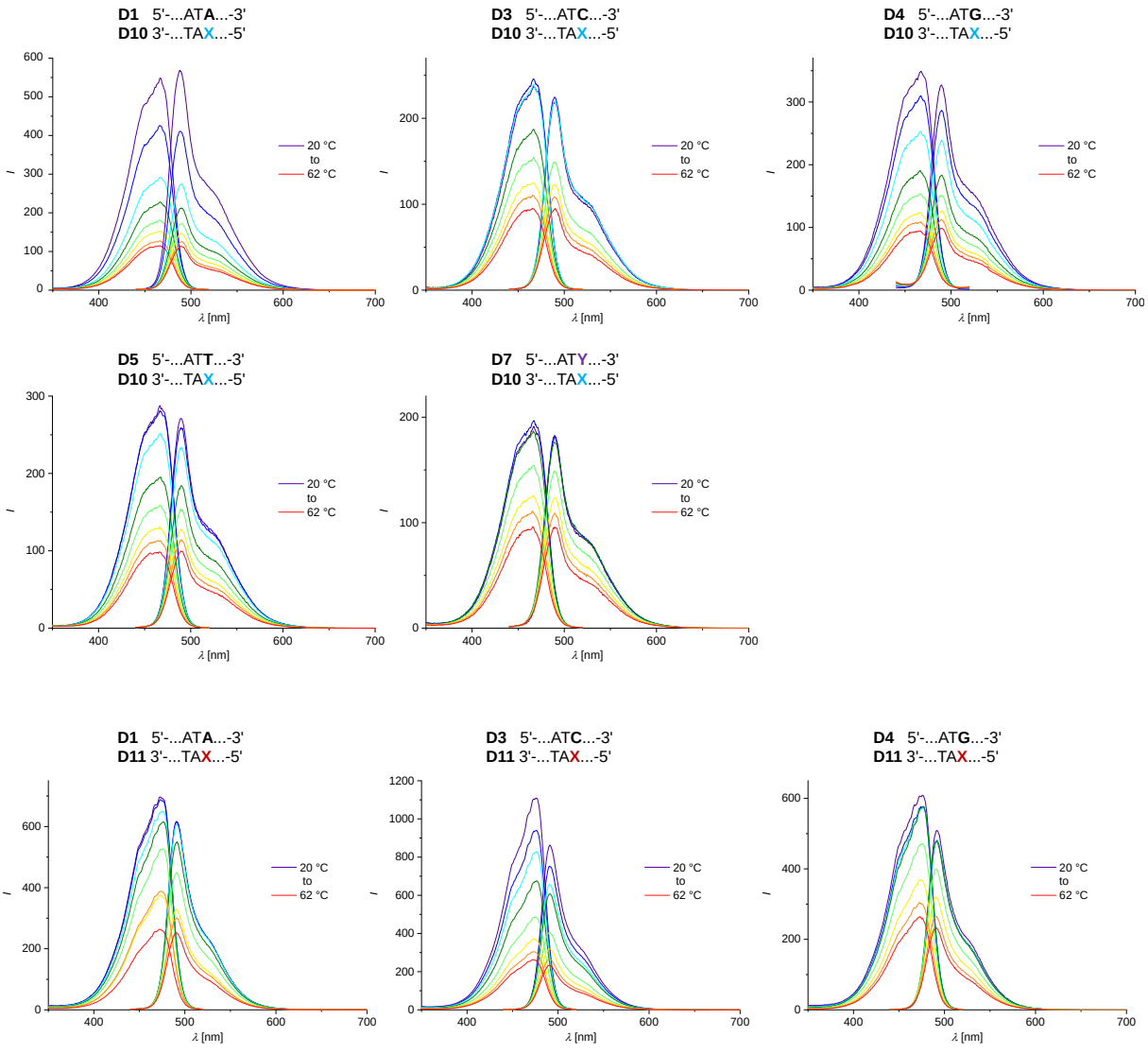

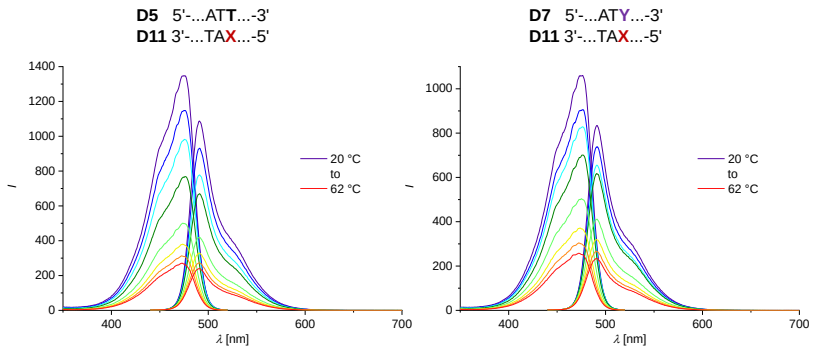

6.3.1.3 GNA

Temperature-dependent fluorescence spectra were recorded for 1 µM oligonucleotides in 1× PBS (100 mM NaCl, 10 mM phosphate, pH 7.0). Excitation and emission wavelengths were 420 and 540 nm, respectively.
Y = C3-linker (abasic site), **X** = gBAM, **X** = gmBAM

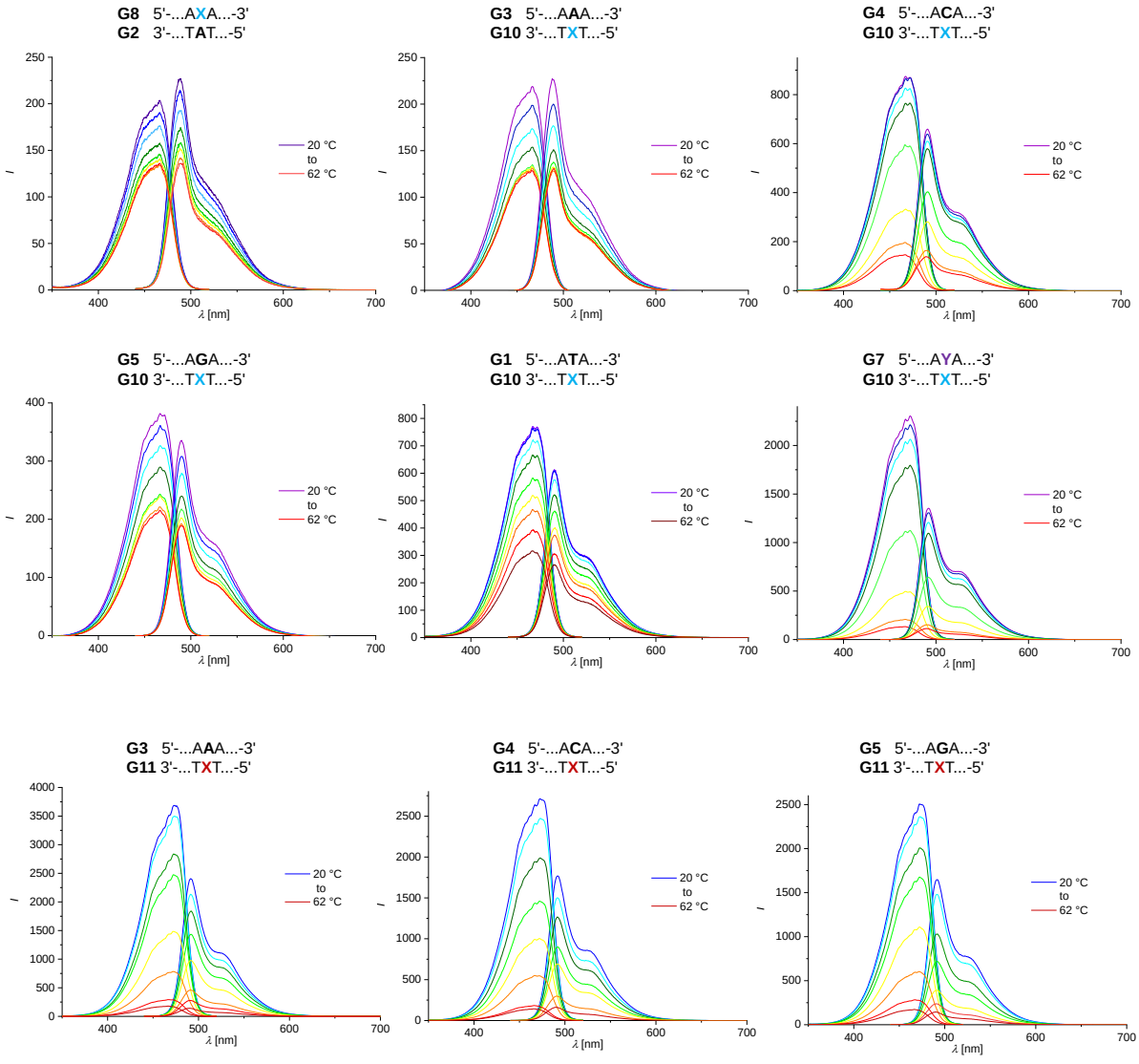

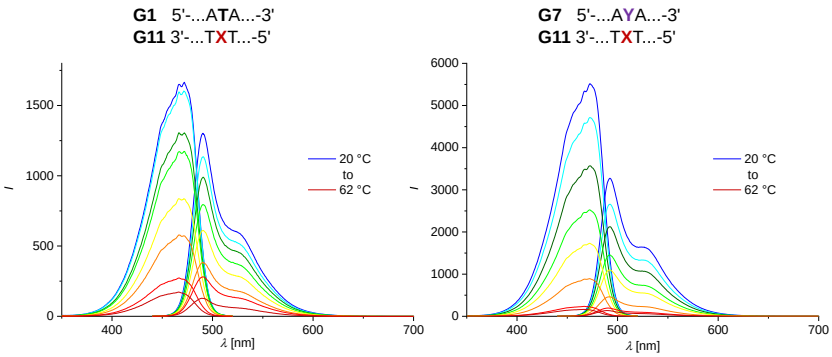

6.3.1.4 DNA/GNA hybrids

Temperature-dependent fluorescence spectra were recorded for 1 µM oligonucleotides in 1× PBS (100 mM NaCl, 10 mM phosphate, pH 7.0). Excitation and emission wavelengths were 420 and 540 nm, respectively.
X = gBAM, X = gmBAM, x = gmBAM^{b}, X = gBAM^{F}, X = gBAM^{OMe}, X for (*R*)-gBAM.

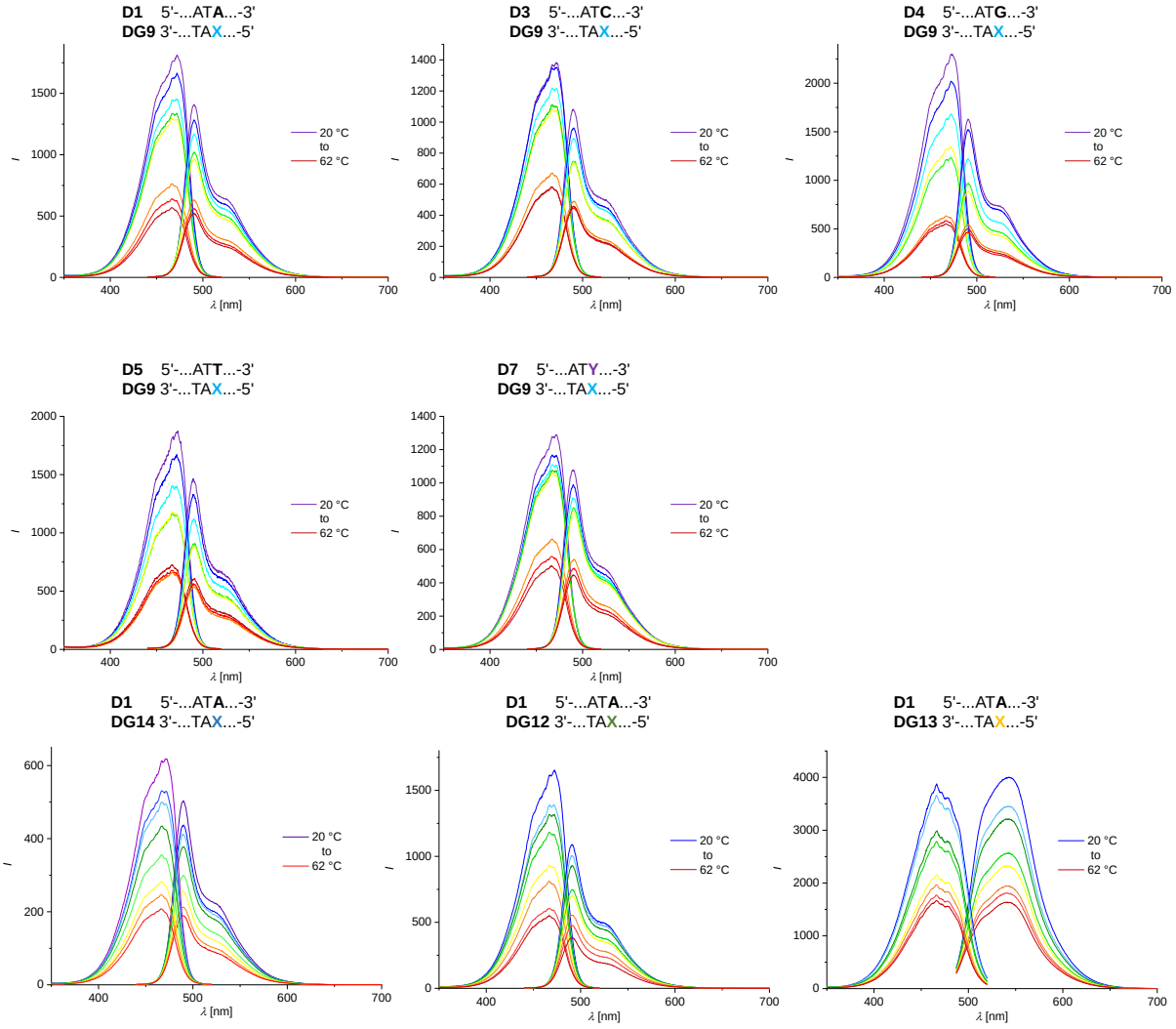

D1 5'-...AT**A**...-3'
DG11 3'-...TA**X**...-5'

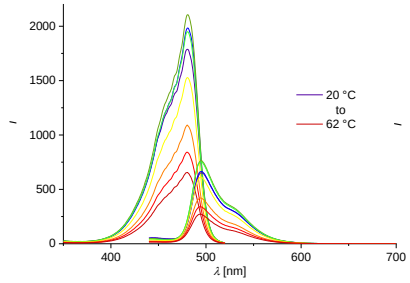

DG7 5'-...A**X**A...-3'
DG14 3'-...TA**X**...-5'

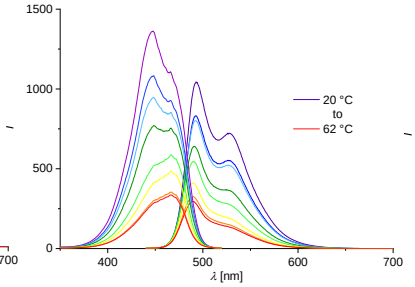

DG2 5'-...A**X**A...-3'
DG14 3'-...TA**X**...-5'

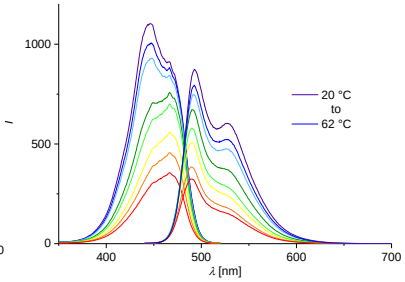

DG7 5'-...A**X**A...-3'
DG18 3'-...T**X**T...-5'

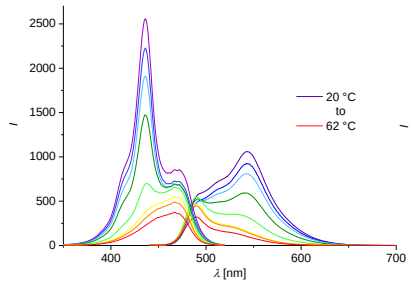

DG2 5'-...A**X**A...-3'
DG18 3'-...T**X**T...-5'

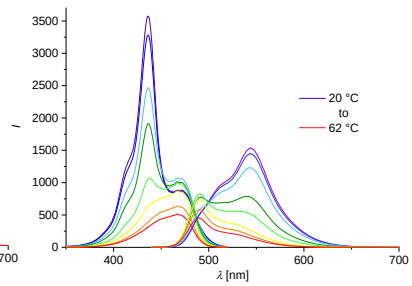

DG29 5'-...TT**X**TT...-3'
DG33 3'-...A**X**XXA...-5'

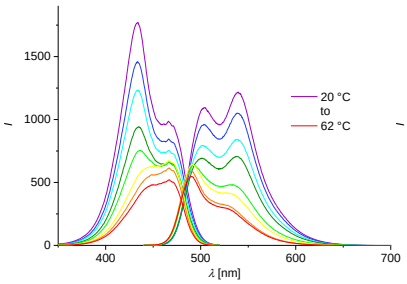

DG32 5'-...T**X**XXT...-3'
DG33 3'-...A**X**XXA...-5'

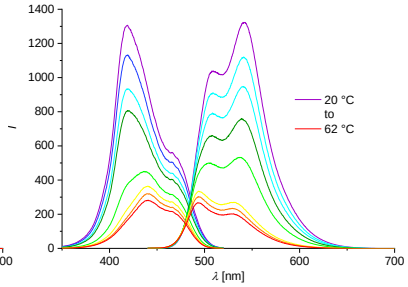

DG31 5'-...TT**X**XT...-3'
DG35 3'-...**X**XXXX...-5'

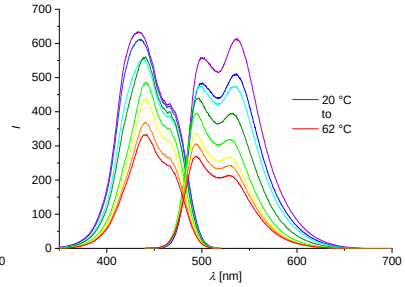

DG34 5'-...**X**XXXX...-3'
DG33 3'-...A**X**XXA...-5'

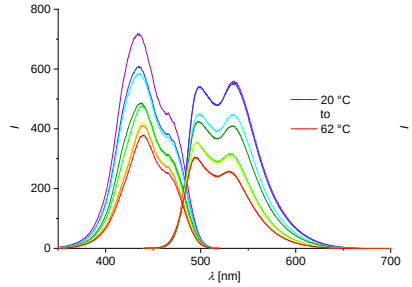

DG32 5'-...T**X**XXT...-3'
DG35 3'-...**X**XXXX...-5'

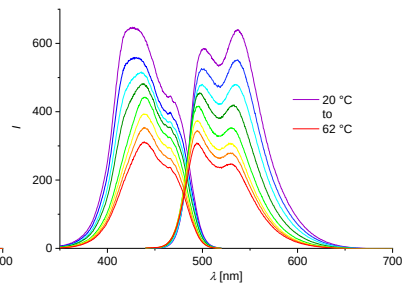

6.3.2 Screening of HBI variants

Fluorescence excitation and emission spectra for HBI chromophores in the presence of the Chili aptamer (in addition Broccoli and Baby Spinach in the case of DFHBI-NH_2). Spectra were blank corrected. Conditions: 0.5 µM chromophore, 0.5 µM Chili, 125 mM KCl, 5 mM $MgCl_2$, 80 mM HEPES pH 7.5; emission and excitation at the maximum.

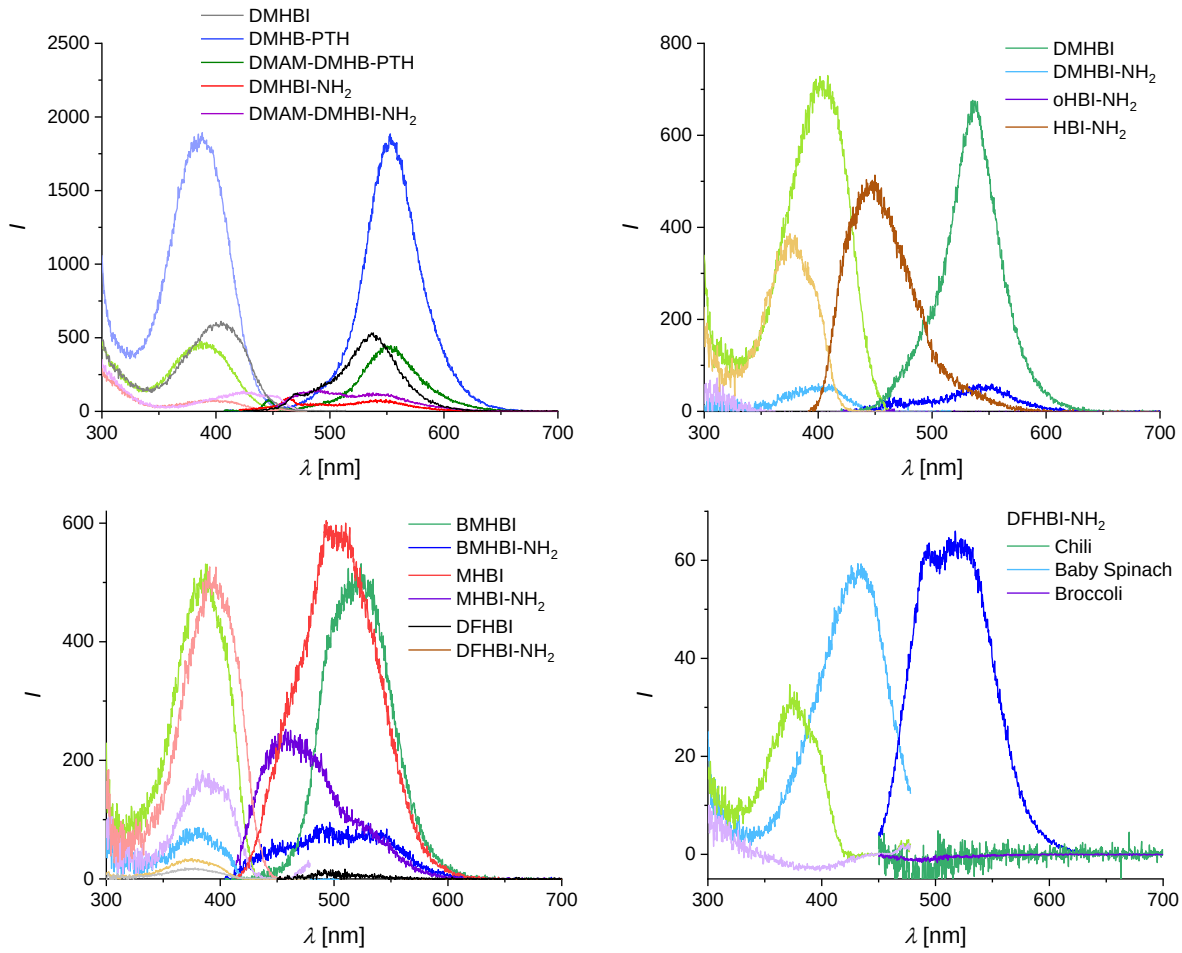

6.3.3 Fluorescence lifetime measurements

Fluorescence lifetimes were measured for 1 µM samples with the given excitation and detection wavelengths and the parameters described in the experimental part of this thesis. Lifetimes were calculated by fitting according to a three-exponential function. Shown are the decay of the sample (red), the instrument response function (prompt, black) and the three-exponential fit (blue) in the top panel and the weighted residuals in the bottom panel.

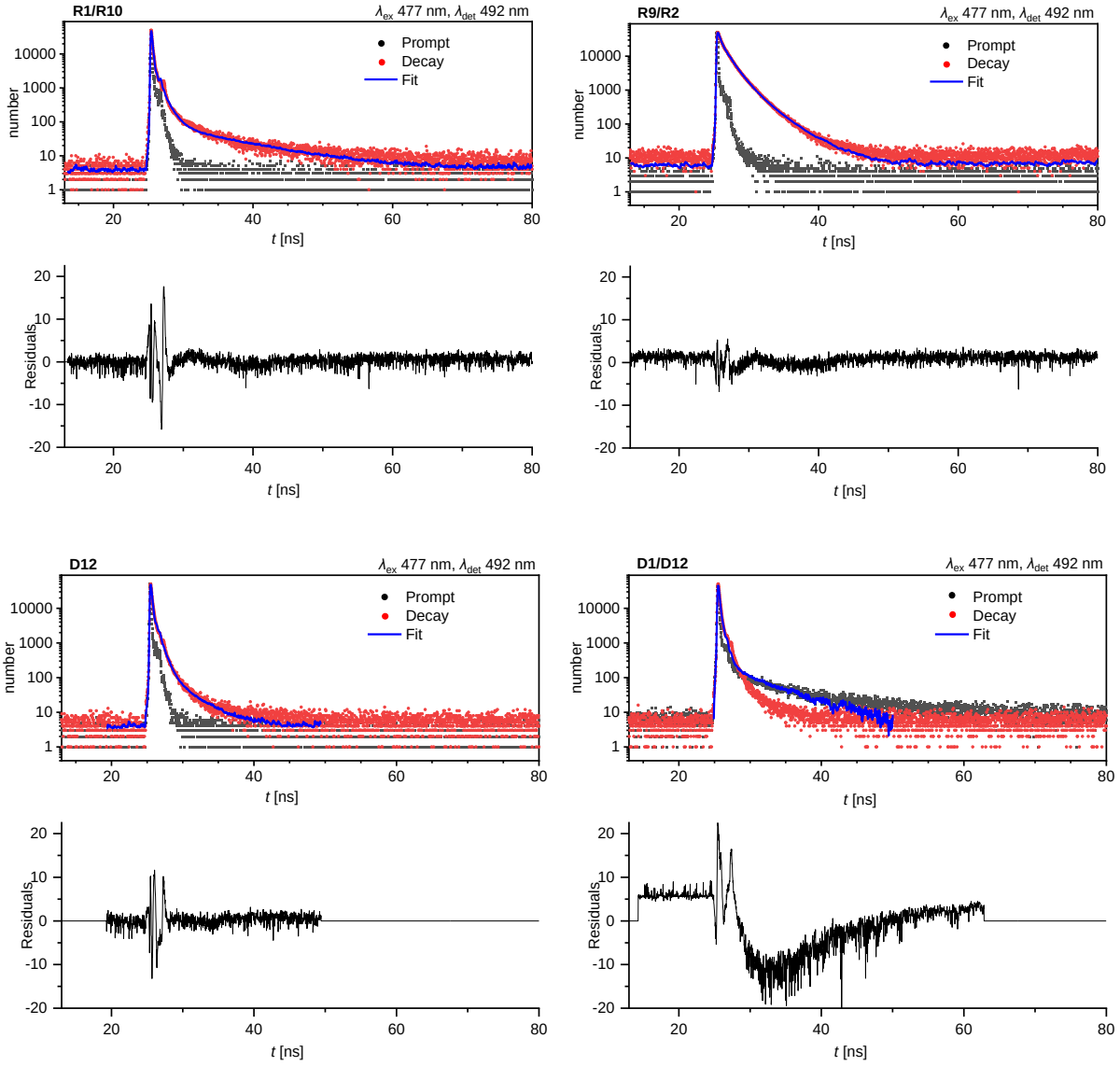

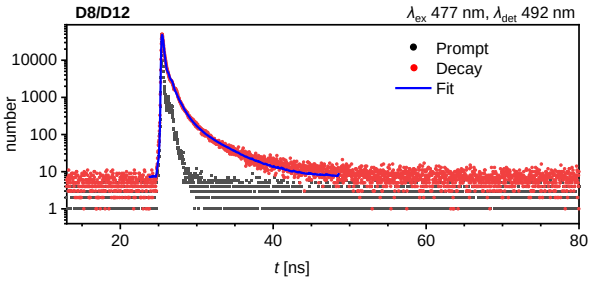
D8/D12
λ_{ex} 477 nm, λ_{det} 492 nm
Prompt
Decay
Fit
number
t [ns]

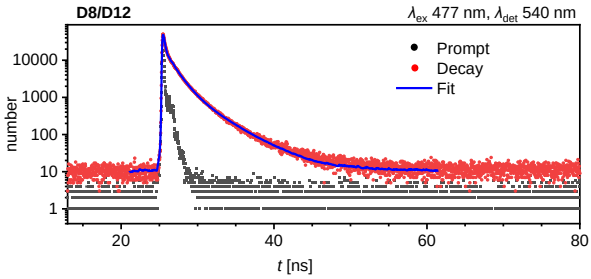
D8/D12
λ_{ex} 477 nm, λ_{det} 540 nm
Prompt
Decay
Fit
number
t [ns]

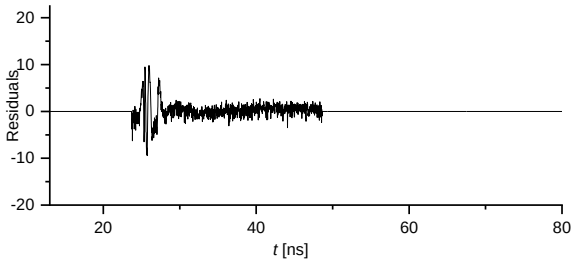
Residuals
t [ns]

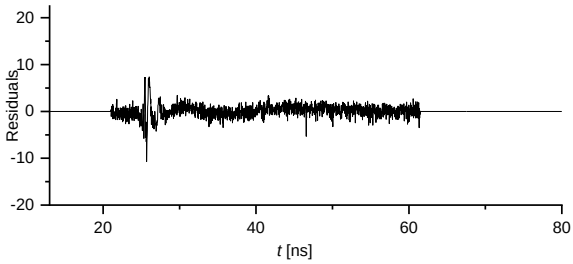
Residuals
t [ns]

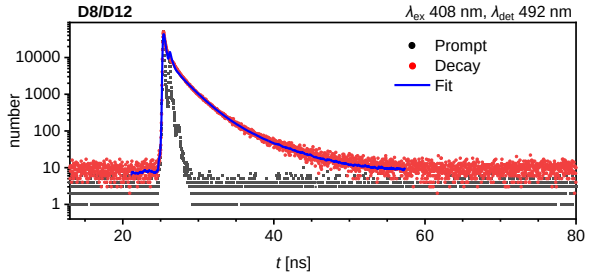
D8/D12
λ_{ex} 408 nm, λ_{det} 492 nm
Prompt
Decay
Fit
number
t [ns]

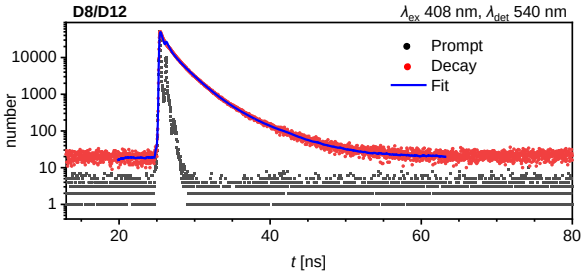
D8/D12
λ_{ex} 408 nm, λ_{det} 540 nm
Prompt
Decay
Fit
number
t [ns]

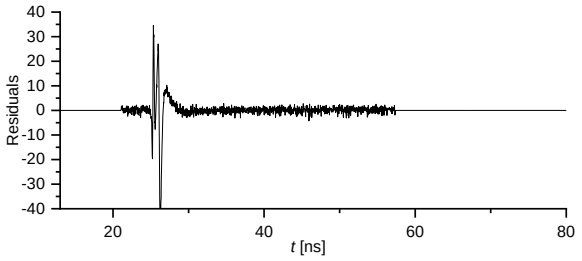
Residuals
t [ns]

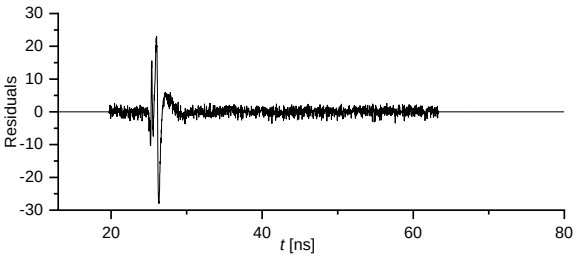
Residuals
t [ns]

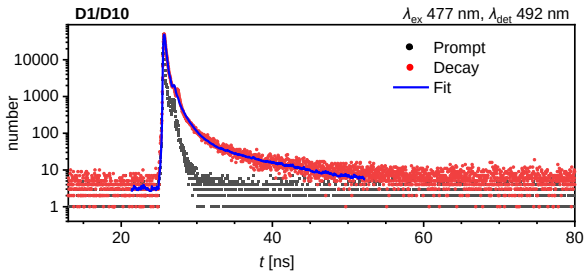
D1/D10
λ_{ex} 477 nm, λ_{det} 492 nm
Prompt
Decay
Fit
number
t [ns]

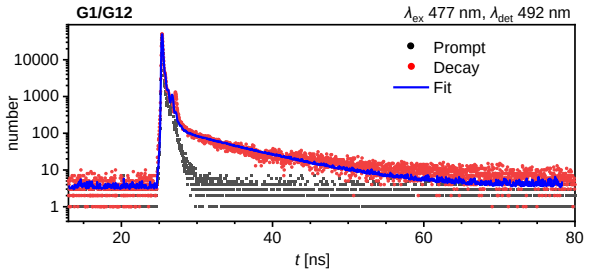
G1/G12
λ_{ex} 477 nm, λ_{det} 492 nm
Prompt
Decay
Fit
number
t [ns]

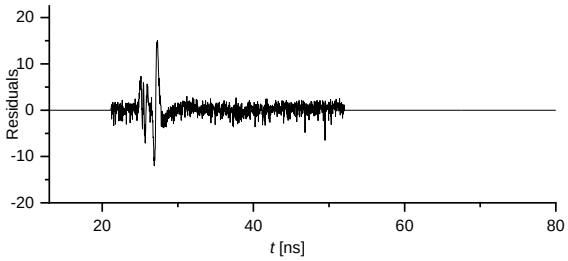
Residuals
t [ns]

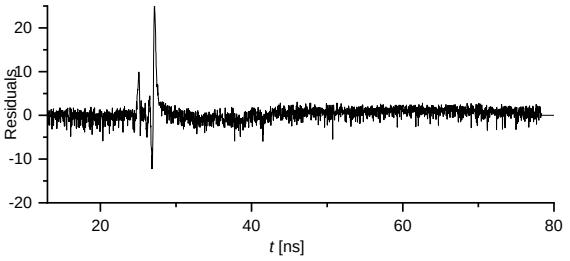
Residuals
t [ns]

6.3.4 K_D measurements

Concentration-dependent fluorescence spectra (left) and titration curves (right) of different HBI derivatives with the Chili aptamer. Fluorescence spectra were integrated after blank correction and the error bars indicate the standard deviation of the mean of duplicates. Conditions: 8.00 µM to 0.49 µM RNA (15-step dilution series with water), 0.1 µM ligand, 125 mM KCl, 5 mM $MgCl_2$, 80 mM HEPES pH 7.5.

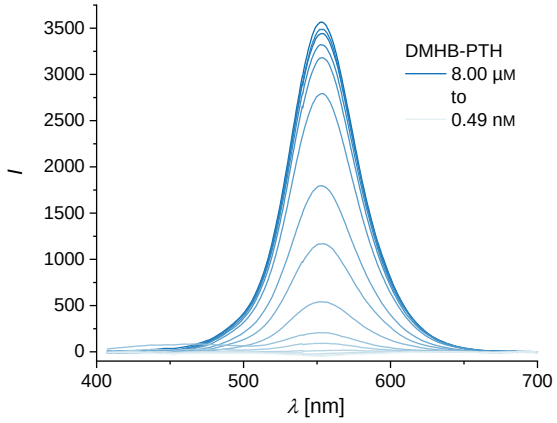

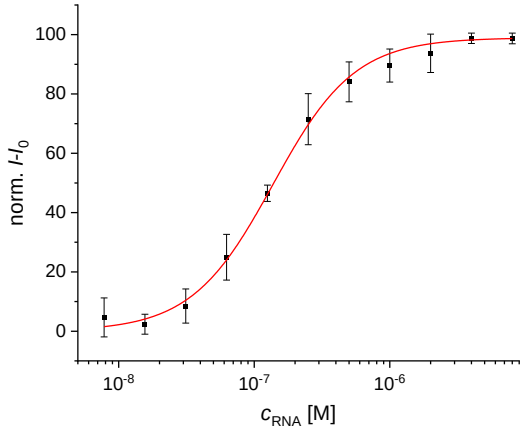

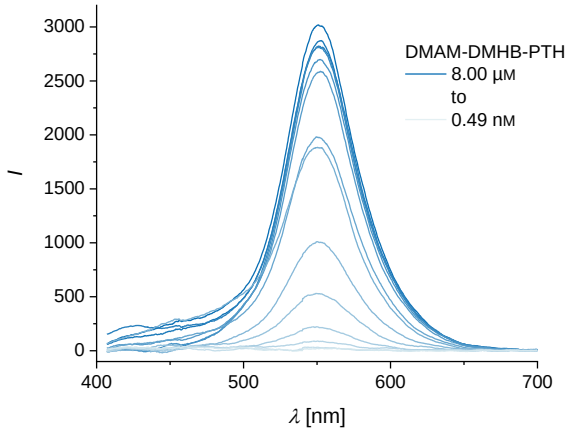

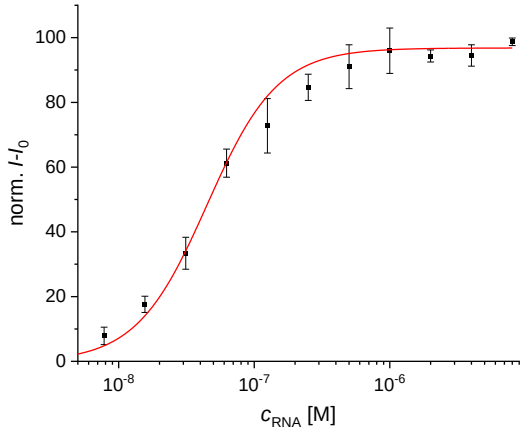

6.3.5 Quantum yield determination

6.3.6 Merocyanine chromophores

The relative quantum yield ϕ_{rel} of merocyanine-modified oligonucleotides was estimated from fluorescence and absorption measurements of 1, 2, and 5 µM samples in 1× PBS (100 mM NaCl, 10 mM phosphate, pH 7.0). Shown here are the respective spectra and a plot of the integral of the fluorescence intensity F *versus* the absorption factor a with a linear fit. Details are given in the experimental part of this thesis in section 5.4.3.6.

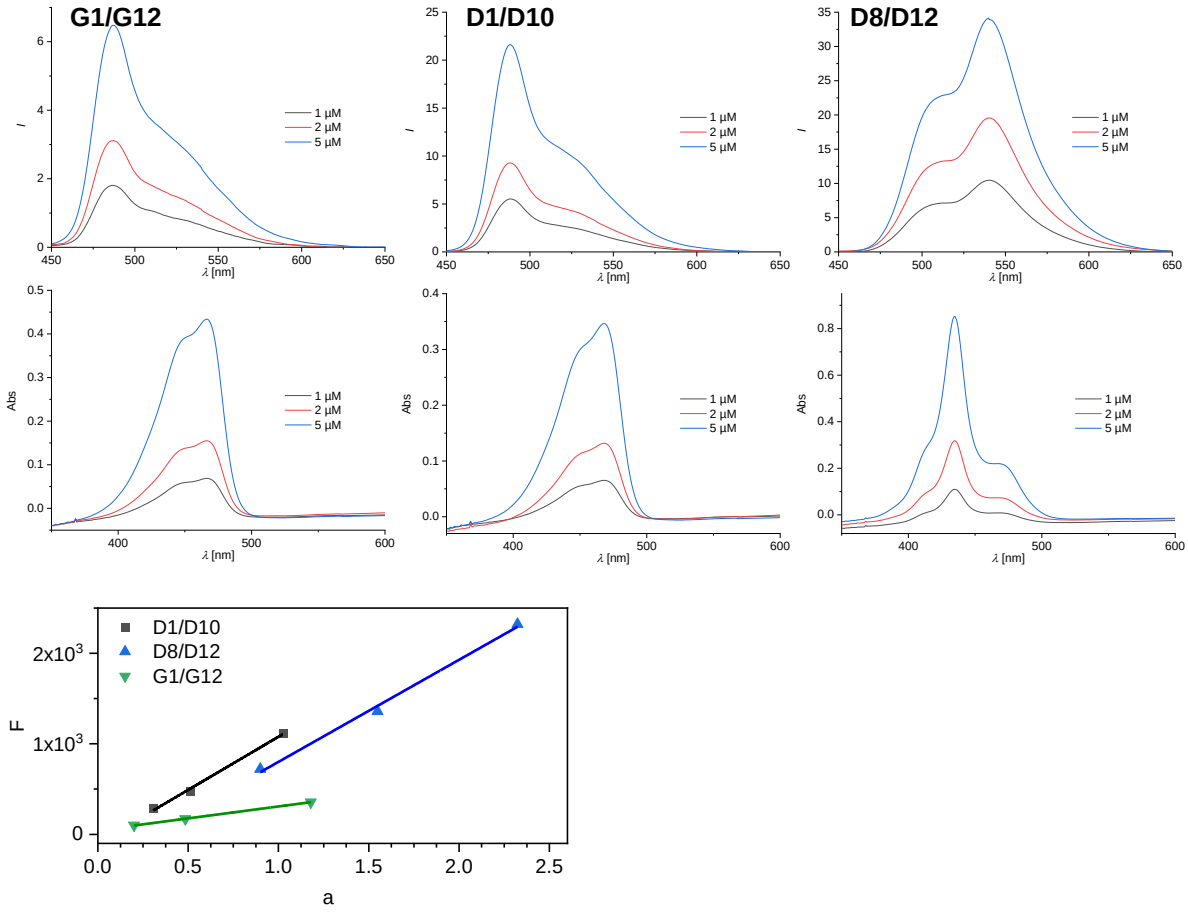

6.3.7 DMHBI variants

The relative quantum yield ϕ_{rel} of DMHBI variants as free chromophores or in complex with Chili was estimated from fluorescence and absorption measurements of 3.33, 6.66 and 10 µM samples in buffer. Shown here are the respective spectra and a plot of the integral of the fluorescence intensity F *versus* the absorption factor a with a linear fit. Details are given in the experimental part of this thesis in section 5.4.3.6.

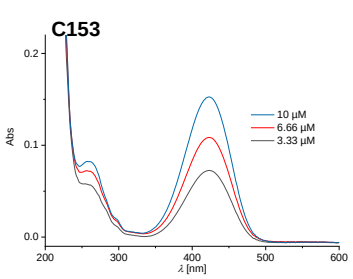
C153
Abs
λ [nm]
10 μM
6.66 μM
3.33 μM

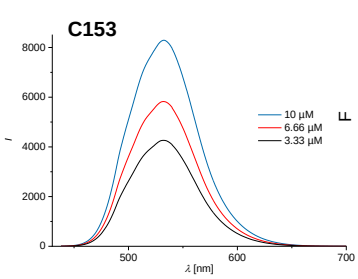
C153
I
λ [nm]
10 μM
6.66 μM
3.33 μM

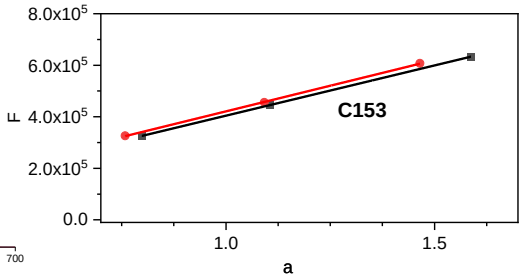
C153
F
a

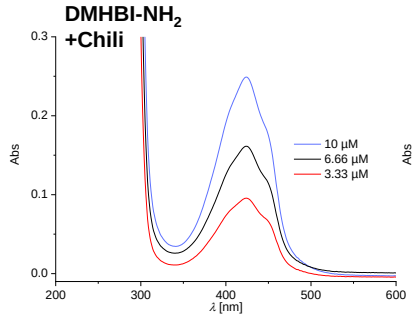
DMHBI-NH2
+Chili
Abs
λ [nm]
10 μM
6.66 μM
3.33 μM

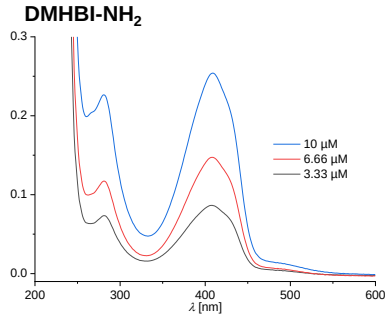
DMHBI-NH2
Abs
λ [nm]
10 μM
6.66 μM
3.33 μM

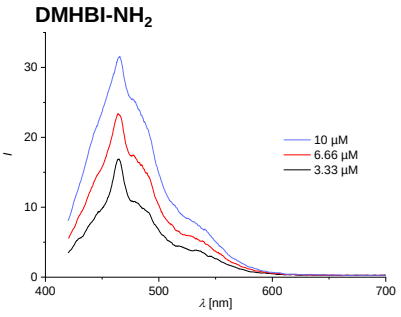
DMHBI-NH2
I
λ [nm]
10 μM
6.66 μM
3.33 μM

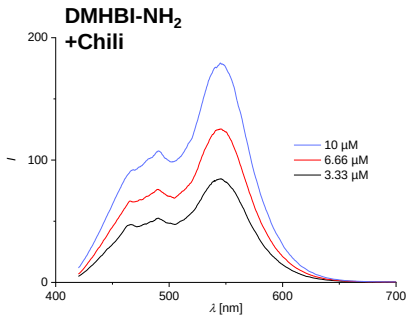
DMHBI-NH2
+Chili
I
λ [nm]
10 μM
6.66 μM
3.33 μM

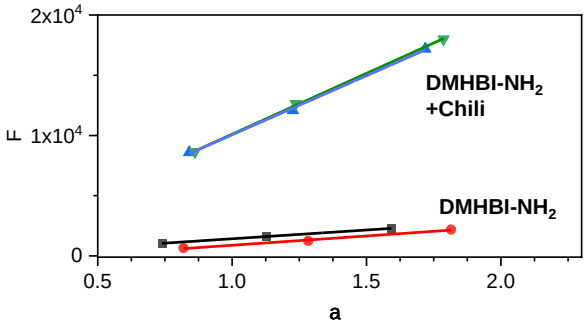
DMHBI-NH2
+Chili
DMHBI-NH2
F
a

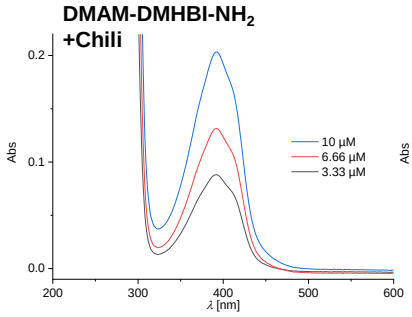
DMAM-DMHBI-NH2
+Chili
Abs
λ [nm]
10 μM
6.66 μM
3.33 μM

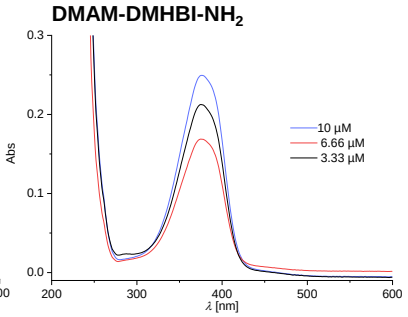
DMAM-DMHBI-NH2
Abs
λ [nm]
10 μM
6.66 μM
3.33 μM

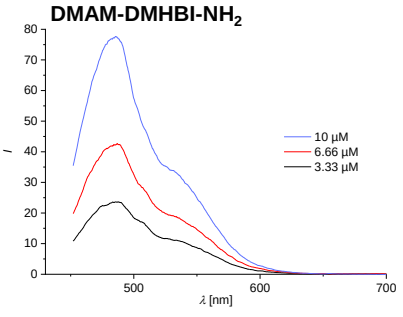
DMAM-DMHBI-NH2
I
λ [nm]
10 μM
6.66 μM
3.33 μM

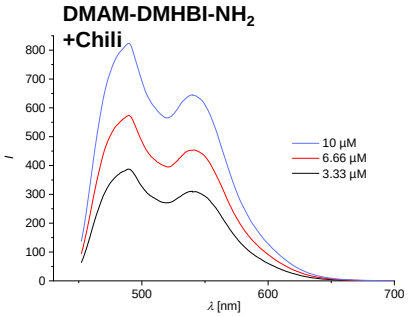
DMAM-DMHBI-NH2
+Chili
I
λ [nm]
10 μM
6.66 μM
3.33 μM

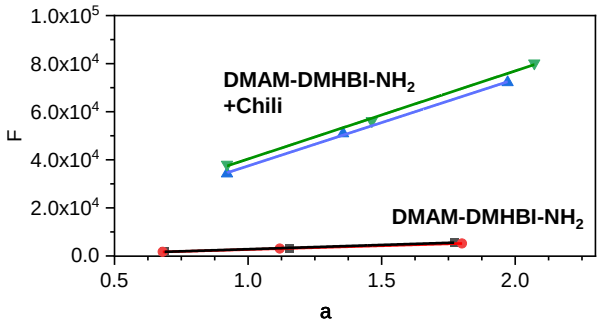
DMAM-DMHBI-NH2
+Chili
DMAM-DMHBI-NH2
F
a

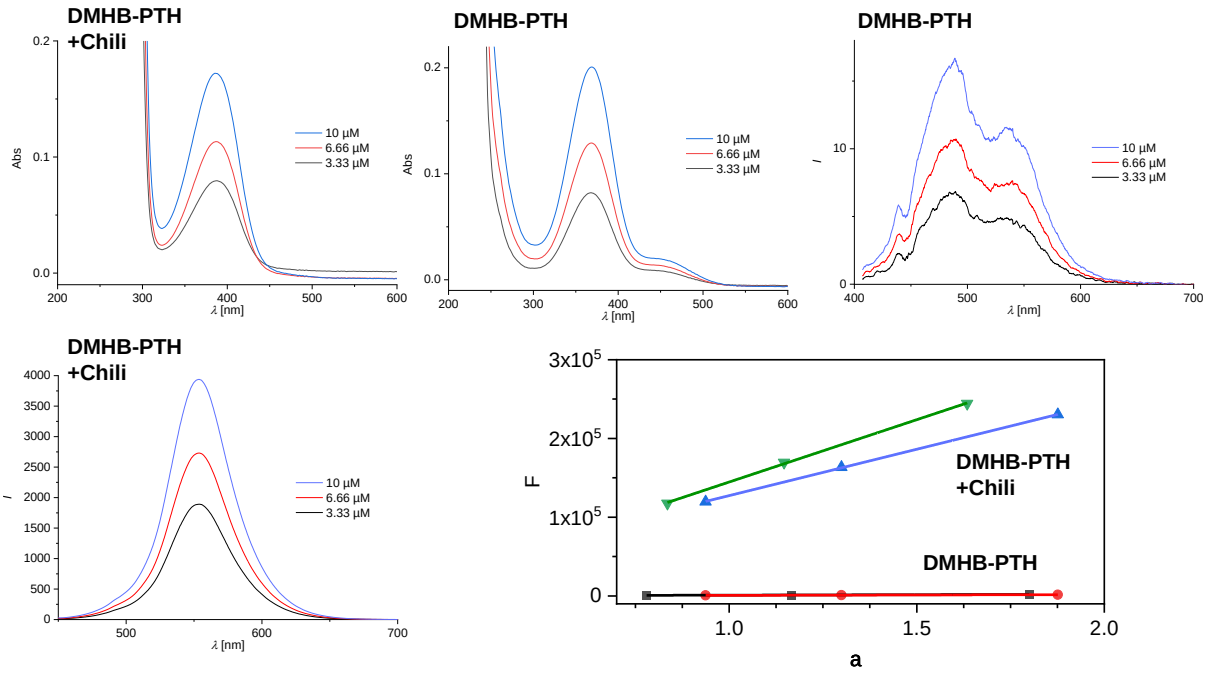
DMHB-PTH
+Chili
Abs
λ [nm]
10 μM
6.66 μM
3.33 μM
DMHB-PTH
Abs
λ [nm]
10 μM
6.66 μM
3.33 μM
DMHB-PTH
I
λ [nm]
10 μM
6.66 μM
3.33 μM
DMHB-PTH
+Chili
I
λ [nm]
10 μM
6.66 μM
3.33 μM
F
DMHB-PTH
+Chili
DMHB-PTH
a

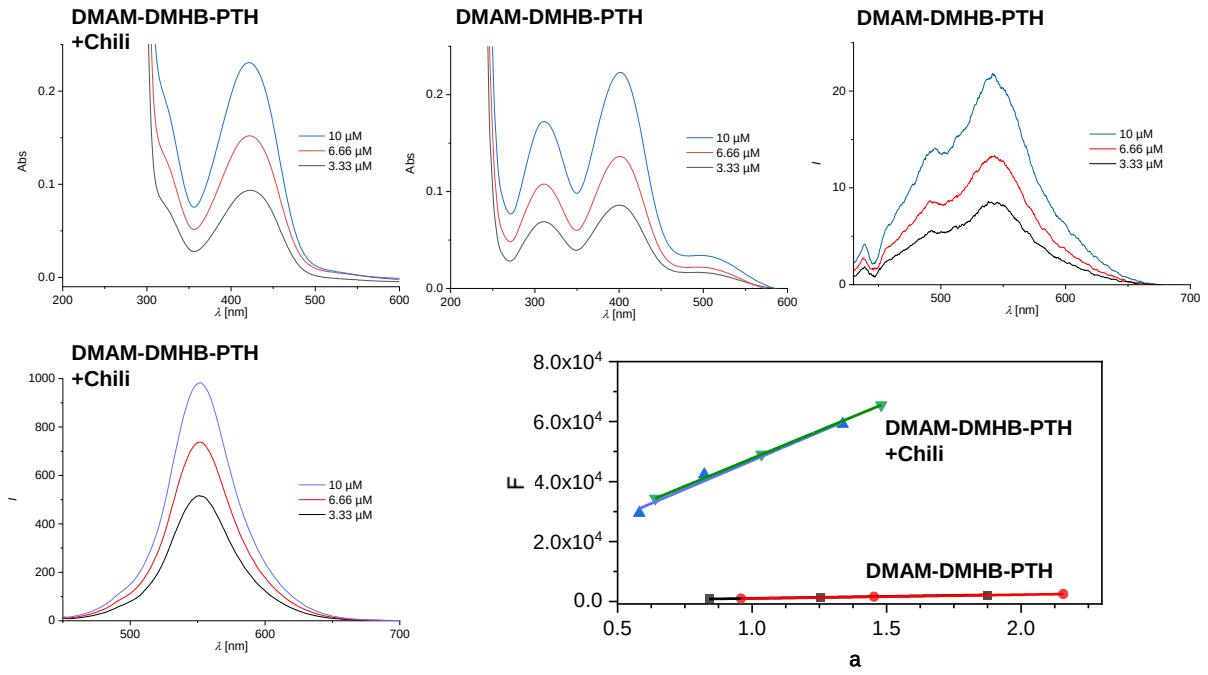
DMAM-DMHB-PTH
+Chili
Abs
λ [nm]
10 μM
6.66 μM
3.33 μM
DMAM-DMHB-PTH
Abs
λ [nm]
10 μM
6.66 μM
3.33 μM
DMAM-DMHB-PTH
I
λ [nm]
10 μM
6.66 μM
3.33 μM
DMAM-DMHB-PTH
+Chili
I
λ [nm]
10 μM
6.66 μM
3.33 μM
F
DMAM-DMHB-PTH
+Chili
DMAM-DMHB-PTH
a

6.4 Supplementary melting curves

Shown are the melting curves for 1, 2, 5, 10 and 20 µM samples in 1× PBS (100 mM NaCl, 10 mM phosphate, pH 7.0) for the second heating ramp. In addition, the van't Hoff plot with the linear fit for the calculation of thermodynamic parameters is provided for every duplex. Data points which were excluded from fitting are shown as empty symbols.

6.4.1 Melting curves for RNA duplexes

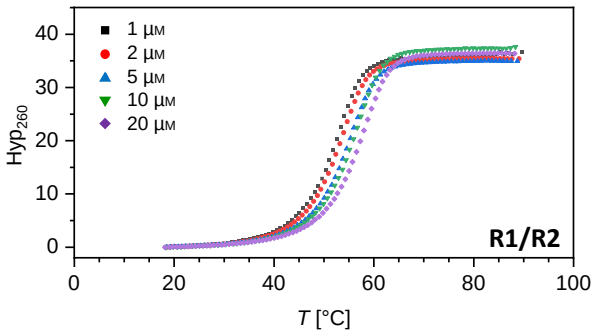

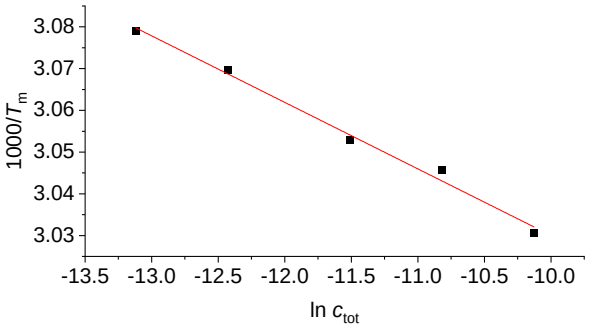

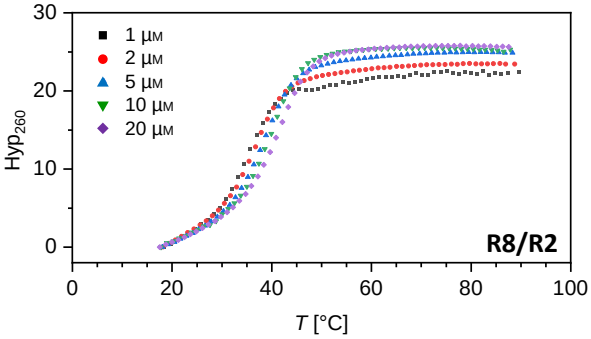

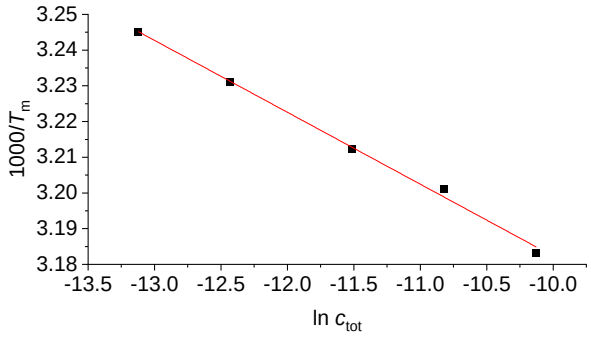

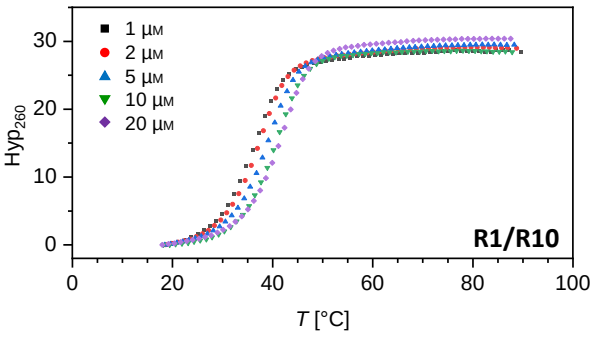

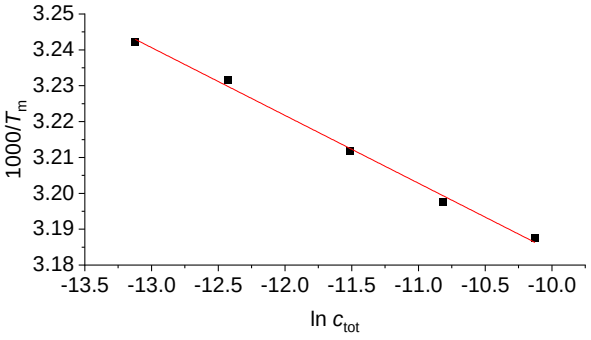

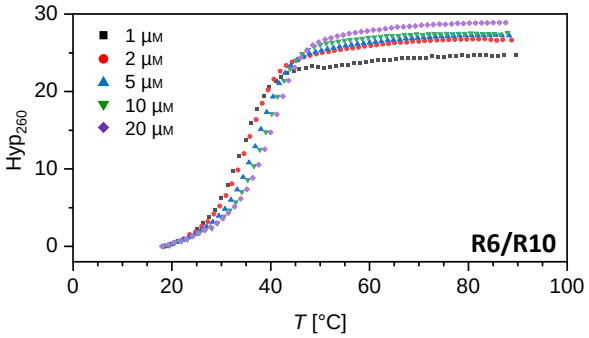

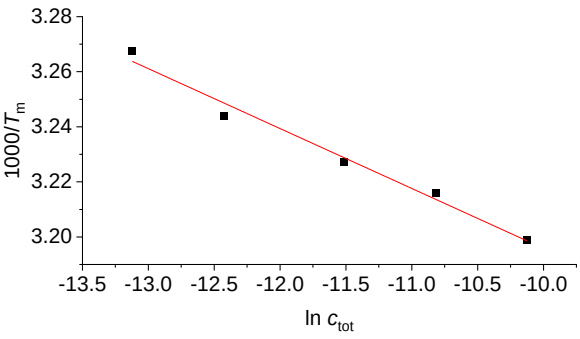

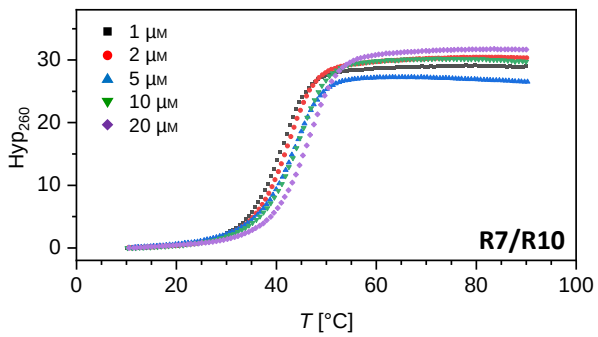
1 µM
2 µM
5 µM
10 µM
20 µM
Hyp260
T [°C]
R7/R10

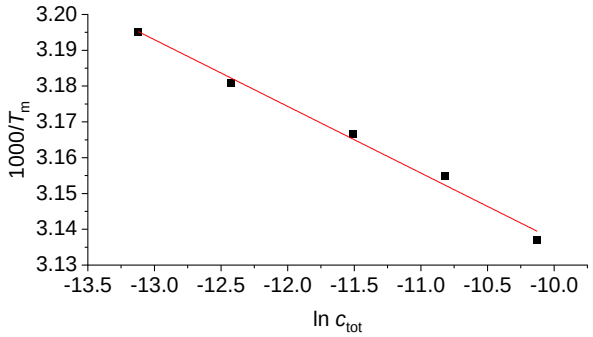
1000/Tm
ln ctot

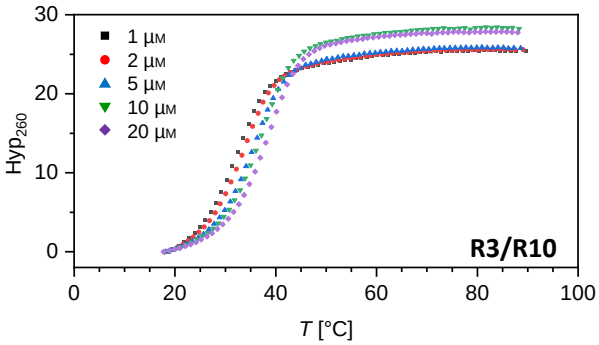
1 µM
2 µM
5 µM
10 µM
20 µM
Hyp260
T [°C]
R3/R10

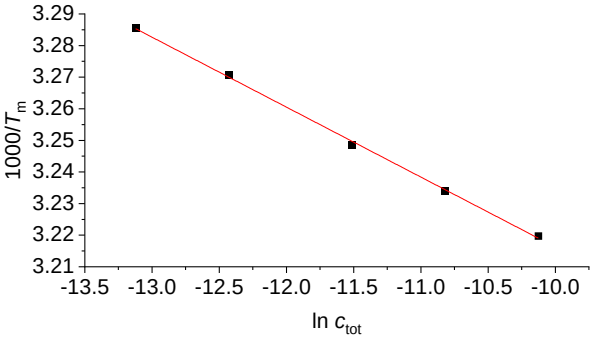
1000/Tm
ln ctot

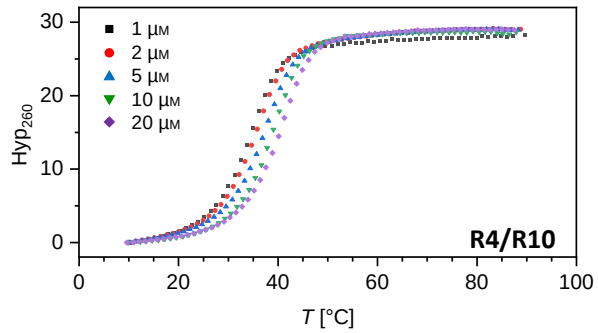
1 µM
2 µM
5 µM
10 µM
20 µM
Hyp260
T [°C]
R4/R10

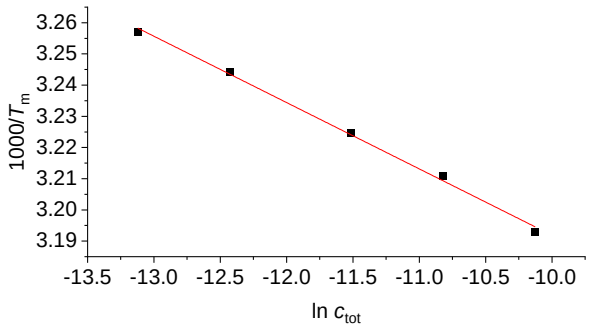
1000/Tm
ln ctot

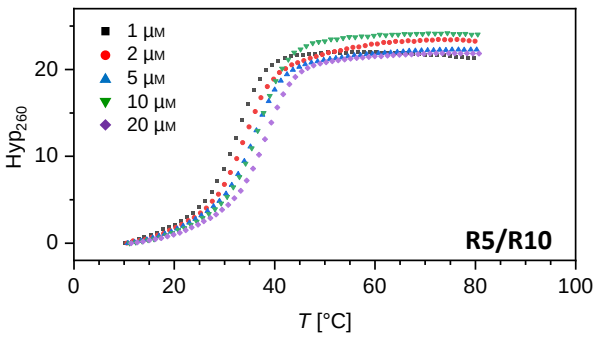
1 µM
2 µM
5 µM
10 µM
20 µM
Hyp260
T [°C]
R5/R10

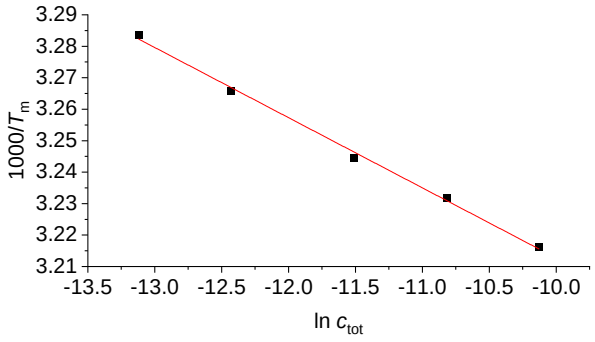
1000/Tm
ln ctot

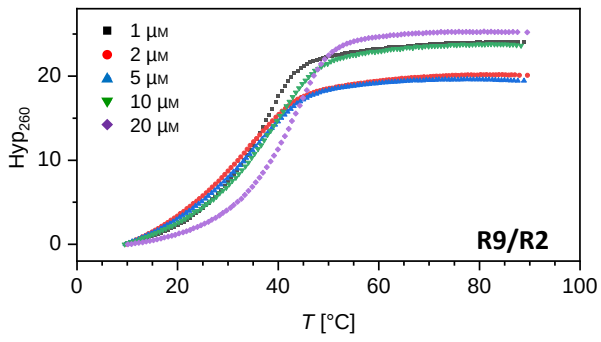
1 µM
2 µM
5 µM
10 µM
20 µM
Hyp260
T [°C]
R9/R2

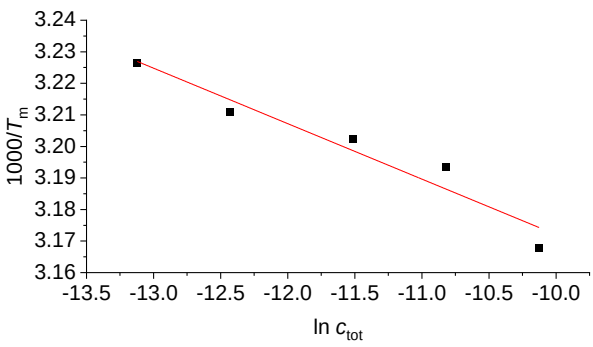
1000/Tm
ln ctot

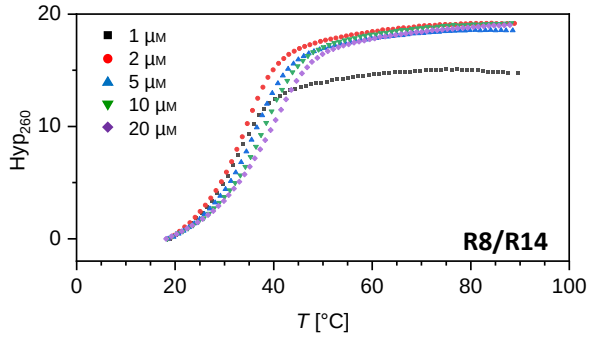
1 µM
2 µM
5 µM
10 µM
20 µM
Hyp260
T [°C]
R8/R14

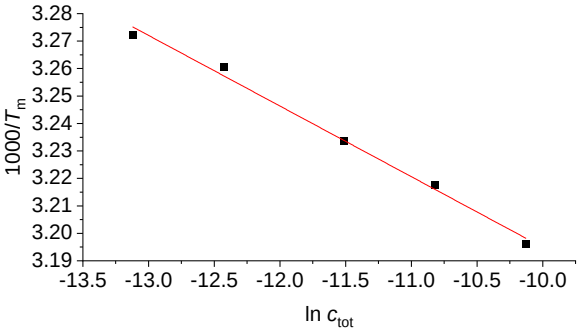
1000/Tm
ln ctot

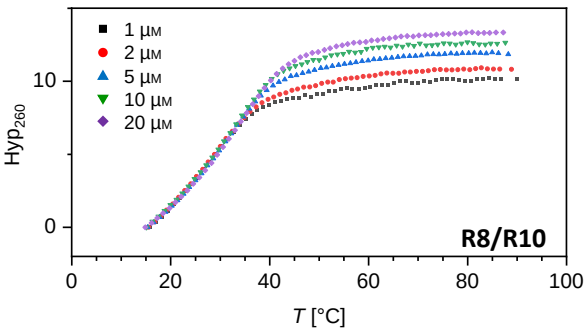
1 µM
2 µM
5 µM
10 µM
20 µM
Hyp260
T [°C]
R8/R10

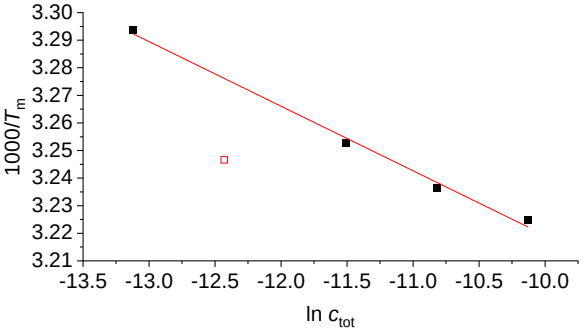
1000/Tm
ln ctot

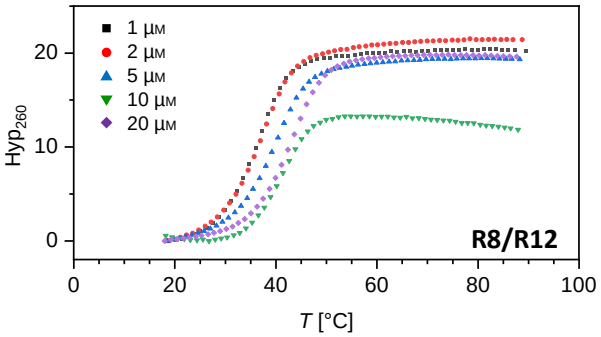
1 µM
2 µM
5 µM
10 µM
20 µM
Hyp260
T [°C]
R8/R12

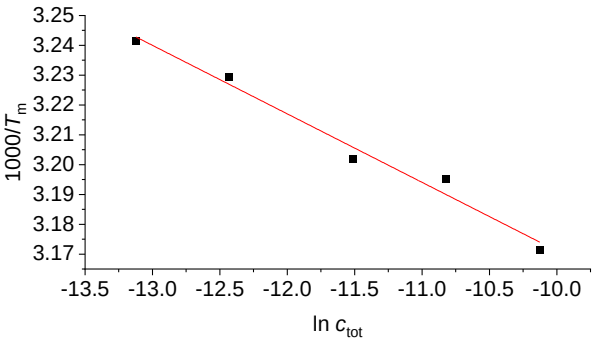
1000/Tm
ln ctot

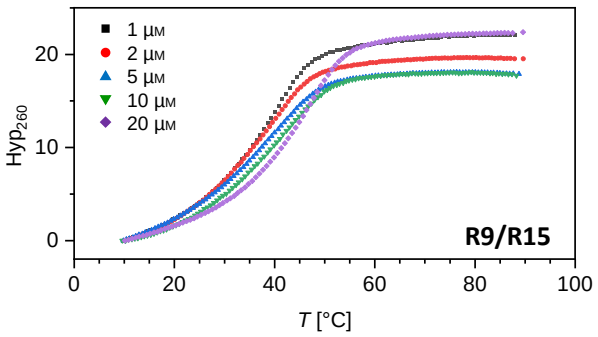
1 µM
2 µM
5 µM
10 µM
20 µM
Hyp260
T [°C]
R9/R15

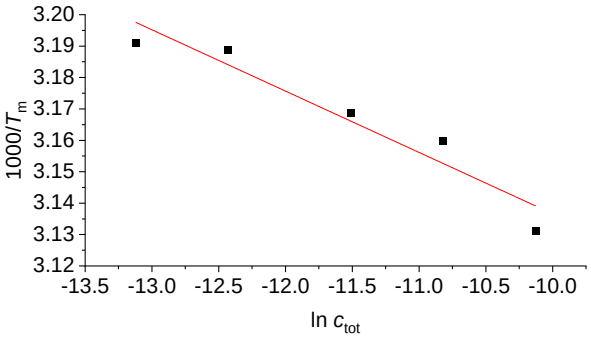
1000/Tm
ln ctot

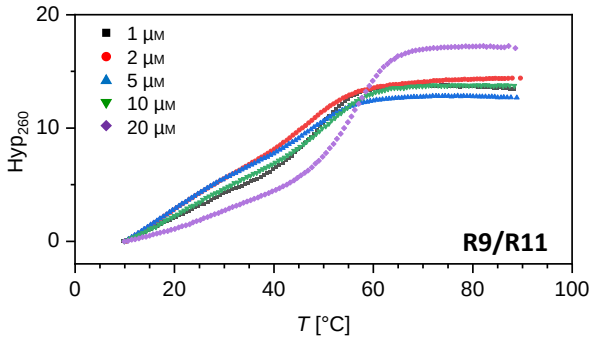
1 µM
2 µM
5 µM
10 µM
20 µM
Hyp260
T [°C]
R9/R11

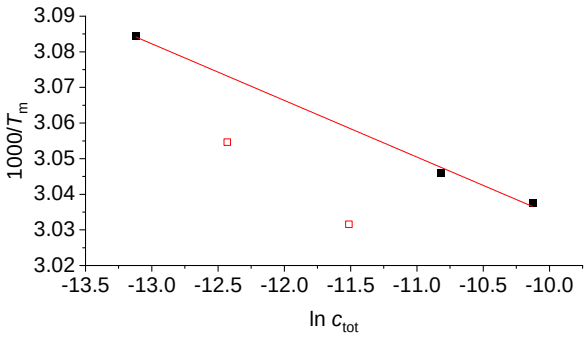
1000/Tm
ln ctot

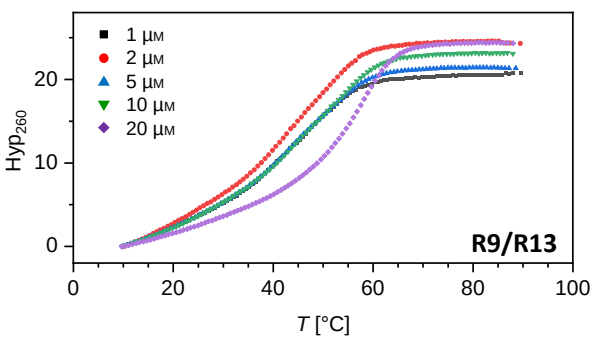

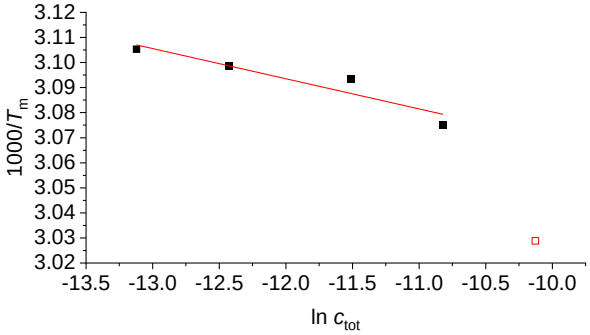

6.4.2 Melting curves for DNA duplexes

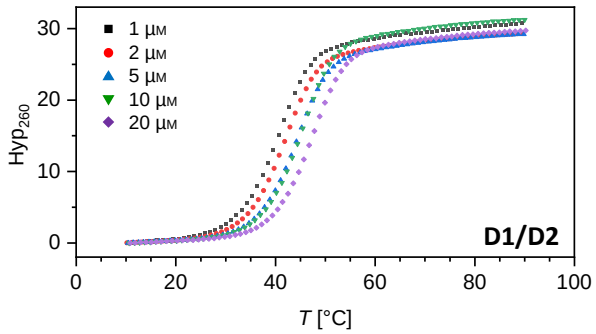

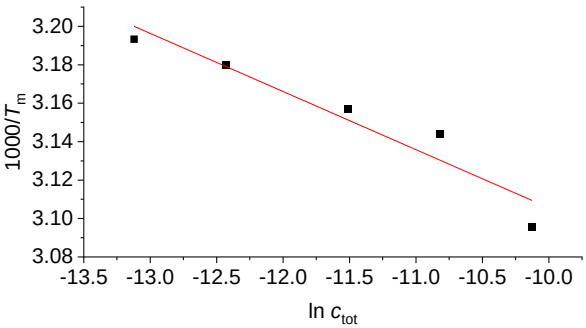

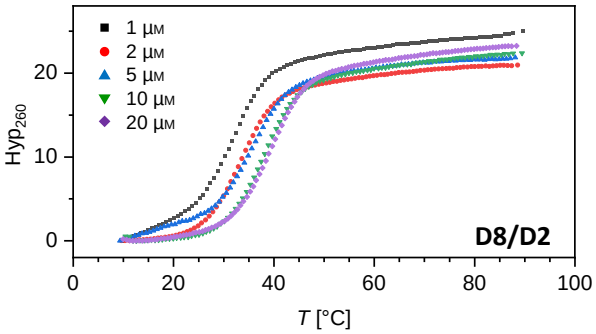

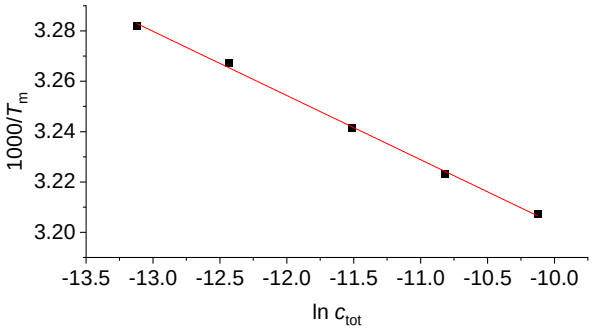

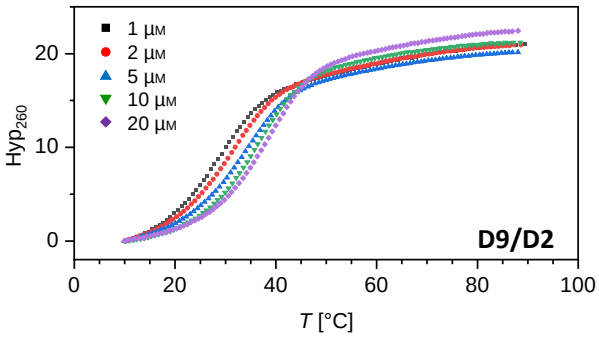

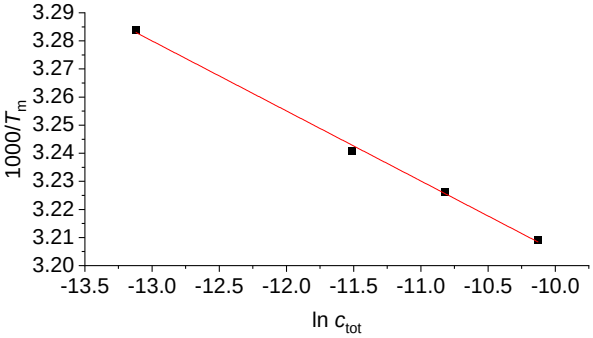

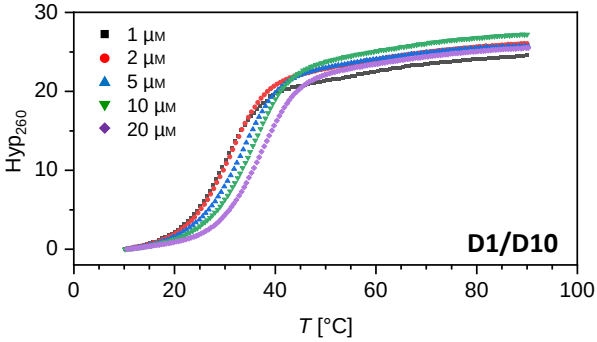

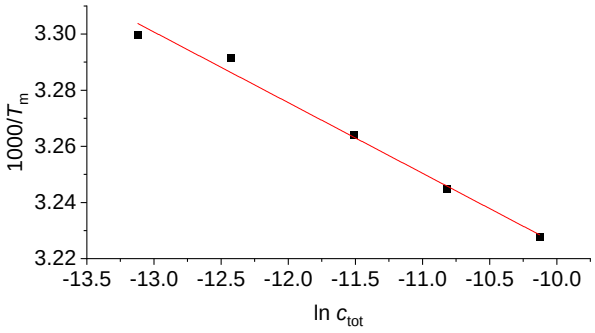

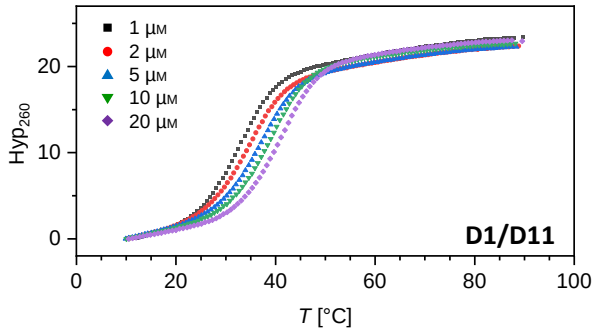
1 µM
2 µM
5 µM
10 µM
20 µM
Hyp260
T [°C]
D1/D11

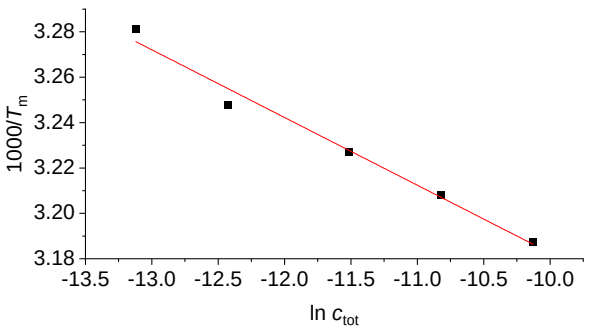
1000/Tm
ln ctot

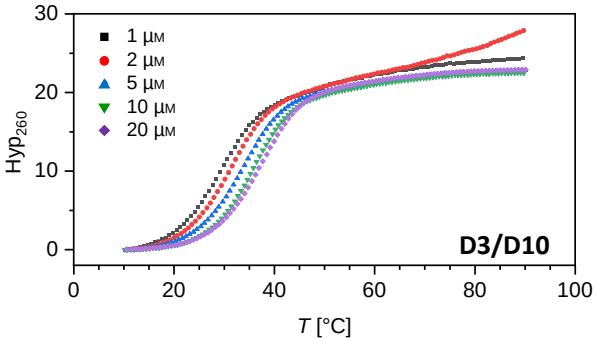
1 µM
2 µM
5 µM
10 µM
20 µM
Hyp260
T [°C]
D3/D10

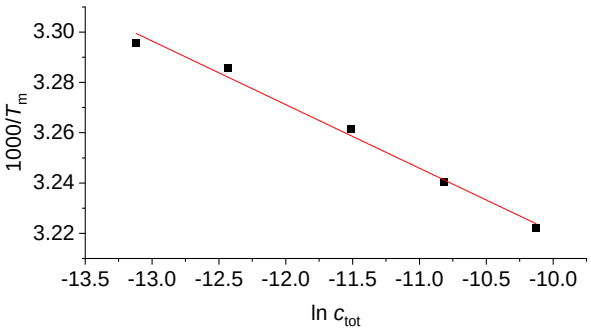
1000/Tm
ln ctot

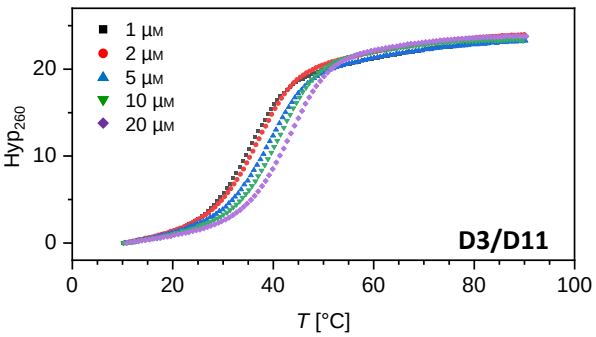
1 µM
2 µM
5 µM
10 µM
20 µM
Hyp260
T [°C]
D3/D11

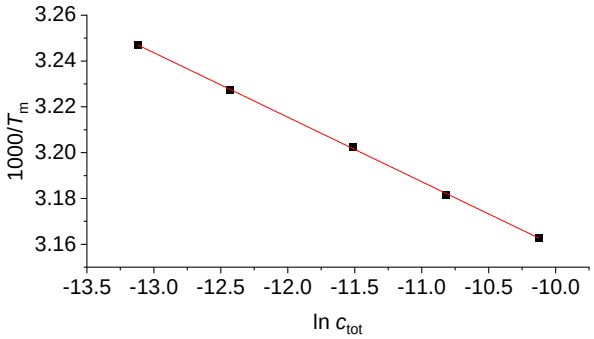
1000/Tm
ln ctot

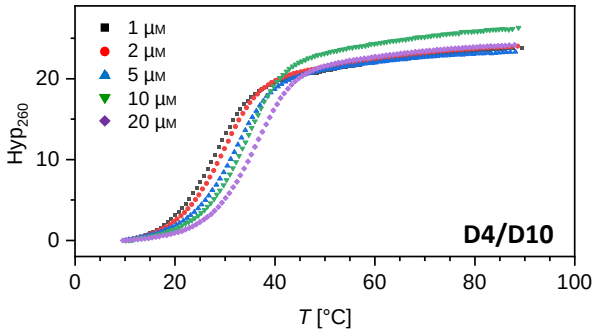
1 µM
2 µM
5 µM
10 µM
20 µM
Hyp260
T [°C]
D4/D10

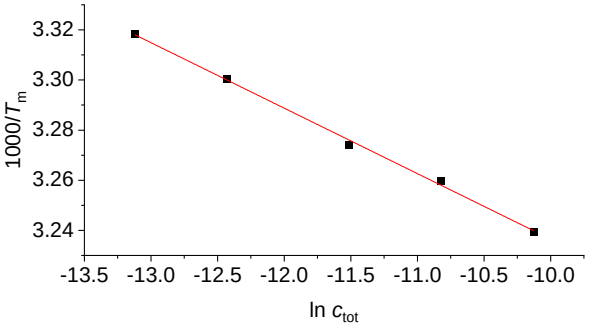
1000/Tm
ln ctot

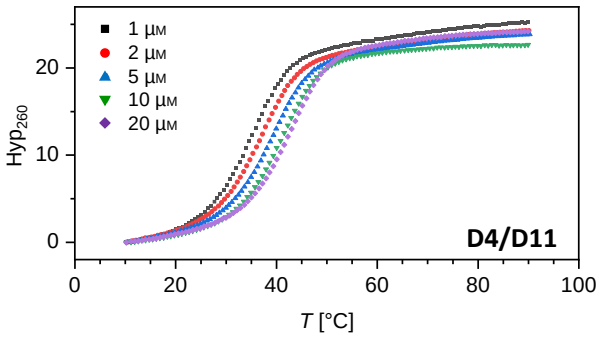
1 µM
2 µM
5 µM
10 µM
20 µM
Hyp260
T [°C]
D4/D11

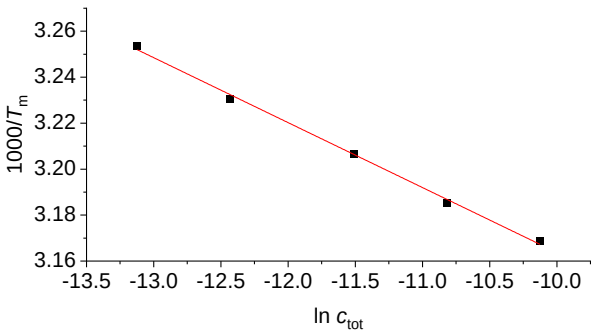
1000/Tm
ln ctot

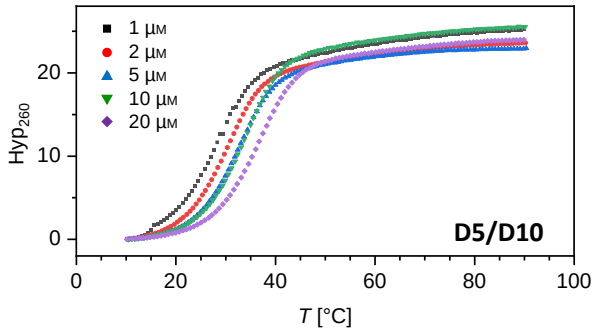
1 µM
2 µM
5 µM
10 µM
20 µM
Hyp260
T [°C]
D5/D10

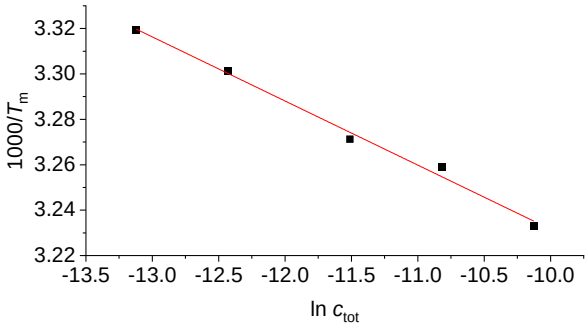
1000/Tm
ln ctot

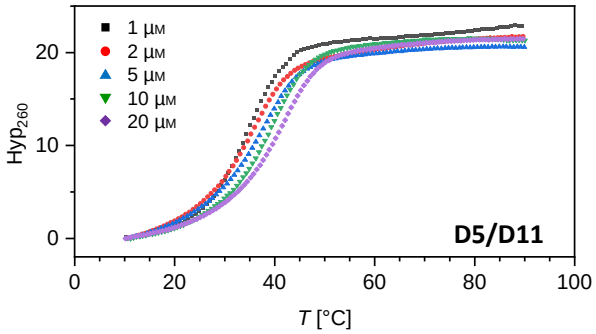
1 µM
2 µM
5 µM
10 µM
20 µM
Hyp260
T [°C]
D5/D11

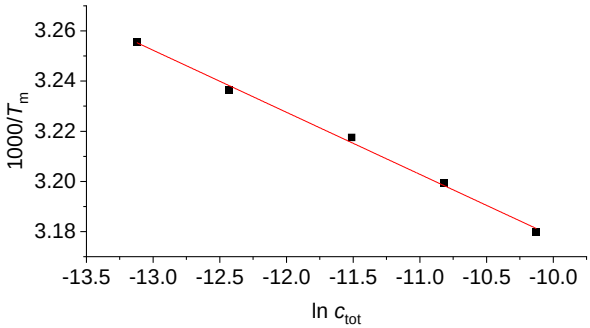
1000/Tm
ln ctot

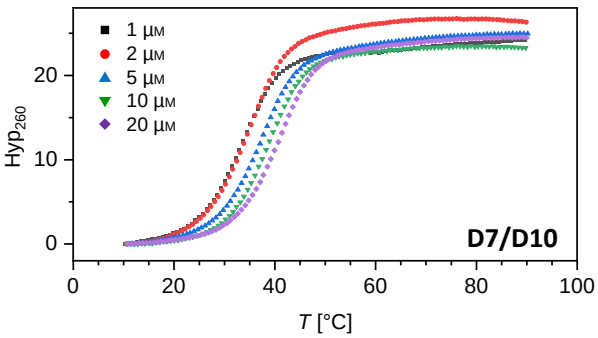
1 µM
2 µM
5 µM
10 µM
20 µM
Hyp260
T [°C]
D7/D10

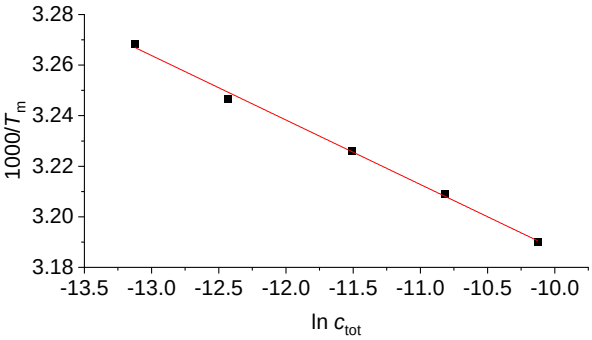
1000/Tm
ln ctot

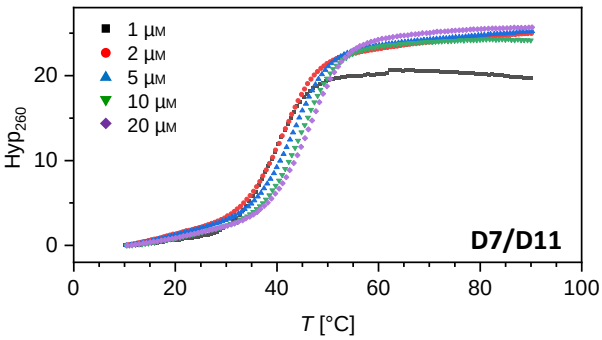
1 µM
2 µM
5 µM
10 µM
20 µM
Hyp260
T [°C]
D7/D11

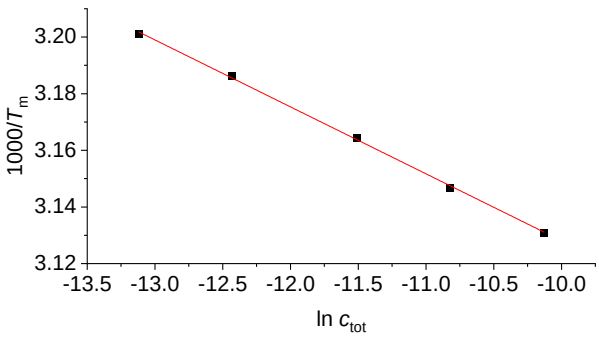
1000/Tm
ln ctot

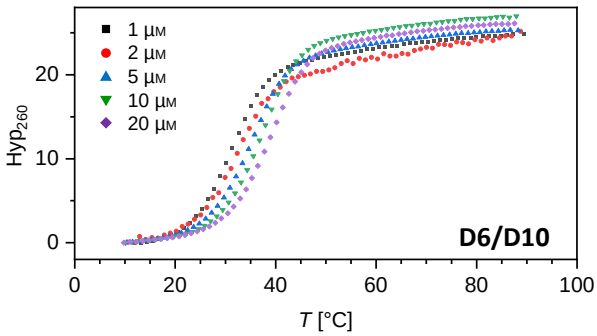
1 µM
2 µM
5 µM
10 µM
20 µM
Hyp260
T [°C]
D6/D10

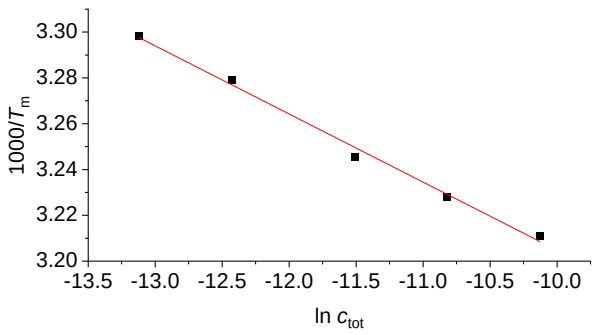
1000/Tm
ln ctot

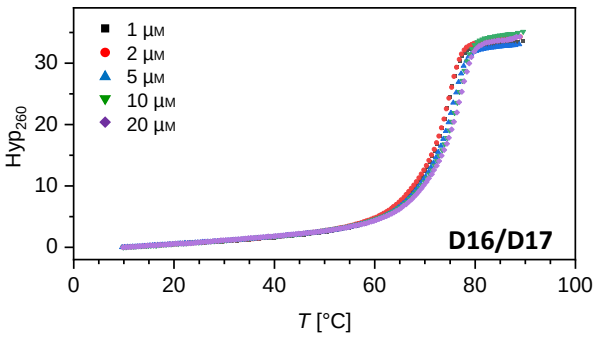
1 µM
2 µM
5 µM
10 µM
20 µM
Hyp260
T [°C]
D16/D17

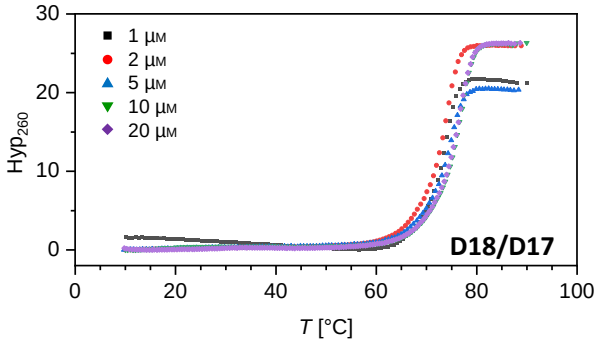
1 µM
2 µM
5 µM
10 µM
20 µM
Hyp260
T [°C]
D18/D17

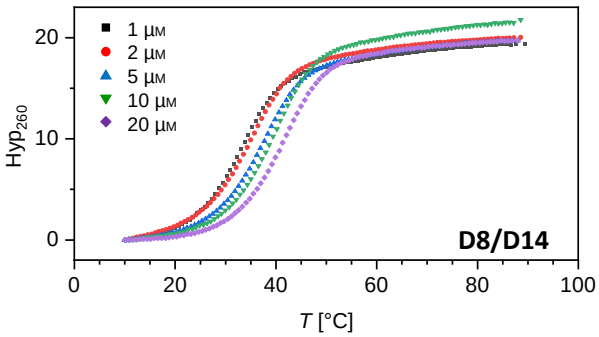
1 µM
2 µM
5 µM
10 µM
20 µM
Hyp260
T [°C]
D8/D14

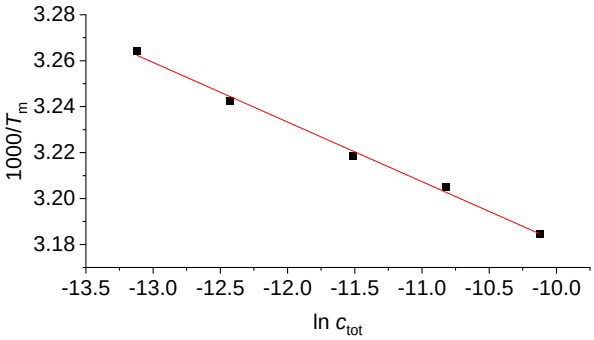
1000/Tm
ln ctot

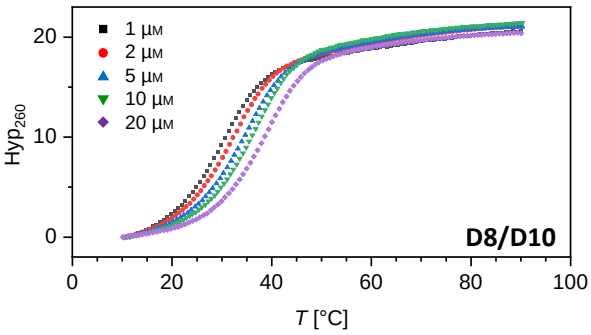
1 µM
2 µM
5 µM
10 µM
20 µM
Hyp260
T [°C]
D8/D10

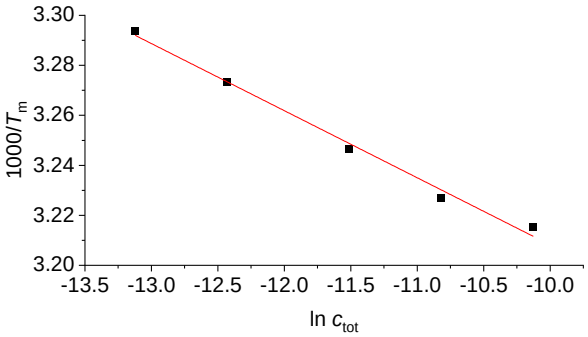
1000/Tm
ln ctot

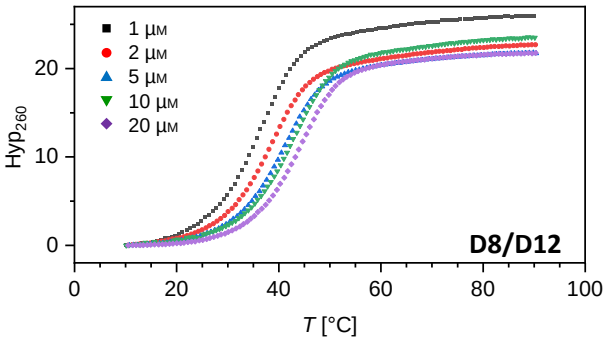
1 µM
2 µM
5 µM
10 µM
20 µM
Hyp260
T [°C]
D8/D12

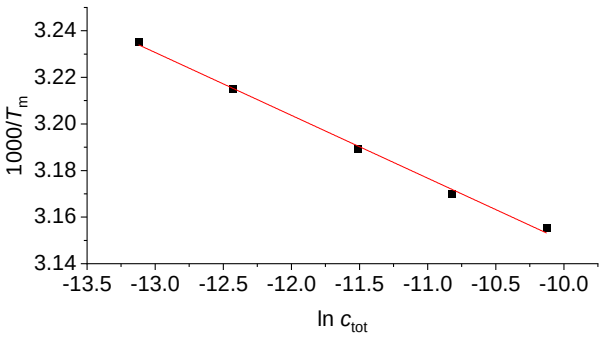
1000/Tm
ln ctot

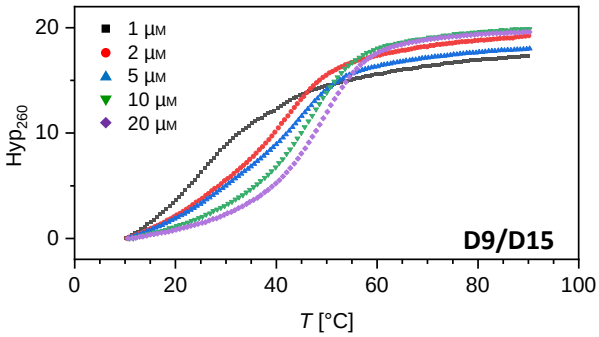
1 µM
2 µM
5 µM
10 µM
20 µM
Hyp260
T [°C]
D9/D15

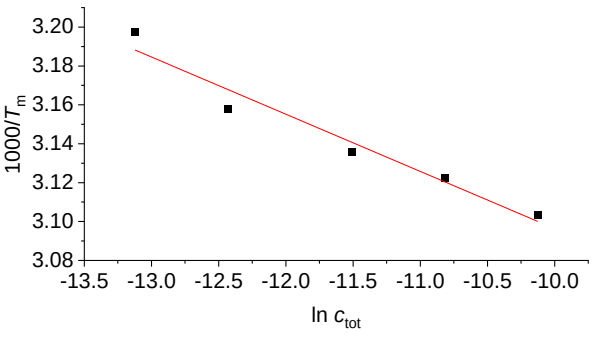
1000/Tm
ln ctot

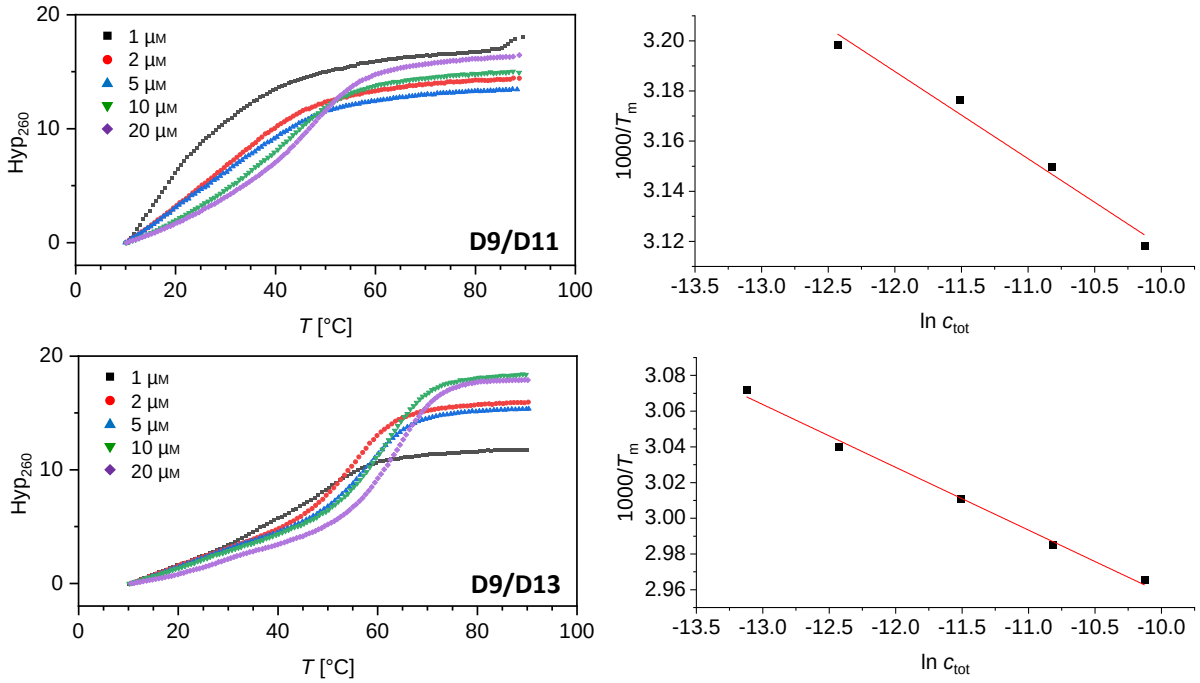

6.4.3 Melting curves for GNA duplexes

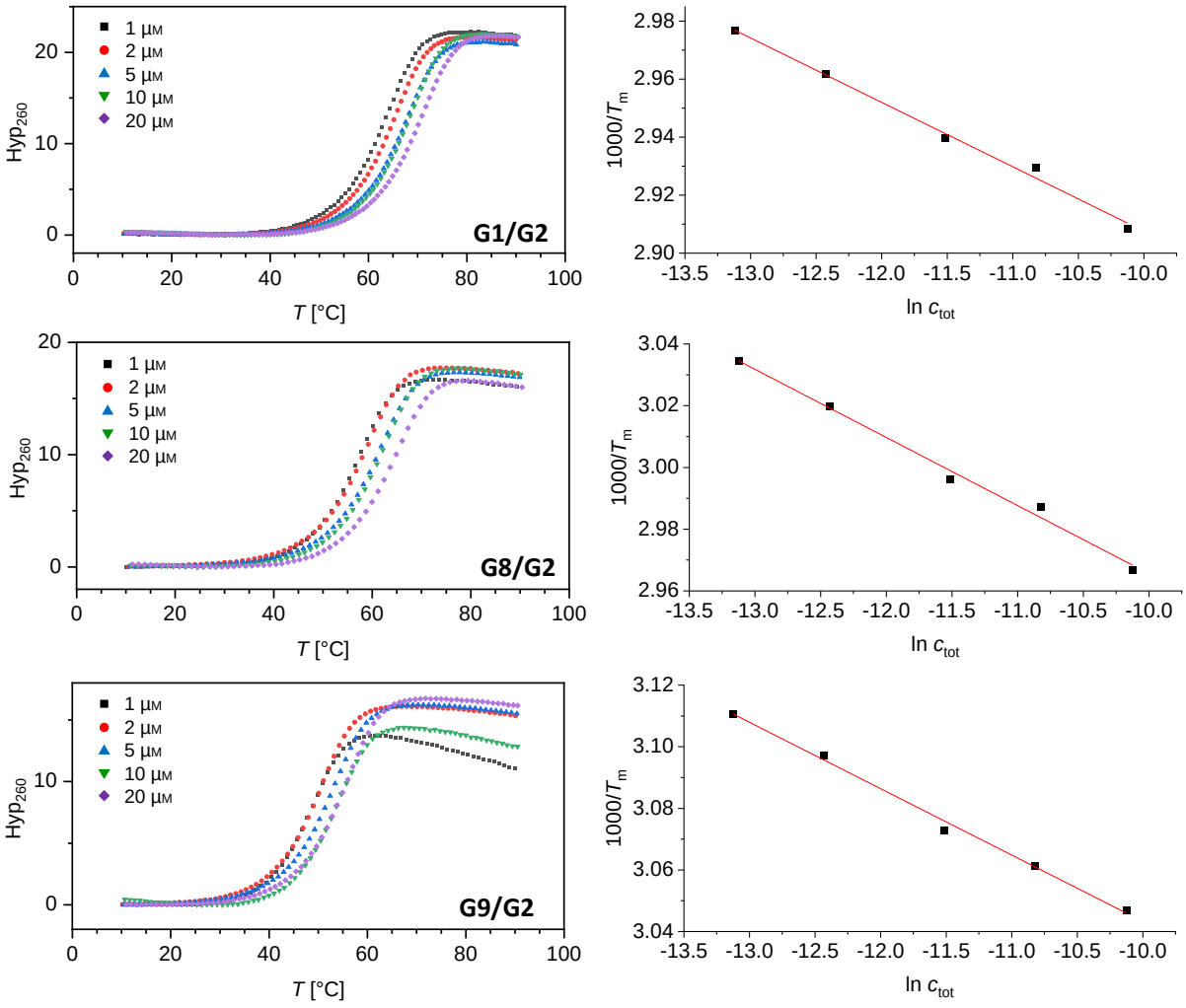

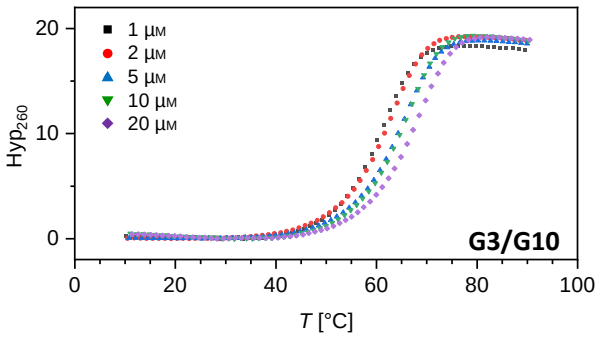
1 µM
2 µM
5 µM
10 µM
20 µM
G3/G10
Hyp260
T [°C]

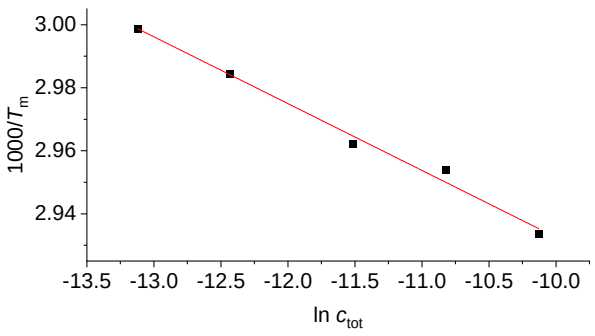
1000/Tm
ln ctot

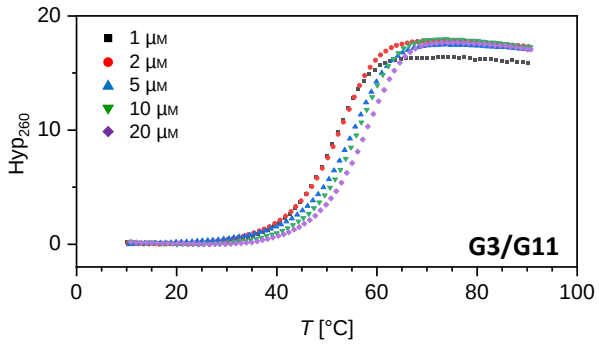
1 µM
2 µM
5 µM
10 µM
20 µM
G3/G11
Hyp260
T [°C]

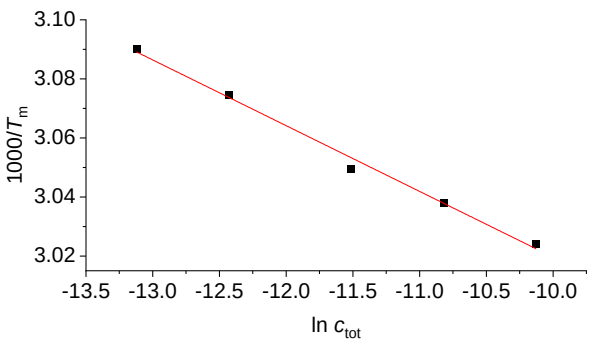
1000/Tm
ln ctot

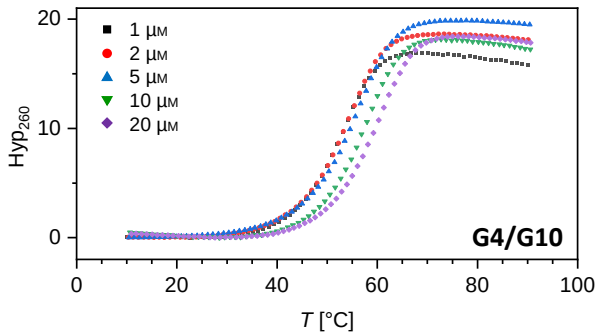
1 µM
2 µM
5 µM
10 µM
20 µM
G4/G10
Hyp260
T [°C]

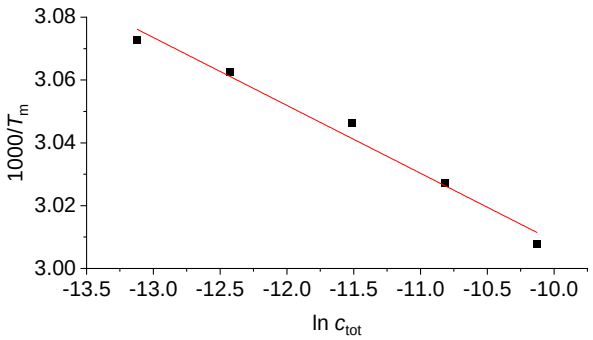
1000/Tm
ln ctot

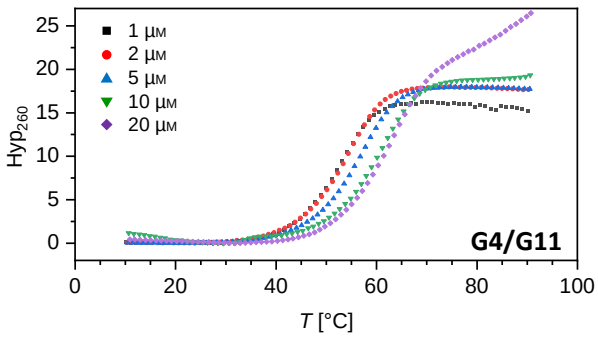
1 µM
2 µM
5 µM
10 µM
20 µM
G4/G11
Hyp260
T [°C]

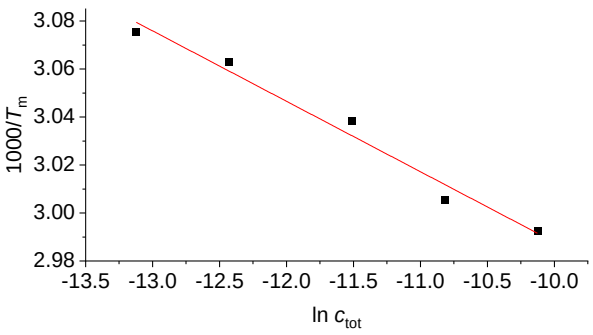
1000/Tm
ln ctot

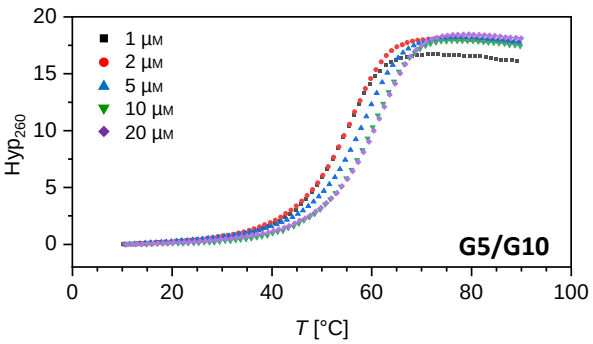
1 µM
2 µM
5 µM
10 µM
20 µM
G5/G10
Hyp260
T [°C]

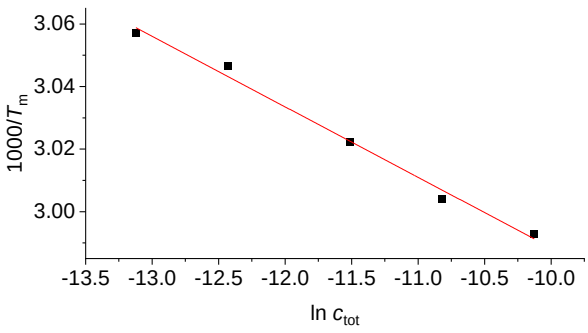
1000/Tm
ln ctot

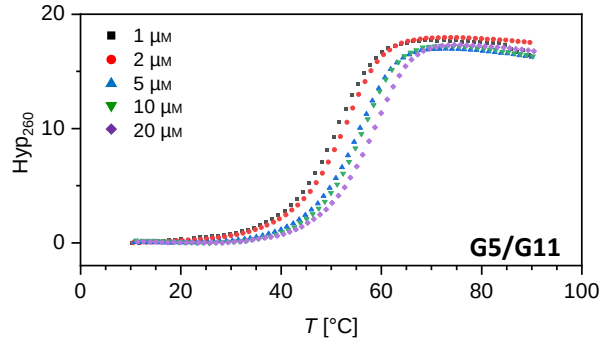
1 μM
2 μM
5 μM
10 μM
20 μM
Hyp260
T [°C]
G5/G11

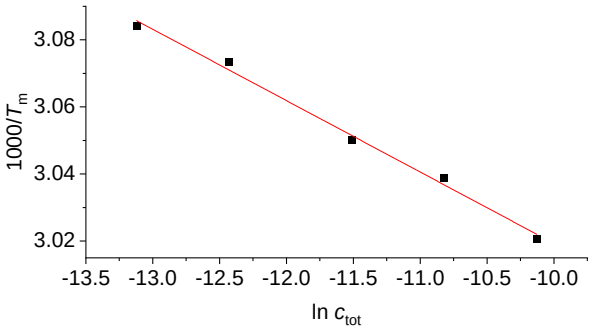
1000/Tm
ln ctot

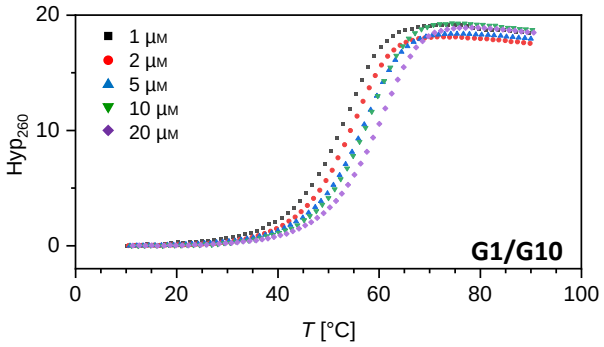
1 μM
2 μM
5 μM
10 μM
20 μM
Hyp260
T [°C]
G1/G10

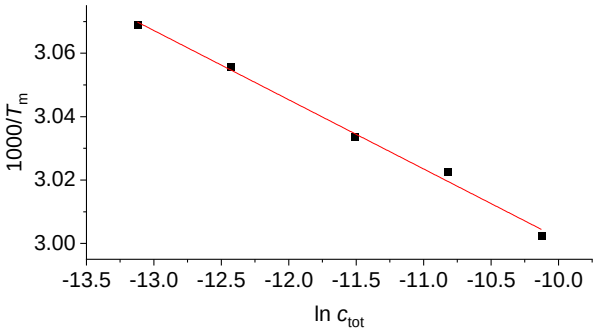
1000/Tm
ln ctot

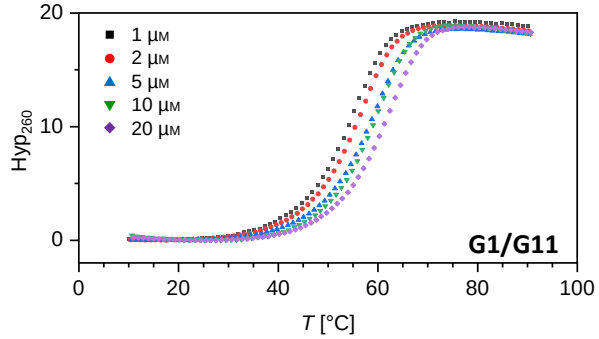
1 μM
2 μM
5 μM
10 μM
20 μM
Hyp260
T [°C]
G1/G11

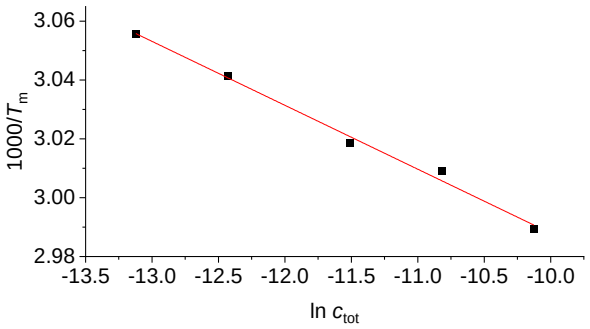
1000/Tm
ln ctot

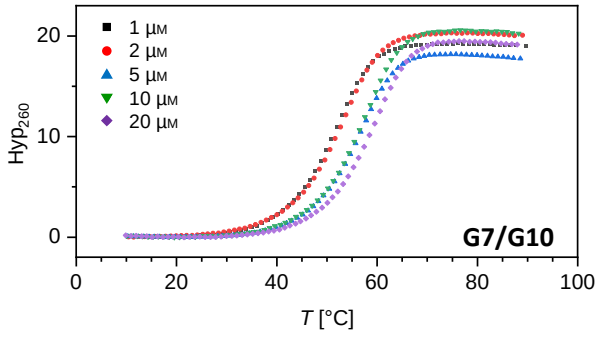
1 μM
2 μM
5 μM
10 μM
20 μM
Hyp260
T [°C]
G7/G10

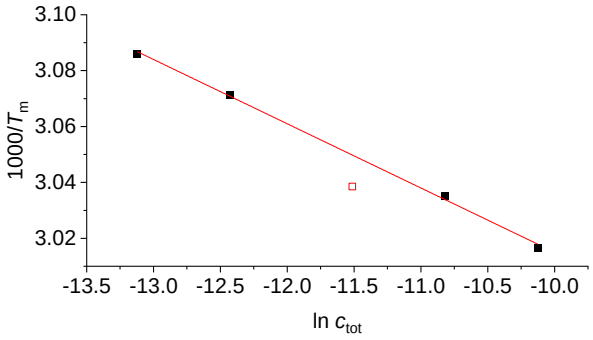
1000/Tm
ln ctot

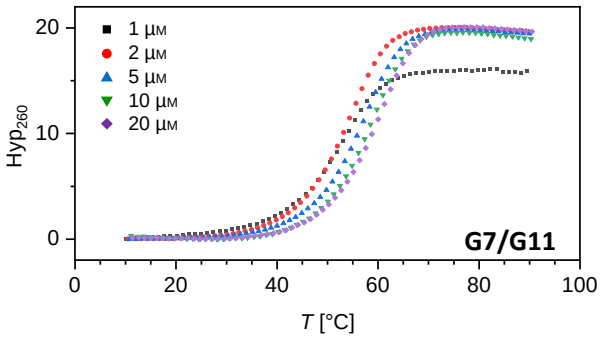
1 μM
2 μM
5 μM
10 μM
20 μM
Hyp260
T [°C]
G7/G11

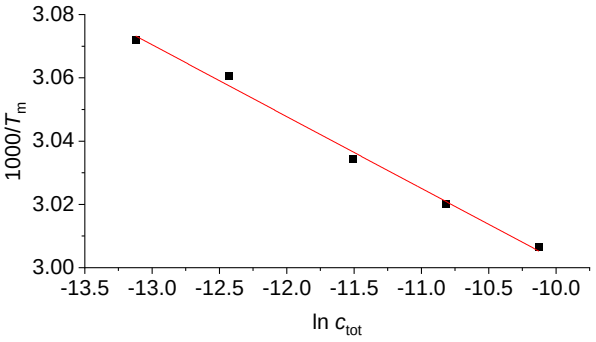
1000/Tm
ln ctot

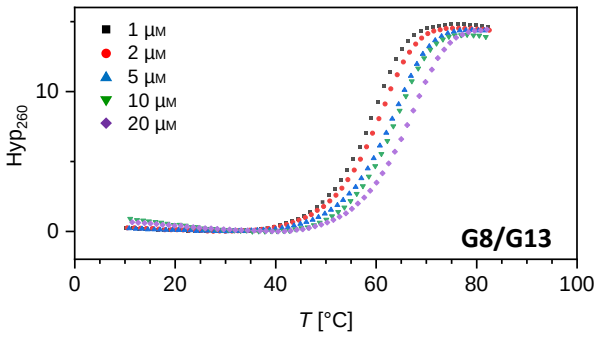
1 µM
2 µM
5 µM
10 µM
20 µM
G8/G13
Hyp260
T [°C]

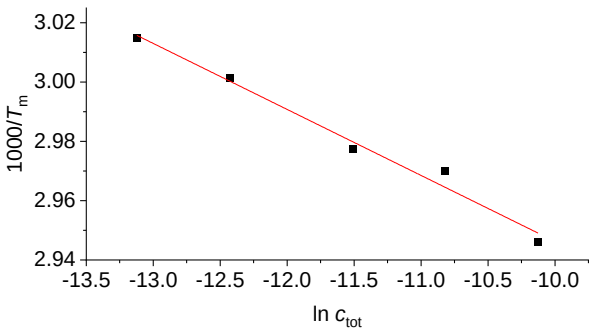
1000/Tm
ln ctot

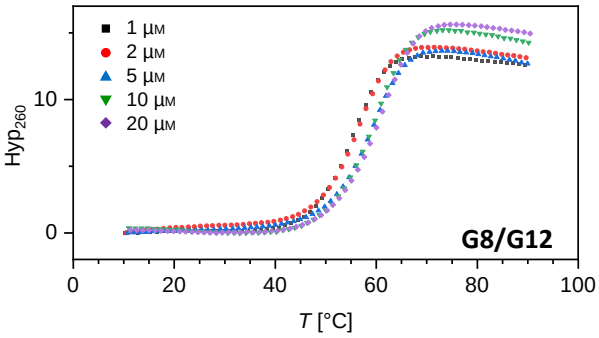
1 µM
2 µM
5 µM
10 µM
20 µM
G8/G12
Hyp260
T [°C]

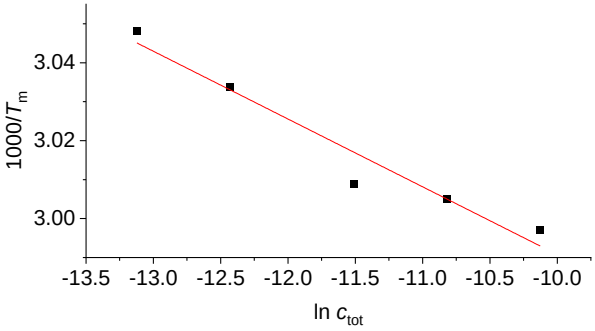
1000/Tm
ln ctot

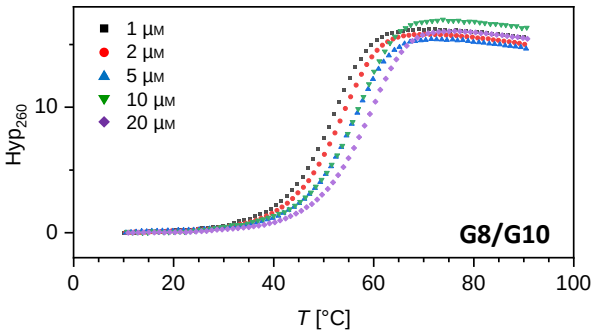
1 µM
2 µM
5 µM
10 µM
20 µM
G8/G10
Hyp260
T [°C]

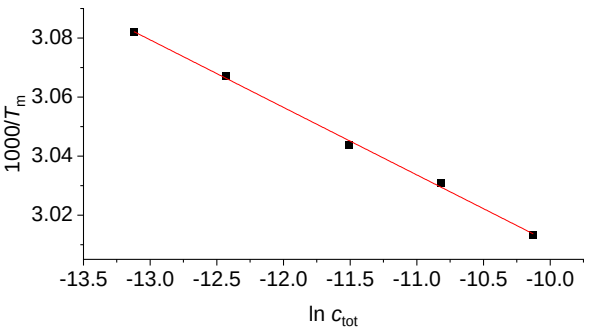
1000/Tm
ln ctot

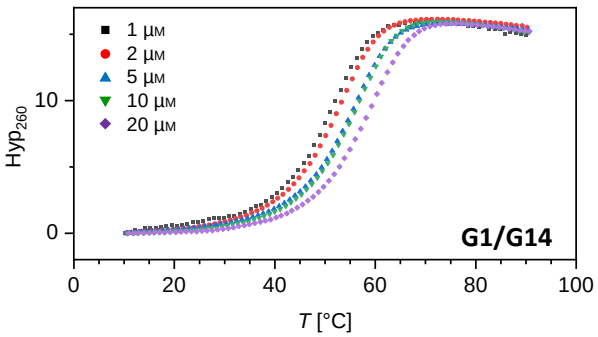
1 µM
2 µM
5 µM
10 µM
20 µM
G1/G14
Hyp260
T [°C]

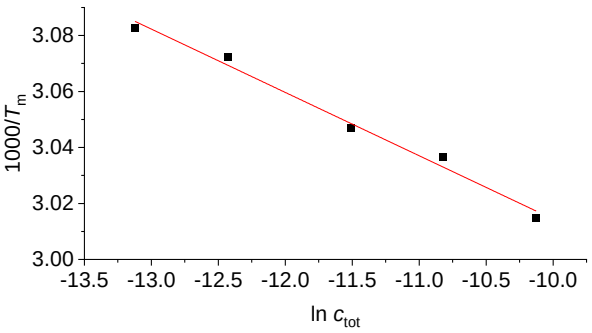
1000/Tm
ln ctot

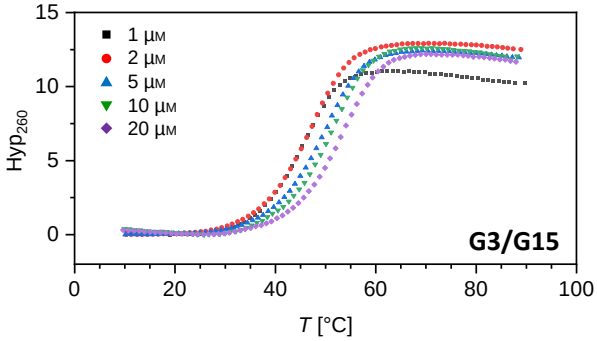
1 µM
2 µM
5 µM
10 µM
20 µM
G3/G15
Hyp260
T [°C]

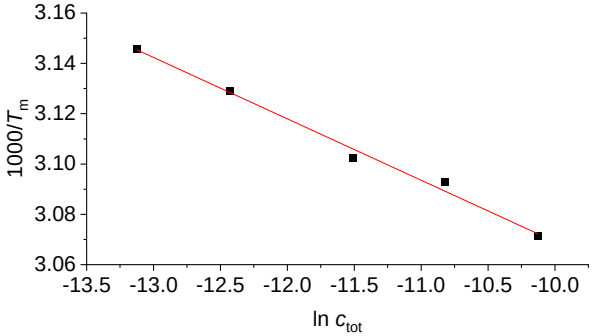
1000/Tm
ln ctot

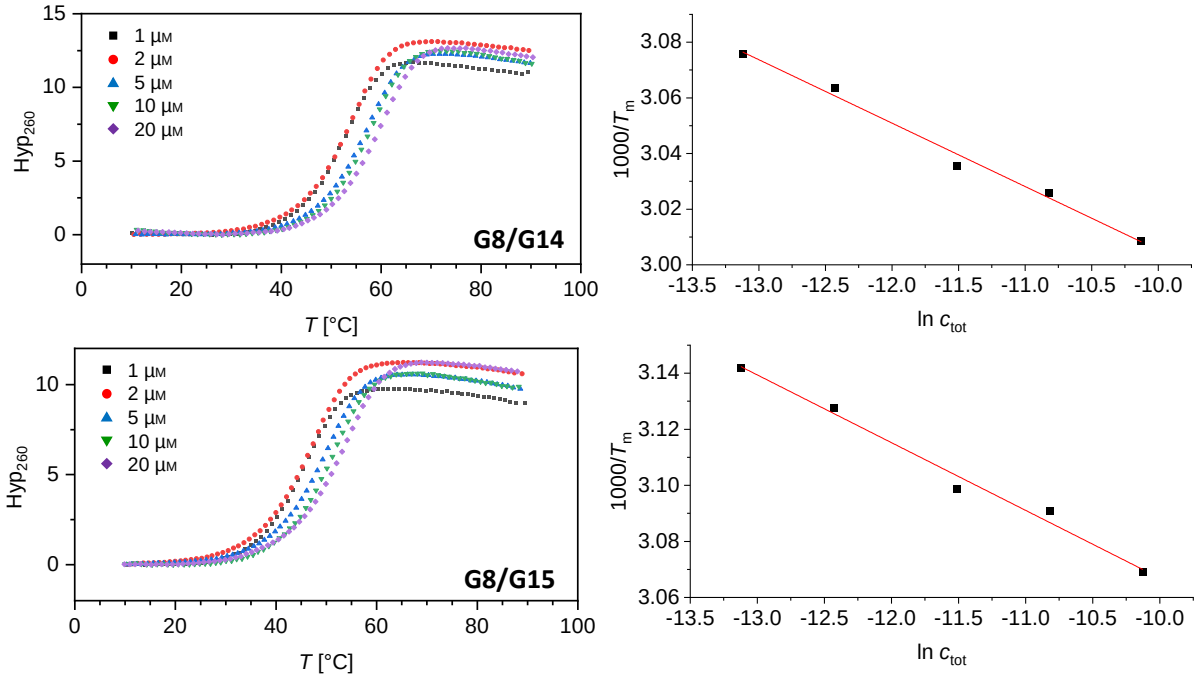

6.4.4 Melting curves for DNA/GNA hybrid duplexes

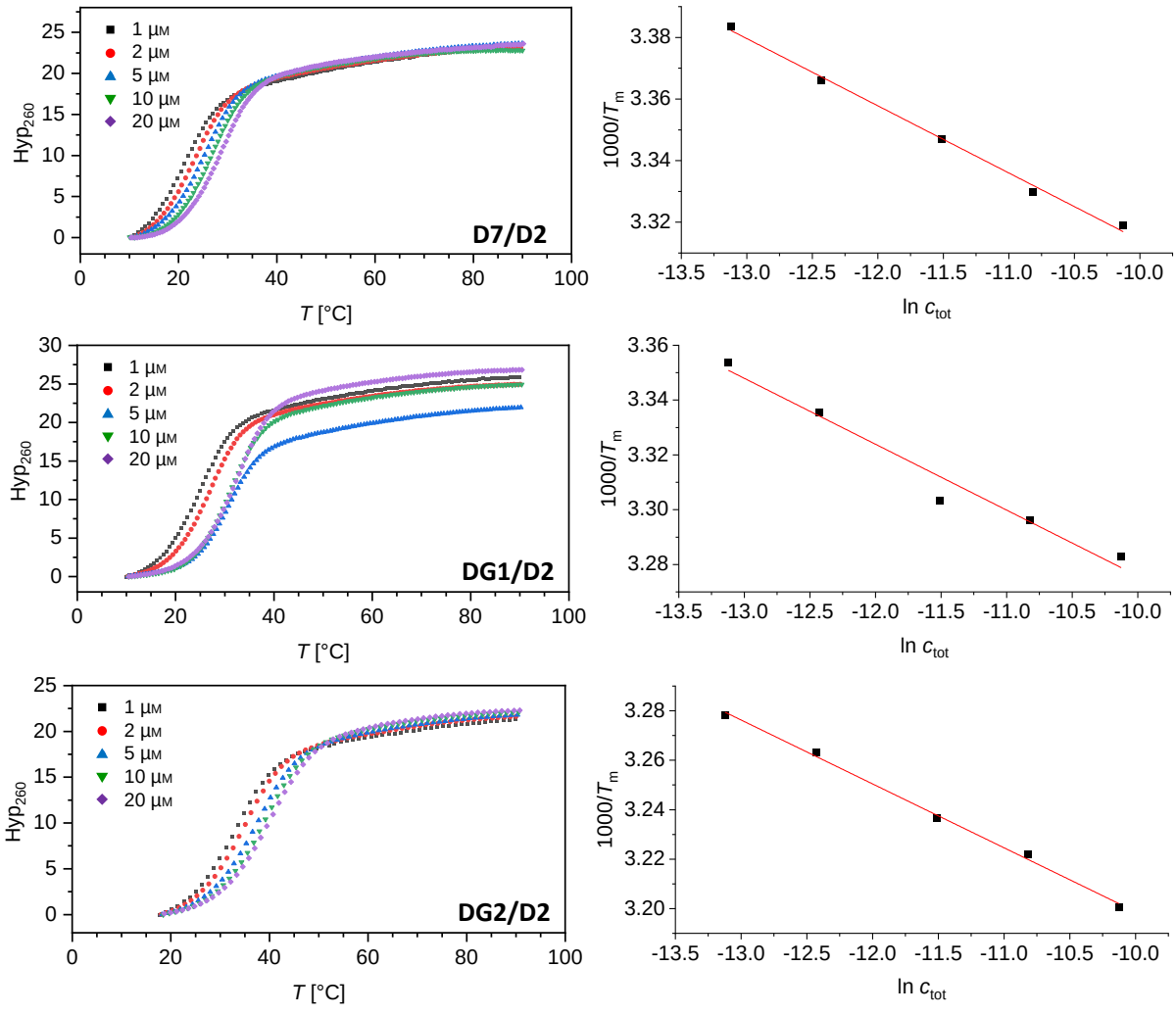

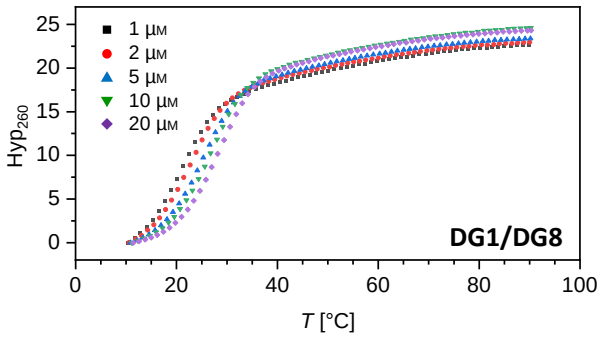
1 µM
2 µM
5 µM
10 µM
20 µM
Hyp260
T [°C]
DG1/DG8

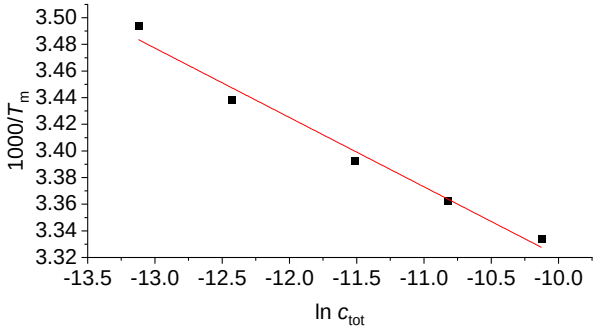
1000/Tm
ln ctot

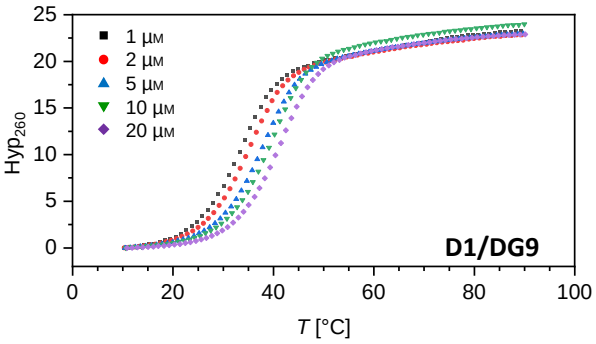
1 µM
2 µM
5 µM
10 µM
20 µM
Hyp260
T [°C]
D1/DG9

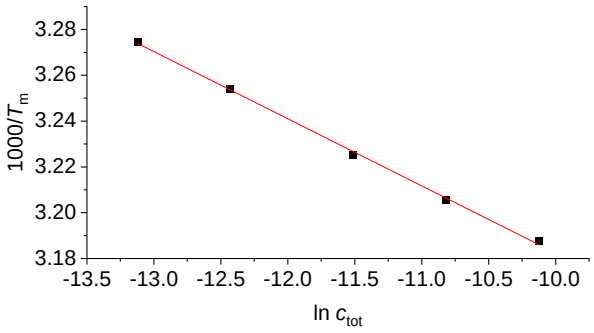
1000/Tm
ln ctot

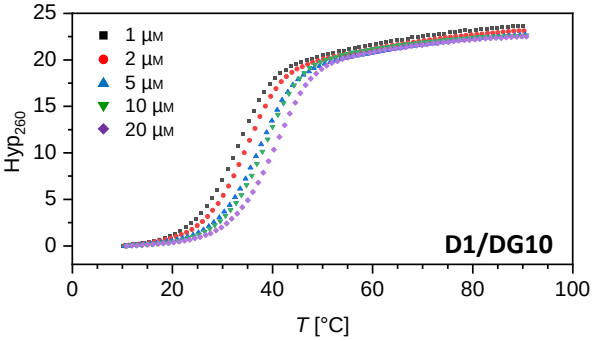
1 µM
2 µM
5 µM
10 µM
20 µM
Hyp260
T [°C]
D1/DG10

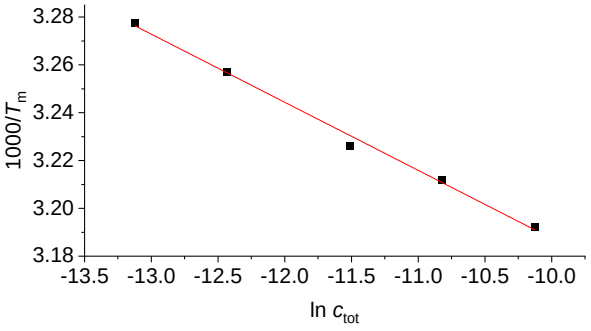
1000/Tm
ln ctot

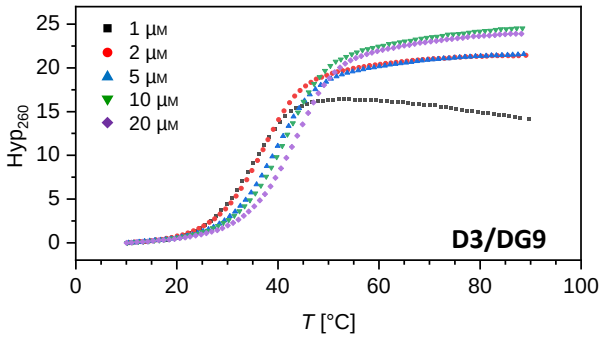
1 µM
2 µM
5 µM
10 µM
20 µM
Hyp260
T [°C]
D3/DG9

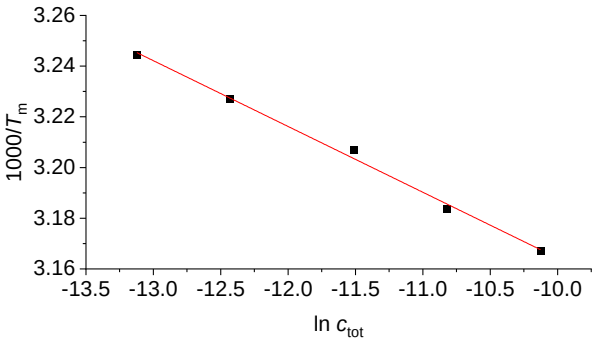
1000/Tm
ln ctot

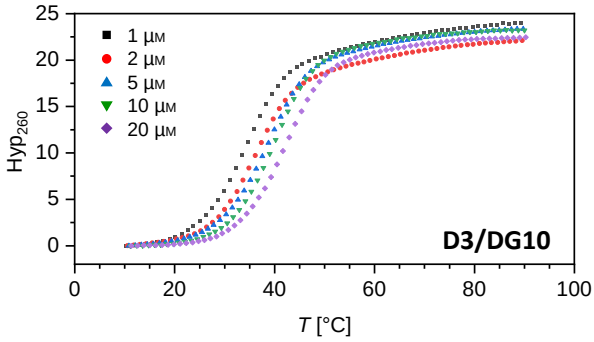
1 µM
2 µM
5 µM
10 µM
20 µM
Hyp260
T [°C]
D3/DG10

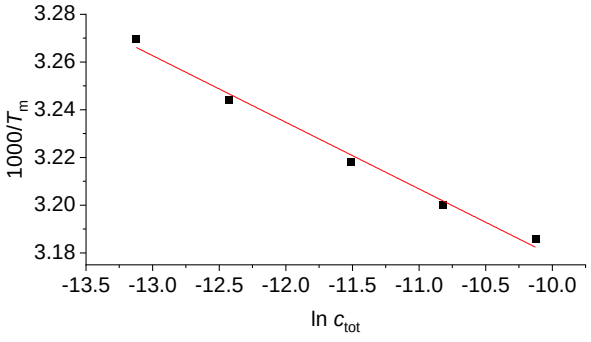
1000/Tm
ln ctot

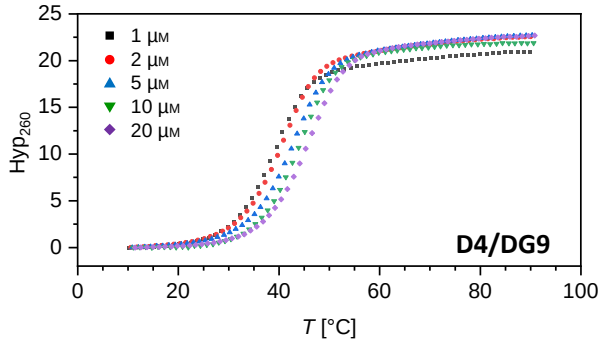
1 µM
2 µM
5 µM
10 µM
20 µM
Hyp260
T [°C]
D4/DG9

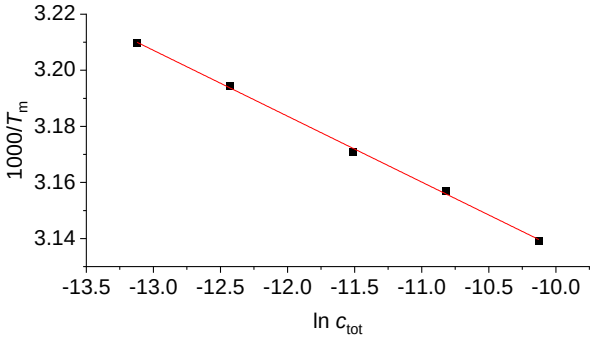
1000/Tm
ln ctot

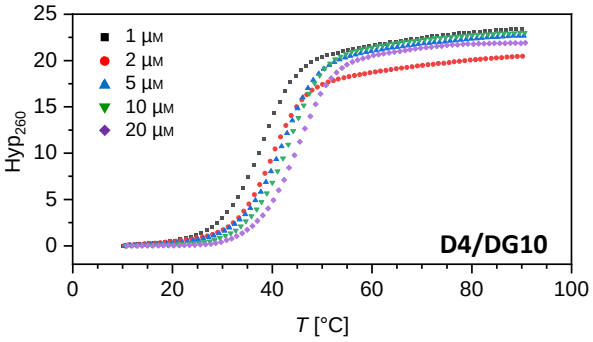
1 µM
2 µM
5 µM
10 µM
20 µM
Hyp260
T [°C]
D4/DG10

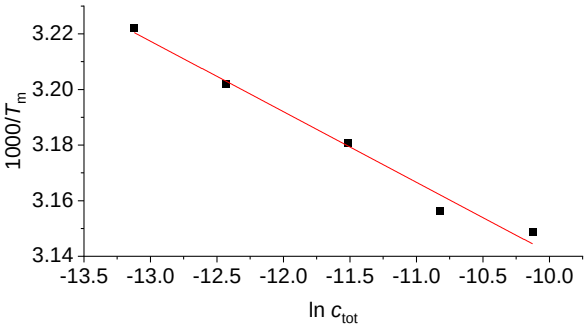
1000/Tm
ln ctot

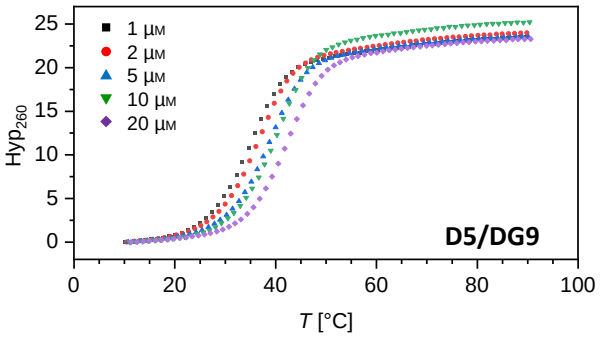
1 µM
2 µM
5 µM
10 µM
20 µM
Hyp260
T [°C]
D5/DG9

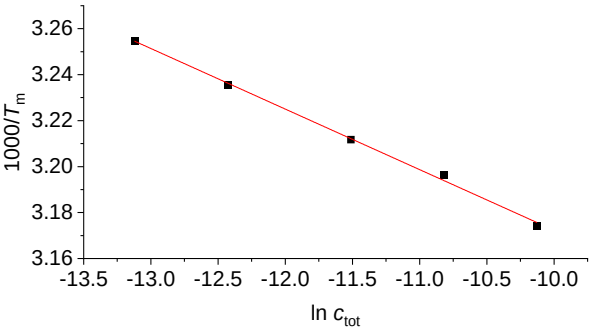
1000/Tm
ln ctot

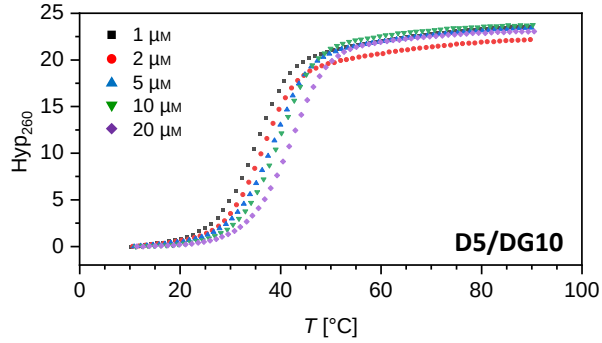
1 µM
2 µM
5 µM
10 µM
20 µM
Hyp260
T [°C]
D5/DG10

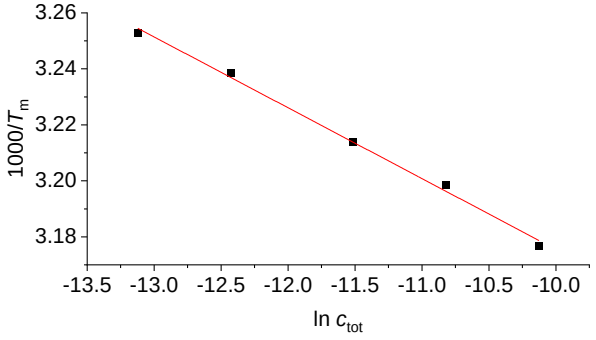
1000/Tm
ln ctot

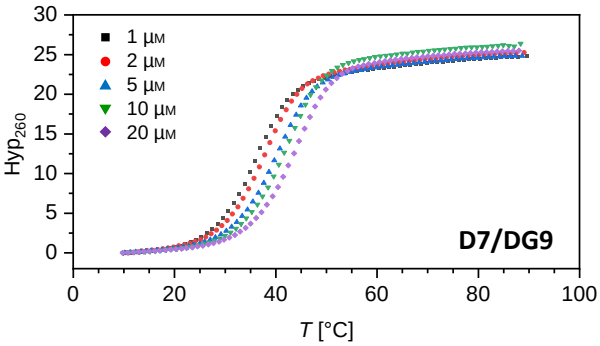
1 µM
2 µM
5 µM
10 µM
20 µM
Hyp260
T [°C]
D7/DG9

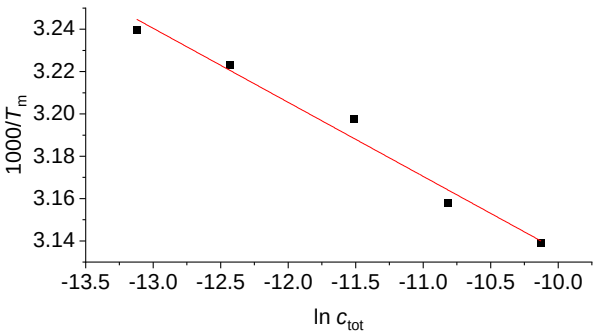
1000/Tm
ln ctot

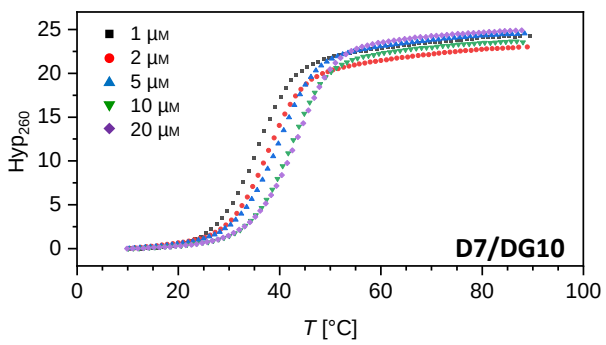
1 µM
2 µM
5 µM
10 µM
20 µM
Hyp260
T [°C]
D7/DG10

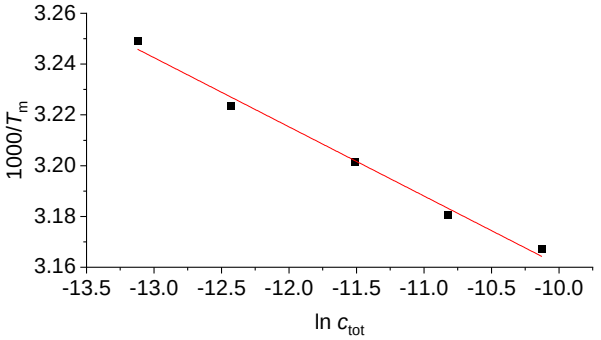
1000/Tm
ln ctot

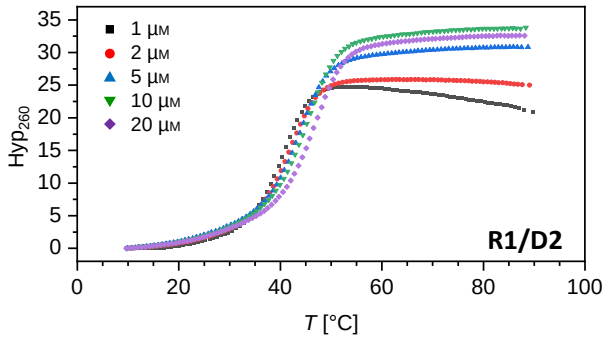
1 µM
2 µM
5 µM
10 µM
20 µM
Hyp260
T [°C]
R1/D2

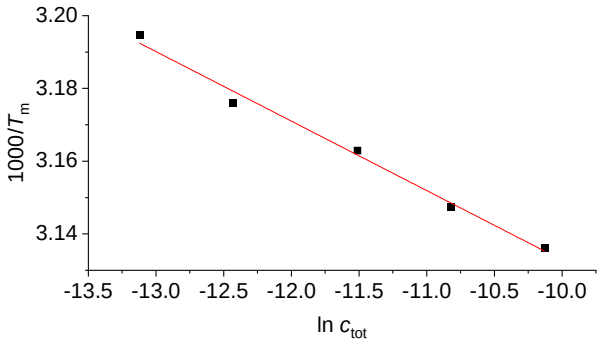
1000/Tm
ln ctot

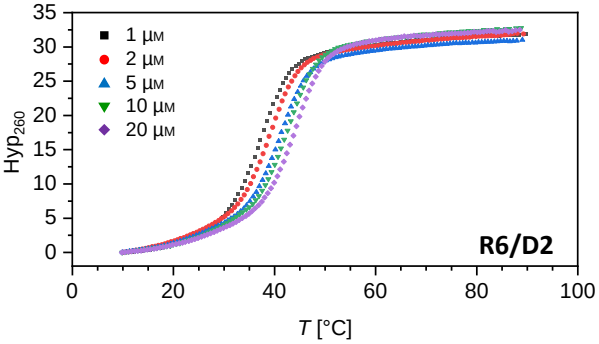
1 µM
2 µM
5 µM
10 µM
20 µM
Hyp260
T [°C]
R6/D2

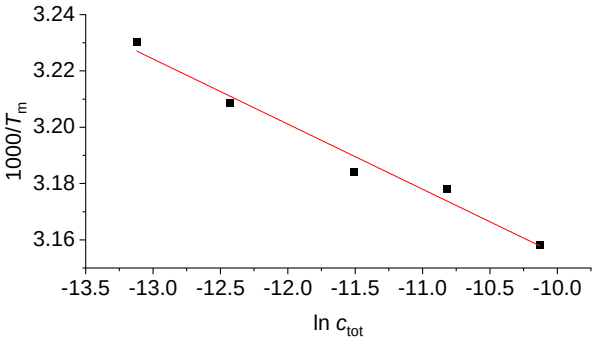
1000/Tm
ln ctot

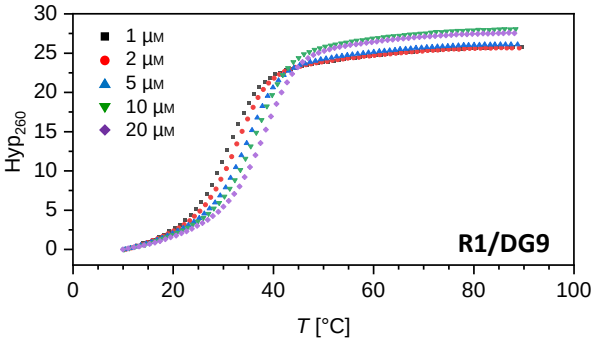
1 µM
2 µM
5 µM
10 µM
20 µM
Hyp260
T [°C]
R1/DG9

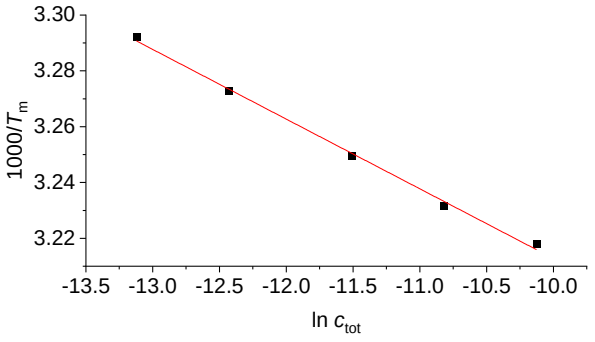
1000/Tm
ln ctot

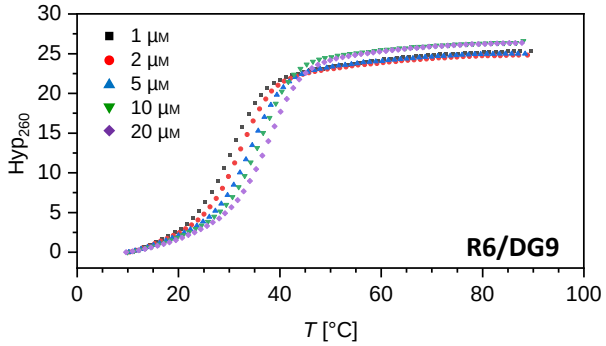
1 µM
2 µM
5 µM
10 µM
20 µM
Hyp260
T [°C]
R6/DG9

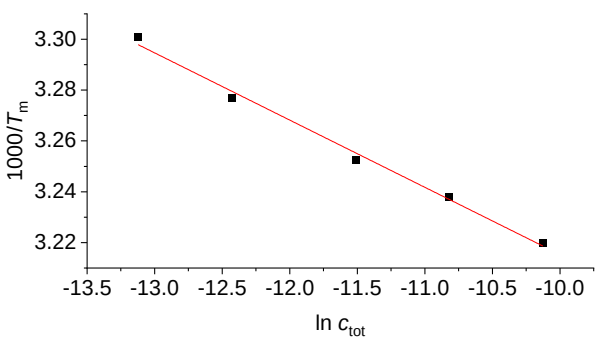
1000/Tm
ln ctot

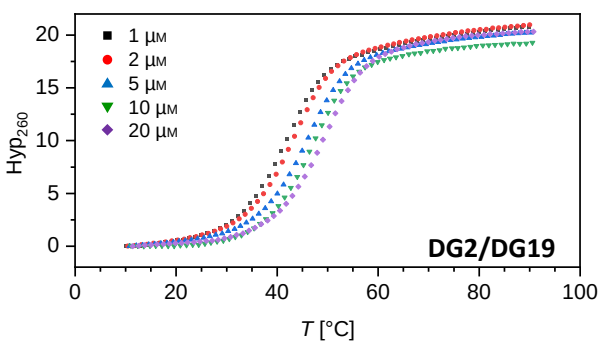
1 μM
2 μM
5 μM
10 μM
20 μM
Hyp260
T [°C]
DG2/DG19

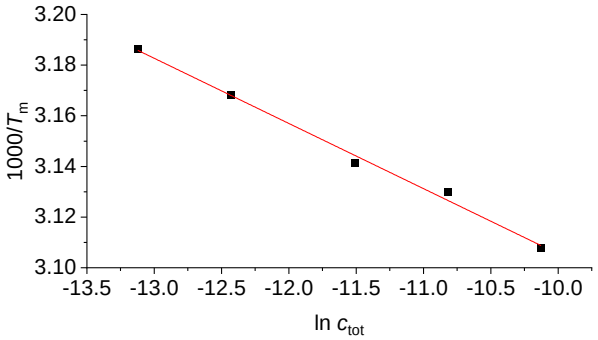
1000/Tm
ln ctot

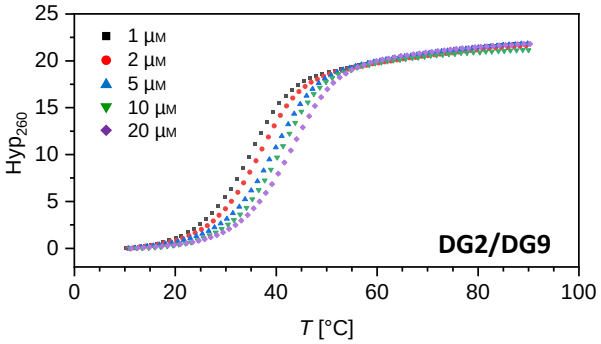
1 μM
2 μM
5 μM
10 μM
20 μM
Hyp260
T [°C]
DG2/DG9

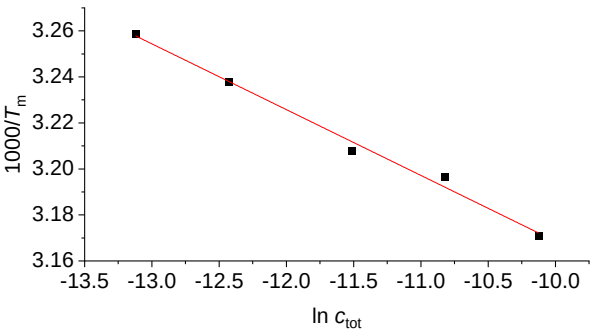
1000/Tm
ln ctot

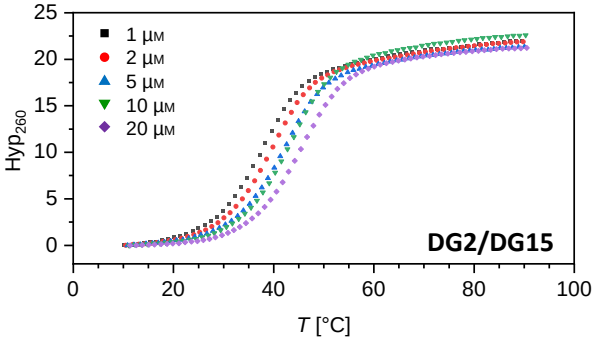
1 μM
2 μM
5 μM
10 μM
20 μM
Hyp260
T [°C]
DG2/DG15

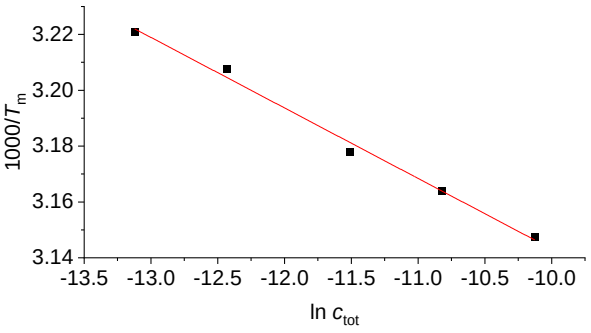
1000/Tm
ln ctot

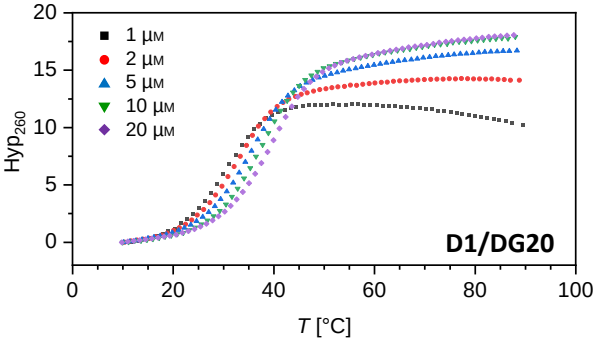
1 μM
2 μM
5 μM
10 μM
20 μM
Hyp260
T [°C]
D1/DG20

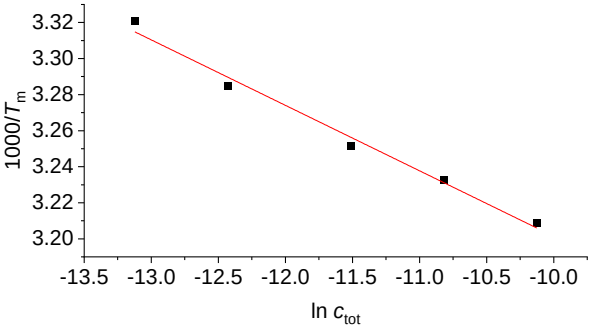
1000/Tm
ln ctot

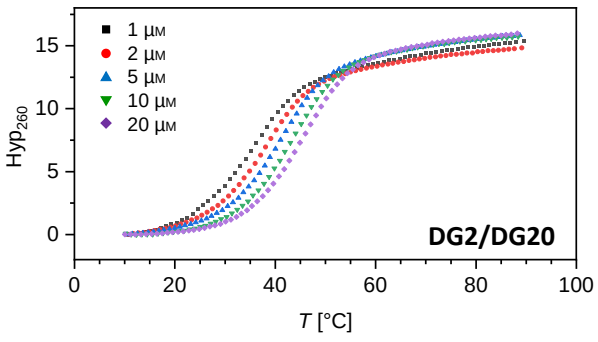
1 μM
2 μM
5 μM
10 μM
20 μM
Hyp260
T [°C]
DG2/DG20

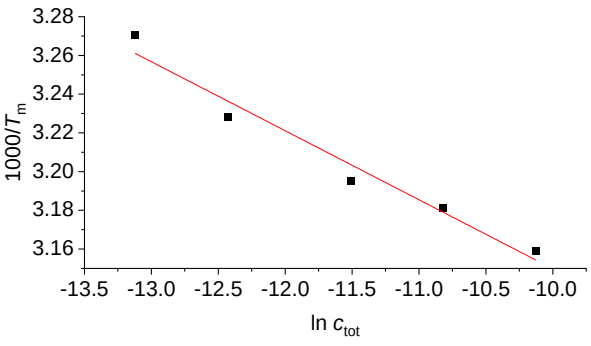
1000/Tm
ln ctot

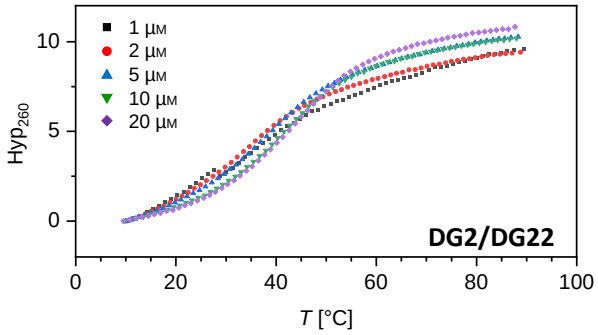
1 µM
2 µM
5 µM
10 µM
20 µM
Hyp260
T [°C]
DG2/DG22

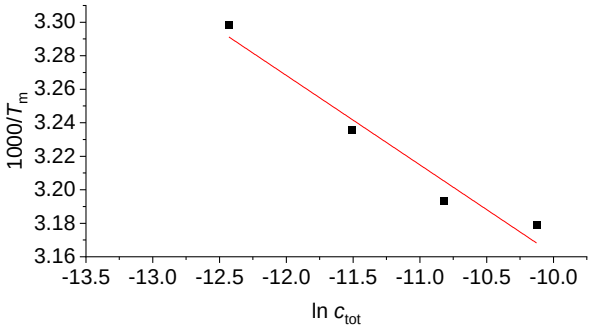
1000/Tm
ln ctot

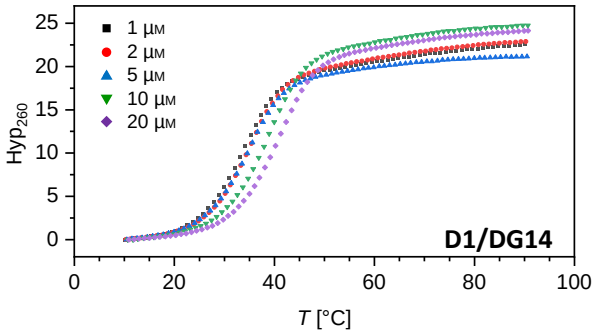
1 µM
2 µM
5 µM
10 µM
20 µM
Hyp260
T [°C]
D1/DG14

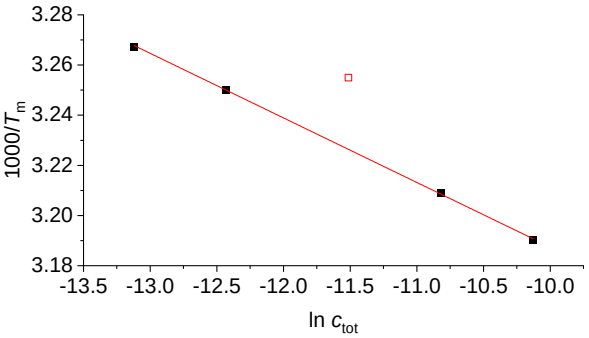
1000/Tm
ln ctot

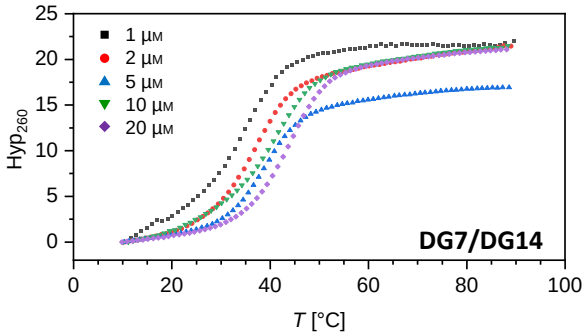
1 µM
2 µM
5 µM
10 µM
20 µM
Hyp260
T [°C]
DG7/DG14

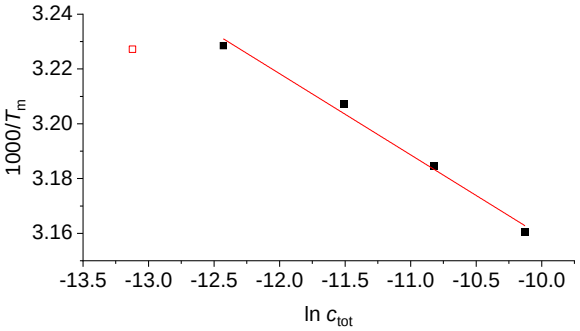
1000/Tm
ln ctot

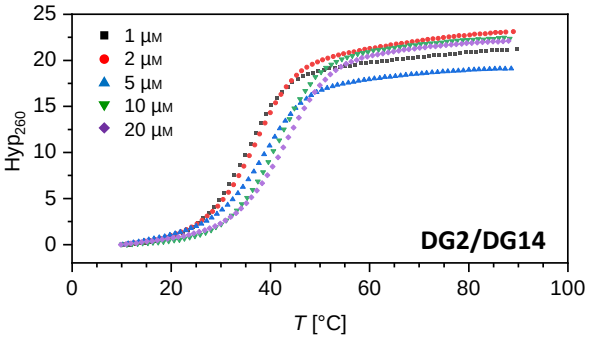
1 µM
2 µM
5 µM
10 µM
20 µM
Hyp260
T [°C]
DG2/DG14

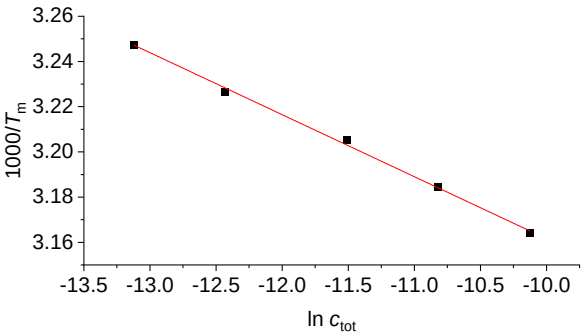
1000/Tm
ln ctot

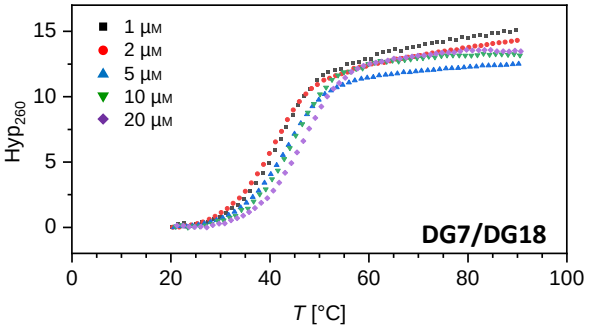
1 µM
2 µM
5 µM
10 µM
20 µM
Hyp260
T [°C]
DG7/DG18

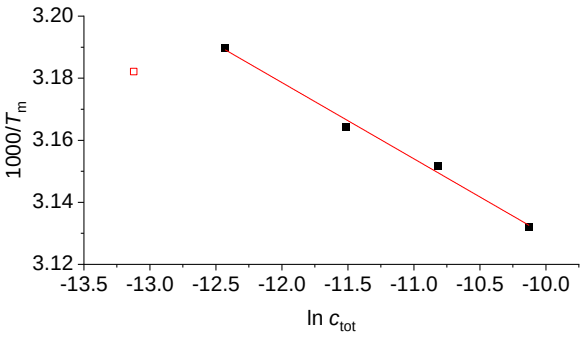
1000/Tm
ln ctot

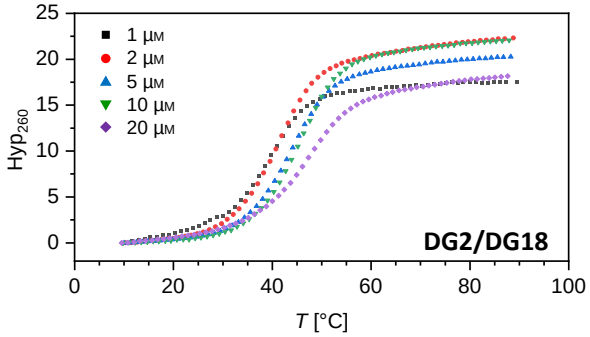
1 μM
2 μM
5 μM
10 μM
20 μM
Hyp260
T [°C]
DG2/DG18

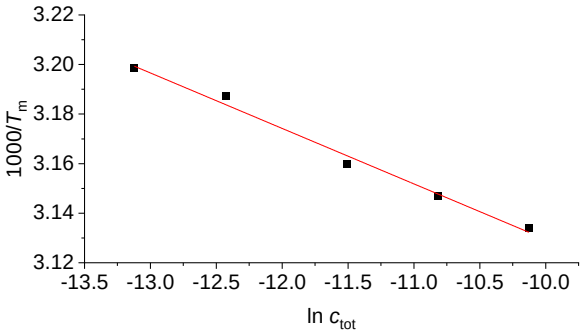
1000/Tm
ln ctot

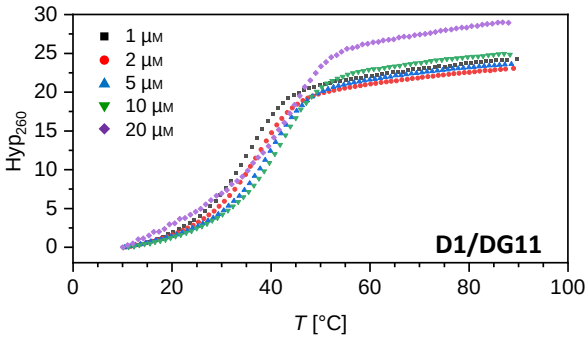
1 μM
2 μM
5 μM
10 μM
20 μM
Hyp260
T [°C]
D1/DG11

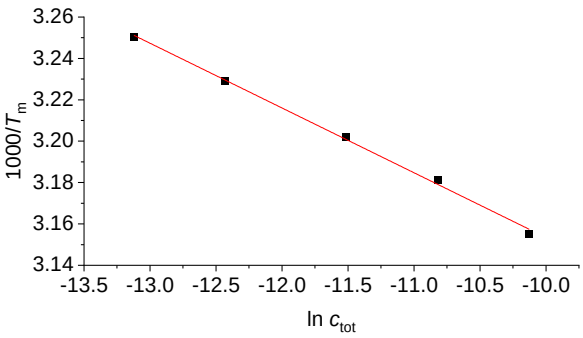
1000/Tm
ln ctot

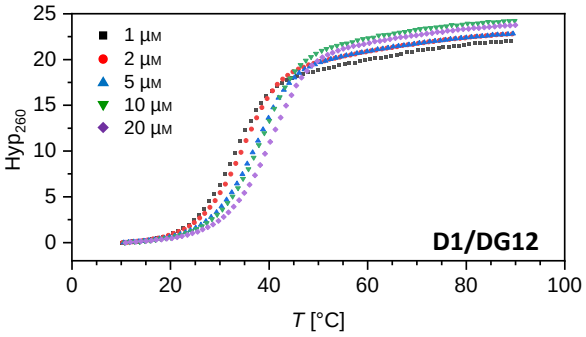
1 μM
2 μM
5 μM
10 μM
20 μM
Hyp260
T [°C]
D1/DG12

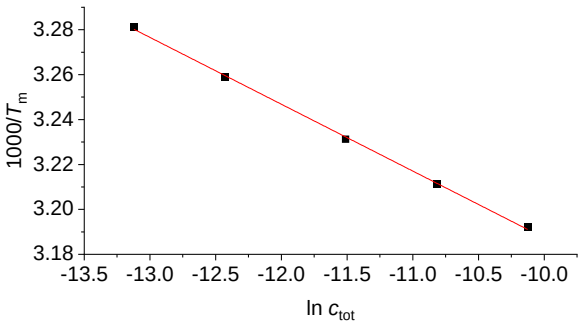
1000/Tm
ln ctot

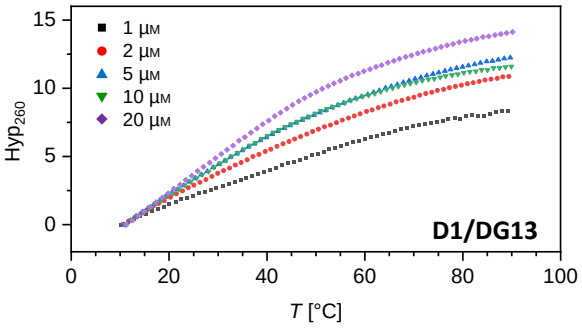
1 μM
2 μM
5 μM
10 μM
20 μM
Hyp260
T [°C]
D1/DG13

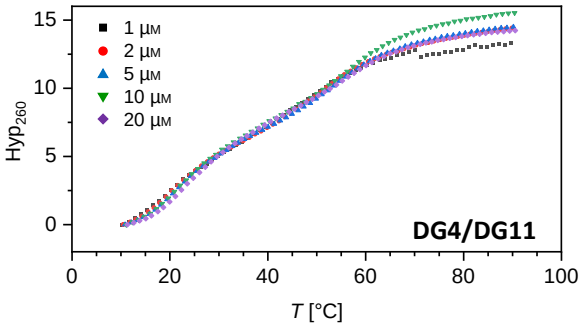
1 μM
2 μM
5 μM
10 μM
20 μM
Hyp260
T [°C]
DG4/DG11

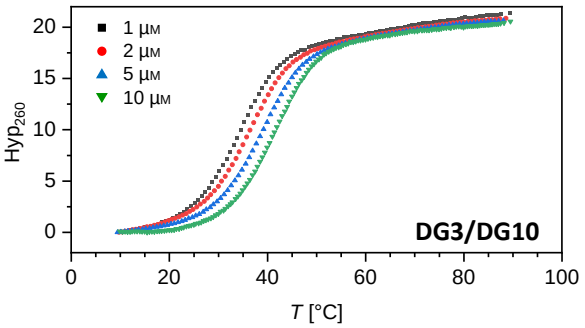
1 μM
2 μM
5 μM
10 μM
Hyp260
T [°C]
DG3/DG10

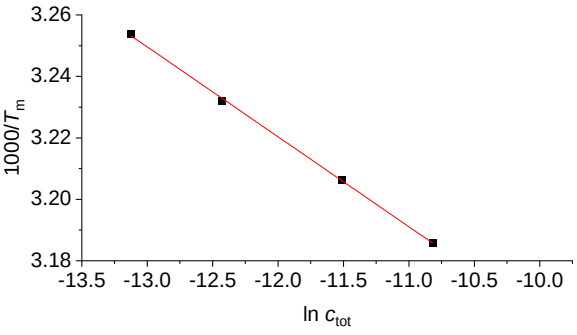
1000/Tm
ln ctot

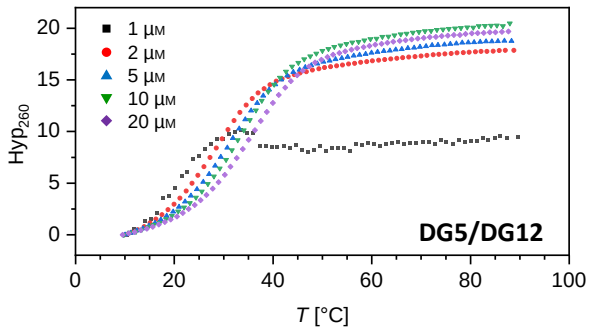
1 µM
2 µM
5 µM
10 µM
20 µM
Hyp260
T [°C]
DG5/DG12

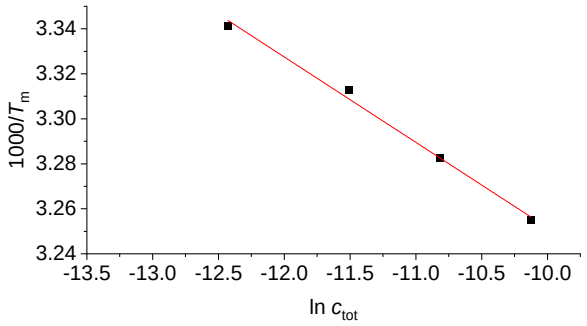
1000/Tm
ln ctot

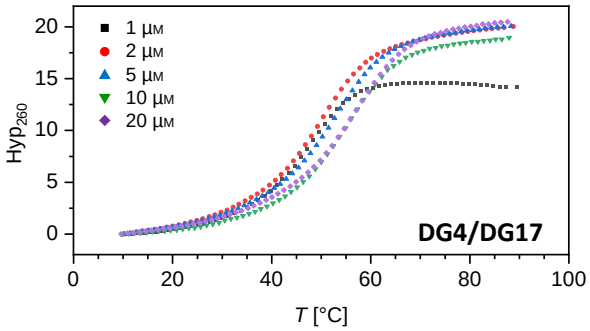
1 µM
2 µM
5 µM
10 µM
20 µM
Hyp260
T [°C]
DG4/DG17

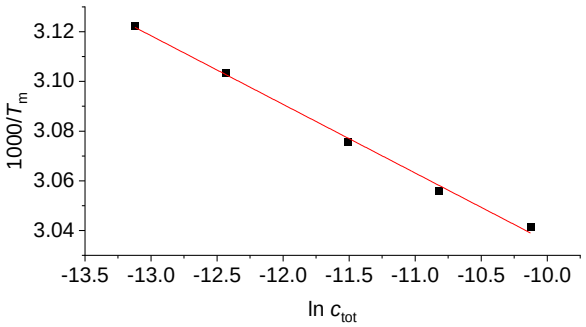
1000/Tm
ln ctot

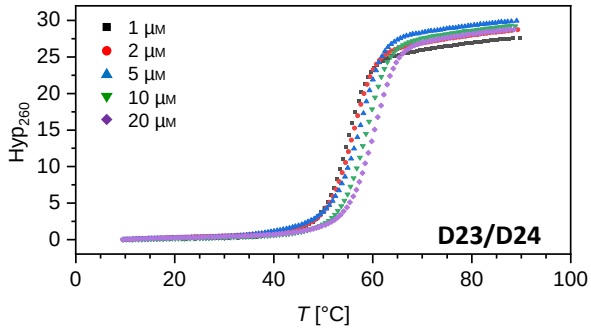
1 µM
2 µM
5 µM
10 µM
20 µM
Hyp260
T [°C]
D23/D24

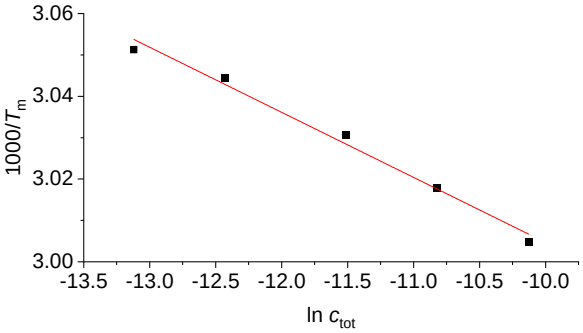
1000/Tm
ln ctot

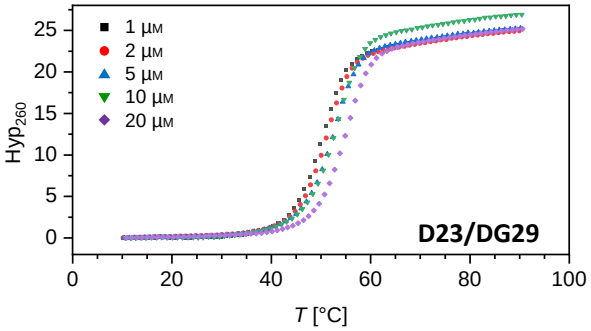
1 µM
2 µM
5 µM
10 µM
20 µM
Hyp260
T [°C]
D23/DG29

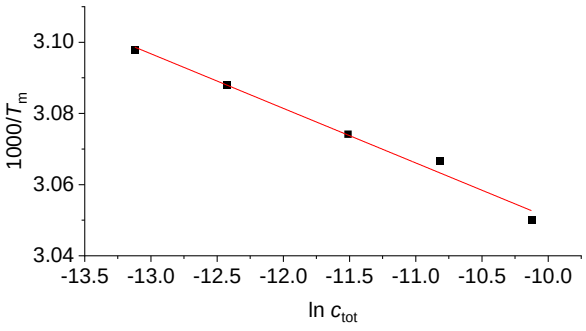
1000/Tm
ln ctot

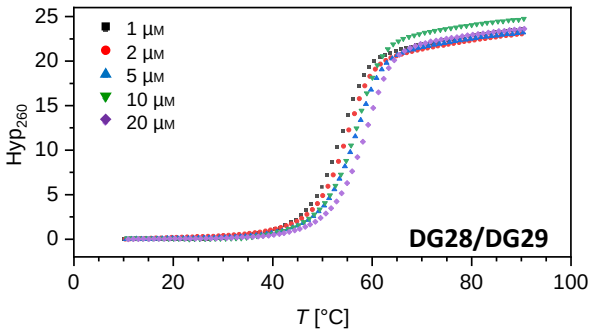
1 µM
2 µM
5 µM
10 µM
20 µM
Hyp260
T [°C]
DG28/DG29

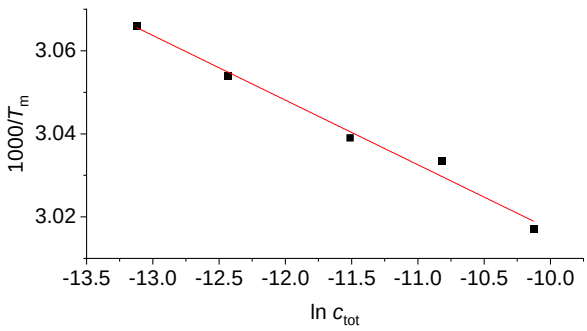
1000/Tm
ln ctot

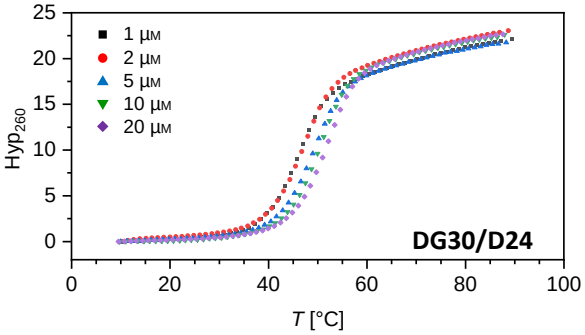
1 µM
2 µM
5 µM
10 µM
20 µM
Hyp260
T [°C]
DG30/D24

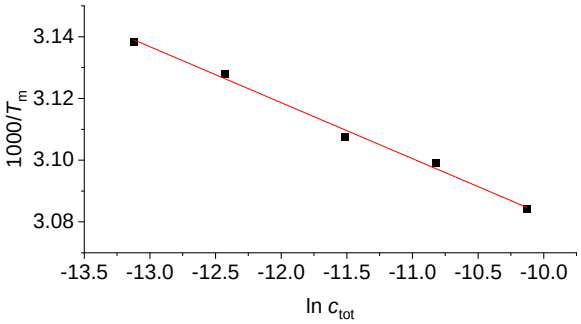
1000/Tm
ln ctot

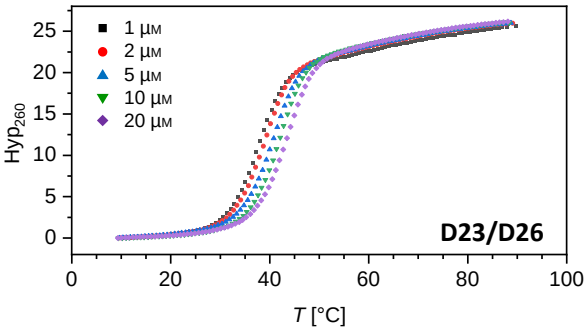
1 µM
2 µM
5 µM
10 µM
20 µM
Hyp260
T [°C]
D23/D26

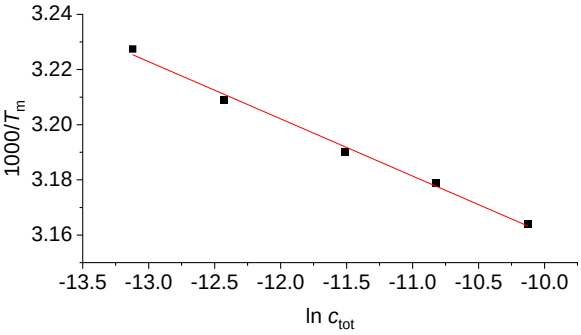
1000/Tm
ln ctot

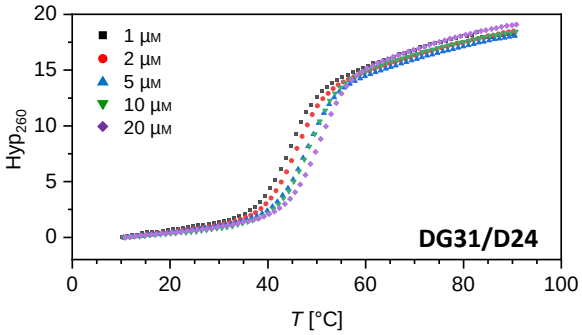
1 µM
2 µM
5 µM
10 µM
20 µM
Hyp260
T [°C]
DG31/D24

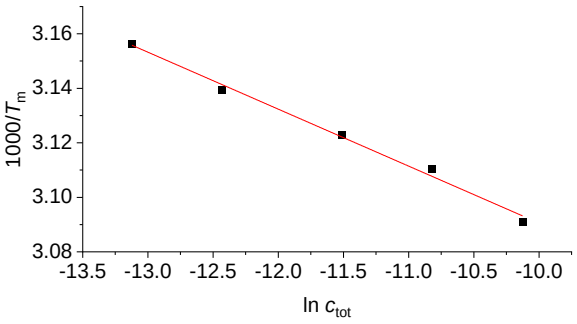
1000/Tm
ln ctot

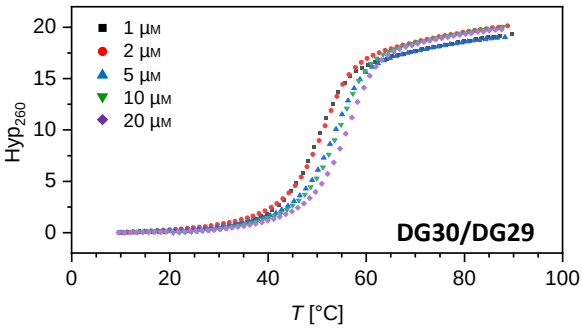
1 µM
2 µM
5 µM
10 µM
20 µM
Hyp260
T [°C]
DG30/DG29

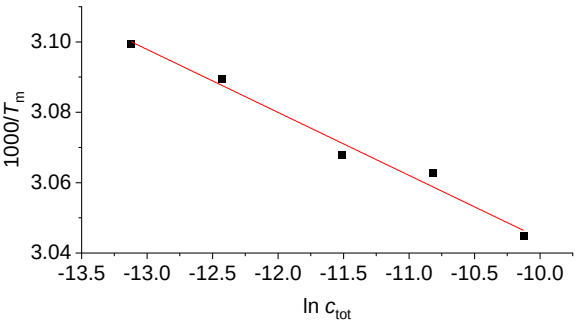
1000/Tm
ln ctot

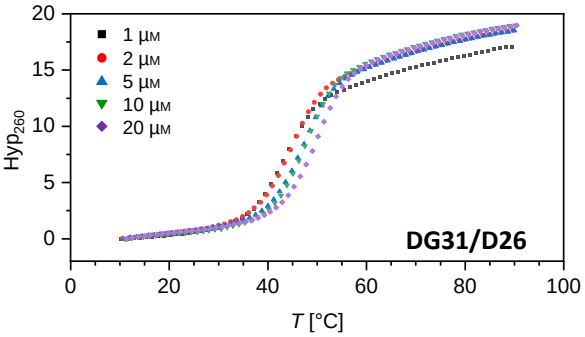
1 µM
2 µM
5 µM
10 µM
20 µM
Hyp260
T [°C]
DG31/D26

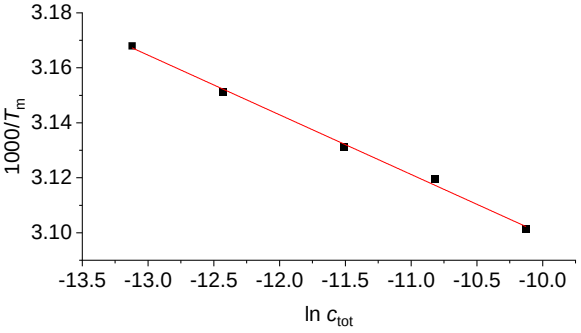
1000/Tm
ln ctot

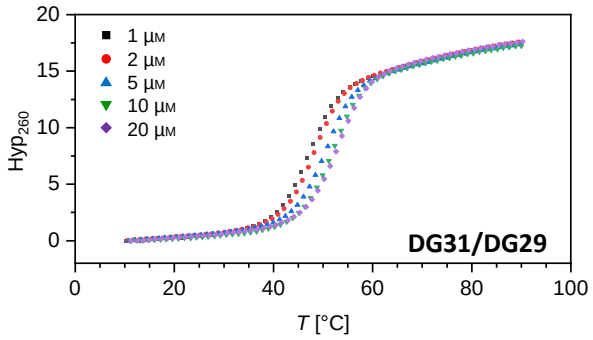
1 µM
2 µM
5 µM
10 µM
20 µM
Hyp260
T [°C]
DG31/DG29

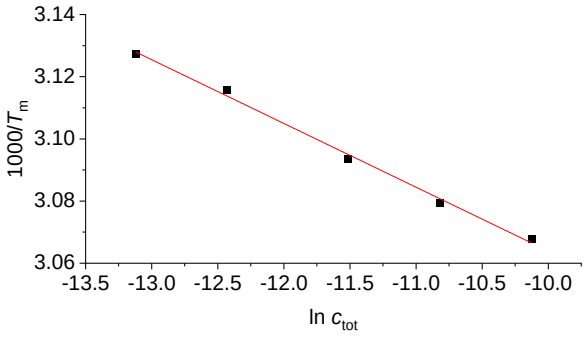
1000/Tm
ln ctot

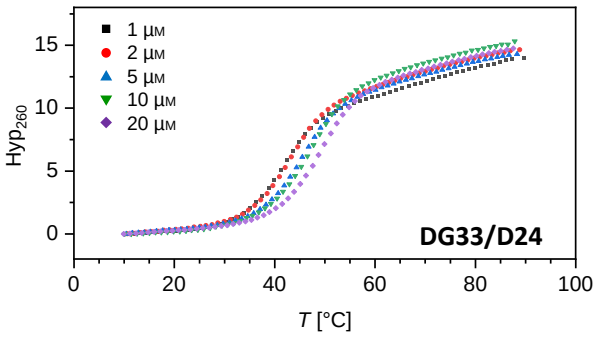
1 µM
2 µM
5 µM
10 µM
20 µM
Hyp260
T [°C]
DG33/D24

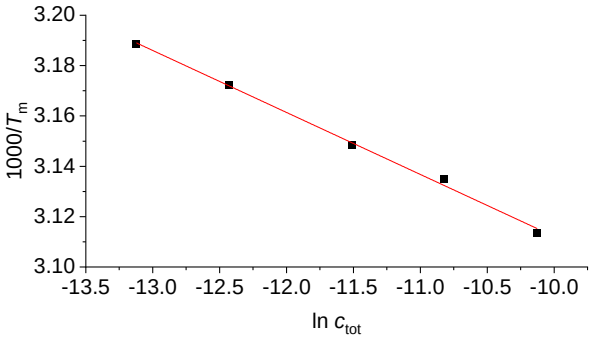
1000/Tm
ln ctot

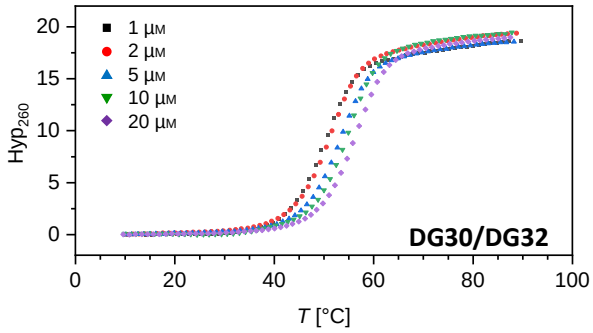
1 µM
2 µM
5 µM
10 µM
20 µM
Hyp260
T [°C]
DG30/DG32

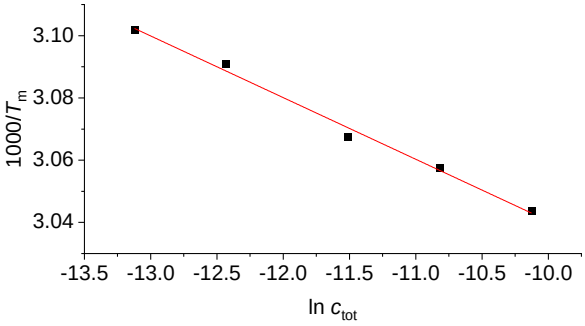
1000/Tm
ln ctot

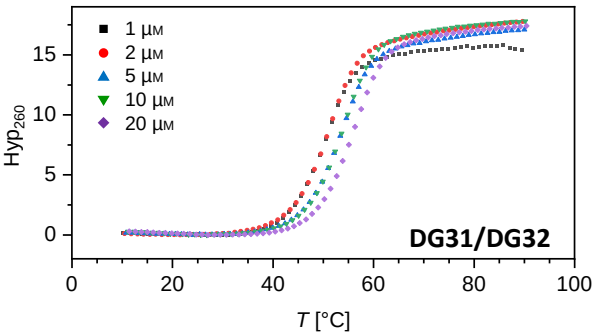
1 µM
2 µM
5 µM
10 µM
20 µM
Hyp260
T [°C]
DG31/DG32

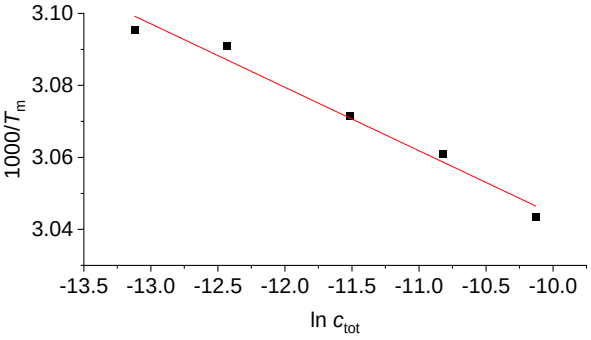
1000/Tm
ln ctot

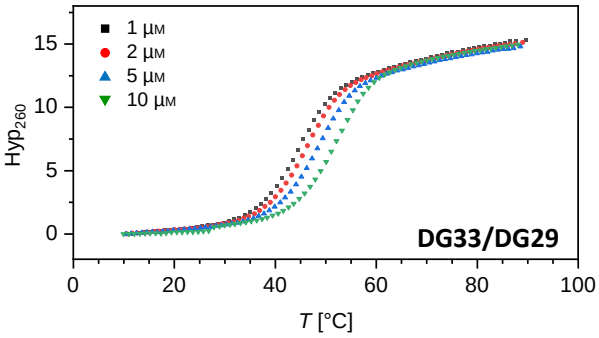
1 µM
2 µM
5 µM
10 µM
Hyp260
T [°C]
DG33/DG29

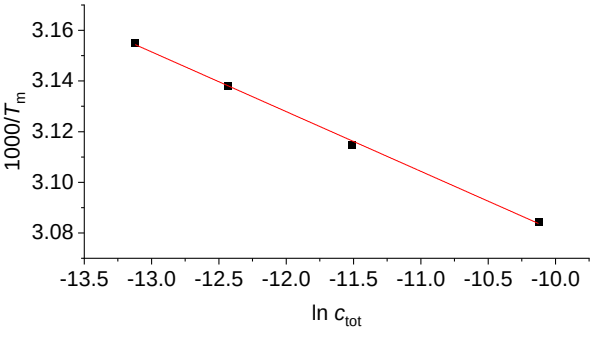
1000/Tm
ln ctot

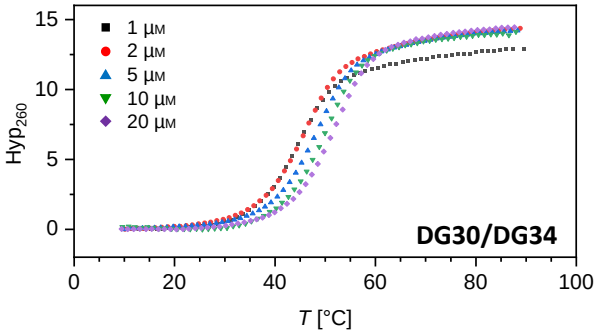
1 μM
2 μM
5 μM
10 μM
20 μM
Hyp260
T [°C]
DG30/DG34

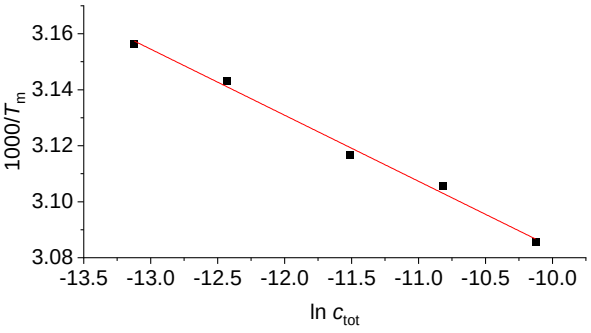
1000/Tm
ln ctot

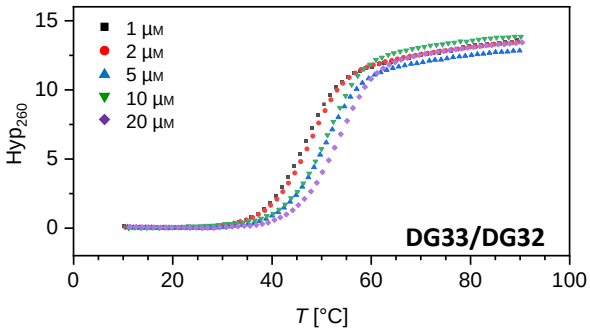
1 μM
2 μM
5 μM
10 μM
20 μM
Hyp260
T [°C]
DG33/DG32

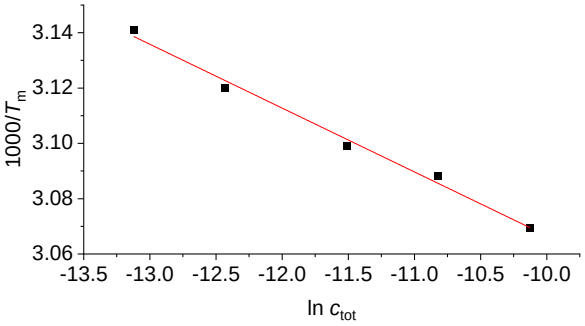
1000/Tm
ln ctot

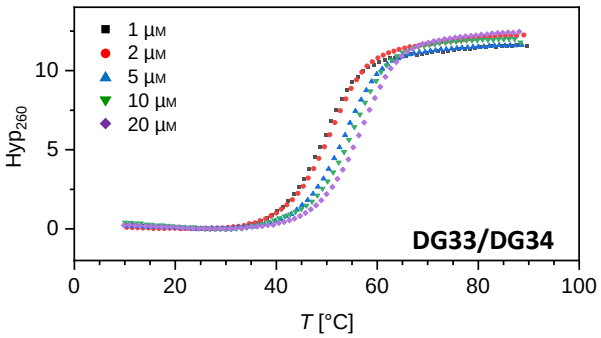
1 μM
2 μM
5 μM
10 μM
20 μM
Hyp260
T [°C]
DG33/DG34

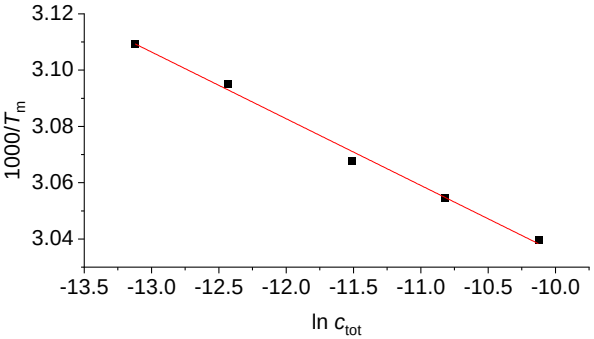
1000/Tm
ln ctot

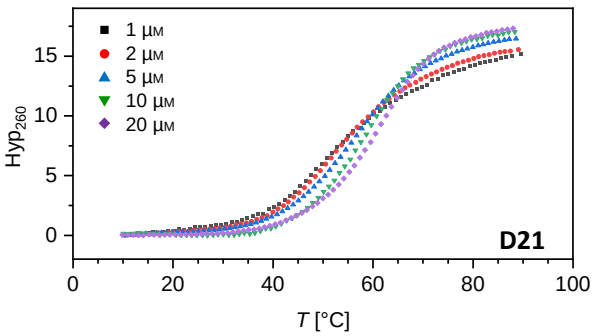
1 μM
2 μM
5 μM
10 μM
20 μM
Hyp260
T [°C]
D21

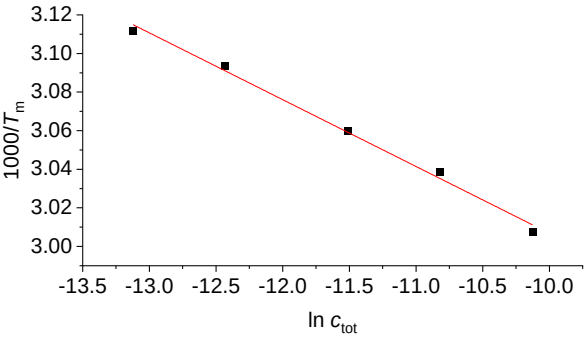
1000/Tm
ln ctot

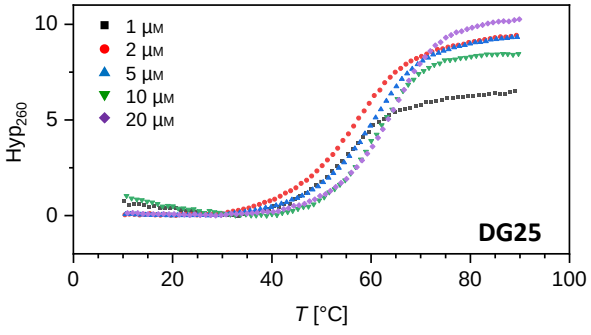
1 μM
2 μM
5 μM
10 μM
20 μM
Hyp260
T [°C]
DG25

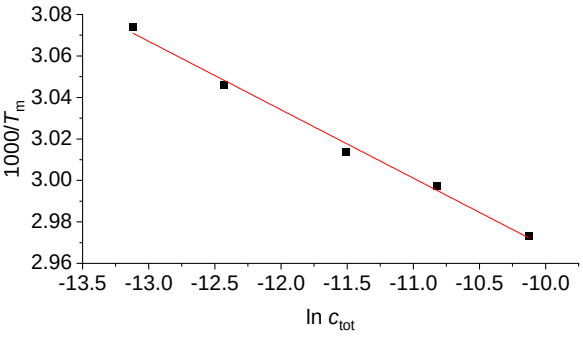
1000/Tm
ln ctot

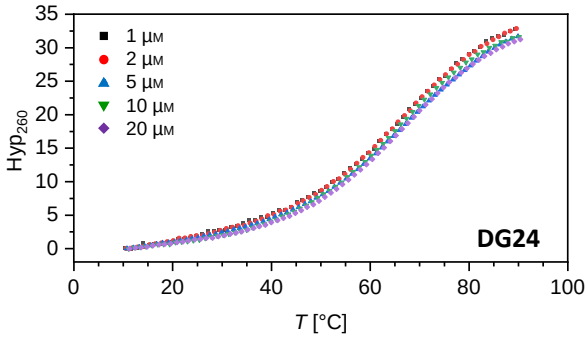
1 µM
2 µM
5 µM
10 µM
20 µM
Hyp260
T [°C]
DG24

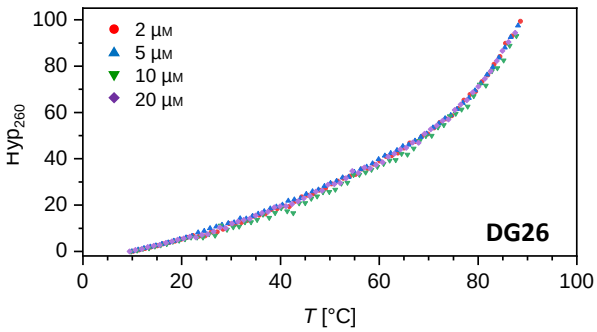
2 µM
5 µM
10 µM
20 µM
Hyp260
T [°C]
DG26

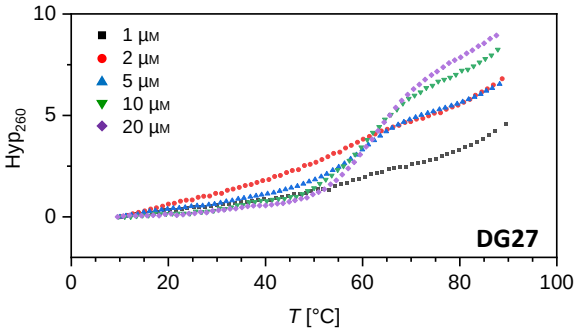
1 µM
2 µM
5 µM
10 µM
20 µM
Hyp260
T [°C]
DG27

6.5 Cartesian coordinates for geometry-optimized structures

6.5.1 Merocyanine chromophores

Table 6.1: Cartesian coordinates for BAM (**1**) in Å.

C	-0.986857	-1.322892	0.229757
C	-1.019070	-2.790895	-0.290484
N	0.234969	-3.404993	-0.397901
C	1.482008	-2.801040	-0.454580
N	1.436082	-1.416776	-0.388020
C	0.304171	-0.604380	-0.277802
C	-2.123095	-0.537366	-0.127914
C	-3.470116	-0.956690	-0.066520
C	-4.560333	-0.109485	0.035818
C	-4.610105	1.430341	0.106822
C	-6.110298	1.675993	0.209503
C	-6.785007	0.446326	0.193858
N	-5.841617	-0.591932	0.090489
C	-6.829503	2.861239	0.307082
C	-8.230688	2.807657	0.388759
C	-8.890161	1.574516	0.371665
C	-8.176719	0.371471	0.273942
C	-3.888956	1.969821	1.364963
C	-4.046359	2.081415	-1.178637
C	-6.168788	-2.004109	0.044276
O	0.430374	0.608489	-0.229473
O	-2.021128	-3.491703	-0.255616
O	2.515649	-3.426096	-0.552445
H	0.234069	-4.420280	-0.442961
H	2.333272	-0.940971	-0.425131
H	-1.894645	0.530570	-0.094904
H	-3.641422	-2.031413	-0.102708
H	-6.316604	3.826941	0.320666
H	-8.806981	3.732596	0.466043
H	-9.980862	1.541803	0.435516
H	-8.706924	-0.582424	0.262617
H	-4.053632	3.055541	1.450032
H	-2.804627	1.794719	1.319904
H	-4.277828	1.494888	2.278513
H	-4.548176	1.686336	-2.075039
H	-4.213709	3.169547	-1.147818
H	-2.965954	1.907257	-1.283326
H	-7.255332	-2.132580	0.104691
H	-5.810611	-2.459009	-0.893458
H	-5.702486	-2.542434	0.885337

Table 6.2: Cartesian coordinates for BAM[b] (**7**) in Å.

C	-1.094363	-0.848358	-0.228422
C	-1.132042	-2.315996	-0.271192
N	0.116357	-2.935949	-0.397985
C	1.364129	-2.335864	-0.484154
N	1.322813	-0.951399	-0.434385
C	0.195242	-0.132703	-0.310139
C	-2.234306	-0.068624	-0.118443
C	-3.573387	-0.494960	-0.032075
C	-4.642206	0.382895	0.070050
S	-4.505801	2.143529	0.119621
C	-6.254683	2.309470	0.242848
C	-6.879841	1.045674	0.243406
N	-5.959175	-0.002427	0.145999
C	-6.995413	3.487643	0.331145
C	-8.388235	3.397344	0.421494
C	-9.016382	2.145298	0.422429
C	-8.275331	0.962881	0.334101
C	-6.323318	-1.412125	0.119998
O	0.326077	1.079390	-0.279776
O	-2.137232	-3.011672	-0.207758
O	2.393672	-2.966078	-0.593155
H	0.111974	-3.951637	-0.430644
H	2.220349	-0.478623	-0.494357
H	-2.022567	1.008178	-0.103341
H	-3.763932	-1.566715	-0.049340
H	-6.496157	4.459180	0.329302
H	-8.985481	4.309194	0.491658
H	-10.104997	2.084505	0.493237
H	-8.787513	-0.000250	0.337393
H	-7.412037	-1.512324	0.175167
H	-5.970215	-1.884399	-0.809910
H	-5.873997	-1.944078	0.973228

Table 6.3: Cartesian coordinates for BAM^F (**2**) in Å.

C	-2.729166	3.108300	-0.634939
C	-2.181200	1.855209	-0.390155
C	-3.011468	0.760253	-0.107959
C	-4.400716	0.889504	-0.064545
C	-4.955166	2.153008	-0.311104
C	-4.122052	3.234429	-0.590371
N	-2.211654	-0.378630	0.100248
C	-0.878370	-0.092850	-0.033554
C	-0.726115	1.406098	-0.366800
C	0.048642	2.163070	0.738349
C	-0.075023	1.623840	-1.753367
C	-2.720979	-1.699482	0.413955
C	0.093320	-1.065906	0.125048
C	1.483776	-0.846341	0.009805
C	2.510883	-1.762996	0.158598
F	-4.669687	4.436869	-0.824457
C	2.293830	-3.181287	0.477808
N	3.461463	-3.945853	0.593080
C	4.775956	-3.528810	0.444361
N	4.904230	-2.181554	0.141897
C	3.883084	-1.241775	-0.019282
O	4.160164	-0.083937	-0.287152
O	5.724408	-4.272825	0.567609
O	1.210521	-3.723771	0.645826
H	-2.118754	3.985914	-0.858638
H	-5.055862	0.044652	0.153300
H	-6.035641	2.307915	-0.288869
H	0.027627	3.244809	0.532444
H	1.100651	1.848047	0.785862
H	-0.406666	1.995979	1.726256
H	-0.617794	1.073490	-2.536842
H	-0.097730	2.694231	-2.011798
H	0.973526	1.294792	-1.764763
H	-3.814157	-1.666737	0.484543
H	-2.438865	-2.424875	-0.366512
H	-2.317157	-2.056841	1.375041
H	-0.215857	-2.083531	0.359277
H	1.847215	0.157305	-0.223113
H	3.332832	-4.929353	0.814731
H	5.854950	-1.842361	0.024183

Table 6.4: Cartesian coordinates for BAM^{OMe} (**3**) in Å.

C	-4.383956	0.334403	0.316689
C	-4.423115	-1.072390	0.319929
C	-3.253628	-1.830180	0.244896
C	-2.033008	-1.154087	0.165235
C	-1.979670	0.242075	0.160965
C	-3.145262	1.001071	0.236607
N	-0.721952	-1.667011	0.080100
C	0.207306	-0.667358	0.013726
C	-0.525550	0.689823	0.064499
C	-0.129917	1.507014	1.316928
C	-0.299972	1.508445	-1.229019
O	-5.586308	0.961641	0.393227
C	-5.633789	2.370277	0.395194
C	-0.387864	-3.077409	0.051556
C	1.563874	-0.937909	-0.085530
C	2.580830	0.036022	-0.161286
C	3.949489	-0.160720	-0.268700
C	4.575489	-1.488008	-0.320189
N	5.972310	-1.478844	-0.432643
C	6.817410	-0.382082	-0.503233
N	6.158098	0.836003	-0.443383
C	4.782113	1.057343	-0.332668
O	4.353599	2.199969	-0.297957
O	3.992749	-2.563128	-0.275965
O	8.021061	-0.479607	-0.609142
H	-5.399215	-1.557524	0.382665
H	-3.314316	-2.920019	0.248361
H	-3.090471	2.090258	0.232597
H	-0.755847	2.410881	1.383830
H	0.921616	1.825412	1.280260
H	-0.280865	0.920423	2.235875
H	-0.564690	0.919821	-2.120508
H	-0.933330	2.409529	-1.216645
H	0.746016	1.831287	-1.328048
H	-6.694213	2.648116	0.465722
H	-5.094494	2.800016	1.259373
H	-5.214335	2.798841	-0.533751
H	-1.301904	-3.675236	0.143175
H	0.115878	-3.343466	-0.892205
H	0.287109	-3.336310	0.883155
H	1.888790	-1.976895	-0.112032
H	2.309514	1.094174	-0.138827
H	6.424154	-2.388108	-0.473722
H	6.747264	1.662450	-0.492111

6.5.2 DMHBI derivatives

Table 6.5: Cartesian coordinates for DMHBI (**102**) in Å.

C	-2.308439	-1.412998	0.386546
C	-2.153075	-2.816245	0.306330
C	-0.884546	-3.355533	0.010032
C	0.213446	-2.527200	-0.204203
C	0.063112	-1.122892	-0.124890
C	-1.209516	-0.580621	0.171301
C	1.233006	-0.297850	-0.347565
C	1.368333	1.059949	-0.310485
O	-3.560995	-0.986802	0.678104
C	-3.798123	0.399083	0.782916
O	-3.208514	-3.627322	0.512207
O	-0.882696	-4.724940	-0.034504
C	0.318779	-5.403367	-0.331418
C	2.685710	1.728290	-0.517993
N	2.375631	3.086575	-0.315568
C	1.013550	3.177748	-0.041657
N	0.400539	2.030208	-0.033923
C	0.356991	4.493280	0.209821
O	3.786479	1.286392	-0.786309
C	3.348855	4.151246	-0.401216
H	1.193553	-2.946408	-0.433232
H	-1.302082	0.502144	0.226973
H	2.165479	-0.827905	-0.570492
H	-4.862639	0.514215	1.029185
H	-3.189845	0.861039	1.581561
H	-3.588341	0.925939	-0.165699
H	-2.883370	-4.537353	0.410168
H	0.086886	-6.476977	-0.317984
H	0.703400	-5.130344	-1.330518
H	1.100501	-5.194268	0.420841
H	-0.713831	4.329966	0.384826
H	0.791522	4.995529	1.091078
H	0.480429	5.176267	-0.647811
H	4.313036	3.683103	-0.646959
H	3.093220	4.876885	-1.191018
H	3.449559	4.690169	0.555557

Table 6.6: Cartesian coordinates for DMHBI-NH_2 (**111**) in Å.

C	-2.318464	-1.403214	0.343017
C	-2.164683	-2.804976	0.277377
C	-0.888820	-3.345072	0.022770
C	0.216871	-2.519218	-0.167492
C	0.067134	-1.115132	-0.101278
C	-1.211763	-0.571202	0.156552
C	1.243164	-0.288472	-0.305059
C	1.370411	1.067376	-0.273852
O	-3.580619	-0.969388	0.591781
C	-3.813222	0.416588	0.677138
O	-3.228875	-3.616873	0.457197
O	-0.881935	-4.716168	-0.010973
C	0.328100	-5.390821	-0.273533
C	2.685699	1.733102	-0.516698
N	2.373683	3.102955	-0.385687
C	1.016647	3.188461	-0.100659
N	0.401121	2.041582	-0.027232
N	0.424671	4.394584	0.077318
O	3.787992	1.292390	-0.771099
C	3.332465	4.168150	-0.548345
H	1.201909	-2.942077	-0.366584
H	-1.304163	0.511702	0.206649
H	2.177177	-0.817485	-0.521371
H	-4.885431	0.541429	0.883786
H	-3.232181	0.882887	1.493974
H	-3.565649	0.935713	-0.267059
H	-2.898531	-4.526236	0.371604
H	0.102088	-6.465929	-0.257450
H	0.736094	-5.124031	-1.265272
H	1.091558	-5.172264	0.494904
H	-0.563566	4.410948	0.289619
H	0.939316	5.261045	0.039380
H	4.297439	3.694423	-0.781276
H	3.061861	4.841133	-1.380706
H	3.448501	4.763089	0.374560

Table 6.7: Cartesian coordinates for DMHB-PTH (**113**) in Å.

C	-2.310325	-1.277195	0.294249
C	-2.149612	-2.679059	0.249059
C	-0.857056	-3.219397	0.101218
C	0.260191	-2.392787	0.001515
C	0.109053	-0.989865	0.058996
C	-1.187284	-0.448509	0.201945
C	1.313732	-0.179457	-0.036860
C	1.546338	1.141976	0.137705
O	-3.587672	-0.844890	0.426451
C	-3.839187	0.540165	0.478561
O	-3.223867	-3.488213	0.341251
O	-0.848518	-4.587251	0.068278
C	0.381211	-5.268252	-0.066361
C	2.954760	1.707732	-0.018555
N	2.991622	3.091134	0.161859
C	1.837792	3.582804	0.458711
S	0.443847	2.447010	0.591087
N	1.607240	4.887304	0.690684
O	3.912884	1.014066	-0.277650
H	1.258232	-2.814573	-0.116603
H	-1.320525	0.631069	0.223161
H	2.240782	-0.712060	-0.283201
H	-4.926336	0.656317	0.585622
H	-3.341040	1.017570	1.342605
H	-3.513346	1.053424	-0.444849
H	-2.890959	-4.399383	0.287303
H	0.149872	-6.341977	-0.057602
H	0.883198	-5.016073	-1.017524
H	1.064883	-5.039383	0.770484
H	0.686139	5.235804	0.917225
H	2.388951	5.529949	0.638236

Table 6.8: Cartesian coordinates for DMAM-DMHBI-NH_2 (**115**) in Å.

C	-1.705819	-2.360019	-0.052744
C	-1.584013	-3.725360	-0.391328
C	-0.390003	-4.182418	-0.982867
C	0.664467	-3.309467	-1.239566
C	0.548342	-1.942058	-0.898720
C	-0.648430	-1.482431	-0.302738
C	1.670484	-1.068272	-1.184606
C	1.838839	0.261432	-0.931612
O	-2.891739	-2.007823	0.508679
C	-3.092629	-0.664654	0.875014
O	-2.600540	-4.581212	-0.151599
O	-0.406493	-5.525969	-1.256807
C	0.720982	-6.117828	-1.863334
C	3.094152	0.973411	-1.334423
N	2.857141	2.285219	-0.907381
C	1.599655	2.320871	-0.312125
N	0.978564	1.165630	-0.316130
N	1.164531	3.516983	0.191536
O	4.098920	0.574541	-1.891883
C	0.084768	3.514424	0.908573
N	-0.472712	4.633646	1.413792
C	-1.656725	4.573711	2.247279
C	0.100873	5.946245	1.170475
C	3.786717	3.379099	-1.068224
H	1.585774	-3.666793	-1.700146
H	-0.716271	-0.426649	-0.049112
H	2.529969	-1.531512	-1.680829
H	-4.102083	-0.605906	1.306076
H	-2.358788	-0.329506	1.631716
H	-3.031870	0.015302	0.005085
H	-2.303197	-5.453305	-0.459179
H	0.489361	-7.184252	-1.990445
H	0.930257	-5.674379	-2.853549
H	1.622201	-6.018052	-1.231915
H	-0.445975	2.579629	1.152300
H	-1.995267	3.533079	2.347038
H	-1.452009	4.972268	3.257398
H	-2.478141	5.168345	1.809198
H	0.970988	5.833240	0.513467
H	-0.641602	6.607664	0.690974
H	0.416786	6.414047	2.119762
H	4.672168	2.974415	-1.578866
H	3.350905	4.188027	-1.675618
H	4.085463	3.798638	-0.094616

Table 6.9: Cartesian coordinates for DMAM-DMHB-PTH (**114**) in Å.

C	-2.359769	-2.981839	-0.135489
C	-2.149013	-4.310797	-0.561923
C	-0.882296	-4.681074	-1.055379
C	0.159045	-3.758737	-1.123133
C	-0.041269	-2.428092	-0.690960
C	-1.312616	-2.057494	-0.201423
C	1.091296	-1.519945	-0.782488
C	1.267454	-0.228020	-0.413982
O	-3.608584	-2.708941	0.316792
C	-3.901985	-1.407190	0.765594
O	-3.149613	-5.212683	-0.499914
O	-0.817925	-5.994307	-1.435646
C	0.383991	-6.497482	-1.979877
C	2.605829	0.453358	-0.636163
N	2.621336	1.769892	-0.165383
C	1.507299	2.151052	0.354337
S	0.163525	0.891475	0.376822
N	1.315669	3.379729	0.896319
O	3.547796	-0.094787	-1.167110
C	0.132355	3.830356	1.164734
N	-0.081672	5.004224	1.786814
C	-1.423057	5.494370	2.036514
C	1.025370	5.839822	2.227644
H	1.137567	-4.049820	-1.505074
H	-1.485286	-1.034270	0.124892
H	1.999363	-1.944973	-1.226687
H	-4.953720	-1.416285	1.083511
H	-3.270160	-1.113602	1.624395
H	-3.777388	-0.655599	-0.036009
H	-2.790735	-6.047946	-0.842584
H	0.202415	-7.552890	-2.224216
H	0.669637	-5.957809	-2.900432
H	1.215509	-6.433270	-1.255527
H	-0.794865	3.297709	0.883905
H	-2.165616	4.771314	1.670927
H	-1.588884	5.649960	3.117045
H	-1.592460	6.458475	1.524952
H	1.966512	5.367198	1.922415
H	0.949786	6.842494	1.773334
H	1.008156	5.953423	3.325451

6.6 Geometry-optimized structures

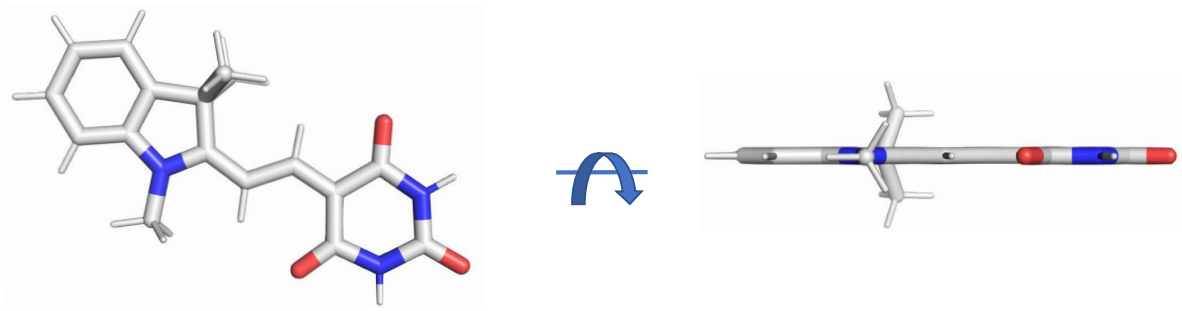

Figure 6.2: Geometry-optimized structure of BAM (**1**).

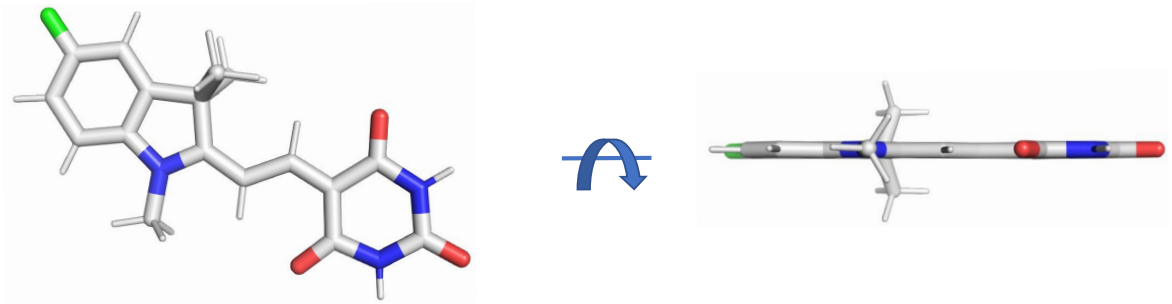

Figure 6.3: Geometry-optimized structure of BAM^{F} (**2**).

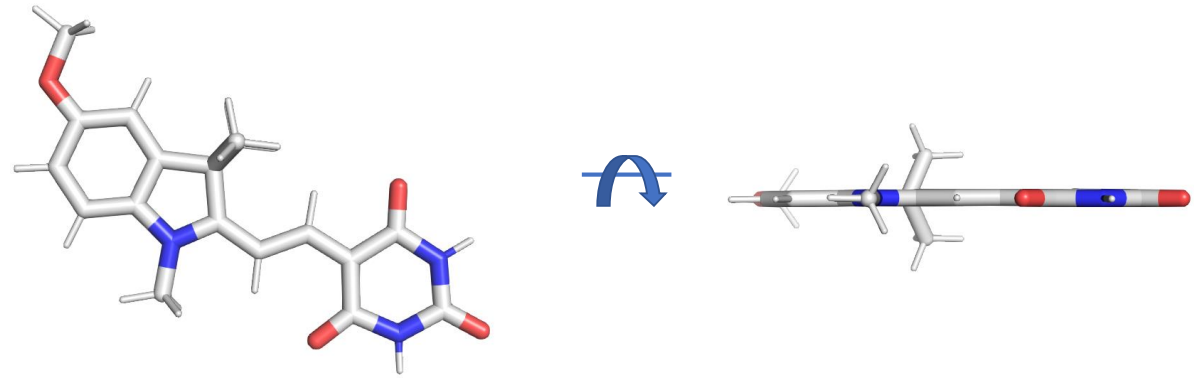

Figure 6.4: Geometry-optimized structure of BAM^{OMe} (**3**).

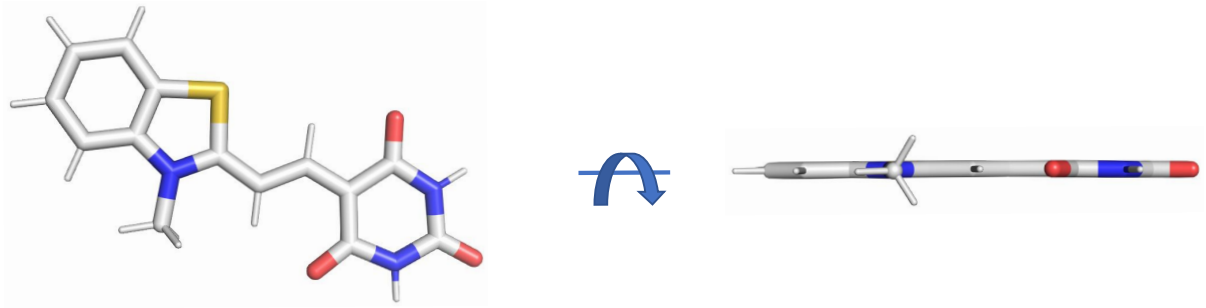

Figure 6.5: Geometry-optimized structure of BAM^{b} (**7**).

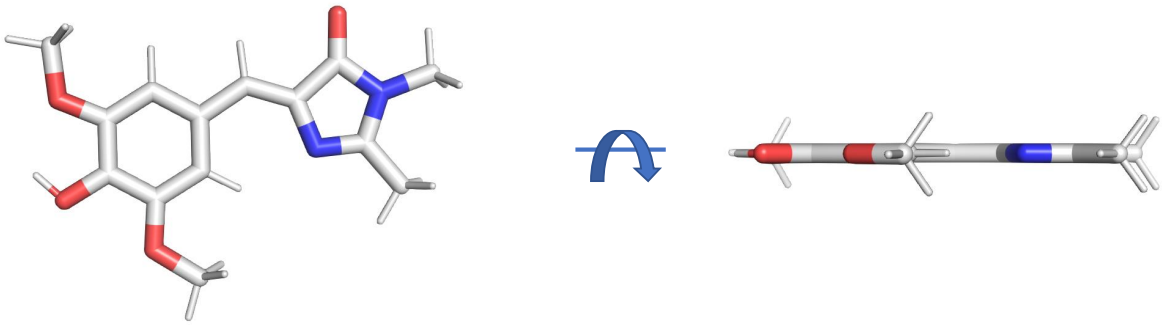

Figure 6.6: Geometry-optimized structure of DMHBI (**102**).

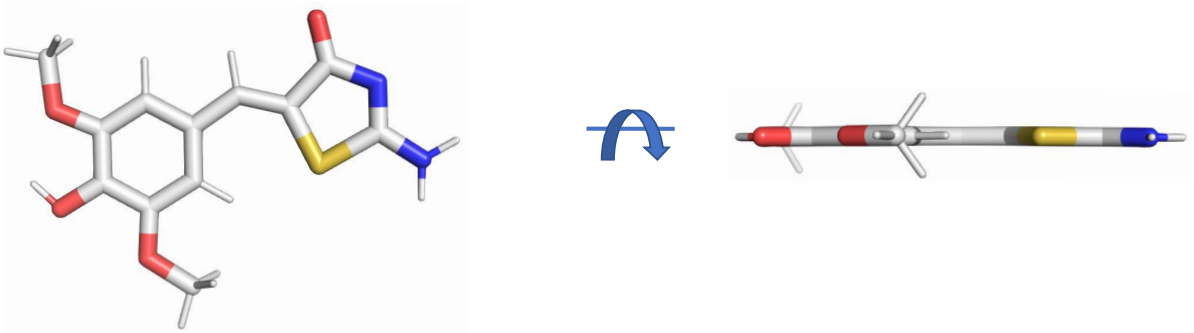

Figure 6.7: Geometry-optimized structure of DMHB-PTH (**113**).

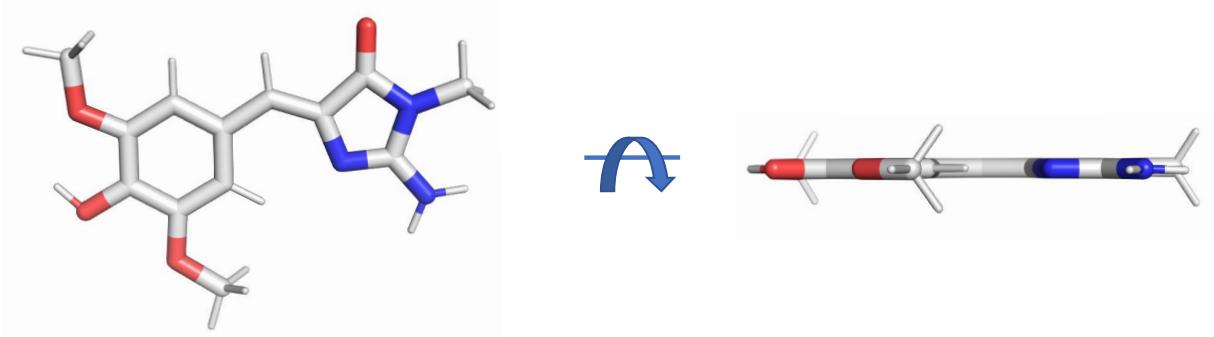

Figure 6.8: Geometry-optimized structure of DMHBI-NH_2 (**111**).

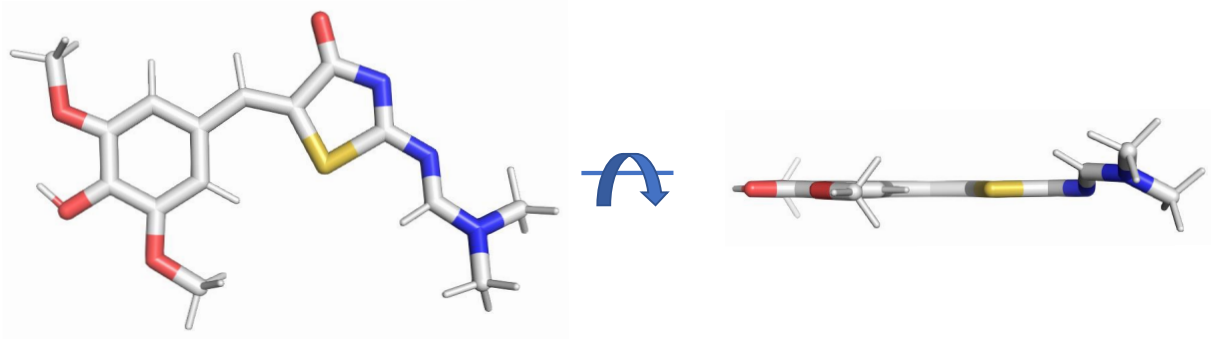

Figure 6.9: Geometry-optimized structure of DMAM-DMHB-PTH (**114**).

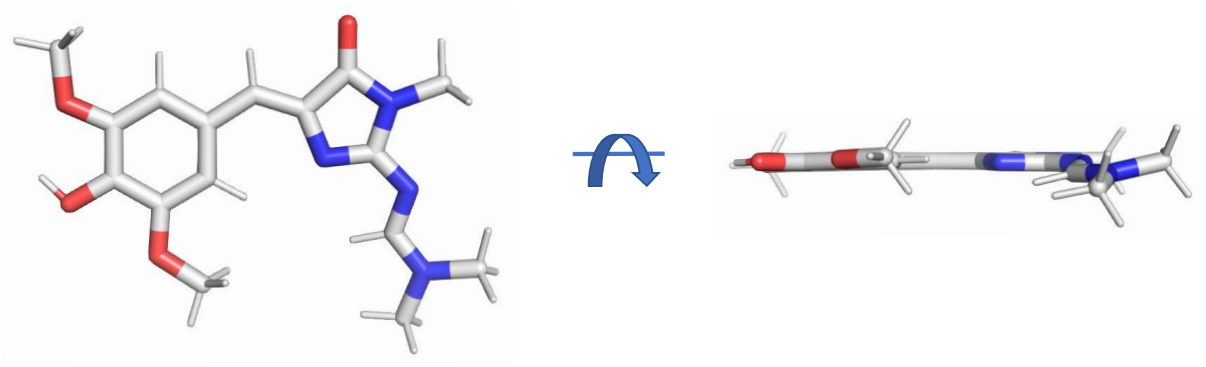

Figure 6.10: Geometry-optimized structure of DMAM-DMHBI-NH_2 (**115**).

6.7 Abbreviations

2AP	2-aminopurine
Ac	acetyl
AFM	atomic force microscopy
ANA	arabino nucleic acid
APS	ammonium peroxodisulfate
ASO	antisense oligonucleotides
BAM	barbituric acid merocyanine
Bn	benzyl
BNA	bridged nucleic acid
BOP	(benzotriazol-1-yloxy)tris(dimethylamino)phosphonium hexafluorophosphate
BPP	benzopyridopyrimidine
BSA	*N,O*-bis(trimethylsilyl)acetamide
BuNA	butyl nucleic acid
Bz	benzoyl
C153	Coumarin 153
CD	circular dichroism
CEP-Cl	2-cyanoethyl-*N,N*-di-*iso*-propylchlorophosphoramidite
COSY	correlation spectroscopy
CPG	controlled pore glass
CPL	circularly polarized luminescence
CT	charge transfer
CuAAC	copper-catalyzed azide-alkyne cycloaddition
d	doublet
2,6-DAP	2,6-diaminopurine
DCE	1,2-dichloroethane
DCM	dichloromethane
DDD	Dickerson Drew dodecamer
DFT	density functional theory
DFHBI	3,5-difluoro-4-hydroxybenzylidene imidazolinone
DFHO	3,5-difluoro-4-hydroxybenzylidene imidazolinone-2-oxime
$(DHQD)_2PHAL$	hydrochinidin-1,4-phthalazindiyl-diether
DIPEA	*N,N*-di-*iso*-propylethylamine
DIR	dimethyl indole red
DiSC	3,3'-diethylthiadicarbocyanine
DMAM	*N,N*-dimethylaminomethylene
DMAP	4-dimethylaminopyridine
DMF	*N,N*-dimethylformamide
DMFDMA	dimethylformamide dimethyacetal
DMHBI	3,5-dimethoxy-4-hydroxybenzylidene imidazolinone
DMHBO	3,5-dimethoxy-4-hydroxybenzyli-dene imidazolinone-2-oxime
DMSO	dimethylsulfoxide
DMT-Cl	4,4'-dimethoxytrityl chloride
DNA	deoxyribonucleic acid

dsDNA	double-stranded DNA
DTT	dithiothreitol
ECHO	exciton-controlled hybridization-sensitive fluorescence emission
EDTA	ethylenediaminetetraacetic acid
EIT	electron transfer
EnT	energy transfer
EPR	electron paramagnetic resonance
ESI-MS	electrospray ionization mass spectrometry
ESPT	excited state proton transfer
^{eth}A	etheno adenine
ETT	5-ethylthio-1*H*-tetrazole
FANA	fluoro arabino nucleic acid
FBD	fluorophore binding domain
FIT	forced intercalation
FNA	flexible nucleic acid, fluorescent nucleobase analog
FP	forward primer
FRET	Förster resonance energy transfer
GFP	green fluorescent protein
GNA	glycol nucleic acid
HBC	(4-((2-hydroxyethyl)(methyl)amino)-benzylidene)-cyanophenylacetonitrile
HBI	hydroxybenzylidene imidazolone
HBMR	4-hydroxymethylbenzylidene-rhodanine
HBR	4-hydroxybenzylidene-rhodanine
HEPES	2-(4-(2-hydroxyethyl)piperazin-1-yl)ethanesulfonic acid
HFIP	hexafluoro-*iso*-propanol
HIV	human immunodeficiency virus
HMBC	heteronuclear multiple bond correlation
HMDS	hexamethyldisilazane
HNA	hexitol nucleic acid
HOMO	highest occupied molecular orbital
HOTAIR	HOX transcript antisense RNA
HPLC	high-performance liquid chromatography
HSQC	heteronuclear single quantum coherence spectroscopy
HT	high tension
I	inosine
Ib	*iso*-butyryl
IC	internal conversion
IEX	ion exchange
IQ	intramolecular quenching
ISC	intersystem crossing
LNA	locked nucleic acid
lncRNA	long noncoding RNA
LUMO	lowest unoccupied molecular orbital
*m*CPBA	*meta*-chloroperoxybenzoic acid
m	multiplet
MAP	4-amino-6-methyl pteridone
MD	molecular dynamics

MI	methyl isoxanthopterin
miRNA	micro RNA
mRNA	messenger ribonucleic acid
ncRNA	noncoding RNA
NMI	*N*-methylimidazole
NMO	*N*-methylmorpholine-*N*-oxide
NMR	nuclear magnetic resonance
NOESY	nuclear Overhauser enhancement spectroscopy
nt	nucleotides
NT	naphthalene
NTP	nucleoside triphosphate
ODF	oligodeoxyfluoroside
OPVT	oligo(*p*-phenylene)vinylene
OTB	oxazole thiazole blue
PAc	phenoxy acetyl
PAGE	polyacrylamide gel electrophoresis
PBI	perylenebisimide
PBS	phosphate-buffered saline
pC	pyrrolo cytosine
PCR	polymerase chain reaction
PDB	protein data bank
Pe	perylene
PET	photoinduced electron transfer
PMT	photomultiplier tube
PNA	peptide nucleic acid
PP_i	pyrophosphate
PTH	pseudothiohydantoin
p-TSA	*para*-toluene sulfonic acid
Py	pyrene
q	quartet
Q	queuosine
QY	quantum yield
RNA	ribonucleic acid
RP	reversed phase, reverse primer
rpm	rounds per minute
s	singlet
s_{br}	broad singlet
SELEX	systematic evolution of ligands by exponential enrichment
siRNA	small interfering RNA
sncRNA	short noncoding RNA
SNP	single-nucleotide polymorphisms
ssDNA	single-stranded DNA
t	triplet
TBAF	tetra-*n*-butylammonium fluoride
TBDMS	*tert*-butyldimethylsilyl
TBE	TRIS/borate/EDTA
TCSPC	time-correlated single photon counting

TEAA	triethylammonium acetate
TEAB	triethylammonium bicarbonate
TEMED	tetramethylethylenediamine
TEN	Tris/EDTA/NaCl
TET	ten-eleven-translocation
THF	tetrahydrofuran
TICT	twisted intramolecular charge transfer
TIPS	tri-*iso*-propylsilyl
TLC	thin layer chromatography
T_m	melting temperature
TMSOTf	trimethylsilyl trifluoromethanesulfonate
TNA	threose nucleic acid
TO	thiazole orange
TOM-Cl	(tris-*iso*-propylsilyloxy)methyl chloride
TRIS	tris(hydroxymethyl)aminomethane
tRNA	transfer ribonucleic acid
UDG	uracil DNA glycosylase
UV	ultraviolet
VR	vibrational relaxation
2WJ	two-way junction
3WJ	three-way junction
Xist	X-inactive specific transcript
XNA	xeno nucleic acid
Y-FAST	yellow fluorescence-activating and absorption-shifting tag
YO	oxazole yellow

Bibliography

[1] J. D. Watson; F. H. C. Crick "Molecular Structure of Nucleic Acids: A Structure for Deoxyribose Nucleic Acid", *Nature* **1953**, *171*, 737–738.

[2] R. E. Franklin; R. G. Gosling "Evidence for 2-Chain Helix in Crystalline Structure of Sodium Deoxyribonucleate", *Nature* **1953**, *172*, 156–157.

[3] R. Wing; H. Drew; T. Takano; C. Broka; S. Tanaka; K. Itakura; R. E. Dickerson "Crystal structure analysis of a complete turn of B-DNA", *Nature* **1980**, *287*, 755–758.

[4] C. Altona; M. Sundaralingam "Conformational analysis of the sugar ring in nucleosides and nucleotides. New description using the concept of pseudorotation", *J. Am. Chem. Soc.* **1972**, *94*, 8205–8212.

[5] I. Tinoco; C. Bustamante "How RNA folds", *J. Mol. Biol.* **1999**, *293*, 271–281.

[6] T. Carell; C. Brandmayr; A. Hienzsch; M. Müller; D. Pearson; V. Reiter; I. Thoma; P. Thumbs; M. Wagner "Structure and Function of Noncanonical Nucleobases", *Angew. Chem. Int. Ed.* **2012**, *51*, 7110–7131.

[7] S. Minchin; J. Lodge "Understanding biochemistry: structure and function of nucleic acids", *Essays Biochem.* **2019**, *63*, 433–456.

[8] J. S. Mattick "Non-coding RNAs: the architects of eukaryotic complexity", *EMBO reports* **2001**, *2*, 986–991.

[9] J. S. Mattick "Challenging the dogma: the hidden layer of non-protein-coding RNAs in complex organisms", *BioEssays* **2003**, *25*, 930–939.

[10] E. Anastasiadou; L. S. Jacob; F. J. Slack "Non-coding RNA networks in cancer", *Nat. Rev. Cancer* **2017**, *18*, 5–18.

[11] Y. Zhang; Y. Zhao; X. Ao; W. Yu; L. Zhang; Y. Wang; W. Chang "The Role of Non-coding RNAs in Alzheimer's Disease: From Regulated Mechanism to Therapeutic Targets and Diagnostic Biomarkers", *Front. Aging Neurosci.* **2021**, *13*, DOI 10.3389/fnagi.2021.654978.

[12] J. Beermann; M.-T. Piccoli; J. Viereck; T. Thum "Non-coding RNAs in Development and Disease: Background, Mechanisms, and Therapeutic Approaches", *Physiol Rev* **2016**, *96*, 1297–1325.

[13] T. Carell; M. Q. Kurz; M. Müller; M. Rossa; F. Spada "Nichtkanonische Basen im Genom: die regulative Informationsebene in der DNA", *Angew. Chem.* **2018**, *130*, 4377–4394.

[14] Y. Chen; T. Hong; S. Wang; J. Mo; T. Tian; X. Zhou "Epigenetic modification of nucleic acids: from basic studies to medical applications", *Chem. Soc. Rev.* **2017**, *46*, 2844–2872.

[15] A. Shaw; M. Gullerova "Home and Away: The Role of Non-Coding RNA in Intracellular and Intercellular DNA Damage Response", *Genes* **2021**, *12*, 1475.

[16] S. Ochoa; V. T. Milam "Modified Nucleic Acids: Expanding the Capabilities of Functional Oligonucleotides", *Molecules* **2020**, *25*, 4659.

[17] J. A. Kulkarni; D. Witzigmann; S. B. Thomson; S. Chen; B. R. Leavitt; P. R. Cullis; R. van der Meel "The current landscape of nucleic acid therapeutics", *Nat. Nanotechnology* **2021**, *16*, 630–643.
[18] K. L. Seley-Radtke; M. K. Yates "The evolution of nucleoside analogue antivirals: A review for chemists and non-chemists. Part 1: Early structural modifications to the nucleoside scaffold", *Antiviral Res.* **2018**, *154*, 66–86.
[19] J. Micklefield "Backbone Modification of Nucleic Acids: Synthesis, Structure and Therapeutic Applications", *Curr. Med. Chem.* **2001**, *8*, 1157–1179.
[20] I. Anosova; E. A. Kowal; M. R. Dunn; J. C. Chaput; W. D. Van Horn; M. Egli "The structural diversity of artificial genetic polymers", *Nucleic Acids Res.* **2015**, *44*, 1007–1021.
[21] K. Morihiro; Y. Kasahara; S. Obika "Biological applications of xeno nucleic acids", *Mol. BioSyst.* **2017**, *13*, 235–245.
[22] K. Murayama; H. Asanuma "Design and Hybridization Properties of Acyclic Xeno Nucleic Acid Oligomers", *ChemBioChem* **2021**, *22*, 2507–2515.
[23] T. Vilaivan "Fluorogenic PNA probes", *Beilstein J. Org. Chem.* **2018**, *14*, 253–281.
[24] N. Michelotti; A. Johnson-Buck; A. J. Manzo; N. G. Walter "Beyond DNA origami: the unfolding prospects of nucleic acid nanotechnology", *WIREs Nanomedicine and Nanobiotechnology* **2011**, *4*, 139–152.
[25] A. Grunweller "Comparison of different antisense strategies in mammalian cells using locked nucleic acids, 2'-*O*-methyl RNA, phosphorothioates and small interfering RNA", *Nucleic Acids Res.* **2003**, *31*, 3185–3193.
[26] M. J. Damha; N. Usman; K. K. Ogilvie "Solution and solid phase chemical synthesis of arabinonucleotides", *Can. J. Chem.* **1989**, *67*, 831–839.
[27] R. El-Khoury; M. J. Damha "2'-Fluoro-arabinonucleic Acid (FANA): A Versatile Tool for Probing Biomolecular Interactions", *Acc. Chem. Res.* **2021**, *54*, 2287–2297.
[28] I. A. Ferreira-Bravo; J. J. DeStefano "Xeno-nucleic Acid (XNA) 2'-Fluoro-Arabino Nucleic Acid (FANA) Aptamers to the Receptor Binding Domain of SARS-CoV-2 S Protein Block ACE2 Binding", **2021**, DOI 10.1101/2021.07.13.452259.
[29] K.-U. Schoning "Chemical Etiology of Nucleic Acid Structure: The alpha -Threofuranosyl-(3'-2') Oligonucleotide System", *Science* **2000**, *290*, 1347–1351.
[30] M. R. Dunn; C. M. McCloskey; P. Buckley; K. Rhea; J. C. Chaput "Generating Biologically Stable TNA Aptamers that Function with High Affinity and Thermal Stability", *J. Am. Chem. Soc.* **2020**, *142*, 7721–7724.
[31] S. Obika; D. Nanbu; Y. Hari; K.-i. Morio; Y. In; T. Ishida; T. Imanishi "Synthesis of 2'-O,4'-C-methyleneuridine and -cytidine. Novel bicyclic nucleosides having a fixed C3, -endo sugar puckering", *Tetrahedron Lett.* **1997**, *38*, 8735–8738.
[32] A. A. Koshkin; S. K. Singh; P. Nielsen; V. K. Rajwanshi; R. Kumar; M. Meldgaard; C. E. Olsen; J. Wengel "LNA (Locked Nucleic Acids): Synthesis of the adenine, cytosine, guanine, 5-methylcytosine, thymine and uracil bicyclonucleoside monomers, oligomerisation, and unprecedented nucleic acid recognition", *Tetrahedron* **1998**, *54*, 3607–3630.
[33] D. D'Alonzo; A. Guaragna; G. Palumbo "Exploring the Role of Chirality in Nucleic Acid Recognition", *Chemistry & Biodiversity* **2011**, *8*, 373–413.
[34] B. D. Bouvere; L. Kerreinans; C. Hendrix; H. D. Winter; G. Schepers; A. V. Aerschot; P. Herdewijn "Hexitol Nucleic Acids (HNA): Synthesis and Properties", *Nucleosides Nucleotides* **1997**, *16*, 973–976.

[35] E. Lescrinier; R. Esnouf; J. Schraml; R. Busson; H. Heus; C. Hilbers; P. Herdewijn "Solution structure of a HNA–RNA hybrid", *Chemistry & Biology* **2000**, *7*, 719–731.
[36] E. Eremeeva; A. Fikatas; L. Margamuljana; M. Abramov; D. Schols; E. Groaz; P. Herdewijn "Highly stable hexitol based XNA aptamers targeting the vascular endothelial growth factor", *Nucleic Acids Res.* **2019**, *47*, 4927–4939.
[37] L. K. McKenzie; R. El-Khoury; J. D. Thorpe; M. J. Damha; M. Hollenstein "Recent progress in non-native nucleic acid modifications", *Chem. Soc. Rev.* **2021**, *50*, 5126–5164.
[38] F. Hövelmann; O. Seitz "DNA Stains as Surrogate Nucleobases in Fluorogenic Hybridization Probes", *Acc. Chem. Res.* **2016**, *49*, 714–723.
[39] E. Rooij; S. Kauppinen "Development of micro RNA therapeutics is coming of age", *EMBO Mol. Med.* **2014**, *6*, 851–864.
[40] P. Nielsen; M. Egholm; R. Berg; O. Buchardt "Sequence-selective recognition of DNA by strand displacement with a thymine-substituted polyamide", *Science* **1991**, *254*, 1497–1500.
[41] K. K. Jensen; H. Ørum; P. E. Nielsen; B. Nordén "Kinetics for Hybridization of Peptide Nucleic Acids (PNA) with DNA and RNA Studied with the BIAcore Technique", *Biochemistry* **1997**, *36*, 5072–5077.
[42] J. Saarbach; P. M. Sabale; N. Winssinger "Peptide nucleic acid (PNA) and its applications in chemical biology, diagnostics, and therapeutics", *Curr. Opin. Chem. Biol.* **2019**, *52*, 112–124.
[43] V. Demidov; M. D. Frank-Kamenetskii; M. Egholm; O. Buchardt; P. E. Nielsen "Sequence selective double strand DNA cleavage by Peptide Nucleic Acid (PNA) targeting using nuclease S1", *Nucleic Acids Res.* **1993**, *21*, 2103–2107.
[44] G. F. Joyce; A. W. Schwartz; S. L. Miller; L. E. Orgel "The case for an ancestral genetic system involving simple analogues of the nucleotides.", *PNAS* **1987**, *84*, 4398–4402.
[45] Y. Merle; E. Bonneil; L. Merle; J. Sági; A. Szemzö "Acyclic oligonucleotide analogues", *Int. J. Biol. Macromol.* **1995**, *17*, 239–246.
[46] M. Chemama; C. Switzer in *Methods in Molecular Biology*, Springer New York, **2019**, pp. 213–236.
[47] L. Zhang; A. Peritz; E. Meggers "A Simple Glycol Nucleic Acid", *J. Am. Chem. Soc.* **2005**, *127*, 4174–4175.
[48] M. Schlegel; X. Xie; L. Zhang; E. Meggers "Insight into the High Duplex Stability of the Simplified Nucleic Acid GNA", *Angew. Chem. Int. Ed.* **2009**, *48*, 960–963.
[49] M. K. Schlegel; D. J. Foster; A. V. Kel'in; I. Zlatev; A. Bisbe; M. Jayaraman; J. G. Lackey; K. G. Rajeev; K. Charissé; J. Harp; P. S. Pallan; M. A. Maier; M. Egli; M. Manoharan "Chirality Dependent Potency Enhancement and Structural Impact of Glycol Nucleic Acid Modification on siRNA", *J. Am. Chem. Soc.* **2017**, *139*, 8537–8546.
[50] S. Zhang; J. C. Chaput "Synthesis of Glycerol Nucleic Acid (GNA) Phosphoramidite Monomers and Oligonucleotide Polymers", *Curr. Protoc. Nucleic Acid Chem.* **2010**, *42*, DOI 10.1002/0471142700.nc0440s42.
[51] M. K. Schlegel; L.-O. Essen; E. Meggers "Atomic resolution duplex structure of the simplified nucleic acidGNA", *Chem. Commun.* **2010**, *46*, 1094–1096.
[52] M. K. Schlegel; L.-O. Essen; E. Meggers "Duplex Structure of a Minimal Nucleic Acid", *J. Am. Chem. Soc.* **2008**, *130*, 8158–8159.
[53] A. T. Johnson; M. K. Schlegel; E. Meggers; L.-O. Essen; O. Wiest "On the Structure and Dynamics of Duplex GNA", *J. Org. Chem.* **2011**, *76*, 7964–7974.

[54] H. Zhou; A. T. Johnson; O. Wiest; L. Zhang "Incorporation of porphyrin acetylides into duplexes of the simplified nucleic acid GNA", *Org. Biomol. Chem.* **2011**, *9*, 2840–2849.

[55] R. S. Zhang; E. O. McCullum; J. C. Chaput "Synthesis of Two Mirror Image 4-Helix Junctions Derived from Glycerol Nucleic Acid", *J. Am. Chem. Soc.* **2008**, *130*, 5846–5847.

[56] M. Luo; E. Groaz; M. Froeyen; V. Pezo; F. Jaziri; P. Leonczak; G. Schepers; J. Rozenski; P. Marlière; P. Herdewijn "Invading Escherichia coli Genetics with a Xenobiotic Nucleic Acid Carrying an Acyclic Phosphonate Backbone (ZNA)", *J. Am. Chem. Soc.* **2019**, *141*, 10844–10851.

[57] P. Karri; V. Punna; K. Kim; R. Krishnamurthy "Base-Pairing Properties of a Structural Isomer of Glycerol Nucleic Acid", *Angew. Chem. Int. Ed.* **2013**, *125*, 5952–5956.

[58] V. Kumar; K. R. Gore; P. I. Pradeepkumar; V. Kesavan "Design, synthesis, biophysical and primer extension studies of novel acyclic butyl nucleic acid (BuNA)", *Org. Biomol. Chem.* **2013**, *11*, 5853–5865.

[59] S. H. Boo; Y. K. Kim "The emerging role of RNA modifications in the regulation of mRNA stability", *Experimental & Molecular Medicine* **2020**, *52*, 400–408.

[60] M. V. C. Greenberg; D. Bourc'his "The diverse roles of DNA methylation in mammalian development and disease", *Nat. Rev. Mol. Cell Biol.* **2019**, *20*, 590–607.

[61] R. Desrosiers; K. Friderici; F. Rottman "Identification of Methylated Nucleosides in Messenger RNA from Novikoff Hepatoma Cells", *PNAS* **1974**, *71*, 3971–3975.

[62] J. M. Adams; S. Cory "Modified nucleosides and bizarre 5'-termini in mouse myeloma mRNA", *Nature* **1975**, *255*, 28–33.

[63] X. Jiang; B. Liu; Z. Nie; L. Duan; Q. Xiong; Z. Jin; C. Yang; Y. Chen "The role of m6A modification in the biological functions and diseases", *Signal Transduct Target Ther* **2021**, *6*, 74.

[64] B. Wu; L. Li; Y. Huang; J. Ma; J. Min "Readers, writers and erasers of N6-methylated adenosine modification", *Curr. Opin. Struct. Biol.* **2017**, *47*, 67–76.

[65] M. Ehrlich; G. G. Wilson; K. C. Kuo; C. W. Gehrke "*N*4-methylcytosine as a minor base in bacterial DNA", *J. Bacteriol. Res.* **1987**, *169*, 939–943.

[66] J. H. Gommers-Ampt; F. V. Leeuwen; A. L. de Beer; J. F. Vliegenthart; M. Dizdaroglu; J. A. Kowalak; P. F. Crain; P. Borst "β-D-glucosyl-hydroxymethyluracil: A novel modified base present in the DNA of the parasitic protozoan T. brucei", *Cell* **1993**, *75*, 1129–1136.

[67] T. F. Kraus; D. Globisch; M. Wagner; S. Eigenbrod; D. Widmann; M. Münzel; M. Müller; T. Pfaffeneder; B. Hackner; W. Feiden; U. Schüller; T. Carell; H. A. Kretzschmar "Low values of 5-hydroxymethylcytosine (5hmC), the "sixth base," are associated with anaplasia in human brain tumors", *Int. J. Cancer* **2012**, *131*, 1577–1590.

[68] H. Yang; Y. Liu; F. Bai; J.-Y. Zhang; S.-H. Ma; J. Liu; Z.-D. Xu; H.-G. Zhu; Z.-Q. Ling; D. Ye; K.-L. Guan; Y. Xiong "Tumor development is associated with decrease of TET gene expression and 5-methylcytosine hydroxylation", *Oncogene* **2012**, *32*, 663–669.

[69] T. Carell; M. Q. Kurz; M. Müller; M. Rossa; F. Spada "Non-canonical Bases in the Genome: The Regulatory Information Layer in DNA", *Angew. Chem. Int. Ed.* **2018**, *57*, 4296–4312.

[70] Y.-F. He; B.-Z. Li; Z. Li; P. Liu; Y. Wang; Q. Tang; J. Ding; Y. Jia; Z. Chen; L. Li; Y. Sun; X. Li; Q. Dai; C.-X. Song; K. Zhang; C. He; G.-L. Xu "Tet-Mediated Formation

of 5-Carboxylcytosine and Its Excision by TDG in Mammalian DNA", *Science* **2011**, *333*, 1303–1307.

[71] F. Schelter; A. Kirchner; F. R. Traube; M. Müller; W. Steglich; T. Carell "5-Hydroxymethyl-, 5-Formyl- and 5-Carboxydeoxycytidines as Oxidative Lesions and Epigenetic Marks", *Chem. Eur. J.* **2021**, *27*, 8100–8104.

[72] M. Bienz; E. Kubli "Wild-type tRNATyrG reads the TMV RNA stop codon, but Q base-modified tRNATyrQ does not", *Nature* **1981**, *294*, 188–190.

[73] R. C. Morris; K. G. Brown; M. S. Elliott "The Effect of Queuosine on tRNA Structure and Function", *J. Biomol. Struct. Dyn.* **1999**, *16*, 757–774.

[74] C. Valadon; O. Namy "The Importance of the Epi-Transcriptome in Translation Fidelity", *Non-Coding RNA* **2021**, *7*, 51.

[75] M. Vinayak; C. Pathak "Queuosine modification of tRNA: its divergent role in cellular machinery", *Biosci. Rep.* **2009**, *30*, 135–148.

[76] P. Thumbs; T. T. Ensfelder; M. Hillmeier; M. Wagner; M. Heiss; C. Scheel; A. Schön; M. Müller; S. Michalakis; S. Kellner; T. Carell "Synthesis of Galactosyl-Queuosine and Distribution of Hypermodified Q-Nucleosides in Mouse Tissues", *Angew. Chem. Int. Ed.* **2020**, *59*, 12352–12356.

[77] W. E. Cohn "Pseudouridine, a Carbon-Carbon Linked Ribonucleoside in Ribonucleic Acids: Isolation, Structure, and Chemical Characteristics", *J. Biol. Chem.* **1960**, *235*, 1488–1498.

[78] T. Suzuki "Taurine as a constituent of mitochondrial tRNAs: new insights into the functions of taurine and human mitochondrial diseases", *EMBO J.* **2002**, *21*, 6581–6589.

[79] J. Y. Feng "Addressing the selectivity and toxicity of antiviral nucleosides", *Antivir. Chem. Chemother.* **2018**, *26*, 204020661875852.

[80] R. Grunewald; H. Kantarjian; M. Du; K. Faucher; P. Tarassoff; W. Plunkett "Gemcitabine in leukemia: a phase I clinical, plasma, and cellular pharmacology study.", *J. Clin. Oncol.* **1992**, *10*, 406–413.

[81] M. Cornberg; H. Wedemeyer; M. P. Manns "Treatment of chronic hepatitis C with PEGylated interferon and ribavirin", *Curr. Gastroenterol. Rep.* **2002**, *4*, 23–30.

[82] R. M. Cox; J. D. Wolf; R. K. Plemper "Therapeutically administered ribonucleoside analogue MK-4482/EIDD-2801 blocks SARS-CoV-2 transmission in ferrets", *Nat. Microbiol.* **2020**, *6*, 11–18.

[83] F. Kabinger; C. Stiller; J. Schmitzová; C. Dienemann; H. S. Hillen; C. Höbartner; P. Cramer "Mechanism of molnupiravir-induced SARS-CoV-2 mutagenesis", *Nature* **2021**, *28*, 740–746.

[84] D. B. Gophane; S. T. Sigurdsson "TEMPO-derived spin labels linked to the nucleobases adenine and cytosine for probing local structural perturbations in DNA by EPR spectroscopy", *Beilstein J. Org. Chem.* **2015**, *11*, 219–227.

[85] P. Cekan; A. L. Smith; N. Barhate; B. H. Robinson; S. T. Sigurdsson "Rigid spin-labeled nucleoside Ç: a nonperturbing EPR probe of nucleic acid conformation", *Nucleic Acids Res.* **2008**, *36*, 5946–5954.

[86] H. Cahová; L. Havran; P. Brázdilová; H. Pivoňková; R. Pohl; M. Fojta; M. Hocek "Aminophenyl- and Nitrophenyl-Labeled Nucleoside Triphosphates: Synthesis, Enzymatic Incorporation, and Electrochemical Detection", *Ange. Chem. Int. Ed.* **2008**, *47*, 2059–2062.

[87] D. A. D. Giusto; W. A. Wlassoff; S. Giesebrecht; J. J. Gooding; G. C. King "Multipotential Electrochemical Detection of Primer Extension Reactions on DNA Self-Assembled Monolayers", *J. Am. Chem. Soc.* **2004**, *126*, 4120–4121.

[88] M. Hocek; M. Fojta "Nucleobase modification as redox DNA labelling for electrochemical detection", *Chem. Soc. Rev.* **2011**, *40*, 5802.

[89] J. N. Wilson; E. T. Kool "Fluorescent DNA base replacements: reporters and sensors for biological systems", *Org. Biomol. Chem* **2006**, *4*, 4265–4274.

[90] S. G. Srivatsan; A. A. Sawant "Fluorescent ribonucleoside analogues as probes for investigating RNA structure and function", *Pure Appl. Chem.* **2010**, *83*, 213–232.

[91] W. Xu; K. M. Chan; E. T. Kool "Fluorescent nucleobases as tools for studying DNA and RNA", *Nat. Chem.* **2017**, *9*, 1043–1055.

[92] A. Podder; H. J. Lee; B. H. Kim "Fluorescent Nucleic Acid Systems for Biosensors", *Bull. Chem. Soc. Jpn.* **2021**, *94*, 1010–1035.

[93] P. R. Callis "Electronic States and Luminescence of Nucleic Acid Systems", *Annu. Rev. Phys. Chem.* **1983**, *34*, 329–357.

[94] C. E. Crespo-Hernández; B. Cohen; P. M. Hare; B. Kohler "Ultrafast Excited-State Dynamics in Nucleic Acids", *Chem. Rev.* **2004**, *104*, 1977–2020.

[95] L. M. Wilhelmsson "Fluorescent nucleic acid base analogues", *Q. Rev. Biophys.* **2010**, *43*, 159–183.

[96] B. Y. Michel; D. Dziuba; R. Benhida; A. P. Demchenko; A. Burger "Probing of Nucleic Acid Structures, Dynamics, and Interactions With Environment-Sensitive Fluorescent Labels", *Front. Chem.* **2020**, *8*, DOI `10.3389/fchem.2020.00112`.

[97] N. Klöcker; F. P. Weissenboeck; A. Rentmeister "Covalent labeling of nucleic acids", *Chem. Soc. Rev.* **2020**, *49*, 8749–8773.

[98] J. R. Lakowicz *Principles of Fluorescence Spectroscopy*, Third Edition, Springer, New York, **2010**.

[99] B. Valeur; M. N. Berberan-Santos *Molecular Fluorescence: Principles and Applications*, second edition, Wiley-VCH, Weinheim, **2013**.

[100] D. Dziuba; P. Didier; S. Ciaco; A. Barth; C. A. M. Seidel; Y. Mély "Fundamental photophysics of isomorphic and expanded fluorescent nucleoside analogues", *Chem. Soc. Rev.* **2021**, *50*, 7062–7107.

[101] D. C. Ward; E. Reich; L. Stryer "Fluorescence Studies of Nucleotides and Polynucleotides", *J. Biol. Chem.* **1969**, *244*, 1228–1237.

[102] O. O. Brovarets'; H. Pérez-Sánchez; D. M. Hovorun "Structural grounds for the 2-aminopurine mutagenicity: a novel insight into the old problem of the replication errors", *RSC Adv.* **2016**, *6*, 99546–99557.

[103] A. Holmén; B. Nordén; B. Albinsson "Electronic Transition Moments of 2-Aminopurine", *J. Am. Chem. Soc.* **1997**, *119*, 3114–3121.

[104] M. A. O'Neil; J. K. Barton "2-Aminopurine: A Probe of Structural Dynamics and Charge Transfer in DNA and DNA:RNA Hybrids", *J. Am. Chem. Soc.* **2002**, *124*, 13053–13066.

[105] S. Lobsiger; S. Blaser; R. K. Sinha; H.-M. Frey; S. Leutwyler "Switching on the fluorescence of 2-aminopurine by site-selective microhydration", *Nat. Chem.* **2014**, *6*, 989–993.

[106] A. C. Jones; R. K. Neely "2-aminopurine as a fluorescent probe of DNA conformation and the DNA–enzyme interface", *Q. Rev. Biophys.* **2015**, *48*, 244–279.

[107] X. Zhao; Z. Zhu; R. Zou; L. Wang; H. Gong; C. Cai "An enzyme-free three-dimensional DNA walker powered by catalytic hairpin assembly for H5N1 DNA ratiometric detection", *Microchem. J.* **2021**, *170*, 106728.

[108] C. Ma; H. Liu; K. Wu; M. Chen; L. Zheng; J. Wang "An Exonuclease I-Based Quencher-Free Fluorescent Method Using DNA Hairpin Probes for Rapid Detection of MicroRNA", *Sens.* **2017**, *17*, 760.

[109] W. Zhou; J. Ding; J. Liu "A highly specific sodium aptamer probed by 2-aminopurine for robust Na+ sensing", *Nucleic Acids Res.* **2016**, gkw845.

[110] M. Li; Y. Sato; S. Nishizawa; T. Seino; K. Nakamura; N. Teramae "2-Aminopurine-Modified Abasic-Site-Containing Duplex DNA for Highly Selective Detection of Theophylline", *J. Am. Chem. Soc.* **2009**, *131*, 2448–2449.

[111] N. B. Gaied "8-vinyl-deoxyadenosine, an alternative fluorescent nucleoside analog to 2'-deoxyribosyl-2-aminopurine with improved properties", *Nucleic Acids Res.* **2005**, *33*, 1031–1039.

[112] A. Nadler; J. Strohmeier; U. Diederichsen "8-Vinyl-2'-deoxyguanosine as a Fluorescent 2'-Deoxyguanosine Mimic for Investigating DNA Hybridization and Topology", *Angew. Chem. Int. Ed.* **2011**, *50*, 5392–5396.

[113] S. Müllar; J. Strohmeier; U. Diederichsen "8-Vinylguanine Nucleo Amino Acid: A Fluorescent PNA Building Block", *Org. Lett.* **2012**, *14*, 1382–1385.

[114] M. E. Hawkins "Fluorescent Pteridine Nucleoside Analogs: A Window on DNA Interactions", *Cell Biochem. Biophys.* **2001**, *34*, 257–281.

[115] K. Wojtuszewski; M. E. Hawkins; J. L. Cole; I. Mukerji "HU Binding to DNA: Evidence for Multiple Complex Formation and DNA Bending", *Biochemistry* **2001**, *40*, 2588–2598.

[116] B. Gildea; L. W. McLaughlin "The synthesis of 2-pyrimidinone nucleosides and their incorporation into oligodeoxynucleotides", *Nucleic Acids Res.* **1989**, *17*, 2261–2281.

[117] S. F. Singleton; F. Shan; M. W. Kanan; C. M. McIntosh; C. J. Stearman; J. S. Helm; K. J. Webb "Facile Synthesis of a Fluorescent Deoxycytidine Analogue Suitable for Probing the RecA Nucleoprotein Filament", *Org. Lett.* **2001**, *3*, 3919–3922.

[118] S. Laland; G. Serck-Hanssen "Synthesis of pyrimidin-2-one deoxyribosides and their ability to support the growth of the deoxyriboside-requiring organism Lactobacillus acidophilus R26", *Biochem. J.* **1964**, *90*, 76–81.

[119] Y. Zhou; P. O. P. Tso "Solid-Phase Synthesis of Oligo-2-Pyrimidinone-2'-Deoxyribonucleotides and Oligo-2-Pyrimidinone-2'-Deoxyriboside Methylphosphonates", *Nucleic Acids Res.* **1996**, *24*, 2652–2659.

[120] G. Ryseck; T. Schmierer; K. Haiser; W. Schreier; W. Zinth; P. Gilch "The Excited-State Decay of 1-Methyl-2(1*H*)-pyrimidinone is an Activated Process", *ChemPhysChem* **2011**, *12*, 1880–1888.

[121] V. Vendrell-Criado; G. M. Rodrıéguez-Muñiz; M. C. Cuquerella; V. Lhiaubet-Vallet; M. A. Miranda "Photosensitization of DNA by 5-Methyl-2-Pyrimidone Deoxyribonucleoside: (6-4) Photoproduct as a Possible Trojan Horse", *Angew. Chem. Int. Ed.* **2013**, *52*, 6476–6479.

[122] H. Yokoyama; R. Mizutani "Structural Biology of DNA (6-4) Photoproducts Formed by Ultraviolet Radiation and Interactions with Their Binding Proteins", *Int. J. Mol. Sci.* **2014**, *15*, 20321–20338.

[123] L. Zhou; X. Cheng; B. Connolly; M. Dickman; P. Hurd; D. Hornby "Zebularine: A Novel DNA Methylation Inhibitor that Forms a Covalent Complex with DNA Methyltransferases", *J. Mol. Biol.* **2002**, *321*, 591–599.

[124] D. Shin; R. W. Sinkeldam; Y. Tor "Emissive RNA Alphabet", *J. Am. Chem. Soc.* **2011**, *133*, 14912–14915.

[125] A. R. Rovira; A. Fin; Y. Tor "Expanding a fluorescent RNA alphabet: synthesis, photophysics and utility of isothiazole-derived purine nucleoside surrogates", *Chem. Sci.* **2017**, *8*, 2983–2993.

[126] L. S. McCoy; D. Shin; Y. Tor "Isomorphic Emissive GTP Surrogate Facilitates Initiation and Elongation of in Vitro Transcription Reactions", *J. Am. Chem. Soc.* **2014**, *136*, 15176–15184.

[127] Y. Li; A. Fin; L. McCoy; Y. Tor "Polymerase-Mediated Site-Specific Incorporation of a Synthetic Fluorescent Isomorphic G Surrogate into RNA", *Angew. Chem. Int. Ed.* **2016**, *56*, 1303–1307.

[128] V. Kilin; K. Gavvala; N. P. F. Barthes; B. Y. Michel; D. Shin; C. Boudier; O. Mauffret; V. Yashchuk; M. Mousli; M. Ruff; F. Granger; S. Eiler; C. Bronner; Y. Tor; A. Burger; Y. Mély "Dynamics of Methylated Cytosine Flipping by UHRF1", *J. Am. Chem. Soc.* **2017**, *139*, 2520–2528.

[129] D. A. Berry; K.-Y. Jung; D. S. Wise; A. D. Sercel; W. H. Pearson; H. Mackie; J. B. Randolph; R. L. Somers "Pyrrolo-dC and pyrrolo-C: fluorescent analogs of cytidine and 2'-deoxycytidine for the study of oligonucleotides", *Tetrahedron Lett.* **2004**, *45*, 2457–2461.

[130] S. J. O. Hardman; S. W. Botchway; K. C. Thompson "Evidence for a Nonbase Stacking Effect for the Environment-sensitive Fluorescent Base Pyrrolocytosine-Comparison with 2-Aminopurine", *Photochem. Photobiol.* **2008**, *84*, 1473–1479.

[131] R. A. Tinsley "Pyrrolo-C as a fluorescent probe for monitoring RNA secondary structure formation", *RNA* **2006**, *12*, 522–529.

[132] S. Taherpour; T. Lönnberg "Fluorescence probing of metal-ion-mediated hybridization of oligonucleotides", *RSC Adv.* **2015**, *5*, 10837–10844.

[133] K.-Y. Lin; R. J. Jones; M. Matteucci "Tricyclic 2'-Deoxycytidine Analogs: Syntheses and Incorporation into Oligodeoxynucleotides Which Have Enhanced Binding to Complementary RNA", *J. Am. Chem. Soc.* **1995**, *117*, 3873–3874.

[134] L. M. Wilhelmsson; P. Sandin; A. Holmén; B. Albinsson; P. Lincoln; B. Nordén "Photophysical Characterization of Fluorescent DNA Base Analogue, tC", *J. Phys. Chem. B* **2003**, *107*, 9094–9101.

[135] P. Sandin; K. Börjesson; H. Li; J. Mårtensson; T. Brown; L. M. Wilhelmsson; B. Albinsson "Characterization and use of an unprecedentedly bright and structurally non-perturbing fluorescent DNA base analogue", *Nucleic Acids Res.* **2007**, *36*, 157–167.

[136] K. Börjesson; S. Preus; A. H. El-Sagheer; T. Brown; B. Albinsson; L. M. Wilhelmsson "Nucleic Acid Base Analog FRET-Pair Facilitating Detailed Structural Measurements in Nucleic Acid Containing Systems", *J. Am. Chem. Soc.* **2009**, *131*, 4288–4293.

[137] A. Okamoto; K. Tainaka; I. Saito "Clear Distinction of Purine Bases on the Complementary Strand by a Fluorescence Change of a Novel Fluorescent Nucleoside", *J. Am. Chem. Soc.* **2003**, *125*, 4972–4973.

[138] A. Okamoto; Y. Saito; I. Saito "Design of base-discriminating fluorescent nucleosides", *J. Photochem. Photobiol. C: Photochem. Rev.* **2005**, *6*, 108–122.

[139] F. Godde; J.-J. Toulmé; S. Moreau "Benzoquinazoli-ne Derivatives as Substitutes for Thymine in Nucleic Acid Complexes. Use of Fluorescence Emission of Benzo[*g*]quinazoline-2,4-(1H*H*,3*H*)-dione in Probing Duplex and Triplex Formation", *Biochemistry* **1998**, *37*, 13765–13775.

[140] H. Liu; J. Gao; L. Maynard; Y. D. Saito; E. T. Kool "Toward a New Genetic System with Expanded Dimensions: Size-Expanded Analogues of Deoxyadenosine and Thymidine", *J. Am. Chem. Soc.* **2004**, *126*, 1102–1109.

[141] J. Gao; H. Liu; E. T. Kool "Expanded-Size Bases in Naturally Sized DNA: Evaluation of Steric Effects in Watson-Crick Pairing", *J. Am. Chem. Soc.* **2004**, *126*, 11826–11831.

[142] A. T. Krueger; E. T. Kool "Fluorescence of Size-Expanded DNA Bases: Reporting on DNA Sequence and Structure with an Unnatural Genetic Set", *J. Am. Chem. Soc.* **2008**, *130*, 3989–3999.

[143] S. K. Jarchow-Choy; A. T. Krueger; H. Liu; J. Gao; E. T. Kool "Fluorescent xDNA nucleotides as efficient substrates for a template-independent polymerase", *Nucleic Acids Res.* **2010**, *39*, 1586–1594.

[144] A. Okamoto; K. Tanaka; T. Fukuta; I. Saito "Design of Base-Discriminating Fluorescent Nucleoside and Its Application to T/C SNP Typing", *J. Am. Chem. Soc.* **2003**, *125*, 9296–9297.

[145] A. Okamoto; K. Tanaka; T. Fukuta; I. Saito "Cytosine Detection by a Fluorescein-Labeled Probe Containing Base-Discriminating Fluorescent Nucleobase", *ChemBioChem* **2004**, *5*, 958–963.

[146] J. R. Barrio; J. A. Secrist; N. J. Leonard "A Fluorescent Analog of Nicotinamide Adenine Dinucleotide", *PNAS* **1972**, *69*, 2039–2042.

[147] G. G. Revich; K. L. Beatitie "Utilization of 1, *N*6-Etheno-2'-deoxyadenosine 5'-triphosphate during DNA synthesis on natural templates, catalyzed by DNA polymerase I of Escherichia coli", *Carcinogenesis* **1986**, *7*, 1569–1576.

[148] M. Kouchakdjian; M. Eisenberg; F. Johnson; A. P. Grollman; D. J. Patel "Structural features of an exocyclic adduct positioned opposite an abasic site in a DNA duplex", *Biochemistry* **1991**, *30*, 3262–3270.

[149] A. P. de Silva; H. Q. N. Gunaratne; T. Gunnlaugsson; A. J. M. Huxley; C. P. McCoy; J. T. Rademacher; T. E. Rice "Signaling Recognition Events with Fluorescent Sensors and Switches", *Chem. Rev.* **1997**, *97*, 1515–1566.

[150] Y. Saito; M. Koda; Y. Shinohara; I. Saito "Synthesis and photophysical properties of 8-arylbutadienyl 2'-deoxyguanosines", *Tetrahedron Lett.* **2011**, *52*, 491–494.

[151] *Fluorescent Analogues of Biomolecular Building Blocks: Design and Applications*, (Eds.: M. Wilhelmsson; Y. Tor), John Wiley & Sons, **2016**.

[152] Y. J. Seo; J. H. Ryu; B. H. Kim "Quencher-Free, End-Stacking Oligonucleotides for Probing Single-Base Mismatches in DNA", *Org. Lett.* **2005**, *7*, 4931–4933.

[153] D. J. Hurley; Y. Tor "Donor/Acceptor Interactions in Systematically Modified RuII-OsII-Oligonucleotides", *J. Am. Chem. Soc.* **2002**, *124*, 13231–13241.

[154] M. Vrábel; P. Horáková; H. Pivoňková; L. Kalachova; H. Černocká; H. Cahová; R. Pohl; P. Šebest; L. Havran; M. Hocek; M. Fojta "Base-Modified DNA Labeled by [Ru(bpy)3]2+ and [Os(bpy)3]2+Complexes: Construction by Polymerase Incorporation of Modified Nucleoside Triphosphates, Electrochemical and Luminescent Properties, and Applications", *Chem. Eur. J* **2008**, *15*, 1144–1154.

[155] K. Ayyavoo; P. Velusamy "Pyrene based materials as fluorescent probes in chemical and biological fields", *New J Chem* **2021**, *45*, 10997–11017.

[156] E. T. Kool "Active Site Tightness and Substrate Fit in DNA Replication", *Annu. Rev. Biochem.* **2002**, *71*, 191–219.

[157] Y. Cho; E. T. Kool "Enzymatic Synthesis of Fluorescent Oligomers Assembled on a DNA Backbone", *ChemBioChem* **2006**, *7*, 669–672.

[158] M. Hollenstein; F. Wojciechowski; C. J. Leumann "Polymerase incorporation of pyrene-nucleoside triphosphates", *Bioorg. Med. Chem. Lett.* **2012**, *22*, 4428–4430.
[159] R. X.-F. Ren; N. C. Chaudhuri; P. L. Paris; Rumney; E. T. Kool "Naphthalene, Phenanthrene, and Pyrene as DNA Base Analogues: Synthesis, Structure, and Fluorescence in DNA", *J. Am. Chem. Soc.* **1996**, *118*, 7671–7678.
[160] T. Ono; S. Wang; C.-K. Koo; L. Engstrom; S. S. David; E. T. Kool "Direct Fluorescence Monitoring of DNA Base Excision Repair", *Angew. Chem. Int. Ed.* **2012**, *51*, 1689–1692.
[161] E. T. Kool "Replacing the Nucleobases in DNA with Designer Molecules", *Acc. Chem. Res.* **2002**, *35*, 936–943.
[162] F. Wojciechowski; J. Lietard; C. J. Leumann "2-Pyrenyl-DNA: Synthesis, Pairing, and Fluorescence Properties", *Org. Lett.* **2012**, *14*, 5176–5179.
[163] L. Zhang; H. Long; G. E. Boldt; K. D. Janda; G. C. Schatz; F. D. Lewis "α- and β-Stilbenosides as base-pair surrogates in DNA hairpins", *Org. Biomol. Chem.* **2006**, *4*, 314–322.
[164] R. S. Coleman; M. L. Madaras "Synthesis of a Novel Coumarin C-Riboside as a Photophysical Probe of Oligonucleotide Dynamics", *J. Org. Chem.* **1998**, *63*, 5700–5703.
[165] H. Morales-Rojas; E. T. Kool "A Porphyrin C-Nucleoside Incorporated into DNA", *Org. Lett* **2002**, *4*, 4377–4380.
[166] L.-A. Fendt; I. Bouamaied; S. Thöni; N. Amiot; E. Stulz "DNA as Supramolecular Scaffold for Porphyrin Arrays on the Nanometer Scale", *J. Am. Chem. Soc.* **2007**, *129*, 15319–15329.
[167] E. B. Brauns; M. L. Madaras; R. S. Coleman; C. J. Murphy; M. A. Berg "Measurement of Local DNA Reorganization on the Picosecond and Nanosecond Time Scales", *J. Am. Chem. Soc.* **1999**, *121*, 11644–11649.
[168] K. Abravaya; J. Huff; R. Marshall; B. Merchant; C. Mullen; G. Schneider; J. Robinson "Molecular Beacons as Diagnostic Tools: Technology and Applications", *Clin. Chem. Lab. Med.* **2003**, *41*, 468–474.
[169] M. F. Fouz; D. H. Appella "PNA Clamping in Nucleic Acid Amplification Protocols to Detect Single Nucleotide Mutations Related to Cancer", *Molecules* **2020**, *25*, 786.
[170] S. Kelley "Single-base mismatch detection based on charge transduction through DNA", *Nucleic Acids Res.* **1999**, *27*, 4830–4837.
[171] A. Okamoto; T. Kamei; I. Saito "DNA Hole Transport on an Electrode: Application to Effective Photoelectrochemical SNP Typing", *J. Am. Chem. Soc.* **2005**, *128*, 658–662.
[172] D. Dodd; R. Hudson "Intrinsically Fluorescent Base-Discriminating Nucleoside Analogs", *Mini Rev. Org. Chem.* **2009**, *6*, 378–391.
[173] R. H. E. Hudson; A. Ghorbani-Choghamarani "Oligodeoxynucleotides incorporating structurally simple 5-alkynyl-2'-deoxyuridines fluorometrically respond to hybridization", *Org. Biomol. Chem.* **2007**, *5*, 1845–1848.
[174] A. A. Beharry; S. Lacoste; T. R. O'Connor; E. T. Kool "Fluorescence Monitoring of the Oxidative Repair of DNA Alkylation Damage by ALKBH3, a Prostate Cancer Marker", *J. Am. Chem. Soc.* **2016**, *138*, 3647–3650.
[175] S. K. Edwards; T. Ono; S. Wang; W. Jiang; R. M. Franzini; J. W. Jung; K. M. Chan; E. T. Kool "In Vitro Fluorogenic Real-Time Assay of the Repair of Oxidative DNA Damage", *ChemBioChem* **2015**, *16*, 1637–1646.
[176] Y. Xu "Formation of the G-quadruplex and i-motif structures in retinoblastoma susceptibility genes (Rb)", *Nucleic Acids Res.* **2006**, *34*, 949–954.

[177] T. Kimura; K. Kawai; M. Fujitsuka; T. Majima "Fluorescence properties of 2-aminopurine in human telomeric DNA", *Chem. Commun.* **2004**, 1438–1439.

[178] T. Kimura; K. Kawai; M. Fujitsuka; T. Majima "Monitoring G-quadruplex structures and G-quadruplex–ligand complex using 2-aminopurine modified oligonucleotides", *Tetrahedron* **2007**, *63*, 3585–3590.

[179] Y. Saito; Y. Miyauchi; A. Okamoto; I. Saito "Synthesis and properties of novel base-discriminating fluorescent (BDF) nucleosides: a highly polarity-sensitive fluorophore for SNP typing", *Tetrahedron Lett.* **2004**, *45*, 7827–7831.

[180] O. P. Schmidt; G. Mata; N. W. Luedtke "Fluorescent Base Analogue Reveals T-HgII-T Base Pairs Have High Kinetic Stabilities That Perturb DNA Metabolism", *J. Am. Chem. Soc.* **2016**, *138*, 14733–14739.

[181] R. A. Mizrahi; D. Shin; R. W. Sinkeldam; K. J. Phelps; A. Fin; D. J. Tantillo; Y. Tor; P. A. Beal "A Fluorescent Adenosine Analogue as a Substrate for an A-to-I RNA Editing Enzyme", *Angew. Chem. Int. Ed.* **2015**, *54*, 8713–8716.

[182] A. Claudio-Montero; I. Pinilla-Macua; P. Fernández-Calotti; C. Sancho-Mateo; M. P. Lostao; D. Colomer; A. Grandas; M. Pastor-Anglada "Fluorescent Nucleoside Derivatives as a Tool for the Detection of Concentrative Nucleoside Transporter Activity Using Confocal Microscopy and Flow Cytometry", *Mol. Pharm.* **2015**, *12*, 2158–2166.

[183] P. Ensslen; H.-A. Wagenknecht "One-Dimensional Multichromophor Arrays Based on DNA: From Self-Assembly to Light-Harvesting", *Acc. Chem. Res.* **2015**, *48*, 2724–2733.

[184] G.-F. Luo; Y. Biniuri; W.-H. Chen; J. Wang; E. Neumann; H.-B. Marjault; R. Nechushtai; M. Winkler; T. Happe; I. Willner "Modelling Photosynthesis with Zn II -Protoporphyrin All-DNA G-Quadruplex/Aptamer Scaffolds", *Angew. Chem. Int. Ed.* **2020**, *59*, 9163–9170.

[185] S. Müller; F. Manger; L. G. von Reventlow; A. Colsmann; H.-A. Wagenknecht "Molecular Chromophore-DNA Architectures With Fullerenes: Optical Properties and Solar Cells", *Front. Chem.* **2021**, *9*, DOI 10.3389/fchem.2021.645006.

[186] M. Nakamura; K. Tsuto; A. Jomura; T. Takada; K. Yamana "Donor-Acceptor Heterojunction Configurations Based on DNA-Multichromophore Arrays", *Chem. Eur. J.* **2015**, *21*, 11788–11792.

[187] Y. N. Teo; E. T. Kool "DNA-Multichromophore Systems", *Chem. Rev.* **2012**, *112*, 4221–4245.

[188] G. Scheibe "Über die Veränderlichkeit der Absorptionsspektren in Lösungen und die Nebenvalenzen als ihre Ursache", *Angew. Chem.* **1937**, *50*, 212–219.

[189] E. E. Jelley "Spectral Absorption and Fluorescence of Dyes in the Molecular State", *Nature* **1936**, *138*, 1009–1010.

[190] M. Kasha; H. R. Rawls; M. A. El-Bayoumi "The exciton model in molecular spectroscopy", *Pure Appl. Chem.* **1965**, *11*, 371–392.

[191] M. Bayda; F. Dumoulin; G. L. Hug; J. Koput; R. Gorniak; A. Wojcik "Fluorescent H-aggregates of an asymmetrically substituted mono-amino Zn(II) phthalocyanine", *Dalton Trans.* **2017**, *46*, 1914–1926.

[192] M. Kasha "Characterization of electronic transitions in complex molecules", *Faraday Discuss.* **1950**, *9*, 14.

[193] U. Rösch; S. Yao; R. Wortmann; F. Würthner "Fluorescent H-Aggregates of Merocyanine Dyes", *Angew. Chem. Int. Ed.* **2006**, *118*, 7184–7188.

[194] A. Eisfeld; J. Briggs "The J- and H-bands of organic dye aggregates", *Chem. Phys.* **2006**, *324*, 376–384.

[195] M. Surin "From nucleobase to DNA templates for precision supramolecular assemblies and synthetic polymers", *Polym. Chem.* **2016**, *7*, 4137–4150.
[196] M. Surin; S. Ulrich "From Interaction to Function in DNA-Templated Supramolecular Self-Assemblies", *ChemistryOpen* **2020**, *9*, 480–498.
[197] T. Kato; H. Kashida; H. Kishida; H. Yada; H. Okamoto; H. Asanuma "Development of a Robust Model System of FRET using Base Surrogates Tethering Fluorophores for Strict Control of Their Position and Orientation within DNA Duplex", *J. Am. Chem. Soc.* **2013**, *135*, 741–750.
[198] S. Hirashima; H. Sugiyama; S. Park "Construction of a FRET System in a Double-Stranded DNA Using Fluorescent Thymidine and Cytidine Analogs", *J. Phys. Chem. B* **2020**, *124*, 8794–8800.
[199] J. Gao; S. Watanabe; E. T. Kool "Modified DNA Analogues That Sense Light Exposure with Color Changes", *J. Am. Chem. Soc.* **2004**, *126*, 12748–12749.
[200] A. Cuppoletti; Y. Cho; J.-S. Park; C. Strässler; E. T. Kool "Oligomeric Fluorescent Labels for DNA", *Bioconjugate Chem.* **2005**, *16*, 528–534.
[201] Y. N. Teo; J. N. Wilson; E. T. Kool "Polyfluorophores on a DNA Backbone: A Multicolor Set of Labels Excited at One Wavelength", *J. Am. Chem. Soc.* **2009**, *131*, 3923–3933.
[202] C. Brotschi; G. Mathis; C. J. Leumann "Bipyridyl- and Biphenyl-DNA: A Recognition Motif Based on Interstrand Aromatic Stacking", *Chem. Eur. J* **2005**, *11*, 1911–1923.
[203] T. J. Matray; E. T. Kool "Selective and Stable DNA Base Pairing without Hydrogen Bonds", *J. Am. Chem. Soc.* **1998**, *120*, 6191–6192.
[204] A. Zahn; C. Brotschi; C. J. Leumann "Pentafluorophenyl-Phenyl Interactions in Biphenyl-DNA", *Chem. Eur. J* **2005**, *11*, 2125–2129.
[205] A. Zahn; C. J. Leumann "Recognition Properties of Donor- and Acceptor-Modified Biphenyl-DNA", *Chem. Eur. J* **2008**, *14*, 1087–1094.
[206] Z. Johar; A. Zahn; C. J. Leumann; B. Jaun "Solution Structure of a DNA Duplex Containing a Biphenyl Pair", *Chem. Eur. J* **2008**, *14*, 1080–1086.
[207] H. Asanuma; K. Shirasuka; T. Takarada; H. Kashida; M. Komiyama "DNA-Dye Conjugates for Controllable H-Aggregation", *J. Am. Chem. Soc.* **2003**, *125*, 2217–2223.
[208] H. Kashida; H. Asanuma; M. Komiyama "Alternating Hetero H Aggregation of Different Dyes by Interstrand Stacking from Two DNA-Dye Conjugates", *Angew. Chem. Int. Ed.* **2004**, *43*, 6522–6525.
[209] H. Kashida; M. Tanaka; S. Baba; T. Sakamoto; G. Kawai; H. Asanuma; M. Komiyama "Covalent Incorporation of Methyl Red Dyes into Double-Stranded DNA for Their Ordered Clustering", *Chem. Eur. J* **2006**, *12*, 777–784.
[210] D. Baumstark; H.-A. Wagenknecht "Perylene Bisimide Dimers as Fluorescent "Glue" for DNA and for Base-Mismatch Detection", *Angew. Chem. Int. Ed.* **2008**, *47*, 2612–2614.
[211] D. Baumstark; H.-A. Wagenknecht "Fluorescent Hydrophobic Zippers inside Duplex DNA: Interstrand Stacking of Perylene-3,4:9,10-tetracarboxylic Acid Bisimides as Artificial DNA Base Dyes", *Chem. Eur. J* **2008**, *14*, 6640–6645.
[212] I. Bouamaied; T. Nguyen; T. Rühl; E. Stulz "Supramolecular helical porphyrin arrays using DNA as a scaffold", *Org. Biomol. Chem.* **2008**, *6*, 3888.
[213] T. Nguyen; A. Brewer; E. Stulz "Duplex Stabilization and Energy Transfer in Zipper Porphyrin-DNA", *Angew. Chem. Int. Ed.* **2009**, *121*, 2008–2011.

[214] E. Mayer-Enthart; H.-A. Wagenknecht "Structure-Sensitive and Self-Assembled Helical Pyrene Array Based on DNA Architecture", *Angew. Chem. Int. Ed.* **2006**, *45*, 3372–3375.

[215] P. Ensslen; F. Brandl; S. Sezi; R. Varghese; R.-J. Kutta; B. Dick; H.-A. Wagenknecht "DNA-Based Oligochromophores as Light-Harvesting Systems", *Chem. Eur. J* **2015**, *21*, 9349–9354.

[216] S. M. Langenegger; R. Häner "Excimer formation by interstrand stacked pyrenes", *Chem. Commun.* **2004**, 2792–2793.

[217] S. Langenegger; R. Häner "The Effect of a Non-nucleosidic Phenanthrene Building Block on DNA Duplex Stability", *Helv. Chim. Acta* **2002**, *85*, 3414–3421.

[218] S. M. Langenegger; R. Häner "A DNA Mimic Made of Non-Nucleosidic Phenanthrene Building Blocks", *ChemBioChem* **2005**, *6*, 2149–2152.

[219] S. M. Langenegger; R. Häner "DNA containing phenanthroline- and phenanthrene-derived, non-nucleosidic base surrogates", *Tetrahedron Lett.* **2004**, *45*, 9273–9276.

[220] R. Häner; F. Samain; V. Malinovskii "DNA-Assisted Self-Assembly of Pyrene Foldamers", *Chem. Eur. J* **2009**, *15*, 5701–5708.

[221] A. N. Glazer in *Methods Enzymol.* Elsevier, **1988**, pp. 291–303.

[222] A. L. Benvin; Y. Creeger; G. W. Fisher; B. Ballou; A. S. Waggoner; B. A. Armitage "Fluorescent DNA Nanotags: Supramolecular Fluorescent Labels Based on Intercalating Dye Arrays Assembled on Nanostructured DNA Templates", *J. Am. Chem. Soc.* **2007**, *129*, 2025–2034.

[223] H. Özhalıcı-Ünal; B. A. Armitage "Fluorescent DNA Nanotags Based on a Self-Assembled DNA Tetrahedron", *ACS Nano* **2009**, *3*, 425–433.

[224] J. L. Seifert; R. E. Connor; S. A. Kushon; M. Wang; B. A. Armitage "Spontaneous Assembly of Helical Cyanine Dye Aggregates on DNA Nanotemplates", *J. Am. Chem. Soc.* **1999**, *121*, 2987–2995.

[225] K. C. Hannah; B. A. Armitage "DNA-Templated Assembly of Helical Cyanine Dye Aggregates: A Supramolecular Chain Polymerization", *Acc. Chem. Res.* **2004**, *37*, 845–853.

[226] K. C. Hannah; R. R. Gil; B. A. Armitage "1H NMR and Optical Spectroscopic Investigation of the Sequence-Dependent Dimerization of a Symmetrical Cyanine Dye in the DNA Minor Groove", *Biochemistry* **2005**, *44*, 15924–15929.

[227] M. Wang; G. L. Silva; B. A. Armitage "DNA-Templated Formation of a Helical Cyanine Dye J-Aggregate", *J. Am. Chem. Soc.* **2000**, *122*, 9977–9986.

[228] S. Müller; Y. Fritz; H.-A. Wagenknecht "Control of Energy Transfer Between Pyrene- and Perylene-Nucleosides by the Sequence of DNA-Templated Supramolecular Assemblies", *ChemistryOpen* **2020**, *9*, 389–392.

[229] G. Sargsyan; A. A. Schatz; J. Kubelka; M. Balaz "Formation and helicity control of ssDNA templated porphyrin nanoassemblies", *Chem. Commun.* **2013**, *49*, 1020–1022.

[230] P. G. A. Janssen; J. Vandenbergh; J. L. J. van Dongen; E. W. Meijer; A. P. H. J. Schenning "ssDNA Templated Self-Assembly of Chromophores", *J. Am. Chem. Soc.* **2007**, *129*, 6078–6079.

[231] S. Sezi; H.-A. Wagenknecht "DNA-templated formation of fluorescent self-assembly of ethynyl pyrenes", *Chem. Commun.* **2013**, *49*, 9257.

[232] P. Ensslen; Y. Fritz; H.-A. Wagenknecht "Mixed non-covalent assemblies of ethynyl nile red and ethynyl pyrene along oligonucleotide templates", *Org. Biomol. Chem.* **2015**, *13*, 487–492.

[233] R. Hofsäß; S. Sinn; F. Biedermann; H.-A. Wagenknecht "Programmable and Sequence-Selective Supramolecular Assembly of Two Different Chromophores along DNA Templates", *Chem. Eur. J* **2018**, *24*, 16257–16261.

[234] P. Ensslen; S. Gärtner; K. Glaser; A. Colsmann; H.-A. Wagenknecht "A DNA-Fullerene Conjugate as a Template for Supramolecular Chromophore Assemblies: Towards DNA-Based Solar Cells", *Angew. Chem. Int. Ed.* **2015**, *55*, 1904–1908.

[235] M. V. Ishutkina; A. R. Berry; R. Hussain; O. G. Khelevina; G. Siligardi; E. Stulz "Self-Assembled Porphyrazine Nucleosides on DNA Templates: Highly Fluorescent Chromophore Arrays and Sizing Forensic Tandem Repeat Sequences", *Eur. J. Org. Chem.* **2018**, *2018*, 5054–5059.

[236] P. Janssen; J. van Dongen; E. Meijer; A. Schenning "Electrospray-Ionization Mass Spectrometry for Screening the Specificity and Stability of Single-Stranded-DNA Templated Self-Assemblies", *Chem. Eur. J* **2008**, *15*, 352–360.

[237] P. G. A. Janssen; S. Jabbari-Farouji; M. Surin; X. Vila; J. C. Gielen; T. F. A. de Greef; M. R. J. Vos; P. H. H. Bomans; N. A. J. M. Sommerdijk; P. C. M. Christianen; P. Leclère; R. Lazzaroni; P. van der Schoot; E. W. Meijer; A. P. H. J. Schenning "Insights into Templated Supramolecular Polymerization: Binding of Naphthalene Derivatives to ssDNA Templates of Different Lengths", *J. Am. Chem. Soc.* **2008**, *131*, 1222–1231.

[238] M. Surin; P. G. A. Janssen; R. Lazzaroni; P. Leclère; E. W. Meijer; A. P. H. J. Schenning "Supramolecular Organization of ssDNA-Templated π-Conjugated Oligomers via Hydrogen Bonding", *Adv. Mater.* **2009**, *21*, 1126–1130.

[239] P. Janssen; A. Ruiz-Carretero; D. González-Rodrıéguez; E. Meijer; A. Schenning "pH-Switchable Helicity of DNA-Templated Assemblies", *Angew. Chem. Int. Ed.* **2009**, *48*, 8103–8106.

[240] P. G. A. Janssen; N. J. M. Brankaert; X. Vila; A. P. H. J. Schenning "ssDNA templated assembly of oligonucleotides and bivalent naphthalene guests", *Soft Matter* **2010**, *6*, 1494.

[241] Z. Guo; I. D. Cat; B. V. Averbeke; J. Lin; G. Wang; H. Xu; R. Lazzaroni; D. Beljonne; E. W. Meijer; A. P. H. J. Schenning; S. D. Feyter "Nucleoside-Assisted Self-Assembly of Oligo(p-phenylenevinylene)s at Liquid/Solid Interface: Chirality and Nanostructures", *J. Am. Chem. Soc.* **2011**, *133*, 17764–17771.

[242] A. de la Escosura; P. Janssen; A. Schenning; R. Nolte; J. Cornelissen "Encapsulation of DNA-Templated Chromophore Assemblies within Virus Protein Nanotubes", *Angew. Chem. Int. Ed.* **2010**, *49*, 5335–5338.

[243] P. G. A. Janssen; N. Meeuwenoord; G. van der Marel; S. Jabbari-Farouji; P. van der Schoot; M. Surin; Ž. Tomović; E. W. Meijer; A. P. H. J. Schenning "ssPNA templated assembly of oligo(p-phenylenevinylene)s", *Chem. Commun.* **2010**, *46*, 109–111.

[244] A. L. Stevens; P. G. A. Janssen; A. Ruiz-Carretero; M. Surin; A. P. H. J. Schenning; L. M. Herz "Energy Transfer in Single-Stranded DNA-Templated Stacks of Naphthalene Chromophores", *J. Phys. Chem. C* **2011**, *115*, 10550–10560.

[245] O. Shimomura; F. H. Johnson; Y. Saiga "Extraction, Purification and Properties of Aequorin, a Bioluminescent Protein from the Luminous Hydromedusan,Aequorea", *J. Cell. Physiol.* **1962**, *59*, 223–239.

[246] M. Pertea "The Human Transcriptome: An Unfinished Story", *Genes* **2012**, *3*, 344–360.

[247] C. Tuerk; L. Gold "Systematic evolution of ligands by exponential enrichment: RNA ligands to bacteriophage T4 DNA polymerase", *Science* **1990**, *249*, 505–510.

[248] A. S. Klymchenko "Solvatochromic and Fluorogenic Dyes as Environment-Sensitive Probes: Design and Biological Applications", *Acc. Chem. Res.* **2017**, *50*, 366–375.
[249] D. Grate; C. Wilson "Laser-mediated, site-specific inactivation of RNA transcripts", *PNAS* **1999**, *96*, 6131–6136.
[250] L. Truong; A. R. Ferré-D'Amaré "From fluorescent proteins to fluorogenic RNAs: Tools for imaging cellular macromolecules", *Protein Sci.* **2019**, *28*, 1374–1386.
[251] J. S. Paige; K. Y. Wu; S. R. Jaffrey "RNA Mimics of Green Fluorescent Protein", *Science* **2011**, *333*, 642–646.
[252] K. D. Warner; M. C. Chen; W. Song; R. L. Strack; A. Thorn; S. R. Jaffrey; A. R. Ferré-D'Amaré "Structural basis for activity of highly efficient RNA mimics of green fluorescent protein", *Nat. Struct. Mol. Biol.* **2014**, *21*, 658–663.
[253] H. Huang; N. B. Suslov; N.-S. Li; S. A. Shelke; M. E. Evans; Y. Koldobskaya; P. A. Rice; J. A. Piccirilli "A G-quadruplex–containing RNA activates fluorescence in a GFP-like fluorophore", *Nat. Chem. Biol.* **2014**, *10*, 686–691.
[254] G. S. Filonov; J. D. Moon; N. Svensen; S. R. Jaffrey "Broccoli: Rapid Selection of an RNA Mimic of Green Fluorescent Protein by Fluorescence-Based Selection and Directed Evolution", *J. Am. Chem. Soc.* **2014**, *136*, 16299–16308.
[255] W. Song; G. S. Filonov; H. Kim; M. Hirsch; X. Li; J. D. Moon; S. R. Jaffrey "Imaging RNA polymerase III transcription using a photostable RNA–fluorophore complex", *Nat. Chem. Biol.* **2017**, *13*, 1187–1194.
[256] L. Sjekloća; A. R. Ferré-D'Amaré "Binding between G Quadruplexes at the Homodimer Interface of the Corn RNA Aptamer Strongly Activates Thioflavin T Fluorescence", *Cell Chem. Biol.* **2019**, *26*, 1159–1168.e4.
[257] C. Steinmetzger; N. Palanisamy; K. R. Gore; C. Höbartner "A Multicolor Large Stokes Shift Fluorogen-Activating RNA Aptamer with Cationic Chromophores", *Chem. Eur. J* **2019**, *25*, 1931–1935.
[258] C. Steinmetzger; I. Bessi; A.-K. Lenz; C. Höbartner "Structure–fluorescence activation relationships of a large Stokes shift fluorogenic RNA aptamer", *Nucleic Acids Res.* **2019**, *47*, 11538–11550.
[259] M. Mieczkowski; C. Steinmetzger; I. Bessi; A.-K. Lenz; A. Schmiedel; M. Holzapfel; C. Lambert; V. Pena; C. Höbartner "Large Stokes shift fluorescence activation in an RNA aptamer by intermolecular proton transfer to guanine", *Nat. Commun.* **2021**, *12*, 3549–3559.
[260] E. V. Dolgosheina; S. C. Y. Jeng; S. S. S. Panchapakesan; R. Cojocaru; P. S. K. Chen; P. D. Wilson; N. Hawkins; P. A. Wiggins; P. J. Unrau "RNA Mango Aptamer-Fluorophore: A Bright, High-Affinity Complex for RNA Labeling and Tracking", *ACS Chem. Biol.* **2014**, *9*, 2412–2420.
[261] A. Autour; S. C. Y. Jeng; A. D. Cawte; A. Abdolahzadeh; A. Galli; S. S. S. Panchapakesan; D. Rueda; M. Ryckelynck; P. J. Unrau "Fluorogenic RNA Mango aptamers for imaging small non-coding RNAs in mammalian cells", *Nat. Commun.* **2018**, *9*, 656.
[262] R. J. Trachman; A. Abdolahzadeh; A. Andreoni; R. Cojocaru; J. R. Knutson; M. Ryckelynck; P. J. Unrau; A. R. Ferré-D'Amaré "Crystal Structures of the Mango-II RNA Aptamer Reveal Heterogeneous Fluorophore Binding and Guide Engineering of Variants with Improved Selectivity and Brightness", *Biochemistry* **2018**, *57*, 3544–3548.
[263] R. J. Trachman; A. Autour; S. C. Y. Jeng; A. Abdolahzadeh; A. Andreoni; R. Cojocaru; R. Garipov; E. V. Dolgosheina; J. R. Knutson; M. Ryckelynck; P. J. Unrau; A. R. Ferré-D'Amaré "Structure and functional reselection of the Mango-III fluorogenic RNA aptamer", *Nat. Chem. Biol.* **2019**, *15*, 472–479.

[264] X. Chen; D. Zhang; N. Su; B. Bao; X. Xie; F. Zuo; L. Yang; H. Wang; L. Jiang; Q. Lin; M. Fang; N. Li; X. Hua; Z. Chen; C. Bao; J. Xu; W. Du; L. Zhang; Y. Zhao; L. Zhu; J. Loscalzo; Y. Yang "Visualizing RNA dynamics in live cells with bright and stable fluorescent RNAs", *Nat. Biotechnol.* **2019**, *37*, 1287–1293.

[265] K. Huang; X. Chen; C. Li; Q. Song; H. Li; L. Zhu; Y. Yang; A. Ren "Structure-based investigation of fluorogenic Pepper aptamer", *Nat. Chem. Biol.* **2021**, 1289–1295.

[266] X. Tan; T. P. Constantin; K. L. Sloane; A. S. Waggoner; M. P. Bruchez; B. A. Armitage "Fluoromodules Consisting of a Promiscuous RNA Aptamer and Red or Blue Fluorogenic Cyanine Dyes: Selection, Characterization, and Bioimaging", *J. Am. Chem. Soc.* **2017**, *139*, 9001–9009.

[267] S. A. Shelke; Y. Shao; A. Laski; D. Koirala; B. P. Weissman; J. R. Fuller; X. Tan; T. P. Constantin; A. S. Waggoner; M. P. Bruchez; B. A. Armitage; J. A. Piccirilli "Structural basis for activation of fluorogenic dyes by an RNA aptamer lacking a G-quadruplex motif", *Nat. Commun.* **2018**, *9*, 4542.

[268] D. M. Shcherbakova; M. A. Hink; L. Joosen; T. W. J. Gadella; V. V. Verkhusha "An Orange Fluorescent Protein with a Large Stokes Shift for Single-Excitation Multicolor FCCS and FRET Imaging", *J. Am. Chem. Soc.* **2012**, *134*, 7913–7923.

[269] K. D. Piatkevich; J. Hulit; O. M. Subach; B. Wu; A. Abdulla; J. E. Segall; V. V. Verkhusha "Monomeric red fluorescent proteins with a large Stokes shift", *PNAS* **2010**, *107*, 5369–5374.

[270] C. Steinmetzger; C. Bäuerlein; C. Höbartner "Supramolecular Fluorescence Resonance Energy Transfer in Nucleobase-Modified Fluorogenic RNA Aptamers", *Angew. Chem. Int. Ed.* **2020**, *59*, 6760–6764.

[271] A. A. Ishchenko "Laser media based on polymethine dyes", *Quantum Elec.* **1994**, *24*, 471–492.

[272] X. Ma; J. Hua; W. Wu; Y. Jin; F. Meng; W. Zhan; H. Tian "A high-efficiency cyanine dye for dye-sensitized solar cells", *Tetrahedron* **2008**, *64*, 345–350.

[273] M. Levitus; S. Ranjit "Cyanine dyes in biophysical research: the photophysics of polymethine fluorescent dyes in biomolecular environments", *Q. Rev. Biophys.* **2010**, *44*, 123–151.

[274] H. Shindy "Basics, Mechanisms and Properties in the Chemistry of Cyanine Dyes: A Review Paper", *Mini Rev Org Chem* **2012**, *9*, 352–360.

[275] V. Z. Shirinian; A. A. Shimkin in *Top Heterocycl Chem*, Springer Berlin Heidelberg, pp. 75–105.

[276] V. F. Traven; V. S. Miroshnikov; T. A. Chibisova; V. A. Barachevsky; O. V. Venidiktova; Y. P. Strokach "Synthesis and structure of indoline spiropyrans of the coumarin series", *Russ. Chem. Bull.* **2005**, *54*, 2417–2424.

[277] Y. Kovtun "Metallochromic merocyanines of 8-hydroxyquinoline series. II. Dyes with end nuclei of low basicity", *Dyes Pigm.* **2004**, *60*, 215–221.

[278] J. Wang; W.-F. Cao; J.-H. Su; H. Tian; Y.-H. Huang; Z.-R. Sun "Syntheses and nonlinear absorption of novel unsymmetrical cyanines", *Dyes Pigm.* **2003**, *57*, 171–179.

[279] F. Würthner; S. Yao "Merocyanine Dyes Containing Imide Functional Groups: Synthesis and Studies on Hydrogen Bonding to Melamine Receptors", *J. Org. Chem.* **2003**, *68*, 8943–8949.

[280] A. J. Kay; A. D. Woolhouse; G. J. Gainsford; T. G. Haskell; T. H. Barnes; I. T. McKinnie; C. P. Wyss "A simple, novel method for the preparation of polymer-tetherable, zwitterionic merocyanine NLO-chromophores", *J. Mater. Chem.* **2001**, *11*, 996–1002.

[281] S. Yao; U. Beginn; T. Gress; M. Lysetska; F. Würthner "Supramolecular Polymerization and Gel Formation of Bis(Merocyanine) Dyes Driven by Dipolar Aggregation", *J. Am. Chem. Soc.* **2004**, *126*, 8336–8348.

[282] F. Würthner "DMF in Acetic Anhydride: A Useful Reagent for Multiple-Component Syntheses of Merocyanine Dyes", *Synthesis* **1999**, *1999*, 2103–2113.

[283] S. Yagai; M. Higashi; T. Karatsu; A. Kitamura "Binary Supramolecular Gels Based on Bismelamine·Cyanurate/Barbiturate Noncovalent Polymers", *Chem. Mater.* **2004**, *16*, 3582–3585.

[284] S. Seifert; A. Seifert; G. Brunklaus; K. Hofmann; T. Rüffer; H. Lang; S. Spange "Probing the surface polarity of inorganic oxides using merocyanine-type dyes derived from barbituric acid", *New J. Chem.* **2012**, *36*, 674–684.

[285] R. Schmidt; S. Uemura; F. Würthner "Solvent- and Guest-Responsive Self-Assembly of Hamilton Receptor Tethered Bis(merocyanine) Dyes", *Chem. Eur. J.* **2010**, *16*, 13706–13715.

[286] R. Schmidt; M. Stolte; M. Grüne; F. Würthner "Hydrogen-Bond-Directed Formation of Supramolecular Polymers Incorporating Head-to-Tail Oriented Dipolar Merocyanine Dyes", *Macromolecules* **2011**, *44*, 3766–3776.

[287] A. A. Ishchenko; A. V. Kulinich "The unusual solvatochromism and solvatofluorochromism of longwave absorbing and emitting barbiturate merocyanine dyes", *Methods Appl. Fluoresc.* **2016**, *4*, 034001.

[288] B. J. Cafferty; D. M. Fialho; J. Khanam; R. Krishnamurthy; N. V. Hud "Spontaneous formation and base pairing of plausible prebiotic nucleotides in water", *Nat. Commun.* **2016**, *7*, 11328.

[289] C. V. Mungi; S. K. Singh; J. Chugh; S. Rajamani "Synthesis of barbituric acid containing nucleotides and their implications for the origin of primitive informational polymers", *Phys. Chem. Chem. Phys.* **2016**, *18*, 20144–20152.

[290] A. V. Kulinich; N. A. Derevyanko; A. A. Ishchenko "Synthesis, structure, and solvatochromism of merocyanine dyes based on barbituric acid", *Russ. J. Gen. Chem.* **2006**, *76*, 1441–1457.

[291] A. A. Ishchenko; A. V. Kulinich; S. L. Bondarev; V. N. Knyukshto "Structure and fluorescence properties of merocyanine dyes derived from dimethylbarbituric acid", *Russ. J. Gen. Chem.* **2007**, *77*, 1787–1798.

[292] A. V. Kulinich; N. A. Derevyanko; A. A. Ishchenko; N. B. Gusyak; I. M. Kobasa; P. P. Romańczyk; S. S. Kurek "Structure and redox properties of polymethine dyes: Electrochemical and DFT/TD-DFT study", *Dyes Pigm.* **2019**, *161*, 24–33.

[293] A. L. Stadler; B. R. Renikuntla; D. Yaron; A. S. Fang; B. A. Armitage "Substituent Effects on the Assembly of Helical Cyanine Dye Aggregates in the Minor Groove of a DNA Template", *Langmuir* **2010**, *27*, 1472–1479.

[294] A. Nano; A. N. Boynton; J. K. Barton "A Rhodium-Cyanine Fluorescent Probe: Detection and Signaling of Mismatches in DNA", *J. Am. Chem. Soc.* **2017**, *139*, 17301–17304.

[295] M. Henary; S. Paranjpe; E. A. Owens "Synthesis and applications of benzothiazole containing cyanine dyes", *Heterocycl. Commun.* **2013**, *19*, 1–11.

[296] X. Song; H. Bian; C. Wang; M. Hu; N. Li; Y. Xiao "Development and applications of a near-infrared dye–benzylguanine conjugate to specifically label SNAP-tagged proteins", *Org. Biomol. Chem.* **2017**, *15*, 8091–8101.

[297] N. A. Pianovich; M. Dean; A. Lassak; K. Reiss; B. S. Jursic "Anticancer potential of aminomethylidene-diazinanes I. Synthesis of arylaminomethylidene of diazinetriones

and its cytotoxic effects tested in glioblastoma cells", *Bioorg. Med. Chem.* **2017**, *25*, 5068–5076.

[298] Y.-C. Jeong; M. Moloney "Antibacterial Barbituric Acid Analogues Inspired from Natural 3-Acyltetramic Acids' Synthesis, Tautomerism and Structure and Physicochemical Property-Antibacterial Activity Relationships", *Molecules* **2015**, *20*, 3582–3627.

[299] J. O. Morley; R. M. Morley; A. L. Fitton "Spectroscopic Studies on Brooker's Merocyanine", *J. Am. Chem. Soc.* **1998**, *120*, 11479–11488.

[300] U. Steiner; M. H. Abdel-Kader; P. Fischer; H. E. A. Kramer "Photochemical cis/trans isomerization of a stilbazolium betaine. A protolytic/photochemical reaction cycle", *J. Am. Chem. Soc.* **1978**, *100*, 3190–3197.

[301] J. Catalan; E. Mena; W. Meutermans; J. Elguero "Solvatochromism of a typical merocyanine: stilbazolium betaine and its 2,6-di-tert-butyl derivative", *J. Phy. Chem.* **1992**, *96*, 3615–3621.

[302] W. Leng; F. Würthner; A. M. Kelley "Solvent-Dependent Vibrational Frequencies and Reorganization Energies of Two Merocyanine Chromophores", *J. Phys. Chem. A* **2005**, *109*, 1570–1575.

[303] P.-A. Bouit; C. Aronica; L. Toupet; B. L. Guennic; C. Andraud; O. Maury "Continuous Symmetry Breaking Induced by Ion Pairing Effect in Heptamethine Cyanine Dyes: Beyond the Cyanine Limit", *J. Am. Chem. Soc.* **2010**, *132*, 4328–4335.

[304] A. V. Kulinich; E. K. Mikitenko; A. A. Ishchenko "Scope of negative solvatochromism and solvatofluorochromism of merocyanines", *Phys. Chem. Chem. Phys.* **2016**, *18*, 3444–3453.

[305] G. Pepe; J. M. Cole; P. G. Waddell; S. McKechnie "Molecular engineering of cyanine dyes to design a panchromatic response in co-sensitized dye-sensitized solar cells", *MSDE* **2016**, *1*, 86–98.

[306] R. Pei; J. Rothman; Y. Xie; M. N. Stojanovic "Light-up properties of complexes between thiazole orange-small molecule conjugates and aptamers", *Nucleic Acids Res.* **2009**, *37*, e59–e59.

[307] J. R. Rumble *CRC Handbook of Chemistry and Physics*, *Vol. 99*, Taylor and Francis, **2018**.

[308] A. Toutchkine; V. Kraynov; K. Hahn "Solvent-Sensitive Dyes to Report Protein Conformational Changes in Living Cells", *J. Am. Chem. Soc.* **2003**, *125*, 4132–4145.

[309] A. Megia-Fernandez; M. Klausen; B. Mills; G. E. Brown; H. McEwan; N. Finlayson; K. Dhaliwal; M. Bradley "Red-Shifted Environmental Fluorophores and Their Use for the Detection of Gram-Negative Bacteria", *Chemosensors* **2021**, *9*, 117.

[310] F. Neese; F. Wennmohs; U. Becker; C. Riplinger "The ORCA quantum chemistry program package", *J. Chem. Phys.* **2020**, *152*, 224108.

[311] C. Lee; W. Yang; R. G. Parr "Development of the Colle-Salvetti correlation-energy formula into a functional of the electron density", *Phys. Rev. B* **1988**, *37*, 785–789.

[312] A. D. Becke "Density-functional thermochemistry. III. The role of exact exchange", *J. Chem. Phys.* **1993**, *98*, 5648–5652.

[313] F. Weigend; R. Ahlrichs "Balanced basis sets of split valence, triple zeta valence and quadruple zeta valence quality for H to Rn: Design and assessment of accuracy", *Phys. Chem. Chem. Phys.* **2005**, *7*, 3297.

[314] T. Lu; F. Chen "Multiwfn: A multifunctional wavefunction analyzer", *J. Comput. Chem.* **2011**, *33*, 580–592.

[315] T. Lu; F. Chen "Quantitative analysis of molecular surface based on improved Marching Tetrahedra algorithm", *J. Mol. Graph. Model.* **2012**, *38*, 314–323.

[316] J. Zhang "libreta: Computerized Optimization and Code Synthesis for Electron Repulsion Integral Evaluation", *J. Chem. Theory Comput.* **2018**, *14*, 572–587.
[317] J.-W. Yan; W.-J. Ye; S.-B. Chen; W.-B. Wu; J.-Q. Hou; T.-M. Ou; J.-H. Tan; D. Li; L.-Q. Gu; Z.-S. Huang "Development of a Universal Colorimetric Indicator for G-Quadruplex Structures by the Fusion of Thiazole Orange and Isaindigotone Skeleton", *Anal. Chem.* **2012**, *84*, 6288–6292.
[318] W. Koenigs; E. Knorr "Ueber einige Derivate des Traubenzuckers und der Galactose", *Chem. Ber.* **1901**, *34*, 957–981.
[319] E. Fischer "Synthese neuer Glucoside", *Chem. Ber.* **1914**, *47*, 1377–1393.
[320] G. E. Hilbert; T. B. Johnson "Researches on pyrimidines. CXVII. A method for the synthesis of nucleosides", *J. Am. Chem. Soc.* **1930**, *52*, 4489–4494.
[321] U. Niedballa; H. Vorbrueggen "Synthesis of nucleosides. 9. General synthesis of *N*-glycosides. I. Synthesis of pyrimidine nucleosides", *J. Org. Chem.* **1974**, *39*, 3654–3660.
[322] H. Vorbrüggen; B. Bennua "Nucleoside syntheses, XXV1) A new simplified nucleoside synthesis", *Chem. Ber.* **1981**, *114*, 1279–1286.
[323] C. Liang; W. Ju; S. Ding; H. Sun; G. Mao "Effective Synthesis of Nucleosides Utilizing *O*-Acetyl-Glycosyl Chlorides as Glycosyl Donors in the Absence of Catalyst: Mechanism Revision and Application to Silyl-Hilbert-Johnson Reaction", *Molecules* **2017**, *22*, 84.
[324] M. W. Winkley; R. K. Robins "Pyrimidine nucleosides. Part II. The direct glycosidation of 2,6-di-substituted 4-pyrimidones", *J. Chem. Soc. C* **1969**, 791.
[325] M. R. Harnden; R. L. Jarvest "Synthesis of Analogues of Ribosylbarbituric Acid", *Nucleosides and Nucleotides* **1985**, *4*, 465–476.
[326] H. L. Levine; R. S. Brody; F. H. Westheimer "Inhibition of orotidine-5'-phosphate decarboxylase by 1-(5'-phospho-β-D-ribofuranosyl)barbituric acid, 6-azauridine 5'-phosphate, and uridine 5'-phosphate", *Biochemistry* **1980**, *19*, 4993–4999.
[327] C. Hu; Z. Chen; H. Xiao; Z. Zhen; X. Liu; S. Bo "Synthesis and characterization of a novel indoline based nonlinear optical chromophore with excellent electro-optic activity and high thermal stability by modifying the π-conjugated bridges", *J. Mater. Chem. C* **2017**, *5*, 5111–5118.
[328] T. Yanai; D. P. Tew; N. C. Handy "A new hybrid exchange–correlation functional using the Coulomb-attenuating method (CAM-B3LYP)", *Chem. Phys. Lett.* **2004**, *393*, 51–57.
[329] M. J. Frisch; G. W. Trucks; H. B. Schlegel; G. E. Scuseria; M. A. Robb; J. R. Cheeseman; G. Scalmani; V. Barone; G. A. Petersson; H. Nakatsuji; X. Li; M. Caricato; A. V. Marenich; J. Bloino; B. G. Janesko; R. Gomperts; B. Mennucci; H. P. Hratchian; J. V. Ortiz; A. F. Izmaylov; J. L. Sonnenberg; D. Williams-Young; F. Ding; F. Lipparini; F. Egidi; J. Goings; B. Peng; A. Petrone; T. Henderson; D. Ranasinghe; V. G. Zakrzewski; J. Gao; N. Rega; G. Zheng; W. Liang; M. Hada; M. Ehara; K. Toyota; R. Fukuda; J. Hasegawa; M. Ishida; T. Nakajima; Y. Honda; O. Kitao; H. Nakai; T. Vreven; K. Throssell; J. A. Montgomery, Jr.; J. E. Peralta; F. Ogliaro; M. J. Bearpark; J. J. Heyd; E. N. Brothers; K. N. Kudin; V. N. Staroverov; T. A. Keith; R. Kobayashi; J. Normand; K. Raghavachari; A. P. Rendell; J. C. Burant; S. S. Iyengar; J. Tomasi; M. Cossi; J. M. Millam; M. Klene; C. Adamo; R. Cammi; J. W. Ochterski; R. L. Martin; K. Morokuma; O. Farkas; J. B. Foresman; D. J. Fox Gaussian 09, Revision D.01, Gaussian Inc. Wallingford CT.
[330] H. Mustroph "Merocyanine dyes", *Phys. Sci. Rev.* **2021**, *0*, DOI 10.1515/psr-2020-0145.

[331] S. L. Bondarev; V. N. Knyukshto; A. A. Turban; A. A. Ishchenko; A. V. Kulinich "Effect of the polymethine chain length, the polarity and temperature of the medium on the spectroscopic properties of merocyanine dyes", *J. Appl. Spectrosc.* **2006**, *73*, 25–34.
[332] M.-C. Chen; D.-G. Chen; P.-T. Chou "Fluorescent Chromophores Containing the Nitro Group: Relatively Unexplored Emissive Properties", *ChemPlusChem* **2020**, *86*, 11–27.
[333] S. K. Panja; N. Dwivedi; S. Saha "Tuning the intramolecular charge transfer (ICT) process in push–pull systems: effect of nitro groups", *RSC Advances* **2016**, *6*, 105786–105794.
[334] J. P. Zobel; J. J. Nogueira; L. González "Mechanism of Ultrafast Intersystem Crossing in 2-Nitronaphthalene", *Chem. Eur. J.* **2018**, *24*, 5379–5387.
[335] S. Beaucage; M. Caruthers "Deoxynucleoside phosphoramidites – A new class of key intermediates for deoxypolynucleotide synthesis", *Tetrahedron Lett.* **1981**, *22*, 1859–1862.
[336] M. D. Matteucci; M. H. Caruthers "Synthesis of deoxyoligonucleotides on a polymer support", *J. Am. Chem. Soc.* **1981**, *103*, 3185–3191.
[337] H. Vu; C. McCollum; K. Jacobson; P. Theisen; R. Vinayak; E. Spiess; A. Andrus "Fast oligonucleotide deprotection phosphoramidite chemistry for DNA synthesis", *Tetrahedron Lett.* **1990**, *31*, 7269–7272.
[338] J. Boal "Cleavage of oligodeoxyribonucleotides from controlled-pore glass supports and their rapid deprotection by gaseous amines", *Nucl. Acids Res.* **1996**, *24*, 3115–3117.
[339] A. Stutz; S. Pitsch "Automated RNA-Synthesis with Photocleavable Sugar and Nucleobase Protecting Groups", *Synlett* **1999**, *1999*, 930–934.
[340] A. Stutz; C. Höbartner; S. Pitsch "Novel Fluoride-Labile Nucleobase-Protecting Groups for the Synthesis of 3'(2')-*O*-Aminoacylated RNA Sequences", *Helv. Chim. Acta* **2000**, *83*, 2477–2503.
[341] S. L. Beaucage; M. H. Caruthers "Synthetic Strategies and Parameters Involved in the Synthesis of Oligodeoxyribonucleotides According to the Phosphoramidite Method", *Curr Protoc Nucleic Acid Chem* **2000**, *00*, Chapter 3, Unit 3.3.
[342] M. Oivanen; S. Kuusela; H. Lönnberg "Kinetics and Mechanisms for the Cleavage and Isomerization of the Phosphodiester Bonds of RNA by Brønsted Acids and Bases", *Chem. Rev.* **1998**, *98*, 961–990.
[343] Á. Somoza "Protecting groups for RNA synthesis: an increasing need for selective preparative methods", *Chem. Soc. Rev.* **2008**, *37*, 2668.
[344] S. Pitsch; P. Weiss; L. Jenny; A. Stutz; X. Wu "Reliable Chemical Synthesis of Oligoribonucleotides (RNA) with 2'-*O*-[(Triisopropylsilyl)oxy]methyl(2'-*O*-tom)-Protected Phosphoramidites", *Helv. Chim. Acta* **2001**, *84*, 3773–3795.
[345] K. K. Ogilvie; G. H. Hakimelahi; Z. A. Proba; N. Usman "Conversion of ribonucleosides to protected 3'-deoxynucleosides", *Tetrahedron Lett.* **1983**, *24*, 865–868.
[346] C. Höbartner; F. Wachowius in (Ed.: G. Mayer), John Wiley and Sons, **2010**, Chapter Chemical Synthesis of Modified RNA, pp. 1–37.
[347] R. Eritja "Solid-Phase Synthesis of Modified Oligonucleotides", *Int. J. Pept. Res. Ther.* **2006**, *13*, 53–68.
[348] A. A. Rodriguez; I. Cedillo; B. P. Mowery; H. J. Gaus; S. S. Krishnamoorthy; A. K. McPherson "Formation of the *N*2-acetyl-2,6-diaminopurine oligonucleotide impurity caused by acetyl capping", *Bioorganic Med. Chem. Lett.* **2014**, *24*, 3243–3246.
[349] G. E. Plum "Optical Methods", *Curr. Protoc. Nucleic Acid Chem.* **2000**, 7.3.1–7.3.17.
[350] J.-L. Mergny; L. Lacroix "Analysis of Thermal Melting Curves", *Oligonucleotides* **2003**, *13*, 515–537.

[351] T. Xia; J. SantaLucia; M. E. Burkard; R. Kierzek; S. J. Schroeder; X. Jiao; C. Cox; D. H. Turner "Thermodynamic Parameters for an Expanded Nearest-Neighbor Model for Formation of RNA Duplexes with Watson-Crick Base Pairs", *Biochemistry* **1998**, *37*, 14719–14735.

[352] W. A. Kibbe "OligoCalc: an online oligonucleotide properties calculator", *Nucl. Acids Res.* **2007**, *35*, W43–W46.

[353] M. Petersheim; D. H. Turner "Base-stacking and base-pairing contributions to helix stability: thermodynamics of double-helix formation with CCGG, CCGGp, CCGGAp, ACCGGp, CCGGUp, and ACCGGUp", *Biochemistry* **1983**, *22*, 256–263.

[354] B. A. Schweitzer; E. T. Kool "Hydrophobic, Non-Hydrogen-Bonding Bases and Base Pairs in DNA", *J. Am. Chem. Soc.* **1995**, *117*, 1863–1872.

[355] T. Takada; K. Nishida; Y. Honda; A. Nakano; M. Nakamura; S. Fan; K. Kawai; M. Fujitsuka; K. Yamana "Stacked Thiazole Orange Dyes in DNA Capable of Switching Emissive Behavior in Response to Structural Transitions", *ChemBioChem* **2021**, 2729–2735.

[356] Y. Vonhausen; A. Lohr; M. Stolte; F. Würthner "Two-step anti-cooperative self-assembly process into defined π-stacked dye oligomers: insights into aggregation-induced enhanced emission", *Chem. Sci.* **2021**, *12*, 12302–12314.

[357] F. Würthner "Dipole–Dipole Interaction Driven Self-Assembly of Merocyanine Dyes: From Dimers to Nanoscale Objects and Supramolecular Materials", *Acc. Chem. Res.* **2016**, *49*, 868–876.

[358] H. S. Rye; S. Yue; D. E. Wemmer; M. A. Quesada; R. P. Haugland; R. A. Mathies; A. N. Glazer "Stable fluorescent complexes of double-stranded DNA with bis-intercalating asymmetric cyanine dyes: properties and applications", *Nucleic Acids Res.* **1992**, *20*, 2803–2812.

[359] S. Ikeda; A. Okamoto "Hybridization-Sensitive On–Off DNA Probe: Application of the Exciton Coupling Effect to Effective Fluorescence Quenching", *Chem. Asian J.* **2008**, *3*, 958–968.

[360] F. Menacher; M. Rubner; S. Berndl; H.-A. Wagenknecht "Thiazole Orange and Cy3: Improvement of Fluorescent DNA Probes with Use of Short Range Electron Transfer", *J. Org. Chem.* **2008**, *73*, 4263–4266.

[361] S. Berndl; H.-A. Wagenknecht "Fluorescent Color Readout of DNA Hybridization with Thiazole Orange as an Artificial DNA Base", *Angew. Chem. Int. Ed.* **2009**, *48*, 2418–2421.

[362] L. Bethge; I. Singh; O. Seitz "Designed thiazole orange nucleotides for the synthesis of single labelled oligonucleotides that fluoresce upon matched hybridization", *Org. Biomol. Chem.* **2010**, *8*, 2439.

[363] S. Berndl; S. D. Dimitrov; F. Menacher; T. Fiebig; H.-A. Wagenknecht "Thiazole Orange Dimers in DNA: Fluorescent Base Substitutions with Hybridization Readout", *Chem. Eur. J.* **2016**, *22*, 2386–2395.

[364] V. Karunakaran; J. L. P. Lustres; L. Zhao; N. P. Ernsting; O. Seitz "Large Dynamic Stokes Shift of DNA Intercalation Dye Thiazole Orange has Contribution from a High-Frequency Mode", *J. Am. Chem. Soc.* **2006**, *128*, 2954–2962.

[365] R. Lartia; U. Asseline "New Cyanine–Oligonucleotide Conjugates: Relationships between Chemical Structures and Properties", *Chem. Eur. J.* **2006**, *12*, 2270–2281.

[366] D. Boger "Thiazole orange as the fluorescent intercalator in a high resolution fid assay for determining DNA binding affinity and sequence selectivity of small molecules", *Bioorg. Med. Chem.* **2001**, *9*, 2511–2518.

[367] O. Suss; L. Motiei; D. Margulies "Broad Applications of Thiazole Orange in Fluorescent Sensing of Biomolecules and Ions", *Molecules* **2021**, *26*, 2828.
[368] M. Y. Berezin; S. Achilefu "Fluorescence Lifetime Measurements and Biological Imaging", *Chem. Rev.* **2010**, *110*, 2641–2684.
[369] A. K. Chibisov "Photonics of dimers of cyanine dyes", *High Energy Chem.* **2007**, *41*, 200–209.
[370] L. I. Markova; V. L. Malinovskii; L. D. Patsenker; R. Häner "J- vs. H-type assembly: pentamethine cyanine (Cy5) as a near-IR chiroptical reporter", *Chem. Commun.* **2013**, *49*, 5298.
[371] F. Nicoli; M. K. Roos; E. A. Hemmig; M. D. Antonio; R. de Vivie-Riedle; T. Liedl "Proximity-Induced H-Aggregation of Cyanine Dyes on DNA-Duplexes", *J. Phys. Chem. A* **2016**, *120*, 9941–9947.
[372] Y. Sang; J. Han; T. Zhao; P. Duan; M. Liu "Circularly Polarized Luminescence in Nanoassemblies: Generation, Amplification, and Application", *Adv. Mat.* **2019**, *32*, 1900110.
[373] N. Berova; N. Harada; K. Nakanishi in *Encyclopedia of Spectroscopy and Spectrometry*, Elsevier, **1999**, pp. 542–558.
[374] N. Harada; K. Nakanishi; N. Berova in *Comprehensive Chiroptical Spectroscopy*, John Wiley & Sons, Inc., **2012**, pp. 115–166.
[375] G. Bobba; R. S. Dickins; S. D. Kean; C. E. Mathieu; D. Parker; R. D. Peacock; G. Siligardi; M. J. Smith; J. A. G. Williams; C. F. G. C. Geraldes "Chiroptical, ESMS and NMR spectroscopic study of the interaction of enantiopure lanthanide complexes with selected self-complementary dodecamer oligonucleotides", *J. Chem. Soc. Perkin Trans. 2* **2001**, 1729–1737.
[376] T.-A. Uchida; K. Nozaki; M. Iwamura "Chiral Sensing of Various Amino Acids Using Induced Circularly Polarized Luminescence from Europium(III) Complexes of Phenanthroline Dicarboxylic Acid Derivatives", *Chem. Asian J.* **2016**, *11*, 2415–2422.
[377] M. Nakamura; J. Suzuki; F. Ota; T. Takada; K. Akagi; K. Yamana "Helically Assembled Pyrene Arrays on an RNA Duplex That Exhibit Circularly Polarized Luminescence with Excimer Formation", *Chem. Eur. J.* **2016**, *22*, 9121–9124.
[378] S. Abdollahi; W. R. Harris; J. P. Riehl "Application of Circularly Polarized Luminescence Spectroscopy to Tb(III) and Eu(III) Complexes of Transferrins", *J. Phys. Chem.* **1996**, *100*, 1950–1956.
[379] Y. Gao; C. Ren; X. Lin; T. He "The Progress and Perspective of Organic Molecules With Switchable Circularly Polarized Luminescence", *Front. Chem.* **2020**, *8*, 458.
[380] Y. Inai; M. Sisido; Y. Imanishi "Strong circular polarization in the excimer emission from a pair of pyrenyl groups linked to a polypeptide chain", *J. Phys. Chem.* **1990**, *94*, 2734–2735.
[381] H. Kashida; K. Nishikawa; Y. Ito; K. Murayama; I. Hayashi; T. Kakuta; T. Ogoshi; H. Asanuma "Pyrene modified serinol nucleic acid nanostructure converts chirality of threoninol nucleic acids into circularly polarized luminescence signals", *Chem. Eur. J.* **2021**, 14582–14585.
[382] K. Burgess; D. Cook "Syntheses of Nucleoside Triphosphates", *Chem. Rev.* **2000**, *100*, 2047–2060.
[383] M. Hollenstein "Nucleoside Triphosphates – Building Blocks for the Modification of Nucleic Acids", *Molecules* **2012**, *17*, 13569–13591.
[384] S. Gallo; M. Furler; R. K. Sigel "In vitro Transcription and Purification of RNAs of Different Size", *Chimia* **2005**, *59*, 812–816.

[385] C. J. Wienken; P. Baaske; S. Duhr; D. Braun "Thermophoretic melting curves quantify the conformation and stability of RNA and DNA", *Nucl. Acids Res.* **2011**, *39*, e52–e52.
[386] H. Bittermann; D. Siegemund; V. L. Malinovskii; R. Häner "Dialkynylpyrenes: Strongly Fluorescent, Environment-Sensitive DNA Building Blocks", *J. Am. Chem. Soc.* **2008**, *130*, 15285–15287.
[387] N. Bouquin; V. L. Malinovskii; R. Häner "Highly efficient quenching of excimer fluorescence by perylene diimide in DNA", *Chem. Comm.* **2008**, 1974.
[388] D. Wenger; V. L. Malinovskii; R. Häner "Modulation of chiroptical properties by DNA-guided assembly of fluorenes", *Chem. Comm.* **2011**, *47*, 3168.
[389] A. Fürstenberg; E. Vauthey "Ultrafast Excited-State Dynamics of Oxazole Yellow DNA Intercalators", *J. Phys. Chem. B* **2007**, *111*, 12610–12620.
[390] P. D. Cunningham; W. P. Bricker; S. A. Dıéaz; I. L. Medintz; M. Bathe; J. S. Melinger "Optical determination of the electronic coupling and intercalation geometry of thiazole orange homodimer in DNA", *J. Chem. Phys.* **2017**, *147*, 055101.
[391] C. A. M. Seidel; A. Schulz; M. H. M. Sauer "Nucleobase-Specific Quenching of Fluorescent Dyes. 1. Nucleobase One-Electron Redox Potentials and Their Correlation with Static and Dynamic Quenching Efficiencies", *J. Phys. Chem.* **1996**, *100*, 5541–5553.
[392] I. Nazarenko "Effect of primary and secondary structure of oligodeoxyribonucleotides on the fluorescent properties of conjugated dyes", *Nucleic Acids Res.* **2002**, *30*, 2089–2195.
[393] D. Bialas; E. Kirchner; F. Würthner "Folding-induced exciton coupling in homo- and heterodimers of merocyanine dyes", *Chem. Commun.* **2016**, *52*, 3777–3780.
[394] E. Kirchner; D. Bialas; M. Wehner; D. Schmidt; F. Würthner "Bis(merocyanine) Homo-Folda-Dimers: Evaluation of Electronic and Spectral Changes in Well-Defined Dye Aggregate Geometries", *Chem. Eur. J.* **2019**, 11285–11293.
[395] S. H. Sohail; J. P. Otto; P. D. Cunningham; Y. C. Kim; R. E. Wood; M. A. Allodi; J. S. Higgins; J. S. Melinger; G. S. Engel "DNA scaffold supports long-lived vibronic coherence in an indodicarbocyanine (Cy5) dimer", *Chem. Sci.* **2020**, *11*, 8546–8557.
[396] S. M. Hart; W. J. Chen; J. L. Banal; W. P. Bricker; A. Dodin; L. Markova; Y. Vyborna; A. P. Willard; R. Häner; M. Bathe; G. S. Schlau-Cohen "Engineering couplings for exciton transport using synthetic DNA scaffolds", *Chem* **2021**, *7*, 752–773.
[397] T. Holstein "Studies of polaron motion", *Ann. Phys.* **1959**, *8*, 325–342.
[398] F. C. Spano "The Spectral Signatures of Frenkel Polarons in H- and J-Aggregates", *Acc. Chem. Res.* **2009**, *43*, 429–439.
[399] F. C. Spano "Absorption in regio-regular poly(3-hexyl)thiophene thin films: Fermi resonances, interband coupling and disorder", *Chem. Phys.* **2006**, *325*, 22–35.
[400] K. A. Kistler; C. M. Pochas; H. Yamagata; S. Matsika; F. C. Spano "Absorption, Circular Dichroism, and Photoluminescence in Perylene Diimide Bichromophores: Polarization-Dependent H- and J-Aggregate Behavior", *J. Phys. Chem. B* **2011**, *116*, 77–86.
[401] M. I. Sorour; K. A. Kistler; A. H. Marcus; S. Matsika "Accurate Modeling of Excitonic Coupling in Cyanine Dye Cy3", *J. Phys. Chem. A* **2021**, *125*, 7852–7866.
[402] D. Bialas; C. Zhong; F. Würthner; F. C. Spano "Essential States Model for Merocyanine Dye Stacks: Bridging Electronic and Optical Absorption Properties", *J. Phys. Chem. C* **2019**, *123*, 18654–18664.
[403] E. Kirchner; D. Bialas; F. Würthner "Bis(merocyanine) Hetero-Folda-Dimers: Evaluation of Exciton Coupling between Different Types of π-Stacked Chromphores", *Chem. Eur. J.* **2019**, 11294–11301.

[404] A. Fürstenberg; M. D. Julliard; T. G. Deligeorgiev; N. I. Gadjev; A. A. Vasilev; E. Vauthey "Ultrafast Excited-State Dynamics of DNA Fluorescent Intercalators: New Insight into the Fluorescence Enhancement Mechanism", *J. Am. Chem. Soc.* **2006**, *128*, 7661–7669.

[405] J. S. Huff; P. H. Davis; A. Christy; D. L. Kellis; N. Kandadai; Z. S. D. Toa; G. D. Scholes; B. Yurke; W. B. Knowlton; R. D. Pensack "DNA-Templated Aggregates of Strongly Coupled Cyanine Dyes: Nonradiative Decay Governs Exciton Lifetimes", *J. Phys. Chem. Lett.* **2019**, *10*, 2386–2392.

[406] S. G. Telfer; T. M. McLean; M. R. Waterland "Exciton coupling in coordination compounds", *Dalton Trans.* **2011**, *40*, 3097.

[407] K. Okano; M. Taguchi; M. Fujiki; T. Yamashita "Circularly Polarized Luminescence of Rhodamine B in a Supramolecular Chiral Medium Formed by a Vortex Flow", *Angew. Chem. Int. Ed.* **2011**, *50*, 12474–12477.

[408] D. Stigter "Evaluation of the counterion condensation theory of polyelectrolytes", *Biophys. J.* **1995**, *69*, 380–388.

[409] P. L. Hansen; R. Podgornik; V. A. Parsegian "Osmotic properties of DNA: Critical evaluation of counterion condensation theory", *Phys. Rev. E* **2001**, *64*, 021907.

[410] G. Bonner; A. M. Klibanov "Structural stability of DNA in nonaqueous solvents", *Biotechnol. Bioeng.* **2000**, *68*, 339–344.

[411] F. Ke; Y. K. Luu; M. Hadjiargyrou; D. Liang "Characterizing DNA Condensation and Conformational Changes in Organic Solvents", *PLoS ONE* **2010**, *5*, (Ed.: R. C. Willson), e13308.

[412] A. Arcella; G. Portella; R. Collepardo-Guevara; D. Chakraborty; D. J. Wales; M. Orozco "Structure and Properties of DNA in Apolar Solvents", *J. Phys. Chem. B* **2014**, *118*, 8540–8548.

[413] Y. Miyake; H. Togashi; M. Tashiro; H. Yamaguchi; S. Oda; M. Kudo; Y. Tanaka; Y. Kondo; R. Sawa; T. Fujimoto; T. Machinami; A. Ono "Mercury-II-Mediated Formation of Thymine-Hg-II-Thymine Base Pairs in DNA Duplexes", *J. Am. Chem. Soc.* **2006**, *128*, 2172–2173.

[414] O. P. Schmidt; S. Jurt; S. Johannsen; A. Karimi; R. K. O. Sigel; N. W. Luedtke "Concerted dynamics of metallo-base pairs in an A/B-form helical transition", *Nat. Commun.* **2019**, *10*, 4818.

[415] A. Marsh; E. G. Nolen; K. M. Gardinier; J.-M. Lehn "Janus molecules: Synthesis of double-headed heterocycles containing two identical hydrogen bonding arrays", *Tetrahedron Lett.* **1994**, *35*, 397–400.

[416] M. C. Chen; B. J. Cafferty; I. Mamajanov; I. Gállego; J. Khanam; R. Krishnamurthy; N. V. Hud "Spontaneous Prebiotic Formation of a β-Ribofuranoside That Self-Assembles with a Complementary Heterocycle", *J. Am. Chem. Soc.* **2013**, *136*, 5640–5646.

[417] B. J. Cafferty; I. Gállego; M. C. Chen; K. I. Farley; R. Eritja; N. V. Hud "Efficient Self-Assembly in Water of Long Noncovalent Polymers by Nucleobase Analogues", *J. Am. Chem. Soc.* **2013**, *135*, 2447–2450.

[418] C. Li; B. J. Cafferty; S. C. Karunakaran; G. B. Schuster; N. V. Hud "Formation of supramolecular assemblies and liquid crystals by purine nucleobases and cyanuric acid in water: implications for the possible origins of RNA", *Phys. Chem. Chem. Phys.* **2016**, *18*, 20091–20096.

[419] H. Kashida; Y. Hattori; K. Tazoe; T. Inoue; K. Nishikawa; K. Ishii; S. Uchiyama; H. Yamashita; M. Abe; Y. Kamiya; H. Asanuma "Bifacial Nucleobases for Hexaplex Formation in Aqueous Solution", *J. Am. Chem. Soc.* **2018**, *140*, 8456–8462.

[420] G. B. Schuster; B. J. Cafferty; S. C. Karunakaran; N. V. Hud "Water-Soluble Supramolecular Polymers of Paired and Stacked Heterocycles: Assembly, Structure, Properties, and a Possible Path to Pre-RNA", *J. Am. Chem. Soc.* **2021**, *143*, 9279–9296.

[421] D. M. Fialho; S. C. Karunakaran; K. W. Greeson; I. Martıénez; G. B. Schuster; R. Krishnamurthy; N. V. Hud "Depsipeptide Nucleic Acids: Prebiotic Formation, Oligomerization, and Self-Assembly of a New Proto-Nucleic Acid Candidate", *J. Am. Chem. Soc.* **2021**, *143*, 13525–13537.

[422] B. A. Anderson; K. Fauché; S. C. Karunakaran; J. R. Yerabolu; N. V. Hud; R. Krishnamurthy "The Unexpected Base-Pairing Behavior of Cyanuric Acid in RNA and Ribose versus Cyanuric Acid Induced Helicene Assembly of Nucleic Acids: Implications for the Pre-RNA Paradigm", *Chem. Eur. J.* **2021**, *27*, 4033–4042.

[423] A. Alenaizan; K. Fauché; R. Krishnamurthy; C. D. Sherrill "Noncovalent Helicene Structure between Nucleic Acids and Cyanuric Acid", *Chem. Eur. J.* **2021**, *27*, 4043–4052.

[424] C. Lachance-Brais; C. D. Hennecker; A. Alenaizan; X. Luo; V. Toader; M. Taing; C. D. Sherrill; A. K. Mittermaier; H. F. Sleiman "Tuning DNA Supramolecular Polymers by the Addition of Small, Functionalized Nucleobase Mimics", *J. Am. Chem. Soc.* **2021**, 19824–19833.

[425] Q. Li; J. Zhao; L. Liu; S. Jonchhe; F. J. Rizzuto; S. Mandal; H. He; S. Wei; H. F. Sleiman; H. Mao; C. Mao "A poly(thymine)–melamine duplex for the assembly of DNA nanomaterials", *Nat. Mater.* **2020**, *19*, 1012–1018.

[426] F. Würthner; S. Yao; B. Heise; C. Tschierske "Hydrogen bond directed formation of liquid-crystalline merocyanine dye assemblies", *Chem. Comm.* **2001**, 2260–2261.

[427] L. J. Prins; C. Thalacker; F. Würthner; P. Timmerman; D. N. Reinhoudt "Chiral exciton coupling of merocyanine dyes within a well defined hydrogen-bonded assembly", *PNAS* **2001**, *98*, 10042–10045.

[428] V. Verdolino; R. Cammi; B. H. Munk; H. B. Schlegel "Calculation of pKa Values of Nucleobases and the Guanine Oxidation Products Guanidinohydantoin and Spiroiminodihydantoin using Density Functional Theory and a Polarizable Continuum Model", *J. Phys. Chem. B* **2008**, *112*, 16860–16873.

[429] L. An; W. Tang; T. A. Ranalli; H.-J. Kim; J. Wytiaz; H. Kong "Characterization of a Thermostable UvrD Helicase and Its Participation in Helicase-dependent Amplification", *J. Biol. Chem.* **2005**, *280*, 28952–28958.

[430] R. E. Dale; J. Eisinger "Intramolecular distances determined by energy transfer. Dependence on orientational freedom of donor and acceptor", *Biopolymers* **1974**, *13*, 1573–1605.

[431] W. R. Algar; M. Massey; U. J. Krull "Fluorescence Resonance Energy Transfer and Complex Formation Between Thiazole Orange and Various Dye-DNA Conjugates: Implications in Signaling Nucleic Acid Hybridization", *J. Fluoresc.* **2006**, *16*, 555–567.

[432] L. Zidek; R. Stefl; V. Sklenar "NMR methodology for the study of nucleic acids", *Curr. Opin. Struct. Biol.* **2001**, *11*, 275–281.

[433] B. Fürtig; C. Richter; J. Wöhnert; H. Schwalbe "NMR Spectroscopy of RNA", *ChemBioChem* **2003**, *4*, 936–962.

[434] A. M. Spring-Connell; M. Evich; M. W. Germann "NMR Structure Determination for Oligonucleotides", *Curr Protoc Nucleic Acid Chem* **2018**, *72*, 7.2.1–7.2.16.

[435] Z. Gáspári; A. Perczel in *Annu. Rep. NMR Spectrosc.* Elsevier, **2010**, pp. 35–75.

[436] E. Meggers; L. Zhang; A. E. Peritz; P. J. Carroll "Synthesis of Glycol Nucleic Acids", *Synthesis* **2006**, *2006*, 645–653.

[437] M. K. Schlegel; E. Meggers "Improved Phosphoramidite Building Blocks for the Synthesis of the Simplified Nucleic Acid GNA", *J. Org. Chem.* **2009**, *74*, 4615–4618.
[438] T. Hansen; P. Vermeeren; A. Haim; M. J. H. van Dorp; J. D. C. Codée; F. M. Bickelhaupt; T. A. Hamlin "Regioselectivity of Epoxide Ring-Openings via SN 2 Reactions Under Basic and Acidic Conditions", *Eur. J. Org. Chem.* **2020**, *2020*, 3822–3828.
[439] S. Zhang; J. C. Chaput "Synthesis of glycerol nucleic acid (GNA) phosphoramidite monomers and oligonucleotide polymers", *Curr Protoc Nucleic Acid Chem.* **2010**, Chapter 4, Unit 4.40.
[440] C.-H. Tsai; J. Chen; J. W. Szostak "Enzymatic synthesis of DNA on glycerol nucleic acid templates without stable duplex formation between product and template", *PNAS* **2007**, *104*, 14598–14603.
[441] M. Schroeder "Osmium tetraoxide cis hydroxylation of unsaturated substrates", *Chem. Rev.* **1980**, *80*, 187–213.
[442] M. Rougee; B. Faucon; J. L. Mergny; F. Barcelo; C. Giovannangeli; T. Garestier; C. Helene "Kinetics and thermodynamics of triple-helix formation: effects of ionic strength and mismatched", *Biochemistry* **1992**, *31*, 9269–9278.
[443] L. Markova; M. Probst; R. Häner "Assembly and functionalization of supramolecular polymers from DNA-conjugated squaraine oligomers", *RCS Adv.* **2020**, *10*, 44841–44845.
[444] T. F. A. D. Greef; M. M. J. Smulders; M. Wolffs; A. P. H. J. Schenning; R. P. Sijbesma; E. W. Meijer "Supramolecular Polymerization", *Chem. Rev.* **2009**, *109*, 5687–5754.
[445] A. Okamoto "ECHO probes: a concept of fluorescence control for practical nucleic acid sensing", *Chem. Soc. Rev.* **2011**, *40*, 5815.
[446] D. O. Wang; A. Okamoto "ECHO probes: Fluorescence emission control for nucleic acid imaging", *J. Photochem* **2012**, *13*, 112–123.
[447] F. Würthner; T. E. Kaiser; C. R. Saha-Möller "J-Aggregates: From Serendipitous Discovery to Supramolecular Engineering of Functional Dye Materials", *Angew. Chem. Int. Ed.* **2011**, *50*, 3376–3410.
[448] N. Jalili; K. Laxminarayana "A review of atomic force microscopy imaging systems: application to molecular metrology and biological sciences", *Mechatronics* **2004**, *14*, 907–945.
[449] H. R. Drew; R. M. Wing; T. Takano; C. Broka; S. Tanaka; K. Itakura; R. E. Dickerson "Structure of a B-DNA dodecamer: conformation and dynamics.", *PNAS* **1981**, *78*, 2179–2183.
[450] F. Seela; A. Kehne "Palindromic octa- and dodecanucleotides containing 2'-deoxytubercidin: synthesis, hairpin formation, and recognition by the endodeoxyribonuclease EcoRI", *Biochemistry* **1987**, *26*, 2232–2238.
[451] P. Nielsen; L. H. Dreiøe; J. Wengel "Synthesis and evaluation of oligodeoxynucleotides containing acyclic nucleosides: Introduction of three novel analogues and a summary", *Bioorg. Med. Chem.* **1995**, *3*, 19–28.
[452] D. Zhou; I. M. Lagoja; J. Rozenski; R. Busson; A. V. Aerschot; P. Herdewijn "Synthesis and Properties of Aminopropyl Nucleic Acids", *ChemBioChem* **2005**, *6*, 2298–2304.
[453] M. K. Schlegel; A. E. Peritz; K. Kittigowittana; L. Zhang; E. Meggers "Duplex Formation of the Simplified Nucleic Acid GNA", *ChemBioChem* **2007**, *8*, 927–932.
[454] F. Garo; R. Häner "A DNA-Based Light-Harvesting Antenna", *Angew. Chem. Int. Ed.* **2011**, *51*, 916–919.

[455] L. A. Marky; K. S. Blumenfeld; S. Kozlowski; K. J. Breslauer "Salt-dependent conformational transitions in the self-complementary deoxydodecanucleotide d(CGCAATTCGCG): Evidence for hairpin formation", *Biopolymers* **1983**, *22*, 1247–1257.

[456] S. Rothenbühler; I. Iacovache; S. M. Langenegger; B. Zuber; R. Häner "Supramolecular assembly of DNA-constructed vesicles", *Nanoscale* **2020**, *12*, 21118–21123.

[457] M. Miar; A. Shiroudi; K. Pourshamsian; A. R. Oliaey; F. Hatamjafari "Theoretical investigations on the HOMO–LUMO gap and global reactivity descriptor studies, natural bond orbital, and nucleus-independent chemical shifts analyses of 3-phenylbenzo[d*d*]thiazole-2(3*H*)-imine and its para-substituted derivatives: Solvent and substituent effects", *J. Chem. Res.* **2020**, *45*, 147–158.

[458] G. L. Silva; V. Ediz; D. Yaron; B. A. Armitage "Experimental and Computational Investigation of Unsymmetrical Cyanine Dyes: Understanding Torsionally Responsive Fluorogenic Dyes", *J. Am. Chem. Soc.* **2007**, *129*, 5710–5718.

[459] A. A. Vasilev; M. I. Kandinska; S. S. Stoyanov; S. B. Yordanova; D. Sucunza; J. J. Vaquero; O. D. Castaño; S. Baluschev; S. E. Angelova "Halogen-containing thiazole orange analogues – new fluorogenic DNA stains", *Beilstein J. Org. Chem.* **2017**, *13*, 2902–2914.

[460] G. S. Manning "The Persistence Length of DNA Is Reached from the Persistence Length of Its Null Isomer through an Internal Electrostatic Stretching Force", *Biophys. J.* **2006**, *91*, 3607–3616.

[461] H. G. Hansma; I. Revenko; K. Kim; D. E. Laney "Atomic Force Microscopy of Long and Short Double-Stranded, Single-Stranded and Triple-Stranded Nucleic Acids", *Nucleic Acids Res.* **1996**, *24*, 713–720.

[462] J. M. Clark; C. M. Joyce; G. Beardsley "Novel blunt-end addition reactions catalyzed by DNA polymerase I of Escherichia coli", *J. Mol. Biol.* **1987**, *198*, 123–127.

[463] L. Garibyan; N. Avashia "Polymerase Chain Reaction", *J. Invest. Dermatol.* **2013**, *133*, 1–4.

[464] K. D. Warner; L. Sjekloća; W. Song; G. S. Filonov; S. R. Jaffrey; A. R. Ferré-D'Amaré "A homodimer interface without base pairs in an RNA mimic of red fluorescent protein", *Nat Chem Biol* **2017**, *13*, 1195–1201.

[465] J. Ouellet "RNA Fluorescence with Light-Up Aptamers", *Front Chem.* **2016**, *4*, DOI 10.3389/fchem.2016.00029.

[466] F. Bouhedda; A. Autour; M. Ryckelynck "Light-Up RNA Aptamers and Their Cognate Fluorogens: From Their Development to Their Applications", *Int. J. Mol. Sci.* **2017**, *19*, 44.

[467] M.-A. Plamont; E. Billon-Denis; S. Maurin; C. Gauron; F. M. Pimenta; C. G. Specht; J. Shi; J. Quérard; B. Pan; J. Rossignol; K. Moncoq; N. Morellet; M. Volovitch; E. Lescop; Y. Chen; A. Triller; S. Vriz; T. L. Saux; L. Jullien; A. Gautier "Small fluorescence-activating and absorption-shifting tag for tunable protein imaging in vivo", *PNAS* **2015**, *113*, 497–502.

[468] L. Wu; K. Burgess "Syntheses of Highly Fluorescent GFP-Chromophore Analogues", *J. Am. Chem. Soc.* **2008**, *130*, 4089–4096.

[469] J. M. Lerestif; J. Perrocheau; F. Tonnard; J. P. Bazureau; J. Hamelin "1,3-Dipolar cycloaddition of imidate ylides on imino-alcohols: Synthesis of new imidazolones using solvent free conditions", *Tetrahedron* **1995**, *51*, 6757–6774.

[470] N. J. Lawrence; L. A. Hepworth; D. Rennison; A. T. McGown; J. A. Hadfield "Synthesis and anticancer activity of fluorinated analogues of combretastatin A-4", *J. Fluor. Chem.* **2003**, *123*, 101–108.

[471] S. Guihéneuf; L. Paquin; F. Carreaux; E. Durieu; L. Meijer; J. P. Bazureau "An efficient approach to dispacamide A and its derivatives", *Org. Biomol. Chem.* **2012**, *10*, 978–987.

[472] K. van Beurden; S. de Koning; D. Molendijk; J. van Schijndel "The Knoevenagel reaction: a review of the unfinished treasure map to formingcarbon–carbon bonds", *Green Chem Lett Rev* **2020**, *13*, 349–364.

[473] Y. Luo; L. Ma; H. Zheng; L. Chen; R. Li; C. He; S. Yang; X. Ye; Z. Chen; Z. Li; Y. Gao; J. Han; G. He; L. Yang; Y. Wei "Discovery of (*Z*)-5-(4-Methoxybenzylidene)thiazolidine-2,4-dione, a Readily Available and Orally Active Glitazone for the Treatment of Concanavalin A-Induced Acute Liver Injury of BALB/c Mice", *J. Med. Chem.* **2009**, *53*, 273–281.

[474] Y. Shen; Y. Chen; J. Wu; N. C. Shaner; R. E. Campbell "Engineering of mCherry variants with long Stokes shift, red-shifted fluorescence, and low cytotoxicity", *PLOS ONE* **2017**, *12*, (Ed.: K. I. Anderson), e0171257.

[475] A. F. Bell; X. He; R. M. Wachter; P. J. Tonge "Probing the Ground State Structure of the Green Fluorescent Protein Chromophore Using Raman Spectroscopy", *Biochemistry* **2000**, *39*, 4423–4431.

[476] S. P. Laptenok; J. Conyard; P. C. B. Page; Y. Chan; M. You; S. R. Jaffrey; S. R. Meech "Photoacid behaviour in a fluorinated green fluorescent protein chromophore: ultrafast formation of anion and zwitterion states", *Chem. Sci.* **2016**, *7*, 5747–5752.

[477] J. Dong; K. M. Solntsev; L. M. Tolbert "Solvatochromism of the Green Fluorescence Protein Chromophore and Its Derivatives", *J. Am. Chem. Soc.* **2006**, *128*, 12038–12039.

[478] N. M. Webber; S. R. Meech "Electronic spectroscopy and solvatochromism in the chromophore of GFP and the Y66F mutant", *Photochem. Photobiol. Sci.* **2007**, *6*, 976.

[479] G. Szalóki; L. Sanguinet "Silica-Mediated Synthesis of Indolinooxazolidine-Based Molecular Switches", *J. Org. Chem.* **2015**, *80*, 3949–3956.

[480] E. I. Balmond; B. K. Tautges; A. L. Faulkner; V. W. Or; B. M. Hodur; J. T. Shaw; A. Y. Louie "Comparative Evaluation of Substituent Effect on the Photochromic Properties of Spiropyrans and Spirooxazines", *J. Org. Chem.* **2016**, *81*, 8744–8758.

[481] H. Li; Z.-J. Luan; G.-W. Zheng; J.-H. Xu "Efficient Synthesis of Chiral Indolines using an Imine Reductase from Paenibacillus lactis", *Adv. Synth. Catal* **2015**, *357*, 1692–1696.

[482] M. Tomasulo; S. L. Kaanumal; S. Sortino; F. M. Raymo "Synthesis and Properties of Benzophenone-Spiropyran and Naphthalene-Spiropyran Conjugates", *J. Org. Chem.* **2006**, *72*, 595–605.

[483] G. Chen; F. Song; X. Wang; S. Sun; J. Fan; X. Peng "Bright and stable Cy3-encapsulated fluorescent silica nanoparticles with a large Stokes shift", *Dyes Pigm* **2012**, *93*, 1532–1537.

[484] B. A. Dar; S. N. Ahmad; M. A. Wagay; A. Hussain; N. Ahmad; K. A. Bhat; M. A. Khuroo; M. Sharma; B. Singh "Ultrasound promoted expeditious, catalyst-free and solvent-free approach for the synthesis of *N,N'*-diarylsubstituted formamidines at room temperature", *Tetrahedron Lett.* **2013**, *54*, 4880–4884.

[485] W. E. Lindsell; C. Murray; P. N. Preston; T. A. Woodman "Synthesis of 1,3-Diynes in the Purine, Pyrimidine, 1,3,5-Triazine and Acridine Series", *Tetrahedron* **2000**, *56*, 1233–1245.

[486] C.-Y. Lin; M. G. Romei; L. M. Oltrogge; I. I. Mathews; S. G. Boxer "Unified Model for Photophysical and Electro-Optical Properties of Green Fluorescent Proteins", *J. Am. Chem. Soc.* **2019**, *141*, 15250–15265.

[487] D. C. Rio "Expression and Purification of Active Recombinant T7 RNA Polymerase from E. coli", *Cold Spring Harb. Protoc.* **2013**, *2013*, 1094–1098.

[488] J. N. Weiss "The Hill equation revisited: uses and misuses", *FASEB J.* **1997**, *11*, 835–841.

[489] L. Porrès; A. Holland; L.-O. Pålsson; A. P. Monkman; C. Kemp; A. Beeby "Absolute Measurements of Photoluminescence Quantum Yields of Solutions Using an Integrating Sphere", *J. Fluoresc.* **2006**, *16*, 267–273.

[490] P. J. Stephens; F. J. Devlin; C. F. Chabalowski; M. J. Frisch "Ab Initio Calculation of Vibrational Absorption and Circular Dichroism Spectra Using Density Functional Force Fields", *J. Phys. Chem.* **1994**, *98*, 11623–11627.

[491] W. Humphrey; A. Dalke; K. Schulten "VMD: Visual molecular dynamics", *J. Mol. Graph.* **1996**, *14*, 33–38.